VOLUME 31 NUMBER
JANUARY 1970

THE JOURNAL OF PHYSICS AND CHEMISTRY OF SOLIDS

AN INTERNATIONAL JOURNAL

Editor-in-Chief
HARVEY BROOKS
Cambridge, Mass.

Associate Editors

H. B. G. CASIMIR
Eindhoven

B. CHALMERS FRAZER
and
DAVID E. COX
Brookhaven

JACQUES FRIEDEL
Paris

I. M. LIFSHITZ
Khar'kov

PERGAMON PRESS NEW YORK · OXFORD · LONDON · PARIS

THE JOURNAL OF PHYSICS AND CHEMISTRY OF SOLIDS

Editors

Prof. Harvey Brooks (*Editor-in-Chief*), 217 *Pierce Hall, Harvard University, Cambridge* 38, *Mass., U.S.A.*
Prof. Dr. H. B. G. Casimir, *N.V. Philips' Gloeilampenfabrieken, Eindhoven, The Netherlands*
Dr. B. Chalmers Frazer and Dr. David E. Cox (*Assistant Editor*), *Brookhaven National Laboratory, Upton, Long Island, New York, U.S.A.*
Prof. Jacques Friedel, *Laboratoire de Physique des Solides, Bâtiment* 210, *Faculté des Sciences,* 91-*Orsay, France*
Prof. I. M. Lifshitz, *Physico-Technical Institute, Academy of Science, Yumorskii tupik, Khar'kov, U.S.S.R.*

Editorial Advisory Board

U.S.A.
E. N. Adams, White Plains, N.Y.
D. Alpert, Urbana, Ill.
L. Apker, Schenectady, N.Y.
J. Bardeen, Urbana, Ill.
D. S. Billington, Oak Ridge, Tenn.
R. G. Breckenridge, Canoga Pk., Calif.
Leo Brewer, Berkeley, Calif.
E. Burstein, Philadelphia, Penn.
J. A. Burton, Murray Hill, N.J.
N. Cabrera, Charlottesville, Va.
G. C. Danielson, Ames, Iowa
G. J. Dienes, Long Island, N.Y.
J. C. Fisher, Schenectady, N.Y.
F. G. Fumi, Chicago, Ill.
H. K. Henisch, University Park, Penn.
F. Herman, San Jose, Calif.
C. Herring, Murray Hill, N.J.
A. R. von Hippel, Cambridge, Mass.
J. H. Hollomon, Washington, D.C.
W. V. Houston, Houston, Texas
H. B. Huntington, Troy, N.Y.
H. M. James, Lafayette, Ind.
C. Kittel, Berkeley, Calif.
W. Kohn, La Jolla, Calif.
J. A. Krumhansl, Ithaca, N.Y.
A. W. Lawson, Riverside, Calif.
H. W. Leverenz, Princeton, N.J.
O. T. Marzke, Pittsburgh, Penn.
B. T. Matthias, La Jolla, Calif.
L. R. Maxwell, Silver Spring, Md.
J. E. Mayer, La Jolla, Calif.
J. W. Mitchell, Charlottesville, Va.
E. W. Montroll, Rochester, N.Y.
D. Pines, Urbana, Ill.
M. H. L. Pryce, Los Angeles, Calif.
G. T. Rado, Washington, D.C.
H. Reiss, Thousand Oaks, Calif.
J. R. Reitz, Dearborn, Mich.
A. Rose, Princeton, N.J.
R. A. Smith, Cambridge, Mass.
R. Smoluchowski, Princeton, N.J.
F. H. Spedding, Ames, Iowa
D. Turnbull, Cambridge, Mass.
J. H. Van Vleck, Cambridge, Mass.
B. E. Warren, Cambridge, Mass.
E. P. Wigner, Princeton, N.J.
B. H. Zimm, La Jolla, Calif.

Canada
R. E. Burgess, Vancouver
W. B. Pearson, Ottawa

United Kingdom
M. Born, Bad Pyrmont
A. Charlesby, Shrivenham, Berks.
W. J. Dunning, Bristol
F. C. Frank, Bristol
H. Jones, London
A. B. Pippard, Cambridge
O. C. Simpson, Baldock, Herts.
K. W. H. Stevens, Nottingham
F. C. Tompkins, London

Czechoslovakia
J. Tauc, Praha

France
E. F. Bertaut, Grenoble
J. Bok, Paris
B. Dreyfus, Grenoble
A. Guinier, Orsay
A. Herpin, Gif-sur-Yvette
B. Jacrot, Grenoble
Louis Néel, Grenoble

Germany
Ulrich Dehlinger, Stuttgart
R. Hilsch, Göttingen
G. Leibfried, Aachen
E. Mollwo, Erlangen
H. Pick, Stuttgart
W. Welker, Erlangen

Israel
I. Estermann, Haifa

Italy
F. G. Fumi, Palermo

Japan
Toshinosuke Muto, Tokyo

The Netherlands
A. Michels, Amsterdam
G. W. Rathenau, Eindhoven

Sweden
J. O. Linde, Stockholm
Per-Olov Löwdin, Uppsala

Switzerland
G. Busch, Zurich
P. Scherrer, Zurich

U.S.S.R.
G. S. Zhdanov, Moscow

Publishing Offices

American Continent: Pergamon Press Inc., Maxwell House, Fairview Park, Elmsford, N.Y. 10523.
Rest of the World: Pergamon Press Ltd., 84–86 *Malahide Road, Coolock, Dublin* 5.

Published monthly. *Annual subscription for libraries, research establishments and all other multiple-reader institutions,* £60 ($150.00); ***private individuals,*** *whose departmental libraries subscribe, may obtain this Journal for their personal use at a reduced price of* £6 ($15.00) ***per annum,*** *including postage. All subscription enquiries are to be addressed to The Manager, Subscriptions Department,* ***Pergamon Press,*** *Headington Hill Hall, Oxford OX3 0BW, England. Back issues are available, write for Back Issues Price Lists.*

Copyright © 1970 Pergamon Press Ltd.

PERGAMON PRESS INC.
MAXWELL HOUSE, FAIRVIEW PARK, ELMSFORD, N.Y. 10523
HEADINGTON HILL HALL, OXFORD OX3 0BW

THE JOURNAL OF PHYSICS AND CHEMISTRY OF SOLIDS

AN INTERNATIONAL JOURNAL

VOLUME 31 1970

EDITORS

Editor-in-Chief: **HARVEY BROOKS** *Cambridge, Mass.*

Associate Editors:

H. B. G. CASIMIR
Eindhoven

B. CHALMERS FRAZER
and
DAVID E. COX
Brookhaven

JACQUES FRIEDEL
Paris

I. M. LIFSHITZ
Khar'kov

Supported by an International Editorial Advisory Board

Copyright © 1970
Pergamon

PERGAMON PRESS
OXFORD . NEW YORK . LONDON . PARIS

LIST OF CONTENTS

JANUARY

V. A. Rowe and P. A. Schroeder: Thermopower of Mg, Cd and Zn between 1·2° and 300°K . . . 1

P. Raj and S. K. Kulshreshtha: Mössbauer studies of the lithium ferrite–aluminate system . . . 9

D. P. Spitzer: Lattice thermal conductivity of semiconductors: a chemical bond approach . . . 19

Č. Jech and R. Kelly: On the formation of ion-bombardment-induced disorder in zircon, corundum and diamond (Studies on bombardment-induced disorder – II) . . . 41

B. Khurgin, I. Nowik, M. Rakavy and S. Ofer: Spin relaxation phenomena in Mössbauer spectra of magnetically ordered dysprosium intermetallic compounds . . . 49

P. D. Southgate: The derivation of recombination rate constants from time-dependent bulk electroluminescent spectra in compensated GaAs . . . 55

H. Mathieu: Etudes des queues de bandes dans le Ga Sb fortement dopé . . . 67

M. Hirabayashi, S. Yamaguchi, K. Hiraga, N. Ino, H. Sato and R. S. Toth: A new type of long period superlattice with hexagonal symmetry in Au–Cd alloys . . . 77

K. Baumann, P. Kocevar and M. Kriechbaum: Anisotropic phonon excitation by hot electrons in n-Ge . . . 95

M. E. Lines: The quadratic-layer antiferromagnet . . . 101

R. W. Vaughan, D. D. Elleman and D. G. McDonald: The de Haas–van Alphen effect in white tin . . . 117

P. Novák: Some aspects of the cooperative Jahn–Teller effect in spinel and perovskite systems . . . 125

R. E. Schmunk and D. R. Winder: Lattice dynamics of sodium chloride at room temperature . . . 131

S. B. Palmer: Debye temperatures of holmium and dysprosium from single crystal elastic constant measurements . . . 143

O. V. Kovalev and A. G. Gorbanyuk: Irreducible representations of magnetic groups of quantum-mechanical operators . . . 149

J. F. Verwey: Time and intensity dependence of the photolysis of lead halides . . . 163

M. M. Blouke, N. Holonyak, Jr., B. G. Streetman and H. R. Zwicker: Solid solubility of Zn in Si . . . 173

D. C. Finbow, P. Makhurane and P. Gaunt: Lattice distortion, specific heat and antiferromagnetic ordering in AuMn . . . 179

Technical Note:

R. J. Smith and D. A. Otterson: Electrical resistivity of PdH$_x$ system for H/Pd atom ratios to 0·97 . . . 187

FEBRUARY

M. V. Rao and W. A. Tiller: Excess free energies in the Ge, Si and Ga binary systems – the α-parameter approach . . . 191

E. Dormann: Die optischen Absorptionsspektren von Ni^{2+} in Cl$^-$ und J-Boraziten . . . 199

K. Sekizawa, H. Sekizawa and C. T. Tomizuka: Effect of pressure on the Néel temperature of rare earth intermetallic compounds . . . 215

S. Radelaar: On the relation between the relaxation time for short-range order and self-diffusion coefficients . . . 219

R. A. Forman, D. E. Aspnes and M. Cardona: Transverse electroreflectance in semi-insulating silicon and gallium arsenide . . . 227

J. B. Clark and Eliezer Rapoport: Effect of pressure on solid–solid transitions in some silver and cuprous chalcogenides . . . 247

T. H. Kwon and H. A. Gersch: Dynamical spin correlations in the B–P–W cluster model as applied to inelastic neutron scattering . . . 255

A. Barry Kunz: Electron energy bands and the optical properties of potassium iodide and rubidium iodide . . . 265

C. Marti, R. Parrot et G. Roger: Déplacements lineaires par un champ électrique de la resonance paramagnétique électronique de ZnS/Mn^{2+} . . . 275

A. Ikushima: Ultrasonic attenuation in MnF$_2$ near the Néel temperature . . . 283

R. Caudron, F. Ducastelle et P. Costa: Chaleur spécifique électronique et susceptibilité magnétique des carbures de transition hexagonaux de formule M$_2$C . . . 291

J. W. Twidell: Radiation induced movement of charge compensating ions in CaF$_2$ . . . 299

M. Mostoller: The scaling of the phonon frequencies in the diamond-type crystals . . . 307

M. Gerl: Energie de formation de monolacunes dans les métaux de transition . . . 315

H. P Baltes, M. Tosi and F. K. Kneubühl: Two phonon processes and phase transitions in KMnF$_3$: temperature discontinuities in the i.r. spectrum and group theoretical analysis . . . 321

A. R. PATEL and K. S. RAJU: Radiation damage in gypsum 331
J. SCHNEIDER, B. DISCHLER and A. RÄUBER: Defects in ZnS/ZnSe mixed crystals – II. The paramagnetic A-centers in cubic $ZnS_{1-x}Se_x$ 337
R. BESERMAN and M. BALKANSKI: Optical properties of impurities in blende type II–VI semiconductors compounds 355
B. BOUCHER, R. BUHL et M. PERRIN: Structures magnétiques et étude des propriétés magnétiques des spinelles cubiques $NiMn_2O_4$ 363
C. W. F. T. PISTORIUS: Phase relations of $KClO_4$ and KBF_4 to high pressures 385
K. BINDER, H. RAUCH and V. WILDPANER: Monte Carlo calculation of the magnetization of superparamagnetic particles 391
J. H. CRAWFORD, JR.: Aggregation of divalent metal impurity in alkali halide crystals 399

Technical Note:

C. BENOIT à la GUILLAUME and P. LAVALLARD: Piezoemission of gallium antimonide 411

MARCH

M. HASS: Raman spectra of vitreous silica, germania and sodium silicate glasses 415
M. ROBBINS, A. MENTH, M. A. MIKSOVSKY and R. C. SHERWOOD: Magnetic and crystallographic evidence for localization to delocalization of V d-electron levels in $CuCr_{2-x}V_xS_4$ spinels 423
L. NOVAKOVIĆ: Quantum theory of ferroelectricity – I. Spectral analysis 431
M. NATTA and P. JOYES: Singularities in the Auger emission spectrum of metals 447
E. EJDER: Some optical properties of Hg_2Cl_2 453
H. R. PATIL and H. B. HUNTINGTON: Electromigration and associated void formation in silver. 463
N. VAN DOAN et G. BREBEC: Migration sous l'effet d'un champ électrique de ^{110}Ag et de ^{124}Sb dans l'argent . 475
E. R. VANCE and J. H. SMITH: Paramagnetic diffuse scattering of neutrons by a 90 at % manganese copper alloy 485
C. KORN and D. ZAMIR. NMR study of hydrogen diffusion in the three different phases of the titanium–hydrogen system. 489
G. BAMBAKIDIS: Effect of band structure on the Ruderman–Kittel–Kasuya–Yosida interaction in the heavy rare earths 503
J. E. RALPH: Cathodoluminescence of Er^{3+} in YGaG and YAG 507
A. B. Y. YOUNG and G. L. PEARSON: Diffusion of sulfur in gallium phosphide and gallium arsenide 517
G. WILLIAMS: Electrical resistivity of the dilute PdCo system 529
R. SHARAN and E. L. HEASELL: Deformation potential constants of acceptor impurities in InSb 541
M. BREUIL et G. TOURAND: Détermination de la fonction de distribution de paire du cuivre liquide par diffraction de neutrons 549
M. WILHELM und B. HILLENBRAND: Über die Praparation und das supraleitende Verhalten von $CeRu_2$ und seiner Gd-, Mn-, Fe-, Co- und Ni-haltigen Mischphasen 559
L. B. ZLATKIN, YU. F. MARKOV, A. I. STEKHANOV and M. S. SHUR: The investigation of the vibrational spectrum, optical constants and ionicity of bond of $GdGeAs_2$ in crystal and amorphous phases by i.r. reflection 567

Technical Note:

L. R. EDWARDS and R. W. LYNCH: The high pressure compressibility and Grüneisen parameter of strontium titanate. 573

APRIL

F. J. FEIGL and J. H. ANDERSON: Defects in crystalline quartz: electron paramagnetic resonance of E' vacancy centers associated with germanium impurities 575
A. H. M. KIPPERMAN and H. F. VAN LEIDEN: Electrical properties of metal surface barriers on the layer structures of GaS and GaSe 597
K. B. WOLFSTIRN: Survey analysis of impurities in gallium arsenide by instrumental neutron activation . . 601
J. L. ANDERSON, J. NASISE, K. PHILIPSON and F. E. PRETZEL: Isotopic effects on the thermal expansion of lithium hydride 613
R. W. ROBERTS and C. S. SMITH: Ultrasonic parameters in the Born model of the sodium and potassium halides 619
B. L. MORRIS, P. RUSSO and A. WOLD: Magnetic properties of ACr_2Se_4 (A = Fe, Co, Ni) and $NiCr_2S_4$ . . 635
C. GRESKOVICH and H. SCHMALZRIED: Nonstoichiometry and electronic defects in Co_2SiO_4 and in $CoAl_2O_4$ $MgAl_2O_4$ crystalline solutions 639

J. J. Fontanella and D. E. Schuele: Low temperature Grüneisen parameter of RbI from elasticity data . 647
L. L. Hirst: A Mössbauer-effect study of paramagnetic relaxation of Er impurities in Zr 655
G. Quezel, R. Ballestracci et J. Rossat-Mignod: Propriétés magnétiques des oxysulfures de terres rares 669
S. D. Devine and R. C. Newman: One phonon absorption from aluminium complexes in silicon compensated by lithium or electron irradiation 685
G. J. Dienes, R. D. Hatcher and R. Smoluchowski: Formation and structure of H′ centers 701
G. Blasse and A. Bril: Some observations on the luminescence of β-Ga_2O_3 707
R. Benz: Entropies of mixing of solids with a retrograde solidus 713
R. E. Seevers and A. B. Scott: Electrical conductivity of additively colored potassium chloride . . . 729
A. R. Bean, R. C. Newman and R. S. Smith: Electron irradiation damage in silicon containing carbon and oxygen 739
Hj. Matzke and C. Jech: High mobility of heavy rare gases in potassium halides at low temperatures (20–100°C) 753
J. W. Loram, P. J. Ford and T. E. Whall: The resistivity of dilute *Au* Co alloys 763
R. S. Crandall: Application of the electron temperature model to low-temperature non-ohmic transport in GaAs 771
C. S. Ting: Thermodynamic properties of dilute magnetic alloys 777
C. Crevecoeur and H. J. De Wit: Electrical conductivity of Li Doped MnO 783
S. Geller, R. W. Grant and L. D. Fullmer: Magnetic structures in the $Ca_2Fe_{2-x}Al_xO_5$ system . . . 793
A. J. Darnell and W. A. McCollum: Thermodynamics of the Fm3m $\rightleftarrows$ Pm3m transition in the potassium and rubidium halides 805
Antione J. F. Bastin, Colette Lewiner and Noëlle Fayet: Anomalous Hall effect in semiconductors . 817
V. C. Nelson and R. J. Friauf: Diffusion of vacancies and vacancy pairs in NaCl 825
H. L. Downing, Jr. and R. J. Friauf: Self-diffusion of Na in NaCl 845
L. C. E. Miller and C. R. Kannewurf: Optical properties of single crystal silicon arsenide 849
L. L. Hirst and E. R. Seidel: A Mössbauer effect study of local moments of erbium in zirconium . . . 857
W. Young and J. Callaway: *t*-Matrix approximation in spin wave calculation 865

Technical Notes:

C.-Y. Huang, F. Rachford, J. A. Lock and M. A. Mostrom: The Debye temperature and temperature-dependent hyperfine coupling constants of Mn^{2+} in SrF_2 and CdF_2 871
R. Kamal and R. G. Mendiratta: Magnetically induced nuclear quadrupole interaction in cubic Fe^{2+}: Pseudo-quadrupole interaction 872
J. N. Plendl and P. J. M. Gielisse: Structural stability of inorganic polymorphs 874
K. Veerabhadra Rao and T. S. Narasimhamurty: Photoelastic constants of CaF_2 and BaF_2 . . 876
C. E. McCain and K. Schröder: Optical properties of chromium rich chromium iron alloys at room temperature 898
G. Davies: Inhomogeneous broadening of edge recombination radiation 883
J. Millstein: Thermal conductivity and Lorenz ratio of RuO_2 886
K. V. Krishna Rao and K. Satyanarayana Murthy: Precision lattice parameters and thermal expansion of sodium nitrate 887
C. K. R. Varma: Evidence of deformation twinning in natural diamond crystals 890

Erratum 893

MAY

C. C. Robinson and J. T. Fournier: Co-ordination of Yb^{3+} in phosphate, silicate, and germanate glasses . 895
G. G. P. Van Gorkom: A new Mn^{2+} centre in CaF_2 905
R. J. Kearney, T. G. Worlton and R. E. Schmunk: Application of group theory to the lattice dynamics of magnesium stannide 913
H. Heinrich and M. Kriechbaum: Galvanomagnetic effects of hot electrons in *n*-type silicon 927
A. Ikushima: Anisotropy of the ultrasonic attenuation in MnF_2 near the Néel temperature 939
M. O'Keeffe and M. Valigi: The electrical properties and defect structure of pure and chromium-doped MnO 947
G. Susila: Recombination and trapping in *n*-type cobalt-doped germanium 963
J. E. Evetts and J. M. A. Wade: Superconducting properties and the phase diagrams of the Pb–Bi and Pb–In alloy systems 973
J. M. Caywood and C. A. Mead: Charge transport through α-monoclinic selenium 983
U. Scherz: Calculation of *g*-factors of Cu^{2+}-centers in II–VI-compounds 995
Maria T. Causa, D. Raoux et C. Taupin: Etude par resonance électronique du tritium atomique forme au sein de cristaux de fluorure de lithium irradié aux neutrons 1011

K. C. Kao, W. Whitham and J. H. Calderwood: Time dependent polarisation in alkali halides . . . 1019
E. Šimánek and K. A. Müller: Covalency and hyperfine structure constant A of iron group impurities in crystals . . . 1027
M. H. Reilly: Temperature dependence of the short wavelength transmittance limit of vacuum ultraviolet window materials – II. Theoretical, including interpretations for u.v. spectra of SiO_2, GeO_2, and Al_2O_3 . 1041
K. Anzenhofer, J. M. Van Den Berg, P. Cossee and J. N. Helle: The crystal structure and magnetic susceptibilities of $MnNb_3S_6$, $FeNb_3S_6$, $CoNb_3S_6$ and $NiNb_3S_6$ . . . 1057
H. W. Newkirk and H. R. Leider: Thermal annealing of irradiated lithium hydride – I. Measurement of stored energy . . . 1069
A. A. Maradudin and S. Ushioda: A theory of the first order Raman scattering of light by polaritons in crystals of the rocksalt structure . . . 1075
R. J. Kearney, T. G. Worlton and R. E. Schmunk: Lattice dynamics of magnesium stannide at room temperature . . . 1085
D. J. Amit: Expansions of the free energy near a phase transition . . . 1099
R. D. Fouchaux: Thermodynamics of point defects with explicit concentration dependent interactions . . 1113
S. Gradsztajn, J. Conard et H. Benoit: Etude de la surface de solides par RMN de liquides adsorbé – I. Origine du déplacement et de la largeur des raies dans le cas des carbones . . . 1121
P. Brüesch and M. Lietz: Dipole sums for hexagonal, tetragonal and orthorhombic lattices with a basis . . 1137
D. J. Newman: Many-body perturbation theory for non-orthogonal basis states . . . 1143
E. Bonek, H. W. Pötzl and K. Richter: High-frequency behavior of hot electrons in one-valley polar semiconductors . . . 1151
K. Baumann, M. Kriechbaum and H. Kahlert: Time dependent phonon distribution in hot electron experiments . . . 1163
G. Buisson: Etude par rayons X et neutrons de la série isomorphe $ATiTO_5$ ($A = Cr$, Mn, Fe, $T =$ Terres rares) . . . 1171

Technical Notes:

R. B. Murray, H. B. Dietrich and F. J. Keller: Recombination luminescence in NaCl . . . 1185
D. Gerlich: Mode Grüneisen parameters for single crystal Al_2O_3 . . . 1188
R. N. Blumenthal and R. J. Panlener: Electron mobility in nonstoichiometric cerium dioxide at high temperatures . . . 1190
J. L. Anderson, A. L. Bowman and G. P. Arnold: Low temperature neutron diffraction studies on Li(D, T) . . . 1193
N. Erickson and N. Elliott: Magnetic susceptibility and Mössbauer spectrum of $NH_4Fe^{3+}Fe^{II}(CN)_6$. 1195

JUNE

G. E. Stillman, C. M. Wolfe and J. O. Dimmock: Hall coefficient factor for polar mode scattering in n-type GaAs . . . 1199
F. Beniere, M. Beniere et M. Chemla: Conductibilité, nombres de transport et autodiffusion des ions dans différents monocristaux de chlorure de sodium . . . 1205
H. R. Leider: Thermal annealing of irradiated lithium hydride – II. A proposed mechanism . . . 1221
Y. Ishikawa, Y. Endoh and T. Takimoto: Antiferromagnetism of a γ iron–nickel–chromium alloy (non-magnetic stainless steel) . . . 1225
J. J. Curry and S. R. Pollack: The thermoelectric properties of quaternary chalcogenides . . . 1235
F. Ducastelle, R. Caudron et P. Costa: Etude du système tantale–hydrogène: diagramme d'équilibre et structure électronique . . . 1247
W. A. Nordland and L. G. Van Uitert: Anomalies in the dielectric constant of the $Pr_{1-x}Nd_xAlO_3$ system . 1257
Jean Bletry: Effets de taille dans les solutions solides de l'aluminium avec les métaux de transition de la première série . . . 1263
B. A. Cruz-Vidal and H. J. Gomberg: The role of K shell ionization in the formation of F centers in alkali halides at 78°K – I. KBr . . . 1273
B. A. Cruz-Vidal, F. Díaz-Hernández and H. J. Gomberg: The role of K shell ionization in the formation of F centers in alkali halides at 78°K – II. RbBr . . . 1281
B. A. Cruz-Vidal, L. Nino-Rojas and H. J. Gomberg: The role of K-shell ionization in the formation of F centers in alkali halides at 78°K – III. KCl . . . 1287
T. G. Stoebe: Distribution of hydroxide ions in doped alkali halide crystals . . . 1291
F. Ducastelle and F. Cyrot-Lackmann: Moments developments and their application to the electronic charge distribution of d bands . . . 1295
P. W. France and H. O. Hooper: Nuclear magnetic resonance study of semiconducting vanadium phosphate glass . . . 1307

D. T. KEATING: A note on the determination of the density of phonon eigenstates from the inelastic incoherent neutron scattering 1317
Y. YAMAGUCHI, T. AOKI and J. O. BRITTAIN: Electronic structure of β-NiAl 1325
L.-G. LIU, T. TAKAHASHI and W. A. BASSETT: Effect of pressure and temperature on the lattice parameters of rhenium 1345
C. B. BURGETT and C. C. LIN: Infrared quenching of the luminescence and photo-Hall effect of ZnS:Cu and CdS:Cu crystals 1353
K. L. VANDER LUGT, J. COMAS and E. A. WOLICKI: Coloration of LiF by 3·0 MeV^{3}He, ^{40}Ar ^{84}Kr and 2·0 MeV ^{129}Xe ions 1361
N. E. GEACINTOV, M. POPE and S. FOX: Magnetic field effects on photo-enhanced currents in organic crystals. 1375
F. D. WÖHLER, H. ALEXANDER and W. SANDER: The annealing of the EPR-signal produced in silicon by plastic deformation 1381
K. S. SONG: On the migration of V_K-centers in alkali halides 1389
P. B. FABRITCHNYI, A. M. BABECHKIN et A. N. NESMEIANOV: Etude des effets superficiels dans les transformations des acides stanniques par l'effet Mössbauer et par diffraction des rayons X 1399

Technical Notes:

A. ELGSAETER and I. SVARE: Thermal properties of nickel hexammine salts at the phase transition . . 1405
B. V. R. CHOWDARI: Electron paramagnetic resonance study of Mn^{2+} in $(NH_4)_2Mg_2(SO_4)_3$ and $(NH_4)_2Zn_2(SO_4)_3$ crystals 1408
J. NOVOTNÝ, Z. SPURNÝ and M. BÍNOVA: Exo-electron emission from activated $CaSO_4$ phosphors . . 1412
M. SHIMSHONI and E. HARNIK: Ultrasonic measurement of the electrocaloric effect in KH_2PO_4 . . 1416
I. CAMLIBEL, M. DIDOMENICO, JR. and S. H. WEMPLE: Dielectric properties of single-domain melt-grown $BaTiO_3$ 1417
R. JANAKIRAMAN and G. C. UPRETI: Electron paramagnetic resonance of Mn^{2+} in zinc acetate dihydrate. 1419

JULY

A. N. BUCKLEY, I. R. HERBERT, B. D. RUMBOLD, G. V. H. WILSON and K. S. MURRAY: Mössbauer effect studies of some dimeric iron compounds 1423
J. INGLESFIELD: The Mössbauer isomer shift in ^{119}Sn – I. Pseudopotential approach 1435
J. E. INGLESFIELD: The Mössbauer isomer shift in ^{119}Sn – II. Effects of crystal structure 1443
L. J. VIELAND: The system $Nb_3Sn_{1-x}Sb_x$ and the density of states model for Nb_3Sn 1449
C. PARACCHINI and G. SCHIANCHI: Electroluminescence due to internal field emission in KI 1455
P. C. SOUERS, T. IMAI, T. S. BLAKE, R. M. PENPRAZE and H. R. LEIDER: NMR and electron microscopy studies on irradiated lithium hydride 1461
N. G. PACE, G. A. SAUNDERS and Z. SÜMENGEN: The elastic constants and interatomic binding forces in arsenic 1467
G. D. MAHAN: Relaxation time of electron–phonon systems 1477
C. S. N. MURTHY and Y. V. G. S. MURTI: Cohesive energies of NH_4Cl and NH_4Br 1485
H. A. FARACH, E. F. STROTHER and C. P. POOLE, JR.: Solution to the Anderson exchange narrowing model for $I > \frac{1}{2}$ 1491
K. S. V. L. NARASIMHAN, W. M. REIFF, H. STEINFINK and R. L. COLLINS: Magnetism and bonding in a $D8_8$ structure; Mössbauer and magnetic investigation of the system Mn_5Si_3–Fe_5Si_3 1511
K. BACHMANN and H. PEISL: Elastic distortions and interactions of point defects in KBr 1525
P. SPITZLI, R. FLÜKIGER, F. HEINIGER, A. JUNOD, J. MULLER et J. L. STAUDENMANN: Chaleur spécifique, supraconductivité et ordre cristallin d'alliages de structure A15 à base de vanadium 1531
R. G. FULLER and F. W. PATTEN: Electrical conductivity in NH_4Cl and ND_4Cl single crystals. . . . 1539
R. P. VAN STAPELE and F. K. LOTGERING: Trivalent and tetravalent chromium in the seleno-spinel series $CuCr_{0\cdot3}Rh_{1\cdot7-x}Sn_xSe_4$ 1547
H. HOSHINO and M. SHIMOJI: Thermoelectric power of ionic crystals – V. Thermoelectric power of potassium bromide and sodium bromide using bromine gas electrodes. 1553
H. Z. DOKUZOGUZ, L. H. BOWEN and H. H. STADELMAIER: Mössbauer effect in B8 alloys of nickel with ^{121}Sb and ^{119}Sn 1565
J. A. BLACKMAN: Theory of impurity states in systems with long range interactions – spin waves in Tb–Ho alloys 1573
G. E. STEDMAN and D. J. NEWMAN: Force-constant models of lattice vibrations in rare-earth halides . . 1587
R. SANDSTRÖM and T. HÖGBERG: Anharmonic widths and shifts in simple metals. Application to aluminium . 1595
R. J. D. TILLEY and B. G. HYDE: An electron microscopic investigation of the decomposition of V_2O_5 . . 1613
M. WEGER: Some considerations regarding the application of a linear chain model to some compounds of the β-W structure 1621

Technical Notes:

J. Tateno: Ionicity of some polar crystals 1641
C. Sánchez, F. Jaque and F. Agulló-López: On the anomalous F-coulouring behaviour of irradiated alkali halides 1642
S. Rajagopalan: Watchman's equation and the temperature dependence of bulk modulus in nonoxide solids 1644
B. Alascio and A. López: Magnon–phonon interaction in the itinerant electron model of ferromagnetism. 1647
D. J. Flood: Field emission in high magnetic fields 1649
J. D. Taynai and M. A. Nicolet: The density of α-monoclinic selenium 1651

AUGUST

Foreword 1655
E. Roi and Dobbs: Electromagnetic generation of ultrasonic waves in metals 1657
H. L. Grubin and T. Kjeldaas, Jr.: Application of translationally invariant wavefunctions in a magnetic field to frequency and wavelength dependent transport phenomena 1669
J. Zucker and S. Zemon: Nonlinear attenuation of microsound in semiconducting CdS 1673
J. L. Stevens and A. Houghton: Change in velocity of high frequency transverse sound at the superconducting transition temperature 1677
Hilda A. Cerdeira, W. N. Cottingham and A. Houghton: Longitudinal ultrasonic attenuation in type II superconductors: clean limit 1681
B. R. Tittmann: Ultrasonic attenuation in a type II superconducting alloy 1687
J. N. Lange: Hypersonic attenuation in niobium in the mixed state 1693
J. J. Quinn: Direct generation of sound in metals and acoustic nuclear spin resonance 1701
A. J. Budreau and P. H. Carr: Performance and applications of microwave photon–phonon double-quantum detection in MgO 1709
B. A. Huberman, R. Ito, E. Burstein and Y. Sawada: The propagation and attenuation of acoustic waves in ferromagnetic metals 1719
T. Ishiguro and N. Mikoshiba: Ultrasonic donor-spin resonance in germanium 1729
T. J. Moran and B. Lüthi: Elastic and magnetoelastic effects in rare earth metals 1735
B. Lüthi, T. J. Moran and R. J. Pollina: Sound propagation near magnetic phase transitions 1741
C. W. Garland and D. D. Snyder: Ultrasonic attenuation near the lambda transition in NH_4Cl at high pressures 1759
G. Alefeld, J. Völkl and J. Tretkowski: Thermodynamic properties of interstitial solid solutions by relaxation methods 1765
C. A. Wert. Damping of interstitial atoms in bcc metals 1771
V. S Postnikov, V. S. Pavlov and S. K. Turkov: Internal friction in ferroelectrics due to interaction of domain boundaries and point defects 1785
C. Wert, D. O. Thompson and O. Buck: Internal friction of Nb–H alloys 1793
M. S. Ahmad and Z. C. Szkopiak: Snoek relaxation peaks in solid solutions of niobium 1799
J. Völkl, G. Schaumann and G. Alefeld: Diffusional relaxation of H and D in V and Nb 1805
R. Cantelli, F. M. Mazzolai and M. Nuovo: Internal friction due to long-range diffusion of hydrogen and deuterium in vanadium 1811
A. S. Nowick: Kinetics of anelastic and dielectric relaxation due to reacting point defects 1819
B. S. Berry: Anelastic relaxation in silicon doped with lithium and boron 1827
K. Ehrensperger, V. Fischer, J. Kerscher and H. Wenzl: Internal friction maxima due to relaxation of point defects in neutron irradiated aluminium 1835
V. Hivert, R. Pichon, H. Bilger, P. Bichon, J. Verdone, D. Dautreppe and P. Moser: Internal friction in low temperature irradiated bcc metals 1843
J. C. Worley, A. B. Smith and M. Kestigian: Anomalous attenuation in lithium tantalate 1857
J. A. Garber and A. V. Granato: Reradiation and viscous dislocation damping 1863
R. O. Schwenker and A. V. Granato: The frequency dependence of sound radiation from mobile dislocation walls 1869
B. K. Ganguly, C. Baker and H. K. Birnbaum: The frequency dependence of dislocation damping in niobium 1877
N. Igata, K. Domoto and R. R. Hasiguti: Frictional force coefficient of a moving dislocation in uranium dioxide with excess oxygen. 1883
R. Gibala, M. K. Korenko, M. F. Amateau and T. E. Mitchell: Dislocation relaxation in single crystals of bcc metals 1889
J. de Fouquet, P. Boch, J. Petit and G. Rieu: A contribution to the study of internal friction peaks associated with dislocations in various metals, and their relations with cold-work 1901

W. Benoit, B. Bays, P. A. Grandchamp, B. Vittoz, G. Fantozzi, J. Perez and P. Gobin: Modulus effects and Hasiguti peaks on two coldworked fcc metals: gold and aluminium 1907

G. Cannelli and F. M. Mazzolai: Anelastic relaxation effects in coldworked and hydrogen doped vanadium . 1913

D. N. Beshers: Anelasticity of dislocation dipoles 1921

W. P. Mason and J. Wehr: Internal friction and ultrasonic yield stress of the alloy 90 Ti 6 Al 4 V . . . 1925

V. S. Postnikov, S. A. Ammer, B. M. Darinsky, I. V. Zolotukhin and A. T. Kosilov: Internal friction in whiskers and thin films 1935

H. Akita and N. F. Fiore: Dislocation damping in copper single crystals of controlled substructure . . 1941

J. Dralla and J. C. Bilello: Dislocation structure and low frequency mechanical hysteresis in copper single crystals 1947

W. Sachse and R. E. Green, Jr.: Deformation rate effects on the attenuation during loading, unloading and reloading of aluminum crystals 1955

SEPTEMBER

W. Fawcett, A. D. Boardman and S. Swain: Monte Carlo determination of electron transport properties in gallium arsenide 1963

J. A. Tunheim, E. E. Kohnke, M. D. Bell and W. J. Leivo: EPR of Ni^{3+} in stannic oxide and oxidation-reduction effects on the EPR spectra observed in flux-grown crystals 1991

M. L. Yu and J. T. H. Chang: The temperature dependence of the Planar Hall Effect in iron, cobalt and nickel. 1997

L. Thomsen: On the fourth-order anharmonic equation of state of solids 2003

R. W. Cunningham and J. B. Gruber: Quantum mechanical treatment of polar optical mode mobility and application to InSb 2017

S. H. Groves, C. R. Pidgeon, A. W. Ewald and R. J. Wagner: Interband magnetoreflection of α-Sn . . 2031

K. F. Loje and D. E. Schuele: The pressure and temperature derivatives of the elastic constants of AgBr and AgCl 2051

R. S. Crandall: Current controlled negative resistance in semiconductors 2069

N. van Doan: Effet de valence en électromigration dans l'argent 2079

R. Riedinger: Structure électronique des alliages à base de métaux de transition et de métaux nobles – II. Calcul de la structure électronique de l'alliage CuNi 2087

R. Riedinger et F. Gautier: Etude de l'hybridation entre bandes *s* et *d* due au potential d'impureté dans les alliages dilues à base de métaux nobles ou de transition 2099

A. N. Men', M. P. Bogdanovič, Ju P. Vorobjov, R. Ju. Dobrovinski and G. J. Chufarov: Cluster theory of solutions 2117

H. Böhm and G. Bayer: ESR-spectra of sodium–titanium–silicate glasses and of titanium-containing oxide compounds 2125

Technical Notes:

J. P. Fillard and J. Gasiot: Thermally stimulated currents in Cu$_2$O 2139

J. P. Charles and J. P. Fillard: Electrical conductivity and space charge Cu$_2$O 2141

H. Gobrecht, G. Willers and D. Wobig: Transformations of red amorphous and monoclinic selenium . 2145

T. J. Wieting: Electrical conductivity of thin single crystals of the IVB–VIB dichalcogenides . . . 2148

D. C. Look: Conduction electron hyperfine interaction in semiconducting CdS 2151

B. N. Srivastava and R. N. Tyagi: The effect of rigidity and density on the temperature variation of Mössbauer effect 2154

J. Przystawa: On the magnetic structure of U$_3$P$_4$ and U$_3$As$_4$ 2158

D. R. Fredkin and H. B. Shore: Linear spin wave theory with single anisotropy 2159

D. G. Schweitzer and P. D. Adams: The effect of localized surface changes on transport current distributions in plates of type I superconductors 2161

M. Shimada, S. Kume and M. Koizumi: Cation distributions in ferrimagnetic garnets 2165

P. S. Nayar: Valence band of thallium selenide 2167

OCTOBER

J. Onstott and G. Lucovsky: Directional dispersion of extraordinary optical phonons in α-quartz in the frequency domain from 380 to 640 cm^{-1} 2171

W. E. Wallace, T. V. Volkmann and R. S. Craig: Structures and magnetic properties of the pseudobinary systems CeNi$_2$–CeCu$_2$ and GdNi$_2$–GdCu$_2$ 2185

F. Bonsignori and A. Desalvo: A dielectric calculation of energy loss to valence electrons under channeling conditions 2191

P. J. Lin-chung: Optical properties and electronic band structures of group V and IV–VI materials . . 2199

Shinji Muramatsu and Takeshi Iida: A possibility of orthorhombic Jahn–Teller distortion 2209
Y. Suzuki, Y. Hamakawa, H. Kimura, H. Komiya and S. Ibuki: Electro-reflectance near the fundamental edge of GaSe 2217
P. W. France and H. O. Hooper: Asymmetric nuclear magnetic resonance line shapes due to nuclear quadrupole and anisotropic shift interactions 2223
C. E. Bailey: Effect of uniaxial stress on *F*-center hyperfine interactions 2229
F. E. Maranzana: Contribution to the theory of Kondo resistivity in magnetic compounds 2245
B. Boucher, R. Buhl et M. Perrin: Structures magnétiques anisotropes dans les spinelles 2251
T. Gavan and B. G. S. Doman: A green function approach to the problem of two magnetic impurities in a non-magnetic metal 2267
R. R. Sharp and E. L. Pace: Direct observation of impurity motion in quartz using the Raman effect 2275
N. C. Halder: Effect of dilation on the Knight shift in liquid alloys 2281
A. J. Strauss and R. F. Brebrick: Vapor-crystal equilibrium and electrical properties of HgTe 2293
M. A. Khan: *g*-Factor and effective mass of electrons in the conduction and the valence bands of CuCl 2309
A. K. Hochberg and C. R. Westgate: Band structure of silicon by pseudo-OPW 2317
S. N. Vaidya and G. C. Kennedy: Compressibility of 18 metals to 45 kbar 2329
R. Grover: Comments on the comparison of dynamic and static compression data 2347
J. McK. Nobbs and F. C. Gillespie: Properties of thin films of zinc oxide prepared by a chemical spray method 2353
W. Gissler, G. Alefeld and T. Springer: Quasielastic neutron scattering by hydrogen in niobium 2361

Technical Notes:

S. M. Silverman: Disorder in the normal paraffin from $8 \leq n \leq 16$ 2371
R. Carter, A. Davidson and P. A. Schroeder: Thermopower of cubic transition metals 2374

NOVEMBER

H. Kiess: High field behaviour of ZnO – I Investigation of the dark current 2379
H. Kiess: High field behaviour of ZnO – II. Investigation of the photocurrents 2391
R. W. Roberts and C. S. Smith: Ultrasonic parameters in the Born model of the rubidium halides 2397
E. Müller and D. K. Ferry: Hall studies of instabilities occurring in impact ionization of *n*-type indium antimonide 2401
J. R. Carter, Jr.: Effect of electron irradiation on lithium-doped silicon 2405
G. Schaack and J. A. Koningstein: Phonon frequencies of rare earth trichlorides with unit cells of different dimensions 2417
J. A. C. Marples: The effect of alloying additions of plutonium and neptunium on the lattice parameters of α-uranium between 4 and 300°K 2421
J. A. C. Marples: An X-ray study of the structures of UN, UP, US and USe at cryogenic temperatures 2431
M. L. Klein, V. V. Goldman and G. K. Horton: Thermodynamic properties of solid Ar, Kr and Xe based upon a short range central force and the improved self-consistent phonon scheme 2441
A. Myszkowski: Phonon-induced hopping transitions in germanium and silicon 2453
O. C. Kopp and P. A. Staats: Characterization of RbOH-grown quartz by infrared and mass spectroscopy 2469
W. B. Fowler and Diane N. Cope: Electronic states of interstitial ions in alkali halide crystals 2477
M. G. Townsend: On the dichroism of tourmaline 2481
J. J. Davies and J. E. Wertz: The EPR spectrum of trivalent titanium in orthorhombic symmetry in MgO 2489
G. A. Saunders and T. Seddon: Effect of ordered vacancies on ultrasonic wave propagation in some mercury-indium tellurides 2495
A. S. Koster and G. D. Rieck: Determination of valence and coordination of iron in oxidic compounds by means of the iron X-ray fluorescence emission spectrum 2505
A. S. Koster and H. Mendel: X-ray $K\beta$ emission spectra and energy levels of compounds of $3D$-transition metals – I. Oxides 2511
A. S. Koster and H. Mendel: X-ray $K\beta$ emission spectra and energy levels of compounds of $3D$-transition metals – II. Non-oxidic compounds 2523
D. B. Watson and W. Heyes: Time lags in the breakdown of NaCl at high temperatures 2531
T. A. Uhrig: Ferromagnetic and spin wave resonance at high pressure 2539
S. Chou: The Boltzmann equation for (111) valleys in germanium 2549
N. A. Goryunova, L. B. Zlatkin and E. K. Ivanov: Optical anisotropy of $A^2B^4C_2^5$ crystals 2557
M. Kriechbaum and H. Heinrich: Galvanomagnetic effects of hot electrons in *n*-type germanium 2563
P. D. Dernier: The crystal structure of V_2O_3 and $(V_{0.962}Cr_{0.038})_2O_3$ near the metal-insulator transition 2569

Technical Notes:

J. J. Mills: Non-stoichiometric defects in sapphire 2577

S. Maniv and A. Gabay: Electron paramagnetic resonance of Gd^{3+} in Cs$_2$ZrCl$_6$ single crystal . . . 2579
L. L. Isaacs and D. J. Lam: The magnetic susceptibilities of hexagonal Tc–Ru, Tc–Rh and Ru–Rh alloys. 2581

Errata 2585

DECEMBER

B. Bjensjö, B. Solly and P. Wikefeldt: Mössbauer spectroscopy of ^{57}Fe as a magnetic impurity in Heusler alloys 2589
E. Gross, S. Permogorov, V. Travnikov and A. Selkin: Hot excitons and exciton excitation spectra . . 2595
H. A. Combet: Surface impedance of gold films on bulk superconducting tin 2607
J. T. Fournier and R. H. Bartram: Inhomogeneous broadening of the optical spectra of Yb^{3+} in phosphate glass 2615
O. Röder, U. Heim and M. H. Pilkuhn: Electron mobilities and photoluminescence of solution grown indiumphosphide single crystals 2625
D. N. Yoon and R. N. Jeffery: Pressure and composition dependence of the order-disorder critical temperature of α-CoFe 2635
S. Kern, P. M. Raccah and A. Tveten: Magnetic susceptibility of europium trifluoride 2639
P. R. Locher and R. P. Van Stapele: Supertransferred hyperfine fields on tetrahedral sites in some chromium sulpho- and seleno spinels 2643
E. E. Havinga, H. Damsma and M. H. Van Maaren: Oscillatory dependence of superconductive critical temperature on number of valency electrons in Cu$_3$Au-type alloys 2653
R. A. Craig: A calculation of the contribution of quasiparticle anisotropy to the isotropic Knight shift . . 2663
L. Ramqvist, K. Hamrin, G. Johansson, U. Gelius and C. Nordling: VC, NbC and TaC with varying carbon content studied by ESCA 2669
Mary M. Conway, N. E. Phillips, T. H. Geballe and N. A. Kuebler: Low-temperature heat capacities of the clathrate salts Ag$_7$O$_8$NO$_3$ and Ag$_7$O$_8$HF$_2$ 2673
D. F. Barbe and C. R. Westgate: Surface state parameters of metal-free phthalocyanine single crystals. . 2679
J. S. Reid and T. Smith: Improved Debye–Waller factors for some alkali halides 2689
G. Pfister and M. Bösch: Orbach type reorientation processes in the paraelastic relaxation of O_2^- in KCl . 2699
C. M. Perrott: Cationic transport in α-AgI and α-Ag$_2$S 2709
F. Y. Fradin: The dynamic effects of localized magnetic moments on nuclear spins in metallic systems . . 2715
D. C. Dobson, J. W. Linnett and M. M. Rahman: Mössbauer studies of the charge transfer process in the system Zn$_x$Fe$_{3-x}$O$_4$ 2727
P. J. Tsang and J. B. Darby, Jr.: The low-temperature specific-heats of several palladium-rich palladium-antimony alloys 2735
B. C. Tofield and B. E. F. Fender: Covalency parameters for Cr^{3+}, Fe^{3+} and Mn^{4+} in an oxide environment. 2741
K. Alex and R. B. McLellan: A zeroth order mixing treatment of interstitial solid solutions 2751
D. J. Olechna: Directional dispersion of extraordinary optical phonons in uniaxial crystals 2755
S. B. S. Sastry, R. B. Tripathi and C. Ramasastry: Perturbation of fundamental band edge absorption of NaClO$_3$ crystals at high temperatures 2765
J. Durand et F. Gautier: Conduction à deux bandes et effet de période dans les alliages à base de nickel et de cobalt 2773

Technical Notes:

A. Ferro and G. Griffa: Quench enhanced ordering of Fe Ni$_3$. 2789
A. E. Ringwood and A. F. Reid: Olivine-spinel transformation in MgMnGeO$_4$, FeMnGeO$_4$ and CoMnGeO$_4$. 2791
J. H. Hendriks and F. J. Dijkstra: Acoustic relaxation in manganese ferrites (Mn$_x$Fe$_{3-x}$O$_4$) at temperatures between 90 and 400 K for $1{\cdot}0 < x < 1{\cdot}6$ 2793
D. C. Parashar: Cation diffusion and electrical conduction in KCl crystals 2795

J. Phys. Chem. Solids Pergamon Press 1970. Vol. 31, pp. 1–8. Printed in Great Britain.

THERMOPOWER OF Mg, Cd AND Zn BETWEEN 1·2° AND 300°K*

V. A. ROWE† and **P. A. SCHROEDER**
Department of Physics, Michigan State University, East Lansing, Mich. 48823, U.S.A.

(*Received* 7 *July* 1969)

Abstract—The two independent components of the thermopower tensors for the hexagonal group II metals Mg, Zn, and Cd have been measured between 1·1° and 300°K. Throughout this temperature range the results are highly anisotropic. Extrema at low temperatures (< 40°K) are ascribed to phonon drag effects. Many correlations suggest that these extrema can be directly associated with the dimensions of the various sheets of the Fermi surfaces of the three metals.

1. INTRODUCTION

This project was commenced with a view to testing the hypothesis that various sheets of the Fermi surface of a polyvalent metal would make discernible contributions to the phonon drag thermopower. A similar project has been carried out by Jan and Pearson[1] on the intermetallic compound AuSn, but from a rather different point of view. From the anistropy of the phonon drag thermopower they attempted to deduce information about the then unknown Fermi surface. In contrast we have chosen metals with well known Fermi surfaces which are topologically similar, but which at the same time have significant differences that aid in the correlation of the phonon drag thermopower with the known Fermi surface topology.

2. EXPERIMENTAL

The thermoelectric tensor in hexagonal materials has two independent coefficients corresponding to measurements made parallel and perpendicular to the hexagonal axis. If we make a thermocouple consisting of a crystal with its axis parallel to the hexagonal axis with junctions to two Pb wires then

$$S_{\parallel} = \frac{\Delta\phi}{\Delta T} + S_{\mathrm{Pb}}$$

where $S_{\parallel}$ is the parallel component of the thermopower tensor; ΔT is an incremental temperature drop between junctions; $\Delta\phi$ is the thermo-e.m.f. of the thermocouple so formed; and S_{Pb} is the absolute thermopower of Pb, which is well-known over the range of our measurements. A similar expression holds for $S_{\perp}$ the perpendicular component of the thermoelectric tensor.

In our experiments the sample was maintained electronically at a mean temperature, T, while a small temperature gradient, also electronically stabilized, was produced by an electrical heater at one end. ΔT and T were measured by Au, 0·028% Fe–chromel thermocouples. The output of the ΔT thermocouple fed into a Keithley 149 millimicrovoltmeter, which in turn drove the X-axis of a Moseley 2D2 X–Y recorder. $\Delta\phi$ was measured by a Keithley 147 nanovoltmeter which drove the Y-axis of the X–Y recorder. To eliminate spurious thermal e.m.f.s in the $\Delta\phi$ and ΔT measurements, at a given temperature, ΔT was given various values up to 0·50°K at room temperature and up to 0·1° at 1°K. For each ΔT value a $\Delta\phi$ value was recorded on the X–Y recorder. The slope of the straight line so obtained gave $\Delta\phi/\Delta T$ independent of any steady thermo-e.m.f.s generated in the leads to the measuring instruments.

The cryostat

The cryostat is illustrated in Fig. 1. It is

---

*This work was supported by the National Science Foundation.

†Now at Argonne National Laboratory.

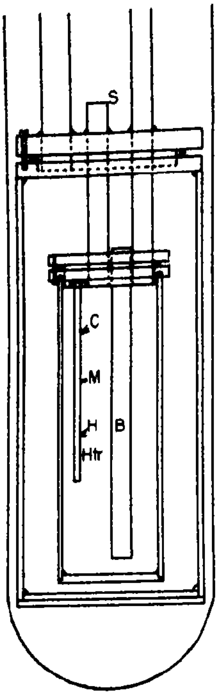

Fig. 1 The cryostat. C and H refer to cold and hot junctions of Au, 0·028% Fe–chromel thermocouples attached to the crystal at the same point as the Pb–crystal thermocouple junction. M is another Au, 0·028% Fe–chromel thermocouple junction for measuring the crystal temperature. Htr refers to the heater wound on the crystal. B is a binding post and S an epoxy seal through which the ΔT and T thermocouple leads were extracted.

designed so that measurements can be made from 1° to 300°K in the same apparatus. For measurements below 4·2°K the outer can is removed and the temperature of the inner can and crystal is adjusted by pumping on the surrounding liquid helium. Between 4·2° and 35°K the space between cans is filled with helium at a controlled pressure. This is essential to give a larger heat leak to the bath, since large heater powers are necessary in this range to give a measurable temperature gradient down the crystal. Above 35°K the space is evacuated during a measurement, but helium can be introduced at any time to lower the crystal temperature between measurements. Above 77°K nitrogen is used as the cryogenic fluid. The inner can is always evacuated and all leads are wrapped many times about the binding post B before going to the crystal. The Pb leads of the $\Delta\phi$ thermocouple were lead up the pumping tube and eventually were taken out through an epoxy seal. The leads from the ΔT and T thermocouples were taken through the epoxy seal S and joined to copper leads below the liquid helium or nitrogen level.

Samples

Measurement of absolute thermopower was made on single crystal rods of magnesium, zinc and cadmium, oriented parallel and perpendicular to the hexagonal axis. In Table 1 we give the sources of the single crystals used, the purities of the starting materials and the residual resistance ratios, $\rho(300°\text{K})/\rho(4{\cdot}2°\text{K})$.

The cadmium crystals were made in a horizontal zone refiner using a heat lamp focused on the crystal to produce the molten zone. The starting material, '69' Cominco Cadmium, was melted in a carbon crucible in an atmosphere of hydrogen and carefully seeded to give the required orientation.

Table 1. *Sources of samples, purity of starting materials and residual resistance ratios* ($\rho(300°K)/\rho(4{\cdot}2°K)$) *of the crystal samples*

		Source	Purity	R.R.R.
Cd	⊥	M.S.U.	'69'	24000
	∥	M.S.U.	'69'	44000
Zn	⊥	Alfa inorganics	'69'	2600
	∥	R.C.I.	'59'	15000
Mg	⊥	Aremco	'49'	24
	∥	Aremco	'49'	65

3. FERMI SURFACES

In this section we describe features of the Fermi surfaces of Cd, Zn and Mg important to this investigation.

Figure 2 is an O.P.W. model for the Fermi surface of magnesium[2]. Shown reduced into the 1st Brillouin zone (a) is a 2nd band hole surface usually referred to as the 'monster'. The piece labelled (b) is a 1st band hole pocket, hereafter referred to as a 'cap'. Inset (c) pictures a 3rd band electron surface usually called the 'needle'. Inset (d) is the 3rd band 'lens'. Inset (e) is the last electron sheet in the 3rd band often called the 'butterfly'. The last sheet, (f) is an electron surface in the 4th band referred to in this work as the 'cigar'.

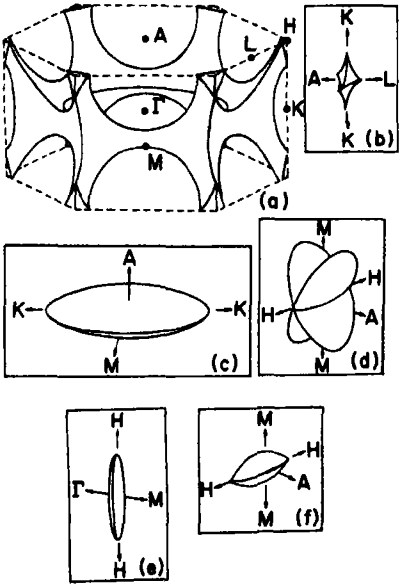

Fig. 2. O.P.W. model for the Fermi surface of magnesium (after Ketterson and Stark[2]): (a) monster (holes); (b) caps (holes); (c) lens (electrons); (d) butterflies (electrons); (e) needles (electrons); (f) cigars (electrons).

This surface is typical of all three of the hexagonal metals we have studied. Certain changes in the O.P.W. picture for the other two metals result from their differing c/a ratios. For zinc with c/a ratio approximately 1·831[3], the needles shrink considerably in girth and tend to become more representative of their name, while the first zone caps and the monster tentacles enlarge[4]. For cadmium the c/a ratio, 1·864, has exceeded the critical value of 1·8607 at which Harrison[4] has calculated that the needles will disappear. There is also evidence that the monster waist is pinched off in Cd, breaking its < 1100 > connectivity. Furthermore it is likely that the third zone butterflies and 4th zone cigars lie above the Fermi level and consequently are empty[5].

A host of experimental evidence supports the topological truth of the above statements concerning the Fermi surfaces of these Group II metals. We cite the most recent and complete work here for Cd[3,6,7] Zn[3,8,11] and Mg[2,9,10].

The calipers of each of the various Fermi surfaces, for directions perpendicular and parallel to the c-axis, are shown in Table 2. Caliper data were culled from the sources listed above. Where only areas are quoted, simple assumptions were made with the O.P.W. model as a guide in converting to calipers.

4. RESULTS

The thermopowers for Mg, Zn and Cd are shown in Figs. 3–6. The results for Zn and Cd agree quite well with those of Gruneisen and Goens[12], but their results extend down to 20°K only. Furthermore their data were taken with copper as the reference metal, and it is well-known that the thermopower of copper is very sensitive to iron impurity at the low temperatures in which we are primarily interested. We notice that for each metal there is a pronounced peak in the thermo-

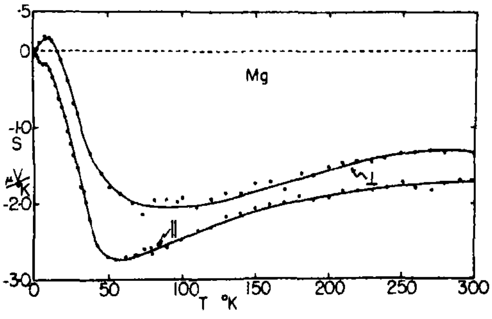

Fig. 3. Thermopower of magnesium.

Table 2. Caliper dimensions D associated with different sheets of the Fermi surfaces of Cd, Zn, and Mg. Questionmarks stand for caliper dimensions we were unable to attain from present data on the Fermi surfaces. Blank entries indicate the absence of these parts of the Fermi surface. 'e' and 'h' represent electrons and holes respectively

Metal		Cd	Zn	Mg
Surface		$D(\text{Å}^{-1})$	$D(\text{Å}^{-1})$	$D(\text{Å}^{-1})$
1st band caps (*h*)	⊥	0·3	0·3	0·045
	∥	0·505	?	0·166
2nd band monster waist (*h*)	⊥	—	0·074	0·189
	∥	—	0·026	0·242
2nd band monster tentacles (*h*)	⊥	0·384	0·33	?
	∥	--	?	0·09
3rd band needles (*e*)	⊥	—	0·02	0·189
	∥	–	—	?
3rd band lens (*e*)	⊥	1·56	1 59	1·17
	∥	0·552	0·53	0·30
3rd band butterfly (*e*)	⊥	—	?	0·68
	∥	–	0·73	0·77
4th band cigars (*e*)	⊥	—	0·11	0·16
	∥	—	0·11	0·16

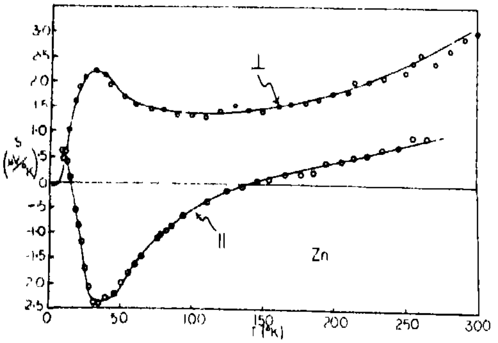

Fig. 4. Thermopower of zinc.

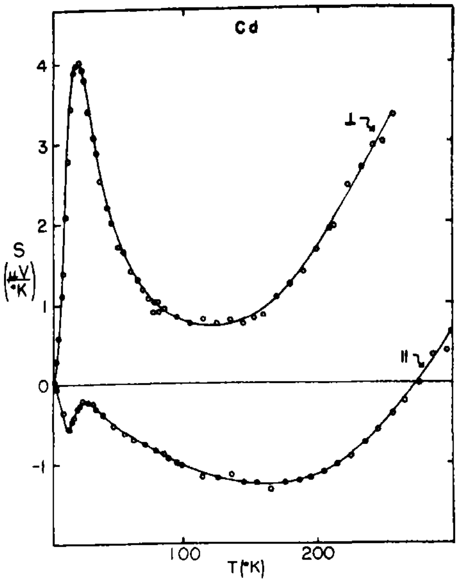

Fig. 5. Thermopower of cadmium.

power for T between $\theta_D/10$ and $\theta_D/5$ ($\theta_D =$ 188°K, 308°K and 350°K, for Cd, Zn and Mg respectively[13]). This is the region where the phonon drag peak commonly occurs in many metals including the noble and alkali metals[14–18], tin[19], and lead[20]. Furthermore, it is in this region that the peak in the lattice thermal conductivity occurs in many metals[21,22]. We assume that the phonon drag thermopower begins to decrease here because the effect of the diminishing relaxation time for phonon–phonon umklapps begins to be appreciable at this point. The sharpness of the peak will depend on the purity of the metal and we suggest below that it will also depend on the shape of the Fermi surface. By comparison with other metals we expect that phonon drag effects may be appreciable up to room temperature, but at that stage we would anticipate that diffusion thermopower becomes the larger component. It is clear from the data near room temperature that the diffusion thermopower is highly anisotropic especially in zinc and cadmium. The separation of the diffusion and phonon drag thermopower cannot be performed with any degree of

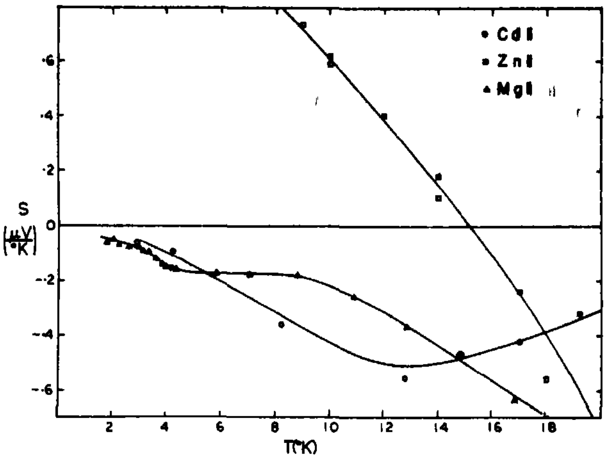

Fig. 6. Comparison of $S_{\parallel}$ for magnesium, zinc and cadmium at low temperatures.

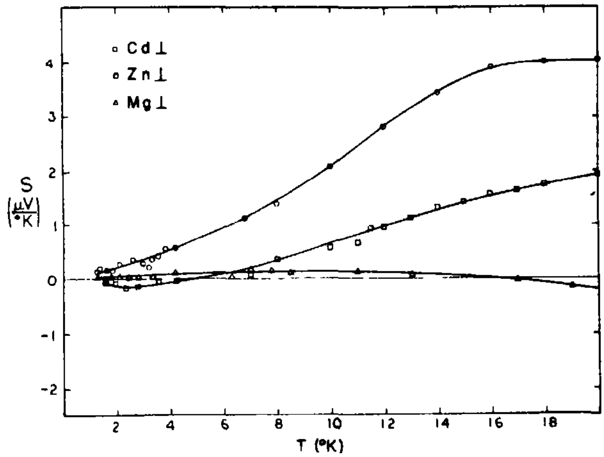

Fig. 7. Comparison of $S_{\perp}$ for magnesium, zinc and cadmium at low temperatures.

confidence at this stage, but we tentatively assume that the diffusion thermopower is a monotonically increasing function of temperature with the same sign as the high temperature thermopower. In the following discussion we refer to the parallel and perpendicular components of thermopower by the appropriate subscripts to the chemical symbol for the metal.

5. DISCUSSION

We consider first $Cd_{\perp}$ and $Zn_{\perp}$. These are rather similar in general appearance. However, there is one significant difference. At the lowest temperatures the thermopower of $Cd_{\perp}$ remains positive whereas in $Zn_{\perp}$ there is a distinct negative dip. We suggest that this difference arises from the presence of the needles in Zn and their absence in Cd. For $S_{\perp}$ the phonon flux is perpendicular to the major axis of the needles as shown in Fig. 8a. A phonon $\mathbf{q}$ interacts with an electron with initial velocity $\mathbf{v}_i$ and causes the transition to the state of final velocity $\mathbf{v}_f$. In the process

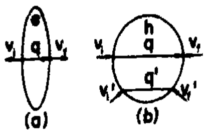

Fig. 8. Electron scattering by phonons across (a) electron and (b) hole sheets of the Fermi surface.

the electron velocity is reversed and this leads to a negative component of phonon drag thermopower. Order of magnitude calculations indicate that at ~ 2–3°K there are sufficient phonons with appropriate wave vector to produce an effect of the observed size.

Notice that a transition across a full region (Fig. 8) usually leads to negative phonon drag contributions, and transitions across an *empty region lead to* a positive phonon drag thermopower. More precisely the contribution of a phonon of wave vector **q** to the phonon drag thermopower is proportional to $\nabla_q\omega.(\tau_i\mathbf{v}_i-\tau_f\mathbf{v}_f)$ where ω is the phonon frequency, τ_i and τ_f are electron relaxation times for electrons in initial and final states respectively, and $\mathbf{v}_i$, $\mathbf{v}_f$ are electron velocities in initial and final states respectively[23–25] $\nabla_q\omega$ is just the sound velocity. If we assume $\nabla_q\omega$ and **q** to have the same direction and $\tau_i=\tau_f$ then the contribution of the phonon of wave vector **q** is proportional to $\mathbf{q}.(\mathbf{v}_i-\mathbf{v}_f)$. On this simplified basis phonons like those labelled **q** in Fig. 8 make a larger contribution than those labelled **q**'. In what follows we will therefore concentrate our attention on those phonons which have $|\mathbf{q}|$ equal to the caliper dimension of the Fermi surface in the direction of the phonon flux.

At higher temperatures we expect that the number of phonons capable of crossing the next largest piece of Fermi surface to increase to the stage when they make the predominant contribution. The next largest pieces of Fermi surface as far as $Cd_\perp$ and $Zn_\perp$ are concerned are the caps and monster tentacles (Table 2) and possibly the waists of the second band monster in *Zn*. These are hole surfaces, and the caps and monster tentacles are nearly the same size for the two metals. We, therefore, propose that the large peaks at ~ 30° are caused by contributions from the caps and tentacles. At this temperature it would appear that phonon–phonon scattering begins to predominate causing the observed rapid decrease in thermopower and tending to obliterate further detail which might be ascribed to Fermi surface topography, though the rapidity of the decrease in $Cd_\perp$ in particular might be in part caused by negative contributions from the larger pieces of Fermi surface most of which are electron surfaces.

The Fermi surface of magnesium suggests that we might find significant differences in $S_\perp$. The needles are comparatively gross objects and the smallest pieces of Fermi surface are the caps. At the lowest temperatures we propose that the caps make the predominant positive contribution, but as the temperature increases the negative contributions from the needles, the fourth band cigars and later the butterflies and lens take over the leading role.

For $Zn_\parallel$ the data have two distinct extrema, although we can only guess at the exact position of the lowest temperature peak. (The crystal fractured before the measurements below 4·2°K could be taken). The piece of Fermi surface with the smallest caliper dimension is the monster waist. This being a hole surface we expect the observed positive contribution at the lowest temperatures. We ascribe the large negative thermopower thereafter to the electron surfaces, the fourth band cigars, third band lens and butterflies which have caliper dimensions ascending in that order. *Cd* has the monster waists pinched off and an initial positive contribution like that observed in $Zn_\parallel$ is absent in $Cd_\parallel$. The caps for this direction present much less area to the phonon flux and contributions from the monster tentacles which were important in $Cd_\perp$ and $Zn_\perp$ will be negligible in this direction. We, therefore, anticipate the comparatively small positive contribution from the caps observed at ~ 30°K. In $Zn_\parallel$ this contribution appears to be swamped by the much larger negative components.

There is no obvious reason for the small kink at 6°K in *Mg* (Figs. 3,6). Considering the low sample purity it is possible that it is associated with a resistance anomaly observed by Rosenberg[26]. Here we have a collection of surfaces which are not appreciably different in caliper dimension. It appears that the electron sheets, the cigars, and lens win out over the hole sheets, the caps and monster waist in producing the negative extremum at 50°K. This is not surprising since both hole surfaces present small areas to the phonon flux compared with the electron surfaces. Indeed the fact that $S_{\parallel}$ is always less than $S_{\perp}$ in the three metals in all but the lowest temperature regions may be caused by the large area (and thus the number of scatterable electrons) which the lens presents to phonons in the measurement of $S_{\parallel}$.

6. CONCLUSIONS

The low temperature thermopower data generally supports the hypotheses:

(1) The sign of the thermopower at the lowest temperature is determined by the nature, hole or electron, of the piece of Fermi surface with the smallest caliper dimension.

(2) As the temperature is increased, contributions from other regions of the Fermi surface successively predominate in the same order as their caliper dimension increases. The agreement is particularly strong in the following instances:

(a) The initial negative thermopower in $Zn_{\perp}$ correlates well with the presence of small needles in zinc. Conversely the absence of this initial negative dip in $Cd_{\perp}$ and $Mg_{\perp}$ is consistent with the complete absence of needles in *Cd* and with the presence of very gross needles in magnesium.

(b) The initial positive thermopower in $Zn_{\parallel}$ appears to be associated with the small monster waists in zinc. Again the absence of this positive thermopower in $Cd_{\parallel}$ and $Mg_{\parallel}$ is consistent with the absence of monster waists in cadmium and with the presence of larger waists in magnesium.

(c) The similar positive peaks in $Zn_{\perp}$ and $Cd_{\perp}$ appear to arise from the approximately equal caps in these metals. The smaller peak at lower temperatures in $Mg_{\perp}$ is in agreement with this picture.

At higher temperatures where many portions of the Fermi surface contribute to phonon drag, the correlations between thermopower and the Fermi surface are not so distinct and the effects are further confused by the incidence of phonon–phonon umklapp processes.

Perhaps more reliable correlations, particularly at the higher temperatures could be made if the phonon drag contribution could be unambiguously separated from the diffusion thermopower. For metals with complicated Fermi surfaces this is a difficult problem to solve analytically. An experimental separation could be made in magnesium by making a dilute alloy of cadmium in magnesium. The heavy cadmium atoms would then act as good phonon scatterers and reduce the phonon drag contribution markedly, while producing minimal changes in the diffusion thermopower, since the two metals are isoelectronic.

Acknowledgement—The authors are indebted to Dr. F. J. Blatt for numerous discussions and his critical reading of the manuscript.

REFERENCES

1. JAN J. P. and PEARSON W. B., *Phil. Mag.* **8**, 911 (1963).
2. KETTERSON J. B. and STARK R. W., *Phys. Rev.* **156**, 748 (1967).
3. GIBBONS D. F. and FALIKOV L. M., *Phil. Mag.* **8**, 177 (1963).
4. HARRISON W. A., *Phys. Rev.* **118**, 1190 (1960).
5. JONES R. C., GOODRICH R. G. and FALIKOV L. M., *Phys. Rev.* **174**, 672 (1968).
6. TSUI D. C. and STARK R. W., *Phys. Rev. Lett.* **16**, 19 (1965).
7. GRASSIE A. D. C., *Phil. Mag.* **9**, 847 (1964).
8. HARRISON W. A., *Phys. Rev.* **126**, 497 (1962).
9. PRIESTLY M. E., *Proc. R. Soc.* **A276**, 258 (1963).

10. FALIKOV L. M., *Phil. Trans. R. Soc.* **A255**, 55 (1963).
11. JOSEPH A. S. and GORDON W. L., *Phys. Rev.* **126**, 489 (1962).
12. GRUNEISEN E and GOENS E., *Z. Phys.* **37**, 278 (1926).
13. SMITH P. L. and WOLCOTT N. M., *Phil. Mag.* **8**, 854 (1956).
14. MACDONALD D. K. C., PEARSON W. B. and TEMPLETON I. M., *Proc. R. Soc.* **248A**, 107 (1958).
15. GOLD A. V., MACDONALD D. K. C., PEARSON W. B. and TEMPLETON I. M., *Phil. Mag.* **5**, 765 (1960).
16. PEARSON W. B., *Phys. Rev.* **119**, 549 (1960).
17. PEARSON W. B., *Can. J. Phys.* **38**, 1048 (1960).
18. BLATT F. J. and KROPSCHOT R. H., *Phys. Rev.* **118**, 480 (1960).
19. FRYER R., LEE C. C., ROWE V. A. and SCHROEDER P. A., *Physica* **41**, 1491 (1965).
20. GOLD A. V. and PEARSON W. B., *Can. J. Phys.* **39**, 445 (1961).
21. KEMP W. R. E., KLEMENS P. E., TAINSH R. J. and WHITE E. K., *Acta Met.* **5**, 303 (1957).
22. KEMP W. R. E., KLEMENS P. E., SREADHAR A. K. and WHITE E. K., *Proc. R. Soc.* **A233**, 480, (1956).
23. ZIMAN J. M., *Adv. Phys.* **10**, 1 (1961).
24. BAILYN M., *Phys. Rev.* **112**, 1587 (1958).
25. BAILYN M., *Phys. Rev.* **120**, 381 (1960).
26. ROSENBERG H. M., *Phil. Mag.* **45**, 73 (1954).

J. Phys. Chem. Solids Pergamon Press 1970. Vol. 31, pp. 9–18. Printed in Great Britain.

MÖSSBAUER STUDIES OF THE LITHIUM FERRITE-ALUMINATE SYSTEM

P. RAJ and S. K. KULSHRESHTHA
Bhabha Atomic Research Centre, Chemistry Division, Trombay, Bombay-85, India

(*Received* 18 *December* 1968; *in revised form* 2 *July* 1969)

Abstract—Mossbauer studies of the series $Li_{0.5}Fe_{2.5-a}Al_aO_4$ where 'a' has values from 0 to 2·5 have been carried out. It is observed that in addition to the six line nuclear Zeeman spectrum, a doublet also appears at the centre and the intensity of this doublet increases with the increasing aluminium content. As a consequence of magnetic dilution, some iron species are isolated from the other magnetic species and have a short range of magnetic order. This results in varying sizes of magnetic clusters; the regions which as a whole have very little magnetic interaction with the surroundings but within which there can be any type of magnetic ordering. The relaxation rate is much faster in the smaller clusters (also referred to in literature as superparamagnetic clusters) and give rise to paramagnetic spectrum. An attempt has been made to find the relative number of iron species which give rise to paramagnetic spectrum in terms of the surrounding non-magnetic neighbours. The anomalous magnetisation behaviour of this series of compounds and the temperature dependence of the hyperfine magnetic fields at the two sites has been discussed.

INTRODUCTION

MÖSSBAUER studies of a number of ferrimagnetic spinels have already been carried out[1–6]. The initial experiments[1] have shown that the magnetic fields at the tetrahedral and octahedral sites are about equal and therefore one obtains only one sextet with rather broad lines. There is now ample experimental evidence[3, 6] showing that the experimentally observed spectra can in general be resolved into two sextets with their centroids shifted with respect to each other. The splittings of the two sets determine the hyperfine magnetic fields and their centroids give the isomeric shifts at the corresponding sites.

It has been shown in numerous other experiments[7–9] that the value of the magnetic field at the nucleus is closely related to the saturation magnetisation, a macroscopic property. Extensive crystallographic and magnetic studies[10, 11] of the series under study have shown that all types of anomalous magnetisation curves are obtained. This anomalous magnetisation behaviour is expected on the basis of Neel's Molecular field theory[12] of ferrimagnetism which predicts a different temperature dependence of the two sublattice magnetisations. We therefore expected a different temperature dependence of the magnetic fields at the two sublattice sites. It was with this point of view that the Mössbauer study of the above series was undertaken.

EXPERIMENTAL

The compounds with compositions $a = 0{\cdot}67$, 0·88, 1·08, 1·20 and 1·80 were prepared by mixing the $Li_{0.5}Fe_{2.5}O_4$ and $Li_{0.5}Al_{2.5}O_4$ at about 1250°C followed by cooling in the furnace itself, as it is known[10] that there is no miscibility gap above 1180°C. $Li_{0.5}Fe_{2.5}O_4$ and $Li_{0.5}Al_{2.5}O_4$ were prepared from the metal nitrates by first heating at low temperature till decomposition followed by heat treatment at about 1210°C for 40 hr. The samples were left to cool in the furnace itself. The identity of the compounds was confirmed by taking their X-ray powder diffraction patterns.

The Mössbauer spectra of these compounds have been taken using a constant velocity cam drive with a single channel analyser. The detector used is a proportional counter with a resolution of about 15 per cent for the 14·4 keV γ-rays. The source used is ^{57}Co in Pd-matrix (unless specified otherwise in the spectra). The absorbers used for room temperature measurements were prepared by spreading the compounds containing approximately 0·7 mg $^{57}Fe/cm^2$ on thin mylar foils and holding them by use of binding material. The absorbers used at other temperatures were in the form of coins made by pressing the compound after mixing with Li_2CO_3. The absorber used for the measurements at liquid nitrogen temperature contained approximately 0·5 mg $^{57}Fe/cm^2$.

RESULTS AND DISCUSSION

The room temperature spectra in Figs. 1(a)–(e) correspond to 'a' values 0, 0·67, 0·88, 1·20 and 1·80 all normalised to the same maximum count rate. Figure 1(a) which corresponds to $Li_{0.5}Fe_{2.5}O_4$ shows only one sextet but the line widths are too broad to characterise a single pattern. It can be resolved into two sets of six line spectra corresponding to the two sublattice sites as has been reported in a recent study[6]. Their reported values of the magnetic fields at the tetrahedral and octahedral sites are 505 and 510 kOe respectively. These values are in close agreement with our average value of (508 ± 5) kOe. In Figs. 1(b)–(e), we find that in addition to the six line pattern a new set of two lines appears at the centre and the intensity of this doublet increases with increasing aluminium content. The centroids of the magnetic and quadrupole patterns are shifted with respect to each other, the later being more negative by approximately 0·13 mm/sec. The splittings of the doublets are found to be almost independent of temperature and aluminium concentration. At room temperature, the average value of the magnetic field of the aluminium substituted compounds does not decrease monotonically with increasing aluminium content, as should be expected from the large variation of their Neel temperatures T_N. The value of the magnetic field when calculated from the separation between the outermost lines of the magnetic pattern is of the same order of magnitude and is equal to (487 ± 7) kOe, but the field measured from the innermost lines of the sextet decreases with increasing value of 'a'.

Figures 2(a)–(d) correspond to 'a' value 1·08 and show spectra at −195°, 24°, 180° and 380°C respectively. Figure 2(a) shows that at liquid nitrogen temperature the value of the magnetic field is (511 ± 5) kOe and the doublet does not disappear. However, it may disappear if we go down to still lower temperatures. Figures 2(b) and (c) show that the average magnetic fields are (480 ± 5) kOe at 24°C and (405 ± 5) kOe at 180°C. At 380°C in Fig. 2(d), the spectrum is only a doublet showing that the Neel temperature is below this temperature. The magnetic hyperfine split lines are numbered as W_1 $W_2 \ldots W_6$ in order of increasing energy and W_{16} stands for the separation between W_1 and W_2.

A salient feature of these spectra is that on increasing the aluminium content or on increasing the temperature of a given composition, the outermost lines (W_1 and W_6) of the magnetic hyperfine split spectra broaden considerably as compared to the inner ones and also the ratio (W_{16}/W_{34}) increases. The broadening of the outermost peaks is partly due to the instrumental broadening and varying environments for iron species resulting in a spread of magnetic fields. However the increase of the ratio (W_{16}/W_{34}) shows that the relaxation effects are responsible for this type of behaviour.

The observed Zeeman patterns do not show any asymmetry in spite of the fact that the nuclei giving rise to the magnetic pattern are also subjected to nuclear quadrupole interactions. The fact that electric field gradient does exist at the iron sites is clear from the Mössbauer spectra of $Li_{0.5}Fe_{2.5}O_4$ [6] above its T_N and for $a = 1.08$ at 380°C Fig. 2(d), both showing quadrupole doublets.

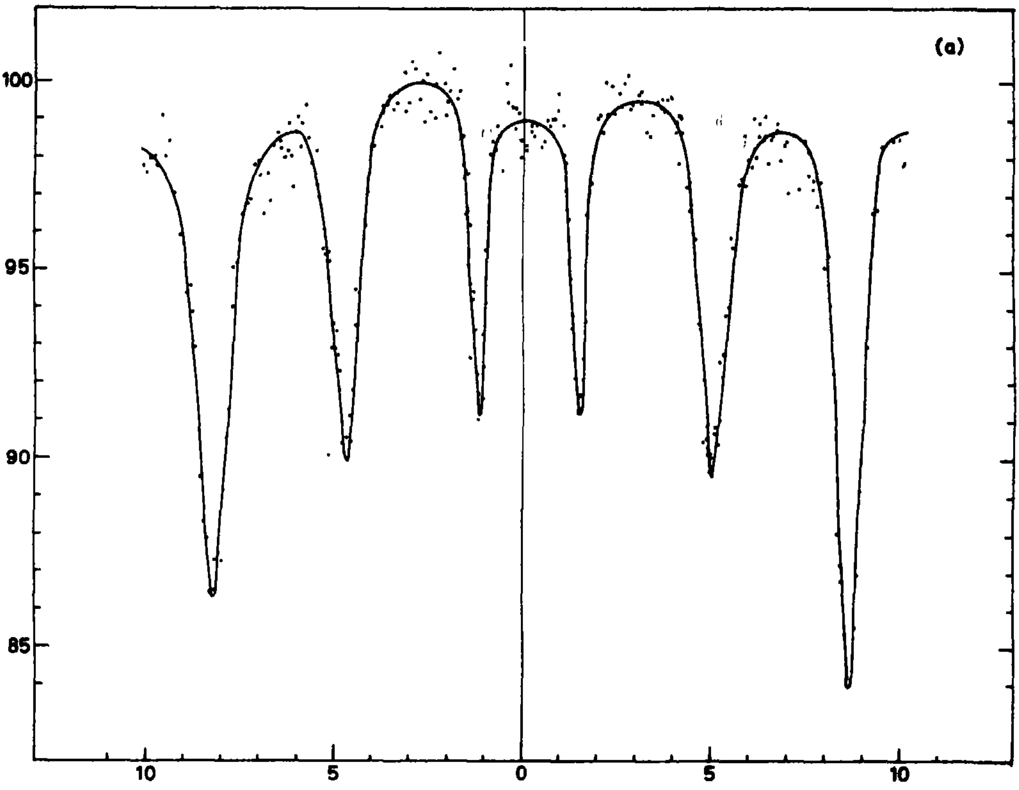

Fig. 1(a).

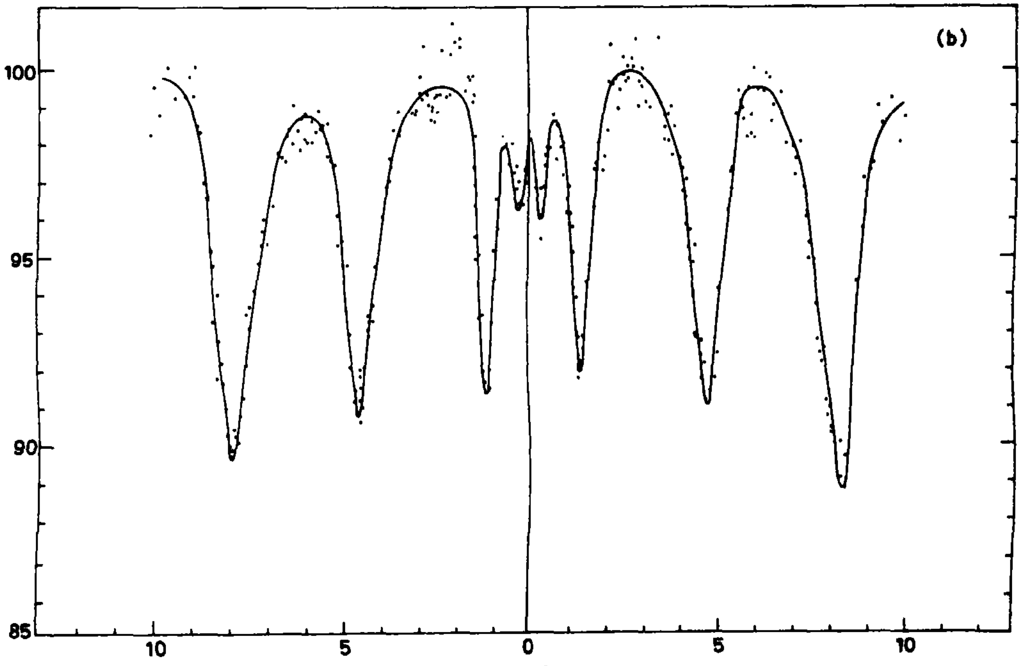

Fig. 1(b).

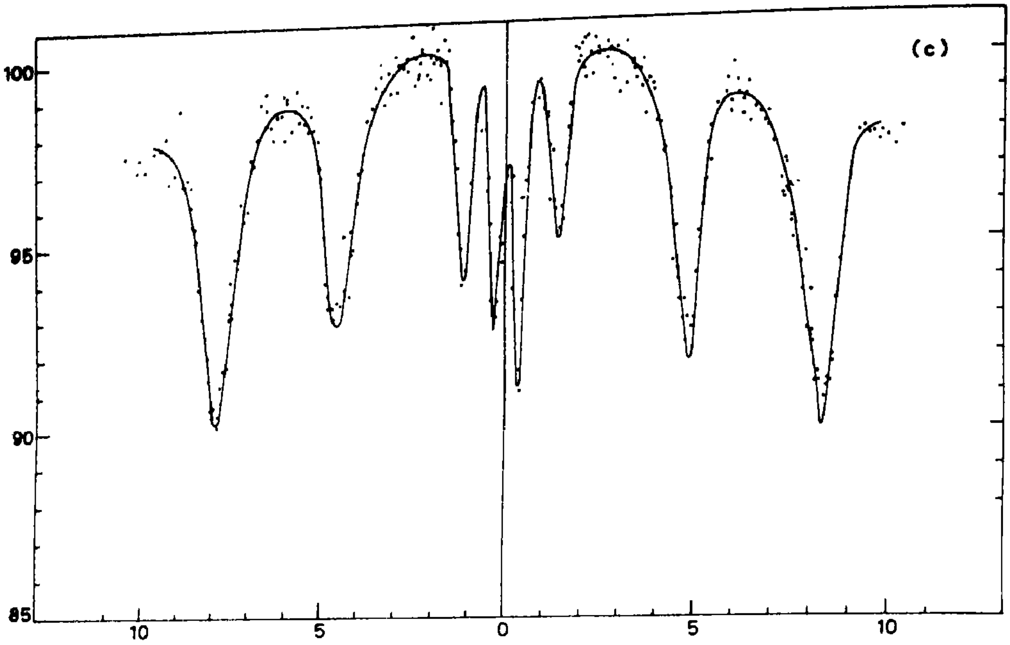

Fig. 1(c).

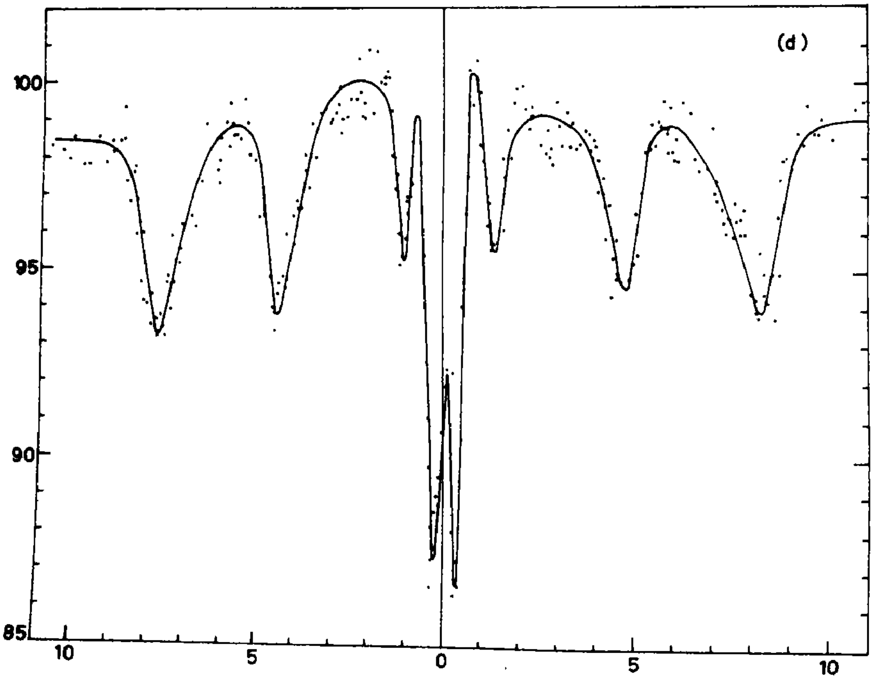

Fig. 1(d).

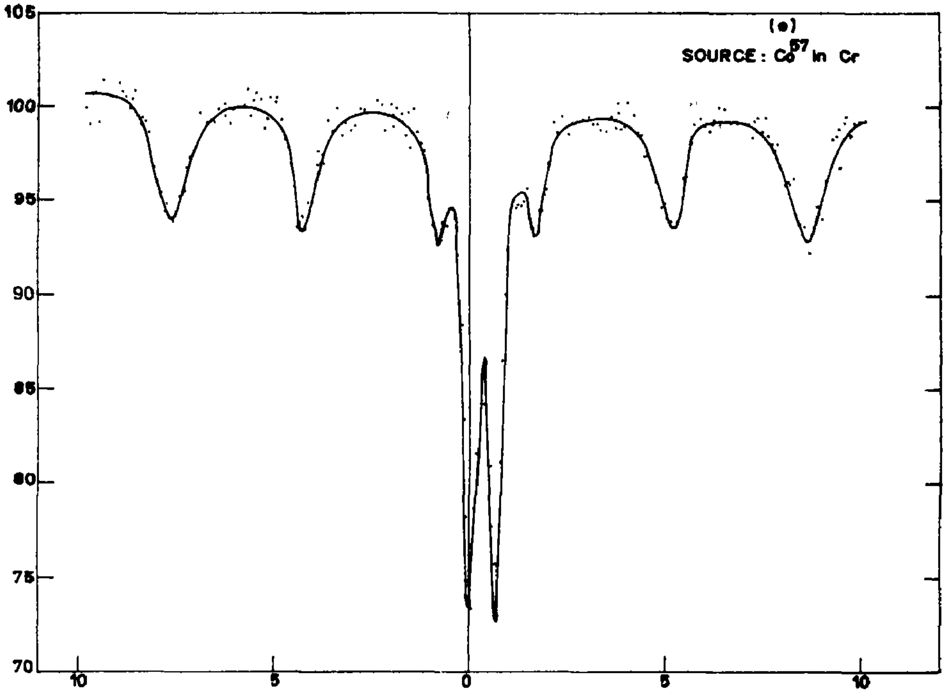

Fig. 1(e).

Fig. 1. Mossbauer spectra of $Li_{0.5}Fe_{2.5-a}Al_aO_4$ containing approximately 0·7 mg ^{57}Fe/cm^2 at 24°C. (a) '*a*' = 0 and source in Palladium matrix. (b) '*a*' = 0·67 and source in Palladium matrix. (c) '*a*' = 0·88 and source in Palladium matrix. (d) '*a*' = 1·20 and source in Palladium matrix. (e) '*a*' = 1·80 and source in Chromium matrix.

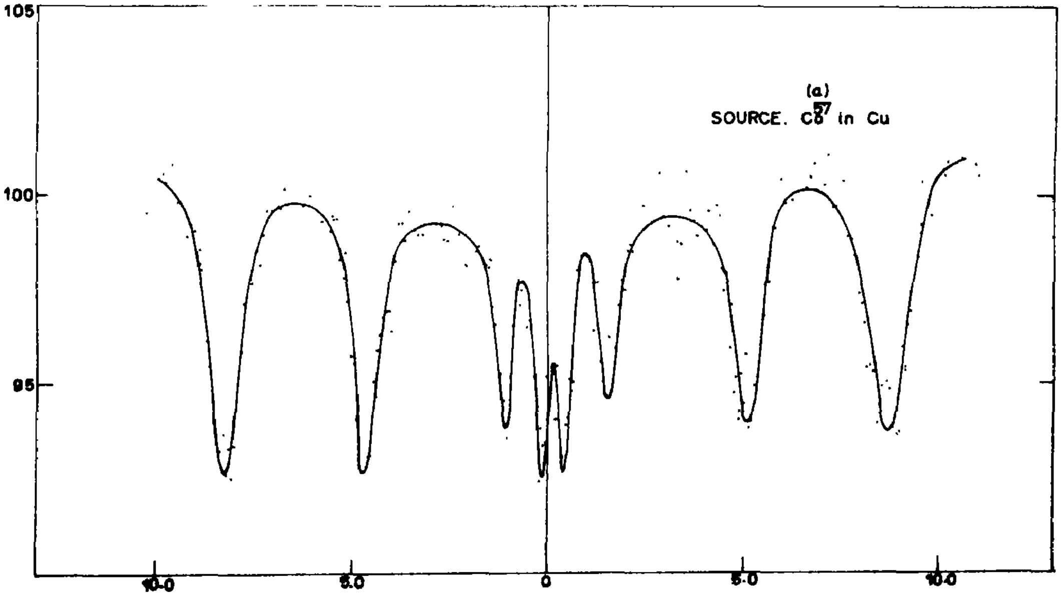

Fig. 2(a).

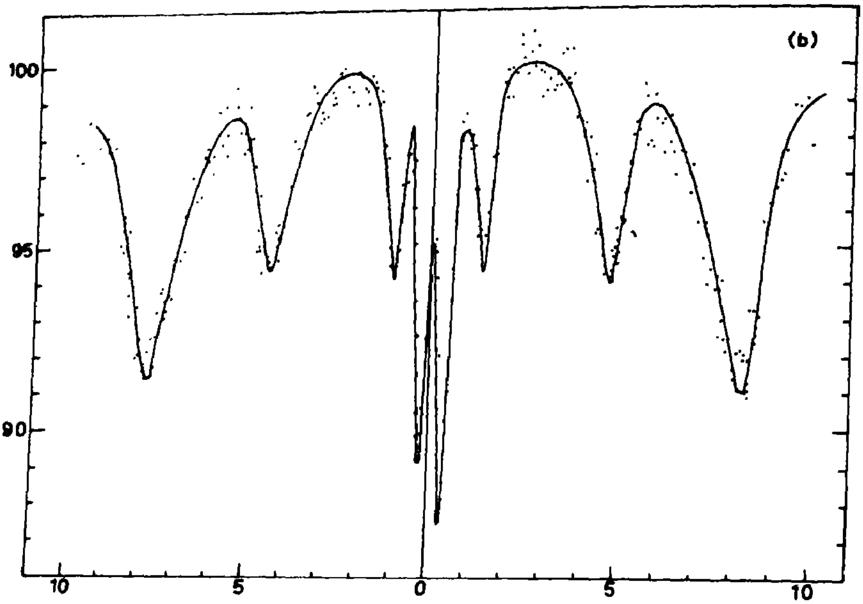

Fig. 2(b).

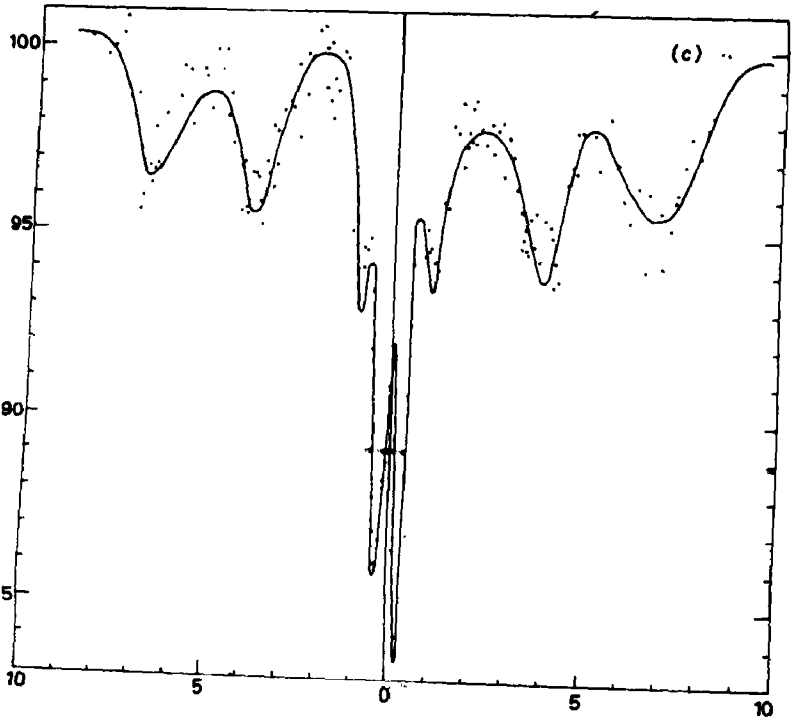

Fig. 2(c).

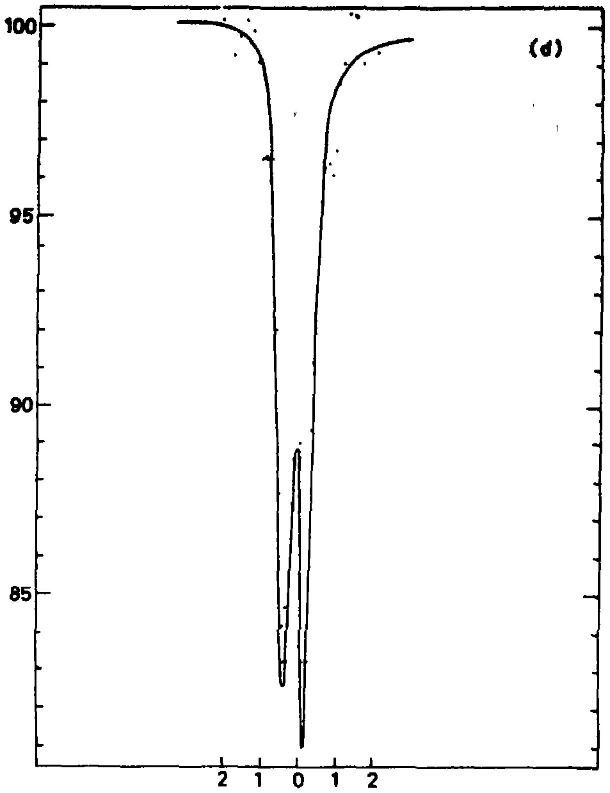

Fig. 2(d).

Fig. 2. Mossbauer spectra for '*a*' = 1·08. (a) Temperature −195°C, absorber thickness ≃ 0·5 mg ^{57}Fe/cm^2 and source in copper matrix. (b) Temperature 24°C, absorber thickness ≃ 0·7 mg ^{57}Fe/cm^2 and source in Palladium matrix. (c) Temperature 180°C, absorber thickness ≃ 0·7 mg ^{57}Fe/cm^2 and source in Palladium matrix. (d) Temperature 380,C, absorber thickness ≃ 0·7 mg ^{57}Fe/cm^2 and source in Palladium matrix.

This type of symmetric pattern[13] is expected when the principal *e.f.g.* axis is inclined to the magnetic field direction at an angle $\text{Cos}^{-1}(1/\sqrt{3})$.

The appearance of the doublet in addition to the sextet can be understood in the following way. The direct exchange or super-exchange interactions with the magnetic neighbours are responsible for the magnetic ordering. In the present system under study, replacement of the magnetic atoms involved in an exchange interaction with a given iron atom by non-magnetic Al^{3+} ions, isolates some of the iron species from the rest of the lattice as far as magnetic interactions are concerned. The isolated iron species should relax relatively rapidly while the introduction of additional iron species into the neighbourhood of original one increases the relaxation time. There are a number of papers in literature which have reported Mössbauer effect studies on systems either known or assumed to be superpara-magnetic, some authors have used the term 'short range magnetic order'. Mössbauer spectra of superparamagnetic systems are similar to those of paramagnetic system due to the relaxation effects. The system[14–16] $(1-x)$ $FeTiO_3-x(\alpha-Fe_2O_3)$ has been studied by static magnetisation measurements, Neutron diffraction and Mössbauer studies. The results indicate that in the temperature range where short range magnetic ordering was observed in neutron diffraction studies, the Mössbauer pattern was a single line characteristic of a paramagnetic state. Their results also indicate that for certain region of composition, the superparamagnetic region coexisted with the large clusters having long range magnetic ordering. Ishikawa's study[17] of the Zn Fe_2O_4-$NiFe_2O_4$ system is an evidence of the copresence of clusters of varying sizes. The coexistence of quadrupole doublet and magnetic hyperfine sextet has also been reported in the experiments[18] with ultrafine particles of $\alpha -$ FeOOH (dimensions specified as < 200 Å). The extremely small particles ≈ 50 Å are contributing to the motionally narrowed doublet where as the larger particles are giving rise to the sextet. Nakamura *et al.*[19] have shown that in Ni–Fe alloys the paramagnetic absorption line coexists with the normal ferromagnetic ones. Huffman and Fisher[20] have also obtained similar results in Fe–Al alloys and they have explained their results in terms of nearest neighbour interactions with small correction for the next nearest neighbours.

The presence of the well defined doublets superposed on the magnetic sextets for all aluminium substituted compounds can be explained by assuming (a) that the major contribution to the paramagnetic part of the spectrum arises from the A-site iron atoms. (b) That the change produced by substituting each non-magnetic atom at B-site in the nearest neighbourhood of A-site is quite large as compared to the corresponding change produced when A-site iron atom is replaced. The justification for making these assumptions is based on the following facts.

1. The most important interactions in the spinel compounds are the A–B interactions.
2. Most of the aluminium atoms replace iron atoms at the B-site[11].
3. The centroids of the quadrupole doublets are more negative with respect to the sextets and the tetrahedral sites are characterised by larger covalency i.e. $4s$-augmentation, thus more negative isomeric shifts and lesser magnetic fields.
4. The calculated and observed ratios of the areas under these sextets and doublets are in fairly good agreement if we assume that ten or more nearest nonmagnetic B-site neighbours around A-site Fe-atoms make them behave like paramagnetic species; the other environments contribute very little to the paramagnetic doublets as the corresponding relaxation times are large enough to give rise to magnetic sextets. The above analysis is subject to the following treatment.

Following Richardson[21] we represent a spinel as $M_mN_nO_4$ and its cation distribution as

$$M_{xm}N_{1-xm}[M_{m(1-x)}N_{n-1+xm}]O_4$$

where M and N represent respectively the magnetic and nonmagnetic atoms, the B-site cations are enclosed within the brackets. In our case, $m = (2{\cdot}5 - a)$ and $n = (0{\cdot}5 + a)$. If $F_k{}^{AB}$ represents the probability that out of Z_{AB} i.e. maximum B-site neighbours of any A-site cation, K are nonmagnetic, then $F_k{}^{AB}$ is given by binomial distribution such that

$$F_k^{AB} = {}^{Z_{AB}}C_k\left[\frac{n-1+xm}{2}\right]^k\left[1-\frac{n-1+xm}{2}\right]^{Z_{AB}-K}$$

Similar expressions can be written for $F_k{}^{AA}$, $F_k{}^{BB}$ and $F_k{}^{BA}$. For nearest neighbour interactions, $Z_{AA} = 4$, $Z_{AB} = 12$, $Z_{BB} = 6$ and $Z_{BA} = 6$. As stated above, the sum $(F_{10}^{AB} + F_{11}^{AB} + F_{12}^{AB})$ determines the fraction of A-site magnetic species contributing to the quadrupole doublet. For the above analysis the cation distribution was taken from Schulkes and Blasse[11] where the distribution is known only up to 'a' $= 1{\cdot}0$. An exact cation distribution is required for extending the calculation to higher aluminium concentrations because the ratio of the area of the doublet to sextet sensitively depends on cation distribution.

For higher '*a*' values, considerable amount of aluminium enters into *A*-sites also and therefore it becomes necessary to take into account the fraction of *B*-site atoms which also contribute to the doublet.

Observation of nuclear Zeeman splitting requires two conditions[22] to be fulfilled. (I) The splitting of the nuclear energy levels should be greater than or of the order of natural line width i.e.

$$|g|\beta_n H_z \gtrsim \Gamma \quad \text{or} \quad \frac{|g|\beta_n H_z}{\hbar} \gtrsim \frac{1}{\tau_n}$$

or $\omega_L\,\tau_n \gtrsim 1$ where $\omega_L = |g|\beta_n H_z/\hbar$ represents the nuclear Larmor precession frequency and τ_n is the mean life time of the nuclear excited state. (II) The spin correlation time should be greater than or comparable to the time required for the nucleus to carry out a Larmor precession of one radian i.e. $\omega_L\,\tau_s \gtrsim 1$ or $\omega_L \gtrsim \Omega$ where τ_s is the spin correlation time and $\Omega = 1/\tau_s$ is the spin flip frequency and determines the rate at which the field at the nucleus flips. Ω depends on variables such as temperature and concentration of magnetic species. In view of the largely varying environments as in our case and the complicated expression for the line shape for the case of spin 5/2(Fe^{3+}), we discuss here the essential features of the spectrum assuming that the ion can make transitions between $m_s = +1/2$ and $-1/2$ only. The relaxation rate dependence of the line shape and the nuclear magnetic field as measured from the Mössbauer spectra has been discussed by Blume and Tjon[23], Wickman and Trozzolo [24], Bradford and Marshal[25] and Vander Woude and Dekker[22]. For ordered state the iron spin spends more time in one state as compared to the other. Following Van der Woude and Dekker[22] this partial order can be described by an order parameter such that the probability for $m_s = +1/2$ is $(1+\eta/1-\eta)$ times as large as for $m_s = -1/2$. The order parameter described in this way is proportional to the magnetisation. For nuclear transition between $m_t = -1/2$ to $m_t{}^* = -3/2$, the line shape is given by

$$\mathrm{I}(W) = \frac{2\Omega}{1-\eta}\left[\frac{W^2\eta^2 - \delta^2}{(W^2-\delta^2) + \dfrac{4\Omega^2}{(1-\eta)^2}(W+\eta\delta)^2}\right]$$

where Ω now represents the probability per unit time that an electron spin in the ground state $m_s = +1/2$ jumps to $m_s = -1/2$. For ^{57}Fe there are three values of δ such that $\delta_1 = \frac{1}{2}[W_6 - W_1]$; $\delta_2 = \frac{1}{2}[W_5 - W_2]$; $\delta_3 = \frac{1}{2}[W_4 - W_3]$. Under varying relaxation rates e.g. (I) For slow modulation i.e. $\Omega \ll \delta$, the above equation gives two maxima at $W = \pm\delta$ i.e. peak positions are independent of degree of order. (II) Fast modulation i.e. $\Omega \gg \delta$, one sharp peak is observed at $W = -\eta\delta$. Under this condition the field measured from Mössbauer spectrum is proportional to η i.e. the magnetisation. (III) For $\Omega \approx \delta$. We know that $\delta_1 > \delta_2 > \delta_3$ such that $(\delta_1/\delta_3) = 6{\cdot}35$. A situation can arise such that $\Omega \approx \delta_3$ but much lesser than δ_1, the innermost lines of the sextet appear at about $\pm\eta\delta_3$ but the position of the outermost lines is not much affected. As a result the ratio (W_{16}/W_{34}) increases and outermost lines broaden more than the inner ones. This is what we also observe in our spectra.

From the three cases discussed above, we conclude that for all Al-substituted compounds the relaxation rate for the species giving rise to the sextet is of the same order as δ i.e. 10^8 rad./sec. The magnetic field as determined from the peak positions of the outermost lines of the Mössbauer spectra does not follow the magnetisation. In view of these considerations, the anomalous magnetisation behaviour may not be truly represented in the Mössbauer studies. It is also suggested that the deviation of the magnetic moment value from that given by Neel's theory of Ferrimagnetism may be due to the presence of paramagnetic state and not necessarily due to canted spin alignment.

Acknowledgement—We are very grateful to Dr. P. G. Khubchandani for many valuable discussions and suggestions.

REFERENCES

1. BAUMINGER R., COHEN S. G., MARINOV A., OFER S and SEGAL E. *Phys. Rev.* **122**, 1447 (1961).
2. KELLY W. H., FOLEN V. J., HASS M., SCHREINER W. N. and BEARD G. B., *Phys. Rev.* **124**, 80 (1961).
3. GOLDANSKY V. I., BELOV V. F. *et al., Zh. eksp. teo. Fiz.* **49**, 1681 (1961).
4. HRYNKIEWIEZ *et al., Acta phys. Polon.* **27**, 423 (1965).
5. CHAPPERT J. and FRANKEL R. B., *Phys. Rev. Lett.* **19**, 570 (1967).
6. DES BARROWS F., VICCARO P. J. and ARTMAN J. O., *Phys. Lett.* **27(A)**, 374 (1968).
7. NAGLE D. E., FRAUENFELDER H., TAYLOR R. D., COCHRON D. R. F. and MATTHIAS B. T., *Phys Rev. Lett.* **5**, 364 (1960).
8. VINCENT D. H., PRESTON R. S., HEBERLE J. and HANNA S. S., *Bull. Am. Phys Soc.* **5**, 428 (1960).
9. BAUMINGER R., COHEN S. G., MARINOV A. and OFER S., *Phys. Rev.* **122**, 743 (1961).
10. STRICKER D. and ROY R., *J. Am. ceram. Soc.* **44**, 225 (1961).
11. SCHULKES J. A. and BLASSE G., *J. Phys. Chem. Solids* **24**, 1651 (1963).
12. NEEL L. *Ann. Phys. Paris* **3**, 137 (1948).
13. MATHUR H. B. *et al., Ind. J. Pure appl. Phys.* **5**, 155 (1967).
14. RUBY S. L. and SHIRANE G., *Phys. Rev.* **123**, 1239 (1961).
15. ISHIKAVA Y., *J. phys. Soc. Japan* **17**, 1835 (1962), *J. phys. Soc. Japan* **17**, (Suppl. B-1) 239 (1962).
16. SHIRANE G., COX D. E., TAKEI W. J. and RUBY S. L., *J. phys. Soc. Japan* **17**, 1598 (1962).
17. ISHIKAWA Y., *J. phys. Soc. Japan* **17**, 1877 (1962); *J. appl. Phys.* **35**, 1054 (1964).
18. VAN DER KRAAM A. M. and VAN LOEF J. J., *Phys. Lett.* **20**, 614 (1966).
19. NAKAMURA Y., SHIZA MASAYUKI and SHIKAZONO MAOMOTO, *J. phys. Soc. Japan* **19**, 1177 (1964).
20. HUFFMAN G. P. and FISHER R. M., *J. appl. Phys.* **38**, 735 (1967).
21. RICHARDSON JAMES T., *J. appl. Phys.* **35**, 664 (1964).
22. VAN DER WOUDE and DEKKER A. J., *Phys. Status Solidi* **9**, 775 (1965); *Physica* **33**, 195 (1967).
23. BLUME M. *Phys. Rev. Lett.* **14**, 96 (1965); *Phys. Rev. Lett.* **18**, 305 (1967); BLUME M. and TJON J. A., *Phys. Rev.* **165**, 446 (1968).
24. WICKMAN H. H. and TROZZOLO A. M., *Phys. Rev. Lett.* **15**, 156 (1965).
25. BRADFORD E. and MARSHAL W., *Proc. phys. Soc.* **87**, 731 (1966).

J. Phys. Chem. Solids Pergamon Press 1970. Vol. 31, pp. 19–40. Printed in Great Britain.

LATTICE THERMAL CONDUCTIVITY OF SEMI-CONDUCTORS: A CHEMICAL BOND APPROACH

D. P. SPITZER
American Cyanamid Company, Stamford, Conn. 06904, U.S.A.

(*Received* 16 *April* 1969; *in revised form* 2 *July* 1969)

Abstract – Lattice thermal conductivity data at room temperature are compiled for more than 200 semiconductors. The data for over seventy semiconductors were obtained at our laboratory and are previously unpublished. It is found that lattice thermal conductivity may be correlated rather reliably with crystal structure. In general, increasing coordination of the ions is associated with decreasing thermal conductivity. Low thermal conductivity may also be caused by cation or anion vacancies. Only compounds which have predominantly tetrahedral bonding have thermal conductivities greater than 100 mW/cm-°C. All tetrahedrally-bonded compounds tend to have relatively high thermal conductivity, regardless of the complexity of their structure. At the other extreme, many compounds with higher coordination and partially-filled lattice sites have thermal conductivities below 10 mW/cm-°C. A majority of semiconductors have intermediate structures, and thermal conductivities within the range of values mentioned. Using these correlations, an unknown thermal conductivity can generally be estimated to within a factor of 2.

INTRODUCTION

MOST data on thermal conductivities of semiconductors (at or near room temperature) have been collected during the past ten years, and have been associated with the interest in finding more efficient materials for thermoelectric energy conversion. An extensive study of lattice thermal conductivities of semiconductors was also made at our laboratory in connection with a program on thermoelectric materials. The present paper summarizes our work on thermal conductivity of semiconductors and has two purposes: to discuss the relation between lattice thermal conductivity and chemical bonding and to collect together available data on thermal conductivity of semiconductors (limited collections of semiconductor thermal conductivities have been previously available[1, 2]).

Lattice thermal conductivity data at room temperature are here compiled for more than 200 semiconductors. The data for seventy semiconductors were obtained at our laboratory and are previously unpublished. These latter measurements include those on about twenty compounds not yet reported in the literature. We have attempted to make the data as inclusive as possible, through mid-1968. To limit coverage, however, borides, carbides, nitrides and oxides are not included, although a few of these are semiconductors.

The problem of correlating thermal conductivity data with other parameters and making estimates of thermal conductivities of new materials received a good deal of attention during the more active periods of research on thermoelectric materials. A discussion of most of the methods used to estimate lattice thermal conductivities, k_l, has been given by Goldsmid[3]. These methods include: (1) the formula of Liebfried and Schlomann, which requires an accurate knowledge of the Debye temperature; (2) the formula of Dugdale and MacDonald, which requires the expansion coefficient and velocity of sound; (3) Keyes' relation of k_l to the melting point, density and atomic weight; (4) Goldsmid's own observation that thermal conductivity falls with increasing average atomic weight; and (5) Ioffe and Ioffe's observation that thermal conductivity decreases with increasing ionicity of the bonds between the atoms.

Relations 1–3 are of limited use in predicting thermal conductivities because they require knowledge of data which are even less likely to be known than the thermal conductivity. Generally, by making educated guesses at the parameters involved one may arrive within an order of magnitude of the correct thermal conductivity. An order-of-magnitude guess is of little advantage, however, considering that the entire range of thermal conductivities of dense solids spans a range of only three orders of magnitude at room temperature, from about 2.10^{-3} to 2 W/cm-°C. Keyes' relation does have an adjustable parameter, which varies over an order of magnitude depending on ionicity of the bonds; by reasonable choice of this parameter, one may be fairly confident of estimating thermal conductivity within a factor of about five.

For predicting thermal conductivities of new materials, the qualitative observations 4 and 5 are probably as useful as the formulas of 1–3. By considering the molecular weight and making a reasonable judgement of the extent of ionicity in a particular compound, it is also generally possible to estimate thermal conductivities of new materials within a factor of five to ten.

The dependence of thermal conductivity on ionicity, first discussed by the Ioffes, has been much elaborated by Suchet *et al.*[4, 5]. This group has extensively correlated lattice thermal conductivity with an ionicity parameter, λ, which depends on crystallographic structure, atomic number, and ionic charge and radius. There is indeed a general trend for decreasing thermal conductivity with increasing λ, but even at a given λ there is a variation of about a factor of ten in thermal conductivity. The correlation with ionicity supposedly takes into account the crystal structure but, in fact, a different curve (k_l vs. λ) results for each structure.

The crystal structure itself actually turns out to be most reliably correlated with thermal conductivity. It has been recognized qualitatively, of course, that thermal conductivity does depend on crystal structure. It is generally known, e.g. that NaCl-type compounds have lower thermal conductivities than zinc blende-type compounds. However, by a more detailed consideration of the type of bonding (in particular, the coordination) for each type of atom in a crystal and, to a lesser extent, the atomic weight, we have found that it is possible to predict thermal conductivities within a factor of two of the correct ones. Our correlations are elaborated in the Discussion section.

EXPERIMENTAL

Most of our own measurements have been made on dense, polycrystalline samples cut from ingots prepared by fusion of a mixture of the elements, as follows. High purity elements (all at least 99·99% pure, except for V and Nb (99·7%) and Ta (99·9%)) were weighed in stoichiometric amounts into a 96% silica glass ampule and sealed at a pressure of less than 10^{-3} Torr. In the case of phosphides and arsenides, the inside surface of the ampule was first carbon-coated by the pyrolysis of acetone. The loaded ampules were heated in a furnace to at least 50°C above the melting temperature in about 4 hr, with the furnace slowly rocking during the heating and holding stages The maximum temperature was held for 2–4 hr, then the rocking was stopped and the furnace cooled, generally at a rate of about 40°C/hr. Samples were ground from these ingots to sizes of about 5 mm × 5 mm cross-section and 4–12 mm in length. For compounds which could not be melted without decomposition, measurements had to be made on pressed and sintered pellets. These were prepared by first reacting stoichiometric amounts of the elements at 300°–500°C for several days in a sealed glass ampule, after which the material was ground up, pressed into pellets, and sintered for several more days. A few compounds which form by peritectic reaction were similarly prepared by lengthy annealings at appropriate low temperatures. Samples that were not prepared by simple fusion are indicated in the tables. A few measurements were made on natural mineral samples (95+% pure) and are so indicated.

At least twenty compounds listed in Tables 1–5 appear to be new and not previously reported. Evidence for the existence of these compounds is based on microscopic examination, differential thermal analysis, and, in a few cases, on X-ray powder diffraction patterns. Some of these new compounds will be reported on in more detail in another publication[6].

Thermal conductivity measurements were made in a steady-state apparatus[7], with an accuracy of 3–5 per cent. Where necessary, direct current electrical conductivities and Seebeck coefficients were also measured, as previously described[8].

THERMAL CONDUCTIVITY DATA

The 200+ semiconductors for which we have lattice thermal conductivity data (at approximately 300°K) are divided among Tables 1–5 according to stoichiometry and whether they are normal or non-normal valence compounds (see Discussion section). For a majority of the compounds, only one reference to thermal conductivity measurement exists. Where several measurements have been made on the same compounds and are in substantial agreement with one another, the earliest measurement is generally cited, unless a later measurement has been made on a sample of significantly better quality. Collected references and selected values are available for some of the compounds that have been frequently measured, e.g. the 3–5 compounds[9]. When quite different results are reported by different workers for the same compounds, two or more entries are made in the table. Possible reasons for some of the discrepancies are discussed below, but gross differences are almost certainly due to differences in the samples themselves rather than to measurement errors. It is, after all, a relatively easy matter to make thermal conductivity measurements with 10–20 per cent accuracy, even though 1–2 per cent accuracy may be very difficult to achieve.

Original publications must be consulted for accuracy of the measurement method used, but they are generally not better than ± 5 per cent and not worse than ± 10 per cent. For nearly all types of thermal conductivity measurements, 5 per cent accuracy is quite adequate, since the thermal conductivities of different samples of the same material generally vary more than this anyway. In compounds where disorder is possible, especially in defect compounds, thermal conductivity has been shown to vary by as much as a factor of three or more, depending on the amount of disorder[10, 11]. Generally, the variance is far less than this, however, and wherever a range of conductivities due to disorder has been found, it is indicated in the tables.

Unless otherwise specified, thermal conductivity measurements were made on a dense polycrystalline ingot, obtained from a melt or by sublimation. Sintered pellets were generally used for compounds of transition elements or rare earths, and such samples are so noted in the tables.

For the great majority of compounds, anisotropy of thermal conductivity is either non-existent or quite small. For isotropic structures, it has always been found that there is no significant difference between measurements made on single crystals and on polycrystals (at least at room temperature). At the extreme, anisotropy in thermal conductivity can be as much as a factor of about ten (for layer compounds, where the bonding in one direction is of the van der Waals type). In most of those cases where large anisotropy is expected (on the basis of the crystal structure), measurements have been made on single crystals.

Data on the following 'compounds' of doubtful existence are not included in the table: $AgFeTe_2$[12, 13], SiTe[14, 15], and $TlBiTe_3$[16, 17, 18] (the first reference in each set of brackets is the original report of thermal conductivity and the second and third references question the existence of the compounds).

Many of the literature references report lattice thermal conductivity specifically. In our own work and for those references that report only total thermal conductivity, we have estimated an electronic component as usual from the Wiedemann–Franz law, and subtracted this from the total thermal conductivity to obtain the lattice component. Electronic thermal conductivity, k_e, is negligible for any semiconductor with an electrical conductivity, σ, less than about $10\,\Omega^{-1}\mathrm{cm}^{-1}$. Less than 20 per cent of the compounds in the tables have an electronic thermal conductivity that is significant compared to the lattice thermal conductivity.

There is generally some uncertainty as to what value to use for the Lorenz number, L, in the Wiedemann–Franz law, $k_e = L\sigma T$, where T = absolute temperature. Fortunately, in all cases where electronic conduction is significant, the Seebeck coefficient has been given together with the electrical conductivity. In principle, one can calculate the position of the Fermi level from the Seebeck coefficient, and the Lorenz number, in turn, may be calculated from the Fermi level, provided the scattering law for the charge carriers is known[19, 20]. Since the scattering law is not generally known (as determined from temperature dependence of carrier mobility), such a calculation is hardly justified. We have instead simply assumed that the Lorenz number is $2(k/e)^2$ (completely non-degenerate case) if the absolute value of the Seebeck coefficient is greater than $150\,\mu V/°C$, and the Lorenz number is $(\pi^2/3)\,(k/e)^2$ (complete degeneracy) if the absolute value of the Seebeck coefficient is less than 50 $\mu V/°C$; for intermediate Seebeck coefficients we interpolate appropriate Lorenz numbers. Any resultant uncertainty in the electronic thermal conductivity is probably always negligible compared to the measurement error in k_{total}, and is definitely negligible compared to the uncertainty in the absolute value of any k_{total} (due to sample imperfections, etc.). Any more accurate estimate of k_e is therefore unnecessary.

We have tried not to include any compounds that are definitely metallic (i.e. do not have a finite energy gap), although it was not always clear from the literature source to which category a material belonged. The Mooser–Pearson criteria[21] for semiconductors were then applied. The reason for not including metallic compounds is primarily that their lattice conductivities are not reliably known when the large electronic thermal conductivity can be only poorly estimated. Generally, trends similar to those we describe for semiconductors are expected among metallic compounds.

The structure data for most of the compounds may be found in the collections by Pearson[22]. Strukturbericht symbols are used wherever they are known.

To give some feeling for the thermal conductivities involved, we recall that 100 mW/cm-°C is approximately the thermal conductivity of stainless steels and 10 mW/cm-°C is approximately the thermal conductivity of ordinary silicate glasses. About half of the semiconductors have thermal conductivities within this range. Thermal conductivities above 100 mW/cm-°C are high for semiconductors; only about an eighth of the compounds in our tables have such high conductivity. At the other extreme, thermal conductivities below 10 mW/cm-°C are certainly very low for crystalline compounds, since such low conductivities are more typical of glasses and polymers (most polymers have conductivities of 2–6 mW/cm-°C).

DISCUSSION

It is first useful to divide all semiconductors into two general groups: normal valence[*] semiconductors are defined as those in which all of their elements appear to have normal chemical valences; non-normal valence semiconductors are those which require anion–anion and/or cation–cation bonds. This causes rather fundamental differences in crystal structures, and it is for this reason that we consider the normal and non-normal valence semiconductors separately at first and later compare the two groups.

Normal valences are considered to be those which the elements have in, say, their halogen salts. For elements in the periodic groups I through IV, this is usually the same as the group number, with the exceptions that Tl may have a valence of either 1 or 3 (generally 1), the valences of Si, Ge and Sn may be either 2 or 4, and that of Pb is always 2. For elements in groups V through VII, the normal valence is 8 minus the group number, with the exception that the phosphorus group elements may also have a valence of 5. For the transition metals, we consider that either 2 or 3 is a normal valence for Fe or Cr, 2 is the normal valence for Mn, Co or Ni, 4 is the normal valence for Ti, and 5 is the valence of V, Nb and Ta. The valences of the rare earths are as given, for example, by Moeller[23], i.e. the valence of 3 is possible for all of the rare earths, with 2 also possible for Sm, Eu and Yb, and a valence of 4 possible for Ce, Pr and Tb. The only actinide element that occurs in our tables is Th, for which the valence is 4.

Further, these two main classifications (normal and non-normal) are also subdivided according to stoichiometry, i.e. according to whether there are more cations than anions, or vice versa, or equal numbers. This helps to group compounds with similar structures together.

Normal valence semiconductors

Most normal valence semiconductors have in common the fact that the anions form a close-packed arrangement—either face-centered cubic (FCC) or hexagonal. These anion arrays contains two tetrahedrally- and one octahedrally-coordinated hole per anion site[24]. If we start with a FCC anion array and fill one of the tetrahedral holes, the zinc blende structure results. The fluorite structure results from filling both of the tetrahedral holes. The NaCl structure results from filling the one octahedral hole. No example is given [24] where one tetrahedral and one octahedral hole are filled, but the structure of Ag_2Se and other I_2–6 compounds may be related to this case, or they may be somewhere between this and the fluorite structure; it is fairly certain at least that there are some cations in both tetrahedral and octahedral sites. Examples are also known where both sets of tetrahedral holes and the octahedral holes are filled, such as in Li_3Bi, but no such compounds are included in our tables. The coordination numbers of the cations and/or anions increase as we fill up the holes in the order listed, and we shall see that lattice thermal conductivities decrease regularly in this order.

Two of the hexagonal analogs are also known; wurtzite is the hexagonal analog of zinc blende, and NiAs is the hexagonal analog of NaCl.

Other normal valence structures can be derived from the structures mentioned above, by having various holes only partially filled. For example, Cd_3As_2 may be derived from the fluorite structure by systematic cation absences in a quarter of the tetrahedral holes, accompanied by some distortion from the cubic symmetry. There are similarly many semiconductors with structures similar to that of zinc blende, but with up to a third of the cation sites vacant. Thermal conductivities of these types of structures are invariably considerably lower than those of the filled structures from which they may be considered to be derived.

We now wish to discuss specific examples to show that lattice thermal conductivities of normal valence semiconductors are related to the coordination of the ions in their structures. Refer first to Table 1, where there are equal numbers of cations and anions. Although this group contains eighty-six compounds, nearly all of them have structures which are either zinc blende type or related, or are sodium chloride or similar.

---

[*] The term normal valence is used here in the same manner as it was by Mooser and Pearson[21]. Various names have been applied to those compounds that are not of normal valence, such as polycationic, polyanionic and anomalous. We refer to them simply as non-normal valence compounds.

Table 1. Lattice thermal conductivity of normal valence semiconductors with cation to anion ratio = 1

No.	Compound	Thermal conductivity mW/cm-°C	Thermal conductivity Reference	Structure (reference)
1	$AgAsSe_2$	4·5	12	Monoclinic – $AgAsS_2$?
2	$AgBiSe_2$	10·3	25	Trigonal; B1 above 287°C
		7·3	12	
3	$AgBiTe_2$	7·6	26	Trigonal; B1 at elevated temp.
4	$AgCeSe_2$	8[a]	4	[33][c]
5	$AgCeTe_2$	6·6[a]	4	[33][c]
6	$AgGaTe_2$	9·5	12	$E1_1$
7	$AgGeBiSe_3$	5·2	27	B1
8	$AgGeSbSe_3$[b]	5·2	27	B1
9	$AgInSe_2$	5[d]	28, 27	$E1_1$
10	$AgGdSe_2$	5·5[a]	4	[33][c]
11	$AgGdTe_2$	4[a]	4	[33][c]
12	$AgInTe_2$	63	26, 29	$E1_1$
		14·8	30, 4	
		12	12	
13	$AgPbBiSe_3$	6·5	27	B1
14	$AgPbSbSe_3$	5·2	27	B1
15	$AgSbS_2$	4·9	12	Monoclinic; B1 at elevated temp.
16	$AgSbSe_2$	10·5	25	B1
		7·5	12	
		4·6	26	
17	$AgSbTe_2$	7	31, 32	B1
18	$AgSnSbSe_3$[b]	5·2	27	B1
19	$AgYTe_2$	7[a]	4	[33][c]
20	AlAs	800	34	B3
21	AlP	900	34, 9	B3
22	AlSb	570	34, 9	B3
23	CdS	200	35	B3
24	CdSe	44	36	B3
25	CdTe	63	10	B3
26	$CdGeAs_2$	40	37	$E1_1$
27	$CdGeP_2$	110	38	$E1_1$
28	$CdSnAs_2$	75	39	$E1_1$
29	$CuAlTe_2$	32·5	28	$E1_1$
30	Cu_3AsS_4	23[e]	27	$H2_5$
		14	40	
31	$CuAsSe_2$	32	12	B3 or hexagonal [41]
32	Cu_3AsSe_4	14	40	Related to B3
33	$CuBiS_2$	5	12	Orthorhombic; similar to $F5_6$
34	$CuBiSe_2$	11	42	Cubic; similar to $F5_6$?
35	$CuFeS_2$[f]	78	27	$E1_1$
36	$CuFeSe_2$	65	12	$E1_1$
37	$CuGaTe_2$	64	12	$E1_1$
		22	43	
38	Cu_2GeS_3	12	44	Tetragonal; distorted B3
		7·7	45	
39	Cu_2GeSe_3	24	44	Tetragonal; distorted B3
		6·9	45	
40	$Cu_2HgGeSe_4$	20	46	Related to B3
41	$Cu_2HgGeTe_4$	13	46	Related to B3
42	$Cu_2HgSnSe_4$	22	46	Related to B3
43	$CuInSe_2$	37	12	$E1_1$
44	$CuInTe_2$	63	29	$E1_1$
		54	26	
		49	12	

Table 1 *(cont.)*

No.	Compound	Thermal conductivity		Structure (reference)
		mW/cm-°C	Reference	
45	$CuPbBiSe_3$	5·6	27	
46	$CuPbSbS_3$[g]	10·1	27	Orthorhombic
47	$CuSbS_2$	15	12	$F5_6$
		20[h]	47	
48	Cu_3SbS_4	27	40	B3
49	$CuSbSe_2$	18	42	$F5_6$
		16[h]	47	
50	Cu_3SbSe_4	26·5	48	B3
		18	40	
51	$CuSbTe_2$	13	26	Rhombohedral; similar to C33
52	Cu_2SiS_3	23	44	Tetragonal; distorted B3
53	Cu_2SnS_3	28	44	B3
54	Cu_2SnSe_3	33	44	B3
		26	27	
55	FeS[i]	33	27	Monoclinic; similar to B8
56	GaAs	440	49, 35, 9	B3
57	GaP	1100	50	B3
		770	34, 9	
58	GaSb	380	35	B3
		330	34, 9	
59	GeTe	13	51	B1
60	HgSe	19	52	B3
		11	53	
61	HgTe	25	54	B3
62	InAs	265	55, 9	B3
63	InP	680	56, 9	B3
64	InSb	165	57, 35, 58, 9	B3
65	InTe[k]	17	103	B37
		6	27	
66	MnTe	15[j]	59	B8
67	PbS	25	60	B1
68	PbSe	17	61	B1
69	PbTe	23	61	B1
70	SmS	25[j]	62	B1
71	SnS	17, $\parallel c$	63	B16
72	SnSe	18	27	B16
		19, $\parallel c$	63	
73	SnTe	15	51	B1
74	TlS[k]	32	103	B37
75	TlSe[k]	20, $\perp c$	103	B37
		12, $\parallel c$	103	
		12	27	
76	TlTe[k]	29	103	Tetragonal; similar to B37
		6	27	
77	$TlBiTe_2$	12	17	$F5_1$
78	$TlGeSbSe_3$	5·1	27	
79	Tl_3NbSe_4	3·3[j]	27	Cubic; similar to B2
80	$TlPbBiS_3$	8·8	27	
81	$TlPbBiSe_3$[b]	9·9	27	
82	Tl_3TaS_4	3·5[j]	27	Cubic; similar to B2
83	Tl_3VSe_4	3·1[j]	27	Cubic; similar to B2
84	ZnS	270	64	B3
85	ZnSe	130	58	B3
86	ZnTe	110	58	B3

Table 1 (*cont.*)

No.	Compound	Thermal conductivity mW/cm-°C	Thermal conductivity Reference	Structure (reference)
87	$ZnGeAs_2$	114	37	$E1_1$
88	$ZnGeP_2$	180	38	$E1_1$
89	$ZnSiAs_2$	140	38	$E1_1$
90	$ZnSnAs_2$	115	39	$E1_1$, ordered
		70	39	$E1_1$, disordered

[a] Presumably for a pressed and sintered pellet.

[b] Reported in reference [77].

[c] Structure of this compound is not known. However, in the structures of some analogous sulfides, $AgTS_2$ (where T = rare earth or Y) [33], the cations have distorted octahedral environments, and some of the compounds have NaCl structure at elevated temperatures. Coordination in these selenides is, therefore, almost certainly octahedral also.

[d] It was thought that the very low value for $AgInSe_2$ might be due to the peritectic nature of the silver 1-3-6_2 compounds. Without sufficient annealing, one might have a mixture of Ag_2Se and In_2Se_3 instead of the ternary phase. Our preparations, however, were definitely single phase, and the same conductivities were measured on samples annealed at 600°C and at 400°C.

[e] Mineral, enargite (from Superior, Arizona).

[f] Mineral, chalcopyrite (from Ajo, Arizona).

[g] Mineral, bournonite (from Wells, British Columbia).

[h] For single crystal, but direction not stated.

[i] Mineral, pyrrhotite (from Devonshire, England).

[j] Pressed and sintered pellet.

[k] $In^{+1}In^{+3}Te_2$, $Tl^{+1}Tl^{+3}S_2$, etc.

The lowest overall coordination we can have in a semiconductor is four. This is the case for the zinc blende structure (B3), its hexagonal analog wurtzite (B4), and the ternary chalcopyrite ($E1_1$), where both the cations and anions occupy tetrahedral holes in the sublattices. We therefore expect compounds with these structures to have relatively high thermal conductivities. All of the 3–5 and 2–6 semiconductors, which have either the B3 or B4 structure, do indeed have high thermal conductivities. The lighter 3–5 compounds have the highest lattice thermal conductivities of all semiconducting compounds.

The 3–5 and 2–6 semiconductors well illustrate the two general trends in lattice thermal conductivity that have been known for some time. Namely: (1) lattice thermal conductivity within a given family of compounds decreases with increasing (mean) atomic weight (CdSe and HgSe are exceptions to this trend); (2) lattice thermal conductivity also decreases with increasing ionicity of bonding. The 2–6 compounds, where there are greater differences in electronegativity between cations and anions (more ionic bonds), always have lower thermal conductivities than adjacent 3–5 compounds (of similar atomic weights); e.g. ZnSe has a lower thermal conductivity than GaAs, etc.

Ternary compounds based on cross-substitution in 3–5 or 2–6 compounds (i.e. 2-4-5_2 and 1-3-6_2 compounds, respectively) also have completely tetrahedral coordination. Relatively high thermal conductivities therefore are expected, but not as high as the binary compounds, due to increased phonon scattering caused by the mass differences of the two cations. Broadly, this is what is found, but the experimental data are not so reliable for the 1-3-6_2 compounds, especially those containing silver.

Similarly, there are several ternary copper compounds (1_3-5-6_4 and 1_2-4-6_3 stoichiometries) with either $H2_5$ or a tetragonally distorted B3 structure. These are still tetrahedrally coordinated compounds, although the tetrahedra are distorted. Thermal conductivities are still rather high, but not quite as high as some of the similar undistorted compounds. Quite disparate conductivities are reported for some of these compounds, especially for Cu_2GeSe_3 (#39). It is possible that the lower value corresponds to more disorder among the cations, but whatever the cause, we prefer the higher value since it is more consistent with the structure.

The $F5_6$ structure consists of weakly-bound wurtzite type layers. Thermal conductivity would be expected to be good (greater than 20 mW/cm-°C) within these layers, but poor (less than 10 mW/cm-°C) across them. The value for $CuBiS_2$ (#33) seems too low for a polycrystalline sample, and may be across the layers. Values reported for #34, 47 and 49 seem reasonable for polycrystalline samples. Single crystal measurements are reported for #47 and 49, but we do not know the direction to which the measurements refer.

There are still other semiconductors where the bonding is primarily tetrahedral and thermal conductivities are consequently high, but these are non-normal valence compounds, which are to be discussed later.

With the NaCl structure (resulting from filling the octahedral hole in a FCC anion array), the coordination of both the cations and anions is increased to six and thermal conductivities are generally considerably lower than for the tetrahedral compounds discussed above. Most ternary compounds with NaCl structure have lattice thermal conductivities below 10 mW/cm-°C.

Other structures which have coordination similar to that in NaCl also have similar thermal conductivities. Here we would like to make the point that one should not take the nearest neighbor coordination number too literally. A second or third nearest neighbor may be close in some structures and far away in others. Generally, it seems best to approximate a more complicated structure by the simpler one to which it is related. SnSe is a good illustration. SnS is considered by Parthe [65] to be a tetrahedral compound, but the structure (B16) has also been described as a deformed NaCl type. Each atom in SnSe has four nearest neighbors, but there are two more atoms only slightly farther away. The thermal conductivity of SnSe is clearly considerably less than expected for a tetrahedral compound of similar atomic weights (compare InAs, CdSe, InSe), but is consistent with the thermal conductivities for SnTe and the lead chalcogenides, which are all NaCl type compounds. From the point of view of thermal conductivity, therefore, SnSe should be considered a distorted NaCl type compound.

Several compounds in Table 1 that do not have NaCl structure are still essentially octahedrally coordinated. It was already mentioned that the B8 (NiAs) structure is the hexagonal analog of B1. Only two compounds with this structure are represented, FeS and MnTe. Thermal conductivities of these compounds are consistent with those of other compounds with octahedral coordination, with the relatively high thermal conductivity of FeS partly due to the low atomic weights.

The atoms in $CuSbTe_2$ (C33) and $TlBiTe_2$ ($F5_1$) also have distorted octahedral coordination, with thermal conductivities in the same range as other octahedral compounds. The structures of $AgCeSe_2$ and related compounds (#5, 10, 11, 19) are not known, but those for many of the analogous sulfides have been reported[33]. The sulfides have either monoclinic or tetragonal symmetry, with distorted octahedral coordination. Even though structures of the selenides (or tellurides) may be different, it is likely that the coordination will be essentially the same. The very low thermal conductivities are consistent with those for other ternary octahedral compounds. This is particularly significant, since it was originally suggested[4] on the basis of magnetic measurements, on $AgGdTe_2$, that the coordination was tetrahedral. Tetrahedral bonding, however, should be associated with considerably higher thermal conductivities than are observed.

Note also that there are three thallium compounds with 8-fold coordination similar to the B2 (CsCl) structure. Their thermal conductivities are all extremely low.

The rather striking difference between tetrahedrally- and octahedrally-coordinated compounds is illustrated graphically in Fig. 1. To be sure, there is considerable overlap, but the difference is well emphasized by the median values, which are about 60 and 7·5 mW/cm-°C for the tetrahedral and octahedral compounds, respectively. A greater distinction between the two classes of compounds is apparent if binary and ternary compounds are distinguished. The highest thermal conductivity for a ternary octahedral compound is only 13 mW/cm-°C, while the corresponding *number for a tetrahedral compound is 180* mW/cm-°C. Note that even the quaternary tetrahedral copper compounds (#40–42) do not have quite such low thermal conductivities as ternary octahedral compounds.

Regarding Table 2—compounds with more cations than anions—detailed structures are not known for many of the compounds. Cu_3AsS_3, Cu_3BiSe_3 and Cu_3SbSe_3 have a defective B3 or $E1_1$ structure, with a quarter of the anion sites vacant. As expected, their thermal conductivities are lower than those of the corresponding filled compounds (compare with Cu_3AsS_4 and Cu_3SbSe_4 of Table 1).

The next simplest structure is the anti-fluorite (C1), represented by Mg_2Si, Mg_2Ge and Mg_2Sn. (Many more compounds with the C1 structure are known, of course, but most are metallic.) As indicated earlier, the anti-fluorite structure is intermediate in coordination between zinc blende and NaCl, with cations in both of the tetrahedral holes, and anions 8-coordinated. Thermal conductivities of these Mg compounds are accordingly intermediate between those of binary zinc blende and NaCl type compounds. Actually, they are rather on the high side, but this is probably connected with the very light atomic weight of Mg.

The structure of the $D5_9$ compounds Cd_3As_2, Cd_3P_2 and Zn_3As_2 has been described as a distorted anti-fluorite, with only three-quarters of the cation sites filled. As always, this lowering of the symmetry of the lattice and partial filling of sites leads to lower thermal conductivities. The structure of Mg_3Sb_2 ($D5_2$) is similar to the $D5_9$ structure, except that the former is based on a hexagonal close-packed anion array rather than a cubic close-packed anion array. The thermal conductivity of Mg_3Sb_2 is about the same as for the $D5_9$ compounds mentioned. A similar argument can probably be applied to $ZnMn_2As_2$.

The rest of the compounds in Table 2 are all compounds of monovalent Ag, Cu or Tl. Symmetries for many of the compounds are known, but detailed structures are generally *not known (with perhaps one or two exceptions*)*. (Crystal symmetry itself is not of particular significance, except that low symmetry is often indicative of complex structure and high coordinations.) Most of the binary Ag or Cu chalcogenides have a high temperature form that consists of a close-packed cubic anion sublattice, with one set of its tetrahedral holes completely filled by half of the cations and the other half of the cations randomly distributed among the remaining holes, both tetrahedral and octahedral. Room temperature structures are probably similar to this, at least in the important respect that cations are in both tetrahedral and octahedral holes. These structures are probably as close as one comes to the case mentioned by Pearson[24] where the cations fill one set of tetrahedral holes and the octahedral holes in a close-packed anion sublattice. This combination of rather high average coordination and especially the partially-filled sites is associated with very low thermal conductivities, as one may judge from the compounds previously discussed. Lattice thermal conductivities of these binary compounds are indeed low, ranging from 4 to 9 mW/cm-°C.

---

*A detailed structure reported for α-Ag_2Se[75] is not consistent with its semiconducting character.

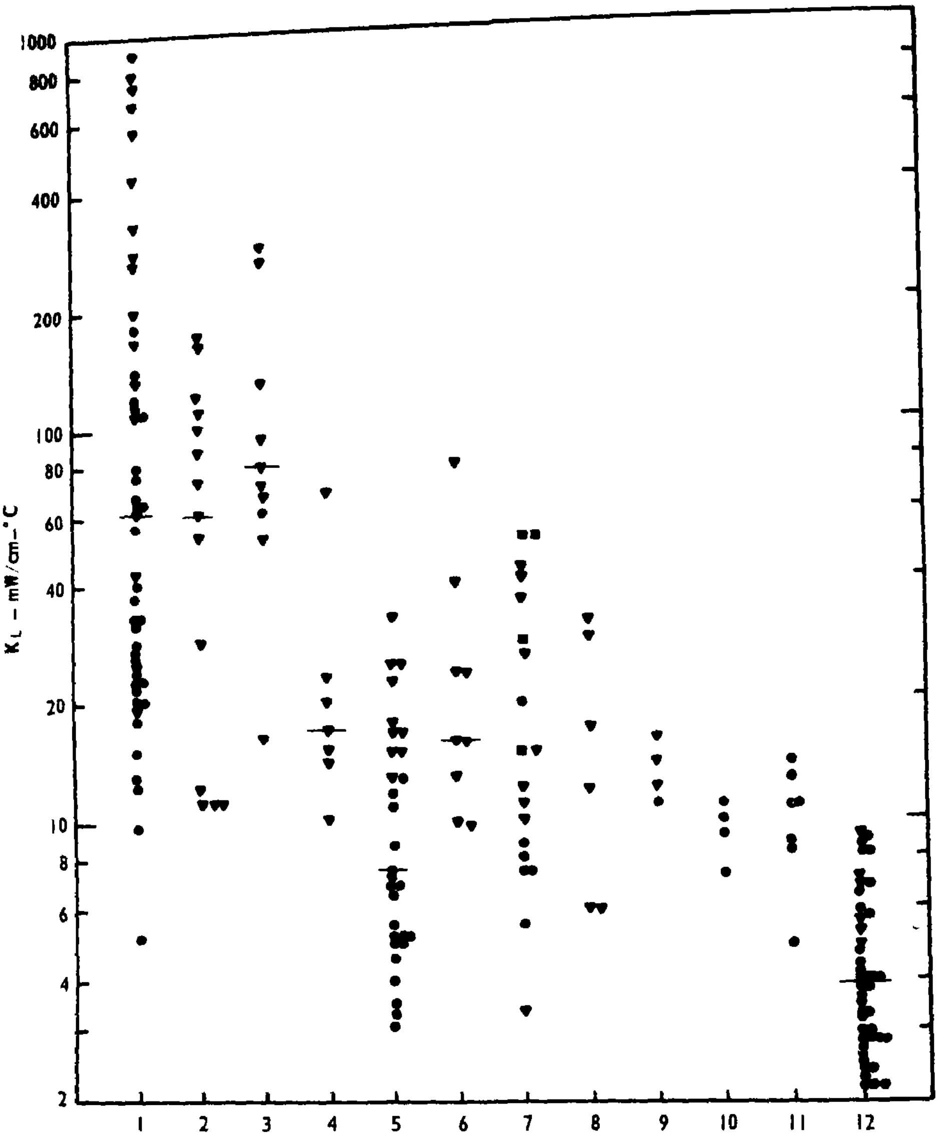

Fig. 1. Lattice thermal conductivities of semiconductors, according to coordination. ▼, binary compounds; ●, ternary or quaternary compounds. Group 1, B3 (or closely related) normal valence compounds. Group 2, non-normal valence compounds, primarily tetrahedral (GaS, GaSe, GaTe, GeAs, InS, InSe, $GeAs_2$, $CoAs_3$, $CdAs_2$, $ZnAs_2$, AgP_2, CuP_2, CdSb, ZnSb). Group 3, C1, C2, C18 and $E0_7$ compounds. Group 4, C6 and C7 compounds. Group 5, B1 (or closely related) normal valence compounds. Group 6, C33, $D5_8$, B20 and BiSe (compounds with predominantly octahedral coordination). Group 7, $D7_3$ (represented by ■) and defect $D7_3$ compounds. Group 8, B37 and similar compounds. Group 9, $D5_2$ and $D5_9$ compounds. Group 10, $H1_1$ and distorted B8 compounds. Group 11, Defect B3 or related compounds. Group 12, All normal valence compounds with cation : anion ratio greater than one, except C1, $D5_2$, $D5_9$ and defect B3 types.

Table 2. Lattice thermal conductivity of normal valence semiconductors with cation to anion ratio greater than 1

No.	Compound	Thermal conductivity		Structure (reference)
		mW/cm-°C	Reference	
91	Ag_2S	9	66	Monoclinic
92	Ag_2Se	4·6	67	Orthorhombic
93	Ag_2Te	7·2	68	Monoclinic
94	Ag_3AuTe_2	8·9	69	Cubic
95	$Ag_2Ge_2S_3$[a]	3·7	27	
96	Ag_4GeS_4[a]	2·2	27	Anisotropic
97	Ag_8GeS_6	2·7	27	Cubic [70]
98	Ag_8GeSe_6	2·9	27	Cubic [70]
99	Ag_8GeTe_6	2·3	27	Same as Ag_8GeSe_6?
100	Ag_5SbS_4	3·4	27	
101	Ag_9SbS_6	4·2	27	
102	Ag_8SiTe_6	2·2	27	Same as Ag_8GeSe_6?
103	Ag_8SnS_6	2·9	27	Cubic [70]
104	Ag_8SnSe_6	3·6	27	Cubic [70]
105	AgTlS	4·5	27	
106	AgTlSe	4·0	27	
107	AgTlTe	3·4	27	
108	Cd_3As_2	14[c]	8	$D5_9$
109	Cd_3P_2	16	27	$D5_9$
110	Cu_2S	5	27	Orthorhombic
111	Cu_2Se	5·4	27	Tetragonal
112	Cu_2Te	7	27	Hexagonal
113	Cu_3AsS_3	11	41	Defect $E1_1$
114	Cu_5BiS_4[a,d]	3·0	27	
115	Cu_9BiS_6[a]	3·9	27	
116	Cu_3BiSe_3	11	42	Defect $E1_1$
117	Cu_5FeS_4	6[e]	27	Tetragonal [67]
118	Cu_4GeS_4[a]	2·5	27	Cu_4SiS_4? [78]
119	Cu_8GeS_6	2·9	27	Cubic [70]
120	Cu_8GeSe_6[a]	2·4	27	Cubic [70]
121	$Cu_2Ge_2Se_3$[a]	8·4	27	
122	Cu_5SbS_4[a,d]	3·3	27	
123	$Cu_6Sb_4S_9$[a]	8·3	27	
124	Cu_9SbS_6[a]	3·9	27	
125	Cu_3SbSe_3	8·5	42	Defect B3
126	Cu_4SnS_4[a]	3·0	27	Cu_4SiS_4? [78]
127	Cu_8SnS_6	2·9	27	Cubic [70]
128	CuTlS	9	27	
129	Cu_3TlS_2[a]	4·3	27	
130	CuTlSe	7	27	
131	Cu_3TlSe_2[a]	4·7	27	
132	Cu_3TlTe_2[a]	6·9	27	
133	Mg_2Ge	66	73	C1
134	Mg_3Sb_2[f]	13	27	$D5_2$
135	Mg_2Si	78	73	C1
136	Mg_2Sn	130	74	C1
137	Tl_2S	5·7	27	Rhombohedral[g]
138	Tl_2Se	4	27	Tetragonal[g]
139	Tl_4GeSe_4[a]	2·4	27	
140	Tl_3SbS_3	4·2	27	
141	Tl_4SiSe_4[a]	2·2	27	
142	Tl_4SnS_4	5·9	27	
143	Tl_4SnSe_4[a]	2·6	27	
144	Zn_3As_2	12	8	$D5_9$
145	$ZnMn_2As_2$	11	27	Hexagonal; similar to $D5_9$?

[a] Compounds not yet reported in the literature.

[b] Reported in reference [77].

[c] The thermal conductivity of Cd_3As_2 has been a subject of considerable attention. All of our own samples have had conductivities about as quoted. Some samples prepared by French workers apparently have much higher conductivities, up to 50 mW/cm-°C [71, 72]. Armitage and Goldsmid [72] measured $K_l = 8$ mW/cm-°C for an undoped sample supplied by us, but obtained $K_l = 50$ mW/cm-°C for an In-doped Cd_3As_2 supplied by N. Sexer.

[d] Analog of mineral stephanite, Ag_5SbS_4.

[e] Similar conductivities measured for both synthetic and mineral (bornite) samples.

[f] Sample from F. Hulliger.

[g] The Tl_2S structure is similar to anti-CdI_2, with layers of Tl atoms above and below an hexagonal array of S atoms. Tl_2Se also contains adjacent layers of Tl atoms [115]. There do not appear to be real bonds between the Tl atoms, however, since metallic conductivity should then be required, contrary to observations.

Regarding the ternary compounds, even less is known of their structures, except for Cu_5FeS_4 (bornite). Bornite has a high temperature form which is known[76] to be a FCC sulfur lattice with the tetrahedral holes three-quarters filled at random. This should be associated with a moderately low thermal conductivity (about like Cd_3As_2), but not so low as is observed. It may be that in the room temperature tetragonal form, the cations also occupy some of the octahedral holes, similar to the binary compounds above.

For the many other ternary compounds for which we have no information on coordination, it is nevertheless instructive to make some observations based on empirical rules for site preferences for various ions, as given, e.g. by Busch and Hulliger[77]*. For example, in compounds which contain trivalent Sb or Bi (#100, 101, 114, 115, 122, 123, 124, 125, 140), it seems quite sure that the Sb (or Bi) will be in octahedral holes. This means that at least some of the monovalent cations must be in tetrahedral holes. Again, therefore, we have the situation where both octahedral and tetrahedral holes are partially filled.

A fairly large number of compounds contain tetravalent Si, Ge, or Sn, which almost certainly occupy tetrahedral sites (#96, 97, 98, 99, 102, 103, 104, 118, 119, 120, 126, 127, 139, 141, 142, 143). The monovalent cations, therefore, could be all in tetrahedral sites also. However, it seems more likely that both octahedral and tetrahedral sites are occupied by the monovalent cations. The odd stoichiometries themselves ensure that all types of sites cannot be completely filled. (It has been suggested that in Cu_4SiS_4[78], the Si are on tetrahedral sites and the Cu are on octahedral sites.)

It is certainly more than coincidence that all of the ternary compounds mentioned in the preceding two paragraphs, where cations partially fill both the tetrahedral and octahedral sites, have extremely low thermal conductivities – all in the range of 2·2–5·9 mW/cm-°C.

Of the compounds in Table 3, with more anions than cations, a number of them are cation defective versions of other structures. First, several compounds have a cation-defective zinc blende or chalcopyrite structure; namely, #149, 164, 165 and 166. Lattice thermal conductivities of these compounds are considerably lower than those similar compounds with the regular filled zinc blende type structure. It has already been mentioned in connection with anion-defective structures above that the vacancies are responsible for the low thermal conductivities. Note that for Ga_2Te_3 and In_2Te_3, conductivities are given for the cases where the vacancies are ordered or disordered. Ordering of the vacancies produces a 2–3 fold increase in thermal conductivity. The low values for the disordered forms are of the same magnitude as for the many compounds of Table 2, where cations were distributed in rather disorderly fashion.

It should be borne in mind that various kinds of disorder are possible with many compounds. With ternary compounds, there may be disorder between two cations which occupy the same type of site, e.g. $ZnSnAs_2$. In general, it must be recognized that effects of ordering are probably largely responsible for gross discrepancies among various observers.

Several compounds have the Th_3P_4 ($D7_3$), or defect $D7_3$ structure. The thorium pnictides are an example that does not fit in well with our general correlations. In the Th_3P_4 structure, the cation is surrounded by eight anions arranged as an octaverticon (strongly distorted cube) and each anion is surrounded by a distorted octahedron of cations. Therefore, thermal conductivities should be less than those of NaCl type compounds, where the coordination is all octahedral. Th_3As_4 and Th_3Sb_4, in particular, have thermal conductivities that are a factor of 2–3 higher than expected on the basis of their coordination and quite high atomic weights (by comparison with NaCl type compounds). No rationaliza-

---

*One should make the addition that Cu^I also can be in an octahedral site, although this is not so likely as for Ag.

Table 3. Lattice thermal conductivity of normal valence semiconductors with cation to anion ratio less than 1

No.	Compound	Thermal conductivity mW/cm-°C	Thermal conductivity Reference	Structure (reference)
146	$AgBi_3S_5$[a]	6·8	27	
147	$AgCe_2Se_{3.5}$	8·0[b]	79	Defect $D7_3$
148	$AgGd_2Se_{3.5}$	7·5[b]	79	Defect $D7_3$
149	$AgIn_3Te_5$	9	80	Defect $E1_1$
150	$AgLa_2Se_{3.5}$	7·4[b]	79	Defect $D7_3$
151	$AgNd_2Se_{3.5}$	8·6[b]	79	Defect $D7_3$
152	$AgPr_2Se_{3.5}$	5·5[b]	79	Defect $D7_3$
153	$AgSm_2Se_{3.5}$	20[b]	79	Defect $D7_3$
154	As_2Te_3	22	81	Monoclinic
		10	82	
155	Bi_2S_3	16	83	$D5_8$
		20·6, ⊥c	84	
156	Bi_2Se_3	24	85	C33
157	Bi_2Te_3	16	86	C33
		17, ⊥ c	87	
		7·5, ∥c	87	
158	Ce_2S_3	35[c] (42[d])	88	?; defect $D7_3$ at elevated temp.
159	Ce_3S_4	15[c]	90	$D7_3$
160	Ce_2Te_3	11[c]	91	Defect $D7_3$
161	$CuBi_3S_5$[e]	11·2	27	Anisotropic
162	$FeCr_2S_4$	10[b]	27	$H1_1$
163	$FeCr_2Se_4$	11[c]	91	$H1_1$ or distorted B8
164	Ga_2Se_3	5	93	Defect B3
165	Ga_2Te_3	5	10	Defect B3
		13	11	Defect B3, ordered
166	In_2Te_3	7	10	Defect B3
		14	11	Defect B3, ordered
167	La_2S_3	23[c] (26[d])	88	?; defect $D7_3$ at elevated temp.
168	La_2Te_3	12[c]	91	Defect $D7_3$
169	$MoSe_2$	23[a]	114	C7
170	$MoTe_2$	20[a]	114	C7
171	Nd_2S_3	34[c] (41[d])	88	?; defect $D7_3$ at elevated temp.
172	Nd_2Te_3	10[c]	91	Defect $D7_3$
173	$NiCr_2Se_4$	9·2[c]	92	$H1_1$ or distorted B8
174	$PbBi_2Se_4$	4	94	
175	$PbBi_4Se_7$	10	94	$GeSb_4Se_7$? [95]
176	$Pb_3Bi_4Se_9$	6	94	
177	$Pb_5Sb_4S_{11}$[f]	5·5	27	
178	$PbSb_2Se_4$	4	96	
179	Pr_2S_3	27[c] (36[d])	88	?; defect $D7_3$ at elevated temp.
180	Pr_2Se_3	3·3[c]	97	Defect $D7_3$
181	Pr_2Te_3	15[c]	91	Defect $D7_3$
182	Sb_2S_3[g]	13	27	$D5_8$
183	Sb_2Se_3	10	36	$D5_8$
184	Sb_2Te_3	24	85, 36	C33
185	$SnSe_2$	67, ⊥c	98	C6
		15, ∥c		
186	Th_3As_4	52[c]	99	$D7_3$
187	Th_3P_4	28[c]	99	$D7_3$
188	Th_3Sb_4	52[c]	99	$D7_3$
189	TiS_2	10[c]	100	C6
190	Tl_2Te_3	4·0	27	Monoclinic
191	VCr_2Se_4	7·3[c]	92	Cr_3S_4, distorted B8
192	WSe_2	17[a]	114	C7
193	WTe_2	14[a]	114	Orthorhombic; stacking variation of C6

[a] Synthetic pavonite.

[b] For pressed, unsintered pellet.

[c] For pressed and sintered pellet.

[d] Corrected for porosity; *k*(corrected) = *k*(observed)/(1-volume fraction porosity)[89].

[e] Compound not reported in the literature.

[f] Mineral, boulangerite, (from Cleveland Co., Washington).

[g] Mineral, stibnite (from Oaxaca, Mexico).

tion can be given for this discrepancy. Only Ce_3S_4 is also listed with the $D7_3$ structure. Its low thermal conductivity is more in line with our correlations.

Given the unexpectedly high thermal conductivity of some of the $D7_3$ compounds, we should still expect defect $D7_3$ compounds to have lower thermal conductivities. Actually, the one direct comparison, between Ce_2S_3 and Ce_3S_4, apparently contradicts this. However, the room temperature structure of Ce_2S_3 is apparently still unsure. Other rare earth sulfides (La_2S_3, Nd_2S_3 and Pr_2S_3) also have rather high conductivities and the same structure. The thermal conductivity data suggest to us that these compounds have a different structure, with lower coordination, but there is no proof for this at present.

Other defect $D7_3$ compounds (#147, 148, 150, 151, 152, 153, 160, 168, 172, 180, 181) have thermal conductivities ranging from 3·3 to 20 mW/cm-°C. This seems reasonable for a defect structure. The lower values presumably reflect some disordering of the vacancies on the cation sites.

The well-known Bi_2Te_3 and other 5–6 compounds have related structures, C33 or $D5_8$ (#155, 156, 157, 182, 183, 184) that are primarily octahedrally coordinated (the cations are in octahedral holes in the close-packed anion sub-lattice). The fact that the octahedral sites are only fractionally occupied is compensated for by the fact that some of the anions have only three-coordination instead of six-coordination. Thermal conductivities of the Bi and Sb chalcogenides are about identical to those of their neighboring Pb and Sn chalcogenides with the octahedral NaCl structure.

A few compounds have the spinel ($H1_1$) or distorted B8 structure (#159, 160, 168, 188). In the spinel structure, the tetrahedral holes are an eighth filled and the octahedral holes are half filled (both in an orderly fashion) and a distorted B8 structure would, of course, have cations only in octahedral holes. In either case, it should be apparent by now that such a structure (with partially-filled sites and primarily octahedral coordination) should be associated with rather low thermal conductivities. These conductivities are, in fact, all about 10 mW/cm-°C.

In the C6 (CdI_2) structure, represented by $SnSe_2$ and TiS_2, the cation coordination is the same as in NiAs, i.e. octahedral. The anions, however, are bonded to only three cations, with three anions considerably farther away. That is, the structure is made up of NiAs-like layers connected via anion–anion layers; within the NiAs-like layers we expect thermal conductivity similar to NiAs or NaCl type compounds; along the anion network we expect better thermal conductivity to be associated with its more open structure. Accordingly, thermal conductivity parallel to the c axis in a C6 structure (i.e. across the layers, where thermal conductivity is limited by the NiAs type layers) is about the same as in a pure NiAs (or NaCl) compound. Such is the case for $k_{\parallel c}$ in $SnSe_2$ (15 mW/cm-°C) and k in SnSe (18 mW/cm-°C). Perpendicular to the c axis, however, where the layers are parallel to one another, thermal conductivity is determined more by the higher conductivity anion network, and for $SnSe_2$, $k_{\perp c} = 67$ mW/cm-°C. The thermal conductivity given for TiS_2 is presumably for a randomly oriented polycrystal, but the number is more consistent with a measurement across the layers.

The C7 structure of $MoSe_2$, $MoTe_2$ and WSe_2 is described as made up of layers of anion prisms in which the centers of half of the prisms are occupied by cations. The coordination is therefore much the same as that in the CdI_2 (C6) structure. In fact, the WTe_2 structure is a stacking variation of the CdI_2 structure. It can only be noted that the thermal conductivities of these W and Mo compounds are of the same order as those for the C6 compounds $SnSe_2$ and TiS_2. It is expected, however, that these compounds should have anisotropic conductivities such as was found for $SnSe_2$. (Anisotropy in thermal conductivity would also be expected on the basis of the physical properties of these compounds, which make them useful as lubricants.) Thermal conductivities parallel to the layers ($\perp c$) should be 2–4 times the values listed (which are for polycrystalline samples).

Regarding the rest of the compounds in Table 3, for which structures are not completely known, it can be said that the cations in them (divalent Pb, trivalent Bi and Sb, etc.) are ones which should be mainly octahedrally coordinated. From the stoichiometries, it can also be certain that neither the octahedral nor the tetrahedral holes can be completely filled. Low thermal conductivities are therefore consistent for all of these compounds.

Non-normal valence semiconductors

In general, non-normal valence compounds do not have a common anion network, and anions may be bonded to one another in pairs, or as a one-, two-, or three-dimensional array. With but one exception in our tables, the number of anions is greater than or equal to the number of cations in these compounds. The anions are generally bonded to one another tetrahedrally, and when the anion–anion bonds form a continuous array, relatively high thermal conductivities result. Even when no continuous array is formed, tetrahedral bonding generally predominates and thermal conductivities of non-normal valence semiconductors tend to be higher than for the normal valence compounds.

In Table 4, the Ga chalcogenides and GeAs have similar structures, with tetrahedrally bonded layers stuck together only with van

Table 4. Lattice thermal conductivity of non-normal valence semiconductors with cation to anion ratio = 1, or greater than 1

No.	Compound	Thermal conductivity		Structure (reference)
		mW/cm-°C	Reference	
194	BiSe	10	27	Trigonal
195	CdSb	11	106	B_e
		21[a]	101	
196	$CdTlS_2$	17·0	102	[102]
197	CoSi	80[b]	42	B20
198	GaS	98, $\perp c$	103	Hexagonal
		10·5, $\parallel c$	103	
199	GaSe	160, $\perp c$	103	Hexagonal, GaS
		21, $\parallel c$	103	
200	GaTe	87, $\perp c$	103	Hexagonal, GaS
		14, $\parallel c$	103	
201	GeAs	30–90[c]	27	Monoclinic; similar to GaSe
202	$HgTlS_2$	43, $\perp c$	104	[102]
		17, $\parallel c$	104	
203	InS	71	103	Orthorhombic
204	InSe	120, $\perp c$	103	Hexagonal
		37, $\parallel c$	103	
		69	27	
205	MnSi	40[b]	105	B20
206	ZnSb	11	106	B_e
		38, $\parallel c$	107	
		34, $\parallel b$	107	
		32, $\parallel a$	107	
207	Zn_4Sb_3	6·5	27	Monoclinic

[a] Average of three single crystals.

[b] For pressed and sintered pellet.

[c] Measured in different directions on a large-grained polycrystal.

der Waals bonding [65] (different stacking sequences are possible, but the bonding is all the same). There are metal-metal pairs in the tetrahedral layers, but this does not seem to have any special significance for thermal conductivity, the important fact being only that the bonding within the layers is tetrahedral. Thermal conductivity within the layers, or parallel to the layers, should therefore be high – not much less than for a zinc blende compound. Conductivity across the layers, however, should be determined primarily by the weak bonding between the layers, and should be quite low. These expectations are exactly in accordance with what is observed. Thermal conductivity in these compounds is quite anisotropic, being quite high parallel to the layers and low across the layers.

InS and InSe are also predominantly tetrahedral compounds [65], but not so anisotropic as those above. The rather high thermal conductivities are in accord with the tetrahedral bonding. Note that InS should have the same sort of anisotropy as InSe, but only a single value is available, for an unspecified sample. The remaining 3–6 compounds have either the B37 structure (InTe, TlS, TlSe) or a similar one (TlTe) (these compounds are actually normal valence ones, with a mixture of mono- and trivalent cations, and were included in Table 1). In the B37 structure, some of the cations are tetrahedrally coordinated, but some are 8-coordinated. Average coordination of the anions is also thus necessarily greater than four. Thermal conductivities of these B37 compounds should thus be considerably less than those of all the other 3–6 compounds, and also less anisotropic. These observations are again in agreement with the measured thermal conductivities.

The BiSe structure has been said to be rather similar to the NaCl structure; however, to be a semiconductor, this stoichiometry must contain Bi–Bi bonds. Whatever the details of the structure, the important point is that the Bi is almost certainly octahedrally coordinated. The thermal conductivity of BiSe is indeed close to that of its neighboring NaCl type compounds, e.g. PbSe.

The silicides CoSi and MnSi, with the B20 structure, are an interesting case. The B20 (FeSi) structure appears at first to be quite complex. On examining a model of the structure, however, it is seen to be strikingly similar to the NaCl structure. (The difference is that the rows of alternating cations and anions in FeSi form a zigzag line instead of a straight one as in NaCl.) Thermal conductivities of these silicides are indeed about what we would have expected for NaCl type compounds, considering that the elements in these compounds are of rather low atomic weight. Since the B20 structure is somewhat more complex than the NaCl structure, these thermal conductivities really should be somewhat lower (say by a factor of about 2), but the discrepancy is not too serious.

The B_e structure of CdSb and ZnSb does not fit well with our general correlations. This orthorhombic structure may be regarded as a very strongly deformed zinc blende lattice; each atom is surrounded by 3 of the opposite kind and one of its own kind. The bonding is not really tetrahedral, since one of the Cd (or Zn) surrounding an Sb is not bound to it. Still, because of the low coordinations, we would not have predicted that ZnSb and CdSb have such low thermal conductivities as they do. ZnTe and CdTe, their closest tetrahedral neighbors, have lattice thermal conductivities of 110 and 63 mW/cm-°C, respectively. We would have predicted the thermal conductivities of CdSb and ZnSb to be somewhat more than half of these values. It should be noted here that there may yet be some uncertainty as to the correct lattice conductivities for CdSb and ZnSb, since the more recent references [90, 107] give values that are appreciably higher than the generally accepted low ones. These higher values that have been reported are within a factor of two of the expected conductivities. (Note that the presence of anion–anion pairs in CdSb and ZnSb does not, by itself, lead to low thermal conductivity; compounds with high conductivity also contain anion–anion pairs (e.g. the pyrite type compounds to be discussed next).)

Arriving finally at Table 5, note first that several of the compounds have the pyrite (C2) or related marcasite (C18) or arsenopyrite (EO_7) structures ($FeAs_2$, FeS_2, FeAsS, $FeSb_2$, $MnTe_2$, and PtP_2). In these structures, the cations are bonded to 6 anions which form a slightly distorted octahedron, while the anions are bonded to 3 cations and one anion, which form a slightly distorted tetrahedron. Thermal conductivities should, therefore, be intermediate between zinc blende and NaCl type compounds, which have pure tetrahedral bonding and pure octahedral bonding, respectively. This is the case, although the thermal conductivities are generally more like those of zinc blende structures than of NaCl structures. Only $MnTe_2$ seems to be unusually low, for which we see no explanation.

FeS_2 is the only compound for which we have thermal conductivities for two different polymorphs. As expected, the more distorted marcasite structure is associated with a lower thermal conductivity than the pyrite structure. It is only fair to note, however, that the difference between pyrite and marcasite may not really be quite so great as indicated, because the pyrite samples were single crystals and probably of better purity than the marcasite. Further thermal conductivity measurements

Table 5. Lattice thermal conductivity of non-normal valence semiconductors with cation to anion ratio less than 1

No.	Compound	Thermal conductivity		Structure (reference)
		mW/cm-°C	Reference	
208	AgP_2	12[a]	27	[108]
209	$BaSi_2$	16[a]	109	C32
210	$CdAs_2$	28	27	Tetragonal
211	$CoAs_3$	110[a]	42	DO_2
212	$CrSi_2$	70	110	C40
		84[a]	111	
213	CuP_2	11[a]	27	[108]
214	$FeAs_2$[b]	70	112	C18
215	FeAsS[c]	60	27	$E0_7$
216a	FeS_2[d]	280	27, 112	C2
216b	FeS_2[e]	91	27	C18
217	$FeSb_2$	51[a]	27	C18
218	$FeSi_2$	50[a]	113	Tetragonal
219	$GeAs_2$	168, $\perp c$	27	Orthorhombic
		10·7, $\parallel c$	27	
220	In_2Te_5	12	27	Monoclinic
221	$MnSi_2$	30[a]	105	Tetragonal
222	$MnTe_2$	16[a]	27, 112	C2
223	$PrSe_2$	12[a]	97	Tetragonal
224	PtP_2	260[a]	112	C2
225	$ReSi_2$	89[a]	111	$C11_b$
226	Si_2Te_3	5	15	
227	$ZnAs_2$	54	27	Similar to ZnP_2

[a] For pressed and sintered pellet.

[b] Mineral (from South Lorraine, Ontario).

[c] Mineral, arsenopyrite (from Cornwall, England).

[d] Mineral, pyrite (from Washington Camp, Arizona, for [27]; from Rio Marina, Island of Elba, for [112]).

[e] Mineral, marcasite (from Jackson, Mississippi).

on other polymorphic sets would be a valuable adjunct to the present thermal conductivity correlations.

The relatively high thermal conductivities of the disilicides $CrSi_2$, $FeSi_2$ and $MnSi_2$ are expected from the fact that their structures are essentially a continuous tetrahedral Si network with metal atoms in some of the sites.

In $CoAs_3$, tetrahedral bonding definitely predominates since there are three tetrahedrally-bonded As atoms (2 As and 2 Co neighbors) for every octahedrally-bonded Co atom. The high thermal conductivity is consistent with this structure.

The $GeAs_2$ structure, although complicated, is similar to that of GeAs if As atoms are replaced by As pairs. Like GeAs, there are tetrahedral layers connected by van der Waals bonding. Accordingly, parallel to the layers ($\perp c$) the thermal conductivity is high, while across the layers the thermal conductivity is poor. Incidentally, the anisotropy of the thermal conductivity of $GeAs_2$ is the largest known, with the thermal conductivity parallel to the layers over 15 times that across the layers.

The structure of $ZnAs_2$ is close to that of ZnP_2, and $CdAs_2$ is also similar. The ZnP_2 structure is truly complex. There are two different zinc and four different phosphorus sites. Half of the Zn atoms form bonds with 3 P and 1 Zn; the other half form bonds with 4 P atoms. One quarter of the P atoms form bonds with 3 P and 1 Zn and three-fourths form bonds with 2 P and 2 Zn. The P atoms form continuous chains. In spite of the complexity of structure, the bonding is all basically tetrahedral. The relatively high thermal conductivities (especially of $ZnAs_2$) should therefore not be surprising.

The structure of AgP_2 and CuP_2 has some similarities to the ZnP_2 structure also. The P atoms form infinite puckered layers, where some P atoms are bonded to two and some to three other P atoms; the Cu or Ag atoms are surrounded by very distorted tetrahedra of P atoms. The overall coordination is therefore rather low, and like the ZnP_2 structure, we expected higher thermal conductivities. No explanation for the low values observed is apparent.

$BaSi_2$ has the C32 (AlB_2) structure, which is quite simple, but highly coordinated. Each cation has 12 equidistant anion neighbors, and each anion has 6 equidistant cation neighbors. The low thermal conductivity of $BaSi_2$, in spite of the light anion, is consistent with high coordination.

CONCLUSIONS

It is hoped that it has been demonstrated by the preceding discussion that a great deal of self-consistent correlation of lattice thermal conductivity with coordination is possible, allowing only a few discrepancies. To further emphasize the effect of coordination on thermal conductivity, we have placed most of the compounds in Tables 1–5 in one of the twelve groups in Fig. 1. These groups are approximately arranged according to increasing coordination, going from left to right. The relative positions of the first six groups and the last one are thought to be quite well fixed. As has been repeatedly mentioned, however, low thermal conductivity does not correlate only with high coordination, but also with partially filled sites. Vacancies in normally filled sites may be as effective in reducing thermal conductivity as is high coordination. Groups 7–11 might therefore be arranged in a different sequence. Group 7 doesn't really fit in too well any place, and the conductivities in groups 8–11 are so similar that interchanging them would have little effect on the appearance of the figure.

The range of values within any group partially reflects the range of atomic weights (decreasing conductivity with increasing atomic weights). The horizontal lines in most of the groups are to indicate median values. Groups 1, 5 and 12 contain many more ternary compounds than do the other groups, which lower the medians for these groups.

A better comparison might be made by considering only the binary compounds.

The rather striking difference between normal valence tetrahedral and octahedral compounds has already been mentioned. Note also especially that the high values of the non-normal tetrahedral compounds (group 2) are quite comparable to those of the zinc blende compounds (group 1). It is generally felt that complex crystal structures are associated with low thermal conductivities. The high thermal conductivities of some of the complex structures in group 2, however, emphasize the point that the coordination is more important than the superficial complexity of structure.

The compounds of groups 3 and 4, with 1 : 2 or 2 : 1 stoichiometries, have mixed coordination, with 3- or 4-coordination for one ion and 6- or 8-coordination for the other. Thermal conductivities are correspondingly between the cases of pure tetrahedral and pure octahedral coordination. Groups 5 and 6 are quite similar, as they should be (at least if one considers the binary compounds only), since bonding in all of these compounds is essentially octahedral. Group 7 compounds have a mixture of 6- and 8-coordination. They should accordingly be below the octahedral compounds in conductivity, but some of their conductivities are unexplainably high. Low conductivities in groups 8–10 are associated with multiple coordinations for the cations and/or partially filled sites. The low conductivities of group 11 are entirely due to the incomplete filling of normal zinc blende sites. Group 12 contains most of the compounds with more cations than anions, where coordination is mixed and any one set of cation sites is almost never filled.

Many types of semiconductors have not been discussed at all because we have no data for them. It is hoped, however, that the reader will be able to apply these correlations to the estimation of thermal conductivities of other materials. We ourselves found the guidelines useful when looking for compounds of low thermal conductivity. This is, in fact, the reason for the unusually large number of compounds with very low conductivity.

It may be predicted, for example, that Li_3Bi type compounds (all holes in the anion lattice filled) will have very low thermal conductivities (10 mW/cm-°C or less); an olivine structure should be similar to the spinel in thermal conductivity (order of 10 mW/cm-°C); CuAsS, $CuGe_2As_3$, and similar compounds should have rather high thermal conductivities (40–100 mW/cm-°C), because of their tetrahedral bonding[65]; C23 ($PbCl_2$) compounds (e.g. US_2) would be similar to C1 compounds in conductivity, i.e. fairly high (order of 50 mW/cm-°C); a CdP_4 type compound would also be expected to have relatively high thermal conductivity because of its tetrahedral anion network; a perovskite semiconductor should have low thermal conductivity (order of 10 mW/cm-°C or less), since the Ti and O have octahedral coordination and the Ca has 12 nearest neighbors; and so on.

Even if a crystal structure is not known, a reasonable estimate of thermal conductivity can usually be made just on the basis of stoichiometry. For example, a normal valence compound with equal numbers of cations and anions will generally be either all tetrahedral or all octahedral. Which bonding applies can usually be judged on the basis of the known site preferences[77]. A normal valence compound with more cations than anions will either clearly be of the type C1, $D5_2$, $D5_9$, etc., or more likely, will belong to the large group that is similar to Ag_2Se. Normal valence compounds with more anions than cations are likely to be either defect structures, primarily octahedral, or of mixed coordination. The nature of non-normal valence compounds is much harder to predict; the only generalization that can be made is that tetrahedral coordination tends to predominate. In general, also, chemically similar compounds tend to have similar coordinations, even though the crystal symmetry may vary considerably.

These correlations have been presented

only as empirical observations. It would be helpful to have some explanation for why there should be correlations such as have been observed. In view of the very qualitative nature of the correlations, an attempt at a quantitative explanation is hardly justified. Only the following observation seems appropriate: In order to propagate a phonon through a lattice, atoms must vibrate. Naively, it would appear that the more neighbors a particular atom is coordinated to, the less free it is to vibrate. Hence, the higher the coordination, the lower the thermal conductivity.

Finally, we will close with a remark not directly related to our correlations. There has been some conjecture[93] as to whether a relation of the form $k = \frac{1}{3}(C \cdot V \cdot L)$ (where C is heat capacity per unit volume, V is the group velocity of the phonons, and L is the phonon mean free path), is still applicable to compounds of very low thermal conductivity. If one takes L as one lattice spacing, k is of the order of a few mW/cm-°C. It is argued that an L of only about one lattice spacing has little real physical significance, and it might be preferable to think of the vibrations as 'hopping' from one atom to another. Depending on the time between hops, then, thermal conductivity might be as low as we please. We should like to point out, however, that for all of the many compounds of low thermal conductivity that we have measured, there does indeed appear to be a lower limit to the thermal conductivity of solids (counting, of course, only completely dense solids, i.e., not porous). For room temperature, this lower limit is about 2 mW/cm-°C. This corresponds essentially to the case for L equal to one lattice spacing (allowing for some uncertainty in V). Thus, it would seem that the concept of phonons with various mean free paths should be retained for all solids, especially since it provides a natural lower limit to the thermal conductivity of a solid which is in good agreement with the facts.

Acknowledgement—We are very grateful for the assistance of Mr. D. L. Wiegand, who prepared most of the samples on which we made measurements. He also assisted with many of the measurements.

REFERENCES

1. AIGRAIN P. and BALKANSKI J., *Tables de Constantes. Semiconducteurs.* Pergamon Press, Paris (1962).
2. RODOT H., *Les Materiaux Semi-conducteurs.* Dunod, Paris (1965).
3. GOLDSMID H. J., *Thermoelectric Refrigeration,* p. 64. Plenum Press, New York (1964).
4. SUCHET J. P., RODOT H., LEROUX-HUGON P. and RODOT M., *Adv. Energy Conv.* **3**, 569 (1963).
5. LEROUX-HUGON P., RODOT M. and SUCHET J., *C. r hebd. Séanc. Acad. Sci., Paris* **245**, 1250 (1960).
6. SPITZER D. P., Semiconducting properties of some new ternary chalcogenides of Ag, Cu and Tl. In preparation.
7. HAACKE G. and SPITZER D. P., *J. scient. Instrum.* **42**, 702 (1965).
8. SPITZER D. P., CASTELLION G. A. and HAACKE G., *J. appl. Phys.* **37**, 3795 (1966).
9. MAYCOCK P. D., *Solid-St. Electron.* **10**, 161 (1967).
10. ZASLAVSKII A. I., SERGEEVA V. M. and SMIRNOV I. A., *Soviet Phys. solid St.* **2**, 2565 (1961).
11. WOOLLEY J. C. and PAMPLIN B. R., *J. electrochem. Soc.* **108**, 874 (1961).
12. ROSI F. D., DISMUKES J. P. and HOCKINGS E. F., *Elect. Engng, N Y.* **79**, 450 (1960).
13. VEALE C. R., *J. less-common Metals* **11**, 50 (1966).
14. SMIROUS K., STOURAC L. and BEDNAR J., *Czech J. Phys.* **7**, 120 (1957).
15. BAILEY L. G., *J. Phys. Chem. Solids* **27**, 1593 (1966).
16. BORISOVA L. A., EFREMOVA M. V. and VLASOV V. V., *Dokl. Akad. Nauk SSSR* **149**, 117 (1963).
17. SPITZER D. P. and SYKES J. A., *J. appl. Phys.* **37**, 1563 (1966).
18. CHIANG PING-WANG and GLUCK J. V., *J. appl Phys.* **38**, 4671 (1967).
19. Reference [3], p. 46.
20. HEIKES R. R. and URE R. W., Jr., *Thermoelectricity: Science and Engineering,* p. 342. Interscience, New York (1961).
21. MOOSER E. and PEARSON W. B., In *Progress in Semiconductors* (Edited by A. F. Gibson), Vol. 5, p. 103. Wiley, New York (1960).
22. PEARSON W. B., *A Handbook of Lattice Spacings and Structures of Metals and Alloys.* Pergamon Press, New York (1958); *Handbook of Lattice Spacings and Structure of Metals* (2nd Edn). Pergamon Press, Oxford (1967).
23. MOELLER T., *Inorganic Chemistry,* p. 896. Wiley, New York (1952).
24. PEARSON W. B., *Acta crystallogr.* **17**, 1 (1964).
25. DUDKIN L. D. and OSTRANITZA A. P., *Dokl. Akad. Nauk SSSR* **124**, 94 (1959).

26. PETROV A. V. and SHTRUM E. L., *Soviet Phys. solid St.* **4**, 1061 (1962).
27. SPITZER D. P., Unpublished.
28. POWELL R. W., In *Proc. Black Hills Summer Conference on Transport Phenomena*, p. 95. ASTIA 289 290 (August 1962).
29. ZALAR S. N. and CADOFF I. B., *Trans. Am. Inst. Metall. Engrs.* **224**, 436 (1962).
30. RODOT H., In *International Conference on Semiconductor Physics*, Prague, p. 1010. Academic Press, New York (1960).
31. HOCKINGS E. F., *J. Phys. Chem. Solids* **10**, 341 (1959).
32. NENSBERG E. D. and SHTRUM E. L., *Soviet Phys. solid St.* **5**, 2463 (1963).
33. BALLESTRACCI R., *C. r. hebd. Séanc. Acad. Sci., Paris* **262**, 1253 (1966).
34. STEIGMEIER E. F. and KUDMAN I., *Phys. Rev.* **141**, 767 (1966).
35. HOLLAND M. G., *Phys. Rev.* **134A**, 471 (1964).
36. IOFFE A. V. and IOFFE A. F., *Soviet Phys. solid St.* **2**, 719 (1960).
37. LEROUX-HUGON P., *C. r. hebd. Séanc. Acad. Sci., Paris* **256**, 118 (1963).
38. MASUMOTO K., ISOMURA S. and GOTO W., *J. Phys. Chem. Solids* **27**, 1939 (1966).
39. GASSON D. B., HOLMES P. J., JENNINGS I. C., MARATHE B. R. and PARROTT J. E., *J. Phys. Chem. Solids* **23**, 1291 (1962).
40. CARPENTER R. L., MURRAY J. S. and ROBERTS T. D., U.S. Bureau of Mines, Rept. Invest. No. 6200 (1963).
41. IMAMOV R. M. and PETROV I. I., *Kristallografiya* **13**, 412 (1968).
42. STAMBAUGH E. P., SIMON R., LOGAN M. J., KOEHL B. G. and LOUGHER E. M., *Materials and Techniques for Thermoelectric Cooling*. Batelle Research Institute (1964).
43. BOBONE R., KENDALL L. F., and VOUGHT R. H., *Adv. Energy Conv.* **1**, 149 (1961).
44. RIVET J., GOROCHOV O. and FLAHAUT J., *C. r. hebd. Séanc. Acad. Sci., Paris* **260**, 178 (1965).
45. BALANEVSKAYA A. E., BERGER L. I. and PETROV V. M., *Inorg. Mater.* **2**, 691 (1966).
46. HIRAI T., KURATA K. and TAKEDA Y., *Solid-St. Electron.* **10**, 975 (1967).
47. ABDULLAEV G. B., NANI R. KH., NASIROV YA. N. and OSMANOV T. G., *Izv. Akad. Nauk S.S.R.*, Ser. Fiz. **28**, 1096 (1964).
48. BERGER L. I. and ANNAMAMADOV R., *Inorg. Mater.* **1**, 470 (1965).
49. AMITH A., KUDMAN I. and STEIGMEIER E. F., *Phys. Rev.* **138**, A1270 (1965).
50. WEISS H., *Annln. Phys.* **4**, 121 (1959).
51. ROSI F. D., HOCKINGS E. F. and LINDENBALD N. E., *RCA Rev.* **22**, 82 (1961).
52. GAVRILITSA E. I. and RADAUTSAN S. I., *Phys. Status Solidi* **19**, 609 (1967).
53. HARMAN T. C., *J. Phys. Chem. Solids* **25**, 931 (1964).
54. CARLSON R. O., *Phys. Rev.* **111**, 476 (1958).
55. STEIGMEIER E. F. and KUDMAN I., *Phys. Rev.* **132**, 508 (1963).
56. KUDMAN I. and STEIGMEIER E. F., *Phys. Rev.* **133**, 1665 (1964).
57. BUSCH G. and STEIGMEIER E. F., *Helv. phys. Acta* **34**, 1 (1961).
58. IOFFE A. V., *Soviet Phys. solid St.* **5**, 2446 (1963).
59. DEVYATKOVA E. D., GOLUBKOV A. V., KUDNOV E. K. and SMIRNOV I. A., *Soviet Phys. solid St.* **6**, 1425 (1964).
60. FARAG B. S., SMIRNOV I. A. and YOUSEF Y. L., *Physica, Eindhoven* **31**, 1673 (1965).
61. IOFFE A. F., *Can. J. Phys.* **34**, 1342 (1956).
62. DEVYATKOVA E. D., ZHUZE V. P., GOLUBKOV A. V., SERGEEVA V. M. and SMIRNOV I. A., *Soviet Phys. solid St.* **6**, 343 (1964).
63. WASSCHER J. D., ALBERS W. and HAAS C., *Solid-St. Electron.* **6**, 261 (1963).
64. Quoted in reference [58]. Original source unknown.
65. PARTHÉ E., *Crystal Chemistry of Tetrahedral Structures*. Gordon & Breach, New York (1964).
66. COPE R. G. and GOLDSMID H. J., *Br. J. appl. Phys.* **16**, 1501 (1965).
67. CONN J. B. and TAYLOR R. C., *J. electrochem. Soc.* **107**, 977 (1960).
68. TAYLOR P. F. and WOOD C., *J. appl. Phys.* **32**, 1 (1961).
69. *Thermoelectric Materials for Power Conversion* (Edited by F. D. Rosi and E. F. Hockings). U.S. Bureau of Ships, Contract No. NOBS-77057 (1961).
70. HAHN H., SCHULZE H. and SECHSER L., *Naturwissenschaften* **15**, 451 (1965).
71. GIRAUDIER L., *J. Phys.* **26**, 129A (1965).
72. ARMITAGE D. and GOLDSMID H. J., Thermomagnetic effects in Cd_3As_2. Presented at the Fifth Annual Solid State Conference, Bath University of Technology (January 1968).
73. LABOTZ R. J. and MASON D. R., *J. electrochem. Soc.* **110**, 121 (1963).
74. NIKITIN E. N., BAZANOV V. G. and TARASOV V. I., *Soviet Phys. solid St.* **3**, 2648 (1962).
75. PINSKER Z. G., CHOU CHING-LIANG, IMAMOV R. M. and LAPIDUS E. L., *Soviet Phys. Crystallogr.* **10**, 225 (1965).
76. MORIMOTO N., *Acta crystallogr.* **17**, 351 (1964).
77. BUSCH G. and HULLIGER F., *Helv. phys. Acta* **33**, 657 (1960).
78. THOMAS D. and TRIDOT G., *C. r. hebd. Séanc. Acad. Sci., Paris* **264**, 1385 (1967).
79. SUCHET J. P., DRUILLE R. and LORIERS, *J. Inorg. Mater.* **2**, 679 (1966).
80. O'KANE D. F. and MASON D. R., *J. electrochem. Soc.* **111**, 546 (1964).
81. HARMAN T. C., PARIS B., MILLER S. E. and GOERING H. L., *J. Phys. Chem. Solids* **2**, 181 (1957).
82. UPHOFF H. L. and HEALY J. H., *J. appl. Phys.* **32**, 950 (1961).
83. GLATZ A. C. and MEIKLEHAM V. F., *J. electrochem. Soc.* **110**, 1231 (1963).
84. GILDART L., KLINE J. M. and MATTOX D. M., *J. Phys. Chem. Solids* **18**, 286 (1961).
85. BIRKHOLZ U., *Z. Naturf.* **13A**, 780 (1958).
86. GOLDSMID H. J., *Proc. phys. Soc* **72**, 17 (1958).
87. GOLDSMID H. J., *Proc. phys. Soc.* **69**, 203 (1956).

88. MARCHENKO V. I. and BARANTSEVA I. G., *Inzh.-fiz. Zh., Akad. Nauk Belorussk. SSR* **7**, 120 (1964).
89. KINGERY W. D., FRANCL J., COBLE R. L. and VASILOS T., *J. Am. Ceram. Soc.* **37**, 107 (1954).
90. RYAN F. M., GREENBERG I. N., CARTER F. L. and MILLER R. C., *J. appl. Phys.* **33**, 864 (1962).
91. MULARZ W. D. and WOLNIK S. J., In *Proc. 3rd Conf. Rare Earth Res.*, Clearwater, Florida 1963, p. 473. (1964).
92. IVANOVA V. A., ABDINOV D. SH. and ALIEV G. M., *Phys. Status Solidi* **24**, K23 (1967).
93. IOFFE A. F., *Soviet Phys. solid St.* **1**, 141 (1959).
94. ELAGINA E. I., In *Proc. 4th All-Union Conf. Semiconductor Materials* (Edited by N. Kh. Abrikosov), p. 123. Consultants Bureau, New York (1961).
95. PETROV I. I., IMAMOV R. M. and PINSKER Z. G., *Soviet Phys. Crystallogr.* **13**, 339 (1968).
96. ELAGINA E. I., Reference [94], p. 119.
97. LISKER I. S., MALKOVICH B. E. Sh., YAREMBASH E. I. and KALITIN V. I., *Inorg. Mater.* **3**, 700 (1967).
98. BUSCH G., FROHLICH C. and HULLIGER F., *Helv. phys. Acta* **34**, 359 (1961).
99. PRICE C. E. and WARREN I. H., *J. electrochem. Soc.* **112**, 510 (1965).
100. *Status Report on Thermoelectricity* (Edited by J. W. Davisson and J. Pasternak). Naval Research Laboratory Memorandum Report 1127 (1960).
101. PILAT I. M., ANATYCHUK L. I. and LYUBCHENKO A. V., *Soviet Phys. solid St.* **4**, 1210 (1962).
102. GUSEINOV G. D., ISMAILOV M. Z. and GUSEINOV G. G., *Mater. Res. Bull.* **2**, 765 (1967).
103. GUSEINOV G. D., RASULOV A. I., KERIMOVA E. M. and IZMAILOV M. Z., *Phys. Status Solidi* **19**, K7 (1967).
104. GUSEINOV G. D., ISMAILOV M. Z. and TALYLOV A. G., *Phys. Status Solidi* **18**, 929 (1966).
105. NIKITIN E. N., *Zh. tekh. Fiz.* **28**, 23 (1958).
106. TURNER W. J., FISCHLER A. S. and REESE W. E., *Phys. Rev.* **121**, 759 (1961).
107. SHAVER P. J. and BLAIR J., *Phys. Rev.* **141**, 649 (1966).
108. OLOFSSON O., *Acta chem. scand.* **19**, 229 (1965).
109. NESHPOR V. S. and YUPKO V. L., *Zh. prikl. Khim.* **36**, 1139 (1963).
110. NIKITIN E. N., *Soviet Phys. solid St.* **2**, 2389 (1961).
111. NESHPOR V. S. and SAMSONOV G. V., *Inorg. Mater.* **1**, 599 (1965).
112. JOHNSTON W. D., MILLER R. C. and DAMON D. H., *J. less-common Metals* **8**, 272 (1965).
113. WARE R. M. and MCNEILL D. J., *Proc. Inst. elect. Engrs.* **111**, 178 (1964).
114. BRIXNER L. H., *J. inorg. nucl. Chem.* **24**, 257 (1962).
115. STASOVA M. M. and VAINSTHEIN B. K., *Soviet Phys. Crystallogr.* **3**, 140 (1958).

J. Phys. Chem. Solids . Pergamon Press 1970. Vol. 31, pp. 41–48. Printed in Great Britain.

ON THE FORMATION OF ION-BOMBARDMENT INDUCED DISORDER IN ZIRCON, CORUNDUM AND DIAMOND

(STUDIES ON BOMBARDMENT-INDUCED DISORDER – II)*

ČESTMIR JECH† and **ROGER KELLY**
Institute for Materials Research, McMaster University, Hamilton, Ontario, Canada.

(*Received* 20 *June* 1969)

Abstract – The release of Kr-85 from zircon, corundum, and diamond, following its injection at 10 keV, can be effected both by dissolution of surface layers disordered by the ion bombardment or alternatively by thermal annealing of the disorder. Such release was used to investigate the progress of disordering as a function of ion-bombardment dose. Both techniques were found to give comparable results and with zircon a close agreement with disordering by alpha recoils, as studied by Holland and Gottfried, was also found. The results are interpreted in terms of a threshold dose and a subsequent, rapid transformation of the crystalline solid into a disordered (amorphous) state. The mean numbers of atoms transferred to the disordered phase per ion impact were determined and found to be 300 for zircon, 150 for corundum, and 110 for diamond. A tentative explanation for this sequence is suggested based on the ease with which the disorder anneals.

1. INTRODUCTION

THERE are a number of experimental techniques which can be used to study the disordering of crystalline solids resulting from low-energy ion bombardment. The most direct information is probably that gained using electron diffraction[1], electron microscopy[2], or the newly developed technique based on channeling effects in the scattering of light ions[3]. The considerable changes in the various properties of solids connected with their disordering make it possible, however, for a number of other methods, somewhat less direct in nature, to be used in ion-bombardment disordering studies as well. The basic criterion of their usefullness is that they permit measurement of the properties of the extremely thin surface layers to which the effects of low-energy ion bombardment are generally confined. Valuable information on disorder in the surface layer can be gained e.g. by following the behaviour of trace amounts of radioactive inert gas injected into the surface layer by ion bombardment. It was noted earlier[1, 4] that a dose-dependent fraction of inert gas, which had been injected into corundum and a number of other substances by ion bombardment, is released simultaneously with the thermal annealing of the bombardment-induced disorder. It was demonstrated also in radioactive tracer experiments that bombardment-disordered corundum exhibits enhanced solubility in concentrated potassium hydroxide solution [5]. These effects are fairly well understood to be due to conversion of the originally single-crystalline material to an apparently amorphous state which in some, though not all, cases seems to be the ultimate stage of ion-bombardment damage.

In the present experiments the influence of ion dose on the fractional release of injected Kr-85 occurring either during disorder annealing or else resulting from the attack of a disorder-selective solvent was investigated in detail with zircon ($ZrSiO_4$), corundum (α-Al_2O_3), and diamond (C). The aims of this study were twofold: (a) to learn more about the doses necessary to cause breakdown of the crystalline structure as the ion-bombardment damage accumulates; (b) to find out whether annealing-release and dissolution-release are equivalent as 'disorder probes'[6].

---

* For Part I, see reference [4].

†*Permanent address:* Institute of Physical Chemistry, Czechoslovak Academy of Sciences, Praha, Czechoslovakia.

2. EXPERIMENTAL

The experiments were done with single crystals of natural gem-quality zircon from Thailand (donated by Dr. H. R. Steacy of the Geological Survey of Canada), with natural gem-quality diamond, and with artificial corundum (purchased from Linde). The samples, which had the form of about 1 mm thick plates of various sizes, were optically polished. In addition, before each experiment they were either treated with a disorder-selective solvent or were annealed.

Radioactive Kr-85 ions were injected into the samples at 10 keV and various doses, i.e. integrated ion currents, using a simple accelerator without mass separation. Doses in excess of 2×10^{14} ions/cm^2 were realised by bombarding first to this dose with Kr-85 followed by additional bombardment with inactive Kr to the required dose. The fractional release of injected Kr-85 occurring during the anneal of the disorder or resulting from the attack of a disorder-selective solvent was determined by measuring the β-activity of the samples before and after the annealing or solvent exposure.

Annealings were carried out using He as carrier gas and with a linear temperature rise of 25°C/min. This was accompanied by the release of inert gas into the He stream, thence by activity measurements which in differential representation had the form of well-defined peaks with maxima at 730°C for corundum and 760°C for zircon (Fig. 1). Gas release from ion-bombardment disordered diamond seems to be complicated by other factors and fractional-release data based on annealing will not be considered here. The maximum temperatures of annealing of zircon and corundum were chosen as 70°C above the midpoint of the disordered-crystalline gas-release peaks (See Note added in proof).

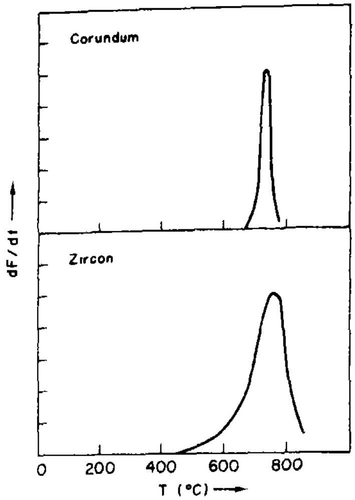

Fig. 1. Typical heating curves showing release rate of Kr-85 from zircon and corundum in the temperature range where the annealing of the bombardment-induced disorder occurs. The bombardment energy was 10 keV.

A parallel series of measurements of fractional release was carried out on samples subjected to the action of disorder-selective solvents. As the respective solvents the following were used: For zircon, 12 N KOH at 95°C for 10 min; for corundum, 12 N KOH at room temperature for 2 min; and for diamond, concentrated sulphuric acid saturated with potassium bichromate at 185°C for 10 min, the latter choice being based on the work of Vavilov *et al.*[7]. These dissolution treatment conditions were adopted after kinetic studies in which it was shown possible to resolve the rapid release of Kr-85 due to dissolution of the disordered phase from a negligible or much slower release due to attack on the underlying less damaged lattice (Fig. 2.) There was no noticeable loss of residual activity from corundum and zircon when they were exposed to

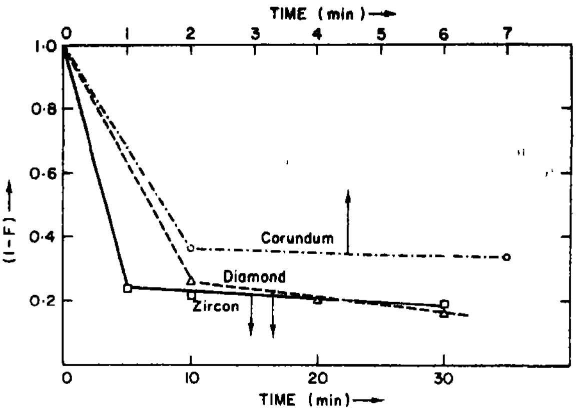

Fig. 2. Typical dissolution curves showing rapid initial drop of the remaining Kr fraction $(1-F)$ due to dissolution of the disordered surface layer. The bombardment energy was 10 keV.

the respective solvents after annealing; conversely, the usual solubility was observed for specimens heated to just below the disordered-crystalline gas-release peaks.

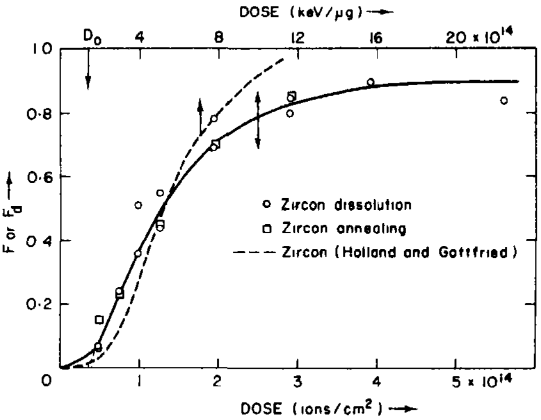

Fig. 3. Fraction F of Kr-85 released from zircon by the action of annealing or a disorder-selective solvent as a function of ion-bombardment dose. Upper scale permits comparison of the present results with the fractional disordering (F_d) measurements of Holland and Gottfried[14] in terms of deposited energy. The bombardment energy was 10 keV.

3. RESULTS

The results of fractional-release measurements obtained by comparing Kr-85 activities in the samples before and after the respective annealing or dissolution treatments are represented in Figs. 3 and 4. We note that the data points fall on sigmoidal curves which suggest the presence of a threshold dose, D_0, upon attainment of which a relatively rapid increase of fractional release, F, is observed to values ranging from 0·8 to 0·9. In effect, there is apparently a change in structure of the solids resulting from bombardment effects at doses beyond D_0.

Another significant feature of the results is that the annealing and dissolution experiments carried out with zircon and corundum yielded similar results, for this indicates that annealing-release and dissolution-release are equivalent as 'disorder probes'.

There were no visually perceptible changes in color or appearance of bombarded zircon and corundum. Diamond developed, however, a grayish reflecting layer at the bombarded surface, the intensity of which increased over the dose range investigated. This layer was completely removed by the sulphuric-acid–bichromate-solution treatment and was also removed by annealing the samples to 650°C in helium. Similar changes in color have been noted also by other authors in reactor-irradiated[8] and ion-bombarded diamond[7]. In addition, the temperature ~ 650°C for the annealing of the disordered layer agrees reasonably with the value >

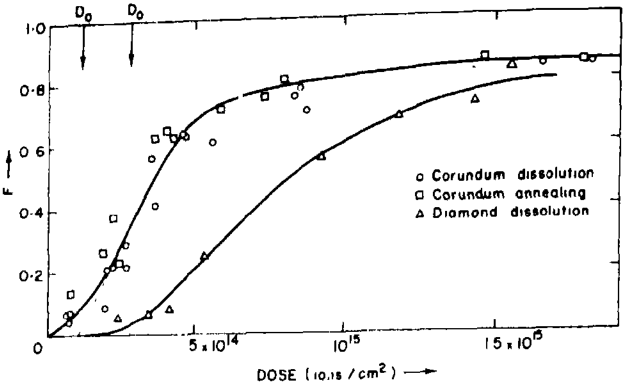

Fig. 4. Fraction F of Kr-85 released from corundum and diamond by the action of annealing (corundum only) or a disorder-selective solvent as a function of ion-bombardment dose. The bombardment energy was 10 keV.

400°C, < 700°C proposed for the conversion of *assumed* amorphous diamond to graphite [7], and the value 650°–750°C found for the final elimination of a bombardment-induced increase in the refractive index [9].

4. DISCUSSION

In attempting to discuss the present results two major problems present themselves. First, it is necessary to adopt a model for the damage distribution resulting from ion bombardment, considering in so doing the distributions both parallel and normal to the surface. Second, one must try to establish a relation between the fractional release of Kr, which is the main experimentally observable parameter, and the state of disorder of the surface layer which it reflects.

4.1 *The geometry of the disordered layer*

It is generally assumed that the damaging of a solid due to ion bombardment originates from atoms being displaced from their normal lattice positions by collision cascades. This damage is, however, not homogeneous (e.g. [10] and the problem therefore arises of describing its distribution. Concerning the distribution parallel to the surface, we note that most of the displacements due to the impact of an individual ion are contained within regions having dimensions similar to the median range of the ion in the solid, thence within regions which are 45–75 Å in dia. for an amorphous solid [11]. It follows that for doses greater than about 10^{13} ions/cm^2, i.e. for doses as used in the present work, the surface is covered with so many overlapping median-range volumes that the damage is effectively homogeneous in the plane of the surface. As far as the distribution of damage normal to the surface is concerned, the work of Sigmund and Sanders [12] is relevant. They showed that the depth distribution of the deposited energy had the form of a truncated Gaussian-type curve similar to the depth distribution of the ions and accordingly that most of the damage was concentrated within a surface layer having a thickness somewhat greater than the median range.

We will accordingly assume in what follows a simplified damage distribution by supposing it to be uniform up to a depth equal to αR_m where α is a numerical factor somewhat greater than unity and R_m is the median range, and with zero concentration deeper in. A similar damage distribution was used also in work by Hines [9] on diamond, by Nelson and Mazey [13] on Si, by Mayer *et al.* [3] on Ge and Si, and by the present authors

(4) when setting up a diffusion model for disorder annealing.

4.2 *Zircon*

In view of the somewhat indirect nature of our evidence for disordering we have found it useful to compare the present results on zircon with those of a closely related study by Holland and Gottfried[14]. These authors were able to obtain more direct information on the disordering of zircon which had received various doses of irradiation from alpha-emitting impurities by measurements of density, optical properties, and X-ray diffraction. With increasing dose an increasing fraction of zircon was found transformed into a disordered phase. This was attributed mainly to the action of the recoil atoms accompanying the alpha decay (average energy 93 keV) rather than to the alphas themselves. The mechanism of disordering should thus be much the same as during a 10-keV Kr bombardment, the main difference being that the recoils were distributed homogeneously throughout the zircon specimens and that their energy was 9·3 times higher. In further work by Bursill *et al.*[15] disordered zircon which showed a glassy structure on X-ray evidence was found by electron microscopy and diffraction to be composed of misoriented crystallites about 100 Å in size. This suggests that the interpretation of the word 'disordered' as meaning 'amorphous' is open to some question but does not change the basic result of Holland and Gottfried that bombardment of zircon leads to a breakdown of the original single-crystal lattice.

Holland and Gottfried's values for the fractional disordering, F_d, are plotted in Fig. 3 (broken line) as a function of the density of deposited energy in keV/μg (upper scale). Our data on fractional release, F, are represented so that both scales are applicable, the units keV/μg being established by assuming, as outlined in Section 4.1, that the damage accumulates uniformly up to a depth of 55 Å or 2·5 μg/cm². Here 55 Å is the median range of 10-keV Kr in zircon as inferred by interpolating the values for Al_2O_3 and WO_3[11] and assuming a density of 4·56 g/cm³.

The outstanding feature in the zircon data of Fig. 3 is probably the close numerical similarity between F_d of Holland and Gottfried and F of the present work. We would propose, in fact, that this result suggests that F_d for the present ion-bombardment experiments, which was not directly observed, is also similar to F, at least in the surface layer of thickness αR_m.

A further point of interest is the presence of a threshold dose in both types of data, for this suggests that the disordering of zircon proceeds in two more or less separated stages. At doses below the threshold, D_0, the accumulation of damage in the form of displaced atoms and vacancies proceeds without a major breakdown of the original lattice structure and thus there is only a slight response in the release behaviour:

$$F \simeq F_d \simeq 0 \qquad D < D_0$$

When the threshold dose is reached, however, the solid is apparently saturated with displacements and a relatively rapid conversion to a disordered state sets in. This latter stage of disordering, provided one can assume that it proceeds homogeneously in a surface layer of thickness αR_m can be described in a way similar to that used by Primak and Kampwirth[16]. The rate of disorder accumulation would thus be given by

$$\mathrm{d}F_d/\mathrm{d}D = (N_t\Omega/\alpha R_m)(1-F_d)$$

whence

$$F_d = 1-\exp[-(N_t\Omega/\alpha R_m)(D-D_0)] \qquad D > D_0 \qquad (1)$$

Here D is the bombardment dose in ions/cm², N_t the number of atoms transferred to the disordered state per ion impact, and Ω the mean atomic volume in cm^3. We now make the assumption that the fractional disordering, F_d, is equal to the fractional gas release, F, so that equation (1) also applies to F. This is not the only possible relation that one might assume between F_d and F (cf. [17, 24]), though, as pointed out above, it can be justified by the similarity of the present data with those of Holland and Gottfried.

When one compares the actual dependence of F vs. dose with that described by equation (1), one finds that the experimental data approach the value $F = 1$ at too slow a rate. We do not consider this significant, for it can be explained on the grounds that the actual damage and inert-gas distributions extend in the form of penetrating tails beyond αR_m[11, 12]. That portion of the inert gas contained in these tails would necessarily not be released until the energy deposited beyond αR_m had reached the value necessary for disordering, thence not until relatively high doses.

Equation (1) is thus probably applicable to that part of the experimental curve just beyond D_0, and this enables N_t/α, which should be similar to the number of atoms transferred to the disordered state per ion impact to be calculated. A value of about 300 atoms/ion results (Table 1). It is of interest that this is a similar value to the estimated number of atoms displaced by a 10-keV ion, namely

$$E/2E_d \simeq 10^4/50 = 200$$

where E_d is the displacement energy, here assumed somewhat arbitrarily to be 25 eV. N_t/α is, however, much lower than the number of atoms in the median range volume, 8× 10^3 assuming R_m is 55 Å.

Finally, it is worth pointing out that the present data show zircon to have a similar, high sensitivity to ion impact as mica[5] and quartz[18] and that these materials are also known to be highly sensitive to damage formation by electron excitation along the tracks of heavy ionizing particles[19]. The common factor is a silicate structure, which thus appears to be particularly susceptible to the production and retention of radiation damage.

4.3 *Corundum and diamond*

Although there has been much work done on radiation damage in corundum and diamond, most of it is not directly comparable with ours. The main exception is perhaps the work of Hines[9], which showed significant changes in the optical properties of diamond bombarded with 20-keV carbon to occur at similar doses to those encountered in the present work, namely at doses of 6× 10^{14} ions/cm^2 and greater. The remaining work is of interest mainly in giving evidence that the accumulation of radiation damage in corundum and diamond leads to the formation of a disordered state. This was shown (a) in an electron-diffraction study of Xe-bombarded corundum by Matzke and Whitton[1], (b) in an X-ray

Table 1. Parameters relating to bombardment-induced disordering

Material	R_m, the median range for 10-keV Kr (μg/cm^2)	Number of atoms in median range volume	N_t/α (atoms/ion)‡	D_0 (ions/cm^2)‡
Zircon	2·5*	8000	300	3×10^{13}
Corundum	2·4†	13000	150	1×10^{14}
Diamond	2·3*	27000	110	3×10^{14}

*Inferred from a graph of R_m for Al_2O_3 and WO_3[11] vs. mean atomic weight.

†From [11].

‡From Figs. 3 and 4.

diffraction study of fission-fragment bombarded corundum by Berman[20], and (c) in an X-ray diffraction study of reactor-irradiated diamond by Levy and Kammerer[8]. In addition, electron microscope studies on corundum indicate the presence of small, disordered regions both (d) after Ar bombardment[21] and (e) after high doses of fast neutrons[22]. The optical measurements of Vavilov *et al.*[7] on (f) Li-bombarded diamond should also be mentioned, as they were interpreted in terms of disordering.

This experimental evidence indicating disordering as the ultimate stage of the damaging of corundum and diamond, together with the similarity in the shapes of the fractional-release-versus-dose curves with that of zircon, has led us to adopt the same procedure for the analysis of the data as with zircon. The respective values of the threshold doses D_0 and of N_t/α are contained in Table 1.

The main point of interest is probably that D_0 for corundum and diamond is greater than for zircon, while N_t/α is lower. We can only speculate at present on the origin of this difference, though one possibility is that it arises due to disorder annealing [4] being easier with corundum and diamond. Perhaps the lesser complexity of the corundum and diamond lattices could be significant here, a point which has also been discussed by Mader *et al.*[23] in connection with the occurrence of amorphousness in Cu–Ag alloys prepared by vapor quenching. Or else the important factor could be the somewhat decreased reordering temperatures. For example, the present work suggests that the re-ordering temperatures for C, Al_2O_3, and $ZrSiO_4$ are respectively ~ 650, 730, and 760°C and this is also the sequence in which D_0 and N_t/α vary.

5. SUMMARY

(a) The release of Kr-85 from zircon, corundum, and diamond, following its injection at 10 keV at doses sufficient to cause disordering of the surface layers, can be effected both by dissolution of the disordered layers or, alternatively, by thermal annealing of the disorder.

(b) Thermal release and dissolution release lead to closely similar results at all bombardment doses and are thus shown to be equivalent as 'disorder probes'.

(c) The dependence of gas release on dose is sigmoidal and thus suggests the existence of a threshold dose followed by a rapid transition of the crystalline solid to a disordered state. The threshold doses were $\sim 3 \times 10^{13}$ ions/cm^2 for zircon, $\sim 1 \times 10^{14}$ for corundum, and $\sim 3 \times 10^{14}$ for diamond, while the rates of transition were, respectively, 300, 150, and 110 atoms/ion.

(d) The order of increasing sensitivity to bombardment-induced disorder, namely diamond–corundum–zircon, is also the order of increasing structural complexity and of increasing re-ordering temperature. For example, the reordering temperatures are ~ 650°C with diamond, 730°C with corundum, and 760°C with zircon. This suggests that the extent of bombardment-induced disordering with a given substance depends on the ease with which the disorder anneals.

Acknowledgements—The authors are indebted to Dr. H. R. Steacy of the Geological Survey of Canada (Ottawa) for supplying the zircons, and to Dr. P. Pronko of this Institute for discussions during the course of the work.

Note added in proof. It is worth emphasizing that the assumption, with corundum and zircon, that gas released at 600°–800°C is due to disorder annealing rests on fairly safe ground. With corundum this follows from an electron-diffraction study of Xe-bombarded specimens carried out by Matzke and Whitton[1]; with zircon it follows from the fact that the gas-release maximum, 760°C, is similar to the value 810°C found by Fleischer *et al.*[25] for fission-fragment track annealing for a 1-min time scale.

6. REFERENCES

1. MATZKE H. J. and WHITTON J. L., *Can. J. Phys.* **44**, 995 (1966).
2. PARSONS J. R., *Phil. Mag.* **12**, 1159 (1965).
3. MAYER J. W., ERIKSSON L., PICRAUX S. T. and DAVIES J. A., *Can. J. Phys.* **46**, 663 (1968).
4. JECH Č. and KELLY R., *J. Phys. Chem. Solids* **30**, 465 (1969).

5. JECH Č., *Phys. Status Solidi* **21**, 481 (1967).
6. KELLY R. and JECH Č., *Proc. Br. Ceram. Soc.* **9**, 243 (1967).
7. VAVILOV V. S., GALKIN V. V., GUSSEVA M. I., ERSHOVA L. M., KISSELEVA K. V., KRASNOPEVTSEV V. V. and MILUTIN YU. V., *Radiation Effects in Semiconductors*, p. 346. Plenum Press, New York (1968).
8. LEVY P. W. and KAMMERER O. F., *Phys. Rev.* **100**, 1787 (1955).
9. HINES R. L., *Phys. Rev.* **138**, A1747 (1965).
10. YOSHIDA M., *J. Phys. Soc. Japan* **16**, 44 (1961).
11. DOMEIJ B., BROWN F., DAVIES J. A., and McCARGO M., *Can. J. Phys.* **42**, 1624 (1964).
12. SIGMUND P. and SANDERS J. B., *Proc. int. Conf. Applications of Ion Beams to Semiconductor Technology*, p. 215 Editions Ophrys, Gap, France (1967).
13. NELSON R. S. and MAZEY D. J., *Can. J. Phys.* **46**, 689 (1968).
14. HOLLAND H. D. and GOTTFRIED D., *Acta Cryst.* **8**, 291 (1955).
15. BURSILL L. A., McLAREN A. C., and PHAKEY P. P., *Proc. int. Conf. Electron Diffraction and Crystal Defects*, p. II B-3. Melbourne (1965).
16. PRIMAK W. and KAMPWIRTH R., *J. appl. Phys.* **39**, 5651 (1968).
17. KELLY R., Submitted to *Radiat. Effects*.
18. MATZKE HJ., *Phys. Status Solidi* **18**, 285 (1966).
19. FLEISCHER R. L., PRICE P. B. and WALKER R. M., *J. appl. Phys.* **36**, 3645 (1965).
20. BERMAN R. M., Bettis (U.S.A.) Report WAPD-TM-350 (1962).
21. DRUM C. M., *Phys. Status Solidi* **9**, 635 (1965).
22. HICKMAN B. S. and WALKER D. G., *J. Nucl. Mat.* **18**, 197 (1966).
23. MADER, S., NOWICK, A. S. and WIDMER, H., *Acta Met.* **15**, 203 (1967).
24. KELLY R. and JECH Č., *J. Nucl. Mat.* **30**, 122 (1969).
25. FLEISCHER R. L., PRICE P. B. and WALKER R. M., General Electric (U.S.A.) Report 64-RL-3831M (1964).

J. Phys. Chem. Solids Pergamon Press 1970. Vol. 31, pp. 49–54. Printed in Great Britain.

SPIN RELAXATION PHENOMENA IN MÖSSBAUER SPECTRA OF MAGNETICALLY ORDERED DYSPROSIUM INTERMETALLIC COMPOUNDS*

B. KHURGIN, I. NOWIK, M. RAKAVY and S. OFER
Department of Physics, The Hebrew University, Jerusalem, Israel

(*Received* 29 *May* 1969)

Abstract—Mössbauer studies of dysprosium metal and cubic Laves intermetallic compounds ($DyAl_2$, $DyNi_2$ and $DyCo_2$) were carried out at various temperatures in the range between 4·2° and 147°K. The measurements show that relaxation processes modify the Mössbauer spectra, especially at temperatures close to the Curie points. The rate equation method of relaxation theory was employed to interpret the observed experimental spectra. Assuming that the crystalline fields do not significantly modify the level structure of Dy^{3+} ions obtained due to exchange interactions, and considering only direct relaxation processes ($\Delta J_z = \pm 1$), fair agreement between theory and experiment is obtained.

INTRODUCTION

SPIN RELAXATION phenomena in Mössbauer spectra have already been observed in paramagnetic insulators[1], ferrimagnetic insulators[2, 3], paramagnetic metals[4] and also in ferromagnetic metals[5].

In the present work, Mössbauer measurements of the 25·6 keV transition of ^{161}Dy in ferromagnetic dysprosium metal and cubic Laves intermetallic compounds ($DyAl_2$, $DyNi_2$ and $DyCo_2$) were carried out. In these measurements, spin relaxation phenomena were observed for a wide range of temperatures: We have succeeded to fit the observed low temperature spectra (below 80°K) by theoretical spectra involving only two adjustable parameters. The calculations of these spectra are based on the assumption that the crystalline fields do not significantly modify the structure of the ionic levels which would be obtained in the case of pure exchange interactions and that the relaxation processes are direct, between adjacent levels only. Thus the only adjustable parameters are the molecular field splitting at a given temperature and the relaxation rate at that temperature.

THEORY

Relaxation phenomena in Mössbauer spectra of magnetically ordered systems can be treated by the rate equation method[2, 6, 7]. In this method, the principal formula, describing the Mössbauer spectrum is:

$$S(\omega) = W \,.\, \mathrm{A}^{-1} \,.\, 1 \qquad (1)$$

where $W = (W_1, W_2, \ldots, W_n)$, and 1 is a column vector of ones. n is the total number of possible different energy nuclear transitions (oscillatory states[7]) and W_k is given by:

$$W_k = C_k \,.\, p_k \qquad (2)$$

where C_k is the nuclear transition probability and p_k is the relative probability of the system being in the oscillatory state $|k\rangle$[7]. The matrix A is given by:

$$\mathrm{A} = -\Gamma \,.\, \mathrm{I} + i(\Omega - \omega \mathrm{I}) + \boldsymbol{\pi} \qquad (3)$$

where Γ is the Mössbauer line width, $\Omega_{kl} = \omega_k \,.\, \delta_{kl}$ $(k, l = 1, \ldots, n)$ and π_{kl} is the probability of the system going by relaxation processes from the oscillatory state $|k\rangle$ to the oscillatory state $|l\rangle$.

The following assumptions were made in

---

*Supported by the Israel Academy of Sciences and Humanities.

the calculations of the theoretical spectra of ^{161}Dy in intermetallic compounds:

(a) The structure of the sublevels of the Dy^{3+} ground level ($^6H_{15/2}$ state) is identical to that obtained in the case of pure exchange interactions, without crystalline fields. Each sublevel is characterized by the wave function $|J, J_z\rangle$. The energy of the state $|J, J_z\rangle$ is given by:

$$E(J_z) = -g_J\beta H_m(T)\,.\,J_z \tag{4}$$

where $H_m(T)$ is the molecular field acting on the Dy^{3+} ion at the temperature T. The relative population of this state is given by:

$$p(J_z) = \exp\{-E(J_z)/kT\}\Big/\sum_{J_z=-J}^{J} \exp\{-E(J_z)/kT\}. \tag{5}$$

The hyperfine fields acting on the ^{161}Dy nucleus while the ion is in the state $|J, J_z\rangle$, are given by

$$H_{\text{eff}}(J_z) = 2\beta\langle 1/r^3\rangle\langle J\|N\|J\rangle J_z \tag{6}$$

and

$$q_{\text{eff}}(J_z) = -e\langle J\|\alpha\|J\rangle\langle 1/r^3\rangle\,[3J_z^2 - J(J+1)]. \tag{7}$$

(b) The relaxation processes occur only between adjacent states, namely, only direct processes in which $\Delta J_z = \pm 1$ are involved. In this case

$$\pi(J_z \to J_z \pm 1) = \pi_0|\langle J_z \pm 1|J_\pm|J_z\rangle|^2 p(J_z \pm 1).$$
$$\pi(J_z \to J'_z) = 0 \quad \text{for} \quad |J'_z - J_z| \neq 1. \tag{8}$$

The assumption that only $\Delta J_z = \pm 1$ transitions are responsible for the relaxation process can be justified if only spin–spin and spin–conduction electrons relaxation have to be considered. Under the above two assumptions we can treat each Mössbauer nuclear transition m, $(I_e, I_e^z) \to (I_g, I_g^z)$, separately. For each allowed nuclear transition m, the formula describing the corresponding Mössbauer spectrum will be

$$S_m(\omega) = W_m\,.\,\mathbf{A}_m^{-1}\,.\,1 \tag{9}$$

where

$$W_m \equiv C_m(p(J), p(J-1), \ldots, p(-J))$$

and

$$\hbar\omega_m(J_z) = H_{\text{eff}}(J_z)\{g_e\beta_N I_e^z - g_g\beta_N I_g^z\} + q_{\text{eff}}(J_z)\left\{\frac{eQ_e}{4I_e(2I_e-1)}(3(I_e^z)^2 - I_e(I_e+1)) - \frac{eQ_g}{4I_g(2I_g-1)}(3(I_g^z)^2 - I_g(I_g+1))\right\}.$$

Since for the 25·6 keV γ-ray of ^{161}Dy there are 16 allowed nuclear transitions ($m = 1, \ldots, 16$) and J_z can have 16 different values ($J = 15/2$), the matrix $\mathbf{A}$ (equation (1)) which was of order 256 (number of oscillatory states $|k\rangle$) is reduced to 16 (complex) matrices each of order 16. At low temperatures only a few lowest ionic levels are populated, and we can further decrease the order of the matrices $\mathbf{A}_m$ according to the number of appreciably populated ionic levels. In our case, only matrices of 4×4 up to 10×10 had to be inverted, which simplified the calculations.

Experimental details

The radioactive source for the Mössbauer studies of the 25·6 keV transition in ^{161}Dy was ^{161}Tb in GdF$_3$. 1/2H$_2$O. This source has, at room temperature, an unsplit emission line with a width of about 5 mm/sec at half height. The source was produced by neutron irradiation of GdF$_3$. 1/2H$_2$O enriched to 96 per cent with Gd^{160}. The 25·6 keV γ-rays were detected by a 4 mm NaI(Tl) scintillation counter.

The absorbers used were DyAl$_2$(40 mg/cm^2), DyNi$_2$(70 mg/cm^2), DyCo$_2$(41 mg/cm^2) and Dy metal (50 mg/cm^2). Measurements were carried out at various absorber temperatures in the range between 4·2° to 147°K. The temperature was measured by a Copper–Constantan thermocouple. The stability of temperatures was better than 0·5°K. The radioactive source was at room temperature.

A linear velocity Mössbauer drive with a multichannel analyzer in the multiscaler mode was used[8].

Experimental results and discussion

The measurements of Mössbauer spectra were carried out with the following absorbers: $DyAl_2$ at 4·2, 20·1, 32·5, 38 and 45°K; $DyNi_2$ at 20·1°K; $DyCo_2$ at 20·1, 76·7, 108 and 128°K and Dy metal at 84, 115 and 147°K. The experimental spectra are given in Figs. 1–4 (dotted lines).

In all the cases, except those of $DyAl_2$ at 4·2°, $DyCo_2$ at 20·1° and Dy metal at 84°K, the Mössbauer spectra are modified by the relaxation processes. The modifications due to

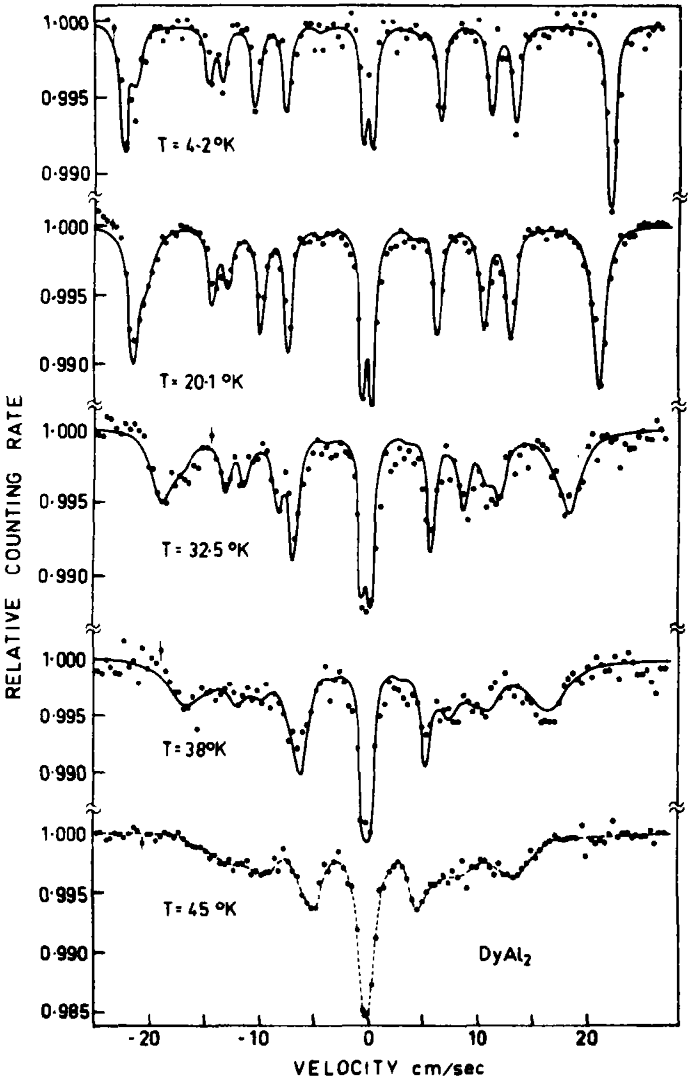

Fig. 1. Mössbauer spectra of $DyAl_2$. The solid lines represent theoretical spectra.

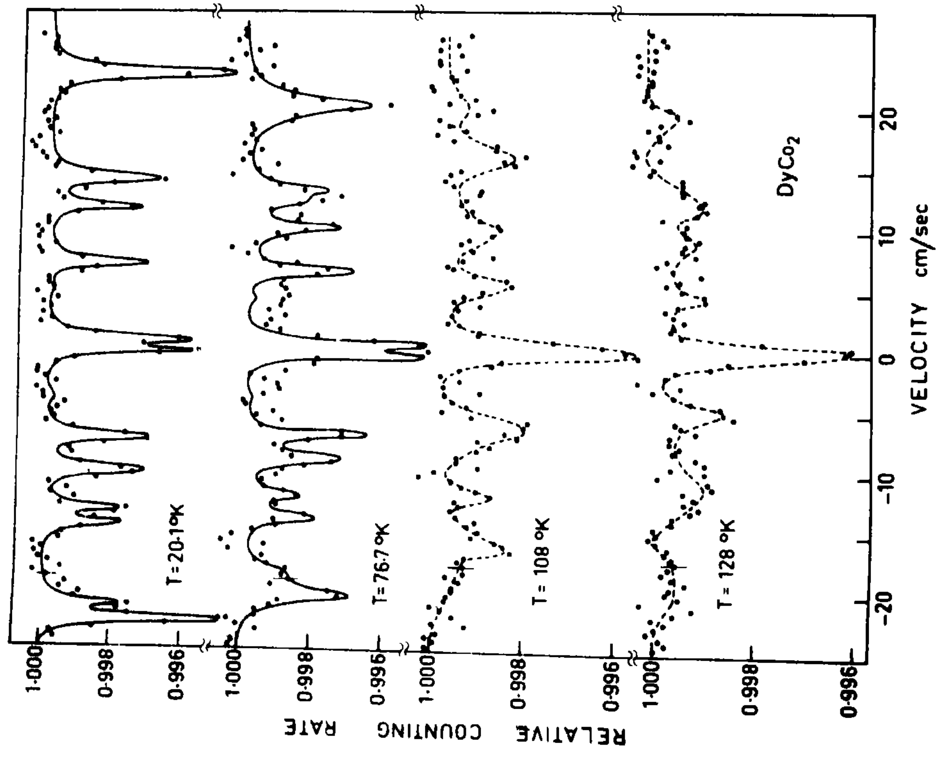

Fig. 2. The Mössbauer spectra of $DyCo_2$. The solid lines represent theoretical spectra.

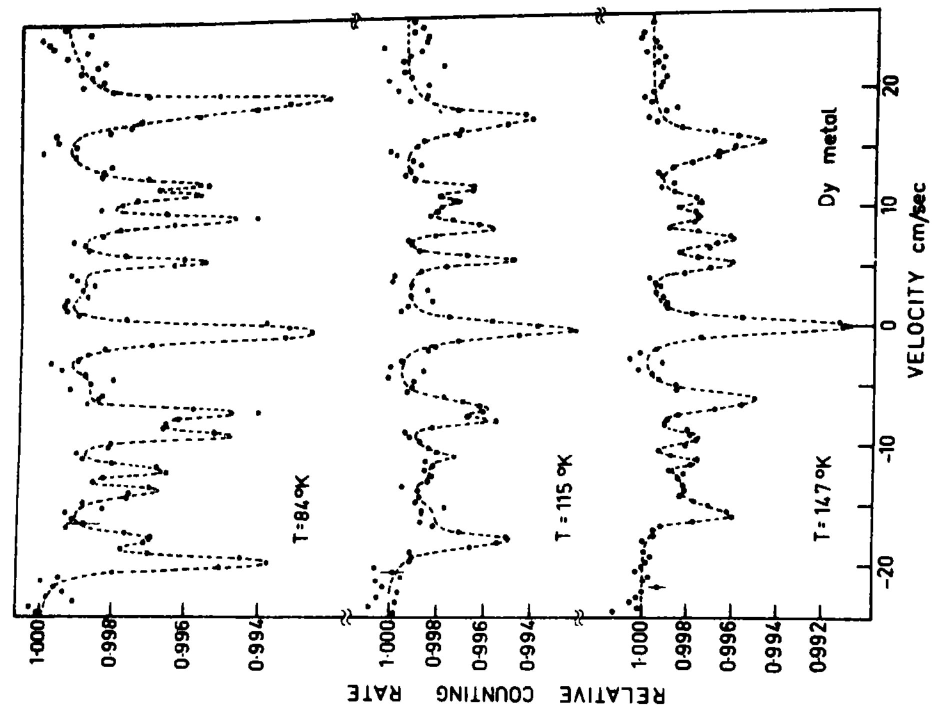

Fig. 3. Mössbauer spectra of Dy metal.

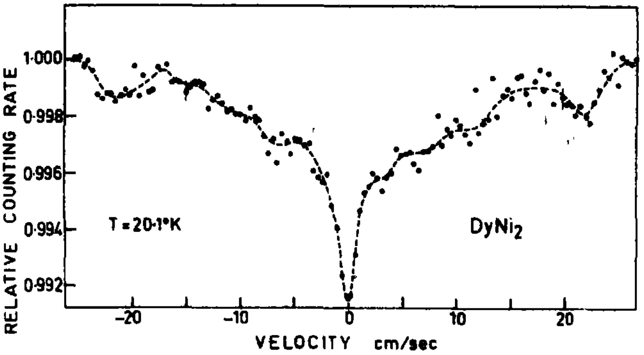

Fig. 4. The Mössbauer spectrum of $DyNi_2$ at 20·1°K.

relaxation processes are especially pronounced at temperatures near the Curie points (62° for $DyAl_2$, 150° for $DyCo_2$ and 179°K for Dy metal).

Theoretical spectra were calculated for the following cases: $DyAl_2$ at 4·2, 20·1, 32·5 and 38°K and $DyCo_2$ at 20·1° and 76·7°K. The two adjustable parameters used in the calculations were: (1) π_0 – the relaxation rate (see equation (8)) and (2) Δ – the separation between the ionic sublevels split by the exchange interaction. (According to equation (4), $\Delta(T) = g_J \beta H_m(T)$.) The solid lines shown in Figs. 1 and 2 represent theoretical spectra which are in quite good agreement with the experimental spectra. The values of π_0 and Δ which gave the best fits are given in Table 1. We have not tried to fit the spectra taken at higher temperatures because the model used and the assumptions made are probably not valid at relatively high temperatures.

In order to justify our assumption that the structure, at low temperatures, of the sublevels of the Dy^{3+} ground level in $DyAl_2$ (and in $DyCo_2$) is similar to that obtained in the case of pure exchange interactions, we have diagonalized the Hamiltonian of the ion in the presence of both exchange and cubic crystalline field interactions (the point symmetry of the Dy^{3+} ions in the Laves intermetallic compounds is cubic). The ratio of the magnitudes of these interactions was used as a free parameter. The calculations were performed for two possible directions of magnetization (100) and (111) and the charge of the Al ions was assumed to be either 0, 1, 2 or 3. The results of the computations show that even for crystalline fields as strong as those predicted by the point charge model[10] (and exchange fields consistent with the Curie temperature of $DyAl_2$) the level structure of the Dy^{3+} ion is similar to that obtained in the case of pure exchange interactions and J_z stays a good quantum number. (Previous susceptibility measurements carried out on Ce^{3+} ions in $LaAl_2$, which has the cubic Laves structure

Table 1. *Molecular field splittings and relaxation rates with which agreement was obtained between theoretical and experimental Mössbauer spectra*

	$DyAl_2$				$DyCo_2$	
T(°K)	4·2	20·1	32·5	38	20·1	76·7
Δ(°K)	> 25	24	16	12	60	55
π_0(sec^{-1})		4.10^{10}	4.10^{11}	$7{\cdot}6.10^{11}$		4.10^{10}

show that the crystalline field interactions are not larger than those predicted by the point charge model[11]).

In a recent work on $ErAl_2$[5], Wiedemann and Zinn assume that the level scheme of the Er^{3+} ions is determined mainly by the crystalline field and that the ground ionic state is the $|J_z = \pm 15/2\rangle$ Kramers' doublet. It is extremely difficult to accept this assumption as the ionic states corresponding to a cubic crystalline field are not eigenfunctions of J_z. The fact that the local symmetry at the Er^{3+} ions in $ErAl_2$ is indeed cubic (and not a lower symmetry which may produce a $|\pm 15/2\rangle$ ground state) is strongly supported by the disappearance of any quadrupole interactions above the Curie point[5]. We believe that in $ErAl_2$ too, the exchange interactions are strong relative to the crystalline field interactions. The temperature dependence of the magnetic hyperfine fields at the Er nuclei in $ErAl_2$ can be fitted by a Brillouin function corresponding to $J = 15/2[B_{15/2}(x)]$ as well as by a $B_{1/2}(x)$ Brillouin function.

Using equation (8) and the values of π_0 and Δ given in Table 1, we can calculate the effective spin relaxation times between adjacent levels and compare them with spin relaxation times which were previously determined in other rare earth magnetic metallic systems. The effective relaxation time between two adjacent levels is given by

$$\frac{1}{\tau_{\text{eff}}} = \pi(J_z \rightleftarrows J_z+1) = \pi_0 |\langle J_z+1|J_+|J_z\rangle|^2 (p(J_z)+p(J_z+1)).$$

τ_{eff} for the two lowest levels in $DyAl_2$ at 20°K is found to be $0{\cdot}2 \times 10^{-11}$ sec. This value of τ_{eff} is of the same order of magnitude as spin relaxation times observed in other metallic systems, like $YbNi_5[\tau(20°K) = 0{\cdot}7 \times 10^{-11}$ sec] and $YbPd_3[\tau(20°K) = 1{\cdot}0 \times 10^{-11}$ sec) [4]. These relatively short relaxation times correspond, probably, mainly to spin–spin and spin–conduction electron interactions.

REFERENCES

1. See Review by WICKMAN H. H., In *Mössbauer Methodology*, Vol. II, p. 34. Plenum Press, New York (1966).
2. NOWIK I. and WICKMAN H. H., *Phys. Rev. Lett.* **17**, 949 (1966).
3. OFER S. and NOWIK I., *Phys. Lett.* **24A**, 88 (1967).
4. NOWIK I., OFER S. and WERNICK J. H., *Phys. Lett.* **24A**, 89 (1967).
5. WIEDEMANN W. and ZINN W., *Phys. Lett.* **24A**, 506 (1967); ZINN W. and WIEDEMANN W., *J. appl. Phys.* **39**, 839 (1968).
6. WICKMAN H. H., KLEIN H. P. and SHIRLEY D. A., *Phys. Rev.* **152**, 345 (1966).
7. NOWIK I., *Phys. Lett.* **24A**, 487 (1967).
8. COHEN R. L., McMULLIN P. G. and WERTHEIM G. K., *Rev. scient. Instrum.* **34**, 671 (1963).
9. NOWIK I., OFER S. and WERNICK J. H., *Phys. Lett.* **20**, 232 (1966).
10. BLEANEY B., *Proc. R. Soc.* **276**, 28 (1963).
11. WHITE J. A., WILLIAMS J. H., WERNICK J. H. and SHERWOOD R. C., *Phys. Rev.* **131**, 1039 (1963).

J. Phys. Chem. Solids Pergamon Press 1970. Vol. 31, pp. 55–66. Printed in Great Britain.

THE DERIVATION OF RECOMBINATION RATE CONSTANTS FROM TIME-DEPENDENT BULK ELECTROLUMINESCENT SPECTRA IN COMPENSATED GaAs

P. D. SOUTHGATE
RCA Laboratories, Princeton, N.J. 08540, U.S.A.

(*Received* 27 *November* 1968; *in revised form* 19 *May* 1969)

Abstract – Time-resolved spectra are taken during the decay of near-band-gap recombination radiation from *n*-GaAs ionized by a 10 nsec current pulse. Comparison of these bulk electroluminescent spectra with photoluminescent spectra in Ge-doped GaAs at 77°K shows that they are composed of two peaks of constant energy but variable relative height, which are identified with band-to-band and band-to-acceptor transitions. Self-absorption is an important factor in the bulk electroluminescent spectra. The decay curves of both components, having time constants of the order of 10 nsec, when fitted to theoretical curves derived from a simple model, allow approximate values of the recombination constants involved to be derived. The radiative band-to-band constant is of order 10^{-9} cm^3 sec^{-1}, and the radiative conduction band-to-acceptor constant, 10^{-10} cm^3 sec^{-1}; both a little smaller than anticipated from theory. A significant difference is found between the hole capture constant, also 10^{-10} cm^3 sec^{-1}, and the much larger value given by the theory of Ascarelli and Rodriguez. Results are also given on heavily compensated Te–Zn doped material, where a continuous shift of emission peak energy with excitation occurs and the interpretation of this paper cannot readily be applied.

1. INTRODUCTION

GERMANIUM in gallium arsenide acts as an amphoteric dopant, producing mainly donors at low doping levels and an increasingly large proportion of acceptors as the total germanium concentration is increased above 10^{17} cm^{-3}. Kressel *et al.*[1] have analyzed photoluminescent data on both *n*- and *p*-type Ge-doped GaAs, and shown that two acceptor levels are associated with the germanium, at 30 meV and 70 meV above the valence band. The intensity of the photoluminescent bands arising from radiative recombination to either acceptor level decreases relative to the band-to-band recombination as the incident exciting radiation level is increased, an effect attributed to changes in the relative hole population of the valence band and acceptor levels.

The work to be described here analyzes the recombination processes in *n*-type Ge-doped GaAs in more detail. Since all time constants involved in the various recombination paths are of approximately the same order, the kinetics of the recombination is of importance. It is not possible to determine the mechanism from steady-state photoluminescent data alone; there are too many parameters involved, and the most important one, the excitation level, can only be estimated. An alternative method is therefore employed, that of time-resolved spectroscopy of pulse-excited bulk electroluminescence. The resolution time of this method is that of the detector, of the order of 3 nsec, which is less than the time-constants involved. It has the advantages of using a bulk ionization process and thus minimizing diffusion problems, and of allowing direct measurement of the initial ionization density, in addition to adding the dimension of time to the experiment.

Pulse-excited bulk electroluminescence has been described earlier[2] in connection with the comparison of radiative and non-radiative recombination processes. It occurs following the passage of inhomogeneously nucleated Gunn domains through moderately heavily doped GaAs to which a field in excess of

2200 V cm^{-1} is applied. For material having an electron density of greater than $10^{17}\,\text{cm}^{-3}$, the ionization usually reaches a steady state in about 5 nsec and is essentially uniform throughout the active part of the sample. Radiation occurs from the whole bulk of the sample, and therefore the total power is greater than that obtained from injection across a junction where the active volume is very thin. In combination with the well defined starting time this makes the system very suitable for the study of recombination kinetics.

2. EXPERIMENTAL

The doping, properties, and method of growth of the materials studied is shown in Table 1. Epitaxial crystals were grown from solution by the method of Nelson[3]; the boat grown Ge-doped crystal G3 was supplied by RCA Electronic Components and Devices Division, and the Te–Zn doped crystal Z1 was obtained from the Monsanto Corporation. The nominal concentration of impurities is derived from the level of melt doping and the conditions of growth rather than by direct chemical analysis. The crystal Z1 in fact seems to be quite closely compensated and is rather inhomogeneous, samples cut from adjacent regions of the same wafer having resistivities varying by up to 50 per cent, and also showing differences in the emission spectra.

For bulk electroluminescence (BEL) measurements, samples were cut with cross-section of about $0{\cdot}1 \times 0{\cdot}15\,\text{mm}^2$ and with active length of about 0·5 mm, either as straight bars or in dumbbell form. Alloyed indium contacts were used. The purpose of the broadened ends of the dumbbell was primarily to allow higher ionization levels to be achieved without burning out the contacts: it was ascertained that the form of the radiation spectra does not depend directly upon the shape of the sample. Samples were excited into BEL by a 1·5 Ω delay line pulser which uses a low-impedance mechanical relay to give a pulse 5 or 10 nsec long. The recombination radiation rises during the first 5 nsec concurrent with the achievement of steady state ionization, and then rises again as the applied voltage switches off. These initial changes occurring under the applied field are attributed to hot carrier effects, and will not be considered in this paper. The measurement technique uses the voltage pulse across the sample to trigger a Tektronix 661 sampling oscilloscope, to which is fed the output from the sample, passed through a Bausch and Lomb 33-86-45 monochromator and detected by an RCA 7102 photomultiplier with a 50 Ω load. The internal delay on the oscilloscope is fixed at a sequence of positions, and spectra taken at each time position.

Table 1. Constitution of experimental materials

	Nominal concn. ($\times 10^{17}\,\text{cm}^{-3}$) Ge	Te	Zn	Electron concn. ($\times 10^{17}\,\text{cm}^{-3}$)	Mobility ($\text{cm}^2\text{V}^{-1}\text{sec}^{-1}$)	Growth method
G1	5			1·1	2900	Epitaxial
G2	5			1·2	3200	Epitaxial
G3	5			1·8	2700	Boat
Z1		12	10	0·5	500	Boat

The mechanism of ionization in BEL involves high and inhomogeneous fields, which affect the recombination of electrons and holes. Observations with a deflectable image convertor tube have shown that although during the ionizing pulse, the infrared emission is not uniform over the active part of the sample, it becomes fairly uniform once the ionizing field is removed. An exception is the presence of a thin surface layer of lower ionization. The non-uniformity is mainly due to hot carrier effects on the self-absorption, rather than non-uniform ionization, and since all measurements described in the paper are made after the applied field has reduced to zero and the hot carriers relaxed to the lattice temperature, details of these effects are not of present significance.

Photoluminescence (PL) has been studied in small samples with chemically polished surfaces. Samples were excited by either a 20 mW He–Ne laser, modulated by a disc chopper, or by a GaAs–P junction laser pulsed with 200 nsec pulses at 1 kHz. In both cases the laser beam may be focussed to a small spot, which in the case of the junction laser can create flux densities as high as 10^4 W cm^{-2}. The same monochromator and photomultiplier as before are used, with a 10 kΩ load on the photomultiplier, followed by a PAR JB-5 phase-sensitive amplifier. The response of the SI photocathode of the photomultiplier is sufficiently flat in the region of interest that no correction is required. For both PL and BEL, measurements are made at 77°K, with the sample immersed in liquid nitrogen.

3. RECOMBINATION KINETICS

It will be convenient first to describe the model which will be used in analyzing the experimental data. Although simple, it appears to embody most features of the behavior of the near-band-gap recombination radiation. Three energy levels are considered: conduction band, valence band, and acceptor level; and these are taken to behave as if they always had the same location and spread of energies within the level, so that radiative transitions between any pair of levels will always give a fixed spectrum. Transitions to other levels are included as non-radiative components. The effective recombination rate coefficients are assumed to be independent of the population of any level. The analysis is a simple variant of many others such as the Shockley and Read[4] analysis; it differs in retaining non-linear terms and including self-absorption. Band-tails are considered to produce only a spectral broadening. Experimental observations in the material studied support the concept of fixed levels; the radiative band-to-band and band-to-acceptor recombination peaks which occur near 1·51 and 1·48 eV, the A1 and A2 peaks, show only a slight shape and location variation over a wide range of excitation levels.

The various recombination processes following the initial ionization are shown in Fig. 1, the recombination rate coefficients being: band-to-band (radiative), B_1, (non-radiative), B_4; conduction band to acceptor, (radiative) B_3, (non-radiative) B_5; and acceptor to valence band, B_2. It will be assumed that the non-radiative recombination rate is proportional to the product of the hole and electron densities, although this is a simplification since intermediate states may be involved, resulting in a more complicated recombination mechanism. The radiative recombination rate is also supposed proportional to the same product, the effect of possible momentum selection restrictions being ignored. In addition to the recombination, two carrier generation mechanisms are considered. The first is the thermal excitation of electrons from the valence band into unoccupied acceptor levels. The second arises from the self-absorption of the band-gap radiation, which is a large effect. A fraction f of the radiation emitted from any

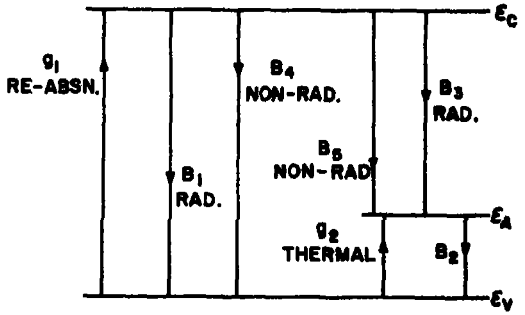

Fig. 1. Electron transitions involved in the present interpretation.

region in the bulk will be taken to emerge from the surface, the remainder being reabsorbed to produce further electron-hole pairs with a quantum efficiency close to 100 per cent. The assumption of spatial uniformity is made, which is a fairly good approximation since most of the reabsorption takes place in the first few microns after emission. Detailed considerations of the nature of the self-absorption and its effect on spectral distribution lead to some anomalies, which will be discussed in Section 5.

The recombination equations, then, may be written

$$\begin{aligned} r_1 &= (n+n_0)p_1B_1 \\ r_2 &= (N_a-p_2)p_1B_2 \\ r_3 &= (n+n_0)p_2(B_3+B_5) \\ r_4 &= (n+n_0)p_1B_4 \end{aligned}$$

with: n_0 density of free electrons in the unionized material
n density of excess electrons after ionization
p_1 density of holes in the valence band
p_2 density of holes in the acceptors
N_a total acceptor density
B_{1-5} recombination rate coefficients.

The band-to-band generation rate is

$$g_1 = (1-f)r_1$$

while the thermal generation of electrons into acceptors must be proportional to both the density of holes trapped on acceptors and the recombination coefficient:

$$g_2 = N_1p_2B_2.$$

The constant N_1 is calculated by considering the special case of a thermal equilibrium situation, (breaking communication with the conduction band) with a quasi-Fermi level E_f. Under these conditions

$$g_2 = r_2$$

and

$$n_1\bar{p}_2B_2 = (N_a-\bar{p}_2)\bar{p}_1B_2.$$

Semiconductor statistics[5] give

$$(N_a-\bar{p}_2)/N_a = 1/(2\exp(E_a-E_f)/kT+1)$$
$$\bar{p}_1/N_v = 1/(\exp(E_f-E_v)/kT+1)$$

where N_v is the effective valence density of states. Thus, if the hole distribution is not degenerate,

$$N_1 = (\tfrac{1}{2})N_v\exp((E_v-E_a)/kT). \quad (1)$$

Expressing the rates of change of hole density in terms of the recombination rates now leads to the rate equations

$$\begin{aligned} \mathrm{d}p_1/\mathrm{d}t &= -(n_0+p_1+p_2)p_1(B_1f+B_4) \\ &\quad -(N_a-p_2)p_1B_2+N_1p_2B_2 \quad (2) \\ \mathrm{d}p_2/\mathrm{d}t &= -(n_0+p_1+p_2)p_2(B_3+B_5) \\ &\quad +(N_a-p_2)p_1B_2-N_1p_2B_2 \quad (3) \end{aligned}$$

while the observed relative radiation intensities emitted from the sample will be

$$\text{band-to-band } \Phi_1 = (n_0+p_1+p_2)p_1B_1f \quad (4)$$

$$\text{band-to-acceptor } \Phi_2 = (n_0+p_1+p_2)p_2B_3 \quad (5)$$

An exact analytic solution of equations (2) and (3) to give the time dependence of the parameters (4) and (5) is not feasible. Equations similar to these have been discussed in the past for a number of recombination situations; Friedrich and Jungk[6] have treated the two-center case and given approximate solutions for various regions of dominance by different recombination coefficients. In the present paper, computer solutions of the equations have been used.

The intensity dependence of the steady state PL spectrum is treated by inserting a photogeneration rate g_3 into equation (2) and equating the rates of change of p_1 and p_2 to zero. The exciting radiation is essentially non-penetrating, and emission occurs within the hole diffusion length of the surface. The self-absorption factor f will therefore be close to unity, significant absorption occurring only at energies greater than the band-gap.

The steady state equations are now

$$\begin{aligned} g_3 &= (n_0+p_1+p_2)(p_1[B_1f+B_4] \\ &\quad +p_2[B_3+B_5]) \\ 0 &= (n_0+p_1+p_2)p_2(B_3+B_5) \\ &\quad +(p_2N_1-p_1[N_a-p_2])B_2 \qquad (6) \end{aligned}$$

These give simple solutions only in the linear limit when the carrier densities are small, and the ratio of the A_1 and A_2 peaks remain constant. A detailed analysis of the non-linear situation, when A_2/A_1 diminishes as g_3 increases, is not made here, mainly because it is not possible to get accurate experimental values for g_3 to fit the theory. The approximate region of onset of non-linearity is found from the linear theory by allowing the proportion of holes in the acceptors to become significant, putting $p_2 \sim N_2/2$. This yields, ignoring second-order terms in equation (6),

$$\begin{aligned} g_{3\text{sat}} &= n_0[N_aB_2(B_3+B_5)/2 \\ &\quad +[N_1B_2+n_0(B_3+B_5)] \\ &\quad \times(B_1f+B_4)]/B_2 \qquad (7) \end{aligned}$$

The parameters derived from the time-dependent spectra should be only approximately applicable to this formula, since the presence of the surface will introduce additional recombination mechanisms.

The analysis of this paper will be applied only to the Ge-doped material where compensation is not heavy, and the acceptor forms a fairly discrete level. In principle, the argument could be extended to a range of non-communicating levels having a range of B_2 and B_3 values; and the model applied to the situation when acceptor levels have become spread until they combine into a continuous valence band tail. This would contrast with the model in which a quasi-Fermi level is defined for the tail, that is, when communication between tail states is fast. In practice, however, the validity of such a model of non-communicating states would have to be determined by curve fitting of a large number of decay curves taken at different excitation levels and temperatures. Such a task is of a considerable magnitude, and in the present paper this question, of the communication between acceptor levels which have been spread out into a continuous band tail, will not be examined.

4. EXPERIMENTAL RESULTS

A. *Photoluminescence*

Spectra which are typical of photoluminescence in both epitaxially grown and boat grown Ge-doped GaAs at 77°K appear in Fig. 2. Over most of the range of excitation levels obtained with the He–Ne laser, the spectrum retains the constant form shown in

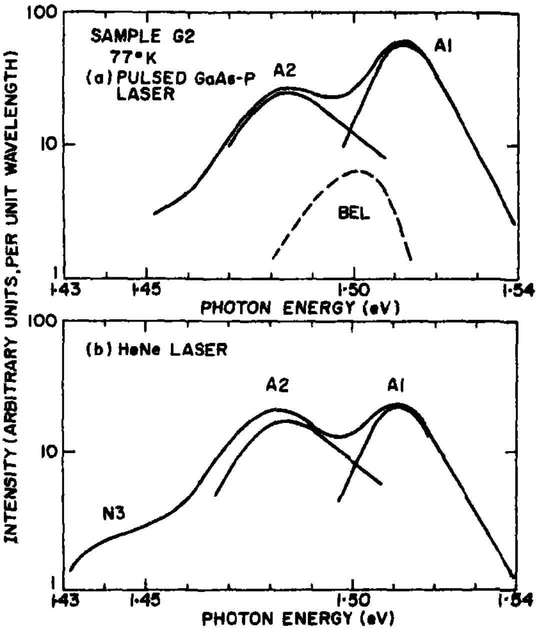

Fig. 2. Photoluminescent spectra of sample G2 at 77°K with moderate and high excitation levels. Approximate resolution into separate peaks shown: broken line is temperature-corrected A1 component of BEL spectrum.

the lower part (b) of the figure, while at the most intense excitation, obtained with a well-focussed GaAs–P pulsed laser, a saturation of the lower energy peak (A2) occurs, as in part (a). The two main component peaks A1 and A2, identified with band-to-band and band-to-acceptor transitions, are indicated in (a); A1 retains its shape in (b) while A2 shows some broadening to lower energies, the significance of which is minimized in this analysis. The peak N3, identified with a deep acceptor level, shows a continuous gradual change of shape with excitation. The nature of these changes in *n*- and *p*-type material has been discussed[1]. Present experimental data do not give an adequate specification of the time-dependence of this peak, and in the interpretation transitions involving the deeper level will be included in other non-radiative transitions (both B_4 and B_5 in Fig. 1).

The shape of the PL A1 peak is only approximately as expected from detailed balance arguments[7] using the optical attenuation curve, measured for the present samples up to attenuation values of $10^3\,\mathrm{cm}^{-1}$ and extrapolated above that on the basis of experience with similar material. Above the band-gap energy, where the attenuation only varies slowly, the emission intensity does indeed fall off as the black-body radiation $\epsilon^2 \exp(-\epsilon/kT)$. At energies below the peak, however, the slope is much steeper than expected from the sum of the slopes of the attenuation constant and the black-body radiation. Some factors involved in this difference are discussed in Section 5. Small changes in peak location between different samples at a given excitation level can be attributed to self-absorption, with differences in active layer depth of less than 1 μm. The slight increase in peak width at lower excitation levels cannot be adequately explained. For the purposes of this paper, the changes are sufficiently small that the peak heights are a good measure of the corresponding radiative recombination rates.

By way of contrast to this discrete acceptor behavior, measurements have been made in the heavily compensated Z1 material where band-tailing dominates. The excitation level dependence of PL is shown in Fig. 3. The dependence is marked at quite low excitations, when little laser spot focussing is required.

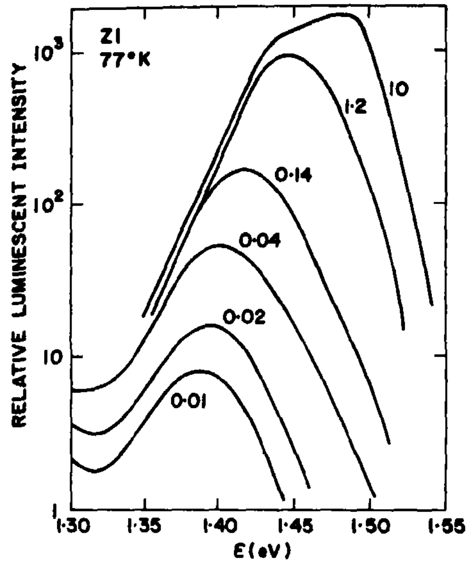

Fig. 3. Photoluminescent spectra of heavily compensated sample Z1 as a function of excitation level. Estimated incident flux in W cm^{-2} shown. Scale of curves adjusted as described in text.

The spot size may be measured and incident flux estimated, and these estimates are given on the curve. The scale of each of the luminescence curves is adjusted so that it corresponds to a given total input power, i.e. plotted as if the same proportion of the radiation were collected each time and the focussing only of the excitation radiation changed. No analysis of the spectra into discrete curves is possible, apart from the suggestion of an emerging peak at 1·485 eV. The direct band-to-band transition in the high density-of-states region near 1·51 eV does not appear at all in this material. It is evident that the analysis given in Section 3 cannot be applied without modification.

B. *Bulk electroluminescence*

Very similar BEL behavior is seen in all Ge doped samples measured. Spectra were taken every 10 nsec or so, the decay time being sufficiently long in the one sample to give data 200 nsec after the ionizing pulse. The time development of a typical set of spectra appears in Fig. 4, the spectra being normalized on the low energy side to demonstrate the shift more clearly. Pulse-to-pulse variability of the output causes the spectra to be rather more noisy than the PL spectra, and the figure shows smoothed spectra. The times indicated are in nanoseconds after the onset of ionization, as indicated by the light output; it occurs about 3–5 nsec after pulse initiation. By 15 nsec after ionization onset the applied field has already decayed to a small value.

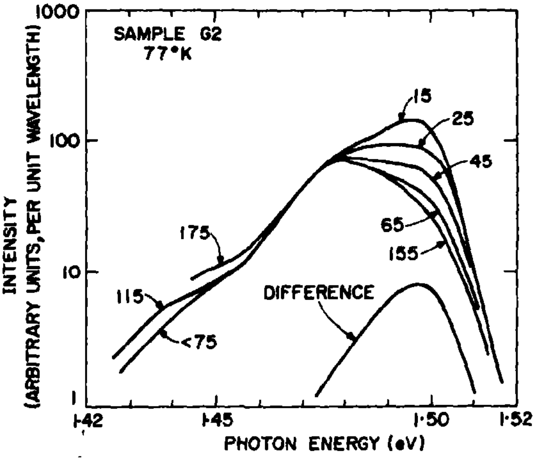

Fig. 4. Bulk electroluminescent spectra for sample G2 measured at a series of different times (in 17 sec) after the start of the ionizing pulse. Spectra all differ by a multiple of lower peak.

It was found that all time-dependent spectra could be derived from the components, A1, A2 and N3, decaying at different rates. The A1 spectrum is derived from the difference between earlier and later spectra of Fig. 4, and is shown below the main series. It is strongly self-absorbed, in contrast to the A2 peak, for which self-absorption may be neglected at the peak maximum. There is an uncertainty in the height of the A1 component towards the end of the decay since the shape of the A2 peak is not accurately known; an increment which is a fixed proportion of the A2 peak must be included. This increment was determined in such a way that good fit to the theoretical decay curves was obtained. It is a small proportion of the total, and its magnitude does not affect the final conclusions significantly.

The curves from which the recombination rates are deduced are shown in Fig. 5: the relative decay rates of the A1 and A2 peaks. The points are experimental; the curves are fitted from equations (2–5) as discussed in Section 6. The zero time is taken as that at which ionization is established, rather than the commencement of the ionizing pulse. Any drift of the apparatus sensitivity during the sequence was corrected by comparing the spectral height with a single decay curve taken at fixed frequency. The current through the sample during the exciting pulse for these

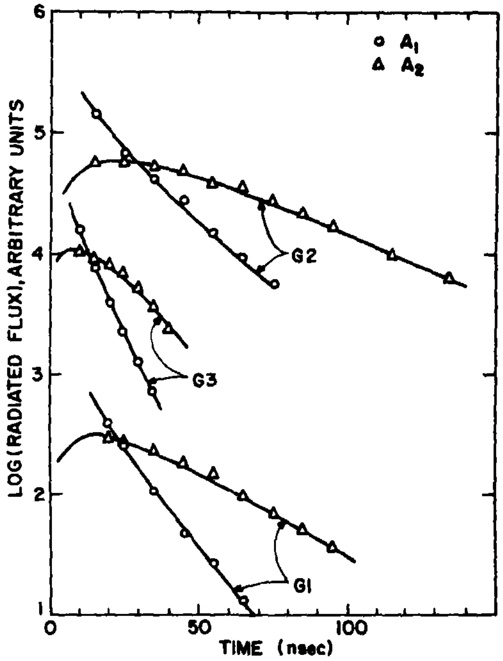

Fig. 5. Measured decay curves of A1 and A2 peaks for three samples compared with curves fitted using the theory. Zero time taken at beginning of ionization.

runs was about twice the critical current, corresponding to a created hole density approximately equal to the original electron density[2]. Measurements at substantially greater ionization levels produced curves of similar appearance. The ionization level dependence was not investigated in detail since the theory does not predict any strong dependence within the attainable range, and also because the samples tended to break down rather frequently at higher pulse currents.

The time-dependent BEL spectra of the Zn compensated material Z1 are shown in Fig. 6. A continuous shift to lower energies occurs during the decay. The spectra appear similar to those in Fig. 3 taken with the incident flux in the 1 W cm^{-2} region; but in fact they correspond to even higher excitation levels, as is known from the measured excess electron density. The correspondence becomes evident when the curves are corrected for self-absorption, as indicated by the broken line in Fig. 6. The measured absorption curve is used, extrapolated beyond 1·47 eV on the basis of measurements on similar samples. As discussed in the next section, use of a measured curve is not completely justified, and the broken line will only be an approximate indication of the intrinsic emission. The higher energy of the corrected peak corresponds, on a rough extrapolation, to a PL peak with incident energy of the order 300 W cm^{-2}; the recombination rates are not sufficiently well known to allow an estimate of the ionization level produced.

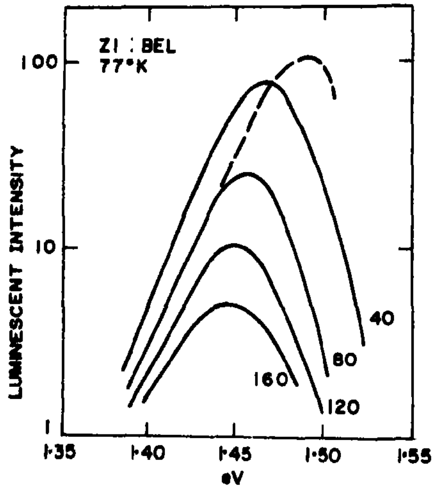

Fig. 6. BEL spectra of sample Z1 at various times (nsec) during the decay. Broken line: approximate correction for self-absorption.

In total, the data on the Z1 material does not appear necessarily to require any assumptions of time-dependent processes, or allow an unambiguous interpretation along these lines. The spectral shift might be accounted for by a steady shift of the hole quasi-Fermi level through a continuum of states, which may be either an extended band tail or a range of essentially separated acceptor states. A detailed analysis of similar situations has been made [8] in which time-dependent transitions between band tail states are considered. The object of describing the data here is to show that BEL results are not inconsistent with the steady state PL results.

Time-resolved spectra have also been taken for BEL in Te and Sn doped GaAs. The time constants tend to be a little shorter in these materials, so that the range of measurement can be extended over only about 70 nsec. No change in shape or position of the spectra is observed during the decay time. In these materials, which are only slightly compensated, the lack of change could be due either to the absence of acceptor states or to a difference in the nature of the band tails.

5. SELF-ABSORPTION: COMPARISON OF PL AND BEL

The major difference between the PL and BEL spectra lies in the truncation of the latter at high energies due to self-absorption. Figure 2(a) compares the A1 peak in PL with that in BEL (broken line; temperature corrected). If the absorption constant at any photon energy is α per unit length, then the observed spectrum in a uniformly excited material of thickness d will be

$$\Phi_0(\epsilon) = \int_0^d \exp(-\alpha x) P_i(\epsilon)\,dx = P_i(\epsilon)(1-\exp(-\alpha d))/\alpha \qquad (8)$$

where $P_1(\epsilon)$ is the intrinsic radiation spectrum. Thus when αd is small, the intrinsic spectrum shape will be followed, and when αd is large, at higher energies, the intrinsic spectrum will be divided by α. Since detailed balance arguments [7] give the intrinsic spectrum equal to the black-body spectrum multiplied by α, one is left with a predicted high-energy emission having the black-body distribution. Observation does not bear this out, the high energy cut-off being much steeper. The reason is that excitation is not uniform, a surface layer of lower ionization density being formed both by the higher surface recombination rate and by radiation 'cooling' of the surface. Confirmation of this explanation is seen in a sample in which about 10 microns of low-conductivity substrate is left on the sample. When viewed from the substrate side an appropriately sharper high-energy cut-off is seen. The existence of the surface layer cut-off does not affect the peak height significantly.

There are difficulties in correlating the ratio of PL to BEL with the measured absorption. These are demonstrated in Fig. 7. The BEL spectrum, taken at a late time when its shape had stabilized, is compared with the high-excitation PL spectrum. Broken lines show small estimated corrections, for a cool surface layer in the case of BEL, and for self-absorption in the case of PL. Although there is no way of knowing how close the hole densities are in the two samples, the similarity of spectral shape at low energies where there is no self-absorption shows that the conditions are at least similar for the two modes of excitation. The ratio of the two corrected radiation intensities, together with the thickness of the sample, 100 μm, now yields a deduced absorption curve, labelled PL/BEL. It varies considerably from the curve measured in the ionized sample, also shown, Any comparison of PL with BEL spectra which seems reasonable yields a similar discrepancy; self-absorption is not large between 1·48 and 1·5 eV. Part of this discrepancy is due to the filling of the valence band tail by holes at the finite excitation levels of the BEL compared with the very low levels at which absorption measurements are made. However, this cannot be the complete explanation, since the effective absorption curve would then approach the low-level curve as the hole density decayed away, and this does not occur. The difficulty has not been resolved; but since the main arguments of this paper do not depend on the origin of the shape of the individual spectra discussion of the point will not be pursued.

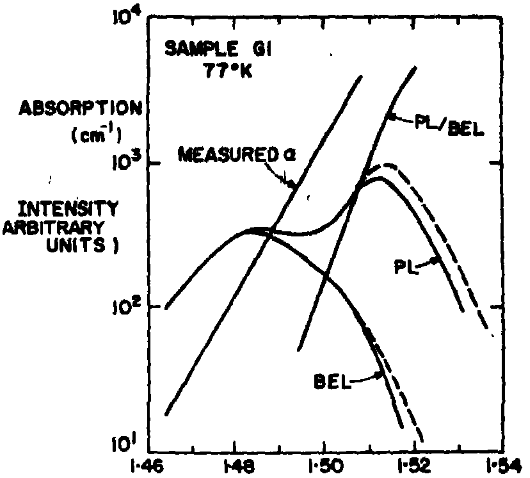

Fig. 7. Measured absorption curve of G1 at 77°K, compared with effective absorption curve derived from comparison of PL with BEL spectra. Broken lines: correction for surface layer absorption.

The BEL spectrum in Fig. 7 has been shifted by 5 MeV to compensate for sample heating during the ionizing pulse. The necessary amount of shift was ascertained by extending the ionizing pulse and measuring the extra shift. The heating is of order 15°K, and does not change the spectral shape significantly.

6. RECOMBINATION RATES

Examination of the equations (2–5) shows that there are no single features of the experimental data that allow individual determinations of the unknown parameters involved; initial slope, final slope, relative height of A1 and A2 peaks and the maximum of A2 all depend on several parameters. A curve-fitting method is required to find a consistent set of parameters. The method employed used computer adjustment of parameters to fit the curve shape, and a set of trial values of other parameters (B_2 and N_a) to obtain the best fit and most reasonable relative height of the two peak decay curves.

The acceptor density may be estimated from the knowledge of the composition of the melt from which the crystal was grown, as described by Kressel *et al.*[1]. The method may possibly over-estimate the density since other acceptor centers are also present. A Ge acceptor density of about twice the free carrier density, i.e. a total Ge concentration of about $5\times10^{17}\,\text{cm}^{-3}$, seems consistent with the initial doping and melt growth conditions for all crystals. The factor N_1 requires the separation of the acceptor level from the valence band to be known: this is given by the PL spectra, corrected for the small self-absorption, as 30 meV. The effective density of states in the valence band at 77°K is $1{\cdot}5\times10^{18}\,\text{cm}^{-3}$, using an effective hole mass of $0{\cdot}7\,m$. Thus $N_1 = 9\times10^{15}\,\text{cm}^{-3}$ from equation (1). Self-absorption in the BEL material may be estimated by comparing the A1 peak with that for PL, and matching them in the non-absorbed low energy region. The PI peak must be corrected for self-absorption and the BEL peak for temperature shift. The resulting ratio of peak heights now gives the fraction f of radiation escaping as equal to about 0·2.

Table 2. Values of parameters used in fitting decay curves of Fig. 5 ($\times10^{-10}\,\text{cm}^3\,\text{sec}^{-1}$)

	B_2	B_3+B_5	fB_1+B_4
G1	0·9	3·0	5·0
G2	0·8	1·8	2·8
G3	1·1	4·0	4·0

The best fits obtained are shown as solid lines in Fig. 5, and the values of parameters required for these curves in Table 2. Curve shapes are insensitive to values of B_2 less than about $2\times10^{-10}\,\text{cm}^3\,\text{sec}^{-1}$, but it is important to note that all curves calculated with $B_2 > 4\times10^{-10}$ give too sharp a drop-off of the A2 peak. A value of $N_a = 2\,n_0$ was used in Table 2; values somewhat less than this give similar shapes but change the relative magnitudes of the curves, an uncertainty in N_a giving an equal uncertainty in the curve magnitude ratio. This ratio is used as follows. From equations (4) and (5) one deduces

$$(p_2/p_1)_{\text{calc}}/(\Phi_2/\Phi_1)_{\text{meas}} = fB_1/B_3 \qquad (9)$$

Both B_1 and B_3 are radiative constants and should not vary greatly between similar materials, and the required constancy of the ratio (9) has been used to further restrict the range of possible parameters. The best consistency is obtained with a ratio of about 0·8. Now, examining Table 2, noting that the values of B are all rather small, as discussed in the next section, so that the radiative component must be a large proportion of the total, the conclusion may be drawn that a good compromise set of values is:

$$B_1 = 0{\cdot}5 \text{ to } 2\times10^{-9}\ \text{cm}^3\,\text{sec}^{-1}$$
$$B_2 = 0{\cdot}5 \text{ to } 2\times10^{-10}\,\text{cm}^3\,\text{sec}^{-1}$$
$$B_3 = 1 \text{ to } 2\times10^{-10}\ \ \text{cm}^3\,\text{sec}^{-1}$$

for each sample, with the remaining non-radiative components varying by a factor of about 3 between samples.

7. DISCUSSION

The purpose of this paper has been to examine the possibility of obtaining a fairly good fit to the experimental data by a simplified model. It is evident that the model used cannot be simplified to the point where the valence-acceptor transition rate is indefinitely fast and a quasi-Fermi level defined since the calculations show that a marked flattening of the initial part of the A2 decay is not possible in the limit $B_2 \rightarrow \infty$ over the range of intensities observed. The question now arises, whether the derived values of B_{1-3} are reasonable. The van Roosbroeck and Shockley theory[7] may be applied to calculate B_1. Discussion is given elsewhere[9] on the possible modifications of the procedure to take account of band tails in such a way as to yield the observed spectrum. If this is done, the value at 77°K is seen to be close to the $2{\cdot}1 \times 10^{-9}\,\mathrm{cm}^3\,\mathrm{sec}^{-1}$ quoted by Varshni[20] for a material with an ideal band-structure. Alternatively, the recombination might be regarded as taking place between the donor states very close to the band and free holes, and Aukerman *et al.*[10] use the Dumke theory to derive a value of $1{\cdot}5 \times 10^{-9}\,\mathrm{cm}^3\,\mathrm{sec}^{-1}$ on this basis. Thus on a theoretical basis one would expect B_1 to have a value close to that obtained from the measurements of this paper. Experimental results for B_1 have been obtained by Wittry and Kyser[11], using diffusion length techniques. The technique is difficult and there is considerable scatter in the results. Sushkov and Moma[12] give reasons for believing that the Wittry and Kyser values tend to be high; in some cases non-radiative recombination can increase the apparent B_1. In *n*-type GaAs the lowest values derived were of order $2 \times 10^{-10}\,\mathrm{cm}^3\,\mathrm{sec}^{-1}$. Thus, within the error of our methods, the value of B_1 deduced from the present experiments may be regarded as not in disagreement with theory and with other experiments. A number of other values of recombination constant have been published, but these cannot be identified with band-to-band rather than band-to-impurity transitions.

The agreement for B_3 is also quite good. The theory of Dumke[13], which takes hydrogenic acceptor wave functions and calculates recombination rates from the matrix element with the $k \sim 0$ conduction electrons, gives $B_3 = 8 \times 10^{-10}\,\mathrm{cm}^3\,\mathrm{sec}^{-1}$ for a 30 meV level. Vilms and Spicer[14] obtain, with order-of-magnitude accuracy, experimental values of $B_3 \sim 10^{-9}\,\mathrm{cm}^3\,\mathrm{sec}^{-1}$ for Cd and Zn acceptors in fairly heavily doped material. The value derived from the present experiments is fairly close to these. In contrast, the hole capture constant B_2 has a small value which deviates significantly from expectation. The theory of Ascarelli and Rodriguez[15] describes the phonon-radiative cascade capture of charge carriers. A marked cascade through the acceptor excited states is predicted only at low temperatures; at 77°K only the ground and first excited states play an important role. Thus, in the Ascarelli and Rodriguez notation, using the carrier effective mass appropriate to holes in GaAs and $n_0 = 2$, the factor $\exp(E_i/n_0^2kT)$, to which B_2 is proportional, is of order unity. The value of B_2 is calculated from theory to be $6 \times 10^{-9}\,\mathrm{cm}^3\,\mathrm{sec}^{-1}$, much larger than that of Table 2. Direct experimental measurements of hole capture rates under conditions comparable to present experiments have not been found. As a poor substitute for these, one may estimate the rate of hole capture by acceptors such as Zn in a luminescent GaAs diode, since the radiated flux and the volume of recombination are known. Stern[16] discusses results[17] in which the acceptor density is $6 \times 10^{18}\,\mathrm{cm}^{-3}$, and the injected current leads to a recombination rate of $5 \times 10^{27}\,\mathrm{cm}^{-3}\,\mathrm{sec}^{-1}$ at 300°K. If the acceptor levels are to maintain a hole occupancy of more than 50 per cent, then the corresponding values of B_2 must exceed $2{\cdot}5 \times 10^{-10}\,\mathrm{cm}^3\,\mathrm{sec}^{-1}$. A strong temperature dependence of B_2 is not expected; one is therefore led to anticipate a value at 77° at least somewhat in excess of that in Table 2.

As a possible interpretation of the disagreement with the theoretical B_2, it is suggested that holes may be localized in fairly small regions. The band-tail model of Redfield[18] describes spatial energy fluctuations which could lead to such localization under the conditions of these experiments. If the regions in which the holes are held are so limited that they do not in general also contain an acceptor center, then hole capture will be markedly reduced from that given by an ideal model with a flat valence band. Such a situation could occur if there were many other negatively charged centers besides the filled Ge acceptor which attract holes (without necessarily completely capturing them) or if a large proportion of Ge acceptors are located close to Ge donors, which will be positively charged and repel holes. The statistics of such a situation have not been studied and the suggestion is made only tentatively.

Values of B_2 and B_3 of similar magnitude to those derived here were obtained by J. A. W. van der Does de Bye[19], using decay of electron-beam excited luminescence. The acceptor centers he observed, however, were different. Although the data were interpreted to show acceptor levels as low as 30 meV, the radiation emitted due to the conduction-band-to-acceptor recombination peaked always at energies 150 meV or more below the band gap. Thus direct comparison with the present data is not valid.

The incident flux at which saturation of the PL A2 peak sets in may be estimated from the measured output of the GaAs–P laser, 0·1 W. The minimum image size is determined by diffraction and by the degree of coherence of the incident radiation; an estimate of $10 \times 50\ \mu m^2$ is reasonable, leading to a flux of 2×10^4 W cm^{-2}. The flux anticipated to approach saturation of A2 may be calculated from equation (7), using values of recombination rate constants derived (Table 2). With a penetration depth of 3 μm due to hole diffusion, and $f \sim 1$, the flux is calculated to be 5×10^3 W cm^{-2}. If system losses are included, it appears there is good order-of-magnitude agreement between the two figures; better agreement involving a more accurate measure of incident flux would be difficult to achieve. Both PL and BEL observations can therefore be explained with some success using similar B values.

In summary, it appears that the model presented here can give a consistent approximate explanation of the kinetics of recombination via germanium acceptor centers in n-GaAs. It has the characteristic of requiring a limited communication between holes in the valence band and shallow acceptors; thus the definition of a quasi-Fermi level for the valence band region is not possible if this region is taken to include the acceptor states. The model is presented with some reservations: clearly there is a discrepancy in the account given of self-absorption, and also the curve-fitting is not entirely unambiguous. Whether a modified approach, involving perhaps a more sophisticated model of band-tails and the communication between tail states, can give a better account of the system, remains to be seen.

Acknowledgements—I wish to thank R. T. Mazzochi for preparing the samples, performing many of the measurements and assisting in the computation, F. Hawrylo for growing the epitaxial material, and H. Kressel and D. Redfield for discussions.

REFERENCES

1. KRESSEL H., HAWRYLO F. A. and LeFUR P., *J. appl. Phys.* **39** 4059 (1968).
2. SOUTHGATE P D., *J. appl. Phys.* **38** 4589 (1967).
3. NELSON H., *RCA Rev.* **24** 603 (1963).
4. SHOCKLEY W., READ W. T., *Phys. Rev.* **87** 835 (1952).
5. BLAKEMORE J. S., *Semiconductor Statistics*. Pergamon Press, New York (1962).
6. FRIEDRICH H. and JUNGK G., *Phys. Status Solidi* **27** 237 (1968).
7. VAN ROOSBROECK W. and SHOCKLEY W., *Phys. Rev.* **94** 1558 (1954).
8. REDFIELD D. and WITTKE J. P., *Proc. Third Intl Conf. Photocond.*, Stanford, Aug. 1969.
9. SOUTHGATE P. D., *J. appl. Phys.* In press.
10. AUKERMAN L. W., MILLEA M. F. and McCOLL M., *J. appl. Phys.* **38** 685 (1967).
11. WITTRY D. B. and KYSER D. F., *J. appl. Phys.* **38** 375 (1967).
12. SUSHKOV V. P. and MOMA YU. A., *Fiz. Tech. Pol.* **1** 1531 (1967); Transl. *Sov. Phys-Semics* **1** 1273 (1968).
13. DUMKE W. P., *Phys. Rev.* **132** 1998 (1963).
14. VILMS J. and SPICER W. E., *J. appl. Phys.* **36** 2815 (1965).
15. ASCARELLI G. and RODRIGUEZ S., *Phys. Rev.* **127** 167 (1962).
16. STERN F., *Phys. Rev.* **148** 186 (1966).
17. PILKUHN M, RUPPRECHT H. and BLUM S., *Solid-St. Electron.* **7** 905 (1964).
18. REDFIELD D., *Phys. Rev.* **130** 916 (1963).
19. VAN DER DOES DE BYE J. A. W., *J. Phys. Chem. Solids* **28** 1485 (1967).
20. VARSHNI Y. P., *Phys. Status Solidi* **19** 459 (1967).

J. Phys. Chem. Solids Pergamon Press 1970. Vol. 31, pp. 67–76. Printed in Great Britain.

ETUDES DES QUEUES DE BANDES DANS LE Ga Sb FORTEMENT DOPE

H. MATHIEU
Centre d'Etudes d'Electronique des Solides associé au CNRS,
Faculté des Sciences de Montpellier, France

(*Received* 21 *January* 1969; *in revised form* 8 *May* 1969)

Résumé—On calcule les taux d'émissions spontanée et stimulée de diodes lasers au Ga Sb en adoptant le modèle de queues de bandes de E. O. Kane. On en déduit les variations du gain avec l'injection et du seuil d'émission stimulée avec la température. Les résultats théoriques sont comparés aux mesures expérimentales obtenues sur les diodes dont les concentrations en impuretés sont $N_A = 10^{19}$ cm^{-3} et $N_D = 10^{18}$ cm^{-3}.

1. INTRODUCTION

LORSQU'UN semiconducteur contient une concentration d'impuretés suffisamment grande, les états électroniques ainsi introduits peuvent former des queues de bandes. C'est en particulier le cas dans les lasers à jonction *p–n*, qui se prêtent donc relativement bien à l'étude des matériaux fortement dopés.

Nous nous intéresserons ici à des lasers à injection au Ga Sb; la jonction est obtenue par dopage alterné du bain au cours du tirage du monocristal par la méthode de Czochralski; le bain est dopé au tellure de façon à ce que le cristal contienne initialement une densité de donneurs de l'ordre de $N_D = 10^{18}$ cm^{-3}, on ajoute alors du zinc dans le creuset de façon à obtenir une région de type *p* avec $N_A = 10^{19}$ cm^{-3}. Ainsi dans la région du type *p* les bandes de conduction et de valence se prolongent par des queues de bandes, on étudie l'émission dans cette région. Des études de répartition d'énergie à la surface de la diode et d'ouverture de faisceau lumineux nous ont permis d'apprécier à 40 μ dans le plan de la jonction et 4,5 μ dans le plan perpendiculaire les dimensions du spot lumineux. D'autre part nos jonctions étant fabriquées par tirage la zone d'inversion est probablement inférieure à 1 μ; ainsi nous supposerons que la région active se situe dans une zone où le matériau est relativement homogène.

2. CALCUL DES DENSITES D'ETATS ET DES TAUX D'EMISSION SPONTANEE ET STIMULEE

La théorie de l'émission stimulée dans les lasers à injection a été développée par Lasher et Stern[1]en adoptant un modèle de bandes paraboliques. En fait les conditions de dopage sont telles que le modèle de bandes paraboliques n'est pas satisfaisant, surtout à faible niveau d'injection et à basse température. La variation exponentielle de l'intensité du rayonnement émis en fonction de l'énergie de la raie[1–6] a suggéré à certains auteurs la participation de queues de bandes dans lesquelles la densité d'état varie exponentiellement avec l'énergie[5]. F. Stern, notamment, a repris les calculs des taux d'émissions spontanée et stimulée de diodes lasers à Ga As[7] en adoptant le modèle de queues de bandes de E. O. Kane[8]. En ce qui concerne les lasers à injection au Ga Sb, aucune théorie de ce genre n'a été développée, seuls Kryukova et ses collaborateurs[9] ont émis l'hypothèse de l'existence de queues de bandes exponentielles pour interpréter phénoménologiquement certains résultats expérimentaux. Nous allons calculer les taux d'emission spontanée et stimulée dans nos diodes suivant la méthode développée par F. Stern dans le cas du Ga As, en utilisant le modèle de queues de bandes de E. O. Kane. Nous comparerons les variations théoriques de certains paramètres avec les résultats expérimentaux.

Nous ne reviendrons pas sur les avantages et les inconvénients du modèle de E. O. Kane dont la discussion a été développée par F. Stern. Toutefois il faut remarquer que ce modèle que a été développé dans le cas de matériaux non compensés prévoit l'apparition de queues de densité d'états à l'extrémum de chacune des bandes. En fait dans un semiconducteur ne contenant qu'un seul type d'impureté, des donneurs par exemple, les amas de centres ionisés jouent un rôle attractif pour les électrons mais répulsif pour les trous, de sorte que s'il apparait des états liés pour les électrons, ce qui se traduit par l'existence d'une queue de densité d'états au bas de la bande de conduction, il n'apparaît pas d'états semblables pour les trous, et par conséquent pas de queue de densité d'états au sommet de la bande de valence. En ce qui concerne les matériaux compensés par contre il existe à la fois dans le semiconducteur des agglomérats attractifs pour les électrons et des agglomérats attractifs pour les trous ce qui entraine un effet de queue de densité d'états sur chacune des bandes. Les études de C. Benoit a la Guillaume et J. Cernogora[10] sur l'évolution de ces queues de bande avec les concentrations d'impuretés N_D-N_A ont effectivement montré (Fig. 5 réf. 10) l'existence d'une seule queue de bande si le matériau est très peu compensé et de deux queues de bande s'il y a compensation, même partielle.

En ce qui concerne nos échantillons que sont partiellement compensés nous calculerons les densités d'états dans chacune des queues de bande en utilisant le modèle de E. O. Kane, les paramètres caractérisant ces queues de bandes étant respectivement fonction du nombre de donneurs (bande de conduction) et du nombre d'accepteurs (bande de valence), ainsi que de la differénce N_A-N_D par l'intermédiaire du nombre de porteurs libres qui jouent un rôle d'écran vis-à-vis du potentiel coulombien des impuretés.

Rappelons les expressions des taux d'émissions spontanée et stimulée du coefficient d'amplification[1].

$$r_{sp}(E) = B\int \rho_c(E')\,\rho_v(E'-E)f_n(E')[1-f_p(E'-E)]dE' \qquad (1)$$

$$r_{st}(E) = B\int \rho_c(E')\rho_v(E'-E)[f_n(E')-f_p(E'-E)]dE' \qquad (2)$$

où

$$B = \frac{4ne^2E}{m^2\hbar^2c^3}\cdot\overline{|M|^2}V \qquad (3)$$

$$\alpha(E) = \frac{\pi^2c^2\hbar^3}{n^2E^2}r_{st}(E) \qquad (4)$$

Dans le modèle de bandes de Kane les densités d'états ρ_c et ρ_v sont données par:

$$\rho_c(E) = \pi^{-2}\hbar^{-3}m_c^{3/2}(2\eta_c)^{1/2}Y\left(\frac{E-E_c}{\eta_c}\right) \qquad (5a)$$

$$\rho_v(E) = \pi^{-2}\hbar^{-3}m_v^{3/2}(2\eta_v)^{1/2}Y\left(\frac{E-E_v}{\eta_v}\right) \qquad (5b)$$

où m_c et m_v sont les masses effectives des électrons et des trous et E_c et E_v les extrema des bandes non perturbées.

$$Y(x) = \pi^{-1/2}\int_{-\infty}^{x}(x-z)^{1/2}e^{-z^2}dz \qquad (6)$$

η_c et η_v sont des paramètres caractérisant la forme des queues de bandes donnés par:

$$\eta_c = \frac{e^2}{k}(4\pi N_D L)^{1/2} \qquad (7a)$$

$$\eta_v = \frac{e^2}{k}(4\pi N_A L)^{1/2} \qquad (7b)$$

où k est la constante diélectrique statique, N_D et N_A les densités de donneurs et d'accepteurs et L la longuer d'écran.

La longueur d'écran est essentiellement fonction du nombre de porteurs et de la forme des bandes; quand le semiconducteur est dégénéré, elle est donnée [11] par l'expression:

$$L^{-2} = \frac{4\pi e^2}{k}[\rho_c(F'_n) + \rho_v(F'_p)] \qquad (8)$$

oú F'_n et F'_p représentent les distances à la bande de conduction et à la bande de valence respectivement des pseudo-niveaux de Fermi des électrons et des trous, comptés positivement à l'intérieur des bandes.

En ce qui concerne nos échantillons, $N_A - N_D = 0{,}9.10^{19}\,\text{cm}^{-3}$; ainsi le nombre de trous est très important et leur pseudo-niveau de Fermi se situe à l'intérieur de la bande de valence proprement dite, en conséquence $\rho_v(F'_p)$ reste toujours très supèrieur à $\rho_c(F'n)$ et on peut négliger la participation des électrons à l'effet d'écran devant celle des trous. L^{-2} s'écrit alors:

$$L^{-2} \simeq \frac{4\pi e^2}{k}\pi^{-2}\hbar^{-3}m_v^{3/2}(2\eta_v)^{1/2}Y\left(\frac{F'_p}{\eta_v}\right) \qquad (9)$$

Les densités d'états sont essentiellement fonction du paramètre L par l'intermédiaire de η_c ou η_v, L étant lui-même fonction des densités d'états par l'équation (8). On devra donc faire un calcul global de $\rho_c, \rho_v, \eta_c, \eta_v$ et L

Principe de calcul

Les densités de porteurs dans chaque bande sont données par les expressions:

$$n = \pi^{-2}\hbar^{-3}m_c^{3/2}(2\eta_c)^{1/2}\int_{-\infty}^{+\infty} Y\left(\frac{E'}{\eta_c}\right)\left[1 + \exp\left(\frac{E' - F'n}{kT}\right)\right]^{-1}dE' \qquad (10a)$$

$$p = \pi^{-2}\hbar^{-3}m_v^{3/2}(2\eta_v)^{1/2}\int_{-\infty}^{+\infty} Y\left(\frac{E'}{\eta_v}\right)\left[1 + \exp\left(\frac{E' - F'p}{kT}\right)\right]^{-1}dE' \qquad (10b)$$

Les paramètres de départ sont N_A et N_D. On choisit arbitrairement une valeur de L; on en déduit séparément à l'aide des expressions (7a) et (7b), η_c et η_v.

À partir de η_v l'expression (9) permet d'obtenir F'_p et par suite p par (10b).

À partir de η_c on calcule à l'aide de l'équation (10a) les valeurs de n correspondant à une série de valeurs de F'_n.

Pour déterminer dans la série des valeurs de n la valeur adéquate et le F'_n correspondant, nous écrivons la condition de neutralité électrique:

$$p - n = \text{Cte} = N_A - N_D$$

Les calculs effectués sur ordinateur IBM 360, nous permettent ainsi de dresser en fonction de L le tableau des paramètres η_c, η_v, F'_n et F'_p à différentes températures. Nous avons pris dans le cas du Ga Sb:

$m_c = 0{,}05$ m $\quad m_v = 0{,}5$ m $\quad k = 15 \quad n = 3{,}9$

Pour caractériser le niveau d'injection nous utiliserons comme Stern [7], un courant nominal défini de la façon suivante:

le taux d'émission spontanée total $R = B$ np[1] représente le nombre de photons émis par seconde par l'unité de volume du cristal. Si la zone active a une épaisseur d et si une fraction η des porteurs injectés donne naissance à des photons, il faudra, pour maintenir le taux de recombinaison R dans cette épaisseur, injecter $R\ d/\eta$ électrons par seconde, c'est-à-dire injecter un courant:

$$J = R\frac{d}{\eta}e\,\text{A.cm}^{-2} \qquad (11)$$

On définit le courant nominal J_0 comme le courant nécessaire au maintien du taux de recombinaison $R\,\mathrm{cm}^{-3}s^{-1}$ sur une épaisseur de $1\,\mu$ si le rendement interne est $\eta = 100\%$, soit:

$$J_0 = 1{,}6.10^{-23}Bnp \tag{12}$$

Le facteur de conversion permettant de passer du courant nominal au courant mesuré dépend de trois quantités: l'épaisseur de la zone active d, le rendement interne η et un troisième facteur Γ introduit phénoménologiquement qui tient compte du fait que le courant n'est pas péparti de façon homogène sur toute la section de la diode.

$$J_m = J_0\frac{d}{\eta}\Gamma$$

On calcule alors $r_{sp}(E)$ et $r_{st}(E)$ pour divers niveaux d'injection. Si on prend comme origine des énergies le bas de la bande de conduction non perturbée, les expressions s'écrivent:

Les courbes représentant $r_{st}(E)$ coupent l'axe des énergies pour des valeurs de l'énergie telles que $E = F_n - F_p$; pour des valeurs supérieures, $r_{st}(E)$ devient négatif: on retrouve la condition d'inversion de population de Bernard et Duraffourg[12] $F_n - F_p \geqslant h\nu$

La Fig. 2 représente les variations du gain G_0 (maximum de $\alpha(E)$) en fonction du courant nominal. Ce courant étant directement proportionnel au courant traversant la diode, on obtiendra les variations du courant de seuil avec la température à partir du réseau de courbes précédent, en déterminant les valeurs de J_0 nécessaires au maintien d'un gain constant quand la température varie; il suffit pour cela de tracer sur la Fig. 2 une droite horizontale représentant un gain constant. On obtient ainsi les courbes de variation du seuil avec la température de la Fig. 3. On constate que pour des températures supérieures à 100°K le seuil varie sensiblement comme T^3.

$$r_{sp}(E) = C(\eta_c\eta_v)^{1/2}\int_{-2\eta_c}^{E-E_g+2\eta_v} Y\left(\frac{E'}{\eta_c}\right)Y\left(\frac{E-E_g-E'}{\eta_v}\right)\left[1+\exp\left(\frac{E'-F'_n}{kT}\right)\right]^{-1}$$
$$\left\{1-\left[1+\exp\left(\frac{E'+E_g+F'_p-E}{kT}\right)\right]^{-1}\right\}dE' \tag{13a}$$

$$r_{st}(E) = C(\eta_c\eta_v)^{1/2}\int_{-2\eta_c}^{E-E_g+2\eta_v} Y\left(\frac{E'}{\eta_c}\right)Y\left(\frac{E-E_g-E'}{\eta_v}\right)\left\{\left[1+exp\left(\frac{E'-F'_n}{kT}\right)\right]^{-1}\right.$$
$$\left.-\left[1+\exp\left(\frac{E'+E_g+F'_p-E}{kT}\right)\right]^{-1}\right\}dE' \tag{13b}$$

où $C = 2\pi^{-4}\hbar^{-6}m_c^{3/2}m_v^{3/2}B$.

Le choix des bornes d'intégration $-2\eta_c$ et $E-E_g+2\eta_v$ est justifié par la décroissance très rapide de la densité d'états dans les queues de bandes.

Les taux d'émissions spontanée et stimulée qui traduisent la forme spectrale de la raie sont représentés sur la Fig. 1. On remarque que $r_{st}(E)$ tend vers $r_{sp}(E)$ quand l'injection augmente et quand la température diminue.

3. INTERPRETATION DES RESULTATS EXPERIMENTAUX

Les caractéristiques du rayonnement émis par nos diodes sont résumées sur les Figs. 4 et 5. La Fig. 4, représentant l'intensité de ce rayonnement en fonction de l'injection, montre que le courant de seuil de l'émission stimulée est de l'ordre de $1000\,\mathrm{A\,cm}^{-2}$. L'étude de l'évolution du spectre avec l'injec-

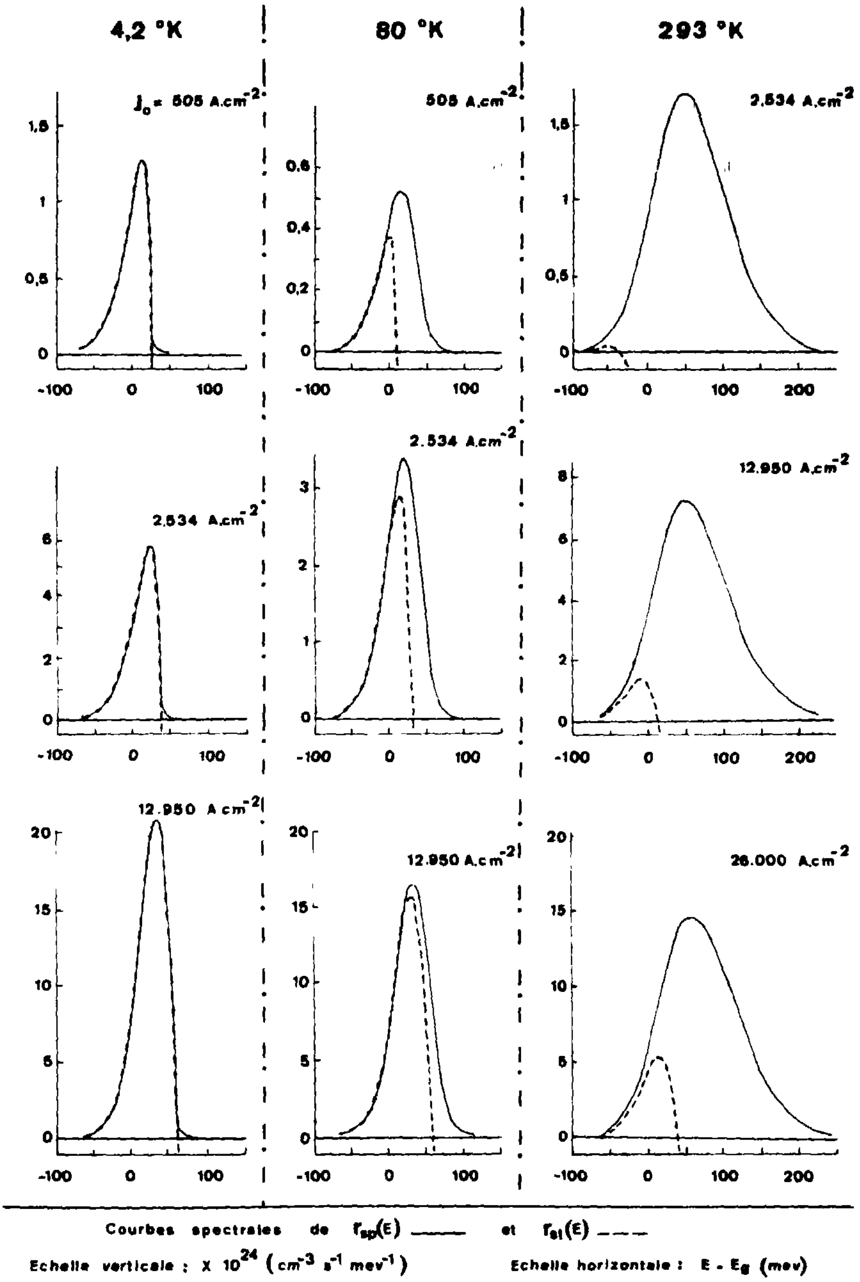

Fig. 1. Spectres d'émissions spontanée et stimulée à 4,2°, 80° et 293°K pour différentes valeurs de l'injection.

tion (Fig. 5) montre que la raie d'émission stimulée apparaît pratiquement au milieu du spectre d'émission spontanée. On constate que l'énergie de cette raie ne varie pas avec l'injection. Or les spectres de la figure 1 montrent que les taux d'émissions spontanée et stimulée se déplacent vers les grandes énergies quand l'injection augmente. Ces varia-

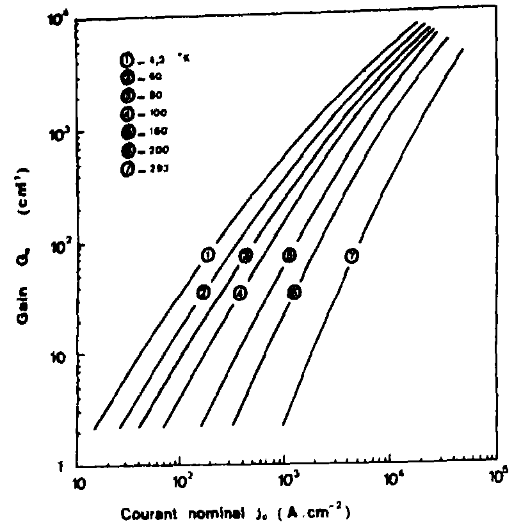

Fig. 2. Variation du gain avec le courant nominal pour différentes températures.

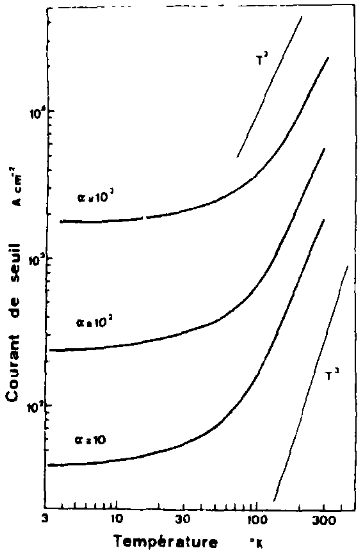

Fig. 3. Variation du courant de seuil avec la température.

tions d'énergie directement liées aux déplacements des pseudo-niveaux de Fermi F'_n et F'_p, peuvent être attribués au seul remplissage de la bande de conduction, le pseudo-niveau de Fermi des trous variant très peu avec l'injection. En fait les calculs sont effectués en supposant une durée de vie

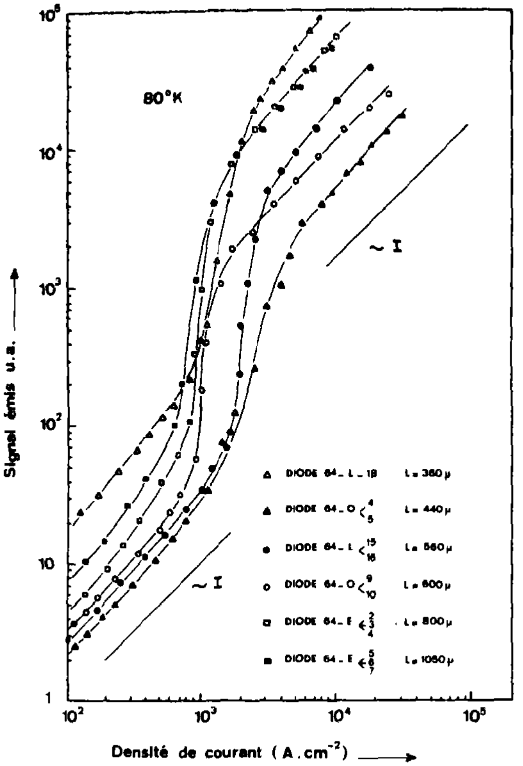

Fig. 4. Intensité émise en fonction de l'injection à 80°K pour des diodes de différentes longueurs L = distance entre les faces clivées.

des porteurs injectés constante avec l'injection. Ceci est justifié dans la mesure où les recombinaisons présentes dans le semiconducteur sont spontanées; si ces recombinaisons sont provoquées par des photons (émission stimulée) la durée de vie des porteurs doit diminuer à mesure que le nombre de ces photons augmente, c'est-à-dire à mesure que l'émission stimulée présente dans le semiconducteur augmente. Ainsi, si l'émission spontanée existe seule, la durée de vie des électrons est constante, l'augmentation de l'injection se traduit par un déplacement vers les grandes énergies du pseudo-niveau de Fermi des électrons thermalisés et par suite de la raie d'émission. Quand l'émission est stimulée, l'augmentation de l'injection se traduit par une diminution de la durée de vie des porteurs, le pseudo-niveau de Fermi de ces

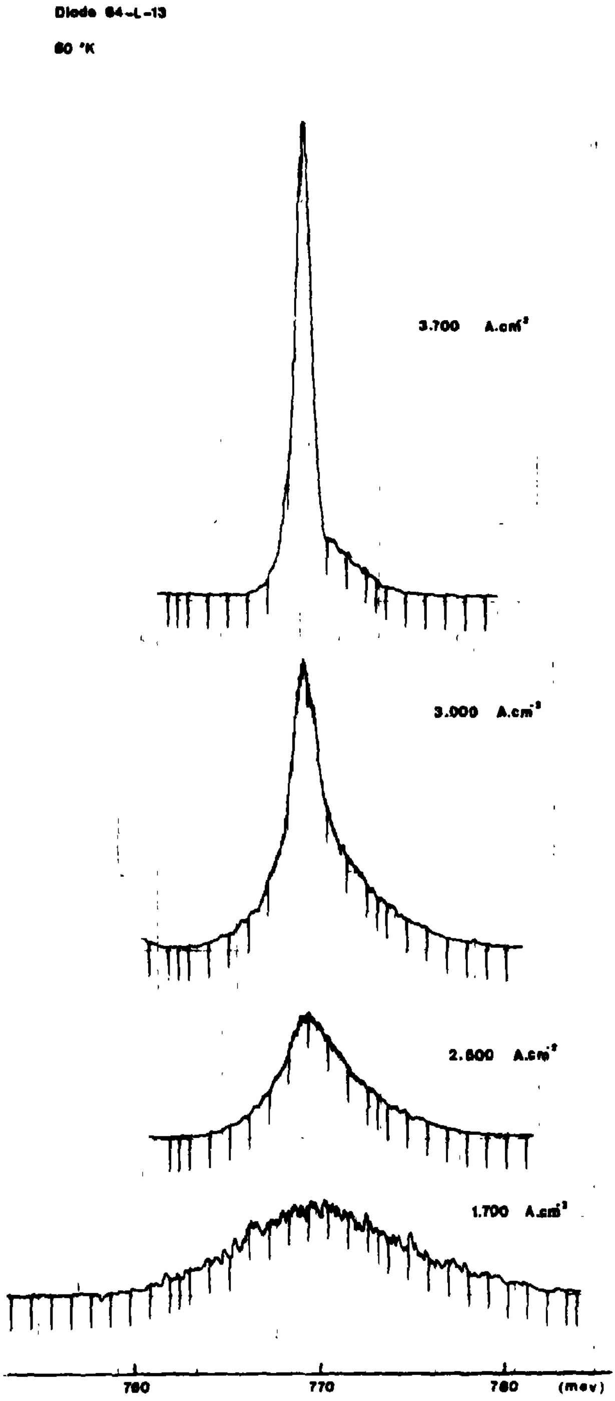

Fig. 5. Evolution du spectre d'émission avec le courant, émission spontanée et émission stimulée.

porteurs reste fixe, il en est de même de la raie d'émission. Les résultats expérimentaux concernant les déplacements des raies d'émissions sont représentés sur la Fig. 6. La diode 44-E-3 émet un rayonnement spontané dont le déplacement est observé jusqu'à un courant de l'ordre de 2000 A cm^{-2} qui correspond au courant de seuil de la diode; pour des courants supérieurs la diode émet un rayonnement stimulé dont l'énergie reste constante avec l'injection. La diode 64-E-23 ayant un seuil d'émission stimulée beaucoup plus important nous avons pu mesurer le déplacement de la raie d'émission spontanée jusqu'à un courant de l'ordre de 10^4 A cm^{-2}; au-delà la présence d'émission stimulée entraine une saturation du déplacement. D'une manière générale nous avons constaté que la raie d'émission stimulée ne se déplaçait pas avec l'injection; par contre l'énergie de cette raie est d'autant plus importante que le courant de seuil de la diode est plus grand.

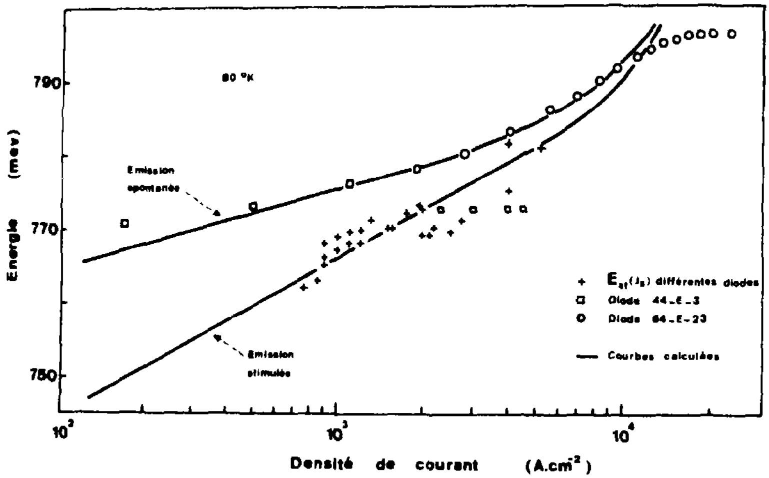

Fig. 6. Déplacement des raies d'émissions spontanée et stimulée avec l'injection. □ = diode 44-E-3; ○ = diode 64-E-23; + = énergie de la raie d'émission stimulée de différentes diodes en fonction de leur courant de seuil.

Nous avons porté sur la fig. 6 les points (+) représentant la position du pic d'émission stimulée d'une série de diodes en fonction de leur courant de seuil.

On constate un accord satisfaisant entre les trois séries de points expérimentaux et les courbes théoriques représentant en fonction de l'injection l'énergie des maxima de $r_{sp}(E)$ et $r_{st}(E)$ définis par les équations (13a) et (13b). Les courbes théoriques ont été calculées en prenant $\Gamma d/\eta = 0{,}5$ et $Eg = 756$ MeV. L'abaissement du gap de 44 meV, nécessaire à l'accord des résultats est dû à la grande densité d'impuretés qui entrainent, outre la formation de queues de bandes, une diminution du gap[13]. En ce qui concerne le paramètre $\Gamma d/\eta$, sa valeur peut être comparée à celle obtenue par Lasher et Stern[1] dans le cas du Ga As et de bandes paraboliques $\Gamma d/\eta = 0{,}6$. Toutefois les inhomogénéités de courant variant de façon tout à fait aléatoire d'une diode à l'autre, le paramétre $\Gamma d/\eta$ varie de même, ce qui explique en particulier la dispersion des points expérimentaux représentant sur la Fig. 6 l'énergie de la raie d'émission stimulée en fonction du courant de seuil.

Outre le déplacement des raies d'émission avec l'injection, l'intensité du rayonnement est directement liée aux fonctions densités d'états. Les résultats que nous avons obtenus dans ce sens sont représentés sur la Fig. 7. Le changement de pente qui apparaît à un courant

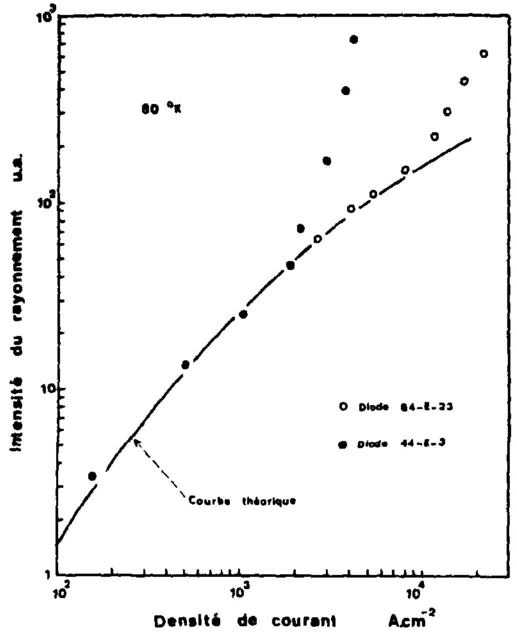

Fig. 7. Intensité du rayonnement en fonction du courant.

déterminé, différent d'une diode à l'autre, traduit l'apparition d'émission stimulée.

Ainsi pour accorder la théorie avec nos résultats expérimentaux, il faut prendre $J_0 \approx 2J$. Le courant de seuil sur l'ensemble de nos diodes est de l'ordre de 1000 A cm^{-2} ce qui correspond à un courant nominal de l'ordre de 2000 A cm^{-2}. Si on se réfère aux courbes de la Fig. 8 représentant le déplacement du pseudo-niveau de Fermi des électrons avec l'injection, on constate que ce courant de seuil correspond sensiblement au moment où le pseudo-niveau de Fermi des électrons atteint le bas de la bande de conduction proprement dite. Ceci est en accord avec les résultats que nous avons obtenus dans l'étude du déplacement de la raie d'émission stimulée avec le champ magnétique[14]. En se rapportant aux courbes de la Fig. 2 on peut remarquer qu'un courant nominal de 2000 A cm^{-2} correspond à un coefficient d'amplification de l'ordre de 500 cm^{-1}. Si l'on suppose que la principale cause d'absorption est la présence de porteurs libres, on obtient pour les trous, qui sont nettement majoritaires une section efficace de capture $\sigma_p \approx 0{,}5\ 10^{-16}$ cm^2 en accord avec la valeur citée par Duraffourg[15].

Enfin les fonctions densités d'états déterminent la valeur du coefficient d'amplification à une température donnée, ainsi elles sont directement liées au seuil d'émission stimulée. Les courbes expérimentales de variation du seuil en fonction de la température (Fig. 9) présentent, au-delà de 100°K, une pente de variation en T^3 en accord avec la théorie. Toutefois rappelons que le seuil d'émission

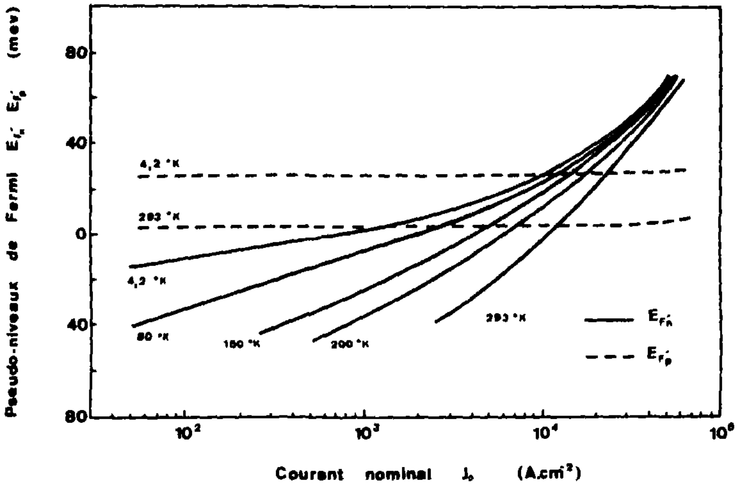

Fig. 8. Evolution des pseudo-niveaux de Fermi des électrons et des trous avec l'injection.

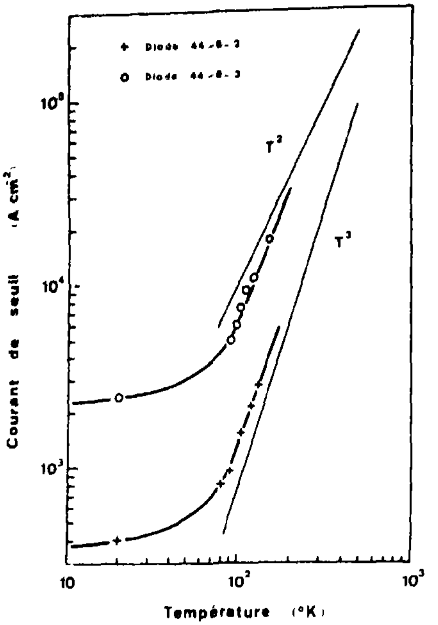

Fig. 9. Variation du courant de seuil avec la température, résultats expérimentaux.

stimulée de nos diodes correspond au moment où le pseudo-niveau de Fermi des électrons atteint le bas de la bande de conduction proprement dite. Ainsi la variation en T^3 est due à la partie quasi-parabolique de la bande de conduction ce qui ne permet pas de distinguer de façon notable des variations de seuil différentes suivant que la structure de bande est parabolique [1] ou exponentielle.

CONCLUSION

Nous avons calculé les taux démissions spontanée et stimulée de diodes lasers au Ga Sb en adoptant le modèle de queues de bandes de E. O. Kane. Les résultats expérimentaux que nous avons obtenus sur l'étude de l'intensité et du spectre de la raie d'émission et sur l'évolution avec la température du seuil d'émission stimulée présentent un accord satisfaisant avec les courbes théoriques. Ainsi dans les conditions de dopage qui sont celles de nos diodes, nous pensons que le modèle de E. O. Kane constitue une représentation satisfaisante des densités d'états dans les queues de bandes.

BIBLIOGRAPHIE

1. LASHER G. et STERNE F., *Phys. Rev.* **133A**, 553 (1964)
2. NELSON D. F., GERSHENZON M., ASHKIN A., D'ASARO L. A. et SARACE J. C., *Appl. Phys. Lett.* **2**, 182 (1963).
3. ARCHER R. J., LEITE R. C. C., YARIV A., PORTO S. P. S. et WHELAN J. M., *Phys. Rev. Lett* **10**, 483 (1963).
4. LEITE R. C. C., RIPPER J. E. et GUGLIELMI P A., *Appl Phys. Lett.* **5**, 188 (1964)
5. DOUSMANIS G. C., MUELLER C. W., NELSON H. et PETZINER K G., *Appl. Phys. Lett.* **3**, 133 (1963).
6. BURNS G. et NATHAN M. I., *Proc. IEEE* **52**, 770 (1964)
7. STERN F., *Phys. Rev.* **148**, 186 (1966).
8. KANE E. O., *Phys. Rev.* **131**, 79 (1963).
9. KRYNKOVA I. V., MIRGALOVSKAYA M. S., KARNAUKHOV V. G., BARANOVA A. M et STREL'NIKOVA I. A., *Soviet. Phys. solid St.* **8**, 822 (1966).
10. CENOIT C., LA GUILLAUME A. et CERNOGORA J., *Phys. Status Solidi* **11**, 295 (1965).
11. HALPERIN B. I. et LAX M., *Phys. Rev.* **148**, 722 (1966).
12. BERNARD M. G. A. et DURAFFOURG G., *J. Phys. Radium, Paris* **22**, 836 (1961); *Phys. Status Solidi* **1**, 659 (1961).
13. WOLFF P. A., *Phys. Rev.* **126**, 405 (1962).
14. PISTOULET B., MATHIEU H., Congrès sur la Physique des Semiconducteurs, Moscow (1968)
15. DURAFFOURG G., Thèse de doctorat, Paris (1965).

J. Phys. Chem. Solids Pergamon Press 1970. Vol. 31, pp. 77–94. Printed in Great Britain.

A NEW TYPE OF LONG PERIOD SUPERLATTICE WITH HEXAGONAL SYMMETRY IN Au–Cd ALLOYS

M. HIRABAYASHI, S. YAMAGUCHI, K. HIRAGA and N. INO
The Research Institute for Iron, Steel and Other Metals, Tohoku University, Sendai, Japan
and
H. SATO and R. S. TOTH*
Scientific Laboratory, Ford Motor Company, Dearborn, Michigan, U.S.A.

(*Received* 24 *April* 1969)

Abstract—The existence of a new type of long period superlattice having hexagonal symmetry, whose period is determined by the critical contact of the Brillouin zone boundaries with the Fermi surface, has been established. The ordering of the atoms on the close packed hexagonal plane of these structures is derived from that of the A_3B type (Cu_3Au type) structure, but the long period is produced in the basal plane by the existence of antiphase boundaries in three directions perpendicular to the close packed plane and making 120° with each other, thus creating the hexagonal symmetry. The stacking of the close packed layers is of either the $2H$ or $4H$ type. The size of this hexagonal unit cell is found to be between seven and nine times as large as that of the hexagonal unit cell of the disordered close packed lattice, these limiting cases being called the $7a_0$ structure and the $9a_0$ structure respectively. Significantly, the period of this structure is found to respond to a change of e/a in a fashion similar to that found in the one dimensional long period superlattice, which has been investigated in detail. In the case of the Au–Cd alloys the stacking is of the $2H$ type and the $7a_0$ structure is identified as $Au_{72}Cd_{28}$ with space group $P6_3/mmc$, and the $9a_0$ structure as $Au_{42}Cd_{12}$ with $P6_3/mcm$. The geometry of the Brillouin zone structure indicates that the structure is stabilized by creating superlattice Brillouin zone boundaries at the flat part of the Fermi surface (in the ⟨110⟩ directions in the case of the fcc structure), as in the case of the one dimensional long period superlattice. Examples of these new structures are found, other than in the Au–Cd alloys reported here, in Au–Mg alloys, Cu–Sb alloys, etc. near the A_3B composition range. These structures are usually found among the long period stacking variants of a one dimensional long period superlattice with non variable period ($M = 1$, $M = 2$, etc.), occurring in these alloys.

INTRODUCTION

IT HAS recently been recognized that various types of long period structures exist in alloys, particularly in those having basically close packed structures. Intensive studies into the nature of long range forces which are responsible for stabilizing such long period structures indicate the essential role of the conduction electrons in the cohesion of metals in determining the crystal structure[1, 2]. In order to reduce their energy, conduction electrons tend to create Brillouin zone boundaries at the Fermi surface by creating extra periodicities in a crystal, for example by appropriate atomic order. The energy required to create such extra periodicities, on the other hand, then opposes the energy gained by the conduction electrons. Hence, a compromise among these energy terms essentially leads to a specific type of extra periodicities created in the crystal, or a specific type of long period structure is stabilized. Therefore, a systematic study of the nature of the energy terms involved in creating such periodicities should give us an enlightening insight into the nature of the stabilization of metallic structures in general.

Considerable progress has been made in this direction starting from the one dimensional long period superlattices (1D LPS), where the superperiod of these alloys is found to be determined by a critical contact of the Brillouin zone boundaries with the Fermi surface, and hence, the period of the structure can be readily obtained from the size of the

---

*Present address: Sensors, Inc., Ann Arbor, Mich.

Fermi surface (or the electron-atom ratio (e/a) of the system)[3-6]. The fact that the stabilization occurs at the critical contact of the Brillouin zone boundaries with the Fermi surface is due to the flatness of the Fermi surface in the ⟨110⟩ directions where the newly created Brillouin zone boundaries contact, so that a sharp minimum in energy is expected[5, 7]. This concept was extended to the short period limit, $M = 1$ or $M = 2$, for example, (M being the half period of the structure in terms of the number of fcc unit cells), where the period can no longer respond to the change in the size of the Fermi surface. In such a case, it was found that the alloy tends to either be distorted tetragonally[8] or create a stacking order modulation[9] without changing its basic structure, so that the Brillouin zone boundaries are kept at the Fermi surface. In this way, the stability of the series of stacking variants which appear in the Au–Mn alloys with the $M = 1$ structure [9], in the Au–Mg alloys near Au_3Mg[10] and in the Au–Cd alloys near Au_3Cd[11, 12] both with the $M = 2$ structures, has been explained.

However, as is easily visualized, the position of the contact of the Brillouin zone boundaries with the Fermi surface tends to deviate more and more from the ⟨110⟩ directions as the period M becomes smaller and as the stacking order modulation is created, and the advantage of the critical contact described above tends to be lost, although a part of this loss may be compensated by the distortion of the Fermi surface due to the change in the symmetry of the crystal. However, if this disadvantage increases too much, the crystal can no longer tolerate the stacking modulation and would eventually change into an other type of structure.

While the stacking variants in the Au–Mg alloys were investigated, Sato *et al.* found the existence of a long period structure of hexagonal symmetry among the existing stacking variants[10] and the structure has subsequently been identified as $Au_{77}Mg_{23}$[13]. A similar structure which apparently belongs to the same family of structures was also found in Au–Cd alloys by Toth *et al.*[14] and, independently, by Hirabayashi *et al.* among the stacking variants of this alloy system[12]. This situation has led us to believe that a family of long period structures of hexagonal symmetry is stabilized by a similar mechanism to that of other long period structures and that this type of structure must be stabilized by a critical contact of the Brillouin zone boundaries with the Fermi surface. On this assumption, a joint effort of the above mentioned two groups has been made to investigate this structure in the Au–Cd alloys and it was found that the period of the structure responded to the change in the size of the Fermi surface in the same fashion as that found in the 1D LPS. In the following, we will give fairly detailed explanations of the structural determination and of the characteristics of the alloys, and will give discussions dealing with the stability aspects of this structure in relation to other long period structures. The emphasis is to make the understanding of the stabilization of this structure a further step toward the understanding of more general crystal structures.

EXPERIMENTAL PROCEDURES AND RESULTS

It has been established in the previous work on the Au–Cd alloy system, that stacking variants of the $M = 2$ structure exist in the composition range around 25 ~ 30 per cen Cd,* with modulations $1R$-$4H$-$6H$-$3R$† occurring with increasing Cd contents[11, 12]. O the other hand, above 45 per cent Cd, martensites, most of which are stacking variants of CuAu ordered structure, are formed whe

---

*Atomic per cent is used exclusively in the following.

†The characteristics of the stacking of close pack structures can be specified by L which corresponds to t period of the structure with a long period stacking ord and by H or R which specifies the symmetry of stacki [9]. The actual number of close packed layers included a unit cell of hexaorthorhombic symmetry is L in the ca of H symmetry but $3L$ in the case of R symmetry[Although Hirabayashi *et al.* have been using $L' =$ in the case of R symmetry[11, 12], we adopt L here stead of L' according to the usage of Sato *et al.*[9].

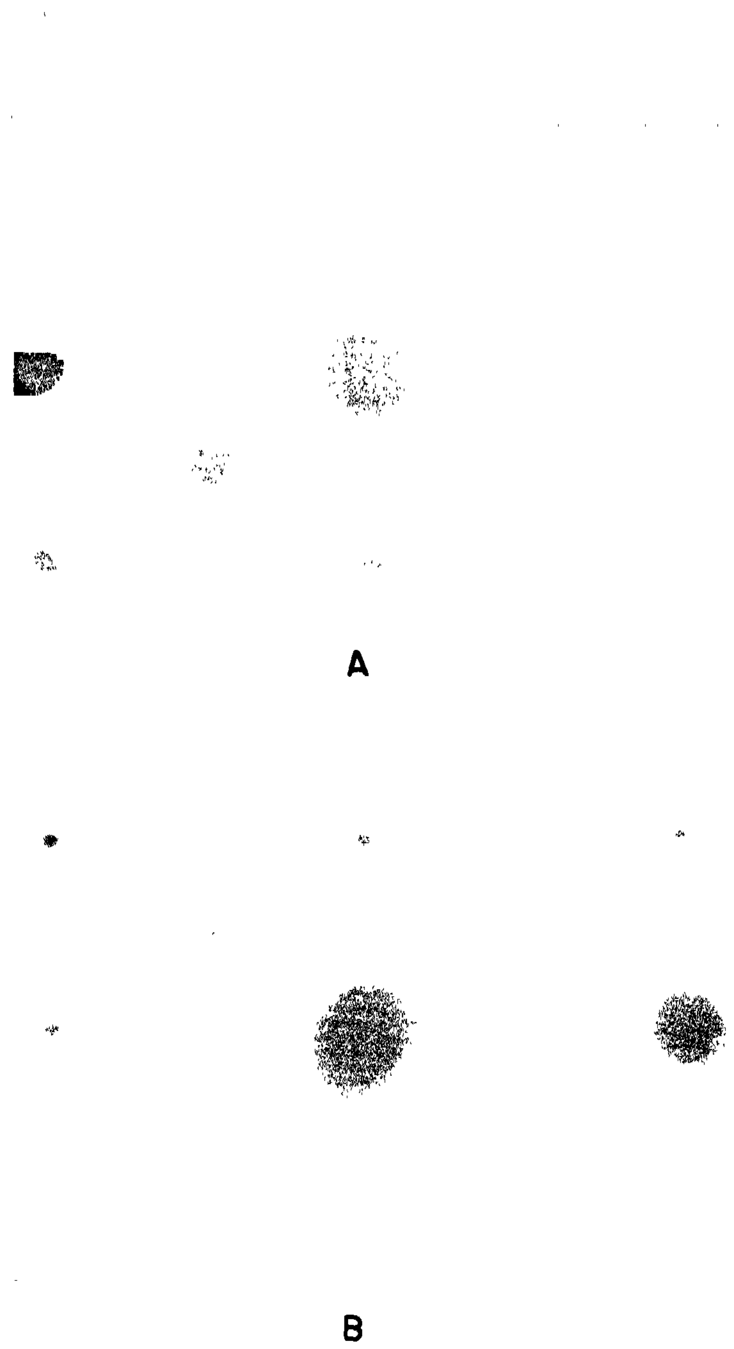

Fig. 1. Electron diffraction patterns corresponding to the basal plane ((00·1) plane). (A) $7a_0$ Structure. (B) $9a_0$ Structure.

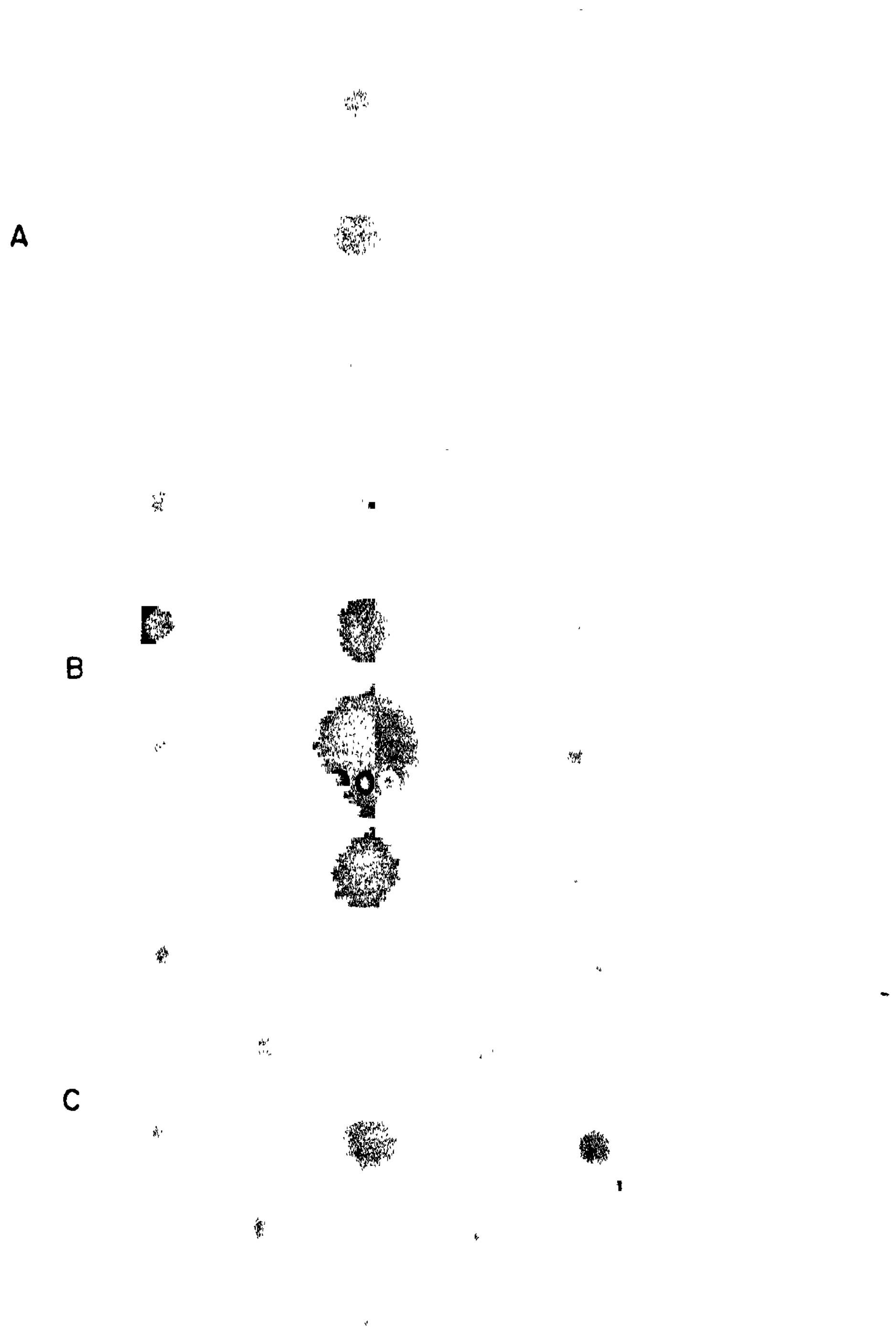

Fig. 3. Diffraction patterns of the $7a_0$ structure representing sections of reciprocal space normal to the basal plane containing the c-axis. A pattern indicating the (11·1) rel. plane is added. Important spots are indexed in terms of the original hexagonal cell (A) (10·0) (B) (11·0), (C) (11·1).

rapidly cooled from the β_1-phase of this alloy system[14]. The hexagonal structure in question was found to appear mostly in the composition range between these limiting compositions. Our concern here is the description of this long period structure of hexagonal symmetry which appears in this composition range. In the joint effort to investigate this structure, the main effort of Hirabayashi *et al.* was limited to the lower Cd composition range up to 35 per cent Cd, whereas the effort of Sato *et al.* was mainly in the high Cd composition range and in the ternary Au–Cd–In alloys in the composition range of $Au_3(Cd_{1-x}In_x)$.

The methods of preparation of required specimens are also different for these two groups. Hirabayashi *et al.* prepared the desired specimens by annealing appropriate amounts of gold foil and cadmium chips together, except for those for X-ray powder patterns which will be described later, while Sato *et al.* prepared the specimens by melting Au and Cd together in an atmosphere of argon by a high frequency furnace. Both methods give satisfactory results and the results between the two groups agree satisfactorily where the composition ranges overlap. The details of the preparation of the specimens and the experimental methods adopted are adequately described in previous papers[12, 14]. However, the experimental results and the structural analysis presented here are based mostly on the work of Hirabayashi *et al.* supplimented by data obtained by Sato *et al.*

Here, many specimens containing various compositions between 28 and 35 per cent Cd and properly heat treated* were investigated by both electron diffraction and electron microscopy as well as X-ray diffraction methods. A Guinier-de Wolff camera was utilized to take X-ray powder patterns using monochromatic Cu K_α radiation.

There exist two distinct structures which belong to the same family of the structure. Electron diffraction patterns of these two structures which correspond to the basal rel. plane ((00·1) in the hexagonal notation) are shown in Fig. 1. The diffraction patterns of these two structures are extremely similar and are characterized by the existence of superlattice spots. The relation of the reciprocal lattice of this superstructure to that of the standard superstructure in this composition range, Cu_3Au type, is shown in Fig. 2. The main characteristic is a splitting of the {110} (cubic notation) type superlattice spots shown in Fig. 2 by small hollow circles, in one of the ⟨110⟩ directions, indicating that new periodicities in atomic ordering are created in the basal plane in three symmetric directions, thus creating again a hexagonal symmetry. The characteristic difference in the diffraction patterns of Fig. 1A and 1B is simply a difference in the amount of splitting, such that in Fig. 1A, the reciprocal unit cell period is $a_0^*/7$ while in Fig. 1B, the reciprocal unit cell period corresponds to $a_0^*/9$, where a_0^* is the reciprocal lattice constant for the fundamental hexagonal cell, marked with large hollow circles in Fig. 2. Conse-

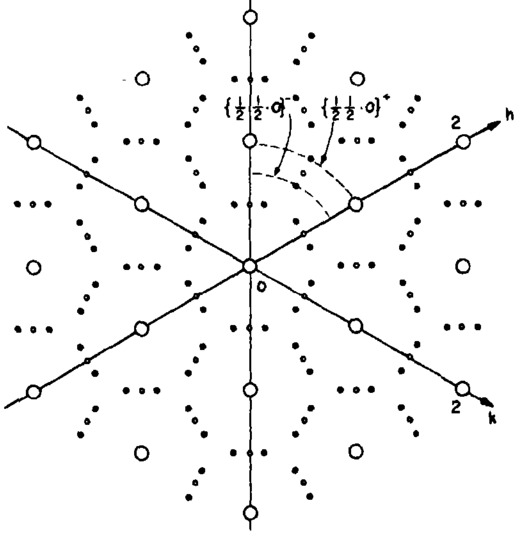
$\{\frac{1}{2}\frac{1}{2}\cdot0\}^-$
$\{\frac{1}{2}\frac{1}{2}\cdot0\}^+$
2
h
0
2
k

Fig. 2. The projection of reciprocal lattice lines on the basal plane of the reciprocal hexagonal lattice for hexagonal long period superlattice (●), Cu_3Au type (o) and fundamental (disordered) structure (O).

---

*After being homogenized, the specimens were slowly cooled from 450°C to room temperature at an approximate rate of 90 degrees a day.

quently, these two distinct structures will hereafter be referred to as the $7a_0$ and $9a_0$ structure respectively.

The $7a_0$ structure can easily be observed in specimens having compositions between 29 and 35 per cent Cd[12]. This structure was also found in a specimen with 45 per cent Cd as a mixture with other structures and had been referred to as the α_{20} structure[14]. On the other hand, the $9a_0$ structure is rather rarely detected. This has been found to exist either in the composition range between 27 and 30 per cent Cd but always in coexistence with the $3R$ stacking variant of the $M = 2$ ordered structure or in specimens having initially the $7a_0$ structure which are later heated in the electron microscope to reduce the Cd content. This indicates that the stability of the $9a_0$ structure is close to that of the $3R$ stacking variant in this composition range. An equilibrium phase diagram in this composition range is now being investigated in detail. A similar structure with a unit cell size of $9a_0$ has also been found in the Au–Mg alloys under similar condition[10, 13]. In the composition range between $7a_0$ and $9a_0$ there appear similar structures whose periods were found to change with a change of the composition and to assume non integral values. Thus, the situation seems to be very similar to the case of the ID LPS. In other words, it appears that we are dealing with the case of the stabilization of a long period structure with much the same origin as that of a ID LPS which has been investigated in detail[3, 4, 5]. However, before we discuss the stability of these structures, it is necessary to analyse the structure itself. For this, it seems sufficient to deal with the $7a_0$ and $9a_0$ structure only since the structures with periods in between can be interpreted as appropriate mixtures of these two structures in a coherent region, as in the case of the ID LPS.

STRUCTURAL ANALYSIS

(A) $7a_0$ *Structure*

A diffraction pattern corresponding to the basal plane (Fig. 1A) and a schematic interpretation of the splitting of the superlattice reflections in this plane, utilizing hexagonal coordinates (Fig. 2), have already been discussed. The diffraction patterns which include the c-axis (such as shown in Fig. 3A) indicate that the stacking of the close packed layers is of the $2H$ type. This indicates that the structure itself has hexagonal symmetry and that hexagonal indexing is more appropriate. The reciprocal lattice of this structure can then be constructed qualitatively from the knowledge of the basal plane. Several reciprocal planes such as (10·0), (11·0) and (11·1) were examined by selecting appropriately oriented crystal grains with the aid of a tilting device and the diffraction patterns are shown in Fig. 3. All these patterns agree with the constructed reciprocal lattice. The diffraction spots can be indexed in terms of hexagonal coordinates utilizing the lattice constants $a \cong 7a_0$ and $c = c_0$. Consequently this structure seems to be identical with that of the phase designated as α_{20} found earlier at higher Cd content[14] (refer to Fig. 13 of [14]). The space group of this structure is then given as P6$_3$/mmc (No. 194), as deduced from the symmetry as well as from the observed extinction rule that no reflections appear for $H-K=3n$ and $L=2n'\pm 1$, where n and n' are integers ($H = 7h$, $K = 7k$ and $L = l$)*.

The unit cell containing 98 atoms and their positions are then determined by comparing the observed patterns with the calculated structure factors. The basic model is deduced from the following considerations:

1. All atoms are on the ideal positions of the hexagonal close packed lattice. No refinements are attempted.
2. Equivalent atomic positions are occupied by the same kind of atoms.

---

*h, k, and l are indices in terms of the fundamental cell and H, K and L are indices in terms of the super cell. Although H's are to be used for indexing, h's are used mostly in the text since we are dealing with structures with different periods and, therefore, these will indicate more visually the relation of the superlattice spots with the original fundamental cell.

3. The intensity of the split spots, ($\frac{2}{7}\frac{1}{7}\cdot 0$) and ($\frac{3}{7}\frac{3}{7}\cdot 0$) are made maximum while those of all other superlattice spots are made weak under the condition that the composition of alloys is kept close to Au_3Cd.

The atomic distribution of such an ideal structure which satisfies the above conditions is shown in Fig. 4A for the two close packed planes included in the unit cell. Note that the resulting structure is such that no Cd atoms are in nearest neighbouring positions as in the case of the Cu_3Au structure. This unit cell contains 26 Cd atoms and 72 Au atoms, which corresponds to a composition of 26·5 per cent Cd. The classification of the lattice sites and the occupations of these sites by Au and Cd atoms respectively are given in Table 1, and is regarded as the basic model. The structure is essentially an antiphase modulation in three directions of the 2*H* version of the Cu_3Au type ordered structure (or Ni_3Sn type, DO_{19}) as is more clearly visualized in Fig. 4B.

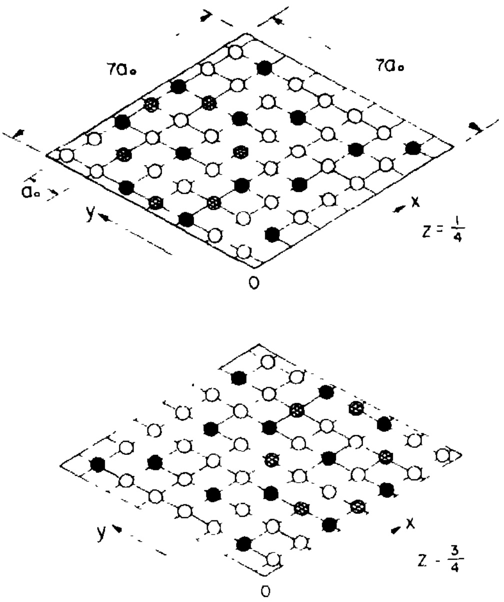

Fig. 4 (A). Atomic arrangement in the two close packed planes of the $7a_0$ structure. Open and full circles correspond to gold and cadmium atoms, respectively. Cross hatched circles indicate the 6*h*′ sites where excess Cd atoms replace Au atoms.

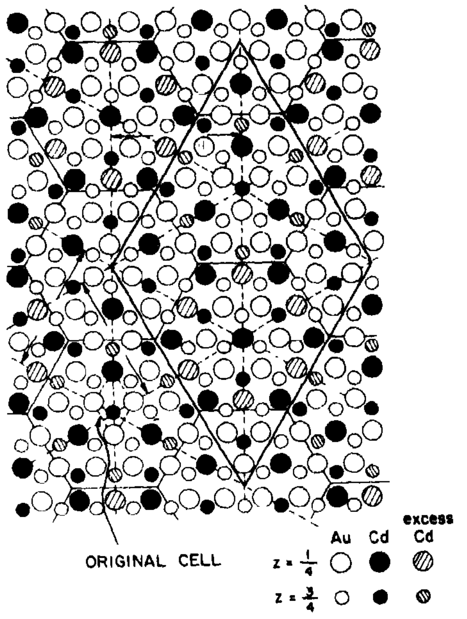

Fig. 4 (B). Basal plane of the hexagonal long period superlattice, the $7a_0$ structure, indicating the atomic positions in the two layer structure. The unit cell of the structure is outlined by heavy lines. Broken lines indicate the antiphase boundaries, and the arrows indicate the long lattice period created by the antiphase boundaries.

An attempt was made to interpret the diffraction data in terms of other models which belong to space groups P3ml (No. 156), $P6_3/m$ (No. 176) and P$\bar{6}$2c (No. 190), but the present model appears to give the best agreement with data.

The composition where the $7a_0$ structure is observed is, however, not at the ideal composition of 26·5 per cent Cd, but in the higher composition range of 29 ~ 35 per cent Cd. Then the excess Cd atoms should be distributed over the Au sites. A reasonable assumption would be to distribute the excess Cd atoms on the Au sites randomly. The relative intensity among the superlattice spots for this case for any composition would be the same as that of the ideal composition, and its geometrical structure factors are calculated in Table 2 under Model 1. The composition of the alloy taken here is $Au_{64}Cd_{34}$ in order to

Table 1. *Atomic position of the* $7a_0$ *structure. Space group* $P6_3/mmc$ (No. 194)

<table>
<tr><th colspan="2" rowspan="2">Coordinates</th><th colspan="2">Parameters</th><th colspan="8">Atoms</th></tr>
<tr><th>x</th><th>y</th><th>Basic model</th><th>Model 2</th><th>Model 3</th><th>Model 4</th><th>Model 5</th><th>Model 6</th><th>Model 7</th><th>Model 8</th></tr>
<tr><td rowspan="5">12j</td><td rowspan="5">$x, y, 1/4; \bar{x}, \bar{y}, 3/4$
$\bar{y}, x-y, 1/4; y, y-x, 3/4$
$y-x, \bar{x}, 1/4; x-y, x, 3/4$
$\bar{y}, \bar{x}, 1/4; y, x, 3/4$
$x, x-y, 1/4; \bar{x}, y-x, 3/4$
$y-x, y, 1/4; x-y, \bar{y}, 3/4$</td><td>1/21</td><td>5/21</td><td colspan="2" rowspan="4">48 Au</td><td rowspan="4">48 Au</td><td>4 Au + 8 Cd</td><td>12 Au</td><td rowspan="2">24 Au</td><td rowspan="3">36 Au</td><td rowspan="2">20 Au + 4 Cd</td></tr>
<tr><td>4/21</td><td>11/21</td><td rowspan="3">36 Au</td><td>4 Au + 8 Cd</td></tr>
<tr><td>7/21</td><td>2/21</td><td rowspan="2">24 Au</td><td>4 Au + 8 Cd</td><td rowspan="2">24 Au</td></tr>
<tr><td>10/21</td><td>2/21</td><td>12 Au</td><td>4 Au + 8 Cd</td></tr>
<tr><td>1/21</td><td>8/21</td><td colspan="3">12 Cd</td><td colspan="5">12 Cd</td></tr>
<tr><td rowspan="6">6h</td><td rowspan="6">$x, 2x, 1/4; \bar{x}, 2\bar{x}, 3/4$
$2\bar{x}, \bar{x}, 1/4; 2x, x, 3/4$
$x, \bar{x}, 1/4; \bar{x}, x, 3/4$</td><td>1/21</td><td></td><td rowspan="4">24 Au</td><td rowspan="2">12 Au</td><td rowspan="2">4 Au + 8 Cd</td><td rowspan="4">24 Au</td><td colspan="3" rowspan="4">24 Au</td><td rowspan="4">20 Au + 4 Cd</td></tr>
<tr><td>13/21</td><td></td></tr>
<tr><td>4/21</td><td rowspan="2">} (6h')</td><td rowspan="2">4 Au + 8 Cd</td><td rowspan="2">12 Au</td></tr>
<tr><td>10/21</td></tr>
<tr><td>16/21</td><td></td><td colspan="3" rowspan="2">12 Cd</td><td colspan="5" rowspan="2">12 Cd</td></tr>
<tr><td>19/21</td><td></td></tr>
<tr><td>2d</td><td>2/3 1/3 1/4; 1/3 2/3 3/4</td><td>—</td><td></td><td colspan="8">12 Cd</td></tr>
</table>

Table 2. Calculated geometrical structure factors of the 7a$_0$ structure. The italicised numbers indicate those whose disagreement with observed intensities is large

Index			Index for the fundamental cell			I_{obs}	Structure factor |F|							
H	K	$\cdot L$	h	k	$\cdot$ l		Model 1	Model 2	Model 3	Model 4	Model 5	Model 6	Model 7	Model 8
1	0	0	1/7	0	0	—	0·22	1·1	2·0	2·8	*4·0*	2·1	1·3	1·6
2	0	0	2/7	0	0	*vvw*	1·3	0·35	0·13	3·8	2·2	4·4	2·3	0·14
3	0	0	3/7	0	0	—	5·0	2·5	*8·3*	*4·3*	3·5	*7·1*	4·3	*4·6*
4	0	0	4/7	0	0	—	2·5	1·2	*4·2*	0·91	1·7	3·5	*5·2*	3·1
5	0	0	5/7	0	0	*vvw*	1·3	0·35	0·13	2·3	2·2	4·4	3·8	
6	0	0	6/7	0	0	—	0·44	2·2	*4·1*	1·8	*5·5*	2·6	1·8	0·48
1	1	0	1/7	1/7	0	*vvw*	1·0	3·3	4·8	2·5	1·6	4·3	2·5	0·15
2	1	0	2/7	1/7	0	*vvw*	0·89	1·7	1·7	2·2	1·7	1·7	0·86	1·4
3	1	0	3/7	1/7	0	m	6·7	8·3	6·5	6·9	6·0	5·8	6·9	6·9
4	1	0	4/7	1/7	0	vvw	1·8	3·3	3·3	1·3	3·3	3·3	1·3	1·2
5	1	0	5/7	1/7	0	vvw	0·52	1·7	2·4	1·3	0·78	2·2	1·3	0·07
6	1	0	6/7	1/7	0	—	0·22	1·1	2·0	2·1	2·8	1·3	4·0	
2	2	0	2/7	2/7	0	—	5·3	0·07	*4·4*	*7·3*	*9·5*	3·2	*7·3*	*5·3*
3	2	0	3/7	2/7	0	—	2·6	0·04	2·2	3·6	*4·8*	1·6	3·6	2·6
4	2	0	4/7	2/7	0	vvw	0·89	1·7	1·7	0·86	1·7	1·7	2·2	
5	2	0	5/7	2/7	0	vvw	2·6	0·75	0·25	1·6	4·4	8·9	1·6	1·2
3	3	0	3/7	3/7	0	m	13·4	16·6	13·0	13·8	11·9	11·5	13·8	13·8
4	3	0	4/7	3/7	0	—	2·5	1·2	*4·2*	*5·2*	1·7	3·5	0·91	
1	0	1	1/7	0	1	—	0·38	1·9	3·5	0·18	*4·8*	2·3	3·4	
2	0	1	2/7	0	1	—	2·2	0·61	0·22	0·42	3·8	*7·7*	3·1	
4	0	1	4/7	0	1	—	4·3	2·1	*7·2*	*5·5*	3·0	*6·1*	1·9	
2	1	1	2/7	1/7	1	—	1·5	2·9	3·7	0·27	2·9	2·9	2·0	
3	1	1	3/7	1/7	1	m	11·6	14·4	11·2	11·9	10·0	10·3	11·9	

compare to that shown as Model 2. The result of such a calculation shows that the superlattice spots split and that higher order split spots exist, and that only a pair of the split spots for each superlattice spot of the Cu_3Au type, such as $(\frac{3}{7}\frac{3}{7}\cdot 0)$ and $(\frac{4}{7}\frac{4}{7}\cdot 0)$, have high intensities, agreeing with observation. However, the intensity distribution of superlattice spots other than these pairs of split spots still seems to be too strong. In order to bring the intensity distribution closer to that of observation, it is necessary to assume a preferential distribution of Cd atoms on selected Au sites. In other words, the effect of additional Cd atoms seems to make the intensities of particular pairs of split spots stronger, while reducing the intensity of other spots. Many possible models including those whose atomic distribution range from Cu_3Au type to that of CuAu type ordering have been examined. However, the best model among those examined which brings on this effect is cited in Table 1 as Model 2. Referring to Table 1, only twelve of the $6h$ sites with parameters $x = 4/21$ and $x = 10/21$ are substituted by excess Cd atoms in this model. These sites are marked with cross-hatched circles in Fig. 4A and will be designated as $6h'$. Thus eight cadmium atoms and four gold atoms are thought to be distributed statistically on the $6h'$ sites, giving a composition of 34·7 per cent Cd. As is seen in Fig. 4B, such excess Cd atoms tend to distribute in the antiphase boundaries. The structure factors for this model are calculated in Table 2 under Model 2, and it can thus be seen that it gives better agreement with observation than Model 1. The approximate intensity distribution in the reciprocal lattice (based on this model) is shown in Fig. 5. Since multiple diffraction effects seem to contribute so much to the observed intensities in electron diffraction, a quantitative comparison could not be made. The model chosen, therefore, remains tentative in this sense. The atomic distribution and the intensity distribution for other models in the excess Cd case (Model 3–Model 8) are also tabulated in Tables 1 and 2 for comparison and for possible identification of a better model (if any) when more reliable measurements of the intensity distribution in the reciprocal lattice by X-rays are obtained.

By taking the two split spots, (3/7 3/7·0) and (4/7 4/7·0), for example, into the objective aperture of the electron microscope, we should be able to observe a particular set of the antiphase boundaries which modulate the crystal. In Fig. 6, stripes having a width of about $10Å = (7a_0)/2$ corresponding to such antiphase boundaries (refer to Fig. 4B) are shown. The specimen used had a composition of 35 per cent Cd, and was electrothinned from the bulk using a cyanide solution.

(B) $9a_0$ *Structure*

Using the same procedure as in the case of the $7a_0$ structure, this structure can be described by a hexagonal cell with $a \cong 9a_0$ and $c = c_0$. However, the unit cell can be reduced to a smaller hexagonal cell with the lattice constants $a = 3\sqrt{3}a_0$ and $c = c_0$ as is shown in Fig. 7, based on the systematic absence of reflections with H'-$K' = 3n \pm 1$ where H' and K' are the indices for this cell.* Thus the space group for this structure would be $P6_3/mcm$ (No. 193) and 54 atoms are included in a unit cell. The atomic arrangement in the unit cell was derived utilizing the same conditions as those in the case of the $7a_0$ structure, and is shown in Fig. 7. The atomic sites and their distribution are given in Table 3. The unit cell of the basic model contains 12 cadmium atoms and 42 gold atoms which corresponds to a composition of 22·2 per cent Cd. This is again well below the composition range where the $9a_0$ structure is observed. The geometrical structure factors are calculated from this model and are compared with

---

*The relation between hs and H's can be seen in Fig. 8 and Table 4. hs will generally be used because these will indicate more visually the relation of the superlattice spots with the original fundamental cell.

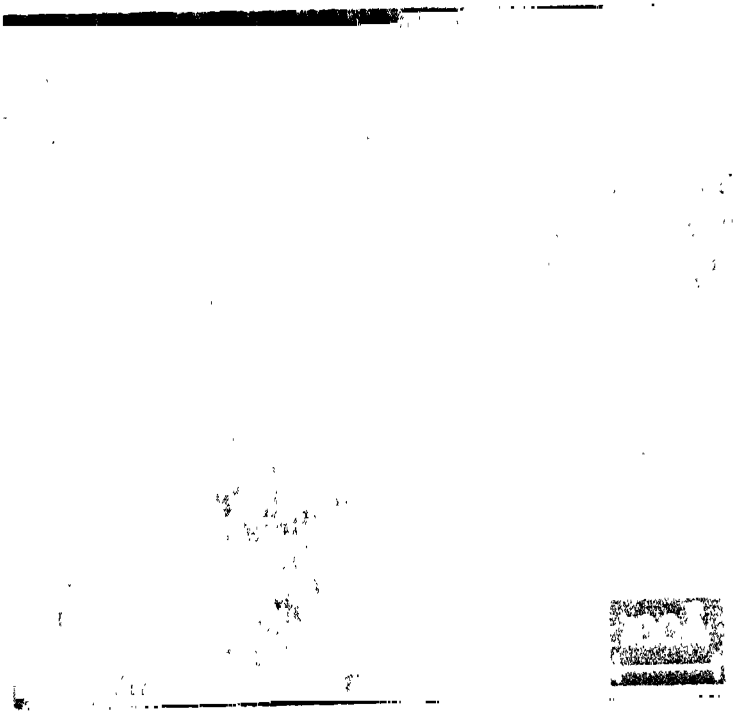

Fig. 6. Dark field micrograph indicating the direct resolution of a set of antiphase boundaries of the $7a_0$ structure. The distance between stripes is about 10·0 Å (35 per cent Cd).

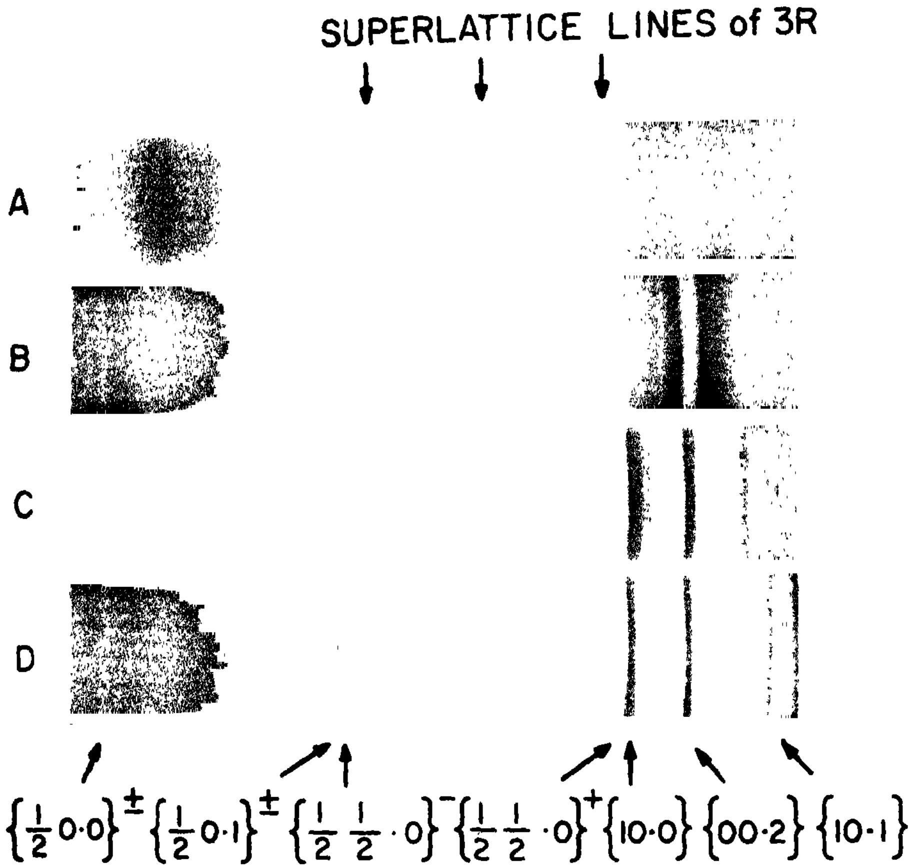
SUPERLATTICE LINES of 3R
A
B
C
D
$\{\frac{1}{2}0\cdot0\}^{\pm}$
$\{\frac{1}{2}0\cdot1\}^{\pm}$
$\{\frac{1}{2}\frac{1}{2}\cdot0\}^{-}$
$\{\frac{1}{2}\frac{1}{2}\cdot0\}^{+}$
$\{10\cdot0\}$
$\{00\cdot2\}$
$\{10\cdot1\}$

Fig. 9. X-ray powder patterns with variable periods showing the coexistence of the $7a_0$ structure and the $3R$ stacking variant of the $M = 2$ structure. A, B, C and D correspond to alloys with 27·5, 28·7, 29·9 and 32·2 per cent Cd respectively.

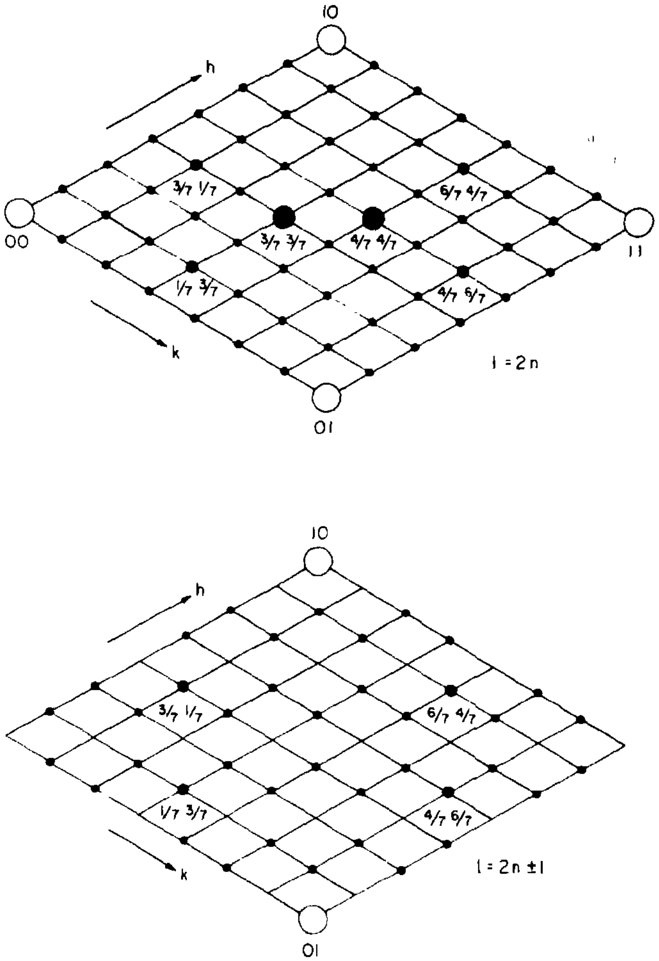

Fig. 5. Schematic intensity distribution in the two basal planes of the reciprocal lattice of the $7a_0$ structure based on calculation. Open and full circles are fundamental and superlattice spots, respectively.

the observed intensity in Table 4. Again, the intensities of spots other than particular pairs of split superlattice spots are stronger than those observed experimentally and therefore Model 1 for excess Cd atoms, where a random distribution of excess Cd atoms on all Au sites is assumed, will not fit the data. In Model 2 on the other hand, four cadmium atoms and eight gold atoms are assumed to occupy statistically twelve lattice sites $12j'$ which are particular sites of $12j$ with $x = 2/9$ and $y = 5/9$. As can be seen in Table 4, Model 2 gives better agreement with observation than Model 1. An approximate intensity distribution in the reciprocal lattice based on this calculation is shown in Fig. 8. The distribution of such excess Cd atoms is shown in Fig. 7. Again, a segregation of such excess atoms into particular locations of low bond energy is seen, as in the case of the $7a_0$ structure. The atomic distribution and the intensity distribution for other models with excess Cd (Model 3–Model 8) are also included in Tables 3 and 4.

Table 3. Atomic positions of the $9a_0$ *structure. Space group* $P6_3/mcm$ (No. 193)

Coordinates		Parameters		Atoms							
		x	y	Basic model	Model 2	Model 3	Model 4	Model 5	Model 6	Model 7	Model 8
$12j$	$x, y, 1/4; \bar{x}, \bar{y}, 3/4$ $\bar{y}, x-y, 1/4; y, y-x, 3/4$ $y-x, \bar{x}, 1/4; x-y, x, 3/4$	1/9	3/9	36 Au	24 Au	36 Au	8 Au + 4 Cd	12 Au	24 Au	10 Au + 2 Cd	12 Au
		1/9	6/9				24 Au	8 Au + 4 Cd		12 Au	20 Au + 4 Cd
	$y, x, 1/4; \bar{y}, \bar{x}, 3/4$ $\bar{x}, y-x, 1/4; x, x-y, 3/4$ $x-y, y, 1/4; y-x, y, 3/4$	2/9 ($12j'$)	5/9		8 Au + 4 Cd			12 Au	14 Au + 4 Cd	10 Au + 2 Cd	
$6g$	$x, 0, 1/4; \bar{x}, 0, 3/4$	1/9		6 Au	6 Au	2 Au + 4 Cd	6 Au	6 Au		6 Au	6 Au
	$0, x, 1/4; 0, \bar{x}, 3/4$	4/9		12 Cd	12 Cd	12 Cd	12 Cd	12 Cd	12 Cd	12 Cd	12 Cd
	$\bar{x}, \bar{x}, 1/4; x, x, 3/4$	7/9									

Table 4. Calculated geometrical structure factors of the $9a_0$ *structure. The italicised numbers indicate those whose disagreement with observed intensities is large*

Index			Index for the fundamental cell			I_{obs}	Structure factor $\|F\|$							
H'	K'	L'	h	k	l		Model 1	Model 2	Model 3	Model 4	Model 5	Model 6	Model 7	Model 8
1	0	0	1/9	1/9	0	—	0·85	0·75	4·3	1·5	0·04	1·8	0·38	0·36
2	0	0	2/9	2/9	0	—	3·0	2·4	*5·1*	1·6	*3·9*	*3·8*	2·0	*3·2*
4	0	0	4/9	4/9	0	m	7·0	8·3	7·2	6·9	6·0	7·8	7·6	7·2
1	1	0	0	3/9	0	vvw	3·1	1·1	1·1	4·9	4·2	1·1	*3·0*	2·7
2	1	0	1/9	4/9	0	m	3·5	4·2	3·3	3·4	3·0	3·7	3·8	3·6
3	1	0	2/9	5/9	0	vvw	1·5	1·2	2·6	0·81	2·0	1·9	*1·0*	1·6
4	1	0	3/9	6/9	0	vvw	2·0	0·74	0·74	0·96	4·5	0·74	0·85	2·6
2	2	0	0	6/9	0	—	1·1	0·39	0·39	*3·5*	0·30	0·39	1·9	0·05
3	2	0	1/9	7/9	0	—	0·42	0·38	2·2	0·80	0·02	0·89	0·21	0·18
1	1	1	0	3/9	1	—	0·54	0·20	0·20	1·2	*2·8*			
2	1	1	1/9	4/9	1	m	6·1	7·2	5·7	5·9	5·2			
3	1	1	2/9	5/9	1	—	2·6	2·1	*4·4*	1·4	3·4			
2	2	1	0	6/9	1	—	3·0	1·1	1·1	*3·7*	*5·0*			

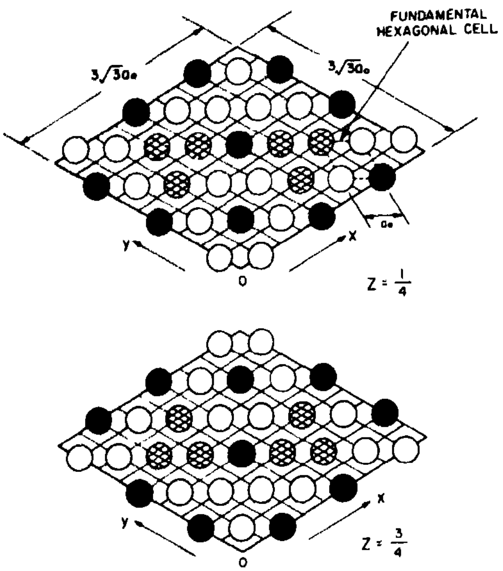

Fig. 7 (A) Atomic arrangement in the two close packed planes of the $9a_0$ structure. Open and full circles correspond to Au and Cd atoms, respectively Cross hatched circles indicate the $12j'$ sites where excess Cd atoms replace Au atoms.

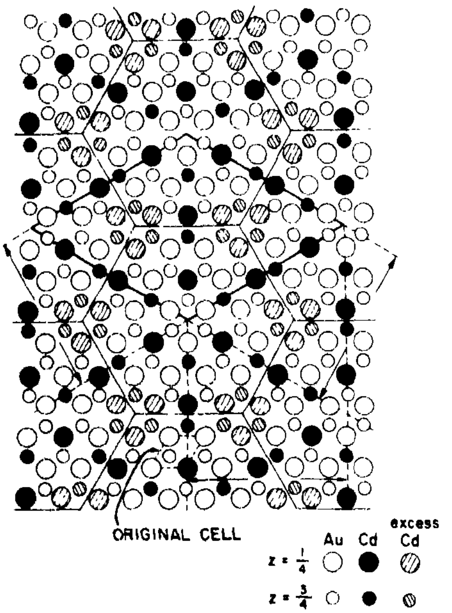

Fig. 7 (B). Basal plane of the hexagonal long period superlattice, the $9a_0$ structure, indicating the atomic positions in the two layer structure. The unit cell of the structure is outlined by heavy lines. Broken lines indicate the antiphase boundaries.

The proposed arrangement of atoms for the $9a_0$ structure is very closely related to that of $Au_{77}Mg_{23}$ which has recently been identified by Burkhardt *et al.*[13]. The only difference between the two is in the stacking of the layers, which was found to be of the $4H$ type for Au–Mg rather than the $2H$ type as for Au–Cd, so that the unit cell there is given as $a = 9a_0$ and $c = 2c_0$. The close packed layers determined for this structure[13] are equivalent to that of the $9a_0$ structure in the Au–Cd alloys except for one, and in fact, a structure with $2H$ stacking has since been found rather frequently in the Au–Mg alloys [15]. Thus, the $2H$ version of $Au_{77}Mg_{23}$ would be identical with the $9a_0$ structure here.

The Fourier synthesis of two split superlattice spots of this structure in the electron microscope gives a stripe pattern which indicates a particular set of antiphase boundaries. Since a direct resolution of the antiphase boundaries of the $9a_0$ structure in the Au–Mg alloys has already been given [10] and is similar to that of the $7a_0$ structure (Fig. 6) except for their width, the picture is not reproduced here. Basal planes of these two structures, indicating the atomic position in the two layers along with the unit cells and antiphase boundaries are shown in Fig. 7B.

(C) *Intermediate structures*

As was indicated before, the apparent period of the structures is not fixed, but changes with composition. The period can be measured from the separation of the pair of split superlattice spots in the electron diffraction pattern. In addition, a series of X-ray powder patterns are shown in Fig. 9 for alloys in the composition range between 27·5 and 32·2 per cent Cd. Specimens for the powder X-ray method were obtained from filings from solid ingots prepared inside evacuated quartz capsules. The patterns of the alloys with the lowest and the highest cadmium content are interpreted as being of the $3R$ and the $7a_0$ structures, respectively, while the patterns for alloys with intermediate compositions

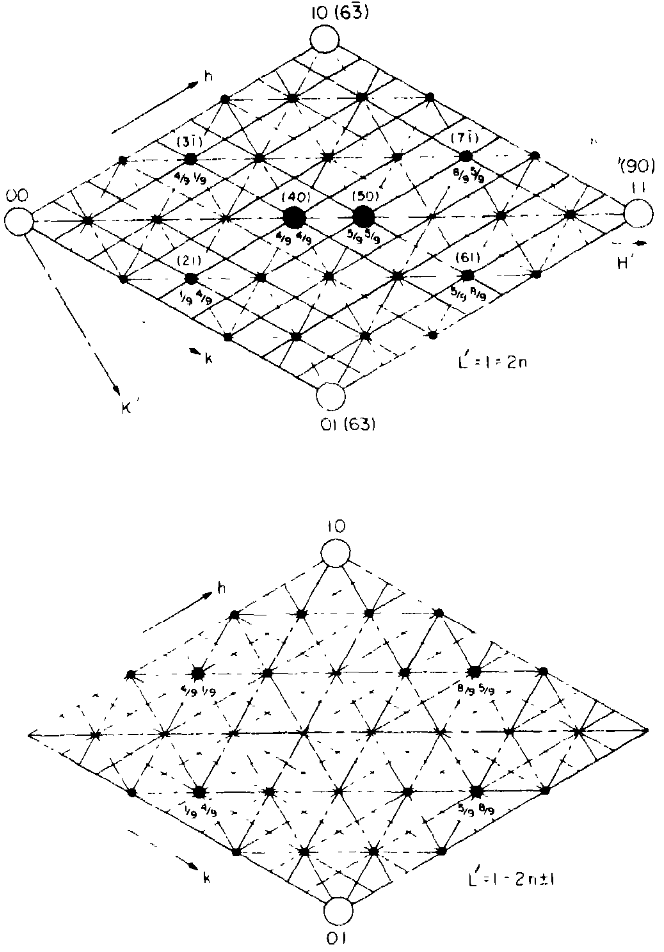

Fig. 8. Schematic intensity distribution in the two basal planes of reciprocal lattice of the $9a_0$ structure based on calculation. Open and full circles are fundamental and superlattice spots, respectively.

show the coexistence of both structures. At the same time, however, one can notice that the separation between the lines $\{1/2\ 1/2 \cdot 0\}^-$ and $\{1/2\ 1/2 \cdot 0\}^+$ of the pattern corresponding to the $7a_0$ structure, which corresponds to the amount of the splitting of superlattice spots (refer to Fig. 2), varies with the cadmium content in these alloys. The period M (in terms of a_0) of this structure is thus defined in the same way as in the case of the 1D LPS as the amount of splitting $x = 1/(Ma_0)$ (refer to Fig. 11) and the value of M as determined by X-ray powder patterns and electron diffraction patterns is thus plotted as a function of the valence electron concentration in Fig. 10. The fact that M generally takes non integral values and that it changes with e/a in a regular fashion indicates a close similarity to the case of the 1D LPS. Sharp diffraction maxima appear at the fractional sites in the reciprocal lattice, as in the case of the 1D LPS. Therefore, it seems safe to assume that domains of different periods, most probably those of the $7a_0$ structure and $9a_0$ structure, are mixed in a coherent

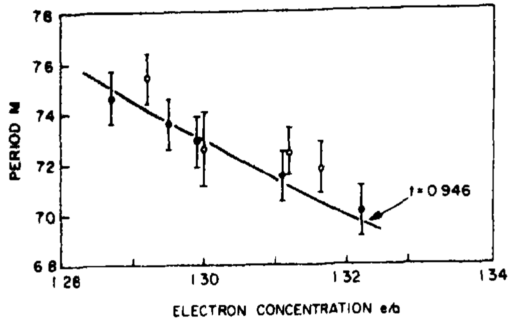

Fig. 10. Period M of the $7a_0$ structure plotted against the valence electron concentration e/a. Open and full circles are results obtained from electron and X-ray diffraction patterns, respectively. The line through the data spots is the theoretical curve for $t = 0{\cdot}946$.

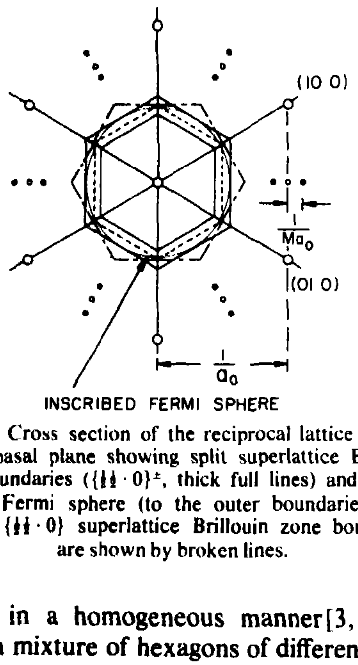

Fig. 11. Cross section of the reciprocal lattice parallel to the basal plane showing split superlattice Brillouin zone boundaries ($\{\frac{1}{2}\frac{1}{2}\cdot 0\}^{\pm}$, thick full lines) and the inscribed Fermi sphere (to the outer boundaries). The original $\{\frac{1}{2}\frac{1}{2}\cdot 0\}$ superlattice Brillouin zone boundaries are shown by broken lines.

region in a homogeneous manner[3, 5, 16]. Since a mixture of hexagons of different sizes cannot fill up the plane homogeneously, distorted hexagons with different side lengths should also mix properly in such a case and such mixtures may affect the distribution of excess Cd atoms. The exact manner of mixing of these domains, however, was not examined in detail here.

Lattice constants of the $7a_0$ structure in this composition range were also measured by the powder method. The camera radius used was 116 mm and the measurements were made utilizing an asymmetric film mounting to eliminate the uncertainty of the film radius. The lattice constants were thus obtained utilizing the Nelson–Riley extrapolation method. The results are shown in Fig. 12. The values of the lattice constants are sensitive to the heat treatment and c_0, and hence c_0/a_0, decreases by disordering (as shown by filled circles) compared to those of the ordered state obtained by annealing for 12 hr at 200 ~ 300°C (~ 50° below the transition points)[12]. Although both c_0 and a_0 increase linearly with Cd content, c_0/a_0 is kept almost constant, $\simeq 1{\cdot}651 \pm 0{\cdot}001$, in this composition range. Lattice constant measurements in this alloy system have also been made by Wegst and Schubert[17]. The alloy which corresponded to the $7a_0$ structure included 32·5 per cent Cd and was designated as A3Ü by them. Their data is shown in Fig. 12 by triangles and agrees very well with the present data. On the

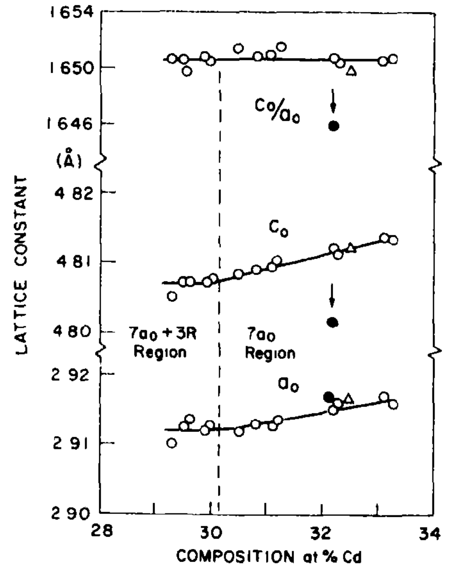

Fig. 12. Composition dependence of the lattice constant and the axial ratios of the $7a_0$ structure. The lattice constants are given in terms of the original hexagonal cell, a_0 and c_0. Values corresponding to a disordered hexagonal state are also added. Open circles, the ordered state (the $7a_0$ structure); triangles, also the ordered state (data by Wegst and Schubert[17]); filled circles, the disordered state.

other hand, Massalski[18] presented data which apparently correspond to the disordered state. Here, c_0/a_0 has also been found to be almost constant in this composition range.

DISCUSSION

It has now been established that long period structures with hexagonal symmetry exist in the Au–Cd alloys in the composition range of 28–35 per cent Cd and coexist with stacking variants, especially the $3R$ variant, of the $M = 2$ structure. The two distinct structures with definite periods, the $7a_0$ structure at higher Cd compositions and the $9a_0$ structure at lower Cd compositions, have been identified. They belong to the space groups $P6_3/mmc$ and $P6_3/mcm$ and their basic compositions correspond to $Au_{72}Cd_{26}$ and $Au_{42}Cd_{12}$ respectively. The basic compositions given above are, however, found to be substantially lower than the composition range where these structures appear. The excess Cd atoms were found to distribute preferentially on specific Au sites of the basic model, which corresponds to the distribution of excess Cd atoms in the antiphase domain boundaries, in a way to increase the intensities of specific pairs of split superlattice spots while reducing those of other superlattice spots. Moreover, the period M of the structure defined in terms of a_0 is found to vary between 9 and 7 with composition and hence with the electron–atom ratio of the system. The appearance of a non-integral value of M is presumably due to a mixture of domains of structures of different periods.

The mechanism of the stabilization of such long period structures should be closely related to the stabilization of other long period structures for the reasons discussed in the Introduction. In the first place they have long periods in a basically closed packed lattice and coexist with the stacking variants of the $M = 2$ structure, which are typical long period structures. The stability of these structures therefore is in close competition with the structures with long period stacking order. Secondly, they exist over a wide composition range which does not particularly correspond to the stoichiometric compositions characterized by the structure, and, more importantly, the period was found to change in this composition range as a function of e/a. Thirdly, similar structures exist under similar conditions in other alloy systems, such as the Au–Mg alloys. This indicates that this type of structure is not determined by a particular combination of metallic elements but is a common characteristic of solid solutions. All these characteristics are common to the known long period structures which have been investigated in detail.

If the above concept is true, the relation between the superperiod of the structure and the electron–atom ratio, as shown in Fig. 10, should be explained, as in the case of the ID LPS, in terms of the size of the Fermi surface. From the value of the e/a of the alloys, the newly created Brillouin zone boundaries at the Fermi surface due to the antiphase boundary modulation must be one of the pair of split {110} superlattice Brillouin zone boundaries (cubic notation). In Fig. 11, such a situation is illustrated. Here, on the basal plane, the {1/2 1/2·0} spots correspond to the cubic {110} spots and these spots split into two along the direction of lines which connect these spots to the origin. Then the two split {110} Brillouin zone boundaries correspond to the two hexagons with heavy lines while the dotted hexagon corresponds to the original unsplit one. The volume V of the inscribed sphere within the split zone boundaries is found to be

$$V = \frac{\pi}{6a_0^3}\left(1 \pm \frac{1}{M}\right)^3 \qquad (1)$$

where the plus and the minus signs correspond to the cases where the sphere is inscribed within the outer zone or the inner zone respectively. Since the hexagonal prism bounded by the planes {10·0} and {00·2} contains just two electrons per atom, the relation between e/a and M can be given for a Fermi surface of simple shape by the following equation:

$$e/a=\frac{\sqrt{3}}{12}\frac{\pi}{t^3}\frac{c_0}{a_0}\left(1\pm\frac{1}{M}\right)^3 \tag{2}$$

where t is a truncation factor as defined in the case of the 1D LPS[3, 4, 5]. The solid line in Fig. 10 represents the theoretical curve for the outer zone according to equation (2), with $t = 0{\cdot}946$ and $c_0/a_0 = 1{\cdot}65$. The theoretical curve agrees very well with the experimental results. Such a good agreement with a reasonable value of t (which should be close to 1) indicates, as in the case of the 1D LPS, that the above interpretation is reasonable.

Several comments must be made in connection with the stabilization mechanism mentioned above. First, the value of t, 0·946, is numerically very close to the value of t(0·950) obtained in the case of 1D LPS[4, 5]. In the latter case, the stability of the structure is determined by the critical contact of the Brillouin zone boundaries with the Fermi surface in the ⟨110⟩ direction and this situation is due to the fact that the Fermi surface of the fcc metals or alloys is flat in the ⟨110⟩ direction. In the present case of the hexagonal LPS, the stabilization is found to occur again due to the contact of the Brillouin zone boundaries with the Fermi surface in the ⟨110⟩ directions (cubic notation) which lie on the basal plane. Although the symmetries of the crystals are different in these two cases, it is not unreasonable to assume that the shape of the Fermi surface around the six areas in the ⟨110⟩ directions where the new Brillouin zone boundaries contact is not very different from that of the fcc crystals. As is well known, the main factor which determines the shape of the Fermi surface in the case of fcc crystals is the location of the {111} Brillouin zone boundaries. Due to the $2H$ stacking modulation, six out of eight {111} reciprocal lattice spots of the fcc crystals each split into two in the c-direction and the basic Brillouin zone of the fcc crystals change[9]. The corresponding Brillouin zone boundaries in these two cases are

fcc (1R)		$2H$
2 {111}	unsplit	{00·2}
6 {111}	split	{10·0} {10·1}

and the shape of the Fermi surface of monovalent fcc metals changes accordingly, pulled by shifted Brillouin zone boundaries. However, as the cross section of the Brillouin zone boundaries of the hexagonal crystals (Fig. 13) indicates, six ⟨110⟩ spots which lie on the basal planes are rather far from the split {111} spots which again lie on the basal plane. Then the shape of the Fermi surface near the six remaining ⟨110⟩ directions would probably not be changed much from that of the fcc metals, and remains flat. If this is the case, we can again expect a stabilization of

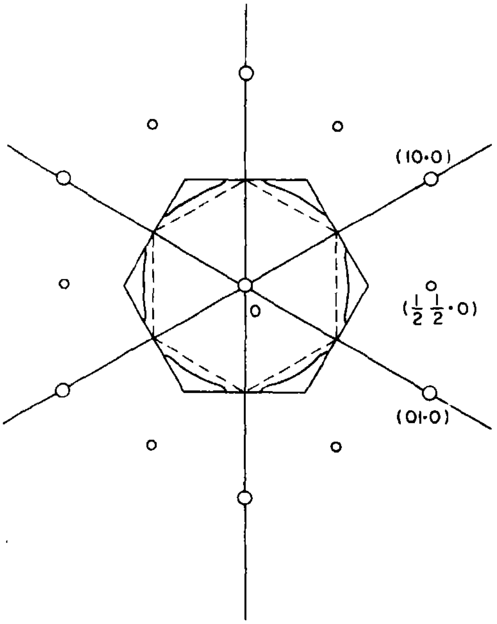

Fig. 13. Cross section of the first Brillouin zone through the center parallel to the basal plane indicating the relation of the {10·0} Brillouin zone boundaries and the Fermi surface of a monovalent hexagonal metal (schematic).

this structure by the critical contact of the Brillouin zone boundaries with the Fermi surface just as in the case of the 1D LPS. This situation not only explains the value of t in equation (1), but also explains the stability of the hexagonal LPS. Although the cost in energy to create such complicated antiphase domain boundaries may be larger than in the 1D LPS, the accomodation of the Fermi surface is more advantageous in the hexagonal LPS than for a 1D LPS with small M since in the latter case the place of contact deviates from the $\langle 110 \rangle$ direction. This may be the reason why a hexagonal LPS appears among the stacking variants of a 1D LPS with small M. In any case the existence of the hexagonal LPS emphasizes the importance of the flatness of the Fermi surface for the existence of a strong energy minimum at the critical contact of the Brillouin zone boundaries with the Fermi surface[5]. Unfortunately, pure monovalent hcp metals do not exist and their Fermi surface cannot be measured directly to prove this conclusion.

Another interesting feature of the problem is that the hexagonal LPS always appears at far higher compositions of Cd atoms (or Mg atoms in the case of Au–Mg alloys) than the ideal composition where no Cd atoms contact. This indicates either that the energy minimum with respect to Cd content occurs at higher Cd content where considerable Cd–Cd contact is expected or that, at least, the energy–composition curve has an extremely flat minimum over a wide composition range. However, as was emphasized in the section on structural analysis, the effect of excess Cd atoms occurs in a way to increase the intensity of specific pairs of split superlattice spots while reducing the intensities of other superlattice spots so that the stabilization based on the above mechanism becomes more favorable than for the stoichiometric case. In other words, the excess Cd atoms, by a preferential distribution on some of the Au sites, tend to reduce the electron energy, compensating for the increase in energy due to the contact of Cd atoms. This not only explains the appearance of this structure at higher compositions than the ideal composition, but gives strong support to the mechanism of the stabilization itself. The locations of excess atoms which satisfy the above condition turn out to be in the antiphase boundaries, which are physically reasonable.

Almost exactly the same structure appears in the Au–Mg alloys, identified as $Au_{77}Mg_{23}$ [10, 13]. Similar diffraction patterns have been reported also in Au–Cd–In alloys[19] ($Au_{70}Cd_{25}In_5$) and in Au–In alloys[19] ($Au_{78\cdot3}In_{21\cdot7}(h)$) and in Cu–Sb alloys[20] ($Cu_{4\cdot5}Sb(\delta)$), etc. Some of these alloys are being investigated by the present authors in light of the present knowledge and results will be published in due course. Among these, the dependence of the period on composition has been confirmed in Cu–Sb alloys[21]. It appears that the hexagonal LPS exists in a wide variety of alloy systems.

The existence of series of long period structures; long period superlattices, structures with long period stacking order, hexagonal long period superlattices, etc; in alloys has been confirmed and it has been established that these structures are stabilized by similar mechanisms. Naturally, there are important differences in stabilization mechanisms among different classes of structures and a systematic survey of these would be another stepping stone towards the understanding of more general structures.

Acknowledgement—We would like to thank Dr. H. Iwasaki for letting us use his computer program and for his helpful discussions.

REFERENCES

1. SATO H., *J. Crystallogr. Soc. Japan* **10**, 50 (1968).
2. SATO H. and TOTH R. S., *Bull. Soc. fr. Minér. Cristallogr.* **91**, 557 (1968).
3. SATO H. and TOTH R. S., *Phys. Rev.* **124**, 1833 (1961).
4. SATO H. and TOTH R. S., *Phys. Rev.* **127**, 469 (1962).
5. SATO H. and TOTH R. S., In *Alloying Behavior and Effects in Concentrated Solid Solutions* (Edited by T. B. Massalski), p. 265. Gordon & Breach, (1965).

6. SATO H. and TOTH R. S., *Phys. Rev. Lett.* **8**, 239 (1962).
7. TACHIKI M. and TERAMOTO K., *J. Phys. Chem. Solids* **27**, 335 (1966).
8. SATO H. and TOTH R. S., *Phys. Rev.* **139A**, 1581 (1964).
9. SATO H., TOTH R. S. and HONJO G., *J. Phys. Chem. Solids* **28**, 137 (1967).
10. SATO H. and TOTH R. S., *J. Phys. Chem. Solids* **29**, 2015 (1968).
11. HIRABAYASHI M., INO N. and HIRAGA K., *J. Phys. Soc. Japan* **22**, 1509 (1967).
12. HIRABAYASHI M., HIRAGA K., YAMAGUCHI S. and INO N., *J. Phys. Soc. Japan* **27**, 80 (1969).
13. BURKHARDT K., SCHUBERT K., TOTH R. S. and SATO H., *Acta crystallogr.* **B24**, 137 (1968).
14. TOTH R. S. and SATO H., *Acta Met.* **16**, 413 (1968).
15. TOTH R. S. and SATO H., Unpublished data.
16. FUJIWARA K., *J. Phys. Soc. Japan* **12**, 7 (1957).
17. WEGST J. and SCHUBERT K., *Z. Metallk.* **49**, 533 (1958).
18. MASSALSKI T. B., *Acta Met.* **5**, 541 (1957).
19. BAHN S. and SCHUBERT K., *Z. Metallk.* **51**, 327 (1960).
20. GÜNZEL E. and SCHUBERT K., *Z. Metallk.* **49**, 124 (1958).
21. HIRABAYASHI M. and YAMAGUCHI S., Unpublished data.

J. Phys. Chem. Solids Pergamon Press 1970. Vol. 31, pp. 95–100. Printed in Great Britain.

ANISOTROPIC PHONON EXCITATION BY HOT ELECTRONS IN *n*-Ge

K. BAUMANN, P. KOCEVAR, and M. KRIECHBAUM
Institute for Theoretical Physics of the University of Graz, Graz, Austria

(*Received* 1 *April* 1969)

Abstract—The build up of a disturbed phonon distribution is studied for *n*-germanium at complete low-temperature breakdown. During the first microsecond after application of the voltage pulse, no stationary state is established. The angular distribution of phonons differs substantially for the two transverse phonon branches. At high wave-number, the phonons are sharply peaked in the 111 directions.

1. INTRODUCTION

A THEORY of phonon excitation by hot electrons at low temperatures has first been given by Paranjape[1]. This theory has been extended in two directions. Conwell[2] has studied the effect of replacing the simple band structure by the many-valley structure of *n*-type germanium. Paranjape and Paranjape[3], on the other hand, have dropped the assumption of a stationary phonon distribution.

In the present paper, both of these problems will be re-examined. We shall derive a differential equation for the phonons which differs in many respects from the one used by Conwell. Some of the differences are:

(i) Our equation looks different for the two transverse phonon branches.

(ii) The elastic anisotropy of germanium is taken into account.

(iii) No phonon loss mechanism is introduced, apart from phonon absorption by the electrons.

We shall carry out a numerical evaluation of the phonon distribution one microsecond after the voltage is switched on.

2. DISCUSSION OF PHONON RELAXATION MECHANISMS

The rate of change of phonon number depends on the rate at which the created phonons are lost or transformed into other phonons. At low temperature, the free path of acoustic phonons is long compared with the dimensions of the crystal. Thus the only process which the phonons undergo is surface scattering. There have been conflicting views about the influence which this process has on the energy relaxation time of the phonons. Conwell[2] has assumed that the phonons disappear as soon as they reach the surface of the sample. To support this assumption, Conwell refers to Casimir's treatment of thermal resistivity at low temperature[4].

Casimir compares the flow of heat through a crystal with the flow of electromagnetic energy through a long and narrow tube. He considers two possibilities: (i) the walls of the tube are perfect mirrors, and (ii) the walls are such that the light is diffusely scattered, i.e. the walls are 'perfectly white'. Casimir supposes that the second possibility corresponds to the situation in the experiments on thermal conductivity. But clearly, the energy relaxation time of the phonons is infinite in any case, since the energy is not lost at all. The only question is the kind of deflection the phonons suffer at the surface of the sample.

A finite energy relaxation time is deduced by Gurevich and Gasymov[5] who take into account the finite transmission coefficient of the sample surface for elastic waves. For germanium immersed in liquid helium this transmission coefficient is small because of the very different densities of germanium and helium, respectively. Hence a phonon, on the average, suffers a large number of surface reflections before it is lost. Now in a hot electron experiment the duration of the voltage pulse is typically of the order of 1 μsec. On the assumption of a sample thickness of a few millimeters, a phonon is scattered only once or twice during one microsecond. Hence we are justified in neglecting this relaxation mechanism.

To summarize, for the effects to be discussed in this paper no phonon loss mechanism need to be taken into account. Practically all phonons which are emitted by the hot carriers are kept in the sample. The only relaxation they experience concerns deviations from isotropy and from equal distribution among polarizations. Deviations of these types decay within a time of the order of cross dimension of sample divided by velocity of sound.

3. DISCUSSION OF APPROXIMATIONS TO BE USED

The conditions for observation as well as for computation of phonon excitation are favourable for germanium containing 5.10^{15} shallow donors per cm^3 at a temperature of 4°K and at a field strength somewhat above complete low temperature breakdown. The binding energy of the donor levels is about 10 meV. If the distribution of the electrons is a Maxwell–Boltzmann one and the electron temperature T_e equals 40°, 90 per cent of the electrons are in the conduction band; at $T_e = 60°$, 94 per cent are in the conduction band.

In this energy range a theoretical analysis meets with rather favourable conditions. The electron energy is not high enough for optical phonon emission to be important. Thus, the electrons emit and absorb long wave acoustic phonons only. Since these processes are nearly elastic the diffusion approximation is applicable. That is, the average velocity of the carriers may be assumed to be large compared with their drift velocity. Furthermore, electron–electron scattering is still strong enough to produce a Maxwell distribution of the electrons. According to Fröhlich and Paranjape[6] the energy loss rate of an electron due to collisions with other electrons exceeds the rate of loss of energy to the lattice if

$$n \geqslant \frac{1}{4\pi}\frac{E^{3/2}m^{3/2}s^2\epsilon^2}{KT\,e^4\,\tau}$$

(n carrier concentration, E energy of carriers, m effective mass of carriers, s sound velocity, ϵ dielectric constant, K Boltzmann's constant; T, lattice temperature; e electronic charge, τ, collision time). If $E = 10\,\text{meV}$, $m = 2.10^{-28}g$, $s = 5.10^5\,\text{cm/sec}$, $T = 4{\cdot}2°\text{K}$, and $\tau = 10^{-11}$ sec, this inequality defines a critical electron density of $10^{14}\,\text{cm}^{-3}$. Therefore the use of a Maxwell distribution is well justified.

4. CALCULATION OF PHONON NUMBERS

The equation

$$\left(\frac{\partial N_{\mathbf{q}\alpha}}{\partial t}\right)^{(i)} = \frac{2V}{4\pi^2\hbar}\int \{|\langle \mathbf{k}, N_{\mathbf{q}\alpha}+1|H'|\mathbf{k} + \mathbf{q}, N_{\mathbf{q}\alpha}\rangle|^2 f^{(i)}(\mathbf{k}+\mathbf{q}) - |\langle \mathbf{k}+\mathbf{q}, N_{\mathbf{q}\alpha}-1|H'|\mathbf{k}, N_{\mathbf{q}\alpha}\rangle|^2 f^{(i)}(\mathbf{k})\}\, \delta(E_{\mathbf{k+q}} - E_{\mathbf{k}} - \hbar\omega_\alpha(\mathbf{q}))\,\mathrm{d}^3k \qquad (1)$$

describes the rate of change due to the electrons in the i-th valley of the number of acoustic phonons. The matrix elements for absorption of an acoustic phonon can be expressed as

$$\langle \mathbf{k}+\mathbf{q}, N_{\mathbf{q}\alpha}-1|H'|\mathbf{k}, N_{\mathbf{q}\alpha}\rangle = \sum_{s=1}^{6} \Xi_s f_s \left(\frac{\hbar q^2}{2\rho\,\omega_\alpha V}\right)^{1/2} N_{\mathbf{q}\alpha}{}^{1/2}. \qquad (2)$$

Here, Ξ_s are the deformation potential constants listed by Herring and Vogt[7]. For germanium-like valleys they are equal to $\Xi_d+\frac{1}{3}\Xi_u$ for $s=1,2,3$, and equal to $\frac{1}{3}\Xi_u$ for $s=4,5,6$; Ξ_d and Ξ_u are the deformation potential constants for volume dilatation and for uniaxial shear.

The numbers f_s are defined by

$$f_{kl}=(2|\mathbf{q}|)^{-1}(e_{q\alpha k}q_l+e_{q\alpha l}q_k), \tag{3}$$

and by $f_1=f_{xx}$, $f_2=f_{yy}$, $f_3=f_{zz}$, $f_4=2f_{yz}$, $f_5=2f_{zx}$, $f_6=2f_{xy}$. It should be mentioned that the numbers defined by equation (3) are *not* integers, whereas Herring and Vogt's polarization factors are. The $e_{q\alpha l}$ are the components of the polarization unit vector of the lattice mode of wave number $\mathbf{q}$ and polarization α. For $\mathbf{q}$ parallel to a symmetry direction, there are longitudinal and transverse phonons. In Table 1, we have defined the transverse polarization vectors denoted by $\mathbf{e}_{t1}$ and $\mathbf{e}_{t2}$ for the various symmetry directions. In Table 2, the quantities $(\Sigma\,\Xi_r f_r)^2$ are given for the 111 valley, with $\mathbf{q}$ pointing in a symmetry direction.

Table 1. *Directions of* $\mathbf{q}$, $\mathbf{e}_{t1}$, *and* $\mathbf{e}_{t2}$

$\mathbf{q}$	$\mathbf{e}_{t1}$	$\mathbf{e}_{t2}$
111	$1\bar{1}0$	$11\bar{2}$
110	001	$1\bar{1}0$
100	010	001

Table 2. *The quantities* $(\Sigma\,\Xi_s f_s)^2$ *for the* 111 *valley*

Direction of $\mathbf{q}$	Longitudinal	Transverse 1	Transverse 2
111	$(\Xi_d+\Xi_u)^2$	0	0
110	$(\Xi_d+\frac{2}{3}\Xi_u)^2$	$\frac{2}{9}\Xi_u{}^2$	0
100	$(\Xi_d+\frac{1}{3}\Xi_u)^2$	$\frac{1}{9}\Xi_u{}^2$	$\frac{1}{9}\Xi_u{}^2$
$1\bar{1}1$	$(\Xi_d+\frac{1}{9}\Xi_u)^2$	$\frac{2}{27}\Xi_u{}^2$	$\frac{2}{81}\Xi_u{}^2$
$1\bar{1}0$	$\Xi_d{}^2$	0	0

We shall express the phonon frequencies as

$$\omega_\alpha=s_\alpha q. \tag{4}$$

The sound velocity s_α is found from the equation

$$\rho s_\alpha{}^2=\sum_{r=1}^{6}\sum_{s=1}^{6}c_{rs}f_rf_s, \tag{5}$$

the c_{rs} being the elastic constants. The $s_\alpha{}^2$ resulting from equation (5) are listed in Table 3.

For $\mathbf{q}$ not pointing in a symmetry direction, the entries of Tables 2 and 3 will be interpolated by linear combinations of spherical harmonics. For Table 3 the three lowest cubic harmonics are needed, whereas for Table 2 we need the five simplest functions with the symmetry of the 111 valley. These are

$$\begin{gathered}1,\ \cos^2\theta,\ \cos^4\theta,\ \cos^6\theta,\\ \sin^3\theta\cos\theta\cos3\phi,\end{gathered} \tag{6}$$

where θ is the angle of $\mathbf{q}$ with the 111 direction, and ϕ the azimuthal angle relative to a 110 plane. For the $t2$ entries of Table 2, our interpolation method does not provide positive definite results. Whenever a negative value is obtained for some direction $\mathbf{q}$, we have replaced it by zero.

After having determined the matrix elements of H' we consider the electron distribution functions $f^{(i)}$. If the applied electric field points in a 100 direction the electron distribution must be the same in all four valleys. We approximate the $f^{(i)}$ by Maxwell distributions,

$$f^{(i)}(\mathbf{k})=\frac{n}{4N_c(T_e)}e^{-Ek/KT}. \tag{7}$$

Here n is the total number of conduction electrons per unit volume, and

$$N_c(T_e)=2(2\pi m_\perp^{2/3}m_\parallel^{1/3}KT_e/h^2)^{3/2} \tag{8}$$

is the effective density of states. The longitudinal and the transverse mass has been denoted by $m_\parallel$ and $m_\perp$.

Our next task is to perform the integral in equation (1). Following Herring and Vogt[7], we transform the energy ellipsoids into spheres,

Table 3. The quantities $\Sigma c_{rs} f_r f_s/\rho$; $c^* = c_{11} - c_{12} - 2c_{44}$ measures the elastic anisotropy

Direction of q	Longitudinal	Transverse 1	Transverse 2
111	$c_{12}+2c_{44}+\frac{1}{3}c^*$	$c_{44}+\frac{1}{3}c^*$	$c_{44}+\frac{1}{3}c^*$
110	$c_{12}+2c_{44}+\frac{1}{2}c^*$	c_{44}	$c_{44}+\frac{1}{2}c^*$
100	$c_{12}+2c_{44}+c^*$	c_{44}	c_{44}

$$E_k = \frac{\hbar^2 k^{*2}}{2m_0}, \tag{9}$$

by putting

$$k_\parallel = \left(\frac{m_\parallel}{m_0}\right)^{1/2} k_\parallel^*, k_\perp = \left(\frac{m_\perp}{m_0}\right)^{1/2} k_\perp^*. \tag{10}$$

m_0 may be chosen equal to the free electron mass. $k_\parallel$ and $k_\perp$ means components parallel and perpendicular to the axis of the energy valley considered.

The angular integrations in equation (1) are easily performed in k^* space. We have

$$\int_0^\pi \delta(E_{k+q} - E_k - \hbar\omega_\alpha) \sin\theta^* \, d\theta^* \, d\phi^*$$

$$= 2\pi \int_{-1}^{1} \delta\left(\frac{\hbar^2 k^* q^*}{m_0} \cos\theta^* + \frac{\hbar^2 q^{*2}}{2m_0} - \hbar\omega_\alpha\right)$$

$$\times d \cos\theta^*$$

$$= \frac{2\pi m_0}{\hbar^2 k^* q^*} \text{ if } k^* \geqslant \frac{1}{2} q^* - \frac{m_0\omega_\alpha}{\hbar q^*}, \tag{11}$$

$= 0$ otherwise.

Next we integrate over k^*. The result is

$$\left(\frac{\partial N_{q\alpha}}{\partial t}\right)^{(i)} = \frac{n\Xi_{i\alpha}^2}{8\hbar s_\alpha} \left(\frac{2\pi m_0}{\rho K T_e}\right)^{1/2} \frac{q}{q^*}$$

$$\{(N_{q\alpha}+1)\, e^{-\hbar\omega_\alpha/KT_e} - N_{q\alpha}\}$$

$$\exp\left\{\frac{-\hbar^2}{2m_0 K T_e} \left(\frac{q^*}{2} - \frac{m_0\omega_\alpha}{\hbar q^*}\right)^2\right\} \tag{12}$$

or

$$\frac{\partial N_{q\alpha}}{\partial t} = \sum_{i=1}^{4} (Q_{i\alpha} - P_{i\alpha} N_{q\alpha}), \tag{13}$$

where

$$P_{i\alpha} = (e^{\hbar\omega_\alpha/KT_e} - 1)\, Q_{i\alpha}, \tag{14}$$

$$Q_{i\alpha} = \frac{n\Xi_{i\alpha}^2}{8\hbar s_\alpha} \left(\frac{2\pi m_0}{\rho K T_e}\right)^{1/2} \frac{q}{q^*}$$

$$\times \exp\left\{\frac{-\hbar^2}{2m_0 K T_e} \left(\frac{q^*}{2} + \frac{m_0\omega_\alpha}{\hbar q^*}\right)^2\right\}. \tag{15}$$

By $\Xi_{i\alpha}^2$ we have denoted the interpolated entries of Table 2. q^*, according to (10), is given by

$$q^* = q\left(\frac{m_0}{m_\perp} \sin^2\theta_i + \frac{m_0}{m_\parallel} \cos^2\theta_i\right)^{1/2}, \tag{16}$$

where θ_i is the angle between q and the axis of the i-th valley.

Equation (13) can be solved immediately. We have prescribed a fixed value for the electron temperature. In order to estimate the error introduced by the use of a time-independent electron temperature one has to study the reaction of the changing state of the lattice on the conduction electrons. We have done this for the standard band model, and we have found that for a pulse length of 1 μsec the error is not greater than 5 per cent.

Plots of the phonon numbers one microsecond after the voltage is switched on are given in the figures. In Figs. 1–3 the angular distribution of the phonons emitted in the

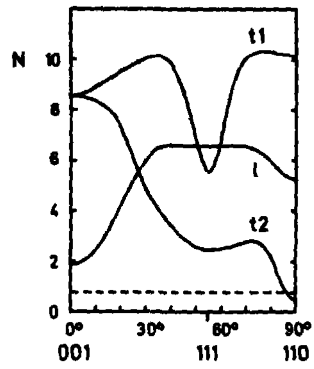

Fig. 1. Angular distribution in the $1\bar{1}0$ plane of longitudinal (l) and transverse ($t1$, $t2$) phonons of wave number $Q = 2{\cdot}29.10^6\ \mathrm{cm}^{-1}$ at time $t = 1\ \mu$s. Parameters assumed are $T = 4{\cdot}2$°K, $T_e = 70$°K, and $n = 5 \times 10^{15}\ \mathrm{cm}^{-3}$. The dashed line gives the number of thermal phonons.

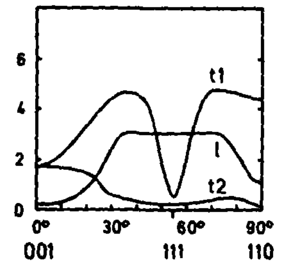

Fig. 2. Angular distribution of phonons of wave number $2Q$.

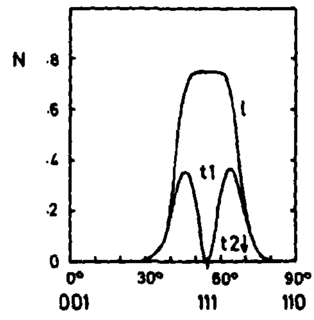

Fig. 3. Angular distribution of phonons of wave number $6Q$.

$1\bar{1}0$ plane is given. The value of q chosen for presentation is Q, $2Q$, and $6Q$, where

$$Q = (3m_{\parallel}^{1/3}\, m_{\perp}^{2/3}\, KT_e/\hbar^2)^{1/2}.$$

In Fig. 1, the thermal phonon distribution is also plotted for comparison. In Fig. 4, the ratios of the phonon numbers at time $t = 1$ μs and $t = 0$ are plotted for $\mathbf{q} \parallel 100$.

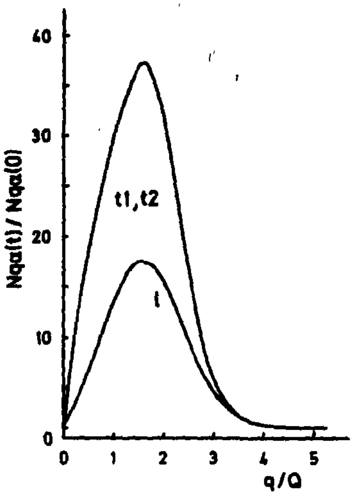

Fig. 4. Phonon numbers as a function of q (in the 001 direction) at time $t = 1\ \mu$sec.

From the last figure it is seen that the phonons emitted most frequently are those with wave number $\sim Q$. Practically no phonons with $q > 3Q$ are emitted in the 100 directions. However, it can be seen from Fig. 3 that the limit is shifted towards much larger wave numbers in the 111 directions. A sharp pencil of high frequency phonons is emitted along each valley axis.

5. CONCLUDING REMARKS

As far as the model we have used is correct, there will be a continuous increase of phonon number and no saturation. If phonon loss mechanisms come into play the phonon number will increase less quickly and eventually will saturate. It is quite possible, however, that the steady state cannot be observed at all since the saturation time is too long for a clean hot electron experiment.

If a phonon reaches the surface of the sample its wave vector changes direction, and also its polarization may change. Therefore equation (13) holds for sufficiently large samples only. If the sample is small the excited phonons will be distributed much more isotropic, and the numbers of phonons of different branches will be approximately equal. Figures 2 and 3 suggest the use of a sample cut in a 111 direction in order to observe the strong high frequency phonon emission in this direction.

As a consequence of the increasing phonon number, the mobility of the electrons will also change with time. A more or less linear decrease of the electric current has been observed by Kahlert and Seeger[8]. During the first microsecond the current decreases by a few per cent only, in agreement with simple standard band estimates.

Acknowledgements – We have profited from discussions with Drs. Conwell, Kahlert, Seeger, and Zylbersztejn. Our thanks are also to the Grazer Rechenzentrum and to the Mathematisches Institut der Technischen Hochschule Wien for making available their computer.

REFERENCES

1. PARANJAPE V. V., *Proc. phys. Soc. Lond* **80**, 971 (1962).
2. CONWELL E. M., *Phys. Rev.* **135**. A 814 (1964).
3. PARANJAPE V. V. and PARANJAPE B. V., *Phys. Rev.* **166**, 757 (1968).
4. CASIMIR H. B. G., *Physica* **5**, 495 (1938).
5. GUREVICH L. G. and GASYMOV T. M., *Sov. Phys. Solid State* **9**, 78 (1967).
6. FRÖHLICH H. and PARANJAPE B. V., *Proc. phys. Soc.* **B69**, 21 (1956).
7. HERRING C. and VOGT E., *Phys. Rev* **101**, 944 (1956).
8. BAUMANN K., KOCEVAR P., KRIECHBAUM M., KAHLERT H. and SEEGER K., *Proc. Int. Conf. Semicond. Physics*, p 757. Moscow (1968).

J. Phys. Chem. Solids Pergamon Press 1970. Vol. 31, pp. 101-116. Printed in Great Britain.

THE QUADRATIC-LAYER ANTIFERROMAGNET

M. E. LINES

Bell Telephone Laboratories Inc., Murray Hill, N.J. 07974, U.S.A.

(*Received* 28 *March* 1969)

Abstract—This paper discusses the statistical mechanics of the isotropic and the weakly anisotropic quadratic-layer antiferromagnet. This system is of current interest since it appears to be quite a good model for the less anisotropic members of two recently discovered isomorphic series of antiferromagnetic layer crystals. The antiferromagnetic phase, depending for its very existence on anisotropy, is discussed using spin-wave and Green's function methods, and comparisons are made with a typical three-dimensional (simple-cubic) system. The paramagnetic phase is investigated by Green's function and high temperature series expansion techniques, with particular attention paid to magnetic susceptibility and spin correlations. By expanding the Green's function results as a high temperature series, a test of the extrapolation techniques, which are frequently used in conjunction with this type of series and are particularly controversial for the two-dimensional Heisenberg system, can be made in the Green's function context.

1. INTRODUCTION

THIS paper discusses the statistical mechanics of the isotropic and the quasi-isotropic quadratic-layer Heisenberg antiferromagnet. This system is of some current interest since it appears to be quite a good model for less anisotropic members of two recently discovered series of antiferromagnetic layer crystals; namely, the K_2NiF_4 series[1] and the Ba_2NiF_6 series[2]. Of particular interest, in view of the inherent instability of ordered two-dimensional isotropic Heisenberg magnetic systems against thermal excitations[3], is the dependence of magnetic properties on anisotropy for these systems.

The antiferromagnetic phase, depending for its very existence on anisotropy, is critically dependent on the presence of even minute quantities of anisotropy from whatever source. Paramagnetic properties, on the other hand, are comparatively insensitive to the small values of the ratio of anisotropy energy to exchange energy typical of many of the layer salts with well isolated singlet ground state magnetic cations. For these, use can be made of the well established high temperature series expansions of statistical magnetism.

Section 2 examines in detail the paramagnetic susceptibility curves, making use of the known high temperature series expansion coefficients, and notes a simple relationship between the temperature of the susceptibility maxima, spin quantum number, and exchange parameter, which provides a very simple and quite accurate method of estimating exchange for these weakly anisotropic quadratic-layer antiferromagnets. Intraplanar exchange J is calculated from this relationship for several examples.

Section 3 discusses the antiferromagnetically ordered phase and the very important role played by anisotropy. The results of simple spin-wave theory are displayed for low temperatures, and direct comparison made with a weakly anisotropic three dimensional (simple-cubic) antiferromagnet. Calculations are extended over the entire ordered phase by use of the random phase Green's function approximation, and sublattice magnetization curves are computed as functions of temperature and anisotropy. The anisotropy is included as an anisotropy field H_A and the results displayed for the case where $H_A \propto$ sublattice magnetization, a situation which (within the present Green's function approximation) holds for most two-spin anisotropies (exchange anisotropy, dipolar anisotropy, etc.) but not for single spin crystal-field forms.

Section 4 considers two-spin correlation functions in the paramagnetic phase as functions of temperature and spin separation. In particular, Green's function susceptibility results are expanded as series in powers of reciprocal temperature and used to test the accuracy of high temperature series extrapolation procedures for the two-dimensional Heisenberg case.

2. HIGH TEMPERATURE SUSCEPTIBILITY

The exact series expansion for paramagnetic susceptibility in powers of reciprocal temperature has been calculated for arbitrary spin, and over a wide range of lattice structures, out to sixth order terms for the nearest neighbor Heisenberg spin system[4]. The series are valid for either sign of exchange parameter J, but the sign change in going from the ferromagnetic to antiferromagnetic system has a very marked effect, causing the antiferromagnetic series terms to alternate in sign and the resulting susceptibility to exhibit no singularity at the phase transition temperature. To estimate a Néel temperature T_n from such a series, an analysis in terms of a staggered susceptibility is necessary[5].

For the quadratic layer Heisenberg antiferromagnet with exchange Hamiltonian

$$\mathscr{H} = \sum_{nn} J\mathbf{S}_i \cdot \mathbf{S}_j \qquad (2.1)$$

where Σ_{nn} runs over all pairs of nearest neighbor spins i and j, the simplest series (numerically) is that for reciprocal susceptibility χ^{-1} for which we find[4]

$$\frac{Ng^2\mu_B^2}{\chi J} = 3\theta + \sum_{n=1}^{\infty} \frac{C_n}{\theta^{n-1}}, \qquad (2.2)$$

where $\theta = kT/JS(S+1)$, g is the Lande g-factor, μ_B the Bohr magneton, N the number of spins in the lattice, and where the coefficients C_n (calculated from the general formalism of Ref. [4]*) are displayed in Table 1.

Using this series, best theoretical estimates for susceptibility as a function of temperature are obtained by plotting χ^{-1} as a function of $1/n$ (up to $n = 6$) and extrapolating graphically to $n = \infty$. The errors involved in the extrapolation may be roughly estimated, and increase with decreasing temperature. The results of such a procedure are shown in Fig. 1 where $Ng^2\mu_B^2/\chi J$ is plotted as a function of $kT/JS(S+1)$ for various values of spin quantum number S. Also shown are the typical errors (resulting from the knowledge of only a small number of terms in the infinite series for reciprocal susceptibility) as a function of temperature, the method ceasing to be of much quantitative value below $kT \sim 0{\cdot}9JS(S+1)$.

Table 1. *Coefficients* C_n *of series* (2.2) *for several different values of spin S*

	$S=\frac{1}{2}$	1	3/2	2	5/2	∞
C_1	4	4	4	4	4	4
C_2	2·667	1·834	1·600	1·500	1·448	1·333
C_3	1·185	0·445	0·304	0·252	0·228	0·178
C_4	0·149	0·224	0·249	0·258	0·262	0·267
C_5	−0·191	0·132	0·132	0·124	0·119	0·104
C_6	0·001	0·019	0·013	0·015	0·017	0·022

Despite this shortcoming, the curves are clearly able to reproduce the broad susceptibility maxima which, experimentally, seem to characterize the two-dimensional quasi-Heisenberg antiferromagnet.

The likely error in the theoretical estimate for the temperature $T_{\chi\max.}$ at which the susceptibility reaches its maximum value is only some ±5 per cent. To this accuracy we find, from Fig. 1,

$$kT_{\chi\max.}/J = 1{\cdot}12S(S+1) + 0{\cdot}10. \qquad (2.3)$$

---

*One or two coefficients beyond $n=6$ are now available for $S = \infty$ (see Ref. [23]) and for spin $\frac{1}{2}$ (Domb C. and Wood, D. W. *Proc. R. Soc.* **86**, 1 1965).

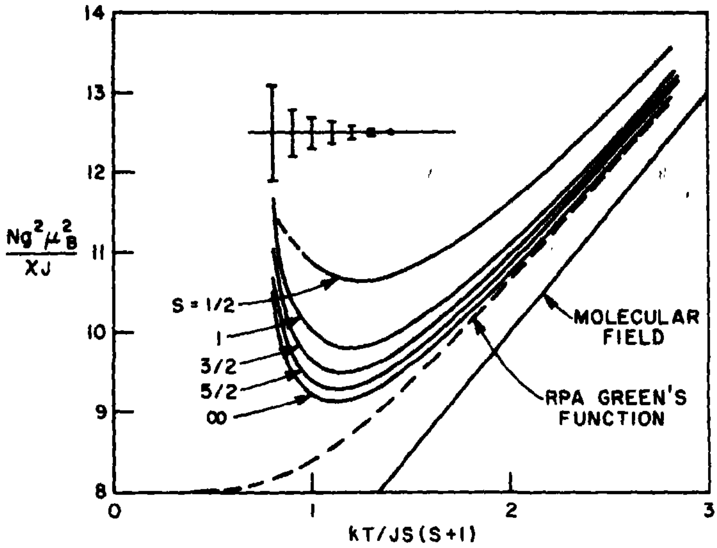

Fig. 1. Reciprocal paramagnetic susceptibility for the quadratic-layer Heisenberg antiferromagnet calculated as a function of temperature by extrapolating the high temperature exact series expansion graphically (see text). Typical errors resulting from the extrapolation procedure are indicated on the figure and increase with decreasing temperature. They are roughly appropriate for all spin except $S = \frac{1}{2}$ for which the extrapolation is less well defined with the present number of known series coefficients. Also plotted are the molecular-field and *RPA* Green's function susceptibility curves (both valid for all values of spin).

Since, for two-dimensional magnetic systems, a stable long-range order at nonzero temperatures can only be maintained in the presence of anisotropy[3, 6], any meaningful estimate for Néel temperature T_n must involve anisotropy in a fundamental way even for quasi-isotropic structures, so that a simple quantitative equation relating T_n to exchange J alone, may not exist. Thus, for two-dimensional quasi-Heisenberg antiferromagnets, $T_{\chi\max}$ replaces T_n as the observable most simply and accurately related to the exchange parameter. Equation (2.3) expresses the required relationship for the case of a square lattice and it is worthwhile to note that the equation is still valid in the presence of any temperature independent (e.g. Van Vleck) contributions to susceptibility, which would complicate the interpretation of high temperature susceptibility in terms of a Curie–Weiss law.

Using (2.3) we are immediately able to estimate fairly accurately the (intraplane) exchange J for the series of quasi-Heisenberg planar antiferromagnets in Table 2. Using Fig. 1 and allowing for possible diamagnetic and Van Vleck contributions to susceptibility it is possible to analyze paramagnetic susceptibility results in detail. As an example we have taken Ca_2MnO_4, for which $g \approx 1{\cdot}99$, fitting theory to the experimental measurements of Davis[7]. The best fit curve is shown in Fig. 2, yielding parameters

$$J(Ca_2MnO_4) = 52 \pm 1\,°K \qquad (2.4)$$

$$\chi(\text{diamag}) + \chi(\text{Van Vleck}) = (-1{\cdot}2 \pm 0{\cdot}5) \times 10^{-6}\ \text{e.m.u./g},$$

the error brackets reflecting the accuracy of the fit but excluding, of course, any possible systematic errors resulting from experimental uncertainties. The discrepancy between theory and experiment for temperatures below $T_{\chi\text{max}}$. is probably due to the existence of a weakly canted rather than a strictly antiferromagnetic spin arrangement below the ordering temperature, leading to a divergence of susceptibility at T_N.

Table 2. Exchange J *calculated from $T_{\chi\text{max}}$. by use of* (2.3)

Salt	$T_{\chi max.}$ (°K)	Spin S	Exchange J(°K)
Rb_2MnF_4	68*	5/2	6·9 ± 0·4
K_2MnF_4	78*	5/2	7·9 ± 0·4
K_2NiF_4	250†	1	107 ± 5
K_2NiF_4	235‡	1	100 ± 5
Ca_2MnO_4	225§	3/2	52 ± 3
Ba_2NiF_6	~ 200#	1	~ 85

*BREED D. J., *Physica* **37**, 35 (1967).

†SRIVASTAVA K. G., *Phys. Lett.* **4**. 55 (1963).

‡MAARSCHALL E P., BOTTERMAN A. C., VEGA S. and MIEDEMA A. R., *Physica* **44**, 224 (1969).

§DAVIS J. L., See MACCHESNEY J. B., WILLIAMS H. J., POTTER J. F. and SHERWOOD R. C., *Phys. Rev.* **164**, 779 (1967).

#VON SCHNERING H. G., *Z. anorg. allg. Chem.* **353**, 1 (1967).

3. THE ORDERED PHASE

(a) *Spin-wave theory*

The isotropic Heisenberg exchange Hamiltonian (2.1) cannot support a long-range antiferromagnetic order at nonzero temperatures [3]. The result is exact, and supports the usual interpretation of simple spin-wave theory in two dimensions. In the presence of a small anisotropy field H_A, the general consensus of theory and experiment is that an ordered state is stabilized up to a well defined Néel temperature. There are, as yet, no exact results for the anisotropic case in question. In this section, we shall adapt conventional spin-wave and Green's function theories to describe the ordered phase knowing that they, at least, will behave in a qualitatively correct manner in the isotropic limit, but thereby accepting the neglect of any possible significance of bound magnon effects [8]. We take comfort from the fact that no effects attributable to the presence of bound magnon states have yet been diagnosed from any failure of conventional spin-wave approximations to account for low temperature experimental observations in

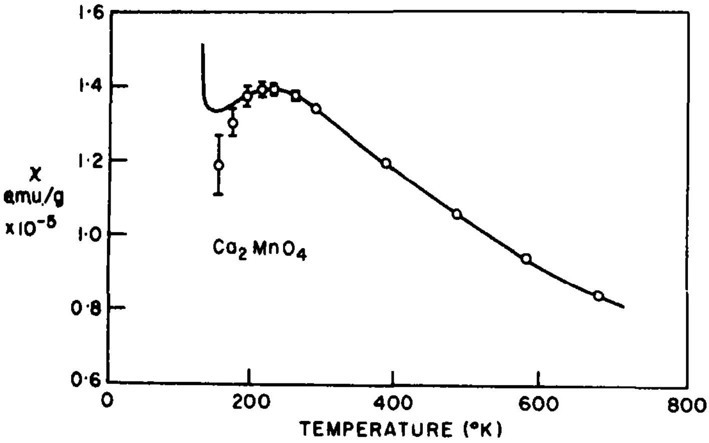

Fig. 2. The paramagnetic susceptibility for Ca_2MnO_4, as measured by Davis [7], is shown (full curve) and compared with the best theoretical fit (open circles) to the data, using the $S = 3/2$ curve of Fig. 1 with $J = 52°$ K and allowing for a temperature independent contribution of $-1{\cdot}2 \times 10^{-6}$ e.m.u./g.

layer salts[9–11]. It should be emphasized, however, that the validity of the 'neglect bound magnon effects' conjecture is far from proven for quasi-Heisenberg magnetic systems in two dimensions.

We describe the quadratic layer quasi-Heisenberg antiferromagnet by a Hamiltonian

$$\mathscr{H} = \sum_{nn} J\mathbf{S}_u \cdot \mathbf{S}_d - \sum_{u} g\mu_B H_A S_u{}^z + \sum_{d} g\mu_B H_A S_d{}^z, \tag{3.1}$$

where the subscript **u**(**d**) labels spins on 'up' ('down') sites in the ordered phase, and where Σ_{nn} runs over all nearest neighbor spin pairs $\mathbf{S}_u$ and $\mathbf{S}_d$. The formal procedures introducing the Holstein–Primakoff spin-deviation operators for the antiferromagnetic case, and the subsequent diagonalization of the resulting Hamiltonian by the Bogolyubov transformation, are well known[12] and only the results need be reproduced here. In the simple (non-interacting) spin-wave approximation we find eigenvalues

$$E(n_1, n_2) = -\tfrac{1}{2}NzJS(S+1) - Ng\mu_B H_A(S+\tfrac{1}{2}) + \sum_{\mathbf{K}} (n_{1\mathbf{K}} + n_{2\mathbf{K}} + 1)(\mu^2 - \lambda_{\mathbf{K}}{}^2)^{1/2}, \tag{3.2}$$

$$\mu = zJS + g\mu_B H_A, \tag{3.3}$$

$$\lambda_{\mathbf{K}} = S \sum_{nn}^{\mathbf{u}-\mathbf{d}} J e^{i\mathbf{K}.(\mathbf{u}-\mathbf{d})} \tag{3.4}$$

where **K** is a wave vector running over $N/2$ allowed values in the first Brillouin-zone of the reciprocal sublattice, $n_{1\mathbf{K}}$ and $n_{2\mathbf{K}}$ are quantum numbers labeling the number of spin-waves present with wave vector **K** in the two degenerate spin-wave bands, and $\Sigma_{nn}^{\mathbf{u}-\mathbf{d}}$— in (3.4) runs over the z nearest neighbor inter-spin distances $\mathbf{u}-\mathbf{d}$. In the same approximations[13, 14] we calculate the ensemble average $\langle S_{\mathbf{u}}^z \rangle = -\langle S_{\mathbf{d}}^z \rangle = \bar{S}$, which measures the temperature dependence of sublattice magnetization per site, as

$$\bar{S} = S + \tfrac{1}{2} - \tfrac{1}{2}x, \tag{3.5}$$

where

$$x = \left\langle \frac{\mu}{(\mu^2 - \lambda_{\mathbf{K}}^2)^{1/2}} \coth\left[\frac{(\mu^2 - \lambda_{\mathbf{K}}{}^2)^{1/2}}{2kT}\right] \right\rangle_{\mathbf{K}}, \tag{3.6}$$

and where $\langle \ldots \rangle_{\mathbf{K}}$ refers to an average of **K** over all its allowed values. For the particular case of the quadratic layer antiferromagnet, we find

$$x = \left\langle \frac{1+D}{[(1+D)^2 - \frac{1}{4}\gamma_{\mathbf{K}}{}^2]^{1/2}} \coth \left\{ \frac{2JS}{kT} [(1+D)^2 - \tfrac{1}{4}\gamma_{\mathbf{K}}{}^2]^{1/2} \right\} \right\rangle_{\mathbf{K}}, \tag{3.7}$$

in which

$$\gamma_{\mathbf{K}} = \cos(K_x a) + \cos(K_y a), \tag{3.8}$$

$$D = g\mu_B H_A / zJS, (z = 4), \tag{3.9}$$

and where the components K_x and K_y of wave vector **K** run independently in $\langle \ldots \rangle_{\mathbf{K}}$ between $-\pi/a$ and π/a, 'a' being the nearest neighbor interspin distance.

Evaluating the average $\langle \ldots \rangle_{\mathbf{K}}$ directly by computer, we have calculated the temperature variation of sublattice magnetization for four values of anisotropy $D = 10^{-1}$, 10^{-2}, 10^{-3}, 10^{-4}. The results are shown in Fig. 3 where the deviation of spin $\bar{S}_0 - \bar{S}$ from the zero temperature value $\bar{S}_0$ is plotted as a function of temperature. Also plotted for comparison are the equivalent results for the quasi-Heisenberg simple-cubic antiferromagnet, where the latter curves are computed from (3.5), (3.7) but with $\gamma_{\mathbf{K}}$ for the simple cubic lattice given by $(\frac{2}{3})[\cos(K_x a) + \cos(K_y a) + \cos(K_z a)]$ and the average $\langle \ldots \rangle_{\mathbf{K}}$ taken over all three components of wave vector. The parameter D is still defined from (3.9) but with $z = 6$.

We see that the sublattice magnetization varies much more rapidly with temperature for the two-dimensional system (this is still true if the curves are plotted as a function of reduced temperature T/T_n) reflecting the fact that, in two dimensions, a much higher den-

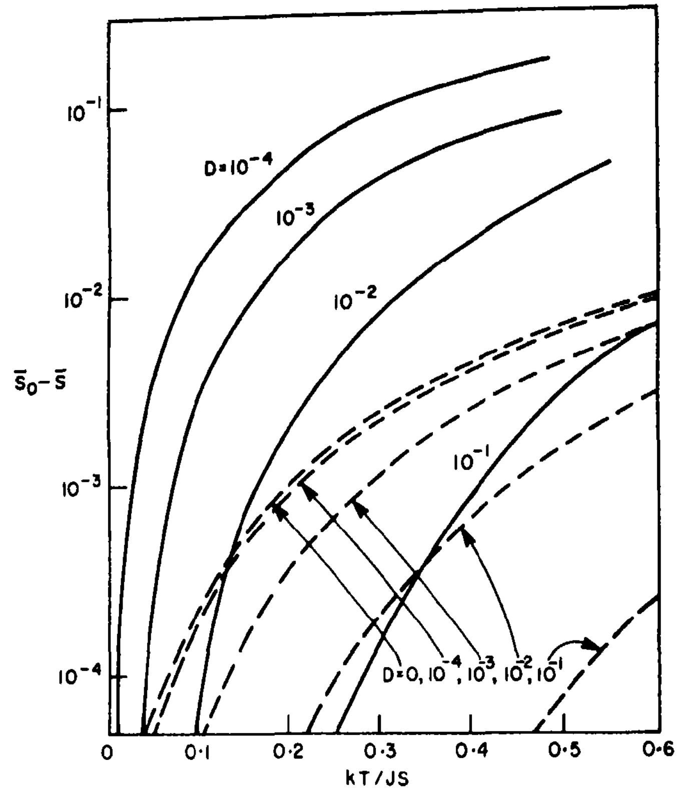

Fig. 3. The variation with temperature of the deviation of sublattice spin $\bar{S}$ from its value $\bar{S}_0$ at absolute zero is shown for the quadratic-layer (full curves) and simple-cubic (dashed curves) antiferromagnets for a series of values of anisotropy $D = g\mu_B H_A/zJS$.

sity of states exists for low energy magnons than in three dimensions. This same property also produces much larger zero-point spin deviations in two dimensions than in three. This is demonstrated in Table 3 where we have computed spin deviation $S-\bar{S}_0$ as a function of anisotropy and compared the results for the quadratic-layer and simple-cubic antiferromagnetic lattices.

(b) *The random-phase Green's function approximation*

To extend the spin-wave findings up to and beyond the phase transition temperature T_n,

Table 3. Zero point spin deviation $(S-\bar{S}_0)$ *as a function of anisotropy parameter*

D	Quadratic-layer lattice	Simple-cubic lattice
0	0·197	0·078
10^{-4}	0·192	0·078
10^{-3}	0·183	0·077
10^{-2}	0·156	0·073
10^{-1}	0·092	0·051

it is necessary to renormalize the spin-waves in some manner to account for magnon interactions. The simplest approximation which allows both for a meaningful description of the phase transition and the inherent instability of the isotropic layer system is the random-phase Green's function approximation, which renormalizes the spin-waves according to the magnetization. The approximation is undoubtedly crude [6] (underestimating, as it does, the short range correlations in the system) and is likely to be exposed, like most other theoretical approximations, far more mercilessly in two dimensions than in three, but it does seem to be qualitatively sound and should provide, at the very least, a sounding board for more sophisticated schemes perhaps to follow.

The random-phase Green's function approximation has already been discussed for the general case of a Heisenberg antiferromagnet describable in terms of two translationally invariant sublattices [15]. The relevant equations for the isotropic quadratic-layer and simple-cubic antiferromagnets can therefore be quoted directly and are very easily adapted to allow for the inclusion of a small anisotropy term as in (3.1).

In the present section we shall be particularly interested in the temperature dependence of sublattice magnetization, and the anisotropy dependence of Néel temperature. In the RPA Green's function approximation, the average value of spin per site $\bar{S}$ in the ordered phase is given by [15]

$$\frac{2\bar{S}+x}{2S+1}=\frac{(x+1)^{2S+1}+(x-1)^{2S+1}}{(x+1)^{2S+1}-(x-1)^{2S+1}}, \qquad (3.10)$$

where x is given in (3.6) but where now the functions μ and λ_K of (3.3) and (3.4) require the simple modification of replacing quantum number S by ensemble average $\bar{S}$. As a result, equations (3.7)–(3.9) are still valid for the quadratic-layer antiferromagnet except for the $S \rightarrow \bar{S}$ substitution.

Equation (3.10) is now an implicit equation for $\bar{S}$ and may be solved numerically by computer. The resulting curves are most usefully presented in the form reduced magnetization $\bar{S}/\bar{S}_0$ as a function of reduced temperature T/T_n and are shown in Figs. 4–6. For larger values of anisotropy ($D \sim 0{\cdot}1$) the curve shapes are very closely equal to the molecular-field (isotropic) Brillouin curves, namely

$$\bar{S}/\bar{S}_0=\bar{S}/S=B_s[(3S/S+1)(T_n/T)(\bar{S}/S)], \qquad (3.11)$$

where B_s is the Brillouin function

$$B_s(y)=(1/2S)\{(2S+1)\coth[(2S+1)y/2S] -\coth[y/2S]\}. \qquad (3.12)$$

However, as anisotropy is reduced for the two-dimensional system, the curves fall progressively further inside the Brillouin curves, the effect being most marked for spin $\frac{1}{2}$, but becoming less pronounced with increasing spin quantum number and finally vanishing completely in the classical spin limit (Fig. 6), for which the Green's function curves reduce to the Brillouin curve for all D. One interesting observation for smaller values of anisotropy ($D \lesssim 10^{-3}$) is that the sequence of curves $S=\frac{1}{2}, 1, 3/2, 2, 5/2, 3$ for a fixed value D of anisotropy field to exchange field ratio, is reversed from the usual (molecular-field) situation, the spin $\frac{1}{2}$ curve being on the inside of the series.

The computations for the simple-cubic antiferromagnet are most insensitive to anisotropy for values of D up to $0{\cdot}1$. The reduced magnetization curves are very closely equal to the isotropic Brillouin curves (3.11) for all cases. The detailed curves are not exactly the molecular-field ones but, on the scale of Figs. 4–6, the differences are negligible except for $S=\frac{1}{2}$, for which the deviations are just discernible on this scale.

The general conclusion is that in three dimensions the reduced magnetization curves for weakly anisotropic Heisenberg antiferromagnets are the Brillouin curves to a good approximation, but that in two dimensions, the

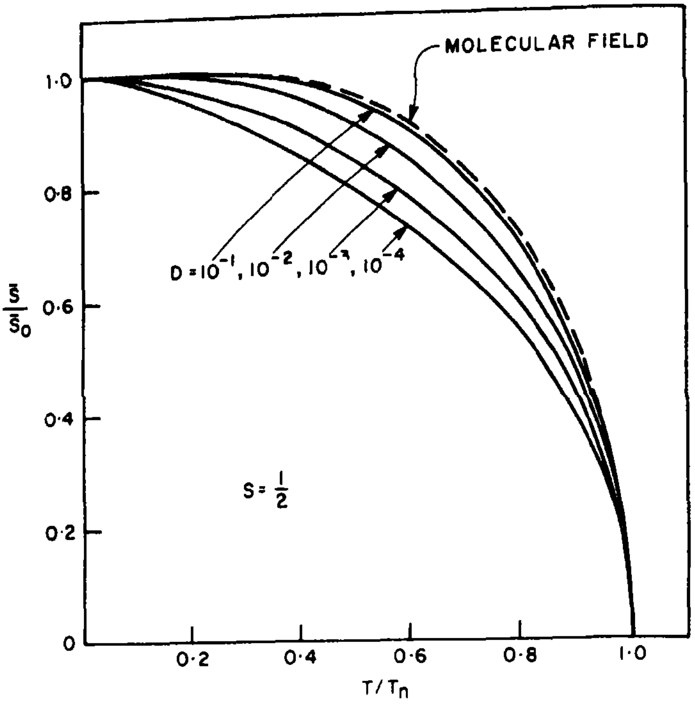

Fig. 4. Curves of reduced sublattice magnetization $\bar{S}/\bar{S}_0$ as a function of reduced temperature T/T_n for the spin $\frac{1}{2}$ quadratic-layer antiferromagnet, as calculated in the *RPA* Green's function approximation for a range of values of anisotropy parameter $D = g\mu_B H_A/zJ\bar{S}$. These curves are valid in their explicit form (D constant, $H_A \propto \bar{S}$) only for two-spin anisotropy forms e.g. anisotropic exchange, dipole-dipole anisotropy (see text). Also shown for comparison is the molecular-field Brillouin curve (dashed) for $S = \frac{1}{2}$.

curves may differ quite markedly from molecular-field shapes. However, a word of caution is necessary. The curves in Figs. 4–6 have been displayed and interpreted above as if $H_A \propto \bar{S}$ (i.e. D independent of temperature). Within the Green's function approximation, this is valid for most two spin forms of anisotropy (e.g. anisotropic exchange and dipole-dipole forms) but is almost certainly quite invalid for crystal field anisotropy. For the latter case, curves 4–6 cannot be interpreted without a knowledge of the temperature dependence of H_A. Secondly, the present theory is still of basic Landau form near the phase transition and must not, therefore, be taken as quantitative in the critical region. The real phase transition in two dimensions is likely to be even less Landau-like than in three dimensions.

Finally, and again subject to the interpretational restrictions alluded to above, the Néel temperature may be computed in the present approximation as a function of D, by considering the $\bar{S} \to 0$ limit of (3.10). Details have been given in Ref.[15] and result in the equation

$$S(S+1)/3kT_n\bar{S} = \langle \mu/(\mu^2 - \lambda_{\mathbf{K}}^2)\rangle_{\mathbf{K}}, \quad (3.13)$$

from which we have computed the Néel temperature curves of Fig. 7 for the quadratic-layer and simple-cubic cases.

4. TWO-SPIN CORRELATION FUNCTIONS

Of particular interest in the study of statistical magnetism is the spin-correlation function

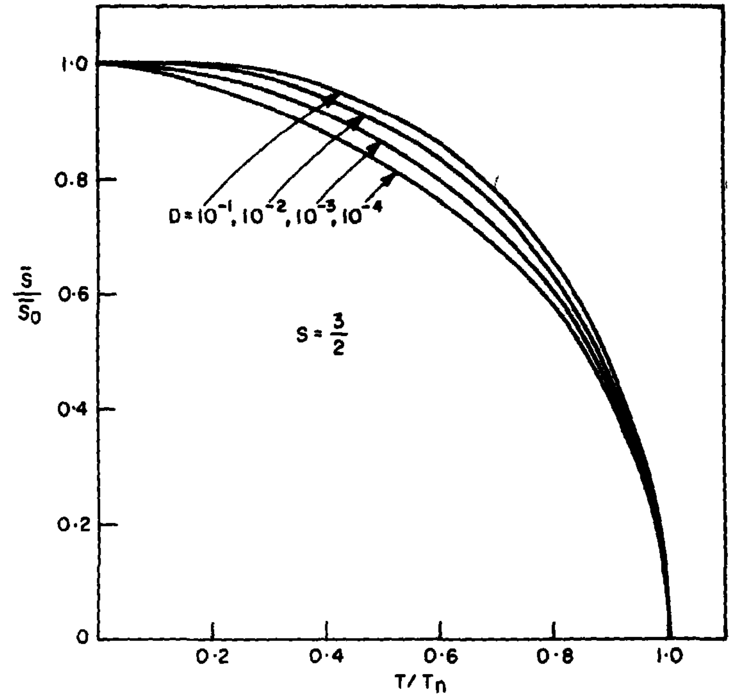

Fig. 5. As Fig. 4 but for spin $S = 3/2$. The molecular-field Brillouin ($S = 3/2$) curve, on this scale, coincides with the $D = 10^{-1}$ curve.

$\langle \mathbf{S}_0(t)\,.\,\mathbf{S}_R(t')\rangle$, where subscripts **O** and **R** label spin sites at the origin and at vector **R** respectively. There has been much recent conjecture about the frequency and wave-vector form of its Fourier transform for temperatures close to a magnetic phase transition, since this determines the nature of the magnetic excitations in the critical region[16–18]. The weight of evidence[1, 19, 20] points to the existence of propagating spin-wave modes above the phase transition, and these modes are presumably best defined for systems possessing the largest degree of short-range order in the paramagnetic phase. It is in this capacity that two-dimensional systems are particularly relevant. In fact, if we define a correlation length L_c in conventional fashion writing, for $T > T_n$ (or T_c for a ferromagnet)

$$|\langle \mathbf{S}_O(t)\,.\,\mathbf{S}_R(t)\rangle| = |\langle \mathbf{S}_O\,.\,\mathbf{S}_R\rangle \propto \exp(-R/L_c). \tag{4.1}$$

in the limit $R \to \infty$, then the best theoretical estimates presently available for isotropic two-dimensional Heisenberg systems[1, 21] indicate that L_c actually diverges when

$$kT = kT_c^{(2)} \approx (J/10)\,(z-1)\,[2S(S+1)-1], \tag{4.2}$$

even though, for these systems, there is no long-range order at nonzero temperatures[3]. The *RPA* Green's function approximation (which, in terms of accuracy cannot, of course, compete with the best high temperature series extrapolation methods in the paramagnetic phase) does not exhibit such a divergence at nonzero temperatures. It does, however, demonstrate quite clearly a very marked difference in the temperature dependence of L_c for two- and three-dimensional systems and shows even in this approximation, which clearly underestimates spin correlations, that L_c approaches macroscopic dimensions over a sizeable range of temperature.

We shall compute spin correlations in the paramagnetic phase using the well established

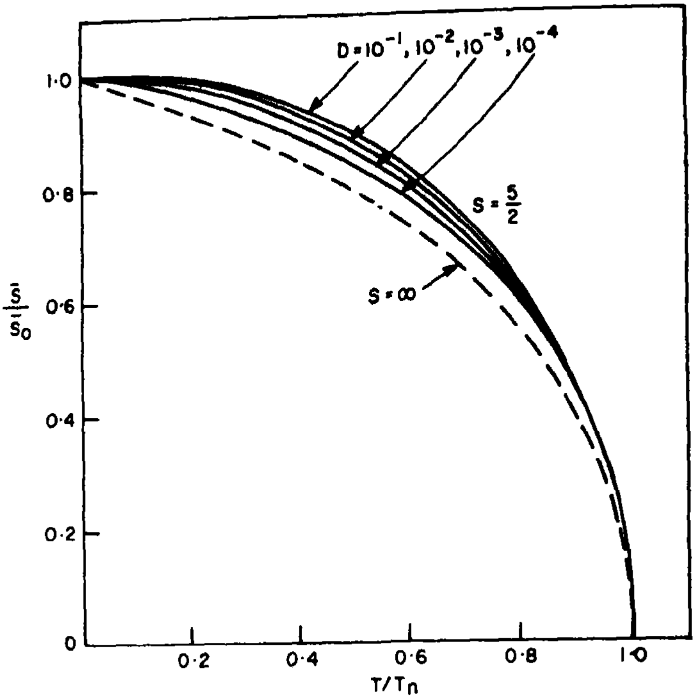

Fig. 6. As Fig. 4 but for spin $S = 5/2$. The molecular-field Brillouin ($S = 5/2$) curve, on this scale, coincides with the $D = 10^{-1}$ curve. Also plotted (dashed) is the result for classical spin $S = \infty$, for which the curve is independent of D and coincides exactly with the molecular-field Brillouin curve for the classical spin limit.

RPA Green's function formalism. In spite of the expected comparative crudeness of the approximation, there is an additional interest in generating it. The accuracy of the high temperature series expansion extrapolation procedures can be tested in the RPA Green's function context. Since the suggestion of a divergent L_c (and the associated questions surrounding the possible interpretation of this finding in two dimensions[1, 21]) results from an extrapolation and cannot yet be demonstrated rigorously, it is important to check the accuracy of the procedure for cases where an exact result is known. In the *RPA* Green's function approximation, $T_c^{(2)}$, the temperature for which L_c diverges, is zero for the isotropic Heisenberg quadratic-layer ferromagnet or antiferromagnet. By expanding the *RPA* Green's function paramagnetic susceptibility as a high temperature power series and to about that number of terms usually available in an exact series calculation, we shall test whether the typical extrapolation procedures are capable of indicating $T_c^{(2)} = 0$ for this case. Such a test can never, of course, establish the validity of the high temperature expansion procedures for the general case; it could, however, destroy the significance of Stanley and Kaplan's finding (4.2) if the method fails. It should, moreover, be quite a good test case in view of the extremely large (though still finite) values attained by L_c at low temperatures in the Green's function description.

The general formalism for the *RPA* Green's function approximation is well known[15, 22] and is valid in the paramagnetic phase for either sign of exchange parameter. We shall

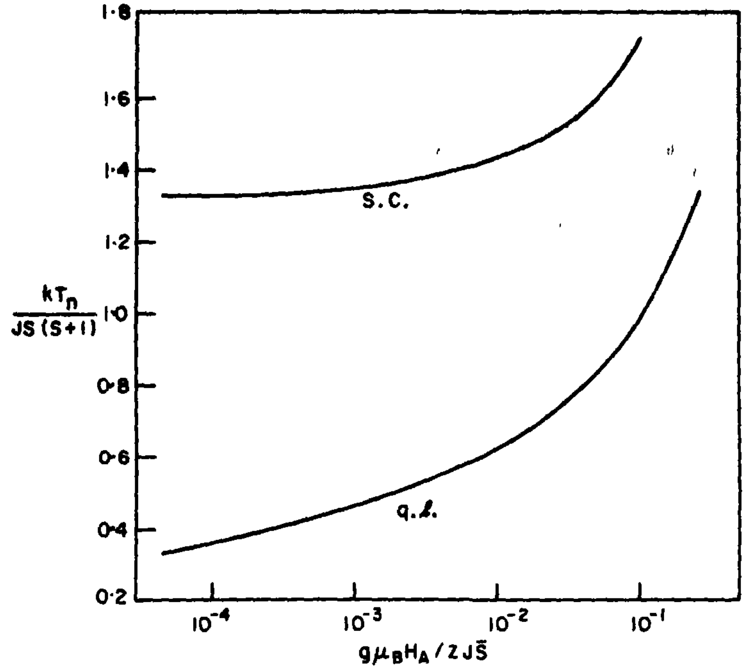

Fig. 7. The Néel temperature T_n as a function of anisotropy $g\mu_B H_A/zJ\bar{S}$ for the quadratic-layer (*q.l.*) and simple-cubic (*s.c.*) antiferromagnets calculated in the *RPA* Green's function approximation.

consider the isotropic quadratic layer system with Hamiltonian (2.1) for which [22]

$$\langle \mathbf{S}_0 . \mathbf{S}_\mathbf{R}\rangle = 3kT\langle \exp(i\mathbf{K}.\mathbf{R})/(\chi_0^{-1}+\rho)\rangle_\mathbf{K}, \tag{4.3}$$

in which

$$\rho = \sum_{nn} J[\exp(i\mathbf{K}.\mathbf{R}_{nn})-1], \tag{4.4}$$

with Σ_{nn} running over nearest-neighbor position vectors $\mathbf{R}_{nn}$, and where χ_0 is a reduced susceptibility $\chi_0 = \chi/Ng^2\mu_B{}^2$ and can be computed in the present approximation from [22]

$$S(S+1)/3kT\chi_0 = \langle 1/(1+\chi_0\rho)\rangle_\mathbf{K}. \tag{4.5}$$

More specifically, we have for the quadratic layer case

$$\rho = 2J[\cos(K_x a)+\cos(K_y a)-2], \tag{4.6}$$

and the average $\langle\ldots\rangle_\mathbf{K}$ is taken for values K_x and K_y running independently between $-\pi/a$ and π/a. The corresponding expression for the simple-cubic lattice is

$$\rho = 2J[\cos(K_x a)+\cos(K_y a) + \cos(K_z a)-3], \tag{4.7}$$

with $\langle\ldots\rangle_\mathbf{K}$ now running independently over all three wave vector components.

Defining a Fourier transform $\mathbf{S}_\mathbf{K}$ of spin operator $\mathbf{S}_\mathbf{R}$ by

$$\mathbf{S}_\mathbf{R} = N^{-1/2}\sum_\mathbf{K} \mathbf{S}_\mathbf{K}\exp(-i\mathbf{K}.\mathbf{R}), \tag{4.8}$$

we find the Fourier transform of the correlation function in the form

$$\langle \mathbf{S}_\mathbf{K} . \mathbf{S}_{-\mathbf{K}}\rangle = 3kT/(\chi_0^{-1}-\rho), \tag{4.9}$$

from which one readily verifies the Ornstein–Zernike form for the long wavelength (ferromagnetic) or staggered long wavelength (antiferromagnetic) cases as follows;

(a) *Ferromagnetic*

$$\langle \mathbf{S}_K \cdot \mathbf{S}_{-K} \rangle = (3kT/|J|)/(K_c^2+K^2)a^2, K \to 0, \quad (4.10)$$

in which

$$a^2K_c^2 = a^2/L_c^2 = (\chi_0|J|)^{-1}, \quad (4.11)$$

and goes to zero as the susceptibility diverges. In the present approximation this occurs at the same temperature T_c at which a long-range order sets in.

(b) *Antiferromagnetic*

$$\langle \mathbf{S}_{q-K} \cdot \mathbf{S}_{-q+K} \rangle = (3kT/J)/(K_c^2+K^2)a^2, K \to 0, \quad (4.12)$$

in which

$$a^2K_c^2 = a^2/L_c^2 = (\chi_0 J)^{-1} - 2z, \quad (4.13)$$

and where q is a reciprocal lattice vector $[(\pi/a, \pi/a)$ for the quadratic-layer lattice, $(\pi/a, \pi/a, \pi/a)$ for the simple-cubic lattice]. Since the antiferromagnetic reduced susceptibility $\chi_0 = (2zJ)^{-1}$ at the Néel temperature [15], K_c again goes to zero in this limit.

Thus, in the *RPA* Green's function approximation, the correlation length L_c diverges at the onset of long-range order. Fourier transforming (4.10) or (4.12) immediately identifies the L_c of (4.11) and (4.13) with that of (4.1).

Computing the correlation length from (4.13) and (4.5) for the isotropic quadratic-layer and simple-cubic antiferromagnets ([$(\chi_0 J)^{-1}$ as a function of temperature in this approximation is displayed in Fig. 1) we obtain the results plotted in Fig. 8, where the reciprocal correlation length is shown as a function of temperature for the paramagnetic phase. The figure is actually valid for the equivalent ferromagnetic lattices also. This is readily proved by using equations (4.5)–(4.7) to establish, in *RPA* Green's function approximation, the result

$$(\chi_0|J|)^{-1}_{\text{ferro}} = (\chi_0|J|)^{-1}_{\text{antiferro}} - 2z. \quad (4.14)$$

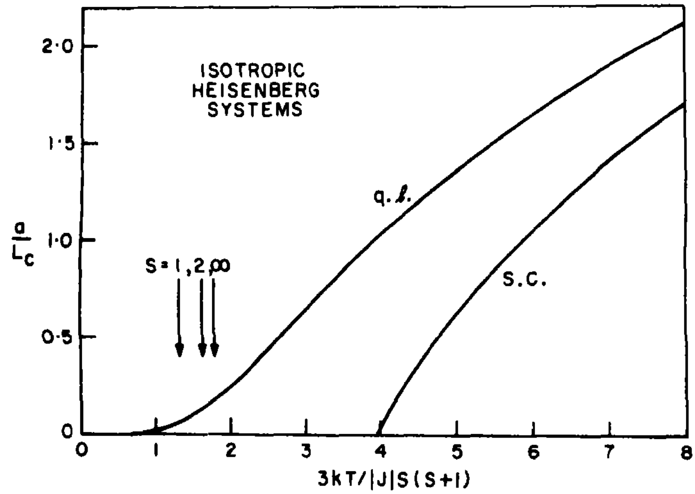

Fig. 8. The ratio of lattice spacing '*a*' to spin correlation length L_c calculated in the *RPA* Green's function approximation for the isotropic Heisenberg quadratic-layer (*q.l.*) and simple-cubic (*s.c.*) systems. The curves are valid for either sign of exchange *J* (see text). Also marked (arrows) are the temperatures (as a function of spin)) for which the high temperature series expansion techniques [equation (4.2)] indicate L_c to diverge for the quadratic-layer case.

We note that the two-dimensional situation shows a sizeable temperature range for which L_c is orders of magnitude larger than the lattice spacing 'a'. A corresponding region for the simple cubic case is vanishingly small. As mentioned earlier, this Green's function estimate for L_c for the two-dimensional system is almost certainly an underestimate, and the high temperature series work suggests that L_c diverges at $T_c^{(2)}$ of equation (4.2) (which is marked on Fig. 8).

Spin correlations for near neighbor spins may be computed directly from (4.3) in conjunction with (4.5). Results out to sixth nearest neighbors along an axis for the quadratic layer-system are shown in Fig. 9 for a number of different temperatures. The correlations are observed to follow the law

$$|\langle \mathbf{S}_0 \,.\, \mathbf{S}_R \rangle| \propto R^{-\beta} \exp(-K_c R), \qquad (4.15)$$

where β is, to a good approximation, temperature independent and equal to $0{\cdot}4 \pm 0{\cdot}1$. The corresponding result for the simple cubic lattice may also be expressed by (4.15) but with $\beta = 1{\cdot}0 \pm 0{\cdot}1$ and where, this time, the nearest neighbor correlation is an exception to the rule, having a larger value than would result from (4.15). The radial dependence of $\langle \mathbf{S}_0 \,.\, \mathbf{S}_R \rangle$ in the limit of $R \to \infty$ can be obtained algebraically by Fourier inverting (4.10) or (4.12) when one obtains

$$|\langle \mathbf{S}_0 \,.\, \mathbf{S}_R \rangle| \propto R^{-(d-1)/2} \exp(-K_c R), \; R \to \infty \qquad (4.16)$$

in which d is the dimensionality. This gives the famous result of Ornstein and Zernike for

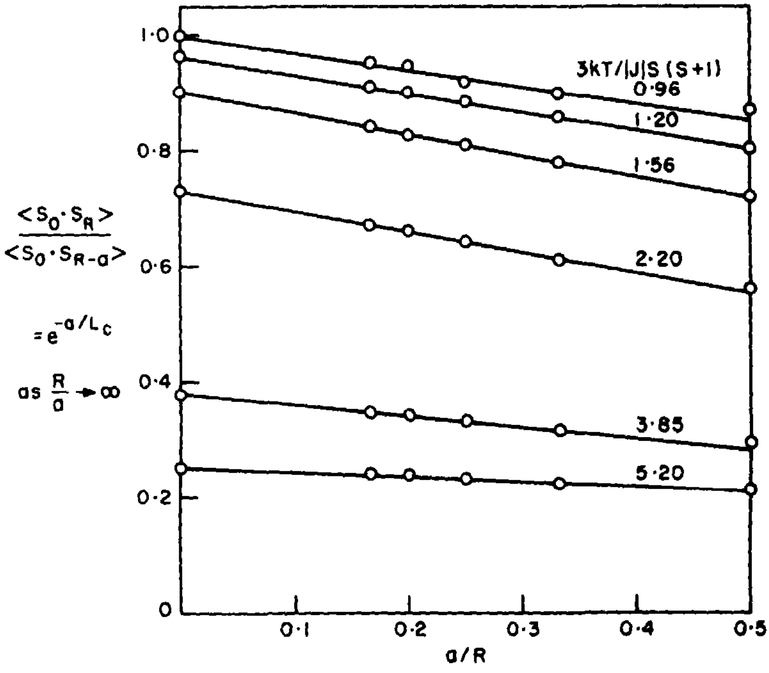

Fig. 9. The correlation function ratio $\langle \mathbf{S}_0 . \mathbf{S}_R \rangle / \langle \mathbf{S}_0 . \mathbf{S}_{R-a} \rangle$ for the first five pairs of nearest-neighbor spins $\mathbf{S}_0$, $\mathbf{S}_{R-a}$ along a quadratic axis are shown for a number of different temperatures for the isotropic Heisenberg quadratic-layer system [computed directly from (4.3) and (4.5)]. The results are valid for either sign of exchange J if allowance is made for an obvious change of sign of ordinate axis for the antiferromagnetic case. Also shown is the limiting behavior as $a/R \to 0$, for which the correlation function ratio is directly related to the correlation length and can be calculated from Fig. 8.

$d=3$ (β of equation (4.15) equal to unity) and, for two dimensions, gives $\beta=\frac{1}{2}$. Thus, the relationship (4.16) for $R\to\infty$ appears to be valid, to a good approximation, right down to very near neighbor distances but with the possible exception of nearest-neighbors themselves.

We now use (4.5) to expand the paramagnetic reduced susceptibility χ_0 as a power series in reciprocal temperature. We first look for the series for reciprocal susceptibility in the form

$$(\chi_0 J)^{-1}=3\theta\left[1+\sum_{i=1}^{\infty}A_i/\theta^i\right], \qquad (4.17)$$

where $\theta=kT/JS(S+1)$. Substituting (4.17) into (4.5) we obtain

$$\left\langle\left[1+(\rho/3J\theta)+\sum_{i=1}^{\infty}A_i/\theta^i\right]^{-1}\right\rangle_K=1. \qquad (4.18)$$

Expanding the left hand side as a power series in θ^{-1}, equating coefficients, and making use of (4.6) and (4.7), we find for the coefficients A_i the values shown in Table 4. Inverting the series we obtain, for the reduced susceptibility

$$\chi_0 J=(1/3\theta)\left[1-\sum_{i=1}^{\infty}B_i/\theta^i\right], \qquad (4.19)$$

where the coefficients B_i for $i\leq 10$ are also given in Table 4 for both the quadratic-layer and simple-cubic cases. We note that the series (4.19) has terms oscillating in sign for the antiferromagnet (positive J) but of constant sign for the ferromagnet.

For the ferromagnetic cases, we may compare these Green's function results with those from the exact series expansion [23]. We make the comparison for the classical spin case ($S=\infty$) for which the largest number of exact coefficients are available (the Green's function approximation is, of course, applicable for arbitrary spin). Plotting the ratio B_i/B_1B_{i-1} as a function of i we obtain the curves of Fig. 10. The extrapolated values of the ordinate for $i\to\infty$ are the respective values of the ratio T_c/T_{mf} of Curie temperature T_c to molecular-field transition temperature T_{mf}. The 'exact' results are known for the Green's function curves, being 0·659 for the simple-cubic case, and zero for the quadratic-layer case. We see

Table 4. The coefficients A_i *of series expansion* (4.17)

Simple cubic lattice		Quadratic layer lattice
2·00000	A_1	1·33333
0·66667	A_2	0·44444
0·22222	A_4	0·04938
0·18107	A_6	−0·02195
0·12346	A_8	−0·00427
0·09693	A_{10}	0·00298
0·00000	$A_{2i+1}\,(i\geq 1)$	0·00000

The coefficients B_i *of series expansion* (4.19)

Simple cubic lattice		Quadratic layer lattice
2·0000	B_1	1·3333
−3·3333	B_2	−1·3333
5·3333	B_3	1·1852
−8·2222	B_4	−0·9383
12·4444	B_5	0·6584
−18·4856	B_6	−0·4170
27·1276	B_7	0·2341
−39·3772	B_8	−0·1140
56·6914	B_9	0·04718
−81·0260	B_{10}	−0·01494

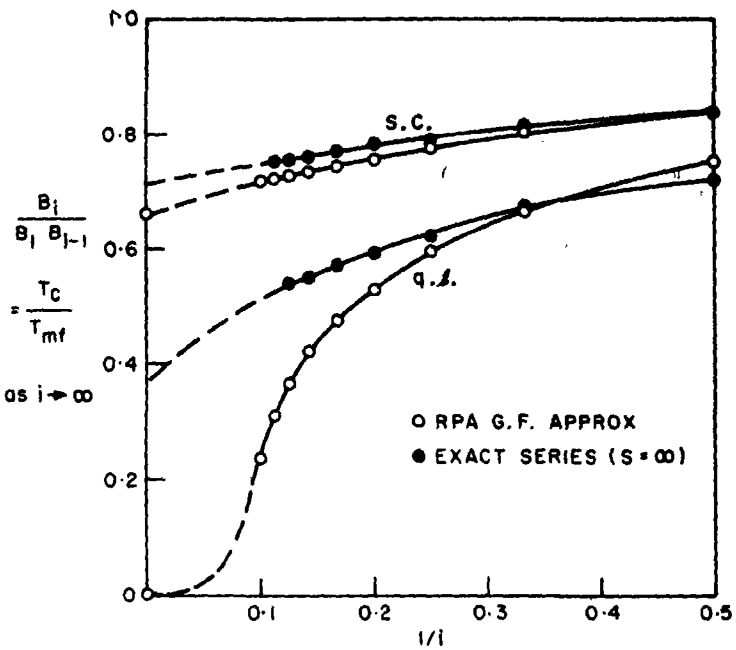

Fig. 10. The ratio of coefficients B_i/B_1B_{i-1} from series (4.19) are plotted as a function of $1/i$ and extrapolated graphically to $1/i \to 0$ for which limit the ordinate equals the ratio of phase transition temperature T_c to molecular-field estimate T_{mf}. The filled circles are the exact series coefficients for the classical spin limit, taken from Ref. [23], and the open circles are the RPA Green's function approximation. Results are shown both for the isotropic Heisenberg quadratic-layer (*q.l.*) and simple-cubic (*s.c.*) ferromagnetic lattices. The correct limiting values for the Green's function approximation can be computed directly and are shown.

that the series extrapolation method is quite valid for both cases. Thus, the Green's function test is not able to point to any obvious weakness in the reliability of the extrapolation procedure. We must therefore still accept the possibility of the existence of a phase transition at nonzero temperatures for the two-dimensional system (see Fig. 10) even though the divergence of susceptibility (which is indicated by the positive intercept on the ordinate axis) and the associated divergence of the correlation length cannot be indicative of a long-range order for this case [3].

Making use of the general relationship

$$\chi_0 = (1/kT) \sum_{\mathbf{R}} \langle S_0^z S_{\mathbf{R}}^z \rangle, \qquad (4.20)$$

for the paramagnetic phase which, for isotropic systems, becomes

$$\chi_0 = (1/3kT) \sum_{\mathbf{R}} \langle \mathbf{S}_0 \cdot \mathbf{S}_{\mathbf{R}} \rangle, \qquad (4.21)$$

it would seem very probable that the *RPA* Green's function approximation underestimates long-range spin correlations and that, in this limit, it is a very much poorer approximation in two dimensions than in three.

Acknowledgement—The author has greatly benefited from numerous discussions with R. J. Birgeneau and is pleased to acknowledge the value of these verbal exchanges.

REFERENCES

1. LINES M. E., *J. appl. Phys.* **40**, 1352 (1969) (A wide selection of relevant references).
2. VON SCHNERING H. G., *Z. anorg. allg. Chem.* **353**, No. 1–2, 1 and 13 (1967).
3. MERMIN N. D. and WAGNER H., *Phys. Rev. Lett.* **17**, 1133 (1966).

4. RUSHBROOKE G. S. and WOOD P. J., *Molec. Phys.* **1**, 257 (1958).
5. RUSHBROOKE G. S. and WOOD P. J., *Molec. Phys.* **6**, 409 (1963).
6. LINES M. E., *Phys. Rev.* **164**, 736 (1967).
7. DAVIS J. L., Private communication, see also MACCHESNEY J. B., WILLIAMS H. J., POTTER J. F. and SHERWOOD R. C., *Phys. Rev.* **164**, 779 (1967).
8. WORTIS M., *Phys. Rev.* **132**, 85 (1963).
9. BREED D. J., *Physica* **37**, 35 (1967).
10. NARATH A., *Phys. Rev.* **131**, 1929 (1963).
11. NARATH A. and DAVIES H. L., *Phys. Rev.* **137**, A163 (1965).
12. KEFFER F., *Handb. Phys.*, Vol. 18, p. 1. Springer, Berlin.
13. ANDERSON P. W., *Phys. Rev.* **86**, 694 (1952).
14. KUBO R., *Phys. Rev.* **87**, 568 (1952).
15. LINES M. E., *Phys. Rev.* **135**, A1336 (1964).
16. MARSHALL W., *Critical Phenomena*, NBS Misc. Publ. No. 273 p. 135.
17. FISHER M. E., *Rep. Prog. Phys.* **32**, 615 (1967).
18. HALPERIN B. I. and HOHENBERG P. C., *Phys. Rev.* **177**, 952 (1969).
19. BENNETT H. S., *Phys. Rev.* **174**, 629 (1968).
20. NATHANS R., MENZINGER F. and PICKART S. J., *J. appl. Phys.* **39**, 1237 (1968).
21. STANLEY H. E. and KAPLAN T. A., *Phys. Rev. Lett.* **17**, 913 (1966).
22. LINES M. E., *Phys. Rev.* **139**, A1304 (1965).
23. STANLEY H. E., *Phys. Rev.* **158**, 546 (1967).

J. Phys. Chem. Solids Pergamon Press 1970. Vol. 31, pp. 117–124. Printed in Great Britain.

THE DE HAAS–VAN ALPHEN EFFECT IN WHITE TIN[†]

R. W. VAUGHAN[‡] D. D. ELLEMAN and D. G. McDONALD[§]
Jet Propulsion Laboratory, California Institute of Technology, Pasadena, Calif. 91103, U.S.A.

(*Received* 7 *March* 1969)

Abstract – A low frequency field modulation differential magnetometer has been adapted to allow numerical Fourier analysis of data taken in de Hass–van Alphen (DHVA) effect studies. The technique is used to determine the effect mass of those sections of the Fermi surface in white, metallic, tin contributing to the DHVA with the magnetic field parallel to the (100) and (001) crystallographic axes. In addition, the observation of anomalous, intense oscillations whose frequencies are high order (greater than sixth) linear combinations of the frequencies of the fundamental DHVA oscillations are reported and discussed.

INTRODUCTION

THE FERMI surface and electronic structure of metallic, 'white,' tin have been extensively investigated in the past few years[1–7]. We wish to report additional information which has been obtained on the Fermi surface in white tin using the de Haas–van Alphen (DHVA) effect. First discovered in tin by Shoenberg[7], the DHVA has since been used for investigations of this material by a number of authors[1–6]. With the development of the field modulation DHVA techniques and their increased sensitivity, two groups[1, 2] have re-examined the DHVA in white tin in detail, reporting both new oscillations and more accurate values of the frequencies of those previously known. No attempt was made in these later studies to accurately determine the amplitudes of the numerous superimposed oscillations.

We have developed a numerical Fourier analysis scheme for use in conjunction with a field modulated magnetometer to allow an accurate determination of both the frequencies and amplitudes of such multiple oscillations. This numerical technique has been used to determine the effective mass of several sections of the Fermi surface contributing to the DHVA from the dependence of the amplitude of the oscillations upon the temperature. In addition, we report the observation of a phenomenon in tin which results in the occurrence of intense oscillations of harmonic and combinational frequencies of high order (greater than sixth) when the magnetic field is orientated parallel to a (100) crystallographic axis.

The numerical Fourier techniques described here are directly applicable to the analysis of data in many other experimental situations. In addition to allowing a straightforward determination of the amplitude and frequency of all oscillatory components in the data, they allow an effective increase in the signal-to-noise ratio of the experimental apparatus and thus can offer significant advantages compared to analog signal processing.

EXPERIMENTAL TECHNIQUES

The modulated field magnetometer which was constructed and used for this work is similar to that described by several authors

---

[†] This paper presents the results of one phase of research carried out at the Jet Propulsion Laboratory, California Institute of Technology, under Contract No. NAS 7-100 sponsored by the National Aeronautics and Space Administration.

[‡] U.S. Army assigned to the Jet Propulsion Laboratory under Contract No. NAS 7-100. *Present address*: Division of Chemistry and Chemical Engineering, California Institite of Technology, Pasadena, Calif. 91109, U.S.A.

[§] *Present address*: National Bureau of Standards, Boulder, Colo. 80302, U.S.A.

[2, 8] and will only be briefly described here. The sample orientation device used the spiral-gear arrangement devised by Thorsen and Berlincourt[9], and a vacuum system connected to the inner Dewar allows accurate temperature control down to 1·2°K. The balance coils are connected in series opposition to the detection coils to reduce the pickup of the modulation signal, and the detection coil is tuned for parallel resonance at the second harmonic frequency. A 500 Hz modulation signal was used, phase sensitive detection was at the second harmonic, and the analog signal F.M. recorded on magnetic tape. A record of the changing d.c. magnetic field was obtained by measuring the voltage drop across a small resistor in series with the superconducting magnet (Westinghouse 50 kG).

The analog data were converted to digital form suitable for direct read into an IBM 7094 computer by means of a Digital Equipment Corporation 'PDP-4' system. This digitization system was used because of its availability, and at present, data is being digitized in real time using a Nuclear Data 160 system, thereby avoiding the need for the intermediate analog recording.

The tin samples used for this work were cut by acid erosion from a single crystal bar and oriented by standard Laue X-ray techniques to within 1° of the desired orientation.

Numerical Fourier analysis of DHVA data has been recently reported by several authors [10-12]. The numerical techniques used in this work differ considerably from what has been reported and therefore a more detailed discussion of the numerical methods has been included in the form of an Appendix. Briefly, the experimental data, sampled at equal intervals of the independent variable, $(1/B_0)$, is used to calculate an autocorrelation function and then the Fourier transform of the autocorrelation function is calculated to determine the frequency spectrum of the original data. Proceeding by initially calculating the autocorrelation function has several distinct advantages: (1) it allows an improvement in the effective signal-to-noise ratio of the experimental apparatus; (2) provides a convenient means of minimizing the distortions in the final frequency spectrum due to the finite length of the experimental record; and (3) allows a considerable reduction in computer time usage. These points and the detailed interpretation of the final frequency spectrum are discussed in the Appendix.

DISCUSSION OF RESULTS

The de Haas-van Alphen signal obtained from a modulated field magnetometer with detection at the second harmonic frequency is [8, 13],

$$
\begin{aligned}
V_{\mathrm{DHVA}} &\propto \sum_i J_2(\alpha_i) M_i(B_0) \sin(2\pi F_i/B_0 + \phi_i) \\
&= \sum_i a_i(B_0) \sin(2\pi F_i/B_0 + \phi_i) \qquad (1)
\end{aligned}
$$

$J_2(\alpha_i)$ is the second order Bessel function of argument, $\alpha_i = 2\pi F_i B_m / B_0^2$, with B_m being the size of the modulating field and B_0 the large external magnetic field. $M_i(B_0)$ is the amplitude of the oscillating magnetization produced by the sample, and is a slowly varying function of B_0.

A low modulation amplitude, $B_m = 2.$G, was used here to accentuate the higher frequency DHVA oscillations. With analog signal processing techniques the amplitude of the modulating field is chosen to preferentially select or reject specific oscillations [8], while with numerical analysis (as used in these experiments) it is desirable to select a value of B_m which will allow the various oscillations to contribute to the data with near equal amplitudes as then a single experimental record will furnish all the desired information.

Figure 1(a) illustrates an experimental DHVA record and the frequency of 'power' spectrum of this specific record is illustrated in Figs. 1(b) and 1(c). The numerically calculated have been connected with straight lines to produce the envelope indicated in Figs.

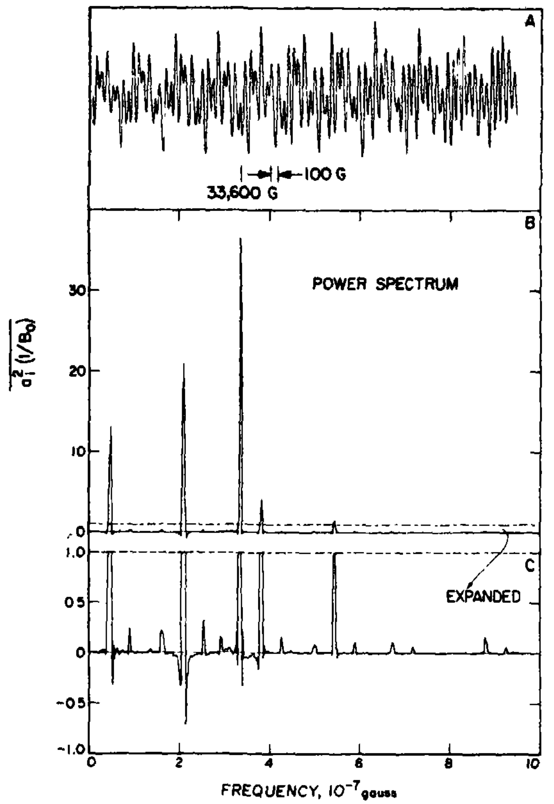

Fig. 1. (a) de Haas-van Alphen data for tin taken with B_0 parallel to the (100) axis at 1·93°K between 32 and 35·4 kG. (b) and (c) power spectrum of tin data in (a).

1(b) and 1(c), and the height of each peak is proportional to the average of the intensity, $a_i(1/B_0)$, of that particular frequency in the experimental record. The negative values in the power spectrum located near the base of each large peak are distortions due to the finite length of the experimental record and do not represent either signal or noise. The importance of making some efforts to minimize these distortions in the frequency spectra (as discussed in the Appendix) caused by the finite length of the data record can be appreciated here as the aberrations would have been an order of magnitude greater otherwise, and it would have been difficult, it not impossible, to observe the low intensity oscillations near in frequency to the most intense ones. The frequency resolution in Figs. 1(b) and 1(c) allow separation of frequencies differing by approximately 10^6 G, which is more than sufficient for the data presented here. As the frequency resolution is determined by the length of the data record, one could obtain higher resolution simply by extending the experimental record beyond that shown in Fig. 1(a).

It should also be pointed out that the large number of low intensity oscillations visible in the expanded view of the low intensity part of the power spectrum, Fig. 1(c), are not artifacts of the numerical analysis, but are representative of the actual data. The ability of the numerical techniques to allow observation of weak oscillations in the presence of strong ones is clearly demonstrated here as there are over four orders of magnitude difference between the strong and weak oscillations in this spectrum.

These frequencies are more clearly indicated in Fig. 2 which is a frequency spectrum of data taken at a somewhat lower temperature, 1·22°K compared to 1·93°K for Fig. 1.

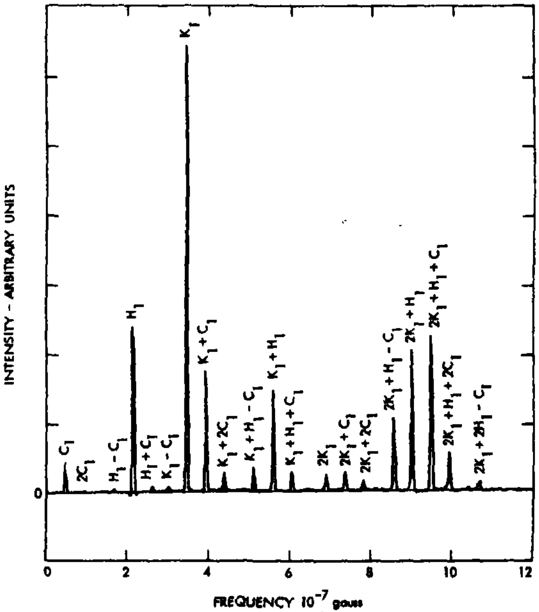

Fig. 2. Power spectrum of DHVA data for tin taken at 1·22°K with the magnetic field between 36·0 and 32·0 kG and parallel to the (100) crystallographic axis.

Only the three oscillations labeled C_1, H_1, and K_1 in Fig. 2 are fundamental as the frequencies of all other oscillations present in Figs. 1 and 2 are linear combinations of the frequencies of these three osicllations. This is indicated in Fig. 2 by the labels given the more intense sum and difference frequencies. The physical phenomena responsible for the generation of such a large number of combinational frequencies is presently not fully understood. It appears to be operative only when the magnetic field is orientated within several degrees of the [100] crystallographic axis in tin as the generation of such combinational frequencies was not observed at other orientations although rotation studies were made in (100), (001), (110), and (011) symmetry planes.

Previous publications of the DHVA effect in tin have not reported observing such excessive generation of combinational frequencies. However, the work of both Gold and Priestley[3] and Stafleu and de Vroomen[2] reported frequencies above the K_1 oscillation with the magnetic field orientated along the [100] symmetry axis in tin. These frequencies can be identified (within the accuracy reported) with the most intense of the sum and difference frequencies in Fig. 2, although these authors treated such frequencies as independent oscillations. Craven and Stark [1] in their more precise measurements reported no independent frequencies above the k_1 oscillation with the field along the [100] axis. They stated only that they saw some harmonic and mixing frequencies generally in their data at various orientations. Our results show an extremely complex spectrum made up of multiple harmonics and linear combinations of the three fundamental oscillations (greater than sixth order) where the intensity of the harmonic and combinational frequency oscillations are comparable to the intensity of the fundamental oscillations.

Presently, additional work is in progress to characterize the generation of these combinational frequencies of such large amplitude in terms of possible mechanisms such as the Schoenberg-B-H effect[14], magnetic breakdown, nonlinear interactions through skin-depth modulation or through the de Haas–Shubnikov effect, etc. Because of the complexity of the field, temperature, and orientation dependence of these oscillations, further discussion of this phenomena will be delayed until publication of that work[15].

The temperature, T, dependence of the amplitude of the DHVA oscillations, M_t, is [13],

$$\frac{M_t}{T} \infty \left[\sin h \frac{\pi^2 KT}{\beta H} \frac{m^*}{m}\right]^{-1} \sim e - \left[\frac{\pi^2 KT}{\beta H}\left(\frac{m^*}{m}\right)\right],$$

$$\beta = \text{Bohr magneton} \quad (2)$$

and thus, the slope of a plot of $\ln(M_t/T)$ vs. T can be used to determine the effective mass, m^*/m, of those parts of the Fermi surface contributing to the DHVA effect.

The Fermi surface of tin is complex and numerous oscillations are observed simultaneously with similar frequencies. This makes determining the amplitude of the separate oscillations difficult using analog signal processing techniques and thus although two detailed investigations of the band structure of tin using the DHVA effect have been made with the more sensitive field modulation techniques[1, 2] no attempt was made to measure the effective masses. The numerical technique described in this work is well suited for sorting out the amplitude of the various oscillations and has been used to determine the effective mass of those sections of the Fermi surface contributing to the DHVA effect along two symmetry axes.

Figure 3 is such a plot for the K_1 oscillation [15] in tin with the magnetic field parallel to the [100] axis, where values for the amplitudes have been obtained from the power spectrum as discussed in the Appendix. The standard deviation of the effective mass, calculated from the slope of the four least square fitted lines in Fig. 4 is 0·005 (units of m^*/m), and indicates the consistency of the data obtained with the numerical techniques.

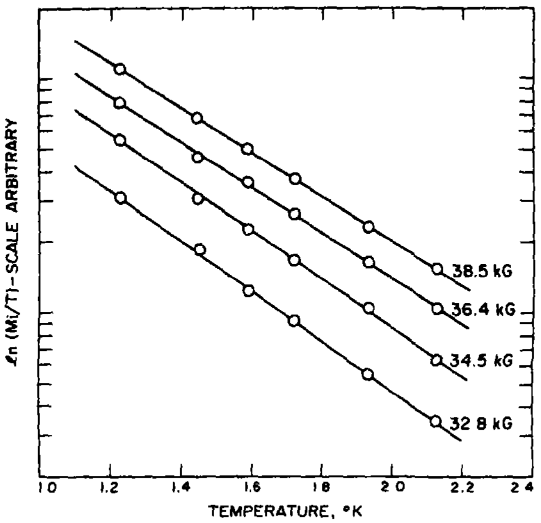

Fig. 3. Plot to determine effective mass of K_1 oscillation [18] in white tin. The field values with each line indicate the mean field around which Fourier transforms were taken for the points on that line. The four sets of data have been shifted vertically for clarity of presentation.

The effective mass values obtained from such plots are presented in Table 1 along with previously reported values[17]. The latter are primarily those taken from the earlier pulsed field studies of Gold and Priestley[3]. Somewhat more conservative error estimates have been placed on the values in Table 1 than indicated by standard deviations. This was done to allow for possible systematic errors particularly for those values obtained along the [001] axis where data was only taken at three temperatures.

The difference between the effective mass values obtained in this work with previously reported values, as indicated in Table 1, differs significantly and consistently only for those values reported with the magnetic field orientated in the [100] direction. It is precisely here that the intense harmonic and combinational frequencies were noted. Previous investigations[14, 17, 18] have indicated that plots such as Fig. 3 may show nonlinearities when a second harmonic, sum or difference frequency is present; therefore, considerable effort was expended to determine if that was the case here where an array of such anomalous combinational frequencies are observed. Data taken in a minimum of four different field ranges and at a minimum of six different temperatures was analyzed for each oscillation without detecting any abnormalities from that expected from equation (3). All lines were linear over the whole temperature range, 1·2°–2·2°K, and the effective mass values calculated for the data taken in the different 1·2°–2·2°K, and the effective mass values calculated for the data taken in the different field ranges agreed excellently. Thus, it does not appear as the difference between current and previously reported values can be accounted for, as has been suggested in the case of Silver[17], due to deviations from

Table 1. *Effective mass values for tin*

Orientation of sample	Oscillation[a]	Previously determined m^*/m[b]		m^*/m Determined in this work[d]
(100)	C	0·26	0·22[c]	0·31 ± 0·01
	K_1	0·50		0·56 ± 0·01
	H_1	0·45		0·55 ± 0·01
(001)	B	0·15		0·16 ± 0·02
	E	0·51		0·51 ± 0·03
	F_1	0·64		0·57 ± 0·03

[a] Nomenclature of [2].

[b] Values from [3] unless otherwise noted.

[c] From [5].

[d] The inaccuracy in approximating the sinh in equation (3) as an exponential was taken into account in determining the m^*/m for the smallest m^*/m's.

temperature dependence of the amplitudes of the oscillations from that predicted by equation (3).

SUMMARY

Digital handling facilities have been combined with a low-frequency field modulation differential magnetometer to allow numerical Fourier analysis of data obtained in DHVA experiments. This system has been applied to a reexamination of the DHVA in white tin and resulted in the discovery and characterization of a phenomena responsible for the generation of oscillations with anomalously high harmonics and combinational frequencies (greater than sixth order). The numerical analysis techniques are well suited for sorting out the frequencies and amplitudes of numerous superimposed oscillations as occur in tin and have been used to evaluate the effective mass of several sections of the Fermi surface contributing to the DHVA effect in tin along two symmetry axes. Particular emphasis was placed on the discrepancy between current values and previously reported effective mass values with the magnetic field orientated parallel to the [100] crystallographic axis.

Acknowledgements—We wish to thank Edwin Olli for technical assistance in many phases of this work and R. W. Iverson, F. W. Hafner, and J. R. Schoeni for informative discussions and aid in establishing the techniques for conversion of the anolog data to digital form.

REFERENCES

1. CRAVEN J. E. and STARK R. W., *Phys. Rev.* **168**, 849 (1967), and the first 29 references therein.
2. STAFLEU M. D. and De VROOMEN A. R., *Phys. Lett.* **23**, 179 (1966); *Phys. Status Solidi* **23**, 675 (1967).
3. GOLD A. V and PREISTLEY M. G., *Phil. Mag.* **5**, 1089 (1960).
4. VERKIN, LAZAREV and RUDENKO, *Dokl. Akad. Nauk. USSR* **69**, 773 (1949); *J. exp. theor. Phys. USSR* **20**, 995 (1950).
5. BERLINCOURT T. G., *Phys. Rev.* **88**, 242 (1952).
6. CROFT G. T., LOVE W. F. and NIX F. C., *Phys. Rev.* **95**, 1403 (1954).
7. SCHOENBERG D., *Nature* **164**, 225 (1949); *Phil. Trans.* **A245**, 1 (1952).
8. WILLIAMSON S. J., FONER S. and SMITH R. A., *Phys. Rev.* **136**, A1065 (1964).
9. THORSEN A. C. and BERLINCOURT T. G., *Rev. Scient. Instrum.* **34**, 435 (1963).
10. GRAEBNER J. E. and MARCUS J. A., *Phys. Rev.* **175**, 659 (1968).
11. GIRVAN R. F., GOLD A. V. and PHILLIPS R. A., *J. Phys. Chem. Solids* **29**, 1485 (1968).
12. SCHOENBERG D. and TEMPLETON I. M., *Can. J. Phys.* **46**, 1925 (1968).
13. LIFSHITZ I. M. and KOSEVICH A. M., *Soviet Phys. JETP* **2**, 636 (1956).
14. SCHOENBERG D., *Can. J. Phys.* **46**, 1915 (1968) and references therein.
15. VAUGHAN R. W. and ELLEMAN D. D., To be published.
16. Nomenclature of [2].
17. A portion of these results were presented at an APS Meeting, *Bull. Am. Phys. Soc.* **13**, 1454 (1968).
18. SCHOENBERG D., *Phil. Trans. Roy. Soc.* (Lond.) **A255**, 85 (1962).
19. JOSEPH A. S. and THORSEN A. C., *Phys. Rev.* **138**, A1159 (1965).
20. BLACKMAN R. B. and TUKEY J. W., *The Measurement of Power Spectra.* Dover Publications, New York (1958).
21. LEE Y. W., *Statistical Theory of Communication.* Wiley, New York (1960).
22. BENDAT J. S. and PIERSOL A. G., *Measurement and Analysis of Random Data.* Wiley, New York (1966).
23. ROSENBLATT M. (Editor), *Time Series Analysis.* Wiley, New York (1963).
24. McDONALD D. G., *Bull. Am. Phys. Soc.* **10**, 605 (1965).
25. COOLEY J. W. and TUKEY J. W., *Mathematics of Computation* **19**, 297 (1965).
26. STOCKHAM T. G., *AFIPS Conference Proceedings, Spring Joint Computer Conference*, Vol. 28, p. 229. Spartan Books, Washington, D.C. (1966).
27. GENTLEMAN W. M. and SANDE G., *AFIPS Conference Proceedings, Fall Joint Computer Conference*, Vol. 29, p. 563. Spartan Books, Washington, D.C. (1966).

APPENDIX

Details of numerical calculations

The numerical Fourier analysis technique used in this work has been discussed in the literature[20–24] particularly under the title, 'power Spectrum Analysis'. It consists of initially calculating an autocorrelation function and then taking its Fourier transform rather than directly Fourier transforming the original data. Equation (Ia) defines the autocorrelation function, while equation (Ib) gives the approximate function which can be determined from a finite experimental record (G = length of experimental record).

$$L(g) = \lim_{G\to\infty} \frac{1}{G} \int_{-G/2}^{G/2} x(\gamma+g/2)x(\gamma-g/2)\mathrm{d}\gamma \qquad \text{(Ia)}$$

$$= \frac{1}{G-|g|} \int_{-1/2(G-|g|)}^{1/2(G-|g|)} x(\gamma+g/2)x(\gamma-g/2)\mathrm{d}\gamma \qquad \text{(Ib)}$$

The autocorrelation function contains all the frequency and amplitude information in the original data and, additionally, is symmetric in the independent variable, γ. Thus, the calculation of the Fourier transform of the autocorrelation function reduces to the determination of a simpler cosine transform. This, together with the fact that g_m (the maximum difference in γ for which the autocorrelation function is calculated is normally considerably less than G results in substantial savings in computer time as there are less terms to be transformed. Mention should also be made here of the fast Fourier transform algorithms[25–27] which are available to further reduce computer time usage.

The intermediate calculation of the autocorrelation function provides a means of improving the signal-to-noise ratio in the final frequency spectrum and for minimizing distortions of the frequency spectrum which are due to the finite length of data record available.

Equation (Ib) is only an estimate of the true autocorrelation function, and it is by improving this estimate that one improves the final power spectrum. In particular, an effective increase in the signal-to-noise ratio can be obtained by effectively averaging out the noise power. This can be done by increasing the range of integration over the independent variable, γ, (increasing the field range), or by ensemble averaging; i.e. by obtaining more than one independent experimental record, calculating the estimated autocorrelation function for each record, and then averaging these for each value of g. This point is discussed quantitatively below.

The best estimate of the autocorrelation function obtainable is, however, undefined for g greater than g_m, and it is not possible to calculate its true Fourier (cosine) transform as one cannot integrate above g_m. One can modify the estimated lag-product function,

$$\{L'(g)\} = W(g)\{L(g)\} \qquad \text{(II)}$$

$\{L'(g)\}$ is the modified lag-product function and $W(g)$ is a function having $W(0) = 1$ and $W(g) = 0$ for $g > g_m$. Thus, $\{L'(g)\}$ is defined for all values of (g) and has a definite Fourier transform, $\{P'(f)\}$. It can be shown[18] that

$$\{P'(f_1)\} = \int_0^\infty [Q(f_1-f)+Q(f_1+f)]P(f)\mathrm{d}f \qquad \text{(III)}$$

where $Q(f)$ is the Fourier transform of $W(g)$ and $P(f)$ is the desired but indeterminate Fourier transform of $\{L(g)\}$. The integral is a modified convolution integral and allows interpretation of $\{P'(f)\}$ as an average-over-frequency estimate of $P(f)$ as seen through the scanning function, $Q(f)$. $\{P'(f)\}$ is thus, an average of $P(f)$ over frequencies near (f) weighed according to $Q(f)$, and the frequency resolution with which $\{P'(f)\}$ approximates $P(f)$ depends upon choosing $W(g)$ such that its Fourier transform, $Q(f)$, will be concentrated near $f = 0$. As of necessity, however, $W(g) = 0$ for $g > g_m$ and this forces a finite width on $Q(f)$ proportional to $1/g_m$ whatever the form of $W(g)$ for $g < g_m$. The greater the frequency resolution required of the analysis, therefore, the greater must be the range, g_m, over which the lag-product function is calculated. A proper choice of $W(g)$ for $g < g_m$ is important for minimizing distortions in the spectrum. Fourier transforming truncked sinusoidal functions, for instance, results in the occurance of large subsidiary peaks or sidebands in the final frequency spectrum, but a proper choice of $W(g)$ can reduce these by an order of magnitude and this is essential if one is to resolve weak oscillations in the presence of much stronger ones. The $W(g)$ used in this work goes under the name 'Hanning' and is:

$$W_H(g) = \tfrac{1}{2}\left(1+\cos\frac{\pi g}{g_m}\right), \quad |g| < g_m \qquad \text{(IVa)}$$

$$= 0 \qquad |g| > g_m \qquad \text{(IVb)}$$

For further discussion of this aspect, reference is made to the Literature[20–22].

So far the data available have been discussed as if it were of a continuous nature, but the analysis is actually performed by sampling the continuous DHVA data at equal intervals of the independent variable, $\gamma = 1/B_0$, and performing the analysis on a digital computer. This presents no additional conceptual difficulty, but some care has to be taken in choosing the interval, $\Delta\gamma$, at which the continuous data is to be sampled. If the data contain frequencies above f_c, $f_c = 1(2\,\Delta\gamma)$, these will be 'folded back' and appear at some anomalous point in the power spectrum. This phenomena, known as 'frequency aliasing' [20–22], makes it necessary to adjust $\Delta\gamma$ so no frequency which might contribute significantly to the spectrum is above f_c.

In practice, both the analog DHVA signal and a voltage proportional to the external magnetic field are initially samples at equal intervals of time. These points are taken close enough together to allow extrapolation between them to obtain the desired points equispaced in the inverse magnetic field, withough introducing errors due to extrapolation. The autocorrelation function is them calculated at the chosen intervals and a finite cosine series transformation made to obtain the final frequency spectrum. As the final power spectrum is an average of the true spectrum through a scanning function, $Q(f)$, of finite width, it is only necessary to calculate the cosine transformation at intervals of frequency of the same order as the width of the scanning function. The final frequency of 'power' spectrum has been calculated at intervals of $1/2\Delta\gamma$ in this work. The Hanning $Q(f)$ is approximately twice as wide as this frequency interval and thus neighboring values calculated in the frequency spectrum are averaged in some sense by the scanning function, while all nonadjacent values are essentially independent.

The final power spectrum is a superposition of both signal and noise frequency spectra. Sharp spikes corresponding to the DHVA frequencies together with fluctuations in the noise are superimposed on a smoothly varying background noise power spectrum. For discriminating between signal and noise the significant measure is the size of the fluctuations in the noise compared to the heights of the signal spikes. For the case where the noise can be approximated as guassian the size of the noise fluctuations can be estimated[20],

$$\sigma(f) = \left(\sqrt{\frac{g_m}{1\cdot 3\,G}}\right)\overline{P_n(f)} \qquad \text{(V)}$$

where $\sigma(f)$ is the standard deviation of the measurement of the noise power and $P_n(f)$ is the ensemble average of the noise power at frequency, f. The ratio, g_m/G is thus seen as the factor which determines how well fluctuations in the power spectrum due to noise are eliminated. (In cases where more than one experimental record is used to calculate the lag-product function, G represents the 'total effective length' of the record[20].

The height of the signal spike in the final power spectrum due to a sinusoidal function of amplitude a_i is:

$$\{P'(F_i)\} = \frac{a_i^2}{2} g_m \qquad \text{(VI)}$$

Thus, the signal to noise ratio for such a signal in the presence of guassian noise is:

$$\frac{\{P'(F_i)\}}{\sigma(f_i)} = \frac{\frac{a_i^2}{2} g_m}{\left(\sqrt{\frac{g_m}{1\cdot 3\, G}}\right)\overline{P_n(f_i)}} \propto \sqrt{g_m G} \qquad \text{(VII)}$$

and is seen to increase with both G and g_m.

The increase in signal to noise ratio due to increased frequency resolution (i.e. increased g_m), will apply up to the point where the frequency resolution of the analysis approaches the 'experimental width' of the signal, while that due to increased length of record, G, is theoretically unlimited. The actual increase in signal-to-noise ratio available from this technique is, thus, controlled by the amount of effort one chooses to spend in data collection and analysis.

The DHVA signal obtained from a modulated field magnetometer with detection at the second harmonic frequency is expressed in equation 2. Thus, the DHVA signal is seen to differ from a simple sum of sinusoidal terms only in that the coefficients of the sinusoidal terms, $a_i(\gamma)$, are not constants, but are functions of the independent variable, $\gamma \sim 1/B_0$. This presents some complications to interpretation of the intensity of the oscillations as observed from the frequency spectrum, but as long as the $a_i(\gamma)$ are smoothly varying functions which do not change greatly over the data record the power spectrum still lends itself to a simple interpretation. One can obtain a relationship between the peak height in the power spectrum and the varying amplitude of the corresponding oscillatory components. Using the definition of the lag-product function from equation (Ib) and taking into consideration the field dependency of the a_i's one obtains:

$$\{L(g)\} \sim \sum_i \left[\frac{1}{2(G-|g|)} \int_{-1/2(G-|g|)}^{1/2(G-|g|)} a_i(\gamma+g/2)\,a_i(\gamma-g/2)\,d\gamma\right] \cos 2\pi F_i g \qquad \text{(VIII)}$$
$$= \sum_i A_i(G, g) \cos 2\pi F_i g$$

Using the Hanning form of $W(b)$ and the fact that the even character of $\{L(g)\}$ reduces its Fourier transform to a cosine transformation, one obtains,

$$\{P'(F_i)\} = \int_0^{g_m} A_i(G, g)\left(1+\cos\frac{\pi g}{g_m}\right) dg \qquad \text{(IX)}$$

for the height of the peak in the power spectrum.

The relationship can, thus, be calculated for any particular functional dependency of the amplitude on field. To take a simple example, and one which suffices for the results presented in this paper, one can approximate the field dependency as linear,

$$a_i = a_{0i} + a_{1i}\gamma \qquad \text{(X)}$$

and in this case

$$\{P'(f_i)\} = a_i^2(\gamma) g_m \left[1 - \frac{\Delta a_i}{\overline{a_i^2(\gamma)}} \frac{1}{12} \left\{\frac{g_m}{G}\left(1-\frac{4}{\pi^2}\right) - \left(\frac{g_m}{G}\right)^2 \left(\frac{2}{3}-\frac{4}{\pi^2}\right)\right\}\right] \qquad \text{(XI)}$$

where $a_i^2(\gamma)$ is the average value of $a_i^2(\gamma)$ over the record, $[-G/2, G/2]$ and Δa_i is the total change in the amplitude over the record. Thus, when $g_m/G < \frac{1}{2}$ (the usual case) even though the amplitude changes by a factor of two over the record one can replace the a_i^2 in equation (VI) by $\overline{a_i^2(\gamma)}$ with an error of less than 1 per cent. For the determination of quantities such as the effective mass from DHVA oscillations, as in this work, this error tends to cancel since its effect is to shift all points nearly equal amounts vertically on plots such as Fig. 3, which does not affect the slope of the line.

J. Phys. Chem. Solids Pergamon Press 1970. Vol. 31, pp. 125–130. Printed in Great Britain.

SOME ASPECTS OF THE COOPERATIVE JAHN–TELLER EFFECT IN SPINEL AND PEROVSKITE SYSTEMS

PAVEL NOVÁK
Institute of Solid State Physics, Prague 6, Czechoslovakia

(*Received* 18 *February* 1969)

Abstract—Theory of the pair interactions between the octahedrally co-ordinated E_g Jahn–Teller ions is applied to the case of the cooperative Jahn–Teller effect. The close connection between the topology of Jahn–Teller ions and the character of resultant deformations is illustrated for a spinel and perovskite lattices. Linear approximation is used through the paper (anharmonicity of the crystal lattice neglected) and only the interactions between nearest Jahn–Teller ions are taken into account.

1. INTRODUCTION

IN A RECENT paper the present author has studied the interaction between the isolated pair of the octahedrally co-ordinated E_g Jahn–Teller ions[1]. It is natural to apply the results of this study to an experimentally more accessible problem of the cooperative Jahn–Teller effect.

First, the cluster of Jahn–Teller ions, located in an infinite crystal will be considered. The results obtained may contribute to the understanding of the effects connected with the supposed existence of Jahn–Teller ion clusters[2]. Later, taking into account the effect of the free surface, conclusions will be made concerning the character of the equilibrium configurations of the systems exhibiting the cooperative effect. It will be shown that the different character of the cooperative effects in the spinel and perovskite lattices is a natural consequence of the topology of Jahn–Teller ions (Fig. 1) in these systems.

With the use of the notation of paper[1] it can be immediately deduced from Fig. 1 that the configurations of the nearest octahedrally co-ordinated ions are of the type $A(1)$ in a spinel structure ($B(1)$ configurations are not present in this structure), while they are of the type $B(1)$ in a perovskite structure ($A(1)$ configurations not present).

It was shown in [1] that the interaction energy of a $A(1)$ or $B(1)$-type pair of Jahn–Teller ions may be written in a simple form:

$$\epsilon_i = J_2 \sin\varphi_a \sin\varphi_b + J_3 \cos\varphi_a \cos\varphi_b. \qquad (1)$$

The angles φ_a, φ_b determine the configuration of the octahedron of the respective Jahn–Teller ion. For the quantities J_2, J_3 following inequalities may be deduced[1]:

$$J_2, J_3 < 0 \text{ for } A(1) \text{ configurations} \qquad (2)$$

$$J_2 < 0, J_3 > 0 \; |J_2| \ll J_3 \text{ for } B(1) \text{ configurations.} \qquad (3)$$

The conditions under which (1) is valid are summarized in [1]. One of these conditions, neglection of the induced interaction, will be considered in greater detail in Appendix A. In the following analysis we shall suppose that it is sufficient to take into account only the interaction of those Jahn–Teller ions, which are the nearest neighbours in the sublattice of the octahedrally coordinated ions. In addition to the pair interaction energy, the Jahn–Teller anisotropy energy which may be for each Jahn–Teller ion approximated by the term

$$\epsilon_{an} = K \cos 3\varphi \qquad (4)$$

will be considered in the following analysis.

2. CLUSTERS

For the characterization of the cluster in which the number of Jahn–Teller ions is N,

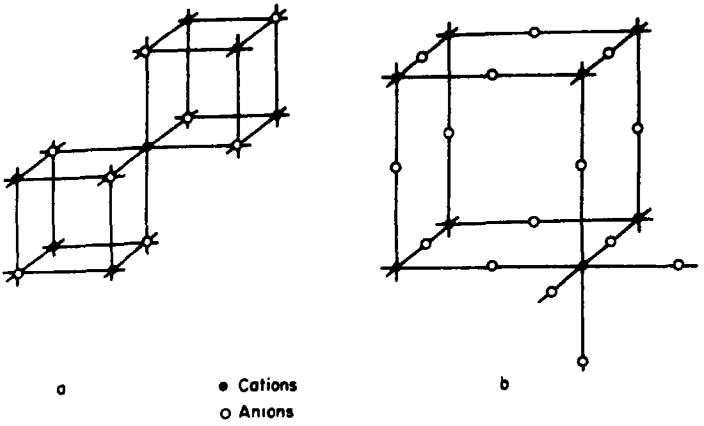

Fig. 1. Arrangement of the octahedrally co-ordinated sites in the spinel (a) and perovskite (b) structures.

we shall introduce $3N$ occupation numbers z_{xj}, z_{yj}, z_{zj} ($j = 1, 2, \dots N$). z_{xj} equals to the number of nearest Jahn–Teller neighbours of the j-th Jahn–Teller ion, where these neighbours lie in the (yz) plane for the cluster in a spinel structure or on the x axis for the cluster in a perovskite structure. Analogously are defined z_{yj}, z_{zj}. In spinel as well as in perovskite structure $z_{\alpha j}$ can acquire three values, $z_{\alpha j} = 0; 1; 2$.

The total interaction energy of the cluster may be evaluated by summing the pair interaction potentials[1]. Taking into account that interchanging the coordinate axes is equivalent to the substitution $\varphi \rightarrow \varphi \pm 2\pi/3$ in (1), the total interaction energy can be written in the form:

$$\epsilon_{l} = \frac{1}{4} \sum_{j=1}^{N} \sum_{j'} z_{\alpha j} [(j_2 + j_3) \cos(\varphi_j - \varphi_{j'}) + (j_3 - j_2) \cos(\varphi_j + \varphi_{j'} + \omega_\alpha)] \tag{5}$$

where the second summation is only over the nearest neighbours of the j-th ion;

$$\omega_x = -\frac{2\pi}{3}, \quad \omega_y = \frac{2\pi}{3}, \quad \omega_z = 0.$$

It is difficult to minimise the energy[5] for a general distribution of Jahn–Teller ions. The present author discussed in his PhD thesis[3] various types (linear, planar) of the clusters. In the asymmetrical clusters the interaction energy per one bond may be greater than in the symmetrical one. However, the number of bonds between Jahn–Teller ions is raised for a symmetrical form of cluster. For this reason the symmetrical forms should be preferred (at least for large N).

A cluster will be called symmetrical, if for any j $z_{xj} = z_{yj} = z_{zj}$. If all octahedral sites shown on Fig. 1 are occupied by the Jahn–Teller ions, the groups illustrated are examples of a simple symmetrical cluster. If only symmetrical clusters are considered, it can be shown[3], that there are four configurations in which the necessary conditions are fulfilled for an extremum of the interaction energy. It is convenient to use the notation of the theory of magnetism (first used in similar problem by Kanamori[4], for the extremal configurations). Characteristic data for these configurations are summarized in Table 1. In Fig. 2 extremal configurations, corresponding to $\varphi_j = 0$, are shown for the simplest symmetrical cluster in a perovskite structure. It is to be noted, that since octahedrally coordinated sites in a spinel structure cannot be divided into two equivalent sublattices, only

Table 1. Extremal configurations of the symmetrical cluster. Ions j, j′ belong to different sublattices, $z = \frac{1}{2}\sum_{\alpha i j} z_{\alpha j}$ *is the number of bonds between Jahn–Teller ions*

Type	Ferromagnetic	Antiferromagnetic				
Notation in Fig. 2	*a*	*b*	*c*		*d*	
Extremal angles	$\varphi_j = \varphi$	$\varphi_j = \varphi$ $\varphi_j' = \varphi + \pi$	$\varphi_j = 0$ $\varphi_j' = \pi$	$\varphi_j = \frac{\pi}{2}$ $\varphi_j' = \frac{3}{2}\pi$	$\varphi_j = 0$ $\varphi_j' = \pi$	$\varphi_j = \frac{\pi}{2}$ $\varphi_j' = \frac{3}{2}\pi$
Interaction energy ϵ_i/z	$\frac{1}{2}(J_2+J_3)$	$-\frac{1}{2}(J_2+J_3)$	$-\frac{1}{2}(J_2-\frac{1}{3}J_3)$	$-\frac{1}{2}(J_3-\frac{1}{3}J_3)$	$\frac{1}{2}(J_2-\frac{1}{3}J_3)$	$\frac{1}{2}(J_3-\frac{1}{3}J_2)$

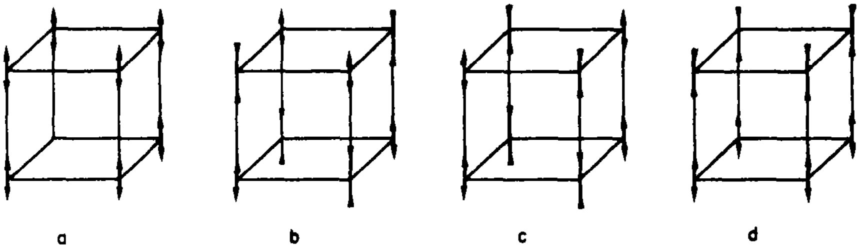

Fig. 2. Extremal configurations of the simplest symmetrical cluster in a perovskite structure pictured for $\varphi_j = 0$. Meaning of symbols: ↕ tetragonally elongated octahedron; tetragonally compressed octahedron.

the configurations *a* and *c* may be realized in this structure.

Taking into account the inequalities (2, 3), it follows from Table 1 that the lowest energy configurations of a cluster in a spinel structure correspond to the ferromagnetic case *a*, while for a perovskite structure the ground states correspond to the antiferromagnetic case *c* ($\varphi_j = \pi/2$). However, the energy difference between the configurations *c* ($\varphi_j = \pi/2$) and *b* is small compared with the total interaction energy.

For a spinel structure the anisotropy energy [4] can be taken into account in a simple way. The result gives three configurations (all octahedrons tetragonally distorted along one of the cubic axis), which give the maximum gain in anisotropy as well as in the interaction energy.

For antiferromagnetic configurations the anisotropy gives no contribution. However, the energy of the system can be lowered, if the angles φ_j, φ_j' are slightly changed. This situation (Fig. 3), is similar to the one described by Kanamori [4] and is analogous to the case of weak ferromagnetism.

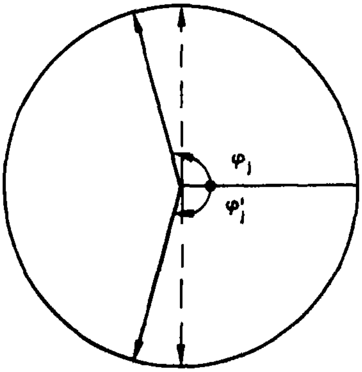

Fig. 3. Angles specifying the antiferromagnetic configuration before (dotted) and after the anisotropy is taken into account.

For configurations b and c ($\varphi_j = \pi/2$) the energy gain and the change of φ_j is given by the expressions:

$$\delta\varphi_j(b) = \frac{3}{4}\frac{K}{z(j_2+j_3)}\cdot\sin 3\varphi;$$

$$\delta\epsilon(b) = -\frac{9}{4}\cdot\frac{K^2}{z(j_2+j_3)}\cdot\sin^2 3\varphi;$$

$$\delta\varphi_j(c) = \frac{3}{4}\frac{K}{z(j_3-\frac{1}{3}j_2)};$$

$$\delta\epsilon(c) = -\frac{9}{4}\cdot\frac{K^2}{z(j_3-\frac{1}{3}j_2)}.$$

It is to be noted that the configuration b, which has $\varphi_j = \pi/2$ is stabilized by the anisotropy.

For extremely strong anisotropy the lowest state of a symmetrical cluster in a perovskite structure is shown in Fig. 4. Corresponding energy is given by the expression:

$$\epsilon = -\tfrac{1}{6}z(j_3-j_2) - N|K|.$$

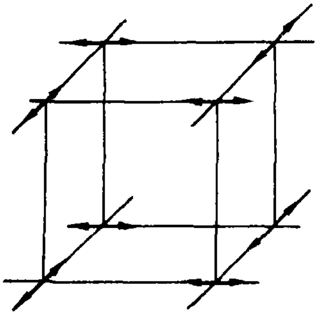

Fig. 4. The lowest energy configuration of a cluster in a perovskite structure in the case of strong anisotropy.

3. EFFECT OF A FREE SURFACE

It is well known that a free surface can have a profound effect in point defect problems[5] and it is, therefore, necessary to consider its role before going on to the discussion of the cooperative Jahn–Teller effect.

Let us consider a body in which the distribution of the Jahn–Teller ions is macroscopically homogeneous. In the case of antiferromagnetic ordering of Jahn–Teller distortions, there is no net force on the surface of the body, and it is therefore not necessary to take the surface into account. For the same reason the effect of the surface can be neglected in the case of uncorrelated distortions or clusters.

If the distortions are ferromagnetically ordered, the total displacement field can be formally represented as a sum of the displacement field in an infinite crystal and the displacement field, usually called the image field, which arises as a consequence of the existence of the free surface[5]. If the body considered has a cubic or spherical symmetry, it follows from the symmetry of the problem that the image part of the energy of the system does not depend on the angle φ, which specifies the ferromagnetic configuration. Furthermore, the image part of the energy is negative (see Appendix B), and will therefore lower the energy of the ferromagnetically ordered system.

4. COOPERATIVE JAHN-TELLER EFFECT

If the concentration of the Jahn–Teller ions in the crystal is high enough, long range ordering of Jahn–Teller distortions will appear. For the analysis of this cooperative effect the results of preceeding discussion of the symmetrical clusters will be used. It is an approximation to suppose that the crystal in which only part of the octahedrally co-ordinated sites is occupied by Jahn–Teller ions can be treated as a symmetrical cluster. With respect to the character of the pair interactions[1] it is probable, however, that the deviation from the symmetrical arrangement of Jahn–Teller ions should not cause any substantial changes in our results.

It follows from the discussions of symmetrical clusters and the effect of a free surface that the co-operative Jahn–Teller effect in a spinel structure will be connected with the tetragonal deformation of the crystal lattice. The temperature dependence of the deformation may be easily found using the molecular field approximation. The results are a classical analogy of the results obtained by Kanamori[4]. The deformation is a linear function of the concentration of the Jahn–Teller ions (Appendix B).

If the anisotropy is neglected, the energy of the system is invariant with respect to the change of the angle φ. From this invariance it follows that a continuous spectrum of low lying collective excitations will exist[6]. These excitations will be studied in a subsequent paper.

The anisotropy constant K could be in principle determined from the equilibrium configuration of a system under external stress.

Perovskite structures

Let us consider a system MnF_3 in which the arrangement of the octahedrally co-ordinated ions is the same as in the perovskite structure. Our theory is therefore applicable to this case. We expect that the antiferromagnetic configuration denoted as c ($\varphi = \pi/2$) in Table 1. will represent the ground state of this system. However, X-ray analysis at room temperature indicates the presence of the distorted antiferromagnetic configuration b, with $\varphi = \pi/2$[7, 4]. The source of this inconsistency may be sought, for instance in the neglection of higher order terms in the defect potential, or in the anharmonicity of the crystal lattice (the energy difference between the ground states of b and c ($\varphi_j = \pi/2$) configurations is small). However, one interesting explanation of this inconsistency might exist. As for ferromagnetic configuration low lying collective excitations also exist in the case b (assuming the anisotropy to be small). For this reason two configurations in consideration b and c ($\varphi_j = \pi/2$) have qualitatively different energy level scheme, the density of states in case b being greater than in case c ($\varphi_j = \pi/2$). corresponding difference in entropies may cause, the configuration b to be realized at finite temperature.

If the theory is slightly generalized to include the interactions between more distant Jahn–Teller ions, these interactions being small compared with the nearest neighbour interactions, the presence of various phases in the perovskite system $La_xCa_{1-x}MnO_3$ can be explained[8, 3].

It is to be noticed that a detailed theory for perovskite systems would be often complicated by the existence of the non Jahn–Teller distortions.

5. DISCUSSION

The main achievement of the theory presented in [1] and this paper can perhaps be seen in the clear demonstration of the connection between the topology of Jahn–Teller ions and the character of the resultant deformation. The 'exchange integrals' J_2 and J_3 can be calculated, as it was shown in [1], for given crystal lattice and therefore there is a direct connection between the one-ion and the cooperative Jahn–Teller effects. Another advantage of the presented theory is, that the weak and strong anisotropy cases can be treated in the same manner.

On the other hand, the theory suffers from a number of simplifications. One of these simplifications, which was not mentioned in [1], nor in the above analysis, is the neglection of the anharmonicity of the crystal lattice. This anharmonicity will cause a nonlinear dependence of the lattice constants on the concentration of Jahn–Teller ions.

Acknowledgement—The author would like to express his sincere thanks to Dr. S. Krupička for valuable discussions and his continuous interest during the course of this work.

REFERENCES

1. NOVÁK P., *J. Phys. Chem. Solids* **30**, 2357 (1969).
2. KRUPICKA, SIMSA Z., and SMETANA Z., *Czech. J. Phys.* **18B** 1016 (1968).
3. NOVÁK P., Thesis, Prague (1968).
4. KANAMORI J., *J. appl. Phys.* **3**, 79 (1956).
6. See for instance BROUT R., *Phase Transitions*, Chap. 1. Benjamin, New York (1965).
7. HEPHWORTH M. A. and JACK K. H., *Acta crystallogr.* **10**, 345 (1957).
8. WOLLAN E. O. and KOEHLER W. C., *Phys. Rev.* **100**, 545 (1955).
9. HARDY J. R., and BULLOUGH R., *Phil. Mag.* **16**, 405 (1967).
10. TOWNSEND J. R., *Acta Metall.* **13**, 325 (1965).

APPENDIX A

Effect of the induced interaction

Let us consider two Jahn–Teller ions a, b located in the lattice. If the interaction between ions a, b is switched off, the configurations of the octahedrons of these ions are characterized by the angles φ_a°, φ_b°. The expression (1) for the iteration energy is valid only if the change of these angles due to the ineraction is neglected. If we are interested only in the energetically lowest configuration of both ions, the contribution to the iteraction caused by changing φ_a°, φ_b° need not be considered, as both angles are allowed to change independently in the interval $\langle 0, 2\pi\rangle$, while the interaction energy is minimized. The same statement holds for the clusters. The only case in which this induced interaction may affect the configuration, is the strong anisotropy case in a perovskite structure (Fig. 4).

Another source of the induced interaction may be a nonlinear vibronic coupling. The one-ion effect of this coupling is included in the anisotropy energy, the corresponding part of the interaction energy may be determined using the expression given by Hardy and Bullough[9] for the induced interaction. The nonlinear vibronic coupling seems to have little influence on the interaction of an isolated pair of Jahn–Teller ions, but it can have a more profound effect in concentrated systems.

APPENDIX B

Elasticity treatment of the Jahn–Teller effect

The deformation of a crystal caused by one Jahn–Teller ion can be simulated by the effect of a point defect which is characterized by three orthogonal double forces. The force per unit volume can be written as:

$$\mathbf{F}_\varphi = \sin\varphi \,.\, \mathbf{F}_2 + \cos\varphi\,\mathbf{F}_3$$

$$\mathbf{F}_2 = -\frac{P}{2}\left(-\frac{\partial}{\partial x}\delta(\mathbf{r}), \frac{\partial}{\partial y}\delta(\mathbf{r}), 0\right);$$

$$\mathbf{F}_3 = \frac{P}{2\sqrt{3}}\left(\frac{\partial}{\partial x}\delta(\mathbf{r}), \frac{\partial}{\partial y}\delta(\mathbf{r}), -2\frac{\partial}{\partial z}\delta(\mathbf{r})\right).$$

Angle φ has analogous meaning as in the discrete theory, P is the strength of the Jahn–Teller force. A simple relation $P = \alpha R_0$ can be deduced, where α is the linear vibronic coupling constant, R_0 is the shortest cation–anion distance.

Let us consider an elastically isotropic sphere, in which the Jahn–Teller ions are uniformly distributed. If Jahn–Teller forces are ferromagnetically ordered, we can superpose the results given by Townsend[10] for defects, characterized by one double force. The parts of the strain tensor, which correspond to an infinite medium ($\mathbf{e}^\infty$) and to the effect of a free surface (e^{im}), may be expressed in the form:

$$e^\infty_{xx} = A\left(\frac{1}{2}\sin\varphi + \frac{1}{\sqrt{3}}\cdot\cos\varphi\right);$$

$$e^\infty_{yy} = A\left(-\frac{1}{2}\sin\varphi + \frac{1}{\sqrt{3}}\cos\varphi\right) e^\infty_{zz} = -\frac{A}{\sqrt{3}}\cos\varphi$$

$$e^{im} = A'e^\infty;\ A = Pn\cdot\frac{1}{\lambda+2\mu}\,\frac{8\mu+3\lambda}{15\mu}, A' = \frac{1}{2}\,\frac{14\mu+9\lambda}{8\mu+3\lambda}$$

n is the density of Jahn–Teller ions, μ and λ are the shear and Lame elastic constants for an isotropis media. The part of the energy density, which is caused by the presence of a free surface, can be written as:

$$\epsilon^{im} = -n^2P^2\frac{14\mu+9\lambda}{60\mu(\lambda+2\mu)}$$

ϵ^{im} is negative and does not depend on φ. Similar analysis can also be done for nonspherical samples.

J. Phys. Chem. Solids Pergamon Press 1970. Vol. 31, pp. 131–141. Printed in Great Britain.

LATTICE DYNAMICS OF SODIUM CHLORIDE AT ROOM TEMPERATURE*

R. E. SCHMUNK
Idaho Nuclear Corporation, Idaho Falls, Idaho 83401, U.S.A.
and
D. R. WINDER
Colorado State University, Ft. Collins, Colo. 80521, U.S.A.

(*Received* 8 *April* 1969; *in revised form* 24 *July* 1969)

Abstract—The phonon dispersion relation has been measured for sodium chloride at room temperature for waves propagating along the symmetry directions [00ζ], [ζζ0], and [ζζζ] by slow neutron inelastic scattering using the Materials Testing Reactor three axis spectrometer. These data are in reasonable agreement with the low temperature (80°K) data obtained by Almqvist *et al.* and with the X-ray scattering data of Buyers and Smith. The shell model has been fit to the present data using a non-linear least squares routine with the fourteen parameter version giving the best overall agreement when the fitting to the elastic constants is also included. In the text comparison is made with a seven parameter rigid-ion model along with eleven and fourteen parameter versions of the shell model. The fourteen parameter shell model has been applied in calculating a frequency distribution from which the Debye temperature was evaluated for comparison with thermodynamic data, and the combined density-of-states distribution was computed and compared with second order Raman scattering data, both with good agreement.

INTRODUCTION

DURING the past ten years there has been a considerable amount of research done on phonon spectra by the method of slow neutron scattering, and these investigations have encompassed most of the different types of binding that are encountered in solids. Ionic crystals are undoubtedly the best understood of the different types, and more specifically the shell model has been applied with considerable success to the alkali halides[1]. This model is expressed in terms of the long range Coulomb forces and the short range repulsive interactions in the solid and allows for the polarizability of the ions. Until the present measurements were undertaken it appears that sodium chloride had not been considered seriously for phonon studies, presumably because of the unfavorable neutron absorption cross section for chlorine (33·6 barn) and the low Debye temperature (320°K) for the solid. The specific interests in sodium chloride at this time are related to the fact that it is used for pressure calibration in the high pressure neutron diffraction[3] experiments at the Materials Testing Reactor (MTR) and also because of an interest in developing the experimental and computational techniques for use in studying other materials having the same crystal structure, such as uranium carbide. The phonon measurements are also expected to be helpful in evaluating the Debye–Waller factor for accurate intensity calibrations in the diffraction experiments.

In the present work we have made slow neutron inelastic scattering measurements in the (110) plane of NaCl using a three axis spectrometer installed at the MTR[3] to obtain phonon dispersion relation data for the symmetry directions [00ζ], [ζζ0] and [ζζζ]. These data have been compared with the low temperature dispersion relation data of Almqvist *et al.*[4] and also with the X-ray scattering data of Buyers and Smith[5] and were found to be in good agreement in both cases. A seven parameter rigid-ion model and several versions of the shell model have been fitted to the data. The eleven parameter shell model fits the neutron data satisfactorily, but fourteen parameters are necessary if the elastic constants are to be fitted in addition to the neutron data. Based on the results of fitting the fourteen parameter model to the data we have calculated the frequency distribution and a two phonon combined density-of-states distribution which includes sum and overtone frequencies, both distributions being evaluated by the extrapolation technique of Gilat and Dolling[6]. The frequency distribution has been used to calculate Θ_D which was compared with Θ_D derived from experimental specific heat data[7] and found to be in agreement in the neighborhood of room temperature. The combined density of states distribution has been compared with the second order Raman scattering data of Welsh *et al.*[8] and found to be in very good agreement.

---

*Work done under the auspices of the U.S. Atomic Energy Commission.

EXPERIMENTAL METHOD AND RESULTS

The fundamental basis for using slow neutron inelastic scattering to study the normal modes of vibration in a crystal has been discussed by a number of authors and will not be elaborated on here[9]. Experimental measurements were made on a NaCl single crystal using a triple axis spectrometer installed at the HT-1 south beam port of the MTR. The sample was a Harshaw crystal with purity 99·997 per cent and dimensions $3\frac{1}{2}\times 1\frac{1}{2}\times\frac{1}{2}$ in. in the form of a rectangular parallelepiped. All crystal surfaces were parallel to (002) planes. No special effort was made to measure the mosaic spread of the sample, but from the data obtained in orienting the sample it is estimated to be less than 3 min of arc.

The sample crystal was oriented so that the (110) mirror plane was parallel to the scattering (horizontal) plane of the experiment. In this configuration it was possible to experimentally investigate all phonon branches for the [001] and [111] directions of wave propagation and 4 of the 6 phonon branches for wave propagation along the [110] direction with only the transverse branches having their polarization normal to the scattering plane being excluded for the latter direction. The symmetry directions [001], [110] and [111] for which measurements have been made are also referred to as Δ, Σ, and Λ, respectively [10].

The spectrometer which was used in the experiment consists of two separate units: (1) a shielded monochromator facility which was used to obtain a diffracted monoenergetic beam for the experiment; and (2) a sample platform and energy analyzer unit which were mounted on a large diameter rotary table. Because of the lack of coupling between the two units all measurements were made using the same incident neutron energy of 54·2 meV. A beryllium crystal with a mosaic spread of 12 min (on the (0002) planes) served as monochromator giving a beam intensity at the sample position of 5×10^6 neutrons/cm^{2}sec and the (111) planes of an aluminum crystal were used for the analyzer. The sample orientation angle, scattering angle, analyzer arm angle and analyzer crystal angle were controlled by Slo-Syn stepping motors through worm gears which permitted angle changes in increments of 0·01° for the first three angles and in increments of 0·005° for the last angle. Beam collimators with a horizontal angular divergence of 30 min were positioned between monochromator and sample and between sample and analyzer crystals.

All data were obtained with the spectrometer operated in the constant Q mode using a preset monitor scaler to control the duration of the count on the analyzer arm for each spectrometer setting. This method requires changing the sample, scattering and analyzer angle settings for each energy that is observed in such a way that the momentum transfer remains constant. Angle settings for the constant Q runs were generated by a computer program. At the start of a run the spectrometer angles were set manually and then advanced automatically from one setting to the next after each counting period, using a drum programmer to introduce angle correction instructions to control circuits for stepping the angle drive motors.

The dynamic structure factor $g_j^2(\vec{q}, \vec{\tau})$ has not been evaluated for NaCl. Instead we have used the results of Woods *et al.*[1] for NaI as an approximation, with good results. The only difficulties encountered were in connection with the longitudinal optical modes which generally gave broad resonances of low intensity. Because of the presence of incoherent scattering from the sample which gave an energy dependent background to the scattering data, care was exercised in evaluating the data, and special background runs were taken to aid in this evaluation. Background data were obtained by taking constant Q scans in ω,k space as close as possible to the region in which a particular mode was investigated yet removed far enough that the polarization factor $(\vec{Q}\cdot\vec{\xi})$ ruled out the possibility of observing one phonon coherent scattering. For example, the transverse optical branch Δ_5 (TO) was mapped along a line in k-space given by $(3,3,1\text{-}\zeta)$ while a background scan for the same branch was obtained at the point (3·2, 3·2, 1) in k-space. With the background scans taken in this way the spectrometer angle settings closely approximated the settings used during the phonon scans, and the background data were subtracted directly to correct phonon data taken at small ζ and used as a guide in evaluating the background for measurements made at larger ζ. Figure 1 shows the data obtained in four separate phonon scans, each

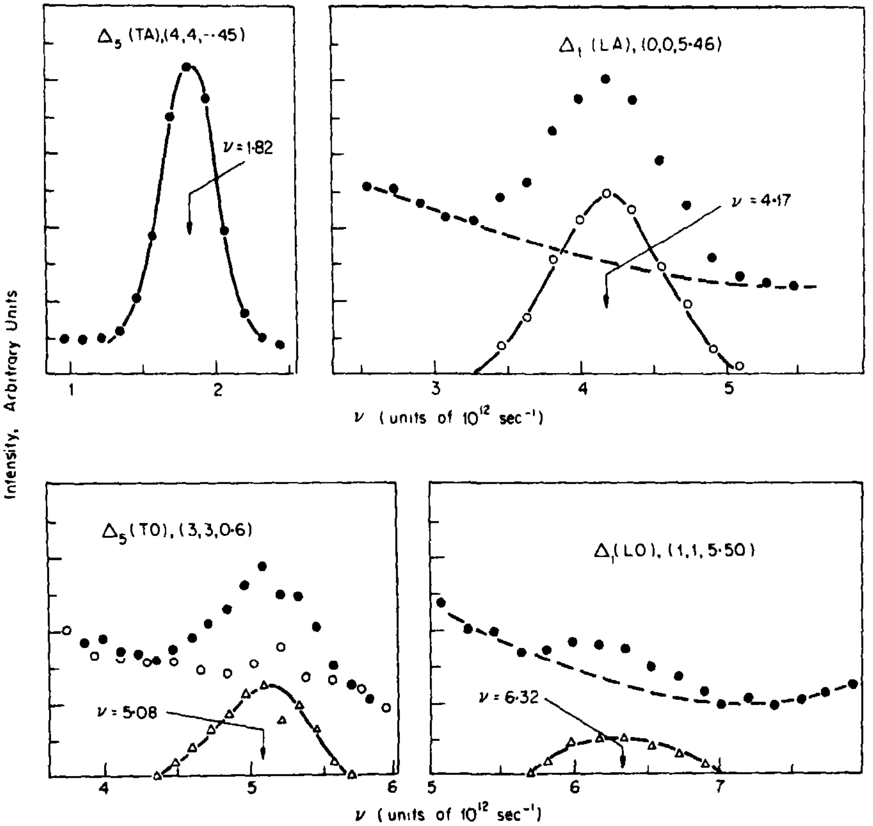

Fig. 1. Examples of neutron scattering data obtained in constant Q scans for the present experiment.

made in the constant Q mode. Generally speaking the transverse modes gave sharper peaks than the longitudinal modes, and in the case of the LO modes it was difficult to identify the resonance data from background in many of the scans. The Δ_1 (LO) mode in Fig. 1 is one of the better LO scans. Data from one of the background scans are included with the Δ_5 (TO) mode in the figure along with the results of subtracting the background.

The dispersion relation data are displayed in Fig. 2 for the three symmetry directions, the transverse modes as round points and the longitudinal modes as diamonds. Errors on the data points are generally in the range 2-3 per cent excepting the longitudinal optical modes for which the errors are larger. In Table 1 we have compiled a list of the various mode frequencies observed at points of high symmetry in the Brillouin zone. The frequencies listed in the table vary somewhat from the values first reported[11], the new values being due to a remeasurement and re-evaluation of many of the modes. The discrepancies were apparently due to poor initial alignment of the spectrometer as this was the first experiment undertaken with a three axis spectrometer at the MTR. A value has not been reported for the L(TO) mode because of strong interference from the L(TA) mode which made it difficult to evaluate. Also included in the table are the data of Almqvist *et al.*[4] for measurements at 80°K. The present data run 2-3 per cent lower in frequency than the 80°K data except for the modes Γ(LO), X(LA) and X(TA). The general trend of the room temperature data is in the direction one would expect, and considering the errors quoted the overall agreement is good, including the excepted modes.

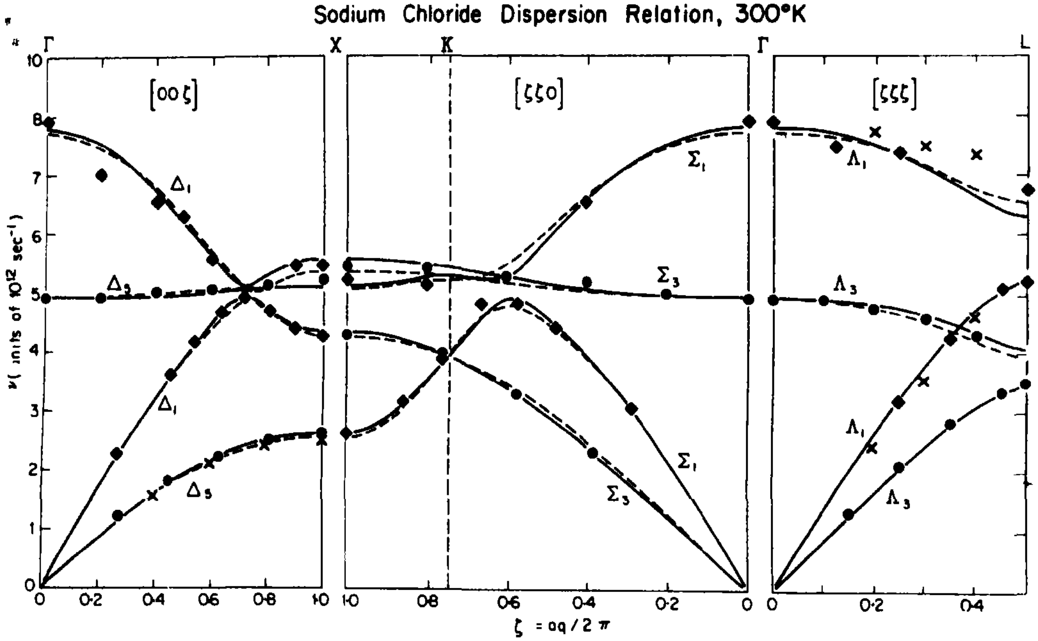

Fig. 2. Phonon dispersion relation for sodium chloride along the symmetry directions indicated in the figure. The solid (dashed) curves represent a fourteen (eleven) parameter shell model which was fit to the data.

Very good agreement is obtained comparing the Γ(TO) mode with the reported value of the infrared absorption frequency[12] of $4{\cdot}92 \times 10^{12}$ sec^{-1}. Further, the square of the

Table 1. Observed phonon frequencies for certain symmetry points compared with the low temperature data of Almqvist et al. [4]

Symmetry point	Mode	ν(units of 10^{12} sec^{-1}) This experiment, 300°K	Almqvist *et al.* 80°K
Γ	TO	4·90 ± 0·10	5·17 ± 0·03
	LO	7·85 ± 0·20	7·83 ± 0·06
X	LO	5·46 ± 0·12	5·79 ± 0·03
	TO	5·22 ± 0·10	5·41 ± 0·03
	LA	4·28 ± 0·08	4·23 ± 0·016
	TA	2·60 ± 0·07	2·63 ± 0·016
L	LO	6·77 ± 0·20	6·89 ± 0·06
	TO	—	4·28 ± 0·03
	LA	5·22 ± 0·10	5·36 ± 0·03
	TA	3·53 ± 0·08	3·63 ± 0·03

ratio of the Γ(LO) to Γ(TO) mode frequencies is 2·57 which compares very well with the ratio of the static to high frequency dielectric constants[12] $(\epsilon_0 \epsilon_\infty) = 2{\cdot}56$ indicating that the Lyddane-Sachs-Teller relation[13] $[\{\nu_{LO}/\nu_{TO}\} = \{\epsilon_0/\epsilon_\infty\}^{1/2}]$ is well satisfied.

The *x*'s displayed in Fig. 2 are the results of X-ray scattering measurements by Buyers and Smith[5]. Very good agreement is obtained for the TA[00ζ] branch while only fair agreement is observed for the [ζζζ] LA and LO branches.

MODELS

The data obtained in the present experiment have been compared with several lattice dynamics models. With one exception these models are variations of the dipole approximation or shell model, details of which have been discussed by a number of different authors. As applied here we refer specifically to the work by Cochran *et al.*[14] on lead telluride, the work by Cowley *et al.*[15] on sodium iodide and potassium bromide, and the theoretical paper by Cowley[16]. In the first two of these references additional parameters are introduced which are not generally included in other work while the third reference gives considerable detail for the matrices which appear in the dynamic equations.

The equations of motion for the shell model have been given by the above authors in matrix notation as:

$$\mathbf{m}\omega^2\mathbf{U} = (\mathbf{R} + \mathbf{ZCZ})\mathbf{U} + (\mathbf{T} + \mathbf{ZCY})\mathbf{W},$$

$$O = (\mathbf{T}^T + \mathbf{YCZ})\mathbf{U} + (\mathcal{S} + \mathbf{YCY})\mathbf{W},$$

$$\mathcal{S}_{\alpha\beta}(\kappa\kappa') = S_{\alpha\beta}(\kappa\kappa') + \delta_{\alpha\beta}\delta_{\kappa\kappa'}\{k_\kappa + (T_{\alpha\alpha}(\kappa\kappa)_{q=0}) - (S_{\alpha\alpha}(\kappa\kappa)_{q=0})\}$$

In these equations the matrices **R**, **T**, and **S** specify the short-range ion–ion, ion–shell and shell–shell interactions respectively while **C** is the Coulomb matrix for the long-range interactions. Matrices **m**, **Z** and **Y** are diagonal matrices representing the mass, ionic charge and charge on the shells while **U** and **W** are the displacement vectors for the ions and shells respectively. The constant k_κ is the spring constant coupling ion core and electron shell charges for the κth atom while the indices α, β denote cartesian coordinates. In most cases in which the shell model has been compared with experimental data the assumption has been made that the short-range forces act entirely through the shells resulting in the condition $\mathbf{R} = \mathbf{T} = \mathbf{S}$. In the work by Cowley *et al.* it was assumed that the **S** matrix was of the form $\mathbf{S} = \gamma_s\mathbf{R}$ which introduced another adjustable parameter into the problem. Then in the work by Cochran *et al.* the restriction that the **T** matrix be symmetric with respect to the ions was relaxed through the introduction of the parameters $\beta_T(12)$ and $\beta_T(21)$. In comparing the present data with the shell model we have employed these additional parameters γ_s, $\beta_T(12)$, and $\beta_T(21)$ or in briefer notation γ, $\beta(12)$ and $\beta(21)$. A recent variation of the shell model is the breathing shell model[17] (BSM) in which new cordinates are introduced which allow for the compression of the electron shells. Dolling *et al.* in their work on LiF[18] applied the BSM and discussed it qualitatively, indicating that it is merely another phenomenological variation of the shell model. Rather than include the BSM we chose to compare the present data with versions of the shell model employing the parameters indicated above.

Model parameters were evaluated using a non-linear least squares program[19] which fit the models to the dispersion relation data and in addition to the elastic constants and high frequency dielectric constant. Because the neutron scattering data were not all obtained with the proper interval on the phonon wave vector as required by the least squares program, smooth curves were drawn through the data points for some branches and the frequencies read off at the appropriate q values. Errors assigned to these frequencies were estimated in terms of the errors on nearby data points, and for the longitudinal optical modes large errors were assigned so that the LO data were given very little weight in the least squares analysis. Several experimental determinations of the elastic constants of sodium chloride have been made recently[20], and because of differences in the values reported we have arbitrarily averaged these sets of data. Values assigned to C_{11}, C_{12} and C_{44} in the program were $4·94 \pm 0·05$, $1·28 \pm 0·05$ and $1·280 \pm 0·011$ respectively, all in units of 10^{11} dyne-cm^{-2}.

Table 2. Parameter values for three models which were fitted to the dispersion relation data. The values quoted for the dielectric constant and elastic constants are those predicted by the models, and v refers to the volume of the primitive unit cell

		Model		
Parameter	units	I	II	III
A	$(e^2/2v)$	6·276	10·264	5·885
B	$(e^2/2v)$	−0·127	−0·971	−0·734
A'	$(e^2/2v)$	0·750	−0·427	0·106
B'	$(e^2/2v)$	−0·140	0·022	−0·122
A''	$(e^2/2v)$	0·646	0·597	1·581
B''	$(e^2/2v)$	−0·003	−0·025	0·241
Z	e	0·630	0·968	0·664
α_1	$(1/v)$		0·011	0
d_1	e		−0·035	−0·019
α_2	$(1/v)$		0·058	0·079
d_2	e		0·194	0·054
γ				−4·191
$\beta(12)$				10·921
$\beta(21)$				−1·889
χ		2·82	1·13	0·950
ϵ		1·00	2·19	2·30
C_{11}	10^{11} dyne cm^{-2}	5·021	5·149	4·964
C_{12}	10^{11} dyne cm^{-2}	1·164	1·164	1·259
C_{44}	10^{11} dyne cm^{-2}	1·250	1·371	1·291

In Table 2 we have listed the final parameter values for three of the models which were evaluated. Model I is a seven parameter rigid-ion model, model II, an eleven parameter shell model and model III, a fourteen parameter shell model. Also listed in the table are the fitting error χ, the calculated value of the high frequency dielectric constant ϵ (to be compared with the experimental value of 2·31), and the calculated values of the elastic constants. Model I gave generally poor results in comparison with both the dispersion relation and elastic constant data. Inclusion of the electrical and mechanical polarizabilities for one or both the sodium and chlorine ions gave improved fits to the data, but the difficulties experienced with the rigid-ion model of fitting to both the neutron scattering data and elastic constants seemed to carry over to the shell model as well. Model II represents a fit which was obtained after increasing the errors assigned to the elastic constants so that these data were given less weight in the fitting process, and therefore, comparison of the calculated elastic constants with the values quoted in the previous paragraph should not be taken too seriously.

In Fig. 2 the results of both models II (dashed curves) and III (solid curves) are compared with the dispersion relation data from which it can be seen that there is very little difference between the calculated frequencies of the two models for these symmetry directions. The results of fitting model II display features similar to those found in other experiments on alkali halides[15], namely that the electrical polarizabilities are shared more equally than expected and that the mechanical polarizability of the sodium ion is negative. In going to model III, the additional parameters γ, $\beta(12)$ and $\beta(21)$ were introduced which improved the fit in that good agreement is obtained with the dispersion relation, dielectric constant, and elastic constant data. As evidenced in Table 2, the addition of the last three parameters has caused considerable change in the values of the other parameters, and made the physical significance of the model more obscure. The constraint placed on model III of having to satisfy the elastic constants as well as the neutron scattering

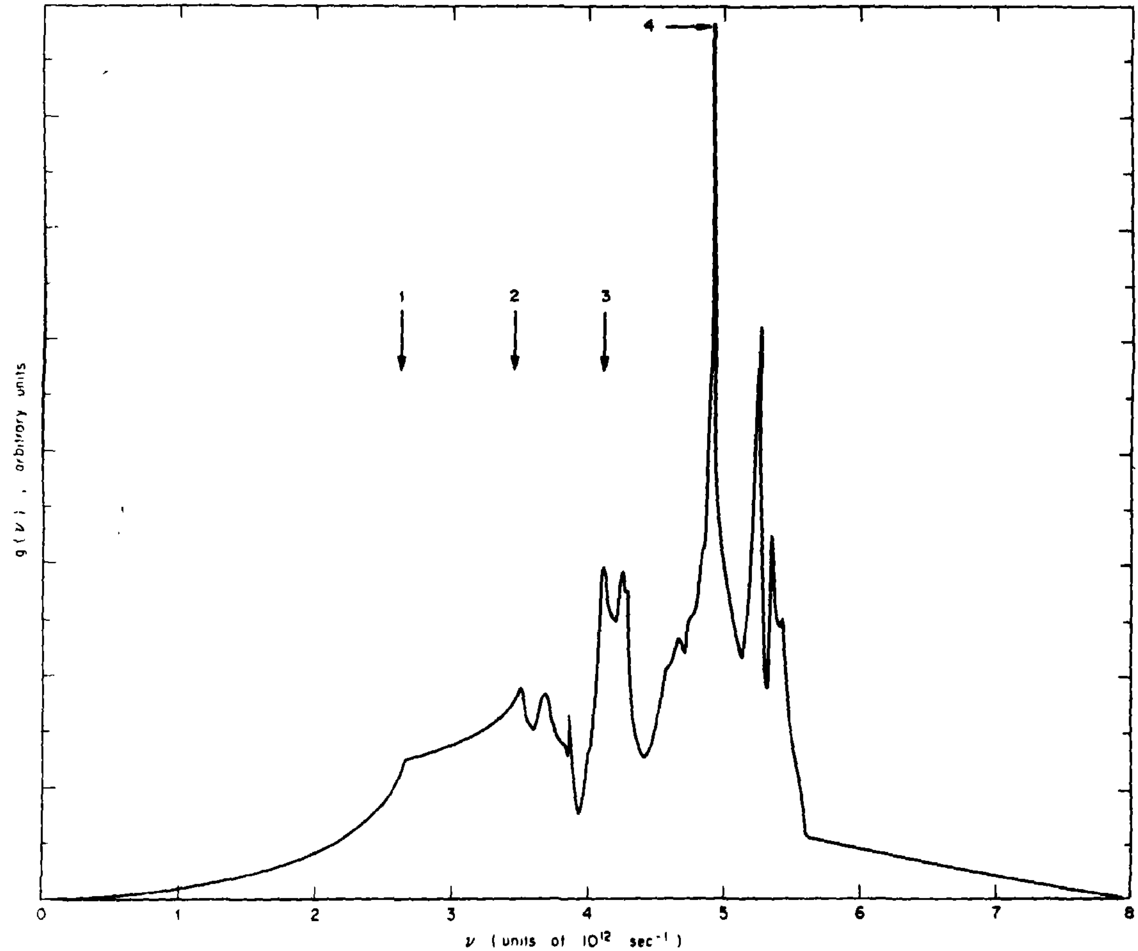

Fig. 3. Frequency distribution of sodium chloride based on the fourteen parameter shell model (III) calculated using the extrapolation method of Gilat and Dolling. Singularities labeled in the figure can be related to specific modes in the dispersion relation as discussed in the text.

data appears to be reasonable in view of the agreement at low q of the neutron scattering data and velocities determined by ultrasonics.

CALCULATIONS BASED ON MODELS

A. *Frequency distribution*

Based on the fit which was obtained for model III we have calculated the phonon frequency distribution using a computer program which is based on the extrapolation method of Gilat and Dolling[6]. The frequencies and frequency gradients have been determined for 977 reduced wave vectors in three subsections for $\frac{1}{48}$ of the Brillouin zone. Frequencies in the distribution are sorted in a histogram plot with a channel width of $\delta\nu = 0{\cdot}005 \times 10^{12}$ sec^{-1} and are displayed in Fig. 3. With this narrow channel width the histogram plot is essentially a smooth curve. Particular singularities in the frequency distribution which have been numbered 1 through 4 have been correlated with the modes TA(X), TA(L), TO(L), TO(Γ) and LA(Σ_1), respectively, the latter two modes both contributing to singularity number 4. (The point Σ_1 occurs at $\zeta = 0{\cdot}60$ along the Σ direction.) The other singularities relate to directions other than those for which measurements were made.

B. Θ_D

From the frequency distribution which was obtained from model III we have evaluated Θ_D(T) which is shown as the solid curve in Fig. 4. The calculated Θ_D(T) is compared with the Θ_D of Morrison and Patterson[7] which was determined from their specific heat data for bulk NaCl. The disagreement at low temperature is in the direction one would expect from using a frequency distribution applicable at room temperature, while the agreement near room temperature is very good considering the low value of Θ_D and that no corrections have been made for anharmonic effects.

C. *Combined density of states*

In the same program which was used to compute the phonon frequency distribution the capability existed for evaluating the two phonon density of states. For each point $\vec{q}$ in the Brillouin zone for which the frequencies

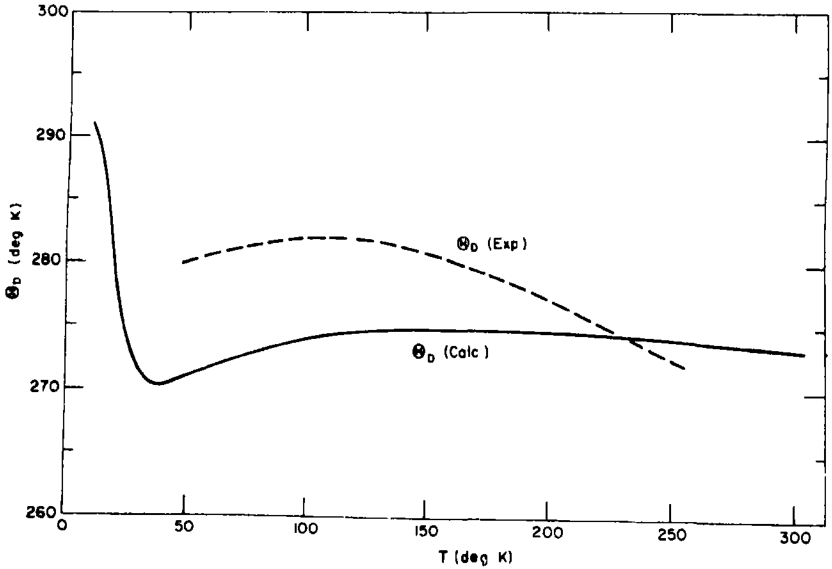

Fig. 4. Temperature dependence of the Debye temperature based on the calculated frequency distribution Θ_D (calc.) compared with the same quantity determined in the experiment of Morrison and Patterson[7] Θ_D(exp.).

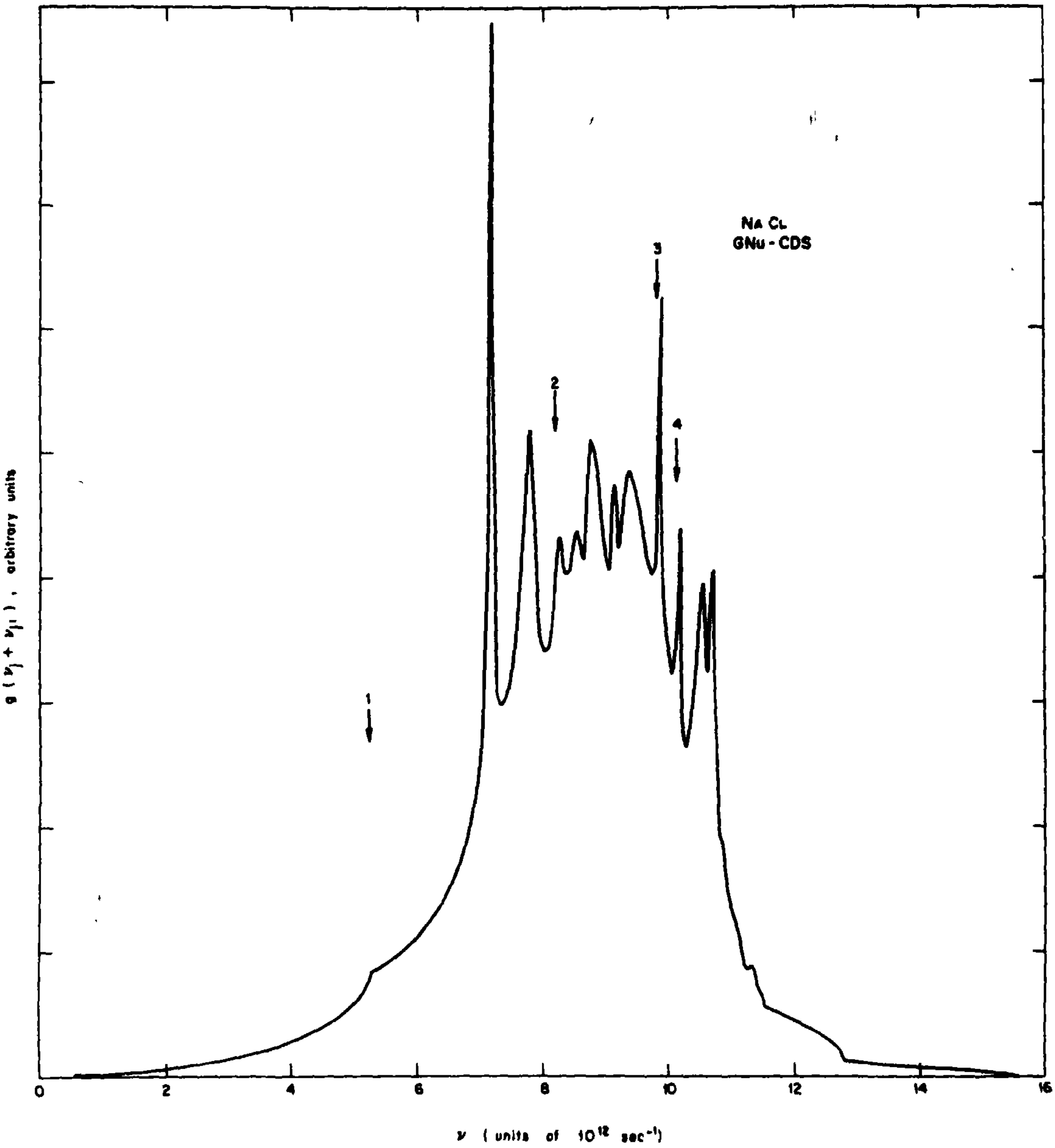

Fig. 5. Combined density of states distribution for sodium chloride based on the fourteen parameter shell model which includes summation and overtone frequencies. The singularities indicated in the figure are discussed in the text where comparison is made with Raman scattering data.

were determined the sum $\nu_j+\nu_{j'}$ was formed for all pairs of modes including the self terms ($j=j'$). These sum frequencies which include all summations and overtones were then sorted into a histogram with a channel width $\Delta\nu = 0{\cdot}01 \times 10^{12}\,\text{sec}^{-1}$.

The resulting density-of-states (CDS) distribution $g(\nu_j+\nu_{j'})$ is plotted versus the sum frequency in Fig. 5. A considerable amount of structure is exhibited in the CDS spectrum, and the four arrows in Fig. 5 indicate structure (overtones) which relate directly to critical points in the single phonon frequency distribution and observed mode frequencies for the symmetry directions of this experiment. The CDS spectrum can be compared with the spectrum obtained in second order Raman scattering although not directly due to experimental conditions and selection rules which apply to Raman scattering. In general the second order Raman spectrum is expected to have less structure than the CDS spectrum due to these selection rules, and experimental conditions may bias that Raman spectrum which is observed. Because of small differences between the observed mode frequencies and the frequencies computed using model III we have used the observed frequencies listed in Table 1 for making a detailed comparison with the second order Raman scattering data of Welsh *et al.* Results of this comparison are summarized in Table 3. Agreement is quite good, being within 1 per cent on all but two of the transitions. The data are all related to phonon modes which correspond to either the point Γ or zone boundary points X and L except for the assignment of $(LA+TO^{xy})$ (Σ_1) which occurs at $\zeta = 0{\cdot}6$, i.e. at the maximum in the Σ_1 longitudinal acoustic branch.

Table 3. Comparison of second-order Raman scattering data[8] *and neutron scattering data for NaCl*

Raman		Neutron	
$\omega(\text{cm}^{-1})$ →	$\nu(10^{12}\,\text{sec}^{-1})$	$\nu(10^{12}\,\text{sec}^{-1})$	Mode
415	12·44	12·75	$(TO+LO)(\Gamma)$
346	10·37	10·44	$2TO(X), 2LA(L)$
314	9·41	9·50	$(TO+LA)(X)$
299	8·96	9·05	$(LA+TO^{xy})(\Sigma_1)$
285	8·54	8·56	$2LA(X)$
275	8·24	8·24	$2TO(L)$
256	7·67	7·82	$(TO+TA)(X)$
234	7·01	7·06	$2TA(L)$
174	5·22	5·20	$2TA(X)$

SUMMARY

The dispersion relation has been measured along the three principle symmetry directions for sodium chloride at room temperature. These data are in good agreement with X-ray scattering data and low temperature neutron scattering data. A fourteen parameter version of the shell model which was fit to the data has been used to generate a frequency distribution and combined-density-of-states distribution. From the frequency distribution the Θ_D parameter was calculated which agrees fairly well with the same parameter derived from specific heat data. Finally a comparison was made between the critical points in the combined-density-of-states distribution and second order Raman scattering data for sodium chloride.

Acknowledgements—The authors would like to thank the slow neutron inelastic scattering group at Oak Ridge National Laboratory for providing the computer programs which were used in the present work, particularly visiting scientists who wrote the programs in Fortran (Dr. G. Dolling), assisted with the programming of the combined-density-of-states calculation (Dr. G. Gilat) and prepared the program listings and card decks for use (Dr. P. R. Vijayaraghavan). Mr. J. K. Boyter provided programming assistance; Mr. D. E. Jackson and Mr. R. E. Brown built and maintained the spectrometer electronics, and the mechanical parts of the spectrometer were designed and built by Mr. H. G. Miller. We would like to thank Dr. W. R. Myers for comments regarding the operation of the spectrometer and Dr. R. M. Brugger for his support. One of us (DRW) would like to thank the Associated Western Universities for financial support.

REFERENCES

1. WOODS A. D. B., COCHRAN W. and BROCKHOUSE B. N., *Phys. Rev.* **119**, 980 (1960).
2. BRUGGER R. M., BENNION R. B., WORLTON T. G., *Phys. Lett.* **24A**, 714 (1967).
3. OSTHELLER G. L., SCHMUNK R. E., BRUGGER R. M. and KEARNEY R. J., In *Inelastic Scattering of Neutrons in Solids and Liquids*, Vol. 1, p. 315. IAEA, Vienna (1968).
4. ALMQVIST L., RAUNIO G. and STEDMAN R., In *Inelastic Scattering of Neutrons in Solids and Liquids*, Vol. 1, p. 295. IAEA, Vienna (1968).

5. BUYERS W. J. L. and SMITH T., *Phys. Rev.* **150**, 758 (1966). More recent work by ELDRIDGE J. E., *J. Phys. Chem. Solids* **29**, 1059 (1968) is essentially in agreement with the work of BUYERS and SMITH but is less extensive.
6. GILAT G. and DOLLING G., *Phys. Lett.* **8**, 304 (1964).
7. MORRISON J. A., and PATTERSON D., *Trans. Faraday Soc.* **52**, 764 (1956).
8. WELSH H. L., CRAWFORD M. F. and STAPLE W. J., *Nature* **164**, 737 (1949).
9. DOLLING G. and WOODS A. D. B., In *Thermal Neutron Scattering* (Edited by P. A. Egelstaff), Chapter V. Academic Press, New York (1965).
10. BOUCKAERT L. P., SMOLUCHOWSKI R. and WIGNER E., *Phys. Rev.* **50**, 58 (1936).
11. SCHMUNK R. E., *Bull. Am. Phys. Soc.* **12**, 281 (1967).
12. MARTIN D. H., *Adv. Phys.* **14**, 39 (1965).
13. LYDDANE R. H., SACHS R. G. and TELLER E., *Phys. Rev.* **59**, 673 (1941).
14. COCHRAN W., COWLEY R. A., DOLLING G. and ELCOMBE M. M., *Proc. R. Soc.* **A293**, 433 (1966).
15. COWLEY R. A., COCHRAN W., BROCKHOUSE B. N. and WOODS A. D. B., *Phys. Rev.* **131**, 1030 (1963).
16. COWLEY R. A., *Proc. R. Soc.* **A268**, 121 (1962).
17. NÜSSLEIN V. and SCHRÖDER U., *Phys. Status Solidi* **21**, 309 (1967).
18. DOLLING G., SMITH H. G., NICKLOW R. M., VIJAYARAGHAVAN P. R. and WILKINSON M. K., *Phys. Rev.* **168**, 970 (1968).
19. The non-linear least squares program which was used in the present experiment was obtained from Oak Ridge National Laboratory and is the same as that described in [18] except that the additional parameters referred to in the text have been added.
20. HAUSSÜHL S., *Z. Phys.* **159**, 223 (1960); BARTELS R. A. and SCHEULE D. E., *J. Phys. Chem. Solids* **26**, 537 (1966); ZANG Z. P., *Phys. Rev.* **140**, A1788 (1968); SLAGLE O. D. and McKINSTRY H. A., *J. appl. Phys.* **38**, 437 (1967); GLUYAS M., *Br. J. appl. Phys.* **18**, 913 (1967).

J. Phys. Chem. Solids Pergamon Press 1970. Vol. 31, pp. 143–147. Printed in Great Britain.

DEBYE TEMPERATURES OF HOLMIUM AND DYSPROSIUM FROM SINGLE CRYSTAL ELASTIC CONSTANT MEASUREMENTS

S. B. PALMER
Department of Applied Physics, The University of Hull, England

(*Received* 20 *June* 1969)

Abstract—The elastic constants of single crystals of Dy and Ho have been measured from 330° to 1·5°K. The moduli at 0°K, obtained by extrapolation, are used to calculate the Debye temperature, θ, of the two materials. Values obtained are for Dy, $\theta = 183$°K and for Ho, $\theta = 188{\cdot}5$°K. These are compared to the values of θ obtained from specific heat measurements.

INTRODUCTION

THE DEBYE temperature, θ, although based on sweeping assumptions about the frequency spectrum of the lattice vibrations in a solid, nevertheless provides a useful means of comparing the thermal properties of different solids. θ can be evaluated from the elastic constants at 0°K from:

$$\theta = \frac{h}{k}\left[\frac{3q}{4\pi}\frac{N\rho}{M}\right]^{1/3} V_m \qquad (1)$$

where h is Plank's constant, k is Boltzmann's constant, N is Avegadro's number, ρ is the density, M is the molecular weight of the solid, q is the number of atoms in the molecule and V_m is the averaged sound velocity given by [1]

$$V_m = \left(\frac{1}{3}\sum_{i=1}^{3}\int_V \frac{1}{V_i^3}\cdot\frac{d\Omega}{4\pi}\right)^{-1/3} \qquad (2)$$

where V_1, V_2, V_3 are the three sound velocities in an arbitrary direction in the material.

Values of θ obtained from the elastic constants should agree with those obtained from the specific heat at low temperatures.

In the heavy rare earths, the total specific heat C_p at low temperatures has four different components, the lattice specific heat C_L, the electronic specific heat C_E, the magnetic specific heat C_M and the nuclear specific heat C_N. Difficulties are encountered in separating out the individual components from C_p, particularly in separating C_M from C_L since the exact temperature dependence of C_M is unknown. This has unavoidably led to a lack of knowledge of θ for the heavy rare earth metals. This problem is further complicated by the fact that the total specific heat results obtained by different investigators differ widely; in the case of dysprosium, by factors of two or more at 4°K [2].

A direct calculation of θ from the elastic constants at 0°K avoids these difficulties and is also insensitive to any small errors in the individual elastic constants.

The original specific heat measurements on dysprosium by Spedding *et al.* [3] indicated that $\theta = 158$°K. These measurements, however, extended only to 15°K and the authors seem to have taken a value for C_E which is now known to be too low. If this were corrected, their value for θ would increase. More recent work by Dreyfus *et al.* [4] yielded a value for θ of 207°K. However, their analysis assumed that $C_M = 0$ and the reliability of this estimate is thrown into doubt by the measurements of Lounasmaa *et al.* [5–7] which indicate that this assumption is not justified and at 4°K could affect the calculated θ appreciably.

In 1964, Lounasmaa [8] argued that the

Debye temperatures of the rare earth metals could be calculated by a linear interpolation between the θ's for lanthanum, at the beginning of the series, and lutetium at the end. This argument was based on the velocity of sound measurements of Smith *et al.*[9] who found that at room temperature the θ's for all the trivalent rare earths followed a straight line when plotted against atomic number. This yielded for Dy a value for θ of 186° ± 5°K. It seems likely that the Debye temperature should increase on progressing through the series because the atomic distances become smaller and the bonding strength between atoms increases as the heavier members of the series are approached. However, the more recent work of Lounasmaa and Sundstrom[5] indicates that the θ's for the heavy rare earths could all be about the same value and that Dreyfus'[4] original estimate of θ for dysprosium is of about the correct magnitude.

The evaluation of C_L and hence θ for holmium is further complicated, firstly by C_N which is appreciable up to 10°K and by C_M which, in Ho, dominates C_p. Early specific heat measurements by Spedding *et al.*[10] yielded a value of $\theta = 161°K$ for Ho. Dreyfus *et al.*[11] arrived at a value of $\theta = 114°K$ from the combined lattice and magnetic specific heat. Lounasmaa's interpolation leads to a value of $\theta = 191° \pm 5°K$.

In view of the present confusion over these Debye temperatures, it seems that values evaluated directly from the elastic moduli at 0°K would be useful. Elastic constant measurements have been made by Rosen[12, 13] on polycrystalline material at 4·2°K for most of the rare earth metals. He obtained Debye temperatures of 178°K for Dy and 195°K for Ho. Estimates of θ from polycrystalline data are complicated by the dependence of the sound velocity on size of crystallite, especially where the grain size is of the order of the sound wavelength. Polycrystalline specimens have to be very carefully prepared to ensure a uniform isotropic density close to the single crystal density. Also polycrystalline samples of Dy and Ho can never be magnetically saturated due to the magnetically hard hexagonal axis. Hence the ΔE effect cannot be eliminated.

The present work extends the elastic constant measurements to single crystals, eliminating any crystallite size effects. The single crystals can be saturated by applying a magnetic field along the easy direction in the basal plane.

EXPERIMENTAL

The dysprosium and holmium single crystals were purchased from Metals Research. They were of 99·9 per cent purity starting material and were grown by a floating zone technique using r.f. heating. The five independent elastic moduli of the hexagonal close packed rare earths were measured by a 15 Mc/s ultrasonic pulse-echo technique[14] from 330° to 1·5°K. The detailed elastic constants will be published elsewhere[15]. The elastic moduli were measured in an applied field of 25 K.Oe. to eliminate the large contributions due to domain and spin rotation effects below the Néel Temperature. The values at 0°K were obtained by extrapolation.

RESULTS

The five independent elastic constants at 0°K for both Dy and Ho are listed in Table 1. The estimated experimental error in these values is 0·5 per cent. The θ's were evaluated from the moduli in Table 1 by two separate techniques.

The first used the simplified method due to Anderson[16]. Here, the single crystal moduli are used to evaluate the polycrystalline moduli using the Voigt[1]–Reuss[1]–Hill[17]–Gilvarry[18] approximation. This then allows a simple estimation of the mean sound velocity V_m provided the density of the material is known. The densities at 0°K were calculated from the most suitable data in the literature [19–22] and are listed together with V_m in Table 1.

The θ's were also calculated using a velocity

Table 1

Metal	Elastic moduli at 0°K and $H_{app.} = 25$ K.Oe. (10^{11} dynes cm^{-2})					Density at 0°K (g.cm^{-3})	Mean sound velocity (10^5 cm. sec^{-1})
	C_{11}	C_{33}	C_{44}	C_{12}	C_{13}		
Dy	8·104	8·506	2·677	3·740	1·875	8·575	1·941
Ho	7·990	8·223	2·847	2·660	1·845	8·840	1·988

averaging computer programme similar to that of Robie and Edwards[23]. Briefly the method involves evaluating the three independent sound velocities for an arbitrary direction, storing them and repeating the process for a large sample of directions throughout space. A numerical summation is used in place of the volume integral in equation (2). The summations were made using intervals of 5° in θ and ϕ the polar angles. (The difference in θ obtained by using $\Delta\theta = \Delta\phi = 2°$ rather than $\Delta\theta = \Delta\phi = 5°$ was of the order of 0·1 per cent). These calculations were made using an I.C.L. 1905E computer.

The values obtained for θ from the two different methods for both Ho and Dy are shown in Table 2, where they are compared to those of other workers. It can be seen that the simple Anderson method leads to a value for θ in close agreement with the computed one.

DISCUSSION

The values for θ obtained here are in reasonable agreement with those of Rosen, and seem to favour the interpolation approach of Lounasmaa yielding a Debye temperature increasing with atomic number. However, results on gadolinium, terbium, erbium and thulium will be necessary to confirm this.

The computer technique allows us to examine the variation of the three wave velocities with propogation direction. The results for Dy and Ho are very similar in that the materials are very isotropic in a plane containing the c-axis and the basal plane. (The elastic moduli for a hexagonal system are isotropic in the basal plane.) The three wave surfaces for Dy in the (100) plane are shown in Fig. 1. This isotropy is surprising in view of the large anisotropy present in the magnetic properties of these materials. Anderson points out that his simplified method of calculating θ only breaks down for highly anisotropic materials; the accuracy of this approach in our case seems to be due to the absence of anisotropy.

At the very lowest temperature ~ 0·001°K, where the phonon frequencies are too low for domain wall movement to occur then it seems that it is the elastic constant values at zero field (i.e. $I = 0$) that are appropriate. However, using these values makes very little difference to the values obtained for θ for Ho.

Table 2. *Comparison of Debye temperatures for* Dy *and* Ho *from both elastic constant and specific heat measurements*

Metal	Present work θ (Anderson's approximation)	θ (Computer programme)	θ (Rosen)	θ (Lounasmaa interpolation)	θ (Dreyfus)
Dy	183·0° ± 1·0°K	182·8° ± 1·0°K	178°K	186° ± 5°K	207°K
Ho	188·5° ± 1·0°K	188·5° ± 1·0°K	195°K	191° ± 5°K	114°K
			[12,13]	[8]	[4,11]

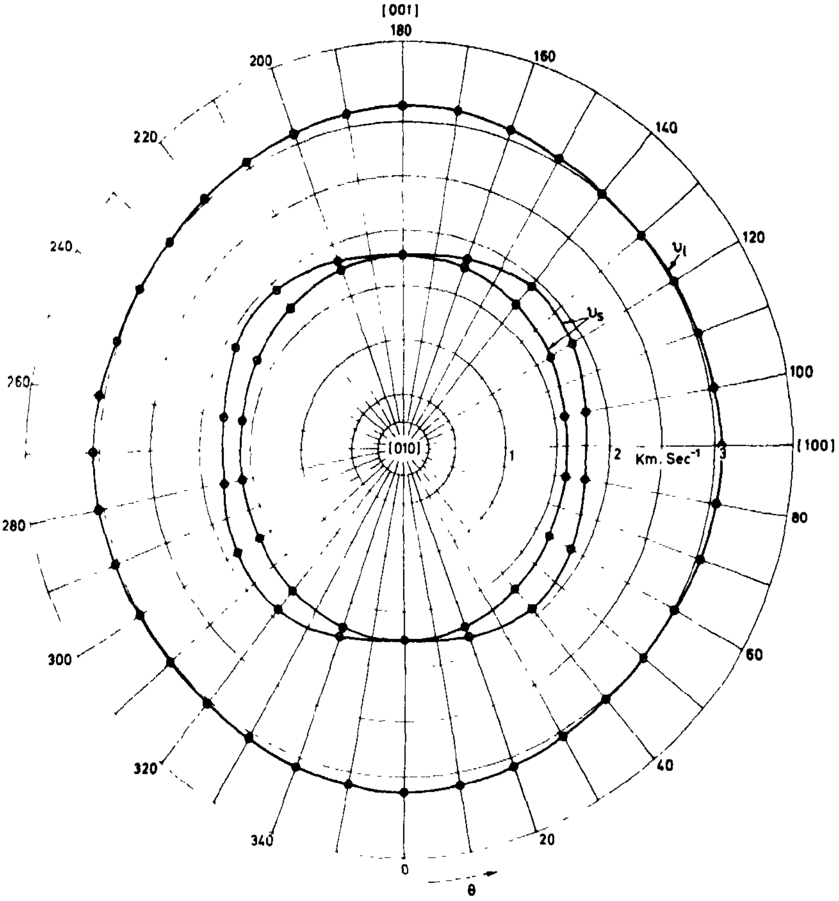

Fig. 1. Cross section of the wave velocity surface in the (010) plane of dysprosium calculated from the elastic constants in Table 1.

The zero-field results could not be obtained for Dy because of ultrasonic couplant problems.

The transition to ferromagnetism in these materials is accompanied by a 1 per cent strain to an orthorhombic structure. We have ignored this in our elastic constant measurements.

Acknowledgements—The author wishes to thank the Department of Physics at the University of Sheffield for providing facilities during the experimental work. Professor E. W. Lee for suggesting the project and for many helpful discussions. Mr. Norman for assistance with the computer programme and S.R.C. for financial support.

REFERENCES

1. HUNTINGTON H. B., *Solid State Physics* (Edited by F. Seitz and D. Turnbull), Vol. 7. Academic Press, New York (1958).
2. LOUNASMAA O. V. and GUENTHER R. A., *Phys. Rev.* **126**, 1357 (1962).
3. SKOCHDOPOLE R. E., GRIFFEL M. and SPEDDING F. H., *J. Chem. Phys.* **23**, 2258 (1955).
4. DREYFUS B., GOODMAN B. B., TROLLIET G. and WEIL L. *C. r. hebd. Séanc. Acad. Sci., Paris* **253**, 1085 (1961).
5. LOUNASMAA O. V. and SUNDSTROM L. J., *Phys. Rev.* **150**, 399 (1966).
6. LOUNASMAA O. V., *Proc. Ninth Intl. Conf. on Low Temperature Physics, Columbus, Ohio, 1964* (Edited by J. G. Daunt, D. O. Edwards, F. J. Millward and M. Yagub), pp. 901–904. Plenum Press, New York (1965).
7. LOUNASMAA O. V. and SUNDSTROM L. J., *Ann. Acad. Sci., Fennicae*, AVI **210**, 202 (1967).
8. LOUNASMAA O. V. *Phys. Rev.* **133**, A219 (1964).
9. SMITH J. F., CARLSON C. E. and SPEDDING F. H., *J. Metals* **9**, 121 (1957).

10. GERSTEIN B. C., GRIFFEL M., JENNINGS L. D., MILLER R. E., SKOCHDOPOLE R. E. and SPEDDING F. H., *J. chem. Phys.* **27**, 394 (1957).
11. DREYFUS B., GOODMAN B. B., LACAZE A. and TROLLIET G. *C. r. hebd. Séanc. Acad. Sci., Paris* **253**, 1764 (1961).
12. ROSEN M., *Phys. Rev. Lett.* **19**, 695 (1967).
13. ROSEN M., *Phys. Rev.* **174**, 504 (1968).
14. HUNTINGTON H. B., *Phys. Rev.* **72**, 321 (1947).
15. PALMER S. B. and LEE E. W., To be published.
16. ANDERSON O. L., *J. Phys. Chem. Solids* **24**, 909 (1963).
17. HILL R., *Proc. phys. Soc.* **65**, 350 (1952).
18. GILVARRY J. J., *Phys. Rev.* **103**, 1701 (1956).
19. LEGVOLD S., ALSTAD J. and RHYNE J. J., *Phys. Rev. Lett.* **10**, 509 (1963).
20. CLARKE A. E., DESAVAGE B. F. and BOZORTH R., *Phys. Rev.* **138**, 216 (1965).
21. RHYNE J. J., LEGVOLD S. and RODINE E. T., *Phys. Rev.* **154**, 266 (1967).
22. DARNELL F. J. and MOORE E. P., *J. appl. Phys.* **34**, 1337 (1963).
23. ROBIE R. A. and EDWARDS J. L., *J. appl. Phys.* **37**, 2659 (1966).

J. Phys. Chem. Solids Pergamon Press 1970. Vol. 31, pp. 149–161. Printed in Great Britain.

IRREDUCIBLE REPRESENTATIONS OF MAGNETIC GROUPS OF QUANTUM-MECHANICAL OPERATORS

O. V. KOVALEV and A. G. GORBANYUK
Physico-Technical Institute, Academy of Sciences, Yumovskii Tupik, Khar'Kov, U.S.S.R.

(*Received* 25 *April* 1969)

Abstract – The methods of constructions of Wigner corepresentations in all those cases which can be met in considering all 674 magnetic space groups, are discussed. In order to use known tables of the irreducible representations of usual space groups, it is necessary to change the description of many magnetic groups. All cases of such changes are considered in detail. The examples of direct calculations of corepresentations are given.

1. INTRODUCTION

IRREDUCIBLE representations of the magnetic space groups are used to obtain physical consequences from the magnetic symmetry of crystals with non-vanishing current density. Representations consist of all (or nearly all) information about the magnetic symmetry and, besides, in a form which is the most suitable for physical applications. Magnetic space groups (1191 Shubnicov groups) have been found[1, 2]. In these groups the antisymmetry operation is not an element of the group itself, but inserts as product by any geometrical symmetry operation (rotation, rotation with inversion, translation). In physics, the antisymmetry operation corresponds to the time reversal operation $R: t \rightarrow -t$. In particular, the operation R changes a sign of the magnetic moment. The representations of such group considering as a set of operations of the geometrical and time symmetry, obviously coincide with those of the space group which is obtained if the operation R is replaced by the identical operation in the magnetic group ('isomorphism' noted by Indenbom[3]). The representations of all space groups are presented in [4, 5].

However, for quantum-mechanical problems these representations are not to be used, but the representations of groups of operators g which are corresponded to operations of the geometrical and time symmetry and are defined over functions ψ which are the solutions of Schrödinger or Pauly equations[6]. These equations must be invariant with respect to those operators. If operation R is not taken into account, the group of operators for Schrödinger equation is isomorphic to that of the geometrical symmetry of physical system, and the group of operators for Pauly equation is isomorphic to that of two-dimensional unimodular unitary matrices [SU(2)]. Odd representations of unitary group is called "double-valued" representations of geometrical operation group. In accordance with Wigner theory[7], when the time symmetry is taken into account, it is necessary to confront the operation R with time reversal operator θ. According to this, the magnetic group reflect oneself over the group $G+\bar{G}\theta$ of operators, half of them containing θ. Since the operator θ is antiunitary, the group $G+\bar{G}\theta$ contains both unitary g and antiunitary $\theta\bar{g}$ operators. These last contain complex conjugate operation.

Let us note that for Schrödinger equation $\theta^2 = 1$ and for Pauly equation $\theta^2 = -1$.

Operators g form a unitary subgroup G of the group $G+\bar{G}\theta$. Matrix forms of operators defined over the wave functions ψ, which are the solutions of correspondent equation, are called corepresentations. Under the time reversaling and the rotating and reflecting allowed by crystal symmetry the wave functions are transformed by corepresentations.

The corepresentations of group $G+\bar{G}\theta$ are constructed with usual irreducible representations of the unitary subgroup G. In the present work we shall show how one can (1) use known representations of the space groups [5] for obtaining those of unitary subgroups G and (2) carry out real construction of the corepresentations. We will limit ourselves to those 674 magnetic groups, in which the operator θ is contained as a product by the rotation operator or rotation with inversion operator. For such groups the chemical and magnetic unit cells coincide, and operators g and $\bar{g}$ are different. Further, the operators g or $\bar{g}$ and antiunitary operators $\theta\bar{g}$ will be called simply "elements" and "antiunitary elements", respectively. Any point operator h_i will be called "rotation".

The method of constructing the corepresentations of such groups is based on following simple speculation. The unitary subgroup G of a magnetic group is any usual space group G' which, of course, is in the list of all space groups. Since the representations of all space groups are known[5], we shall use them for constructing the corepresentations. In accordance with it, we shall denote sometimes the magnetic group by two symbols $G^i(H^j)$ [10], the first being Shoenflies symbol of a space group $G+\bar{G}$ and the second (near the brackets) being that of a unitary subgroup. So, for instance, $O_h{}^1(O^1)$ is the magnetic group which reduces to $O_h{}^1$ in replacing R by unity; O^1 is the unitary subgroup of $O_h{}^1(O^1)$. Analogical symbols are used for denoting of magnetic classes.

2. UNITARY SUBGROUPS AND THEIR REPRESENTATIONS

Here we shall show how it should describe the group $G+\bar{G}\theta$ and the unitary subgroup G of this group to coincide G with a space group G' from the group list[5] and to use then the representations of the group G' for constructing those of G.

We suppose that the description of a magnetic group is known in some kind. It means we know all symmetry elements g and $\bar{g}$. The set of these elements forms a usual group $G+\bar{G}$ which is in the space group list[5]. The elements of every space group in[5] have been described as $(\boldsymbol{\alpha}_i/h_i)$ where h_i and $\boldsymbol{\alpha}_i$ is the rotation and the subsequent translation, respectively. Under such description all axes and planes intersect in one point (point group center). This point is chosen as an origin of Cartesian coordinate system. Every rotation h_i inserts into the group description the only one time. The translations $\boldsymbol{\alpha}_i$ associated to rotations are defined by the position of the coordinate system origin in the crystal cell. If the coordinate system origin is displaced be a vector $\mathbf{R}$, a space group takes up other description, that is, an element $(\boldsymbol{\alpha}_i/h_i)$ must be replaced by an element $(\boldsymbol{\beta}_i/h_i')$ where

$$\boldsymbol{\beta}_i=\boldsymbol{\alpha}_i+h_i\mathbf{R}-\mathbf{R}=\boldsymbol{\alpha}_i+\boldsymbol{\gamma}_i. \qquad (1)$$

Here $h_i\mathbf{R}$ the vector to which vector $\mathbf{R}$ is changed under the operation h_i. The rotation h_i' is made around a new coordinate system origin. For the consecutive application of an element g_1 and then g their product corresponds

$$gg_1=(\boldsymbol{\alpha}/h)(\boldsymbol{\alpha}_1/h_1)=(\boldsymbol{\alpha}+h\boldsymbol{\alpha}_1/hh_1).$$

The product table of rotations h_i is in [5].

Further we shall deal with "small" representations of the wave vector K_j group G_{Kj}. Let us remind, that group G_{Kj} consist of elements of G, which being applied to K_j produce h_iK_j that differs from K_j not more than by a translation of the reciprocal lattice. The representations $t(g_i)$ and $\pi(g_i)$ of the group G_{Kj} is called "small". Side by side with them loaded representations $\tau(h_i)=\exp[iK_j,\boldsymbol{\alpha}_i]\tau(g_i)$ and $\pi(h_i)=\exp[iK_j,\boldsymbol{\alpha}_i]\pi(g_i)$ are introduced[8, 5]. It is very important that matrices of loaded representations of elements

g_i and (a_n/g_i) – where a_n is lattice translation – are identical. Our aim is to obtain loaded representations of G with the help of loaded representations of G' for all vectors $\mathbf{K}_j$ which form Brillouin zone.

Let us deduce a formula, needed below, showing how the loaded representation is changed under displacement $\mathbf{R}$ of the coordinate system origin. It is clear that matrix $\tau(g_i)$ assigned to element g_i does not depend on the choice of the coordinate system origin. Therefore, if $(\boldsymbol{\alpha}_i/h_i)$ and $(\boldsymbol{\beta}_i/h_i')$ is the same element described in the different coordinate systems, $\exp[-iK_j, \boldsymbol{\alpha}_i]\boldsymbol{\tau}(h_i) = \exp[-iK_j, \boldsymbol{\beta}_i]\boldsymbol{\tau}'(h_i')$ where $\boldsymbol{\tau}(h_i)$ and $\boldsymbol{\tau}'(h_i')$ are matrices before and after displacement, respectively. Using (1), we have

$$\boldsymbol{\tau}'(h_i') = \lambda_i\boldsymbol{\tau}(h_i)$$

$$\boldsymbol{\pi}'(h_i') = \lambda_i\boldsymbol{\pi}(h_i) \tag{2}$$

where $\lambda_i = \exp[iK_j, \boldsymbol{\gamma}_i]$. The factor λ_i is the same for $\mathbf{R}$ and $\mathbf{R}+a_n$, since

$$(K_j, h_ia_n - a_n) = (h_i^{-1}K_j - K_j, a_n) = b_ma_n = 2\pi\delta_{mn}.$$

Later on we shall suppose that $G+\bar{G}$ has description as it is in [5]. *Therefore, for the* use of rules given here the reader must describe the considered group with regard to [5].

As it turned out for aims of the present work, it is suitable to change some of the data [5] and add something. This is done in the Appendix. So §1 contains the description and representations of groups $D_{2d}^{9,10}$; §2 contains the description of the lattices Γ_m and $\Gamma_m{}^b$. Some corrections of [5] (Russian edition, 1961) are in §7.

We shall show further how it should identify the groups G and G' and determine representations of G. We shall pick out three essential different cases which, in his turn, are divided into subcases.

Case A

Magnetic classes of cubic, hexagonal, trigonal system and magnetic classes $D_{4h}(C_{4h})$, $D_{4h}(D_4)$, $D_{4h}(D_{2d})$, $D_{4h}(C_{4v})$, $D_4(C_4)$, $D_{2d}(S_4)$, $C_{4h}(C_4)$, $C_{4h}(S_4)$, $C_{4v}(C_4)$, $D_{2h}(D_2)$, $D_{2h}(C_{2v})$, $C_{2h}(C_2)$, $C_{2h}(C_s)$, $C_i(C_0)$.

Group $G+\bar{G}$ and subgroup G considered as a some space group belong to the same system and have the same type of Bravais lattice. For all systems except orthorhombic, which we consider apart, a set of rotations h_i of G coincides with one of some group G'. The group G' should be sick among groups of the same lattice Γ and the same class $\mathbf{G}$ which the group G belong to. However, the description of G can appear different than that of G' in [5]. There are the following possible cases.

A-1. There is a group G' among groups of corresponding lattice Γ and class $\mathbf{G}$, the description of which differs from that of G no more than by the lattice translations for vectors $\boldsymbol{\alpha}_i$. It is clear that $G = G'$. Loaded representations $\mathbf{t}(h_i)$ and $\boldsymbol{\pi}(h_i)$ of the group G_{Kj} of vector K_j, adduced in [5] for the group G', are those of $\mathbf{t}(h_i)$ and $\mathbf{p}(h_i)$ of the group G_{Kj} of the same vector K_j for the unitary subgroup G.

A-2. For the group of lattice Γ and class $\mathbf{G}$ in the list [5], there is no description that coincides with that of G in sense discussed above. In this case, in order to identify G with some group G' of the class $\mathbf{G}$ in the list [5], it should change the description of G' in just degree by displacing of the coordinate system origin by a vector $\mathbf{R}$ in latter. Let us show how one can determine the vector $\mathbf{R}$ and the group G'. Let us assume we have p groups $G_1', G_2', \ldots, G_p'$ of class $\mathbf{G}$ and lattice Γ in the list [5]. Choosing q generating elements in a class $\mathbf{G}$ (that is, such ones which generate the group $\mathbf{G}$ by multiplying), let us then displace the coordinate origin in the groups G_m' by a vector $\mathbf{R}$. The description of these groups must be changed and new translations $\boldsymbol{\beta}_{im}$ associated to rotations h_i in elements g_i [1].

$$\boldsymbol{\beta}_{im} = \boldsymbol{\alpha}_{im} + h\mathbf{R} - \mathbf{R} \quad (m = 1, 2, \ldots, p; \quad i = 1, 2, \ldots, q)$$

where $\boldsymbol{\alpha}_{lm}$ is the translation associated to h_l before displacement. Demand now $\boldsymbol{\beta}_{lm} = \boldsymbol{\alpha}_l + a_n$ where $\boldsymbol{\alpha}_l$ is the translation associated to h_l in G and a_n is a lattice translation which can be different for different i. We shall obtain p systems of equations, the total number of equations in everyone being q. Only one of them is compatible. The group G'_m, corresponding to a compatible system, must be identified with G. In order to make the description of G'_m coincide with that of G with accuracy to the lattice translations, we must displace the coordinate origin in G'_m by a vector $\mathbf{R}$ determined from this compatible system. The following rule is useful, helping to determine $\mathbf{R}$ and G_m: the displacement of the coordinate origin along a symmetry axis or reflection plane do not change the translation along these elements. Formula (1) allows verification of this rule and deduction of other ones, but we do not consider it here.

Example 1. Magnetic group $D_6{}^3(D_3{}^n)$, Γ_h. With [5] $D_6{}^3 = G\{h_1, (2\boldsymbol{\alpha}'/h_3), (4\boldsymbol{\alpha}'/h_5), (\boldsymbol{\alpha}'/h_8), (3\boldsymbol{\alpha}'/h_{10}), (5\boldsymbol{\alpha}'/h_{12})\} + \bar{G}\{(\boldsymbol{\alpha}'/h_2), (3\boldsymbol{\alpha}'/h_4), (5\boldsymbol{\alpha}'/h_6), h_7, (2\boldsymbol{\alpha}'/h_9), (4\boldsymbol{\alpha}'/h_{11})\}$ where

$$\boldsymbol{\alpha}' = \frac{a_3}{6} = (0, 0, \tau_z/3.$$

It is easy true, if we displace the coordinate origin in the group $D_3{}^5$[5] by a vector $\mathbf{R} = -\alpha'/2$, its description will coincide with that of G, hence $D_3{}^n = D_3{}^5$. Loaded representations of G are obtained with those of $D_3{}^5$ in [5] by multiplying them by factors λ_i. For instance, for $K = \frac{1}{3}b_3$, $\lambda_1 = \lambda_3 = \lambda_5 = 1$ and $\lambda_8 = \lambda_{10} = \lambda_{12} = e^{i\pi/6} = \nu$. Using, with Ref. [5], *T* 18 we find the representations $\mathbf{t}(h_i)$ and $t(g_1)$ of G

	h_1	h_3	h_5	h_8	h_{10}	h_{12}
$\mathbf{t}^1$	1	ν^8	ν^4	ν	ν^9	ν^5
$\mathbf{t}^2$	1	ν^8	ν^4	ν^7	ν^3	ν^{11}
$\mathbf{t}^3$	$\begin{pmatrix}10\\01\end{pmatrix}$	$\begin{pmatrix}10\\0\nu^4\end{pmatrix}$	$\begin{pmatrix}10\\0\nu^8\end{pmatrix}$	$\begin{pmatrix}0\nu\\\nu0\end{pmatrix}$	$\begin{pmatrix}0\nu\\\nu^5 0\end{pmatrix}$	$\begin{pmatrix}0\nu\\\nu^9 0\end{pmatrix}$

A-3. Magnetic class $D_{2h}(C_{2v})$, lattices Γ_0, $\Gamma_0{}^v$, $\Gamma_0{}^f$. In [5], the only one variant of the space group description of class C_{2v} has been given. Nevertheless, the groups of this class allow six variants of the description differing from each other by the orientation of the axis C_2 and the reflection planes respect to coordinate axes (variants, corresponding to the same position of axis C_2, can coincide for some groups). In real magnetic crystal, axis C_2 of subgroup G has been oriented definitely along x, y or z axis. It should be compared to the description of G with those two descriptions of the group C_{2v}^n in which axis C_2 has been oriented along the same coordinate axis. Therefore, it is convenient to have five more variants of the group C_{2v} description, besides that given in [5]. One can obtain them from the description cited in [5] by formal replacing rotations and translations for every element g apart with agree Table 1.

Table 1. *Six variants of the class* C_{2v} *group description, the lattices* $\Gamma_0, \Gamma_0{}^v, \Gamma_0{}^f$. ν_1, ν_2, ν_3 *are* 0 *or* 1 *in the description of groups* $C_{2v}{}^n$ *in* [5] τ_X, τ_Y, τ_Z *are half-periods along* X, Y, Z *axes;* h_1 *is rotation*

$C_2 \parallel z, a$	h_4	h_{26}	h_{27}	$(\nu_1\tau_x, \nu_2\tau_y, \nu_3\tau_z)$
$C_2 \parallel z, b$	h_4	h_{27}	h_{26}	$(\nu_2\tau_x, \nu_1\tau_y, \nu_3\tau_z)$
$C_2 \parallel x, a$	h_2	h_{27}	h_{28}	$(\nu_3\tau_x, \nu_1\tau_y, \nu_2\tau_z)$
$C_2 \parallel x, b$	h_2	h_{28}	h_{27}	$(\nu_3\tau_x, \nu_2\tau_y, \nu_1\tau_z)$
$C_2 \parallel y, a$	h_3	h_{28}	h_{26}	$(\nu_2\tau_x, \nu_3\tau_y, \nu_1\tau_z)$
$C_2 \parallel y, b$	h_3	h_{26}	h_{28}	$(\nu_1\tau_x, \nu_3\tau_y, \nu_2\tau_z)$

Example 2. Magnetic group $D_{2h}^5(C_{2v}^n)$, $C_2 \parallel x$, Γ_0. It follows from the description of D_{2h}^5 in [5] that $G = C_{2v}^n\{h_1, h_4, (0,0,\tau_z/h_{27},h_{28})\}$. With agree to the third and fourth rows of

	g_1	g_3	g_5	g_8	g_{10}	g_{12}
t^1	1	-1	1	1	-1	1
t^2	1	-1	1	-1	1	-1
t^3	$\begin{pmatrix}10\\01\end{pmatrix}$	$\begin{pmatrix}\nu^{10}0\\0\nu^2\end{pmatrix}$	$\begin{pmatrix}\nu^8 0\\0\nu^4\end{pmatrix}$	$\begin{pmatrix}01\\10\end{pmatrix}$	$\begin{pmatrix}0\nu^{10}\\\nu^2 0\end{pmatrix}$	$\begin{pmatrix}0\nu^8\\\nu^4 0\end{pmatrix}$

Table 1, we replace h_4, h_{26}, h_{27} by h_2, h_{27}, h_{28} (a) and by h_2, h_{28}, h_{27} (b) in all ten groups of the class C_{2v}. Accordingly, we replace translations. In particular, we obtain two new descriptions for C_{2v}^4: $\{h_1, (0, \tau_y, 0/h_2), h_{27}, (0, \tau_y, 0/h_{28})\}$ (a) and $\{h_1, (0{,}0{,}\tau_z/h_2), h_{28}, (0{,}0{,}\tau_z/h_{27})\}$ (b). If we now carry out the displacement by $R = (0{,}0{,}\tau_z/2)$, the latter is described as $\{h_1, h_2, (0{,}0{,}\tau_z/h_{28}), (0{,}0{,}\tau_z/h_{27})\}$. With the accuracy to the lattice translations, it coincides with the description of the subgroup $G = G_{2v}^n$, that is, $n = 4$.

If in G $C_2\|y$, it should be realized the replacements with agree to the fifth and sixth rows of Table 1. If in G $C_2\|z$, one must use the description given in [5] and that, which we will obtain from it with the help of the second row of Table 1.

In order to obtain representations of groups G, one should have representations of C_{2v} class groups for all six variants of the description. For the description given in [5] representations are in [5]. For other variants of description representations are in Appendix §3. Obviously, the loaded representations **t** and $\boldsymbol{\pi}$ of G' are bound up with **t** and **p** of G on formula (2).

Let us obtain **t** of $D_{2h}^5(C_{2v}^4)$ for the vector $\mathbf{K}_{11} = \mu_1 b_1 + \frac{1}{2}(b_2 + b_3)$. In this case $R = (0{,}0{,}\tau_z/2)$. It follows from appendix ($C_2\|x$, b, C_{2v}^4) that the set $T12$ is bound up with $\mathbf{K}_{11}$

$T12$	h_1	h_2	h_{28}	h_{27}
$\boldsymbol{\tau}^1$	$\begin{pmatrix}1&0\\0&1\end{pmatrix}$	$\begin{pmatrix}i&0\\0&-i\end{pmatrix}$	$\begin{pmatrix}0&1\\1&0\end{pmatrix}$	$\begin{pmatrix}0&i\\-i&0\end{pmatrix}$

Since $\lambda_i = \exp[iK.h_i R - R]$, we have $\lambda_1 = \lambda_{27} = 1$ and $\lambda_2 = \lambda_{28} = -i$. Hence, the loaded representations of G are equal to

	h_1	h_2	h_{28}	h_{27}
$\mathbf{t}^1$	$\begin{pmatrix}1&0\\0&1\end{pmatrix}$	$\begin{pmatrix}1&0\\0&-1\end{pmatrix}$	$\begin{pmatrix}0&-i\\-i&0\end{pmatrix}$	$\begin{pmatrix}0&i\\-i&0\end{pmatrix}$

A-4. Magnetic class $D_{2h}(C_{2v})$, lattice Γ_0^b, $C_2\|z$. The group G is identified with groups $C_{2v}^{11,12,13}$ in the way of A-1 or A-2, the group C_{2v}^{12} allowing two descriptions which are different from one another by the orientation of the glide plane respect to the coordinate system. One of them is given in [5] (a), another is following: $C_{2v}^{12}\{h_1, h_{27}, (0, 0, \tau_z/h_4, h_{26})\}$ (b). The description of G should be compared with both, since, if G is C_{2v}^{12}, its description differs from (a) or (b) only by shift of the coordinate origin. The loaded representations, corresponding to these descriptions, are identical. $C_2\|x$. In the way A-1 or A-2, G is identified with one of groups $C_{2v}^{14,15,16,17}$ described in [5].

$C_2\|y$. In the way A-1 or A-2, G is identified with one of groups $C_{2v}^{14,15,16,17}$ described in Table 2. The representations of groups $C_{2v}^{14,15,16,17}$ (Table 2) are given in Appendix §4.

Table 2. The description of groups $C_{2v}^{14\text{-}17}$

Group	Type	h_3	h_{26}	h_{28}
C_{2v}^{14}	Γ_0^b			
C_{2v}^{15}	Γ_0^b		$\tau_x 00$	$\tau_x 00$
C_{2v}^{16}	Γ_0^b		$00\tau_z$	$00\tau_z$
C_{2v}^{17}	Γ_0^b		$\tau_x 0\tau_z$	$\tau_x 0\tau_z$

Case B

Systems S and S', which the magnetic group belongs to, are different. For instance, the group $C_4^2(C_2^n)$ belongs to tetragonal system and the group C_2^n belongs to monoclinic one. In any list of the space groups, as in [5], groups $G + \bar{G}$, which we must identify with the subgroup G, are found in sections with different lattices Γ and Γ' or, as we shall speak, $G + \bar{G}$ refers to lattice Γ and G refers to lattice Γ'. It connects with the rule (not proved, but also, apparently, not be broken), according to which, any space group is realized in nature with the least symmetrical lattice, allowing its constructions. It is the rule which the distribution of the space groups over lattices conform to. In our case, the elements of G form a subgroup of $G + \bar{G}$. Here, they are realized with lattice Γ, since $G + \bar{G}$ refers to Γ. However, if these elements do not form a subgroup of other group, but are considered as some space group G', then G' must refer to lattice Γ′. In above example, C_4^2 refers to lattice Γ_q, however, C_2^n should be referred to lattice Γ_m or Γ_m^b. Thus, two problems arise. One of them is to determine the lattice Γ′ to which the group G' refers; the other is to choose the basic periods in such a way that their arrangement with respect to the coordinate system is the same, as in Γ′. After solving these problems, it is possible to compare the subgroup G with groups, referring to the lattice Γ′. The system S' of the group G' is determined in the simple way, since G and G' refer to the same class, that is, $\mathbf{G} = \mathbf{G}'$. To determine Γ′ one can use the following consideration: Γ′ is obtained from Γ as a result of such infinitesimal deformation which transfers the crystal from the system S to system S'. In given example, the rotation of the vector a_1 of the lattice Γ_q by an infinitesimal angle in the plane $z = 0$ results the lattice Γ_m (latter Γ_m^b, thus, fall away). Comparing now elements of $G = C_2^n\{h_1, (0, 0, \tau_z/h_4)\}$ with elements of class C_2 of the lattice Γ_m, we see that $C_2^n = C_2^2$.

Below we shall show the accordance Γ → Γ′ and those combinations of vectors $\mathbf{a}_i$ which must be taken as basic periods a_i' of the lattice Γ′.

If periods a_i' of Γ′ do not coincide with periods a_i of Γ, then reciprocal lattice vectors b_i' and b_i will not coincide also. In connection with this, the same Brillouin zone point is expressed by vectors b_i and b_i' in a different way. From relations between a_i' and a_i these follow for b_i' and b_i. These last are adduced also.

B-1. Letters of rotations h_i of the subgroup G coincide with those of class **G** groups in [5]. Magnetic classes $C_{4v}(C_{2h})$, $C_4(C_2)$, $S_4(C_2)$, $C_{2v}(C_2)$, $C_{2h}(C_i)$, $C_s(C_0)$, $D_{4h}(1D_{2h})$, $C_{4v}(1C_{2v})$, $D_4(1D_2)$, $D_{2d}(1D_2)$, $D_{2d}(1C_{2v})$, $C_2(C_0)$, where the figure 1 means that symmetry axes and planes of the subgroup G coincide with coordinate axes and planes, the Γ_q and Γ_q^v orienting with agree [5]. The accordance Γ → Γ′ is following. For $C_{4h}(C_{2h})$, $C_4(C_2)$, $S_4(C_2)$, $C_{2v}(C_2)$, $C_{2h}(C_i)$, $C_s(C_0)$, $C_2(C_0)$

$$\left.\begin{array}{r} \Gamma_q, \Gamma_0 \to \Gamma_m \\ \Gamma_m, \Gamma_m^b \to \Gamma_{t2} \\ \Gamma_0^b \to \Gamma_m \end{array}\right\}, a_i = a_i', b_i = b_i'$$

$$\Gamma_q^v, \Gamma_0^v \to \Gamma_m^b, a_2 + a_3 = a_1', -a_2 = a_2', a_1 = a_3',$$
$$b_1 = b_3', b_2 = b_1' - b_2', b_3 = b_1'.$$

$$\Gamma_0^f \to \Gamma_m^b, a_3 = a_1', a_3 - a_2 = a_2', a_1 = a_3',$$
$$b_1 = b_3', b_2 = -b_2', b_3 = b_1' + b_2'.$$

For $D_{4h}(1D_{2h})$, $C_{4v}(1C_{2v})$, $D_4(1D_2)$, $D_{2d}(1D_2)$, $D_{2d}(1C_{2v})$

$$\left.\begin{array}{r} \Gamma_q \to \Gamma_0 \\ \Gamma_q^v \to \Gamma_0^v \end{array}\right\} a_i = a_i', b_i = b_i'.$$

If the group G now are considered as referring to the lattice with periods a_i', its description may differ from that of some group in [5], referring to the lattice Γ′, only by a coordinate origin displacement. The displacement vector $\mathbf{R}$ is determined in the way pointed out in A-2.

Example 3. Group $C_{4h}^6(C_{2h}^n)$, Γ_q^v. In accordance with [5] $C_{4h}^6 = G\{h_1, h_4, (0, \tau, \tau_z/2 \,|\, h_{25}, h_{28})\} + \bar{G}\{h_{38}, h_{39}, (0, \tau, \tau_z/2 \,|\, h_{14}, h_{15})\}$. Introduce new periods $a_1' = a_2 + a_3 = (\tau, \bar{\tau}, \tau_z) + (\tau, \tau, \bar{\tau}_z) = (2\tau, 0, 0)$, $a_2' = \bar{a}_2 = (\bar{\tau}, \tau, \tau_z)$, $a' = a_1 = (\tau, \tau, \tau_z)$, as it pointed out in the above list. Hence, it appears $(0, \tau, \tau_z/2) = \frac{1}{2}a_1' + \frac{1}{4}(a_2' - a_3')$. In accordance with A-2, for groups C_{2h}^3 and C_{2h}^6 referring to the lattice Γ_m^b, we obtain two systems of equations

$$\text{(I)} \quad \begin{cases} h_4\mathbf{R} - \mathbf{R} = a_{n1}' \\ h_{25}\mathbf{R} - \mathbf{R} = a_{n2}' + \frac{1}{2}a_1' + \frac{1}{4}(a_2' - a_3') \end{cases}$$

$$\text{(II)} \quad \begin{cases} h_4\mathbf{R} - \mathbf{R} = a_{n1}' \\ \frac{1}{2}a_1' + h_{25}\mathbf{R} - \mathbf{R} = a_{n2}' + \frac{1}{2}a_1' + \frac{1}{4}(a_2' - a_3') \end{cases}$$

One makes sure that system (II) has solution $R = \frac{1}{8}(a_3' - a_2')$. Therefore, $n = 6$.

Example 4. Group $D_4^{10}(1D_2^n)$, Γ_q^v. In accordance with [5]

$$D_4^{10} = G\{h_1, h_4, (0, \tau, \tau_z/2/h_2, h_3)\} \\ + \bar{G}\{h_{13}, h_{16}, (0, \tau, \tau_z/2/h_{14}, h_{15})\}.$$

It follows from the list that one should compare the group G with groups of the lattice Γ_0^v. Periods of Γ_q^v are considered to coincide with those of Γ_0^v (for this, it is necessary to put $\tau_x = \tau_y = \tau$ in Γ_0^v). If we displace the coordinate origin by the vector $R = (0, \bar{\tau}/2, \tau_z/4)$ in D_2^9, we shall obtain the description of D_2^9 as following $D_2^9\{h_1, (0, 2\tau, 0/h_4), (0, \tau, \tau_z/2 | h_2), (\tau, 0, \bar{\tau}_z/2 | h_3)\}$ which differs only by the lattice translations from that of G. Therefore, $n = 9$.

It is possible to determine easily the small representations of the subgroup G with the help of above adduced lists. Let us interest the representation bound up with the vector $K = \mu_1 b_1 + \mu_2 b_2 + \mu_3 b_3$. With the help of obtained formulae in the list, we express K_j by vectors b_i. We have $K = \mu_1' b_1' + \mu_2 b_2' + \mu_3' b_3'$. In [5], we find the loaded representations of the group G' bound up with this vector. Multiplying them by factors $\lambda_i = \exp[iK, \gamma_i]$, where $\gamma_i = h_i\mathbf{R} - \mathbf{R}$, we obtain the loaded representations $\mathbf{t}$ of the group G. The same is true for $\mathbf{p}$.

As an example, we will construct some representations of groups considered above.

Group $C_{4h}^6(C_{2h}^6)$, Γ_q^v, $R = \frac{1}{8}(a_3' - a_2')$. Let us take, for example, $K = \mu(b_1 - b_2) + \frac{1}{2}b_3$ ($K = K_8$ for Γ_q^v). In accordance with the list, we replace b_i by b_i' and obtain $K = \mu(b_3' + b_2' - b_1') + \frac{1}{2}b_1'$. Loaded representations of this vector for Γ_m^b[5] coincide with those τ and π of vector $\mu_1 b_1 + \mu(b_2 + b_3)$ (this is K_1 for Γ_m^b)

$T2$	h_1	h_{28}	$P2$	h_1	h_{28}
τ^1	1	1	π^1	1	i
τ^2	1	-1	π^2	1	$-i$

Since $\gamma_1 = 0$, $\gamma_{28} = \frac{1}{4}(a_2' - a_3')$, then $\lambda_1 = 1$, $\lambda_{28} = e^{i(\pi/4)} = \delta$. Hence, it appears

	h_1	h_{28}		h_1	h_{28}
$\mathbf{t}^1$	1	δ	$\mathbf{p}^1$	1	δ^3
$\mathbf{t}^2$	1	δ^5	$\mathbf{p}^2$	1	δ^7

From them, the small representations are obtained

	g_1	g_{28}		g_1	g_{28}
t^1	1	$\delta^7\mu'$	p^1	1	$\delta\mu'$
t^2	1	$\delta^3\mu'$	p^2	1	$\delta^5\mu'$

where $\mu' = \exp[-i\pi\mu]$.

Group $D_4^{10}(1D_2^9)$, Γ_q^v, $\mathbf{R} = (0, \bar{\tau}/2, \bar{\tau}_z/4)$. Here $b_i = b_i'$; therefore, the loaded representations of the unitary subgroup bound up with a vector K, are obtained from those of group D_2^9 bound up with the same vector. For example, let $K = \mu(b_1 + b_2 - b_3) + \frac{1}{2}b_3$. In accordance with [5], the loaded representations $T24$ and $P24$ have bound up with this vector

$T24$	h_1	h_4	$P24$	h_1	h_4
τ^1	1	i	π^1	1	1
τ^2	1	$-i$	π^2	1	-1

Here $\gamma_1 = 0$, $\gamma_4 = (0, \tau, 0)$ and $\lambda_1 = 1$, $\lambda_4 = i$. Therefore,

	h_1	h_4		h_1	h_4
$\mathbf{t}^1$	1	-1	$\mathbf{p}^1$	1	i
$\mathbf{t}^2$	1	1	$\mathbf{p}^2$	1	$-i$

Since for $D_4^{10}(1D_2^9)$ $g_4 = h_4$ then small representations are equal to ones loaded.

B-2. Rotations h of the subgroup have been denoted not the same way as it has been done in groups of class G in [5]. Magnetic classes $D_{4h}(2D_{2h})$, $C_{4v}(2C_{2v})$, $D_4(2D_2)$, $D_{2d}(2C_{2v})$, $D_{2d}(2D_2)$. The figure 2 means that symmetry axes and planes oriented at an angle of 45° with respect to axis x. Tables 3, 4, 5 contain the description of all subgroups allowed in this case. Appendix §5 contains their repre-

Table 3. The description of groups $C_{2v}^{11,13,18,19}$

Group	Type	h_4	h_{37}	h_{40}
C_{2v}^{11}	Γ_q			
C_{2v}^{13}	Γ_q		$00\tau_z$	$00\tau_z$
C_{2v}^{18}	Γ_q^v			
C_{2v}^{19}	Γ_q^v		$0\tau\frac{\tau_z}{2}$	$0\tau\frac{\tau_z}{2}$

Table 4. The description of groups $D_2^{5,6,7}$

Group	Type	h_{13}	h_{16}	h_4
D_2^5	Γ_q	$00\tau_z$		$00\tau_z$
D_2^6	Γ_q			
D_2^7	Γ_q^v			

Table 5. The description of groups D_{2h}^{19-24}

Group	Type	h_{13}	h_{16}	h_4	h_{25}	h_{37}	h_{40}	h_{28}
D_{2h}^{19}	Γ_q							
D_{2h}^{20}	Γ_q				$00\tau_z$	$00\tau_z$	$00\tau_z$	$00\tau_z$
D_{2h}^{21}	Γ_q				$\tau\tau 0$	$\tau\tau 0$	$\tau\tau 0$	$\tau\tau 0$
D_{2h}^{22}	Γ_q				$\tau\tau\tau_z$	$\tau\tau\tau_z$	$\tau\tau\tau_z$	$\tau\tau\tau_z$
D_{2h}^{23}	Γ_q^v							
D_{2h}^{24}	Γ_q^v				$0\tau\frac{\tau_z}{2}$	$0\tau\frac{\tau_z}{2}$	$0\tau\frac{\tau_z}{2}$	$0\tau\frac{\tau_z}{2}$

sentations. Subgroups G were denoted in the same way, as groups G' of orthorombic system which the subgroups may be identified with. In real magnetic crystal, the description of the subgroup G differs from that of corresponding subgroup in Table 3 no more than by a coordinate origin displacement. The comparison of subgroups and obtaining of the loaded representations is carried out by analogy with A-1 or A-2.

Case C

Magnetic classes $D_{2h}(C_{2h})$, $D_2(C_2)$, $C_{2v}(C_s)$. It turned out that the description of ways of obtaining the representations of subgroups G from those of groups G' are bulky. In this case, it is more expedient to give the method of direct constructing of the unitary subgroup representations, the more so, as it can be applied to case both magnetic groups and usual space groups (in [5] the method is not given).

In a group G, let us select elements $g_i = (\alpha_i/h_i)$ which do not change the vector K or add to it the reciprocal lattice vector. The set of these elements forms the group G_K of the vector K. If $g_i = (\alpha_i/h_i)$ and $g_K = (\alpha_K/h_K)$, then matrices of loaded representations satisfy the relation

$$\mathbf{t}(h_i)\mathbf{t}(h_K) = \Psi_{iK}\mathbf{t}(h_ih_K)$$

where $\Psi_{iK} = \exp\left[i(K - h_i^{-1}K, \alpha_K)\right]$ and $K - h_i^{-1}K$ is the reciprocal lattice vector. Calculating Ψ_{iK} for all g from G_K and using the product table of h_i [5], we compose the product table of matrices $\mathbf{t}(h_i)$. With the help of it, the matrices $\mathbf{t}(h_i)$ are determined. Selecting the simplest sets of figures or matrices, satisfying the product table, we obtain irreducible representations.

Irreducible representations $\mathbf{p}(h_i)$ are determined in the same way with the difference that some Ψ_{iK} must be multiplied by -1, as it pointed out in the product table in [5].

Example. Group $D_{2h}^6(C_{2h}^2)$, Γ_0, $C_2 \| y$. In accordance with the description of D_{2h}^6 [5], $G = C_{2h}^2\{h_1, (0.0.\tau_z/h_3), (\tau_x, \tau_y, 0/h_{25}), (\tau_x, \tau_y, \tau_z/h_{27})\}$. Let us consider $K = \frac{1}{2}b_1$. The group G_K consists of all elements of the group G. It is true that $\Psi_{3,25} = \Psi_{3,27} = \Psi_{25,25} = \Psi_{27,27} = -1$; the rest of Ψ_{iK} is equal to 1.

Taking into account product rules of rotations h (see [5]), we will obtain the product tables for $\mathbf{t}(h_i)$ and $\mathbf{p}(h_i)$.

$\mathbf{t}(h_1)$	$\mathbf{t}(h_3)$	$\mathbf{t}(h_{25})$	$\mathbf{t}(h_{27})$	$\mathbf{p}(h_1)$	$\mathbf{p}(h_3)$	$\mathbf{p}(h_{25})$	$\mathbf{p}(h_{27})$
$\mathbf{t}(h_3)$	$\mathbf{t}(h_1)$	$-\mathbf{t}(h_{27})$	$-\mathbf{t}(h_{25})$	$\mathbf{p}(h_3)$	$-\mathbf{p}(h_1)$	$-\mathbf{p}(h_{27})$	$\mathbf{p}(h_{25})$
$\mathbf{t}(h_{25})$	$\mathbf{t}(h_{27})$	$-\mathbf{t}(h_1)$	$-\mathbf{t}(h_3)$	$\mathbf{p}(h_{25})$	$\mathbf{p}(h_{27})$	$-\mathbf{p}(h_1)$	$-\mathbf{p}(h_3)$
$\mathbf{t}(h_{27})$	$\mathbf{t}(h_{25})$	$\mathbf{t}(h_3)$	$\mathbf{t}(h_1)$	$\mathbf{p}(h_{27})$	$-\mathbf{p}(h_{25})$	$\mathbf{p}(h_3)$	$-\mathbf{p}(h_1)$

The only matrices of order two can satisfy such tables.

	h_1	h_3	h_{25}	h_{27}
t	$\begin{pmatrix}1&0\\0&1\end{pmatrix}$	$\begin{pmatrix}1&0\\0&-1\end{pmatrix}$	$\begin{pmatrix}0&-1\\1&0\end{pmatrix}$	$\begin{pmatrix}0&1\\1&0\end{pmatrix}$
p	$\begin{pmatrix}1&0\\0&1\end{pmatrix}$	$\begin{pmatrix}i&0\\0&-i\end{pmatrix}$	$\begin{pmatrix}0&-1\\1&0\end{pmatrix}$	$\begin{pmatrix}0&i\\i&0\end{pmatrix}$

3. COREPRESENTATIONS OF GROUPS $G_{K,-K}$

Corepresentations of group $G_{K,-K}$ are constructed with the irreducible representations of the group G_K. There are three types of corepresentations ($g_0K = -K + b$).

(a) Representations $\Delta(g)$ and $\bar{\Delta}(g) = \Delta^*(g_0^{-1}gg_0)$ are equivalent, that is, $\bar{\Delta}(g) = \beta^{-1}\Delta(g)\beta$ the matrix β satisfies the equation $\beta\beta^* = \Delta(\theta^2 g_0^2)$. Corepresentation D is constructed by formulae [7]

$$D(g) = \Delta(g), D(\bar{g}\theta) = \Delta(\bar{g}g_0^{-1})\beta$$

where g and $\bar{g}\theta$ is unitary and antiunitary element of $G_{K,-K}$, respectively.

(b) Representations $\Delta(g)$ and $\bar{\Delta}(g)$ are equivalent, but matrix β satisfies the equation $\beta\beta^* = -\Delta(\theta^2 g_0^2)$. Then

$$D(g) = \begin{pmatrix}\Delta(g) & 0\\ 0 & \Delta(g)\end{pmatrix},$$

$$D(\bar{g}\theta) = \begin{pmatrix}0 & \Delta(\bar{g}g_0^{-1})\beta\\ -\Delta(\bar{g}g_0^{-1})\beta & 0\end{pmatrix}.$$

(c) Representations $\bar{\Delta}(g)$ and $\Delta(g)$ are inequivalent, but $\bar{\Delta}(g)$ is equivalent to some other representation of the group G_K, for example $\bar{\Delta}^1(g) = \beta^{-1}\Delta^2(g)\beta$. Two representations $\Delta^1(g)$ and $\Delta^2(g)$ form one corepresentation

$$D(g) = \begin{pmatrix}\Delta^1(g) & 0\\ 0 & \beta^{-1}\Delta^2(g)\beta\end{pmatrix},$$

$$D(\bar{g}\theta) = \begin{pmatrix}0 & \Delta^1(\bar{g}g_0\theta^2)\\ \beta^{-1}\Delta^2(\bar{g}g_0^{-1})\beta & 0\end{pmatrix}.$$

In order to determine the type of the corepresentation, it is convenient to use the criterion [9]

$$S = \frac{\kappa}{h}\sum \exp\left[-iK,\langle\alpha + h\alpha)\right]\mathbf{x}\,[h^2] = \begin{cases} 1\,(\mathrm{a})\\ -1\,(\mathrm{b})\\ 0\,(\mathrm{c})\end{cases}$$

where summation is over all different rotations h_i associated to antiunitary elements $\bar{g}\theta = (\alpha/h\theta)$ of the group $G_{K,-K}$; h and $\mathbf{x}$ is number of rotations and matrix character of a loaded representation, respectively; $\kappa = 1$ for **t** and $\kappa = -1$ for **p**.

The matrix β is determined by foregoing relations, being enough to consider only those which generate the group G_K.

Example. $D_6^3(D_3^5)$, $K = \frac{1}{2}b_3$. The description of the group is in example 1. In the group $G_{K,-K}$, rotations h_2, h_4, h_6, h_9, h_{11} associate to antiunitary elements. One can calculate the summation S, as is shown in Table 6. It follows from the table that $S_t^1 = S_t^2 = 0$ and $S_t^3 = 1$, that is, t^1 and t^2 form the type (c)

Table 6. The calculation of sum S. $\alpha' = (00(\tau_z/3))$; $w = e^{i(\pi/3)}$; $\alpha + h\alpha$ *is translation associated with* h^2; $x_t\bar{l}$ *is matrix loaded character of representation* **t**

	h_2	h_4	h_6	h_7	h_9	h_{11}
h_l^2	h_3	h_1	h_5	h_1	h_1	h_1
$\alpha + h\alpha$	$2\alpha'$	$6\alpha'$	$10\alpha'$	0	0	0
$\exp[-ik.\alpha + h\alpha]$	w^5	w^3	w	1	1	1
$x_t^1 = x_t^2$	w^4	1	w^2	1	1	1
x_t^3	w	2	w^5	2	2	2

corepresentation and t^3 forms the type (a) corepresentation. Let $g_0 = g_4 = (3\alpha'/h_4)$. Then $g_4^{-1} = (3\alpha'/h_4)$. Productions $\bar{g}g_4$ and $\bar{g}g_4^{-1}$, where $\bar{g}$ is element, belonging to set of $\bar{G}$, are given in Table 7. For corepresentation $D^{1,2}$ formed by one-dimentional representation t^1 and t^2, $\beta = 1$. For D^3, matrix β is determined by equations

$$\beta\beta\dagger = 1, \beta\beta^* = t^3(g_4^2) = t^3(a_3) = -1,$$

$$\beta t^{3*}(g_4^{-1}g_3g_4) = t^3(g_3)\beta,$$

$$\beta t^{3*}(g_4^{-1}g_8g_4) = t^3(g_8)\beta.$$

Since $g_4^{-1}g_3g_4 = g_3$ and $g_4^{-1}g_8g_4 = (-a_3/g_8)$, then we have

$$\beta = \begin{pmatrix} 0 & 1 \\ -1 & 0 \end{pmatrix}.$$

Finally, matrices of corepresentations are (for some elements)

	g_3	g_8	$g_2\theta$	$g_7\theta$
$D^{1,2}$	$\begin{pmatrix} -1 & 0 \\ 0 & -1 \end{pmatrix}$	$\begin{pmatrix} 1 & 0 \\ 0 & -1 \end{pmatrix}$	$\begin{pmatrix} 0 & 1 \\ -1 & 0 \end{pmatrix}$	$\begin{pmatrix} 0 & 1 \\ 1 & 0 \end{pmatrix}$
D^3	$\begin{pmatrix} \nu^{10} & 0 \\ 0 & \nu^2 \end{pmatrix}$	$\begin{pmatrix} 0 & 1 \\ 1 & 0 \end{pmatrix}$	$\begin{pmatrix} 0 & \nu^2 \\ \nu^{10} & 0 \end{pmatrix}$	$\begin{pmatrix} \nu^4 & 0 \\ 0 & \nu^2 \end{pmatrix}$

Table 7. The productions gg_4 *and* gg_4^{-1}

	g_2	g_4	g_6	g_7	g_9	g_{11}
gg_4	g_5	(a_3/g_1)	(a_3/g_3)	$(-a_3/g_{10})$	$(-a_3/g_{12})$	g_8
$\bar{g}g_4^{-1}$	$(-a_3/g_5)$	g_1	g_3	g_{10}	g_{12}	(a_3/g_8)

Corepresentations with **p** are constructed in the analogical way.

4. CONCLUSION

If element θ is added to the magnetic group, it results in a neutral group in which elements g and $g\theta$ are contained together. In many cases, the neutral group is a group of the chemical symmetry of the crystal and coincides with the whole group of a magnetic crystal in the non-magnetic phase. Corepresentations of some neutral groups were considered in [11, 12, 13]. Thus, the transition from the nonmagnetic phase to the magnetic one are accompanied by lowering of the symmetry and, possibly, partial or whole splitting of the energy-levels. To determine the splitting, it should be compared with the corepresentations of the neutral group with those of the magnetic group.

Later on, authors intend to publish corepresentations of all neutral and magnetic groups.

Acknowledgements—The authors wish to thank Professor Akhiezer A.I. and Professor Lifshitz I.M. for the interest shown in the work.

REFERENCES

1. BELOV N. V., NERONOVA N. N. and SMIR-

NOVA T. S., *Trudy-Inst. Krist. Akad. Nauk SSSR*, **11**, 33 (1955).
2. ZAMORZAEV A. M., *Kristallografiya* **2**, 15 (1957).
3. INDEMBOM V. L., *Kristallografiya* **4**, 619 (1959); **5**, 513 (1960).
4. FADDEYEV D. K., *Tables of Basic Unitary Representations of Fedorov Groups*. Moscow (1961).
5. KOVALEV O. V., *Irreducible Representations of the Space Groups*. Kiev (1961); English edition; Gordon & Breach, New York (1965).
6. DIMMOCK J. O. and WHEELER R. G., *Phys. Rev.* **127**, 391 (1962).
7. WIGNER E. P., *Group Theory* (Russian translation). Moscow (1961).
8. LYUBARSKY G. J., *Group Theory and its Application in Physics*. Moscow (1957).
9. CHALDISHEV V. A., KUDRYAVTZEVA N. V. and KARAVAYEV G. F., *Izv. vuzov SSSR. Fiz.* **2**, 46 (1963).
10. KOPTZIK V. A., *Shubnikov Groups*. Moscow University edition (1966).
11. HERING C., *Phys. Rev.* **52**, 365 (1937).
12. ELLIOTT R. J., *Phys. Rev.* **96**, 266, 280, (1954).
13. PARMENTER R. H., *Phys. Rev.* **100**, 573, (1955).

APPENDIX

§1. *Description and representations of* $D_{2d}^{9,10}\Gamma_q^v$

Both groups contain rotations h_1, h_{38}, h_4, h_{39}, h_{16}, h_{26}, h_{13}, h_{27}; for $D_{2d}^{9}\alpha_i = 0$. for $D_{2d}^{10}\alpha_{16,26,13,27} = (0, 0, \tau_z)$. Representations: $K_1, K_6, K_{11} - 10$. $K_2, K_3, K_4, K_5 - 0$. $K_7 - 130$. $K_8 - 171$. $K_9 - 3$. $K_{10} - 11$. $K_{12} - 117$. $K_{13} - 172$. $K_{14}, K_{15} - 131$.

§2.

$\Gamma_m - a_1$ and a_2 are in plane $z = 0$, $a_3 = (0, 0, 2\tau_z)$. $\Gamma_m{}^b - a_1$ is in plane $z = 0$; a_2 and a_3 symmetrically arranged with respect to plane $Z = 0$.

§3. *Representations of groups of class* C_{2v}, *lattices* $\Gamma_0, \Gamma_0^f, \Gamma_0^v$

$C_{2v}{}^2(C_2\|z, b)$ $K_1, K_2, K_8, K_{13}, K_{14}, K_{15} - 9$. $K_3, K_4, K_7, K_{10}, K_{11}, K_{12} - 10$. $K_5, K_6 - 0$. K_9, K_{16}–$K_{26} - 11$.

$C_{2v}^{5,6}(C_2\|z, b)$. $K_1, K_2, K_8, K_{13}, K_{14}, K_{15} - 9$. $K_3, K_4, K_7, K_{10}, K_{11}, K_{12} - 10$. $K_5, K_6 - 0$. $K_9, K_{16}, K_{19}, K_{20}, K_{22}, K_{24} - 11$.
$K_{17}, K_{18}, K_{21}, K_{23}, K_{25}, K_{26} - 345$.

$C_{2v}^{9}(C_2\|z, b)$. $K_1, K_2, K_8, K_{13}, K_{14}, K_{15} - 9$. $K_3, K_4, K_7, K_{10}, K_{11}, K_{12} - 10$. $K_5, K_6 - 0$. $K_9, K_{19}, K_{22} - 11$.
$K_{16}, K_{20}, K_{24} - 346$. $K_{17}, H_{25}, K_{26} - 13$. $K_{18}, K_{21}, K_{23} - 345$.

$C_{2v}^{1,2}(C_2\|x, a)$. $K_1, K_2 - 0$. $K_3, K_4, K_9, K_{16}, K_{17}, K_{18} - 10$. $K_5, K_6, K_8, K_{13}, K_{14}, K_{15} - 2$. $K_7, K_{10}, K_{11}, K_{12}, K_{19}$–$K_{26} - 30$.

$C^{5-7}(C_2\|x, a)$. $K_1, K_2 - 0$. K_3, K_4, K_9, K_{16}–$K_{18} - 10$. K_5, K_6, K_8, K_{13}–$K_{15} - 2$.
$K_7, K_{12}, K_{19}, K_{20}, K_{22}, K_{24} - 30$. $K_{10}, K_{11}, K_{21}, K_{23}, K_{25}, K_{26} - 63$.

$C_{2v}^{8,9}(C_2\|x, a)$. $K_1, K_2 - 0$. K_3, K_4, K_9, K_{16}–$K_{18} - 10$. K_5, K_6, K_8, K_{13}–$K_{15} - 2$. $K_7, K_{19}, K_{20} - 30$.
$K_{10}, K_{21}, K_{25} - 63$. $K_{11}, K_{23}, K_{26} - 340$. $K_{12}, K_{22}, K_{24} - 341$.

$C_{2v}^{4,7}(C_2\|x, b)$. $K_1, K_2 - 0$. K_3, K_4, K_9, K_{16}–$K_{18} - 10$. K_5, K_6, K_8, K_{13}–$K_{15} - 2$. K_7, K_{10}, K_{19}–$K_{21}, K_{25} - 30$.
K_{11}, K_{12}, K_{22}–$K_{24}, K_{26} - 341$.

$C_{2v}^{9,10}(C_2\|x, b)$. $K_1, K_2 - 0$. K_3, K_4, K_9, K_{16}–$K_{18} - 10$. K_5, K_6, K_8, K_{13}–$K_{15} - 2$. $K_7, K_{19}, K_{20} - 30$.
$K_{10}, K_{21}, K_{25} - 63$. $K_{11}, K_{23}, K_{26} - 340$. $K_{12}, K_{22}, K_{24} - 341$.

$C_{2v}^{1,3}(C_2\|y, b)$, $C_{2v}^{2}(C_2\|y, a)$. K_1, K_2, K_9, K_{16}–$K_{18} - 9$. $K_3, K_4 - 0$. K_5–K_7, K_{10}–$K_{12} - 2$. K_8, K_{13}–K_{15}, K_{19}–$K_{26} - 31$.

$C_{2v}^{4,6}(C_2\|y, b)$. K_1, K_2, K_9, K_{16}–$K_{18} - 9$. $K_3, K_4 - 0$. K_5–K_7, K_{10}–$K_{12} - 2$.
$K_8, K_{15}, K_{19}, K_{21}$–$K_{23} - 31$. $K_{13}, K_{14}, K_{20}, K_{24}$–$K_{26} - 342$.

$C_{2v}^{9}(C_2\|y, b)$. $K_1, K_2, K_9, K_{16}, K_{17}, K_{18} - 9$. $K_3, K_4 - 0$. $K_5, K_6, K_7, K_{10}, K_{11}, K_{12} - 2$.
$K_8, K_{19}, K_{21} - 31$. $K_{13}, K_{20}, K_{25} - 64$. $K_{14}, K_{24}, K_{26} - 343$. $K_{15}, K_{22}, K_{23} - 344$.

$C^{18}(C_2\|x, a)$. $K_1, K_{10}, K_{11}, K_{12}, K_{13} - 0$. $K_2, K_8, K_9, K_{18} - 10$. $K_3, K_6, K_7 - 2$. $K_4, K_5, K_{14}, K_{15}, K_{16}, K_{17} - 30$.

$C_{2v}^{19}(C_2\|x, a)$. $K_1, K_{10}, K_{11}, K_{12}, K_{13} - 0$. $K_2, K_9, K_{18} - 10$. $K_3, K_6, K_7 - 2$. $K_4, K_{14}, K_{15} - 30$. $K_5, K_{16} - 63$. $K_{17} - 341$.

$C_{2v}^{20,22}(C_2\parallel x, a)$, $C_{2v}^{21,23}(C_2\parallel x, b)$. K_1, K_5, K_6-0. $K_2, K_9, K_{11}, K_{14}-10$. $K_3, K_8, K_{12}, K_{15}-2$.
$K_1, K_{10}, K_{13}, K_{16}-15$. $K_7, K_{17}, K_{18}-30$.

§4. *Representations of* $C_{2v}^{14,15,16,17}$ *(Table 2)*

$C_{2v}^{14,15}$. K_1, K_6, K_7-9, K_2, K_5-0. $K_3, K_4, K_8, K_9, K_{12}, K_{13}-2$. $K_{10}, K_{11}, K_{14}, K_{15}, K_{16}, K_{17}-31$.

$C_{2v}^{16,17}$. K_1, K_6, K_7-9. K_2, K_5-0. $K_3, K_8, K_{12}-2$. $K_4, K_9, K_{13}-35$. $K_{10}, K_{14}, K_{15}-31$. $K_{11}, K_{16}, K_{17}-43$.

§5. *Representations of groups given in Tables* 3, 4, 5

$C_{2v}^{11,13}$. $K_1, K_2, K_3, K_4, K_6, K_7, K_8, K_9-0$. $K_5, K_{10}, K_{11}-118$. $K_{12}, K_{15}, K_{16}-3$. $K_{13}, K_{14}, K_{17}, K_{18}, K_{19}, K_{20}-126$.

C_{2v}^{18}. $K_1, K_2, K_5, K_6, K_{11}-0$. K_3, K_7-118. K_4, K_8-166. $K_9, K_{10}, K_{12}, K_{13}, K_{14}, K_{15}-126$.

C_{2v}^{19}. $K_1, K_2, K_5, K_6, K_{11}-0$. K_3, K_7-118. K_4, K_8-167. $K_9, K_{12}, K_{13}-168$. $K_{10}, K_{14}, K_{15}-126$.

$D_2^{5,6}$. K_1-$K_7 0$. $K_{10}, K_{11}-130$. K_{12}-$K_{16}-3$. $K_{17}, K_{18}--172$. $K_{19}, K_{20}-338$ (for D_2^5), 172 (for D_2^6).

D_2^7. K_1-K_6, $K_{11}-0$. K_7-130. K_8-171. $K_9, K_{10}, K_{12}-3$. $K_{13}, K_{14}, K_{15}-172$.

$D_{2h}^{19,21}$. $K_1, K_2, K_6, K_7, K_8, K_9-2$. K_3, K_4-0. K_5-118. $K_{10}, K_{11}-146$. $K_{12}-3$. $K_{13}, K_{14}-126$.
$K_{15}, K_{16}-4$ (for D_{2h}^{19}), 99 (for D_{2h}^{21}). K_{17}-$K_{20}-176$.

$D_{2h}^{20,22}$. K_1, K_6, K_8-2. K_2, K_7, K_9-35. K_3, K_4-0. K_5-118. $K_{10}--146$. $K_{11}-148$. $K_{12}-3$. $K_{13}, K_{14}-126$.
$K_{15}-4$ (for D_{2h}^{20}), 99 (for D_{2h}^{22}), $K_{16}-101$ (for D_{2h}^{20}), 102 (for D^{22}). $K_{17}, K_{18}-176$. $K_{19}, K_{20}-300$.

D_{2h}^{23}. K_1, K_5-0. K_2, K_6-2. K_3-118. K_4-166. K_7-146. K_8--175. $K_9, K_{10}, K_{12}-126$. $K_{11}-1$. $K_{13}, K_{14}, K_{15}-176$.

D_{2h}^{24}. K_1, K_5-0. K_2, K_6-2. K_3-118. K_4-167. K_7-146. K_2-172. $K_9, K_{12}-168$.
$K_{10}-126$. $K_{11}-104$. $K_{13}-181$. $K_{14}-176$. $K_{15}-300$.

§6. *Additional representations*

$P340$	h_1	h_2	h_{27}	h_{28}
	$\begin{pmatrix}1&0\\0&1\end{pmatrix}$	$\begin{pmatrix}-i&0\\0&i\end{pmatrix}$	$\begin{pmatrix}0&1\\-1&0\end{pmatrix}$	$\begin{pmatrix}0&-i\\-i&0\end{pmatrix}$

$T338$	h_1	h_{13}	h_{16}	h_4
	$\begin{pmatrix}1&0\\0&1\end{pmatrix}$	$\begin{pmatrix}0&1\\-1&0\end{pmatrix}$	$\begin{pmatrix}0&1\\1&0\end{pmatrix}$	$\begin{pmatrix}1&0\\0&-1\end{pmatrix}$

$T340$	h_1	h_2	h_{27}	h_{28}
$T343$	h_1	h_3	h_{26}	h_{28}
$\mathbf{t}^1$	1	1	1	-1
$\mathbf{t}^2$	1	1	-1	1
$\mathbf{t}^3$	1	-1	1	1
$\mathbf{t}^4$	1	-1	-1	-1

$T341$	h_1	h_2	h_{27}	h_{28}
$T342$	h_1	h_3	h_{28}	h_{26}
$T344$	h_1	h_3	h_{26}	h_{28}
$T345$	h_1	h_4	h_{26}	h_{27}
$T346$	h_1	h_4	h_{27}	h_{26}
	$\begin{pmatrix}1&0\\0&1\end{pmatrix}$	$\begin{pmatrix}-i&0\\0&i\end{pmatrix}$	$\begin{pmatrix}0&1\\1&0\end{pmatrix}$	$\begin{pmatrix}0&i\\-i&0\end{pmatrix}$

$P343$	h_1	h_3	h_{26}	h_{28}
	$\begin{pmatrix}1&0\\0&1\end{pmatrix}$	$\begin{pmatrix}-i&0\\0&i\end{pmatrix}$	$\begin{pmatrix}0&1\\-1&0\end{pmatrix}$	$\begin{pmatrix}0&i\\i&0\end{pmatrix}$

$P338$	h_1	h_{13}	h_{16}	h_4
$P344$	h_1	h_3	h_{26}	h_{28}
$\mathbf{P}^1$	1	1	i	$-i$
$\mathbf{P}^2$	1	1	$-i$	i
$\mathbf{P}^3$	1	-1	i	i
$\mathbf{P}^4$	1	-1	$-i$	$-i$

$P341$	h_1	h_2	h_{27}	$h_{\ 8}$
$P342$	h_1	h_3	h_{26}	h_{28}
$P345$	h_1	h_4	h_{26}	h_{27}
$P346$	h_1	h_4	h_{27}	h_{26}
$\mathbf{P}^1$	1	1	i	i
$\mathbf{P}^2$	1	1	$-i$	$-i$
$\mathbf{P}^3$	1	-1	i	$-i$
$\mathbf{P}^4$	1	-1	$-i$	i

	h_1	h_{13}	h_{16}	h_4	h_{25}	h_{37}	h_{40}	h_{28}
$T300$, $\mathbf{t}^1$	$\begin{pmatrix}1&0\\0&1\end{pmatrix}$	$\begin{pmatrix}1&0\\0&-1\end{pmatrix}$	$\begin{pmatrix}1&0\\0&-1\end{pmatrix}$	$\begin{pmatrix}1&0\\0&1\end{pmatrix}$	$\begin{pmatrix}0&1\\-1&0\end{pmatrix}$	$\begin{pmatrix}0&-1\\-1&0\end{pmatrix}$	$\begin{pmatrix}0&-1\\-1&0\end{pmatrix}$	$\begin{pmatrix}0&1\\-1&0\end{pmatrix}$
$P300$, $\mathbf{P}^1$	$\begin{pmatrix}1&0\\0&1\end{pmatrix}$	$\begin{pmatrix}i&0\\0&-i\end{pmatrix}$	$\begin{pmatrix}0&1\\-1&0\end{pmatrix}$	$\begin{pmatrix}0&-i\\-i&0\end{pmatrix}$	$\begin{pmatrix}0&i\\i&0\end{pmatrix}$	$\begin{pmatrix}0&1\\-1&0\end{pmatrix}$	$\begin{pmatrix}-i&0\\0&i\end{pmatrix}$	$\begin{pmatrix}1&0\\0&1\end{pmatrix}$

$\mathbf{t}^2=\mathbf{t}^1\times\mathbf{t}^5$ ($T176$, $\mathbf{P}^2=\mathbf{P}^1\times\mathbf{t}^5$ ($T176$).

§7. *Corrections of* [5]

$P12.$	h_4	h_{26}	h_{27}
C_{2v}^{21}		$00\tau_z$	$00\tau_z$

$P42$. Add $K_{18}=\mu(b_1+b_2)+\frac{1}{2}(b_2+b_3)|h_1, h_4, h_{26}, h_{27}$.
$P43$. C_{2v}^{19}. K_1-9. K_2-10. K_8-11. K_9-14. $K_{18}-12$. C_{2v}^{18}, D_{2h}^{23}. $K_{18}-11$. $D_2{}^7$. $K_{18}-3$. D_{2h}^{24}. $K_{18}-38$.
$P45$. D_{2h}^{28}. K_8-31. $P48$. D_{2d}^2. K_8-16. D_{2d}^3. $K_{12}-3$. $P51$. D_{4h}^6. $K_{18}-152$. $P61,62$. $T_d{}^{2,5}$. $K_{10}-127$. O^3. K_4-130.
$P63,64$. Add $K_{13}=\frac{1}{2}(1-\mu)(b_1+b_2)+\frac{1}{2}(3\mu-1)b_3|h_1, h_6, h_{11}, h_{37}, h_{42}, h_{47}$. T^3, $T_h{}^5$, O^5. $K_{13}-268$. T^3, $T_h{}^7$, O^8.
$K_{13}=269$. $T_d{}^3$, $O_h{}^9$. $K_{13}-270$. $T_d{}^6$, $O_h{}^{10}$. $K_{13}-271$. $P66$. Hexagonal system. $b_1\perp e_y$, $b_2\perp e_x$. Add ($P74$)

$T29$	h_1	h_2	h_3	h_4
	$\begin{pmatrix}1&0\\0&1\end{pmatrix}$	$\begin{pmatrix}i&0\\0&-i\end{pmatrix}$	$\begin{pmatrix}0&1\\-1&0\end{pmatrix}$	$\begin{pmatrix}0&i\\i&0\end{pmatrix}$

Correct: $P77$. $\mathbf{P}^j(P77)=\mathbf{t}^j(T31)$.

	h_{26}	h_{40}	h_{27}	h_{37}
$P119$	$\begin{pmatrix}1&0\\-1&0\end{pmatrix}$	$\begin{pmatrix}0&\delta\\\delta^3&0\end{pmatrix}$	$\begin{pmatrix}0&-i\\-i&0\end{pmatrix}$	$\begin{pmatrix}0&\delta^3\\\delta&0\end{pmatrix}$
$P120$	$\begin{pmatrix}0&i\\-i&0\end{pmatrix}$	$\begin{pmatrix}0&\delta^7\\\delta^7&0\end{pmatrix}$	$\begin{pmatrix}0&1\\1&0\end{pmatrix}$	$\begin{pmatrix}0&\delta\\\delta^3&0\end{pmatrix}$

$P160$	h_2	h_{13}	h_{25}
$\mathbf{P}^1$	$\begin{pmatrix}i&0\\0&-i\end{pmatrix}$	$\frac{1}{\sqrt{2}}\begin{pmatrix}1&i\\-i&-1\end{pmatrix}$	$\begin{pmatrix}0&1\\1&0\end{pmatrix}$

$\mathbf{P}^2=\mathbf{P}^1\times\mathbf{t}^2(T147)$
$\mathbf{P}^3=\mathbf{P}^1\times\mathbf{t}^5(T147)$
$\mathbf{P}^4=\mathbf{P}^1\times\mathbf{t}^6(T147)$

$P147$, $P149$, $P152$, $P153$. $\mathbf{P}^3=\mathbf{P}^1\times\mathbf{t}^5(T147)$, $\mathbf{P}^4=\mathbf{P}^1\times\mathbf{t}^6(T147)$

		1, 2, 4, 5, 6, 7, 10	3, 8, 9, 11, 12	13, 16, 17, 18, 21, 23, 24	14, 15, 19, 20, 22	25, 26, 28, 29, 30, 31, 34	27, 32, 33, 35, 36	37, 40, 41, 42, 45, 47, 48	38, 39, 33, 44, 46
$P187$	$\mathbf{P}^1$	1	-1						
$P190$	$\mathbf{P}^1$	1	-1			1	-1		
$P200$	$\mathbf{P}^1$	1	-1	δ	δ^5				
$P204$	$\mathbf{P}^1$	1	-1	δ^3	δ^7				
$P231$	$\mathbf{P}^1$	1	-1					i	$-i$

J. Phys. Chem. Solids Pergamon Press 1970. Vol. 31, pp. 163–171. Printed in Great Britain.

TIME AND INTENSITY DEPENDENCE OF THE PHOTOLYSIS OF LEAD HALIDES

J. F. VERWEY*
Solid State Chemistry Department, University of Utrecht, Jutphaas, Netherlands

(*Received* 10 *December* 1968; *in revised form* 14 *April* 1969)

Abstract—The rate of the photochemical decomposition (photolysis) of lead halides by u.v. light was investigated by measuring the change of the optical density ΔD after irradiation. It was found that the time dependence of the photolysis in $PbCl_2$, $PbBr_2$ and PbI_2 is not essentially different. The maximum in the photolysis of $PbCl_2$ as a function of the intensity could be explained by the assumption that photo-enhanced evaporation occurs at high intensities. The mechanism of the photolysis in $PbBr_2$ and $PbCl_2$ is supposedly the transport of photogenerated holes to the surface and trapping at surface halogen ions. The halogen atoms formed are desorbed and the anion vacancies created in this way diffuse into the crystal. The photogenerated electrons react with Pb^{2+} ions to give Pb atoms in an aggregated state accompanied by annihilation of anion vacancies.

INTRODUCTION

THE PHOTOCHEMICAL behavior of the lead halides shows a great similarity to that of the silver halides. Like the latter, they decompose under the action of photons of suitable wavelength[1]. For the silver halides a mechanism for the photochemical decomposition (photolysis) has been proposed[2]. This mechanism is based upon the Gurney–Mott principle[3], which states that the photochemical decomposition of the silver halides consists of an ionic and an electronic part. Absorption of a photon by the crystal excites an electron into the conduction band. This electron moves to a suitable trapping site where it combines with an interstitial silver ion. By the movement and trapping of more electrons and interstitial ions to this site an aggregate of silver atoms is formed. The holes can be trapped at surface halogen ions, followed by the desorption of halogen atoms.

Dawood, Forty and Tubbs[4, 5] have extensively studied the photochemical decomposition of lead iodide. The mechanism they propose is the reaction of two excitons at a suitable surface site, eventually leading to the production of an iodine molecule, a lead atom and two anion vacancies next to the original site[5]. This mechanism accounts for the quadratic dependence of the decomposition rate on irradiation intensity. Furthermore, the photodecomposition varies as the square root of the irradiation time. They explained this by assuming that a surface layer of lead and lead salts is formed; the diffusion through this layer of the iodine formed is rate-determining[5].

De Vries and van Santen[6] pointed to the importance of the transport of anion vacancies during the thermal decomposition of $PbCl_2$. This was concluded from their experiments on ionic conductivity[7, 8]. Kaldor and Somorjai[9] also used the results of ionic conductivity[7, 8, 10] measurements to propose a vacancy mechanism for the photochemical decomposition of $PbCl_2$. The present measurements on the photolysis of $PbCl_2$ doped with cation impurities confirm this proposal. From similar measurements on $PbBr_2$ it can be concluded that also in this substance the mass transport during photolysis is carried by the anion vacancies[12]. To reach this conclusion use was made of the measurements on the ionic conductivity of $PbBr_2$[11, 12]. From these measurements, together with the results of the transport number determinations from the literature[13] it can be concluded that in $PbBr_2$ too the anion vacancies are the dominant mobile lattice defects.

---

*Present address: Philips Research Laboratories, N.V. Philips' Gloeilampenfabrieken, Eindhoven, Netherlands.

Photoconductivity experiments revealed [12, 14] that holes are the mobile charge carriers in $PbBr_2$ and $PbCl_2$.

Electron spin resonance measurements[15] on $PbCl_2$, $PbBr_2$ and PbI_2 irradiated with u.v. light at liquid nitrogen temperature indicate that Pb^+ ions are formed as an initial step in the photochemical decomposition. These Pb^+ ions coagulate to metallic lead particles. Also reaction products of holes with lattice defects have been detected, like a hole trapped at a cation vacancy. At higher temperatures, viz. at room temperature, this centre is not stable. Probably, it dissociates again into a free hole and a vacancy.

In this paper we will present some quantitative optical measurements on the photolysis of $PbCl_2$, $PbBr_2$ and PbI_2. These measurements will be discussed in terms of particle currents to and from the surface, particularly, the migration of anion vacancies and photogenerated holes.

EXPERIMENTAL

The crystals investigated were grown from the melt. The details of crystal preparation have been given elsewhere[8, 11, 12]. The set-up for the optical measurements and irradiation of the crystals is shown schematically in Fig. 1. The optical filter *c* is an interference reflectance filter (UV-R-250) with centre-frequency at 250 nm. The intensity of the irradiation lamp was measured by comparison with a standard high pressure mercury lamp.

With this set-up we were able to measure the optical density D of the crystals as a function of wavelength. D is given by $D = \log(I_0/I)$, where I_0 is the amount of light incident on the crystals and I is the amount of light transmitted by them. The

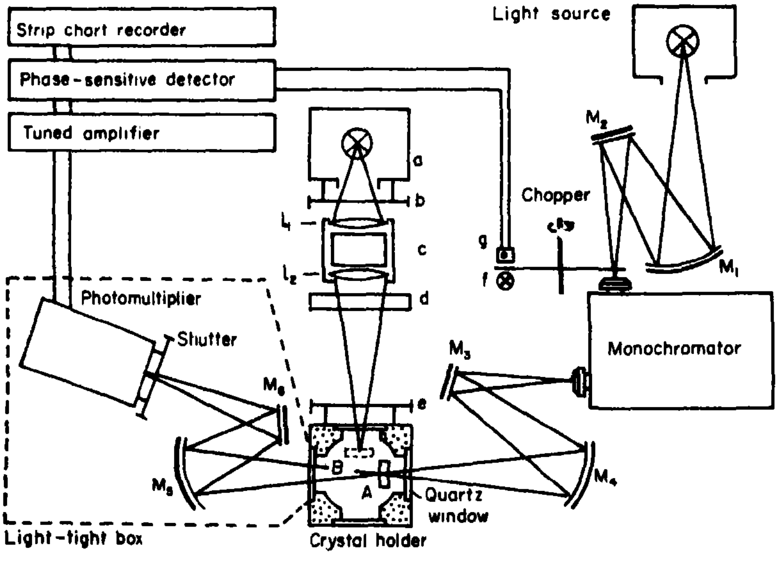

Fig. 1. Spectrophotometer. A = crystal in the position for the measurement of optical transmission, B = position into which the crystal can be turned for irradiation, M = surface-coated mirrors, a–e = irradiation unit, a = irradiation lamp (HBO 200), b = shutter, c = optical filter, d = neutral density filter, e = shutter, l_1, l_2 = quartz lenses, f–g = unit for the production of a reference signal, f = lamp, g = photo-sensitive transistor.

change of the optical density ΔD at one wavelength is a measure of the photodecomposition [1]. The accuracy of D is ±0·001 in the low optical density ranges. Unless otherwise indicated, all measurements were made on crystals mounted and measured immediately after cleavage under red safe-light in air. The crystals were irradiated in a vacuum of 10^{-6} mm Hg, except the crystal in Fig. 6, which was irradiated in alcohol vapour. This vapour was in equilibrium with liquid alcohol of 0°C. $PbCl_2$ and $PbBr_2$ were irradiated at room temperature and PbI_2 at 200°C.

RESULTS

Figure 2 shows the photolysis of PbI_2 as a function of irradiation time t. The curve $\Delta D \propto t^{1/2}$ is also drawn in the figure. The results indicate that ΔD is proportional to the square root of t for a part of the curve. The irradiation did not take place with the irradiation set-up in Fig. 1, but as indicated in the caption of Fig. 2. Figure 3 shows the photodecomposition of two $PbBr_2$ crystals. Irradiation took place with the set-up in Fig. 1 which accounts for the different time scales of Figs. 2 and 3. Here again the lines $\Delta D \propto t^{1/2}$ are shown.

The variation of $PbCl_2$ photolysis with irradiation time is shown in Fig. 4. The first part of the curve appears to be proportional to t.

The intensity dependence of the $PbCl_2$ photolysis is shown in Fig. 5. There is a

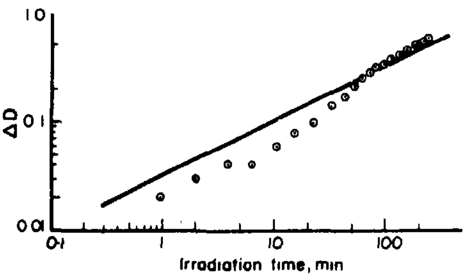

Fig. 2. Change of the optical density ΔD at $\lambda = 589$ nm as a function of the irradiation time of a PbI_2 crystal. Irradiation with a high pressure mercury lamp (HPK 125) at a temperature of about 200°C in vacuum (10^{-6} mm Hg).

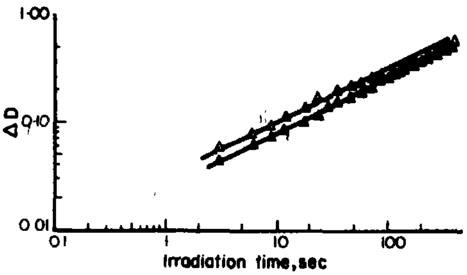

Fig. 3. Optical density change ΔD ($\lambda = 589$ nm) of two $PbBr_2$ crystals as a function of irradiation time ($\lambda = 250$ nm, room temperature). Intensity $(8 \pm 2) \times 10^5\ \mu W/cm^{-2}$. After cleavage the crystals were annealed in vacuum.

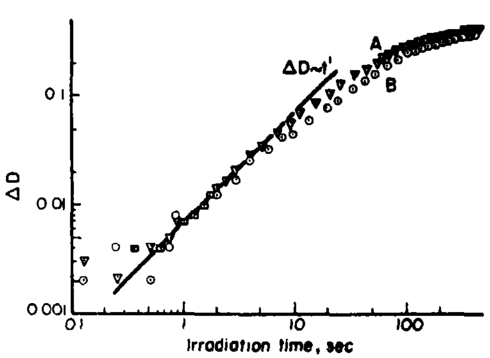

Fig. 4. Optical density change ΔD at $\lambda = 589$ nm as a function of irradiation time. A = $PbCl_2$ doped with 0·01 wt. % Tl, B = undoped $PbCl_2$ crystal. Irradiation in vacuum with $\lambda = 250$ nm at room temperature. Intensity about $6 \times 10^5\ \mu W/cm^{-2}$.

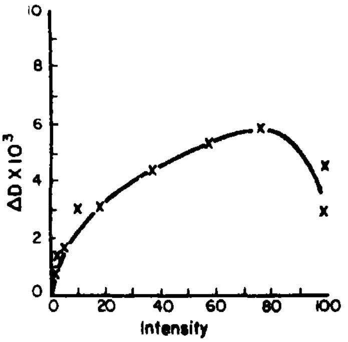

Fig. 5. Optical density change ΔD ($\lambda = 589$ nm) upon irradiating $PbCl_2$ crystals with different intensities ($\lambda = 250$ nm) for 10 seconds. The intensity at $I = 100$ corresponds to $(8 \pm 2) \times 10^5\ \mu W/cm^{-2}$.

maximum in the curve at an incident light intensity of about $6 \times 10^5 \mu W cm^{-2}$.

In Fig. 6 ΔD is plotted as a function of wavelength for a $PbCl_2$ crystal irradiated in alcohol. These curves are shown as an example. Identical curves were obtained after irradiation in air or in vacuum, but at a lower value of ΔD after the same irradiation time.

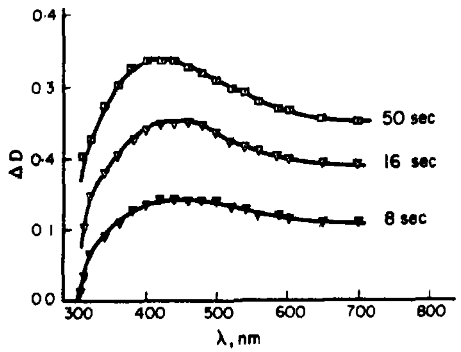

Fig. 6. Optical density change ΔD as a function of wavelength of a $PbCl_2$ crystal. The crystal was irradiated in alcohol vapour ($\lambda = 250$ nm). The irradiation times are indicated in the figure.

DISCUSSION

(*a*) *Three modes of photolysis*

We can describe the photolytic process in the following way. The absorption of a photon gives an electron-hole pair. According to the processes which follow this absorption, we may discern three modes in the photolysis. Firstly, transport and trapping of photogenerated electrons and holes. Irradiation of lead halides at liquid nitrogen temperature gave reaction products of electrons and holes with lattice defects, detectable by electron spin resonance[15]. We call this the colour centre mode.

Secondly, in addition to charge transport there may be mass transport by ionic motion. This happens in lead halides upon irradiation at a temperature near room temperature. This gives small lead particles inside the crystal near the surface. This is the print-out mode.

Thirdly, there is the mode where substance is completely evaporated from the surface, the photo-enhanced evaporation mode.

These effects can also be illustrated with the example of cadmium sulphide. CdS photodecomposes at 400°C[17]. Apparently in this substance the second mode is operative at this temperature. At a higher temperature (700°C) photoenhanced evaporation occurs. Hence, in CdS a transition from one mode to the other takes place as a function of temperature.

(*b*) *The photolysis in* $PbBr_2$ *and* $PbCl_2$

In $PbBr_2$ and $PbCl_2$ the photogenerated hole is trapped at a surface halogen ion, giving a halogen atom. This atom is desorbed which explains the influence of ambient conditions on the photolysis[12]. For instance the rate of photodecomposition is greater in alcohol vapour than in air. The alcohol is assumed to react with halogen.

The electrons produced by the photons are trapped at Pb^{2+} ions, ultimately giving aggregates of lead atoms.

The impurity content of the crystals has a certain influence on the photolysis (cf. Fig. 4), though less than the ambient conditions. Generally the photolysis is faster in crystals doped with monovalent cations[12, 16]. It is known that in this case the crystals contain a higher concentration of anion vacancies, thus fulfilling the condition of electro-neutrality[6, 11]. These vacancies can facilitate the photolysis process in three ways. Firstly, the vacancies carry the mass transport current of anions to the surface. Secondly, because of the Schottky equilibrium an enhanced anion vacancy concentration is accompanied by a reduced concentration of the cation vacancies $V_{Pb^{2+}}$. Presumably the $V_{Pb^{2+}}$ are shallow traps for holes. Therefore, this reduced concentration of $V_{Pb^{2+}}$ increases the hole current to the surface. Thirdly, annihilation of anion vacancies supplies room for the lead nuclei since lead atoms have a larger radius than the lead ions.

The fact, that in reality an aggregation of lead atoms takes place was shown by the qualitative agreement of ΔD as a function of wavelength (Fig. 6) and the calculated absorption of small lead particles [12].

The time dependence of the photolysis (Figs. 2–4) will be discussed below in connection with the photolysis in PbI_2.

(*c*) *The intensity dependence of the photolysis in* $PbCl_2$

The intensity dependence of the photolysis in $PbCl_2$, especially the maximum in ΔD vs. intensity of the irradiation (Fig. 5), can be explained as a transition from one mode of photolysis to another. At intensities below $6\times 10^5\,\mu W/cm^2$ holes are trapped at surface halogen ions, producing surface halogen atoms which can be desorbed. The excess lead condenses inside the crystal (print-out mode). At higher intensities more or less complete $PbCl_2$ molecules are desorbed from the surface (photo-enhanced evaporation mode). This can be understood according to Levine Mark [18] in the following way. Holes trapped at the surface during the photochemical process develop a potential barrier which accelerates the photogenerated electrons towards the surface. If, however, the lifetime, τ_e, of the electrons is shorter than the transit time, t_d, to cross the barrier, then the electrons do not reach the surface. The transit time t_d for these minority carriers can be diminished by increasing the intensity of the irradiation. This, indeed, has been proved [18] to occur in CdS.

In $PbCl_2$ we suppose that at some intensity the relation $t_d \leq \tau_e$ is valid. Then the electrons cross the potential barrier and become trapped at surface states connected with Pb^{2+} ions. These states, customarily called Pb^+ states [19] may form recombination centres for holes and electrons. The Pb^+ states can also initiate chemical instability of the surface in the following way. An electron trapped at a Pb^+ state and a hole at a nearby Cl^- state form a surface Cl atom and a Pb^+ ion. These in turn may form a molecular-like structure, facilitating the surface breakdown by evaporation.

That there is evaporation from the surface can be seen in Fig. 7, which shows the border of an irradiated part of the crystal. The step height measured by the interferometric method is about 530 nm.

Photo-enhanced evaporation contributes to the optical density change ΔD (light scattering by surface roughness) but not to the same extent as the photoreduction of the same amount of lead chloride to metallic lead. Obviously, ΔD in the latter case is higher.

Summarizing, the photolysis rate will increase as the intensity increases but after a certain intensity at which the photo-enhanced evaporation starts the photolysis rate decreases. This will result in a maximum of ΔD vs. intensity.

This is, to some extent, consistent with the observation of Kaldor and Somorjai [9]. They observed an abrupt increase of the 'reflection density' at an intensity of $0{\cdot}7\times 10^5\,\mu W/cm^2$. That the 'knee' in their curves was found at lower intensities than ours ($6\times 10^5\,\mu W/cm^2$) may be due to the difference in material used, viz., lead chloride powder not (single) crystals.

(*d*) *The photolysis in* PbI_2

We will devote part of this paper to a discussion of the photolysis of PbI_2. As mentioned in the introduction, Dawood *et al.* [4, 5] studied the photolysis of PbI_2. The time, intensity and temperature dependence of the photolysis was obtained by measuring the iodide content of thin layers of PbI_2 after irradiation at about 200°C.

To start with the temperature dependence, it appears that the results of Dawood *et al.* [4, 5] are much the same as ours on $PbBr_2$ and $PbCl_2$. This can be seen in Table 1.

Regarding the time dependence, Dawood *et al.* observed that the photolysis of PbI_2 varied as the square root of the irradiation time. We have observed the same dependence

Table 1. Activation energy for the rate of photolysis in lead halides

	E(eV)	Reference
PbI_2	0·17	Dawood *et al.*[9]
$PbCl_2$	0·14±0·03	Verwey[12]
$PbBr_2$	0·13±0·03	Verwey[12]

for $PbBr_2$ (Fig. 3). However, we must emphasize that in $PbBr_2$ this was only found for an intensity of about 10^{18} photons sec^{-1} cm^{-2}. Deviations occurred at other intensities and also at low and high irradiation times t. The same phenomenon occurred for our measurement on PbI_2. Here again, $\Delta D \propto t^{1/2}$, but for a limited range of the curve. $PbCl_2$ showed even $\Delta D \propto t$ in the initial part of the curve (Fig. 4). Furthermore, the shape of the curve depends on the irradiation intensity. Therefore, it seems impossible to correlate the time dependence with a particular mechanism in the photolysis process, viz. the diffusion of halogen through a layer of lead and lead salts formed as proposed by Dawood *et al.* [5] for PbI_2. We can only conclude that the time dependence in PbI_2 is very much the same as in $PbBr_2$ and $PbCl_2$.

Now we will look at the intensity dependence. We have measured this dependence for $PbBr_2$ and $PbCl_2$ for several irradiation times, and found[12] that the intensity dependence of the photolysis is a strong function of that irradiation time. For $PbBr_2$ we found that $\Delta D \propto F$ (F = intensity of the irradiation) at irradiation times shorter than 1 second. The power of F for $PbCl_2$ photolysis[12] lies between 0·93 and 0·17. Kaldor and Somorjai even found for $PbCl_2$ in the high intensity region the relation $\Delta D \propto F^{3\cdot2}$. A comparison of the photolytic processes based on the intensity dependence seems difficult. From the time and temperature dependence we conclude that the photolytic processes in $PbCl_2$, $PbBr_2$ and PbI_2 are the same. This is supported by ESR measurements at liquid nitrogen temperature[15].

There is one significant point to be noted. We were unable to observe photolysis of PbI_2 crystals when they were irradiated at room temperature. One PbI_2 crystal was irradiated for 100 min under the same conditions as in Fig. 2 but now at room temperature. We could not observe a change of the optical density, which means that $\Delta D < 0{\cdot}001$. The absence of any darkening cannot be explained by the temperature dependence of lead iodide photolysis (Table 1). After $t = 10$ min this would give $\Delta D = 0{\cdot}02$. Probably in our PbI_2 crystals a deviation from stoichiometry (excess halogen) existed, which prevented the photodecomposition. This should be compared with the observation that crystals of $PbBr_2$ annealed in bromine vapour show a remarkably reduced sensitivity to photolysis, possibly due to a similar deviation from stoichiometry. In PbI_2 this deviation* seems to be corrected at temperatures of about 200°C.

(*e*) *Quantitative treatment of particle currents*

We will describe our 'dynamic' model for the photolysis of $PbCl_2$ and $PbBr_2$. This model consists of the transport of holes and anion vacancies to and from the surface. We consider transport of holes because, of the photogenerated electron-hole pair, the holes have a longer range[14] than the electrons. At the surface the holes h^+ react with halogen ions X_s^- according to

$$h^+ + X_s^- \rightarrow X_s.$$

A halogen atom X_s thus formed may combine with another halogen atom X_s to give a halogen molecule which can desorb. The halogen atoms may also be desorbed directly. In any case, halogen leaves the surface and anion vacancies are left behind. These anion vacancies in turn are assumed to be transported into the crystal, resetting the halogen

---

*Measurements of Henisch *et al.*[20, 21] show that their gelgrown PbI_2 crystals too are *p*-type, due to a slight deviation from stoichiometry.

Fig. 7. Border of a u.v.-irradiated part of a $PbCl_2$ crystal. Irradiation at room temperature in vacuum for 20 min ($\Delta D = 0{\cdot}435$). Intensity $(8 \pm 2) \times 10^5\ \mu W/cm^{-2}$. Microscope Reichert Zetopan with interferometer attachment according to Nomarski.

ion sites at the surface for subsequent trapping of a hole and desorption of halogen.

Inside the crystal electrons react with Pb^{2+} ions to give first Pb^+ ions and then Pb atoms which flock together in precipitates under annihilation of anion vacancies. Much information about these reaction products could be gained from the electron spin resonance measurements[15] at liquid nitrogen temperature.

We have called this reaction scheme a dynamic model because it takes into account the particle currents during photochemical reaction. It does not only describe the reaction products of the different stages but also tries to describe the way of reacting species; where they come from and where they go. This approach lends itself to a more quantitative description. The primary aim will be to show that the maximum in the curve of Fig. 5 is a transition from the print-out mode of photolysis to photo-enhanced evaporation.

The equations for the particle currents perpendicular to the surface ($x = 0$) are

$$\begin{aligned} j_h &= E_D\mu_h C_h - D_h\frac{\partial C_h}{\partial x},\\ j_e &= -E_D\mu_e C_e - D_e\frac{\partial C_e}{\partial x},\\ j_V &= E_D\mu_V C_V - D_V\frac{\partial C_V}{\partial x}. \end{aligned} \tag{1}$$

The subscripts h, e and V indicate the respective quantities of holes, electrons and vacancies, j indicates the particle currents, μ the mobilities, D the diffusion constants and C the respective concentrations. E_D consists of the Dember field, due to the difference in diffusion velocity, and the barrier field. This barrier field is due to charge carriers in surface states and in the space charge layer below the surface.

No net electrical current flows through the crystal during photolysis, hence,

$$j_h - j_e + j_V = 0. \tag{2}$$

Up to this point the treatment resembles that of the oxidation of metals[22]. In the latter case a set of equations (1) also exists, coupled by the internal electric field E_D together with an additional equation (2) relating the currents.

Some difficulties may arise from the complex continuity equation in our case. For electrons this is

$$\frac{\partial C_e}{\partial t} = -\frac{\partial j_e}{\partial x} + G - R - C. \tag{3}$$

It contains three extra terms G, R and C representing generation, recombination and chemical reaction, respectively. Some explicit relations may be obtained after rigorous simplifications.

We assume that we have a steady state condition, hence, $\partial C_e/\partial t = 0$. One often uses for the recombination term R in equation (3) the relation[23]

$$R = \frac{C_e}{\tau_e} = \frac{C_h}{\tau_h} \tag{4}$$

where τ_e and τ_h are the lifetimes of electrons and holes, respectively. It is not necessary to incorporate a separate term for C in equation (3) if the chemical reaction is monomolecular. In that case it only affects the lifetime τ_e or τ_h. The generation term G is

$$G = FKe^{-Kx} \tag{5}$$

where K is the absorption constant and F is the number of photons ($cm^{-2}\,sec^{-1}$) penetrating the crystal at $x = 0$.

We assume that there exists a barrier field E_D. We disregard diffusion, and we look at a layer near the surface where $x \ll 1/K$. From the continuity equation of the electrons (equation (3)) and equations (4) and (5) it follows that

$$C_e = FK\tau_e. \tag{6}$$

In Fig. 5 we have plotted the photolysis of $PbCl_2$ as a function of the intensity of the irradiation. At the left-hand side of the maximum in the curve we have a photolysis reaction which we called the print-out mode, hence, in equation (2) we have $j_e \approx 0$. We believe that at the right-hand side photo-enhanced evaporation occurs. Then, the electron current j_e is unequal to zero but $j_V \approx 0$. Therefore, it seems likely that at the maximum in Fig. 5

$$|je| = |jV|. \tag{7}$$

From (7) it follows that

$$E_D\mu_e C_e = E_D\mu_V C_V. \tag{8}$$

Combining (6) and (8) in inserting $\sigma_V = \mu_V e C_V$ we obtain

$$eE_D\mu_e F_m K\tau_e = E_D\sigma_V. \tag{9}$$

F_m is the intensity of the irradiation in the maximum of the curve of Fig. 5.

From (9) it follows that

$$F_m = \frac{\sigma_V}{eK\mu_e\tau_e}.$$

We insert the numerical values $\sigma_V = 10^{-6}$ $\Omega^{-1}\,\mathrm{cm}^{-1}$, $e = 1{\cdot}6\times10^{-19}$ C and we assume that $K = 10^5\,\mathrm{cm}^{-1}$.

There remains to be known the electron range per unit field $\mu_e\tau_e$ in $PbCl_2$ at room temperature. We can make an estimate by comparison with $PbBr_2$. At liquid nitrogen temperature $\mu_e\tau_e \approx 1/10\mu_h\tau_h$ in both crystals. For a $PbBr_2$ crystal we estimated[12] $\mu_h\tau_h$ at room temperature by the Haynes–Shockley technique[24]. If we assume that the relation between $\mu_e\tau_e$ and $\mu_h\tau_h$ is the same at room temperature and at liquid nitrogen temperature then $\mu_e\tau_e$ in $PbBr_2$ at room temperature will be $5\times10^{-9}\,\mathrm{cm^2V^{-1}}$. If we try the same value for $\mu_e\tau_e$ in equation (10) and insert the values of the other quantities, then $F_m = 0{\cdot}1 \times 10^5\,\mu\mathrm{W/cm^{-2}}$. This value of F_m is a lower limit because σ_V may be higher than the value used above due to the creation of anion vacancies at the surface. F_m in Fig. 5 is $6\times10^5\,\mu\mathrm{W/cm^{-2}}$. F_{m_2} as observed by Kaldor and Somorjai[9] ($F_m = 0{\cdot}7\times10^5\mu\mathrm{W/cm^{-2}}$) is in better agreement with the value calculated.

We see that this very rough estimate supports the assumption that the maximum in ΔD vs. intensity is due to the transition from the print-out mode to the photo-enhanced evaporation mode of photolysis.

CONCLUSION

The photolysis as a function of irradiation time is not essentially different in $PbCl_2$ and $PbBr_2$ at room temperature and in PbI_2 at about 200°C. However, this time dependence does not give very much information about the mechanism of the photolysis because it is a strong function of the intensity of the irradiation.

The photolysis of the substances mentioned can be understood in terms of the print-out mode of photolysis. This is the separation of lead metal inside the crystal and the desorption of halogen from the surface. An important part of the mechanism is the transport of photogenerated holes to the surface and of anion vacancies from the surface into the crystal.

The variation of the photolysis as a function of intensity in $PbCl_2$ shows a maximum. This is ascribed to a transition from the print-out mode to photo-enhanced evaporation of more or less complete molecules from the surface. This is supported by a rough estimate based on a quantitative description of particle currents in the crystal.

Acknowledgement—The author wishes to thank Professor J. H. van Santen for encouraging this work and for many helpful discussions.

REFERENCES

1. VERWEY J. F., *J. Phys. Chem. Solids* **27**, 468 (1967).
2. MEES C. E. K. and JAMES T. H., *Theory of the Photographic Process*. New York (1966).
3. MOTT N. F. and GURNEY R. W., *Electronic Processes in Ionic Crystals*, 2nd Ed. New York (1964).

4. DAWOOD R. I. and FORTY A. J., *Phil. Mag.* **7**, 1633 (1962).
5. DAWOOD R. I., FORTY A. J. and TUBBS M. R., *Proc. R. Soc.* **284**, 272 (1965).
6. DE VRIES K. J. and VAN SANTEN J. H., *Physica* **30**, 2051 (1964).
7. DE VRIES K. J. and VAN SANTEN J. H., *Physica* **29**, 482 (1963).
8. DE VRIES K. J., Thesis, Utrecht (1967).
9. KALDOR A. and SOMORJAI G. A., *J. phys. Chem.* **70**, 3538 (1966).
10. SIMKOVICH G., *J. Phys. Chem. Solids* **24**, 213 (1963).
11. VERWEY J. F. and SCHOONMAN J., *Physica* **35**, 386 (1967).
12. VERWEY J. F., Thesis, Utrecht (1967).
13. TUBANDT C. and EGGERT S., *Z. anorg. Chem.* **110**, 196 (1920).
14. VERWEY J. F. and WESTERINK N. G., *Physica* **42**, 293 (1969).
15. ARENDS J. and VERWEY J. F., *Phys. Status Solidi* **23**, 137 (1967).
16. SCHOONMAN J. and VERWEY J. F., *Physica* **39**, 244 (1968).
17. SOMORJAI G. A. and LESTER J. E., *J. chem. Phys.* **43**, 1450 (1965).
18. LEVINE J. D. and MARK P., *Phys. Rev.* **144**, 751 (1966).
19. KRÖGER F. A., *The Chemistry of Imperfect Crystals*. Amsterdam (1964).
20. HENISCH H. K. and SRINIVASAGOPALAN C., *Solid State Commun.* **4**, 415 (1966).
21. DUGAN A. E. and HENISCH H. K., *J. Phys. Chem. Solids* **28**, 1885 (1967).
22. FROMHOLD A. T., *J. chem. Phys.* **41**, 509 (1964).
23. TABAK M. D. and WARTER P. J., *Phys. Rev.* **148**, 982 (1966).
24. HAYNES J. R. and SHOCKLEY W., *Phys. Rev.* **82**, 935 (1951).

J. Phys. Chem. Solids Pergamon Press 1970. Vol. 31, pp. 173–177. Printed in Great Britain.

SOLID SOLUBILITY OF Zn IN Si*

M. M. BLOUKE, N. HOLONYAK, JR., B. G. STREETMAN, and H. R. ZWICKER
Department of Electrical Engineering and Materials Research Laboratory, University of Illinois at Urbana-Champaign, Urbana, Ill. 61801, U.S.A.

(*Received* 7 *April* 1969)

Abstract—The solid solubility of Zn in Si has been extended by nearly two decades to include the temperature range from 800° to 1000°C. The data of the present work near 1050°C are consistent with previously published values of solubility. Freeze-out of carriers in both the 0·55 eV and the 0·31 eV acceptor levels has been observed and employed to obtain the Zn impurity solubility. Measurements of the impurity-compensated resistivity and the concentration of Zn atoms agree well with theoretical predictions based on the charge balance equation and the known double acceptor behavior of Zn in Si.

INTRODUCTION

RECENTLY a number of investigators have examined the behavior of Si doped with Zn under a variety of experimental conditions. Holonyak[1] and more recently Lebedev and Sultanov[2] and Maher *et al.*[3] have examined doubled injection Si diodes doped with Zn. Holonyak and Bevacqua[4] have also reported current oscillations in Si *p–i–n* diodes doped with various deep levels including Zn. Other investigators have examined the photoconductivity of Zn doped Si at room temperature[5]. Important in all this work is a knowledge of the solid solubility of Zn in Si, provided such data are available.

Trumbore[6] has presented solid solubility curves for many different elements in Si. The available data on the solid solubility of Zn in Si, however, extend only from about 1400° to 1000°[7, 8] and over a very limited solubility range. In the course of work on *p–i–n* diodes fabricated from Si lightly doped with Zn, we[9] have found desirable a knowledge of Zn solubility in the range $\leq 3{\cdot}3\times 10^{15}$ atoms/cm^3. We present here these data and, along with previous data, show the behavior of Zn solid solubility in Si over a wide temperature and solubility range.

SAMPLE PREPARATION AND DIFFUSION

Crystal slices 750 μm to 1000 μm thick were cut from Czochralski grown, *n*-type, *P*-doped Si ingots. The initial crystal resistivities were: 3·1 Ωcm, 7·9 Ωcm, and 12·2 Ωcm, measured at 300°K. The slices were cleaved into smaller wafers, which were lapped and cleaned by boiling successively in trichloroethane, acetone, and ethanol. They were then etched for about five minutes in a dilute solution of $HNO_3 + 48$ per cent HF and finally were rinsed with distilled water. This process was repeated twice, the final etching and rinse procedure occurring just prior to placing the experimental wafer in a silica ampoule for impurity diffusion. The ampoule was previously cleaned, etched in $3HNO_3 + 1\,HF$, and rinsed in distilled water.

The diffusion of Zn into the wafers took place at temperatures ranging from 820° to 1076° for times of at least four days. The various diffusion schedules are given in Table 1. Four to six mg of 99·999 per cent pure Zn metal was placed in the ampoule with each wafer. The Zn source was cleaned by etching in dilute warm nitric acid. The ampoule containing the wafer and Zn was evacuated to 10^{-5} Torr. and sealed. Since Zn has a vapor pressure of about one atmosphere at the diffusion temperatures, it was not necessary to back-fill the ampoule with any

---

*This work has been supported by the Advanced Research Projects Agency Contract No. SD-131 and by the National Science Foundation Grant No. GK-2657.

Table 1

Sample	Initial resistivity $\rho_0(\Omega$ cm)	Initial impurity content $(N_d^+ - N_a^-)$ atoms/cm^3	Diffusion temperature T(°C)	Diffusion time t(hr)
045	3·1	$1{\cdot}58 \times 10^{15}$	910	120
046	3·1	"	820	120
047	3·1	"	999	96
048	3·1	"	1076	120
050	12·2	$3{\cdot}7 \times 10^{14}$	970	96
051	12·2	"	896	744
055	7·9	$6{\cdot}7 \times 10^{14}$	900	340
056	12·2	$3{\cdot}7 \times 10^{14}$	870	140
057	12·2	"	952	111
058	12·2	"	939	246
059	12·2	"	872	240

auxiliary inert gas. After diffusion annealing of the Si wafer at the desired temperature, the ampoule was removed from the furnace and quenched in water. Condensation of Zn metal on the inside surface of the ampoule after quenching indicated a sufficient atmosphere of Zn atoms during diffusion to guarantee that the diffused Zn density was limited only by the solid solubility at the diffusion temperature.

After diffusion a hot probe measurement invariably indicated a strongly p-type surface on the Si wafer. However, after lapping $\sim 25\,\mu$m from the surfaces, we found the underlying bulk material to be n- or p-type, depending on the diffusion temperature and the initial resistivity of the Si wafer. The heavily p-type surface layer can be attributed to the condensation of Zn on the surfaces of the wafer during quenching and is not a source of concern.

A 4-leaf clover-shaped sample, $\frac{1}{8}$ or $\frac{3}{8}$ in. in dia., was cut from the diffused wafer with an ultrasonic cutter. The experimental sample was used for van der Pauw[10] measurements of resistivity, carrier concentration and mobility. The sample was lapped on both sides with American Optical Company M305 abrasive to the desired thickness (between 250 μm and 650 μm). Metal contacts were alloyed to the edges of the four leaves in a hydrogen atmosphere. An alloy of Au + 0·6 per cent Sb was used for n-type samples and an alloy of Al + 1 per cent B was used for the p-type samples for Ohmic contacts. Rolled and annealed 125 μm Ni leads approximately 1·5 cm long were attached to the metal contacts. The measurement sample was fastened in a holder and the Ni leads soldered to appropriate electrical connectors. The sample holder was inserted in a cryostat of the conventional type for Hall or van der Pauw measurements[11].

THEORETICAL CALCULATIONS

Zinc introduces two acceptor levels into the forbidden gap of Si[8], one located 0·31 eV above the valence band and the other 0·55 eV below the conduction band (essentially mid-gap). When the Zn atom is in the neutral charge state, only the lower level is available for electron capture, and the upper level exists only when the lower level is occupied.

The methods of Shockley and Last[12] can be used to compute the impurity-compensated resistivity of a sample (i.e. a wafer into which Zn has been diffused) as a function of the number of Zn impurity atoms. For a crystal in thermal equilibrium the charge balance equation is

$$n + N_{\mathrm{Zn}}^{-} + 2N_{\mathrm{Zn}}^{--} = p + N_d^{+} - N_a^{-} \qquad (1)$$

and

$$N_{\mathrm{Zn}}^{0} + N_{\mathrm{Zn}}^{-} + N_{\mathrm{Zn}}^{--} = N_{\mathrm{Zn}} \qquad (2)$$

where n is the concentration of conduction band electrons, N^i_{Zn} is the density of Zn atoms in the i^{th} charge state, p is the density of the valence band holes, and N_d^+ and N_a^- are the concentration of ionized donor and acceptor atoms, respectively, which are present initially in the crystal, and N_{Zn} is the total concentration of Zn atoms.

Expressing the concentrations N^-_{Zn} and N^{--}_{Zn} in terms of N_{Zn} and making the substitution $y = e^{-\beta\phi}$, where $\beta = 1/kT$ and ϕ is the Fermi level measured from the valence band, we may solve equation (1) for N_{Zn} and obtain

$$N_{Zn} = [(1 + ye^{\beta E_2} + y^2 e^{\beta(E_1+E_2)})/(2 + ye^{\beta E_2})] \times \{N_v y - N_c e^{-\beta E_g} y^{-1} + N_d ye^{\beta E_d}/(1 + ye^{\beta E_d}) - N_a/(1 + ye^{\beta E_a})\}. \quad (3)$$

In this equation N_c and N_v are the effective density of states in the conduction and valence bands, respectively, E_g is the band gap energy ($E_v \equiv 0$), and E_d, E_a, E_1, and E_2 are the energies of the donor, acceptor, and lower and upper Zn levels, respectively.

The resistivity, ρ_c, of the impurity-compensated sample may be computed from the equation

$$\rho_c = \{q(\mu_n n + \mu_p p)\}^{-1} = \{q(\mu_n N_c e^{-\beta E_g} y^{-1} + \mu_p N_v y)\}^{-1} \quad (4)$$

where q is the magnitude of the electronic charge, and μ_n and μ_p are the electron and hole mobilities, respectively. Equations (3) and (4) express the resistivity, ρ_c, and the Zn density, N_{Zn}, in parametric form with y as the intermediate variable.

The Fermi level $\phi \equiv -kT \ln y$ is allowed to vary within the gap. For each value of ϕ, equations (3) and (4) define a unique value of ρ_c and a corresponding value of N_{Zn} for given values of N_d and N_a. (These latter two parameters determine the initial resistivity of the Si wafer.)

EXPERIMENTAL RESULTS

The resistivity, carrier concentration, Hall coefficient, and Hall mobility were measured over a range of temperatures for each sample. Figure 1 shows the carrier concentration as a function of $1/T$ for three different samples. Curve (a) of Fig. 1 represents measurements on a very lightly Zn-doped n-type sample. Since the Fermi level is well above the upper Zn level for this sample (i.e. $N_d > N_{Zn}$), the number of Zn atoms introduced into the sample can be determined by assuming that each Zn atom is in the doubly negative charge state, i.e. it will have removed two electrons from the conduction band. Hence

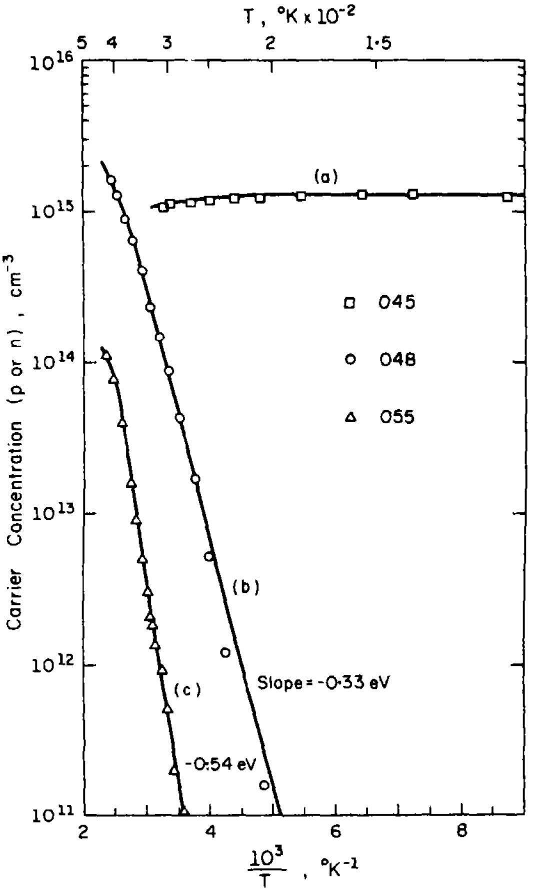

Fig. 1. Carrier concentration vs. reciprocal temperature. Wafers a and c were n-type after impurity-compensation and wafer b was compensated p-type.

$$N_{Zn} = \tfrac{1}{2}(n_0 - n_c) \tag{5}$$

where n_0 is the density of conduction electrons present before Zn diffusion and compensation and n_c is the electron density in the compensated wafer. For the samples compensated to p-type (e.g. curve (b) of Fig. 1), N_{Zn} was computed by taking

$$y = e^{-\beta\phi} = p/N_v, p \gg n.$$

Thus, from equation (3)

$$N_{Zn} = \{p + (N_d^+ - N_a^-)\}\{(1 + (p/N_v)e^{\beta E_2} + (p/N_v)^2 e^{\beta(E_1+E_2)})\} \times [2 + (p/N_v)e^{\beta E_2}]^{-1}. \tag{6}$$

The value of the hole concentration p measured at temperature T was substituted in equation (6) along with the appropriate value of $(N_d^+ - N_a^-)$, and N_{Zn} was then computed. The sample resistivity at 300°K was also measured. A completely analogous procedure was used for those samples that were compensated to high resistivity n-type (e.g. curve (c) of Fig. 1).

Figure 2 shows the resistivity ρ_c of the Zn impurity-compensated samples as a function of N_{Zn} for the three different initial resistivities shown. The data points are the measured values of ρ_c and N_{Zn} as determined from van der Pauw measurements. The solid lines are theoretical curves as computed from equations (3) and (4) using the various measured values of $(N_d^+ - N_a^-)$ for the three different sample initial resistivities. The mobilities used in equation (4) are those given by Ludwig and Watters[13]. No attempt was made to correct the mobilities for impurity scattering, as the density of impurities is quite low. Measurements of the Hall mobility of these samples confirms the validity of this assumption.

Because of the appearance of the previously mentioned heavily doped p-type surface

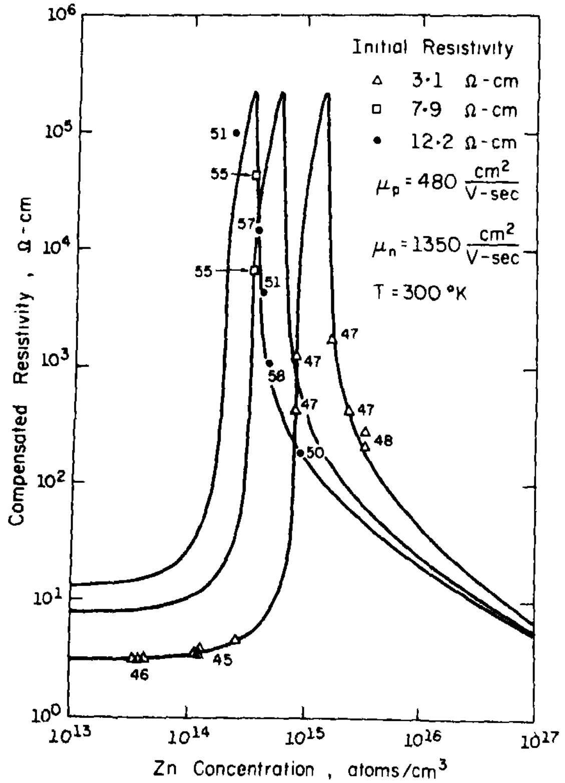

Fig. 2. Compensated resistivity, ρ_c, vs. the concentration of impurities, N_{Zn}, for the three initial resistivities used in this experiment. The numbers adjoining the various data points refer to the diffusions listed in Table 1.

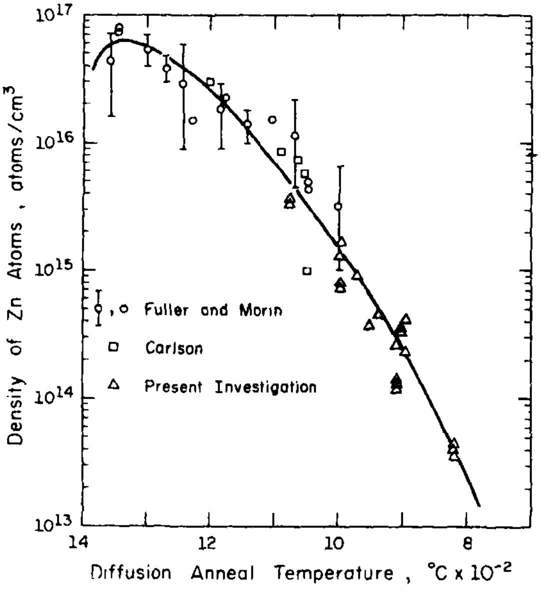

Fig. 3. Solid solubility of Zn in Si. The curve is based on the data of Fuller and Morin[7], Carlson[8], and the present study.

layer upon completion of the Zn diffusion, an experiment was undertaken to determine the uniformity of the underlying bulk of the diffused wafer. van der Pauw samples were cut from different regions of a wafer, and the Zn concentration in these samples was determined. These data indicated that the concentration of Zn in the wafer was uniform within 7 per cent. When more than one wafer was placed in an ampoule for diffusion, the measured concentration of Zn was generally within a factor of two for all pieces.

Finally, Fig. 3 gives the density of electrically active Zn atoms which are introduced during diffusion at various temperatures. Since Carlson[8] has shown that essentially all the Zn atoms in Si are electrically active, Fig. 3 may be taken as the solid solubility of Zn in Si and is so labeled. The curve of Fig. 3 includes the data of Fuller and Morin [7] as corrected and amended by Carlson[8], and is extended into the range from 1000° to 800°C by the data of the present work. The resulting Zn impurity solubility range covers the temperature interval from 800° to 1400°C. Although the additional temperature interval added to the solid solubility curve by the present work is only ~200°C, this corresponds to about two orders of magnitude change in the Zn solid solubility and more than doubles the solubility range previously published.

Acknowledgements—The authors would like to thank Dr. G. E. Stillman and A. B. Wilson who built the cryostat, and G. E. Morris and V. Swanson for technical assistance in portions of this work.

REFERENCES

1. HOLONYAK N., Jr., *Proc. Inst. Radio Engrs* **50**, 2421 (1962).
2. LEBEDEV A. A. and SULTANOV N. A., *Sov. Phys.-Semi.* **2**, 1295 (1969).
3. MAHER A. T., STREETMAN B. G. and HOLONYAK N., Jr., *I.E.E.E. Trans. Electr. Devel.* ED-16 (1969).
4. HOLONYAK N., Jr., and BEVACQUA S. F., *Appl. phys. Letters* **2**, 71 (1963).
5. *H. P. Associates Staff Members, Tech. Rep.* No. AFAL-66-60 (March 1966).
6. TRUMBORE F. A., *Bell Syst. tech. J.* **39**, 205 (1960).
7. FULLER C. A. and MORIN F. J., *Phys. Rev.* **105**, 379 (1957).
8. CARLSON R. O., *Phys. Rev.* **108**, 1390 (1957).
9. BLOUKE M. M., HOLONYAK N., Jr., STREETMAN B. G. and ZWICKER H. R., *Solid State Electron.* In press (1970).
10. VAN DER PAUW L. J., *Philips Res. Rep.* No. **13**, 1 (1958).
11. PUTLEY E. H., *The Hall Effect and Semi-conductor Physics*. Dover, New York (1968).
12. SHOCKLEY W. and LAST J. T., *Phys. Rev.* **107**, 392 (1957).
13. LUDWIG G. W. and WATTERS R. L., *Phys. Rev* **101**, 1699 (1956).

J. Phys. Chem. Solids Pergamon Press 1970. Vol. 31, pp. 179–185. Printed in Great Britain.

LATTICE DISTORTION, SPECIFIC HEAT AND ANTIFERROMAGNETIC ORDERING IN AuMn

D. C. FINBOW*
Physics Department, University of Salford, England

and

P. MAKHURANE*
Physics Department, University of Zambia, Lusaka, Zambia

and

P. GAUNT*
Physics Department, University of Manitoba, Canada

(*Received* 12 *March* 1969)

Abstract – Experiments are reported which show that the tetragonal distortion in an AuMn alloy below the Néel temperature depends on the square of the antiferromagnetic order parameter. This result is shown to be consistent with a distortion dependent magnetic exchange energy.

The specific heat of an AuMn alloy has been measured in the range 100°–600°K and the magnetic part of the specific heat curve agrees in detail with the predictions of a distortion modified molecular field model with $S = 2$.

INTRODUCTION

ALLOYS of AuMn near the equiatomic composition have a cubic CsCl structure which distorts on cooling below the Néel temperature to a t_1 phase with $c/a < 1$. On further cooling alloys containing less than ~ 50 at.% Au distort further to produce a t_2 phase with $c/a > 1$ (Smith and Gaunt[1]). Single crystals of these alloys have been prepared and the crystallography of the transitions has been examined in detail by Finbow and Gaunt[2]. The lattice distortion was measured in an Au 48·1 at.% Mn crystal by a multiple beam interference microscope technique over the temperature range 150°–500°K[2]. These measurements have now been extended to 4°K. using powdered material and X-ray diffraction techniques.

It is found that the distortion, expressed as $(1-c/a)$, is directly proportional to the square of the long range antiferromagnetic order measured in the same crystal using neutron diffraction methods. A similar distortion dependence was found in a Cu 87% Mn alloy [3] where a simple theoretical model, based on a strain dependent exchange, was fitted to the data. A similar model is shown to fit well in the present work.

The specific heat of an AuMn alloy has been measured and is compared with the excess specific heat near the Néel temperature predicted by the distortion modified molecular field model with $S = 2$. The agreement is remarkable and suggests that the magnetic moments in this alloy can be regarded as completely localised with long range interactions between the spins.

MICROSCOPIC SHEAR AND LATTICE PARAMETER MEASUREMENTS

The cubic tetragonal transformation near the Néel temperature shows many of the properties of a martensitic shear transformation and the polished surface of a single cubic crystal shows a characteristic shear distortion which increases as c/a decreases. It can be shown that the measured shear observed should be $(1/3)(1-c/a)$ and this prediction has been confirmed[2]. Measured values of the reduced distortion parameter $(1-c/a)/(1-c/a)_0$, where $(1-c/a)_0$ is the value at absolute zero, are plotted in Fig. 1.

---

*Formerly at: Physics Department, University of Sheffield, England.

The measurements were extended to low temperatures using powdered specimens and a Philips X-ray diffractometer to measure c and a from the 312 and 213 reflections using a copper target. The transformation temperature was somewhat higher, (507°K), in the powdered sample. These results are also plotted in Fig. 1 but with the transition temperature normalised to fit the single crystal results.

NEUTRON DIFFRACTION MEASUREMENTS

The structure of the t_1 phase was deduced by Bacon[4] who found a moment of $\sim 4{\cdot}2\,\mu_B$ per manganese atom the moments being ordered in ferromagnetic sheets perpendicular to the c axis; neighbouring sheets being antiparallel. In the present work the intensity of the $(00\frac{1}{2})$ magnetic neutron diffraction peak was measured over a range of temperature from 4° to 500°K. and the normalised intensity of the peak I/I_0, where I_0 is the intensity at 0°K, is also plotted in Fig. 1. The reduced intensity is proportional to the square of the long range magnetic order. The results show that T_t and T_N are not exactly coincident. This deduction might also be made from some recent results[5]. The significance of this discrepancy is discussed below.

STRAIN DEPENDENT MOLECULAR FIELD MODEL

In reference [3] a strain dependent exchange model for spin $\frac{1}{2}$ was developed. It was found

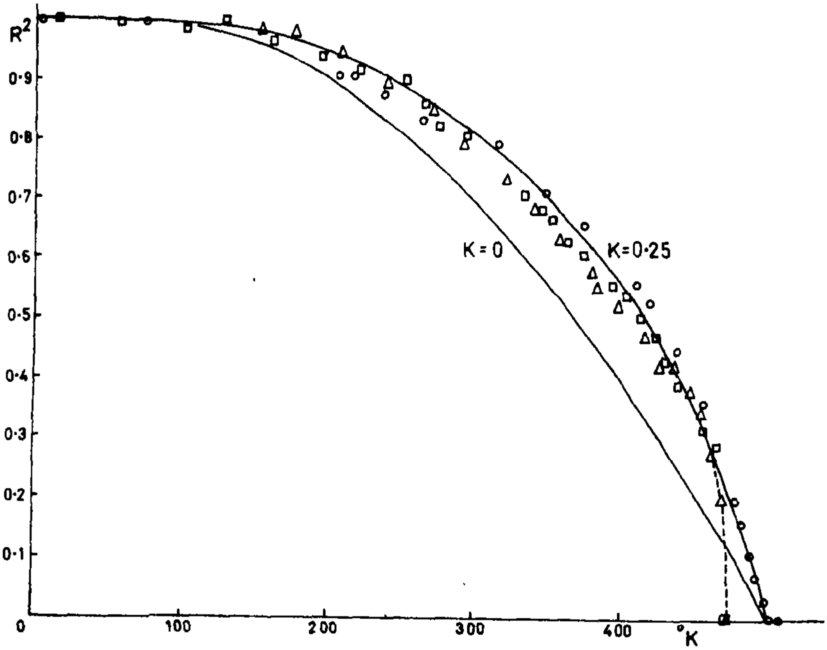

Fig. 1. The square of the long range order parameter deduced from neutron intensity measurements of the $(00\frac{1}{2})$ magnetic peak in an Au 48·1 at.% Mn alloy is plotted against temperature as indicated by circles. Also shown are the reduced distortion parameter $(1-c/a)/(1-c/a)_0$ deduced from shear measurements (triangles) and from X-ray data (squares). The solid curve is theoretical with $S = 2$, $K = 0{\cdot}25$.

that both distortion, $(1-c/a)$, and cell volume showed a dependence on magnetic order in the Cu 87% Mn alloy investigated. In the AuMn alloys the cell volume shows no anomaly below the Néel temperature but as shown in Fig. 1 the distortion depends directly on the square of the magnetic order.

For this alloy, therefore, it is sufficient to discuss the dependence of exchange energy on the distortion. Let x, y, z be the principal strains of the originally cubic lattice. In the absence of external stress x and y are equal because of the symmetry of the exchange interaction and:

$$2(1-c/a) = (x+y-2z)$$

if terms in x^2, y^2 and z^2 can be neglected. Following the methods of [3] and [9] the exchange energy for unpaired spin S in the material can be written as:

$$U_E = -\frac{3}{2}\frac{S}{S+1}kT_NR^2[1+\beta(x+y-2z)] \tag{1}$$

where β is a constant defining the dependence of the exchange energy kT_N on the distortion and R is the ratio of the sub-lattice magnetisation at temperature T to that at 0°K. The strain energy associated with each spin S is given by:

$$U_s = a(x^2+y^2+z^2)+2b(xy+yz+xz) \tag{2}$$

where

$$a = \frac{vY(1-\nu)}{2(1+\nu)(1-2\nu)} \text{ and } b = \frac{v\nu Y}{2(1+\nu)(1-2\nu)}$$

v being the volume per spin S, Y is Young's modulus, and ν Poisson's ratio. This expression applies strictly only for an isotropic solid.

Minimising U_S+U_E with respect to x, y and z gives:

$$2(1-c/a) = \frac{9}{2}\left(\frac{S}{S+1}\right)\frac{kT_N{}^{\beta}R^2}{(a-b)}. \tag{3}$$

Hence:

$$\frac{(1-c/a)}{(1-c/a)_0} = R^2.$$

The free energy per magnetic spin will be:

$$G = U_E+U_S-kT\ln W(R,S)$$

where $W(R,S)$ is the number of spin arrangements consistent with a given R. Thus:

$$\frac{\partial G}{\partial R} = 3\left(\frac{S}{S+1}\right)kT_NR[1+\beta(x+y-2z)] \\ -kT\mathrm{d}(\ln W)$$

Now

$$\frac{\mathrm{d}G}{\mathrm{d}R} = \frac{\partial G}{\partial x}\mathrm{d}x+\frac{\partial G}{\partial y}\mathrm{d}y+\frac{\partial G}{\partial z}\mathrm{d}z+\frac{\partial G}{\partial R}$$

$$\therefore \frac{\mathrm{d}G}{\mathrm{d}R} = 3\left(\frac{S}{S+1}\right)kT_NR \\ \times\left[1+\frac{9}{2}\left(\frac{S}{S+1}\right)\frac{\beta^2R^2kT_N}{(a-b)}\right] \\ -kT\mathrm{d}(\ln W). \tag{4}$$

∴ Minimising G with respect to R gives

$$\frac{T}{T_N} = \frac{3SR}{(S+1)\mathrm{d}(\ln W)}(1+KR^2) \tag{5}$$

where K is the coefficient of R^2 in equation (4). This expression reduces to an analytical one for $S = \frac{1}{2}$ as shown in (3) when:

$$\mathrm{d}(\ln W) = \tfrac{1}{2}\ln[(1+R)/(1-R)].$$

The relation between T and R for $K = 0$ has been tabulated for values of S from $\frac{1}{2}$ to $\frac{7}{2}$[6]. As the first part of equation (5) is not K dependent it is thus possible to calculate the distortion modified relation between T and R using the tabulations and appropriate K values. A curve for $S = 2$ and $K = 0{\cdot}25$ is plotted in Fig. 1 and fits the data well. It was found that a curve for $S = \frac{1}{2}$ could not be made to fit for any value of K, particularly at low temperatures. The value of $S = 2$ is reasonable for the alloy in which Bacon's results[4] indicate $S = 2{\cdot}01$. Ho and Bindloss [7] support the assignment of a localised spin for this material in that they observe only a small linear temperature dependent contribution to specific heat at low temperatures which can be adequately explained in terms of conduction electrons. This implies that the unpaired magnetic spins lie in levels well below the Fermi energy.

SPECIFIC HEAT OF AuMn ALLOYS

Experimental method

The specific heat of an Au 50·2 at. % Mn alloy has been measured in the present work from 90°K to 650°K. A combined heater and incremental thermometer of 'Anodal' wire was used to measure the specific heat by a simple heat pulse method. This wire is pure aluminium insulated by an aluminium oxide coating which does not deteriorate, therefore, at 500°K. The specific heat curve is plotted in Fig. 2 and the error is not more than 3 per cent. The anomaly near 370°K is associated with the $t_1 - t_2$ change as this alloy was found to be t_2 at room temperature with $c/a \sim 1{\cdot}04$.

Separation of magnetic contribution to specific heat

The specific heat curve at 100° and 638°K has been matched to a curve:

$$C_p = f(T/\theta) + cT$$

where $f(T/\theta)$ is the Debye specific heat and C is a constant. A curve with $\theta = 254$°K and $C = 2{\cdot}4 \times 10^{-3}$ cal./deg^2 is shown in Fig. 2. The differences between this curve and the experimental points are plotted in Fig. 3 and represent the magnetic contribution to the specific heat[8].

For any localised spin model the entropy associated with the magnetic transition is given by $k \ln(2S+1)$ per magnetic spin S. From Fig. 3 the total change in entropy associated with the curve is:

$$\int \frac{C_M}{T}\,\mathrm{d}T = 3{\cdot}45 \text{ cal./deg/gm atom manganese.}$$

The alloy measured has a mean S of 2·1[4] so that there could be 90 per cent of sites with spin 2 and 10 per cent spin 3. With this assumption, the predicted entropy change is 3·27 cal./deg/gm atom.

Detailed comparison of specific heat with model

The total entropy calculation gives such a good fit to the results that a detailed comparison of specific heat with the predictions of the

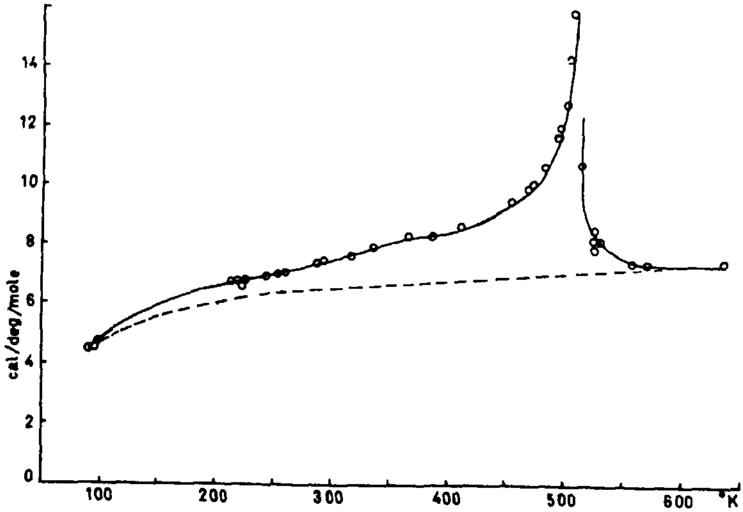

Fig. 2. The specific heat of an Au 50·2 at. % Mn alloy in cal./gm mole of $\mathrm{Au}_{0.498}\mathrm{Mn}_{0.502}$ is indicated by circles. The solid curve is drawn through the experimental points. The dotted curve is a plot of the Debye specific heat with $\theta = 254$°K plus $2{\cdot}4 \times 10^{-3}\,T$ cal./deg.

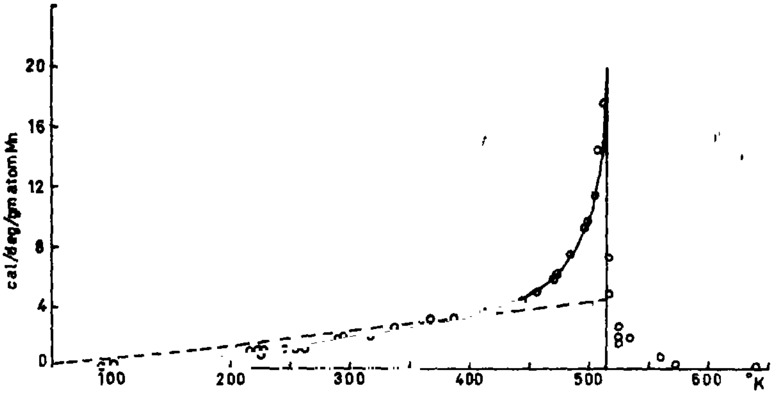

Fig. 3. Magnetic specific heat in cal./gm atom of manganese is indicated by circles. The solid curve is theoretical with $S = 2$, $K = \frac{1}{4}$. The dotted curve is theoretical with $S = 2$, $K = 0$.

model above has been attempted. The magnetic part of the free energy after minimisation with respect to s, y, and z is given by:

$$U_E + U_S = -\frac{3}{2}\left(\frac{S}{S+1}\right)kT_N R^2\left[1+\frac{K}{2}R^2\right].$$

The magnetic specific is given by:

$$C_M = \frac{\partial U}{\partial R}\cdot\frac{dR}{dT} = -3\left(\frac{S}{S+1}\right)kT_N R\frac{dR}{dT} \times[1+KR^2]. \quad (7)$$

Thus from (7) and (5) C_M can be determined. $R\,dR/dT$ was determined from the slope of the theoretical R^2 against T/T_N curve excepting at T_N where an analytical solution is available. Smart[9] gives the relation between R and T near the Néel temperature as:

$$R^2 = \frac{10}{3}\frac{(S+1)^2}{(S+1)^2+S^2}\cdot\frac{T_N-T}{T_N}$$

$$\therefore \frac{T}{T_N} = 1-\frac{3}{10}\left[1+\left(\frac{S}{S+1}\right)^2\right]R^2.$$

This expression corresponds to equation 5 for $K = 0$ and $T \to T_N$. Thus as $T \to T_N$ equation (5) becomes:

$$\frac{T}{T_N} = 1-\frac{3}{10}\left[1-\frac{10}{3}K+\left(\frac{S}{S+1}\right)\right]R^2.$$

The transition is therefore of first order if

$$\frac{10K}{3} > 1+\left(\frac{S}{S+1}\right)^2:$$

For $S = 2$ the critical K is therefore 0·433.

Thus for $R \to 0$

$$\frac{1}{T_N} = -\frac{3}{5}R\frac{dR}{dT}\left[1-\frac{10}{3}K+\left(\frac{S}{S+1}\right)^2\right]$$

Substituting in equation (7) the specific heat as $R \to 0$ is, therefore, given by:

$$C_M = \frac{5Sk}{S+1}\bigg/\left[1-\frac{10}{3}K+\left(\frac{S}{S+1}\right)^2\right]. \quad (8)$$

The steepness of the specific heat curve as $T \to T_N$ thus depends strongly on the value of K. If K is put at $\frac{1}{3}$ the specific heat discontinuity at the Néel temperature is 19·87 cal./deg/gm atom of manganese. The value of $K = \frac{1}{4}$ found for the 48·1 at.% Mn alloy would give a discontinuity of 10·58 while $K = 0$ gives 4·58 cal./deg/gm atom. In Fig. 3 the experimental values of C_M are compared with the theoretical curve calculated from equation (7) with $S = 2$ and $K = \frac{1}{4}$ and $K = 0$. The total enthalpy under the curve for $K = \frac{1}{4}$ is 1195 cal./gm atom compared with an experimental value of 1262 cal./mole.

DISCREPANCY BETWEEN NÉEL TEMPERATURE AND TRANSFORMATION TEMPERATURE

There is a difference between the cubic tetragonal transformation temperature of 472°K and the Néel temperature of 500°K observed in the same crystal of Au 48·1 at.% Mn. The dilation and specific heat measurements reported in [6] also show a discrepancy of ~ 12°K. This difference is not accounted for directly in the model discussed above. The model, however, tacitly assumes that one tetragonal crystal grows from the cubic phase without interference from competing tetragonal orientations. Three different tetragonal orientations are possible corresponding to the ⟨100⟩ axes of the parent cubic crystal. Suppose that initially the tetragonal phase forms uniformly throughout the sample but with C axes oriented at random along the three possible ⟨100⟩ directions. If the volume of each tetragonal region is small (~ 100 Å) and the distortion is small then there will be no martensitic shear and the X-ray reflection will be interpreted as cubic. As the distortion increases, however, the strain energy due to interaction of different tetragonal orientations will increase until it becomes energetically favourable for the crystal to transform martensitically to a finely twinned tetragonal product. The {110} twin boundaries separate two orientations whose C axes are almost at 90° to each other[2]. The strain energy, due to impingement of neighbouring tetragonal nuclei in the randomly transformed tetragonal phase, will be proportional to $(x+y-2z)^2$ and will consist of area and volume contributions for each tetragonal nucleus. In order to transform by a shear transformation a habit plane joining the finely twinned product and the randomly transformed phase must be formed. This habit plane can then move through a region of sample causing transformation to the twinned product accompanied by a shear. In the twinned product there will be an energy associated with the area of the twin walls and an energy associated with the formation of the habit plane boundary. Microscopic observations indicate that habit plane boundaries occur in the same place on successive cycles through the transformation which suggests that particular transformation dislocations are always present in the sample. The energy of the habit plane will be a minimum when the distortion $(x+y-2z)$ exactly matches the shear of the transformation dislocation. Putting $\epsilon = (x+y-2z)$ the extra strain energy in the randomly transformed phase could be written:

$$\Delta U = (P+Q)\epsilon^2$$

where P and Q are constants representing area and volume parts of the energy. This extra energy will slightly reduce the value of K in equation (5). When the habit plane and twin boundaries are introduced the energy will be of the form:

$$\Delta U = (1-\alpha)B\epsilon^2 + W(\epsilon-\epsilon_0)^2 + \alpha Q\epsilon^2 + \alpha P\epsilon^2$$

where α is the untwinned fraction, B is the twin wall energy constant, W is the habit plane energy constant and ϵ_0 is the distortion which exactly matches the shear of the transformation dislocation. Minimising the total U with respect to ϵ gives an equation:

$$\epsilon = \frac{\left[\frac{9}{2}\left(\frac{S}{S+1}\right)kT_N\beta R^2 + 2W\epsilon_0\right]}{(a-b+\text{const.})}.$$

This equation is analogous with equation (3) and shows that in the presence of the habit plane ϵ will be finite even when $R = 0$. This cannot give the lowest possible free energy and therefore, as $R \rightarrow 0$ the randomly transformed free energy with no habit plane (i.e. $W = 0$ and $\alpha = 1$ in equations above) will be the lowest. As $\epsilon \rightarrow \epsilon_0$, however, the twinned situation with a habit wall and $\alpha \rightarrow 0$ will be favoured. As this argument is illustrative only and the values of the various constants are unknown a rigorous analysis of the equations has not been attempted. The main feature of the model which gives the required properties is the $W(\epsilon-\epsilon_0)^2$ term which arises because of the presence of transformation dislocation arrays in the crystals.

CONCLUSION

The work presented above indicates that a distortion modified Weiss molecular field model explains the distortion of the alloy AuMn below the Néel temperature in the tetragonal phase with $c/a < 1$. The same model gives a remarkably close fit to specific heat data around the magnetic anomaly. The model accounts simply for the sharpness of the anomaly which contrasts strongly with the predictions of models not including the distortion term. The distortion term is likely to be important in any antiferromagnet while in ferromagnets a volume dependent exchange energy would produce similar modifications to the properties. The distortion term has been included here in the simplest possible model where it accounts for about 25 per cent of the total enthalpy change from absolute zero to the Néel temperature. More sophisticated models which nevertheless take no account of the distortion could, therefore, be in error by this amount.

The fact that the modified Weiss molecular field model fits the data so closely lends support to the suggestion of Ho and Bindloss[7] that the unpaired spins are essentially localised in this alloy and that exchange interaction extends beyond nearest neighbours.

Acknowledgements—The authors wish to acknowledge the support of Professor G. E. Bacon and the Atomic Energy Research Establishment, Harwell, which enabled this work to be carried out at Sheffield. One of us (P.M.) was supported by a Commonwealth Scholarship. Grateful thanks are due to the Aluminium Wire and Cable Co. for a gift of 'Anodal' wire.

REFERENCES

1. SMITH J. H. and GAUNT P., *Acta Metall.* **9**, 819 (1961).
2. FINBOW D. and GAUNT P., *Acta Metall.* **17**, 41 (1969).
3. MAKHURANE P. and GAUNT P., *Proc. phys. Soc.* In press (1970).
4. BACON G. E., *Proc. phys. Soc.* **79**, 938 (1962).
5. MATSUMOTO S., KANEKO T. and KAMIGAKI K., *J. phys. Soc. Japan* **25**, 631 (1968).
6. DARBY M. I., *Br. J. appl. Phys.* **18**, 1415 (1967).
7. HO J. C. and BINDLOSS W., *Phys. Lett.* **20**, 459 (1966).
8. TITMAN J. M., *Proc. phys. Soc.* **77**, 807 (1961).
9. SMART J. S., In *Effective Field Theories of Magnetism*, p. 28. Saunders, London (1966).

J. Phys. Chem. Solids Pergamon Press 1970. Vol. 31, pp. 187–189. Printed in Great Britain.

TECHNICAL NOTE

Electrical resistivity of PdH_x system for H/Pd atom ratios to 0·97

(*Received* 9 *April* 1969; *in revised form* 9 *June* 1969)

RECENTLY, Bambakidis, Smith, and Otterson [1] presented a model to explain the effect of deuterium concentration on the resistivity of the PdD_x system. The model is based on the screening of the conduction electrons from the deuterium ions for $x < 0·55$ at 4·2°K, and the presence of an NaCl type structure for $x > 0·55$. The predictions of the model were compared to measured PdD_x data in which the maximum D/Pd atom ratio was 0·90. Our purpose is to present experimental results for the PdH_x system up to $x = 0·97$. These results are discussed in terms of the Bambakidis, Smith and Otterson (BSO) model.

In a review by Lewis[2], the highest H/Pd atom ratio, x, cited for the PdH_x system was 0·88. No detailed study of resistivity vs. x at 4·2°K was mentioned. In this work we measured the resistivity of PdH_x at 4·2°K and 273°K for x up to 0·97. We attained these high H/Pd atom ratios by electrolytic deposition of hydrogen into a palladium wire cathode. We used an electrolyte of 0·1 N H_2SO_4 containing Na_2S and formaldehyde. The resistivity was measured potentiometrically with the standard four probe technique. The hydrogen content was determined by mass spectrographic analysis after vacuum desorption at 573°K.

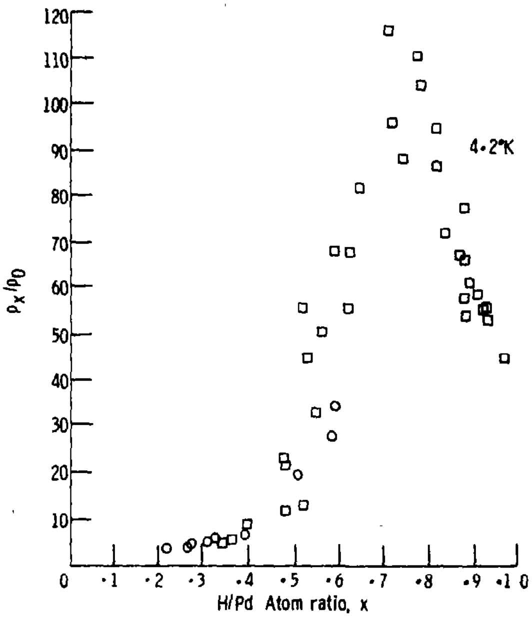

Fig. 1. Resistivity ratio ρ_x/ρ_0 vs. H/Pd atom ratio (x) at 4·2°K. ρ_0 is the resistivity at 4·2°K (annealed prior to absorption). ρ_x is the resistivity after absorption. The PdH_x specimens were cooled from room temperature to 4·2°K in 8 ± 2 sec.

Our experimental results are presented in graphs of ρ_x/ρ_0 vs. x for temperatures of 4·2°K (Fig. 1) and 273°K (Fig. 2); ρ_0 is the resistivity of an annealed palladium specimen and ρ_x is the resistivity of the same specimen after the absorption of hydrogen. At 4·2°K, ρ_x/ρ_0 shows little change up to $x \simeq 0·36$. As x increases above 0·36, ρ_x/ρ_0 increases more rapidly reaching a peak value of approximately 116 for $x \simeq 0·70$. Then ρ_x/ρ_0 decreases to about 40 per cent of its maximum value at $x \simeq 0·97$. At 273°K, (Fig. 2), a knee appears at $x \simeq 0·02$. This has been attributed to the initial appearance of the β-phase[2]. For larger x, ρ_x/ρ_0 increases almost linearly to a maximum value of about 1·9 for x between 0·7 and 0·8. As x increases beyond 0·8, ρ_x/ρ_0 decreases to about 1·35 at $x \simeq 0·97$. The significant difference between the data at 4·2°K and 273°K is the dissimilarity of the ρ_x/ρ_0 vs. x relationship up to $x \simeq 0·7$. Most

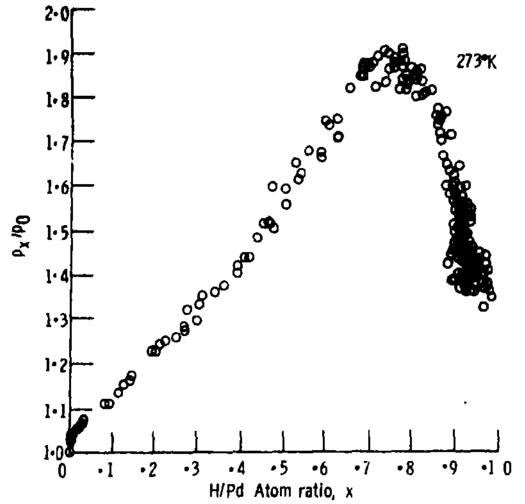

Fig. 2. Resistivity ratio ρ_x/ρ_0 vs. H/Pd atom ratio (x) at 273°K. ρ_0 is the resistivity at 273°K (annealed prior to absorption). ρ_x is the resistivity after absorption.

of the data shown in Fig. 1 were obtained from specimens that were cooled from room temperature to 4·2°K, in 8 ± 2sec. We observed variations in ρ_x (at $x = 0·5$) as large as 10 per cent upon repeated quenching of the same specimen. The only variable was rate of quenching. Below $x = 0·36$, no variation with respect to quench rate was observed. At 4·2°K, the resistivity measurements did not change with time. Upon quenching, the specimen passed through a temperature range where time dependent resistivity changes occurred[3, 4]. Such changes have been attributed to transitions of some of the hydrogen ions from octahedral to tetrahedral palladium lattice sites (O–T transitions or β–β^* transitions)[5]. We believe the scatter due to quench rate is due to differences in time available for O–T transitions to occur.

We shall now use the BSO model to interpret our experimental results for the PdH$_x$ system. The model is divided into two parts, $0 < x \leqslant 0·55$ and $0·55 \leqslant x \leqslant 1$. In the first part, we assume the f.c.c. palladium lattice expands linearly from a lattice parameter of $a = 3·88$ Å at $x = 0$ to approximately 4·02 Å at $x = 0·55$. Actually, a two-phase system exists for $0·02 \leqslant x \leqslant 0·60$; the α-phase with $a = 3·89$ Å, and the β-phase with $a \simeq 4·02$ Å. There are no values of a between 3·89 and 4·02 Å. For $x < 0·02$ a varies continuously from 3·88 to 3·89 Å. For $x > 0·60$, only the β-phase exists. In both the α and β-phases, the hydrogen normally occupies the octahedral sites at room temperature[6]. The BSO model assumes the hydrogen ions are randomly distributed throughout the palladium lattice (i.e. the α and β-phases are randomly distributed). This is supported by the almost linear increase in (ρ_x/ρ_0) with x at 273°K for $0·02 < x < 0·70$; and the absence of appreciable scatter at both 273°K and 4·2°K for $0·02 \leqslant x \leqslant 0·60$ (where the α and β-phases coexist). Vuillemin has deduced from deHaas–vanAphen experiments that pure palladium has 0·36 hole in its d-band[7]. Presumably, the lattice expansion, caused by the hydrogen absorption, and the presence of interstitial hydrogen ion alter the Fermi surface and cause the failure of the rigid band model noted in [1]. This change in the Fermi surface causes the d-band to be filled at 0·55; instead of 0·36. At 4·2°K (Fig. 1), it is assumed that the hydrogen ions are screened from the conduction electrons by the highly localized palladium d-band for $0 < x < 0·36$. For $0·36 < x \leqslant 0·55$ the hydrogen electrons go increasingly into s-states. This results in a decrease in the screening effect and a more rapid increase in ρ_x/ρ_0 as x increases from 0·36 to 0·55.

Above 0·55 the stoichiometry of the NaCl type lattice influences the shape of the curve. Vacancies are filled in the hydrogen lattice and ρ_x/ρ_0 goes through a maximum near $x = 0·75$ and then decreases to approximately one at $x = 1$. The curves resulting from these assumptions combine at $x = 0·55$.

The screening effect decreases for increasing temperature. According to the BSO model, the screening effect is dependent upon the electron donated by the hydrogen atom being associated with the palladium d-band. The electrons are distributed between the s and

d-bands at all temperatures. However, the density of available electron states in the d-band at the Fermi level decreases with increasing temperature[8, 9]. We base the extension of references[8] and [9] to the PdH_x system on the similarity of the curvature of the ρ vs. T curves of pure palladium and PdH_x for x up to 0·40[3], i.e. the curvatures are concave toward the T-axis above approximately 80°K. Also, thermal contributions to the resistivity at 273°K are of the same order as the structural resistivity which is consistent with $\rho(273°K)/\rho(4{\cdot}2°K)$ for the uncharged annealed specimen. This decrease in screening and the thermal contributions result in the differences in the shapes of the curves at 4·2°K and 273°K.

The PdH_x data for ρ_x/ρ_0 vs. x is quite similar to the ρ_x/ρ_0 data for the PdD_x system reported in [1]. The maximum values of ρ_x/ρ_0 are somewhat greater for PdD_x than for PdH_x at both 4·2°K and 273°K. However, for $x < 0{\cdot}36$ at 4·2°K, ρ_x/ρ_0 values of PdH_x and PdDx are essentially equal. Apparently, where screening was dominant, screening obscured any effects due to differences in the two hydrogen isotopes.

Screening can be used to explain other features of the PdH_x system. One is that specific heat measurements[10] suggests that O–T transitions occur down to $x = 0{\cdot}125$ but resistivity measurements imply O–T transitions do not occur below $x = 0{\cdot}48$[11]. Screening prevents the O–T transitions from being seen by resistivity measurements below $x = 0{\cdot}48$ but not by specific heat measurements because specific heat measures the total energy of the system.

Finally, the observation that scatter is observed in the resistivity data at 4·2°K for $x > 0{\cdot}36$ but not for $x < 0{\cdot}36$ is readily explained by screening. Indeed, where the screening effect is dominant, resistivity appears to be independent of the octahedral or tetrahedral position of the hydrogen isotope in the palladium lattice or of such hydrogen isotope differences as mass or spin.

In conclusion, it appears that the model derived to explain the effect of composition on the resistivity of PdDx can be applied to PdHx.

Lewis Research Center,
Cleveland,
Ohio, U.S.A.

R. J. SMITH
D. A. OTTERSON

REFERENCES

1. BAMBAKIDIS G., SMITH R. J. and OTTERSON D. A., *Phys. Rev.* **177**, 1044 (1969).
2. LEWIS F. A., *The Palladium/Hydrogen System.* Academic Press, New York (1967).
3. HAYWOOD C. T. and VERDINI L., *Can. J. Phys.* **46**, 2065 (1968).
4. SMITH R. J., NASA TN D-2568 (1965).
5. FERGUSON G. A., SCHINDLER A. I., TANAKA T., and MORITA T. *Phys. Rev.* **137A**, 483 (1965).
6. MAELAND ARNULF J., *Can. J. Phys.* **46**, 121 (1968).
7. VUILLEMIN J. J., *Phys. Rev.* **144**, 396 (1966).
8. MOTT N. F. and JONES H., *The Theory of the Properties of Metals and Alloys*, pp. 269–271. Dover, New York (1958).
9. JONES H., *Encyclopedia of Physics* (Edited by S. Flugge), Vol. 19, pp. 267–269. Springer, Berlin (1956).
10. ASTON J. G. and MITACEK P., *Non-Stoichiometric Compounds, Advances in Chemistry Series*, No. 39, p. 111. American Chemical Society, Washington, D.C. (1963).
11. SCHINDLER A. I., SMITH R. J. and KAMMER E. W., *Proc. Tenth Intl Conf on Refrigeration*, Vol. 1, p. 74. Pergamon Press, Oxford (1960).

J. Phys. Chem. Solids Pergamon Press 1970. Vol. 31, pp. 191–198. Printed in Great Britain.

EXCESS FREE ENERGIES IN THE Ge, Si AND Ga BINARY SYSTEMS–THE α-PARAMETER APPROACH

M. V. RAO and W. A. TILLER
Department of Materials Science, Stanford University, Stanford, Calif. 94305, U.S.A.

(*Received* 26 *March* 1969; *in revised form* 25 *July* 1969)

Abstract—An equation of the form $\alpha_{12} = -A_2 - A_3N_2 + B_2/T$, where $\alpha_{12} = \ln \gamma_1/(1-N_1)^2$, has been found to fit the solubility data for the Ge and Si systems investigated by Thurmond[5] better than the composition independent form. It has been further shown that evaluation of the quantities $\Delta\bar{S}_1^{XS}$ and $\Delta\bar{H}_1$ from this functional dependence of α is too sensitive to the approximation used to be reliable. The α parameters in the Ga–As and Ga–P systems are also found to fit the proposed formalism, with A_3 being composition dependent in each case. A correlation of α_{12} with atomic 'size factor' has been found in the four systems investigated when all the solute elements are in the same group of the periodic table.

1. INTRODUCTION

THE ACTIVITY coefficient of one element is known to be affected by the presence of other elements present in solution. Wagner[1] proposed a power series expansion in terms of the mole fractions of the various elements present that is expected to hold approximately for the dilute solution case. A quadratic formalism or α-parameter approach proposed and studied by Darken[2–4] is a much more suitable procedure for evaluating the concentration dependence of activity coefficients for alloys of appreciable solute content. In the present investigation, we will use a parameter α differing only by a factor of 2·303 from that of Darken; i.e.

$$\alpha_{12} = \frac{\ln \gamma_1}{(1 \; - N_1)^2} \tag{1}$$

where γ_1 is the activity coefficient of the solvent (subscript 1) and where equation (1) is a consequence of the Margules expansion for the excess partial molar free energy of the solvent in a binary system,

$$\Delta\bar{F}_1^{XS} = RT \ln \gamma_1. \tag{2}$$

In the Margules power series of $(1-N_1)^n$, the $n = 0$ terms must be absent in order to satisfy Roult's Law and the $n = 1$ term must be absent in order to satisfy the Gibbs–Duhem equation. The series therefore reduce to

$$\Delta\bar{S}_1^{XS} = A_2R(1-N_1)^2 + A_3R(1-N_1)^3 + \dots \tag{3}$$

$$\Delta\bar{H}_1 = B_2R(1-N_1)^2 + B_3R(1-N_1)^3 + \dots \tag{4}$$

where $\Delta\bar{H}_1$ and $\Delta\bar{S}_1^{XS}$ are the partial molar enthalpy and partial molar excess entropy respectively.

$$\Delta F_1^{XS} = \Delta\bar{H}_1 - T\Delta\bar{S}_1^{XS}. \tag{5}$$

Therefore, α_{12} is given for a binary system by

$$\alpha_{12} = -A_2 - A_3N_2 + \frac{1}{T}[B_2 + B_3N_2] + \dots \tag{6}$$

where N_2 is the mole fraction of the solute element 2 and the A_i and B_i are constants. As a simplifying approximation for this paper, we shall neglect the higher power terms and will, in addition, presume that B_3 can be neglected, giving

$$\alpha_{12} = -A_2 - A_3N_2 + \frac{B_2}{T}. \tag{7}$$

For a strictly regular solution, defined by $\Delta \bar{S}_1^{xs} = 0$, we find $A_2 = A_3 = 0$ so that $\alpha_{12} = B_2/T$. For a real solution, if we find that A_3 and B_3 need to be either concentration or temperature dependent in order to fit experimental data, we must abandon equation (7) and must use an expanded form of equation (6).

In the interest of simplicity, Thurmond and Kowalchik[5] truncated equation (6) even further by setting $A_3 = 0$ in equation (7) and chose to define α^* as $\alpha^* = RT \ln \gamma_1/(1-N_1)^2$. Thus, they used a relation of the form $\alpha^* = B_2 - A_2/T$ which would give them a temperature independent α^* for a regular solution. They made an extensive study of the Ge and Si systems with numerous binary constituents and, although their simple form of α^* was adequate in many cases, it was clear that in several cases concentration effects were present. It thus seemed appropriate to utilize the somewhat more complete form of α_1 represented by equation (7) as a fitting parameter for this data.

Departure from ideality in solid solutions has been attributed to several reasons including valence and size effects. If Eyring's quasi-solid model of the liquid state (a solid-like structure with a large number of holes) is accepted, it would not be unreasonable to consider roughly similar rationales in liquid solutions. Since α is directly related to the departure from ideality, it is possible that there is a size factor correlation between α_{12}'s where all the '2' elements are in the same group of the periodic table, thus holding the valence effect constant.

Hildebrand[9] investigated several systems and found that k_N defined by $RT \ln \gamma_1/(1-N_1)^2$ varied with composition at a given temperature, whereas k_ϕ defined by $RT \ln \gamma_1/(1-\phi_1)^2$ where ϕ_1 is the volume fraction of solvent '1', was substantially constant with variation of ϕ_1. The two factors entering when volume fractions are substituted for mole fractions are packing density and atomic size. If the Goldschmidt CN12 atomic diameters[6] are used, the only variable factor is atomic size. One may take this as evidence pointing to the fact that atomic size has a correlation with the composition dependence of α; i.e. $\Delta \bar{S}_1^{xs}$, and possibly with $\Delta \bar{F}_1^{xs}$. In the solid state, a size correlation with $\Delta \bar{S}_1^{xs}$ has been suggested by Freedman[10]. Such a correlation has been investigated here for some systems.

2. FIT OF FORMALISM WITH EXPERIMENTAL DATA

Ge *and* Si *systems*

As expected, a better fit to the data of Thurmond and Kowalchik[5] was found using equation (7). The coefficients obtained from a least squares analysis of their data are listed in Tables 1 and 2. In some cases, the fit was strikingly better (see Figs. 1 and 2). The significance of Figs. 1 and 2 is to show that, if the A_3 term is included in the analysis, then α is found to be linearly dependent upon $1/T$ as proposed in equation (7). We do this by correcting, via equation (7), the temperature and concentration dependent data to the single concentration listed in the figures so that only the proper temperature dependance should be revealed if equation (7) is the appropriate fitting function. In the determination of the coefficients, obviously inaccurate points were neglected (such as when three solubilities were tabulated at a single temperature and one was vastly different from the other two). In many cases, the solubility measurements were made at low Ge (or Si) concentrations only; thus, the reliability of the coefficients for use at high Ge (or Si) concentrations is in some doubt. The tables also list the expected limits of reliability. In two particular cases, Si–Pb and Si–Bi, the data covered the region $N_{Si} < 0{\cdot}01$. These coefficients are likely to be very unreliable, consequently, since spurious compositional effects could be introduced by even minor experimental inaccuracies. In each of the foregoing systems, it was found that the composition dependence of α was linear.

Table 1. *Excess free energies in the* Ge *systems: the power series coefficients*

$$\alpha_{12} = -A_2 - A_3N_2 + \frac{B_2}{T}$$

Element '2' in Ge	A_2	A_3	B_2	Expected range of good reliability (N_{Ge})
Au	−0·6499	0·03995	−2515·1	0–1·0
Ag	−1·0352	2·16559	1201·3	0–1·0
Cu	−1·75575	0·367989	−1548·2	0–1·0
Ga	−0·07663	0·363630	57·99	0–0·50
In	−0·06404	−2·42964	−1257·5	0–0·5
Tl	+1·75109	−0·38449	3367·68	0–1·0*
Al	−0·57877	+1·16948	−1270·8	0–1·0
Bi	+0·82808	−0·52725	2398·4	0–0·35
Sb	+0·85088	+0·03465	1189·6	0–1·0
As	−6·4920	−2·60552	−8323·7	0·45–1·0
Cd	+0·8957	−0·71869	1527·5	0–0·45
Zn	+2·2110	+3·68280	4121·6	0–1·0

*Only three data points available.

Table 2. *Excess free energies in the* Si *systems: the power series coefficients*

Element '2' in Si	A_2	A_3	B_2	Expected range of good reliability (N_{Si})
Au	+11·747	+10·220	−24290	0–1·0
Ag	−3·7174	−2·6631	−6725·3	0–1·0
Cu	−5·7915	−4·3019	−11751·6	0–0·9
Ga	+0·46958	+0·3560	+1938·8	0–0·5
In	+2·8389	−2·2214	4501·4	0–0·2
Al	+0·2358	+0·63708	−620·85	0–1·0
Bi	-	-	-	*
Sb	−0·18475	−1·26158	931·88	0–0·25
As	−21·08	−10·310	+37370	†
Pb	-	-	-	*
Sn	+5·1473	−7·0262	1073·7	0–0·10
Zn	+8·8408	−10·078	548·9	0–0·10

*Data covers $N_{Si} < 0{\cdot}01$; coefficients very unreliable and, hence, not listed.
†Only three data points available, in the range 0·60–0·70.

Darken and Gurry[6] plotted α vs. composition (at constant temperature) and found that the dependence was either linear, exhibited two linear segments, or was a smooth curve. This could be expected in our analysis also and was, in fact, found in the next system investigated, Ga–As.

Ga–As *system*

Thurmond[7] investigated the Ga–As system and found that the α^* parameter did not fit an equation of the form $\alpha^* = b + aT$. Arthur[8] conducted further experiments with better accuracy in the estimation of γ_{As} and obtained a fit of α_{AsGa} to an equation

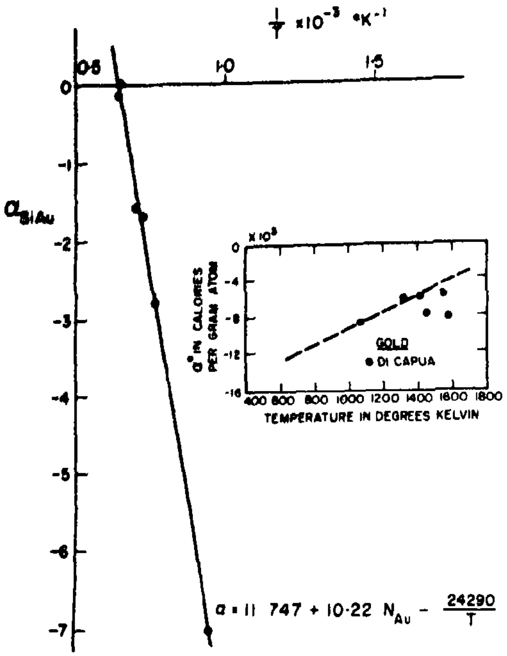

Fig. 1. α_{SiAu} as a function of $1/T$ at constant 40% Au composition compared with α^*_{SiAu} as a function of T[5].

of the form $\alpha^* = -bT$, thus concluding that the heat contribution was zero. He could not, however, get α_{GaAs} to fit equation(8) and attributed this to the γ_{Ga} being 'less reliable' than the γ_{As} since it was calculated from the latter and not determined directly. It must be pointed out here that we concern ourselves only with the α's calculated from Arthur's pressure measurements. He also determines the regular solution model α's by Vieland's method from the liquidus, but these are disregarded as having little significance in this system.

The form indicated by equation (7) was fitted to the activity data of Arthur[8]. It was found that a break in the α_{AsGa} vs. N_{As} line was required to obtain the fit indicated in Fig. 3. Darken and Gurry[6] have suggested that, if the α_{12} line has two linear segments, the α_{21} line will have one linear and one curved segment, the breaks occurring at the same composition. This is exactly what is observed here, as can be seen in Fig. 3.

Ga–P *system*

Thurmond[7] also investigated the Ga–P system in the same study as Ga–As but did not attempt to give a formulation for either α_{GaP} or α_{PGa}. The form of equation (7) was fitted to his activity coefficient data with the use of his Ga–P phase diagram. Once again, the α_{PGa} vs. N_P line was found to be segmented and the α_{GaP} curve also broken into one line and one curve, the two breaks being at roughly the same composition, as shown in Fig. 4. The α_{PGa} equations are given below. For α_{GaP}, the equation at constant composition ($N_P = 0$) is shown; the compositional part can be obtained from Fig. 4.

Results:

$$\alpha_{AsGa} = -2{\cdot}6080 + 0{\cdot}4077\, N_{Ga} + \frac{638}{T} \text{ for } N_{As} \leqslant 0{\cdot}45$$

$$= -2{\cdot}6080 + 0{\cdot}921\, N_{Ga} + \frac{638}{T} \text{ for } N_{As} \geqslant 0{\cdot}45$$

$$\alpha_{GaAs} = -26{\cdot}690 + \frac{47900}{T} \text{ at } N_{As} = 0$$

$$\alpha_{PGa} = -6{\cdot}554 - 5{\cdot}527\, N_{Ga} + \frac{15540}{T} \text{ for for } N_P \leqslant 0{\cdot}32$$

$$= -6{\cdot}554 - 8{\cdot}567\, N_{Ga} + \frac{15540}{T} \text{ for for } N_P \geqslant 0{\cdot}32$$

$$\alpha_{GaP} = -110{\cdot}3 + \frac{191700}{T} \text{ at } N_P = 0.$$

3. SIZE EFFECT CONSIDERATIONS

Solutions of Group I elements (Li, Na, K) in Hg at 25°C were first considered. The values for α at low concentrations were obtained from Dealy and Pehlke[11] and α

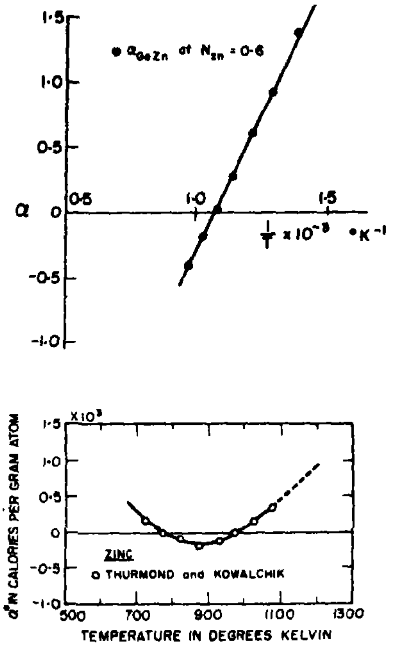

Fig. 2. α_{GeZn} as a function of $1/T$ at constant 60% Zn composition compared with α^*_{GeZn} as a function of T [5].

was seen to have a linear variation with 'size factor' defined by $(R_0-R)/R$ where R_0 and R are the (metallic) radii of solvent and solute atoms respectively (see Fig. 5). When the solutes differ in crystal structure, the Goldschmidt CN12 atomic radii should probably be used. A similar correlation with size factor was found for some Group II elements in Bi as solvent at 600°C. In Fig. 6, the Mg, Cd and Hg values were corrected to 600°C from 700°C, 500°C and 320°C respectively using an approximate relation of the form $\alpha = A/T$. This could be in error, but its magnitude is expected to be small since the α's themselves are small.

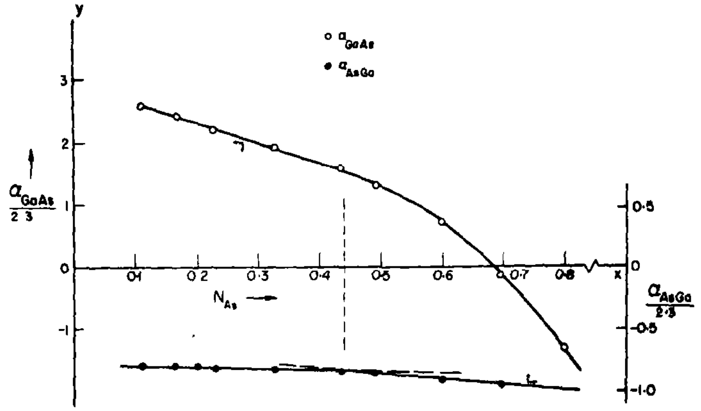

Fig. 3. α_{GaAs} and α_{AsGa} as functions of As composition at 1430°K.

For Group III elements in Ge, α_{GeX} was calculated at $N_X = 0 \cdot 02$ where X = Ga, In, Al and Tl, at 1333°K. The Goldschmidt CN12 atomic radii were used. Ga, In and Al are seen to have a fair correlation (Fig. 6) with size factor whereas Tl is quite far off. A similar odd behavior of Tl was observed in Cd solutions in comparison with Ga and In (data from Turkdogan and Darken[4]). The α_{GeX} computations were made from Table 1 at high Ge($N_{Ge} = 0 \cdot 98$) concentrations where the coefficients could be slightly in error. For Group V elements in Ge, α_{GeX} was calculated at $N_X = 0 \cdot 02$ where X = As, Sb, Bi at 1233°K. A good fit was obtained (Fig. 6). In all the other Ge and Si systems, extrapolations to Ge rich concentrations were either unreasonable or data existed for less than three elements in the same group; thus, no correlations could be attempted.

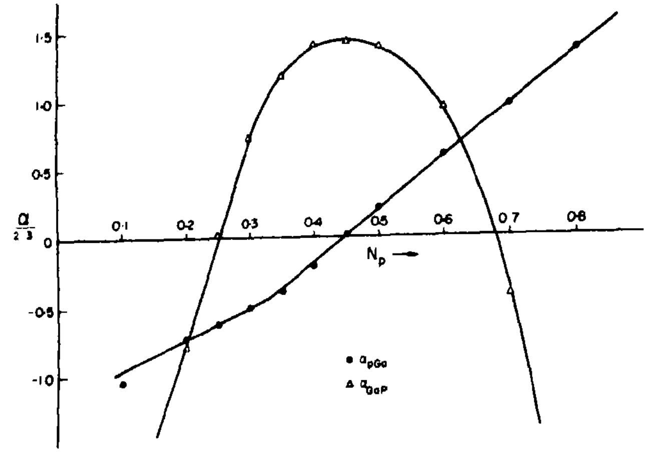

Fig. 4 α_{GaP} and α_{PGa} as functions of P composition at 1668°K.

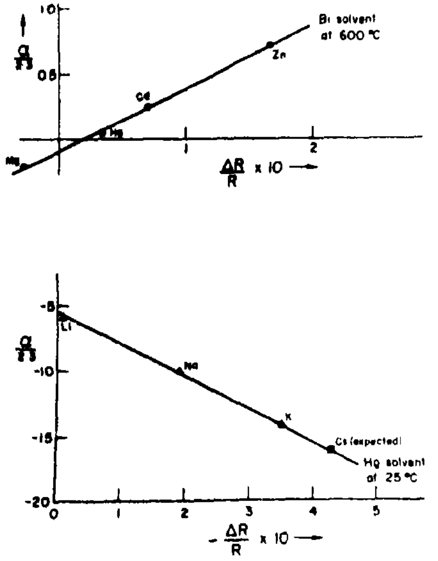

Fig. 5. Size factor dependence of α. Systems: Group I elements in Hg and Group II elements in Bi.

4. DISCUSSION

(i) *Comparison of the fit of the Thurmond and Kowalchik data with equations* (7) *and* (8)

In general, a better fit was obtained for the form of equation (7) than for equation (8). In some cases, the improvement was not significant, especially when the data covered small composition ranges. This is indicated by the small contribution of the A_3 term in these cases. In some other cases, the improvement was striking. Two such are the Ge–Zn and Si–Au systems. For the latter, Thurmond and Kowalchik obtained considerable scatter about the line they drew, and for the former they could not get a linear variation. Equation (7) gives a good fit for both, as seen in Figs. 1 and 2.

(ii) *Effect of taking* $B_3 = 0$

Keeping $B_3 = 0$ in equation (6) appears to give a good fit with the data and the error

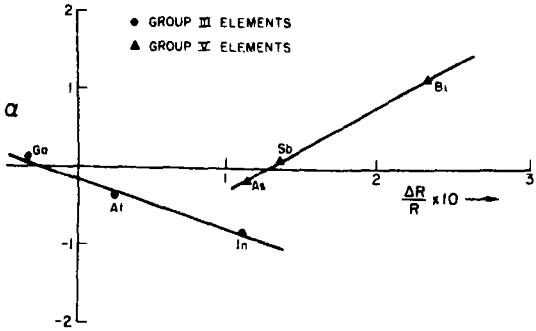

Fig. 6. Size factor dependence of α. Systems: Group III and Group V elements in Ge.

introduced in so doing is generally less than 4 per cent in the estimation of α. Its magnitude depends partly on the relative importance of the heat term. In the Ga-As system for the α_{AsGa} function, the contribution of entropy predominates, so the effect of taking $B_3 = 0$ is very small i.e. leading to an error of the order of 2 per cent in the $\Delta\bar{F}_{As}{}^{XS}$. In the Ge-Au and Ge–Ag systems, both equations were tried. The fit with $B_3 \neq 0$ was necessarily better but whereas (in the Ge–Au system) the $\Delta\bar{F}_1{}^{XS}$ at an arbitrary liquidus part of $N_{\mathrm{Ge}} = 0{\cdot}573$, differed by only 2·75 per cent, the $\Delta\bar{H}_1$ and $\Delta\bar{S}_1{}^{XS}$ values were vastly different.

	ΔH_{Ge} (cal/mole)	$\Delta\bar{S}_{\mathrm{Ge}}{}^{XS}$ (e.u.)	$\Delta\bar{F}_{\mathrm{Ge}}{}^{XS}$ (cal/mole)
$B_3 = 0$	-1063	$-{\cdot}276$	-819
$B_3 \neq 0$	$+8800$	$+10{\cdot}560$	-797

A similar striking difference was observed for the Ge–Ag system and for α_{AsGa}. The apparent conclusion is that the values of $\Delta\bar{S}_1{}^{XS}$ and $\Delta\bar{H}_1$ obtained by these methods is extremely sensitive to the approximation and completely unreliable. There is an indication, however, that successive approximations could lead to a convergence of the $\Delta\bar{H}_1$ and $\Delta\bar{S}_1{}^{XS}$ values. The next three approximations following equation (7), in Ge–Ag, appear to support this view; i.e. convergence is rapid for both $\Delta\bar{H}_{\mathrm{Ge}}$ and $\Delta\bar{S}_{\mathrm{Ge}}{}^{XS}$. Were this always so, a reliable estimate of these two quantities could be obtained; but no conclusions are drawn regarding this at this point.

(iii) *Size factor*

Correlations between α, at dilute concentrations, with size factor have met with some success in the systems studied. The basis for expecting some such correlation appears reasonable and should certainly be extremely useful. If in the solid solution the solute is predominantly interstitial (as opposed to substitutional), one would expect the correlation to break down. A similar rationale may be attributed to the quasi-solid liquid state for an absence of correlation.

(iv) Ga–As

It appears from the functional relationship obtained to express the α_{AsGa} data that $\Delta\bar{H}_1$, though small, is not negligible in comparison with $\Delta\bar{S}_1{}^{XS}$. It has further been shown that estimation of these quantities by such procedures can be erroneous. The system does not appear to be 'athermal' from the relative magnitude of the two quantities. For example, consider the liquidus point at $N_{\mathrm{As}} = 0{\cdot}257$ and $1/T = 0{\cdot}7075 \times 10^{-3}$ °K^{-1}. One finds,

	$\Delta\bar{S}_{\mathrm{As}}{}^{XS}$ (e.u.)	$\Delta\bar{H}_{\mathrm{AS}}$ (cals/mole)	$\Delta\bar{F}_{\mathrm{As}}{}^{XS}$ (cals/mole)
$B_3 = 0$	2·190	600	2860
$B_3 \neq 0$	4·040	3225	2845

Arthur's formulation of $RT \ln \gamma_{\mathrm{As}}/(1 - N_{\mathrm{As}})^2 = -3{\cdot}7T$ gives a very good fit with experimental data; but then it appears that successive approximations do little to change the $\Delta\bar{F}_{\mathrm{As}}{}^{XS}$ whereas the effect on the $\Delta\bar{H}_1$ and $\Delta\bar{S}_1{}^{XS}$ is large. A comparison of $\Delta\bar{F}_{\mathrm{As}}{}^{XS}$ from equation (7) and Arthur's equation and his experiment, shows that the difference is small (Fig. 7). At high As contents, however, the relatively large errors in Arthur's curve would be expected to cause a scatter about the α vs. T line. The equation (7) relationship fits much closer to the experimental data obtained by Arthur. The significant point, however, is that equation (7) fits the γ_{Ga} data whereas fit with the $\alpha^* = a + bT$ equation could not be obtained by Arthur.

(v) Ga–P

Thurmond's data was experimentally obtained only within the range $N_{\mathrm{P}} = 0{\cdot}2$ to 0·4 but he made reasonable extrapolations on either side. Both of these extrapolations

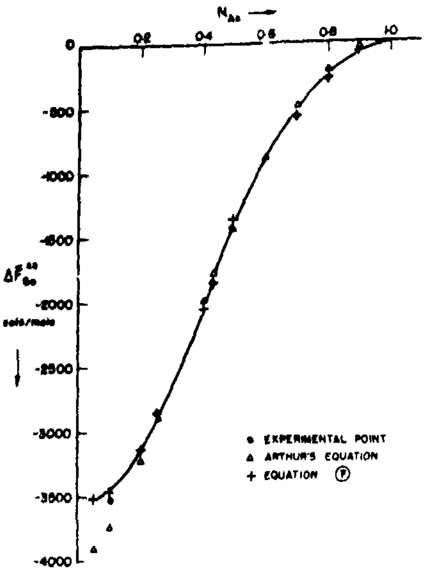

Fig. 7 $\Delta \bar{F}_{Ga}{}^{XS}$ as a function of As composition

appear to be excellent in that they fall on the α vs. composition (at constant temperature) lines predicted from the 0·2–0·4 region (both for α_{GaP} and α_{PGa}). The log γ_P curve has a very slightly lower trajectory with N_P beyond $N_P = 0{\cdot}75$ according to our analysis (with a small corresponding change in the log γ_{Ga} curve). See Fig. 12 in [7].

5. CONCLUSIONS

The $\alpha_{12} = -A_2 - A_3N_2 + B_2/T$ form of representation is seen to fit the Ge and Si systems better than the composition independent form. The inclusion of the next term in the expansion ($B_3 \neq 0$) has been found to produce only marginally different results. However, it is found that the $\Delta \bar{S}_1{}^{XS}$ and $\Delta \bar{H}_1$ quantities change considerably with the different orders of expansion used as the curve fitting expressions. This leads one to conclude that estimation of these quantities by this type of approach is too sensitive to the approximation to make it reliable for a 3 or 4-term expansion. The term A_3 can be expected to sometimes vary with composition over the total composition range of the diagram if one uses only the 3-term expression.

A correlation of the α-parameter in dilute solutions has been found with 'size factor' in the systems investigated. A reasonable basis has been proposed but no unequivocal conclusions drawn regarding the universality of this behavior.

The Ga–As and Ga–P systems have been re-analyzed using the data of Thurmond [7] and Arthur[8] and found to fit the proposed 3-term formalism for α_{AsGa}, α_{GaAs}, α_{PGa} and α_{GaP}. The coefficient A_3 was found to vary over the composition range of the diagram in each of these cases. The results suggest that the Ga–As system is not 'athermal'.

Acknowledgements—The authors are grateful to R. A. Hiskes for his generous assistance. This work was supported by the Air Force Office of Scientific Research, Grant AF-AFOSR-68-1360, and by the Advanced Research Projects Agency through the Center for Materials Research at Stanford University.

REFERENCES

1. WAGNER C., *Thermodynamics of Alloys*. Addison-Wesley, New York (1952).
2. DARKEN L. S., *Trans. AIME* **239**, 80 (1967).
3. DARKEN L. S., *Trans AIME* **239**, 90 (1967).
4. TURKDOGAN E. T. and DARKEN L. S., *Trans. AIME* **242**, 1997 (1968).
5. THURMOND C. D. and KOWALCHIK M., *Bell Syst Tech J.* 169 (1960).
6. DARKEN L. S. and GURRY R. W., *Physical Chemistry of Metals*, pp. 49, 271. McGraw-Hill, New York (1953).
7. THURMOND C D., *J. Phys. Chem. Solids* **26**, 785 (1965)
8. ARTHUR J. R., *J. Phys. Chem. Solids* **28**, 2257 (1967).
9. HILDEBRAND J. H. and SCOTT R. C., *The Solubility of Non-Electrolytes*, p. 239. Dover, New York (1964).
10. FREEDMAN J. F. and NOWICK A. S., *Acta Metall.* **6**, 176 (1958).
11. DEALY J. M. and PEHLKE R. D., *Trans. AIME* **227**, 88 (1963).

J. Phys. Chem. Solids Pergamon Press 1970. Vol. 31, pp. 199–214. Printed in Great Britain.

DIE OPTISCHEN ABSORPTIONSSPEKTREN VON Ni^{2+} IN Cl- und J-BORAZITEN*

E. DORMANN
2, Physikalisches Institut der Technischen Hochschule, Darmstadt, Deutschland

(*Received* 13 *June* 1969; *in revised form* 25 *July* 1969)

Zusammenfassung – Die optischen Absorptionsspektren von Ni^{2+} in Ni–Cl-, Ni–J- und Ni-dotierten Cd–Cl- und Cd–J-Boraziten wurden im Temperaturbereich von etwa 4,2°–635°K gemessen. Bei tiefen Temperaturen wurden vielfach Flankenstrukturen der Absorptionsbänder beobachtet. Eine Beschreibung der gemessenen Spektren im Rahmen des Kristallfeldmodells bei Annahme einer tetragonalen und einer etwas kleineren kubischen Kristallfeldaufspaltung wird vorgeschlagen.

Abstract – The optical absorption spectra of Ni^{2+} in Ni–Cl-, Ni–I- and Ni-doped Cd–Cl- and Cd–I-boracites were measured at temperatures ranging from 4·2° to approximately 635°K. At low temperatures, we often observed fine structures of the absorptionbands. A description of the measured spectra within the frame of the crystal-field-model, assuming a tetragonal and a slightly smaller octahedral crystal-field splitting, is suggested.

EINLEITUNG

Die Borazite, die nach dem in der Natur vorkommenden Kristall $Mg_3B_7O_{13}Cl$ benannt werden, lassen sich durch die Summenformel $Me_3{}^{2+}B_7O_{13}X^-$ beschreiben, wobei Me eins der Metalle: Mg, Cr, Mn, Fe, Co, Ni, Cu, Zn, Cd, und X ein Halogen: Cl, Br, oder J ist. Nach einer Analyse von Ito *et al.*[1] liegt der natürliche Borazit bei Temperaturen $T > 265°C$ in der 'α-Phase' vor mit der Raumgruppe $T_d{}^5$ ($F\bar{4}3c$), bei $T < 265°C$ in der 'β-Phase' mit der Raumgruppe C_{2v}^5 ($Pca2_1$).

Seine Ferroelektrizität in der β-Phase wurde von le Corre[2] vermutet; bei einem Großteil der künstlichen Borazite, die sich nach einem von Schmid[3] angegebenen Transportreaktionsverfahren herstellen lassen und deren Struktur weitgehend mit der des Mg–Cl-Borazits übereinstimmt, wurde die Ferroelektrizität der β-Phase von Ascher *et al.*[4] überprüft.

Durch Mössbauer-, optische und röntgenographische Methoden konnte bei einigen Boraziten bei tieferen Temperaturen auch noch eine trigonale Phase C_{3v}^6 ($R3c$) gefunden werden[5].

Die 3d-Metall-Borazite weisen überdies interessante magnetische Eigenschaften auf [6, 7]. Sie haben, soweit untersucht, negative Curie-Weisstemperaturen; vielfach tritt gebunden an den antiferromagnetischen Ordnungszustand ein ferromagnetisches Moment auf. Beim Ni–J-Borazit beobachtet man unterhalb des α-β-Umwandlungspunktes (64°K) den magneto-elektrischen Effekt[8].

In Tabelle 1 sind einige wichtige Daten der hier behandelten Borazite zusammengefaßt.

Die optischen Absorptionsspektren von Boraziten und ihre Erklärung sind noch nicht bekannt. Die ersten Messungen an einigen 3*d*-Übergangsmetall-Boraziten führte Elschner durch[9]. In dieser Arbeit werden die Absorptionen von Nickel in verschiedenen Boraziten für den sichtbaren und nahen infraroten Spektralbereich wiedergegeben. Die bei Temperaturen unter 100°K auftretenden Strukturen in den Absorptionslinien werden diskutiert. Außerdem wird eine Zuordnung der beobachteten Übergänge zu berechneten Kristallfeldniveaus des Ni^{2+}-Ions vorgeschlagen.

EXPERIMENTELLE ERGEBNISSE

Mit einem Leitz-Infrarot-Spektralphotometer (Modell IIIG) wurden die Absorptionsspektren von Ni–Cl-, Ni–J-, und Ni-dotierten

---

*Auszug aus einer Darmstädter Dissertation, D17.

Tabelle 1. Einige wichtige Daten der hier behandelten Borazite

	Ni–Cl	Ni–J	Cd–Cl	Cd–J	Mg–Cl–B	
α-β-Umwandlungstemp. (°K) = elektr. Curietemperatur	610	64	798	611/623	538	(3)
Gitterkonst. c (Å), 20°C	12,019	12,046	12,49	12,56	12,1	(3)
n_{eff}(Bohrsche Magnetonen) (Hochtemp. extrapolation)	4,13	4,15	–	–	–	(6)
n_{eff}(Tieftemp. extrapolation)	3,69					(7)
T_c (°K), (H. T. Extrap.)	−108	−325				(6)
T_c (°K) (T. T. Extrap.)	−14	–				(7)
T_N (°K)	+15	120: $T_c = 64$°K				(7)

> 80°K keine orthorhombisch-trig. Umwandlung[5]

Cd–Cl- und Cd–J-Boraziten im Bereich von 0,35–19 μ bei Temperaturen zwischen 4,2 und über 600°K aufgenommen. Als Proben wurden unter Verwertung der natürlichen (100)-, (110)- und (111)- Flächen auf etwa 0,05–0,5 mm Dicke geschliffene und polierte Kristallplättchen (etwa 1–6 mm² nutzbare Fläche) verwandt.

Im Wellenlängenbereich > 3,5 μ konnten (bei Vergleich mit Cd- und Fe-Boraziten) keine Ni^{2+}-Absorptionen sicher festgestellt werden. Für den übrigen Spektralbereich zeigt ein Vergleich der Abb. 1–4, daß sich die Spektren von Ni–Cl- und Ni–J-Borazit außer in geringen Intensitäts- und Wellenzahlverschiebungen kaum unterscheiden. Die Absorptionsstärken sind für 3*d*-Ion-Kristallfeldspektren von üblicher Größenordnung ($f \sim 10^{-6} - 10^{-4}$) mit Ausnahme der kurzwelligen Absorptionen, besonders des Ni–J-Borazits bei $\lambda \leqslant 370$ mμ; die nur gering Ni-dotierten Cd–Cl-bzw. Cd–J-Borazite lassen für das Band bei 420 m μ Oszillatorstärken von $10^{-4} - 10^{-3}$ bestimmen, für $\lambda \leqslant 360$ mμ waren auch unter 0,5% Ni-dotierte Cd–J-Borazite undurchlässig. Dieses Verhalten legt die Interpretation als 'Charge-Transfer'-Übergang nahe, der bei den kovalenteren J-Nachbarn[10] bei niedrigerer Energie als bei den Cl-Nachbarn zu erwarten ist.

Mit abnehmender Temperatur ist eine Verschmälerung der Übergänge und das Auftreten von Strukturen in den Absorptionslinien zu beobachten. (siehe z.B. Abb. 1 bei $\lambda = 1050$ m μ) Die Änderung der Absorptionsminima ist für die bei Schmid[3] aufgeführte Thermochromie der Ni–Cl- und Ni–J-B. verantwortlich. Auffällige Änderungen der Spektren beim α-β-Phasenübergang treten nicht auf; ebensowenig Linien- und Intensitätsverschiebungen, die auf mehrere Grundtermkomponenten mit verschiedenem Spin S innerhalb etwa 300 cm⁻¹ hinwiesen. Untersuchungen mit polarisiertem Licht zeigten keine die Messunsicherheit übersteigende Variationen der Absorption. (Die Absorptionsmaxima waren dabei allerdings z.T. apparativ nicht erfassbar.)

Die Spektren von Ni^{2+} (Konz. bereich etwa 0,1–75%) im Cd–Cl–B. (Abb. 5 u. 6) und Cd–J–B. (Abb. 7) unterscheiden sich bis auf kleinere Verschiebungen und entsprechend geringere Intensität nicht von denen der konzentrierten Borazite. Dies gestattet es, selbst für die Analyse der 100% Ni-Borazit-Spektren ein Ein-Ionen-Modell als Näherung zu verwenden.

DISKUSSION DER SPEKTREN

Nach der Strukturanalyse des Mg–Cl-Borazits durch Ito *et al.*[1] besitzen α- und β-Phase des Kristalls ein unverändertes Boroxidgerüst, in dessen Hohlräumen die Mg- und Cl-Ionen verschiebbar angeordnet sind. Die kubische Elementarzelle umfasst 8, die orthorombische 4 Formeleinheiten.

In der kubischen Elementarzelle sind je 8 der 24 identischen Oktaeder um Mg-Ionen

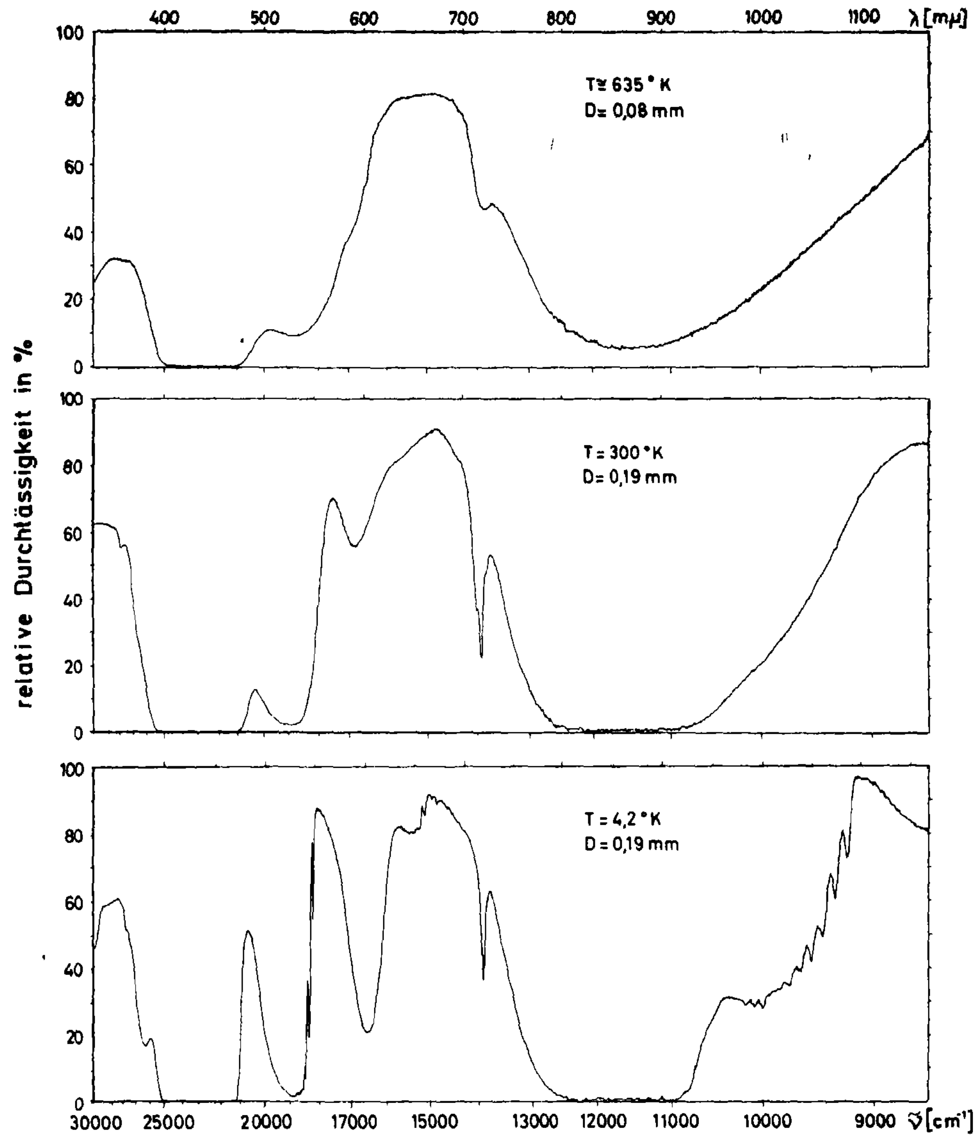

Abb. 1. Absorptionsspektrum des Ni-Cl-Borazits.

parallel zu den 3 Würfelkanten angeordnet. Sie bestehen aus 4 nicht ganz koplanaren O-Ionen und 2 Cl-Ionen in größerem Abstand auf der z-Achse (Abb. 8(a)). Die Punktsymmetrie des Metallions ist S_4, bei Berücksichtigung nur der 6 nächsten Nachbarn D_{2d}.

Jeweils nur 4 der 12 Oktaeder in der orthorhombischen Elementarzelle sind äquivalent. Dabei sind die Mg-Ionen um etwa 0,24 Å entlang der z-Achse gegenüber den entsprechenden Lagen bei der α-Phase verschoben (Abb. 8(b)), die Cl-Ionen um 0,21 Å entlang der kubischen (111)-bzw. ($\bar{1}\bar{1}1$)-Richtungen. Die drei inäquivalenten Oktaedertypen stimmen nicht überein:

1. in den Winkeln θ und ϕ für die Mg-Cl-Verbindungsachsen;

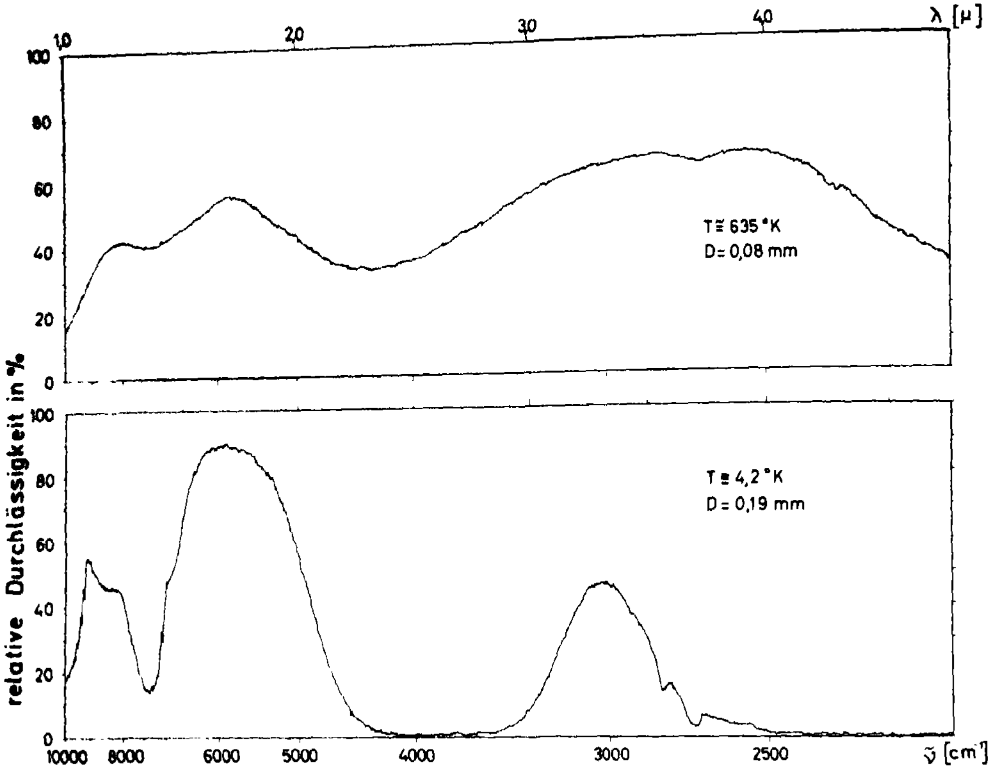

Abb. 2. Absorptionsspektrum des Ni–Cl-Borazits. Bei den Tieftemperaturspektren ist für $\lambda > 3{,}5\,\mu$ die Absorption der Dewar-Quarz-Fenster überlagert Die beiden Absorptionen bei etwa 3,57 und 3,7 μ ($\Delta\tilde{\nu} = 96-96{,}5\,\mathrm{cm}^{-1}$ für Fe–, Ni–, Cd–Cl–B, $\Delta\tilde{\nu} = 92{,}5\,\mathrm{cm}^{-1}$ für Cd–J–B) traten außer bei Ni–J–B, mit leichten Verschiebungen bei allen untersuchten Boraziten auf. (Gitterschwingung in β-Phase?)

2. darin, daß in einem Fall die spontane elektrische Polarisation ∥ zur z-Achse, in den beiden andern senkrecht dazu gerichtet ist. Die Punktsymmetrie des Mg-Ions ist streng nur noch C_1.

Die Gitterkonstanten der künstlichen Borazite unterscheiden sich nur wenig von denen des natürlichen Mg–Cl-Borazits; die Raumgruppen des Ni–Cl- und Ni–J-Borazits stimmen mit denen des Mg-Cl-B. überein; dasselbe ist auch für die Nahumgebung der Ni^{2+}-Jonen zu erwarten[11].

Ni^{2+}-SPEKTRUM NACH DEM KRISTALLFELD-MODELL

Bei Verwendung der Strukturdaten für die 6 nächsten Nachbarn aus[1] ergeben sich nach dem Punktladungsmodell für ein einzelnes Ni^{2+}-$3d$-Elektron die Aufspaltungsbilder aus Abb. 9. ($\langle r^n \rangle$ aus Freeman and Watson[12], D_{2d}-Gruppentafel aus Griffith [10]). Berücksichtigung von 50 nächsten Nachbarn in der α-Phase führt zu keiner prinzipiellen Änderung, wie Trooster[13] im Fall von Fe^{2+} zeigte. In der ferroelektrischen β-Phase sind die permanenten elektrischen Dipolmomente für Abb. 9 vernachlässigt. Da das Punktladungsmodell bestenfalls qualitativ richtige Ergebnisse liefert, soll dieser Rechnung nur entnommen werden, daß die Aufspaltungsbilder für alle 4 Oktaedertypen (Abb. 9) sich weitgehend gleichen.

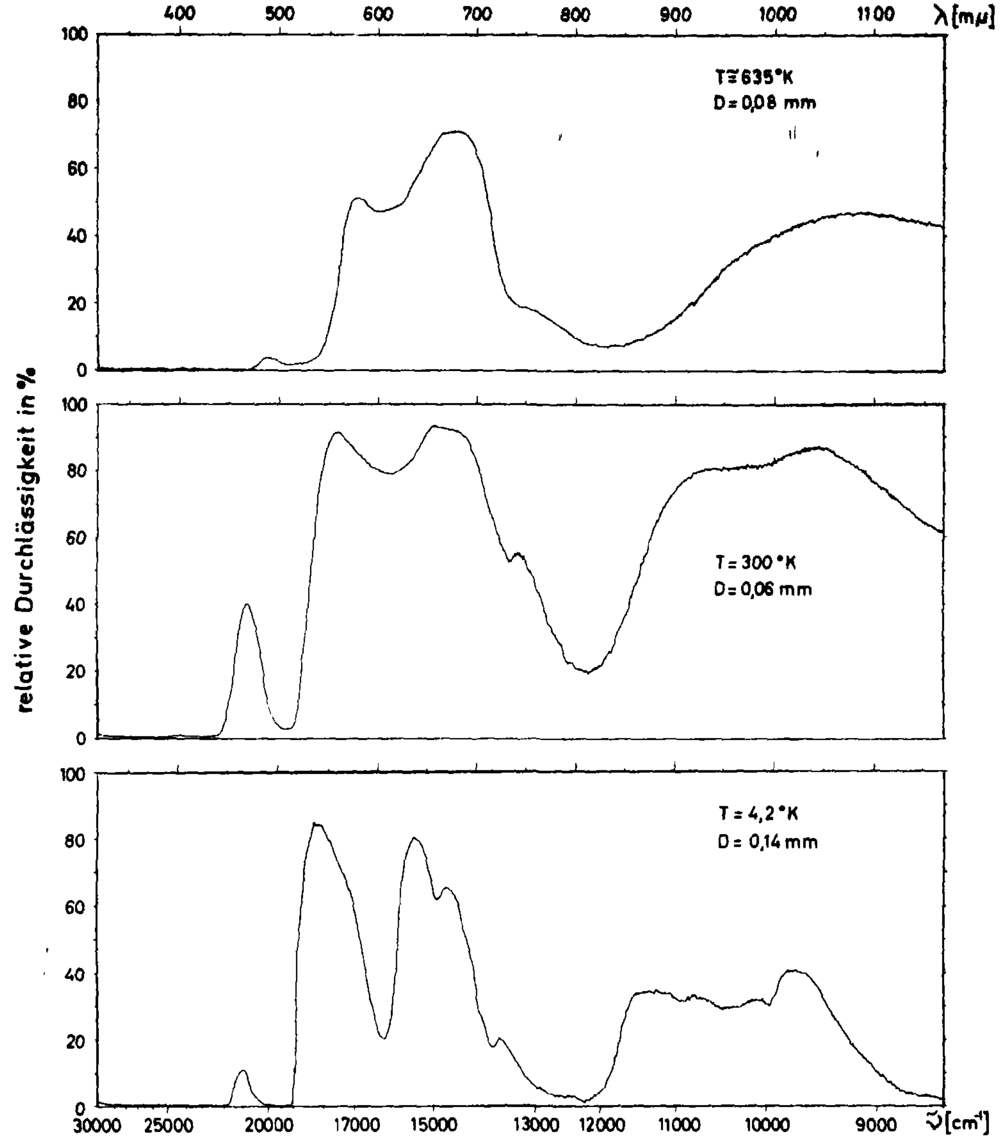

Abb. 3. Absorptionsspektrum des Ni-J-B.

Zur genaueren Analyse wurde eine Kristallfeldrechnung für die d^8-Konfiguration in tetragonaler Symmetrie (D_{2d}-Termbezeichnungen) unter Verwendung der bei Tanabe *et al.*[14, 15] angegebenen Matrixelemente und Clebsch-Gordan-Koeffizienten durchgeführt und mit einer IBM 7090 ausgewertet. (E_x-E_y-Aufspaltung vernachlässigt). Die Parameter $10Dq$, E, F/E (Abb. 9), B und C/B wurden variiert.

Um die Vieldeutigkeit der Termzuordnung (ohne Polarisationsaussagen) nur nach Energielagen einzuschränken, wurden folgende Kriterien berücksichtigt:

(1) Zur Erklärung der beobachteten Ni^{2+}-Suszeptibilitäten[6, 7] muß zumindest bei

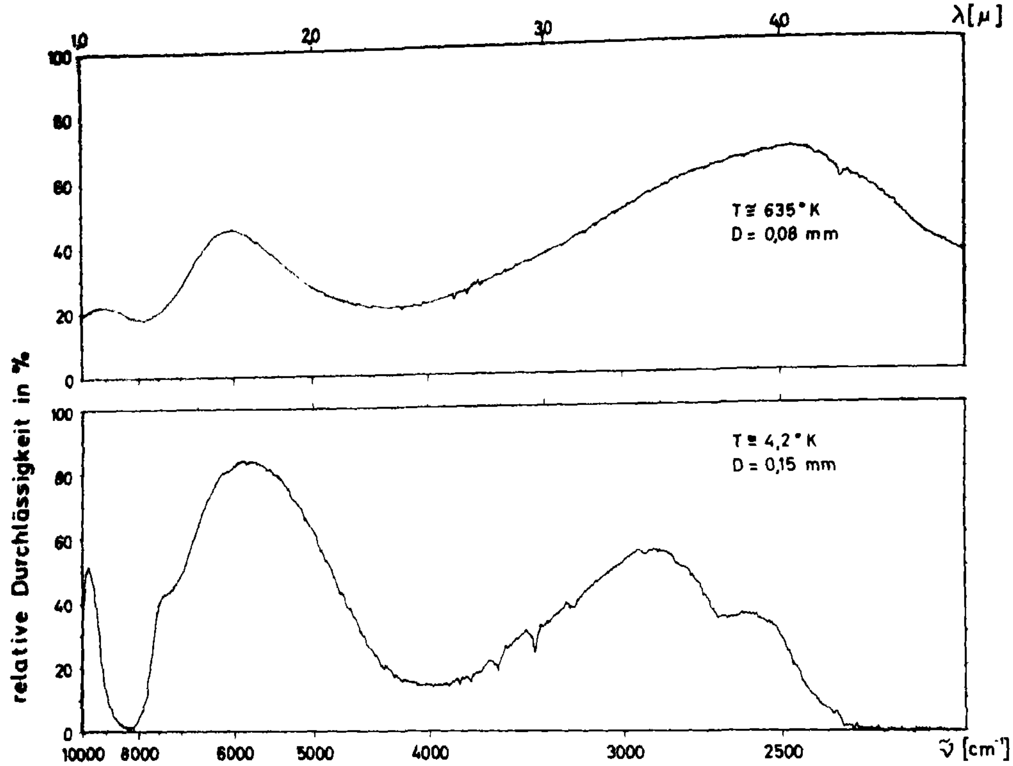

Abb. 4. Absorptionsspektrum des Ni–J–B.

höheren Temperaturen ($T > 15°K$ im Ni–Cl–B., $T \geqslant 120°K$ im Ni–J–B. (α-Phase)) ein Triplettzustand besetzt sein ($^3B_2(d\epsilon^8 d\gamma^2)$ oder $^3A_2(d\epsilon^6 d\gamma^3)$, kubische Orbital-Bezeichnung).

(2) Die Annahme eines tieferliegenden Singuletts $^1A_2(d\epsilon^6 d\gamma^2)$, mit der Heinrich *et al.* [16] die mit der Temperatur abnehmende Suszeptibilität des Ni–J-B. erklären konnten ($\Delta E \approx 160\,\mathrm{cm}^{-1}$), ließe eine starke Intensitätsabnahme einzelner Übergänge zu tiefer Temperatur hin erwarten. Dies wird jedoch nicht beobachtet (Abb. 3 u. 4).

(3) Die Spektren von Ni^{2+} in J- und Cl-B. sind sehr ähnlich. Die sonst bekannte verschiedene Kovalenz und Kristallfeldstärke [10] von J und Cl wirkt sich hier demnach wenig aus. Dies wird durch die geringe Variation der Isomerieverschiebung von Fe^{2+} in Ni–Cl/J/Br–B. bei den Mössbauer-untersuchungen Trooster's [13] unterstrichen.

(4) Die freien-Ni^{2+}-Ion-Werte $B = 1030\ \mathrm{cm}^{-1}$, $C = 4{,}71 \cdot B$ sind in Ionenkristallen in der Regel durch Kovalenzeffekte um 10–20% reduziert.

(5) Der kubische Kristallfeldparameter $10Dq$ berechnet sich nach dem Punktladungsmodell zu

$$10Dq = -\tfrac{5}{18} e \sum_{i=1}^{6} f_i \frac{q_i}{R_i^5} \langle r^4 \rangle ;\ f_i = 1$$

Die hier eingeführten Skalenfaktoren f_i wurden an die experimentellen Daten

NiO; $R = 2{,}09$ Å; $q_i = -2e$;
$10Dq \approx 9100\ \mathrm{cm}^{-1}$
$NiCl_2$; $R = 2{,}55$ Å; $q_i = -1e$;
$10Dq \approx 7000\ \mathrm{cm}^{-1}$

angepasst und danach für Ni^{2+} in der Borazit-

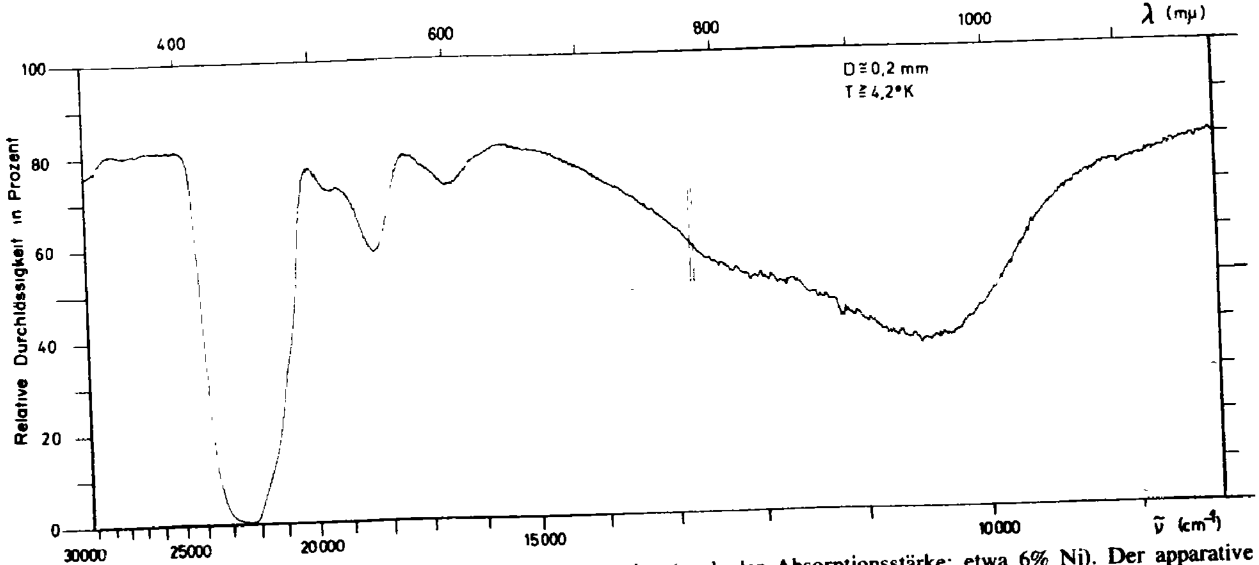

Abb. 5. Absorptionsspektrum eines Ni-dotierten Cd–Cl-Borazits. (nach der Absorptionsstärke: etwa 6% Ni). Der apparative Untergrund ist zwischen 700 und 1100 mμ schwach wellenlängenabhängig (Durchlässigkeitsminimum bei 820 mμ). Im infraroten Spektralbereich dient ein Thermoelement zum Strahlungsnachweis, im kurzwelligen Bereich ein Sekundärelektronenvervielfacher.

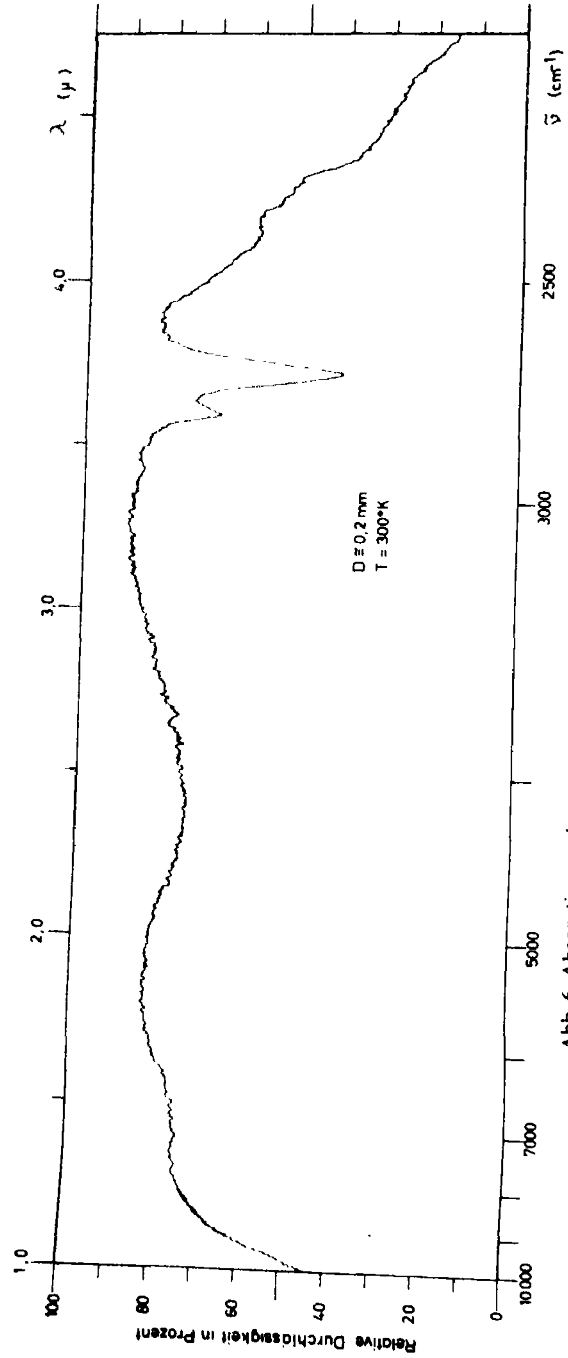

Abb. 6. Absorptionsspektrum eines Ni-dotierten Cd–Cl-Borazits (etwa 6% Ni).

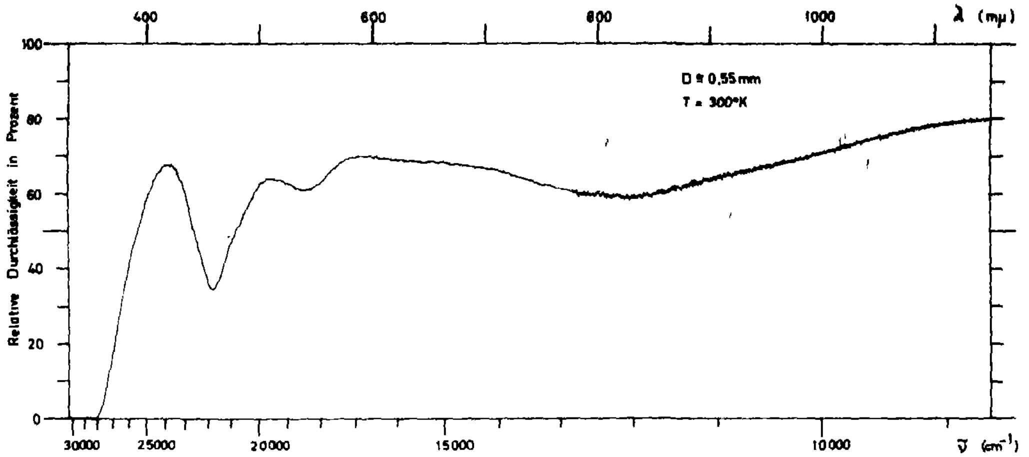

Abb. 7. Absorptionsspektrum eines Ni-dotierten Cd–J-Borazits (etwa 0,3% Ni).

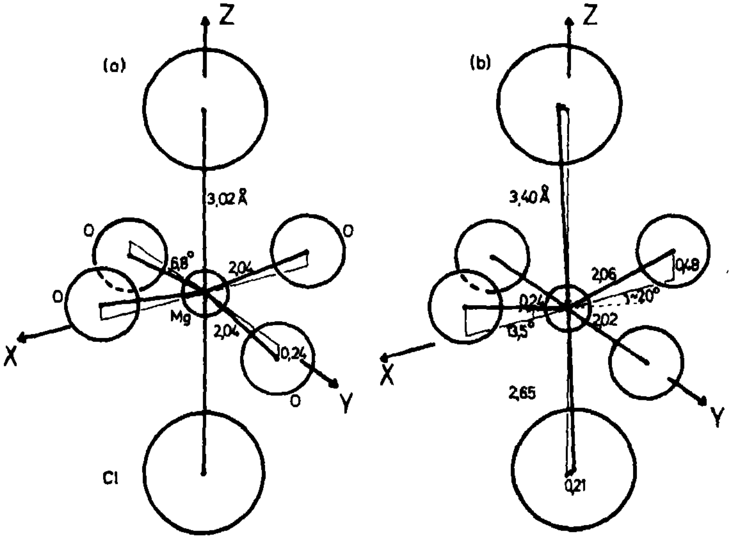

Abb. 8.(a) Mg-Nahumgebung in der α-Phase des Mg-Cl-Borazits nach Ito [1]. 8(b) Mg-Nahumgebung (z.B.) in der β-Phase des Mg–Cl-B. nach Ito[1].

α-wie β-Phase bei Vernachlässigung der Abweichung von tetragonaler Symmetrie $10\,Dq < 8200\,\mathrm{cm}^{-1}$ ermittelt.

(6) Für die Parameter E und F gilt nach dem Punktladungsmodell[10]

$$2E = \frac{-e}{14\sqrt{\pi}}\left(\sqrt{35}\gamma_{44}^{c}\,\langle r^4\rangle - 5\gamma_{40}^{c}\,\langle r^4\rangle - 4\sqrt{5}\gamma_{20}^{c}\,\langle r^2\rangle\right) = X_4 + X_2$$

$$3F = \frac{-e}{14\sqrt{\pi}}\left(-\sqrt{35}\gamma_{44}^{c}\langle r^4\rangle + 5\gamma_{40}^{c}\langle r^4\rangle - 3\sqrt{5}\gamma_{20}^{c}\,\langle r^2\rangle\right) = -X_4 + \tfrac{3}{4}X_2.$$

$X_4 < 1700\,\mathrm{cm}^{-1}$ lässt sich nach dem unter (5) angewandten Verfahren abschätzen, für X_2 ließ sich kein Skalenfaktor bestimmen, es wurde in weiten Grenzen variiert ($X_2 \approx$

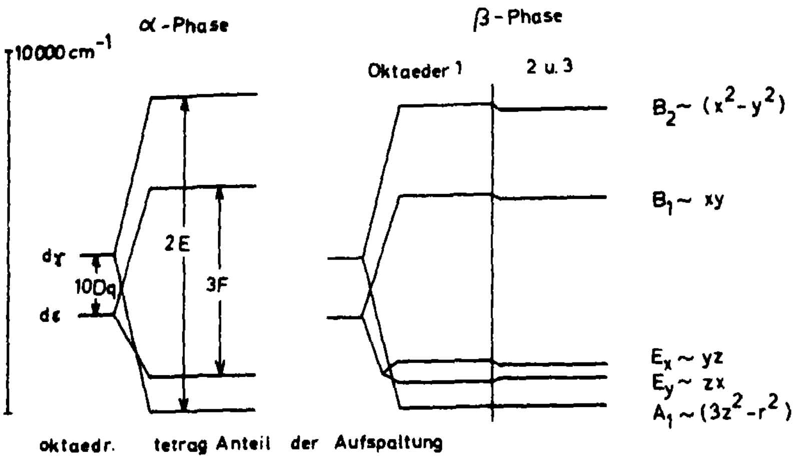

Abb. 9. Aufspaltungsbilder für einzelnes Ni^{2+}-3*d*-Elektron im Borazit nach dem Punktladungsmodell.

$8400\,cm^{-1} \rightarrow E = 5000$, $F/E = 0{,}3$ nach reinem Punktladungsmodell, tetrag. Näherg.)

(7) Auswahlregeln: Bei D_{2d}-Symmetrie transformiert sich der Operator für elektrische Dipolstrahlung nach den Darstellungen E ($\mathscr{E} \parallel x,y$) und B_2 ($\parallel z$), derjenige für magnetische nach $E(\mathscr{H} \parallel x,y)$ bzw. $A_2(\parallel z)$.

Demnach wären die Übergänge

$A_1 \rightarrow E,B_2$; $B_2 \rightarrow E,A_1$; $A_2 \rightarrow E,B_1$ für elektr. Dipol- und $A_1 \rightarrow E,A_2$; $B_2 \rightarrow E,B_1$; $A_2 \rightarrow E,A_1$ für magn. Dipol-Strahlung erlaubt.

In der β-Phase gibt es streng keine Auswahlregeln mehr. In beiden Phasen besitzt die Ni-Umgebung keine Inversionssymmetrie. $\Delta S = 0$-Übergänge sind intensiver als die nur durch Spinbahnkopplung erlaubten $\Delta S \neq 0$-Übergänge.

(8) Schmale Linien in den Spektren der 3*d*-Ionen, wie die im Ni–Cl–B-Spektrum bei etwa 714 mμ treten nur bei elektronischen Übergängen zwischen 2 Niveaus auf, die in gleicher Weise vom Kristallfeld beeinflusst werden[17].

(Diese Bedingung ist bei dem $^3B_2(d\epsilon^6 d\gamma^2) \rightarrow {}^1B_2(d\epsilon^6 d\gamma^2)$-Übergang im Ni–Cl–B erfüllt, bei dem $^3A_2(d\epsilon^5 d\gamma^3) \rightarrow {}^1B_2(d\epsilon^6 d\gamma^2)$-Übergang im Ni–J–B jedoch nicht!)

(9) Der Übergang bei 1,2 μ im Ni–J–B ist auffällig stärker als der Übergang bei 1,35 μ im Ni–Cl–B (Er ist nur im Ni-J-Borazit Spin- und E1-erlaubt).

Unter diesen Bedingungen wurden die in Tabelle 2 und 3 wiedergegebenen Zuordnungen gewählt. Abb. 10 gibt die dabei angenommene Kristallfeldaufspaltung für ein einzelnes 3*d*-Elektron wieder.

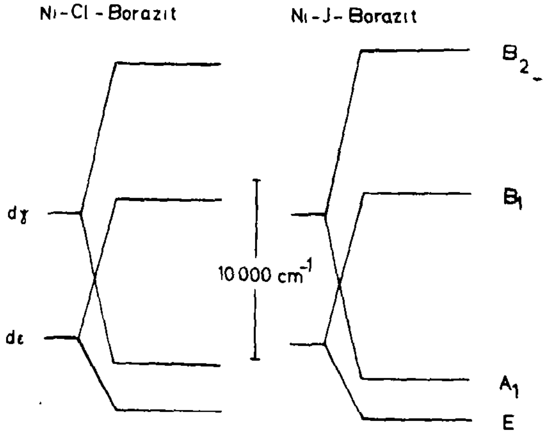

Abb. 10. Angenommenes Aufspaltungsbild für einzelnes Ni^{2+}-Elektron.

(Die Spinbahnkopplung ist bei den Berechnungen vernachlässigt. Sie führt zum Beispiel zur Aufspaltung der beiden tiefsten Triplettzustände mit stärkerer

Tabelle 2. Vergleich der gemessenen Ni^{2+}*-Spektren im* Ni-Cl-B *mit berechneten Werten bei der Parameterwahl:* B = 900 *cm*$^{-1}$; C = 3600 *cm*$^{-1}$; (C/B = 4,0) Dq = 700 *cm*$^{-1}$; E = 8400 *cm*$^{-1}$; F = 3957 *cm*$^{-1}$; (F/E = 0,471)

Beobachteter Übergang $\tilde{\nu}$ (cm^{-1}) ($T \leqslant 100$°K)	Intensität*	$\tilde{\nu}$ ber. (cm^{-1})	Übergang von $^3B_2(^3A_2(6,2))$ nach†	Intensität‡	Spin-Bahn-Komponenten: B_1,E
~ 400§		287	$^3A_2(^3F_1(5,3))$	((+−))	A_1, E
		2063	$^1A_1(^1E(6,2))$	(−+)	A_1
3450–4350(3920)	st	3930	$^3E(^3F_2(5,3))$	++	$E, A_1+A_2+B_1+B_2$
6620–6800(6725)	sw				
6940–7810(7350)	m$^+$	7485	$^3B_1(^3F_2(5,3))$	((+−))	B_2,E
8400–8890(8620)	sw$^+$				
		8685	$^1A_2(^1F_1(5,3))$	((−−))	A_2
9350–10150(9265)	sw$^+$				
10870–12660(11630)	st	11591	$^3E(^3F_1(5,3))$	++	$E, A_1+A_2+B_1+B_2$
14000	sw$^+$	13982	$^1B_2(^1E(6,2))$	(−−)	B_2
15340–15720(15500)	sw	15988	$^1A_1(^1A_1(6,2))$	(−+)	A_1
16310–17240(16735)	m	16788	$^1E(^1F_2(5,3))$	((−+))	E
18520–20000(18980)	st				
		21276	$^1B_1(^1F_2(5,3))$	(−−)	B_1
21510–25320(22990)	sst				
		25813	$^3A_2(^3F_1(4,4))$	((+−))	A_1,E
26810	sw	26121	$^1E(^1F_1(5,3))$	((−+))	E
27955	ssw				
		29936	$^3E(^3F_1(4,4))$	++	$E, A_1+A_2+B_1+B_2$
30440–31250	sw				
		36085	$^1A_1(^1E(4,4))$	(−+)	A_1
		36748	$^1E(^1F_2(4,4))$	((−+))	E
		37633	$^1B_2(^1E(4,4))$	(−−)	B_2
		37824	$^1B_1(^1F_2(4,4))$	( )	B_1
		58650	$^1A_1(^1A_1(4,4))$	(−+)	A_1

**sst, sehr stark; st, stark; m, mittel; sw, schwach; s. sw, sehr schwach.*

†D_{2d}-Termbezeichnung; in Klammern Haupt-Oktaeder-Anteil mit Angabe der besetzten dε und dγ-Orbitalzahlen.

‡ΔS = O-Übergang, in D_{2d}-Symmetrie E l-erlaubt; () durch Spin-Bahn-Kopplung von einer, (()) von beiden Grundterm Komponenten aus erlaubt.

§Nach magnetischem Suszeptibilitätsverlauf.

Absenkung der $M_s = 0$-Komponenten. Dabei werden die Komponenten des $^3A_2$-Niveaus in erster störungstheoretischer Näherung um einen Faktor 6 (Ni–Cl–B-Termsystem) bzw. 9 (Ni–J–B-Termsystem) weiter getrennt als die des $^3B_2$-Niveaus. In diesem Rahmen lassen sich die beobachteten paramagnetischen Suszeptibilitäten (6, 7) erklären. Sie sind beim Ni–J-Borazit in der α-Phase hauptsächlich durch die thermisch besetzten höheren Niveaus bedingt, während beim Ni–Cl–B tiefliegende Niveaus den größten Beitrag liefern.)

Die Zuordnung der schwachen Absorptionen zwischen 9000 und 11000 cm^{-1} zu Übergängen zum $^1A_2$-Niveau und zu Spinbahnkomponenten des ^3E-Terms wurde nicht versucht. Unsicher bleibt noch die Klärung des Ursprungs der starken Übergänge bei 19000 und 23000 cm^{-1}; hierbei kann es sich um die spinerlaubten Übergänge (bis auf einen Zweielektronensprünge) zu den $^3A_2$ ($d\epsilon^4$ $d\gamma^4$)- und ^3E ($d\epsilon^4$ $d\gamma^4$)-Niveaus handeln; zu fordern wäre dann, daß die ($d\epsilon^4$ $d\gamma^4$)-Niveaus durch stärkere Ligandenwechselwirkung gegenüber den ($d\epsilon^5$ $d\gamma^3$)- und ($d\epsilon^6$ $d\gamma^2$)-Niveaus um etwa 7000 cm^{-1} beim Ni–Cl- und etwa 7500 cm^{-1} beim Ni–J-Borazit abgesenkt sind und daß die Übergänge dieser Wechselwirkung auch ihre Intensität verdanken.

(Eine andere Möglichkeit ist, diese Absorptionen als Ni^{3+}-Übergänge zu deuten, deren

Tabelle 3. *Vergleich der gemessenen* Ni^{2+}-*Spektren im* Ni-J-Borazit *mit berechneten Werten bei der Parameterwahl*: B = 900 *cm*$^{-1}$; C = 3420 *cm*$^{-1}$; (C/B = 3,8) Dq = 720 *cm*$^{-1}$; *E* = 9100 *cm*$^{-1}$; *F* = 4204 *cm*$^{-1}$; (F/E = 0.462)

Beobachteter Übergang $\tilde{\nu}$ (cm^{-1}) ($T \leqslant 100°$K)	Intensität*	$\tilde{\nu}$ ber. (cm^{-1})	Übergang von $^3A_2(^3F_1(5,3))$ nach†	Intensität‡	Spin-Bahn Komponenten A_1,E
~150§		624	$^3B_2(^3A_2(6,2))$	((+−))	B_1,E
		985	$^1A_1(^1E(6,2))$	(−−)	A_1
3480–4700 (4065)	m$^+$	4349	$^3E(^3F_2(5,3))$	++	$E,A_1+A_2+B_1+B_2$
6560–7410 (6990)	sw	7955	$^1A_2(^1F_1(5,3))$	(−−)	A_2
7690–8890 (8300)	st	8515	$^3B_1(^3F_2(5,3))$	++	B_2,E
10050	sw				
10500	sw				
11000–11400	sw				
11980–13200 (12400)	st	12455	$^3E(^3F_1(5,3))$	++	$E,A_1+A_2+B_1+B_2$
13950	sw$^+$				
14200	sw$^+$	14260	$^1B_2(^1E(6,2))$	((−−))	B_2
14900–15200 (15100)	sw$^+$	15800	$^1A_1(^1A_1(6,2))$	(−−)	A_1
16100–17000 (16500)	m$^+$	16851	$^1E(^1F_2(5,3))$	((−+))	E
18020	sw				
19250–20800 (19750)	st				
22150	sw$^+$	21963	$^1B_1(^1F_2(5,3))$	(−+)	B_1
22730–?					
22730–24390	sst				
25975–30300	sst	26505	$^1E(^1F_1(5,3))$	((−+))	E
		27248	$^3A_2(^3F_1(4,4))$	((+−))	A_1,E
		31571	$^3E(^3F_1(4,4))$	++	$E,A_1+A_2+B_1+B_2$
		37570	$^1A_1(^1E(4,4))$	(−−)	A_1
		38140	$^1E(^1F_2(4,4))$	((−+))	E
		38775	$^1B_2(^1E(4,4))$	((−−))	B_2
		38965	$^1B_1(^1F_2(4,4))$	(−+)	B_1
		58893	$^1A_1(^1A_1(4,4))$	(−−)	A_1

*sst, sehr stark; st, stark; m, mittel; sw, schwach; s.sw, sehr schwach.

†D_{2d}-Termbezeichnung; in Klammern Haupt-Oktaeder-Anteil mit Angabe der besetzten dϵ und dγ-Orbitalzahlen.

‡$\Delta S = 0$-Übergang, in D_{2d}-Symmetrie *E* 1-erlaubt; () durch Spin-Bahn-Kopplung von einer, (()) von beiden Grundterm Komponenten aus erlaubt.

§Nach magnetischem Suszeptibilitätsverlauf.

große Intensität im nahen Ultraviolett in Al_2O_3 von McClure beobachtet wurde[18]. ESR-Spektren von Nickel dotierten Cd–Cl- und Cd–J-Boraziten, die Rosenhauer[21] mit einem effektiven Spin ½ beschrieben konnte, weisen auf das teilweise Vorliegen nicht zweifach ionisierten Nickels hin. Diese Untersuchungen sind am II. Physikalischen Institut der Technischen Hochschule, Darmstadt, zur Zeit noch im Gang).

STRUKTUREN IN DEN NI-SPEKTREN

Die bei Temperaturen unter 100°K in den Ni-Borazit-Spektren beobachteten Strukturen (siehe z.B. Abb. 1 bei $\lambda = 1{,}050\,\mu$) sind nach Lage und Aussehen zum größten Teil als Schwingungsstrukturen ($\Delta\tilde{\nu} \approx 100$ cm^{-1}, siehe Tabelle 4 und 5) zu erklären[18, 19]. Leider sind von Boraziten noch keine Schwingungsanalysen bekannt, so daß ein direkter Vergleich damit nicht möglich ist. Es ist zu erwarten, daß hauptsächlich Schwingungen des Ni-Ions und seiner Nah-Umgebung beim elektronischen Übergang mit angeregt werden. Alleinige Halogenschwingung führt bei gleicher Federkonstante zu einem Frequenzverhältnis $\nu_{J\text{-}B}/\nu_{Cl\text{-}B} \cong \sqrt{35/127} \cong 0{,}525$, im allgemeinen Fall sollte es wegen Mit-

Tabelle 4. Strukturen in den Ni-Cl-*Borazit-Spektren* (T $\leqslant$ 100°K, $\tilde{\nu}_{ph} \approx$ (104 ± 5) cm^{-1})

Übergang (cm^{-1})	Strukturen (cm^{-1})	*Interpretation, Bemerkungen*
7000 (Abb. 2)	7050 6947 ($T \geqslant 80°K$) 7147, 7262	$0 \to 0$ wegen überlagerten $1 \to 0$ Untergrundes (H_2O- $0 \to 1,2$ Oberschwingungen) unsicher.
9500 (Abb. 1)	9265 ~ 9162 ($T \geqslant 80°K$) 9365, ... 10050 + n·90	$0 \to 0$ $\nu_{ph} \approx (103 \pm 3)\,cm^{-1}$ $1 \to 0$ Huang–Rhys-Faktor $0 \to n, n = 1–6$ $S^{(20)} = 4–5$ anderer elektronischer Übergg.
10870-12660		zu geringe Durchlässigkeit
14000 (Abb. 1)	Siehe Abb. 11(a)	Aufspaltung von etwa 25 cm^{-1} im Grundzustand, von 40 cm^{-1} im angeregten (z.b. Phononen)
15500 (Abb. 1)	15001, 15120, 15275, 15412, 15513	zum Teil bekanntes $\Delta\tilde{\nu}$
19000 (Abb. 12(a))	Siehe Abb. 11(b)	$\tilde{\nu}_{ph} \approx (105 \pm 5)\,cm^{-1}$. Mittlere Zahl von emittierten Phononen etwa 6, d.h. erhebliche Verschiebung der Gleichgewichtslage zwischen Grund- und angeregtem Zustand. $n' = 0$ und $n'' = 0$ rein elektronisch oder durch Emission von 1–2 Phononen verschoben.

(Absolute Verschiebungen von Liniengruppen mit der Temperatur (Größenordnung einige cm^{-1}) sind vernachlässigt. Relative Genauigkeit ± 3 cm^{-1} im roten und ± 5 cm^{-1} im blauen Spektralbereich).

Tabelle 5. Strukturen in den Ni-J-*Borazit-Spektren*
T $\leqslant$ 100°K, $\tilde{\nu}_{ph} \approx$ (95 ± 5) cm^{-1}

Übergang (cm^{-1})	Strukturen (cm^{-1})	*Interpretation, Bemerkungen*
4000 (Abb. 4)	3200 3380 3570	Erklärung unklar; sehr schmal für Spin-Bahn-Komponenten von ${}^3E(d\epsilon^5 d\gamma^3)$ (H_2O-Absorptionen überlagert).
14000 (Abb. 3)	13950 14200	Aufspaltung im angeregten Zustand, z.B. 2 Schwingungsniveaus.
16000 (Abb. 3)	15883	$(15883 + n \cdot (97 \pm 9))\,cm^{-1}$
($T = 4,2°K$)	15987,...	$n = 0...5; S = 7$
19750 (Abb. 12(b))	19300	$(19300 + n \cdot (93 \pm 5))\,cm^{-1}$
($T = 4,2°K$)	19392,...	$n = 0,...4,.; S = 6-7$

schwingens anderer Ionen näher bei 1 liegen. Das tatsächlich beobachtete Verhältnis $\nu_{J\text{-}B}/\nu_{Cl\text{-}B} \approx 0,91$ zeigt die durch die Halogenmassen bedingte Tendenz. Die äquidistanten Folgen von 0, 1, 2 . . . Quanten deuten auf einen 'geraden' Schwingungstyp hin, die Frage nach seiner Symmetrie ist nicht entschieden. Da beim Ni-J-Borazit nicht schon von seinem α-β-Umwandlungspunkt an (also $T \leqslant 64°K$) Schwingungsstrukturen beobachtet werden, müssen bei ihm die Schwingung stärker gedämpft oder

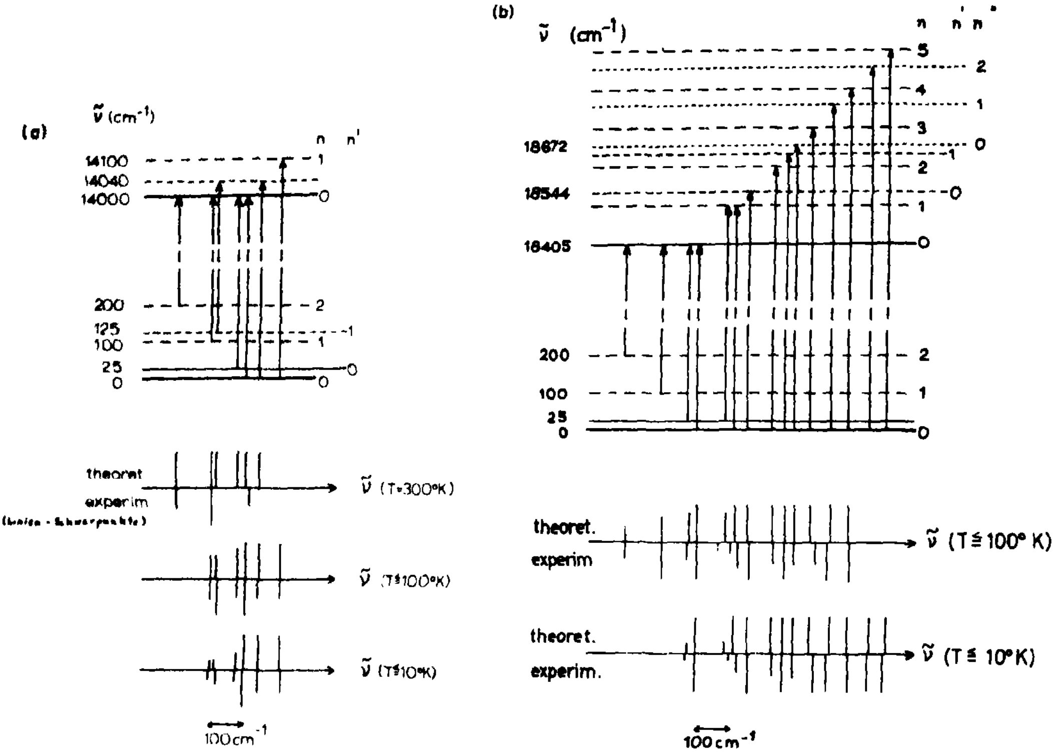

Abb. 11. Vergleich beobachteter Strukturen im Ni–Cl-B- Spektrum mit vorgeschlagenen Interpretationen. (a) Übergang bei 14000 cm^{-1}. (b) Übergang bei 18500 cm^{-1}.

andere beitragende Gitterschwingungen noch thermisch angeregt sein.

RESÜMEE

Die Absorptionsspektren von Nickel in Ni–Cl- und Ni–J-Boraziten unterscheiden sich nur wenig voneinander oder von denen in Ni-dotierten Cd–Cl- und Cd–J-Boraziten. Das Ein-Ionen-Modell wird in dieser Arbeit deshalb als brauchbare Näherung betrachtet und die wesentlichen Absorptionen im sichtbaren und nahen infraroten Spektralbereich werden Kristallfeldübergängen des Ni^{2+}-Ions zugeordnet. Dabei sind die Parameter soweit wie möglich an bekannten Ni^{2+}-Daten orientiert. Der tetragonale Anteil der Kristallfeldaufspaltung ist bei der vorgeschlagenen Zuordnung etwas größer als der kubische. Die Erklärung der bekannten magnetischen Suszeptibilitäten der Ni–Cl- und Ni–J-Borazite ist in diesem Rahmen möglich. Die Beschreibung der intensiven Absorption im blauen und nahen ultravioletten Spektralbereich erfordert aber eine starke Absenkung der beiden höchstliegenden Tripletts gegenüber den errechneten Lagen.

Bei tiefen Temperaturen werden in der niedersymmetrischen Phase von Ni–Cl- wie Ni–J-Borazit äquidistante Flankenstrukturen an vielen Absorptionsbändern gefunden, die zum großen Teil Schwingungsquanten von etwa 100 cm^{-1} zugeschrieben werden können. Auffällige Effekte im Spektrum als Folge der Ferroelektrizität oder des Antiferromagnetismus dieser Borazite treten nicht auf.

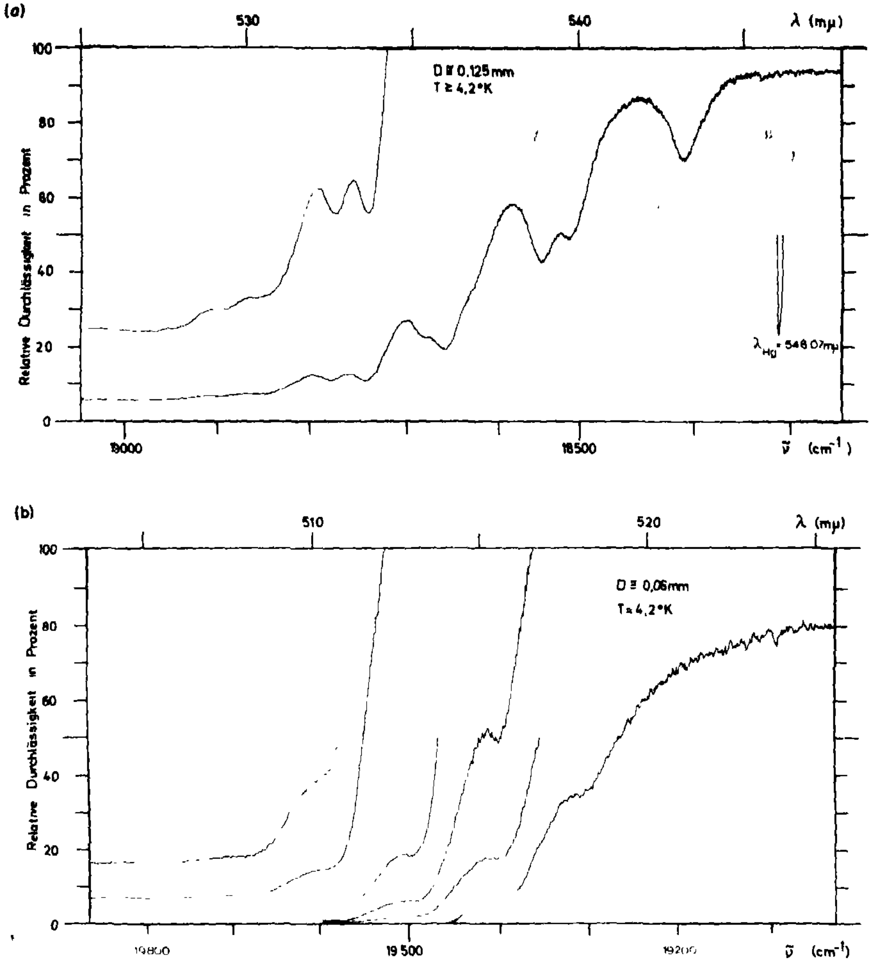

Abb. 12.(a) Struktur des Ni–Cl–B-Ubergangs bei 18980 cm^{-1}. (b) Struktur des Ni–J–B-Übergangs bei 19750 cm^{-1}. (Bei verschiedener Abschwächung des Vergleichsstrahles).

Anerkennung – Die Anregung zu dieser Arbeit verdanke ich Herrn Professor Dr. B. Elschner. Die Herrn M. Rosenhauer, G. Winter, G. Keller sowie Frau H. Ghanouchi stellten die Kristalle her. Die numerischen Rechnungen wurden am Deutschen Rechenzentrum, Darmstadt, ausgeführt.

This research was supported in part by the United States Air Force under Grant No AF61 (052)-817 and monitored by the European Office, Office of Aerospace Research.

LITERATUR

1. ITO T., MORIMOTO N. und SADANAGA R., *Acta crystallogr.* **4**, 310 (1951).
2. LE CORRE Y., *J. Phys. Radium* **18**, 629 (1957).
3. SCHMID H., *J. Phys. Chem. Solids* **26**, 973 (1965).
4. ASCHER E., SCHMID H. und TAR D., *Solid State Commun.* **2**, 45 (1964).
5. SCHMID H. und TROOSTER J. M., *Solid State Commun.* **5**, 31 (1967).
6. SCHMID H., RIEDER H. und ASCHER E., *Solid State Commun.* **3**, 327 (1965).
7. QUÈZEL G. und SCHMID H., *Solid State Commun.* **6**, 447 (1968).
8. ASCHER E., RIEDER H., SCHMID H. und STÖSSEL H., *J. appl. Phys.* **37**, 1404 (1966).
9. ELSCHNER B., Battelle Memorial Institute, Genf, private Mitteilungen (1963).
10. GRIFFITH J. S., *The Theory of Transition Metal Ions*. Cambridge University Press (1961).
11. BECKER J. und WILL G., *Z. Kristallogr.* Erscheint demnächst.

12. FREEMAN A. J. und WATSON R. E., In *Magnetism* 2A (Edited by G. T. Rado und H. Suhl). Academic Press, New York/London (1965).
13. TROOSTER J. M., Proefschrift, Nijmegen (1967).
14. TANABE Y. und SUGANO S., *J. phys. Soc. Japan* **9**, 753, 766 (1954).
15. TANABE Y. und KAMIMURA H., *J. phys. Soc. Japan* **13**, 394 (1958).
16. HEINRICH B., ZITKOVA J. und KACZER F., *Phys. Status Solidi* **26**, 443 (1968).
17. ORGEL L. E., *J. chem. Phys.* **23**, 1824 (1955).
18. McCLURE D. S., *J. chem. Phys* **36**, 2757 (1962).
19. PAPPALARDO R., *Nuovo Cimento* **6**, 392 (1957).
20. HUANG K. und RHYS A., *Proc. R. Soc.* **A204**, 406 (1950).
21. ROSENHAUER M. private Mitteilungen.

Anmerkungen bei der Korrektur – 1. Inzwischen konnte gezeigt werden, daß die ESR-Spektren von Nickel-dotierten Cd-Boraziten durch teilweise vorliegendes Ni^+ verursacht sind. 2. R. V. PISAREV *et al.*, (*Phys. Status Solidi* **35**, 145 (1969)) veröffentlichten u.a. interessante Temperaturabhängigkeiten einiger Absorptionsbänder von Ni-Boraziten.

J. Phys. Chem. Solids Pergamon Press 1970. Vol. 31, pp. 215–218. Printed in Great Britain.

EFFECT OF PRESSURE ON THE NÉEL TEMPERATURE OF RARE EARTH INTERMETALLIC COMPOUNDS*

KAZUKO SEKIZAWA,† HISASHI SEKIZAWA‡ and C. T. TOMIZUKA
Department of Physics, University of Arizona, Tucson, Arizona 85721, U.S.A.

(Received 9 September 1968; in revised form 22 July 1969)

Abstract – The pressure coefficient of the Néel temperature and the compressibility were obtained on two rare earth intermetallic compounds. Samples studied were GdCu and GdAg which have the CsCl type of crystal structure and show antiferromagnetic property at low temperature. The Néel temperature was determined by the abrupt change in the slope of the electrical resistivity vs. temperature curve. The resistivity was measured on polycrystalline samples over the temperature range from 77° to 200°K at a constant hydrostatic pressure. Pressures up to 5 kbar were employed. The Néel temperature was found to increase linearly with pressure at a rate of 0·03 ± 0·04°K/kbar for GdCu and 0·43 ± 0·04°K/kbar for GdAg. Volume compressibilities at room temperature are $2{\cdot}2 \times 10^{-3}$/kbar and $2{\cdot}0 \times 10^{-3}$/kbar for GdCu and GdAg, respectively. Values of $d\ln T_N/d\ln V$ are −0·09 for GdCu and −1·6 for GdAg.

1. INTRODUCTION

SEVERAL investigations [1–6] have shown that magnetic properties of rare earth intermetallic compounds are largely influenced by the number of conduction electrons in the compounds. This fact is qualitatively understood in terms of the indirect exchange interaction via conduction electrons. On the other hand, it was found in some systems of rare earth intermetallic compounds that their magnetic properties depend also on the ratio of the nearest neighbor distance of magnetic ions ($r_{N\text{-}N}$) to the diameter of $4f$ shell (r_{4f}), $r_{N\text{-}N}/r_{4f}$. Ferromagnetism is apt to occur in the region of small $r_{N\text{-}N}/r_{4f}$[7]. Existence of such dependence cannot be explained by the simple Ruderman-Kittel-Yosida theory.

For the purpose of learning the dependence of the exchange interaction on the separation of magnetic ions, the effect of hydrostatic pressure on the Néel temperature has been investigated on two rare earth intermetallic compounds, GdCu and GdAg. These compounds have the CsCl type of crystal structure. According to magnetic studies previously made, compounds GdCu and GdAg show antiferromagnetic properties below 144°K and 138°–150°K, respectively, under atmospheric pressure [1, 8–10]. The present results of high pressure experiments are compared with the exchange interaction curve for R-Cu and R-Ag systems (R: rare earth elements), which is constructed by plotting the ratio of the magnetic transition temperature to the de Gennes factor vs. $r_{N\text{-}N}/r_{4f}$.

2. EXPERIMENTAL

Specimens of the compounds were prepared by arc-melting stoichiometric amounts of component metals under argon atmosphere. The melts were annealed in evacuated silica tubes at 700°C for 10 hr. Bar specimens approximately 0·8 × 0·8 × 25 mm in size required for resistivity measurements were cut out from the melt with a spark cutter. Four copper leads were spot-welded to each specimen. The pressure vessel made of specially heat-treated Cu–Be alloy was mounted inside a liquid nitrogen bath. Helium gas was used as

---

*This work was sponsored in part by the U.S. Air Force Office of Scientific Research through Grant No. AF-AFOSR 105-63.

†On leave of absence from Department of Physics, College of Science and Engineering, Nihon University, Tokyo, Japan.

‡On leave of absence from the Institute of Physical and Chemical Research, Yamato-cho, Saitama, Japan.

a pressure medium. The electrical resistivity was measured by the standard four-probe method while the temperature was raised from 77° to 200°K at a constant pressure. Compressibilities of both compounds were measured by the strain gauge method. Pressures up to 5 kbar were employed. The temperature was measured by means of a chromel–alumel thermocouple and the pressure was measured using the resistance of a suitably calibrated manganin wire. The voltage drop in the sample was determined with an accuracy of 0·5 per cent. The accuracy of the determination of the temperature was ±0·2°K.

3. RESULTS AND DISCUSSION

The relative resistivity vs. temperature curves for GdCu at 2 kbar and for GdAg at 4 kbar are shown in Figs. 1 and 2 as examples. All the curves for both compounds are split clearly into two branches by a narrow transition region in which an abrupt change in the slope takes place. The absolute values of the resistivity at 77°K under atmospheric pressure are approximately 40 $\mu\Omega$cm for GdCu and 12 $\mu\Omega$cm for GdAg. The shape of the resistivity vs. temperature curves and the values of the resistivity of two compounds at atmospheric pressure are in good agreement with the results by Chao[11].

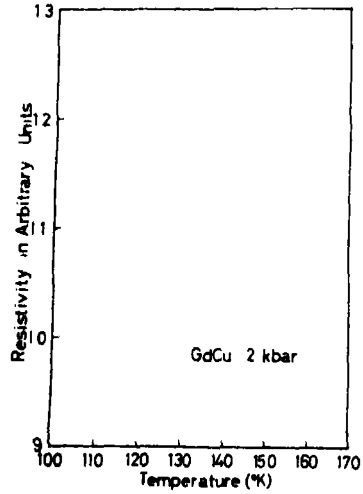

Fig. 1. The resistivity vs. temperature curve for GdCu under the pressure of 2 kbar

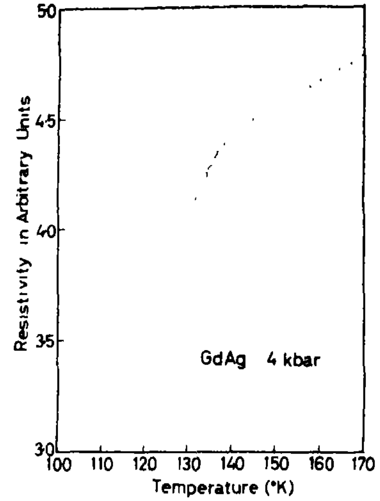

Fig. 2. The resistivity vs. temperature curve for GdAg under the pressure of 4 kbar

Two methods for determining the Néel temperature were tried. In the first method, the Néel temperature is determined as the intersection point of two straight lines drawn by extrapolating the least-squares fit of the two branches of the resistivity vs. temperature curve. The second method is to plot the slope of the curve, dR/dT, vs. temperature, from which two nearly horizontal lines, corresponding to two branches, result with a narrow transition region between them. The Néel temperature in this case, is defined as the temperature at which dR/dT takes the mean value of the slopes of two branches. The pressure dependence of the Néel temperatures determined by both methods coincide well, though the Néel temperature determined as the intersection point of two straight lines are plotted against pressure in Figs. 3 and 4. The Néel temperature increases linearly with pressure with a slope of $dT_N/dP = 0{\cdot}03 \pm 0{\cdot}04$°K/kbar for GdCu and $dT_N/dP = 0{\cdot}43 \pm 0{\cdot}04$°K/kbar for GdAg. The values of the isothermal compressibility at room temperature are $\kappa_{GdCu} = 2{\cdot}2 \times 10^{-3}$/kbar and

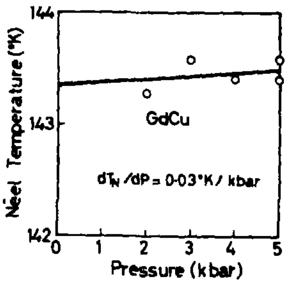

Fig. 3. Néel temperature vs. hydrostatic pressure for GdCu.

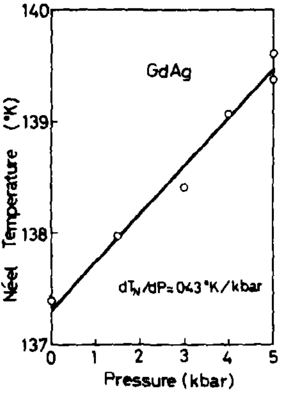

Fig. 4. Néel temperature vs. hydrostatic pressure for GdAg.

$\kappa_{GdAg} = 2{\cdot}0 \times 10^{-3}$/kbar. From these values, the logarithmic dependence of the Néel temperature on volume, $d\ln T_N/d\ln V$, can be calculated. The value of $d\ln T_N/d\ln V$ is $-0{\cdot}1 \pm 0{\cdot}1$ for GdCu and is $-1{\cdot}6 \pm 0{\cdot}1$ for GdAg.

It is interesting to compare the results of high pressure experiments with exchange interaction curves for R-Cu and R-Ag systems. These curves are constructed using the results of magnetic studies by Walline and Wallace[9, 10]. As an indication of the exchange energy, the Néel temperatures of R–Cu and R–Ag systems are divided by the de Gennes factor, $(g-1)^2J(J+1)$, and plotted against the ratio r_{N-N}/r_{4f}, in Fig. 5. The present results calculated from pressure coefficients of the Néel temperature and compressibilities are indicated by two arrows in the figure. These two arrows (experimental slopes) do not coincide with the slopes of the interaction curves for the compounds, whereas the slopes agree well in the case of rare earth metals[12, 13]. Thus, the present result showing the enhancement of the Néel temperature of both compounds with pressure does not agree with what is indicated by the interaction curve, i.e. the tendency toward ferromagnetism with decreasing r_{N-N}/r_{4f}. On the other hand, the fact that the enhancement of the Néel temperature by pressure of GdAg is larger than that of GdCu seems to corroborate the appearance of ferromagnetism in the region of smaller r_{N-N}/r_{4f}. It thus appears that the application of pressure and the replacement of rare earth elements have a different effect on the exchange interaction.

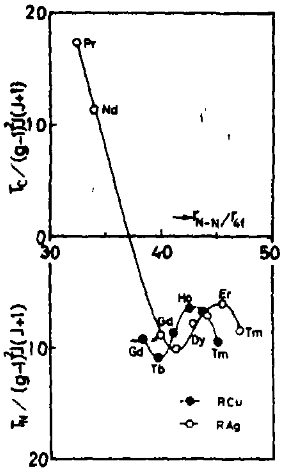

Fig. 5. Exchange interaction curves for R-Cu and R-Ag systems (R: rare earth elements). Two arrows show the results of high pressure experiments.

Acknowledgements—The authors wish to thank Mr. Rodney C. Lowell who assisted them in the operation of the gas-pressure system. The authors are grateful to Mr. Richard Handverger who carried out the major portion of the compressibility measurement. They are also indebted to Professor Kō Yasukōchi for many enlightening and stimulating discussions.

REFERENCES

1. SEKIZAWA K. and YASUKOCHI K., *J. phys. Soc. Japan* **21**, 684 (1966).
2. CABLE J. W., KOEHLER W. C. and WOLLAN E. O., *Phys. Rev.* **136**, A240 (1964).
3. CABLE J. W., KOEHLER W. C. and CHILD H. R., *J. appl. Phys.* **36**, 1096 (1965).
4. ALFIERI G. T., BANKS E. B. and KANEMATSU K., *J. appl. Phys.* **37**, 1254 (1966).
5. HOLZBERG F., McGUIRE T. R., METHFESSEL S. and SUITS J. C., *J. appl. Phys.* **35**, 1033 (1964).
6. HOLZBERG F., McGUIRE T. R., METHFESSEL S. and SUITS J. C., *Proc. Int. Conf. Magnetism*, Nottingham, p. 470 (1964).
7. SEKIZAWA K. and YASUKOCHI K., *J. phys. Soc. Japan* **21**, 274 (1966).
8. PIERRE J. and PAUTHENET R., *C. r. hebd. Séanc. Acad. Sci., Paris* **260**, 2739 (1965).
9. WALLINE R. E. and WALLACE W. E., *J. chem. Phys.* **41**, 3285 (1964).
10. WALLINE R. E. and WALLACE W. E., *J. chem. Phys.* **42**, 604 (1965).
11. CHAO C. C., *J. appl. Phys.* **37**, 2081 (1966).
12. ROBINSON L. B., MILSTEIN F. and JAYARAMAN A., *Phys. Rev.* **134**, A187 (1964).
13. McWHAN D. B. and STEVENS A. L., *Phys. Rev.* **139**, A682 (1965).

J. Phys. Chem. Solids Pergamon Press 1970. Vol. 31, pp. 219–226. Printed in Great Britain.

ON THE RELATION BETWEEN THE RELAXATION TIME FOR SHORT-RANGE ORDER AND SELF-DIFFUSION COEFFICIENTS

S. RADELAAR*
Laboratorium voor Fysische Metaalkunde, Universiteitscomplex Paddepoel, Rijksuniversiteit Groningen, Groningen, The Netherlands

(*Received* 28 *October* 1968; *in revised form* 14 *July* 1969)

Abstract—An equation is derived which relates the relaxation time for short-range ordering in binary f.c.c. alloys with the self-diffusion coefficients of the components of the alloy. The equation shows that for certain conditions the activation energy for short-range ordering can be lower than the activation energy for self-diffusion of the fastest component. The computed relaxation times are compared with experimental data, reasonable agreement is obtained.

1. INTRODUCTION

MEASUREMENTS of the establishment of equilibrium short-range order (s.r.o.) after a small temperature change[1–5] can be used for the study of diffusion at relatively low temperatures. It was shown that the relaxation times for the establishment of s.r.o.-equilibrium and the Zener relaxation-effect are of the same order of magnitude. The precise atomic movements occurring during the Zener relaxation process are more or less unknown. For a study of s.r.o.-kinetics such a problem does not occur. In this paper we will derive an expression which relates the relaxation time for s.r.o. with the self-diffusion coefficients of the components of the alloy. To the author's knowledge two theoretical investigations of s.r.o.-kinetics exist. Iida[6] discussed the kinetics of both long- and short-range order in a (50:50) b.c.c. alloy. A theory of the kinetics of s.r.o. in binary f.c.c. alloys of variable composition has been devised by Kidin and Shtremel' [7]. Their theory is based on a paper by Vineyard[18], which deals with the kinetics of long-range order in AB b.c.c. and A_3B f.c.c. alloys. Kidin and Shtremel' derived expressions for the time rate of change of the number of atom–atom and atom–vacancy pairs. This system of two non-linear simultaneous differential equations was solved by assuming that the vacancy environment reaches equilibrium much faster than s.r.o. As will be shown below this is not true, moreover the above assumption leads to a relation for the relaxation time for s.r.o. which contains only one of the diffusion coefficients, which seems unsatisfactory from a physical point of view.

By linearizing the simultaneous differential equations we are able to derive an expression which relates the relaxation time for s.r.o. with *both* self-diffusion coefficients. Linearization of the differential equations is justified for experiments like those mentioned above[1–5], where only a small temperature change is involved.

2. DEFINITIONS

Let us consider a homogeneous binary f.c.c. alloy AB with concentrations c_A and c_B of A and B-atoms resp. The vacancy concentration cV is assumed to be very small, so with good approximation $c_A + c_B = 1$ holds. The following assumptions are used:

(i) Interactions exist between neighbouring atoms only. The interaction energy of a pair of atoms is independent of its surroundings. The interaction energies between AA, AB and BB-pairs are called V_{AA}, V_{AB}, V_{BB}, resp.

---

[*] Temporarily at: McMaster University, Department of Metallurgy and Materials Science, Hamilton, Ontario, Canada.

(ii) Random distribution of pairs. These are the basic assumptions of the quasi-chemical theory. The numbers of AA, BB and AB-pairs (N_{AA}, N_{BB}, and N_{AB} resp.) are related by:

$$N_{AB}+2N_{AA} = 12Nc_A$$
$$N_{AB}+2N_{BB} = 12Nc_B.$$

From N_{AB} we can determine the possibility that a particular site next to a given A-atom is occupied by a B-atom:

$$p_{AB} = \frac{N_{AB}}{12Nc_A}, \text{ similarly } p_{AA} = \frac{2N_{AA}}{12Nc_A}.$$

The various probabilities are related by:

$$p_{AA}+p_{AB} = p_{BA}+p_{BB} = 1$$
$$c_A p_{AB} = c_B p_{BA}.$$

In exactly the same way we can determine the probability that an A-atom will be the neighbour of a vacancy V:

$$p_{VA} = \frac{N_{VA}}{12Nc_V}, \text{ similarly } p_{VB} = \frac{N_{VB}}{12Nc_V}$$

N_{VA} and N_{VB} are the numbers of VA- and VB-pairs resp. (Note that we have neglected the formation of divacancies). Obviously $p_{VA}+p_{VB} = 1$. The probability p_{AV} that a vacancy occupies a particular site next to a given A-atom is related to p_{VA} by:

$$p_{AV} = \frac{c_V}{c_A} p_{VA}.$$

3. MIGRATION OF ATOMS IN F.C.C. ALLOYS WITH S.R.O.

We assume that the migration energy E^M of an atom depends only on its immediate environment. The migration energy of an A-atom is given by the energy difference $V_2^A - V_1^A$ (Fig. 1), where V_1^A is the energy of an A-atom next to a vacancy and V_2^A is the energy of an A-atom in the saddle-point position. Let us assume that V_2^A is given by a sum of pair interaction energies with the common nearest neighbour atoms only. Let m be the number of B-atoms adjacent to both the A-atom and the vacancy ($m \leq 4$). V_2^A will thus be given by:

$$V_2^A(m) = mS_{AB}+(4-m)S_{AA}.$$

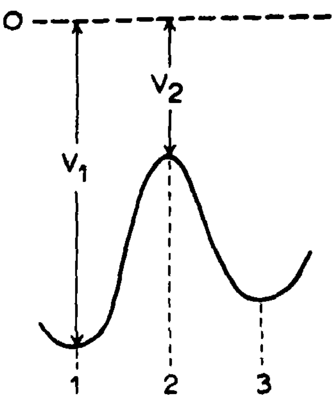

Fig. 1. Potential barrier for the motion of A-atoms.

Let n be the number of the remaining nearest neighbour sites of the A-atom occupied by B-atoms ($n \leq 7$). V_1^A will be given by:

$$V_1^A(m,n) = (11-m-n)V_{AA}+(m+n)V_{AB}.$$

The migration energy of A-atoms with given environment (m, n) will be given by:

$$\begin{aligned} E_A^M(m,n) &= V_2^A(m) - V_1^A(m,n) \\ &= 4S_{AA} - 11V_{AA} + m(S_{AB}-S_{AA}) \\ &\quad -(m+n)(V_{AB}-V_{AA}) \\ &= E_A^M(0) + mS_A - (m+n)U_A \end{aligned}$$

$E_A^M(0)$ is the migration energy of an A-atom in pure A, while we have defined

$$S_A = S_{AB}-S_{AA} \quad \text{and} \quad U_A = V_{AB}-V_{AA}$$

A similar expression can be derived for B-atoms:

$$E_B^M(m,n) = E_B^M(0) + mS_B - (m+n)U_B$$

with $S_B = S_{BA} - S_{BB}$ and $U_B = V_{AB} - V_{BB}$. S_{AB} and S_{BA} are not necessarily the same.

Note that

$$U_A + U_B = 2V_{AB} - (V_{AA} + V_{BB}) = 2W$$

where W is usually called the 'ordering energy.'

4. AVERAGE JUMP FREQUENCIES

The average number of jumps per second of an A-atom will be determined by:

(i) The probability p_V that the atom has a vacancy as one of its nearest neighbours:

$$p_V = 12p_{AV} = 12\frac{c_V p_{VA}}{c_A}. \qquad (1)$$

(ii) The occupation of its nearest neighbour sites. The probability that m common nearest neighbours are of type B will be given by:

$$q_{VAB}(m) = \binom{4}{m} p_{VAB}{}^m (1 - p_{VAB})^{4-m}. \qquad (2)$$

Here p_{VAB} is the probability that a B-atom is adjacent to both the A-atom and the vacancy. The probability p_{VAB} cannot be evaluated from the probabilities p_{AB} and p_{VA} since in the pair-approximation the correlations between the occupation of pairs which share a site are entirely neglected.

However, the occupation of the common nearest neighbour sites is the same before and after the jump of the A-atom. As will be shown below the occupation of the common nearest neighbour sites affects the self-diffusion coefficients and the relaxation time for s.r.o. in precisely the same way as long as we assume that V_2 depends only on the occupation of the common nearest neighbour sites. The probability that n of the remaining lattice sites are occupied by B-atoms is given by

$$q_{AB}(n) = \binom{7}{n} p_{AB}{}^n (1 - p_{AB})^{7-n}. \qquad (3)$$

(iii) The jump probability of A-atoms with given environment (m, n):

$$M_A(m,n) = \nu_A \exp\left(-\frac{E_A^M(m,n)}{kT}\right)$$
$$= \nu_A \exp\left(-\frac{E_A^M(0)}{kT}\right) s_A{}^m u_A{}^{m+n}. \qquad (4)$$

We have defined $s_A = \exp(S_A/kT)$ and $u_A = \exp(U_A/kT)$, while ν_A is a frequency factor approximately equal to the Debye frequency. The average number of jumps/sec of A-atoms is thus given by:

$$\Gamma_A = \sum_m \sum_n \nu_A p_V q_{VAB}(m) q_{AB}(n)$$
$$\times \exp\left(-\frac{E_A^M(0)}{kT}\right) s_A{}^m u_A{}^{m+n}.$$

Substitution of equations (1–4) and summation over m and n yields:

$$\Gamma_A = 12\nu_A \frac{p_{VA}}{c_A} \exp\left(-\frac{E_A^M(0)}{kT}\right)$$
$$\times \{1 + p_{VAB}(s_A u_A - 1)\}^4 \{1 + p_{AB}(u_A - 1)\}^7. \qquad (5)$$

A similar expression can be derived for B-atoms.

It is well known that, neglecting correlation effects, Γ_A is related to the self-diffusion coefficient D_A by:

$$D_A = \frac{a^2}{6}\Gamma_A \ (a = \text{jump distance}).$$

5. KINETICS OF S.R.O.

We will now investigate the influence of the jump of a particular atom on the number of AB-pairs in the alloy. Let us assume again that m of the common nearest neighbours of A and V are of type B. The other nearest neighbour sites of A and V are occupied by n resp. r B-atoms. The probability that r sites next to the vacancy are occupied by r B-atoms is given by:

$$q_{VA}(r) = \binom{7}{r} p_{VA}{}^{r}(1-p_{VA})^{7-r} \qquad (6)$$

If the A-atom and the vacancy change place the numbers of different pairs will change according to:

$$\Delta N_{AB} = -\Delta N_{AA} = \Delta N_{VA} = -\Delta N_{VB} = r-n$$

and

$$\Delta N_{BB} = 0.$$

Since we assume that the probabilities $q_{VA}(r)$, $q_{VAB}(m)$ and $q_{AB}(n)$ are independent, the probability for the occurrence of VA-pairs with environment (r, m, n) will be given by the product

$$q_{VA}(r)q_{VAB}(m)q_{AB}(n).$$

The total number of VA-pairs is $12Nc_V p_{VA}$. The rate of exchange of VA-pairs with environment (r, m, n) will be given by (4) since we assumed that the jump probability depends only on the environment of the A-atom. By a summation over r, m and n we obtain the time rate of change of N_{AB} due to VA-exchanges:

$$\dot{N}_{AB} = 12Nc_V p_{VA} \sum_{r,m,n} \nu_A \exp\left(-\frac{E_A^M(0)}{kT}\right)$$
$$\times (r-n)q_{VA}(r)q_{VAB}(m)q_{AB}(n)u_A{}^{m+n}s_A{}^{m}. \qquad (7)$$

If we designate the triple sum by Σ_A we may write

$$\dot{N}_{AB}(VA) = 12Nc_V p_{VA}\Sigma_A$$

similarly:

$$\dot{N}_{AB}(VB) = 12Nc_V p_{VB}\Sigma_B.$$

Hence the total time rate of change is given by:

$$\dot{N}_{AB} = \dot{N}_{AB}(VA) + \dot{N}_{AB}(VB)$$
$$= 12Nc_V(p_{VA}\Sigma_A + p_{VB}\Sigma_B). \qquad (8)$$

In the same way we find:

$$N_{VA} = 12N(p_{VA}\Sigma_A - p_{VB}\Sigma_B). \qquad (9)$$

The equilibrium values of p_{AB} and p_{VA} can be deduced from the condition that in the equilibrium state both $\dot{N}_{AB}$ and $\dot{N}_{VA}$ must vanish, in which case we obtain the relations:

$$p_{VA}\Sigma_A + p_{VB}\Sigma_B = 0 \qquad (10)$$
$$p_{VA}\Sigma_A - p_{VB}\Sigma_B = 0$$

which are satisfied only if $\Sigma_A = \Sigma_B = 0$. Summation over r, m and n after substitution of (2), (3) and (6) we find for Σ_A:

$$\Sigma_A = 7\nu_A \exp\left(-\frac{E_A^M(0)}{kT}\right)\{1+p_{AB}(u_A-1)\}^6$$
$$\times\{1+p_{VAB}(s_A u_A-1)\}^4\,[p_{VB}\{1+p_{AB}$$
$$\times(u_A-1)\} - p_{AB}u_A] \qquad (11)$$

During the calculation of this expression we used the relation:

$$\sum_{n=0}^{k} \binom{k}{n} a^n b^{k-n} = (a+b)^k$$

It is easy to show that all factors are positive except the last one, so the equilibrium equations $\Sigma_A = \Sigma_B = 0$ reduce to:

$$p_{VB}^{e}\{1+p_{AB}^{e}(u_A-1)\} = p_{AB}^{e}u_A$$
$$p_{VA}^{e}\{1+p_{BA}^{e}(u_B-1)\} = p_{BA}^{e}u_B. \qquad (12)$$

(The superscript e denotes the equilibrium value.)

Eliminating p_{VA}^{e} and p_{VB}^{e} from these expressions and using the relation:

$$w^2 = \exp\frac{2W}{kT} = \exp\frac{U_A+U_B}{kT} = u_A u_B$$

we find:

$$c_A p_{AB}^{e\,2}(w^2-1) + p_{AB}^{e} - c_B = 0. \qquad (13)$$

The root of this equation which satisfies the condition $0 \leq p^e_{AB} \leq 1$ is:

$$p^e_{AB} = \frac{-1+\sqrt{(1+4c_Ac_B(w^2-1))}}{2c_A(w^2-1)}. \quad (14)$$

This result is also obtained by the quasi-chemical theory. From the equilibrium equations (12) we also obtain:

$$p^e_{VA} = \frac{p^e_{BA}u_B}{1+p^e_{BA}(u_B-1)}. \quad (15)$$

Schapink[8], using quasi-chemical theory, has derived an expression for the vacancy concentration in binary alloys. The author[5] derived a value of p^e_{VA} from Schapink's theory, which can be shown to be equivalent to equation (15). Thus both the values of p^e_{AB} and p^e_{VA} derived from this kinetic treatment are in agreement with the results of the quasi-chemical approximation of statistical mechanics.

6. THE RELATION BETWEEN ORDERING KINETICS AND SELF-DIFFUSION

The kinetic equations (10) are nonlinear first order differential equations. We will consider only small deviations from equilibrium order:

$$p_{AB}-p^e_{AB} = \Delta p_{AB} \ll p^e_{AB}$$

$$p_{VA}-p^e_{VA} = \Delta p_{VA} \ll p^e_{VA}$$

$$p_{VAB}-p^e_{VAB} = \Delta p_{VAB} \ll p^e_{VAB}.$$

Obviously: $c_A\Delta p_{AB} = c_B\Delta p_{BA}$ and $\Delta p_{VA} = -\Delta p_{VB}$, neglecting products of small quantities.

$$\begin{aligned}\Sigma_A = 7\nu_A \exp\left(-\frac{E^M_A(0)}{kT}\right)&\{1+p^e_{AB}(u_A-1)\}^6\\ &\times\{1+p^e_{VAB}(s_Au_A-1)\}^4\\ &\times[\Delta p_{VB}\{1+p^e_{AB}(u_A-1)\}\\ &+\{(u_A-1)p^e_{VB}-u_A\}\Delta p_{AB}]\end{aligned} \quad (16)$$

Note that Δp_{AB} etc. only occur in the last term since this term vanishes for equilibrium values of p_{AB} and p_{VA} (equation 12).

Self-diffusion should be measured at equilibrium short-range order. In practice this condition will always be fulfilled, since measurable diffusion will always require a large number of jumps/atom, whereas s.r.o.-equilibrium is established with an average of 1 jump/atom. We can thus insert the equilibrium values of p_{AB} etc. in equation (5). We will henceforth omit the superscript e. Comparison of equations (5) and (16) shows that the kinetic equations may be written as:

$$\begin{aligned}c_A\dot{p}_{AB} = -\frac{7}{2a^2}&\left\{\left(\frac{p_{VB}}{p_{AB}}\right)^2\frac{D_A}{u_A}+\left(\frac{p_{VA}}{p_{BA}}\right)^2\frac{D_B}{u_B}\right\}\\ &\times c_A\Delta p_{AB}-\frac{7}{2a^2}(c_AD_A-c_BD_B)\Delta p_{VA}\end{aligned} \quad (17)$$

$$\begin{aligned}\dot{p}_{VA} = -\frac{7}{2a^2c_V}&\left\{\left(\frac{p_{VB}}{p_{AB}}\right)^2\frac{D_A}{u_A}-\left(\frac{p_{VA}}{p_{BA}}\right)^2\frac{D_B}{u_B}\right\}\\ &\times c_A\Delta p_{AB}-\frac{7}{2a^2c_V}(c_AD_A+c_BD_B)\Delta p_{VA}\end{aligned} \quad (18)$$

We have now two linear first order differential equations which are easily solved. As is shown in the appendix the solution for p_{AB} can be accurately represented by

$$\Delta p_{AB} = (\Delta p_{AB})_0 \exp\left(-\frac{t}{\tau_s}\right)$$

Here $(\Delta p_{AB})_0$ is the value of Δp_{AB} at $t = 0$ and τ_s is given by:

$$\tau_s = \frac{a^2}{7}\frac{c_AD_B{}^{-1}+c_BD_A{}^{-1}}{\left(\frac{P_{VB}}{P_{AB}}\right)^2\frac{c_B}{u_A}+\left(\frac{P_{VA}}{P_{BA}}\right)^2\frac{c_A}{u_B}} \quad (19)$$

For constant V^A_2 and V^B_2 a similar equation can be derived for b.c.c. alloys in which case the numerical factor $a^2/7$ has to be replaced by $2a^2/21$. Using the relations (12) and (13) we can derive a slightly different form of (19):

$$\tau_s = \frac{a^2}{7}\frac{p_{AB}p_{BA}}{p_{VA}p_{VB}}\frac{p_{AB}w'^2}{2c_B - p_{AB}}(c_AD_B^{-1}+c_BD_A^{-1}) \tag{20}$$

The details of formulae (19) or (20) depend of course on the jump model used. However, other jump models pose no serious difficulties if they fulfill the requirement that the correct equilibrium equations for p_{VA} and p_{AB} result. For example it is easy to include binding energies between vacancies and the constituent atoms.

For the purely random distribution one easily finds:

$$\tau_s = \frac{a^2}{7}(c_AD_B^{-1}+c_BD_A^{-1})$$

If $c_A \ll c_B$, $p_{AB} \sim 1$ and $p_{VB} \sim 1$. In this case (19) reduces to:

$$\tau_s = \frac{a^2}{7}D_A^{-1}u_A = \frac{a^2}{7}D_{0A}\exp\frac{Q_A+U_A}{kT} \tag{21}$$

7. DISCUSSION

The linearization of the kinetic equations (8) and (9) is justified for the experiments [1–5] where the change in s.r.o. is small; e.g. for AgZn (70.30) near 200°C the changes in p_{AgZn} and p_{VZn} due to a temperature change of 10°C are resp. 0·2 and 0·5 per cent (using the data of Fig. 2).

It can be shown [17] that for such small variations the solution of the linearized equations (17) and (18) are very good approximations of the solutions of equations (8) and (9).

The following features of (19) are important:

(i) If one of the components diffuses much faster than the other the value of τ_s is determined by the *slowest* diffusing component. Nowick has already pointed out that this is an essential requirement of a correct expression for the relaxation time of the Zener effect. His arguments are also valid for other changes in atomic configurations. If one of the components, say A, diffuses much faster than the other, nearly every jumped A-atom will be replaced by another A-atom, in which case no change in the atomic configuration will occur. The atomic distribution will be changed only by the occasional jump of a B-atom. It must be pointed out, however, that although equation (19) satisfies the above requirement the physical origin cannot be the same, since Nowick considers a *sequence* of jumps of a single vacancy, while in the derivation of equation (19) an average was taken over all *single* jumps.

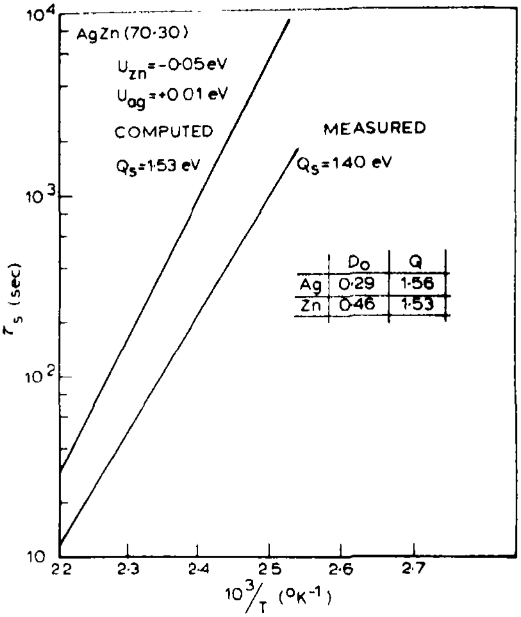

	D_0	Q
Ag	0·29	1·56
Zn	0·46	1·53

Fig. 2. Comparison of computed and experimental relaxation times for AgZn (70,30). Experimental data are from [4], diffusion measurements from [9]. Ordering energy is calculated from heat of mixing [10]. Binding energies are estimated.

(ii) Formula (21) shows that, for low concentrations of solute, τ_s is determined by the self-diffusion coefficient of the dilute component. If A is the fastest component usually $U_A < 0$ (a binding between vacancies and the fastest diffusor e.g. Zn in AgZn). So equation (21) shows that for low concentrations of solute the activation energy for the establishment of s.r.o. can be lower than the activation energy of the fastest diffusing component.

8. COMPARISON WITH EXPERIMENTAL DATA

In Figs. 2–4 we have plotted the relaxation time computed from (19) together with experimental results. In the temperature range, where s.r.o. is usually studied the computed values of τ_s are larger than the experimental results. We must, however, keep in mind that an error of 0·06 eV in the activation energies for self-diffusion causes a difference of a factor 4 in τ_s at $T^{-1} = 2{\cdot}10^{-3}$. The theoretical activation energies have been computed from:

$$Q_s = \frac{\mathrm{d}\ln\tau_s}{\mathrm{d}(1/kT)}.$$

It is obvious that the activation energies computed in this way are not constant. The values quoted in Figs. 2–4 are taken in the middle of the temperature range shown. The variations of Q_s are, however, small, e.g. in the case of AgZn shown in Fig. 2 the variation was only ~0·01 eV over a temperature range from 250°–1000°C.

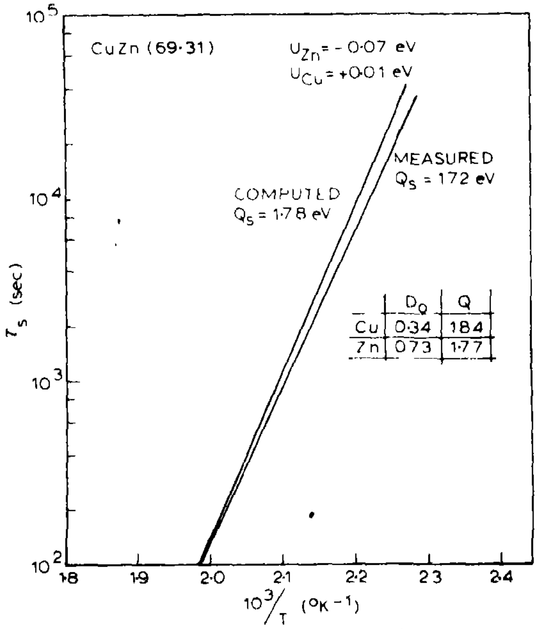

Fig. 3. Comparison of computed and experimental relaxation times for CuZn (69,31). Experimental data are from [15]. diffusion measurements from [11]. Ordering energy is calculated from heat of mixing [10]. Binding energies are estimated.

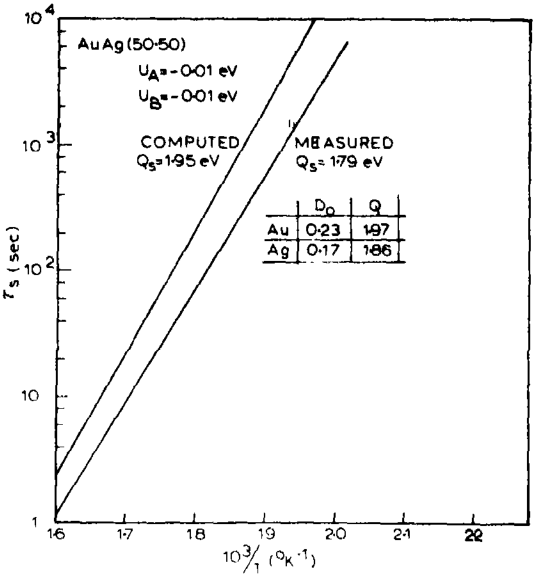

Fig. 4. Comparison of computed and experimental relaxation times for AgAu (50, 50). Experimental data are from [2,5]. Diffusion measurements from [12]. Ordering energy is determined from s.r.o. parameters [13]. Binding energies are supposed to be small.

In all cases shown the computed activation energies are larger than the experimental values. Although the theory given above is admittedly rather crude it is possible that the observed discrepancy can be attributed to a temperature dependence of the activation energies for self-diffusion. In alloys a small curvature of the log D vs. T^{-1} plot is highly probable since the average energy levels of the constituent atoms change with temperature. It is interesting to note that even in pure f.c.c. metals a curvature of the Arrhenius plot is observed. Ermert *et al.*[14] found an activation energy of 1·75 eV in pure gold between 286° and 412°C, whereas e.g. Makin *et al.*[16] found an activation energy of 1·81 eV between 700° and 1000°C.

9. CONCLUSION

The theory given above may be considered as an approximate solution to the problem of relating the relaxation time for s.r.o. with the self-diffusion coefficients of the com-

ponents of the alloy. Agreement with experiment is reasonable, especially if we take into account that the diffusion coefficients used in the calculations had to be extrapolated by roughly ten orders of magnitude.

Acknowledgements—This work is part of the research programme of 'Metals F.O.M.-T.N.O.' and was carried out under the direction of Prof. Dr. M. J. Druyvesteyn. The author wishes to thank his colleagues Dr. A. van den Beukel and Dr. J. L. Verster for stimulating discussions and Dr. G. Boom for writing a required computer programme.

REFERENCES

1. RADELAAR S., *J. Phys. Chem. Solids* **27**, 1375 (1966).
2. RADELAAR S., *Phys. Status Solidi* **27**, K63 (1968).
3. RADELAAR S. and RITZEN J. M. J., *Phys. Status Solidi* **31**, 277 (1969).
4. CHARDON J. Th., and RADELAAR S., *Phys. Status Solidi* **33**, 449 (1969).
5. RADELAAR S., Thesis, Delft (1967).
6. IIDA S., *J. phys. Soc. Japan* **10**, 769 (1955).
7. KIDIN I. I. and SHTREMEL' M. A., *Phys. Metals Metallogr.* **11**, no. 5, 1 (1961).
8. SCHAPINK F. W., *Phil. Mag.* **12**, 1055 (1965).
9. LAZARUS D. and TOMIZUKA C., *Phys. Rev.* **103**, 1155 (1956).
10. HULTGREN R. *et al.*, *Selected Values of Thermodynamic Properties of Metals and Alloys*. Wiley, New York (1963).
11. HINO C. *et al.*, *Acta Met.* **5**, 41 (1957).
12. MALLARD W. C. *et al.*, *Phys. Rev.* **129**, 617 (1963).
13. NORMAN N. and WARREN B. E., *J. appl. Phys.* **22**, 483 (1951).
14. ERMERT U. *et al.*, In *Vacancies and Interstitials* Edited by A. Seeger. North-Holland. Amsterdam (1969).
15. DAMASK A. C., *J. appl. Phys.* **27**, 610 (1956).
16. MAKIN S. M. *et al.*, *Proc. phys. Soc.* **70**, 545 (1957).
17. CODDINGTON E. A. and LEVINSON N., *Theory of Ordinary Differential Equations*. Chap. 15, p. 384. McGraw-Hill, New York (1955).
18. VINEYARD G. H., *Phys. Rev.* **102**, 981 (1956).

APPENDIX

The equations (17, 18) are of the form

$$\begin{aligned} c_A\dot{p}_{AB} &= (\alpha+\beta)c_A\Delta p_{AB} + (\gamma-\delta)p_{VA} \\ \dot{p}_{VA} &= c_V^{-1}(\alpha-\beta)c_A\Delta p_{AB} + c_1^{-1}(\gamma+\delta)\Delta p_{VA} \end{aligned} \tag{A1}$$

or

$$\dot{x}_1 = a_{11}x_1 + a_{12}x_2$$

$$\dot{x}_2 = a_{21}x_1 + a_{22}x_2,$$

in matrix notation

$$\dot{X} = AX, \text{ where } X = (x_1, x_2).$$

Applying a transform $Y = S^{-1}X$ we get the equation $\dot{Y} = S^{-1}ASY$. Choose S in such a way that $S^{-1}AS$ is a diagonal matrix D. The resulting equations $\dot{y}_1 = d_{11}y_1$ and $\dot{y}_2 = d_{22}y_2$ are easily solved. Application of the reverse transform yields the required solution:

$$\begin{aligned} c_A\Delta p_{AB} &= c_A(\Delta p_{AB})_0\left[-\frac{a_{22}-\lambda_1}{\lambda_1-\lambda_2}\exp(\lambda_1 t) + \frac{a_{22}-\lambda_2}{\lambda_1-\lambda_2}\exp(\lambda_2 t)\right] \\ &+ (\Delta p_{VA})_0\left[\frac{a_{12}}{\lambda_1-\lambda_2}\exp(\lambda_1 t) - \frac{a_{12}}{\lambda_1-\lambda_2}\exp(\lambda_2 t)\right] \end{aligned} \tag{A2}$$

with

$$\begin{aligned} \lambda_{1,2} &= \tfrac{1}{2}(a_{11}+a_{22}) \\ &\pm \tfrac{1}{2}\sqrt{((a_{11}+a_{22})^2 - 4(a_{11}a_{22} - a_{12}a_{21}))}. \end{aligned} \tag{A3}$$

The terms α, β, γ and δ in equations (A1) are all of the same order of magnitude, c_1^{-1} is a very large number.

Substituting the values of a_{11} etc. in (A3) and approximating the root by using $\sqrt{(1-\epsilon)} \sim 1-\tfrac{1}{2}\epsilon$ if $\epsilon \ll 1$

$$\begin{aligned} \lambda_{1,2} &\sim \tfrac{1}{2}[\alpha+\beta+c_1^{-1}(\gamma+\delta)] \\ &\pm\frac{1}{2}\left[c_1^{-1}(\gamma+\delta) - (\alpha+\beta) + 2\frac{(\alpha+\beta)(\gamma-\delta)}{\gamma+\delta}\right]. \end{aligned}$$

Hence

$$\lambda_1 = c_V^{-1}(\gamma+\delta) + \frac{(\alpha-\beta)(\gamma-\delta)}{\gamma+\delta} \sim c_V^{-1}(\gamma+\delta)$$

and

$$\lambda_2 = \alpha+\beta - \frac{(\alpha-\beta)(\gamma-\delta)}{\gamma+\delta}.$$

Note that $|\lambda_1| \gg |\lambda_2|$, moreover $a_{22} \sim \lambda_1$ and $a_{12}/\lambda_1 = 0(c_1)$, which shows that the solution is accurately represented by:

$$\Delta p_{AB} = (\Delta p_{AB})_0 \exp(\lambda_2 t).$$

Hence

$$\begin{aligned} \tau_s = -(\lambda_2)^{-1} &= -\frac{\gamma+\delta}{(\alpha+\beta)(\gamma+\delta)-(\alpha-\beta)(\gamma-\delta)} \\ &= \frac{\gamma+\delta}{2(\alpha\delta+\beta\gamma)} \\ &= \frac{a^2}{7}(c_A D_B^{-1} + c_B D_A^{-1})\left[\left(\frac{p_{VB}}{p_{AB}}\right)^2\frac{c_B}{u_A} + \left(\frac{p_{VA}}{p_{BA}}\right)^2\frac{c_A}{u_B}\right]^{-1}. \end{aligned}$$

The solution for the time dependence of p_{VA} shows that apart from a fast decay there exist a slow variation with time constant λ_2^{-1}. This phenomenon, neglected by Kidin and Shtremel', may cause a slowing down of the ordering process, depending on the sign of a_{12} and a_{21}.

J. Phys. Chem. Solids Pergamon Press 1970. Vol. 31, pp. 227–246. Printed in Great Britain.

TRANSVERSE ELECTROREFLECTANCE IN SEMI-INSULATING SILICON AND GALLIUM ARSENIDE*

RICHARD A. FORMAN†, DAVID E. ASPNES‡ and MANUEL CARDONA§
Department of Physics, Brown University, Providence, R. I. 02912, U.S.A.

(*First received* 8 *May* 1969; *in revised form* 7 *July* 1969)

Abstract—The transverse electroreflectance (TER) spectrum of GaAs is measured over an energy range extending from the fundamental absorption edge to the lambda structure. The TER structure in the vicinity of 3·4 eV in Si is also presented. Quantitative measurements of the variation of the spectrum with field have been performed, utilizing the facts that the TER geometry permits the calculation of the value of the electric field, and that the field is essentially uniform in the region of measurement. A detailed investigation of the effect of collision broadening on the electroreflectance response in the one-electron approximation is given, which qualitatively correlates the dependence of peak amplitude, peak location, and number of subsidiary oscillations observed in electroreflectance with the magnitude of the field and collision broadening lifetime. A method of measuring the collision broadening lifetime is applied to the fundamental edge of the GaAs sample used in this experiment. A conformal mapping is presented which enables a calculation of the field at any position in the crystal for the common TER geometries.

1. INTRODUCTION

THE ELECTRO-OPTIC effect has been used with great success for the determination and assignment of interband critical points in the band structure of a wide variety of solids[1–12]. In most of the previously used techniques [1–5] the electric field is non-uniform and quantitative comparison between the experimental lineshapes and existing theories of the elctro-optic effect for a uniform field[13–17] is difficult. These methods, applicable to semiconductors, make use of a space charge region for the production of the electric field and include the field-effect configuration of Seraphin and co-workers[1, 2], the semiconductor–electrolyte-interface technique of Cardona and co-workers[3, 4], and the *p–n* junction method of Handler and co-workers[5]. High-resistivity crystals allow electro-optic measurements to be made in the parallel[11, 12] or transverse[6, 7, 10] electrotransmission or electroreflectance[8–10] configurations, where the modulating field is sufficiently uniform and accurately determined to compare with theory. In this paper, we apply transverse electroreflectance (TER) methods to insulating samples of GaAs and Si, with the objective of obtaining the additional symmetry information available from TER, and also to demonstrate a method of obtaining collision broadening which requires quantitative measurements of the variation of the electro-optic response with field strength. A conformal mapping of the field distribution for typical TER gemoetries is given in the Appendix, which permits field magnitudes to be calculated.

2. EXPERIMENTAL

The basic experimental configuration is similar to that reported previously[3, 4, 10] and is shown in Fig. 1. The source is a 450 W

---

*Supported by the Army Research Office, Durham, and the National Science Foundation.

†On training assignment from the National Bureau of Standards. Permanent address: Solid State Physics Section, National Bureau of Standards, Washington, D.C. 20234, U.S.A.

‡Present address: Bell Telephone Laboratories, Murray Hill, N.J. 07974, U.S.A.

§A. P. Sloan Foundation Research Fellow.

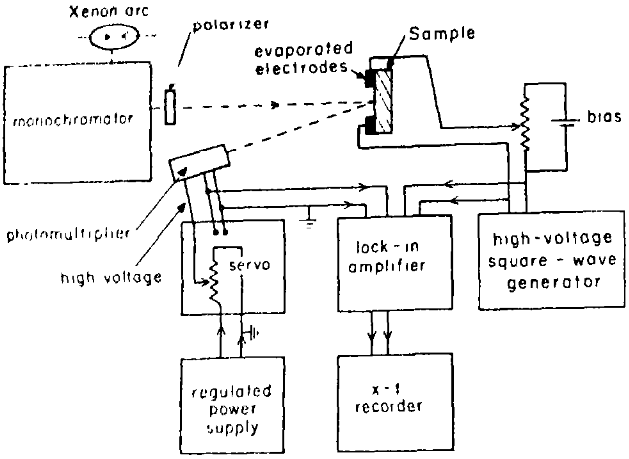

Fig. 1. Diagram of the experimental apparatus. The sample is in the transverse electroreflectance configuration.

XBO450 Osram high-pressure Xenon arc, and the monochromator is a 3/4 m Spex Model 1700-11. A 600 line/mm grating blazed at 500 nm or a 1200 line/mm grating blazed at 200 nm was used in conjunction with a Dumont 6911 photomultiplier with S1 response or an EMI 6256B photomultiplier with S13 response, depending upon the wavelength range of interest. Quartz optics were used throughout, and the light incident on the sample was polarized with a Polaroid HNB'P film polarizer. The effective light intensity I was held constant by controlling the gain of the photomultiplier in the usual manner[4] so that a constant DC current was maintained at the anode. The variation ΔI of light intensity caused by the electric field modulation was phase sensitively detected with a Princeton Applied Research Corp. Model HR-8 lock-in amplifier and the output recorded as a function of wavelength.

The GaAs single crystal samples[18] used in the experiment were chromium doped and had a room temperature resistivity of 10^9 Ω-cm and a liquid nitrogen (LN) temperature resistivity well over 10^{14} Ω-cm. High resistivity Si was produced by diffusing gold into a 100 Ω-cm *p*-type single-crystal silicon slice 1 mm thick at 1260°C for 23 hr, and following this with a rapid quench[19, 20]. All samples were lapped and polished to a thickness of approximately 0·5 mm in order to aid in achieving spatial homogeneity of the applied field (see Appendix). The exposed surface of the silicon crystal was of (110) orientation, so that all three major crystallographic axes were contained in the plane of the surface. Following a suitable light etch, a thick gold film was evaporated onto the surface to be studied, except for bare strips 0·25 to 1·0 mm wide perpendicular to each of the major crystallographic axes. The modulating electric field was developed in the plane of the surface and parallel to the appropriate crystallographic axes by applying a high voltage across these bare strips. This geometry gave the usual TER advantages: [8–10] ER response could be measured for polarizations of normally incident light both parallel and perpendicular to the electric field, no dielectrics were present on the sample surface, and the field was reasonably uniform and could be accurately determined (see Appendix). Limiting field strengths of the order of 10^5 V/cm were determined by electrical breakdown across the surface gap.

In most cases, measurements were taken with the samples in LN to insure high resistivity and to avoid thermal modulation effects [21]. Nitrogen bubbling, a possible source of noise, was eliminated by slowly bubbling helium gas into the LN. The samples were glued to a quartz backing plate at one corner only to eliminate strain; the fine wires used to make electrical contact to the evaporated gold regions were too thin to either support or strain the samples. These wires were soldered to the gold films using Wood's metal. The resistance of the samples was greater than $10^8\,\Omega$, including possible photoconductivity[22] due to the incident light. The experiments were performed using great care to prevent moisture from entering the dewar, for any ice which contaminated the LN would eventually be attracted to the high-field region of the sample.

A square-wave voltage was applied across the contact gap so as to produce a periodic modulating field. The generator[23] was constructed so that both peak-to-peak and DC values of the square wave were independently variable. A 1 kHz frequency was generally used. The use of square waves is essential for the interpretation of line shapes and dependence of electroreflectance on field strength, as will be discussed below.

3. THEORY

A. *Determination of collision broadening*

The theory of the electro-optic or Franz–Keldysh effect has been extensively treated in the literature[13–17]. In the absence of Coulomb effects in the effect of the electric field on the real and imaginary parts of the dielectric function in the vicinity of any critical point can be described analytically in the one-electron approximation in terms of two electro-optic functions[13, 14], $F(\eta)$ and $G(\eta)$. Excited carriers have a finite lifetime due to collisions, which leads to a broadening of the electro-optic spectrum which can be expressed as a Lorentzian convolution of the unbroadened response[2, 15] in terms of a collision broadening parameter Γ_c. This broadening rounds off the singularities of the electro-optic functions[2, 14]. In this section we investigate the effect of this broadening, and show that by measuring its field dependence the broadening energy Γ_c can be experimentally determined. Our treatment does not include exciton effects[17]; analytic expressions are not yet available to describe the general electro-optic effect in the Enderlein formalism[17], and for typical broadening energies and electric fields the analytic results of the one-electron approximation[13, 14] should be adequate to describe moderate bandgap semiconductors such as Si and GaAs where interband transitions dominate the absorption structure.

The Lorentizian boradened electro-optic functions $F(\eta)$ and $G(\eta)$ can be expressed analytically[14]; if Γ_c is the collision broadening parameter (in energy units), then after Lorentzian convolution

$$F(\eta) \rightarrow F\left(\eta, \frac{\Gamma_c}{\hbar\theta}\right)$$

$$G(\eta) \rightarrow G\left(\eta, \frac{\Gamma_c}{\hbar\theta}\right)$$

where $\hbar\theta$ is the characteristic electro-optic energy and

$$\eta = \pm\left(\frac{\omega_g - \omega}{\theta}\right) \qquad (1a)$$

$$\hbar\theta = \left[\frac{e^2 E^2 \hbar^2}{2\mu_\parallel}\right]^{1/3} \qquad (1b)$$

$$\frac{1}{\mu_\parallel} = \frac{1}{E^2}\left[\frac{E_x^2}{\mu_x} + \frac{E_y^2}{\mu_y} + \frac{E_z^2}{\mu_z}\right] \qquad (1c)$$

$\mu_\parallel$ is the interband reduced mass in the field direction[13, 14]. Changes in the real and imaginary parts of the dielectric function are proportional to $F(\eta, \Gamma_c/\hbar\theta)$ or $G(\eta, \Gamma_c/\hbar\theta)$ with the absolute magnitude of the proportionality factor given by

$$B\frac{\theta^{1/2}}{\omega^2} = \frac{4\pi^2 e^2 |\hat{\epsilon}\cdot \mathbf{P}_{cv}|^2}{m^2 \hbar}\cdot\frac{\theta^{1/2}}{\omega^2} \qquad (2)$$

where B is field-independent and contains the optical selection rules in the product of the polarization vector ϵ with the interband momentum matrix element $\mathbf{P}_{cv}$. Changes in the real or imaginary part of the dielectric function for any critical point can be written in the form

$$\Delta\epsilon_{1,2}(\omega, \mathbf{E}, \Gamma_c) = \pm B\frac{\theta^{1/2}}{\omega^2}\cdot F(\eta, \Gamma_c/\hbar\theta) \qquad (3a)$$

or

$$= \pm B\frac{\theta^{1/2}}{\omega^2}\cdot G(\eta, \Gamma_c/\hbar\theta). \qquad (3b)$$

Explicit expressions may be found in Ref. [14].

Determination of Γ_c by measuring the dependence of the peak-to-peak (p–p) value of $\Delta\epsilon$ upon $\mathbf{E}$ is contingent on the dependence of $F(\eta,\Gamma_c/\hbar\theta)$ and $G(\eta,\Gamma_c/\hbar\theta)$ on $(\Gamma_c/\hbar\theta)$, as shown in Fig. 2. We plot $F(\eta, x)$ and $G(\eta, x)$ for four values of $x = \Gamma_c/\hbar\theta$. Figure 2 illustrates the rapid decrease in the p–p value of each function together with a rapid attenuation of the subsidiary oscillations; with sufficiently large broadening the structure is effectively reduced to a positive and negative pair of peaks. As we shall show, the dependence of this decrease upon the ratio of $\hbar\theta$ to Γ_c is sufficiently strong to enable a determination of Γ_c independent of the actual p–p value of the electroreflectance response or type of critical point, provided Γ_c is field-independent.

The broadening energy Γ_c depends primarily upon decay processes such as phonon emission, recombination through traps. Auger electron excitation, etc., which are reasonably independent of externally applied electric fields, hence Γ_c should be field-independent to a good approximation. We examine the dependence of $|\Delta\epsilon(\omega, \mathbf{E}, \Gamma_c)|$, defined in equation (3), upon field for a fixed broadening energy Γ_c. It is convenient to use Γ_c as an energy unit, and to define a field unit E_0 as:

$$\Gamma_c = \hbar\theta_0 = \left[\frac{e^2\mathrm{E}_0{}^2\hbar^2}{2\mu_{\parallel}}\right]^{1/3} \qquad (4)$$

whence

$$\Delta\epsilon_{1,2}(\omega, \mathbf{E}, \Gamma_c) = \pm\frac{B\theta_0{}^{1/2}}{\omega^2}\left\{\left(\frac{\theta}{\theta_0}\right)^{1/2} \times F\left(\pm\left(\frac{\omega_g-\omega}{\theta_0}\right)\cdot\left(\frac{\theta_0}{\theta}\right), \frac{\theta_0}{\theta}\right)\right\} \qquad (5a)$$

or

$$= \pm\frac{B\theta_0{}^{1/2}}{\omega^2}\left\{\left(\frac{\theta}{\theta_0}\right)^{1/2} G\left(\pm\left(\frac{\omega_g-\omega}{\theta_0}\right)\cdot\left(\frac{\theta_0}{\theta}\right), \frac{\theta_0}{\theta}\right)\right\} \qquad (5b)$$

where the entire field dependence is contained in the terms in brackets, which are written as a function of the dimensionless reduced field E/E_0 since

$$\left(\frac{\theta}{\theta_0}\right) = \left(\frac{\mathrm{E}}{\mathrm{E}_0}\right)^{2/3}. \qquad (6)$$

The experimental condition of variable field and constant broadening energy is contained in the bracketed terms, since the proportionality factor is field-independent.

The dominant peaks of the bracketed terms in equation (5) originate from the singularity $\eta = 0$ and from $\eta \cong -0{\cdot}5$ of $F(\eta, 0)$, and from $\eta = 0$ and $\eta \cong -1{\cdot}1$ of $G(\eta, 0)$. We plot the numerical peak-to-peak (p–p) value of the bracketed terms as a function of reduced field for the Lorentzian broadened F and G functions in Fig. 3, and the energy separation (in units of $\Gamma_c = \hbar\theta_0$) between these peaks in Fig. 4. Inspection shows that the theoretical $\mathrm{E}^{1/3}$ dependence of the p–p variation which occurs in the absence of broadening changes substantially when broadening is present. The p–p variation is faster than $\mathrm{E}^{1/3}$ even for very little broadening: it is approximately $\mathrm{E}^{1/3}$ for $\Gamma_c \sim 0{\cdot}01\,\hbar\theta$. Such small broadening (or large field) is difficult to realize even under the best conditions at the lowest threshold and certainly cannot be obtained at interband critical points above the fundamental edge. The energy separation between the peaks retains the unbroadened $\mathrm{E}^{2/3}$ functional dependence

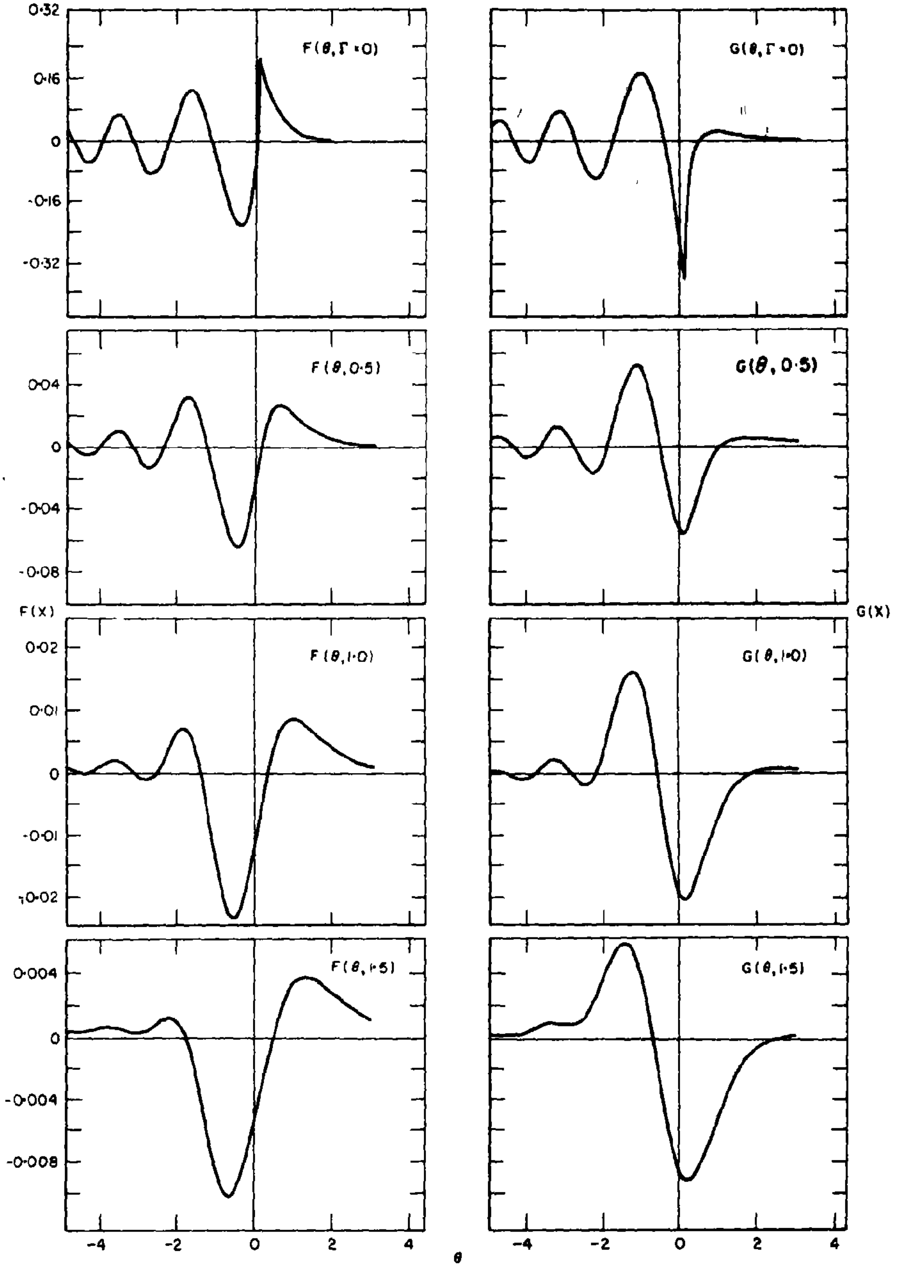

Fig. 2. The effect of Lorentzian broadening on the electro-optic functions $F(\eta, \Gamma_c/\hbar\theta)$ and $G(\eta, \Gamma_c/\hbar\theta)$ for various broadening energies $\Gamma_c = \hbar/\tau$.

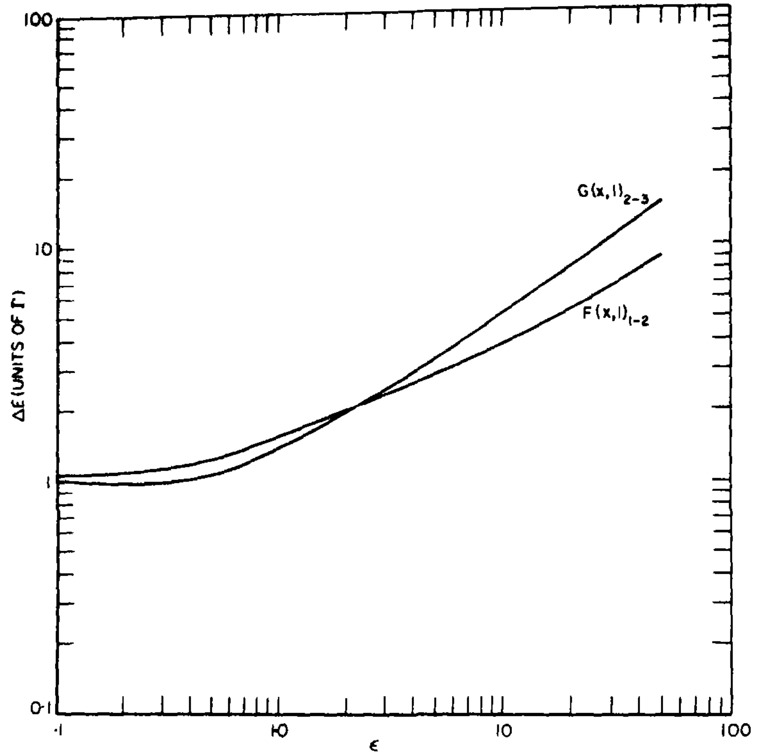

Fig. 3. The energy difference, in units of $\hbar\theta_0$, between the main positive peak and main negative peak for each function in equation (3), as a function of field for a fixed broadening energy Γ_c. The abscissa is in units of E_0, the field at which $\Gamma_c = \hbar\theta_0$.

for fields such that $|\hbar\theta| > \Gamma_c$, but the field dependence vanishes when $|\hbar\theta| \lesssim \Gamma_c$. These statements apply equally well to both F and G functions. Measurements of the electro-optic effect for higher transitions appear at best to have Γ_c comparable to $\hbar\theta$; Figs. 2–4 show that under these conditions the electroreflectance spectrum of any critical point should consist of only two peaks whose positions are nearly independent of the electrical field and whose rate of growth with field is at least linear. It can be shown that in the limit of $|\imath\theta| \ll \Gamma_c$ that the peak to peak amplitude of the signal is proportional to the square of the field.

The rapidly decreasing p–p value for $\Gamma_c \sim |\hbar\theta|$ implies the electroreflectance signal will not be observable experimentally if $\Gamma_c \gtrsim |\hbar\theta|$ which means critical points of one or two small interband reduced mass components will be favored. Since different modulation methods such as thermal[21] and stress[24] modulation depend on other parameters, electroreflectance will not respond with similar intensity to the same critical points in a given crystal.

The field dependence of the p–p values of F and G in Fig. 3 is sufficiently strong to permit a quantitative determination of Γ_c by measuring the field dependence of the p–p amplitude of an ER structure and fitting the experimental points to the curves of Fig. 3. If the field is known for each experimental point, the reduced field E_0 is obtained immediately as that field corresponding to an abscissa of 1 in Fig. 3, whence Γ_c is given by equation (4). Although

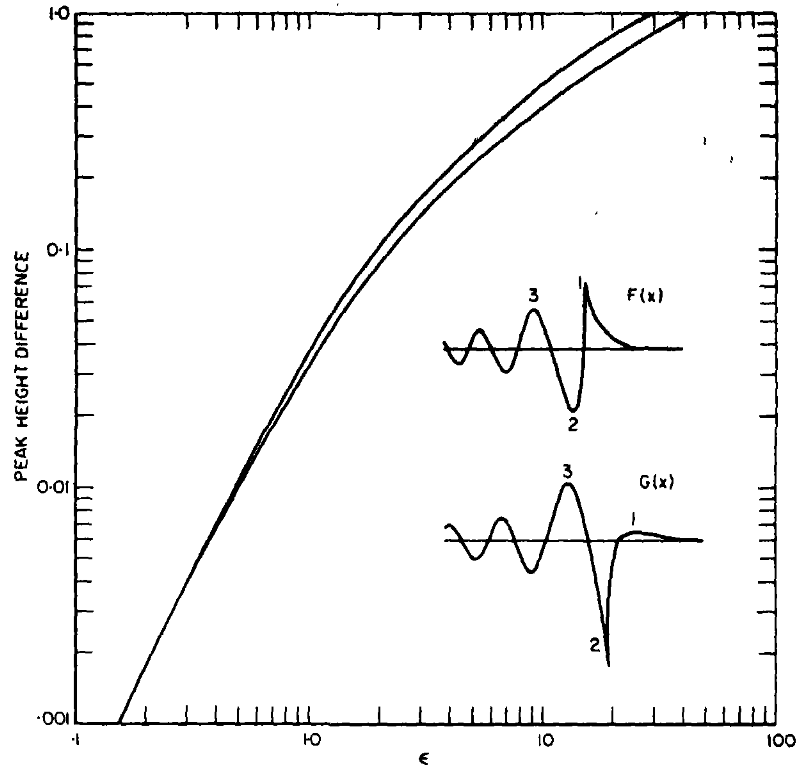

Fig. 4. The peak-to-peak amplitude of each function of equation (3), as a function of field for a fixed broadening energy Γ_c. The abscissa is in units of E_0, the field at which $\Gamma_c = \hbar\theta_0$. To obtain $\Delta\epsilon$, the ordinate is multiplied by the prefactor $B\theta_0^{1/2}/\omega^2$, as defined in the text.

equation (4) contains $\mu_{\parallel}$, Γ_c varies only as $|\mu_{\parallel}|^{-1/3}$, hence $\mu_{\parallel}$ need not be known to high accuracy to extract Γ_c.

The advantage of this method over direct curve fitting lies in the fact that the variation of the *p–p* amplitude with reduced field is practically identical for both *F* and *G* functions, hence it is not necessary to know the nature of the critical point giving rise to the ER structure nor to perform the Kramers–Kronig analysis in order to separate $\Delta R/R$ into $\Delta\epsilon_1$ and $\Delta\epsilon_2$ to obtain Γ_c. We repeat again that excitonic effects are not included and the results should be applied only where interband effects predominate.

The determination of Γ_c by the above method assumes that the dependence of the amplitude upon field is accurately measured. We stress here that an accurate dependence (using any ER method) can only be measured using square-wave modulation since the electro-optic response is nonlinear. The commonly used sine-wave modulation will give erroneous results. The system nonlinearities will in general distort the shape of the sine modulation, inducing both a shape and an amplitude component in the fundamental harmonic extracted by phase-sensitive detection. True amplitude dependence is obtained only by using a modulating waveform which cannot be distorted by system nonlinearities, i.e. a square wave. Errors introduced by using non-square-wave modulation will be less serious in the 'linear' response region discussed above, where $\Gamma_c \sim \hbar\theta$, but may be appreciable if $\Gamma_c < |\hbar\theta|$.

B. *Symmetry determination by transverse electroreflectance*

TER measurements can be performed with light polarized both parallel and perpendicular to the applied electric field, permitting symmetry information to be obtained. The electro-optic effect depends on the interband reduced mass in the direction of the field, producing field-induced changes in the dielectric constant which are anisotropic. The selection rules for polarized light give characteristic changes in the observed response for certain high-symmetry field directions and critical point sets[25, 26]. We consider here only Γ, Δ, and symmetries which permit the use of certain selection rules valid in many cases of interest. We assume that first-forbidden effects and effects arising from absence of inversion symmetry in crystals of zincblende structure are negligible. The electric-field-induced change $\Delta\epsilon$ arising from a nondegenerate critical point at Γ will be scalar under these assumptions, and will exhibit neither polarization nor field directional dependence (although degenerate critical points at Γ may exhibit polarization dependence in electroreflectance[27].

In many cases of interest, the polarization dependence of the optical selection rules for direct transitions can be described by the functional form:

$$W_i = [1 - (\hat{k}_i \cdot \hat{n})^2] \tag{6}$$

where W_i is the weight given to a transition involving a critical point at $\mathbf{k}_i$ in the B.Z. with the incident radiation polarized along $\hat{n}$. Equation (6) simply states that transitions are allowed if $\hat{k}_i \perp \hat{n}$. The change in the electroreflectance spectrum with polarization vector can be calculated in principle, since the electric field gives rise to an ER signal at a critical point which, for nondegenerate critical points, depends entirely on the angle between $\mathbf{k}_i$ and $\mathbf{E}$. A set of equivalent critical points are first grouped according to the angle made by each with the field, then the weights W_i of equation (6) are summed over each subgroup. Table 1 shows groupings and weight sums for equivalent critical points of Δ and Δ symmetry for fields applied in the (001), (110), and (111) directions in a crystal with an exposed $(1\bar{1}0)$ face. The total ER response is the sum of fractions having these weights regardless of the detailed shape of the ER response of any subgroup. The simplest identifications occur for Δ symmetry with (111) fields, and for Λ symmetry with (100) fields, in which cases all critical points make the same angle with the field and no polarization dependence occurs. These simple results do not apply if there is appreciable mixing of the wavefunctions on equivalent critical points, or interband mixing by the electric field, and would be obscured if structures from more than one symmetry coincided in energy.

4. RESULTS AND DISCUSSION

We report here results of measurements taken on Si and GaAs. These semiconductors are representative of the Group IV and III–V compounds, can be obtained in semi-insulating form, and their electro-optic response is given, at least qualitatively, by the one-electron approximation.

A. *Gallium arsenide*

Figure 5 shows the electroreflectance spectrum of the (001) face of GaAs. The experimental conditions are shown in the figure. Unpolarized light was used, for the data presented in this figure and the electric field was oriented in the (100) direction. All GaAs measurements were made on (100) faces since the only high resistivity samples available were (100) slabs. The electric field shown in Fig. 5 was determined by sample dimension measurements (see Appendix).

At the longest wavelengths, there is a large signal which is not a true ER signal, but rather is due to absorption-modulated reflection from the back surface of the sample. A back-reflection signal of this type is present whenever any light scattered from the back surface re-

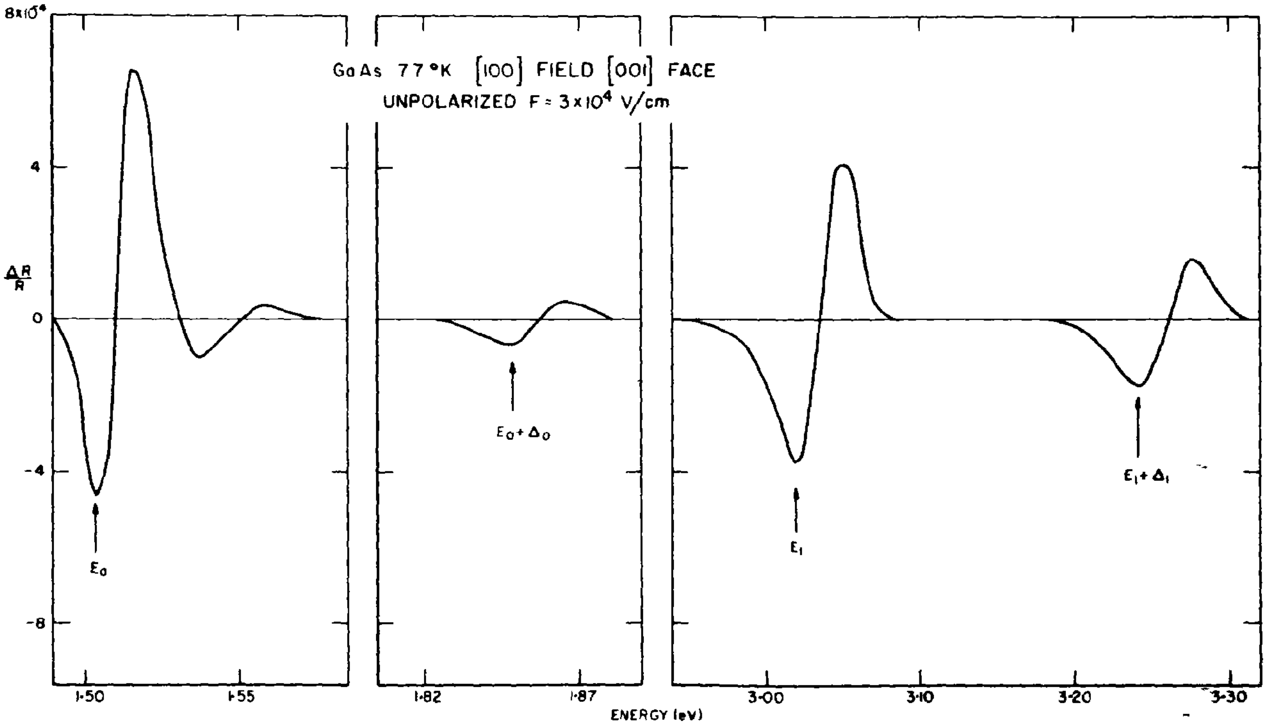

Fig. 5. The transverse electroreflectance spectrum of GaAs for square-wave modulation at LN temperature, to 3·5 eV. The field was oriented in the (100) direction in the (001) face.

Table 1. Electroreflectance subgroups and optical selection rule weights for Γ, Δ, and Λ critical sets for different field orientations on the ⟨110⟩ face of a cubic crystal

Critical point, symmetry	Number equivalent points	Field	Angle with field	Parallel	Perpendicular
(000) Γ	1	Any		1	1
⟨100⟩ Δ, *X*	6	001	0°, 2	0	2
			90°, 4	4	2
		110	45°, 4	2	4
			90°, 2	2	0
		111	54·73°, 6	4	4
⟨111⟩ Λ, *L*	8	001	54·73°, 8	16/3	16/3
		110	35·27°, 4	4/3	20/9
			90°, 4	4	28/9
		111	0°, 2	0	2
			70·53°, 6	16/3	10/3

emerges and is collected by the detector. It may be easily recognized by several characteristic features: its dependence on sample geometry, back surface roughness, and its similarity to electroabsorption. It has a characteristic shape much steeper on the high-energy side than the low-energy side due to the rapid rise of the absorption coefficient. The effect is similar to the internally reflected signals which occur in surface barrier methods under certain conditions[28]. It can be completely eliminated by cutting the back surface at an angle to the front.

The remainder of the signals are true front-surface electroreflectance signals and can be identified, as in previous work[4], with the assignments: 1·50 eV, the fundamental edge E_0, at Γ; 1·85 eV, $E_0+\Delta_0$, the transition from the conduction band minimum to the spin-orbit-split valence band, also at Γ; 3·0 and 3·2 eV, E_1 and $E_1+\Delta_1$, the main and spin-orbit split transitions of Λ symmetry. The E_0 and $E_0+\Delta_0$ ER peaks show no polarization effects to within the accuracy of our measurements, although polarization dependence at E_0 has been detected in EA in similar materials[27]. No polarization dependence was observed in the E_1 and $E_1+\Delta_1$ structures for ⟨100⟩ field directions, consistent with the interpretation of the transition having Λ symmetry.

We estimate the amount of broadening at the E_0 fundamental edge in this sample in two ways: by the best fit of $G(\eta, \Gamma_e/\hbar\theta)$ to the ER spectrum in this region, and by the procedure outlined in Section 3. Figure 6 shows the 'best fit' to the LN ER structure at a field of 3×10^4 V/cm. Since the interband reduced mass at E_0 in GaAs is 0·37 m_e[29], the characteristic energy at $E=3\times10^4$ V/cm is $\hbar\theta = 21$ meV. The 'best fit' occurs for $\Gamma_e/\hbar\theta = 0{\cdot}9$, hence $\Gamma_e \cong 19$ meV.

The method outlined in Section 3 can be used to determine the broadening by measuring the field dependence of the *p–p* amplitude and fitting the experimental points to the curve of Fig. 4. We show the evolution of the complete M_0 structure with increasing field in Fig. 7. The main peak at 824 nm remains fixed, as expected, since this peak is the singularity which occurs at the critical point energy itself. The entire structure changes with increasing field in a manner qualitatively similar to that shown in Fig. 2. The fitting of the *p–p*

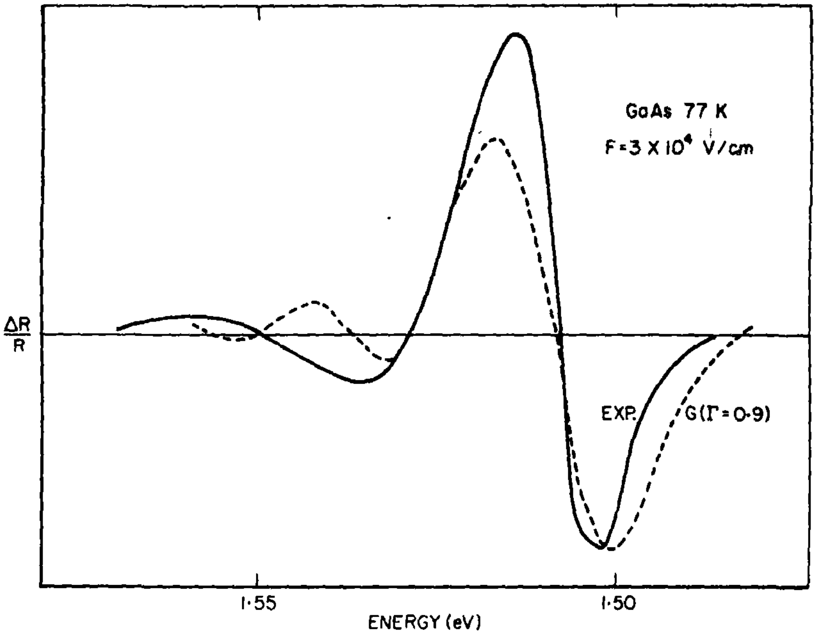

Fig. 6 'Best fit' of theoretical broadened G-function to experimental curve obtained for the fundamental edge of GaAs.

amplitude of the structure to the theoretical curve of Fig. 4 is given in Fig. 8. The experimental points, from 600V to 2000 peak square wave applied across the 0·56 mm gap, are shown as circles. The field unit E_0 corresponds to an applied voltage of 940 V, whence from the crystal dimensions and Appendix A, $E_0 = 10{\cdot}9$ kV/cm and $\Gamma_c \cong 11$ meV. The discrepancy between the two methods of estimating Γ_c may be caused by the definition of best fit; it is expected that the procedure of measuring peak height variation is more accurate since it involves a range of fields. Although exciton effects [17] are not included, the fact that Γ_c is much larger than the exciton binding energy $E_B = 3{\cdot}3$ meV in GaAs [30] means that exciton effects will tend to be washed out and the shape will be primarily determined by interband processes, justifying the use of the one-electron approximation.

The broadening energies obtained in transverse ER at the fundamental edge are larger than those obtained in capacitor[1, 2] or electrolyte [3, 4] configurations, which are estimated to be of the order of 2 or 3 meV even at room temperatures, since deep traps and recombination centers in the semi-insulating materials may make excited carrier lifetimes shorter.

It should be pointed out that the presence of normal fields at the surface due to a space charge region can cause errors in the calculation of the true field in transverse electroreflectance by modulation away from a nonzero field. If a normal field $\mathbf{E}_n$ exists at the surface, the net field obtained in transverse ER is

$$\mathbf{E} = \mathbf{E}_n + \mathbf{E}_t$$

where $\mathbf{E}_t$ is the applied transverse field. Neglect of $\mathbf{E}_n$, if present, can cause serious errors. However, the large concentration of deep traps in semi-insulating semiconductors makes space charge regions fairly short

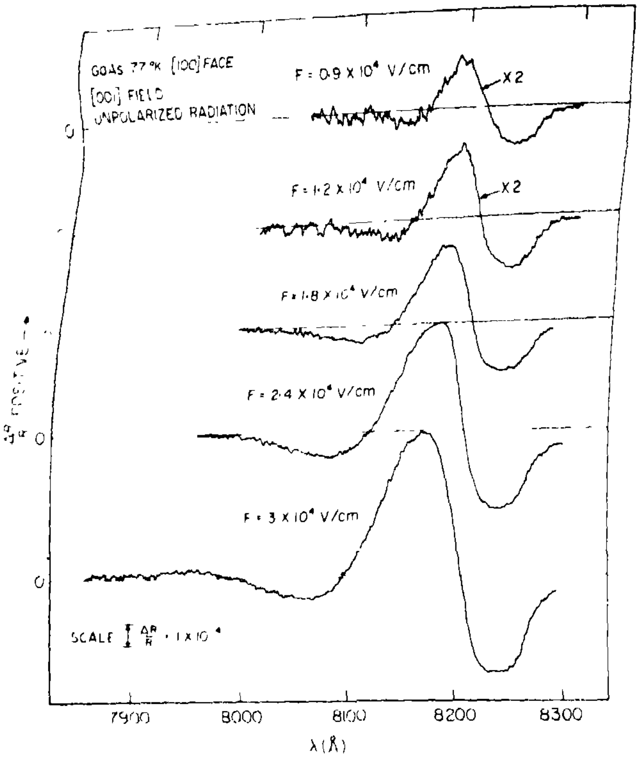

Fig. 7. The evolution of the fundamental ER spectrum of GaAs with increasing field. These curves illustrate typical signal-to-noise ratios obtained in the measurements.

(the Debye length for a semiconductor of dielectric constant 10 and ionized impurity concentration $10^{17}\,\mathrm{cm}^{-3}$ at LN temperature is ~ 10 nm). Also, the surface states on real GaAs[31] and Si surfaces[32] pin the surface Fermi level near the center of the forbidden gap, close to the bulk Fermi level in semi-insulating material. Thus, the true field over most of the light penetration depth, at least near the fundamental edge where light penetration depths are of the order of microns, will be tangential field. Our results are therefore characteristic of the transverse field and not greatly influenced by a normal surface field.

B. *Silicon*

We report only ER results on the structure at 3·4 eV, whose band structure assignment has been the subject of much effort and controversy[2, 4, 33–38]. A tracing of a typical experimental spectrum is shown in Fig. 9. The experimental details are given in the figure. All spectra of Si in the 3·4 eV region show the same characteristics regardless of field or polarization, except for differences in peak amplitudes. The structure is similar in shape to that observed by Seraphin[33], except the higher-energy part is more pronounced.

While this spectrum has the qualitative appearance of structure arising from one equivalent critical point set, a main peak followed by a subsidiary oscillation, detailed measurements show a negligible energy dependence of all peak positions on field amplitude. Since the interpretation of this spectrum as a main peak with a subsidiary oscillation requires a two-thirds power dependence of

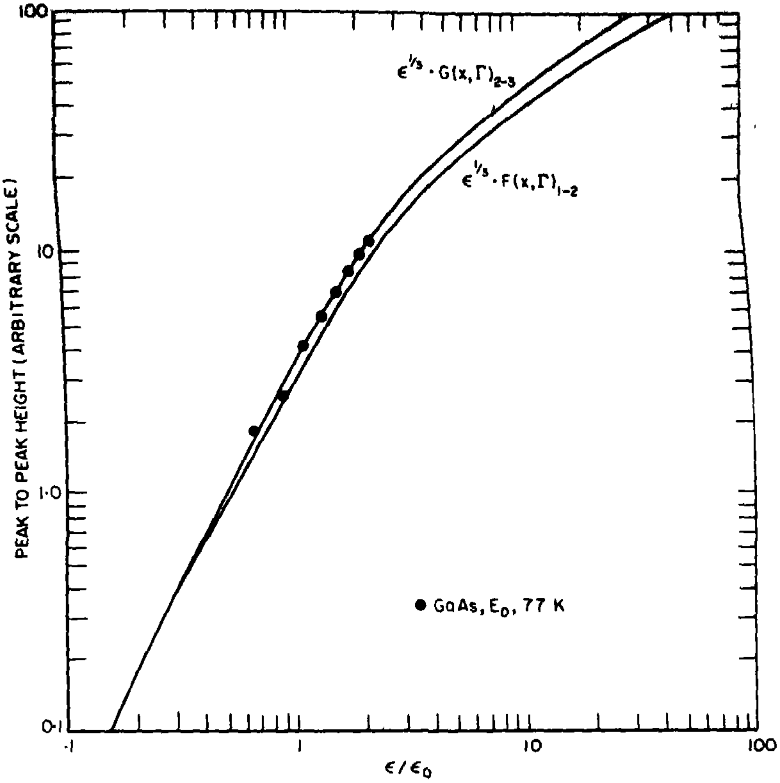

Fig. 8. Fit of the evolution with field of the peak-to-peak amplitudes of spectra similar to those shown in Fig. 7, to the theoretical curve of Fig. 4. The field unit $E_0 = 10·9$ kV/cm corresponds to a simple voltage of 940 V. The correction factor corresponding to the contact spacing of 0·56 mm on a 0·50 mm thick crystal is 0·65 (see Appendix A).

the subsidiary oscillation position with field, it is obvious that the absence of such a shift requires two distinct critical points in the 3·4 eV region. The qualitative features are consistent with the earlier discussion of broadening, provided $\Gamma_c \geqslant |\hbar|$ for the fields attained. Subsidiary oscillations cannot be seen until the $E^{2/3}$ dependence of peak position is well established for the main peaks, which would require $|\hbar\theta| \geqslant \Gamma_c$; since no subsidiary oscillations are observed, then $\Gamma_c \geqslant |\hbar\theta|$. The quantitative dependence of p–p amplitude on field, for various polarizations and field orientations, is also consistent with $\Gamma_c \geqslant |\hbar\theta|$ although this variation was not sufficiently strong to provide a definite location on the curve of Fig. 4. If a typical interband reduced mass of $0·1\, m_e$ is assumed, $\Gamma_c \geqslant 20$ meV, from the highest field applied.

Interpretation of this structure as arising from at least two critical points is also consistent with the interpretation of Seraphin, [2, 33] who observed small shifts of peak position with bias in the surface barrier configuration and assigned an M_0 and M_1 critical point set to the lower and higher energy peaks on the basis of these shifts. Although his fields were nonuniform and the surface magnitudes not known, it is probable that they were larger than those attained here, which made observation of the field shifts possible. A more definite assignment could be made by calculating $\Delta\epsilon_1$ and $\Delta\epsilon_2$ separately from $\Delta R/R$, [39] but the fractional coefficients

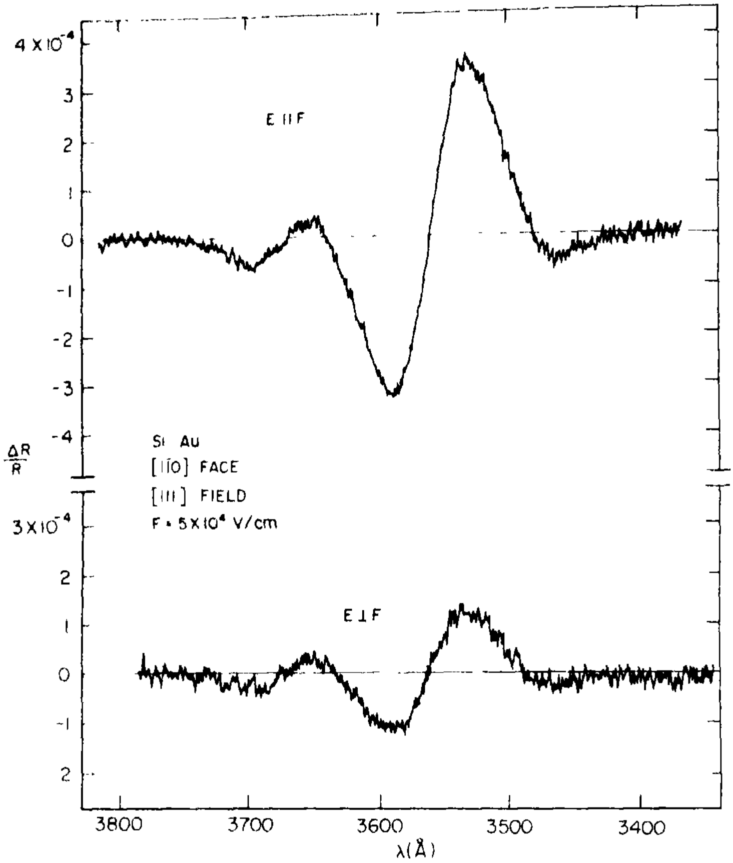

Fig. 9. A typical electroreflectance spectrum for the 3·4 eV region in Si. The field shown corresponds to an applied voltage of 3500 V across the contact gap.

α and β necessary for the separation are not known for Si at LN temperature, and vary too rapidly with energy in this energy range to permit the use of the room-temperature values[2]. A measurement of the relative reflectivity (Fig. 10) of high resistivity silicon was performed at 87°K and indeed also shows the doublet structure found in the electroreflectance. Measurement of the LN temperature optical constants of Si are planned.

We consider next the measurements for different field orientations and polarization directions on the exposed (1$\bar{1}$0) face. The amplitude ratios of polarizations parallel and perpendicular to the field directions for the dominant peaks are given in Table 2 together with the means square deviation for a series

Table 2. Ratio of amplitude of two peaks in the 3·4 eV region of Si for parallel and perpendicular polarizations. The results are averaged for measurements from 2000 to 3500V in all cases. All measurements were made with the field in and light incident perpendicularly onto the (1$\bar{1}$0) face

Peak	Field direction		
	001	110	111
3·6 eV	1·9 ± 0·1	1·67 ± 0·1	2·7 ± 0·3
3·4 eV	2·0 ± 0·2	1·0 ± 0·2	2·0 ± 0·5

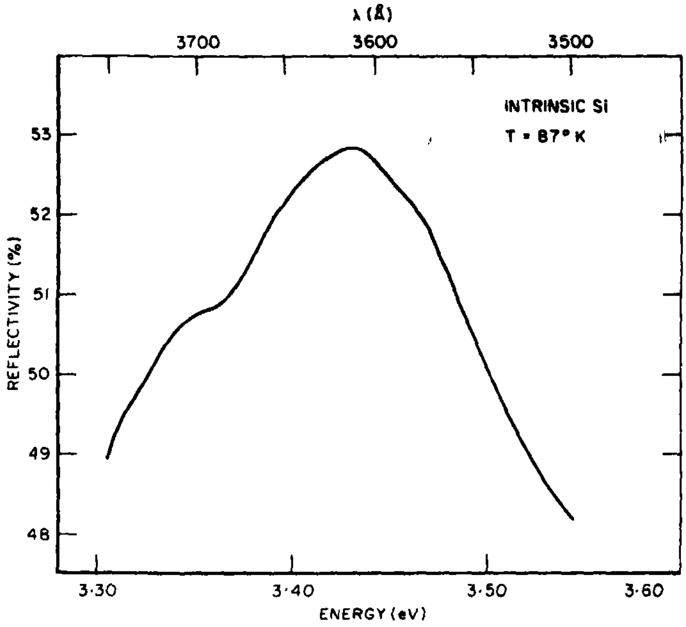

Fig. 10. Reflectivity of Si near 3·4 eV.

of measurements at applied voltages between 2000 and 3500V. Typically, little variation was observed over this voltage range.

The results shown in Table 2 can be compared with the theoretical variations of the high-symmetry critical points given in Table 1. We consider first the larger peak at 3·6 eV. A simple critical point along either Δ or Λ can be immediately ruled out because of the strong polarization dependence exhibited for fields in both (001) and (111) directions. Since simple equivalent critical point sets of lower symmetry should tend to be more isotropic than the high-symmetry Δ and Λ sets, it appears that this peak is not due to a simple equivalent critical point set, but is a result of a more complex system, as for example several nearly degenerate bands[34].

The calculations of Kane[36], Dresselhaus and Dresselhaus[37], and more recently Saravia and Brust[38], show this energy structure as probably arising from a complex set of critical points near Γ, and lying between Δ and Σ. A calculation of the electric-field effect on the dielectric function for each proposed energy band structure could be performed in the one-electron approximation by the convolution formalism[16], but this formalism contains approximations which may not be valid in this region, and the amount of computer time required to do the calculations is at present prohibitive.

Similar conclusions apply to the smaller structure occuring in the region of 3·4 eV. The difference between the two structures with respect to polarization dependence is sufficient to show that they arise from different regions of the B.Z. It appears quite certain that the B.Z. region giving rise to this structure is *not* located in the ⟨111⟩ direction as indicated by Saravia and Brust[38], since the polarization ratio for a (001) field is nearly 2. The agreement is not good enough with any model, however, to allow a definite choice to be made with any particular critical point.

Finally, Ghosh[35] reports seeing structure at 3·25 eV, 3·42 eV, and 3·55 eV in electrolyte electroreflectance measurements. These measurements are not inconsistent with the results presented here, since the maximum fields obtainable in transverse ER are generally an order of magnitude below those obtainable in the semiconductor space charge region. The stronger electric fields presumably present in Ghosh's measurements could bring out additional structure. We have not been able to observe any separate structure in the 3·2–3·3 eV region.

5. CONCLUSION

We have applied the TER method to the measurement of the electroreflectance spectrum of semi-insulating GaAs and the 3·4 eV structure of Si at liquid nitrogen temperatures. The application of known, nearly uniform fields to a crystal enables quantitative electroreflectance measurements to be made. We have shown that these measurements can be used to estimate collision broadening energies by measuring the field dependence of the peak-to-peak variation of the ER structure. A detailed investigation of the effect of collision broadening[2, 14, 15] on the quantitative behavior of the electro-optic functions in the one-electron approximation demonstrates that the generally observed higher interband ER spectra consisting of single oscillations with both peaks field-independent are to be expected whenever the broadening energy $\Gamma_c \cong |\hbar\theta|$, in contrast to the predications of the unbroadened theory. The same relation between Γ_c and $|\hbar\theta|$ constitutes an observability criterion, for unless Γ_c smaller than or of the order of $|\hbar\theta|$, a critical point will not contribute to the ER spectrum.

Our measurements of the field and polarization dependence of the structure of the 3·4 eV peak in Si show conclusively that at least two regions of probably different symmetry give rise to this structure. The data obtained were not sufficient to enable a unique determination of the symmetries, but it appears that simple isolated sets of equivalent critical points are insufficient to explain the results. These results are in general agreement with piezo-electroreflectance experiments[34].

Acknowledgements—One of us (D. E. A.) wishes to thank Bell Telephone Laboratories, Murray Hill, New Jersey, for providing facilities for the preparation of the final manuscript. We would also like to thank Kerry Shaklee and Fred Pollak for many helpful discussions.

REFERENCES

1. SERAPHIN B. O. and HESS R. B., *Phys. Rev. Lett.* **14**, 138 (1965).
2. SERAPHIN B. O. and BOTTKA N., *Phys. Rev.* **145**, 628 (1966).
3. SHAKLEE K. L., POLLAK F. H. and CARDONA M., *Phys. Rev. Lett.* **15**, 883 (1965).
4. CARDONA M., SHAKLEE K. L and POLLAK F. H., *Phys. Rev.* **154**, 696 (1967).
5. FROVA A. and HARDLER P., *Phys. Rev. Lett.* **14**, 178 (1965); FROVA A., HANDLER P., GERMANO F. A. and ASPNES D. E., *Phys. Rev* **145**, 575 (1966).
6. GAHWILLER C., *Helv. Phys. Acta* **39**, 595 (1966); *Solid-St. Commun.* **5**, 65 (1967).
7. PAIGE E. G. S. and REES H. D., *Phys. Rev. Lett.* **16**, 444 (1966).
8. REHN V. and KYSER D. S., *Phys. Rev. Lett.* **18**, 848 (1967).
9. A preliminary report of this work is contained in *Bull. Am. phys. Soc.* **12**, 658 (1967).
10. FORMAN R. A. and CARDONA M., in *II-VI Semiconducting Compounds*, p. 100. Benjamin, New York (1967).
11. FRENCH B. T., *Phys. Rev.* **174**, 991 (1968).
12. HAMAKAWA Y., HANDLER P. and GERMANO, *Phys. Rev.* **167**, 703 (1968).
13. THERMALINGAM K., *Phys. Rev.* **130**, 2204 (1963); ASPNES D. E., *Phys. Rev.* **147**, 554 (1966).
14. ASPNES D. E., *Phys. Rev.* **153**, 972 (1967).
15. ENDERLEIN R., *Phys. Status. Solidi* **20**, 295 (1967); **23**, 127 (1967)
16. ASPNES D. E., HANDLER P. and BLOSSEY D. F., *Phys. Rev.* **166**, 921 (1968); REES H. D., *J. Phys. Chem. Solids* **29**, 143 (1968).
17. ENDERLEIN R., *Phys. Status. Solidi*, **26**, 509 (1968).
18. Obtained from Bell and Howell, Pasadena, Calif.
19. AITCHISON R. E., Standford Electronics Laboratories Tech. Rep. No. 211-2 (1960).
20. ASPNES D. E., Ph.D. Thesis, Univ. of Illinois (1965) (unpublished).
21. BERGLUND C. N., *J. appl. Phys.* **37**, 3019 (1966); MATATAGUI E., THOMPSON A. G. and CARDONA M. *Phys. Rev.* In press.
22. SHAH J. and YACOBY Y., *Phys. Rev.* **174**, 932 (1968).
23. The square-wave generator was designed by L. MARZETTA, National Bureau of Standards, Washington, D.C.
24. ENGELER W. E., FRITSCHE H., GARFINKEL M. and TIEMANN J. J. *Phys. Rev. Lett.* **14**, 1069

(1965); GOBELI G. W. and KANE E. O., *Phys. Rev. Lett.* **15**, 142 (1965).

25. RÖSSLER U. and BOTTKA N., *Solid-St. Commun.* **5**, 939 (1968).
26. AYMERICH F. and BASSANI F., *Nuovo Cim.* **56B**, 295 (1968).
27. BAGAEV V. S., BELOUSOVA TYa., BEROZASHUILI Yu. N. and KELDYSH L. V., *Proc. Int. Conf. on the Physics of Semiconductors.* Vol. 1, p. 384. Publishing House "Nauka", Leningrad (1968).
28. ZOOK J. D., *Phys. Rev. Lett.* **20**, 848 (1968).
29. VREHEN Q. H. F., *J. Phys. Chem. Solids* **29**, 129 (1968), quotes the following effective masses for GaAs at 77°K: $m_e^* = 0{\cdot}067\, m_e$, $m_{hl} = 0{\cdot}082\, m_e$, and $m_{hh}^* = 0{\cdot}45\, m_e$. At the critical point the light hole mass should dominate, whence $\mu = 0{\cdot}037\, m_e$.
30. STURGE M. D., *Phys. Rev.* **127**, 768 (1962).
31. FLINN I., *Surface Sci.* **10**, 32 (1968).
32. ASPNES D. E. and HANDLER P., *Surface Sci.* **3**, (1966).
33. SERAPHIN B. O., *Phys. Rev.* **140**, A1716 (1965).
34. CARDONA M. and POLLAK F. H., *Phys. Rev.* **172**, 816 (1968).
35. GHOSH A., To be published.
36. KANE E. O., *Phys. Rev.* **146**, 558 (1966).
37. DRESSELHAUS G. and DRESSELHAUS M. S., *Phys. Rev.* **160**, 649 (1967).
38. SARAVIA L. R. and BRUST D., *Phys. Rev.* **171**, 916 (1968).
39. EHRENREICH H. and PHILIPP H. R., *Phys. Rev.* **129**. 1550 (1963); CARDONA M. and GREENWAY, *Phys. Rev.* **133**, A1685 (1964).
40. OBERLANDER S. and WILHELM W. E., *Phys. stat. sol.* **12**, 569 (1965).
41. CHURCHILL R. V., *Introduction to Complex Variables and Applications*, p. 171. McGraw-Hill, New York (1948).
42. MILNE-THOMPSON L. M., In *Handbook of Mathematical Functions* (Edited by M. Abramowitz and I. A. Stegun (U.S. Department of Commerce, National Bureau of Standards, Washington, D.C., 1964). *Appl. Math. Series* **55**, pp. 567 ff.
43. *Ibid.*, p. 591.
44. ASPNES D. E. and FROVA A., *Solid-St. Commun.* **7**, 155 (1969).

APPENDIX

Typical transverse electroreflectance geometries [6–10] can be represented quite accurately in cross-section as idealized two-dimensional potential distributions having simple boundary conditions. These potential distributions can usually be expressed in closed form using Jacobi elliptic functions. [20, 40]. In this Appendix, we obtain an analytic approximation for the potential distribution of the crystal in our geometry.

Figure 10(a) shows a cross-section of our crystal taken perpendicular to both crystal surface and contact edges, and plotted in the $W = u + iv$ plane. The crystal is assumed uniform in the direction perpendicular to the cross-section. We approximate the actual geometry by assuming the crystal and contacts continue as shown to infinity in both positive and negative v-directions. Errors are introduced because the crystal is finite in the v direction and nonuniform in the perpendicular direction, but the effects of these errors decrease roughly as $e^{-\alpha(x/L)}$, where x is the distance from the crystal boundary or nonuniformity, L is the sample thickness, (the characteristic length for the geometry) and α is of order unity. The truncation errors are small in the region of interest, the center of the gap between the contacts.

To obtain the analytic approximation, we must further assume that the dielectric constant is isotropic, the contacts define equipotential lines, and the normal component of the electric field vanishes on all remaining crystal surfaces. The first assumption is satisfied for a cubic crystal. The second and third depend primarily upon the absence of surface states, which result in the presence of electric fields in the crystal even if no potential difference is applied between the contacts. Such surface fields are almost always present in crystals and represent the principal limitation upon the results calculated here. The vanishing of the normal field over the contact-free boundaries also requires that the crystal dielectric constant be much larger than the dielectric constant of the ambient. Unless the crystal dielectric constant is infinite, normal fields will be present at the contact-free boundaries. In the absence of surface charge, the normal field inside the crystal is related to the normal external field by the boundary condition $E_{cr}{}^{\perp} = \epsilon\,\text{amb.}/\epsilon\,\text{cr.}\, E_{amb}{}^{\perp}$, where the subscripts cr. and amb. refer to the crystal and ambient respectively, and $\perp$ to the normal component of the electric field at the boundary. Since the external normal field is a result of field fringing, it is expected to be much less than the tangential fields, where internal equals external. For the usual dielectric constants encountered in crystals and ambients, the normal field component inside the crystal due to fringing will be quite small. This is particularly true for the region of interest between the contacts to the crystal. Therefore, to the extent that normal field at free boundaries can be neglected, the potential distribution in the region centered between the contacts will be given fairly accurately by the potential distribution of the idealized geometry and boundary conditions of Fig. 11(a).

The coordinate axes u and v are defined as shown in the complex w-plane in order to utilize the symmetry of the idealized crystal. The potential distribution is completely described by either the upper or lower half of the crystal, and by choosing the upper and lower contacts to be at potentials $+V/2$ and $-V/2$ the line $v = 0$ becomes an equipotential with $\Phi = 0$. We therefore need the potential distribution for only the $v \geqslant 0$ half of the figure, where the boundary conditions are

$$V(w) = \begin{cases} +\dfrac{V}{2}: & \left(u = d, \dfrac{1}{2}s \leqslant v < \infty\right) \\ 0: & (0 \leqslant u \leqslant d, v = 0) \end{cases}$$

$$\frac{dV(w)}{dw} = \begin{cases} 0: (u = 0, 0 \leqslant v < \infty) \\ 0: \left(u = d, 0 \leqslant v \leqslant \dfrac{S}{2}\right). \end{cases}$$

The crystal thickness is d, the spacing between the

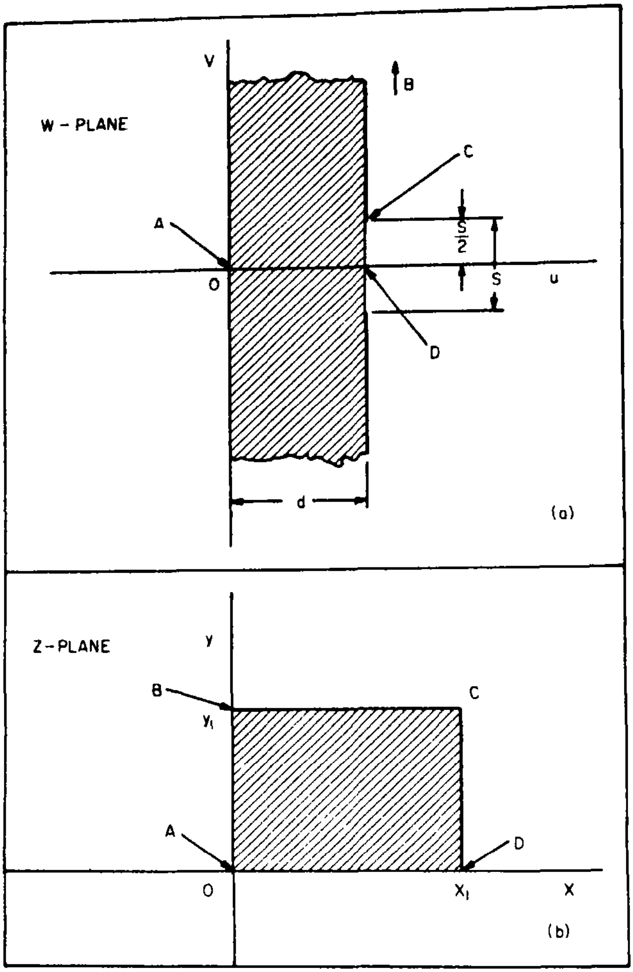

Fig. 11. (a) The idealized sample geometry in the *w*-plane. Contacts are shown as heavy lines, and dimensions are indicated. (b) The *z*-plane diagram of the rectangle conformally mapped onto the upper half of the idealized sample geometry. Equivalent points A, B, C, and D are shown in both diagrams

contacts is *s*, and the voltage difference between contacts is *V*.

The boundary conditions are defined over four straight line segments, which suggests that the idealized crystal represented by the region defined in Fig. 11(a) can be mapped onto the rectangle shown in Fig. 11(b), for which the potential distribution is simply $\phi(z) = yV/2Y_1$. Corresponding image points in Figs. 11(a) and 11(b) are labeled A, B, C and D with B in Fig. 11(a) receding to $v \to +\infty$. We map the rectangle onto the idealized crystal using the conformal mapping $W(z) = u(x,y) + iv(x,y)$ defined in the *z*-plane of Fig. 11(b).

By Schwartz-Christoffel transformation theory[41], the straight line segments of the rectangle will be mapped onto the straight line segments of the idealized geometry if the derivative $\mathrm{d}W(z)/\mathrm{d}z$ of $W(z)$ possesses a symmetric distribution of poles and zeros about each of the infinite lines formed by extending the sides of the rectangle. Therefore, $\mathrm{d}W(z)/\mathrm{d}z$ must be doubly periodic in the complex *z*-plane. In addition $\mathrm{d}W(z)/\mathrm{d}z$ must be analytic everywhere except at those points where the map is not conformal, i.e. at points B and C where the angles are not preserved in the mapping, and all doubly periodic images of B and C. The required angular changes are obtained if $\mathrm{d}W(z)/\mathrm{d}z$ has a pole at B and a zero at C[41]. This determines $\mathrm{d}W/\mathrm{d}z$ to within a multiplicative constant.

Including this constant gives:

$$\frac{dW(z)}{dz} = \frac{2d}{\pi} dn(z) \tag{7a}$$

$$w(z) = u + iv = \frac{2d}{\pi} \sin^{-1}[sn(z)] \tag{7b}$$

where the Jacobian elliptic functions[42] dn(z) and sn(z) are doubly periodic over the fundamental rectangle

$$0 \leqslant x \leqslant x_1 = K(m)$$

$$0 \leqslant y \leqslant y_1 = K'(m) = K(1-m).$$

K is the complete elliptic integral of the second kind and m is a parameter given by the location $w_c = d + i\,s/2$ of C in the w-plane. m is most easily obtained from the inverse transformation

$$z = x + iy = sn^{-1}\left\{\sin\left[\frac{\pi W}{2d}\right]\right\} \tag{8a}$$

$$\equiv \int_0^{\pi w/2d} d\theta[1 - m\sin^2\theta]^{-1/2}. \tag{8b}$$

The integral representative of equation (8b) has a singularity at w_c, where

$$1 - m\sin^2\left(\frac{\pi w_C}{2d}\right) = 0. \tag{9}$$

Using $w_c = d + i\,s/2$, we have

$$m = \cosh^2\left(\frac{\pi s}{4d}\right). \tag{10}$$

Since the potential distribution on the rectangle is

$$\phi(z) = \frac{yV}{2y_1} = \frac{yV}{2K(1-m)} \tag{11}$$

the idealized crystal potential distribution is

$$\Phi(u, v) = \frac{V}{2K(1-m)} \cdot Im \int^{\pi W/2d} d\theta\,[1 - m\sin^2\theta]^{-1/2} \tag{12}$$

and the electric field is

$$E_v + E_u = \frac{-\pi V}{4dK(1-m)}\left[1 - m\sin^2\left(\frac{\pi}{2d}(u+iv)\right)\right]^{-1/2}. \tag{13}$$

One of the objectives of transverse electroreflectance is to obtain a known, nearly uniform field in the region near the center of the gap between the contacts. Equation (13) can be used to calculate the field value at the center of the gap, and to estimate the width of a region where the field is uniform to within a given amount of this value. On the surface in the gap, $w = d + iv$, and

$$E_v = 0\,\frac{\pi V}{4dK(1-m)}\left[1 - m\cosh^2\left(\frac{\pi V}{2d}\right)\right]^{-1/2}$$

$$\left(u = d, 0 \leqslant v \leqslant \frac{s}{2}\right) \tag{14}$$

giving the field minimum in the center of the gap as

$$|E_{V_0}| = \frac{\pi V}{4dK(1-m)\surd(1-m)} = \xi\,(m) \cdot \frac{V}{s}$$

$\zeta(m)$ represents a gap width/crystal thickness $= s/d$ dependent correction to the simplest approximation, which sets the field equal to the voltage across the gap divided by the gap width. The correction $\xi(m)$ is plotted as a function of s/d in Fig. 12. As can be seen, the simple approximation $\epsilon \cong V/s$ is surprisingly accurate, with $\zeta(m)$ varying over the limited range $2/\pi = 0{\cdot}636$ at zero gap, to 1 at large gaps. Greatest uniformity of the tangential field near the center of the gap will result for largest ratios of gap width to crystal thickness. If s/d is large, m is small, and using[43]

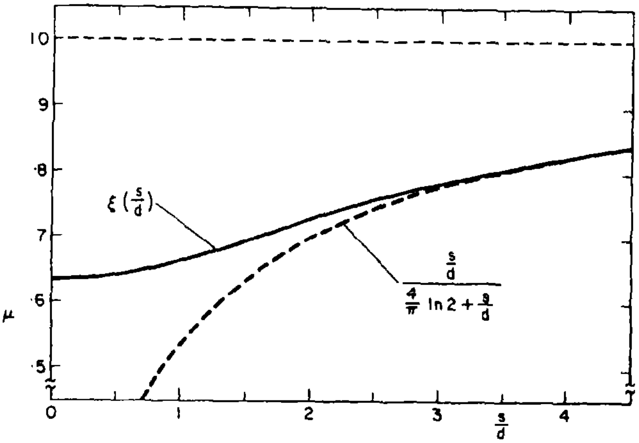

Fig. 12. The correction $\xi(m)$ to the zero-order field approximation, with the asymptotic expansion which includes fringing at the edges of the contacts.

$$\lim_{m\to 0} K(1-m) = \frac{1}{2}\ln\left(\frac{16}{m}\right) \approx \ln 2 + \frac{\pi s}{4d} \tag{16}$$

equation (13) becomes in this limit

$$E_v + iE_u \approx \frac{-V}{s+2\left(\frac{2\ln 2}{\pi}d\right)}\left[1 - m\sin^2\left(\frac{\pi}{2d}(u+iv)\right)\right]^{-1/2}. \tag{17}$$

Each contact edge adds an effective length approximately equal to $(2\ln 2/\pi)d$ to the gap width s for the purpose of calculating the tangential field at the center of the gap. Figure 12 shows that this asymptotic behavior is reached for a quite low s/d ratio. Surface uniformity can be estimated by setting $u = d$ in equation (17) and calculating the range of v for which

$$|E_v(d+iv)| \leqslant \eta \cdot |E_v(d, 0)|, \quad \eta > 1.$$

where η represents the allowable deviation of tangential field from the value at the center. The inequality is satisfied over the entire gap to within distance $L \approx (d/\pi)\ln(\eta^2/\eta^2 - 1)$ of the contact edges. As an example, 10 per cent uniformity is achieved over the gap region which excludes the strips within $L = 0{\cdot}55d$ of the contact edges for any gap width greater than $1{\cdot}1d$. Field uniformity is therefore achieved with quite reasonable gap/length ratios.

It has recently been shown that field inhomogeneities can strongly influence the ER lineshape in surface barrier ER, due to interference in the direction of propagation which is phase-sensitive and mixes the line-shapes of $\Delta\epsilon_1$, and $\Delta\epsilon_2$ as well as averaging them. We prove here our previous statement that such inhomogeneities in transverse ER are negligible, using equation (13) and the criterion given in Ref. [44] for the neglect of inhomogeneity in the propagation direction:

$$\left|\begin{matrix}\frac{1}{2k}\cdot\frac{1}{\Delta\epsilon}\frac{\partial\Delta\epsilon(z)}{\partial z}\\ k^2 = \frac{w^2}{c^2}\epsilon\end{matrix}\right| \ll 1 \tag{18}$$

Taking the most unfavorable cases, we suppose ϵ is real so that $\lambda k = 2\pi n$, where λ is the wavelength in air and n the index of refraction. Also, we suppose broadening is present, in which case according to Fig. 3, the most rapid variation of ϵ with E will be quadratic, at the peak locations when $|\hbar\theta| \ll \Gamma$. Then equation (18) can be written

$$\left|\frac{\lambda}{2\pi nE}\frac{\partial E}{\partial z}\right| \ll 1 \tag{19}$$

which may be evaluated using equation (13), noting that $z \leftrightarrow u$. We find equation (19) is equivalent to

$$\left|\frac{\lambda}{d}\cdot\frac{m\sin\left(\frac{\pi}{d}(u\, l\, iv)\right)}{8n\left[1 - m\sin^2\left(\frac{\pi}{2d}(u+iv)\right)\right]}\right| \ll 1. \tag{20}$$

Since this effect is observable for a distance of the order of several wavelengths in from the surface, we set $u = d$, which neglects terms of second order in λ/d, and obtain,

$$\frac{m\lambda}{8n}\cdot\left|\frac{\sinh v}{1 - m\cosh^2\left(\frac{\pi v}{2d}\right)}\right| \ll 1.$$

But we have already restricted our measurements to regions where the abolute value quantity is not too large. Therefore, TER field inhomogeneity of the type discussed in Ref. [44] is negligible. We should emphasize that this concerns mixing of the real and imaginary parts of $\Delta\epsilon$ due to interference; spatial variation of E parallel to the surface can be included by performing a simple average of $\Delta\epsilon_1$, and $\Delta\epsilon_2$ independently. This effect is also of minor importance in the presence of broadening.

Generalization of the above to the 4-contact configuration used by Rehn and Kyser[8] is obtained by reflecting Fig. 11(a) about the v-axis, which has the effect of replacing d by $d'/2$ in all the above equations, where d' is the thickness of the crystal carrying the four contacts in the Rehn–Kyser configuration. Our solution to the potential distribution of the idealized crystal applied more accurately to the Rehn–Kyser configuration, for the boundary condition of zero normal field on the 'free' boundary opposite the contact face in Fig. 11(a) is now forced by symmetry since this boundary is a mirror plane in the 4-contact configuration. Remaining considerations of surface fields and finite crystal size still apply.

J. Phys. Chem. Solids **Pergamon Press 1970. Vol. 31, pp. 247–254. Printed in Great Britain.**

EFFECT OF PRESSURE ON SOLID-SOLID TRANSITIONS IN SOME SILVER AND CUPROUS CHALCOGENIDES

J. B. CLARK and ELIEZER RAPOPORT*
Chemical Physics Group of the National Physical and National Chemical Research Laboratories,
South African Council for Scientific and Industrial Research, P.O. Box 395,
Pretoria, South Africa

(*Received* 9 *May* 1969; *in revised form* 30 *June* 1969)

Abstract—Phase transitions in Ag_2S, Ag_2Se, Ag_2Te, Cu_2S and Cu_2Se were studied by differential thermal analysis (DTA) to 40 kbar. The transition temperature lines increase with pressure with initial slopes of 1·57, 6, 11·48, and 0·5°C/kbar, respectively, for the first four and −0·6°C/kbar for (probably copper-deficient) Cu_2Se.

INTRODUCTION

THE SILVER and cuprous chalcogenides belong to a class of non-stoichiometric compounds and have interesting electrical properties. Ag_2S, for example, is a semiconductor in its monoclinic room-temperature form and transforms at 177°C into a disordered b.c.c. phase which is a metallic (though poor) conductor[1–3]. The other chalcogenides in this group behave in a similar manner and are also known to undergo phase transformations in the temperature range 100°–200°C [4–5]. The silver and copper chalcogenides are naturally-occurring minerals of some geological interest. Ag_2S in its two modifications (and also Ag_2Se) was suggested to be useful for geologic thermometry [6, 7].

The present work is concerned with phase transformations in these compounds and the dependence of the transition temperatures on pressure. Previously, Roy *et al.*[7] followed the α/β transformations [8] in Ag_2S and Ag_2Se to slightly beyond 1 kbar. More recently, the α/β transformation in Ag_2Se was determined by Banus[9] to 47 kbar in a tetrahedral anvil press and, very recently, Banus and Finn[10] determined the phase diagram of Ag_2Te to 25 kbar and 250°C in a hydrostatic apparatus.

EXPERIMENTAL

Ag_2S of stated purity of 99·99%, and Ag_2Se and Ag_2Te both of stated purity of 99·999% were obtained from Koch-Light Laboratories. Cu_2S and Cu_2Se were obtained from Rocky Mountain Chemicals and were of stated purity of 99% and 99·99%, respectively. The quantities of these substances that were available were sufficient for several differential thermal analysis (DTA) experiments on each substance but not for volumetric (*P-V-T*) work.

Quasihydrostatic pressures to 40 kbar were generated in a piston-cylinder device previously described[11, 12]. The furnace assembly was similar to that described by Cohen *et al.*[13]. Phase transitions were detected by means of differential thermal analysis (DTA)[11, 14] with Chromel–Alumel thermocouples. The heating rate was usually in the range 0·8–2·5°C/sec. Corrections were made for the effect of pressure on the thermocouples[15]. The corrections are, however, quite small in the temperature range of present experiments. The silver compounds were contained in silver capsules and the copper compounds in copper capsules. The capsule design, incorporating a thermocouple well, had been previously described[16]. The longitudinal temperature gradient along the sample capsule was reduced by sandwiching the capsule between two insulated copper plugs[17]. Sliding friction was determined and corrected for by comparing results obtained on increasing and decreasing pressure[14]. The pressures obtained in this way were further corrected for the effect of nonsymmetrical pressure loss[18]. The corrected pressures are believed accurate to ±0·5 kbar. Temperatures could be determined to ± 1°–2°C. Each phase boundary (in a pressure temperature diagram, as the results are presented here) is based on at least four repeated determinations on different samples with consistency of 1°–2°C. The procedure for following phase transitions (and correcting for friction) below ~ 4 kbar has been described elsewhere[19].

---

*Now at Israel Atomic Energy Commission, Soreq Nuclear Research Centre, Yavne, Israel.

RESULTS AND DISCUSSION

Typical DTA signals obtained for some of the transitions studied here are presented in Fig. 1. Experimental results are presented in Figs. 2–6 in the form of temperature–pressure (phase) diagrams. A line in such a p–T diagram, drawn through the experimentally determined transition points, divides the p–T plane into the regions of stability of the two phases and is referred to in the following discussion as a phase boundary or transition line. The points plotted in the p–T diagrams are the averages between transition temperatures on heating and on cooling.

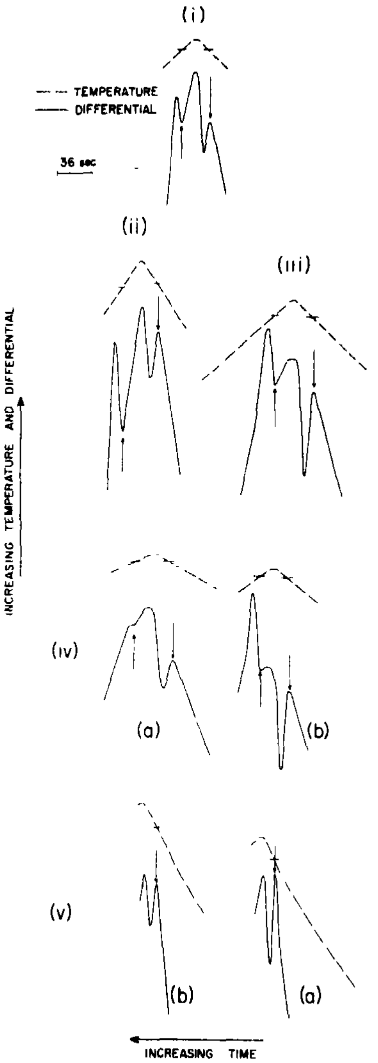

Fig. 1. Typical DTA signals. (i) Signal at 6·3 kbars, 226·5°C on the $Cu_{1.96}S$ I/II boundary. (ii) Signal at 32·9 kbars, 283·5°C on the Ag_2Se I/II boundary. (iii) Signal at 6·4 kbars, 131°C on the I/II boundary in Cu_2Se. (iv) (a) Signal at 6·1 kbars, 105·5°C on the I/III boundary in Cu_2S. (b) Signal at 13·9 kbars, 242·5°C on the Cu_xS I/II boundary. (v) (a) Ag_2Te on the V/II boundary at 25·7 kbars and 316·2°C. (b) Ag_2Te on the VI/II boundary at 28·8 kbars and 332·5°C.

Silver sulphide

The phase diagram of Ag_2S to 40 kbar and 300°C is shown in Fig. 2. The III/II (Kracek's notation[6]) transition temperature increases linearly with pressure with a slope of 1·5 ±0·2°C/kbar. The initial slope estimated previously by Roy *et al.*[7] as ~ 4°C/kbar seems somewhat too high and might be open to question due to the very limited pressure range, viz. ~ 1·2 kbar, and the large hysteresis interval in their experiments. The hysteresis interval in our experiments was slight, ~ 1°C, up to the highest pressure attained. Above 12·3 kbars, 195°C the transition line lies on another straight line section with a different slope, viz. 3·1±0·2°C/kbar. The III/IV transition line determined by Bridgman[20] from 100° to 200°C is also shown in Fig. 2. The only break in the III/II trajectory that might indicate the occurrence

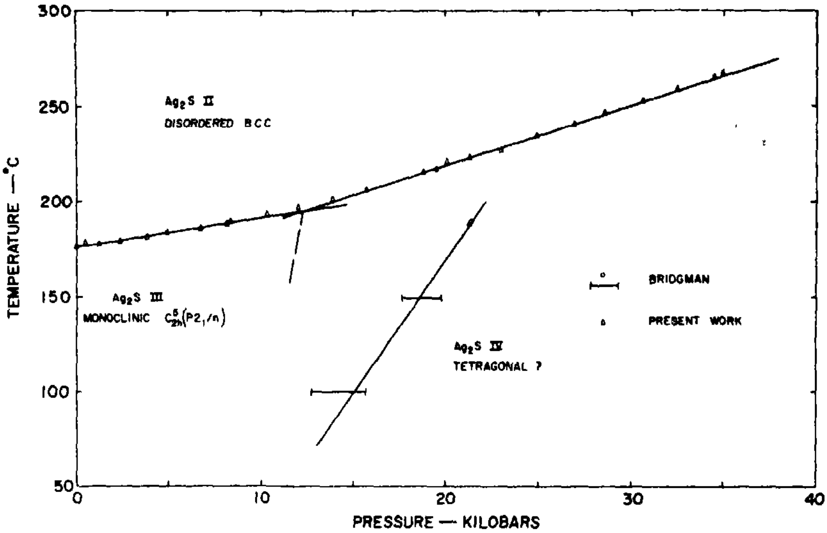

Fig. 2. Phase diagram of Ag_2S.

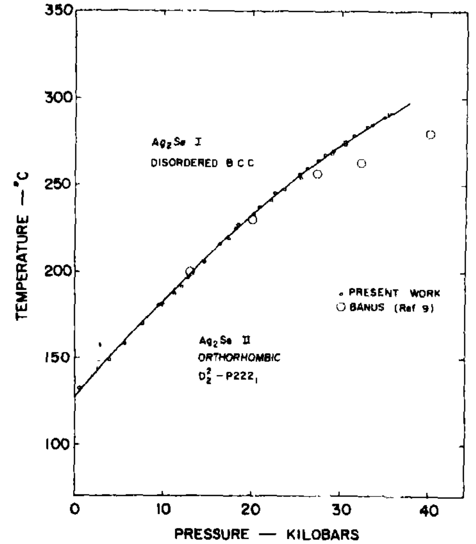

Fig. 3. Phase diagram of Ag_2Se to 300°C and 40 kbars (including the work of Banus).

of the II/III/IV triple point is the one at 12·3 kbar, 195°C. However, its location is not on the extrapolation of Bridgman's III/IV boundary. Unfortunately we did not have a sufficient amount of sample of high purity to repeat Bridgman's volumetric work.

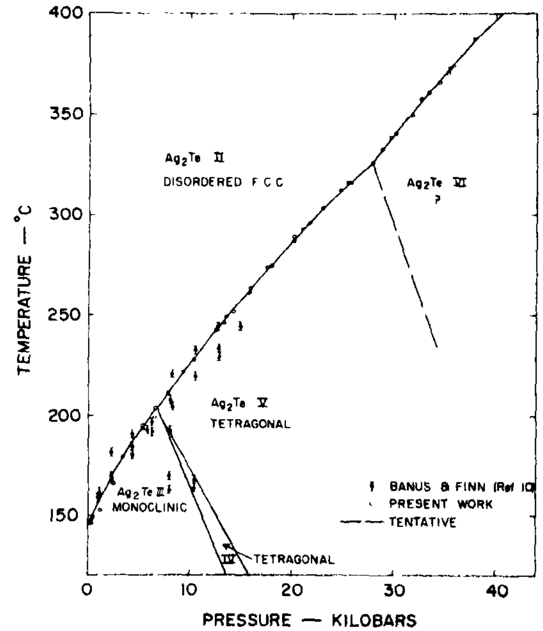

Fig. 4. Phase diagram to 400°C and 40 kbars of Ag_2Te (including the work by Banus and Finn).

Phase relations in the system silver–sulfur and the transitions in silver sulfide were investigated by Kracek[6] and reviewed by Frueh[21]. The temperature–composition phase diagram reveals that the III/II transi-

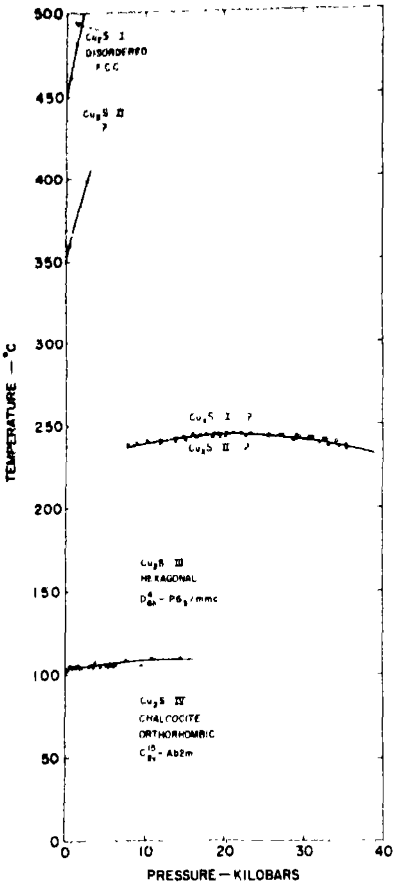

Fig. 5. Phase diagram of Cu_2S with the phase boundary Cu_xS included.

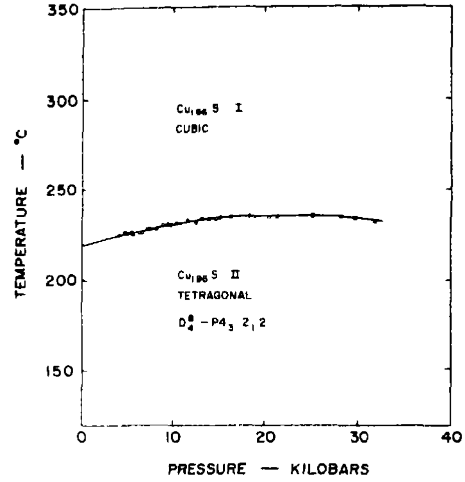

Fig. 6. The I/II phase boundary in $Cu_{1.96}S$.

tion temperature on the silver-rich side is slightly lower than that on the sulfur-rich side (176·3°±0·5°C as compared with 177·8°± 0·7°C). Wagner[22], from EMF measurements on galvanic cells containing solid Ag_2S, concluded that Ag_2S in equilibrium with metallic silver at 200°C contains 2×10^{-3} g atom Ag/mole Ag_2S excess silver whereas Ag_2S in equilibrium with sulfur has nearly the ideal stoichiometric composition. At 160°C the variability in stoichiometry if 3×10^{-5} g atom Ag/mole Ag_2S. He made a thermodynamic calculation to account for the 1·7°C difference between transition temperatures on the Ag-rich and S-rich side. Aside from this small difference the transition temperature does not vary further with excess silver or sulfur, and we consider it safe to have carried out the present experiments on Ag_2S enclosed in silver capsules. The II/I transition is much more sensitive to excess sulfur or silver[6]. We made several attempts to investigate the course of the II/I transition with pressure but encountered a vigorous endothermic sample-capsule reaction above 500°C. This was the only case that such a reaction was encountered, possibly a dissolution of silver in the Ag_2S sample. No such reactions were encountered in the other silver and cuprous chalcogenides at lower temperatures.

Silver selenide

The α/β transformation[8] in Ag_2Se had been studied previously by Roy *et al.*[7] and by Banus[9]. In our experiments we first searched for DTA signals around 130°C, corresponding to the α/β transition. At first no such signals could be obtained, but we found that if the sample was heated in situ to ~350°C for a period of several minutes, sharp DTA signals were obtained after the sample had been cooled and another search was made around 130°C. Such signals were then obtained repeatedly four to five times, gradually diminishing in size. Repeating such preheating procedure reproduced this behavior. No such preheating was necessary above ~ 6 kbar and repeated DTA signals with somewhat gradually increasing size were obtained to the highest pressure attained. Such preheating was also found necessary in the other chalcogenides studied here with the exception of Ag_2S, and is, in our opinion, connected with the non-stiochiometric nature of these compounds. It is possible that the phase transition occurs only over a certain range of deviation from stoichiometric composition and that preheating treatment was necessary in order to introduce a certain amount of excess cation defects. The Ag–Se composition phase diagram is not as well established as those of Ag–S[6] or Ag–Te [23, 21]. The fragmentary diagram given by Hansen and Anderko[5] is based only on some early data and we do not know of any more recent data. The dependence of the transition temperature, mechanism and kinetics on excess Ag or Se in Ag_2Se is not known.

The phase diagram of Ag_2Se to 300°C and 40 kbar is shown in Fig. 3 and includes also the data of Banus[9] for comparison. The agreement with Banus's results is good to 20 kbar. Above 20 kbar Banus's results fall some 10°–15°C below our results. The initial slope, dT/dp, of 6·02°C/kbar is lower than the value 7·2°C/kbar reported by Roy *et al.*[7] as in the case of Ag_2S. The agreement with Banus's data below 20 kbar shows that our preheating treatment did not change the Ag_2Se sample drastically. The mode of preparation of our sample obtained from a commercial source is not known to us. Banus's sample was grown from the melt and had, thus, received a preheating treatment. Differences in behavior (resistance jump at the transition) for samples cooled from 700°–900°C as compared to samples cooled from temperature slightly above the transition were reported by Baer *et al.*[24, 9]. Banus[9] also reported that the hysteresis interval between the transition temperatures on heating and on cooling was 15°–25°C whereas in our experiments it did not exceed 3°C.

Silver telluride

The phase diagram of Ag_2Te to 40 kbars and 400°C is shown in Fig. 4. It also contains recent results of Banus and Finn[10] that appeared after our experimental work was completed. The phase designation has been kept in accord with Frueh[21] and is also consistent with the labelling in the case of Ag_2S [6]. The high-pressure phases recently discovered by Banus and Finn[10] had to be relabelled IV and V (instead of II and III, respectively, as originally labelled by Banus and Finn[10]).

In our experiments the preheating treatment was similar to that given in the case of Ag_2Se, and, similarly, was unnecessary above ~ 6 kbars. Ag_2Te used by Banus and Finn was grown from the melt, and therefore had also received a 'preheating treatment'. The good agreement between the results of Banus and Finn and our data on the III/II boundary demonstrates, again as in the case of Ag_2Se, that the preheating treatment produced essentially a sample of excess silver in the range of deviation from stoichiometry that exhibits the III/II transition. The composition phase diagram of the binary system Ag–Te [23] shows clearly that the III/II transition exists on the silver-rich side at 145° ± 3°C, whereas on the silver-deficient side complicated behavior due to coexistence of $Ag_{5-x}Te_3$, Ag_2Te and a γ-phase was reported by Kracek and Ksanda[25]. The prehating treatment that we used thus ensured equilibrium of Ag_2Te with excess Ag, as is also apparent from our 1 bar value of 147° ± 1°C. The latter value compares favorably with that of Kracek *et al.* [23] and also with the recent value of 148° ± 1°C of Banus and Finn[10] where a sample of known carrier concentration was used. Hysteresis between heating and cooling in our experiments did not exceed 4°C below ~ 6 kbar. Above ~ 6 kbars the transition on cooling (II/III) took place some 20°C lower than on heating (III/II), yielding somewhat broader DTA signals. Banus and Finn[10] reported a triple point at 8 kbar, 200°C, the existence of which is, however, masked by the 10°–15°C scatter in their data on the f.c.c.-monoclinic boundary (II/III boundary in our notation). It can be inferred only from extrapolation of the III/IV or IV/V boundary. The possible slight break in the III/II transition line is not even obvious from our data, but the sudden increase in the hysteresis interval above 8 kbars may be of some indication. Above 30 kbars the DTA signal size was suddenly reduced to less than half of its previous size and the hysteresis interval decreased to about 12°C. Simultaneously, a small but definite upward break occurs on the V/II phase boundary, as is seen in Fig. 4, which is an indication of a new triple point and the appearance of a new high-pressure phase, Ag_2TeVI. The possible V/VI boundary is indicated in Fig. 4 by the dotted line. Unfortunately we did not have a sufficient amount of high purity Ag_2Te sample to perform volumetric work in order to detect the III/IV, IV/V and V/VI transitions by the piston-displacement method.

Cuprous sulfide

Phase behavior in the binary system copper–sulfur is more complex than in the silver chalcogenides discussed before. Djurle[26] studied phase relations in the Cu–S system by high temperature X-ray methods and found in samples prepared from the elements by sintering at temperatures of 320°C or 470°C the compounds Cu_2S, $Cu_{1\cdot96}S$ and $Cu_{1\cdot8}S$ (digenite). The three compounds undergo phase transitions[27]. A composition phase diagram of the binary system Cu–S was recently published by Rau[28] who argued in favor of the formula Cu_7S_4 rather than Cu_9S_5 ($Cu_{1\cdot8}S$) for digenite. Earlier data by Buerger[29] are open to question due to the mode of sample preparation in air[26]. Djurle[26] showed that in the presence of excess copper, samples quenched from 400°C produced only Cu_2S and free copper. Our samples, enclosed in copper capsules and given a preheating treatment at 380°C were, therefore, in the Cu_2S composition. The course of the IV/III transformation [30] with pressure is shown in Fig. 5. The transition temperature increases with pressure from its zero pressure value of 103°C with an initial slope, dT/dp, of 0·5°C/kbar. At about 10 kbars new DTA signals were obtained around 240°C and the new transition line (Fig. 5) could be followed with ease, and without any necessity for preheating, to 40 kbars. At the same time, apart from some metastable extension beyond 10 kbars, the signals corresponding to the original IV/III transition disappeared. On releasing pressure this behavior is reversed and at around 8 kbars the upper transition disappeared and DTA signals corresponding to the lower IV/III transition were regained. The upper transition line varies only slightly with pressure and passes through a shallow maximum around 245°C and 21 kbar, the occurrence of which is probably connected with the disordered structure of the III phase (this will be discussed further). Serebrianaia[31] recently reported that $Cu_{1\cdot96}S$ could be prepared by heating Cu_2S to 900°C. We therefore heated Cu_2S to ~850°C and after cooling we searched for the transition around 103°C with negative results. New, very sharp, DTA signals were, on the other hand, obtained around 220°–230° (see Fig. 6). This boundary is exactly parallel to the upper transition line in Fig. 5, but some ~10°C lower. We therefore think that the upper transition line in Fig. 5 corresponds to Cu_9S_5 (or Cu_7S_4) reversibly formed by a disproportionation reaction from Cu_2S. Both Cu_9S_5 samples formed in situ in the presence of Cu and Cu_2S are probably not very pure, and hence the 10°C difference in transition temperatures.

The temperature-hysteresis interval in the case of Cu_2S IV/III was varied and ranged between 1°–12°C. However, in the case of Cu_xS II/I it varied between 0°–2°C.

The Cu_2S III/II and II/I transitions were reported to exist at room pressure by Serebrianaia[31] and Jensen[35]. The high pressure points shown were not reproducible and were the only points ever obtained in this region.

Cuprous selenide

The transition in Cu_2Se was reported[32, 33] at 110°C. *In our experiments it occurred* at 135°C at 1 bar. This is probably due to the high purity of the sample. Preheating in our experiments as required only once for a given sample. Sharp and strong DTA signals were consistently and repeatedly obtained until a pressure of 30 kbars was reached, where the signal disappeared completely. This behavior was reproducible from run to run and was reversible, as the DTA signals were regained upon decompression. We made a thorough search at higher pressure to 41 kbars and found no indication of any further transitions. We postulate that at ~ 30 kbars the transition line intersects a sluggish high pressure phase transition. Unfortunately the lack of a sufficient amount of sample of high purity prevented us from searching for this transition by the piston-displacement method. The course of the phase transition in Cu_2Se with pressure is shown in Fig. 7. Unlike the other chalcogenides reported here the transition temperature falls with pressure with an initial slope, dT/dp, of $-0{\cdot}6$°C/kbar, and thus implies a negative volume change on passing from the low-temperature tetragonal phase to the high-temperature f.c.c. phase. Crystallographic data[2], on the contrary, yield a *positive value for the volume change for* Cu_2Se of exact stoichiometry. However, it is impossible to prepare Cu_2Se of stoichiometric composition even by using refined methods[2]. The cell constant of the cubic phase shrinks considerably with copper deficency[2], and in addition there is some disagreement in the literature as to the exact values of the cell constants of the tetragonal phase[2]. An analogous case of Cu_2S which transforms at 10 kbars by a disproportionation reaction into a copper-deficient phase $Cu_{1\cdot 96}S$ has been suggested before. Again, at pressures above 24 kbars the transition line in $Cu_{1\cdot 8}S$ has a negative slope (see Fig. 5 and Fig. 6). An analogous maximum in a solid-solid transition involving a defect structure high temperature b.c.c. phase has been found before in CuCl[34].

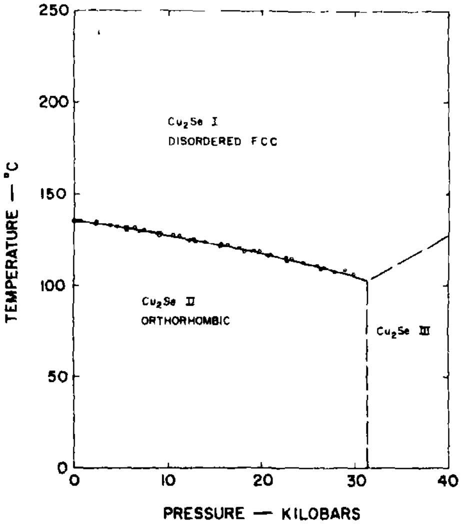

Fig. 7. The phase diagram of Cu_2Se.

The experimentally determined transition points were fitted to cubic equations for interpolation purposes by means of the least mean square method. The results are presented in Table 1.

Table 1. *Phase behavior of* Ag_2S, Ag_2Se, Ag_2Te, Cu_2Se *and* Cu_2S

Transition line	Fit (°C)	Standard deviation (°C)
Ag_2Te II/III	$t = 143{\cdot}7 + 11{\cdot}48P - 0{\cdot}389P^2$	2·1
Ag_2Te II/V	$t = 204 + 7{\cdot}35P - 0{\cdot}069P^2$	0·8
Ag_2Te II/VI	$t = 326{\cdot}6 + 6{\cdot}51P - 0{\cdot}053P^2$	0·8
Ag_2Se I/II	$t = 127 + 6{\cdot}02P - 0{\cdot}038P^2$	1·1
Cu_2Se I/II	$t = 135 - 0{\cdot}624P - 0{\cdot}012P^2$	0·8
Cu_2S II/III	$t = 103{\cdot}5 + 0{\cdot}504P - 0{\cdot}005P^2$	1·2
Cu_xS I/II	$t = 238{\cdot}8 + 0{\cdot}834P - 0{\cdot}031P^2$	1·2
$Cu_{1\cdot 96}S$ I/II	$t = 219 + 1{\cdot}56P - 0{\cdot}036P^2$	0·6
Ag_2S II/III	$t = 176{\cdot}7 + 1{\cdot}57P$	0·8
Ag_2S II/IV	$t = 195 + 3{\cdot}13P$	0·7

Acknowledgements—The authors would like to thank Mrs. Martha C. Pistorius for writing the computer programs used in fitting the data, and Drs. C. W. F. T. Pistorius and R. J. Murphy for valuable discussions. Mr. J. Erasmus and his staff and Mr. G. O'Grady and his staff kept the equipment in good repair, and were responsible for the manufacture of the furnace parts. Calculations were carried out on the IBM System 360/65H of the National Research Institute for Mathematical Sciences.

REFERENCES

1. BUSCH G. and JUNOD P., *Helv. Phys. Acta* **31**, 567 (1958).
2. JUNOD P., *Helv. Phys. Acta* **32**, 567 (1959) contains an extensive list of references to earlier work.
3. Interpretation of the electrical properties of Ag_2S and Ag_2Se is given in: JUNOD P., *Helv. Phys. Acta* **32**, 601 (1959).
4. Crystallographic data and lattice spacings of the various phases of the Ag and Cu chalcogenides are collected in: PEARSON W B., *A Handbook of Lattice Spacings and Structures of Metals and Alloys*, Vol. 1 and especially Vol. 2 Pergamon Press, Oxford. (1958 and 1967).
5. Composition phase diagrams and crystal structures are collected in: HANSEN M. and ANDERKO K., *Constitution of Binary Alloys*. McGraw-Hill, New York (1958).
6. KRACEK F. C., *Trans. Am. geophys. Un.* **27**, 364 (1946).
7. ROY R., MAJUMDAR A. J. and HULBE C. W., *Econ. Geol.* **54**, 1278 (1959)
8. Phase designation of α for the low temperature phase is in accord with the practice in PEARSON [4, Vol. I, p. 1] and HANSEN and ANDERKO[5]. β is the phase stable above 180°C in Ag_2S and above 130°C in Ag_2Se. The corresponding phases in Ag_2S and Ag_2Te are labelled III and II respectively by KRACEK[6] and in PEARSON, Vol. 2.
9. BANUS M. D., *Science* **47**, 732 (1965).
10. BANUS M. D. and FINN M. C., *J. electrochem. Soc.* **116**, 91 (1969).
11. KENNEDY G. C. and NEWTON R C., In *Solids Under Pressure* (Edited by W. Paul and D M. Warschauer). McGraw-Hill, New York (1963).
12. KENNEDY G. C. and LAMORI P. N., *Progress in Very High Pressure Research* (Edited by F. P. Bundy, W. R. Hibbard and H. M. Strong). Wiley, New York (1961).
13. COHEN L. H., KLEMENT W. and KENNEDY G. C., *J. Phys. Chem. Solids* **27**, 179 (1966).
14. JAYARAMAN A., KLEMENT W., NEWTON R. C. and KENNEDY G. C., *J. Phys. Chem. Solids* **27**, 7 (1963).
15. HANNEMAN R. E. and STRONG H. M., *J. appl. Phys.* **36**, 523 (1965); *ibid.* **37**, 612 (1966).
16. PISTORIUS C. W. F. T., *J. Phys. Chem. Solids* **26**, 1543 (1965).
17. RAPOPORT E., *J. chem. Phys.* **45**, 2721 (1966).
18. PISTORIUS C. W. F. T., RAPOPORT E. and CLARK J. B., *Rev. scient. Instrum.* **38**, 1741 (1967).
19. RAPOPORT E., *J. chem. Phys.* **46**, 3279 (1967); PISTORIUS C. W. F. T., *J. Phys. Chem. Solids* **28**, 1811 (1967).
20. BRIDGMAN P. W., *Proc. Am. Acad. Arts Sci.* **72**, 45 (1937).
21. FRUEH A. J., *Am. Miner.* **46**, 654 (1961).
22. WAGNER C., *J. chem. Phys.* **21**, 1819 (1953).
23. KRACEK F. C., KSANDA C. J. and CABRI L. J., *Am. Miner.* **51**, 14 (1966).
24. BAER Y., BUSCH G., FRÖHLICK C and STEIGMEIER E., *Z. Naturf.* **17a**, 886 (1962).
25. See [23], p. 21, Table 2 and Fig. 2 and the reinterpretation by CABRI on p. 21.
26. DJURLE S., *Acta chem. Scand.* **12**, 1415 (1958).
27 See Table 1 in [26] for transition temperatures and crystal systems, also [4], vol. 2.
28. RAU H., *J. Phys. Chem. Solids* **28**, 903 (1967).
29. BUERGER N. W., *Am. Miner.* **27**, 712 (1942), *Econ. Geol.* **36**, 19 (1941).
30. We use the notation according to PEARSON[4, Vol. 2]; see also DJURLE[26]. The phases labelled α, β, γ by RAU[28] are I, II, III respectively. Thus a uniform notation is used for Ag_2S, Ag_2Te and Cu_2S.
31. SEREBRIANAIA N. R., *Geokhimiia* **7**, 866 (1966).
32. KELLEY K. K., Contribution to the data on theoretical metallurgy. *Bureau of Mines Bull.* No. 584 (1960).
33 GATTOW G. and SCHNEIDER A., *Z. anorg Chem.* **286**, 296 (1956).
34. RAPOPORT E. and PISTORIUS C. W. F. T., *Phys. Rev.* **172**, 838 (1968).
35. JENSEN E., *Avh. Norske Vidensk Acad. Oslo, I. Mat. Naturv. Kl* No. 6 (1947).

J. Phys. Chem. Solids Pergamon Press 1970. Vol. 31, pp. 255–264. Printed in Great Britain.

DYNAMICAL SPIN CORRELATIONS IN THE B-P-W CLUSTER MODEL AS APPLIED TO INELASTIC NEUTRON SCATTERING*

T. H. KWON and H. A. GERSCH
School of Physics, Georgia Institute of Technology, Atlanta, Georgia 30332, U.S.A.

(*Received* 8 *April* 1969; *in revised form* 12 *June* 1969)

Abstract—The magnetic neutron scattering function for a Heisenberg antiferromagnet with spin $\frac{1}{2}$ per atom in a bcc lattice at finite temperature is evaluated from first principles in the Bethe–Peierls–Weiss cluster model, and the temperature dependence of the frequencies and half widths of spin excitations is deduced from the scattering function for the temperature range $0 \leq T/T_N \leq 1{\cdot}5$. The results show the essential features observed in recent experiments.

1. INTRODUCTION

THE INELASTIC scattering of neutrons from exchange coupled spin systems has revealed the existence of well defined spin-wave-like peaks in the neighborhood of the transition temperature for numerous substances. Murthy *et al.*[1], for instance, reported such observations in MnO, Turberfield *et al.*[2] in MnF_2, Lowde and Windsor [3] in Ni, Nathans *et al.*[4] in $RbMnF_3$, and Martel *et al.*[5] in CoF_2. The essential features of these observations can be summarized as follows. The neutron spectra in the neighborhood of the transition temperature are clearly resolved into three components—an elastic peak at the center with absorption and excitation peaks on both sides. The position of the elastic peaks is, of course, independent of temperature, although their intensities vary with both temperature and momentum transfer. At low temperatures the absorption peaks are not visible because the spin wave population obeys Bose–Einstein statistics, but the excitation peaks are sharply peaked and clearly visible. As the temperature approaches T_N, both peaks become visible and their positions shift toward lower frequencies with increasing half widths. Past T_N both peaks are still visible in some cases but with markedly reduced tendencies in frequency shift and half width increase. An interesting feature in these is that even above the transition temperature quite well-defined peaks are observed for large momentum transfer in some of the substances.

The purpose of this paper is to show these features of experimental observations result from a model calculation of magnetic neutron cross section. In particular, the magnetic neutron scattering function, which is known to be proportional to the cross section[6], is evaluated from first principles in the Bethe–Peierls–Weiss cluster model of a Heisenberg antiferromagnet at finite temperatures, and the temperature dependence of spin excitations and half widths is examined in the temperature range $0 \leq T/T_N \leq 1{\cdot}5$. The results shown in this paper are informative in that there is no working theory at present that gives an adequate prediction in temperature dependence of magnon energies and half widths in the intermediate temperature range $(0{\cdot}5 \leq T/T_N \leq 1{\cdot}5)$. The Dyson spin wave theory[7] is limited to very low temperatures, while Green's function theories either predict magnon energies proportional to sublattice magnetization with infinite lifetime[8], or have not yet been developed sufficiently to produce adequate quantitative results[9].

---

*Supported in part by the National Science Foundation.

Recently Loly and Doniach[10] presented a computer calculation of magnon energy and line width, but their calculations were still limited to temperatures below T_N. Furthermore, the theories that predict spin-wave modes above the transition temperature are either qualitative [11] or phenomenological [12] in that some analytic form with adjustable parameters is assumed for the scattering function, and very little is known about these theories from first principles. Consequently, a model study of the subject from first principles would serve an informative purpose in understanding the temperature variation of spin excitations below and above the transition temperature.

2. SCATTERING FUNCTION IN THE B–P–W CLUSTER MODEL

The neutron differential cross section for an isotropic Heisenberg sample can be described by the expression [6]

$$\frac{d^2\sigma}{d\Omega d\omega} = A(k_i, k_f)S(\mathbf{k}, \omega) \qquad (1)$$

where $A(k_i, k_f)$ is a known function of scattering parameters and $S(\mathbf{k}, \omega)$ is the scattering function related to the dynamical spin–spin correlation in the following way:

$$S(\mathbf{k}, \omega) = [2\pi s_0(s_0+1)]^{-1} \sum_n e^{i\mathbf{k}\cdot\mathbf{n}} \int_{-\infty}^{\infty} dt\, e^{-i\omega t} \langle \mathbf{S}_0(0)\cdot\mathbf{S}_n(t)\rangle. \qquad (2)$$

Here $\mathbf{k} = \mathbf{k}_f - \mathbf{k}_i$ and $\omega = E_f - E_i$ are the momentum and energy transfers from neutron to crystal with $\hbar = 1$, $\mathbf{S}_n(t)$ is the spin operator for the atom at lattice site n and at time t, s_0 is the spin value per atom, and the dynamical spin–spin correlation is defined as

$$\langle \mathbf{S}_0(0)\cdot\mathbf{S}_n(t)\rangle = Z^{-1} \sum_{ij} e^{-E_i/k_BT} \sum_\alpha \langle i|S_0^\alpha(0)|j\rangle\langle j|S_n^\alpha(t)|i\rangle \qquad (3)$$

where Z is the partition function, $\alpha = (x, y, z)$, i and j are the stationary states of the sample, and the time dependence is given through the Heisenberg picture, i.e.

$$S_n^\alpha(t) = e^{i\mathcal{H}t} S_n^\alpha(0) e^{-i\mathcal{H}t}. \qquad (4)$$

Substitution of (3) and (4) into (2) yields

$$S(\mathbf{k}, \omega) = [Zs_0(s_0+1)]^{-1} \sum_n e^{i\mathbf{k}\cdot\mathbf{n}} \sum_{ij} e^{-E_i/k_BT} \sum_\alpha \langle i|S_0^\alpha|j\rangle\langle j|S_n^\alpha|i\rangle\delta(\omega + E_i - E_j) \qquad (5)$$

where now the dependence on the energy transfer ω is shown explicitly in terms of delta function singularities.

To evaluate the scattering function from first principles, i.e. from (5), requires a specific model for the sample. In order to make calculations as simple as possible and still applicable to physical systems in the intermediate temperature range, the B–P–W cluster model of the Heisenberg system [13, 14] is chosen. Inasmuch as for large $\mathbf{k}$ values ($ka \gtrsim 1$) the scattering function is mostly determined by the degree of local order, the cluster model should be a reasonable approximation in this range of $\mathbf{k}$ values.

The Heisenberg exchange Hamiltonian for a cluster of $z+1$ atoms is usually written in the form [13, 14]

$$\mathcal{H} = -2J\mathbf{S}_0\cdot\mathbf{S}_1 - H_1S_1^z - H_0S_0^z \qquad (6)$$

where J is the exchange integral between nearest neighbor atoms, $\mathbf{S}_0$ is spin of the central atom, $\mathbf{S}_1$ the total spin of z atoms in the first shell, S_0^z and S_1^z are the z-components of the corresponding spins, the z-direction being defined by the applied field H_0, and H_1 denotes the sum of the applied field H_0 and the effective ordering field created by nearest neighbors of the first shell atoms outside the cluster. The fields H_0 and H_1 are expressed in units of $g\mu_B$, where g is the spin g-factor and μ_B is the Bohr magneton. For a ferromagnet J is positive, while for an antiferromagnet J is negative and $\mathbf{S}_0$ and $\mathbf{S}_1$ belong to opposite sublattices.

In the absence of an external applied field the Hamiltonian[6] can be divided into unperturbed and perturbed parts, i.e.

$$\mathscr{H} = \mathscr{H}^0 + \mathscr{H}^1 \tag{7}$$

where each term is given by

$$\mathscr{H}^0 = -2J\mathbf{S}_0\cdot\mathbf{S}_1 - H_1S^z \qquad \mathscr{H}^1 = H_1S_0^z$$

with $\mathbf{S} = \mathbf{S}_0 + \mathbf{S}_1$ representing the total spin of the cluster. Since the operators S_0^2, S_1^2, S^2 and S^z commute with the unperturbed Hamiltonian $\mathscr{H}^0$, $\mathscr{H}^0$ is diagonal in the representation characterized by $|s_0\,s_1\,s\,m\rangle$; i.e.

$$\mathscr{H}^0|s_0s_1sm\rangle = E^0(s_0s_1sm)|s_0s_1sm\rangle \tag{8}$$

with the eigenvalues and eigenfunctions specified by

$$\begin{aligned} E^0(s_0s_1sm) &= -J[s(s+1) - s_1(s_1+1) \\ &\qquad - s_0(s_0+1)] - H_1m \\ |s_0s_1sm\rangle &= \sum_{m_1m_0} |s_0s_1m_0m_1\rangle\langle s_0s_1m_0m_1|s_0s_1sm\rangle. \end{aligned} \tag{9}$$

Here the eigenfunction is expanded in terms of individual spinors, and m_0, m_1, and m are the magnetic quantum numbers for the operators S_0^z, S_1^z, S^z respectively. The quantities $\langle s_0\,s_1\,m_0\,m_1|s_0\,s_1\,s\,m\rangle$ are the Clebsch–Gordan coefficients. For a given spin value s_0 of the central atom and the nearest neighbor coordination number z the various quantum numbers assume following values:

$$\begin{aligned} &s_1 = 0, 1, 2, \ldots, z\,s_0 \\ &s = |s_1 - s_0|, \ldots, s_1 + s_0 - 1, s_1 + s_0 \\ &m_0 = -s_0, \ldots, s_0 - 1, s_0 \\ &m = -s, \ldots, s - 1, s \\ &m_1 = m - m_0. \end{aligned} \tag{10}$$

The perturbing term $H_1S_0^z$ is small compared to the unperturbed Hamiltonian. This can be seen from the fact that near the transition temperature the ordering field H_1 is small, while at low temperatures the average value of S_0^z is $z+1$ times less than the average value of total cluster spin S^z. In view of this fact the perturbing term $H_1S_0^z$ is treated as a first order energy correction to the unperturbed system. The diagonal matrix elements of S_0^z are readily evaluated from the relation[15]

$$\begin{aligned} \langle s_0s_1sm|S_0^z|s_0s_1sm\rangle &= [s(s+1)]^{-1}\langle s_0s_1sm \\ &\times |S^z|s_0s_1sm\rangle\langle s_0s_1sm|\mathbf{S}_0\cdot\mathbf{S}|s_0s_1sm\rangle, \end{aligned}$$

consequently

$$\begin{aligned} &H_1\langle s_0s_1sm|S_0^z|s_0s_1sm\rangle = [2s(s+1)]^{-1} \\ &[s(s+1) + s_0(s_0+1) - s_1(s_1+1)]mH_1. \end{aligned} \tag{11}$$

It still remains to evaluate the effective ordering field H_1 and it is to be determined as a function of temperature by a suitable self-consistency condition. The self-consistency originally proposed by Weiss[13] was to require the average magnetic moment of the central atom and that of the shell atoms be equivalent, but it was pointed out by Anderson[16], later verified by Li[14] for an antiferromagnet, that Weiss' self-consistency leads to a catastrophic property of anti-transition point at low temperature. It was further pointed out by Strieb *et al.*[17] and Radcliffe[18] that the apparent internal inconsistency of the phenomenological cluster methods is resolved when the effective field H_1 is evaluated by minimizing the free energy. The result of Radcliffe[18] for a bcc lattice turned out to be

$$H_1 = 2J(z-1)\langle S_0^z\rangle \tag{12}$$

which is just *P.* Weiss's molecular field approximation[19]. In the present calculation H_1 is evaluated after Radcliffe with an additional simplification of replacing the magnetization $\langle S_0^z\rangle$ by that of the molecular field approximation.*

---

*The actual numerical evaluation by Radcliffe showed only a marginal improvement over the molecular field approximation (see Table 1, Ref. [18]).

Now that the eigenvalues and eigenfunctions are obtained, it is possible to proceed to numerical evaluation of scattering function from (5). In the cluster model the equation (5) can be put into more workable form:

$$S(\mathbf{k},\omega) = [Zs_0(s_0+1)]^{-1}\sum_{ij} e^{-E_i/k_BT} \times [F_{ij}(0)+F_{ij}(\mathbf{k})]\delta(\omega+E_i-E_j) \quad (13)$$

with

$$F_{ij}(0) = |\langle i|S_0{}^z|j\rangle|^2+\tfrac{1}{2}\langle i|S_0{}^+|j\rangle\langle j|S_0{}^-|i\rangle +\tfrac{1}{2}\langle i|S_0{}^-|j\rangle\langle j|S_0{}^+|i\rangle \quad (14)$$

$$F_{ij}(\mathbf{k}) = [\langle i|S_0{}^z|j\rangle\langle j|S_1{}^z|i\rangle+\langle i|S_0{}^+|j\rangle \times \langle j|S_1{}^-|i\rangle]C(\mathbf{k})$$

where $C(\mathbf{k})$ represents the phase factor averaged over solid angle Ω; i.e.

$$C(\mathbf{k}) = \langle e^{i\mathbf{k}\cdot\mathbf{n}}\rangle_\Omega = \int d\Omega\, e^{i\mathbf{k}\cdot\mathbf{n}}\Big/\int d\Omega = \sin(ka)/(ka) \quad (15)$$

a being the average nearest neighbor distance. The partition function is explicitly

$$Z = \sum_i W(s_1)\, e^{-E_i/k_BT} \quad (16)$$

where $W(s_1)$ is the multiplicity of the s_1 quantum numbers obtainable from

$$W(s_1) = L(s_1)-L(s_1+1) \quad (17)$$

with $L(s_1)$ equal to the coefficient of X^{s_1} in the polynomial

$$(X^{s_1}+X^{s_1+1}+\cdots+X^{1-s_1}+X^{-s_1})^z. \quad (18)$$

The values of $W(s_1)$ used in this paper are listed in Table 1. For a bcc lattice with spin $\frac{3}{2}$ per atom, there are altogether 4^9 eigenstates $|s_0\, s_1\, s\, m\rangle$, each of which is constructed as a linear combination of four individual spin states, i.e.

$$\begin{aligned}|i\rangle = |s_0s_1sm\rangle &= c_1|s_0s_1m_0=\tfrac{3}{2}\, m_1=m-\tfrac{3}{2}\rangle \\ &+c_2|s_0s_1m_0=\tfrac{1}{2}\, m_1=m-\tfrac{1}{2}\rangle \\ &+c_3|s_0s_1m_0=-\tfrac{1}{2}\, m_1=m+\tfrac{1}{2}\rangle \\ &+c_4|s_0s_1m_0=-\tfrac{3}{2}\, m_1=m+\tfrac{3}{2}\rangle \qquad (19)\end{aligned}$$

where c's are the appropriate Clebsch–Gordan coefficients. The necessary matrix elements between these states are of the type:

$$\begin{aligned}&\langle s_0s_1m_0m_1|S_0{}^z|s_0s_1m_0m_1\rangle = m_0 \\ &\langle s_0s_1m_0+1m_1|S_0{}^+|s_0s_1m_0m_1\rangle = [(s_0-m_0)(s_0+m_0+1)]^{1/2} \\ &\langle s_0s_1m_0m_1|S_0{}^-|s_0s_1m_0+1m_1\rangle = [(s_0+m_0+1)(s_0-m_0)]^{1/2}; \quad (20)\end{aligned}$$

similarly for the $S_1{}^z$, $S_1{}^+$, $S_1{}^-$ operators.

Table 1. The degeneracy of shell quantum number for a bcc lattice with spin $\frac{3}{2}$ per atom

s_1	$W(s_1)$	s_1	$W(s_1)$
0	358	7	426
1	992	8	212
2	1398	9	88
3	1515	10	29
4	1377	11	7
5	1075	12	1
6	728		

3. RESULTS AND DISCUSSION

The scattering function as given by (13) has been evaluated for a bcc lattice of spin $\frac{3}{2}$ per atom with the nearest neighbor exchange integral set at $k_BT_N/J = -17{\cdot}04$[20]. A typical set of such numerical results is shown in Figs. 1(a–j) for a fixed value of momentum transfer $\mathbf{k}$ ($ka = 3\pi/2$)* as a function of energy transfer ω in the temperature range $0{\cdot}3 \leq T/T_N \leq 1{\cdot}5$. The solid vertical lines denote the delta function singularities in $S(\mathbf{k},\omega)$. The singularities at zero energy constitute elastic peaks labeled D, and heights of these elastic peaks are not shown in scale but rather in numbers at the tip of each line.

At low temperatures the absorption peaks

---

*Inasmuch as the cluster model is a local model, the results for small $\mathbf{k}$ values would not be as meaningful as those for large $\mathbf{k}$.

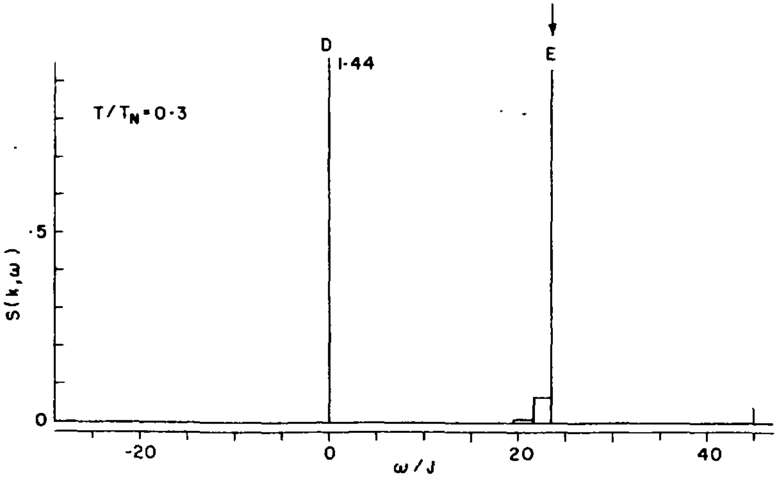

Fig. 1(a).

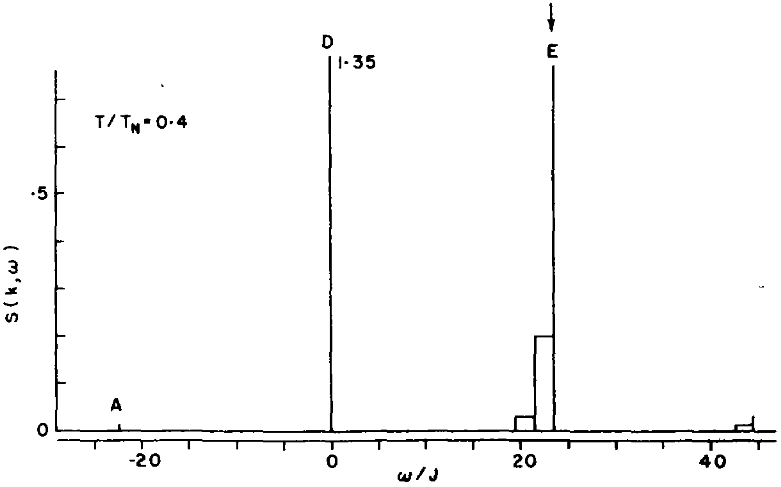

Fig. 1(b).

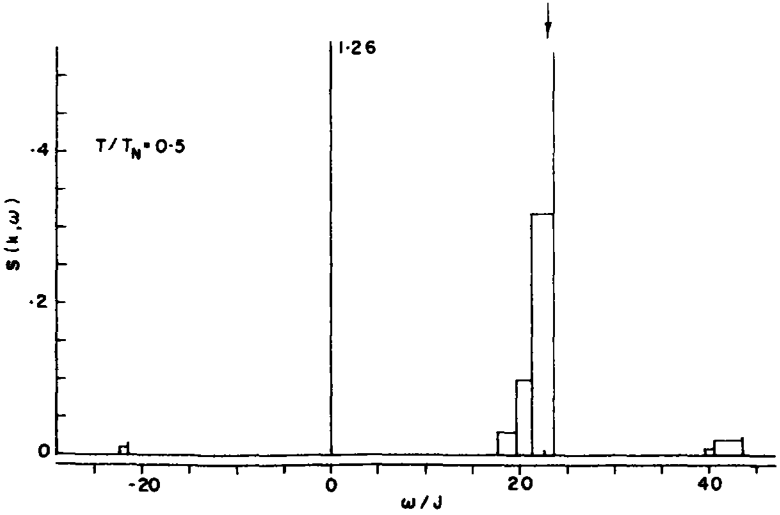

Fig. 1(c).

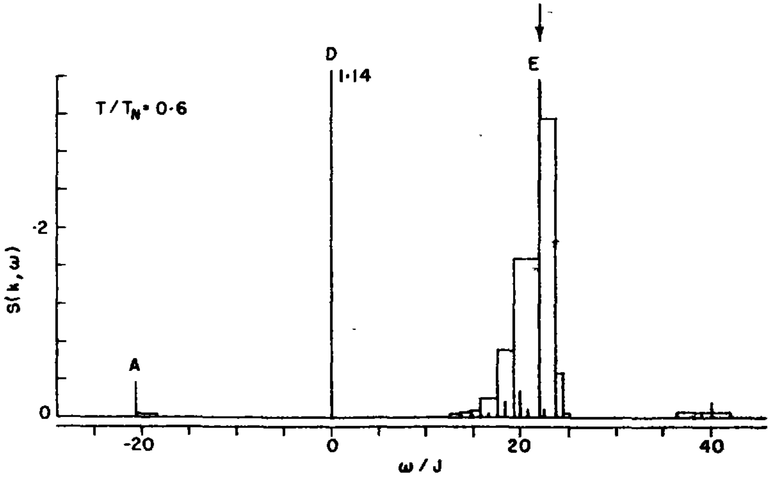

Fig. 1(d).

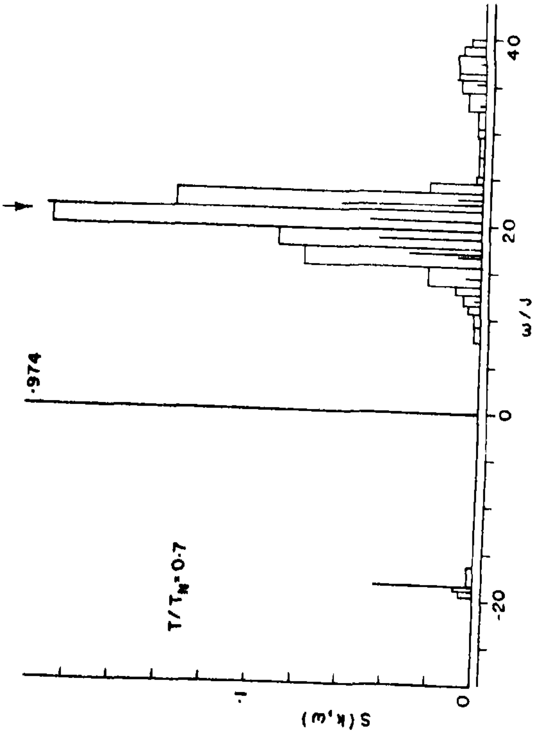

Fig. 1(e).

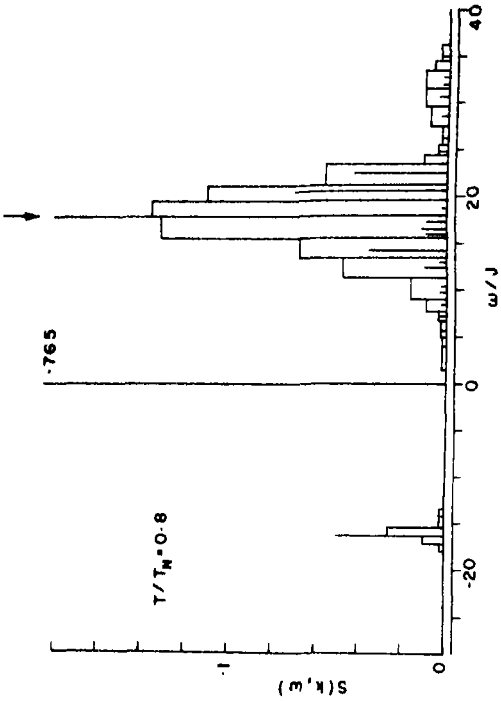

Fig. 1(f).

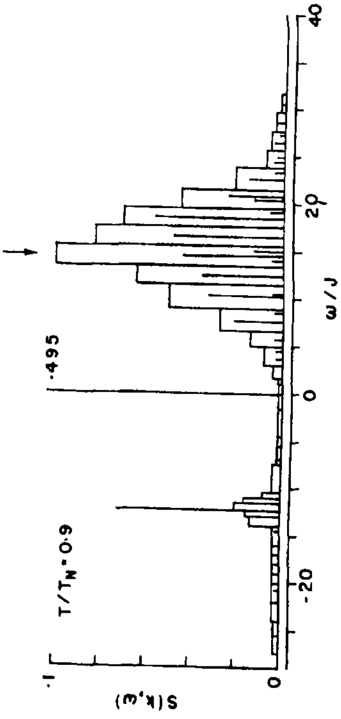

Fig. 1(g).

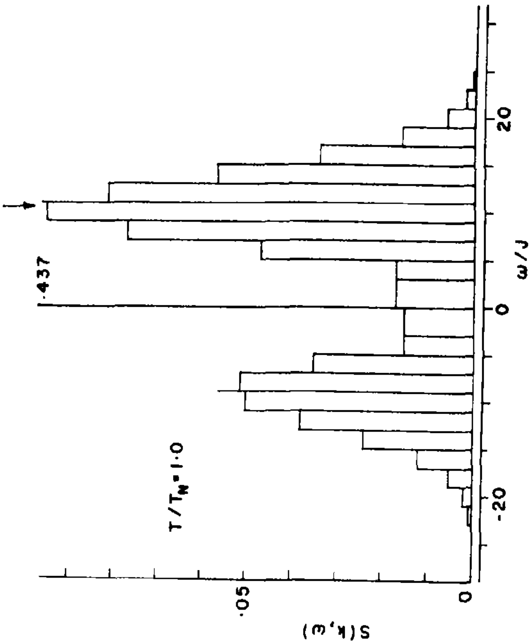

Fig. 1(h).

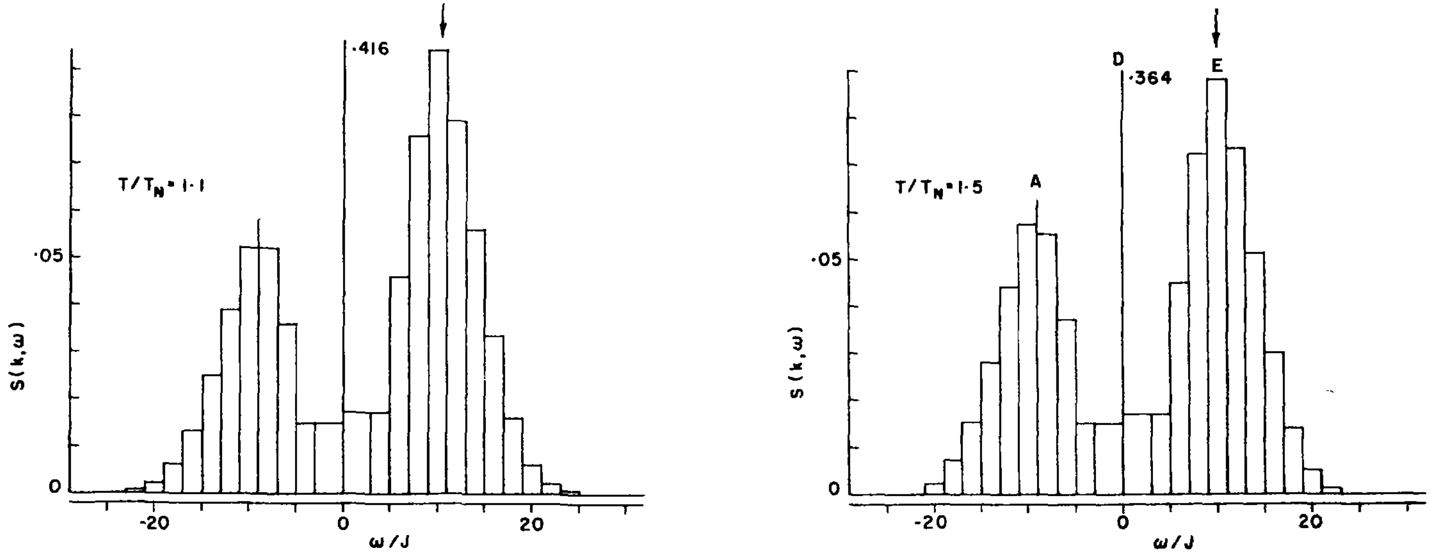

Fig. 1(i).

Fig. 1(j).

Fig. 1(a–j). The scattering function (13) for a bcc lattice of spin $\frac{3}{2}$ per atom with $k_B T_N/J = -17{\cdot}04$ is shown for $ka = 3\pi/2$ as a function of energy in the temperature range $0{\cdot}3 \leqslant T/T_N \leqslant 1{\cdot}5$.

A are hardly visible, while the excitation peaks *E* are seen to be sharply peaked. As the temperature approaches T_N, the absorption peaks become visible, while the excitation peaks become broadened and shifted to lower energies. Past T_N these inelastic peaks, *A* and *E*, remain clearly resolved, but their energies and half widths become nearly independent of temperature. In conformity with experimental practice[5] the excitation energies ω are determined as that position where the maxima of excitation peaks *E* occur as denoted by down pointed arrows* in Fig. 1, and the half widths $\Delta\omega$ are merely the half widths at half maxima of these excitation peaks *E*. The horizontal lines in Fig. 1 are drawn in somewhat arbitrarily between predominant vertical lines,† starting always from the tip of a lower vertical line and ending at the side or tip of a higher neighbor vertical line, to serve merely as visual aids in determining excitation maxima and half widths. The temperature dependence of the excitation energies and half widths thus determined is shown in Fig. 2. The energies ω remain nearly independent of temperature up to about $0{\cdot}5\,T_N$, decrease rapidly to about one half of their low temperature values by T_N, and past T_N vary little with temperature; while the half widths $\Delta\omega$ start with a small value at low temperatures, increase non-linearly as the temperature approaches T_N, and past T_N vary little with temperature.

The intensities of various peaks vary with temperature *T* and momentum transfer **k**. Shown in Fig. 3 are the intensities of $S(\mathbf{k}, \omega)$ for three typical values of **k** and four different values of *T* above T_N. For a given *T* the intensities in general (*A*, *D*, or *E*) increase with **k**, while for a given **k**, each kind of peaks varies differently with *T*. The elastic peaks *D* increase in intensity with increasing *T* for small **k** but decrease with increasing *T* for large **k**. For a fixed **k** the absorption peaks *A* increase in intensity with increasing *T*, while the excitation peaks *E* vary conversely to the absorption peaks. Not only do these general tendencies shown here for *T* above T_N hold for *T* below T_N, but they do so with added pronouncedness as can be seen from Fig. 1 for the case of $ka = 3\pi/2$.

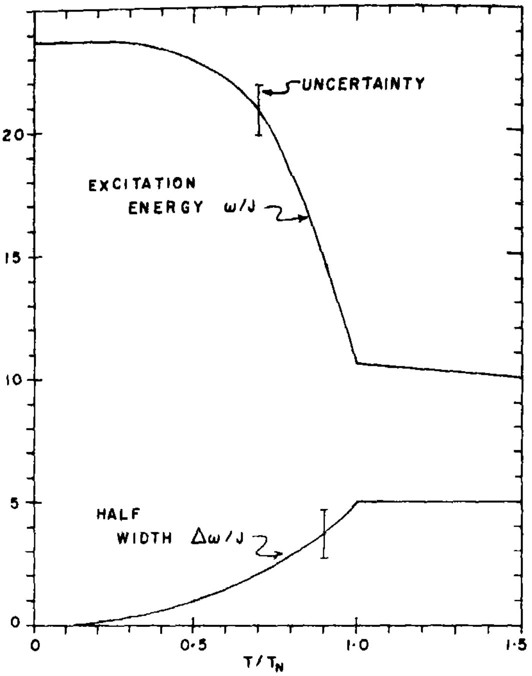

Fig. 2. The excitation energy ω and half width at half maxima $\Delta\omega$ are shown as a function of temperature for $ka = 3\pi/2$ and $k_B T_N/J = -17{\cdot}04$.

There exists no real spin ½ bcc isotropic Heisenberg magnet for which neutron data are available and thus it is not possible to make direct comparison with experiments; it is nevertheless informative to note that all or part of the features obtained from the present model calculation have been observed in each of the experiments mentioned at the outset

---

*The amount of uncertainty associated with the location of these arrows is indicated in Fig. 2.

†It should be noted from equation (9) that below T_N the term $H_1 m$ is finite and because of this fact the energy levels of a spin cluster split into finer increments enabling more transitions between these states. The shorter vertical lines in between predominant vertical lines in Fig. 1 below T_N are the results of these additional transitions. Inasmuch as these finer structures in $S(\mathbf{k}, \omega)$ are not likely to be observed in experiments, they are neglected in determining the line shape of the inelastic peak.

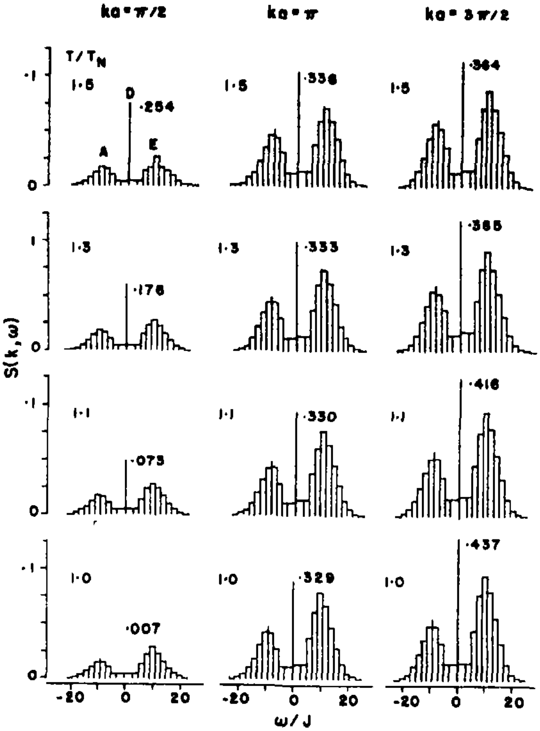

Fig. 3. The intensities of various peaks in $S(\mathbf{k}, \omega)$ are shown for three typical values of **k** and four different temperatures above T_N. The heights of elastic peaks D are shown in numbers at the tip of each line.

[1–5]. The inelastic neutron scattering data for $RbMnF_3$ in the immediate vicinity of transition temperature[4], for instance, show striking qualitative agreement with present results, but here again a quantitative comparison would not be very meaningful since $RbMnF_3$ has *sc* lattice with spin $\frac{5}{2}$.

The results for $T = \infty$ are not very much different from those at $T = 1{\cdot}5\,T_N$ shown in Fig. 3, except for the fact that now at $T = \infty$ the absorption and excitation peaks are symmetric with respect to $\omega = 0$ axis as they should be from the fact that $S(\mathbf{k}, \omega)$ is an even function in ω at $T = \infty$. Unlike the case of *sc* lattice with spin $\frac{1}{2}$[21] in which it was possible to smooth out the curve for $S(\mathbf{k}, \omega)$ and the smoothed version agreed well with the infinite temperature results derived from the method of moments—the Gaussian distribution by de Gennes[22] and its modification by Collins and Marshall[23], it does not seem possible in the present case of a bcc lattice with spin $\frac{3}{2}$ to follow the same procedures and comment on the agreement with the results of the method of moments. The persistence of structure in $S(\mathbf{k}, \omega)$ up to $T = \infty$ for the present case is most probably due to lack of diffusion in the cluster model, the diffusion process being a long-time phenomenon over a wide-range of lattice space. It should be noted, however, that a considerably larger number of frequencies resulted for the present case of bcc and spin $\frac{3}{2}$* than the previous case of *sc* and spin $\frac{1}{2}$, and in this sense the present work may be considered as an improvement over the earlier work[21].

REFERENCES

1. MURTHY N. S. S., VENKATARAMAW G., DENIG K. U., DASANNACHARYA B. A. and IYENGAR P. K., *Symp. on Inelastic Neutron Scattering*, p. 433. Bombay (1964).
2. TURBERFIELD K. C., OKAZAKI A. and STEVENSON R. W. H., *Proc. phys. Soc.* **85**, 743 (1965); TORRIE B. H., *Proc. phys. Soc.* **89**, 77 (1966).
3. LOWDE R D. and WINDSOR C. G., *Solid-St. Commun.* **6**, 189 (1968).
4. NATHANS R. and MENZINGER F., *J. appl. Phys.* **39**, 1237 (1968).
5. MARTEL P., COWLEY R. A. and STEVENSON R. W. H., *Can. J. Phys.* **46**, 1355 (1968); *J. appl. Phys.* **39**, 1116 (1968); *Phys. Rev. Lett.* **18**, 162 (1967).
6. VAN HOVE L., *Phys. Rev.* **95**, 1374 (1954).
7. DYSON F. J., *Phys. Rev.* **102**, 1217 (1956); *ibid* **102**, 1230 (1956).
8. TYABLIKOV S. L., *J. Ukrainian Math.* **11**, 287 (1959); CALLEN H. B., *Phys. Rev.* **130**, 890 (1963); COPELAND J. A. and GERSCH H. A., *Phys. Rev.* **143**, 236 (1966); LEE K. H. and LIU S. H., *Phys. Rev.* **159**, 390 (1967).
9. COOKE J. F. and GERSCH H. A., *Phys. Rev.* **153**, 641 (1967); MARSHALL W. and MURRAY G., *J appl. Phys.* **39**, 380 (1968); TAHIR KHELI R. A., *Phys. Rev.* **159**, 439 (1967).
10. LOLY P. D. and DONIACH S., *Phys. Rev.* **173**, 603 (1968).
11. MARSHALL W. *Conf. on Critical Phenomena*, Washington, p. 135 D.C. (1965). (NBS Misc. Pub. 273).

---

*A table showing the precise frequencies would be useful, but their numerousness below T_N makes it unpractical to list.

12. BENNETT H. S., *Phys. Rev.* **174**, 629 (1968); *ibid* **176**, 650 (1968).
13. WEISS P. R., *Phys. Rev.* **74**, 1493 (1948).
14. LI Y. Y., *Phys. Rev.* **84**, 721 (1951).
15. CONDON E. V. and SHORTLEY G. H., *The Theory of Atomic Spectra*, p. 64. Cambridge University Press, London (1935).
16. ANDERSON P. W., *Phys. Rev.* **80**, 922 (1950).
17. STRIEB B., CALLEN H. B. and HORWITZ G., *Phys. Rev.* **130**, 1798 (1963).
18. RADCLIFFE J. M., *Phys. Rev.* **165**, 635 (1968).
19. WEISS P., *J. Phys. Radium, Paris* **4**, 661 (1907).
20. BROWN H. A. and LUTTINGER J. M., *Phys. Rev.* **100**, 685 (1955).
21. KWON T. H. and GERSCH H. A., *Phys. Rev.* **167**, 458 (1968).
22. DE GENNES P. G., *J. Phys. Chem. Solids* **4**, 223 (1958).
23. COLLINS M F. and MARSHALL W., *Proc. phys. Soc.* **92**, 390 (1967).

J. Phys. Chem. Solids Pergamon Press 1970. Vol. 31, pp. 265–274. Printed in Great Britain.

ELECTRON ENERGY BANDS AND THE OPTICAL PROPERTIES OF POTASSIUM IODIDE AND RUBIDIUM IODIDE*

A. BARRY KUNZ†
Department of Physics, Lehigh University, Bethlehem, Penna. 18015, U.S.A.

(*Received* 12 *June* 1969)

Abstract – Using the relativistic mixed basis (M.B.) technique and the non-relativistic O.P.W. technique, electron energy bands are obtained for KI and RbI under a variety of conditions. It is argued that the previous calculations and interpretations offered for the KI optical absorption spectrum are not in agreement with recent experimental results. The present calculation produces results which eliminate the difficulties associated with previous theoretical models, and the results of this calculation are in good agreement with experiment. It is found that the L_1 and X_3 conduction levels play a substantial role in understanding the experimental results. It is also shown that a stringent 'muffin tin' potential is a poor approximation to the KI potential. The RbI results are similar to the KI results and a similar experimental interpretation is advanced.

1. INTRODUCTION

IN RECENT years the properties of KI have been the subject of many theoretical and experimental papers. In this present paper we use electron energy band theory to investigate certain optical and transport properties of KI and RbI.

The first attempt to obtain a band structure for KI was made by Phillips[1]. In this work it was assumed that the conduction band was free electron like. The valence band was modeled after that which Howland obtained for KCl[2]. The optical absorption spectrum of KI has four sharp peaks in the low energy region. These peaks at 77°K are at 0·430 Ry, 0·496 Ry, 0·507 Ry and 0·526 Ry[3]. Phillips interpreted the first two peaks as being due to exciton transitions from the spin-orbit split I^-5p valence band to the *s*-like conduction band at the point Γ in the first Brillouin zone. The second two peaks were interpreted as being due to exciton transitions from the upper two spin-orbit split I^-5p valence states to the *s*-like conduction band at *L*.

This model has been shown to be far too simple[4, 5]. Firstly, the free electron model places the *d*-like conduction bands above the *s*-like conduction bands, whereas by a more detailed calculation the two conduction bands are seen to overlap[4]. Secondly, the exciton transition at the point *L* would be at a point where the energy separation of the valence and conduction bands is a relative maximum and one need not expect to see sharp exciton lines in this case. Onodera found that at the point *X* the lowest lying state is a *d*-like X_3 state and the separation of valence and conduction band is a relative minimum just as it is at Γ and one may expect to find bound excitons here[4]. Onodera and Toyozawa[5] have developed a very elegant theory of these excitons. It is noted that Onodera identifies the first and fourth prominent absorption peaks as being due to the Γ exciton and the second and third peaks as being due to the *X* exciton.

There are several experimental difficulties with the model of Onodera. Firstly, by a very careful analysis of the absorption spectrum of pure NaI, KI and RbI crystals and mixed NaI–KI and KI–RbI crystals, Nakamura has shown that the first two peaks are due to transitions at the same point in the Brillouin

---

*Work supported in part by the U.S. Air Force Office of Scientific Research, Contract 1276-67.

†Present address: Department of Physics, University of Illinois, Urbana, Ill. 61803, U.S.A.

zone[6, 7]. The first three absorption peaks are seen to have a similar temperature dependence[8]. Previously, the author has shown that the temperature dependence is explained simply by changes in the band structure due to the change in average lattice parameter as the temperature is changed[9]. It seems unlikely that transitions to different symmetry conductions bands should have the same dependence upon lattice parameter. In the case of CsI, Onodera has found that the first few exciton transitions are to *s* and *d* like conduction bands[10]. Lynch and Brothers have measured the pressure dependence of the first few excitons in CsI and find that the sign of the change in energy with pressure of the first two excitons is opposite[11]. It seems likely that transitions to *s* and *d* bands in both KI and CsI would have a similar dependence on lattice parameter.

In this paper we present a calculation of the energy bands in KI which avoids the difficulties of the Phillips model[1] and the Onodera calculation[4]. It is shown that the greatest part of the difference in the calculation of Onodera and the present one is due to a very stringent 'muffin-tin' approximation to the KI potential which is made by Onodera. We have found a similar difficulty in applying a 'muffin-tin' potential to NaCl[12].

In Section 2, we describe the techniques used in this calculation and discuss the various approximations made. In Section 3 the results of the various calculations are presented for KI in its normal lattice and in a distorted lattice. Results for RbI are also presented here. In Section 4 we compute the effective mass of an electron in the KI conduction band and compute the corresponding polaron mass. The results are compared to experiment in Section 5.

2. DETAILS OF THE ENERGY BAND CALCULATION

The energy bands in KI have been computed using both the non-relativistic O.P.W. technique[13,14] and the relativistic M.B. (mixed basis) formalism[15]. In the case of RbI only the non-relativistic O.P.W. method is used. For KI we use a value of 13·236 Bohr units for our normal lattice constant. In the case of RbI we use the value of 13·8 Bohr units for the lattice constant. In the case of KI we also recompute the band structure using a lattice constant of 13·000 Bohr units in order to study the dependence of band structure on temperature or hydrostatic pressure.

For these calculations we chose our usual model of potential[14, 15]. This is a localized version of the Hartree–Fock potential for a valence electron located on a halogen ion. Localization is accomplished using the Slater exchange[16] and imposing a Latter tail[17] so that the potential contributions have the desired asymptotic behavior. By using a localized potential we may not use the eigenvalues of the resulting Schrödinger equation as being the energy needed to remove that electron from the crystal since Koopman's theorem is no longer valid[18]. Thus we might regard the potential chosen as a type of pseudo-potential where it is hoped that the errors introduced by neglecting Koopman's theorem compensate for the errors introduced by neglecting correlation effects. The ultimate test of such an approximation is the comparison with experiment. The normal lattice KI calculation was repeated using a 'mufin-tin' potential formed from the previously described potential using the values for sphere radii and height of the constant term in the potential given by Onodera *et al.*[4]. As will be seen, this 'muffin-tin' potential causes considerable distortion of the band structure.

It is useful at this time to define the types of calculations used. The one electron crystal hamiltonian is given as

$$H = \frac{p^2}{2m} + V(\mathbf{r}) + H_m + H_d + H_{S-O}. \quad (1)$$

In equation (1) p is the momentum of an electron, m is the electron mass, $V(\mathbf{r})$ is the lattice potential, H_m is the relativistic variation of mass with velocity term, H_d is the Darwin or non-physical term and H_{s-o} is the spin orbit operator. In the non-relativistic O.P.W. calculation H_m, H_d and H_{S-O} are set equal to zero. In the M.B. calculation H_{S-O} is included using degenerate state perturbation theory [19].

The states which are included as core states are the K$^+$, $1s$, $2s$, $2p$, $3s$, $3p$, the Rb$^+$ $1s$, $2s$, $2p$, $3s$, $3p$, $3d$, $4s$, $4p$, and the I$^-$ $1s$, $2s$, $2p$, $3s$, $3p$, $3d$, $4s$, $4p$, $4d$. In the case of the O.P.W. calculation the one electron wave function is given as

$$\psi_n^{\alpha\gamma}(k,r) = \sum_m b_{nm}^{\alpha\gamma}(\mathbf{k})\Big[S_{mq}^{\alpha\gamma}(\mathbf{k},\mathbf{r}) - \sum_{m'} \Phi_{m'}^{\alpha\gamma}(\mathbf{k},\mathbf{r}) \Big\langle \Phi_{m'}^{\alpha\gamma} \Big| S_{mq}^{\alpha\gamma}(\mathbf{k},\mathbf{r}) \Big\rangle\Big] \tag{2}$$

and for the M.B. calculation we find

$$\psi_n^{\alpha\gamma}(\mathbf{k},\mathbf{r}) = \sum_{m=1}^{M} a_{mn}^{\alpha\gamma}(\mathbf{k})\Phi_m^{\alpha\gamma}(\mathbf{k},\mathbf{r}) + \sum_{m'} b_{m'n}^{\alpha\gamma}(\mathbf{k}) S_{m'q}^{\alpha\gamma}(\mathbf{k},\mathbf{r}). \tag{3}$$

In equations (2) and (3) $\psi_n^{\alpha\gamma}$ is the nth eigenstate which transforms according to the αth row of the γth irreducible representation of the point group of the wave vector **k**. The Φ's are properly symmetrized combinations of Bloch sums formed from the core orbitals. The S's are properly symmetrized combinations of plane waves which have a common kinetic energy. The a's and b's are variational parameters and are determined by simultaneously diagonalizing the overlap and hamiltonian matrix formed using the plane waves and the core orbitals or the orthogonalized plane waves as an expansion basis. In this calculation about 400 plane waves are used and the convergence of the energy levels is estimated to be better than 0·001 Ry.

3. RESULTS OF THE ENERGY BAND CALCULATIONS

The electronic energy levels of KI were evaluated for the normal lattice constant at ten points in the first Brillouin zone by the M.B. method. These points are Γ, X, L, K, the midpoint of Λ, three equally spaced points along Δ and two points along Σ. The X-ray energy levels obtained from this calculation are given in Table 1. In Table 2 the energies of selected points of high symmetry for the valence and conduction band are given. Spin-orbit effects in the conduction band are neglected due to their small size[4]. The energy bands are shown in Fig. 1.

It is seen that spin-orbit effects split the predominantly $5p$ I$^-$ valence band into two non-overlapping bands. At the center of the zone the splitting is 0·083 Ry. Neglecting

Table 1. The X-ray levels for the KI *crystal are given in column two for the normal lattice parameter* (a = 13·236 *Bohr units) and for a lattice parameter of* 13·000 *Bohr units in column three. In column one the atomic state of origin for the X-ray levels is given. In column four the levels obtained for the normal lattice parameter using a 'muffin tin' potential are given. Results are in Rydbergs*

One	Two	Three	Four
I^-1s	−2433·	−2433·	−2433·
I^-2s	−379·6	−379·6	−379·6
I$^-2p, j = \frac{1}{2}$	−359·6	−359·6	−359·6
I$^-2p, j = \frac{3}{2}$	−339·8	−339·8	−339·8
I^-3s	−77·62	−77·64	−77·62
I$^-3p, j = \frac{1}{2}$	−69·02	−69·03	−69·02
I$^-3p, j = \frac{3}{2}$	−65·24	−65·25	−65·24
I$^-3d, j = \frac{3}{2}$	−50·51	−50·52	−50·51
I$^-3d, j = \frac{5}{2}$	−49·61	−49·62	−49·61
I^-4s	−14·02	−14·04	−14·02
I$^-4p, j = \frac{1}{2}$	−10·87	−10·89	−10·87
I$^-4p, j = \frac{3}{2}$	−10·13	−10·15	−10·13
I$^-4d, j = \frac{3}{2}$	−4·603	−4·612	−4·603
I$^-4d, j = \frac{5}{2}$	−4·468	−4·476	−4·468
K^+1s	−236·7	−236·7	236·7
K^+2s	−27·36	−27·35	−27·36
K$^+2p, j = \frac{1}{2}$	−22·27	−22·25	−22·27
K$^+2p, j = \frac{3}{2}$	−22·05	−22·03	−22·05
K^+3s	−2·962	−2·952	−2·962
K$^+3p\,j = \frac{1}{2}$	−1·731	−1·722	−1·731
K$^+3p, j = \frac{3}{2}$	−1·710	−1·701	−1·710

Table 2. The energies of points of high symmetry in the first Brillouin zone of the KI *crystal are given. Results are presented for the valence and conduction bands. In column one the symmetry of the state is given using the notation of* [24]. *In the second column the results obtained using the relativistic mixed basis method and the model potential described in* [14, 15] *are given. In the third column results obtained using the relativistic mixed basis method and the 'muffin tin' potential described in the text are given. In column four, non-relativistic O.P.W. results are given and in column five, results for* KI *obtained by Onodera* et al.[4] *using a 'muffin tin' potential are given. For the results of columns two to five the lattice parameter is* 13·236 *Bohr radii. In column six, results are presented using a lattice parameter of* 13·000 *Bohr units and the same method as was used for the results of column two. Spin-orbit effects are neglected for the conduction band. All energies are in Rydbergs*

One	Two	Three	Four	Five	Six
		$5sI^-$ valence band			
Γ_1	−1·525	−1·510	−1·369	−1·47	−1·536
X_1	−1·514	−1·503	−1·357	—	−1·524
L_1	−1·519	−1·506	−1·360	—	−1·529
		$5pI$ valence band			
$\Gamma_8^-(\Gamma_{15})$	−0·675	−0·663	−0·659	−0·598	−0·699
Γ_6^-	−0·758	−0·744		−0·691	−0·793
$X_7^-(X_5')$	−0·707	−0·673	−0·678	−0·615	−0·715
$X_6^-(X_4')$	−0·727	−0·689	−0·719	−0·631	−0·737
X_6^-	−0·805	−0·756		−0·710	−0·815
$L_4^-, L_5^-(L_3')$	−0·703	−0·660	−0·671	−0·619	−0·711
$L_6^-\ (L_2')$	−0·731	−0·688	−0·735	−0·639	−0·741
L_6^-	−0·809	−0·764		−0·718	−0·819
		Lower conduction bands			
Γ_1	−0·269	−0·080	−0·236	−0·144	−0·259
Γ_{25}'	0·012	0·160	0·013	−0·042	0·015
Γ_{12}	0·112	0·159	0·115	−0·057	0·115
X_1	−0·058	0·019	−0·048	−0·063	−0·049
X_3	−0·166	0·102	−0·164	−0·097	−0·174
X_5'	0·269	0·462	0·280	0·406	0·295
X_4'	0·009	0·263	0·029	0·225	0·028
X_2	0·219	0·232	0·223	−0·022	0·225
L_1	−0·206	0·026	−0·194	0·005	−0·205
L_3	−0·036	0·061	−0·033	0·020	−0·044
L_2'	−0·009	0·147	0·008	0·027	0·009
L_3	0·155	0·266	0·157	0·067	0·147

spin-orbit splitting the valence band is 0·076 Ry wide. The width of the spin-orbit split valence band is 0·134 Ry. It is noted that using the present I^- potential, the author obtains a value of 0·066 Ry for the spin-orbit splitting of the free ion I^- $5p$ state. The experimental value is 0·065 Ry and the agreement is excellent.

It is found that the band gap is at Γ and is from a p-like Γ_8^- state to the s-like Γ_1 state, and has a value of 0·406 Ry. It is noted that there are other low lying conduction band minima at the points L and X. The minimum at X involves the d-like state X_3. In general, it is noted that there is very poor agreement between this calculation and that of Onodera *et al.*[4] with respect to the details of the conduction band. The most obvious differences are that the order of the d-like states at Γ (Γ_{12} and $\Gamma_{25'}$) are reversed in this calculation from those given by Onodera. It is observed that the order of the d-states obtained here is the same as this author and other authors have obtained for other alkali halides[14,15,20,23].

There are two things one can do to try to understand the differences between the present calculation and that of Onodera *et al.* [4]. Firstly, the energy bands were recomputed at Γ, X, L and the midpoint of Δ using the non-relativistic O.P.W. method. These results are presented in Table 2. It is seen that there is excellent correlation between the authors' results using the two methods. The chief quantitative differences may be attributed to relativistic effects. Certainly the differences between the relativistic and non-relativistic results are similar to those found by the author for NaI.

As a second test, the band structure of KI was computed making a 'muffin-tin' approximation to the author's potential. As a matter of convenience, the author used the values given by Onodera[4] for the 'muffin-tin' constants. The radius of the K^+ sphere was 3·275 Bohr, the radius of the I^- sphere was 3·343 Bohr and the potential outside the 'muffin-tin' spheres was −0·145 Ry. The

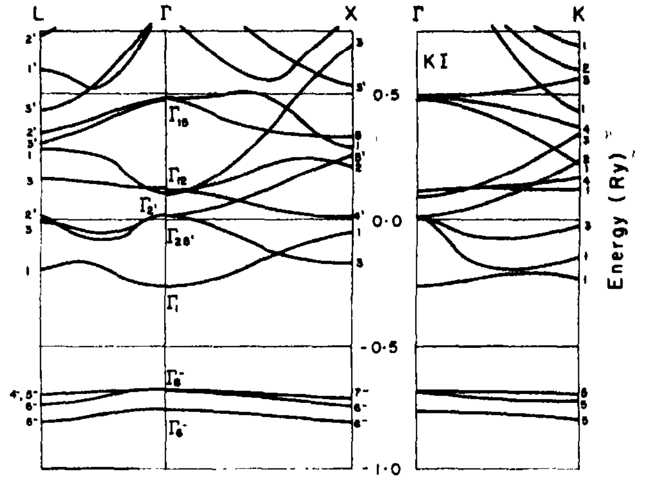

Fig 1. The electron energy bands of KI are shown along lines of high symmetry in the first Brillouin zone. The lattice parameter is 13·236 Bohr radii. The B.S.W. notation is used[24]. The calculation was performed by the relativistic M.B. method.

calculation using the 'muffin-tin' potential was made at Γ, X, L, K and is presented in Tables 1 and 2. It is seen that the results are greatly distorted by the use of a 'muffin-tin' potential. However, the results of Onodera are not obtained. The author believes this is due to remaining differences in the potential used in the two calculations. It does not seem likely that this is due to errors in the present calculation since the author, using his present program and a 'muffin-tin' potential, was able to reproduce the NaCl results obtained by Clark and Kliewer[23] who used a 'muffin-tin' potential and the A.P.W. method. In addition, the author does not believe this technique of including relativistic effects is at fault since the size of the relativistic effects obtained by the author agree well with those of Onodera.

Finally, using a lattice constant of 13·000 Bohr, the band structure of KI was evaluated at the points Γ, X, L, K using the usual potential. Qualitatively, these results are very similar to those obtained using the normal lattice constant. These results are presented in Tables 1, 2. These results will be discussed in Section 5.

In the case of RbI a non-relativistic O.P.W. calculation was performed at the points Γ, X, L and the midpoint of Δ. In a qualitative and quantitative sense the conduction bands of RbI are similar to those of KI. The results of the RbI calculation are presented in Table 3 and Fig. 2. Neglecting spin-orbit effects the valence band is found to be 0·063 Ry wide. The top of the valence band is at Γ_{15} and the bottom of the conduction band is at Γ_1. In these discussions the group theoretical notation of Bouckaert *et al.* is used[24]. The band gap is found to be 0·412 Ry.

It is seen that there is a low lying minimum in the conduction band at X_3. The L_1 conduction level is also very low lying and by comparison of the RbI results with those of KI, the author speculates that L_1 is also a minimum. In presenting all of the above results a halogen ion site is used as the origin.

4. EFFECTIVE MASS AND POLARON MASS OF CONDUCTION ELECTRONS

Using the results of the energy band calculation the author has been able to compute the bare effective mass of an electron in the Γ_1 conduction state. At points of high symmetry such as Γ, X, and L in the first Brillouin

Table 3. The energies of points of high symmetry in the first Brillouin zone of the RbI *crystal are given. These calculations were made using the non-relativistic O.P.W. method as described in* [24]. *The lattice parameter used was* 13·8 *Bohr units. All energies are in Rydbergs*

		$5s$I valence band			
Γ_1	−1·35	X_1	−1·34	L_1	−1·34
		$5p$I$^-$ valence band			
Γ_{15}	−0·646	X'_5	−0·659	L'_3	−0·658
		X'	−0·690	L'	−709
		Lower conduction states			
Γ_1	−0·234	X_1	−0·028	L_1	−0·175
Γ'_{25}	−0·002	X_3	−0·162	L'_2	−0·020
		X'_5	0·268	L_3	0·001
Γ_{12}	0·99	X'_1	0·11	L_3	0·171
		X_2	0·203		
Γ'_2	0·086	X_4	0·650	L_1	0·269
Γ_{15}	0·504	X_1	0·271	L'_3	0·239
		X_5	0·280	L'_2	0·320

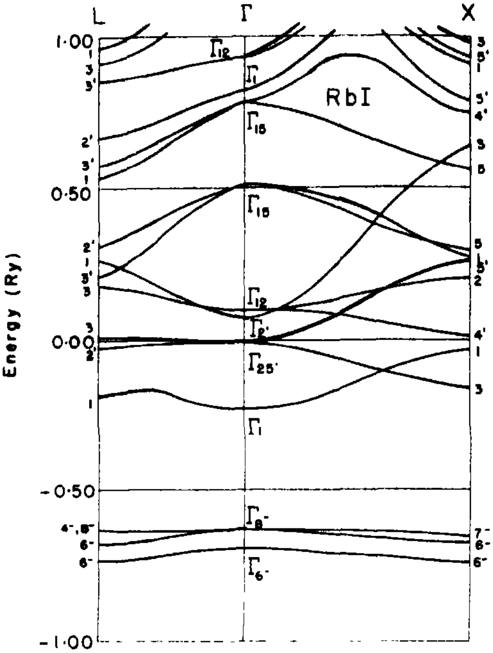

Fig. 2. The electron energy bands of RbI are shown along lines of high symmetry in the first Brillouin zone. A lattice constant of 13·8 Bohr radii was used. The calculation was performed using the O.P.W. method. The BSW notation is used [24].

zone the effective mass of an electron is given by [25]

$$\frac{m_{ij}}{m} = \left(\frac{\delta^2 E(\mathbf{k})}{\delta k_i \delta k_j}\right)^{-1}. \tag{4}$$

At the point Γ_1 this mass m_{ij} is found to be a scalar. The author has computed the effective mass about Γ_1 by several different techniques. Parabolic fits of the computed band structure were made using the point Γ_1 as one of the points fit and several of the points along Δ and Σ for the other point. In addition tight binding fits of $E(\mathbf{k})$ about Γ_1 were made using the methods of Slater and Koster [26]. These tight binding fits seemed well converged and were employed in equation (4).

The results of the several calculations were very consistent and effective mass of 0·44 free electron masses was obtained for the Γ_1 conduction electron using the tight binding method which the authors believe to be the most reliable. The deviation from this value using the other technique was found to be +0·00 to −0·04 electron masses.

In transport measurements the bare effective mass of the electron is not measured but a polaron mass is. Therefore, it is useful to compute the polaron mass from the bare effective mass. To do this, we employ the Langreth interpolation formula to the Feynman polaron mass [27]. Thus, one finds the polaron mass to be

$$m_p = m\left(\frac{1 - 0{\cdot}0008\alpha^2}{1 - {}^1\!/6\alpha + 0{\cdot}0034\alpha^2}\right),$$

$$\alpha = \left(\frac{e^2}{\hbar}\right)\left(\frac{m}{2\hbar\omega_l}\right)^{1/2} \frac{\epsilon_S - \epsilon_\infty}{\epsilon_S \epsilon_\infty}. \tag{5}$$

Here m is the electron bare effective mass, e is the electron charge, ω_l is the frequency of a longitudinal optical phonon, ϵ_s is the static dielectric constant, and ϵ_∞ is the optical dielectric constant.

For KI, the value of α is 2·60 and one finds the polaron mass to be 0·72 electron masses when the value of 0·44 is used for the bare effective mass. It is also possible to compute the polaron mass using the intermediate coupling theory result of Lee, Low and Pines [28]. In this case, the polaron mass is given by

$$m_P = m\left(1+\frac{\alpha}{6}\right) \tag{6}$$

and is found to be 0·63 electron masses if one uses 0·44 for the mass of the bare electron.

5. COMPARISON OF THEORY AND EXPERIMENT

Experimentally, KI has received much attention. The optical absorption spectrum of thin films of KI has been measured by Eby *et al.*[3] Fischer and Hilsch [8] and Teegarden and Baldini [29]. Studies have also been made on the reflection spectrum of bulk crystals of KI by Roessler and Walker [30] and by Baldini and Bosacchi [31]. In addition there is optical absorption data on mixed KI–RbI crystals by Nakamura [6] and on mixed KI–NaI crystals by Nakamura and Nakai [7]. Basically, there is excellent agreement among the various authors on the features of the optical absorption spectrum of KI.

In the analysis that follows the energy values used are those of Teegarden and Baldini obtained at 10°K. The onset of optical absorption begins at about 0·426 Ry with a strong narrow peak identified as the gamma exciton formed by a transition from the Γ_8^- valence state. There is a shoulder in the absorption at about 0·458 Ry which is interpreted as being due to the band to band transition from Γ_8^- to Γ_1. There are other sharp absorption peaks to 0·500, 0·514 and 0·534 Ry for which various interpretations have been proposed. In addition there are certain broad peaks in the absorption spectrum at 0·570, 0·611 and 0·661 Ry. The position of the band to band transition has been confirmed by the two phonon absorption experiments of Hopfield, Worlock and Park [32].

Theoretical attempts to interpret the experimental data has been made by Phillips [1] and Onodera *et al.*[4, 5]. Onodera has demonstrated that the interpretations of Phillips are in error due to Phillips' neglect of the *d*-like conduction levels. In the interpretation of Onodera, the first sharp peak is due to transition from the Γ_8^- valence band to the exciton level associated with the Γ_1 conduction level. He interprets the second sharp peak as being due to transition from X_7^- to the *d*-like exciton state associated with X_3. The third peak is said to be due to an exciton transition from X_6^- to X_3 and the fourth is said to be due to the exciton transition from Γ_6^- to Γ_1.

The interpretations of Onodera *et al.* are not in agreement with recent experimental evidence. Firstly, the analysis of the mixed crystal KI–RbI data [6] and of the KI–NaI data [7] indicates that the first two peaks involve final states of the same symmetry. Hence, since the first peak is generally agreed to be due to a Γ_8^- to Γ_1 transition, the second peak should be due to the Γ_6^- to Γ_1 transition. The analysis of the mixed crystal data by Nakamura is supported by the temperature dependence studies of the sharp peaks in the KI absorption spectrum by Fischer and Hilsch [8]. The first two peaks are seen to have a similar temperature dependence in this work. It is also noted that the third peak has a temperature dependence similar to that of the first two. A shoulder on the high energy side of the fourth peak is found to have the opposite temperature dependence of the first three peaks. That is for the first three peaks the absorption energy shifts to lower energy as the temperature is raised.

It is possible to explain most of the experimentally observed features of the KI absorption spectrum in terms of the present calculation. In Fig. 3 we present a chart of the M_0 type absorption edges associated with the low lying conduction band minima at Γ_1, L_1 and X_3. We also show the first few absorption peaks

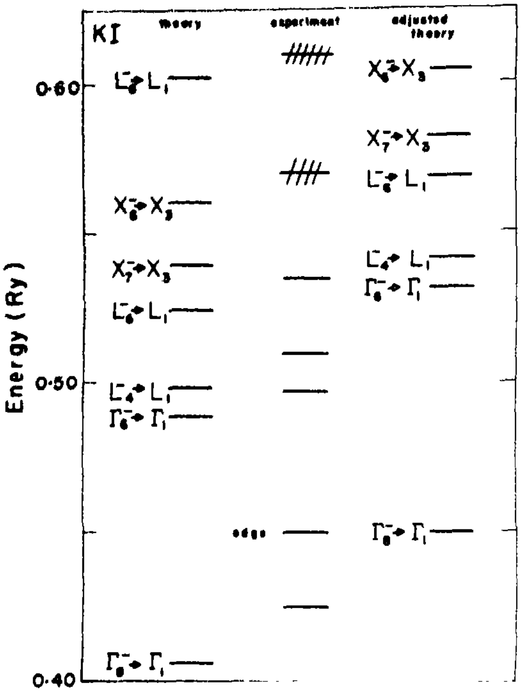

Fig. 3. The theoretical band edges are shown on the left hand side for KI. In the center the experimental peaks and the band to band transition is given. On the right hand side an empirically adjusted set of theoretical band edges are given. The notation of[24]. and the experimental data of[29] are used.

and the band edge obtained from the KI optical absorption spectrum. Finally, we show a revised set of M_0 type edges which we obtain by forcing the calculated band gap to agree with experiment. In doing this, we adjust the structure rigidly. It is noted that the error in the band gap is small (10 per cent). Previous calculations have shown that such readjustments are reasonable[14].

We see that the first four sharp absorption peaks in KI may be due to excitons associated with the $\Gamma_8^-\to\Gamma_1$, $\Gamma_6^-\to\Gamma_1$, $L_{4,5}^-\to L_1$, and $L_6^-\to L_1$ band to band transitions. It is also seen that the shoulder on the high energy side of the fourth peak may be due to an exciton associated with the $X_7^-\to X_3$ band to band transition. There is also good agreement between the higher broad absorption peaks and the low lying M_0 edges shown in Fig. 3.

From calculating the change in band edges with change in lattice parameter we find that the band edges at Γ_1 and L_1 will shift to lower energy as the temperature is raised. We also find that the edges associated with X_3 will go to higher energy as the temperature is raised. We also find that the edges associated with X_3 will go to higher energy as the temperature is raised. Thus, we see that the interpretation of the KI absorption spectrum based upon the present calculation is in agreement with the experiments of Nakamura[16], Nakamura and Nakai[7], and Fischer and Hilsch[8].

Hodby, Borders, Brown and Foner[33] have measured the mass of a polaron in the conduction band of KI. They find the polaron mass to be 0·67 ± 0·05 electron masses, a value which is in excellent agreement with the value of 0·72 electron masses obtained from this calculation.

Finally, using the results of Bridgman[34], we have computed the hydro-static pressure dependence of the KI band edges. They are as follows:

$\Gamma_8^-\to\Gamma_1$ $\quad\partial E/\partial P = 5{\cdot}0\times10^{-6}$ Ry/bar
$\Gamma_6^-\to\Gamma_1$ $\quad\partial E/\partial P = 6{\cdot}4\times10^{-6}$ Ry/bar
$L_{4,5}^- -\to L_1$ $\quad\partial E/\partial P = 1{\cdot}6\times10^{-6}$ Ry/bar
L_6^-(upper) $\to L_1$ $\quad\partial E/\partial P = 1{\cdot}6\times10^{-6}$ Ry/bar
$X_7^-\to X_3$ $\quad\partial E/\partial P \approx -10^{-7}$ Ry/bar
X_6^-(upper) $\to X_3$ $\quad\partial E/\partial P \approx -10^{-7}$ Ry/bar.

The author is not aware of any experimental studies of the pressure dependence of the band edges in KI with which to compare these results.

Recently Fröhlich and Staginnus and also Park and Stafford have measured the two photon spectra of KI and CsI[35]. These studies have included the polarization dependence of optical absorption in the region of the band edges. In the case of CsI a marked change in polarization dependence of the absorption occurs when one shifts from the absorption associated with s-like band edges to *d*-like band edges. This is in agreement with the results of Lynch and Brothers[11]. In the case of KI as measured by Fröhlich and Staginnus there was no observed strong change in absorption with polarization throughout the exciton region. This tends to confirm the assignments proposed in this paper. The less extensive results of Park and Stafford are not in agreement with the more recent work of Fröhlich and Staginnus.

Finally, we consider the soft X-ray absorption measurements of Fujita, Gahwiller and Brown[36]. In these experiments the soft X-ray absorption from the $4dI^-$ states to the *p*-like conduction bands are measured. The onset of this absorption is at about 3·94 Ry. There are sharp peaks observed at about 3·98, 4·10, 4·32 and 4·45 Ry. In addition there are smaller peaks at 4·07, 4·17, 4·19 and 4·23 Ry. These may be due either to exciton or band to band transitions. The splitting between the first two sharp peaks is 0·12 Ry. This corresponds well with the computed spin-orbit splitting of 0·13 Ry of the $4dI^-$ state. The *p* absorption band has a total width of about 0·47 Ry. The computed width of the *p*-like levels associated with the lowest Γ_{15} conduction level is about 0·50 Ry.

In the case of RbI, the interpretation of the optical spectrum is conducted along the line indicated by the KI results. In this case, there are no other calculations available for comparison. In Fig. 4 we show the band edges of RbI associated with Γ_1, L_1 and X_3. To make this chart spin-orbit splittings have been incorporated in the RbI valence band by degenerate state perturbation theory. We also show the band edge and the exciton transitions obtained from experiment[20, 37]. Finally, we show a revised set of edges obtained by having the band gap agree with experiment. It is seen that a similar experimental interpretation to that of KI is possible for RbI. It is clear that the first exciton peak is associated with the $\Gamma_8^- \rightarrow \Gamma_1$ transition. The second and third peaks are associated with the $L_4^- \rightarrow L_1$ and the $\Gamma_6^- \rightarrow \Gamma_1$ transitions respectively although it is possible that if one includes relativistic shifts the $\Gamma_6^- \rightarrow \Gamma_1$ edge would lie lower. However the fourth peak seems associated with the $X_7^- \rightarrow X_3$ transition. Here as in KI low lying minima at Γ, *L*, and *X* in the conduction band are essential in an interpretation of the RbI absorption spectrum.

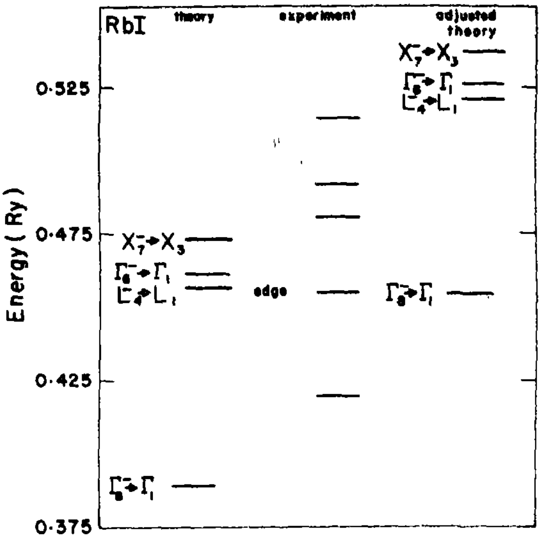

Fig. 4. The theoretical band edges are shown on the left hand side for RbI. In the center the experimental peaks and the band to band transition is given. On the right the empirically adjusted set of theoretical band edges are given. The notation of Ref.[24] is used and the experimental data of [24] and [35] are used.

Recent Stark measurements by Menes on RbI tend to confirm our assignments[38]. However, this would indicate that the spin-orbit splitting in the Γ exciton is smaller than for the Γ band edge. It is also possible that some small structure between the third and fourth peak is the Γ_6^- exciton.

6. CONCLUSIONS

We have seen that by using the relativistic mixed basis technique and a rather simple model potential results for the KI band structure may be obtained which are in good agreement with a wide range of current experimental evidence. A new interpretation of the optical absorption spectrum of KI is proposed which avoids the weak points of the experimental interpretations of Phillips[1] and Onodera *et al.*[4, 5]. In agreement with the results of Onodera[4, 5] we show that the *d*-like conduction bands play a significant role in the fundamental optical absorption of KI. We have also shown, in agreement with Phillips[1], that the L_1 conduction edge is essential in a satisfactory interpretation. We find that this L_1 level is a minimum whereas Phillips found it to be a maximum.

We have also arrived at an interpretation of the RbI spectrum which is similar to that advanced for the KI spectrum. It has also been seen that the use of a stringent 'muffin tin' potential such as used by Onodera[4, 5] produces a considerable distortion of the energy bands.

It is suggested that calculations of the conduction band density of states, and the interband density of states should be performed. An effort should be made using the theory of Page *et al.*[39] to test the connection of the *L* bands of the *F*-center with transitions from the *F*-center ground state to the conduction band, as the results of the present calculation are not in agreement with the simple *L*-band theory proposed by Baldini and Bosacchi[31].

Acknowledgements—The author wishes to thank Professor W. B. Fowler for several stimulating discussions. The author also thanks Mr. Y. Onodera for several discussions relating to his calculation. He thanks Dr. Jozef Devreese for a stimulating discussion relating to polaron theory. He also thanks Dr. D. Fröhlich and Professor F. C. Brown for permission to quote from their unpublished works. Finally, the efficient computing facilities of the Courant Institute are gratefully acknowledged.

REFERENCES

1. PHILLIPS J. C., *Phys. Rev.* **136**, A1705 (1964).
2. HOWLAND L. P., *Phys. Rev.* **109**, 1927 (1958).
3. EBY J. E., TEEGARDEN K. J. and DUTTON D. B., *Phys. Rev.* **116**, 1099 (1959).
4. ONODERA Y., OKAZAKI M. and INUI T., *J. phys. Soc. Japan* **21**, 2229 (1966).
5. ONODERA Y. and TOYOZAWA Y., *J. phys. Soc. Japan* **22**, 833 (1967).
6. NAKAMURA K., *J. phys. Soc. Japan* **22**, 511 (1967).
7. NAKAMURA K. and NAKAI Y., *J. phys. Soc. Japan* **23**, 455 (1967).
8. FISCHER F. and HILSCH R., *Nachrichten Akod. Wiss. Gotingen, Math. Physik. Klasse* 241 (1959).
9. BARRY KUNZ A., *Phys. Rev.* **151**, 620 (1966).
10. ONODERA Y., *J. phys. Soc. Japan* **25**, 465 (1968).
11. LYNCH D., and Brothers, *Phys. Rev. Lett.* **21**. 689 (1968).
12. KUNZ A. B., FOWLER W. B. and SCHNEIDER P. M., *Phys. Lett.* **28A**, 553 (1969).
13. HERRING C., *Phys. Rev.* **57**, 1169 (1940).
14. KUNZ BARRY A., *Phys. Rev.* **175**, 1147 (1968).
15. KUNZ BARRY A., *Phys. Rev.* **180**, 934 (1969).
16. SLATER J. C., *Phys. Rev.* **81**, 385 (1951).
17. LATTER R., *Phys. Rev.* **99**, 510 (1955).
18. LINDGREN I., *Ark. Fys.* **31**. 59 (1965).
19. LIU L., *Phys. Rev* **126**, 1317 (1962).
20. KUNZ A. B., *Phys. Status Solidi* **29**, 115 (1968).
21. OYAMA S. and MIYAKAWA T., *J. phys. Soc. Japan* **21**, 868 (1966).
22. DeCICCO P. D., *Phys. Rev.* **153**. 931 (1967).
23. CLARK T. D and KLIEWER K. L., *Phys. Lett.* **27A**, 167 (1968).
24. BOUCKAERT L P, SMOLUCHOWSKI R. and WIGNER E., *Phys. Rev.* **50**. 58 (1936).
25. BEALL FOWLER W., *Phys. Rev.* **132**, 1591 (1963).
26. SLATER J C. and KOSTER G. F., *Phys Rev.* **94**, 1498 (1954).
27. LANGRETH D. C., *Phys. Rev.* **159**, 717 (1967).
28. LEE T. D., LAW F. E. and PINES D., *Phys. Rev.* **90**, 297 (1953)
29. TEEGARDEN K. J. and BALDINI G., *Phys Rev* **155**, 896 (1967).
30. ROESSLER D. M. and WALKER W. C., *J. opt. Soc. Am.* **57**, 677 (1967).
31. BALDINI G and BOSACCHI B., *Phys. Rev.* **166**. 863 (1968).
32. HOPFIELD J. J., WORLOCK J. M. and PARK K., *Phys. Rev. Lett.* **11**, 414 (1963); HOPFIELD J. J. and WORLOCK J. M., *Phys. Rev.* **137A**, 1455 (1965).
33. HODBY J. W., BORDERS J. A., BROWN F. C and FONER S., *Phys. Rev. Lett.* **19**, 952 (1967).
34. BRIDGMAN P. W., *Proc. Am. Acad. Arts Sci.*, **64**, 19 (1929).
35. FRÖHLICH D. and STAGINNUS B., To be published; PARK J. K. and STAFFORD R. G. *Phys. Rev. Lett.* **22**, 1426 (1969)
36. FUJITA H., GAHWILLER C. and BROWN F. C., *Phys. Rev. Lett.* **22**. 1369 (1969).
37. FRÖHLICH D. and STAGINNUS B., *Phys. Rev. Lett.* **19**, 496 (1967).
38. MENES M., *Bull. Am. phys. Soc.* **14**, 429 (1969).
39. PAGE L. J., STROZIER J. A. and HYGH E. H., *Phys. Rev. Lett.* **21**, 348 (1968).

J. Phys. Chem. Solids Pergamon Press 1970. Vol. 31, pp. 275–282. Printed in Great Britain.

DEPLACEMENTS LINEAIRES PAR UN CHAMP ELECTRIQUE DE LA RESONANCE PARAMAGNETIQUE ELECTRONIQUE DE ZnS/Mn^{2+}

C. MARTI
Faculté des Sciences de Paris, 9 quai St. Bernard, Paris 5°, France
et
R. PARROT et G. ROGER
Faculté des Sciences de Poitiers, avenue du Recteur Pineau, Poitiers, France

(*Received* 7 *February* 1969; *in revised form* 6 *June* 1969)

Abstract—We observe the electronic paramagnetic resonance of Mn^{2+} substituted to zinc in zinc-blende and wurtzite during application of a.c. and d.c. electric fields. The lines of fine structure of wurtzite and of blende are linearly displaced. The components of the third rank tensor describing the effect of external electric fields are $R_{333} - R_{311} = 0{\cdot}14$ g/kV/mm and $R_{223} = 0{\cdot}010$ g/kV/mm for wurtzite and $R = 0{\cdot}09$ g/kV/mm for blende. These values are to be related to the variation of the S–Mn bond length. We also observe a change in absorption due to the influence of this variation on the spin-lattice relaxation.

L'ACTION d'un champ électrique sur un spectre de R.P.E. d'une impureté dans un ZnS doit être relativement importante, car l'effet est linéaire: les sites ne présentent pas de centre d'inversion[1]; elle est simple, car il n'y a pas de sites reliés par un centre d'inversion conduisant à un dédoublement apparent des raies. Nous avons choisi comme impureté le manganèse (Mn^{2+} substitué au zinc) dont les raies R.P.E. normales sont bien connues et bien résolues. Les expériences discutées ici ont été brièvement décrites dans [2].

1. RAPPELS SUR LE SPECTRE NORMAL

L'hamiltonien de spin à employer pour Mn^{2+} dans un site tétraédrique d'un cristal cubique (blende) ou hexagonal (wurtzite) est

$$\begin{aligned}\mathscr{H} &= g\beta\vec{H}\,.\,\vec{S} + D\left[S_z{}^2 - S\frac{(s+1)}{3}\right] \\ &\quad + \frac{a}{6}[S_\eta{}^4 + S_\xi{}^4 + S_\phi{}^4 - \tfrac{707}{16}] \\ &\quad + \tfrac{7}{36}F[S_z{}^4 - \tfrac{95}{14}S_z{}^2 + \tfrac{81}{16}] + A\vec{I}\,.\,S\end{aligned}$$

avec z parallèle à l'axe optique c de l'hexagonal, η, ξ, ϕ parallèles aux côtés du cube, $S = 5/2$ le spin électronique, $I = 5/2$ le spin nucléaire, H le champ magnétique.

Nous utiliserons les valeurs données par [3] qui correspondent bien à nos spectres:

dans la wurtzite—$g = 2{,}0018$; $D = -130{,}9\ 10^{-4}\,cm^{-1}$; $a = 7{,}35\ 10^{-4}\,cm^{-1}$; $a - F = 7{,}68\ 10^{-4}\,cm^{-1}$; $A = -64{,}9\ 10^{-4}\,cm^{-1}$;

et dans la blende—$g = 2{,}0024$; $a = 7{,}87\ 10^{-1}\,cm^{-1}$; $A = -64\ 10^{-4}\,cm^{-1}$.

Nous avons étudié des cristaux possédant des parties cubiques et hexagonales (dont l'axe optique c était parallèle à un axe [111] du cubique). Il est bon de remarquer que le spectre observé (Fig. 1a) montre un certain nombre de différences avec le spectre idéal, que semblent caractéristiques de l'existence de contraintes internes:

1. Les raies sont élargies non seulement par l'interaction spin–spin mais aussi par l'inhomogénéité du champ cristallin comme le prouve l'augmentation de largeur lorsqu'on passe des transitions centrales ($-\frac{1}{2} \leftrightarrow \frac{1}{2}$) (insensibles au champ cristallin) aux transitions de structure fine ($\pm\frac{1}{2} \leftrightarrow \pm\frac{3}{2}$) et surtout ($\pm\frac{3}{2} \leftrightarrow \pm\frac{5}{2}$).

2. Les raies de structure fine sont asymétriques.

3. Le spectre de la partie cubique ne s'interprète avec précision que si on introduit un

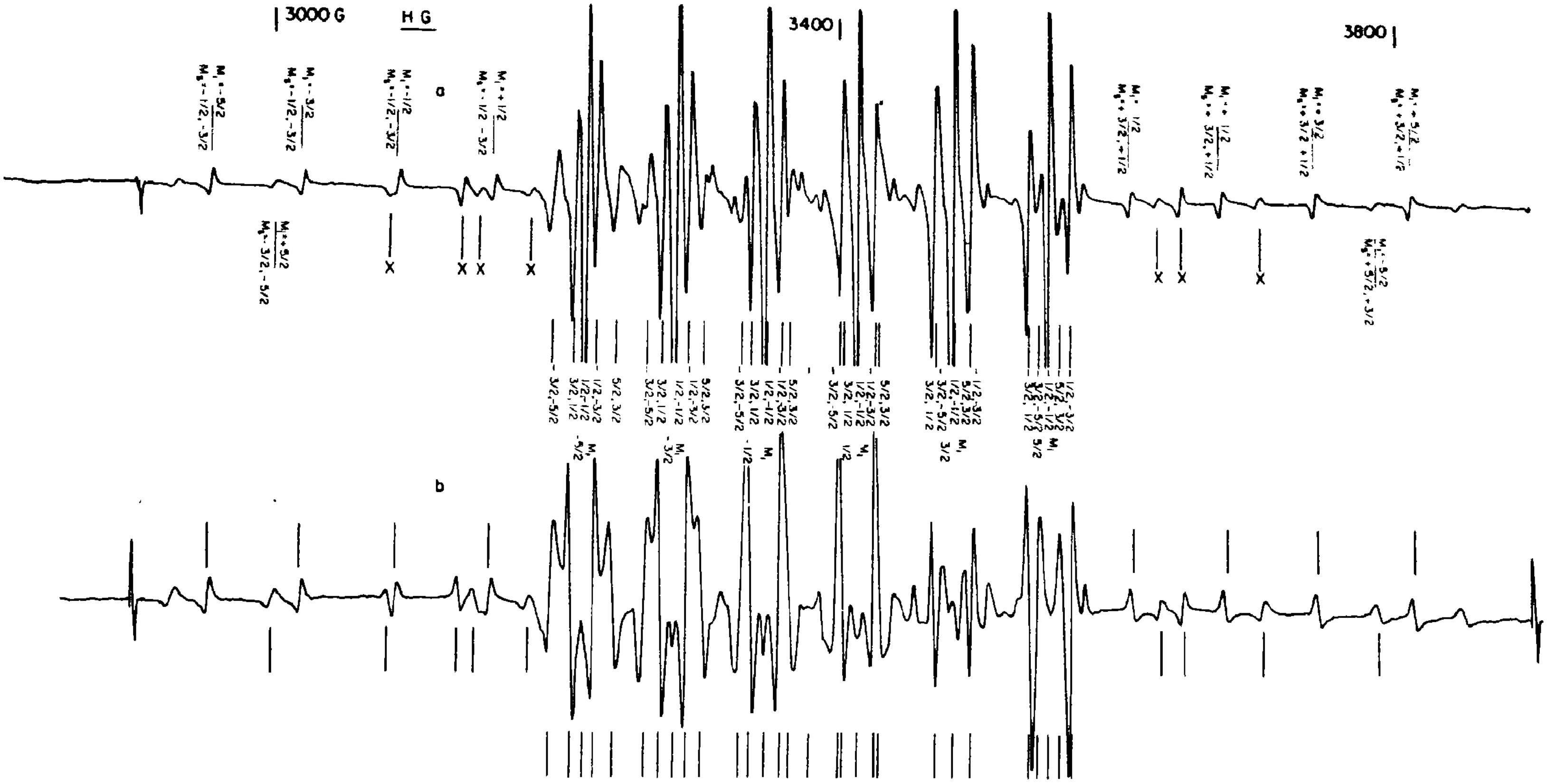

Fig. 1. (a) Spectre obtenu par modulation à 100 kHz du champ magnétique (b) Spectre obtenu par modulation à 400 Hz du champ électrique. Dans les deux cas le champ électrique et le champ magnétique sont parallèles à l'axe optique du cirstal. Les raies marquées d'une croix ne sont pas interprétées actuellement.

faible champ axial

$$\Delta\left[S_z^2-\frac{s(S+1)}{3}\right]$$

avec $\Delta = -10^{-4}\,\mathrm{cm}^{-1}$.

Nous retrouvons là un résultat de Schneider *et al.*[3] avec, simple coïncidence, la même valeur de Δ.

4. Le spectre hexagonal fait appel, dans le cristal étudié, à $|D| \simeq 133\ 10^{-4}\ \mathrm{cm}^{-1}$; la différence avec la valeur donnée par [3] ne peut provenir d'une mauvaise orientation de notre cristal car elle serait alors supérieure: la dispersion des valeurs de D selon les cristaux correspond à celle de Δ.

Notons aussi l'existence de raies supplémentaires d'origine inconnue.

2. CONTRIBUTION D'UN CHAMP ELECTRIQUE EXTERNE A l'HAMILTONIEN DE SPIN

L'action d'un champ électrique externe est décrite par [6]

$$\mathcal{H}_E = R_{ijk}E_iS_jS_k + T_{ijk}E_iS_jH_k$$

et constituée par deux tenseurs **T** et **R**, de rang 3, symétriques par rapport au 2ème et 3ème indice, c'est à dire analogues au tenseur piézoélectrique **d**.

Les restrictions sur le tenseur **d** sont obtenues en considérant le seul groupe ponctuel du cristal (et non le groupe spatial). Ce groupe de symétries est possédé par le manganèse substitué au zinc et les restrictions sur **d** sont donc applicables à **R** et **T**.

Par la suite nous ne faisons plus figurer **T** qui se traduit par une variation de g. Cette variation n'est importante que si g diffère beaucoup de 2,0023 ce qui n'est par le cas; expérimentalement nous n'avons pas observé cette variation qui entraînerait un déplacement des raies centrales ($\frac{1}{2} \leftrightarrow -\frac{1}{2}$). Il n'y a pas de variation de A détectable non plus.

1. *La wurtzite*

Pour la wurtzite appartenant à la classe 6 mm [4] le tenseur piézoélectrique d possède 3 composantes indépendantes. Dans un système d'axes notés 1, 2, 3, l'axe 3 étant pris parallèlement à l'axe optique c et les axes 1 et 2 étant contenus dans deux plans miroirs faisant entre eux un angle de 90°, **d** a sept composantes non nulles soit: Le tenseur **R** a une symétrié plus faible que le tenseur **d** dans le cas de la wurzite, mais on néglige la 4ème composante indépendante pu est nettament plus faible.

$$d_{333}$$

$$d_{311} = d_{322}$$

$$d_{223} = d_{232} = d_{131} = d_{113}$$

(a) *Détermination de* R_{333}-R_{311}. Pour $E//c$, l'hamiltonien $\mathcal{H}_E$ est donc de la forme

$$\begin{aligned}\mathcal{H}_E &= [R_{333}S_3^2 + R_{311}(S_1^2+S_2^2)]\,E_3\\ &= [(R_{333}-R_{311})S_3^2 + R_{311}S(S+1)]E_3\end{aligned}$$

qui peut être considéré comme une modification de la constante de structure fine D. Si l'angle du champ magnétique avec le champ $E//c$ est θ, on obtient immédiatement le déplacement ΔH d'une raie de structure fine $M_S \to M_S - 1$;

$$\Delta H_{\parallel} = (R_{333}-R_{311})E_3\left(\frac{3\cos^2\theta-1}{2}\right)(M_S-\tfrac{1}{2})$$

(b) *Détermination de* R_{223}. Pour $E \perp C$

$$\mathcal{H}_E = R_{223}[E_2(S_2S_3+S_3S_2)+E_1(S_3S_1+S_1S_3)]$$

Dans le cas où on prend H dans le plan (E, c) il n'est pas nécessaire de connaître l'orientation de E par rapport à un plan miroir et on a

$$\Delta H \perp = \sin 2\theta'(M_S-\tfrac{1}{2})$$

θ' étant l'angle de H avec c dans le plan (E, c).

Notons qu'on ne peut atteindre séparément R_{333} et $R_{311} = R_{322}$ à l'intérieur du seul multiplet de l'état fondamental. On adopte généralement la convention $R_{333}+R_{311}+R_{322}=0$ correspondant à une position inchangée du centre de gravité du multiplet.

2. *La blende*

La blende appartenant à la classe $\bar{4}3$ m (Td)

[4] le tenseur n'a qu'une composante indépendante d avec [5]

$$d = d\eta\xi\phi (= d\eta\phi\xi) = d\xi\eta\phi$$
$$= (d\xi\phi\eta) = d\phi\eta\xi (= d\phi\xi\eta)$$

en le rapportant aux arêtes du cube. Nous donnons sa forme dans des axes 'hexagonaux' $(1\bar{1}0), (11\bar{2}), (111)$:

$$d_{333} = \frac{2d}{\sqrt{3}}$$
$$d_{311} = d_{322} = -\frac{d}{\sqrt{3}}$$
$$d_{211} = -d_{222} = -d\sqrt{\tfrac{2}{3}}$$
$$d_{331} (= d_{313}) = d_{223} (= d_{232}) = -d/\sqrt{3}$$
$$d_{321} (= d_{312}) = d\sqrt{\tfrac{2}{3}}$$

Les autres composantes sont nulles.
Pour $E \parallel [1, 1, 1]$ et $H \parallel E$

$$\mathscr{H}_E = R\sqrt{3}\left[S_z{}^2 - \frac{S(S+1)}{3}\right]E$$
$$\text{et } \Delta H = \sqrt{3}ER(M_S - \tfrac{1}{2})$$

3. APPLICATION D'UN ECHELON DE TENSION: MESURE DE $\bar{R}_{333} - \bar{R}_{311}$ ET DE $\bar{R}_{223}$ DANS LA WURTZITE

Le sulfure de zinc est un semi-conducteur dont la résistivité était pour nos échantillons de l'ordre de $10^{14}\,\Omega$/cm. Lorsque le cristal est *isolé* des électrodes le champ y décroît donc avec une constante de temps de quelques dizaines de secondes.

La résistivité dépend naturellement du cristal et de la température, mais aussi du champ et de son histoire électriques. En effet, à champ élevé, les phénomènes d'avalanche se produisent conduisant à des conductibilités apparentes plus fortes et associés à des dépiégeages souvent irréversibles.

Ainsi sur un autre échantillon nous avions pu vérifier la linéarité du déplacement des raies de structure fine hexagonales, le déplacement restant constant au cours du temps. Malheureusement au bout de quelques expériences la conductibilité a fortement augmenté rendant la méthode inutilisable.

Nous avons donc dû appliquer un échelon de tension et observer les variations du phénomène au cours du temps. En particulier nous avons utilisé un champ magnétique statique correspondant au maximum d'une raie au repos électrique et enregistré la dérivée de l'absorption (donnée par modulation du champ magnétique à 100 kHz). A l'application de la tension, le maximum de la raie est déplacé, et la dérivée de l'absorption n'est plus nulle; elle prend la valeur δ_1 puis décroît en quelques vingt secondes sans s'annuler complètement. Si on coupe alors la tension on observe une variation δ_2 de la dérivée mais de signe opposé correspondant à un déplacement en sens contraire; elle décroît ensuite avec une constante de temps qui peut être différente (Fig. 2).

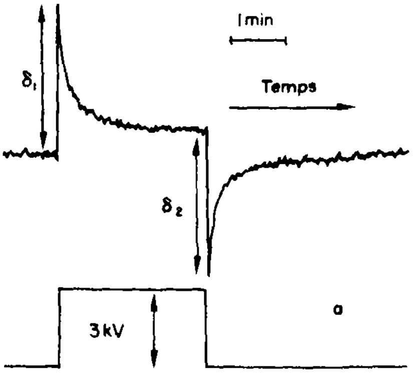

Fig. 2. Déplacement en fonction du temps de la raie hexagonale $M_I = -\frac{3}{2}$, $M_S = -\frac{3}{2}, -\frac{5}{2}$ (trace supérieure) et tension appliquée (trace inférieure).

La variation du déplacement de la raie au cours du temps correspond à l'établissement du champ dépolarisant E_D à l'intérieur du cristal; le champ interne est:

$$E + E_D$$

si E est le champ directeur appliqué. Nous avons constaté que pour les raies isolées $\delta_1 = -\delta_2$ et une variation linéaire de δ_1 et δ_2 avec E pour les champs inférieurs à 5 kV/

mm. Nous en concluons qu'il n'y a pas de dépolarisation établie avec une constante de temps inférieure à celle de nos appareils (0, 1*s*): les valeurs du déplacement correspondant à δ_1 et δ_2 sont bien dues à une variation du champ local E et $-E$. On obtient d'ailleurs la même valeur avec un cristal non isolé.

Pour les raies isolées nous avons constaté que la mesure du déplacement en fonction du temps donne le champ interne instantané intéressant pour l'étude du dépiégeage par le champ électrique.

Mesures

En faisant varier, sans tension, le champ magnétique statique de facon à avoir la même valeur δ_1 de la dérivée de l'absorption, on a une mesure du déplacement de la raie correspondant à un champ électrique donné. Cette méthode s'applique bien aux raies de résonance isolées donc aux raies de structure fine du Mn^{2+} dans la wurtzite. Nous avons vérifié que le déplacement des raies ($\pm\frac{5}{2} \leftrightarrow \pm\frac{3}{2}$) était le double de celui des raies ($\pm\frac{3}{2} \leftrightarrow \pm\frac{1}{2}$).

(a) Avec $E \parallel c$ nous avons obtenue

$$R_{333} - R_{311} = 0.14\ \mathrm{g/kV/mm}$$

Une variation de l'amplitude d'une raie hexagonale en fonction de l'angle θ des champs électriques et magnétiques (Fig. 3) est comparée à la variation théorique en ($3\cos^2\theta - 1$). Pour des angles compris entre 50° et 80° la comparaison est rendue difficile par le dédoublement des raies hexagonales par les termes en a et F du champ cristallin, différent pour les deux positions possibles dans la maille [3].

(b) Nous avons aussi mesuré R_{223} en plaçant $E \perp c$ et $H \parallel c$

$$R_{223} = 0.010\ \mathrm{g/kV/mm}$$

Une variation angulaire pour H dans le plan (E, c) est représentée sur la Fig. 4, elle correspond à celle prévue dans 2.1(b). La superposition des raies ou leur dédoublement n'a pas permis de faire les mesures pour certaines valeurs de θ'.

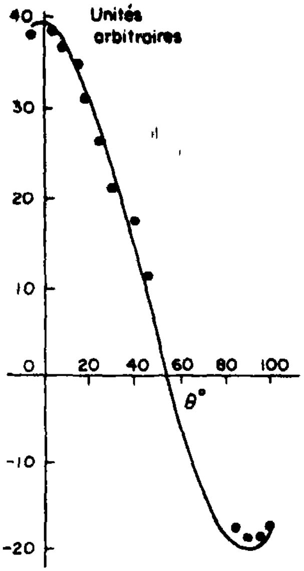

Fig. 3. Variation angulaire du déplacement de la raie hexagonale $M_I = -\frac{5}{2}$, $M_S = -\frac{5}{2}, -\frac{3}{2}$. Le champ électrique est appliqué parallèlement à l'axe optique du cristal. *θ est l'angle formé par le champ magnétique et le champ* électrique. La courbe donne la variation théorique.

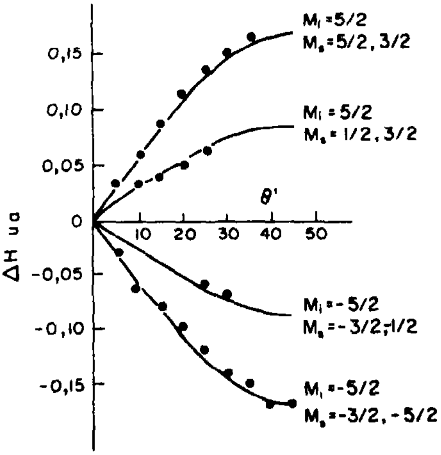

Fig. 4. Déplacement de 4 raies hexagonales, le champ électrique E est perpendiculaire à l'axe optique c, le champ magnétique est dans le plan (E, c). θ' est l'angle formé par le champ magnétique et l'axe c.

4. APPLICATION D'UNE TENSION ALTERNATIVE: MEASURE DE R DANS LA BLENDE

Les raies de résonance de Mn^{2+} dans la blende n'étant pas suffisamment séparées la méthode précédente s'applique difficilement, on constate en effet que $\delta_2 \neq \delta_1$, en effet le déplacement d'une raie est affecté par le déplacement des raies voisines. Nous avons préféré appliquer à l'échantillon un champ électrique alternatif $E_3 \sin \omega_t$, qui doit donner d'après 2.2, si H est aussi parallèle à c, un déplacement de la raie

$$\Delta H = RE\sqrt{3}(M_S - \tfrac{1}{2}) \sin \omega t$$

Avec le montage classique d'un spectromètre R.P.E. on obtient le même signal (forme et intensité) que si on avait effectué une modulation du champ magnétique d'amplitude crête à crête $2RE\sqrt{3}(M_S - \frac{1}{2})$.

En déterminant l'amplitude de modulation magnétique qui donne la même hauteur de raie crête à crête on a une mesure du déplacement.

L'interprétation des raies hexagonales de structure fine sur la Fig. 1b ne pose pas de problème. Dans la partie cubique du spectre il y a chevauchement avec inversion de phases des raies.

$$M_S = \tfrac{3}{2} \leftrightarrow \tfrac{1}{2} \text{ et } -\tfrac{3}{2} \leftrightarrow -\tfrac{5}{2} \text{ ou } -\tfrac{1}{2} \leftrightarrow -\tfrac{3}{2} \text{ et } \tfrac{3}{2} \leftrightarrow \tfrac{5}{2}$$

Dans le groupe hyperfin de champ faible ($M = -\frac{5}{2}$) les raies sont suffisamment séparées pour que le spectre soit clair; on voit nettement que la transition centrale $M_S = \frac{1}{2} \leftrightarrow -\frac{1}{2}$ ne subit pas de déplacement observable, la légère dissymétrie du spectre étant due à la dissymétrie du spectre normal (termes du 3ème ordre).

Les Figs. 5 et 6 donnent l'amplitude crête à crête des 4 raies cubiques et de 2 raies hexagonales en fonction de la tension. La variation est d'abord linéaire, puis on observe une saturation. Ce phénomène est dû à une modulation trop grande car il s'observe aussi pour des modulations magnétiques équivalentes. Il est accompagné d'un élargissement des raies suffisant à l'expliquer.

Des parties linéaires on a déduit [2]

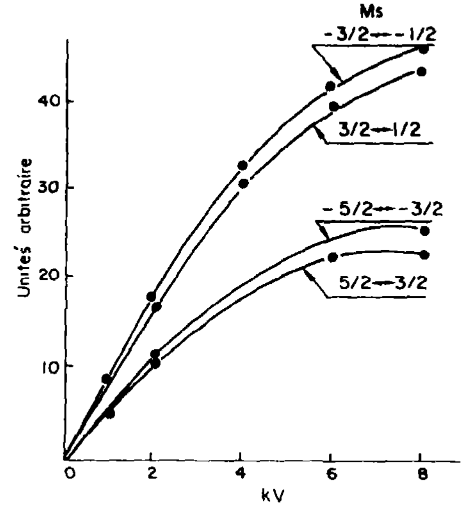

Fig. 5. Amplitude en fonction de la tension de 4 raies cubiques correspondant à $M_I = -\frac{5}{2}$, obtenues par modulation du champ électrique.

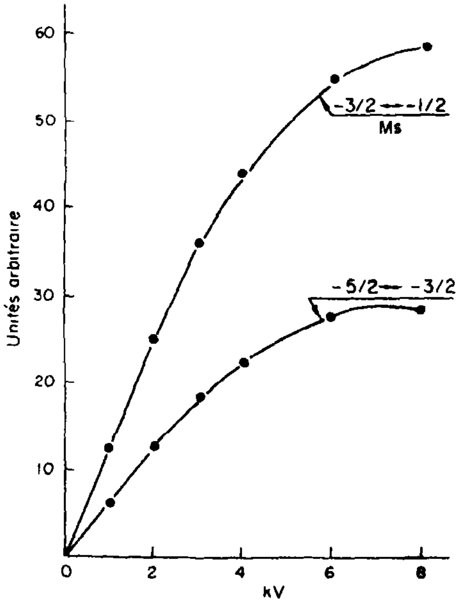

Fig. 6. Amplitude en fonction de la tension de deux raies hexagonales correspondant à $M_I = -\frac{5}{2}$.

$R\sqrt{3} = 0{,}16$ g/kV/mm pour les raies cubiques. On peut donner aussi $T < 10^{-3}$ G/kV/mm.

5. SINGULARITIES DANS LA REGION DES TRANSITIONS CENTRALES

Dans les groupes hyperfins $M_I = -\frac{3}{2}, -\frac{1}{2}$, on peut noter un signal pour le champ correspondant aux transitions centrales. Ce signal n'a pas la forme d'une dérivée de raie: la symétrie par rapport au centre du groupe hyperfin est presque parfaite. Il ne s'agit pas non plus de la superposition de dérivées de raies dont les phases sont opposées: on peut vérifier que l'apparition d'un pic supplémentaire au centre ne peut se produire ni avec des raies gaussiennes ni avec des raies lorentziennes. Ce signal ressemble donc à une raie d'absorption; il y a non pas un déplacement de la raie, mais une variation d'absorption sensiblement linéaire par rapport au champ électrique.

Nous avons d'ailleurs observé directement cette variation de l'intensité des raies à l'oscilloscope (démodulation à 100 kHz synchrone au champ magnétique et déploiement sur l'écran cathodique à 20 Hz) et en faisant agir le champ électrique: les extremums des raies dérivées se déplacent seulement verticalement de façon perceptible.

Notons enfin que l'asymétrie des raies de structure fine hexagonales est peut-être due à la présence d'un signal proportionnel à l'absorption.

Cette variation est de l'ordre du % pour un champ de 1 kV/mm. Elle semble être maximum pour $H \parallel c$ et faible lorsque le déplacement des raies dû au champ électrique est nul.

6. DISCUSSION

1. Dans la blende $d\eta\xi\phi = -3{,}2\ 10^{-12}$ MKSA [7]. L'application d'un champ électrique de 1 kV/mm selon l'axe [111] correspond donc à une compression relative de la maille dans cette direction de $1{,}8\ 10^{-6}$, donnant dans l'hamiltonien de spin un terme en S_Z^2 de $0{,}16\ 10^{-4}\,\mathrm{cm}^{-1}$.

Or dans la wurtzite la hauteur de la maille est [4] $c = 6{,}260$ Å dans la blende la quantité correspondante est

$$`c' = \tfrac{2}{3}a\sqrt{3}$$

avec [4] $a = 5{,}4093$ Å, soit $`c' = 6{,}246$ Å, ce qui correspond à une compression relative de la maille de $2\ 10^{-3}$, soit 1100 fois la compression due à une champ électrique de 1 kV/mm.

Le champ cristallin de la wurtzite donne un terme en S_Z^2 de $130\ 10^{-4}\,\mathrm{cm}^{-1}$ soit 800 fois le terme dû au champ électrique précédent.

La coïncidence est remarquable.

Evidemment la différence entre les mailles de la blende et de la wurtzite n'est pas réduite à une compression de la maille; dans la wurtzite le manganèse occupe un site avoisiné par quatre atomes de soufre pratiquement équivalents à la précision des mesures de diffraction X existantes, alors que dans le cas d'application d'un champ électrique les sous-réseaux des cations et des anions exécutent certainement un mouvement relatif d'un par rapport à l'autre.

Nous interprétons cette coïncidence comme le fait que c'est essentiellement la distance manganèse-soufre qui est le paramètre important.

2. L'existence d'un champ axial dans les parties cubiques du cristal correspond à des contraintes internes équivalentes à des champs de 10^5 V/cm, c'est à dire des distorsions moyennes de 10^{-4}, valeur très acceptable dans nos cristaux.

3. L'action du champ électrique sur les transitions $(-\frac{1}{2}, \frac{1}{2})$ peut être due soit à une variation des probabilités de transition soit à une modification du temps de relaxation.

Une variation des probabilités de transitions peut être due à une modification du mélange avec les autres états Zeeman ou des états excités du cristal.

On sait qu'il y a effectivement mélange des états Zeeman de l'état fondamental dû au champ cristallin axial de la wurtzite, conduisant à des transitions interdites $\Delta M_S = 1$, $\Delta M_I = \pm 1$ [8] ou $\Delta M_S = 2$, $\Delta M_I = 0, \pm 1$ [9]. Mais le mélange est surtout important lorsque le champ magnétique n'est pas parallèle à l'axe optique[10]. L'action d'un champ électrique parallèle à cet axe donnerait la même dépendance à l'intensité vis à vis de l'orientation du champ magnétique que le champ cristallin axial, dépendance tout à fait différente de celle que nous avons observée. Par ailleurs elle serait en $(eER/g\beta H)^2$ soit pour un kV/mm environ 10^{-5} ce qui est nettement insuffisant pour rendre compte du phénomène. Quant à la variation de l'admission des états excités, elle est en $(ER/V_{cr})^2$ où V_{cr} est relié au champ cristallin et vaut quelques dizaines de milliers de cm^{-1}, soit 10^{-8} pour le champ électrique externe.

Les transitions dipolaires électriques ne sont pas à considérer d'une part parce que l'échantillon est dans une région de la cavité où le champ électrique hyperfréquence est nul, d'autre part parce que T est petit[11].

L'effet est donc à rechercher essentiellement du côté de la variation du temps de relaxation. Nous avons effectivement constaté que l'effet dépend de la puissance hyperfréquence de façon correcte qualitativement. La couplage spin–réseau, dans la mesure où l'hybridation des orbitales est importante, doit être très sensible aux distances interatomiques et l'ordre de grandeur devient acceptable.

Nous ne possédons malheureusement pas de cristaux de wurtzite sans parties cubiques, dopés au manganèse qui permettraient d'approfondir en particulier la dépendance angulaire de la relaxation. Nous essayons d'utiliser des cristaux de ZnO meilleurs sur le plan de la monocristallinité mais possédant une conductivité gênante.

BIBLIOGRAPHIE

1. BLOEMBERGER N., *Science*, N.Y. **133**, 1363 (1961).
2. MARTI C., PARROT R., ROGER G. et HERVE J., *C.r. hebd. Séanc. Acad. Sci., Paris* **267**, 931 (1968).
3. SCHNEIDER J., SIRCAR SR. et RÄUBER A., *Z. Naturf.* **18a**, 980 (1963).
4. WYCKOFF. *Crystal Structures*, Vol. 1. Wiley, New York (1965).
5. NYE J. F., *Propriétés Physiques des Christaux*. Dunod Paris (1961); ou Clarendon Press, Oxford (1957).
6. ROYCE E. B. et BLOEMBERGER N., *Phys. Rev.* **131**, 1912 (1963).
7. KNOL K. S., *Kronit Inst. Amsterdam* **35**, 99 (1932).
8. BLEANEY B. et RUBINS R. S., *Proc. phys. Soc.* **77**, 103 (1961).
9. CLERJAUD B., MARTI C. et VISOCEKAS R., *C.r. hebd. Séanc. Acad. Sci., Paris* **266**, 1030 (1968).
10. MARTI C., ROMESTAIN R. et VISOCEKAS R., *Phys. Status Solidi*, **28**, 97 (1968).
11. KIEL A., *Proc. Int. Conf. on Magnetism*, p. 465. The Institute of Physics and Physical Society (1965).

J. Phys. Chem. Solids Pergamon Press 1970. Vol. 31, pp. 283–289. Printed in Great Britain.

ULTRASONIC ATTENUATION IN MnF_2 NEAR THE NÉEL TEMPERATURE*

AKIRA IKUSHIMA†

Department of Physics and Materials Research Laboratory, University of Illinois, Urbana, Ill. 61801, U.S.A.

(*Received* 7 *May* 1969; *in revised form* 28 *July* 1969)

Abstract—The anomalous ultrasonic attenuation in MnF_2 was measured near the Néel temperature, T_N. The measurement was carried out for the [100] longitudinal waves over the frequency range of 10–110 MHz. A log–log plot of the attenuation coefficient vs. $|T-T_N|$ could not be described by a single power-law stage. For the most linear part of this log–log plot, the attenuation coefficient, α, was written as $\alpha \sim \omega^n|T-T_N|^{-\eta}$, where ω is the angular frequency of the sound; $\eta = 0{\cdot}14 \pm 0{\cdot}01$ and $n = 1{\cdot}6 \pm 0{\cdot}1$ for $T > T_N$, whereas η decreases with increasing frequency for $T < T_N$. An anomalous behavior of the attenuation was found in the immediate vicinity of T_N in the paramagnetic phase, where the slope of the log–log plot decreases as the sound frequency increases. Possible explanations will be given for these results.

1. INTRODUCTION

ULTRASONIC studies, both of the attenuation and the velocity measurements, have attracted much attention as useful ways to investigate the dynamical aspect of the critical fluctuation associated with the second-order phase transition. In the case of magnetic transitions, the sound waves are more attenuated as the temperature approaches the critical point, where the spin fluctuation grows and the characteristic relaxation time of the fluctuation slows down. The change of sound velocity is also worth measuring since the sound velocity and the attenuation coefficient should be related to the real and the imaginary parts of a response function for an alternating stress and strain, and one can get an information on the relaxation time of the phenomenon.

Several theoretical treatments[1–9] have been published concerning the sound attenuation near the magnetic transition point. On the other hand, several experimental investigations have also been carried out (in MnF_2 [10–12], $RbMnF_3$[13, 14], EuO[14], rare-earth metals[15, 16], and CoO[17]), showing good agreement with the theoretical predictions in some cases and poor agreement in other cases. It appears that more results of careful experiments are needed to predict a general trend of the present phenomenon.*

This paper reports experimental results in MnF_2, a material regarded as one of the standards in the study of the critical phenomenon and one for which many properties have been measured[19]. A quantitative measurement of the sound attenuation was first made by Neighbours and Moss[11], for the [110] and the [001] longitudinal waves. The present work was carried out for the [100] longitudinal waves, with a great care applied to the question of the tempera-

---

*This work was supported in part by the U.S. Atomic Energy Commission, Contract AT(11-1)-1198.

†Present address: The Institute for Solid State Physics, The University of Tokyo, Minato-ku, Tokyo 106, Japan.

*Lüthi *et al.*[18] have recently proposed from their investigation in rare-earth metals that the attenuation measurements in anisotropic materials are better understood by the theoretical predictions than are those in isotropic ones. However, the present author has still found a discrepancy between theory and his experimental result in FeF_2[23], a strongly anisotropic antiferromagnet. It seems that detailed considerations have to be paid to the actual interaction between spins to make clear the cause of the discrepancy.

ture gradient within the specimen and of the accuracy of the attenuation measurement, which revealed a number of new facts and also makes the present result the most reliable among those so far obtained in MnF_2.

2. EXPERIMENTAL PROCEDURE

A single crystal of about 10 × 10 × 10 mm in size was obtained from Semi-Elements, Inc. The crystal was oriented crystallographically by X-ray technique with an accuracy of 0·5°. A pair of the [100] surfaces was then polished sufficiently flat and parallel for the ultrasonic study.

In this experiment, the specimen was mounted in a massive copper block and the block was set in a vacuum can immersed in a liquid nitrogen bath. The liquid nitrogen was always pumped and kept at its triple point temperature, 63·2°K, during the measurement. The specimen was then heated up by a heater coil wound around the copper block. The temperature of the specimen was measured with a platinum resistance thermometer which had been calibrated and was embedded in the copper block.

The absolute accuracy of the measured temperature was about 0·02°K. However, of much more importance here are the relative accuracy of the temperature and the elimination of the temperature gradient within the specimen. We could achieve a measurement of temperature change as small as 0·0005°K. The temperature gradient in the specimen appeared to depend primarily on the rate of the temperature change in this case. Due to the results of preliminary tests, we changed the temperature at the rate of 0·1°K per hr, especially in the range of $T_N \pm 0{\cdot}5$°K. This means that the temperature difference between any two points in the specimen was less than about 1 millidegree K.

The present measurement of the attenuation was made by the usual pulse-echo method. A combined system of the Matec's Model PR-201 and Model 2470 was used, and the character of the entire amplifier system was respectively checked for every frequency used here. This procedure was found to be necessary for such a delicate experiment as the present one and a mere calibration of the IF amplifier was unsatisfactory. Furthermore, the attenuation variation, which was recorded simultaneously with the temperature change on a multi-point recorder, was converted to the attenuation coefficient in the unit of dB/μsec or dB/cm by the use of an exponential decay oscillator at more than 15 different temperatures during an experimental run. The relation between the recorded value and the attenuation coefficient was always found to be satisfactorily linear. The time constant of the exponential decay was carefully calibrated, and then the absolute accuracy of the attenuation coefficient is considered to be better than 0·01 dB/cm.*

In the present work, only the attenuation associated with the second-order phase transition concerns us, so the remaining attenuation should be subtracted as a background component. The determination of the background level might introduce some error in the final result. The present author deduced the level by extrapolating the behavior of the attenuation coefficient in the temperature range from 20 to 30°C or more above T_N. The level then was assumed to be constant over the entire temperature range of concern. Since the attenuation did not seem to rise linearly, for example, as the temperature was lowered, we do not have any positive reason of using a temperature-dependent residual attenuation in the present case[24].

3. RESULTS

Figure 1 shows a typical example of the variation of the attenuation as a function of

---

*The attenuation coefficient described here contains both the magnetic and the residual parts. Since we introduce a certain amount of error when we determine the level of the residual attenuation, the absolute accuracy of the magnetic part of the attenuation should be considered to be approximately 0·05 dB/cm in the present case. Nevertheless, this experimental error little affects the values of η and n.

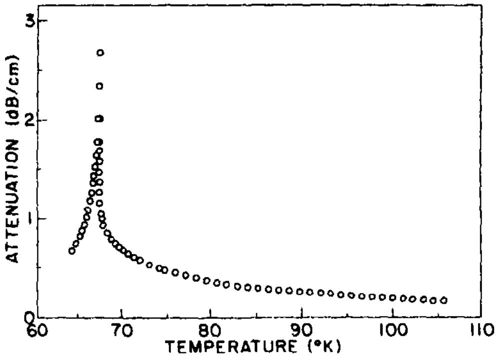

Fig. 1. Critical attenuation of 30 MHz longitudinal waves propagating along the [100] direction in MnF_2.

temperature. Figures 2 and 3 are log–log plots of the attenuation coefficient vs. $T-T_N$ and $\epsilon = |T-T_N|/T_N$ for various frequencies. Clearly, there are more than one stage in these plots in both paramagnetic and antiferromagnetic phases. From the present result alone, we cannot determine whether or not the crossover temperature between these stages depends on the frequency in a systematic manner.

Let us take here a usual power-law formula,

$$\alpha \sim \omega^{n} |T-T_N|^{-\eta} \qquad (1)$$

where ω is the angular frequency of the sound, and n and η are the characteristic parameters to be compared with theory. Table 1 summarizes values of η deduced from the most linear part of the plots in Figs. 2 and 3. We could not deduce reliable values of η for any other possible stages of the plots. For $T > T_N$, the value of η seems to be independent of frequency with an average value of 0·14±0·01. On the other hand, η has a smaller value for higher frequency when $T > T_N$, and is practically constant for 70, 90 and 110 MHz. The attenuation coefficient is also almost constant even for $T > T_N$ if the frequency is high enough and the temperature is close enough to T_N.

Table 1. *Values of* η *for the* [100] *longitudinal waves in* MnF_2

Frequency (MHz)	η for $T > T_N$	η for $T < T_N$
10	$0{\cdot}13_8$	0·090
30	$0{\cdot}13_1$	0·067
50	$0{\cdot}13_1$	0·020
70	$0{\cdot}12_6$	0·005
90	$0{\cdot}15_0$	0·004
110	$0{\cdot}15_2$	0·004
Average	0·14±0·01	

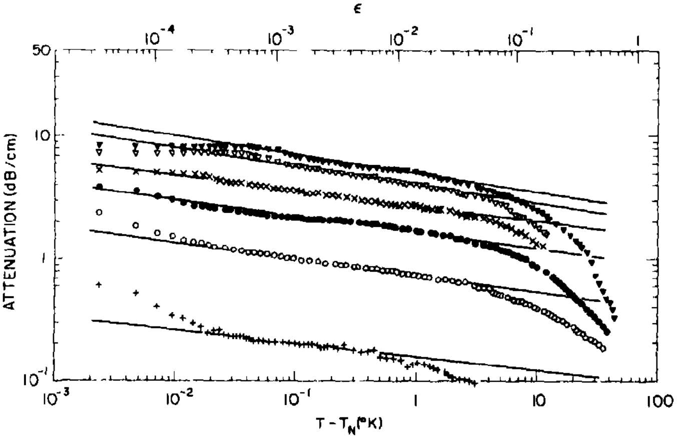

Fig. 2. Temperature dependence of the attenuation coefficient of the [100] longitudinal waves for $T > T_N$. + – 10 MHz. ○ – 30 MHz. ● – 50 MHz. × – 70 MHz. ▽ – 90 MHz. ▼ – 110 MHz.

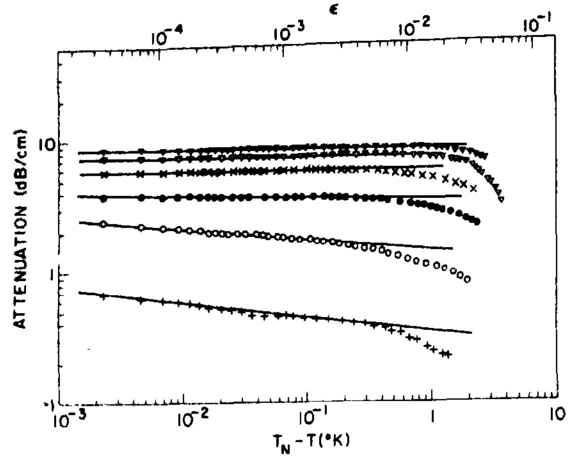

Fig. 3. Temperature dependence of the attenuation coefficient of the [100] longitudinal waves for $T < T_N$. + — 10 MHz, ○ — 30 MHz, ● — 50 MHz, × — 70 MHz, ▽ — 90 MHz, ▼ — 110 MHz.

The frequency dependence of the attenuation obeying the power law is also important. Figure 4 is the plot for $T > T_N$, and the value of n in equation (1) is 1·6±0·1. A comparison is given of the present result with other ones in Table 2.

4. DISCUSSION

The value of η obtained here for the paramagnetic phase is 0·14, which does not agree with the previous value, 0·53, obtained by Evans[11] for the same crystallographic situation. The discrepancy might arise be-

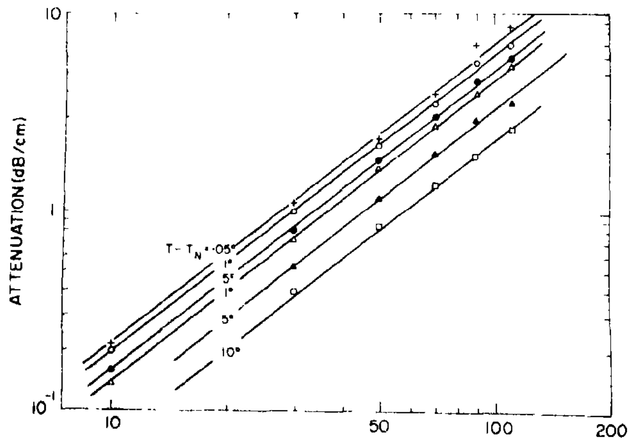

Fig. 4. Frequency dependence of the attenuation for $T > T_N$ in MnF_2. The temperature difference, $\Delta T = T - T_N$, is indicated in the figure.

Table 2. Attenuation in MnF_2

Investigator	Wave propagation	Frequency range (MHz)	$T > T_N$		$T < T_N$		Peak height at 30 MHz (dB/cm)
			η	n	η	n	
Present author	[100]	10–110	0·14±0·01	1·6±0·1	*		2·7
Evans[12]	[100]	10–50	0·53	2	0·29	2	8
Neighbours and Moss[11]	[110]	10–70	0·38	†			0·86
	[001]	10–70	0·42	†	0·18	†	3·5

*The value of η depends on sound frequency. See Table 1.

†They compared the peak height to deduce n, which should therefore be rechecked.

cause Evans would not measure the variation of the attenuation coefficient up to a temperature far enough from T_N to determine the residual attenuation. Although the most important temperature range for determining the values of η would be approximately $T_N \pm 2$°K, we may get a value even three times as large as the present one if we would take the magnitude of the attenuation coefficient at several °K above T_N as the level of the residual attenuation. It should be worth noting here that Lüthi *et al.*[18] have also obtained η equal to 0·2 for the [100] longitudinal waves [24].

As is seen in Table 2, there is another large difference between the present result and the one by Evans, namely, the difference in the peak height of the attenuation. A theory of Tani and Mori[8] predicted that the ratio of the attenuation coefficient for the [001] longitudinal waves to that for [100] in antiferromagnets of the rutile structure is given by

$$\alpha[001]/\alpha[100] \approx (c/a)^2(J_z'/J_x')^2, \quad (2)^*$$

where c and a are the lattice parameters along the z- and x-axis respectively, and $J_z' = \partial J/\partial z$ and $J_x' = \partial J/\partial x$ with J as the most predominant, antiferromagnetic exchange interaction between a spin at (0,0,0) and the one at $(\frac{1}{2},\frac{1}{2},\frac{1}{2})$. In MnF_2, $a = 4·87$ Å, $c = 3·31$ Å, and $|J_z'/J_x'|$ was estimated[8] as 2·1 from the experimental result by Benedek and Kushida[20].† Therefore, the above ratio of the attenuation coefficients should have the value of about 2. From this reason, the peak value by Evans, much larger than the value for [001] in Table 2, seems to be in some doubt.

The present value of η does not seem to be explained by existing theories, all of which predict much larger values. For example, a group of theories[1–5, 8] have given the value of η equal to 5/3 for the isotropic antiferromagnet and 3/2 for the anisotropic antiferromagnet. In these theories, the four spin correlation function is factorized into a product of two pair correlation functions. Since the fluctuation becomes larger, this factorization should be invalid close to T_N. On the other hand, Kadanoff[9] has predicted the value of η equal to 1 and 4/3 for the isotropic and the anisotropic antiferromagnets respectively, where the perturbation treatment was made for the decay rate of one sound wave into two, three or four other sound waves together with the scaling law concept.

The systematic breaking away of the experimental points from the linear variation for larger ϵ in Fig. 2 suggests another power-law stage having a larger η. The larger value of η may crudely be deduced as $0{\cdot}7 \pm 0{\cdot}2$. We may explain that the breaking-away temperature of the stage corresponds to the temperature difference at which the anisotropic energy in MnF_2 is just overcome by thermal energy. If we use a value of 3×10^{-2} as the anisotropic factor in MnF_2[18], the estimated temperature difference is 2°K, which coincides with the observed result. However, the value of the critical exponent is larger for $T - T_N > 2$°K, which appears to contradict the trend of the above theoretical prediction by Kadanoff.

---

*Equation (2) can also be derived considering that the attenuation coefficient is proportional to the square of the coupling strength between the spin system and the sound waves multiplied by the number of the exchange interactions which are affected by the sound waves.

†The present author and his co-worker[21] have recently obtained that $|J_z'/J_x'| = 2·7$, from the anisotropic anomalous change of sound velocity near T_N being based on a theoretical treatment.

The attenuation coefficient in the paramagnetic region has a frequency dependence weaker than ω^2 in this material, at least for the [100] direction. This means that one or more mechanisms predominantly determine a rather long effective relaxation time τ; then the product $\omega\tau$ has a magnitude not far below unity, making the frequency dependence weaker. Such a frequency dependence has also been observed in CoO[17]. From the present result alone, we cannot determine the actual process or processes which give this slow relaxation. Direct interaction between spin system and the lattice might be a possibility, as in the theoretical treatment recently given by Kawasaki[22].

The anomalous behavior of the attenuation in the immediate vicinity of T_N in the paramagnetic phase should also be noted. This anomaly occurs in the temperature range of $T - T_N \lesssim 2 \times 10^{-2}$°K, where the slope of the log–log plot decreases as the sound frequency increases, and the attenuation coefficient is almost flat for 70 MHz and higher. We can roughly estimate the spin fluctuation frequency as $f_s \approx (k_B T_N/h)\epsilon^x$ for the case in which spin diffusion determines the process, where h is the Planck constant and ϵ^x is the factor expressing the critical slowing-down effect. If we take x as 4/3 according to a treatment by Kawasaki[7], then $f_s \approx 2{\cdot}8 \times 10^7$ for $T - T_N = 2 \times 10^{-2}$°K. Therefore, we can conclude here that the spin diffusion process is the mechanism responsible to the attenuation in the range of $T - T_N \lesssim 2 \times 10^{-2}$°K, whereas another mechanism becomes more responsible instead of the spin diffusion process at temperatures further away. A thorough investigation of determining the relaxation time should be much desirable to elucidate the actual mechanism which determines the attenuation coefficient of such a small critical exponent as obtained in this work.

Acknowledgements—The present author would like to thank Dr. A. V. Granato, Dr. K. Kawasaki, Dr. B. Luthi and Dr. G. Laramore for their interests in this work and many valuable discussions. The author is also indebted to Dr. B. B. Chick and Dr. J. T. Holder for their helpful suggestions during the experiment.

REFERENCES

1. TANI K. and MORI H., *Phys. Lett.* **19**, 627 (1966).
2. OKAMOTO H., *Prog. theor. Phys.* **37**, 1348 (1967).
3. BENNETT H. S. and PYTTE E., *Phys. Rev.* **155**, 553 (1967).
4. BENNETT H. S. and PYTTE E., *Phys. Rev.* **164**, 712 (1967).
5. KAWASAKI K., *Solid-St. Commun.* **6**, 57 (1968).
6. KAWASAKI K., *Phys. Lett.* **26A**, 543 (1968).
7. KAWASAKI K., *Prog. theor. Phys.* **39**, 285 (1968).
8. TANI K. and MORI H., *Prog. theor. Phys.* **39**, 876 (1968).
9. KADANOFF L. P., *J. phys. Soc. Japan, Suppl.* **26**, 122 (1969).
10. NEIGHBOURS J. R., OLIVER R. W. and STILLWELL C. H., *Phys. Rev. Lett.* **11**, 125 (1963).
11. NEIGHBOURS J. R. and MOSS R. W., *Phys. Rev* **173**, 542 (1968).
12. EVANS R. G., *Phys. Lett.* **27A**, 451 (1968).
13. GOLDING B., *Phys. Rev. Lett.* **20**, 5 (1968).
14. LUTHI B. and POLLINA R. J., *Bull. Am. phys. Soc. II*, **14**, 418 (1969); *Phys. Rev. Lett.* **22**, 717 (1969).
15. LÜTHI B. and POLLINA R. J., *Phys. Rev.* **167**, 488 (1968).
16. POLLINA R. J. and LÜTHI B., *Phys. Rev.* **177**, 841 (1969).
17. IKUSHIMA A., *Phys. Lett.* **29A**, 417 (1969).
18. LÜTHI B., PAPON P. and POLLINA R. J., *J. appl. Phys.* **40**, 1029 (1969).
19. See, for example, KADANOFF L. P. *et al.*, *Rev. mod. Phys.* **39**, 395 (1967).
20. BENEDEK G. B. and KUSHIDA T., *Phys. Rev.* **118**, 46 (1960).
21. KAWASAKI K. and IKUSHIMA A., To be published in *Phys. Rev.*
22. KAWASAKI K., *Phys. Lett.* **29A**, 406 (1969).
23. $\eta = 0{\cdot}75 \pm 10\%$ for $T > T_N$ and $0{\cdot}45 \pm 10\%$ for $T < T_N$. IKUSHIMA A., To be published.

24. The author has recently made a computer calculation to deduce the level of the residual attenuation as well as the attenuation of the magnetic part. The computer calculation based on the raw data for 30 MHz, for example, gave us the following results:

$$\alpha = a + b(T - 70{\cdot}0) + \frac{c}{\eta}(\epsilon^{-\eta} - 1) \text{ for } T > T_N$$

with

$a = +(0{\cdot}804 \pm 0{\cdot}007)$ dB/cm,
$b = -(0{\cdot}00456 \pm 0{\cdot}00003)$ dB/cm°K,
$\eta = +0{\cdot}1357 \pm 0{\cdot}0044$.

This clearly means that the temperature coefficient of the residual attenuation is very small and also the value of η mentioned in my paper is surely correct.

J. Phys. Chem. Solids Pergamon Press 1970. Vol. 31, pp. 291–297. Printed in Great Britain.

CHALEUR SPECIFIQUE ELECTRONIQUE ET SUSCEPTIBILITE MAGNETIQUE DES CARBURES DE TRANSITION HEXAGONAUX DE FORMULE M_2C

R. CAUDRON, F. DUCASTELLE et P. COSTA
O.N.E.R.A.-29, Avenue de la Division Leclerc, 92 Chatillon, France

(*Received* 19 *March* 1969; *in revised form* 24 *July* 1969)

Résumé—Les chaleurs spécifiques électroniques des sous-carbures hexagonaux de vanadium, de niobium et de molybdène, ainsi que celle du composé (V–Mo)C ont été mesurées. Elles donnent les valeurs suivantes du coefficient γ: V_2C: 2,26 mJ/°K² mole; Nb_2C: 1,47 mJ/°K² mole; $(Mo–V)_2C$: 3,16 mJ/°K² mole; Mo_2C: 3,26 mJ/°K² mole. Ces résultats semblent indiquer l'existence d'un minimum de la densité d'états pour un nombre d'électrons par atome un peu inférieur à celui des composés de la cinquième colonne, sans doute homologue à celui que l'on observe pour les métaux cubiques centrés (VIème colonne) et les carbures cubiques faces centrées (IVème colonne), et qui correspond peut être au remplissage de la partie 'liante' de la bande *d*. Le susceptibilité magnetique de ses composés a été également mesurée et discutié.

Abstract—Specific heats of vanadium, niobium and molybdenum hexagonal hemicarbides and of a (V–Mo)C compound have been measured. They give the following values for the γ coefficient: V_2C: 2,26 mJ°K² mole; Nb_2C: 1,47 mJ/°K² mole; $(Mo–V)_2C$: 3,16 mJ/°K² mole; Mo_2C: 3,26 mJ/°K² mole. These results probably indicate the existence of a minimum of the density of states, vs. the electron concentration, located just before the fifth column. This minimum would be homologous to those which have been observed for the b.c.c. metals (sixth column) and the f.c.c. carbides (fourth column), and might correspond to the filling of the binding part of the *d* band. This paper also includes measurements of the magnetic susceptibilities of these compounds, and a discussion of their origin.

1. INTRODUCTION

L'ÉTUDE des carbures cubiques à faces centrées des métaux de transition a montré l'existence d'un minimum de la densité d'états au niveau de Fermi au voisinage de la IVème colonne (Ti, Zr, Hf). Certains auteurs [1–3], ont associé ce minimum au demi-remplissage d'une bande *d*, analogue à celui qu'on observe pour les métaux eux-mêmes. Cette hypothèse implique un accroissement du nombre des états *d* occupés pour chaque atome. Si elle est correcte, on peut s'attendre à voir apparaître un minimum analogue au voisinage de la Vème colonne pour les sous-carbures de formule M_2C. Nous avons donc cherché à déterminer les densités d'états de ces composés à partir de la chaleur spécifique à basse température et de la susceptibilité magnétique.

Les carbures de formule M_2C des Vème et VIème colonnes ont, on le sait, une structure cristallographique hexagonale, ou tout au moins une structure très voisine. Ceux de la IVème colonne sont, au contraire, des variétés à faible taux en carbone des phases MC de structure NaCl. Dans le présent travail, nous nous sommes limités à la première famille, de façon à éviter des phénomènes trop complexes liés à la structure cristalline. Nous avons donc préparé les carbures V_2C, Nb_2C, Mo_2C. Nous avons en outre cherché à préparer des composés mixtes du type $(A,B)_2C$. Il eût été évidemment préférable de choisir des composés intermédiaires de deux métaux appartenant à la même série de transition; malheureusement [4], les composés mixtes de type $(Mo, Nb)_2C$ sont instables vis à vis du mélange $(Mo, Nb)C +$ (Mo, Nb) en raison de la très forte variation d'enthalpie associée à la réaction correspondante. Par contre, il nous a été possible de préparer des composés mixtes $(Mo, V)_2C$ pour tout le domaine de composition. La situation est, dans ce cas, plus favorable, car:

(1) Le carbure de vanadium a une énergie de formation moins élevée que le carbure de niobium (28 au lieu de 33,7 kcal/mole). (2) Les rayons métalliques du vanadium et du molybdène sont plus proches.

2. PREPARATION DES ECHANTILLONS

Les échantillons ont été obtenus par réaction à 1700°C sous vide de poudres compactées de métaux ou d'hydrures métalliques et de graphite dont les taux d'impuretés étaient inférieurs à 0,07 pour cent. Ils ont été ensuite broyés et homogénéisés au cours d'un frittage final à 1900°C.

Les diagrammes de rayons X (Debye-Scherer, raie Kα du cuivre) sur le carbure de molybdène et le carbure mixte de vanadium et de molybdène ont montré que les corps formés étaient bien les phases hexagonales M_2C. Nous en donnons les paramètres:

Mo–V–C	Mo_2C
a:2,9535 ± 0,001 Å	3,007 ± 0,001 Å
c:4,645 ± 0,002 Å	4.729 ± 0,002 Å

Ces valeurs sont en bon accord avec celles de la bibliographie[5, 6]. En ce qui concerne Mo_2C, notre échantillon se situe bien sur les courbes paramètres-composition fournies par Rudy[7] (Fig. 2). Sa composition effective serait donc de 32 pour cent en carbone (ce qui correspond à $MoC_{0,48}$).

On sait que des distorsions orthorhombiques des carbures V_2C et Nb_2C ont été récemment observées[8]. Nous avons bien retrouvé ce phénomène. En ce qui concerne Nb_2C, la phase orthorhombique subsiste pour des échantillons dont le rapport nominal x = C/Nb (en atomes) varie de 0,4 à 0,5 environ; les rayons X révèlent en outre la coexistence de la phase orthorhombique et du Nb métal. Nous avons au contraire constaté la coexistence de la phase non distordue et du carbure NbC dans un échantillon dont la composition nominale correspond à x = 0,54.

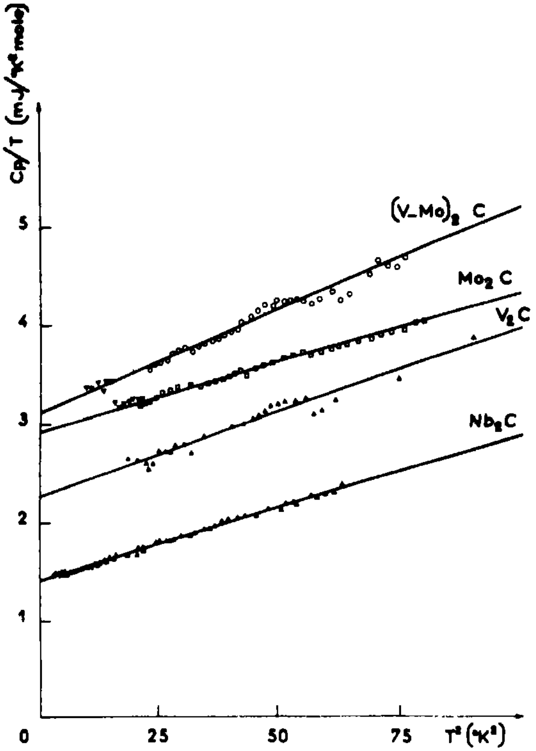

Fig. 1. Diagramme Cp/T en fonction de T^2 (Cp, chaleur spécifique molaire) pour V_2C, $(Mo–V)_2C$, Mo_2C et Nb_2C.

C'est sur ce dernier échantillon qu'a porté la mesure de chaleur spécifique. Les paramètres sont:

V_2C	Nb_2C distordu	Nb_2C non distordu
c = 2,87 ± 0.01 Å	c = 3,095 ± 0,001 Å	a = 3,126 ± 0.001 Å
b = 4,57 ± 0.01 Å	b = 4,967 ± 0,001 Å	c = 4,971 ± 0.001 Å
a = 10.25 ± 0,03 Å	a = 10,904 ± 0,003 Å	

L'analyse des gaz (extraction par fusion-réduction sous hélium, analyse des gaz extraits par chromatographie en phase gazeuse)[9] a donné pour un échantillon-type de Nb_2C:

O_2:270 p.p.m. ± 50
N_2:110 p.p.m. ± 20
H :35 p.p.m. ± 10

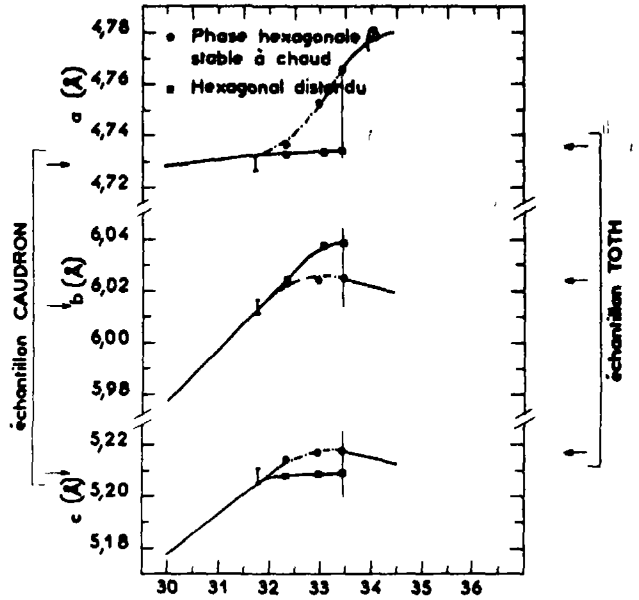

Fig. 2. Courbes paramètres-composition (d'après Rudy[7]) situant notre échantillon de Mo_2C et celui de Toth[15] dans le système Mo–C (en abcisse, la concentration atomique en carbone).

3. MESURES

(1) Les chaleurs spécifiques à basse température ont été mesurées sur un calorimètre adiabatique de type Nernst[10], analogue à celui qui a été mis au point par Conte[11]. Donnons rapidement les principales caractéristiques de cet appareil:

(a) Le refroidissement de l'échantillon à la plus basse température (1,5°K) se fait par gaz d'échange, sauf pour la mesure portant sur Nb_2C, où nous avons utilisé un nouveau calorimètre, équipé d'un contact mécanique, qui nous débarrasse des effets de désorption. (b) L'écart de température entre l'échantillon et l'écran qui l'entoure, et sur lequel sont bobinés tous les fils de connexion qui y aboutissent, est maintenu constant à 0,02°K près. La régulation est assurée par une chaîne comprenant un thermocouple différentiel Au–Fe (5 μV par °K), un amplificateur à faible bruit (< 0,1 μV) et une unité d'asservissement linéaire CAT (Leeds et Northrup). L'action corrective est obtenue par effet Joule dégagé sur l'écran. Cet ensemble est analogue à celui utilisé par Bonnerot[12] sur son calorimètre. Malgré de multiples précautions, une certaine quantité de chaleur est encore transmise par conduction à l'échantillon. Pour la compenser, il nous a fallu imposer un déséquilibre constant de température entre l'échantillon et l'écran. (c) La puissance destinée à accroître la température de l'échantillon est dégagée par effet Joule. Les mesures de tension et de courant sont effectuées à l'aide d'un voltmètre numérique DYMEC de résolution ± 1 μV. La détermination de la chaleur spécifique se fait par chauffage pulsé et l'on suit l'évolution des températures d'équilibre avant et après chauffage, afin d'en déduire l'accroissement de température. (d) La température est mesurée par une sonde au germanium dopé, étalonnée au millidegré par le NBS. Ce thermomètre est traversé par un courant taré, et la tension aux bornes est mesuré par le voltmètre numérique qui sert à déterminer la puissance dissipée. (e) Pour le calorimètre à gaz d'échange, qui a servi aux mesures sur Mo_2C, V_2C, $(Mo\text{–}V)_2C$, la suspension de l'échantillon était réalisée à l'aide de boucles de constantan maintenues par le fil de chauffage. Ce dernier était enroulé directement sur l'échantillon, et le tout était consolidé par du vernis. Nous utilisions également du vernis pour maintenir le thermomètre dans un trou ménagé à cet effet dans l'échantillon. Cet assemblage était modifié à chaque expérience, ce qui entraînait une non-reproductibilité de la chaleur spécifique des accessoires (attributable surtout au vernis, isolant organique à forte chaleur spécifique de réseau, dont la quantité était difficilement contrôlable). Le calorimètre à contact mécanique qui a servi à effectuer la mesure sur Nb_2C, est équipé d'un porte-échantillon, (de chaleur spécifique importante, mais absolument fixe) sur lequel sont enroulés définitivement tous les bobinages, et où le thermomètre est installé à demeure. Le contact avec l'échantillon est assuré par le serrage d'une vis de pression. Les mesures de chaleurs spécifiques ainsi obtenues sont beaucoup plus fidèles, surtout en ce qui concerne le terme de réseau. (f) Les mesures ont été effectuées entre 1,5 et 9°K sur le colorimètre à contact mécanique. Sur le calorimètre à gaz d'échange, les désorptions observées en dessous de 4°K ont rendu inutilisables les résultats correspondants. Toutefois, il nous a été possible de distinguer la transition supraconducteur-normal de Mo_2C.

(2) Les susceptibilités magnétiques ont été mesurées entre 77°K et l'ambiante à l'aide de la balance mise au point par Ducastelle [13].

4. RESULTATS

Nous avons reproduit à la Fig. 1 les valeurs de C_p/T en fonction de T^2, déduction faite d'une valeur moyenne de la chaleur spécifique des accessoires. Nous donnons en outre dans le Tableau 1 les valeurs du coefficient γ associé à la chaleur spécifique électronique, ainsi que les valeurs de la température de Debye.

Sauf pour Nb_2C, la précision sur θ_D n'est pas très bonne. Les valeurs de θ_D sont en effet très élevées, ce qui implique de faibles valeurs de α donc des erreurs relatives importantes, d'autant plus que la non-reproductibilité du dispositif de suspension affecte surtout la chaleur spécifique de réseau.

La différence entre la mesure actuelle sur Nb_2C et celle que nous avons citée à Enschede résulte en partie de l'amélioration apportée grâce au porte-échantillon. Il semble toutefois que les différences observées soient significatives et qu'elles doivent être reliées à la différence de structure cristalline: hexagonal non distordu (cet article) et orthorhombique (Enschede) [14]. Il ne nous a malheureusement pas été possible de refaire l'expérience sur la totalité de l'échantillon d'Enschede qui a été partiellement détruit. Elle a toutefois été refaite sur la partie restante (7 g environ)

Tableau 1

	Nb_2C	V_2C	$(Mo, V)_2C$	Mo_2C
γ(mJ/mole °K^2)	1,47 ± 1%	3,16 ± 5%	3,16 ± 5%	2,93 ± 5%
θ_D (°K)	520 ± 10%	490 ± 20%	468 ± 20%	531 ± 20%

$$\text{on a } C_p = \gamma T + \alpha T^3 \text{ avec} \begin{cases} \alpha = 1{,}941\ \theta_D^{-3} (\mathrm{J/°K^4\ mole}) \\ \gamma = 2{,}355\ N(E_F) (\mathrm{mJ/°K^2\ mole}) \\ N(E_F) \text{ en états/eV pour l'ensemble des} \\ \quad \text{états de spin et par atome de métal.} \end{cases}$$

et elle semble confirmer la différence citée plus haut.

On peut également penser que les différences observées entre nos mesures et celles de Toth sur Mo_2C[15] ont la même origine; la comparaison des diagrammes de Rudy et des paramètres cités par Toth laisse penser que l'échantillon de ce dernier est un mélange de phases hexagonale et orthorhombique (voir Fig. 2).

Les susceptibilités magnétiques sont données dans le tableau suivant:

	Nb_2C (non distordu)	V_2C	Mo_2C	MoVC
χ(en 10^{-6}u.e.m. /mole)	38,5	176,8	25,3	77,3

Ces susceptibilités ne dépendent pratiquement pas de la température, sauf pour Nb_2C où l'on observe une légère croissance avec la température.

5. DISCUSSION

Les coefficients de chaleur spécifique électronique obtenus sur nos échantillons sont portés à la Fig. 3, ainsi que ceux de Costa [1] sur Sc C, TiC, VC, TaC et ceux de Morin et Maita [16] sur les métaux purs de la seconde série de transition. On peut remarquer que la chute de γ de Mo_2C à Nb_2C est plus rapide que la variation observée de Mo_2C à V_2C. C'est en effet normal puisque la densité des états *d* est approximativement 1,5 fois plus élevée pour la première série de transition que pour la seconde.

Ces résultats suggèrent l'existence d'un minimum de la densité d'états pour un nombre d'électrons par atome un peu inférieur à celui des composés de la Vème colonne. Ce minimum se déplace progressivement lorsque l'on passe des métaux cubiques centrés (VIème colonne) aux sous-carbures hexagonaux (Vème colonne). *Ils suggèrent en outre l'existence d'une forme de bande peu sensible à la structure cristallographique.* Pour confirmer cette interprétation, il serait nécessaire de connaître la forme de la bande *d* pour la structure hexagonale compacte, de façon à vérifier qu'elle présente, comme les bandes des cubiques centrés et des cubiques à faces centrées de type NaCl, un minimum de la densité d'états correspondant au remplissage de la partie 'liante' de la bande.

La comparaison entre chaleurs spécifiques et susceptibilités magnétiques montrent que ces dernières ne sont pas de simples susceptibilités de Pauli. L'effet est surtout remarquable pour V_2C et MoVC. Le fait que le rapport $\pi^2 k_B{}^2\chi/3\mu_B{}^2\gamma$ s'écarte de l'unité peut être dû, soit à un effet de renforcement d'échange—ce qui paraît plausible pour les composés du vanadium, dernier élément non magnétique de la première série de transition—soit à *l'existence d'un terme orbital important (Van Vleck).* La comparaison des chaleurs spécifiques, des susceptibilités et du déplacement de Knight pour le vanadium et les deux carbures V_2C et VC[1, 17, 18, 20] semble bien confirmer la seconde hypothèse (Fig. 4): du carbure VC au sous carbure V_2C on observe une croissance de la susceptibilité alors que la chaleur spécifique décroît et que le déplacement de Knight passe de valeurs négatives fortes à des valeurs positives très élevées.

Si l'on admet que les effets d'échange sont responsables de la croissance de la susceptibilité on doit attendre une décroissance parallèle du déplacement de Knight K_S qui contient un terme négatif proportionnel à la susceptibilité de spin *d*. Cet effet n'est pas observé. On serait d'ailleurs conduit à des valeurs énormes du coefficient de renforcement. Si au contraire on fait l'hypothèse que cette croissance est essentiellement due au magnétisme orbital, les résultats sont cohérents: La très forte croissance ($-0{,}2$ à $+0{,}7$ pour cent) du déplacement de Knight est due au terme positif proportionnel à la susceptibilité de Van Vleck. Entre V_2C et V, au contraire, le terme orbital reste à peu près

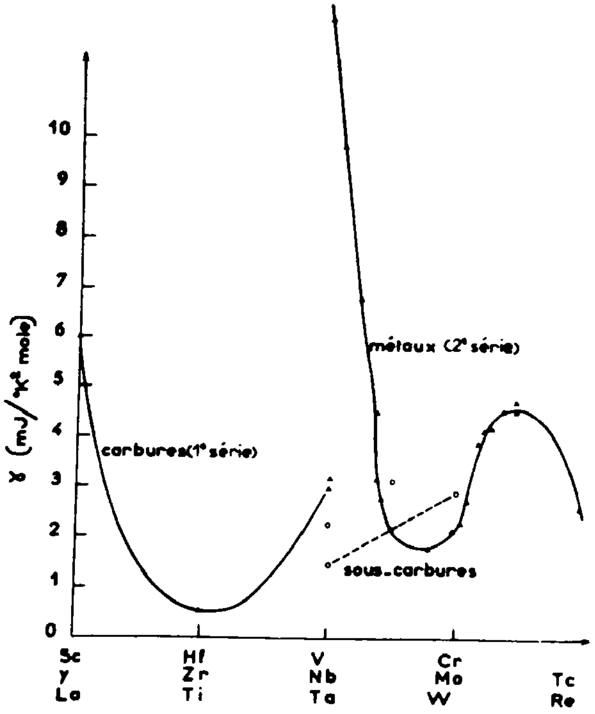

Fig. 3. Comparaison des coefficients de chaleur spécifique électronique des métaux de transition, de leurs carbures CFC et de leurs sous carbures hexagonaux.

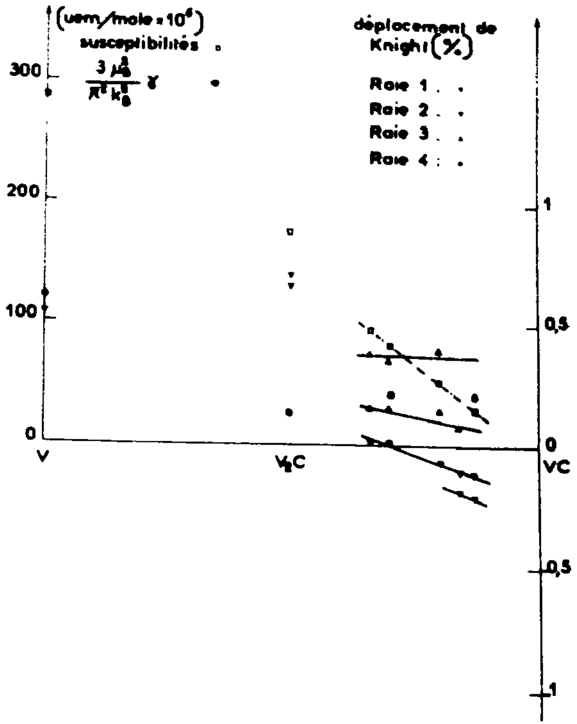

Fig. 4. Chaleurs spécifiques electroniques, susceptibilités magnétiques et déplacements de Knight des composés Vanadium–Carbone. Les différentes valeurs du déplacement de Knight sont extraites de l'article de Froidevaux et Rossier[18]. Elles correspondent, pour chaque composition nominale, à des atomes de Vanadium ayant 0,1, 2 ou 3 lacunes en carbone sur les six sites plus proches voisins (raies 1, 2, 3 et 4 respectivement).

stationnaire, comme le confirme la constance approximative de la quantité $\chi - 3\mu_B{}^2\gamma/\pi^2 k_B$. La densité d'états croît très fortement (croissance de γ et de χ, décroissance de K_s).

On aboutit d'ailleurs ainsi à un découpage de la susceptibilité du vanadium qui néglige les effets de renforcement d'échange et qui est bien celui qui est généralement admis.

La description précédente n'exclut pas un effet secondaire: décroissance du déplacement de Knight de V à VC à travers une décroissance éventuelle de la densité (4*s*).

BIBLIOGRAPHIE

1. COSTA P., *Mat. Int. in Nucl. Techn. AIME.* Boulder (1964).
2. DEMPSEY E., *Phil. Mag.* **86**, 8, 225.
3. LYE R. G., et LOGOTHETIS E. M., *Phys. Rev.* **147**, 622 (1966).
4. RUDY E. et CHANG Y. A., *Plansee proceedings* (1964).
5. PARTHE E., SADAGOPAN V., *Acta crystallogr.* **16**, 202 (1963).
6. KIEFFER R., et BENESOWSKY F., *Hartstoffe.* Springer, Berlin (1963).
7. RUDY E., WINDISCH St., STOSICK A. J. et HOFFMAN J. R., *Trans. Met. Soc. AIME* **239**, 1247, (1967).
8. YVON K., NOWOTNY H., KIEFFER R., *Mh. Chem.* **98**, 34 (1968).
9. ESCOFFIER P., *Chim. Anal.* **49**, No. 4 (1967).
10. NERNST W. et SCHWERS F., *Sitzler Akad. Wiss. Berlin.* **355** (1914).
11. CONTE R., *Rapport* No. CEA R 2854.
12. BONNEROT, *Rev. Phys. Appl.* **1**, 61, (1966).
13. DUCASTELLE F., *Note Technique* ONERA No. 3/1222 MN.
14. CAUDRON R., COSTA et SAULGEOT B., Communication présentée au *2ème Colloque International sur les composés solides des éléments de transition* Enschede-Groningen (1967). (les comptes rendus de cette conférence n'ont pas été publiés)
15. TOTH L. E. et ZBASNIK J., *Acta metallur.* **16**, 1115 (1968).
16. MORIN F. J. et MAITA J. P., *Phys. Rev.* **129**, 1115 (1963).
17. BITTNER H. et GORETZKI H., *Mh. Chem.* **91**, 616 (1960); *ibid.* **93**, 1000 (1962); *ibid.* **94**, 518 (1963).
18. FROIDEVAUX C. et ROSSIER D., *J. phys. Chem. Solids*, **28**, 1197 (1967).
19. VAN OSTENBURG D. O., LAM A. J., TRAP H. D. McLEOD D. E., *Phys. Rev.* **128** 1428 (1962).
20. BONNEROT, Travail non publié, Orsay.

J. Phys. Chem. Solids Pergamon Press 1970. Vol. 31, pp. 299–305. Printed in Great Britain.

RADIATION INDUCED MOVEMENT OF CHARGE COMPENSATING IONS IN CaF_2

J. W. TWIDELL
Department of Physics, University of Essex, Colchester, England

(*Received* 17 *July* 1969)

Abstract—Trivalent rare earth ions have been incorporated substitutionally in CaF_2 where charge compensation has occurred (a) by F^- interstitials and O^{2-} substitutional ions forming complexes with the trivalent ions, or (b) by processes remote from the trivalent ions. The ESR spectra of the magnetic rare earth ions indicate the presence or absence of n.n. compensating ions, and monitor the movement of these ions from or into n.n. sites. Ion movement has been stimulated by u.v. irradiation and electron bombardment, and changes in the valence state of the rare earth ions have occurred. Thermal annealing techniques give an activation energy for F^- interstitial movement of $1{\cdot}0 \pm 0{\cdot}1$ eV. The self-diffusion of oxygen in the CaF_2 lattice has been monitored in a new way.

INTRODUCTION

TRIVALENT rare earth cations may be incorporated substitutionally in the CaF_2 lattice with charge compensating mechanisms either near or remote. A number of authors have shown that there exist similar mechanisms for charge compensation for most rare earth trivalent ions in CaF_2[1–6]. The magnetic ions Er^{3+} and Yb^{3+} have been found particularly useful in investigation since their ESR spectra at 20°K clearly indicate the presence or absence of neighbouring charge compensation mechanisms.

The CaF_2 lattice has O_h^5 space group symmetry and may be visualised as a cubic lattice of F^- ions in which every alternate body centre is occupied by a Ca^{2+} cation. A substitutional trivalent rare earth cation may be compensated (a) by a remote defect or impurity cation that leaves the rare earth ion at a site of cubic symmetry, (b) by a n.n. F^- interstitial that produces a tetragonal distortion on the rare earth ion, (c) by a n.n. O^{2-} substitutional anion that produces a trigonal distortion, or (d) other less common impurity ions at various sites [7–9].

EXPERIMENTAL

X band ESR experiments at 20° and 4·2°K were performed on CaF_2 crystals doped with the rare earth ions La^{3+}, Ho^{3+}, Er^{3+}, Tm^{3+}, and, Yb^{3+} that were grown by the Stockbarger method. It became apparent that some of the crystal samples also contained oxygen ions that had been incorporated in the melt as the crystals were grown. The crystals could be irradiated by u.v. light from a quartz windowed mercury lamp, by 50 kV X-rays and by 4 MeV electrons. The crystals doped with Er^{3+} proved to be of interest for all three types of irradiation, and this system will be described in detail with occasional reference to the other dopant systems.

$CaF_2:Er^{3+}$ (a) *Initial properties*

One crystal of CaF_2 doped with Er^{3+} ions proved to be particularly free of oxygen or hydroxyl impurity ions. This was the same crystal as used by Baker, Hayes and Jones, [2]. Erbium ions have a 77 per cent abundant isotope of nuclear spin $I = 0$ and the ESR spectra of the trivalent ions of this isotope predominate over the spectra from other isotopes so that only the former are discussed here. Basically two types of ESR spectra were detected at 20°K, (i) an isotropic spectrum from ions on cubic sites with $g = 6{\cdot}78 \pm 0{\cdot}01$, (ii) a spectrum axially symmetric about cube edges from a tetragonal distortion with $g_{\parallel} = 7{\cdot}78 \pm 0{\cdot}02$, $g_{\perp} = 6{\cdot}253 \pm 0{\cdot}006$. A further tetragonally distorted spectrum reported by Baker, Hayes and Jones from an excited state could be detected at 20°, but not at 4·2°K.

(b) *X irradiation*

Figure 1(i) shows a group of X band ESR absorption lines at 20°K in the region $g \sim 6{\cdot}8$ in an unirradiated crystal sample of $CaF_2:Er^{3+}$.

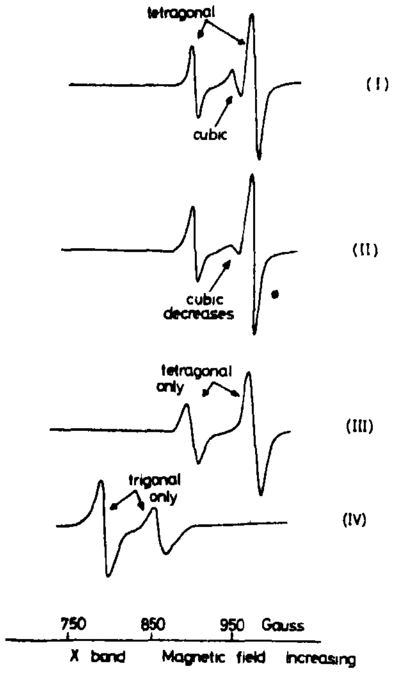

Fig. 1. Er^{3+} ESR spectra at 20°K, ⟨121⟩ direction. (i) Oxygen free crystal unirradiated; (ii) After 1 min X irradiation at 18°C; (iii) After 3 min X irradiation at 18°C; (iv) After heating in dry oxygen at 800°C for 60 hr

The sample was mounted to rotate in a (111) plane and the magnetic field is along a ⟨121⟩ direction. In this direction absorption lines from the different spectra indicated on the figure are clearly resolved. X irradiation at room temperature by a 50 kV Machlett tube producing 10^5 Rad (air) per minute did not colour the samples strongly but resulted in the ESR spectra of Fig. 1(ii) and (iii) after 1 and 3 min respectively. The isotropic spectrum has decreased as Er^{3+} ions on cubic sites have been reduced by the radiation to non-magnetic Er^{2+} ions[10–12]. The isotropic spectrum of Er^{3+} returned after the crystal had been heated above room temperature. The kinetics of this return process were such that the number of cubic Er^{3+} ions, n_t, after heating at T°K for t sec as indicated by the ESR spectrum at 20°K was

$$n_t = n_0 e^{-t/\tau}$$

where

$$1/\tau = \nu e^{-E/kT}$$

and

$$E = 1{\cdot}4 \pm 0{\cdot}2\ \text{eV}$$
$$\nu = 10^{21\pm 6}.$$

(c) *Ultra-violet irradiation*

Oxygen free samples of $CaF_2:Er^{3+}$ that showed the presence of Er^{3+} on cubic and tetragonal sites only were u.v. irradiated for several days at 0°C with a 9 W quartz windowed mercury low pressure lamp emitting mainly at 4·9 and 3·4 eV. The ESR spectra at 20°K then showed a 400 per cent increase in the number of Er^{3+} ions on cubic sites and a corresponding reduction in the number on tetragonally distorted sites. This is indicated in Fig. 2 where the ESR absorption lines are as described previously. It is concluded that the u.v. radiation has caused some of the n.n. F^- charge compensating interstitials to be freed from the $Er^{3+}:F^-$ complex, so leaving an increased number of Er^{3+} ions on cubic sites. It is to be noted that the u.v. radiation did not reduce the Er^{3+} ions on cubic sites to the divalent state. This movement of the F^- charge compensating interstitials at 0°C can be compared with the behaviour found by Friedman and Low[13] who succeeded in breaking up the $Er^{3+}:F^-$ complexes by heating the samples to 1200°C and quenching to room temperature.

After u.v. irradiation moderate heating

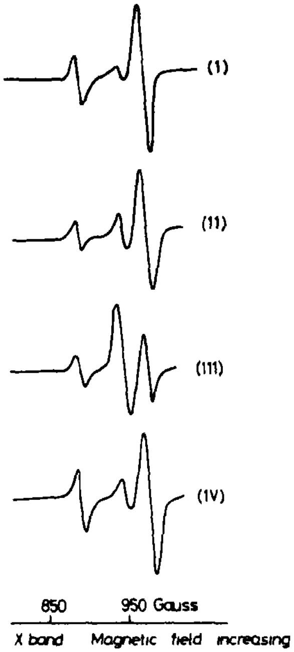

Fig. 2. Er^{3+} ESR spectra at 20°K, ⟨121⟩ direction. (i) Oxygen free crystal unirradiated; (ii) After 12 hr u.v. irradiation at 0°C; (iii) After 250 hr u.v. irradiation at 0°C; (iv) After heating u.v. irradiated sample (iii) to 200°C *in vacuo*.

resulted in the tetragonal spectrum increasing and the cubic spectrum decreasing as the F$^-$ interstitials were trapped to reform the Er^{3+}:F$^-$ complexes, Fig. 2(iv). An estimate can be made of the activation energy E for the return of the F$^-$ interstitials to the tetragonally distorted complexes. The rate dN/dt at which N_0 originally free interstitials are trapped at temperature T may be expressed by

$$-\frac{dN/dt}{N} = \nu e^{-E/kT} \qquad (1)$$

where ν is a pre-exponential constant.

At any time t the number of free interstitials will be therefore

$$N = N_0 e^{-t/\tau} \qquad (2)$$

and so

$$-dN/dt = N/\tau \qquad (3)$$

and from (1) and (3)

$$\ln \tau = E/kT - \ln \nu. \qquad (4)$$

If the number of Er^{3+} ions on cubic sites after total annealing is $C(\infty)$, then the number after time t of the annealing at temperature T is

$$C(t) = C(\infty) + N_0 e^{-t/\tau}. \qquad (5)$$

Likewise if the number of Er^{3+} ions on tetragonal sites at the start of the annealing is $G(0)$, then the number at time t is

$$G(t) = G(0) + N_0(1 - e^{-t/\tau}). \qquad (6)$$

If $R(t) = C(t)/G(t)$, then from (5) and (6) at temperature T

$$\frac{R(0) - R(\infty)}{R(t) - R(\infty)} = e^{t/\tau} \cdot \frac{1 + R(0)}{1 + R(t)} \qquad (7)$$

and if $M = e^{t/\tau}$ (8)

$$M = \frac{R(0) - R(\infty)}{R(t) - R(\infty)} \cdot \frac{1 + R(t)}{1 + R(0)}. \qquad (9)$$

Having found M for each annealing period of duration t, from (8)

$$\tau = t/\ln M \qquad (10)$$

and

$$\ln \tau = \ln (t/\ln M)$$

giving from (4)

$$\ln (t/\ln M) = E/kT - \ln \nu. \qquad (11)$$

The relative populations of Er^{3+} ions on cubic and tetragonal sites, R, was found directly from the relative intensity of the ESR absorption lines weighted according to the number of lines in each type of spectrum, i.e. 1:3.

Thermal annealing experiments indicated

that the return of the F^- interstitials after u.v. irradiation followed the process outlined above. Fig. 3 is a plot of $\ln(t/\ln M)$ against $1/T$, and fitting this to equation (11) gives

$$E = 1{\cdot}0 \pm 0{\cdot}1 \text{ eV}$$
$$\nu = 10^{13\pm 2} \text{ sec}^{-1}$$

and for example

$$\tau_{20°C} = 10^5 \text{ sec (28 hr)}$$
$$\tau_{50°C} = 2{\cdot}5 \times 10^3 \text{ sec (42 min)}.$$

(d) *Heating in dry oxygen*

If the X irradiated or unirradiated crystal samples were heated to about 800°C for 1 hr in dry oxygen both the isotropic and tetragonal ESR spectra at 20°K disappeared and a new trigonally distorted ESR spectrum appeared. This behaviour is indicated in Fig. 1 (iv) where that part of the new ESR spectrum near $g \sim 6{\cdot}8$ is shown. The new spectrum was identical to that reported by Ranon and Low [5] with $g_{\parallel} = 2{\cdot}20 \pm 0{\cdot}02$, $g_{\perp} = 8{\cdot}84 \pm 0{\cdot}03$, and was clearly due to the entry of oxygen O^{2-} ions into n.n. anion sites next to the Er^{3+} ions. X irradiation coloured the oxygenated samples strongly and after the irradiation the ESR spectrum at 77°K of O^{2-} ions was observed [14].

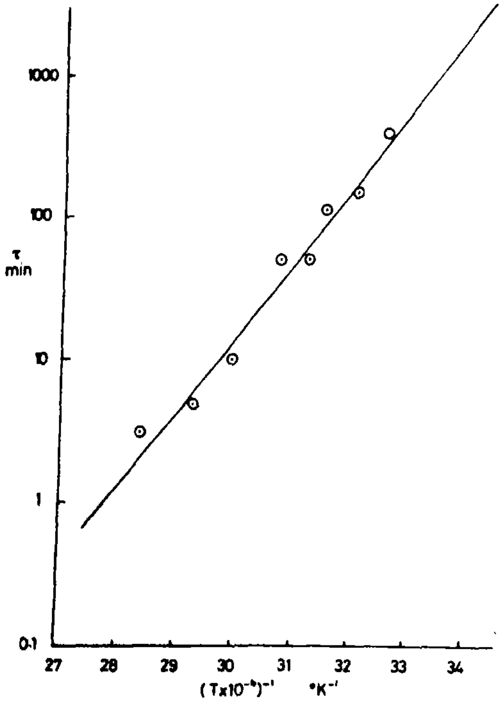

Fig. 3. Thermal annealing of F^- interstitial, equation (11). Slope equivalent to $E = 1{\cdot}0 \pm 0{\cdot}1$ eV.

The change from isotropic and tetragonal spectra to the trigonal spectrum could be followed by heating the samples for about fifteen minute intervals in dry oxygen and recording the changing ESR spectra at 20°K. The change was consistant with a diffusion constant for oxygen entry of $D \sim 10^{-7}$ cm^2 sec^{-1} at 800°C.

(e) *Electron irradiation of* O^{2-} *compensated samples*

Samples of $CaF_2{:}Er^{3+}$ that showed only the trigonal ESR spectrum from O^{2-} n.n. charge compensated complexes were irradiated at room temperature by 4 MeV electrons for one hour at 10^6 Rad (air)/min. After the irradiation ESR at 20°K showed the presence of about 20 per cent of the Er^{3+} ions now on cubic sites. It must be concluded that the electron irradiation collisions caused 20 per cent of the $Er^{3+}{:}O^{2-}$ complexes to break up leaving Er^{3+} ions on cubic sites with remote charge compensation. A high proportion of the oxygen ions removed from the complexes will be expected to remain in n.n.n. substitutional sites after the irradiation, and since no new type of ESR spectrum was observed after the irradiation it must be concluded that removal of an O^{2-} ion to a n.n.n. substitutional anion site leaves the Er^{3+} ion at a site of cubic symmetry. During the irradiation the crystal would be sufficiently hot, > 50°C, to prevent the permanent reduction of Er^{3+} ions on cubic sites to the divalent state.

$CaF_2{:}Yb^{3+}$. Samples of $CaF_2{:}Yb^{3+}$ showed the ESR spectra at 20°K of Yb^{3+} ions on cubic, tetragonal and trigonal sites (6). Heating the samples in dry oxygen at 800°C resulted in the disappearance of the cubic and tetragonal spectra and the appearance of an increased trigonal spectrum as oxygen ions entered the lattice at n.n. charge compensating anion sites. Ultra-violet irradiation at 0°C had no effect on the original crystal, and X irradiation reduced only the Yb^{3+} ions on cubic sites to the non-magnetic divalent state.

Table 1

Divalent ion:		La^{2+}	Er^{2+}	Tm^{2+}	Yb^{2+}
E eV		$0{\cdot}6 \pm 0{\cdot}1$	$1{\cdot}4 \pm 0{\cdot}2$	$0{\cdot}45 \pm 0{\cdot}05$	$1{\cdot}0 \pm 0{\cdot}2$
Produced	u.v.	No	No	Yes	No
by:	X	Yes	Yes	Yes	Yes

$CaF_2:Tm^{3+}$. The Tm^{3+} ion is non-magnetic and ESR does not directly reveal the types of charge compensating mechanisms. 4 MeV electron irradiation and subsequent X irradiation of a crystal thought to contain oxygen produced an increased number of magnetic Tm^{2+} ions on cubic sites than had been the case before electron irradiation. This is consistant with non-magnetic Tm^{3+}: O^{2-} complexes being broken up by the electron irradiation to leave Tm^{3+} ions on sites of cubic symmetry that could then be reduced by X irradiation at room temperature to the divalent state [10]. Ultra-violet irradiation by either the 4·9 or 3·4 eV emission from the mercury lamp caused Tm^{3+} ions on cubic sites to be reduced to Tm^{2+} divalent ions. This is the only instance of a trivalent rare earth ion being reduced by u.v. irradiation that has been found in CaF_2.

$CaF_2:La^{3+}$; $CaF_2:Ho^{3+}$. The La^{3+} and Ho^{3+} ions are non-magnetic and the only radiation effect observed was reduction to the magnetic divalent states of ions on cubic sites by X irradiation[11, 12]. Pulse annealing techniques above room temperature as described previously for the $CaF_2:Er^{3+}$ system enabled the activation energy to reform the trivalent ions to be found for most of the rare earth ions described in this paper. A summary of the activation energies, E, and method of production of the divalent ions from the trivalent ions on cubic sites at room temperature is given in the table below.

DISCUSSION

(a) *Reduction of trivalent ions*

Irradiation by 50 kV X-rays at room temperature reduced only the trivalent rare earth ions on cubic sites to the divalent state. Only Tm^{3+} ions could be also reduced by u.v. irradiation.

(b) *Oxygen diffusion*

The trigonally distorted Er^{3+} spectrum monitored the entry of O^{2-} ions into the doped CaF_2 samples, and could provide a new method for measuring the diffusion constants of oxygen ions in CaF_2.

(c) *4 MeV electron irradiation*

The break up of trigonally distorted Er^{3+}: O^{2-} complexes after electron irradiation provided a clear indication of the extent of damage in the crystal. During the irradiation the sample temperature would be expected to rise to about 50°C at which temperature oxygen substitutional ions would not be mobile and the complexes once broken up would not reform. The straight knock-on energy available in a 4 MeV electron–oxygen ion collision is about 1000 eV, which is ample to cause movement of ions in the lattice. Such experiments with orientated crystals in mono-energetic particle beams would provide a method for analysing displacement damage in crystals.

(d) F^- *interstitial displacement*

Ion displacement resulting from the absorption of u.v. or visible light has been proposed to explain a number of effects in ionic crystals. For example the U band absorption in alkali halide and alkaline earth halide crystals doped with hydrogen[15], Br^- ion displacement in Ag Br[16, 17] and the formation of cubic environments for impurity ions on previously distorted sites[18].

In the instance of the $Er^{3+}:F^-$ complex described here it would seem that the complex absorbs a u.v. photon and the resulting excited state configuration is at a higher energy with the F^- interstitial in a n.n. position than the configuration with the F^- interstitial in a n.n.n. position. Relaxation to the latter would be expected to take place in $\sim 10^{-13}$ sec before the final configuration returned to its groundstate in a time greater than this, typically $\sim 10^{-8}$ sec. The F^- interstitial would then be too far removed to affect the Er^{3+} ion then in a cubic environment, and at 0°C the interstitial would have a low probability of returning by diffusion.

Heating the crystal after u.v. irradiation enabled the F^- interstitials to return to reform the $Er^{3+}:F^-$ tetragonal complexes. The activation energy for this process, $E = 1{\cdot}0 \pm 0{\cdot}1$ eV, is clearly related to that derived from electrical conductivity and dielectric loss measurements for F^- interstitial movement in CaF_2. Chen and McDonough[19] and Southgate[20] investigated the anelastic and dielectric loss in Y doped CaF_2 and obtained an activation energy of $1{\cdot}2 \pm 0{\cdot}1$ eV for F^- jumps within a $Y^{3+}:F^-$ complex. Southgate assumed 0·3 eV of this was associated with the internal energy of the complex and 0·9 eV was associated with the movement of F^- interstitials. Lysiak and Mahendroo[21] postulated an activation energy of $0{\cdot}53 \pm 0{\cdot}05$ eV for F^- interstitial movement in their NMR studies of Sm doped CaF_2 in the extrinsic region below 900°K. Viegle[22] obtained a value of 0·63 eV for F^- interstitial diffusion in his NMR linewidth studies in CaF_2. Arkhangel'skaya *et al.*[23] and Nikitinskaya *et al.*[24] have discussed electrical conductivity determined activation energies for F^- vacancy and interstitial movement in the light of results obtained from oxygen and rare earth doped samples of CaF_2.

The results outlined above seem to be in disagreement with those of Ure[25] who gave an activation energy of $1{\cdot}65 \pm 0{\cdot}35$ eV (38 ± 8 kcal mole^{-1}) from electrical conductivity measurements on CaF_2 for assumed F^- interstitial movement, and of Fong and Hiller [26] who postulated an energy of 1·5 eV (34·8 kcal mole^{-1}) for F^- interstitial movement during reduction of $CaF_2:Dy^{3+}$ samples in calcium vapour. Fong himself however[27] points out the difficulty of interpreting electrical conductivity measurements due to F^- interstitial movement.

Acknowledgements — The author wishes to express his gratitude to Dr. W. Hayes and Mr. A. Legeat for helpful discussion

REFERENCES

1. BAKER J. M., DAVIES E. R. and HURRELL J. P., *Phys Lett.* **26A**, 352 (1968).
2. BAKER J. M., HAYES W. and JONES D. A., *Proc. phys. Soc. Lond.* **73**, 942 (1959).
3. BOBROVNIKOV Y. A., ZVEREV G. M. and SMIRNOV A. I., *Soviet Phys solid St.* **8**, 1750 (1967).
4. DVIR M. and LOW W., *Proc. phys Soc. Lond* **75**, 136 (1960).
5. RANON U. and LOW W., *Phys. Rev.* **132**, 1609 (1963).
6. WEBER M. J. and BIERIG R. W., *Phys. Rev.* **134A**, 1492 (1964).
7. McLAUGHLAN S. D., *Phys. Rev.* **160**, 287 (1967).
8. KAFRI A., KIRO D., YATSIV S. and LOW W., *Solid-St. Commun.* **6**, 573 (1968).
9. RANON U. and YANIV A., *Phys. Lett.* **9**, 17 (1964).
10. HAYES W. and TWIDELL J. W., *J. chem. Phys.* **35**, 1521 (1961)
11. HAYES W., JONES G. D. and TWIDELL J. W., *Proc. phys. Soc.* **81**, 371 (1963).
12. HAYES W. and TWIDELL J. W., *Proc. phys. Soc.* **82**, 330 (1963).
13. FRIEDMAN E. and LOW W., *J. chem. Phys.* **33**, 1275 (1960).
14. BILL H. and LACROIX R., *Phys. Lett.* **22**, 250 (1966); *Helv. phys. Acta* **39**, 189 (1966).
15. POHL R. W., *Proc phys. Soc.* **49**, (Appendix) 3 (1937).

16. MOTT N. F. and GURNEY R. W., *Elect. proc. ionic crystals*, p. 212. Oxford (1948).
17. SIETZ F. and KOEHLER J. S., *Solid-St. Phys.* **2**, 328 (1956).
18. WILKENS J., Thesis, University of Oxford (1961).
19. CHEN J. W. and McDONOUGH M. S., *Bull. Am. phys. Soc.* **9**, 647 (1964).
20. SOUTHGATE P. D., *J. Phys. Chem. Solids* **27**, 1623 (1966).
21. LYSIAK R. J. and MAHENDROO P. P., *J. chem. Phys.* **44**, 4025 (1966).
22. VEIGELE W. J., *Bull. Am. phys. Soc.* **9**, 25 (1964).
23. ARKHANGEL'SKAYA V. A., NIKITINSKAYA T. I., TYUTIN M. S., *Soviet Phys. solid St.* **7**, 2976 (1966).
24. NIKITINSKAYA T. I., SUNTSOV E. V. and TYUTIN M. S., *Soviet Phys. solid St.* **9**, 1656 (1968).
25. URE R. W., *J. chem. Phys.* **26**, 1363 (1957).
26. FONG F. K. and HILLER M. A., *J. phys. Chem.* **71**, 2854 (1967).
27. FONG F. K., In *Progress in Solid State Chemistry* (Edited by H. Reiss), Vol. 3, p. 135. Pergamon Press, London (1967).

J. Phys. Chem. Solids Pergamon Press 1970, Vol. 31, pp. 307-313. Printed in Great Britain.

THE SCALING OF THE PHONON FREQUENCIES IN THE DIAMOND-TYPE CRYSTALS*

MARK MOSTOLLER†
Florida Atlantic University, Boca Raton, Fa. 33432, and Harvard University,
Cambridge, Mass. 02138, U.S.A.

(*Received* 5 *May* 1969; *in revised form* 2 *July* 1969)

Abstract—A simplified point ion model for the phonon force tensors in the diamond-type crystals, derived from Baym's first principles treatment of lattice vibrations in the harmonic approximation, is used in preference to the shell model; in the point ion model, the interaction between a pair of ions in the vibrating lattice is essentially a Coulomb potential screened by the electrons. It is shown that if the screening is weakly dependent on the electron density in Si, Ge, and α-Sn, then the phonon frequencies ω_{qj} in these crystals scale approximately as observed by Kucher, $\omega_{qj}^2 = [(4e)^2/Ma^3]\Omega_{qj}^2$, where Ω_{qj} is a dimensionless frequency that is independent of the particular material being considered. Evidence is presented in the RPA to support this explanation of the scaling.

1. INTRODUCTION

IT IS WELL known that the phonon spectra of the diamond-type crystals are similar, but the approximate analytic form that this similarity takes is perhaps not so familiar. On the basis of experimental information and fitted shell model calculations, Kucher[1] observed that to a first approximation, the phonon frequencies in silicon, germanium, and gray tin scale as

$$\omega_{qj}^2 = \frac{(4e)^2}{Ma^3}\Omega_{qj}^2 \tag{1}$$

where ω_{qj} is the frequency of the phonon mode at wave vector q in the jth branch of the spectrum, e is the magnitude of the electronic charge, M is the ionic mass, a is the lattice constant, and Ω_{qj} is a dimensionless frequency which is independent of the particular material being considered.

The approximate observed scaling[1] of the phonon spectra makes it possible to calculate phonon functions in gray tin, for which little experimental information is available, and it allows simultaneous treatment of silicon, germanium, and gray tin. Diamond, whose ionic cores contain no p electrons, is somewhat anomalous, and it will therefore not be included in the discussion. Kucher notes that $(4e)^2/Ma^3$ is the only combination of ionic charge $4e$, ionic mass M, and lattice constant a which is dimensionally a frequency squared, but he gives no further explanation for the scaling.

The lattice vibrations in the diamond-type crystals have been treated in two ways in the literature. The traditional approach with fitted short range force constants gives poor results for the phonon frequencies[2, 3], while shell model calculations [4-7], although reasonably successful in fitting the phonon spectra with relatively few adjustable parameters, rely on questionable assumptions in Si, Ge, and α-Sn, applying a tight binding picture to materials in which the nearly-free-electron approximation is more appropriate.

As described by Cochran[4], the shell model is a simple phenomenological method of determining the phonon frequencies. Each

---

*Supported by grants from the National Science Foundation, the Advanced Research Projects Agency, and the Air Force Office of Scientific Research.

†This work is based in part on a section of a thesis submitted to Harvard University in partial fulfillment of the requirements for the Ph.D. degree.

atom is assumed to consist of a point ion core and a rigid, spherical shell of valence electrons. The Hamiltonian, expanded to second order in the core and shell displacements, is the sum of the following terms: the kinetic energies of the cores and shells; short range core–core, core–shell, and shell–shell interactions, with the range determined by the number of parameters needed to give a good fit to experiment; long range, bare electrostatic core–core, core–shell, and shell–shell interactions. From the equations of motion for the core and shell displacements, secular equations of twice the usual dimensions are derived, and these reduce to the normal size when the masses of the electron shells are neglected. The phonon dispersion curves are then found by diagonalizing the reduced secular equations and fitting elastic constants and particular frequencies to experiment.

Although in practice the Russian shell model calculations[5–7] are equivalent to Cochran's simple phenomenological description, Tolpygo[8] has also attempted to provide a theoretical basis for the model, using a perturbation expansion based on tight-binding electron wave functions in the Hartree–Fock approximation. If Tolpygo's tight-binding assumptions are not questioned, it is clear how the long range electrostatic interactions of the shell model are obtained, but the short range force constants are never explicitly defined in terms of electronic overlap integrals or matrix elements, and no such explicit definition of the short range interactions is given in the germinal paper[9] to which Tolpygo refers the reader.

The shell model gives reasonably good agreement with experiment in the diamond-type crystals, but it has not been given a sound physical or theoretical explanation. The introduction of weightless electronic shells in the calculation of the phonon frequencies has two major effects. First, because the shells adjust (adiabatically) to ionic motion, the direct core–core interactions are screened, although the screening is not exhibited explicitly. Second, by multiplying the number of phenomenological short range parameters which describe the interaction between two atoms by a factor of three, it makes a fit to experimental data a good deal easier and still allows cut-off of the short range force constants at nearest or next-nearest neighbors. In a very simple way, the shell model allows the electronic response in the crystal to affect the ionic motion, introducing long range dipole–dipole interactions, and it is probably for that reason that fewer parameters are required in the shell model than in the standard approach.

A large number of calculations of electronic properties in the Group IV semiconductors and related solids have, however, indicated that the electrons in these crystals should be treated as nearly-free rather than tightly-bound or highly localized as they are in the shell model. In particular, the electron-phonon interaction in these lattices can be treated by assuming weak ionic pseudo-potentials and 'smooth' electron states[10–13]. It is therefore more reasonable to describe the electrons as a continuous gas that screens the ionic core–core interactions instead of as a collection of movable or deformable shells associated with individual ions.

In Section 2, we discuss a simple point ion model for the phonon force tensors; in this model, the interionic interaction is essentially a Coulomb potential screened by the electrons. If the dielectric response of the electrons is approximately independent of the electron density in Si, Ge, and α-Sn, we find that the phonon frequencies in these crystals calculated from the point ion force constants scale as observed by Kucher,

$$\omega_{qj}^2 = \frac{(4e)^2}{Ma^3}\Omega_{qj}^2 .$$

In Section 3, evidence is presented that in the RPA, the density or lattice constant dependence of the screening is weak in the diamond-type crystals, making the approximate observed scaling plausible. While the point ion model used here to consider the scaling is somewhat oversimplified, similar dielectric screening approaches which include non-central forces have recently been applied to the phonon spectra of semiconductors[14, 15].

2. THE POINT ION MODEL

The determinantal equation for the phonon frequencies in the point ion model is obtained [16] by using an approach based on Baym's [17] first principles treatment of lattice vibrations in the harmonic approximation. Beginning with a crystal Hamiltonian that includes the electronic and ionic kinetic energies and ion–ion, electron–ion, and electron–electron interactions, an equation for the retarded phonon Green's function, correct to second order in the displacements of the ions from their equilibrium positions, is derived by functional derivative techniques. This equation is then simplified by making the following assumptions and approximations:

1. The energy of the system is unchanged by an arbitrary uniform translation of the crystal;
2. The non-Coulombic parts of the unscreened ionic potentials do not overlap when the ions occupy their equilibrium positions;
3. Terms involving the quadrupole moments of the ions can be neglected in comparison to those involving the ionic charges;
4. $\epsilon^{-1}(\mathbf{r},\mathbf{r}';\ \omega_{qj})$, the frequency dependent dielectric response function or inverse longitudinal dielectric constant of the electrons at the phonon frequencies ω_{qj}, can be approximated by the static, translationally invariant form $\epsilon^{-1}(\mathbf{r}-\mathbf{r}')$.

In this procedure for simplifying the equation of motion for the phonon Green's function, the most important approximation made is the use of a translationally invariant electronic dielectric response function. This approximation has been successfully used to treat a variety of problems in crystals in which the valence electronic behavior is free-electron-like[11, 18–21], and in particular, Penn[22] indicates that this is a reasonable approximation in the Group IV semiconductors. With this simplification, the point ion model contains only central forces; this may be unacceptable for calculational purposes, but it facilitates a comparison of the screening effects in similar materials.

The phonon frequencies are the poles of the transform of the retarded phonon Green's function, or the zeroes of the determinant of its inverse. From the Green's function equation derived in the manner outlined, the phonon frequencies are the eigenvalues of a determinantal equation of the familiar form

$$\det\|M\omega_{qj}{}^2\delta_{\mathbf{bb}'}\mathscr{I}-\mathscr{B}_{\mathbf{bb}'}(\mathbf{q})\|=0 \qquad (2)$$

in which $\mathbf{b}$ and $\mathbf{b}'$ are basis vectors to the equilibrium ionic positions in the unit cell and $\mathscr{I}$ is the unit tensor in three dimensions, $\mathscr{I}_{ij}=\delta_{ij}$. $\mathscr{B}_{\mathbf{bb}'}(\mathbf{q})$ is the lattice transform of the force tensors $\mathscr{B}_{\mathbf{bb}'}(\mathbf{R}_l-\mathbf{R}_{l'})$,

$$\mathscr{B}_{\mathbf{bb}'}(\mathbf{q})=\sum_l e^{-iq\cdot R_l}\mathscr{B}_{\mathbf{bb}'}(\mathbf{R}_l) \qquad (3)$$

where $\mathbf{R}_l$ and $\mathbf{R}_{l'}$ are lattice vectors.

In real space, the force tensors in the point ion model are second derivatives of ion–ion interactions screened by the electrons. Denoting the bare ionic potential at r due to an ion at the origin by

$$v(r)=Zef(r), \qquad (4)$$

where $f(r)$ is dimensionally an inverse length, the screened ionic potential is

$$v_s(r)=Zef_s(r), \qquad (5)$$

with f_s defined in terms of f and the dielectric response function ϵ^{-1} of the electrons by

$$f_s(r)=\int d^3r'\epsilon^{-1}(\mathbf{r}-\mathbf{r})f(r') \qquad (6)$$

The point ion model force tensors in a homopolar crystal can then be written as

$$\begin{aligned}&\mathscr{B}_{\mathbf{bb}'}(\mathbf{R}_l-\mathbf{R}_{l'})=\\&-(Ze)^2\Big\{(1-\delta_{ll'}\delta_{\mathbf{bb}'})\mathscr{A}[(\mathbf{R}_l+\mathbf{b})-(\mathbf{R}_{l'}+\mathbf{b}')]\\&-\delta_{ll'}\delta_{\mathbf{bb}'}\sum_{l''\mathbf{b}''}(1-\delta_{ll''}\delta_{\mathbf{bb}''})\mathscr{A}[(\mathbf{R}_l+\mathbf{b})-(\mathbf{R}_{l''}+\mathbf{b}'')]\Big\}\end{aligned} \qquad (7)$$

where

$$\mathscr{A}(\mathbf{r}) = \nabla\nabla f_s(r)$$
$$= (\mathscr{I} - 3\mathbf{rr}/r^2)\frac{1}{r}\frac{df_s(r)}{dr} + (\mathbf{rr}/r^2)\nabla^2 f_s(r) \quad (8)$$

For the discussion of the scaling of the phonon spectra in Si, Ge, and α-Sn, we define dimensionless force constant transforms by

$$\zeta_{\mathbf{bb}'}(\mathbf{q}) = \frac{a^3}{(Ze)^2} e^{-i\mathbf{q}\cdot(\mathbf{b}-\mathbf{b}')}\mathscr{B}_{\mathbf{bb}'}(\mathbf{q}) \quad (9)$$

or, from equations (3) and (7)

$$\zeta_{\mathbf{bb}'}(\mathbf{q})$$
$$= -a^3 \sum_l \Big\{(1-\delta_{l0}\delta_{\mathbf{bb}'})e^{-i\mathbf{q}\cdot(\mathbf{R}_l+\mathbf{b}-\mathbf{b}')}.\mathscr{A}(\mathbf{R}_l+\mathbf{b}-\mathbf{b}')$$
$$-\delta_{\mathbf{bb}'}\sum_{\mathbf{b}''}(1-\delta_{l0}\delta_{\mathbf{b}''}).\mathscr{A}(\mathbf{R}_l+\mathbf{b}-\mathbf{b}'')\Big\} \quad (10)$$

Substituting equations (1) and (9) into equation (2), we obtain

$$\det\|\Omega_{qj}{}^2\delta_{\mathbf{bb}'}.\mathscr{I} - e^{-i\mathbf{q}\cdot(\mathbf{b}-\mathbf{b}')}\zeta_{\mathbf{bb}'}(\mathbf{q})\| = 0 \quad (11)$$

In a group of crystals having the same lattice structure and the same number of valence electrons per atom, the dimensionless frequencies $\Omega_{qj} = [Ma^3/(Ze)^2]^{1/2}\omega_{qj}$ will then be approximately independent of the particular material being considered if the dimensionless force tensors $\zeta_{\mathbf{bb}'}(\mathbf{q})$ are.

3. THE RPA SCREENED COULOMB FORCE TENSORS AND THE SCALING

With the assumptions that the ionic displacements are small, and that the non-Coulombic parts of the bare ionic potentials do not overlap when the ions occupy their equilibrium positions, the force tensors in the point model are derived from what are essentially screened Coulomb interactions. Accordingly, we set $f(r)$ equal to $1/r$, so that the screened ionic potential function $f_s(r)$ defined by equation (6) becomes

$$f_{sc}(r) = \int d^3r' \epsilon^{-1}(\mathbf{r}-\mathbf{r}')\frac{1}{r'} \quad (12)$$

or, in terms of the Fourier transforms of ϵ^{-1} and $1/r$,

$$f_{sc}(r) = \int \frac{d^3k}{8\pi^3} e^{i\mathbf{k}\cdot\mathbf{r}} \frac{4\pi/k^2}{\epsilon(k)} \quad (13)$$

For the static dielectric constant $\epsilon(k)$, we will use the free electron RPA result at $T = 0$ [23, 24],

$$\epsilon_{\mathrm{RPA}}(k) = 1 + \gamma_{FT}^2 \chi(k/k_F) \quad (14)$$

where k_F is the Fermi wave vector, γ_{FT} is the ratio of the Fermi–Thomas and the Fermi wave vectors,

$$\gamma_{FT}^2 = \frac{k_{FT}^2}{k_F{}^2} = \frac{4me^2}{\pi\hbar^2 k_F} \quad (15)$$

and the function χ is given by

$$\chi(x) = \frac{1}{2x^2}\left\{1 - \frac{1}{4x}(x^2-4)\log\left|\frac{x+2}{x-2}\right|\right\} \quad (16)$$

To express the RPA screened Coulomb interaction in terms of quantities more easily related to the lattice constant a, we introduce the usual dimensionless radius r_s defined in terms of the average electron density n_e and the Bohr radius a_0 by $(4\pi/3)a_0{}^3r_s{}^3 = 1/n_e$. The Fermi wave vector is inversely proportional to r_s,

$$k_F = \frac{c}{r_s} = \frac{3{\cdot}627\times 10^8}{r_s}(\text{Å})^{-1} \quad (17)$$

and γ_{FT}^2 is directly proportional to r_s,

$$\gamma_{FT}^2 = dr_s = 0{\cdot}6634\, r_s. \quad (18)$$

For diamond-type crystals, assuming four electrons per atom and measuring the lattice constant a in Angstroms, $r_s = 0{\cdot}3693\,a$; for silicon, germanium, and gray tin, $r_s = 2{\cdot}000$, 2·085, and 2·385 respectively.

As a function of the dimensionless variable

k_Fr and the electron density parameter r_s, it follows from equations (13), (14), (17) and (18) that the RPA screened Coulomb interaction can be written as

$$f_{sc}(r)=\frac{c}{r_s}g_{sc}(k_Fr;r_s) \tag{19}$$

where

$$g_{sc}(k_Fr;r_s)=\frac{2}{\pi k_Fr}\int_0^\infty dx\frac{\sin k_Frx}{x[1+dr_s\chi(x)]} \tag{20}$$

Correspondingly, the tensors $a^3\mathscr{A}^{sc}(r)=a^3\nabla\nabla f_{sc}(r)$ can be written in the form

$$a^3\mathscr{A}^{sc}(\mathbf{r})=\kappa\mathscr{F}(k_F\mathbf{r};r_s) \tag{21}$$

where $\kappa=[c/(r_s/a)]^3$ is a constant equal to $0{\cdot}9947\times10^3$ in the diamond-type crystals, and

$$\mathscr{F}(k_F\mathbf{r};r_s)=\frac{d}{d(k_F\mathbf{r})}\frac{d}{d(k_F\mathbf{r})}g_{sc}(k_Fr;r_s) \tag{22}$$

Substituting equation (21) into equation (10) for the dimensionless force tensors $\zeta_{\mathbf{bb}'}(\mathbf{q})$, we obtain

$$\begin{aligned}\zeta_{\mathbf{bb}'}^{sc}(\mathbf{q})\\ =-\kappa\sum_l\Big\{&(1-\delta_{lo}\delta_{\mathbf{bb}'})[e^{-i(\mathbf{q}/k_F)\cdot k_F\mathbf{r}}\mathscr{F}(k_F\mathbf{r};r_s)]_{\mathbf{r}=\mathbf{R}_l+\mathbf{b}-\mathbf{b}'}\\ &-\delta_{\mathbf{bb}'}\sum_{\mathbf{b}''}(1-\delta_{lo}\delta_{\mathbf{bb}''})[\mathscr{F}(k_F\mathbf{r};r_s)]_{\mathbf{r}=\mathbf{R}_l+\mathbf{b}-\mathbf{b}''}\Big\}\end{aligned} \tag{23}$$

If we neglect the r_s or lattice constant dependence of the screening by using some average value $\langle r_s\rangle_{Av}$ in $g_{sc}(k_Fr;r_s)$ and $\mathscr{F}(k_F\mathbf{r};r_s)$ for a group of crystals which have the same lattice structure and the same number of valence electrons per atom, the dimensionless screened Coulomb force tensors[23] yield the scaling of the phonon frequencies observed in the Group IV semiconductors. If r_s is replaced by $\langle r_s\rangle_{Av}$ over a limited range of electron densities, then since $k_F(\mathbf{R}_l+\mathbf{b}-\mathbf{b}')$ is a dimensionless vector defined by the lattice structure, $\zeta_{\mathbf{bb}'}^{sc}(\mathbf{q})$ becomes a dimensionless function of dimensionless variables which does not depend on the lattice constant, and, from equation (11), the dimensionless phonon frequencies Ω_{qj} are independent of the particular material being considered.

To see whether it is a reasonable approximation to use some average value of r_s to calculate the screened Coulomb force tensors $\zeta_{\mathbf{bb}'}^{sc}(\mathbf{q})$ in Si, Ge and α-Sn, we have used a program written by L. Beeferman and V. O'Donnell[25] to determine the RPA screening charge density $\nabla^2f_{sc}(r)/4\pi$ as a function of k_Fr and r_s in these crystals. Adopting the notation of Langer and Vosko[24], the Laplacian of $f_{sc}(r)$ can be written as

$$\nabla^2f_{sc}(r)=-4\pi\delta(\mathbf{r})+4\pi\Delta n_B(r) \tag{24}$$

or, measuring $\Delta n_B(r)$ in units of $k_F{}^3=(c/r_s)^3$ and indicating its functional dependence on k_Fr and r_s,

$$\nabla^2f_{sc}(r)=-4\pi\delta(\mathbf{r})+4\pi(c/r_s)^3\Delta n_B(k_Fr;r_s) \tag{25}$$

From equations (8), (21) and (22), the contribution of the screening charge density to $\mathscr{F}(k_F\mathbf{r};r_s)$ then is

$$\mathscr{F}(k_F\mathbf{r};r_s)|\nabla^2f_{sc}=4\pi(\mathbf{rr}/r^2)\Delta n_B(k_Fr;r_s) \tag{26}$$

where we have omitted the delta function in $\nabla^2f_{sc}(r)$ because $\mathbf{r}\neq0$ in equation (23) for $\zeta_{\mathbf{bb}'}^{sc}(\mathbf{q})$.

Figures 1 and 2 show the function $\Delta n_B(k_Fr;r_s)$ vs. k_Fr for the values of r_s appropriate for Si, Ge, and α-Sn at room temperature, assuming that four electrons per atom participate in the screening. The positions of the nearest and of the first four next nearest neighbors are marked on the k_Fr axis in Figs. 1 and 2 respectively. Table 1 gives numerical values for the RPA screening charge density $\Delta n_B(k_Fr;r_s)$ at the first five nearest neighbor distances, their

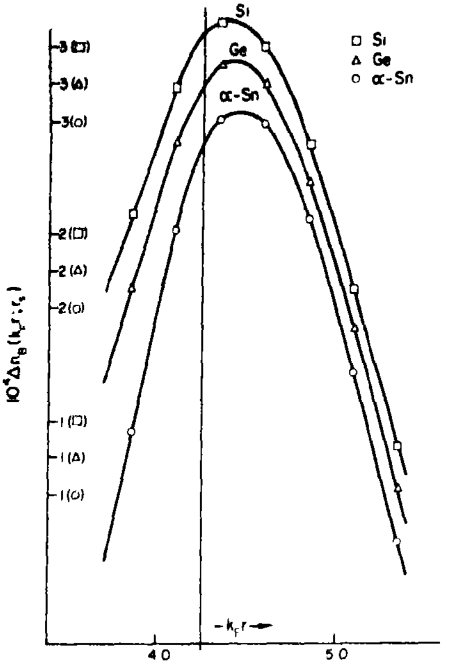

Fig. 1. The RPA screening charge density $\Delta n_B(k_F r; r_s)$ vs. $k_F r$ in Si, Ge and α-Sn. The nearest neighbor distance $k_F r_{nn}$ is marked with a vertical line.

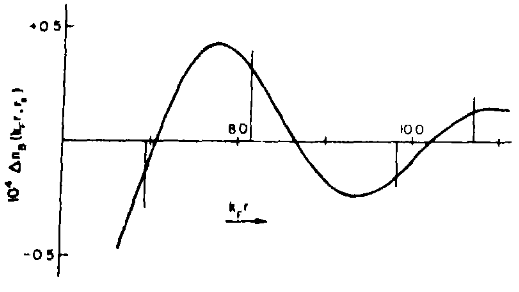

Fig. 2(a). The RPA screening charge density $\Delta n_B(k_F r; r_s)$ vs. $k_F r$ in Si. The first four next-nearest neighbour distances are marked with vertical lines.

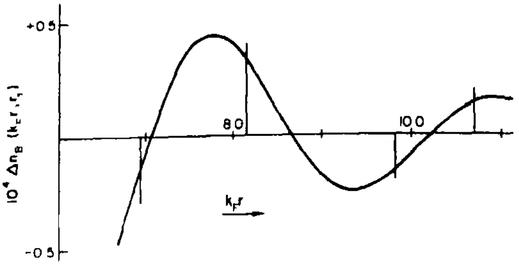

Fig. 2(b). The RPA screening charge density $\Delta n_B(k_F r; r_s)$ vs. $k_F r$ in Ge. The first four next-nearest neighbour distances are marked with vertical lines.

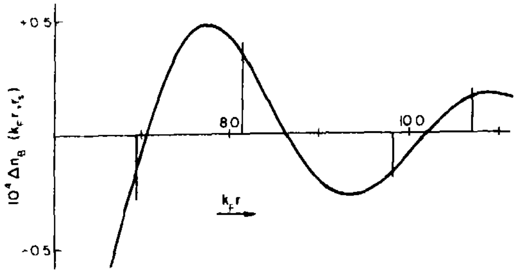

Fig. 2(c). The RPA screening charge density $\Delta n_B(k_F r; r_s)$ vs. $k_F r$ in α-Sn. The first four next neighbour distances are marked with vertical lines.

averages, and the percentage r.m.s. deviations of the values for the three crystals from the averages. The figures and the table show clearly that $\Delta n_B(k_F r; r_s)$ does not change much in going from Si through Ge to α-Sn, and that the values for Si and Ge are particularly close. To a first approximation, some single value $\langle r_s \rangle_{Av}$ may therefore be used to calculate the contributions of the screening charge density to the tensors $\mathcal{F}(k_F \mathbf{r}; r_s)$ and hence to the dimensionless force constants $\zeta^{sc}_{bb'}(\mathbf{q})$.

In a group of crystals having the same lattice structure and the same number of valence electrons per atom, the point ion model yields the approximate scaling $\omega^2 \sim (Ze)^2/Ma^3$ when the r_s dependence of the electron screening is weak. This apparently is the case in the diamond-type crystals. To test the general observation of this scaling, we looked at the phonon spectra of the monovalent metals Li, Na and K, and found that a different and more approximate scaling occurs. Krebs[26] has fitted calculated phonon dispersion curves for these metals to experimental data taken at or near liquid nitrogen temperatures. Using his results to compare the phonon frequencies in Li, Na and K at several symmetry points, we found that something like $\omega^2 \sim (Ze)^2/Ma^2$ is observed, although there is considerable spread about this.

The values of r_s for Li, Na and K are about 2·6, 3·1 and 3·9 respectively, higher than those for Si, Ge and α-Sn, and much more

Table 1. *The dimensionless* RPA *screening charge density* $\Delta n_B(k_F r; r_s)$ *in* $Si(r_s = 2\cdot000)$, $Ge(r_s = 2\cdot085)$ *and* α-$Sn(r_s = 2\cdot385)$ *at the first five nearest neighbor distances*

		$k_F r_{nn}$				
		4·253	6·945	8·144	9·822	10·703
$10^4\Delta n_B(k_F r; r_s)$	*Si*	3·06	−0·135	0·322	−0·149	0·132
	Ge	2·99	−0·135	0·330	−0·153	0·134
	α-Sn	2·87	−0·158	0·353	−0·164	0·150
$10^4\langle\Delta n_B(k_F r; r_s)\rangle_{Av}$*		2·97	−0·143	0·335	−0·155	0·139
$\dfrac{\sqrt{\langle[\delta\Delta n_B(k_F r; r_s)]^2\rangle_{Av}}}{\lvert\langle\Delta n_B(k_F r; r_s)\rangle_{Av}\rvert}$†		0·03	0·08	0·04	0·04	0·06

$$^*\langle\Delta n_B(k_F r; r_s)\rangle_{Av} = \tfrac{1}{3}\sum_{Si,Ge,\alpha\text{-}Sn}\Delta n_B(k_F r; r_s)$$

$$^\dagger\langle[\delta\Delta n_B(k_F r; r_s)]^2\rangle_{Av} = \tfrac{1}{3}\sum_{Si,Ge,\alpha\text{-}Sn}\{\Delta n_B(k_F r; r_s) - \langle\Delta n_B(k_F r; r_s)\rangle_{Av}\}^2.$$

widely spaced. It is therefore less likely that an average value for r_s can adequately describe the screening in the three metals. Langer and Vosko's[24] plots show that the oscillations in $\Delta n_B(k_F r; r_s)$ become more pronounced as r_s changes at a fixed value of $k_F r$. The different and very rough scaling $\omega^2 \sim (Ze)^2/Ma^2$ we find in Li, Na and K is thus not too surprising.

Acknowledgements – The author is particularly grateful to Professor Henry Ehrenreich for his encouragement and guidance. It is also a pleasure to thank Professor Arthur Bienenstock for helpful discussions, and Mr L. Beeferman and Mr. Vincent O'Donnell for providing the program for the RPA screening charge density.

REFERENCES

1. KUCHER T. I., *Soviet Phys. solid St.* **4**, 1747 (1963) [Translated from *Fiz. Tverd Tela* **4**, 2385 (1962)].
2. HSIEH Y. C., *J. chem. Phys.* **22**, 306 (1954).
3. SMITH H. M. J., *Trans. R. Soc. (Lond.)* **A241**, 105 (1948).
4. COCHRAN W., *Proc. R. Soc.* **A253**, 260 (1959).
5. DEMIDENKO Z. A., KUCHER T. I. and TOLPYGO K. B., *Soviet Phys. solid St.* **3**, 1803 (1962) [Translated from *Fiz. Tverd. Tela* **3**, 2482 (1961)].
6. DEMIDENKO Z. A., KUCHER T. I. and TOLPYGO K. B., *Soviet Phys. solid St.* **4**, 73 (1962) [Translated from *Fiz. Tverd. Tela* **4**, 104 (1962)].
7. KUCHER T. I., *Soviet Phys. solid St.* **4**, 729 (1962) [Translated from *Fiz. Tverd. Tela* **4**, 992 (1962)].
8. TOLPYGO K. B., *Soviet Phys. solid St.* **3**, 685 (1961) [Translated from *Fiz. Tverd. Tela* **3**, 943 (1961)].
9. MASHKEVICH V. S. and TOLPYGO K. B., *Soviet Phys. JETP* **5**, 435 (1957).
10. YU S. C. and BROOKS H., Unpublished manuscript; see also YU S. C., Ph.D. Thesis, Harvard University (1964).
11. HARRISON W. A., *Pseudopotentials in the Theory of Metals*. Benjamin, New York (1966).
12. AUSTIN B. J., HEINE V. and SHAM L. J., *Phys. Rev.* **127**, 276 (1962).
13. SHAM L. J. and ZIMAN J. M., In *Solid State Physics* (Edited by F. Seitz and D. Turnbul), Vol. 15, p. 221. Academic Press, New York (1963).
14. MARTIN R. M., *Phys. Rev. Lett.* **21**, 536 (1968).
15. KEATING P. N., *Phys. Rev.* **175**, 1171 (1968).
16. MOSTOLLER M., The temperature dependence of the electron energies in semiconductors, Ph.D. Thesis, Harvard University (1968).
17. BAYM G., *Ann. Phys.* **14**, 1 (1961).
18. KANE E. O., *Phys. Rev.* **146**, 558 (1966).
19. HEINE V. and ABARENKOV I., *Phil. Mag.* **9**, 451 (1964).
20. MORITA A. and NARA H., *Proc. Int. Conf. Physics of Semiconductors*, Kyoto (*J. phys. Soc. Japan* **21**, Suppl. p. 234 (1966).
21. ANIMALU A. O. E., *Phil. Mag.* **11**, 379 (1965).
22. PENN D. R., *Phys. Rev.* **128**, 2093 (1962).
23. PINES D., *Elementary Excitations in Solids*, p. 138. Benjamin, New York (1963).
24. LANGER J. S. and VOSKO S. H., *J. Phys. Chem. Solids* **12**, 196 (1959).
25. BEEFERMAN L. and O'DONNELL V., Private communication.
26. KREBS K., *Phys. Rev.* **138**, A143 (1965).

J. Phys. Chem. Solids Pergamon Press 1970. Vol. 31, pp. 315–319. Printed in Great Britain.

ENERGIE DE FORMATION DE MONOLACUNES DANS LES METAUX DE TRANSITION

MAURICE GERL
Laboratoire de Physique du Solide, E.N.S.M.I.M. 54 Nancy, France

(*Received* 2 *July* 1969)

Résumé – De la variation de densité d'états d'un cristal CC ou CFC quand on y introduit une lacune, on déduit l'énergie de formation E^F_{1V}. On utilise la méthode des moments dans l'approximation des liaisons fortes et on obtient la variation de E^F_{1V} en fonction du remplissage de la bande d pour les trois périodes de métaux de transition.

Abstract – The formation energy E^F_{1V} of a monovacancy is deduced from the modification of the density of states of the *d*-band when a vacancy is introduced in a perfect crystal. By means of the moments of the density of the *d*-band, the variation of E^F_{1V} with respect to the filling of the band is obtained for the transitional metals.

1. INTRODUCTION

COMME l'a mis en évidence Gschneider[1], un grand nombre de propriétés physiques des métaux de transition varient de manière sensiblement parabolique lorsque le coefficient de remplissage de la bande *d* varie de 0 à 1. Telle est l'allure par exemple de l'énergie de cohésion *Ec*, de la chaleur latente de fusion, de l'énergie de sublimation, de la tension superficielle γ_s des métaux de transition liquides, sauf pour les éléments de la première période pour lesquels des complications magnétiques interviennent.

Ce comportement des métaux de transition est bien expliqué en traitant la bande *d* dans l'approximation des liaisons fortes[2, 3]. L'objet de cet article est de chercher si la méthode permet un calcul approché de l'énergie de formation E^F_{1V} des monolacunes dans ces métaux, bien que les résultats expérimentaux dans ce domaine soient assez peu nombreux. Le seul métal où E^F_{1V} a été mesurée directement est Ni[4] pour lequel la valeur $E^F_{1V} = 1{,}4\,\text{eV}$ correspond bien aux valeurs expérimentales $Q = 2{,}9\,\text{eV}$[5] et $E_M = 1{,}5\,\text{eV}$ [6], où Q est l'énergie d'activation pour l'autodiffusion et E_M l'énergie de migration des monolacunes. Un ordre de grandeur de E^F_{1V} peut être déduit de la valeur de Q, mesurée dans un certain nombre de métaux et de la valeur de E_M calculée[6].

2. CALCUL DE E^F_{1V} – METHODE DES MOMENTS

2.1 *Méthode de calcul*

Mme Cyrot a montré[3] que la connaissance des premiers moments

$$\mu_n = \frac{1}{N}\int E^n\, n(E)\, dE$$

de la densité d'états suffit pour déterminer $n(E)$ et certaines propriétés physiques (E_c, γ_s), avec une bonne précision. Dans l'approximation des liaisons fortes, et dans une structure à un atome par maille, ces moments s'écrivent:

$$\mu_n = \sum_{i_2, i_3, \ldots, i_n} \langle i_1|V_{i_1}|i_2\rangle\langle i_2|V_{i_2}|i_3\rangle \ldots \langle i_n|V_{i_n}|i_1\rangle$$

$$\langle i|V_l|j\rangle = \int \psi^*(\mathbf{r}-\mathbf{R}_i)V_l(\mathbf{r}-\mathbf{R}_l)\psi(\mathbf{r}-\mathbf{R}_j)/d_3r$$

est l'intégrale de recouvrement à 2 centres i, j, les intégrales à 3 centres étant négligées.

Les intégrales de dérive $(i = j)$ étant en général beaucoup plus faibles que les intégrales de recouvrement $(i \neq j)$, μ_n s'interprète comme le produit d'intégrales de recouvrement le long d'un circuit fermé de n sauts.

Les approximations inhérentes au calcul

sont présentées dans la référence[3] et nous ne les rappellerons pas ici. La densité d'états $n_0(E)$ du cristal parfait étant connue par ses moments, on peut calculer l'énergie de cohésion

$$E_c = \int^{E_F^0} n_0(E)(E_0 - E)\,dE \qquad (1)$$

où E_0 est l'énergie des électrons d dans l'atome isolé, E_F^0 le niveau de Fermi du cristal parfait. Si la densité d'états varie de $n_0(E)$ à $n(E) = n_0(E) + \delta n(E)$ quand on introduit une lacune dans le cristal en portant un ion à un cran de la surface, l'énergie de formation E^F_{1V} de la lacune est:

$$E^F_{1V} = \int^{E_F^0} \delta n(E)(E - E_F^0)\,dE \qquad (2)$$

où $\delta n(E)$ est connue par l'intermédiaire de ses moments:

$$\delta\mu_n = \int E^n \delta n(E)\,dE$$

Dans l'expression (2) de l'énergie de formation, toute énergie de relaxation des ions autour de la lacune est négligée, ainsi que la polarisation des fonctions d'onde d au voisinage du défaut. L'énergie de formation obtenue sera donc certainement plus forte que les valeurs expérimentales.

2.2 *Détermination de* E_F^0, E_c, E^F_{1V}

Lorsque les moments de $n_0(E)$ sont connus jusqu'à l'ordre n, on peut approximer $n_0(E)$ par une série d'Edgeworth[3] qui a exactement les mêmes moments jusqu'à l'ordre n. Par exemple, avec les moments jusqu'à l'ordre 4:

$$n_0(E) = (2\pi\mu_2)^{-1/2} \exp - \frac{E^2}{2\mu_2} \times [a_0 + a_1E + a_2E^2 + a_3E^3 + a_4E^4]$$

avec les coefficients:

$$a_0 = (1+g);\ a_1 = -\tfrac{1}{2}h(\mu_2)^{-1/2};\ a_2 = -2g(\mu_2)^{-1}$$

$$a_3 = \tfrac{1}{6}h(\mu_2)^{-3/2};\ a_4 = \tfrac{1}{3}g(\mu_2)^{-2}$$

où l'on a posé:

$$g = \frac{1}{8}\frac{\mu_4 - 3\mu_2^2}{\mu_2^2};\ h = \frac{\mu_3}{(\mu_2)^{3/2}}$$

On obtient alors aisément le niveau de Fermi E_F^0 du cristal parfait en fonction du coefficient de remplissage z de la bande d[3]:

$$z = \int_{-\infty}^{E_F^0} n_0(E)\,dE = \sum_{n=0}^{4} a'_n J_n\left(\frac{E_F^0}{\sqrt{2\mu_2}}\right) \qquad (3)$$

où l'on a posé:

$$a'_n = \frac{a_n}{\sqrt{\pi}}(2\mu_2)^{n/2}$$

$$J_n(x) = \int_{-\infty}^{x} u^n e^{-u^2}\,du$$

L'équation (3) permet, par inversion, de déterminer E_F^0 en fonction de z. On obtient de même l'énergie de cohésion en fonction de E_F^0, donc de z:

$$E_c = -\int_{-\infty}^{E_F^0} En_0(E)\,dE = -(2\mu_2)^{1/2} \times \sum_{n=0}^{4} a'_n J_{n+1}\left(\frac{E_F^0}{\sqrt{2\mu_2}}\right) \qquad (4)$$

Pour déterminer E^F_{1V}, on calcule la variation $\delta\mu_n$ des moments jusqu'à l'ordre 4 en analysant le nombre $\delta\mu_n(L)$ de circuits d'ordre n supprimés dans le volume lors de l'introduction de la lacune et le nombre $\delta\mu_n(A)$ de circuits introduits quand l'atome est replacé à la surface:

$$\delta\mu_n = \delta\mu_n(A) - \delta\mu_n(L) \qquad (5)$$

La variation de densité d'états $\delta n(E)$ est alors approximée par la différence de deux séries d'Edgeworth limitées aux deux premiers termes:

$$\delta n(E) = \frac{1}{\sigma_1\sqrt{2\pi}}\exp\left[-\frac{E^2}{2\sigma_1{}^2}\right][1+b_1E]$$

$$-\frac{1}{\sigma_2\sqrt{2\pi}}\exp-\frac{E^2}{2\sigma_2{}^2}[1+b_2E] \quad (6)$$

Les constantes σ_1, σ_2, b_1, b_2 sont déterminées de manière à reproduire les moments de $\delta n(E)$ jusqu'à l'ordre 4:

$$\sigma^2_{1(2)} = \tfrac{1}{2}\left(\pm\delta\mu_2 + \frac{\delta\mu_4}{3\delta\mu_2}\right)$$

$$b_{1(2)} = \frac{1}{\sigma^2_{1(2)}}\cdot\frac{\delta\mu_3}{3\delta\mu_2}$$

On trouve alors aisément pour l'énergie de formation:

$$E^F_{1V} = A(\sigma_1) - A(\sigma_2) \quad (7)$$

avec

$$A(\sigma_i) = \sqrt{\frac{2}{\pi}}\sigma_i[J_1(y_i) + b_i'J_2(y_i)]$$

$$-\frac{E_F{}^0}{\sqrt{\pi}}[J_0(y_i) + b_i'J_1(y_i)] \quad (8)$$

et

$$y_i = \frac{E_F{}^0}{\sigma_i\sqrt{2}}$$

$$b_i' = (\sigma_i\sqrt{2})b_i$$

Le coefficient de remplissage z étant donné, on peut alors calculer $E_F{}^0$, E_c et l'énergie de formation E^F_{1V} en fonction des intégrales de recouvrement non nulles conservées dans le calcul.

3. RESULTATS

3.1 *Structure cubique à faces centrées (CFC)*

Dans la structure CFC les premiers voisins se trouvent à une distance $a/\sqrt{2}$ et les seconds voisins sont distants de a. Il est donc raisonnable de négliger les intégrales de recouvrement entre seconds voisins et de ne conserver que les intégrales entre premiers voisins. Des 5 intégrales de recouvrement ainsi conservées, nous n'en retenons qu'une seule, en fonction de laquelle nous calculons l'énergie de cohésion E_c et l'énergie de formation E^F_{1V}. Si α est la valeur de cette intégrale de recouvrement, nous obtenons les moments de $n_0(E)$ et $\delta n(E)$ (Tableau 1), lorsque A est placé à un cran d'une surface (111) (Fig. 1).

Tableau 1. CFC: *Moments de* $n_0(E)$ *et* $\delta n(E)$, *l'atome* A *étant placé à un cran d'une surface* (111) *et la lacune formée à l'intérieur du volume du cristal*

n	0	1	2	3	4
μ_n/α^n	1	0	12	48	540
$\delta\mu_n(L)/\alpha^n$	0	0	−24	−144	−1872
$\delta\mu_n(A)/\alpha^n$	0	0	12	48	540
$\delta\mu_n/\alpha^n$	0	0	−12	−96	−1332

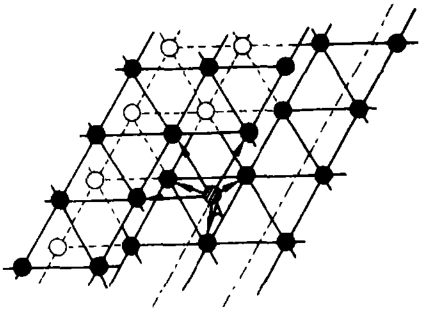

Fig. 1. Replacement d'un atome A à un cran d'une surface (111) d'un cristal CFC.

E_c et E^F_{1V} étant alors fonction du seul paramètre α, $R = E^F_{1V}/E_c$ est un nombre qui ne dépend que du remplissage de la bande *d*. Il est remarquable de noter que, si l'on considère uniquement les moments jusqu'à l'ordre 2, le rapport R est une constante indépendante du remplissage de la bande *d* alors que si l'on considère les moments d'ordre supérieur à 2, R varie avec z. Le modèle de liaisons coupées (circuits de deux sauts coupés) au voisinage de la lacune et rétablies à la surface ne donne donc qu'une estimation grossière de E^F_{1V}.

Connaissant l'énergie de cohésion expérimentale des métaux de transition CFC[1], on

déduit une estimation de l'énergie de formation des monolacunes:

$$E^F_{1V} = R(E_c)_{exp}$$

En supposant les calculs précédents valables pour la structure hexagonale compacte, très voisine de la structure CFC, nous avons calculé ainsi E^F_{1V} pour les métaux de transition HC ou CFC des première, deuxième et troisième périodes de la classification périodique (Figs. 2, 3 et 4).

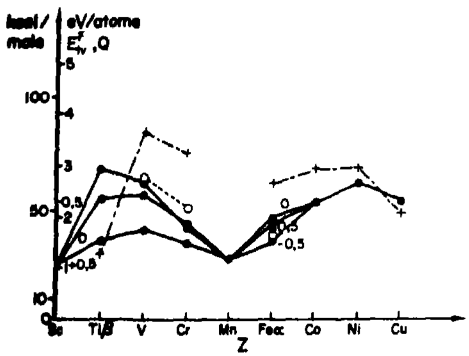

Fig. 2. Eléments de la première période.

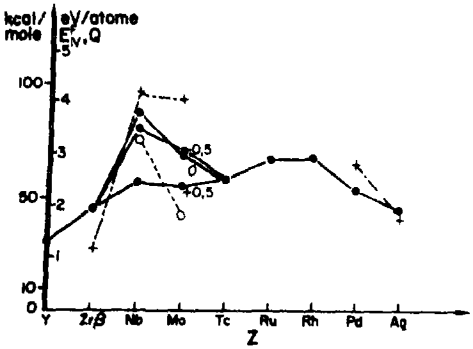

Fig. 3. Eléments de la deuxième période.

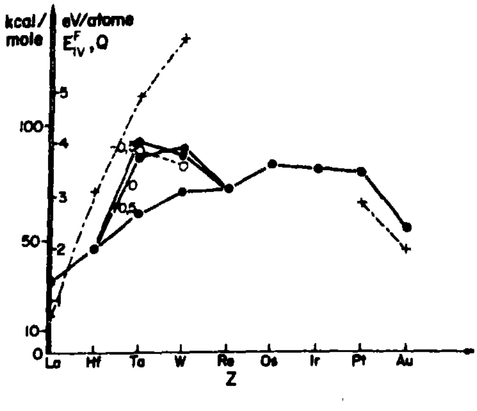

Fig. 4. Eléments de la troisième période.

Figs. 2, 3 et 4. Comparaison de l'énergie de formation E^F_{1V} calculée (——), β/α prenant les valeurs +0,5, 0 et −0,5 à:
(1) l'énergie d'activation Q pour l'autodiffusion (—·—)
(2) l'énergie de formation déduite du calcul de Flynn [6] (-------)

3.2 *Structure cubique centrée (CC)*

Dans la structure CC, les premiers voisins sont distants de $a\sqrt{3}/2$ et une distance égale à a sépare les seconds voisins. Cette différence de 14 pour cent environ entre ces deux distances laisse supposer que les intégrales de recouvrement β entre seconds voisins ne sont pas négligeables par rapport aux intégrales α entre premiers voisins. Les moments μ_n de $n(E)$ et de $\delta n(E)$ sont alors des polynômes de degré n en $\alpha\beta$ soit, en posant $t = \beta/\alpha$:

$$\mu_n = \alpha^n \sum_{m=0}^{n} A^{(n)}_{n-m}\, t^m$$

Les résultats du dénombrement des circuits de n sauts donnent alors les coefficients $A_n^{(m)}$ donnés dans le Tableau 2, pour une lacune L en volume et un atome A placé à un cran d'une surface (100):

On peut alors exprimer le rapport R de l'énergie de formation E^F_{1V} et de l'énergie de cohésion E_c en fonction du seul paramètre $t = \beta/\alpha$ et du remplissage de la bande d. Les Figs. 2, 3 et 4 donnent ainsi les résultats obtenus pour l'ensemble des métaux de transition, en choisissant les valeurs $t = 0,5$, $t = 0$ et $t = -0,5$ pour les cubiques centrés. On a représenté également les valeurs expérimentales de E^F_{1V} ou les valeurs déduites des énergies d'activation Q pour l'autodiffusion et des énergies de migration calculées par Flynn [6].

Tableau 2. Coefficients $A_m^{(n)}$ *intervenant dans l'expression des moments* μ_n*, pour une structure CC, la lacune étant créée en volume et l'atome* A *placé à un cran d'une surface* (100)

	$n = 2$		$n = 3$	$n = 4$		
	$A_2^{(2)}$	$A_0^{(2)}$	$A_2^{(3)}$	$A_4^{(4)}$	$A_2^{(4)}$	$A_0^{(4)}$
μ_n	8	6	72	216	576	90
$\delta\mu_n(L)$	−16	−12	−216	−736	−1824	−288
$\delta\mu_n(A)$	8	6	72	216	576	90
$\delta\mu_n$	−8	−6	−144	−520	−1248	−198

4. CONCLUSION

Ainsi que le montrent les Figs. 2, 3 et 4, la méthode développée par Mme Cyrot[3] conduit à des valeurs de E_{1V}^F reproduisant grossièrement l'évolution de l'énergie de formation le long des trois périodes des métaux de transition. Le calcul est cependant assez grossier, étant donné les hypothèses utilisées:

(i) une seule intégrale de chaque type α et β a été retenue; cette approximation revient à utiliser une intégrale moyenne des différentes intégrales de recouvrement possibles, ce qui est justifié pour le moment d'ordre 2 mais discutable pour les moments d'ordre plus élevé. Cette correction ne devrait pourtant pas modifier radicalement les ordres de grandeur obtenus.

(ii) le fait de négliger les relaxations atomiques autour du défaut lacunaire, ainsi que la polarisation des fonctions d'onde au voisinage du défaut doit introduire une erreur importante dans le calcul de E_{1V}^F. Il est donc difficile de déterminer quelle valeur de β/α conduit au meilleur accord avec les résultats expérimentaux.

Un calcul de relaxation serait théoriquement possible si l'on connaissait la variation des intégrales de recouvrement α et β avec la distance. Une analyse de ce genre permettrait un calcul self-consistant de l'énergie de formation et de l'énergie de migration d'une lacune dans un métal de transition. La variation de α et β avec la distance est cependant trop mal connue à l'heure actuelle[7] pour qu'un tel calcul soit réaliste.

Remerciements—J'ai plaisir à remercier Mme Cyrot, Monsieur Ducastelle et Monsieur le Professeur Friedel pour leurs conseils et critiques.

REFERENCES

1. GSCHNEIDER K. A., *Solid State Physics* (Edited by F. Seitz), Vol. 16, p. 275 (1964).
2. FRIEDEL J., *Transitional Metals. Electronic Structure of the* d *band.*
3. CYROT F., Thèse Orsay (1968); *J. Phys. Chem. Solids* **29**, 1235 (1968).
4. NAKAMURA N., *J. phys. Soc. Japan* **16**, 2167 (1961).
5. HOFFMANN R. E., PIKUS F. W. et WARD R. A., *Trans. AIME* **206**, 483 (1956).
6. FLYNN C. P., *Phys. Rev.* **171**, 682 (1968).
7. DUCASTELLE F. et CYROT F., À paraître.

J. Phys. Chem. Solids Pergamon Press 1970. Vol. 31, pp. 321–329. Printed in Great Britain.

TWO PHONON PROCESSES AND PHASE TRANSITIONS IN $KMnF_3$: TEMPERATURE DISCONTINUITIES IN THE I.R. SPECTRUM AND GROUP THEORETICAL ANALYSIS

H. P. BALTES, M. TOSI and F. K. KNEUBÜHL
Laboratorium für Festkörperphysik, Eidgenössische Technische Hochschule, Zurich, Switzerland

(*Received* 11 *February* 1969; *in revised form* 27 *June* 1969)

Abstract—The far i.r. reflection spectrum of $KMnF_3$ single crystals was measured for various temperatures between 65°K and room temperature. A multi-phonon sideband near 261 cm^{-1} was observed in the low temperature spectra, showing marked temperature discontinuities of the intensity at 88°K (= Néel temperature) and 190°K (= temperature of the transition from cubic to orthorhombic phase). At 190°K, the sideband disappears abruptly. The group theoretical study of two-phonon processes in $KMnF_3$ suggests an interpretation in terms of symmetry dependent multiphonon selection rules. Careful analysis of the behaviour of the critical points of the first Brillouin zone at the phase transition from O_h^1 to D_{2h}^{16} shows the existence of *R* and *M* processes forbidden in the higher and allowed in the lower symmetry phase. A precise assignment of the reflection band can, however, not be given.

1. INTRODUCTION

It is well known to spectroscopists that the qualitative structure of infrared and Raman spectra of solid materials is strongly related to crystal symmetry. As an example we mention the changes in selection rules and the splittings of degeneracies observed for normal mode (one phonon) frequencies in diamond[1], $KTaO_3$[2], and $SrTiO_3$[3, 4] when the symmetry is lowered by the application of electric fields. In our paper we intend to show that i.r. spectra may be useful in revealing the symmetry dependence of multiphonon processes for crystals having phases with different structures. $KMnF_3$ is an attractive material for the study of phase-change dependent phenomena, since its crystallographic structure is well known. X-ray data[5, 6] reveal two phase transitions, at 184°K a change from cubic (O_h^1) to an orthorhombic (D_{2h}^{16}) phase and at 88°K (= Néel temperature) to another orthorhombic phase. Perry and Young[7] recently published infrared reflection and transmission spectra of several perovskite fluorides. In $KMnF_3$ they observed a strong extra reflection band near 270 cm^{-1} which they tentatively assigned to TO_1+LO_1, TO_2+LA, and/or 0_4-TA two phonon transitions. We have measured the temperature dependence of this sideband between 65°K and room temperature in order to study the influence of crystallographic and magnetic phase changes on multiphonon processes. We found discontinuities at 190° and 88°K related to structural and magnetic transitions. Group theoretical considerations indicate symmetry-dependent multi-phonon selection rules.

2. EXPERIMENTAL TECHNIQUES AND RESULTS

Single crystals of $KMnF_3$ were kindly furnished by Dr. D. T. Teaney, IBM New York and by Semielements Inc., Saxonburg Pa. Our data were obtained from cleaved surfaces. The specular reflectance was measured using a Beckman I.R. 12 spectrometer with a spectral resolution better than 3 cm^{-1} and equipped with a Beckman microreflectance cell. Thus the angle of incidence was about 40°. Samples were mounted on the copper finger of a cryostat covering the range between liquid nitrogen and room temperature. The temperatures were determined by a copper-constantan thermocouple welded to the sample holder and the experiment gave evidence that the temperature difference between sample and holder was smaller than 1°.

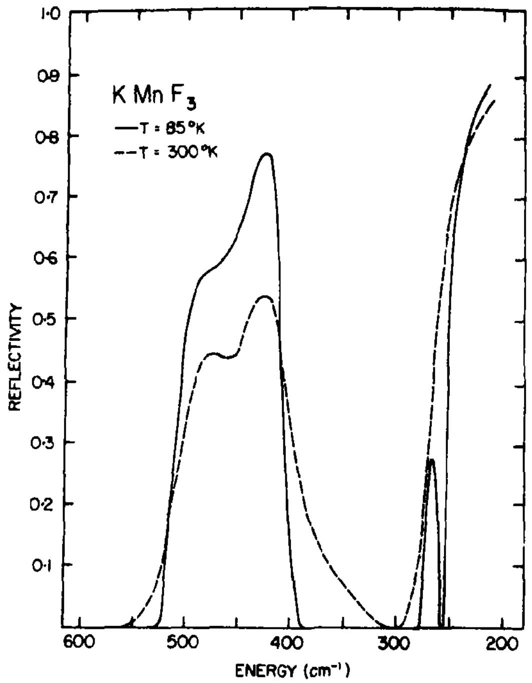

Fig. 1. Spectral reflectivity of a cleaved surface of a $KMnF_3$ crystal measured with an angle of incidence between 35° and 45°.

Figure 1 shows the reflectivity of $KMnF_3$ at 85° and 300°K between 200 and 600 cm^{-1}. The main bands correspond to the TO_2 (Γ') and TO_3 (Γ') single phonon modes[7] at 191 cm^{-1} and 414 cm^{-1}. The sideband appears in the low temperature spectrum near 270 cm^{-1} and it corresponds to two-phonon modes at 261 cm^{-1}[7]. Figures 2 and 3 demonstrate the behaviour of the two-phonon sideband for temperatures in the vicinities of the two phase transitions. Marked discontinuities appear at 190° and 88°K. The sideband vanishes above 190°K. The discontinuity at 190°K corresponding to the cubic-orthorhombic phase change occurs well above the 184°K determined by X-ray structure studies[5, 6]. This may be due to small amounts of Na in the $KMnF_3$ furnished by Semi-Elements. Na impurities are known to increase the transition temperature[8]. The slope of the reflectivity versus temperature curve at 260 cm^{-1} near 190°K (Fig. 2) is relatively flat compared with the slope of

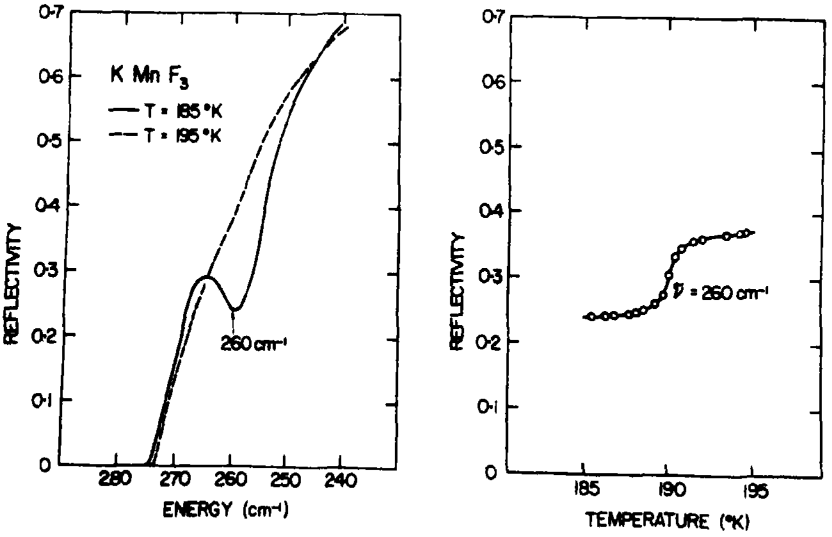

Fig. 2. Variation of the two-phonon sideband near 190°K.

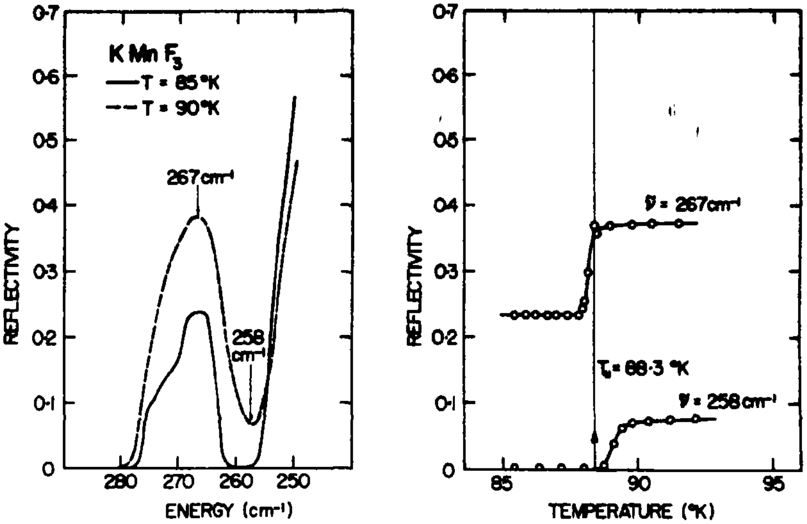

Fig. 3. Variation of the two-phonon sideband near the Néel temperature. The crystal orientation differs from that of Fig. 1. This explains the different peak values of reflectivity at 270 cm^{-1}.

the corresponding curve at 267 cm^{-1} near 88°K (Fig. 3).

According to Beckman and Knox[6] the transition at 88°K is accompanied by a discontinuity of the lattice parameters, whereas at 184°K the arrangement of the atoms in the crystal varies continuously and only the symmetry undergoes a sudden change. Nevertheless, a sharp anomaly in the elasticity of $KMnF_3$ single crystals in the vicinity of the upper phase transition was found[8]. Figure 4 shows a *speculative* phonon-band structure at 85°K compiled from the data and suggestions of Perry and Young [7]. From their calculations we have the impression that the assignments are arrived at from some kind of average energies of phonon branches at the zone boundary. The authors make no allowance for the distortion of the cubic symmetry existing at 85°K and its effects on the selection rules.

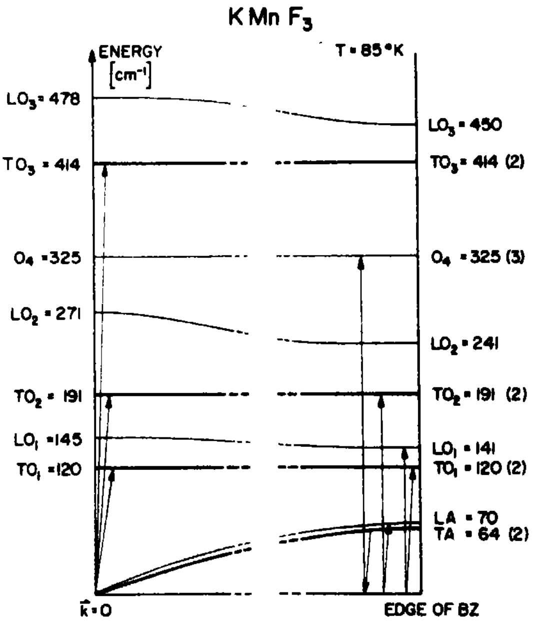

Fig. 4. Speculative dispersion curve compiled from the data given in [7]. The degeneracy of each branch at the zone boundary is given in brackets. The i.r. active one-phonon transitions as well as the possible two-phonon processes with 261 cm^{-1} energy are indicated by arrows. No exact branch assignments at the zone boundary can be given.

3. SELECTION RULES FOR TWO-PHONON PROCESSES

We should like to demonstrate that there may exist two-phonon processes forbidden for the cubic phase of $KMnF_3$ and allowed for lower symmetries. This fact would provide a plausible interpretation of the 190°K discontinuity in the reflection spectrum. The 88°K discontinuity can be explained on a similar basis. At this temperature the symmetry remains unchanged whereas the ratio c/a of the pseudocell dimensions decreases abruptly[6]. This results in a change of the band intensity, because the second order dipole moment responsible for the coupling of the two phonons depends on the atomic arrangement[9].

$KMnF_3$ possesses inversion symmetry in all phases. Thus only combination states may be ir-active whereas two-phonon overtones are forbidden[10, 11]. According to Birman[12–14] a two-phonon transition leading from the zero-phonon to the combination state

$$|(\mathbf{k}, m), (\mathbf{k}' \approx -\mathbf{k}, m')>$$

is dipole forbidden if the product

$$D^m(G(\mathbf{k}))\otimes D^{m'}(G(\mathbf{k}'))$$

does not contain the vector representation

$$D^{\text{vector}}(G(\mathbf{k}'' \approx 0)), \mathbf{k}'' = \mathbf{k}+\mathbf{k}'.$$

Here, $\mathbf{k}$ and $\mathbf{k}'$ are wave vectors of the critical points (c.p.) in the phonon dispersion. $G(\mathbf{k})$ is the space group of $\mathbf{k}$ and $D^m(G(\mathbf{k}))$ indicates its irreducible representation based on the m-th irreducible representation of $P(\mathbf{k}) = G(\mathbf{k})/T(\mathbf{k})$ with the invariant subgroup of translations $T(\mathbf{k})$. The calculation of this selection rule can be simplified using subgroups (e.g. $P(\mathbf{k})$) instead of the full space group symmetry[10, 15, 16]. Following Elliot and Loudon[15] we consider the common factor group of the wave vectors $\mathbf{k}$, $\mathbf{k}'$ and $\mathbf{k}''$. Therefore we have to classify the combination states according to irreducible representations of

$$P(\mathbf{k}) = P(\mathbf{k}' \approx -\mathbf{k}) \wedge P(\mathbf{k}'' \approx 0) = P(\Gamma).$$

According to Phillips[17] critical points in the phonon dispersion of the cubic phase of $KMnF_3$ are located at Γ, R, M and X in the first Brillouin zone[18, 19] with

$$P(\Gamma) = P(R) = 0_h$$

and

$$P(M) = P(X) = D_{4h}.$$

At Γ we have [20]

$$TA+LA, TO_1+LO_1, TO_2+LO_2, TO_3+LO_3 = \Gamma_4^-$$

and

$$0_4 = \Gamma_5^-$$

with the nomenclature of Koster *et al.* [21].

In the orthorhombic phase we have a tetragonal unit cell containing four $KMnF_3$ molecules[6] leading to a somewhat smaller volume of the first Brillouin zone than for the cubic phase (see Appendix A). The Brillouin zones for both phases are given in Fig. 5. It is shown in Appendix A that the c.p. of the cubic BZ (capital letters) become the following c.p. of the tetragonal $D_{2h}{}^{16}$ BZ (small letters),

$$\Gamma, R \rightarrow \gamma$$

$$X, M \rightarrow \gamma \text{ or } m$$

where the nomenclature of Koster[19] is used. As $D_{2h}{}^{16}$ is non-symmorphic, only the irreducible representation for interior points of the first BZ can be constructed from point groups[19]. Thus for the case Γ, R, X, $M \rightarrow \gamma$ the symmetries $P(\Gamma)$, $P(R)$, $P(X)$ and $P(M)$ become D_{2h} in the orthorhombic phase ('symmetry breaking'), as is shown in Appendix B.

The compatibility conditions between 0_h (D_{4h}) and D_{2h} are useful in establishing selection rules for either phase. Thus, at Γ two-phonon transitions are dipole forbidden in the cubic as well as in the orthorhombic phase. Going from Γ to M, the irreducible representations M_m^{+-} of D_{4h} compatible with Γ_4^- respectively Γ_5^- can be found[18]

$$\Gamma_4^- \rightarrow (M_1^+ \text{ or } M_4^+) + (M_2^+ \text{ or } M_3^+) + (M_2^- \text{ or } M_3^-)$$

or

$$M_5^- + (M_2^- \text{ or } M_3^-)$$

$$\Gamma_5^- \rightarrow (M_1^+ \text{ or } M_4^+) + (M_2^+ \text{ or } M_3^+) + (M_1^- \text{ or } M_4^-)$$

or

$$M_5^- + (M_1^- \text{ or } M_4^-).$$

Consider e.g. a combination state transforming according to $M_2^+ \otimes M_3^-$. Two-phonon transitions leading to such states are forbidden in the cubic phase because

$$M_2^+ \otimes M_3^- = M_4^- \in M^{\text{vector}} = M_2^- + M_5^-$$

whereas they are allowed in the lower symmetry phase, the subgroup structure with respect to D_{2h} being

$$M_2^+ \otimes M_3^- \rightarrow \gamma_3^+ + \gamma_1^- = \gamma_3^-$$

and γ_3^- is a component of the vector representation

$$\gamma_2^- + \gamma_3^- + \gamma_4^- \text{ of } D_{2h}.$$

Only few of the many possible two-phonon combination states show a change in the selection rule. At M, these are

$$M_1^\pm \otimes M_4 \text{ and } M_2^\pm \otimes M_3^\mp.$$

They are compatible with any of the three processes suggested by Perry and Young [7]. At R, the two phonon processes having an i.r. activity changing with symmetry are

$$R_1^\pm \otimes R_5^\mp \text{and } R_2^\pm \otimes R_4^\mp$$

which can be correlated only with a combination state involving mixed subgroups of Γ_4^- and Γ_5^-. They are thus compatible only with $O_4 - TA$, but not with $LO_1 + TO_1$ or $LA + TO_2$. At X, none of the processes suggested by Perry and Young[7] is symmetry dependent, as the compatibility and dimension of the representations lead to the assignments

$$LA, LO = X_1^+ \text{ or } X_2^-$$

$$TA, TO = X_5^+ \text{ or } X_5^-$$

$$O_4 = (X_3^+ + X_5^+) \text{ or } (X_4^- + X_5^-).$$

We therefore conclude that the two-phonon sideband at 270 cm^{-1} belongs to a M or R process rather than to an X process, being compatible only with $TO_1(M) + LO_1(M)$, $TO_2(M) + LA(M)$, $O_4(M) - TA(M)$, and $O_4(R) - TA(R)$. This conclusion remains valid when the more involved case $X, M \rightarrow m$ is considered (see Appendix B). The concept of decrease of the volume of the Brillouin zone by phase transition and its implications on phonon selection rules has been used earlier by O'Leary and Wheeler[22].

The main result of these group theoretical considerations is the existence of two-phonon processes in KMnF$_3$ forbidden in one and allowed in the other phase, i.e. the existence of symmetry dependent changes in the selection rules for photon absorption[23] which may explain the striking behaviour of the ir activity of the 261 cm^{-1} frequency. It is not the purpose of our work to give unambiguous branch assignments going essentially beyond the speculations of Perry and Young [7]. Nevertheless, we slightly improved their speculative assignments by excluding all X-processes and part of the R-processes for the 261 cm^{-1} phonon frequency.

4. DISCUSSION

As KMnF$_3$ is antiferromagnetic below $T_N = 88{\cdot}3$°K one might suggest that magnetic effects are involved in the interpretation of the 261 cm^{-1} sideband and its temperature behaviour. The difference of the sideband and TO$_2$ (191 cm^{-1}) energies is approximately the magnon energy in KMnF$_3$ at the edge of the BZ[24, 25]. Thus one might be led to the conclusion that a magnon sideband of TO_2 is observed in the 191 cm^{-1} reflectivity. But this must be excluded, for it has been shown [26] that $KMnF_3$ magnon sidebands usually appear only at temperatures well below T_N. One still might be inclined to ascribe at least the 88°K discontinuity to the effect of magnetic ordering, as the exchange interaction may contribute to the forces between the ions by means of phonon–magnon interaction. The form of the temperature dependence and the order of magnitude of the effect as measured in our case seem to deny this explanation: Weak effects of magnetic coupling on the TO_2 phonon energy in $KNiF_3$ (cubic above *and* below T_N) have been reported recently [27] showing a saturation-like temperature dependence below T_N similar to theoretical results obtained by Baltensperger and Helman[28]. A temperature behaviour of the same kind has been observed for the intensity of an electronic band in the optical spectrum of $KNiF_3$[29]. Thus, also for $KMnF_3$ an influence of magnetic long range ordering on the phonon spectrum may be observed well below T_N. The 88°K discontinuity, however, has to be attributed to the crystallographic change occuring at this temperature.

The interpretation of the 261 cm^{-1} sideband by *one* phonon processes should be rejected as well. The activation of $O_4(\Gamma) = \Gamma_5^-$ (i.r. inactive in the cubic phase[20]) by the lattice distortion below 190°K, though being allowed by group theory, cannot account for the observed sideband because the magnitude of the energies is too high[7, 20]. Group theory would also predict a splitting of the doubly degenerate TO_2 (Γ) mode for the low temperature phase. It is in this way that Last[30] and Ballantyne[31] interpret a sideband occuring in low temperature $BaTiO_3$ spectra. Yet in our case this splitting would be rather large (70 cm^{-1}). Moreover, the nature of the 190°K phase transition [6] ought to lead to a temperature dependent frequency splitting, whereas we observed a sideband with constant frequency but with temperature dependence of the intensity. This clearly has to be explained by temperature dependent transition probabilities of the given processes rather than by a splitting. Thus, the interpretation of the sideband by two-phonon processes in connection with the theory developed in Section 3 seems to be valid.

5. CONCLUSIONS

We measured the temperature dependence of a sideband in the i.r. reflection spectrum of $KMnF_3$ and discovered marked discontinuities at phase transition temperatures. In addition we studied the group theory of two-phonon processes in the D_{2h}^{16} and O_h^1 phases of this solid material. The existence of two-phonon processes undergoing a symmetry dependent change of selection rules was clearly established. We should therefore like to explain the discontinuities observed with the aid of group theoretical selection rules. As a by-product, the group theoretical considerations reveal that the sideband has to be assigned to a two-phonon transition at the c.p. *R* or *M* rather than at *X* without yielding, however, further precise phonon branch assignments.

Crystals with inversion symmetry usually do not have too many i.r.-active two-phonon transitions. Among these, only few can possess symmetry dependent i.r.-activity. Thus the 261 cm^{-1} band of $KMnF_3$ has to be considered as a rather rare case. The study of the temperature dependence of the Raman spectrum of this crystal seems to yield further interesting results in connection with phase transitions[32].

Acknowledgements—We thank Dr. D. T. Teaney, IBM Watson Research Center, Yorktown Heights, New York, who generously loaned us several crystals grown by Professor W. H. Stevenson, Aberdeen. We thank Professor W. Baltensperger, ETH, and Dr. R. Wehner, RCA Laboratories, Zurich, for helpful discussions. This work was supported by the "Eidgenössische Kommission zur Förderung der Forschung" under contract number 7713.7/639.

REFERENCES

1. ANASTASSAKIS E., IWASA S. and BURSTEIN E., *Phys. Rev. Lett.* **17**, 1051 (1966).
2. FLEURY P. A. and WORLOCK J. M., *Phys. Rev. Lett.* **18**, 665 (1967).
3. SCHAUFELE R. F., WEBER M. J. and SILVERMAN B. D., *Phys. Lett.* **25A**, 47 (1967).
4. WORLOCK J. M. and FLEURY P. A., *Phys. Rev. Lett.* **19**, 1176 (1967).
5. OKAZAKI A. and SUEMUNE Y., *J. phys. Soc. Japan* **16**, 671 (1961).
6. BECKMAN O. and KNOX K., *Phys. Rev.* **121**, 376 (1961).
7. PERRY C. H. and YOUNG E. F., *J. appl. Phys.* **38**, 4616, 4624 (1967).
8. ALEXANDROV K. S., RESHCHIKOVA L. M. and BEZNOSIKOV B. V., *Phys. Status Solidi* **18K**, 17 (1966).
9. LAX M. and BURSTEIN E., *Phys. Rev.* **97**, 39 (1955).
10. LAX M., *Phys. Rev.* **138A**, 793 (1965).
11. LOUDON R., *Phys. Rev.* **137A**, 1784 (1965).
12. BIRMAN J. L., *Phys. Rev.* **127**, 1093 (1962).
13. BIRMAN J. L., *Phys. Rev.* **131**, 1489 (1963).
14. BIRMAN J. L., *Phys. Rev.* **150**, 771 (1966).
15. ELLIOT R. J. and LOUDON R., *J. Phys. Chem. Solids* **15**, 146 (1960).
16. LAX M. and HOPEFIELD J. J., *Phys. Rev.* **124**, 115 (1961).
17. PHILLIPS J. C., *Phys. Rev.* **104**, 1263 (1956).
18. BOURCKAERT L. P., SMOLUCHOWSKI R. and WIGNER E., *Phys. Rev.* **50**, 58 (1936).
19. KOSTER G. F., *Solid-St. Phys.* **5**, 173 (1957).
20. NAKAGAWA I., TSUCHIDA A. and SHIMANOUCHI T., *J. Phys. Chem. Solids* **47**, 982 (1967).
21. KOSTER F., DIMMOCK J. O., WHEELER R. G. and STATZ H., *Properties of the Thirty-two Point Groups.* MIT Press, Cambridge, Mass. (1963).
22. O'LEARY G. P. and WHEELER R. G., *Phys. Rev. Lett.* **18**, 1054 (1967).
23. BURSTEIN E., MARADUDIN A. A., ANASTASSAKIS E. and PINCZUK A., *Helv. Phys. Acta* **41**, 730 (1968).
24. STEVENSON R., *Phys. Rev.* **152**, 531 (1966).
25. AOYAGI K., *J. phys. Soc. Japan* **22**, 1516 (1967).
26. SHIONOYA S. and HIRANO M., *Phys. Lett.* **26A**, 533 (1968).
27. SINTANI K., TOMONO Y., TSUCHIDA A. and SIRATORI K., *J. phys. Soc. Japan* **25**, 99 (1968).
28. BALTENSPERGER W. and HELMAN J. S., *Helv. Phys. Acta* **41**, 668 (1968).
29. PISAREV R. V. PROCHOROVA S. D., *Phys. Lett.* **26A**, 356 (1968).
30. LAST J. T., *Phys. Rev.* **105**, 1740 (1957).
31. BALLANTYNE J. M., *Phys. Rev.* **136A**, 429 (1964).
32. STEIGMEIER E., RCA Zürich, Private communication.
33. KOWALSKI H.-J., *Lineare Algebra*, p. 264. Berlin (1963).
34. HENRY N. F. M. and LONSDALE K. (Editors), *International Tables for X-Ray Crystallography, Vol. I, Symmetry Groups. Birmingham, England (1952).*

APPENDIX A. THE BRILLOUIN ZONES FOR CUBIC AND ORTHORHOMBIC KMnF$_3$

Consider a primitive Bravais lattice generated by three vectors $\mathbf{c}_i$. The corresponding reciprocal lattice is spanned by the (up to a factor 2π) dual basis $\{\mathbf{C}_l\}$ defined by

$$\mathbf{c}_i\mathbf{C}_l = 2\pi\delta_{il} \qquad (i, l = 1, 2, 3). \tag{A1}$$

The choice of another unit cell (and, consequently, new basis $\{\mathbf{t}_j\}$) in the direct lattice is equivalent to a linear transformation described by the real matrix $a_{ij} = A$,

$$\mathbf{c}_i = \sum_{j=1}^{3} a_{ij}\mathbf{t}_j. \tag{A2}$$

The corresponding new basis $\mathbf{T}_k$ of the reciprocal lattice is defined by

$$\mathbf{t}_j\mathbf{T}_k = 2\pi\delta_{jk} \qquad (j, k = 1, 2, 3). \tag{A3}$$

The related linear transformation in the reciprocal lattice may be described by the matrix $b_{kl} = B$,

$$\mathbf{T}_k = \sum_{l=1}^{3} b_{kl}\mathbf{C}_l. \tag{A4}$$

In order to determine the matrix B, consider the products $\mathbf{c}_i\,\mathbf{T}_k$. Inserting (A2) and (A4) respectively leads to the equation

$$\sum_{l=1}^{3} b_{kl}\mathbf{c}_i\mathbf{C}_l = \sum_{j=1}^{3} a_{ij}\mathbf{t}_j\mathbf{T}_k.$$

Accounting for (A1) and (A3) yields

$$b_{ki} = a_{ik} \tag{A5}$$

consistent with the well known theorem of linear algebra [33] saying that the dual transformation is described by the transposed matrix, $B = A^T$.

The cubic cell of the high-temperature phase respectively the tetragonal *pseudo*cell of the low-temperature phase of KMnF$_3$ are given by the basis vectors

$$\mathbf{c}_1 = a(1,0,0)$$
$$\mathbf{c}_2 = a(0,1,0)$$
$$\mathbf{c}_3 = c(0,0,1).$$

This being an orthogonal system, the corresponding basis of the reciprocal lattice is

$$\left.\begin{aligned} \mathbf{c}_1 &= \frac{2\pi}{a}(1,0,0) \\ \mathbf{c}_2 &= \frac{2\pi}{a}(0,1,0) \\ \mathbf{c}_3 &= \frac{2\pi}{c}(0,0,1) \end{aligned}\right\} \tag{A6}$$

where we have $c = a$ for the cubic ($O_h{}^1$) phase and $c \approx a$ for the orthorhombic ($D_{2h}{}^{16}$) phase. Following Beckman and Knox [3] the $D_{2h}{}^{16}$ tetragonal cell can be chosen such that the basis vectors for the orthorhombic phase are

$$\mathbf{t}_1 = \mathbf{c}_1 + \mathbf{c}_2$$
$$\mathbf{t}_2 = \mathbf{c}_1 - \mathbf{c}_2$$
$$\mathbf{t}_3 = 2\mathbf{c}_3.$$

Thus, in the sense of (A2), we have

$$A = \frac{1}{2}\begin{pmatrix} 1 & 1 & 0 \\ 1 & -1 & 0 \\ 0 & 0 & 1 \end{pmatrix} = A^T.$$

Using (A5) we obtain the basis $\{\mathbf{T}_i\}$ of the reciprocal lattice for the orthorhombic phase.

$$\left.\begin{aligned} \mathbf{T}_1 &= \frac{1}{2}(\mathbf{C}_1 + \mathbf{C}_2) \\ \mathbf{T}_2 &= \frac{1}{2}(\mathbf{C}_1 - \mathbf{C}_2) \\ \mathbf{T}_3 &= \frac{1}{2}\mathbf{C}_3 \end{aligned}\right\} \qquad \text{(A7)}$$

Now, (A6) and (A7) allow us to draw the first Brillouin zones for both phases as shown in Fig. 5. Furthermore, (A7) helps us to study the behavior of the critical points Γ, R, X, M of the cubic phase for a transition to the orthorhombic phase. As the cubic unit cell becomes the tetragonal *pseudo*cell ($c \neq a$), the c.p. X as well as M split into non equivalent subsets, namely

$$X' = \frac{\pi}{a}(1,0,0)\text{ etc.}, X'' = \frac{\pi}{c}(0,0,1)\text{ etc.},$$
$$M' = \frac{\pi}{a}(1,1,0)\text{ etc.}, M'' = \left(\frac{\pi}{a}, 0, \frac{\pi}{c}\right)\text{ etc.}$$

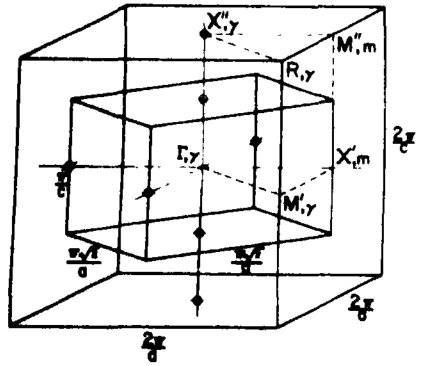

Fig. 5. First Brillouin zones for the cubic lattice and for the tetragonal lattice of KMnF$_3$. Capital letters denote symmetry points for $O_h{}^1$, small letters those for $D_{2h}{}^{16}$. Only those $D_{2h}{}^{16}$ symmetry points needed for our selection rules are given. In the cubic phase ($c = a$) X' and X'' as well as M' and M'' are equivalent, being called X and M.

E.g. we find that

$$R = \left(\frac{\pi}{a}, \frac{\pi}{a}, \frac{\pi}{c}\right) = (\mathbf{C}_1 + \mathbf{C}_2 + \mathbf{C}_3)\cdot\frac{1}{2}$$

of the $O_h{}^1$ Brillouin zone by virtue of (A7) becomes

$$\mathbf{T}_1 + \mathbf{T}_3 = \left(\frac{\pi\sqrt{2}}{a}, 0, \frac{\pi}{c}\right)$$

which is a vector of the $D_{2h}{}^{16}$ reciprocal lattice and therefore is equivalent to $(0,0,0) = \gamma$ of the $D_{2h}{}^{16}$ Brillouin zone. Similarly, the conversion of the other c.p. is computed. The results are

$$\begin{array}{ll} \Gamma \rightarrow \gamma & R \rightarrow \gamma \\ X = X' \rightarrow m, & X = X'' \rightarrow \gamma \\ M = M' \rightarrow \gamma, & M = M'' \rightarrow m. \end{array}$$

Here, capital letters denote the c.p. of the cubic, small letters those of the orthorhombic phase.

APPENDIX B. THE GROUPS OF THE CRITICAL POINTS FOR CUBIC AND ORTHORHOMBIC KMnF$_3$

The space group G of KMnF$_3$ in the low temperature phase is the non-symmorphic group $D_{2h}{}^{16}$ = Pbnm. The symmetry operations $g \in G$ thus have the form

$$g = (\alpha|\mathbf{v}_\alpha + \mathbf{R}_n).$$

The operations

$$\mathbf{R}_n = \sum_{i=1}^{3} n_i\mathbf{t}_i$$

with n_i = integer, $|\mathbf{t}_1| = |\mathbf{t}_2| = a\sqrt{2}$, $|\mathbf{t}_3| = 2c$, and $\mathbf{t}_i$ orthogonal to $\mathbf{t}_{j\neq i}$ (as described in A), form the translation group T of the Bravais lattice. The rotation or reflection part of g is denoted by α. The translation part of those operations involving gliding planes or screw axis is given by $\mathbf{v}_\alpha$. The operations $(\alpha|\mathbf{v}_\alpha)$ are [34]

$$E, (I|0) = I,$$
$$(C_2|\mathbf{v}), (\sigma_h|\mathbf{v})$$
$$(C_2'|\mathbf{v}'), (\sigma_v'|\mathbf{v}')$$
$$(C_2''|\mathbf{v}''), (\sigma_v''|\mathbf{v}'')$$

with the translation vectors

$$\mathbf{v} = \frac{1}{2}(\mathbf{t}_1 + \mathbf{t}_3) = \frac{1}{2}(\mathbf{c}_1 + \mathbf{c}_2 + 2\mathbf{c}_3)$$
$$\mathbf{v}' = \frac{1}{2}(\mathbf{t}_1 + \mathbf{t}_2 + \mathbf{t}_3) = \mathbf{c}_1 + \mathbf{c}_3$$
$$v'' = \frac{1}{2}t_2 = \frac{1}{2}(\mathbf{c}_1 - \mathbf{c}_2)$$

the vectors $\mathbf{v}$ and $\mathbf{v}''$ belong neither to the $D_{2h}{}^{16}$ tetragonal lattice

$$\sum_{i=1}^{3} n_i t_i$$

nor to the tetragonal *pseudo*lattice respectively cubic lattice

$$\sum_{i=1}^{3} n_i \mathbf{c}_i .$$

Thus, $D_{2h}{}^{16}$ is not simply a subgroup of $O_h{}^1$.

According to A, we have to study the groups belonging to the critical points

$$\gamma = (0, 0, 0)$$

and

$$m = \frac{1}{2} C_1 = \frac{1}{2}(T_1 + T_2)$$

only. Up to isomorphism, $P(\gamma)$ is obtained by putting all $\mathbf{v}_a$ equal to zero. Thus $P(\gamma)$ is isomorphic to D_{2h}, which is a subgroup of the symmetries. $P(\Gamma) = P(R) = O_h$ as well as $P(X'') = P(M') = D_{4h}$ valid in the cubic phase, and the compatibility can be studied directly using standard tables [21]. For m, however, we find $P(m) = G/T$ = the complete factor group of $D_{2h}{}^{16}$, which is not a point group or direct product of point groups and thus is not contained in $P(X') = P(M'') = D_{4h}$ as a subgroup. Hence the simple concept of symmetry lowering by going to a subgroup does not work. Our interest is, however, restricted to the implications for selection rules of those symmetry operations that disappear when we go from the cubic to the orthorhombic phase. Therefore we may consider only the compatibitlity of

$$D_{4h} \to D_{4h} \wedge P(m) = C_i .$$

With the aid of standard tables [21] we again find that none of the X'' processes has the quality of being allowed in the orthorhombic and forbidden in the cubic phase.

J. Phys. Chem. Solids Pergamon Press 1970. Vol. 31, pp. 331–335. Printed in Great Britain.

RADIATION DAMAGE IN GYPSUM

A. R. PATEL and K. S. RAJU
Department of Physics, Sardar Patel University, Vallabh Vidyanagar, Gujarat State, India

(*Received* 15 *April* 1969; *in revised form* 16 *June* 1969)

Abstract—Gypsum single crystals have been irradiated with different doses of neutrons and their hardness determined by a Vicker's microhardness indentor. It is observed that the hardness of the irradiated crystal decreases with the increase in the total dose of irradiation with neutrons and the variation of hardness within the irradiated crystal is similar to that of the crystal heated to the dehydration temperature and then allowed to cool. From the Laue X-ray diffraction studies of irradiated crystals, distortion of the lattice is observed and it is shown that similar distortion in the lattice is produced when the crystals are heated to the dehydration temperature and cooled. Infra-red absorption studies of the irradiated, heated and the unirradiated crystals have been made. Less extended peaks relating to lattice water and peaks relating to free sulphate group on the irradiated and heated crystals are identified. The implications are discussed.

INTRODUCTION

IT IS AN established fact that when crystals are irradiated with neutrons, their hardness, mechanical properties and the structure etc., undergo some change. Vaughan and Davisson[1] have reported that lithium fluoride hardens by neutron irradiation. Gilman and Johnston[2] have concluded that the hardening of lithium fluoride, on neutron bombardment, along with a change in colour is due to the formation of cluster defects. Both ordered and disordered alloys of $AuCu_3$ increase in hardness as a result of irradiation according to Dienes' review[3]. He had mentioned that water undergoes dissociation under the action of radiation. Hardness changes were studied by Damask[4] who found that the rate of wear of gramaphone styli was greater after than before irradiation. Wilks[5] has reported that a neutron irradiation reduced the hardness of diamond. Maximum change occurred on the octahedron face and the minimum on the dodecahedron face. Berzina and Berman[6] have studied the propagation of dislocations in proton irradiated ionic crystals by the etch figure star surrounding the indentor. It is observed that the hardening shortens the rays of the etch figure star. Billington and Crawford[7] have reported that the amount of irradiation is measured in terms of increase in the lattice constant in the case of diamond. X-ray diffraction of irradiated diamond has given the evidence of the presence of thermal spikes. Hass and Sutherland[8] have studied the infra-red absorption spectrum of gypsum in detail.

It is well known that the X-ray technique is a powerful tool to diagnose precisely the damage that may have occurred in the crystal lattice due to irradiation. We have utilized this technique in our present investigations.

This paper deals with the studies made on natural and neutron irradiated gypsum crystals. These studies have been classified into three different groups:

1. Studies on measurement of hardness.
2. X-ray diffraction studies.
3. Studies on infra-red absorption spectra.

Irradiation process

Natural single crystals of gypsum supplied by R. F. D. Parkinson, England, of transparent quality were selected for the present investigations. Several matched pairs of these crystals were obtained by cleaving and one part of each of them were placed in polythene bags and sealed. They were then placed in aluminium containers which were hung with threads outside the core of Swimming Pool Apsara Reactor at Trombay, India, and irradiated with neutrons with the dose of 10^{12} n/cm²/sec for 8 hr, 12 hr, 16 hr, 20 hr and 24 hr (i.e. total dose of $2{\cdot}8\times10^{16}$, $4{\cdot}3\times10^{16}$, $5{\cdot}76\times10^{16}$, $7{\cdot}2\times10^{16}$ and $8{\cdot}66\times10^{16}$ nvt) respectively. The containers were then taken out and were allowed to remain at room temperature till the activity of the crystals died down. Their counterparts were preserved in the laboratory.

EXPERIMENTAL

The hardness of the crystals was determined by indenting them with Vicker's hardness indentor. The X-ray diffraction patterns were obtained with the help of Philip's X-ray unit, model P.W. 1012/00 N.R. 1016. Infra-red absorption spectra of irradiated, heated and the unirradiated gypsum have been recorded, on a Carl Zeiss infra-red spectrometer model U.R. 10.

OBSERVATIONS

(a) *Measurement of hardness*

The crystal cleavages, both irradiated and unirradiated were indented with the Vicker's microhardness diamond indentor at different sites with the requisite load (1 g in the present case) and the mean of the diagonals of 25 indented impressions was calculated and from these values, the Vicker's hardness numerals (V.H.N.) were obtained as shown in Table 1.

Table 1

Particulars	V.H.N. (kg/mm²)
Unirradiated	18·60
Irradiated dose	
$2{\cdot}8\times10^{16}$ (nvt)	14·40
$4{\cdot}3\times10^{16}$ (nvt)	11·03
$5{\cdot}76\times10^{16}$ (nvt)	9·00
$7{\cdot}2\times10^{16}$ (nvt)	6·40
$8{\cdot}66\times10^{16}$ (nvt)	5·30

One of the irradiated cleavages was indented and then etched in analar grade nitric acid for 1 min. That analar grade nitric acid is a reliable etchant to reveal dislocation sites in gypsum has been reported by Patel and Raju[9]. The etch pattern produced is shown in Fig. 1. It is clear from the figure that the indented mark turns out to be a single pit during etching as no etch figure is formed around it.

In order to see, whether the load affects the production of etch figure star, they were indented with different loads varying from 1 to 100 g and to our surprise, no etch figure star was produced on etching them. The etch figure star was also not obtained by indenting and etching an unirradiated cleavage.

Variation of microhardness within the body of the irradiated crystal at different depths. In order to study the effect on the microhardness due to irradiation, the crystals, irradiated with different doses, were cleaved into five thinner flakes and their thickness measured. They were then indented with 1 g load and V.H.N. calculated at different depths from the surface. The observations are shown graphically in Fig. 2. It is seen from the figure that the hardness increases as one moves

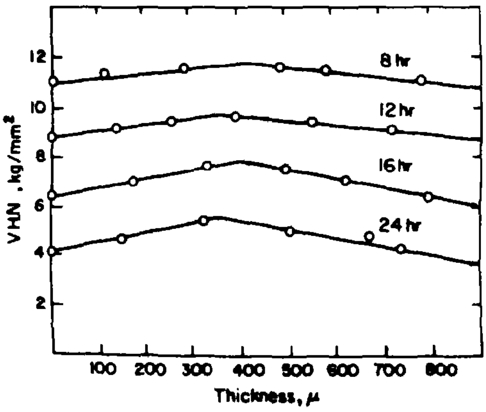

Fig 2. Graph showing variation of microhardness at different thicknesses of irradiated crystals.

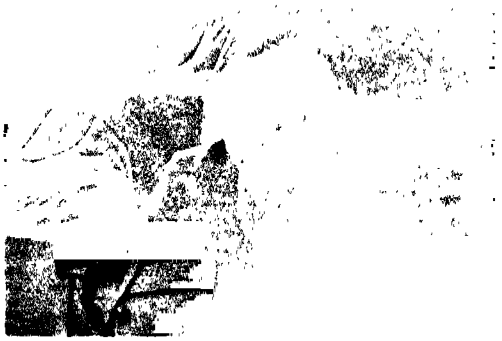

Fig. 1. An indented irradiated cleavage etched in nitric acid. × 350

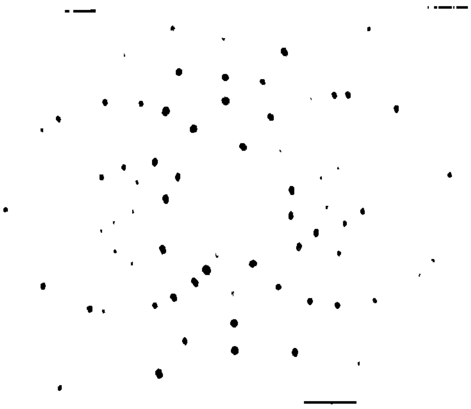

Fig. 3. Laue pattern of unirradiated crystal.

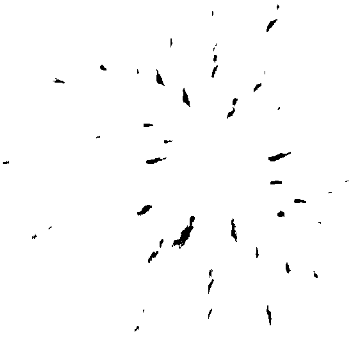

Fig. 4. Laue pattern of irradiated crystal. ($8{\cdot}66 \times 10^{16}$ nvt).

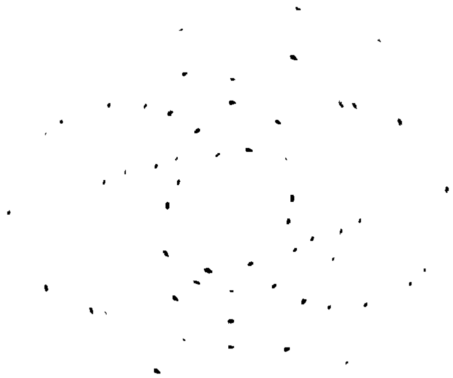

Fig. 5. Laue pattern of heated crystal at 80°C for 50 hr.

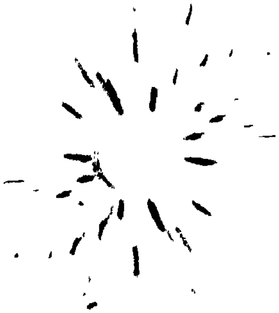

Fig. 6. Laue pattern of heated crystal at 100°C for 50 hr

within the body of the crystal, becomes maximum at the centre and then decreases again. It was verified that etching did not produce the etch figure star around the indentation marks at different depths.

It may be mentioned that the microhardness was practically constant at all depths within the body of the unirradiated crystals.

In order to investigate into the cause of reduction of hardness on irradiation, several freshly cleaved gypsum cleavages were heated in a constant temperature air-oven at 40°, 60°, 80° and 100°C for 24 hr and their microhardness were measured. The microhardness practically remained constant for specimen heated at 40°, 60° and 80°C while the microhardness of the crystal heated at 100°C could not be measured as it turned white due to dehydration. It was thought worthwhile to study the variation of microhardness, if any, when heated at a little lower temperature than 100°C for different periods. Hence the crystal cleavages were heated at 95°C for 4 hr, 8 hr and 12 hr respectively and the V.H.N. were determined as recorded in Table 2.

Table 2

Duration of heating at 95°C	V.H.N. (kg/mm^2)
4 hr	18·54
8 hr	10·77
12 hr	7·50

It is seen from Table 2 that increase in the heating period decreases the hardness of the crystal. It may be mentioned that even at 80°C if the crystal is heated for a prolonged time, an appreciable change in hardness is observed. A crystal was heated at 80°C for 50 hr. It was then cleaved into five flakes when cooled and the V.H.N. at different depths were obtained as recorded in Table 3.

It is seen that the heated crystal is softer at the surface than within the body of the crystal.

Table 3

Face No.	V.H.N. (kg/mm^2)	Thickness (μ) below the top surface
1.	12·87	0
2.	16·19	280
3.	17·02	512
4.	18·40	823
5.	14·27	1080
6.	12·68	1460

(b) *Laue X-ray diffraction*

In order to determine any structural changes in the crystals due to irradiation or heating, Laue X-ray diffraction patterns of the irradiated and heated crystals were obtained. Thus Figs. 3, 4, 5 and 6 show respectively the X-ray diffraction patterns of the unirradiated, irradiated (total dose: 8·66 × 10^{16} nvt), heated at 80°C for 50 hr and the crystal heated at 100°C for 50 hr. It may be mentioned that the crystal heated at 80°C for 50 hr was translucent whereas the crystal heated at 100°C was almost white in colour. The irradiated and unirradiated crystals were transparent.

The following points merit discussion:

1. The symmetry of the diffraction patterns in all the Laue photographs is almost the same.
2. To every 'spot' on the Laue pattern of the unirradiated crystal, there is a corresponding 'streak' on the Laue pattern of the irradiated crystal (compare Figs. 3 and 4).
3. The crystal heated at 80°C for 50 hr shows the beginning of the 'streak formation' in its Laue photograph (compare Fig. 5 and Fig. 3), whereas the crystal heated at the dehydration temperature shows 'elongated streaks' (Fig. 6).

It was verified by obtaining Powder photographs of both irradiated and the unirradiated crystal that there was no significant change in the lattice constant due to neutron irradiation.

(c) *Infra-red absorption spectra*

The infra-red absorption spectra of irradiated, unirradiated and heated gypsum crystals of approximately equal thicknesses are taken under almost identical conditions and the peaks related to free sulphate group and lattice water are compared (Fig. 7). The details of the absorption peaks are recorded in Table 4.

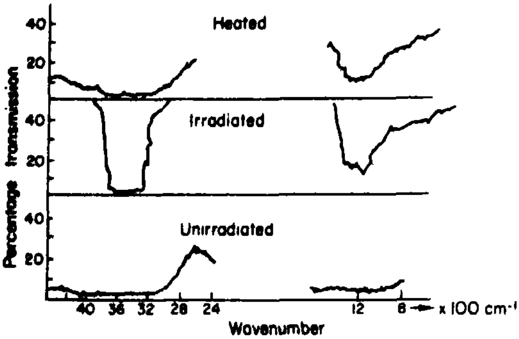

Fig. 7. Infra-red spectra of water and sulphate region of heated, irradiated and unirradiated gypsum crystals

It is clear from Table 4 and Fig. 7 that both irradiated and heated crystals show absorption peaks relating to free $(SO_4)^{2-}$ ions. The breadth of the absorption peak due to lattice water in the case of irradiated crystal is less extended compared to the corresponding peaks of heated and unirradiated crystals.

DISCUSSION

1. The fact that the hardness of the irradiated gypsum within the body of the crystal changes exactly in the same way as those of the unirradiated crystals when they are heated at or near the dehydration temperature and cooled, suggests that the crystals might have been heated due to irradiation. It is also quite probable that associated gamma rays might have contributed to the heat treatment besides the effect of energetic neutrons. In the case of irradiated crystal, the neutrons dissipate energy utilised in rupturing lattice water by breaking OH bonds, as they penetrate the crystal from the surface to the interior. As the lattice water is sandwiched between strong double layers of calcium sulphate[10], the probability of the rupture of water of crystallisation is more at the surface than in the interior. Hence the damage caused in the interior of the crystal will be less than that at the surface. In the case of heated crystals, outer layers are first heated and the lattice water at the surface is first damaged and continues inwards. In this case also, the damage will be more at the surface than in the interior as observed.

By etching an indented cleavage (irradiated or unirradiated), neither new pits emerge around the indentation mark nor the etch figure star is formed, suggest that the plastic flow is practically nil in the crystal at the room temperature.

2. The formation of 'streaks' in the Laue patterns of the irradiated as well as heated crystals corresponding to well defined 'spots' of the unirradiated sample strongly suggests that, due to neutron irradiation and heating, the lattice gets distorted. Comparison of the Laue patterns of the heated crystals reveals that the lattice distortion depends on the temperature at which the crystals are heated and is maximum at dehydration temperature. It may be mentioned that increase in the dose

Table 4. Observed absorption peaks

Region	Unirradiated	Irradiated	Heated
Free $(SO_4)^{2-}$ ions peak at 1200 cm^{-1}	Absent	Predominent	Less predominent
Lattice water peak at (3000–3700) cm^{-1}	(3100–4000) cm^{-1}	(3270–3650) cm^{-1}	(3200–3700) cm^{-1}

of irradiation increases the distortion in the lattice.

3. The less extended (OH) absorption bands of lattice water in the irradiated sample compared to the heated and unirradiated samples, suggest that water molecules fully associated due to O- and H- bondings with $CaSO_4$ molecule in normal untreated gypsum crystal might have been partly dissociated due to rupture of any of its H-bonds with the oxygen of the sulphate ion or with Ca^{2+} ion through its oxygen atom of water. The peak corresponding to free sulphate ion present in irradiated and heated crystals but absent in unirradiated samples strongly suggests that the crystal on irradiation has undergone dissociation.

We, therefore, conjecture that the neutron irradiation of gypsum causes:

1. the reduction in hardness, which may be due to the decrease in the cohesive energy of the ruptured H- and O-bondings of lattice water;
2. 'lattice distortion' revealed by 'streaks' in X-ray diffraction patterns; and
3. nuclear heating due to neutrons and γ-rays which may partly rupture lattice water and in turn sulphate group, causing dissociation.

Acknowledgements—The authors are grateful to the Atomic Energy Establishment Commission, Trombay for getting the crystals irradiated and for financial assistance, without which, this work would not have been done. We thank Professor R. D. Patel, Professor and Head, Department of Chemistry, Sardar Patel University for his kind permission to use infra-red spectrometer and doctors K. C. Patel, R. P. Patel and S. R. Patel for their kind help and valuable suggestions in the infra-red studies.

REFERENCES

1. VAUGHAN W. H. and DAVISSON J. W., *Acta Met.* **6**, 554 (1958).
2. GILMAN J. J. and JOHNSTON W. G., *J. appl. Phys.* **29**, 887 (1958).
3. DIENES, G. J., Particle Radiation effects in solids, *Annual Review of Nuclear Science* Vol. 2, pp. 195, 215 (1953).
4. DAMASK A. C., *J. appl. Phys.* **29**, 1590 (1958).
5. WILKS, E. M., *Ind. Dia. Rev.* **27**, 110 (1967).
6. BERZINA I. G. and BERMAN I. B., *Soviet Phys. Crystallogr.* **9**, 202 (1964).
7. BILLINGTON D. S. and CRAWFORD J. H., *'Radiation Damage in Solids'*. Clarendon Press, Oxford (1961).
8. HASS M. and SUTHERLAND G. B. B. M., *Proc. R. Soc.* **A236**, 427 (1965).
9. PATEL A. R. and RAJU K. S., *Acta crystallogr* **23**, 217 (1967).
10. WELLS A. F., *Structural Inorganic Chemistry*, 2nd Edn, p. 440. Clarendon Press, Oxford (1950).

J. Phys. Chem. Solids Pergamon Press 1970. Vol. 31, pp. 337-353. Printed in Great Britain.

DEFECTS IN ZnS/ZnSe MIXED CRYSTALS-II. THE PARAMAGNETIC *A*-CENTERS IN CUBIC $ZnS_{1-x}Se_x$

JÜRGEN SCHNEIDER
Physikalisches Institut der Universität, and Institut für Elektrowerkstoffe der Fraunhofer-Gesellschaft, Freiburg/Br., Germany

BERNHARD DISCHLER and ARMIN RÄUBER
Institut für Elektrowerkstoffe der Fraunhofer-Gesellschaft, Freiburg/Br., Germany

(*Received* 23 *December* 1968; *in revised form* 5 *June* 1969)

Abstract—Associate defect centers formed by zinc vacancies, V_{Zn}, and substitutional group-VII or group-III impurity ions have been investigated by electron spin resonance in $ZnS_{1-x}Se_x$ mixed crystals. These centers form deep acceptor states and are converted into a paramagnetic state by supplying a photo-excited hole. Apart from the $V_{Zn}S_3Cl$ and $V_{Zn}S_3Br$ cluster (halogen *A*-center), which had been previously analysed in pure ZnS, the following clusters were analysed in detail: $V_{Zn}S_2SeCl$, $V_{Zn}S_2SeBr$, $V_{Zn}SSe_2Cl$ and $V_{Zn}SSe_2Br$. For centers of the type $V_{Zn}S_2SeX$, hyperfine interaction arising from the isotope Se^{77} could be detected. Here, the unpaired hole is found to be strongly localized in an atomic 4*p*-orbital directed towards the zinc vacancy. In centers of the type $V_{Zn}SSe_2X$ the unpaired hole's wavefunction must be described by an antibonding molecular orbital, centered at the two selenium sites. Selective quenching of the paramagnetic centers $V_{Zn}S_3X$, $V_{Zn}S_2SeX$ and $V_{Zn}SSe_2X$ occured by illumination with near-infrared light, peaked at 1·4, 1·6 and 1·8 eV, respectively. The process is interpreted as a hole transfer into states close to the valence band edge.

1. INTRODUCTION

THE HALOGEN A-center is a dominant impurity defect in ZnS. It is formed by the association of a twofold negatively charged zinc vacancy with a Cl^-, Br^- or J^- ion, occupying a nearest sulfur site[1]. Such a complex can be converted into a paramagnetic state by supplying a photoexcited hole. Previous electron spin resonance (ESR) investigations, which were performed mainly on ZnS crystals of the cubic type, have shown that the unpaired spin is mainly localized on the three sulfur sites around the zinc vacancy. Because of this degeneracy, associated with the three sulfur sites, a spontaneous Jahn–Teller type distortion of the complex takes place and the symmetry of the center will be lowered from C_{3v} to C_s. As a result of this distortion, it is now energetically more favorable if the unpaired hole finds itself localized on only one of the three possible sulfur sites[2,3]. However, as the temperature is increased, a thermally activated hopping of the unpaired spin among the three distorted sites occurs and, in the time average, the center regains axial symmetry, C_{3v}. This behaviour had been observed experimentally for the chlorine and bromine *A*-center in ZnS[4].

In cubic ZnS, a different type of *A*-center, formed by association of a twofold negatively charged zinc vacancy with an Al^{3+} or Ga^{3+} impurity ion, occupying a nearest zinc site, has also been observed[3,5]. Here, the symmetry of the *A*-center is C_s, already in its diamagnetic charge state. An unpaired hole is then bound to stay localized on only one sulfur site. Consequently, due to the lack of a site degeneracy, no thermally activated spin hopping can occur in these centers.

The formation of *A*-centers appears to be favoured also in other tetrahedrally coordinated host lattices. ESR of the chlorine *A*-center, in its spontaneously distorted state, has been reported for ZnSe[6], and in BeO, the fluorine and boron *A*-center can be detected by the same technique[7]. On the basis of optical investigations on bound excitons, the existence of halogen and aluminum *A*-centers in CdS has been postulated by Thomas and Dingle[8]. Finally, Williams[9] has presented evidence that *A*-centers are responsible for certain luminescence bands in GaAs. Here, the *A*-center should be formed by association of a gallium vacancy with a group-IV or group-VI donor.

We now come to the motivation of the present paper and ask what happens if one of the three sulfur atoms in a halogen *A*-center in ZnS is replaced by a selenium atom. Such centers are likely to exist in $ZnS_{1-x}Se_x$ mixed crystals. If such a complex traps a photo-excited hole, one expects that the defect electron will show a strong preference for the selenium site, because the valence electrons of the two neighbouring sulfur atoms are more tightly bound. Therefore, the symmetry of the center is again C_s. We then expect that the electronic structure of this center bears a close resemblance to that of the Jahn–Teller distorted chlorine *A*-center in ZnSe[6].

A different case is encountered when in a $ZnS_{1-x}Se_x$ mixed crystal a zinc vacancy is surrounded by two selenium, one sulfur and one chlorine atom. Here, it will be shown that the unpaired spin is localized in a molecular orbital centered at the two selenium atoms.

The notation used in this paper follows that given in our previous paper on paramagnetic point defects in $ZnS_{1-x}Se_x$ mixed crystals [10]. It gives the composition of the first shell around the zinc vacancy, including the group-VII impurity. Calculated relative probabilities for the diamagnetic *A*-centers $V_{Zn}S_3Cl$, $V_{Zn}S_2SeCl$, $V_{Zn}SSe_2Cl$ and $V_{Zn}Se_3Cl$ as a function of the ZnS:ZnSe mixing ratio are shown in Fig. 1. This diagram is valid under the condition that the occupation of the lattice sites around the zinc vacancy is solely governed by the laws of statistics.

For a group-III impurity, the notation has to include the first and second shell around the zinc vacancy. The statistical probabilities for the diamagnetic *A*-centers $V_{Zn}S_4Zn_{11}Al$, $V_{Zn}S_3SeZn_{11}Al$, $V_{Zn}S_2Se_2Zn_{11}Al$, $V_{Zn}SSe_3Zn_{11}Al$ and $V_{Zn}Se_4Zn_{11}Al$ as a function of the ZnS:ZnSe mixing ratio is slightly different from that given in Fig. 1. Here, the diagram given previously in Fig. 1 of [10] applies.

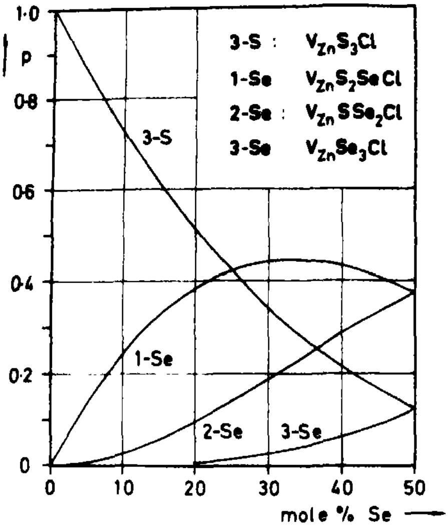

Fig. 1. Statistical probabilities for finding in the first chalcogen shell around the fourfold coordinated zinc vacancy three sulfur atoms, 3-S, or two sulfur and one selenium atom, 1-Se, etc. The extension to the right is a mirror image of the displayed range, where the roles of S and Se are interchanged.

2. EXPERIMENTAL PROCEDURE

The samples investigated in this study were prepared by Mr. F. Friedrich. The chemical transport reaction was used with HCl, HBr or J_2 as transporter. By this method, purely cubic $ZnS_{1-x}Se_x$ crystals were obtained, which showed the ESR spectra of the corresponding halogen *A*-centers. The doping of $ZnS_{1-x}Se_x$ crystals with aluminum or gallium was accomplished by adding traces of these metals to the $ZnS_{1-x}Se_x$ powders and transporting the mixture with iodine. It appears that in the presence of Al or Ga the formation of the iodine *A*-centers is suppressed in favour of the aluminum or gallium *A*-center, respectively. Attempts to grow $ZnS_{1-x}Te_x$ mixed crystals by the chemical transport reaction were not successful.

The ESR spectra were observed at 77°K with a Varian spectrometer operating at 9 GHz. Since the *A*-centers are normally diamagnetic, they had to be converted to the paramagnetic state by u.v. illumination, using the 365 nm Hg line. Reconversion to the diamagnetic state occurs upon subsequent illumination with visible or near infrared light from a tungsten wire lamp. Both processes can be conveniently monitored on the ESR spectrometer, and in this connection we use the words 'excitation' and 'quenching' of a paramagnetic *A*-center. For the investigation of the spectral dependence of the quenching, the intensity of the incident light was kept constant by means of a thermopile.

3. ELECTRON SPIN RESONANCE RESULTS

We have observed the ESR spectra of *A*-centers containing Cl, Br, Al or Ga as impurity. Some of them were analysed in detail.

$V_{Zn}S_2SeCl$

The ESR spectrum of a HCl transported cubic $ZnS_{1-x}Se_x$ ($x = 0{\cdot}005$) single crystal, recorded for H‖[111], is shown in Fig. 2. Most of the lines in the spectrum appeared after u.v. illumination. Three prominent signals are seen in the low and high field part of the spectrum. We assign these lines to the chlorine *A*-center with one selenium and two sulfur atoms around the zinc vacancy, i.e. to the $V_{Zn}S_2SeCl$ center. This interpretation is corroborated by the observation of hyperfine structure (hfs) satellite lines, originating from the interaction of the unpaired spin with the nuclear spin $I = \frac{1}{2}$ of the 7·5 per cent abundant isotope Se^{77}, see Fig. 2. Three additional signals in the ESR spectrum can be assigned to the $M_s = -\frac{1}{2} \rightarrow +\frac{1}{2}$ transition of the photosensitive ions Cr^+[11] and Fe^{3+}[12], occupying undisturbed cubic zinc sites, and to the trigonal FeS_3Se cluster[10]. The single line typical for the ESR spectrum of the $V_{Zn}S_3Cl$ center at 77°K[4] is also apparent. The remaining signals arise possibly from $V_{Zn}S_3Cl$ centers

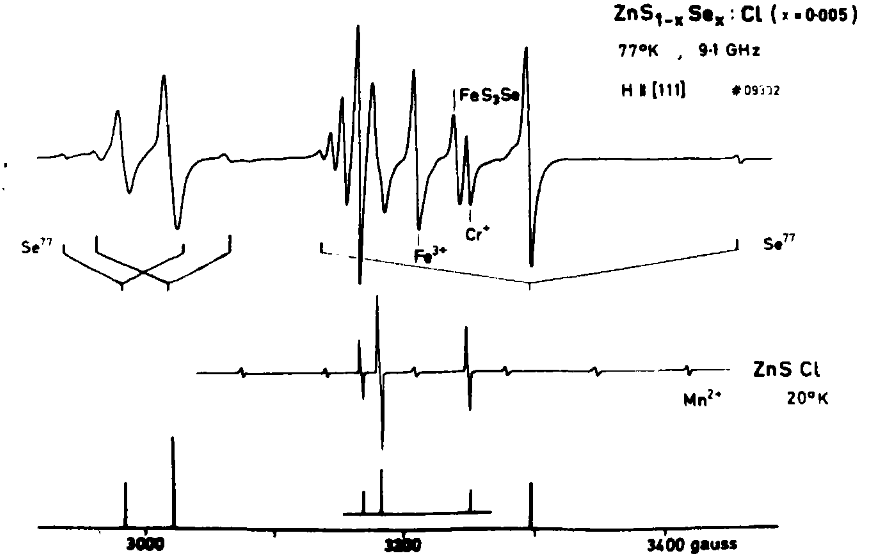

Fig. 2. ESR spectrum of the $V_{Zn}S_2SeCl$ center in an HCl-transported cubic $ZnS_{1-x}Se_x$ crystal under H‖[111]. For comparison, the ESR spectrum of the $V_{Zn}S_3Cl$ center in pure ZnS is shown below. Resonance lines due to the Cr^+ ion and to Fe^{3+} ions on cubic sites and in the trigonal FeS_3Se cluster can also be identified.

which are slightly distorted by the influence of selenium atoms occupying second nearest or more distant sulfur sites*. The angular dependence of the ESR spectrum of the $V_{Zn}S_2SeCl$ center was taken for a rotation of the magnetic field in a $(0\bar{1}1)$ plane and is shown in Fig. 3. Such a diagram results from a center with an orthorhombic g-tensor and twelve possible orientations in the crystals. Under the given geometry, seven lines are discernible which coalesce into three lines for H‖[111]. In this connection it should be mentioned that all experimental data to be reported in this paper were obtained on untwinned cubic crystals. The principal values of the g-tensor and of the Se^{77} hfs-tensor, $K(Se^{77})$ were determined from this angular dependence; they are listed in Tables 1 and 2, respectively.

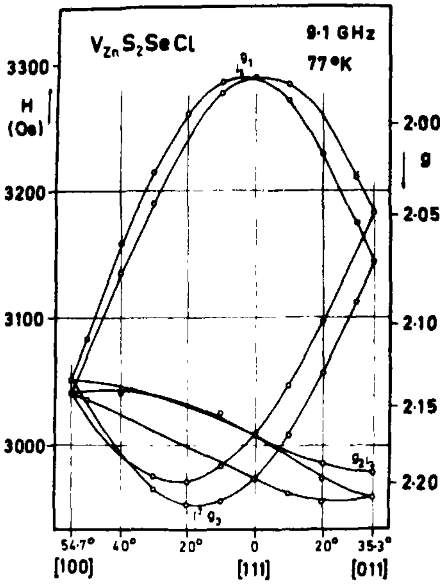

Fig. 3. Angular dependence of the lines in the ESR spectrum of the $V_{Zn}S_2SeCl$ center in $ZnS_{1-x}Se_x$. The crystal was purely cubic and free of stacking faults. The magnetic field is rotated in a $(0\bar{1}1)$ plane.

$V_{Zn}S_2SeBr$

The *A*-center also occurred in a bromine doped $ZnS_{1-x}Se_x$ ($x = 0·007$) crystal and its ESR spectrum is shown in Fig. 5. The essential features are the same as observed for the chlorine doped crystals. However, additional small doublet splittings occur for two of the three strong signals originating from the $V_{Zn}S_2SeBr$ center under H‖[111]. These can be explained by a weak ligand hyperfine structure of the unpaired spin with the bromine isotopes Br^{79} (50·6 per cent) and Br^{81} (49·4 per cent), both having nuclear spin $I = \frac{3}{2}$ and comparable magnetic moments. The appearance of only one or two hfs components, instead of a regular quartet hfs pattern, indicates that the quadrupole interaction and the nuclear Zeeman interaction are not negligible

---

*In Fig. 2, it is a surprising result that the relative intensity of the $V_{Zn}S_2SeCl$ center, as compared to that of the $V_{Zn}S_3Cl$ center, exceeds by far the value expected on the basis of Fig. 1 for 0·5 mole per cent. This discrepancy may be possibly accounted for by (i) preferential association of zinc vacancies with the selenium atoms and (ii) preferential conversion of the $V_{Zn}S_2SeCl$ centers into their paramagnetic state.

Table 1. *Principal values of the* g-*tensor*, g_i, *and tilting angle* τ, *determined for* A-*centers in cubic* $ZnS_{1-x}Se_x$. *The principal axes and the tilting angle are defined in Fig.* 4

Center	g_1	g_2	g_3	τ
$V_{Zn}S_2SeCl$	1·9708	2·1742	2·1941	3·8° ± 0·5°
$V_{Zn}S_2SeBr$	1·9708	2·1825	2·1922	2·0° ± 1·0°
$V_{Zn}SSe_2Cl$	2·0125	2·0976	2·1786	16° ± 2°
$V_{Zn}SSe_2Br$	2·0060	2·1039	2·1840	13° ± 2°

The uncertainty in g_i is ±0·0005 for $V_{Zn}S_2SeX$, and ±0·0020 for $V_{Zn}SSe_2X$.

*Table 2. Principal values, K_i, and tilting angle τ of the Se^{77} hyperfine interaction tensor **K**, determined for the $V_{Zn}S_2SeX$ A-centers in cubic $ZnS_{1-x}Se_x$. The K_i values are given in MHz, and the principal axes coincide with those of the g-tensor (see Fig. 4)*

Center	K_1	K_2	K_3	τ
$V_{Zn}S_2SeCl$	883	219	188	3·8° ± 1·0°
$V_{Zn}S_2SeBr$	876	176	171	2·0° ± 2·0°

The uncertainty in K_i is ± 10 MHz.

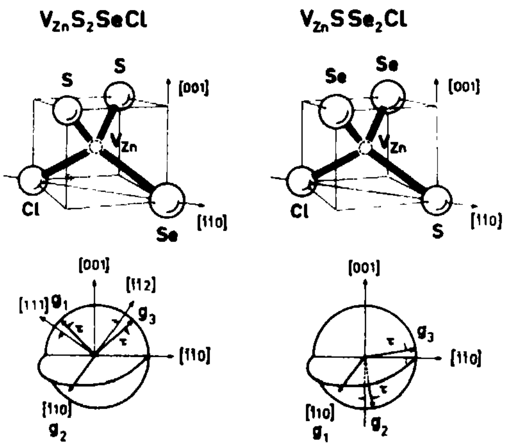

Fig. 4. Orientation of the principal axes of the $V_{Zn}S_2SeCl$ and $V_{Zn}SSe_2Cl$ type *A*-centers.

compared to the magnetic hyperfine interaction. A similar behaviour had been previously observed for the bromine *A*-center, $V_{Zn}S_3Br$, in ZnS[3]. Apart from this ligand hyperfine interaction, the direct hyperfine interaction gives rise to Se^{77} satellite lines, see Fig. 5.

$V_{Zn}S_3SeZn_{11}Al$ and $V_{Zn}S_3SeZn_{11}Ga$

For an *A*-center of the type $V_{Zn}S_3SeZn_{11}Al$, three structurally different centers are expected to exist in the cubic host lattice. They differ by the relative arrangement of the selenium atom in the sulfur shell and of the group-III impurity atom in the zinc shell. Two of these centers have symmetry C_s and one type has only symmetry C_1. Considering the

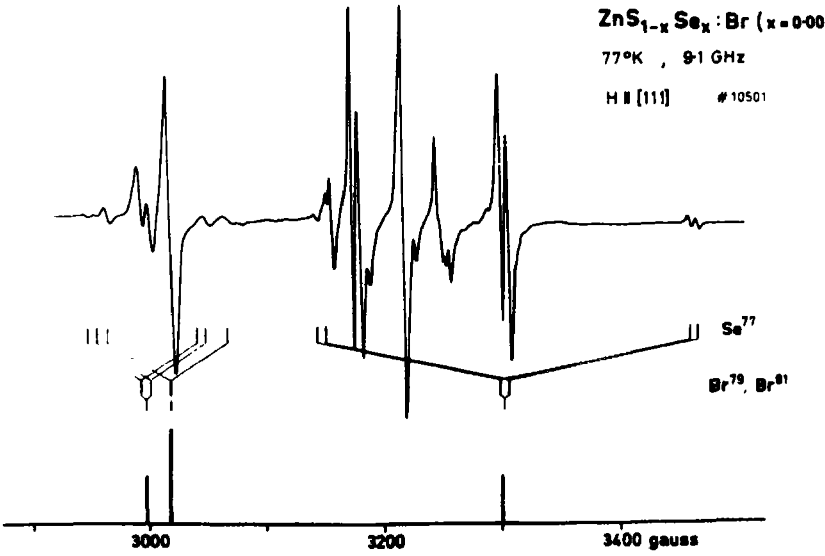

Fig. 5. ESR-spectrum of the $V_{Zn}S_2SeBr$-center in an HBr-transported cubic $ZnS_{1-x}Se_x$ crystal under H∥[111].

possible orientations of the three types of centers in the cubic crystal, a total number of forty-eight centers can be distinguished for a general direction of the magnetic field **H**, twenty-six for a rotation of **H** in the (011) plane and ten centers for **H**‖[111]. Because of this complexity, no attempt was made to analyse the ESR spectra in detail. Only survey spectra, for **H**‖[111], were recorded in $ZnS_{1-x}Se_x$ ($x = 0{\cdot}02$) mixed crystals doped with aluminum or gallium. Strong signals, flanked by Se^{77} satellites, were found to appear at about the same field positions as in the case of the $V_{Zn}S_2SeCl$ or $V_{Zn}S_2SeBr$ center. For the above orientation of the magnetic field, one expects three lines in the high field part and seven lines in the low field part of the spectrum. The ESR signals were found to be inhomogeneously broadened by an unresolved ligand hyperfine structure which was rather pronounced in the case of the $V_{Zn}S_3Se$-$Zn_{11}Ga$ center. Although no detailed analysis of these ESR spectra was possible, the maximum *g*-shifts of the centers responsible appear to be of the same order of magnitude as in the case of the corresponding halogen *A*-centers.

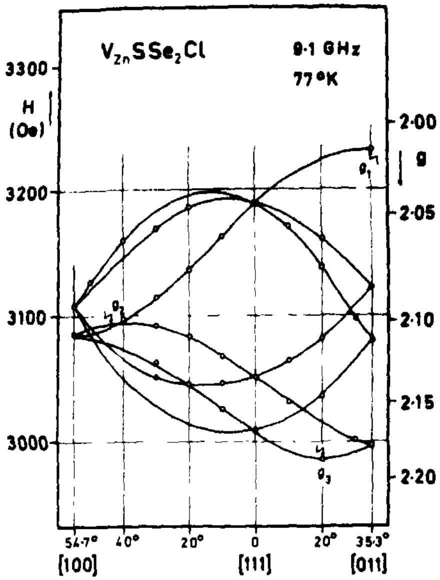

Fig. 6. Angular dependence of the lines in the ESR-spectrum of the $V_{Zn}SSe_2Cl$-center in $ZnS_{1-x}Se_x$. The crystal was purely cubic and free of stacking faults. The magnetic field was rotated in a $(0\bar{1}1)$ plane.

$V_{Zn}SSe_2Cl$

In a chlorine doped $ZnS_{1-x}Se_x$ ($x = 0{\cdot}07$) mixed crystal the ESR spectrum of an additional center was investigated, which we want to attribute to the *A*-center with two selenium and one sulfur atom around the zinc vacancy, $V_{Zn}SSe_2Cl$. There are two main arguments which support this assignment: The relative intensity of these lines increased considerably when the selenium content in the $ZnS_{1-x}Se_x$ crystals was increased from $x = 0{\cdot}005$ over 0·02–0·07. Furthermore, the principal axes of the **g**-tensor were found to point in directions, which are consistent with a two-selenium *A*-center, see Fig. 4, and the principal values of the **g**-tensor have the expected order of magnitude. The angular dependence of the spectrum was taken for a rotation of **H** in a $(0\bar{1}1)$ plane and is shown in Fig. 6. Seven lines are discernible, as in Fig. 3, but now the smallest principal value, g_1, appears exactly at **H**‖[011], whereas the directions of g_2 and g_3 are tilted away from [100] and $[0\bar{1}1]$ by an angle of 16°. Because of the low intensity of these signals, as compared to that of numerous other lines occurring in the ESR spectrum, the components of the Se^{77} hfs tensor could not be determined. We note that the smallest **g**-tensor component, g_1, which occurs along a [011] axis, is considerably greater than the free spin value, 2·0023. This fact will later serve as a strong evidence that the unpaired spin is equally localized at the two selenium atoms.

$V_{Zn}SSe_2Br$

In a bromine doped $ZnS_{1-x}Se_x$ ($x = 0{\cdot}07$) crystal we observed the spectrum of the $V_{Zn}SSe_2Br$ center, which is similar to that of the chlorine analogue. No resolved splitting due to the bromine ligand hyperfine interaction was detected, in contrast to the case of the $V_{Zn}S_2SeBr$ center.

The principal values of the g-tenser and the tilting angle, as determined for the above centers, are compiled in Table 1.

4. RESULTS FROM OPTICAL MEASUREMENTS

Excitation and decay of the paramagnetic A-*centers*

As mentioned before, all paramagnetic *A*-centers were created by illuminating the crystal with the 365 nm line at 77°K. No attempt was made to determine the spectral dependence of the excitation. It was found that the final concentration of paramagnetic *A*-centers in the $ZnS_{1-x}Se_x$ mixed crystals strongly depends on the intensity of the exciting light. Furthermore, a more or less rapid decay of the paramagnetic *A*-centers is observed at 77°K, after turning off the exciting light. These two observations indicate that the final concentration of the paramagnetic centers is determined by the competing effects of optical excitation and thermally enhanced decay. The decay rate depends on the type of center and is fastest for the $V_{Zn}S_3Cl$ center, whereas the $V_{Zn}SSe_2Cl$ centers show the slowest decay among the *A*-centers in chlorine doped $ZnS_{1-x}Se_x$. It should be emphasized that this behaviour of the *A*-centers in $ZnS_{1-x}Se_x$ is quite different from that observed for the $V_{Zn}S_3Cl$ center in pure ZnS. There, the center is stable at 77°K and consequently, the final concentration of paramagnetic *A*-centers does not depend on the intensity of the exciting light. We do not believe that the decay of the *A*-centers in the $ZnS_{1-x}Se_x$ mixed crystals is due to a thermal release of the unpaired hole into the valence band; there is good evidence that the *A*-centers form deep acceptor states in which the unpaired holes are effectively frozen in at 77°K. Instead, we are more inclined to believe that the thermal release of trapped electrons, and their subsequent recombination with the holes trapped at the *A*-centers, is enhanced in the $ZnS_{1-x}Se_x$ mixed crystals. For a better understanding of this effect, more experimental data would be required.

Quenching of the paramagnetic A-*centers*

The decay of the paramagnetic *A*-centers is strongly enhanced by illumination with visible or near infrared light. Figure 7 shows the spectral dependence of this quenching effect for the three different types of *A*-centers observed in the same chlorine doped $ZnS_{1-x}Se_x$ ($x = 0{\cdot}02$) mixed crystal. If we denote the decay constant in the dark by T_d and that upon illumination by T_i, then the diagram shows

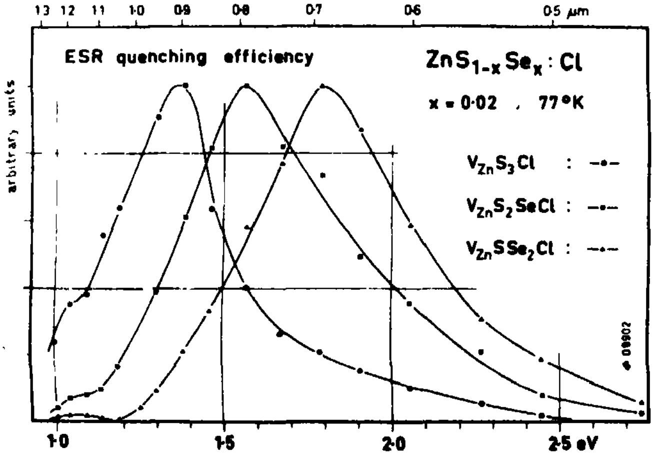

Fig. 7. ESR quenching efficiency of the *A*-centers $V_{Zn}S_3Cl$, $V_{Zn}S_2SeCl$ and $V_{Zn}SSe_2Cl$ in a $ZnS_{1-x}Se_x$ crystal with $x = 0{\cdot}02$.

the difference $1/T = 1/T_l - 1/T_d$ as a function of the energy of the quenching light. We note a distinct shift of the maximum of the quenching efficiency towards higher energies when going from the $V_{Zn}S_3Cl$ over $V_{Zn}S_2SeCl$ to the $V_{Zn}SSe_2Cl$ center. This means that the acceptor states formed by the A-centers in $ZnS_{1-x}Se_x$ become deeper in this same order, since the quenching process can be interpreted as a photo-induced transfer of the trapped hole to valence band like states, as will be discussed in Section 5. It should also be mentioned that halogen doped $ZnS_{1-x}Se_x$ mixed crystals quickly darken upon u.v. illumination at 77°K. This colouration can be bleached by light of that energy which is also efficient in quenching the paramagnetic A-centers. The optical absorption band responsible for this colouration has been investigated by Mr. K. Leutwein of our laboratory. For the $V_{Zn}S_3Cl$ center in pure ZnS, the maximum absorption occurs at 1·3 eV, i.e. at about the same energy as the peak of the quenching band which lies at 1·4 eV, in ZnS as well as in the $ZnS_{1-x}Se_x$ mixed crystals. In the latter case however, the three absorption bands expected for the three types of A-centers could not be separately resolved. Only a broad, structureless absorption was detected in the spectral range of interest. Obviously, more information had been gained from the quenching spectra which are specific for only one type of defect center, see Fig. 7.

Luminescence

Survey measurements of the photo luminescence emission spectra of chlorine doped $ZnS_{1-x}Se_x$ mixed crystals were performed by Dr. G. Schmid of our laboratory. Beside the 470 nm 'self-activated' blue emission band, which is caused by recombination of an electron with the hole in the paramagnetic $V_{Zn}S_3Cl$ center, an additional emission band at about 530 nm was observed on the low energy wing of the blue band. This band rapidly gained in intensity, as the selenium content in the mixed crystal was increased. It might be tentatively assigned to the $V_{Zn}S_2SeCl$ center, although we have not sufficient experimental evidence to make this assignment conclusive.

For a more detailed discussion of the luminscent phenomena in $ZnS_{1-x}Se_x$, and in other related ternary systems we can refer to papers by Lehmann[13], Halsted *et al.*[14] and Fonger[15].

5. DISCUSSION

The experimental data reported in the preceding sections appear to be sufficient to propose rather detailed models for the paramagnetic A-centers occurring in $ZnS_{1-x}Se_x$ mixed crystals.

We start the discussion by considering the four lone-pair orbitals pointing towards the zinc vacancy. The situation is illustrated in Fig. 8(a, b, c) for the case of the halogen A-centers $V_{Zn}S_3Cl$, $V_{Zn}S_2SeCl$ and $V_{Zn}SSe_2Cl$, respectively. Obviously, the two electrons in the halogen orbital are the ones which are

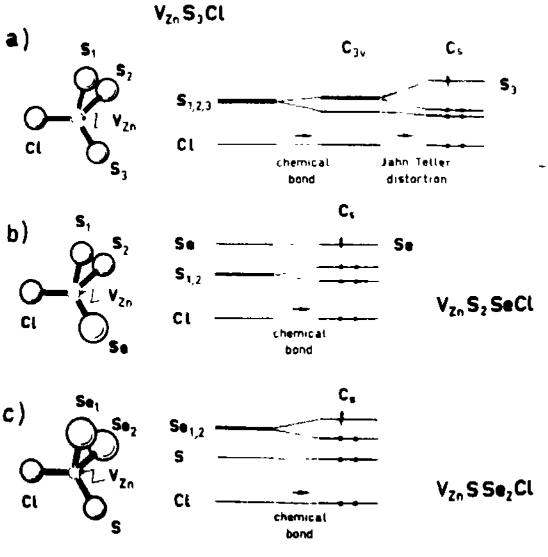

Fig. 8. Simple LCAO molecular orbital model of the electronic structure of the A-centers $V_{Zn}S_3Cl$, $V_{Zn}S_2SeCl$ and $V_{Zn}SSe_2Cl$. The positions of the energy levels are not drawn to scale. A more detailed treatment of the distortion of the $V_{Zn}S_3Cl$ center will be given in Appendix A.

most tightly bound and we expect that the unpaired hole will be mainly localized at the chalcogen sites.

In centers of the type $V_{Zn}S_3X$ or $V_{Zn}Se_3X$, the hole has then the choice between three equivalent chalcogen sites. If overlap between the corresponding orbitals is taken into account, this threefold site degeneracy is lifted, resulting in a lower lying, fully symmetric singlet state and an excited doublet state, in which the unpaired spin has to be accommodated. This upper doublet is further split by a Jahn–Teller type distortion which tends to remove the twofold degeneracy. Thus, the symmetry of the *paramagnetic* state of the centers $V_{Zn}S_3X$ and $V_{Zn}Se_3X$ is lowered from C_{3v} to C_s. The unpaired hole is now dominantly localized at only *one* chalcogen site, see Fig. 8(a). A more detailed discussion of this distortion will be given in Appendix A. At sufficiently high temperatures, a thermally activated hopping of the spin among the three distorted chalcogen sites can be observed[4].

In centers of the type $V_{Zn}S_2SeX$, the two electrons in the selenium lone-pair orbital are the ones which are most weakly bound. Consequently, the unpaired hole must be accommodated at the selenium site, see Fig. 8(b). Because of their inherent lower symmetry, no motional effects resulting from spin-hopping are expected to occur for centers of the type $V_{Zn}S_2SeX$.

In centers of the type $V_{Zn}Se_2SX$, the two selenium orbitals pointing towards the zinc vacancy form a lower lying bonding molecular orbital and a higher lying antibonding orbital, in which the unpaired hole is accommodated, see Fig. 8(c).

Hyperfine interaction

In pure ZnS, the *A*-centers are formed by association of a zinc vacancy with a group-VII or group-III impurity. The presence of these impurity ions in the paramagnetic *A*-centers is unambiguously indicated by the ligand hyperfine structure observed in the ESR spectra[3].* In $ZnS_{1-x}Se_x$, ligand hfs could only be resolved in the ESR spectrum of the $V_{Zn}S_2SeBr$ center. In the case of the $V_{Zn}SSe_2Cl$ and $V_{Zn}SSe_2Br$ centers the unpaired spin is localized in an antibonding molecular orbital centered at the two selenium sites. Therefore, the impurity ligand nuclei are in a nodal plane of the unpaired spin's wavefunction and their hyperfine interaction will be greatly reduced. Finally, the absence of a resolved ligand hfs splitting in the ESR spectrum of the $V_{Zn}S_2SeCl$ center does not appear surprising in view of the very small splitting observed for the $V_{Zn}S_3Cl$ center in pure ZnS.

A quantitative analysis of the *A*-center ligand hyperfine interaction is beyond the scope of this paper. Its observation should merely serve as evidence that the impurity is really part of the center in question. Furthermore, the smallness of the ligand hyperfine splitting indicates that only a very small fraction of the unpaired spin's wavefunction is localized at the group-VII and group-III ligand sites. This appears reasonable since the charge state of these impurities, e.g. Cl^- or Al^{3+}, is repellant for holes.

The large Se^{77} hyperfine interaction observed for the $V_{Zn}S_2SeCl$ and $V_{Zn}S_2SeBr$ center can be interpreted in more detail. For this, we note that the hyperfine interaction tensor **K** can be decomposed into an isotropic part a and into an anisotropic, traceless part **P**,

$$K_1 = a + P_1$$
$$K_2 = a + P_2$$
$$K_3 = a + P_3,$$

---

*Ligand hfs had so far been reported only for the bromine, iodine and gallium *A*-center in ZnS, see [3]. More recently, we have also detected the very small ligand hfs splitting in the ESR spectra of the chlorine and aluminum *A*-center in pure ZnS. The splitting was resolved at 20°K on the high field line in the ESR spectrum H∥[111], giving

$$K(Al^{27}) = 0{\cdot}41\,.\,10^{-4}\,\text{cm}^{-1},\ \text{or}\ 1{\cdot}2\ \text{MHz}$$

and

$$K(Cl^{35}, Cl^{37}) \approx 0{\cdot}1\,.\,10^{-4}\,\text{cm}^{-1},\ \text{or}\ 0{\cdot}3\ \text{MHz}.$$

where $P_1+P_2+P_3=0$. Here, a represents the s-character and P_i dominantly the $4p$-character of the unpaired electron's wavefunction, at the selenium impurity. From the experimental data given in Table 2 we then obtain the values listed in Table 3 under the assumption that K_1 is positive, whereas K_2 and K_3 are negative. This at the moment arbitrary choice will be justified later.

Table 3. Decomposition of the Se^{77} hyperfine interaction tensor determined for A-centers in $ZnS_{1-x}Se_x$ and comparison with corresponding values of the SeO_2^- radical in KCl. All numbers are given in units of MHz, and the principal axes are defined in Fig. 4

Center	a	P_1	P_2	P_3
$V_{Zn}S_2SeCl$	+159	+724	−377	−347
$V_{Zn}S_2SeBr$	+176	+700	−353	−347
SeO_2 :KCl	+66	+622	−320	−302

Comparison is invited with those hyperfine structure parameters which are predicted on the basis of restricted Hartree-Fock calculations of atomic wavefunctions as reported by Clementi[16]. From tables given in his work, the contact interaction a for a pure $4s$-electron and the dipole-dipole interaction b for a pure $4p$-electron can be obtained. We obtain:

	a_{4s}(MHz)	b_{4p}(MHz)
Se^0 (^3P)	+13,200	+379
Se^- (^2P)	+12,700	+315

The theoretical hyperfine structure parameters, as listed above for free Se^0 and Se^-, are exact to a few per cent, within the Hartree-Fock approximation. However, it should be kept in mind that they will be somewhat modified if the electron–electron correlation had been taken into account more rigorously.

The experimentally determined a-values of the $V_{Zn}S_2SeCl$ center, 159 MHz, and of the $V_{Zn}S_2SeBr$ center, 176 MHz, indicate that the unpaired spin has a wavefunction with an s-character of the order of only 1 per cent.

On the other hand, the anisotropic part of the hyperfine interaction b, as predicted on the basis of restricted Hartree–Fock wavefunctions, compares well with the P-values determined experimentally for the A-centers. For this, we neglect the small deviations of the dipole–dipole interaction tensor **P** from axial symmetry, by taking

$$b = -\tfrac{1}{2}(P_2+P_3)$$
$$2b = P_1$$

For $V_{Zn}S_2SeCl$ and $V_{Zn}S_2SeBr$, we then obtain $b = 362$ MHz and $b = 350$ MHz, respectively. These experimental values fall within the range of the theoretically expected b-values for Se^0 and Se^-. Thus, the analysis of the Se^{77} hyperfine structure of the $V_{Zn}S_2SeX$ centers has shown that the unpaired spin is highly localized in a non-bonding, atomic $4p$-orbital of selenium.*

It remains to justify our previous assumption that the sign of K_1 was taken to be

---

*The above discussion of the Se^{77} hyperfine structure of the $V_{Zn}S_2SeX$ centers applies also to the somewhat simpler case of the isolated zinc vacancy in ZnSe, to be labeled in our notation as $V_{Zn}Se_4$. ESR of this intrinsic lattice defect was recently reported by Watkins[17]. The **g**-tensor and the Se^{77} hyperfine interaction tensor, **K**, are axially symmetric around a [111] bond axis, with $K_{\parallel} = 804$ MHz and $K_{\perp} = 150$ MHz.

positive whereas that of K_2 and K_3 was taken to be negative. For this, we summarize the results for the rather similar situation encountered for the SeO_2^- radical in KCl, where the parameter a could be measured very directly from the isotropic, motionally averaged ESR spectrum observed at elevated temperatures [18]. For SeO_2^-, we have without ambiguity $a = +66$ MHz and $b = +311$ MHz. The unpaired spin of this radical is localized in a molecular orbital formed by atomic selenium and oxygen p-orbitals. The spin localization at the central selenium site is about 50–60 per cent.

In the case of the $V_{Zn}S_2SeX$ centers, we can now use the following arguments:

(i) In view of the small deviations of the K-tensor from axial symmetry, we can safely assume that K_2 and K_3 have the same sign.

(ii) Since the spin-localization at the selenium site should be greater than 50–60 per cent, we expect b to be greater than the SeO_2^- value of $+311$ MHz. Only by taking K_1 positive, but K_2 and K_3 negative, this condition can be met. Of course, it has been taken into account that for Se^{77} the dipolar interaction b must have positive sign.

Quenching of the paramagnetic A*-centers*

We had seen above that the unpaired hole of the A-centers shows a strong preference for being localized at the chalcogen sites. Furthermore, if the hole has the choice between a sulfur or a selenium site, localization at the selenium site is energetically more favoured. For centers having the hole localized at only one chalcogen site, i.e. $V_{Zn}S_3X$, $V_{Zn}Se_3X$ and $V_{Zn}S_2SeX$, we can interpret the quenching process by considering a localized 'molecule' made up of the chalcogen atom in question and its three nearest zinc ligands (see Fig. 9). Apart from the non-hybridized lone-pair orbital in which the unpaired spin is accommodated, there are three bonding and three antibonding molecular orbitals. The molecular states corresponding to the bonding orbitals should be viewed as perturbed valence bands states, which have dominantly chalcogen character.

The quenching of the paramagnetic centers by illumination with infrared light is interpreted as a hole transfer from the lone-pair state to the valence band like bonding states from where the hole has then the freedom to leave the complex entirely. For the centers $V_{Zn}S_3Cl$, $V_{Zn}S_2SeCl$ and $V_{Zn}SSe_2Cl$ the maximum quenching rate is observed at 1·4 eV, 1·6 eV and at 1·8 eV, respectively, see Fig.

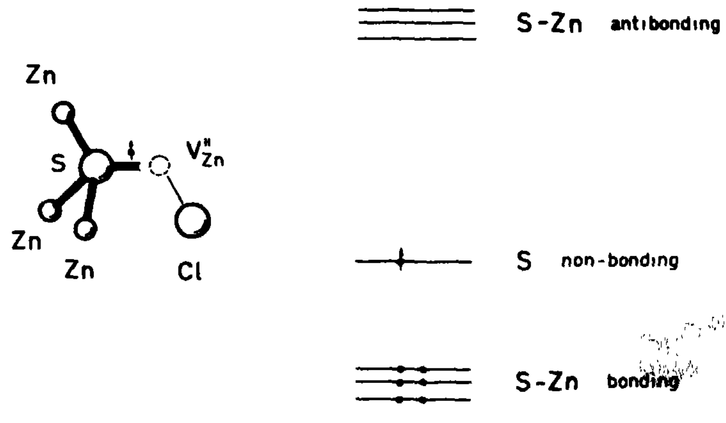

Fig. 9. Localized 'molecule' considered for the explanation of the g-shifts and the optical ESR-quenching of a $V_{Zn}S_3Cl$ center in ZnS.

7. This shows that the energetical separation of the unpaired spin level from the valence band of ZnS is greater for those *A*-centers which contain selenium atoms. In other words, these centers represent deeper hole traps.

g-Tensor

A summary of experimental *g*-shift data obtained for *A*-centers in ZnS, ZnSe and $ZnS_{1-x}Se_x$ is given in Table 4. The deviations of the g-tensor components g_i from the free-spin value of 2·0023 result from the spin–orbit interaction which admixes excited states to the ground state wavefunction. The first-order *g*-shifts can be obtained from the relation

$$\Delta g_{ij} = -2\lambda \sum_n n \frac{\langle 0|L_i|n\rangle\langle n|L_j|0\rangle}{E_n - E_0} \qquad (1)$$

where λ is the spin–orbit coupling constant, and the sum must be taken over all excited states of the paramagnetic center. It should be emphasized that the above relation will only be correct, if the unpaired spin experiences a centrosymmetric electric field.* In the case of the *A*-centers, however, this will be a good approximation, since the analysis of the Se^{77} hyperfine interaction of the $V_{Zn}S_2SeX$ centers had shown that the unpaired spin is dominantly localized in an atomic 4*p*-orbital.

Equation (1) predicts no first-order *g*-shift if the magnetic field is parallel to the axis of the non-bonding *p*-type orbital. As can be seen from Table 4, this is almost exactly true for the *A*-centers in ZnS, where the unpaired spin is localized at one sulfur site. However, for the corresponding selenium *A*-centers in ZnSe and $ZnS_{1-x}Se_x$ small negative *g*-shifts are observed. It will be shown later, that second-order terms in the spin–orbit interaction can account for these negative *g*-shifts.

Large, positive *g*-shifts are observed, when the magnetic field is normal to the non-bonding orbital, see Table 4. The excited states which will dominantly contribute to the *g*-shifts, on the basis of equation (1), can be predicted from the same 'localized molecule' energy scheme, which was previously used to interpret the quenching process, see Fig. 9. For one type of excitation, the unpaired elecelectron of the non-bonding state is lifted to the antibonding states, for the other type, one electron is excited from the occupied bonding states to fill the non-bonding state.

Spin-orbit matrix elements to the antibond-

Table 4. Summary of g-shifts observed for A-centers in cubic ZnS, ZnSe† and $ZnS_{1-x}Se_x$‡. For definition of principal axes and tilting angle τ, see Fig. 4*

Host	Center	Δg_1	Δg_2	Δg_3	$(\Delta g_3/\Delta g_2) - 1$	τ
ZnS	$V_{Zn}S_3Cl$	0·0004	0·0479	0·0542	0·132 ± 0·014	3·9° ± 0·1°
	$V_{Zn}S_3Br$	0·0006	0·0514	0·0546	0·062 ± 0·014	2·3° ± 0·3°
	$V_{Zn}S_4Zn_{11}Al$	0·0007	0·0490	0·0537	0·096 ± 0·014	2·5° ± 0·5°
	$V_{Zn}S_4Zn_{11}Ga$	0·0002	0·0486	0·0533	0·097 ± 0·022	2·9° ± 0·5°
ZnSe	$V_{Zn}Se_3Cl$	−0·0426	0·1589	0·2426	0·527 ± 0·005	6·3° ± 0·1°
$ZnS_{1-x}Se_x$	$V_{Zn}S_2SeCl$	−0·0315	0·1719	0·1918	0·116 ± 0·006	3·8° ± 0·5°
	$V_{Zn}S_2SeBr$	−0·0315	0·1802	0·1899	0·054 ± 0·006	2·0° ± 0·8°
	$V_{Zn}SSe_2Cl$	0·0102	0·0953	0·1763		16° ± 2°
	$V_{Zn}SSe_2Br$	0·0037	0·1016	0·1817		13° ± 2°

*Taken from [3].
†Taken from [6].
‡This work, see Table 1.

---

*Complications which arise in the case of non-centrosymmetric electric fields have been discussed by Watkins and Corbett [19].

ing states yield negative first-order *g*-shifts, whereas the contributions of the bonding states are positive. In view of the strongly positive *g*-shifts observed experimentally for g_2 and g_3, see Table 4, we can safely assume that the dominant contributions to the *g*-shifts result from an admixture of the bonding states. As was pointed out already in the discussion of the quenching process, the bonding states should be viewed as perturbed valence band states which have dominantly chalcogen character.

We can now attempt an order of magnitude estimate of the *g*-shifts. The spin-orbit coupling constant λ of the chalcogen atoms are approximately known and the mean energetical separation between the non-bonding ground state and the bonding states, ΔE_b, has been determined directly by the quenching experiments. In an axial approximation, which neglects the small differences between g_2 and g_3, we then obtain for the *g*-shifts

$$\Delta g_{\parallel} = \Delta g_1 = -(g_0 - 1)\lambda^2/\Delta E_b{}^2$$

$$\Delta g_{\perp} = \tfrac{1}{2}(\Delta g_2 + \Delta g_3) = -2\lambda/\Delta E_b - g_0\lambda^2/\Delta E_b{}^2 \tag{2}$$

where $g_0 = 2{\cdot}0023$. For this, equation (1) had to be extended to include also second order terms in the spin–orbit interaction, which can no longer be neglected for the selenium *A*-centers, where λ is quite large. We note that these second order contributions are always negative, independent of the sign of λ.

For λ we take values corresponding to the singly negatively charged chalcogen ions, viz. $-330\,\mathrm{cm}^{-1}$, or $-0{\cdot}041$ eV, for S^- and $-1620\,\mathrm{cm}^{-1}$, or $-0{\cdot}201$ eV for Se^-.* The quenching peak, ΔE_b, occurred at 1·4 eV for $V_{Zn}S_3X$, and at 1·6 eV for $V_{Zn}S_2SeX$. We then obtain

$V_{Zn}S_3X, V_{Zn}S_4Zn_{11}^{''}X$ $\quad \Delta g_{\parallel} = -0{\cdot}001$
$\Delta g_{\perp} = +0{\cdot}057$

$V_{Zn}S_2SeX$ $\quad \Delta g_{\parallel} = -0{\cdot}016$
$\Delta g_{\perp} = +0{\cdot}219$

We note that the dominant *g*-shifts, $\Delta g_{\perp}$, are greater by about 10 per cent than those observed experimentally for sulfur *A*-centers and by about 20 per cent for the $V_{Zn}S_2SeX$ centers, see Table 4. The reason is that, in our simplified model, we have neglected the *g*-shift contributions resulting from admixture of the antibonding states, which are positive for $\Delta g_{\perp}$, but again negative for $\Delta g_{\parallel}$. In other words, we have neglected the partial covalent bonding of the chalcogen atom to its three zinc ligands.

To summarize the discussion, we can state that the above treatment accounts well for the *g*-shifts observed. In particular, it became apparent that the energy denominators appearing in equation (1) should be essentially identified with the energetical separation of the non-bonding state from the bonding states which should be located close to the edge of the valence band of the host lattice. This means that the *g*-shift contributions from the antibonding states can be neglected to a good approximation.

For this reason, an atomic approach can be used to interpret the *g*-shifts: in Appendix B they will be discussed in the light of crystal field theory of a S^- or Se^- ion, ^2P, subject to a Stark effect from the non-cubic crystalline field arising mainly from the zinc vacancy and the associated donor impurity ion. This treatment will enable us to understand finer details of the g-tensor, like the deviations from axial symmetry, g_3-g_2, and the tilting angle τ, which were neglected in the previous discussion.

It should be mentioned that the molecular orbital description of the centers $V_{Zn}S_3X$, $V_{Zn}Se_3X$ and $V_{Zn}S_2SeX$ is quite analogous to that given by Watkins and Corbett[19] for the isomorphous silicon *E*-center. This defect is formed by association of a silicon vacancy with a group-V donor, as phosphorus. In our notation, the silicon *E*-center should be written as $V_{Si}Si_3P$. The analogous centers $V_{Si}Si_3As$ and $V_{Si}Si_3Sb$ have also been recently investigated[20].

---

*These values were obtained by an extrapolation from isoelectronic np^5 atoms and ions, taking λ equal to two-thirds the difference between the $^2P_{3/2}$ and $^2P_{1/2}$ state. This spin–orbit coupling constant should not be confused with the spin–orbit splitting parameter of the valence band, as used in the preceding paper, see[10].

It remains to discuss the *g*-shifts of the centers $V_{Zn}SSe_2X$, where the unpaired spin is shared between two selenium sites, in an antibonding molecular orbital, see Fig. 8. As a first approximation, we can construct the molecular wavefunction by a superposition of the two dangling selenium orbitals. We note that the smallest *g*-shift, Δg_1, observed for centers of the type $V_{Zn}SSe_2X$ is still positive and occurs along the Se–Se axis, see Table 1 and Fig. 4. This behaviour is to be expected since the molecular orbital in question is formed by two dangling, non-collinear atomic orbitals. One might still argue that the positive *g*-shift, observed for g_1, results from a rapid, thermally activated hopping of the spin between the two selenium sites. In this case, drastic changes in the ESR-spectrum should be observed at lower temperatures, where the hopping rate becomes much slower. This was not observed experimentally, down to 20°K.

REFERENCES

1. SCHNEIDER J., In *II-VI Semiconducting Compounds* (Edited by D. G. Thomas). Benjamin, New York (1967). This article summarizes previous ESR work on ZnS and on other II–VI compounds.
2. SCHNEIDER J., HOLTON W. C., ESTLE T. L. and RÄUBER A., *Phys. Lett.* **5**, 312 (1963).
3. SCHNEIDER J., RÄUBER A., DISCHLER B., ESTLE T. L. and HOLTON W. C., *J. chem. Phys.* **42**, 1839 (1965).
4. DISCHLER B., RÄUBER A. and SCHNEIDER J., *Phys. Status Solidi* **6**, 507 (1964).
5. RÄUBER A. and SCHNEIDER J., *Phys. Lett.* **3**, 230 (1963).
6. HOLTON W. C., deWIT M. and ESTLE T. L., In *Int. Symp. Luminescence* (Edited by N. Riehl and H. Kallmann), p. 454. Verlag Karl Thiemig, München (1966).
7. SCHIRMER O., Private communication.
8. THOMAS D. G. and DINGLE R., See [1], p. 863.
9. WILLIAMS E. W., *Phys. Rev.* **168**, 922 (1968).
10. SCHNEIDER J., DISCHLER B. and RÄUBER A., *J. Phys. Chem. Solids* **29**, 451 (1968).
11. DIELEMAN J., TITLE R. S. and SMITH W. V., *Phys. Lett.* **1**, 334 (1962).
12. RÄUBER A. and SCHNEIDER J., *Z. Naturf.* **17a**, 266 (1962); TITLE R. S., *Phys. Rev.* **131**, 623 (1963).
13. LEHMANN W., *J. Electrochem. Soc.* **113**, 449, 788 (1966); *ibid.* **114**, 83 (1967).
14. HALSTED R. E., AVEN M. and COGHILL H. D., *J. Electrochem. Soc.* **112**, 177 (1965).
15. FONGER W. H., *Phys. Rev.* **137**, A1038 (1965).
16. CLEMENTI E., *IBM J. Res. Devel.* **9**, 2 (1965).
17. WATKINS G. D., *Bull. Am. phys. Soc.* **14**, 312 (1969).
18. SCHNEIDER J., DISCHLER B. and RÄUBER A., *Phys. Status Solidi* **13**, 141 (1966).
19. WATKINS G. D. and CORBETT J. W., *Phys. Rev.* **134**, A1359 (1964).
20. ELKIN E. L. and WATKINS G. D., *Phys. Rev.* **174**, 881 (1968).
21. INUI T., HARASAWA S. and OBATA Y., *J. phys. Soc. Japan* **11**, 612 (1956).
22. CASTNER T. G. and KÄNZIG W., *J. Phys. Chem. Solids* **3**, 178 (1957).

APPENDIX A

Spontaneous distortion from C_{3v} to C_s symmetry

It is an experimental fact that the paramagnetic centers $V_{Zn}S_3Cl$, $V_{Zn}S_3Br$ and $V_{Zn}Se_3Cl$ have orthorhombic hyperfine and g-tensors. Evidently the corresponding molecular clusters, which have originally C_{3v}-symmetry undergo a spontaneous distortion.

In the following, we present a very simple model calculation in order to derive two results, which should be valid also for the more complicated real system. We want to show that the distorted cluster is the more stable configuration and that the wavefunction of the unpaired spin is almost entirely localized on one of the three chalcogen atoms.

In the molecular cluster there are four dangling bonds pointing towards the zinc vacancy. We label the three chalcogen orbitals ϕ_a, ϕ_b and ϕ_c. The halogen orbital is lower in energy and does not enter the calculation. We assume a linear coupling of the energy levels to the distortion Q, a repulsion term proportional to Q^2 and an exchange integral β which is also a function of Q. Then the elements of the energy matrix take the form

$$\begin{aligned} H_{aa} = H_{bb} &= \alpha(1+a_1Q+a_2Q^2) \\ H_{cc} &= \alpha(1+c_1Q+c_2Q^2) \\ H_{ab} &= \beta(1+d_1Q+d_2Q^2) \\ H_{ac} = H_{bc} &= \beta(1+e_1Q+e_2Q^2) \end{aligned} \tag{A1}$$

In the absence of a distortion, i.e. $Q=0$, the eigenfunctions have trigonal symmetry, C_{3v}

$$\begin{aligned} A_1 &: \psi_1 = (\phi_a+\phi_b+\phi_c)/\sqrt{3} \\ E &: \begin{cases} \psi_2 = (\phi_a+\phi_b-2\phi_c)/\sqrt{6} \\ \psi_3 = (\phi_a-\phi_b)/\sqrt{2} \end{cases} \end{aligned} \tag{A2}$$

The corresponding energies are

$$W_1(A_1) = \alpha + 2\beta$$
$$W_{2,3}(E) = \alpha - \beta$$

In the limit of a very strong C_s-distortion, i.e. $|\alpha(a_1 - c_1)Q| \gg |\beta|$, the molecular orbitals are given by

$$\begin{aligned} A':\psi_1 &= (\phi_a + \phi_b)/\sqrt{2} \\ A':\psi_2 &= \phi_c \\ A'':\psi_3 &= (\phi_a - \phi_b)/\sqrt{2} \end{aligned} \tag{A3}$$

with energies

$$W_1(A') = \alpha(1 + a_1Q + a_2Q^2) + \beta(1 + d_1Q + d_2Q^2)$$
$$W_2(A') = \alpha(1 + c_1Q + c_2Q^2)$$
$$W_3(A'') = \alpha(1 + a_1Q + a_2Q^2) - \beta(1 + d_1Q + d_2Q^2)$$

Note that ψ_1 is independent of Q, whereas ψ_1 and ψ_2 approach the functions of equation (A2) when Q goes to zero. The lower part of Fig. 10 shows the energy levels as a function of the distortion Q, where the parameters for this model calculation were chosen freely, viz.: $\alpha = 100$, $\beta = -1$, $a_1 = -0{\cdot}04$, $a_2 = 0{\cdot}01$, $c_1 = 0{\cdot}08$, $c_2 = 0{\cdot}01$, $d_1 = -0{\cdot}1$, $d_2 = -0{\cdot}1$, $e_1 = 0{\cdot}1$, $e_2 = 0{\cdot}1$ We have to accommodate five electrons in the level scheme and summation of the individual energies gives the total energy shown in the upper part of Fig. 10. Two conclusions now can be drawn: (i) the energy is minimized in the distorted configuration and (ii) the unpaired spin is in the upper A' state which means localization in one of the dangling bonds, viz. ϕ_c.

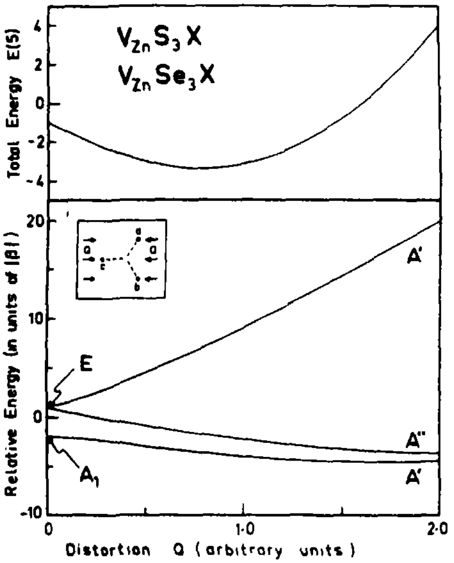

Fig. 10. Results of a model calculation (see text) for the relative energies of the three single electron LCAO-MO states of the $V_{Zn}S_3Cl$ center, as a function of the Jahn–Teller type spontaneous distortion, Q, (lower part). The total energy $E(5)$ for the five-electron system is plotted in the upper part and is seen to be minimized in the distorted configuration.

APPENDIX B

Point charge calculation for the g-tensor

As pointed out in the Discussion, the basic structure of the paramagnetic state of the A-center is characterized by an atomic ^2P state. We subject this state to a Stark effect from the non-cubic crystalline field arising mainly from the zinc vacancy and the associated impurity ion. Neglecting the spin–orbit interaction, the axial field arising from the zinc vacancy splits the threefold orbital degeneracy of the ^2P state of the Se^- or S^- ion into a lower energy singlet, E_z, and a higher energy doublet, $E_x = E_y$. The additional field due to the associated group-VII or group-III impurity lifts the orbital degeneracy of the doublet. Now, if the spin–orbit interaction is taken into account in first and second order, the deviations of the g-tensor components g_i from the free spin value, $g_0 = 2{\cdot}0023$, are given by:

$$\begin{aligned} \Delta g_x &= -\frac{2\lambda}{E_y} - \lambda^2\left[\frac{g_0}{2}\frac{1}{E_x^2} + \frac{1}{E_xE_y}\right] \\ \Delta g_y &= -\frac{2\lambda}{E_x} - \lambda^2\left[\frac{g_0}{2}\frac{1}{E_y^2} + \frac{1}{E_xE_y}\right] \\ \Delta g_z &= -\lambda^2\left[\frac{g_0}{2}\left(\frac{1}{E_x^2} + \frac{1}{E_y^2}\right) - \frac{1}{E_xE_y}\right] \end{aligned} \tag{B1}$$

Here, E_z has been placed at the zero point of the energy scale and λ is the spin–orbit coupling constant of the Se^- or S^- ion. Equations (B1) result from a specialisation of the g-shift calculation reported by Inui *et al.*[21] for the molecular V_k-centers [22] in alkali halides.

A summary of experimental g-shift data obtained for A-centers in ZnS, ZnSe and $ZnS_{1-x}Se_x$ was given in Table 4. Inspection of this table reveals some general trends:

(a) The largest g-shift, Δg_3, always occurs in the mirror symmetry plane of the center, in which also Δg_1 is observed.
(b) A larger tilting angle τ goes parallel with a larger deviation of the g-tensor from axial symmetry, as described by the parameter $(\Delta g_3/\Delta g_2) - 1$.

These observations can be readily understood on the basis of the following naive crystal field calculation; for this, we consider the A-center geometry shown in Fig. 11. The paramagnetic S^- or Se^- ion is at the center of the coordinate system. e_1 and e_2 represent the effective electric charges of the zinc vacancy and of the associated impurity, respectively. In an idealized, purely ionic picture, we would expect $e_1 = -2e$ and $e_2 = +e$. These defect charges induce crystalline electric field gradients at the central chalcogen site, which are given by

$$V = \beta_{20}(3\zeta^2 - \rho^2) + \beta_{21}\xi\zeta + \beta_{22}(\xi^2 - \zeta^2)$$

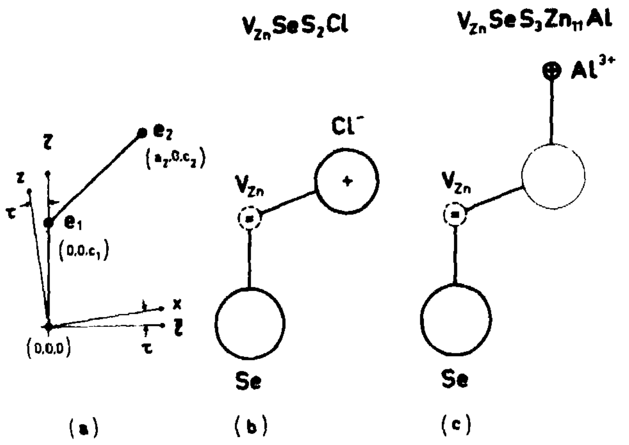

Fig. 11. Coordinate system used for the point charge calculation, (a). The basic structure of the A-centers with a group-VII or group-III impurity is sketched in (b) and (c).

where

$$\beta_{20} = \frac{e_1}{2c_1^3} + \frac{e_2}{2(a_2^2 + c_2^2)^{3/2}}$$

$$\beta_{21} = 3e_2 \cdot \frac{a_2 c_2}{(a_2^2 + c_2^2)^{5/2}} \qquad \text{(B2)}$$

$$\beta_{22} = \frac{3}{2} e_2 \cdot \frac{a_2^2}{(a_2^2 + c_2^2)^{5/2}}$$

Here, the ζ-axis is taken along a [111] bond direction and the η-axis is perpendicular to the mirror symmetry plane of the center, see Fig. 11. Since $|e_1| > |e_2|$, and since e_2 is more distant, the dominant contribution to the field gradient will arise from the zinc vacancy. The threefold orbital degeneracy of the ^2P state is lifted by this perturbation. The energy matrix is most conveniently diagonalized by transformation to a new coordinate system x, y, z in which the mixed term $\xi\zeta$ of the field gradient vanishes. This can be achieved by rotating the coordinate system ξ, η, ζ around the η-axis by the 'tilting' angle τ which is determined by the relation

$$\operatorname{tg} 2\tau = \frac{\beta_{21}}{2\beta_{22} - 3\beta_{20}} \qquad \text{(B3)}$$

In the new coordinate system, the field gradients are written as

$$V = b_{20}(3z^2 - r^2) + b_{22}(x^2 - y^2) \qquad \text{(B4)}$$

where

$$b_{20} = \beta_{20} - b_{22}$$

$$b_{22} = \tfrac{1}{2}(3\beta_{20} \sin^2\tau + \tfrac{1}{2}\beta_{21} \sin 2\tau + \beta_{22} \cos 2\tau)$$

and the energy matrix is diagonalized by the orbital eigenfunctions p_x, p_y, p_z, giving

$$\begin{aligned} E_x &= c(b_{20} - b_{22}) \\ E_y &= c(b_{20} + b_{22}) \qquad \text{(B5)} \\ E_z &= -2cb_{20} \end{aligned}$$

where c is a common constant. For the geometry shown in Fig. 11, where sign $e_2 = -$ sign e_1 and $|e_1| > |e_2|$, b_{20} and b_{22} have opposite signs. This means that the E_x state

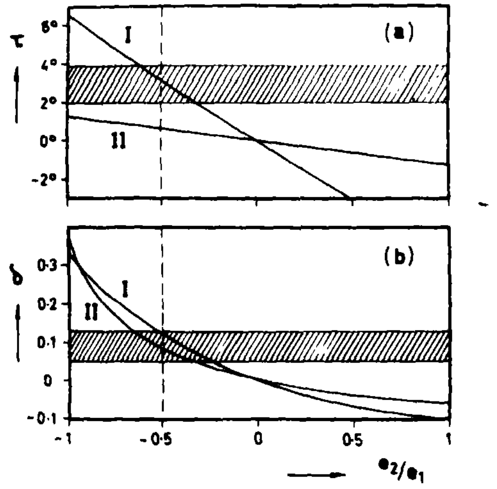

Fig. 12. Results of point charge calculations for the geometry defined in Fig. 11. The charge ratio e_2/e_1 is taken as abscissa. The diagrams show (a) the tilting angle τ and (b) the deviations from axial symmetry of the g-tensor defined by $\delta = (\Delta g_2/\Delta g_3) - 1$. Experimental values, observed for A-centers in ZnS and $ZnS_{1-x}Se_x$, are within the shadowed areas. The broken line at $e_2/e_1 = -0{\cdot}5$ is appropriate for a purely ionic description. Roman numbers refer to A-centers with a group-VII impurity, (I), and with a group-III impurity, (II).

lies above the E_y state, the E_x state being the ground state. Equations (A1) then predict that $\Delta g_x > \Delta g_y$, in agreement with the experimental findings. Note, that the axes x and y correspond to the axes 3 and 2 in Fig. 4. Furthermore, equation (B3) then predicts that the tilting angle τ is always positive.

We have attempted some quantitative estimates of the tilting angle τ and of the asymmetry parameter $\delta = (\Delta g_3/\Delta g_2) - 1$. The latter quantity is determined by the relation

$$\delta = \frac{\Delta g_x}{\Delta g_y} - 1 = -\frac{2b_{22}}{3b_{20} + b_{22}} \tag{B6}$$

if the spin–orbit interaction is treated only in first order. For an order of magnitude estimate, we now make the greatly simplifying assumption that the defect charges e_1 and e_2 are centered at undistorted lattice sites. In the case of the selenium A-centers, we also neglect the electronegativity differences between sulfur and selenium. With the help of the above relations, the quantities τ and δ have been calculated for the group-VII and group-III A-centers, as a function of the defect charge ratio e_2/e_1. The results are shown in Fig. 12. Experimental values observed for A-centers in ZnS and $ZnS_{1-x}Se_x$ fall within the shadowed areas. Curves labeled I and II are valid for group-VII and group-III A-centers, respectively. In most cases, order of magnitude agreement for the tilting angle τ and for the asymmetry parameter δ is achieved if we take $e_2/e_1 = -\frac{1}{2}$. This corresponds to the purely ionic case. However, the experimental values for τ of the group-III A-centers in ZnS and for τ and δ of the chlorine A-center in ZnSe are considerably larger than those calculated within our ionic approximation.

In this connection it must be emphasized, that the distortion of the lattice as treated in Appendix A has been neglected. The calculated parameter δ for instance would be larger in the distorted lattice.

J. Phys. Chem. Solids Pergamon Press 1970. Vol. 31, pp. 355–361. Printed in Great Britain.

OPTICAL PROPERTIES OF IMPURITIES IN BLENDE TYPE II-VI SEMICONDUCTORS COMPOUNDS

R. BESERMAN and M. BALKANSKI
Laboratoire de Physique des Solides de la Faculté des Sciences de Paris, France
(Equipe de Recherche Associée au C.N.R.S.)

(*Received* 27 *March* 1969; *in revised form* 2 *June* 1969)

Abstract– Using infrared techniques, the localized mode frequencies of S in ZnSe and ZnTe, of Se in CdTe, have been measured, as well as the resonnance mode frequencies of Mn and Te in ZnSe.

1. INTRODUCTION

A LARGE amount of experimental results on the lattice vibration spectra of pure and doped II-VI compounds have been accumulated in recent years.

Most of the investigations were directed toward the study of lighter impurity ions in alkali halides, silicon and in some of the III-V compounds.

In the case of II-VI compounds, the infrared absorption due to some light impurities have been investigated such as the Li impurity in CdS[1], CdSe and CdTe[2] of Be in CdTe [3], of S impurity in CdSe[2]. More recently the infrared spectra of the localized vibration of Al, Mg, Li and Cu in ZnS, ZnSe, ZnTe has been studied[4].

In this paper we are presenting the optical spectra of some II-VI compounds doped with light and heavy substitutional impurities. The reflectivity peaks are attributed to localized, resonnance or to gap modes.

The impurity mode frequencies are solutions of the perturbed secular equation

$$\mathrm{Det}\,|1-G(\omega)\,.\,C(\omega)| = 0 \qquad (1.1)$$

$G(\omega)$ and $C(\omega)$ are the Green's function matrix of the perfect crystal and the perturbation matrix related to the defect.

The Green's functions of the perfect crystal are deduced from the phonon density of states $\nu(\omega)$ by:

$$G(\omega) = \int_0^{\omega_M} \frac{\nu(\omega')\mathrm{d}\omega'}{\omega^2\ \omega'^2} + \frac{i\pi}{2\omega}\nu(\omega) \qquad (1.2)$$

When the defect can be considered as an isotopic substitutional atom, the localized and resonnance mode frequencies are then solution of:

$$\epsilon\omega^2 G'(\omega) = 1 \qquad (1.3)$$

$G'(\omega)$ is the real part of $G(\omega)$.

The single phonon density of states for a perfect crystal of CdS has been calculated [5], taking into account the ion polarisibility.

The Green's functions of the perfect crystal have been used to calculate the localized mode frequency for a substitutional mass defect without change of force constants [6].

2. EXPERIMENTAL RESULTS

2.1 *Experimental procedure*

The reflectivity measurements were performed on a far infrared vacuum spectrometer CODERG. The reflectivity is taken point by point comparing the crystal reflectivity to a mirror one. The resolution is 1 cm^{-1} in all the range studied.

The dielectric constant is a complex function of the oscillator strength $4\pi\rho$ of the damping constant γ and of the transverse optical mode ω_{TO}.

$$\epsilon = \epsilon_\infty + \frac{4\pi\rho\,\omega_{TO}^2}{\omega_{TO}^2-\omega^2-i\gamma\omega} \qquad (2.1)$$

the real and the imaginary part of the dielectric constant are respectively

$$\epsilon_r = \epsilon_\infty + \frac{4\pi\rho\omega_{TO}^2(\omega_{TO}^2 - \omega^2)}{(\omega_{TO}^2 - \omega^2)^2 + \gamma^2\omega^2} \qquad (2.2)$$

$$\epsilon_i = \frac{4\pi\rho\omega_{TO}^2\omega\gamma}{(\omega_{TO}^2 - \omega^2)^2 + \gamma^2\omega^2} \qquad (2.3)$$

When the damping is neglected in the real and imaginary parts of the dielectric constant, the ω_{TO} frequency corresponds to ϵ_i maximum, the ω_{LO} frequency to $\epsilon_r = 0$ or $Im(-1/\epsilon)$ maximum given by equations (2.2) and (2.3)

The oscillator strength is then defined from the imaginary part of the dielectric constant by

$$4\pi\rho = \epsilon_{i\,\max}\frac{\Delta\epsilon_i}{\omega_{TO}} \qquad (2.4)$$

$\Delta\epsilon_i$ being the line width

The dielectric constants have been calculated with a 3600 control Data computer, using the Kramers-Krönig relations [7].

The samples have been optically polished, and the composition of the doped II-VI compounds have been determined by X ray fluorescence.

2.2 *Localized modes in II-VI blende type semiconductors*

2.2.1 *Sulfur substitutes selenium of zinc selenide.* The S is a light impurity of mass 32, which substitutes the Se of mass 79, the mass factor is $\epsilon = 0{\cdot}595$ and a local mode of the substitutional impurity is expected.

Figure 1 shows the reflectivity spectrum of ZnSe containing about 1%S. The reflectivity band corresponds to the ZnSe restrahlen, the reflectivity peak which frequency is higher than the ω_{LO} frequency of ZnSe is due to the substitutional S impurity in ZnSe.

The Kramers-Krönig relations analysis of the reflectivity coefficient, leads to the real and imaginary part of the dielectric constant, which are shown in Fig. 2.

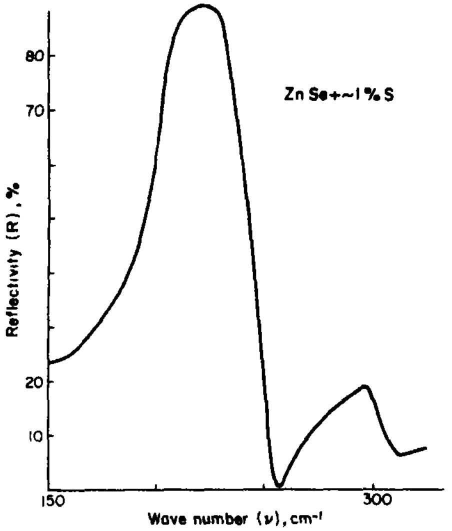

Fig. 1. Reflectivity spectrum of ZnSe containing about 1%S.

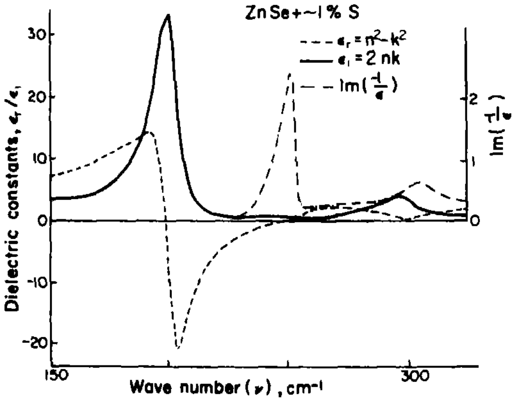

Fig. 2. Dielectric constants of ZnSe containing about 1%S.

The imaginary part of the dielectric constant, has two maxima corresponding respectively to the pure ZnSe and to the S localized transverse optical modes, whose frequencies are

$$\omega_{TO}(\text{ZnSe}) = 202\ \text{cm}^{-1}\ \omega_{TO}^{Loc} = 297\ \text{cm}^{-1}$$

The imaginary part of minus the inverse of the dielectric constant shows two maxima corresponding respectively to the pure ZnSe and to the S localized longitudinal optical modes, whose frequencies are

$$\omega_{LO}(\text{ZnSe}) = 252\ \text{cm}^{-1}\ \omega_{LO}^{Loc} = 305{\cdot}5\ \text{cm}^{-1}.$$

The splitting between the frequencies ω_{TO}^{Loc} and ω_{LO}^{Loc}, is due to the finite concentration in impurities. As shown in the study of mixed crystals, the increase of impurity concentration brings up two constituents of the localized mode having the characters of a transverse and a longitudinal mode, the energy difference between these two modes is a function of the impurity concentration [8].

2.2.2 *Sulfur substitutes tellurium of zinc tellurium.* Substituting Te of mass 127·6, S is a light impurity in ZnTe, the mass factor is $\epsilon = 0{\cdot}75$ and a localized mode is expected.

Figure 3 shows the reflectivity spectrum of ZnTe containing about 1% of S.

The reflectivity band corresponds to the ZnTe restrahlen, the reflectivity peak which is located at frequencies higher than the ω_{LO} frequency of ZnTe is due to the substitutional S impurity.

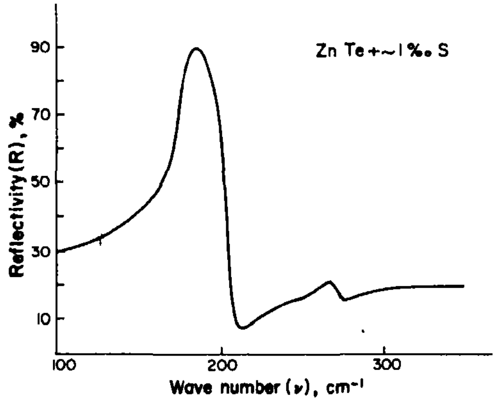

Fig. 3. Reflectivity spectrum of ZnTe containing about 1% S.

The Kramers–Krönig relations analysis of the reflectivity coefficient gives the dielectric constants which are shown in Fig. 4.

The two maxima of ϵ_i correspond to the transverse optical mode frequencies of pure ZnTe and of the S impurity. The frequencies are respectively:

$$\omega_{TO}(\text{ZnTe}) = 177\ \text{cm}^{-1} \quad \omega_{TO}^{Loc} = 269\ \text{cm}^{-1}$$

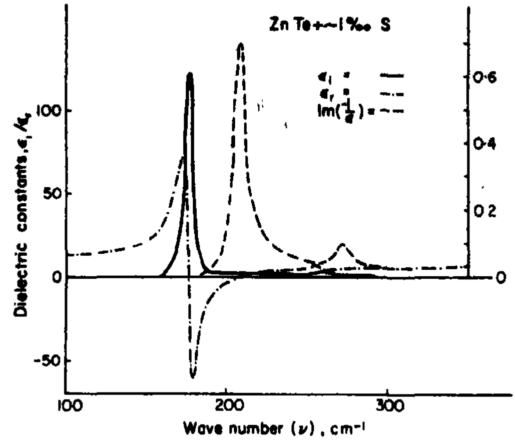

Fig. 4. Dielectric constants of ZnTe containing about 1% S.

The two maxima of $Im(-1/\epsilon)$ correspond to the longitudinal optical mode frequencies of ZnTe and of the S impurity which are

$$\omega_{LO}(\text{ZnTe}) = 208{\cdot}5\ \text{cm}^{-1}\ \omega_{LO}^{Loc} = 272\ \text{cm}^{-1}$$

2.2.3 *Selenium substitutes tellurium of cadmium tellurium.* Se of mass 79 substituting Te which mass is 127·6 is a light impurity and the mass factor is low $\epsilon = 0{\cdot}38$.

Figure 5 shows the reflectivity spectrum of CdTe containing about 1% Se, the impurity peak due to Se appears on the high frequency side of the CdTe restrahlen curve.

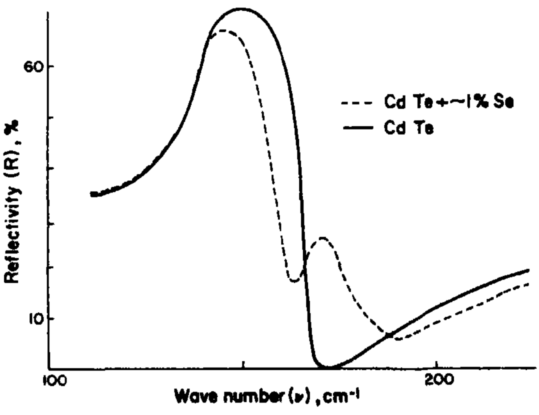

Fig. 5. Reflectivity spectra of pure CdTe and CdTe containing about 1% Se.

The dielectric constants has been calculated from the reflectivity spectrum. As shown on Fig. 6, two transverse optical modes can be seen in the imaginary part of the dielectric constants:

The CdTe one of which the frequency is $\omega_{TO} = 139\,\mathrm{cm}^{-1}$.

The Se impurity one of which the frequency is $\omega_{TO}^{loc} = 170\,\mathrm{cm}^{-1}$.

The longitudinal optical mode primitively situated at $\omega_{LO} = 167\,\mathrm{cm}^{-1}$, is split into two optical mode by the introduction of Se impurities.

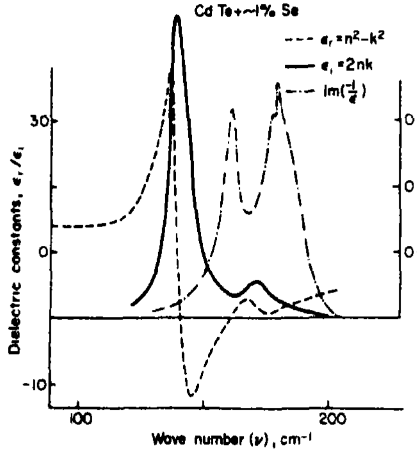

Fig. 6. Dielectric constants of CdTe containing about 1% Se.

These optical modes are the longitudinal optical one of doped CdTe $\omega_{LO} = 162\,\mathrm{cm}^{-1}$; and the optical mode of the Se impurity $\omega_{LO}^{Loc} = 180\,\mathrm{cm}^{-1}$ as shown on Fig. 7.

The ω_{LO} frequency shift of CdTe containing about 1% Se, can be explained by the anharmonic coupling between the CdTe normal modes and the Se localized mode.

In this case the CdTe self energy $\pi(j, \omega)$ is a complex function of the frequency ω[9]

$$\pi(j, \omega) = \Delta(j, \omega) - i\Gamma(j, \omega)$$

when the anharmonicity is low, the CdTe normal mode is defined by

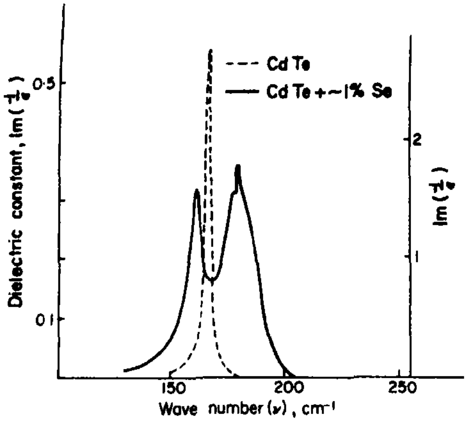

Fig. 7. Imaginary part of the inverse of the dielectric constant of pure CdTe and CdTe containing about 1% Se.

$$\omega_N^2 = \omega_{TO}^2 + 2\Delta(\omega)\omega_{TO} - 2i\Gamma(\omega)\omega_{TO}$$

ω_{TO} is the transverse optical mode in the harmonic approximation, $\Delta(\omega)$ and $\Gamma(\omega)$ are respectively the frequency shift and the damping constant which are related to the dielectric constant by

$$\epsilon(\omega) = \epsilon_\infty + \frac{\Omega_T^2(0)(\epsilon_0 - \epsilon_\infty)}{[\omega_{TO} + \Delta(\omega) - \omega]^2 - 2i\omega_{TO}\Gamma(\omega)}$$

$\Omega_T(0)$ is a constant which is deduced from the sum rules by[10]

$$\Omega_T^2(0) = \frac{\int \omega\, \epsilon_i(\omega)\mathrm{d}\omega}{\int \frac{\epsilon_i(\omega)}{\omega}\mathrm{d}\omega}$$

$\Delta(\omega)$ and $\Gamma(\omega)$ can be calculated from the dielectric constants which are deduced from the reflectivity spectrum.

$$[\omega_{TO} + \Delta(\omega)]^2 = \omega^2 + \frac{\Omega_T^2(0)(\epsilon_0 - \epsilon_\infty)(\epsilon_r(\omega) - \epsilon_\infty)}{\epsilon_i(\omega)^2 + [\epsilon_r(\omega) - \epsilon_\infty]^2}$$

$$\Gamma(\omega) = \frac{\Omega_T^2(0)(\epsilon_0 - \epsilon_\infty\epsilon_i(\omega))}{\epsilon_i(\omega)^2 + [\epsilon_r(\omega) - \epsilon_\infty]^2}$$

The Lyddane Sachs Teller relation can be written in the anharmonic approximation:

$$\frac{\epsilon_0}{\epsilon_\infty} = \frac{\omega_{LO}^2}{\Omega_T^2(0)} + \frac{\Omega_T^2(0) - (\omega_{TO} + \Delta(\omega_{LO}))^2}{\Omega_T^2(0)}$$

As shown in Fig. 8 the damping coefficient is very important near the ω_{LO} frequency of CdTe.

The shift of the longitudinal optical mode frequency due to the anharmonic coupling between the host crystal and the impurities, has been deduced from the anharmonic ω_{LO} frequency $\omega_{LO} = 160\ \mathrm{cm}^{-1}$. This value is in fairly good agreement with the experimental frequency $\omega_{LO} = 162\ \mathrm{cm}^{-1}$.

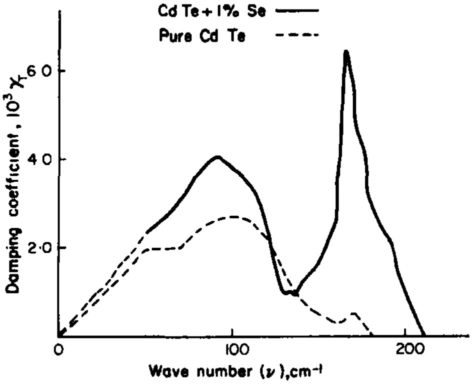

Fig. 8.

2.3 *Resonnant modes in blende type II-VI semiconductors*

2.3.1 *Manganese substitutes zinc of zinc selenide.* The Mn of mass 55 is a light impurity substituting the cation of mass 65·4 in ZnSe. The mass factor is low, $\epsilon = 0{\cdot}25$, so that no localized mode is expected, the impurity will modify the normal mode vibration amplitudes, and a resonnant mode could appear in the band of the allowed frequencies.

Figure 9 compares the reflectivity spectra of ZnSe containing 1·5% Mn, to that of pure ZnSe. The shape of the restrahlen band of ZnSe is modified by the introduction of Mn impurities.

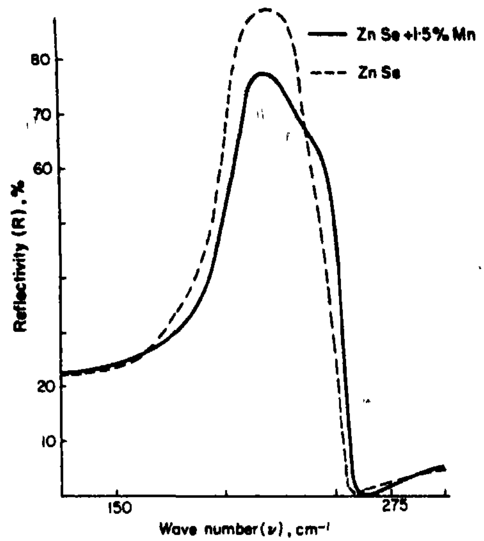

Fig. 9. Reflectivity spectra of pure ZnSe and ZnSe containing 1·5% Mn.

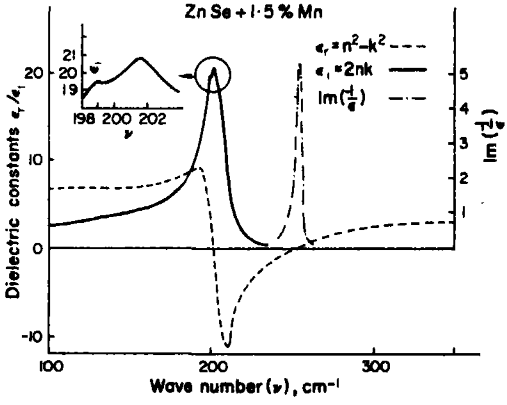

Fig. 10. Dielectric constants of ZnSe containing 1·5% Mn.

A detailed examen of the optical constants displayed in Fig. 10 shows a structure on the imaginary part of the dielectric constant which gives two frequencies for the transverse optical modes: $\omega_R = 199\ \mathrm{cm}^{-1}$ and $\omega_{TO} = 202\ \mathrm{cm}^{-1}$. For the pure ZnSe we have $\omega_{TO} = 202\ \mathrm{cm}^{-1}$.

The presence of impurities shifts the ω_{LO} from $\omega_{LO} = 252\ \mathrm{cm}^{-1}$ to an higher energy $\omega_{LO} = 254\ \mathrm{cm}^{-1}$. The shift of ω_{LO} is due to the anharmonic coupling between Mn impurities and the normal modes of ZnSe, the frequency has been calculated from the Lyddane–Sachs–

Teller relation applied to anharmonic process $\omega_{LO} = 257\,\mathrm{cm}^{-1}$ which corresponds to the experimental frequency $\omega_{LO} = 254\,\mathrm{cm}^{-1}$.

2.3.2 *Tellurium substitutes selenium of zinc selenium.* The Te with $M = 127{\cdot}6$ is a heavy impurity in ZnSe. The mass parameter is negative ($\epsilon = -0{\cdot}615$). A heavy defect in the lattice should lead to a resonance in the allowed frequency region, or to a gap mode if the density of states at the given frequency is very low or practically zero.

The infrared reflectivity spectra of pure and Te doped ZnSe are given in Fig. 11, the latter shows a higher reflectivity coefficient on the low energy side of the restrahlen.

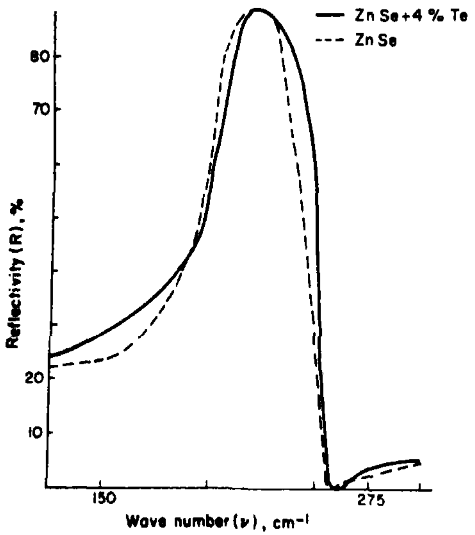

Fig. 11. Reflectivity spectra of pure ZnSe and ZnSe containing 4% Te.

The dielectric constants are displayed in Fig. 12. From the difference between the imaginary part of the dielectric constant of pure ZnSe and Te doped ZnSe, one can deduce the frequency of the resonant mode $\omega_R = 182\,\mathrm{cm}^{-1}$. The width of this band is $\Delta(\omega) = 35\,\mathrm{cm}^{-1}$ which combines the impurity line width, and the band broadening due to the anharmonic coupling.

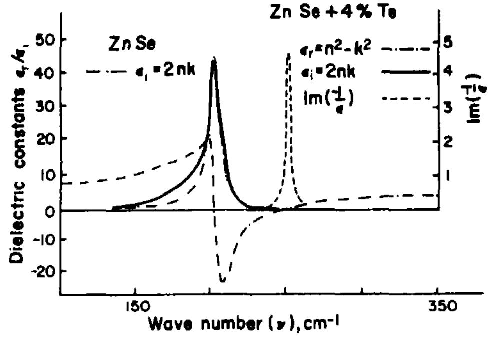

Fig. 12. Dielectric constants of ZnSe containing 4% Te and imaginary part of the dielectric constant of pure ZnSe.

The damping constant of ZnSe increases when the *impurities give rise to a resonnant* mode, as shown in Table 1.

3. DISCUSSION

Recently the dispersion relations, and the density of states have been calculated for the Würtzite type CdS[6] and extrapolated to BeO[11]. Up to now, no theoretical calculations have been performed on zinc blende

Table 1. Optical frequencies and damping constants of doped ZnSe

Crystal	Optical frequencies		Damping constant
	$\omega_{TO}(\mathrm{cm}^{-1})$	$\omega_{LO}(\mathrm{cm}^{-1})$	γ
ZnSe	202	252	0·036
ZnSe + 1·5%Mn	202	254	0·094
ZnSe + 4%Te	202·5	252	0·056

type II-VI semiconductors so that it is not possible to compare the experimental results with calculated values.

The presence of S in ZnSe leads to a localized mode whose frequencies deduced from the Kramers–Krönig analysis of the reflectivity spectrum are $\omega_{TO}^{Loc} = 297\ \mathrm{cm}^{-1}$ and $\omega_{LO}^{Loc} = 305{\cdot}5\ \mathrm{cm}^{-1}$.

Analogous situation has been formed in ZnTe doped with S, the experimental frequencies are $\omega_{TO}^{Loc} = 269\ \mathrm{cm}^{-1}$ and $\omega_{LO}^{Loc} = 272\ \mathrm{cm}^{-1}$.

The experimentally observed frequencies of Se in CdTe are $\omega_{TO}^{Loc} = 170\ \mathrm{cm}^{-1}$ and $\omega_{LO}^{Loc} = 180\ \mathrm{cm}^{-1}$.

Band resonannces have been observed in the case of light substitutional impurity when the mass parameter is not high enough for example Mn in ZnSe where $\omega_R = 199\ \mathrm{cm}^{-1}$.

Gap or band modes have also been observed in the case of heavy impurities as Te in ZnSe, where $\omega_R = 182\ \mathrm{cm}^{-1}$ has been deduced from the Kramers-Krönig analysis of the reflectivity spectrum.

REFERENCES

1. MITSUISHI A., MANABE A., YOSHINAGA H., IBUKI S. and KOMIYA H., *Proc. int. Conf. Semiconductors* Kyoto, Vol. 72, (1966).
2. BALKANSKI M., BESERMAN R. and VODOPIANOV L. K., *Int. Conf. Localized Excitations in Solids* (Edited by Wallis), p. 154. Plenum Press, New York (1968).
3. HAYES W. and SPRAY A., *Solid-St. Commun.* **5**, 1 (1967).
4. IBUKI S., KOMIYA H., MITSUISHI A., MANABE A. and YOSHINAGA H., *Proc. int. Conf. Semiconductors, Moscow*, 1047 (1968).
5. NUSIMOVICI M. A., BALKANSKI M. and BIRMAN J. L., To be published in *Phys. Rev.*
6. PFEUTY P., BIRMAN J. L., NUSIMOVICI M. A. and BALKANSKI M., *Int. Conf. Localized Excitations in Solids, Irvine* (Edited by Wallis), p. 210. Plenum Press, New York (1968).
   NUSIMOVICI M. A., Thesis, Paris (1968).
7. STERN F., *Solid-St. Phys.* **15**, 299 (1963).
8. BALKANSKI M. and BESERMAN R., *Proc. int. Conf. Semiconductors, Moscow*, p. 1042 (1968).
9. COWLEY R. A., *Adv. Phys.* **12**, 421 (1964).
10. LE TOULLEC R., Thesis, Paris (1968).
11. NUSIMOVICI M. A., *C. r. hebd. Séanc. Acad. Sci., Paris*, **268**, 755 (1969).

J. Phys. Chem. Solids Pergamon Press 1970. Vol. 31, pp. 363–383. Printed in Great Britain.

STRUCTURES MAGNETIQUES ET ETUDE DES PROPRIETES MAGNETIQUES DES SPINELLES CUBIQUES $NiMn_2O_4$

B. BOUCHER*, R. BUHL† et M. PERRIN†
Service de Physique du Solide et de Résonance Magnétique, Centre d'Etudes Nucléaires de Saclay,
BP n° 2 – 91, Gif-sur-Yvette, France

(*Received* 21 *March* 1969; *in revised form* 2 *May* 1969)

Resumé – On étudie par des mesures de magnétisme, de chaleur spécifique et de diffraction de neutrons les spinelles cubiques $Mn_\nu Ni_{1-\nu}$ $[Mn_{2-\nu}Ni_\nu]O_4$. L'étude porte sur trois échantillons correspondant à $\nu = 0{,}74$, 0,80 et 0,93. On établit, dans le cas de chaque valeur du degré d'inversion, la structure magnétique à 4,2°K: elle est du type structure 'en étoile'. On explique la faible valeur de l'aimantation spontanée de ces échantillons. L'état de valence des ions des sites A est déterminé. L'évolution de la structure en fonction de la température est étudiée; on montre expérimentalement que la structure 'en étoile' se transforme en une structure ferrimagnétique colinéaire à une température de transition $T_1 < T_c$ comme le prévoit la théorie.

Abstract – Cubic spinels $Mn_\nu Ni_{1-\nu}[Mn_{2-\nu}Ni_\nu]O_4$ are studied by means of magnetic measurements, specific heat and neutron diffraction. Three samples corresponding to $\nu = 0{\cdot}74$, 0·80 and 0·93 are studied. We show that the magnetic structure at 4·2°K is a 'star' structure, whatever the inversion degree. The weak values of the spontaneous magnetization of these samples are explained. The valencies of A site ions are determined. The evolution of the magnetic structure as a function of temperature is studied; we show experimentally that the 'star' structure becomes a collinear ferrimagnetic structure at a transition temperature $T_1 < T_c$ as theoretically predicted.

INTRODUCTION

DANS UN précédent article[1] on a montré que, suivant le traitement thermique auquel est soumis l'échantillon, le degré d'inversion ν du spinelle cubique $Mn_\nu Ni_{1-\nu}[Mn_{2-\nu}Ni_\nu]O_4$ peut varier entre $\nu = 0{,}74$ et $\nu = 0{,}93$. On sait[2] que certaines propriétés magnétiques de ce composé varient avec le traitement thermique et que quelque soit ν, l'aimantation spontanée mesurée à basse temperature est toujours petite. De plus la présence, en proportions presque égales, dans les sites B de deux sortes d'ions amène à penser qu'une structure 'en étoile' décrite et étudiée dans [3] peut exister.

Dans le but d'expliquer les propriétés magnétiques et de vérifier expérimentalement la théorie exposée dans [3] on étudie par des mesures d'aimantation, de chaleur spécifique et de diffraction de neutrons trois échantillons correspondant à $\nu = 0{,}74$, $\nu = 0{,}80$, $\nu = 0{,}93$. L'étude cristallographique de ces corps a été faite dans [1].

Après avoir établi la structure magnétique à basse température, qui est du type 'en étoile', on étudie l'évolution de cette structure en fonction de la température.

A. STRUCTURE MAGNETIQUE DE $NiMn_2O_4$ A 4,2°K

1. *Données expérimentales*

(1) *Mesures d'aimantation (4,2°K).* On a mesuré dans des champs intenses* (jusqu'à 200 kOE), l'aimantation I, des différents échantillons (Fig. 1); on constate: (a) qu'il n'y a pas saturation dans les champs élevés;

---

*Partie de la thèse de doctorat d'état, Paris le 2 Décembre 1968.

†L.M.P.S., C.N.R.S. Bellevue – 92, France.

*Mesures faites par MM. Krebs et Miédan-Gros, DPh/SRM, Saclay.

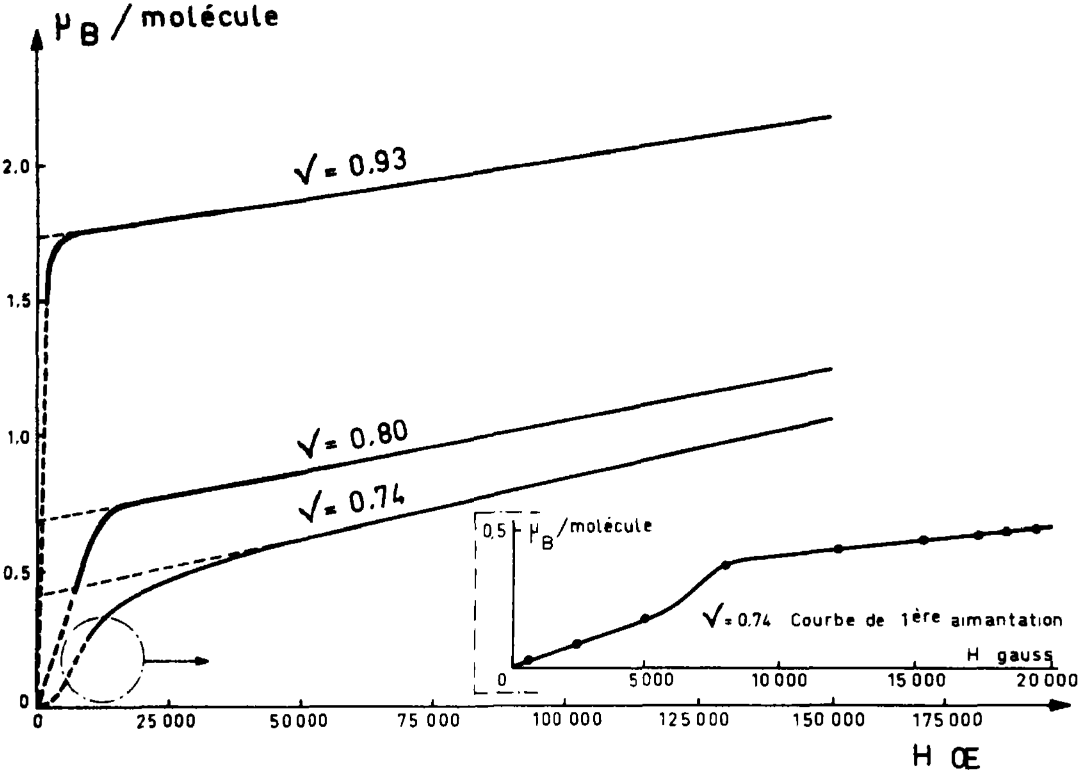

Fig. 1. Variation de l'aimantation en fonction du champ $T = 4{,}2°K$.

on observe une variation linéaire de l'aimantation comme il est usuel dans le cas des composés dont la structure magnétique n'est pas colinéaire. On appelle aimantation spontanée I_0, l'ordonnée à l'origine (H = 0) de la partie linéaire de la courbe I(H) à 4,2°K; (b) que l'anisotropie est forte dans le cas des composés dont le degré d'inversion est faible ($\nu < 0{,}80$). Un champ de 40 kOE est nécessaire ($\nu = 0{,}74$) pour atteindre la partie linéaire de la courbe; (c) que lorsque l'anisotropie est forte la courbe I(H) a une forme inhabituelle dans des champs inférieurs à 8 kOE: l'aimantation croît d'abord linéairement avec le champ, puis croît plus rapidement (entre 6 et 8 kOE), enfin la courbe s'infléchit pour suivre une variation plus régulière (Fig. 1); (d) que l'aimantation spontanée I_0 varie fortement avec l'inversion (Fig. 2; Tableau 1) et que dans tous les cas la valeur de l'aimantation reste faible par rapport à ce que l'on peut attendre d'un ferrimagnétique dont les moments seraient alignés.

Tableau 1

ν	I_0 (μ_B/mol.)	T_c (°K)	$\mu_{\text{eff.}}$ (μ_H/at)	$\theta°_A$
0,74	0,4	161	3,96	−190
0,76	0,4	155		
0,78	0,5	145		
0,80	0,6	130	4,20	−278
0,82	0,78	127		
0,87	1,22	116		
0,93	1,75	114	4,05	

(2) *Mesures de susceptibilité*. On a mesuré la susceptibilité entre 900°K et la température de Curie*. Les courbes $1/\chi(T)$ obtenues,

---

*Mesures faites au laboratoire de M. Allain, DPh/SRM, Saclay.

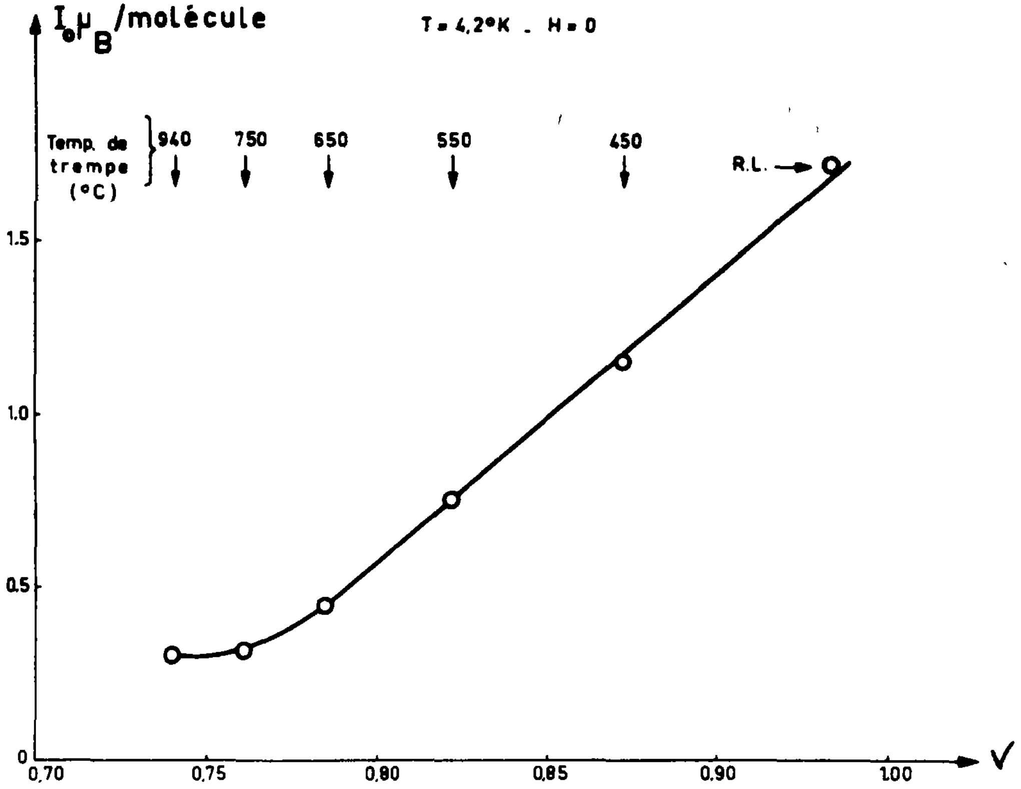

Fig. 2. Variation de l'aimantation spontanée, mesurée à 4,2°K, en fonction du degré d'inversion ν.

dont une est représentée sur la Fig. 3, ont la forme générale de celles des ferrimagnétiques. Ces mesures confirment les températures de Curie déjà déterminées. Les températures de Curie des échantillons varient entre 114° et 161°K; plus le spinelle est inverse plus la température de Curie est faible (Fig. 4). Aux hautes températures $1/\chi(T)$ est une fonction linéaire de T. La valeur du moment paramagnétique effectif déduit des mesures est reportée au Tableau 1.

(3) *Mesures de diffraction X.* Les mesures effectuées à 4,2°K ne mettent en évidence aucun changement de système cristallin (précision relative sur les paramètres de la maille: 10^{-4})†

(4) *Mesures de diffraction de neutrons.* On a fait à 4,2°K, dans le cas de chaque échantillon, les spectres de diffraction de neutrons sans champ appliqué, puis avec un champ de 15 kOE appliqué suivant le vecteur de diffusion K(Fig. 5).

On obtient des spectres qualitativement identiques quelle que soit la valeur de ν. Toutes les raies s'indexent dans la maille chimique. Ces spectres obéissent aux lois d'extinction caractéristiques des réseaux cubiques à faces centrées. De plus la raie (200) nulle à température ambiante reste nulle à 4,2°K (avec ou sans champ).

Quand on applique le champ magnétique, les intensités des raies de diffraction, correspondant à un échantillon donné, varient toutes dans le même sens: toutes croissent ou toutes décroissent (Figs. 6 et 7).

---

†Mesures faites par MM. Jehanno et Kleinberger, DPh/SRM, Saclay.

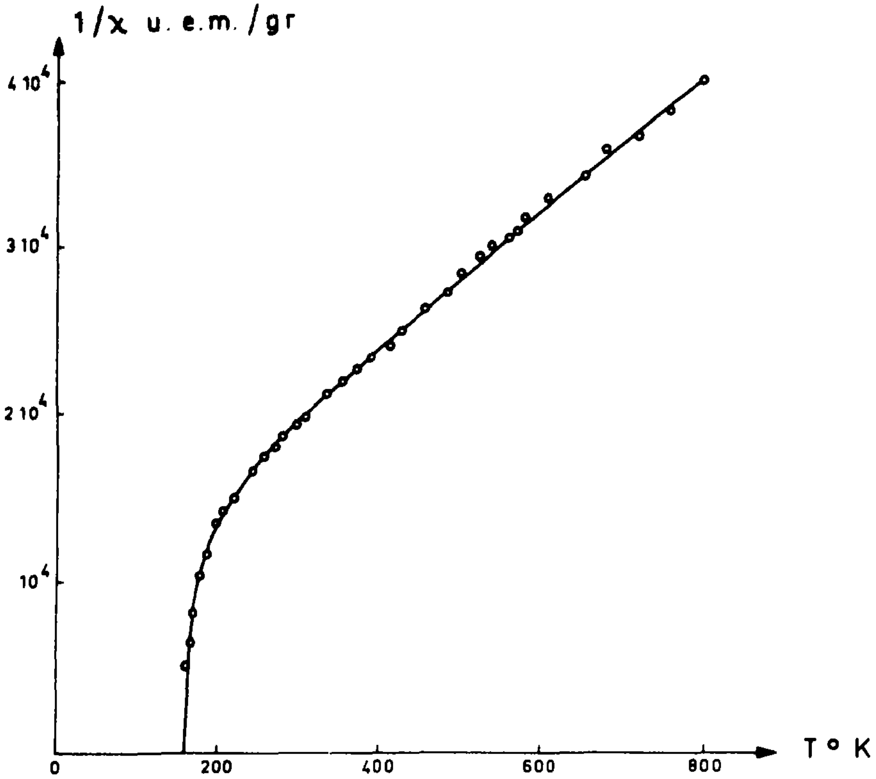

Fig. 3. Variation de l'inverse de la susceptibilité en fonction de la température ($H \simeq 3\,000$ OE), $\nu = 0{,}74$.

2. *Structure magnétique*

Les lois d'extinction caractéristiques des réseaux cubiques à faces centrées étant respectées, on peut subdiviser les sites A et B respectivement en deux sous-réseaux A_1 et A_2 et en 4 sous-réseaux B_1, B_2, B_3 et B_4, tous cubiques à faces centrées. L'étude cristallographique ayant mis en évidence l'absence d'ordre à grande distance entre les ions manganèse et nickel sur les sites A ou B, on affectera à chaque ion A un moment magnétique moyen fictif de module S_A et à chaque ion B un moment moyen fictif de module S_B.

(1) *La raie (200) est nulle en l'absence de champ appliqué.* Ceci entraîne:

(a) *Dans le cas des sites* A:

$$S_{A_1} = S_{A_2} = S_A.$$

Les moments des ions des sites A forment donc un sous-réseau ferromagnétique.

(b) *Dans le cas des sites* B: (les moments magnétiques étant égaux), l'un des quatre modèles suivants (Fig. 8): (α) Il y a 4 sous-réseaux dont les aimantations sont disposées suivant les 4 arêtes d'une pyramide à base rectangulaire, axée sur une des six directions [h00] (la disposition relative des moments $\vec{S}_{B_i}$ sur les arêtes de la pyramide dépend de la direction [h00] considérée). (β) Les quatre sous-réseaux $\vec{S}_{B_i}$ se groupent deux à deux formant deux sous-réseaux dont les aimantations sont symétriques par rapport à un plan de la forme {h00} (le groupement des sous-réseaux dépend également du plan de symétrie considérée). (γ) Les quatre sous-réseaux se confondent en un seul (aimantation de direction quelconque). (δ) Il

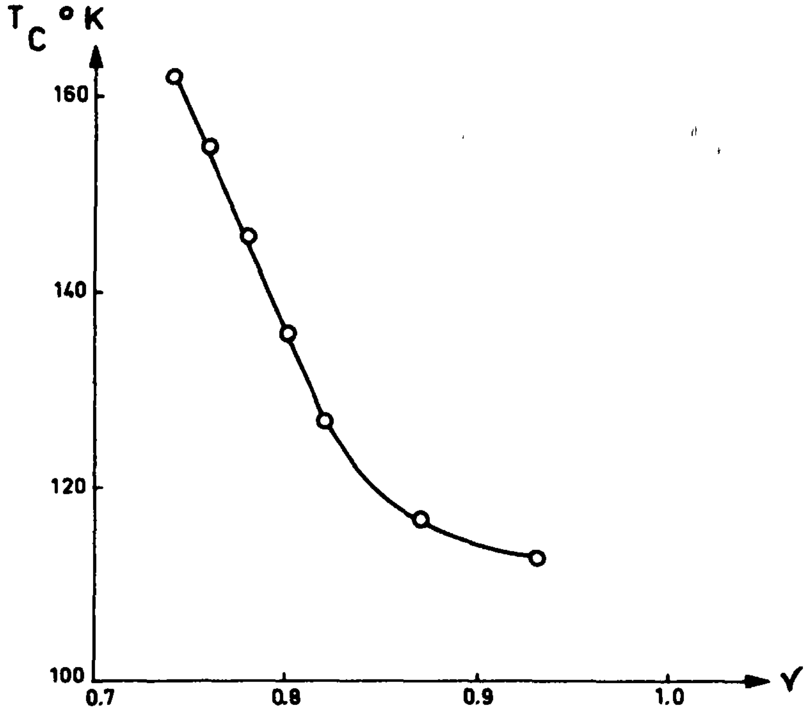

Fig. 4. Variation de la température de Curie en fonction de l'inversion.

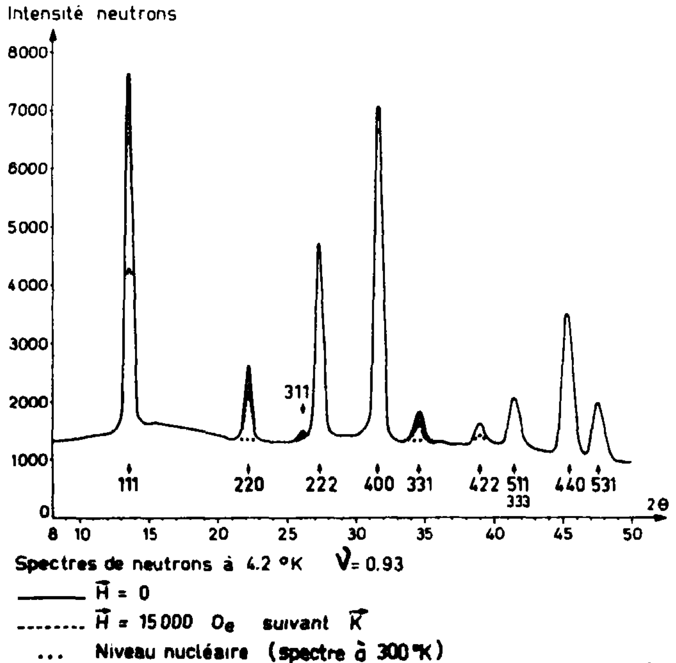

Fig. 5. Spectres de diffraction de neutrons à 4,2°K; $\nu = 0,93$; $\lambda = 1,143$ Å. Trait plein: spectre sans champ; Tirets: spectre avec un champ de 15 kOE appliqué suivant le vecteur de diffusion; Pointillé: niveau nucléaire.

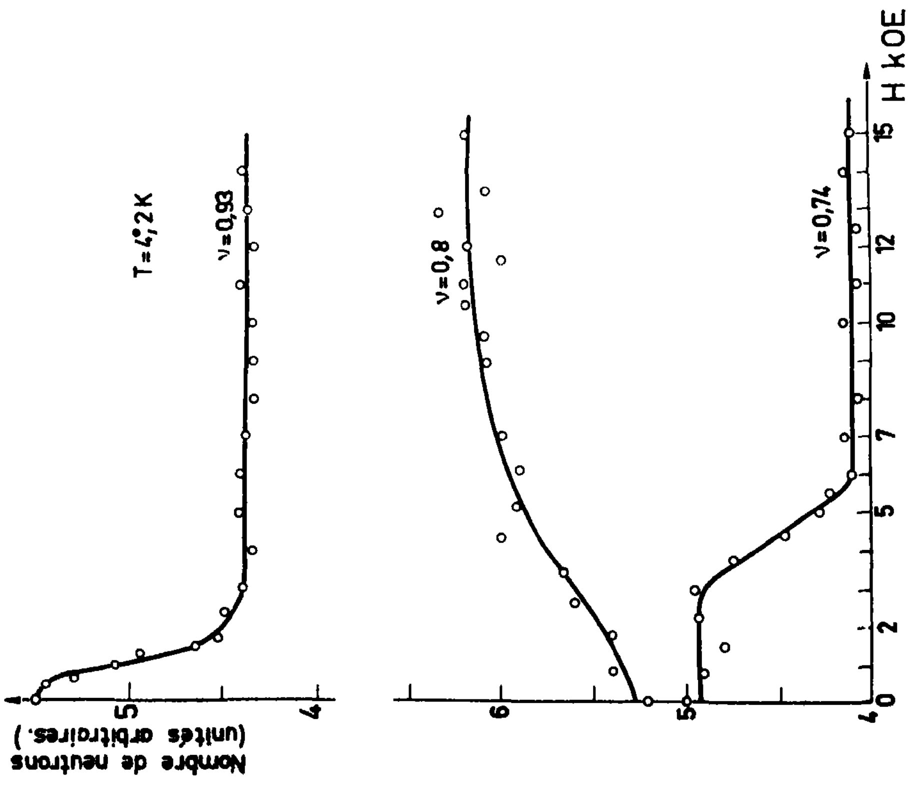

Fig. 6. Evolution du sommet de la raie (220) en fonction du champ appliqué suivant K.

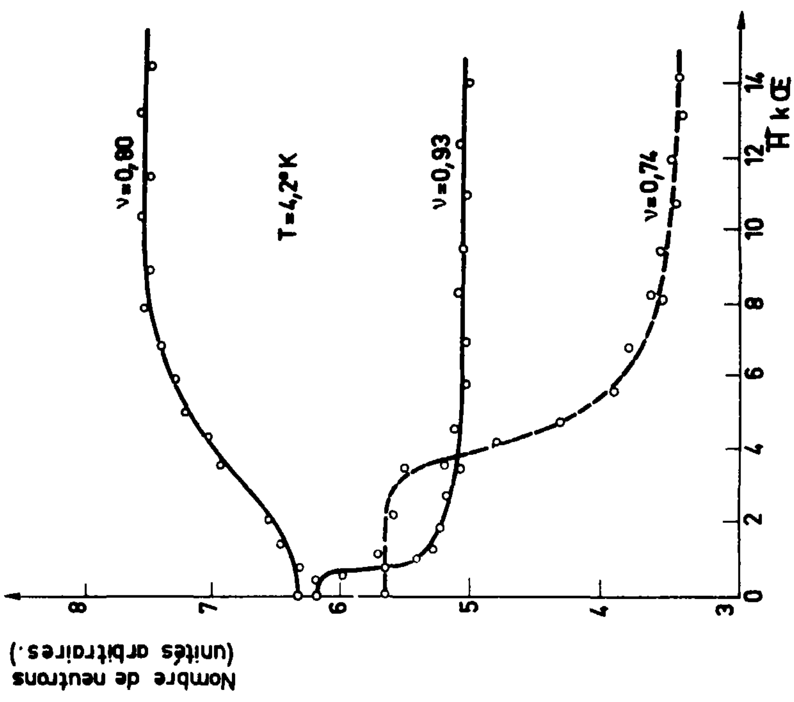

Fig. 7. Evolution du sommet de la raie (111) en fonction du champ appliqué suivant K.

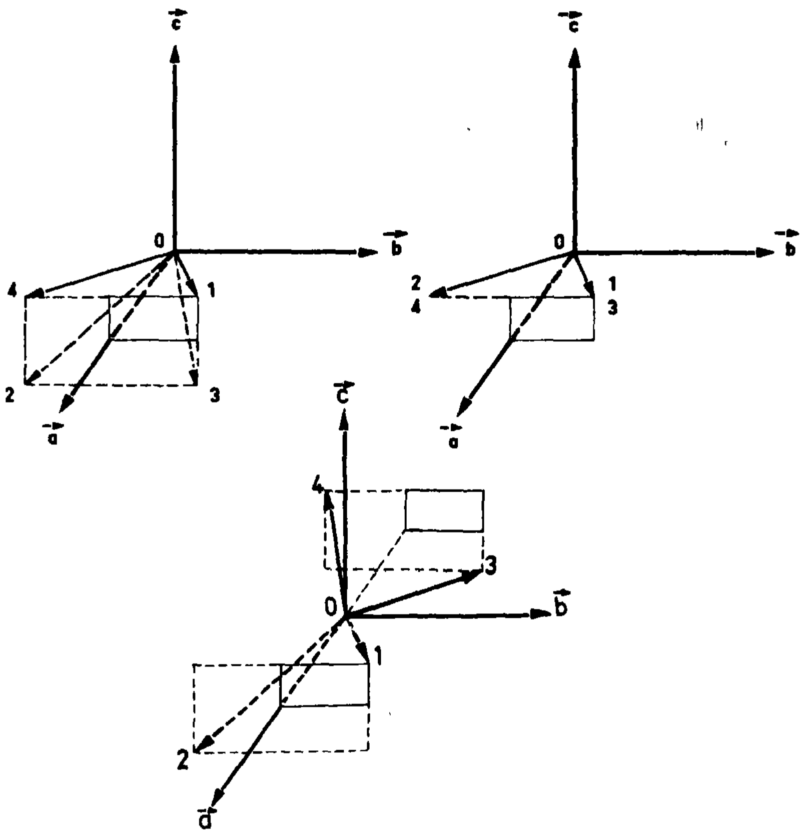

Fig. 8. Configurations de moments magnétiques (site B) rendant nulle l'intensité de la raie (220).

y a quatre sous-réseaux dont les aimantations sont disposées suivant les droites qui joignent le centre d'un tétraèdre à ses sommets. L'aimantation résultante d'un tel motif est nulle.

Cette dernière solution peut immédiatement être rejetée: ce modèle ne peut rendre compte de l'aimantation du corps observée; ce modèle exige que l'intensité magnétique de la raie (222) soit nulle, ce que l'expérience infirme.

Il reste à choisir entre les trois premières solutions.

(2) *Le modèle*. Pour déterminer la structure magnétique on compare les valeurs calculées des intensités de raies de diffraction dans le cas des différents modèles avec les valeurs observées.

De cette comparaison il ressort que seule la structure γ (un sous-réseau A et *un seul sous-réseau* B) peut rendre compte des intensités observées.

Quand on applique un champ de 15 kOE parallèle au vecteur de diffusion, en supposant que ce champ ne modifie pas le motif magnétique et que l'anisotropie est suffisamment faible pour être vaincue par ce champ, (cas $\nu = 0{,}80$ et $0{,}93$), les mesures de diffraction de neutrons montrent *que l'aimantation* $\mathbf{R}_B$ *du sous-réseau* B *n'est pas alignée avec celle du sous-réseau* A (sinon les intensités magnétiques des raies de diffraction seraient nulles).

La structure (Fig. 9) se compose donc de deux sous-réseaux d'aimantation $\mathbf{S}_A$ et $\mathbf{R}_B$ faisant entre eux un angle inférieur à 180°. L'aimantation résultante $\mathbf{I}_0$ est suivant une

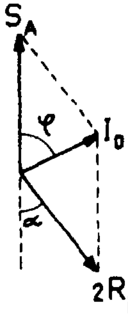

Fig. 9. Schéma de la structure magnétique mise en évidence par les mesures de diffraction de neutrons.

troisième direction. Nous verrons que ce modèle reste valable dans le cas $\nu = 0{,}74$ (anisotropie plus forte que dans les deux cas précédents).

Avec un tel modèle la variation de l'intensité des raies en fonction du champ appliqué suivant le vecteur de diffusion dépend de l'angle que fait l'aimantation résultante $\mathbf{I}_0(\nu)$ avec les aimantations des sous-réseaux $\mathbf{S}_A$ et $\mathbf{R}_B$. Il est donc normal que les intensités des raies dans le cas de certains échantillons croissent toutes quand on applique un champ comme le montre l'expérience.

(3) *Mesure des intensités et comparaison avec les intensités calculées.* (a) *Traitement des mesures expérimentales.* On a obtenu les quantités expérimentales

$$\frac{jf^2F^2_M \exp\left(-2B\dfrac{\sin^2\theta}{\lambda^2}\right)}{\sin\theta\sin 2\theta}$$

en retranchant des intensités obtenues à la température de l'hélium liquide, celles obtenues à la température ambiante corrigées de l'agitation thermique ($B \simeq 0{,}8$ et $0{,}4$ Å^2 pour 300° et 4,2°K).

Le facteur de forme magnétique adopté pour chacun des sites est une moyenne, tenant compte de l'inversion, entre le facteur de forme du manganèse et celui du nickel[4]: (b) ***Détermination des valeurs des paramètres définissant la structure.*** La structure est complètement définie par 3 paramètres: par exemple S_A, R_B (ces 2 paramètres sont chacun rapporté à un atome) et I (rapporté à une molécule). Deux autres 'paramètres' α et φ (Fig. 9) s'en déduisent. Pour déterminer les trois paramètres définissant la structure on connaît dans le cas de chaque échantillon, de façon précise: au moins six intensités de raies magnétiques de diffraction (spectres avec et sans champ) (Tableaux 2 et 3) et la valeur de l'aimantation I_0 obtenue par des mesures classiques, soit 7 informations pour 3 inconnues.

On connaît I_0 par les mesures d'aimantation. L'intensité de la raie (220) sans champ ne dépendant que de S_A, on obtient ainsi directement S_A.

Connaissant I_0 et S_A, on tire de la mesure d'intensité de la raie (111) sans champ la valeur de R_B.

La structure peut donc être entièrement établie à partir des mesures d'aimantation et de diffraction de neutrons faites sans champ. Les mesures de diffraction faites en présence d'un champ permettent de vérifier l'exactitude des paramètres ainsi déterminés: (c) *Résultats.* Il n'y a aucune difficulté pour rendre compte des données expérimentales dans les cas $\nu = 0{,}80$ et $\nu = 0{,}93$.

Par contre dans le cas $\nu = 0{,}74$ l'existence d'une assez forte anisotropie rend plus délicate l'interprétation du spectre de diffraction fait en présence d'un champ (15 kOE). On détermine S_A, R_B, I_0 comme ci-dessus. La valeur de φ tirée de la mesure de l'intensité de la raie (220) avec champ est en très bon accord avec les valeurs calculées (comme indiqué précédemment) à partir des valeurs S_A, R_B et I_0 obtenues expérimentalement. Par contre on ne peut rendre compte de l'intensité de la raie (111) (avec champ) que si l'on admet que $\mathbf{S}_A$ fait un angle de 157° avec la direction [111], c'est-à-dire que l'aimantation résultante $\mathbf{I}_0$ ne s'aligne pas avec le champ et qu'elle fait un angle de 12° avec cette direction. La valeur calculée dans le cas de la raie (111) portée dans le Tableau 3 tient compte de ce fait.

Tableau 2. Comparaison des intensités calculées et observées $\dfrac{jf^2F^2_M \exp\left(-2B\dfrac{\sin^2\theta}{\lambda^2}\right)}{\sin\theta \sin 2\theta}$ *(en μ_B^2/maille) pour* H = 0. *Les valeurs des aimantations* S_A,R_B,I_R *et des angles* α et φ, *déterminées expérimentalement, sont indiquées au bas des colonnes. L'aimantation* I_0 *mesurée par des moyens classiques a été reportée pour mémoire*

	$\nu = 0{,}74$		$\nu = 0{,}80$		$\nu = 0{,}93$	
hkl	Expérim.	Calculée	Expérim.	Calculée	Expérim.	Calculée
111	190 813 9 000	191 195	215 590 ±11 000	204 160	168 790 ± 7 000	162 950
200	0	0	0	0	0	0
220	48 280 2 300	47 800	55 800 ± 2 500	55 750	58 470 ± 2 700	60 140
311 222	24 000 13 000	1 321 20 529 21 850	17 000 ±12 000	25 900	14 000 ±13 000	11·010 10·010 21·020
400	36 000 13 000	33 240	26 000 ±12 000	36 360	14 000 ±12 000	25 970
331	35 420 ± 6 000	30 740	34 260 ± 5 000	37 690	26 860 ± 7 000	25 640
442			15 755 ± 5 000	15 083		
S_A	3,48 μ_B		3,65 μ_B		3.90 μ_B	
R_B	1,91 μ_B		1.92 μ_B		1,33 μ_B	
α	3°25′		9°		21°30′	
φ	145°20′		103°		34°20′	
I_R	0,39 μ_B		0,60 μ_B		1,73 μ_B	
I_0	0,40 μ_B		0,60 μ_B		1,75 μ_B	

Tableau 3. *Comparaison des intensités* $\dfrac{jf^2F^2 \exp\left(-2B\dfrac{\sin^2\theta}{\lambda^2}\right)}{\sin\theta \sin 2\theta}$ *(en μ_B^2/maille) pour* H = 15 kOE *parallèle au vecteur de diffusion* **K**

	$\nu = 0{,}74$		$\nu = 0{,}80$		$\nu = 0{,}93$	
hkl	Expérim.	Calculée	Expérim.	Calculée	Expérim.	Calculée
111	36 650 ± 7 000	36 120	276 380 ±11 000	281 630	103 550 ± 6 000	105 700
200	0	0	0	0	0	0
220	23 120 ± 2 000	23 220	79 600 ± 2 500	79 620	28 530 ± 2 000	28 680
311 222	non mesurable	4 300	32 500 ±12 000	34 600	10 500 ±10 000	11 670
400	10 000 ± 9 000	8 300	33 500 ±15 000	49 670	16 000 ±12 000	18 130
331	12 860 ± 4 000	13 510	48 500 6 000	51 930	14 500 ± 5 000	16 630
422			16 500 ± 5 000	21 563		

Les Tableaux 2 et 3 montrent que le modèle rend bien compte de l'ensemble des résultats expérimentaux *y* compris des faibles valeurs de l'aimantation des corps considérés. La Fig. 10 représente le schéma des structures obtenues.

3. *Remarques sur le modèle*

(1) *Etat de valence des ions*. Les valeurs de $S_A(\nu)$ obtenues par les mesures de diffraction de neutrons sont en très bon accord avec les valeurs calculées (moment orbital bloqué) dans le cas d'un sous-réseau ferromagnétique formé des moments des ions Ni^{2+} et Mn^{3+} (Tableau 4). Le nickel n'étant stable qu'avec la valence 2 la formule du corps s'écrit donc:

$$Mn_{\nu}^{3+}Ni_{(1-\nu)}^{2+}\left[Ni^{2+}Mn_{(2-\nu)}^{3+}\right]O_4.$$

Avec cette formule les valeurs calculées (rapportées à un atome) de l'aimantation $S_B(\nu)$ d'un sous-réseau *B* (moments des ions *B* tous parallèles) sont très différentes des valeurs expérimentales R_B (Tableau 4).

Tableau 4

ν	S_A calc. (μ_B)	S_A expér. (μ_B)	S_B calc (μ_B)	R_B (μ_B)
0,74	3,48	3,48	3,26	1,91
0,80	3,60	3,65	3,20	1,92
0,93	3,86	3,90	3,07	1,35

On a vérifié qu'il n'était pas possible de rendre compte de la valeur de R_B, quelle que soit la répartition des valences.

Ces résultats montrent bien que l'expérience ne met en évidence que la valeur moyenne des ions des sites *B*.

(2) *Structure 'en étoile' de* $NiMn_2O_4$. Le modèle trouvé met en évidence un sous-réseau ferromagnétique (site *A*) (ce sous-réseau correspond à l'alignement pratiquement complet des moments de ce sous-réseau), et un autre sous-réseau d'aimantation $\mathbf{R}_B$ qui correspond à la valeur moyenne des moments des atomes peuplant les sites *B*. $\mathbf{R}_B$ est la résultante d'un ensemble de moments non alignés.

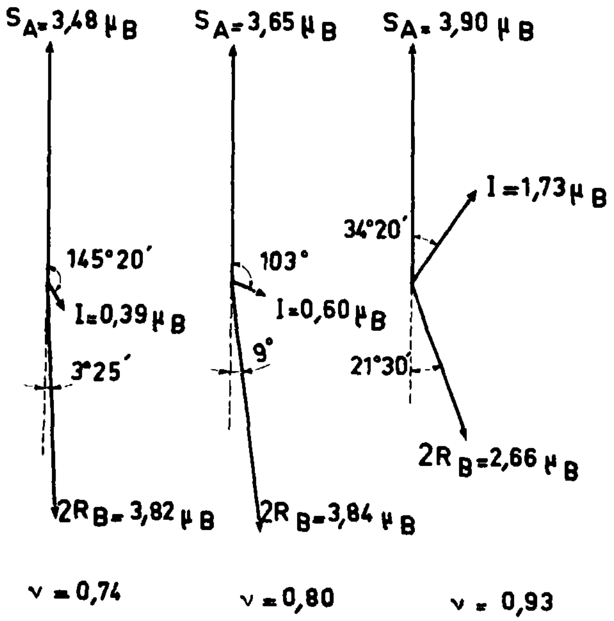

Fig. 10. Evolution de la structure magnétique de $NiMn_2O_4$ en fonction du degré d'inversion.

Ce modèle s'explique, du point de vue théorique, par un modèle à trois sous-réseaux décrit précédemment[3]. Pour celà il suffit d'admettre que *les interactions entre les moments des ions de site* A *avec les moments des ions de site* B *sont différentes suivant la nature de l'ion peuplant une position de site* B (manganèse ou nickel). S'il existait un ordre nucléaire à grande distance entre ces atomes, les mesures de diffraction mettraient en évidence *les trois sous-réseaux ferromagnétiques formés* respectivement des moments *de site* A, des moments des *atomes de manganèse de site* B, des moments des *atomes de nickel de site* B (Fig. 11). En l'absence de cet ordre nucléaire, seule la valeur moyenne $\mathbf{R}_B$ de l'ensemble des moments des sites *B* peut être mise en évidence. Les mesures de diffraction ne montrent donc l'existence que de deux 'sous-réseaux' $\mathbf{S}_A$ et $\mathbf{R}_B$, non alignés.

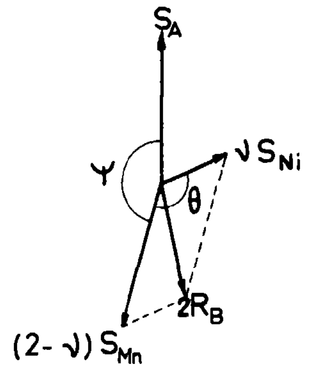

Fig. 11. Schéma de la structure 'en étoile' 'idéale' correspondant à $NiMn_2O_4$.

De plus le désordre nucléaire introduit des fluctuations du champ moléculaire sur le site *B*, perturbations d'autant plus fortes que les premiers voisins d'un atome *B* sont proches (2,97 Å) et peu nombreux (6); au désordre de substitution s'ajoute donc, pour les moments magnétiques des atomes de même nature, un désordre de direction. L'ensemble de ces phénomènes explique la faible valeur mesurée de $\mathbf{R}_B$.

Notons que ce désordre de substitution observé sur les sites *B* perturbe beaucoup moins le champ moléculaire sur les sites *A*. En effet les premiers voisins *B* d'un atome *A* sont loin (3,46 Å) et nombreux (12). Il est donc normal d'observer, par mesure de diffraction, un réseau ferromagnétique dont la valeur mesurée de l'aimantation est proche de la valeur théorique.

B. EVOLUTION EN FONCTION DE LA TEMPERATURE DE LA STRUCTURE MAGNETIQUE DE $NiMn_2O_4$

On sait par la théorie[3] qu'une structure 'en étoile' doit obligatoirement évoluer vers une structure colinéaire quand la température croît.

On a mis expérimentalement en évidence cette propriété. De plus on a précisé l'évolution des différents paramètres définissant la structure 'en étoile' quand $T < T_1$ et l'ordre ferrimagnétique qui s'établit quand $T_1 < T < T_C$.

Etant donné le comportement apparemment particulier de l'échantillon $\nu = 0{,}80$, on traitera en premier lieu les cas $\nu = 0{,}74$ et $\nu = 0{,}93$, puis on abordera le cas $\nu = 0{,}80$.

B-1. ETUDE DU COMPORTEMENT MAGNETIQUE EN FONCTION DE LA TEMPERATURE DES ECHANTILLONS $\nu = 0{,}74$ ET $0{,}93$

1. *Données expérimentales*

(1) *Mesures d'aimantation.* L'aimantation I en fonction du champ a été mesurée à différentes températures. En extrapolant à champ nul la partie linéaire de la courbe $I(H)$ on obtient l'aimantation spontanée $I_0(T)$. On suppose comme précédemment que le champ appliqué ne déforme pas la structure magnétique, cette valeur $I_0(T)$ correspond donc bien à la résultante du motif magnétique.

Les courbes $I_0(T)$ sont représentées sur les Figs. 12a et b.

Ces courbes ont une allure très particulière et présentent à $T \simeq 85°K$ un 'accident' qui

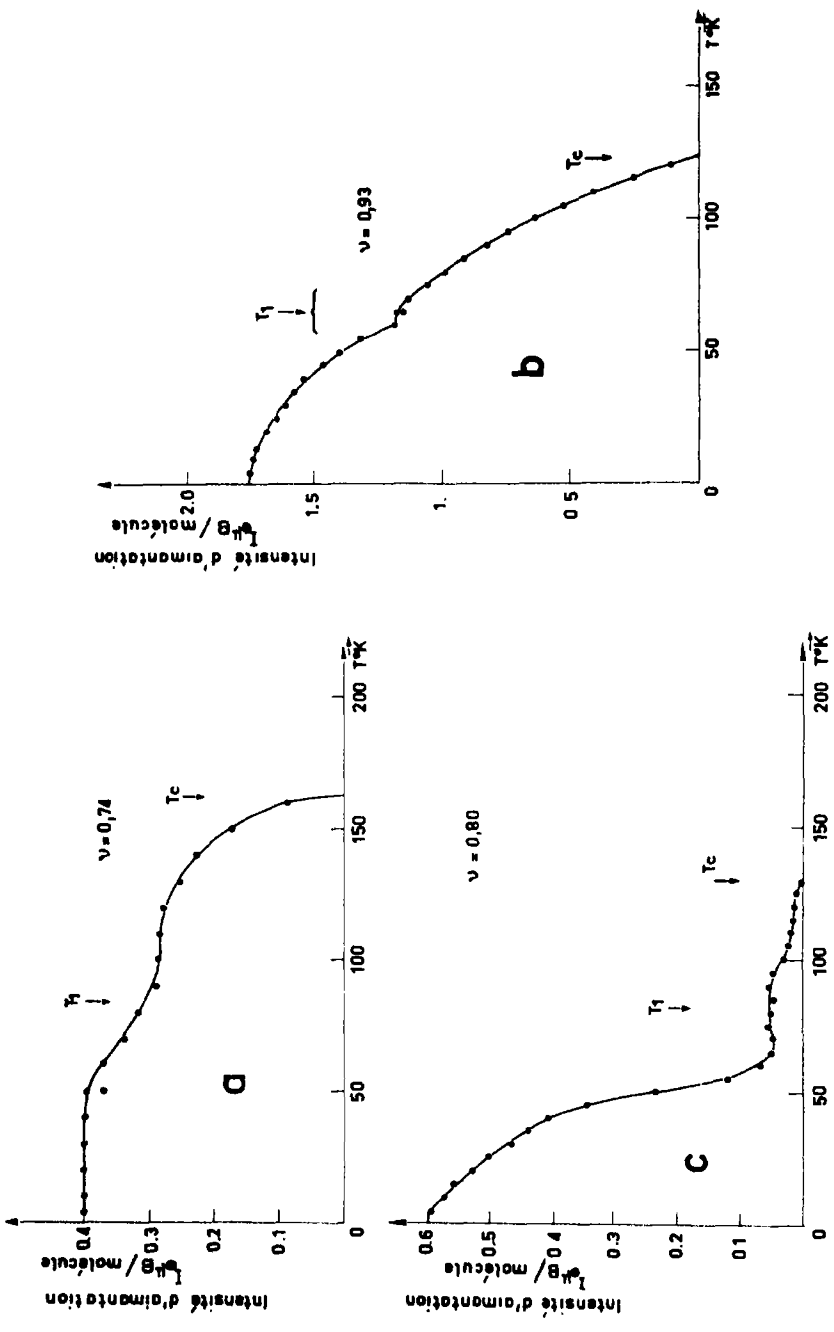

Fig. 12. Variation de l'aimantation spontanée en fonction de la température.

correspond (voir plus loin) au passage de la structure 'en étoile' à la structure colinéaire.

(2) *Mesure de la variation de l'intensité des raies de diffraction de neutrons en fonction de* T (Figs. 13 et 14). On a mesuré ces variations d'une part sans champ extérieur, d'autre part dans un champ de 15 kOE parallèle au vecteur de diffusion **K**.

Le cas $\nu = 0{,}93$ (Fig. 13) est particulièrement intéressant: l'anisotropie de cet échantillon est faible quelle que soit la température et un champ de 15 kOE permet toujours d'aligner l'aimantation résultante avec le champ **H**. En présence d'un champ appliqué les intensités des raies (111), (220), (331) s'annulent toutes à une même température $T_1 < T_C$. Ce résultat montre clairement que la structure devient colinéaire à $T = T_1$, confirmant ainsi la théorie [3].

Dans le cas $\nu = 0{,}74$ la décroissance de l'anisotropie forte à 4,2°K, avec la température est suffisamment rapide pour qu'un champ de 15 kOE puisse mettre en évidence le même phénomène. Les intensités mesurées sous champ s'annulent toutes à $T_1 \simeq 84$°K (Fig. 14).

Les spectres de diffraction mesurés à 95°K avec et sans champ confirment ce résultat.

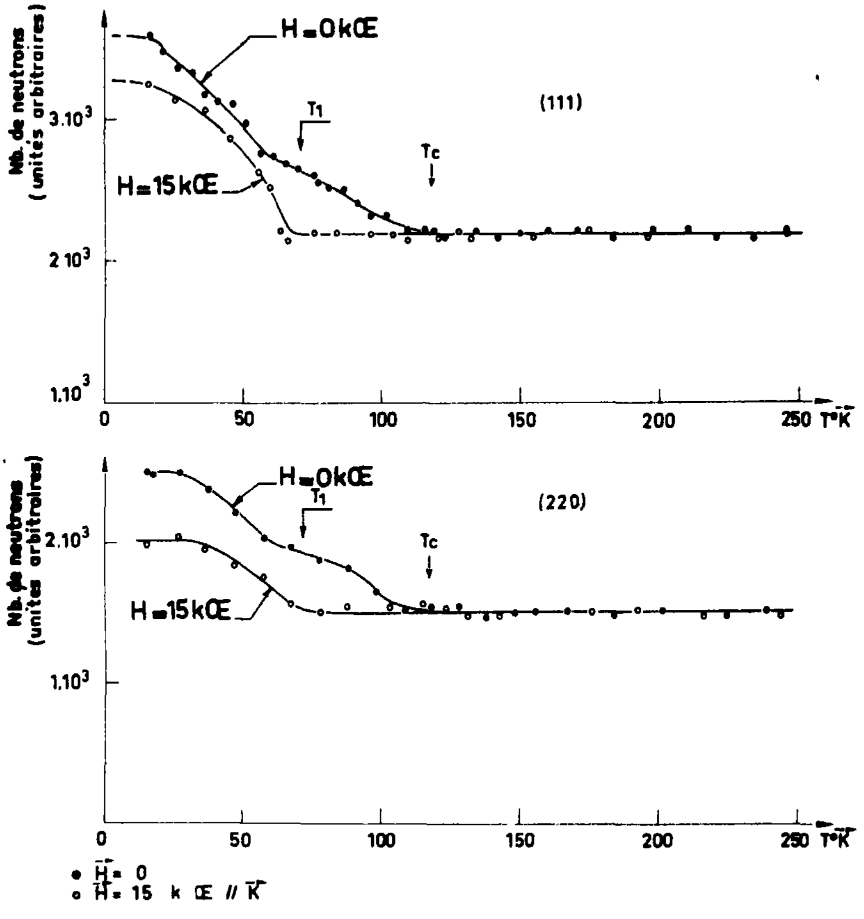

Fig. 13 Variation des intensités magnétiques des raies de diffraction (111) et (220) en fonction de la température, $\nu = 0{,}93$.

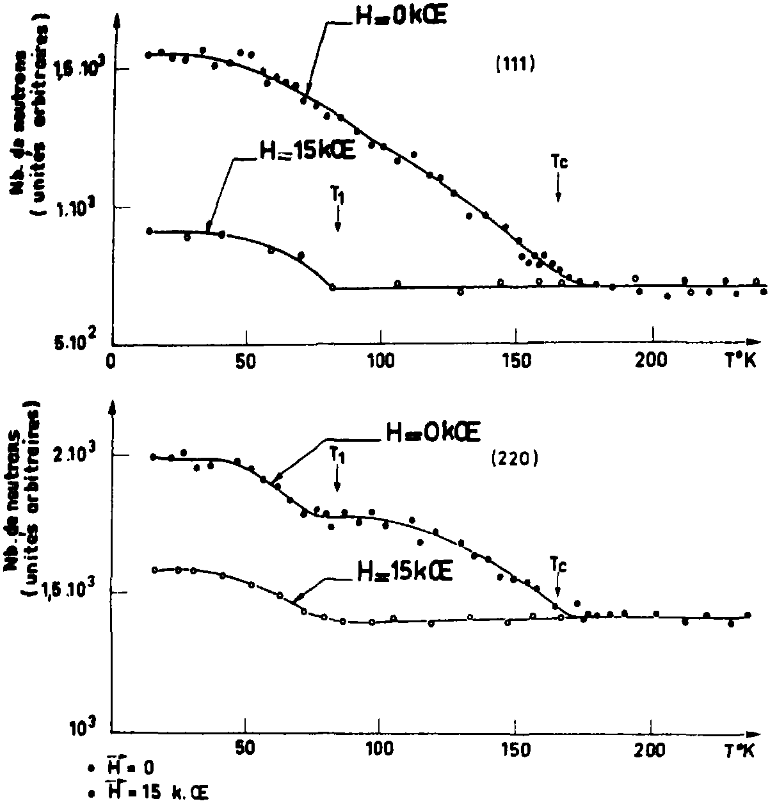

Fig. 14. Variation des intensités magnétiques des raies de diffraction (111) et (220) en fonction de la température, $\nu = 0{,}74$.

2. *Variation, en fonction de la température, des différents paramètres définissant la structure*

(1) *Variation de* $S_A(T)$ *et* $\varphi(T)$. L'intensité de la raie (220) mesurée sans champ et avec champ donne directement la valeur des paramètres $S_A(T)$ et $\varphi(T)$. Connaissant la structure à 4,2°K, il n'y a pas d'ambiguïté sur la valeur φ qui ne peut être confondue avec son supplément. Lorsque T tend vers T_1, φ tend vers 0° ($I_0(T)$ de même sens que S_A) dans le cas $\nu = 0{,}93$ et φ tend vers 180° ($I_0(T)$ opposé à S_A) dans le cas $\nu = 0{,}74$.

Les courbes représentatives $S_A(T)$ (Figs. 15 et 16) présentent un accident à $T_1 = 85$°K. La pente des courbes montre une variation brusque au voisinage de T_1; cette pente est plus petite au-dessous qu'au dessus de T_1. Ces courbes correspondent au 'cas 2' de la théorie[3].

(2) *Variation de* R_B *et* $\cos\alpha$ (Figs. 15 et 16). α tend vers zéro quand T tend vers T_1, c'est-à-dire que la structure évolue avec T vers une structure ferrimagnétique et non ferromagnétique ($\mathbf{R}_B$ opposé à S_A).

Connaissant la variation de φ, on obtient sans ambiguïté, à partir de l'intensité de la raie (111) celle de R_B.

(3) *Structure magnétique quand* $T_1 < T < T_C$. La structure est colinéaire. Il s'agit de définir le sens, par rapport à S_A, des aimantations des deux sous-réseaux magnétiques formés par les moments des ions des sites B.

Il est raisonnable de supposer, étant donné ce que l'on sait sur les interactions magnétiques AB et BB dans les spinelles, que les

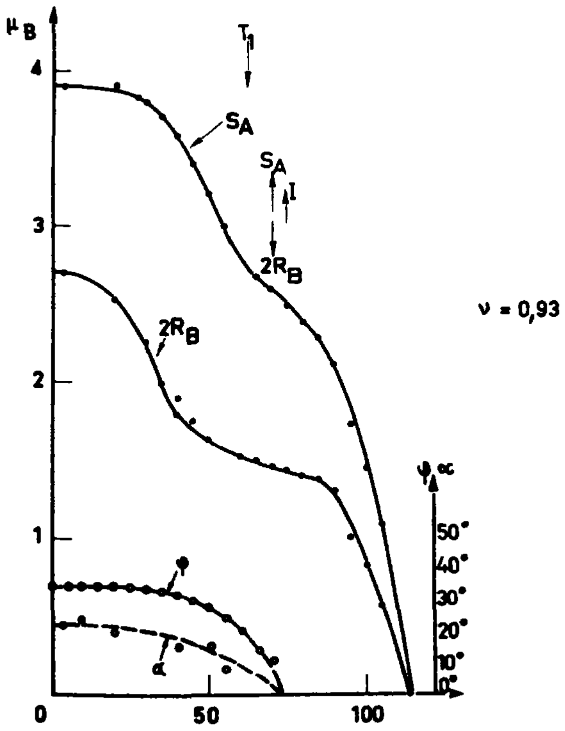

Fig. 15. Variation des différents paramètres définissant la structure en fonction de la température, $\nu = 0{,}93$.

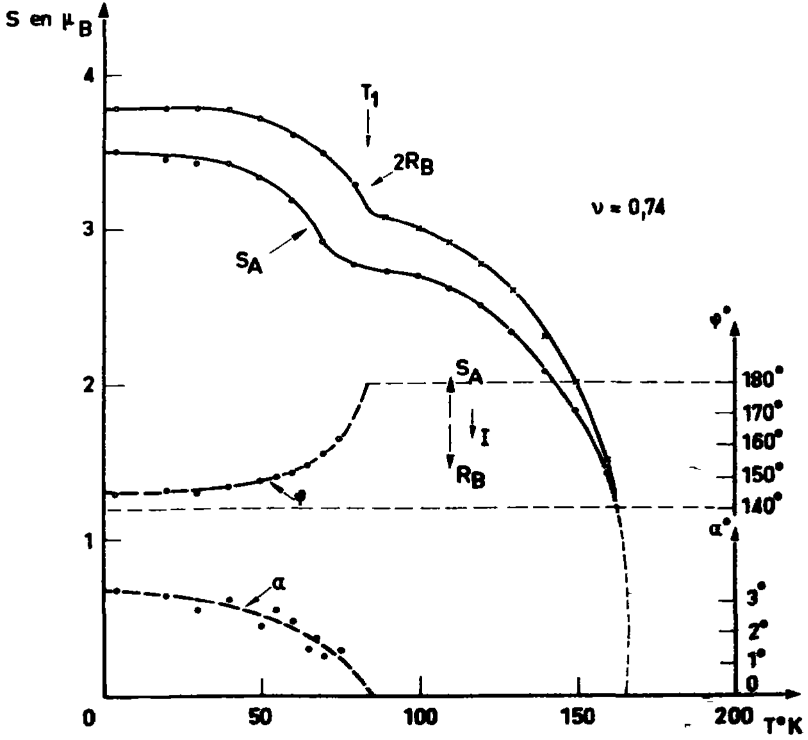

Fig. 16. Variation des différents paramètres définissant la structure en fonction de la température, $\nu = 0{,}74$.

constantes de champ moléculaire α,β,γ sont négatives (α,β,γ correspondent respectivement aux interactions entre les moments $S_{Mn}{}^{B}-S_{Ni}{}^{B}$, $S_{Ni}{}^{B}-S_{A}$, $S_{A}-S_{Mn}{}^{B}$) [3]. Avec cette hypothèse, on déduit, connaissant la forme de la courbe $S_A(T)$ quand $T \simeq T_1$, d'après[3] que les aimantations des deux sous-réseaux des ions des sites B sont antiparallèles.

Les mesures de I, S_A, R_B dans cette région de température sont en accord avec ce résultat.

$$\text{Posons } S_A(T_1) = R_1 S_A(0°\text{K})$$
$$S'_{Mn}(T_1) = R_2 S'_{Mn}(0)$$
$$= R_2(2-\nu)\, S_{Mn}(0)$$
$$S'_{Ni}(T_1) = R_3 S'_{Ni}(0) = R_3 \nu S_{Ni}(0),$$

où S_{Mn} et S_{Ni} représentent la valeur des moments de spin des ions manganèse et nickel peuplant le site B. R_i est un facteur de proportionnalité traduisant la diminution de l'aimantation entre 0°K et T_1.

On sait d'après[3] qu'à $T = T_1$ au moins deux des trois rapports R_i sont peu inférieurs à l'unité. Il faut donc que R_2 ou R_3 soit du même ordre de grandeur que R_1 (qui est connu par les mesures de diffraction de neutrons être de l'ordre de 0,7–0,8).

Ceci est possible compte tenu des valeurs R_B déterminées par diffraction. En effet S'_{Mn} étant antiparallèle à S'_{Ni} on a $2R_B = |R_2 S'_{Mn}(0) - R_3 S'_{Ni}(0)|$.

Cette relation linéaire entre R_2 et R_3 est représentée, dans le cas de chaque valeur de ν, sur la Fig. 17. On voit qu'il est aisé de trouver un couple de valeur R_2, R_3 tel que l'une au moins soit du même ordre de grandeur

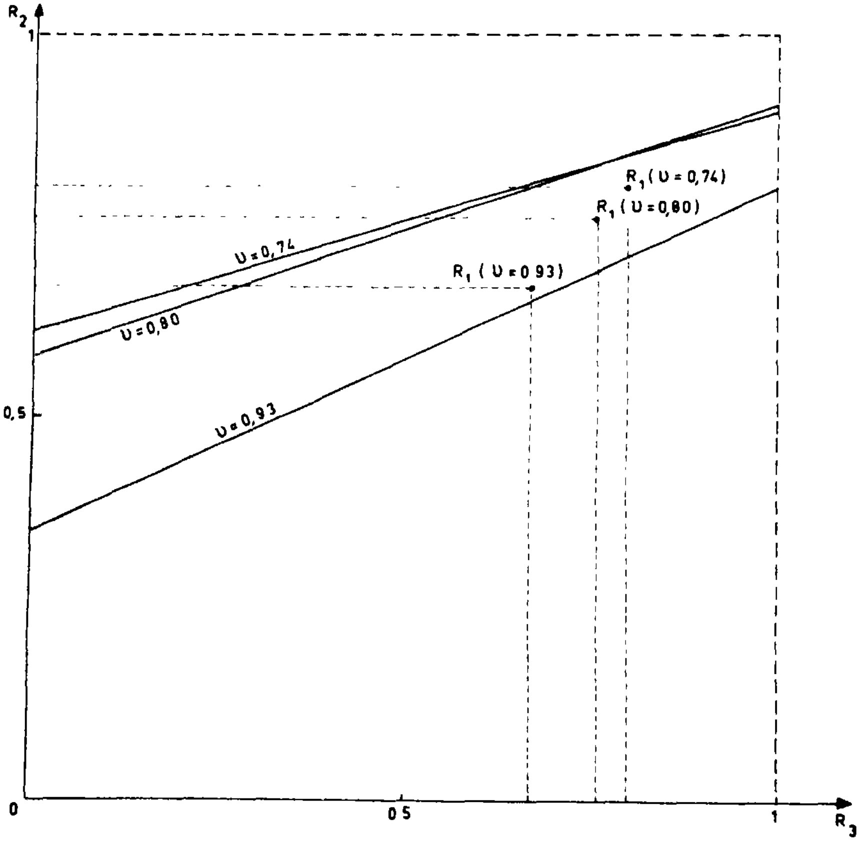

Fig. 17. Représentation de la relation $2R_B = |R_2 S'_{Mn}(0) - R_3 S'_{Ni}(0)|$.

que R_1 et que la relation précédente soit satisfaite.

En outre, S_{Mn}' doit aussi être opposé à S_A pour que $\mathbf{R}_B$ soit, comme le montre l'expérience, antiparallèle à S_A.

La structure haute température peut donc être ainsi décrite: l'aimantation du sous-réseau manganèse des sites B est opposée à l'aimantation du sous-réseau A et à l'aimantation du sous réseau nickel des sites B.

3. *Mesures de chaleur spécifique*

M. Lecomte* a mesuré la chaleur spécifique à pression constante de l'échantillon $\nu = 0{,}74$ (Fig. 18).

On observe deux anomalies: l'une à 160,7° ± 0,2°K correspondant à la température de Curie, l'autre à 84,3° ± 0,2°K correspondant au passage de la structure 'en étoile' à la structure colinéaire. Le pic correspondant à T_1(84,3°K) est plus étroit (~ 5° à la base) que celui correspondant à T_C (20° à 25° à la base), mais correspond à une variation d'entropie au moins égale à la variation d'entropie observée à $T \sim T_C$.

Ainsi les mesures de chaleur spécifique mettent en évidence non seulement la tem-

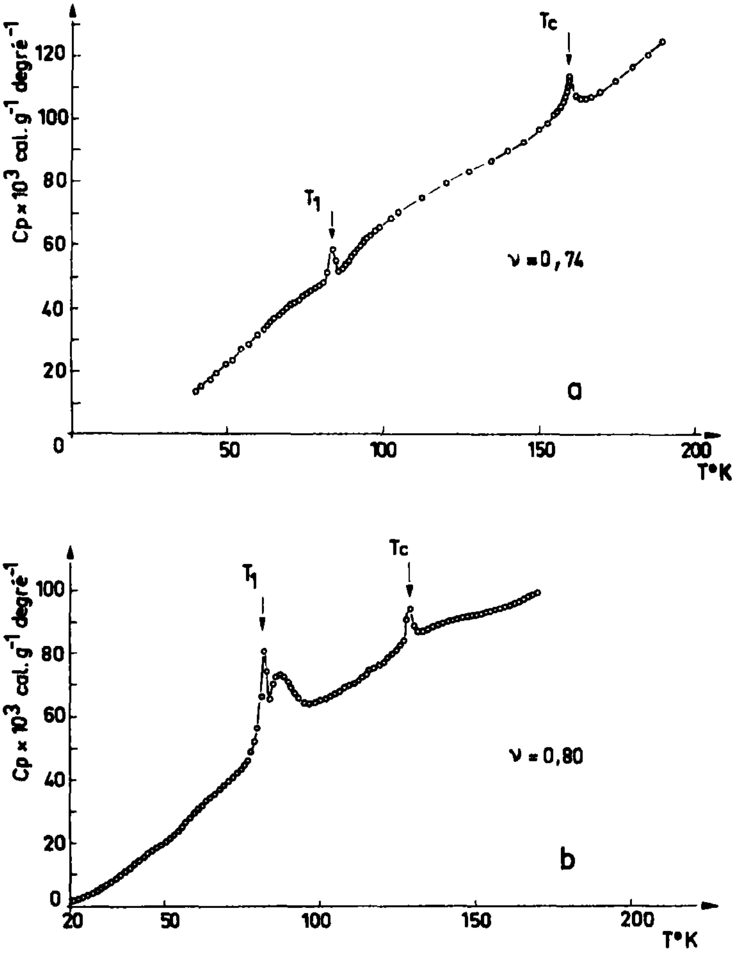

Fig. 18. Variation de la chaleur spécifique à pression constante en fonction de la température, $\nu = 0{,}74$ et $\nu = 0{,}80$.

---

*DPh-SRM, Saclay.

pérature de Curie, mais aussi la température de transition T_1. Cette méthode est la seule qui nous ait permis de déterminer avec précision le température T_1.

B-2. ETUDE DU COMPORTEMENT MAGNETIQUE EN FONCTION DE LA TEMPERATURE DE L'ECHANTILLON $\nu = 0{,}80$

1. *Données expérimentales*

Cet échantillon présente une évolution thermique apparemment originale par rapport aux deux précédents.

(1) *L'aimantation spontanée*, relativement forte à $T = 4{,}2$°K ($I_0 = 0{,}6\,\mu_B$/mol.), décroit rapidement pour atteindre une valeur très faible à $T \simeq 65$°K ($I \simeq 0{,}05\,\mu_B$/mol.) (Fig. 12(c)). Elle reste constante jusque vers 100°K, puis décroît pour atteindre 0 à $T = T_C$.

De plus les courbes $I(\mathrm{H})_T$ à température constante montrent que l'anisotropie est faible.

(2) *Variation avec la température de l'intensité de la raie* (220) *mesurée sans champ par diffraction de neutrons* (Fig. 19). Cette raie décroît régulièrement de 4,2°K à $T_C = 128$°K, sans présenter d''accident', contrairement aux cas précédents. Son intensité ne dépend que de S_A. La valeur de $S_A(T)$ suit la loi de Brillouin avec $J = 2$ (Mn^{3+}); aucun accident de cette courbe ne laisse prévoir une évolution vers une structure colinéaire.

(3) *Variation des raies* (220) *et* (111) *par diffraction de neutrons en présence d'un champ* 15 *kOE parallèle au vecteur de diffu-*

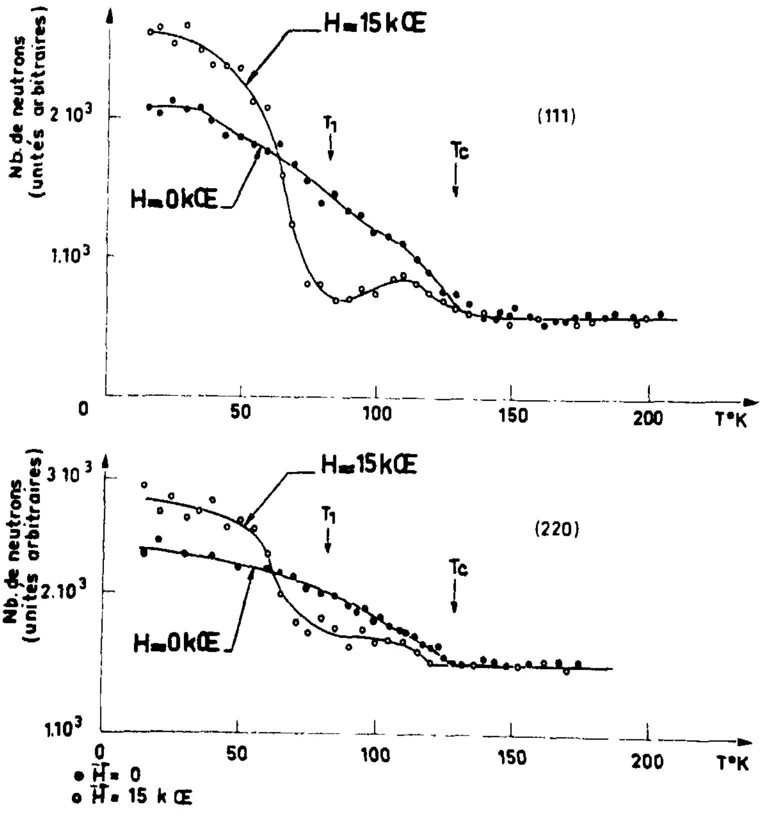

Fig. 19. Variation des intensités magnétiques des raies de diffraction (111) et (220) en fonction de la température, $\nu = 0{,}80$.

sion K (Fig. 19). Les intensités ne s'annulent à aucune température inférieure à T_C, comme cela devrait se produire en présence d'un champ si la structure devenait colinéaire (anisotropie faible). On observe même dans le cas de la raie (111) un maximum entre T_1 et T_C.

(4) *Mesures de chaleur spécifique** (Fig. 18(b)). A température égale, les valeurs de la chaleur spécifique sont légèrement plus faibles dans le cas $\nu = 0{,}80$ que dans le cas précédemment étudié ($\nu = 0{,}74$), l'écart augmentant quand la température $T(< T_C)$ croît.

On observe deux anomalies, l'une à 128,4° ± 0,2°K(T_C), l'autre à 82,4 ± 0,2°K (T_1) présentant les mêmes caractéristiques que celles obtenues dans le cas $\nu = 0{,}74$: le pic à $T \simeq T_1$ est plus étroit que celui à $T \simeq T_C$; la variation d'entropie correspondant au passage de la structure 'en étoile' à la structure alignée est supérieure à celle correspondant à la température de Curie du corps.

La similitude des deux courbes permet d'affirmer que *la structure 'en étoile' se transforme bien dans le cas $\nu = 0{,}80$ en une structure alignée* à $T_1 = 82{,}4$°K.

Il faut de plus signaler que le pic de chaleur spécifique, existant quand $T \simeq T_1$, est superposé à une 'bosse' s'étendant sur 25° à 30° et correspondant à une variation d'entropie beaucoup plus importante que les variations d'entropie correspondant à T_C (ou T_1).

2. *Interprétation du cas $\nu = 0{,}80$*

(1) *Structure haute température.* Les mesures de diffraction faites à 95°K en l'absence de champ conduisent à un modèle ferrimagnétique aligné. La valeur trouvée R_B s'explique comme dans les deux cas précédents en mettant l'aimantation du sous-réseau nickel de site B parallèle à $\mathbf{S}_A$ et de même sens, celle du sous-réseau manganèse de site B antiparallèle à $\mathbf{S}_A$.

(2) *En présence d'un champ.* Dans [3] on a calculé l'énergie magnétique en négligeant le champ intérieur. Ceci est valable dans le cas d'une structure à trois sous-réseaux, tant que l'aimantation I du corps est suffisamment grande. Quand I est petit il n'en est plus de même et en l'absence d'anisotropie le minimum de l'énergie est obtenu pour:

$$\frac{\partial E}{\partial \theta} = \left(\frac{H}{I} + \alpha\right) S'_{\mathrm{Mn}} \sin\theta + \left(\frac{H}{I} + \beta\right) S_A \sin(\theta + \psi) = 0$$

$$\frac{\partial E}{\partial \psi} = \left(\frac{H}{I} + \gamma\right) S'_{\mathrm{Mn}} \sin\psi + \left(\frac{H}{I} + \beta\right) S'_{\mathrm{Ni}} \sin(\theta + \psi) = 0$$

où E est l'énergie magnétique et θ et ψ représentent respectivement les angles des moments entre eux (Fig. 11).

Expérimentalement nous appliquons un champ de 15 kOE; quand I est grand, le terme dépendant de H est négligeable par rapport aux constantes α, β, γ. C'est ce qu'on a vérifié à 4,2°K pour les trois échantillons étudiés. Par contre quand I est petit (par exemple de l'ordre de 0,04 μ_B/mol dans le cas

$$\nu = 0{,}80 \text{ à } T \simeq 85°) \ \frac{H}{I} \sim \frac{15\,000}{0{,}04} \sim 400\,\text{kG}$$

l'ordre de 10^6G et l'aimantation d'un sous-réseau de l'ordre de 3 ou 4 μ_B/mol, les constantes de champ α, β, γ, seront de l'ordre de 300 kG μ_B^{-1} mol.$^{-1}$, valeur de même ordre que $\frac{H}{I}$. Nous n'avons donc plus le droit de négliger ce terme, l'application d'un champ pouvant modifier le type de structure.

Quand on applique un champ extérieur de 15 kOE, les mesures de diffraction de neutrons (spectre à 95°K et variations thermiques (Fig. 19)), montrent qu'on 'induit' une structure 'en étoile' lorsque $T_1 < T < T_C$ avec un angle α de l'ordre de 20 à 30′ et un angle φ de l'ordre de 30° à $T \simeq T_1$. L'importance de ce dernier provient du fait que S_A et $2\mathbf{R}_B$ sont pratiquement égaux en longueur.

---

*Mesures faites par M. Lecomte, DPh-SRM, Saclay.

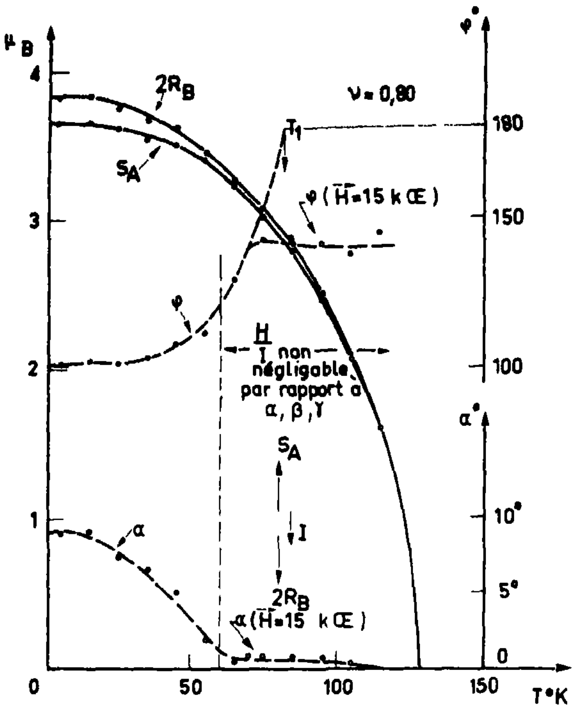

Fig. 20. Variation des différents paramètres définissant la structure en fonction de la température, $\nu = 0{,}80$. Influence de **H** aux hautes températures.

Ainsi à une température donnée, quand I est suffisamment petit, le champ appliqué transforme une structure ferrimagnétique colinéaire en une structure 'en étoile' et quand T est inférieure à T_1, H modifie les angles de la structure 'en étoile'. Il s'ensuit que, lorsqu'à une température donnée on extrapole à $H = 0$ la partie linéaire de la courbe $I(H)$, on obtient (si $I(H)$ est petit) une valeur différente de la résultante du motif magnétique. La courbe représentative $I_0(T)$ (Fig. 12(c)) ne représente pas la variation de la valeur de la résultante du motif magnétique quand $T > 55$°K. Les variations des différents paramètres définissant la structure avec ou sans champ appliqué sont représentées Fig. 20.

CONCLUSION

A basse température cette étude expérimentale a mis en évidence un type nouveau de structure magnétique dite structure 'en étoile' dont on avait prévu l'existence par un calcul théorique[3]. Ce modèle explique les faibles valeurs de l'aimantation spontanée et la grande variation de cette dernière en fonction de l'inversion. Si on ne prend pas la précaution de faire des mesures de diffraction précises en présence d'un champ appliqué la structure peut être confondue avec une structure ferrimagnétique alignée, mais dans ce cas il est impossible d'expliquer la faible valeur de l'aimantation.

Quand la température croît, la structure 'en étoile' évolue vers une structure ferrimagnétique alignée confirmant ainsi la théorie. De la forme des courbes représentatives de la variation des aimantations en fonction de T autour de la température de transition, il est possible de déterminer le type de structure colinéaire obtenue à haute température.

Remerciements—Nous remercions M. le Professeur Herpin qui a suivi de près ce travail et nous a aidé par ses suggestions ainsi que M. Mèriel qui nous a fait largement bénéficier de son expérience lors de nombreuses discussions.

Nous remercions également tous les chercheurs et techniciens que nous avons cités, leur collaboration nous a permis de mener à bien à ce travail.

Enfin nous remercions MM. Tourand et Sougi de l'aide qu'ils nous ont apportée au cours des expériences de diffraction de neutrons.

REFERENCES

1. BOUCHER B., BUHL R. et PERRIN M., *Acta. crystallogr.* À paraître.
2. VILLERS G. et BUHL R., *C.r. hebd. Séanc. Acad. Sci., Paris* **260**, 3406 (1965).
3. BOUCHER B., BUHL R. et PERRIN M., *J. Phys. Chem. Solids* **30**, 2467 (1969).
4. SCATTURIN V., CORLISS L., HELLIOT N. et HASTINGS J., *Acta crystallogr.* **14**, 19 (1961).

J. Phys. Chem. Solids Pergamon Press 1970. Vol. 31, pp. 385–389. Printed in Great Britain.

PHASE RELATIONS OF $KClO_4$ AND KBF_4 TO HIGH PRESSURES

CARL W. F. T. PISTORIUS

Chemical Physics Group of the National Physical and National Chemical Research Laboratories,
South African Council for Scientific and Industrial Research, P.O. Box 395, Pretoria, South Africa

(*Received* 29 *April* 1969)

Abstract—The high-pressure phase diagrams of $KClO_4$ and KBF_4 were studied by means of differential thermal analysis. The $KClO_4$ orthorhombic/cubic transition line rises from 296°C at atmospheric pressure to 566°C at 11·3 kbar, where it decomposes explosively. The melting curve of cubic KBF_4 I rises from 580°C to a triple point at 16·4 kbar, 852°C, where a new phase KBF_4 III appears. It is suggested that the tetrahedral anions rotate freely in KBF_4 III. The KBF_4 II/I (orthorhombic/cubic) transition line rises from 278·6°C to the KBF_4 III/II/I triple point at 33·3 kbar, 928°C, and the resulting II/III transition line was followed to 40·3 kbar, 985°C. The melting curve of KBF_4 III rises steeply to 22·6 kbar, 950°C.

INTRODUCTION

THE CRYSTAL chemistry of XYO_4 substances has been fairly extensively studied and correlated at atmospheric pressure[1–3]. Some scattered work has been done at elevated pressures[4], but in the case of substances closely related to those studied in the present work the only high-pressure results reported have been those of Bridgman[5], who studied the polymorphism of the alkali perchlorates to 50 kbar and ~ 100°C, and a recent study of the phase diagrams of $NaBF_4$ and $NaClO_4$ to 40 kbar[6].

The room-temperature modifications KBF_4 II and $KClO_4$ II have the barite structure [7, 8], and are therefore isostructural with the perchlorates and fluoroborates of rubidium, thallium and caesium[3]. These substances have cubic high-temperature modifications [3] with the space group Fm3m[6]. The disorder in the structure is not caused by free rotation of the anions, but is of a type which maximizes the cation-oxygen (or cation-fluorine) distances[6]. This transition occurs at ~ 300°C for $KClO_4$[9, 10], and at 277°C for KBF_4[11]. KBF_4 I melts at 530°C[12]. while $KClO_4$ I decomposes before melting[13].

EXPERIMENTAL PROCEDURES

$KClO_4$ with a certified purity of 99 per cent was obtained from Koch-Light & Co., and KBF_4 from BDH. The KBF_4 was purified by washing with cold and hot water and with ethanol. The salts were thoroughly dried before use.

Pressures up to 40 kbar were generated in a piston–cylinder device[14]. The furnace assembly was similar to that used by Cohen *et al.*[15]. Phase changes were detected by means of differential thermal analysis (DTA), using Chromel–Alumel thermocouples below ~ 900°C and platinum–platinum–10% rhodium thermocouples above this temperature. The results were corrected for the effect of pressure on the thermocouples[16]. The samples were contained in metal capsules which incorporated thermocouple wells[17]. The work on KBF_4 was done in Cu capsules, while Ni capsules were used for $KClO_4$. $KClO_4$ decomposed explosively at high pressures near ~ 600°C, and its phase boundary could therefore not be followed beyond this point. No capsule attack was observed. The axial thermal gradient along the sample capsule was reduced by sandwiching the capsule between two insulated metal plugs[18]. Each phase boundary was based on several separate runs. The results of different runs were consistent. The heating/cooling rate was in the range 0·2–0·8°C/sec. Sliding friction was determined by comparing results obtained on increasing and on decreasing pressure. The pressures obtained in this way were further corrected for the effect of nonsymmetrical pressure losses[19]. The corrected pressures are believed accurate to ± 0·5 kbar. The points plotted represent the mean of heating and cooling in the case of solid–solid transitions, and melting temperatures in the case of solid–liquid phase changes.

RESULTS

Potassium perchlorate

The $KClO_4$ II/I transition line is shown in Fig. 1. The transition yielded extremely strong and sharp DTA signals at atmospheric pressure. The ~ 10°C thermal hysteresis was independent of the heating/cooling rate in the range 0·2–2·0°C/sec. The present atmospheric pressure transition points are 301·3°C on heating and 291·1°C on cooling, being the mean of 26 determinations. At higher pressures the signals become considerably broader, and the thermal hysteresis increase somewhat. This is a consequence of the large slope of the transition line and the large volume change (see below) associated with the transition, which cause a considerable local change in pressure as the transition occurs, and thereby broaden the DTA signals. The observed points, fitted to a simple power series, are shown in Table 1.

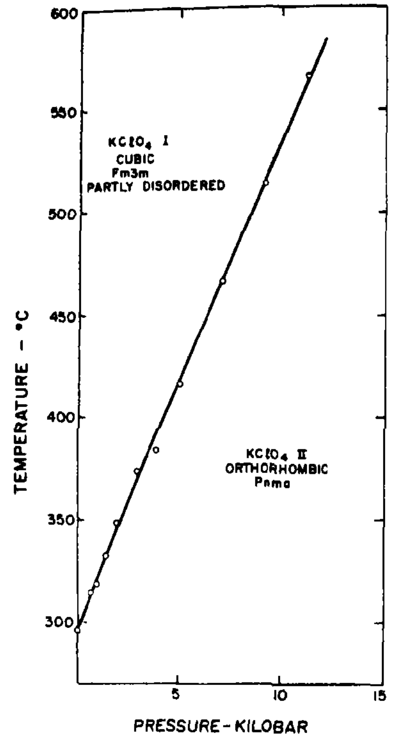

Fig. 1. Phase diagram of $KClO_4$ to 15 kbar.

The latent heat of the $KClO_4$ II/I transition is 15·1 kJ/mole[9]. With the present

Table 1. Phase relations of $KClO_4$ *and* KBF_4

Transition line	Fit	Standard deviation
$KClO_4$ II/I	$t(°C) = 296{\cdot}2 + 23{\cdot}9P - 0{\cdot}0098P^2$	3·6°C
KBF_4 II/I	$t(°C) = 278{\cdot}6 + 22{\cdot}4P - 0{\cdot}086P^2$	4·6°C
KBF_4 I/III	$t(°C) = 852 + 8{\cdot}03(P - 16{\cdot}4) - 0{\cdot}216(P - 16{\cdot}4)^2$	2·8°C
KBF_4 II/III	$t(°C) = 928 + 8{\cdot}70(P - 33{\cdot}3) - 0{\cdot}084(P - 33{\cdot}3)^2$	2·9°C
KBF_4 I/liq.	$P/9{\cdot}625 = (T/853)^{3{\cdot}581} - 1$	0·41 kbar
KBF_4 III/liq.	$(P - 16{\cdot}4)/30{\cdot}27 = (T/1125)^{1{\cdot}998} - 1$	0·07 kbar

Triple point	Pressure (kbar)	Temperature (°C)
KBF_4 III/I/liq.	16·4 ± 1·0	852 ± 5
KBF_4 III/II/I	33·3 ± 0·5	928 ± 4

initial slope of the transition line, viz. 24°C/kbar, the Clapeyron relation yields

$$\Delta V_{II/I} = 6{\cdot}4\,\text{cm}^3/\text{mole},$$

which is ~ 11% of the molar volume of the low-temperature phase.

Potassium tetrafluoroborate

The phase diagram of KBF_4 is shown in Fig. 2. The DTA signals corresponding to the KBF_4 II/I transition behaved in the same fashion as those of the $KClO_4$ II/I transition at low pressures, but slowly became sharper once again above ~ 20 kbar, together with a gradual decrease in thermal hysteresis. The atmospheric pressure transition points are 285·2°C on heating and 272·1°C on cooling, being the mean of 12 determinations. The thermal hysteresis was independent of heating/cooling rate in the range 0·3–2·0°C/sec.

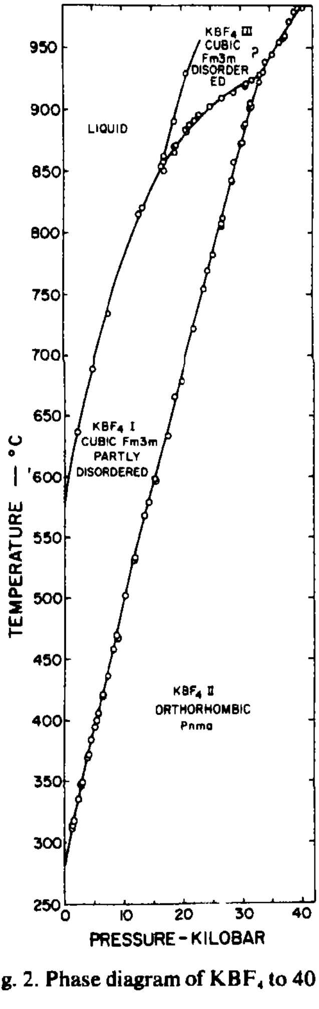

Fig. 2. Phase diagram of KBF_4 to 40 kbar.

The melting line of KBF_4 I yielded sharp signals and rose from an atmospheric pressure value of 580°C to a triple point KBF_4 III/I/liquid at 852°C, 16·4 kbar. At higher pressures two DTA signals are encountered due to the I/III transition and to the melting of KBF_4 III. The I/III transition had a thermal hysteresis of less than 5°C. This transition line meets the II/I transition at a triple point III/II/I at 928°C, 33·3 kbar. The resulting KBF_4 II/III transition line yielded sharp and strong DTA signals, and was followed to 40·2 kbar, 984°C. At heating/cooling rates above ~ 0·7°C the III/II transition, as well as the I/II transition above ~ 28 kbar, tended to supercool by ~ 5°C. Supercooling could be recognized by a sudden reversal of motion of the temperature pen accompanied by a sharp rise in temperature of the sample to the transition temperature observed on heating. The phase relations of KBF_4 are summarized in Table 1. The melting curves were fitted to the Simon equation[20]

$$P - P_0 = A[(T/T_0)^c - 1]$$

where T°K is the melting point at P kbar, P_0 and T_0 are the coordinates of the triple point of the phase in question, and A and c are adjustable constants, determined by means of Babb's method[21].

DISCUSSION

An inspection of Table 1 shows that the II/I transition lines of $KClO_4$ and KBF_4 are closely similar with regard to slope and curvature. Since the crystal structures of the phases II on the one hand, and the phases I on the other, are identical, it can be expected that the entropy of the KBF_4 II/I transition is close to that of the $KClO_4$ II/I transition. The volume changes upon transition are therefore also closely similar.

The room-temperature phases of $RbClO_4$, $TlClO_4$, NH_4ClO_4 and $CsClO_4$ have the same crystal structure as $KClO_4$ II[3]. Bridgman [5] found that in the pressure range to 50 kbar $CsClO_4$ has a transition with a volume change of 3·5 cm^3/mole, while $RbClO_4$, $TlClO_4$ and NH_4ClO_4 each have a transition with a volume change of less than 1·3 cm^3/mole. This suggests that the high-pressure form of $CsClO_4$ has a crystal structure different from that of the high-pressure forms of $RbClO_4$, $TlClO_4$ and NH_4ClO_4. $KClO_4$ did not have a high-pressure transition to 50 kbar. $NaClO_4$ has two high-pressure transitions in this range[5], and it has been shown that $NaClO_4$ III, the phase stable at pressures above ~ 30 kbar, probably has the same structure as $KClO_4$II[6]. It therefore appears probable that for, e.g., the alkali perchlorates, and probably also the alkali tetrafluoroborates, a larger cation radius simulates higher pressure, as is the case with the alkali halides. One can therefore expect $KClO_4$ and KBF_4 to undergo transitions to the structure of the high-pressure form of $RbClO_4$ or $CsClO_4$, or both, at pressures above 50 kbar. If the similarity between the phase diagrams of $KClO_4$ and KBF_4 is real, one can further expect $RbBF_4$ to have a high-pressure transition near 20 kbar as in the case of $RbClO_4$. Work is in progress to check these predictions.

The atmospheric pressure melting point of KBF_4 I is given as 530°C in the literature[12]. Our present value for material contained in a metal capsule is 580°C. The discrepancy is probably due to slow decomposition of the uncontained material as the temperature was raised to the melting point. If this is correct, the present value should be preferred. Similar considerations were found to apply in the case of $NaBF_4$[6].

The structure of the group of cubic high-temperature phases, of which $KClO_4$ I and KBF_4 I are examples, has only recently[6] been clarified. The cations and the central atoms of the anions were known to have the positions of sodium and chlorine, respectively, in NaCl[10, 13]. Originally it was proposed that the space group is T_d^2–$F\bar{4}3m$, but the proposed oxygen or fluorine parameters led to completely unreasonable interatomic distances. Later work[22] suggested that the rotation of the anions does not leave the oxygens in fixed positions. However, in a ~ 7 Å cell with a Cl–O distance of ~ 1·5 Å this requires a minimum cation–oxygen approach of ~ 2 Å, which is not acceptable even for $NaClO_4$, and certainly not for larger cations. A satisfactory description of the structure[6] showed that the disorder in the structure was not caused by free rotation of the anions, but was of a type which maximizes the cation-oxygen distances. The 16 oxygen atoms appear in the $32f$ set of positions of the space group $Fm3m$, with $x = b/\sqrt{3}$, where b represents the ratio of the cation-oxygen distance and the unit-cell edge. The tetrahedral anions can therefore have either of two orientations which might occur either statistically, over limited domains, or alternatively interchange by flipping, i.e. 90° oscillations about a [100] direction of the parent cube of the tetrahedron.

If the temperature is raised considerably, with resulting thermal expansion of the lattice as well as a considerable increase in thermal vibrational energy of the tetrahedra, one would expect that, eventually, a state would be approached where the earlier suggestion of almost free rotation of the tetrahedra became possible. Ordinarily the substance melts before this point is reached. However, if pressure is increased, the melting point rises rapidly with pressure, and we suggest that the new phase KBF_4 III has this structure. If this is the case, KBF_4III will also be cubic, space group $Fm3m$, as is KBF_4I, but with a different structure. The DTA signals corresponding to the KBF_4 I/III transition are sufficiently strong to suggest that the transition is of the first order. The considerable increase in slope of the melting curve at the KBF_4 liquid/III/I triple point further shows that either Δv or Δs, or both, for the I/III transition must be non-zero. A similar phase might be found to occur in the phase diagram of NaBF$_4$[6] at pressures above ~ 40 kbar and temperatures above ~ 850°C, as well as possibly in the phase diagram of RbBF$_4$ in approximately the same position as KBF$_4$ III. Work is in progress to test this prediction.

Acknowledgements—The author would like to thank Mrs Martha C. Pistorius for writing the computer programs used in fitting the data and Drs G. Gafner, J. C. A. Boeyens and R. J. Murphy for valuable discussions. Mr. J. B. Clark assisted with much of the experimental work. Mr. J. Erasmus and his staff and Mr. G. O'Grady and his staff kept the equipment in good repair, and were responsible for the manufacture of the furnace parts. Calculations were carried out on the IBM System 360/65H of the National Research Institute for Mathematical Sciences.

REFERENCES

1. PANNETIER G. and COURTINE P., *Bull. Soc. chim. France* **1966**, 2933 (1966).
2. BOKII G. B. and GOROGOTSKAYA L. I., *Zh. strukt. Khim.* **8**, 662 (1967).
3. WYCKOFF R. W. G., *Crystal Structures*. Wiley, New York (1965).
4. KLEMENT W., Jr. and JAYARAMAN A., *Prog. solid State Chem.* **3**, 289 (1966).
5. BRIDGMAN P. W., *Proc. Am. Acad. Arts Sci.* **72** 45 (1937).
6. PISTORIUS C. W. F. T., BOEYENS J. C. A. and CLARK J. B., *High Temp. High Press.*, **1**, 41 (1969).
7. BALLANCA A. and SGARLATA F., *Rend Soc. Mineral. Ital.* **7**, 42 (1951).
8. GOTTFRIED C. and SCHUSTERIUS C., *Z. Kristallogr.* **84**, 65 (1932).
9. OZAWA T., *Bull. chem. Soc. Japan* **39**, 2071 (1966); OZAWA T., MOMOTA M. and ISOZAKI H., *Bull. chem. Soc. Japan* **40**, 1583 (1967).
10. HERRMANN and ILGE W., *Z. Kristallogr.* **75**, 41 (1930).
11. VORLÄNDER D., HOLLATZ J. and FISCHER J., *Ber. Deut. Chem. Ges.* **65**, 535 (1932).
12. De BOER J. H. and VAN LIEMPT J., *Rec. Trav. Chim. Pays-bas* **46**, 127 (1927).
13. BRAEKKEN H. and HARANG L., *Z. Kristallogr.* **75**, 538 (1930).
14. KENNEDY G. C. and LAMORI P. N., *Progress in Very High Pressure Research* (Edited by F. P. Bundy, W. R. Hibbard and H. M. Strong). Wiley, New York (1961).
15. COHEN L. H., KLEMENT W. Jr. and KENNEDY G. C., *J. Phys. Chem. Solids* **27**, 179 (1966).
16. HANNEMAN R. E. and STRONG H. M., *J. appl. Phys.* **36**, 523 (1965); *ibid.* **37**, 612 (1966).
17. PISTORIUS C. W. F. T., *J. Phys. Chem. Solids* **26**, 1543 (1965).
18. RAPOPORT E., *J. chem. Phys.* **45**, 2721 (1966).
19. PISTORIUS C. W. F. T., RAPOPORT E. and CLARK J. B., *Rev. scient. Instrum.* **38**, 1741 (1967).
20. SIMON F. E. and GLATZEL G., *Z. anorg. allg. Chem.* **78**, 309 (1929).
21. BABB S. E., *Rev. mod. Phys.* **35**, 400 (1963).
22. FINBAK C. and HASSEL O., *Z. phys. Chem. (Leipzig)* **32B**, 130 (1936).

J. Phys. Chem. Solids Pergamon Press 1970. Vol. 31, pp. 391-397. Printed in Great Britain.

MONTE CARLO CALCULATION OF THE MAGNETIZATION OF SUPERPARAMAGNETIC PARTICLES

K. BINDER, H. RAUCH and V. WILDPANER
Atominstitut der Österreichischen Hochschulen, Vienna, Austria

(*Received* 29 *April* 1969)

Abstract—The thermodynamics of single superparamagnetic particles is studied by means of a Monte Carlo technique which we recently derived for the calculation of compact ferromagnets[1, 2]. Using this method, an exact (numerical) calculation of the magnetization and of the internal energy of the particle is obtained. The particle consists of several hundred to thousand spins arranged in a body-centered cubic lattice, interacting with nearest neighbours according to the Heisenberg model of ferromagnetism. It is shown that in the phase transition region the effect of the finiteness of the system cannot be explained by any shift of the Curie point, because the finite system does not exhibit any pronounced phase transition. A marked temperature dependence of the magnetization on the size and shape of the particle is found. With these calculations it is possible to interprete the experiments in a new way.

1. INTRODUCTION

ASSEMBLIES of ferromagnetic particles having particle sizes smaller than a certain 'critical volume' show the behaviour of 'superparamagnetism', i.e. the magnetization of the system in a magnetic field is equal to the corresponding thermodynamic equilibrium value and both remanence and coercitivity vanish[3–5]. These phenomena have been extensively studied both experimentally and theoretically (see [3–5] and references contained therein) and several applications have been proposed. The basic theory is the Néel–Langevin theory[6], in which any interaction between the particles themselves is neglected and it is assumed that the magnetization of the small particle is the same as for the bulk material. We shall give a brief outline of this concept in Section 2, together with other approximate theories. Experimental investigations have shown that it seems to be well justified for many substances[7–11] to neglect the particle interaction, as we do it in this paper, although there have been found some exceptions[12, 13]. It is very difficult to take the interaction between the particles properly into account and therefore only crude approximations have been given[13, 14].

We consider now the question whether the magnetization of the small system can deviate appreciably from the corresponding value of the infinite system. In [14, 15] spin wave theory is applied and it is shown that for low temperatures there is only a small dependence on size and shape, if every linear dimension G of the systems fulfills the condition $G \gg 1$ (G in units of the lattice constant). A theory for all temperatures has been given in [16] by means of a modified mean field theory. Very similar to the results for thin films[17, 18], a shift of the Curie-temperature as a function of the particle size is found[16, 19]. Therefore the experimental results were often interpreted in terms of a Curie-temperature shift [3, 12, 16, 20, 21].

For the calculation of the magnetization and internal energy of small finite particles we now adopt a Monte Carlo method which we previously used for the calculation of the spin correlation functions determining the diffuse magnetic scattering of neutrons[1, 2]. In [2] we have already shown for a finite Ising system that the application of the Monte Carlo method gives useful results, which are exact within the statistical error (can be made very small if the computing time is chosen long enough). In Section 3 we give a short explanation of this technique, while in Section 4 we present numerical results which are derived for a body-centered cubic lattice and nearest neighbour Heisenberg interaction. There the temperature dependence of the magnetization for various sizes and shapes of the particles is shown. Using these results, we are able to discuss approximate theories critically in Section 5 and to give the adequate interpretation of the relevant experiments.

2. APPROXIMATE THEORIES

The simplest theory for the phenomena of superparamagnetism is due to Néel[6]. One considers non-interacting single domain particles with volume V, magnetization $M(T)$ and uniaxial anisotropy $KV\sin^2\theta$. To observe superparamagnetism, the volume V must be smaller than a certain 'critical volume V_c' (if $K=0$ then $V_c \to \infty$). The influence of the anisotropy on the average magnetization of a superparamagnetic system is considered in [3, 22], where it is shown that the anisotropy can be neglected in all cases of cubic symmetry. In the following we always use values of V which are smaller than V_c, wherefore we may neglect the anisotropy. Then the average magnetization of our system of n particles is [6]

$$\bar{M} = M_s(T)\left(cthx - \frac{1}{x}\right) \approx M_s(T)\frac{x}{3} \quad (x \ll 1) \tag{1}$$

with

$$x = \frac{M_s(T)H}{nkT}, \quad M_s(T) = nVM(T)$$

H . . . external magnetic field.

Of course, it is possible to generalize (1) for a distribution of particle sizes[3, 12]. According to [6], the function $M(T)$ does not depend on the particle volume V. For a cubic particle of length G with a simple cubic lattice and $S=\frac{1}{2}$ we have in the spin wave region [14, 15]:

$$m(T) = m_\infty(T)\left(1 - \frac{1\cdot 42}{G}\frac{kT}{4\pi J}\right)$$
$$\left(m(T) = \frac{M(T)}{M(0)}\right) \tag{2}$$

J . . . exchange integral between nearest neighbours. Except for extremely small values of G one can take $m(T) \approx m_\infty(T)$ in this region.

In [16] a treatment based on mean field theory is given. The spins on the surface of the particle and the inner spins are considered to establish two sublattices having different coordination numbers. In this way one derives a system of coupled equations which can be solved numerically. The temperature dependence of the magnetization is similar to the case of an infinite system, but the values of the Curie-points decrease considerably for the mean field theory is especially for temperasmall particles[16]. It is now well known that the mean field theory is especially for temperatures near the critical one only a poor approximation[23].

The best estimates of Curie-points of infinite systems are obtained by an extrapolation of the high temperature series of the susceptibility [24].

$$\frac{\chi}{\chi_0} = \sum_\nu a_\nu\left(\frac{J}{kT}\right)^\nu \tag{3}$$

χ_0 . . . susceptibility of the ideal paramagnet.

From the assumption

$$\left(\frac{\chi}{\chi_0}\right)_{T\to T_c} \infty \left(1 - \frac{T_c}{T}\right)^{-\gamma}$$

one derives

$$a_\nu/a_{\nu-1} = \frac{J}{kT_c}(1 + (\gamma-1)/\nu)$$

In [19] some coefficients a_ν for a finite system have been calculated and the Curie-temperatures were determined from the ratios a_5/a_6.

Extending the arguments on thin films[25], some authors find a dependence of the Curie-temperature of iron on the particle size[12].

3. DESCRIPTION OF THE MONTE CARLO METHOD[1, 2]

The interaction between the spins is described by the Heisenberg model Hamiltonian

$$\mathscr{H} = -\sum_{i \neq j} J_{ij} \vec{S}_i \vec{S}_j \tag{4}$$

and we assume interactions between nearest neighbours only. We use the 'classical Heisenberg model' where the $\vec{S}_i$ are unit vectors instead of spin operators. (This is equivalent to $S \to \infty$ and redefining the exchange integral J_{ij} appropriately). This is justified because the critical properties of Heisenberg magnets are almost independent of the spin value if a suitable normalization of J_{ij} is chosen[26]. An extension to finite S values can be based upon[27, 28].

Now we have to calculate the expectation value

$$\langle \cdots \rangle = Tr\left(\exp\left(-\frac{\mathscr{H}}{kT}\right)\cdots\right) \Big/ Tr \exp\left(-\frac{\mathscr{H}}{kT}\right) \tag{5}$$

where we assume to have N spin vectors $\vec{S}_i$ in a lattice (we chose the body-centered cubic lattice). From a given configuration (i.e. coordinates $\{S_i^\epsilon\}$) we generate a new configuration by changing the coordinates of the lattice point i_1 by

$$S^{\epsilon}_{i_1(\text{new})} = \frac{S^{\epsilon}_{i_1} + x_\epsilon \cdot \Delta}{\sqrt{\sum_{\epsilon} (S^{\epsilon}_{i_1} + x_\epsilon \cdot \Delta)^2}} \qquad \begin{pmatrix} \epsilon = x, y, z \\ -1 \leqslant x_\epsilon \leqslant +1 \\ \text{random numbers} \end{pmatrix}^{*} \tag{6}$$

and calculate the energy change δE according to equation (4). If δE is negative, the new configuration is abandoned with a probability of $1 - \exp(-\delta E/(kT))$ and the old configuration is taken once more. Using a set of L configurations we get the expectation value of a variable F[1, 2, 29] by

$$\langle F \rangle = \frac{1}{L} \sum_{j=1}^{L} F_j. \tag{7}$$

A number of initial configurations has to be excluded from this procedure. To make this number as small as possible, we calculated the magnetization curves starting from the ferromagnetic region and we used the last configuration of a neighbouring temperature as a start configuration for the next value.

The numerical calculations were performed on an IBM 7040 computer and refer to various particle sizes and various particle shapes (a cube, a sphere, a rectangular block with an edge ratio of 2:1:1). The calculated errors are of the same order of magnitude as the size of the points drawn in the diagrams (Figs. 2–5). The computer program can be easily generalized for a more complicated lattice, as well as to include interactions with more distant neighbours, anisotropy terms, an external magnetic field etc. The only limitation for these generalizations is the computing time. In our case the total time was about 60 hr.

4. RESULTS OF THE NUMERICAL CALCULATIONS

A great number of configurations typical for the thermodynamic equilibrium of each temperature is generated by the Monte Carlo method. In Fig. 1 at $J/kT = 0{\cdot}8$ we show an example of a typical instantaneous picture of the spin projections in the xz-plane for three particle shapes. The result with periodic boundary conditions is also given. Although the magnetization has decreased from its maximum value by an amount of about 20 per cent, one can recognize a considerable disorder being statistically distributed. Since at the surface the coordination number is smaller, the disorder is greater in most cases.

In Figs. 2–4 the magnetization for the three particle shapes is shown. This function is compared with the magnetization of an

---

*For a good convergence of the procedure, the parameter Δ has to be chosen suitably (see Ref. [2]).

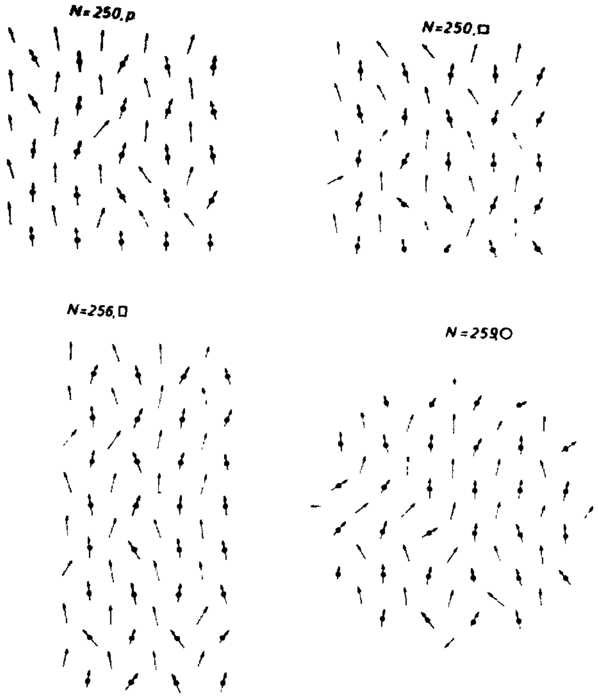

Fig. 1. Instantaneous spin projections into the x–z-plane for a cube ($N = 250$, □), a sphere ($N = 259$, ○) and a rectangular block ($N = 256$, ▭). For $N = 250$, p periodic boundary conditions are applied. In each case a central x–z-plane (↑) of the particle is shown together with an adjacent plane (↑).

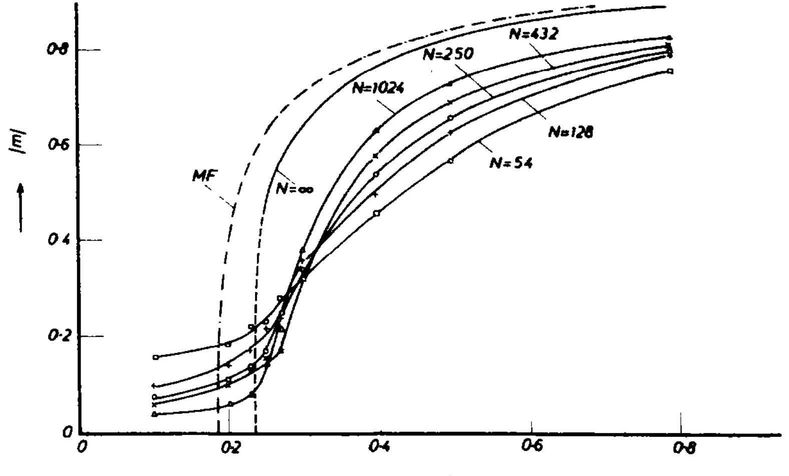

Fig. 2. Absolute values of the magnetization of superparamagnetic particles of cubic shape vs. the reciprocal temperature. Parameters are the numbers of spins. The dashed-dotted curve (MF) is calculated by the mean field theory, the curve for $N = \infty$ is derived from the result for $N = 250$ with periodic boundary conditions extrapolated to the correct value of the Curie temperature (dashed line). The magnetization is given in units of its saturation value.

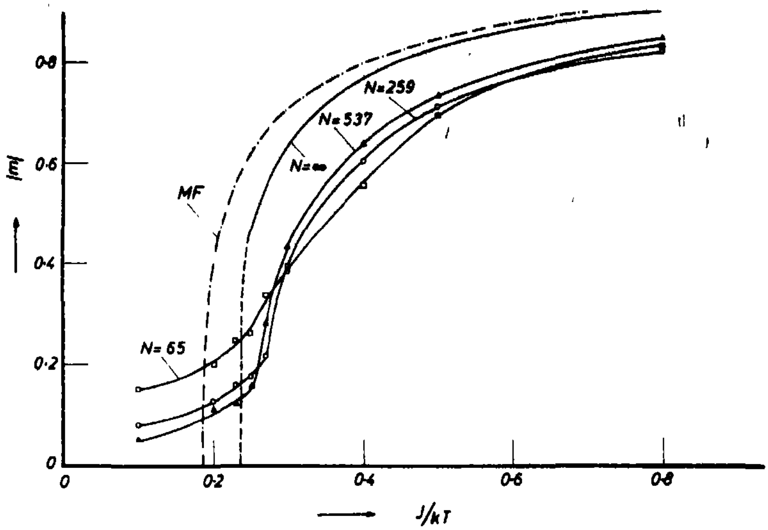

Fig. 3. Absolute values of the magnetization of superparamagnetic particles of spherical shape versus the reciprocal temperature. For explanation see Fig. 2.

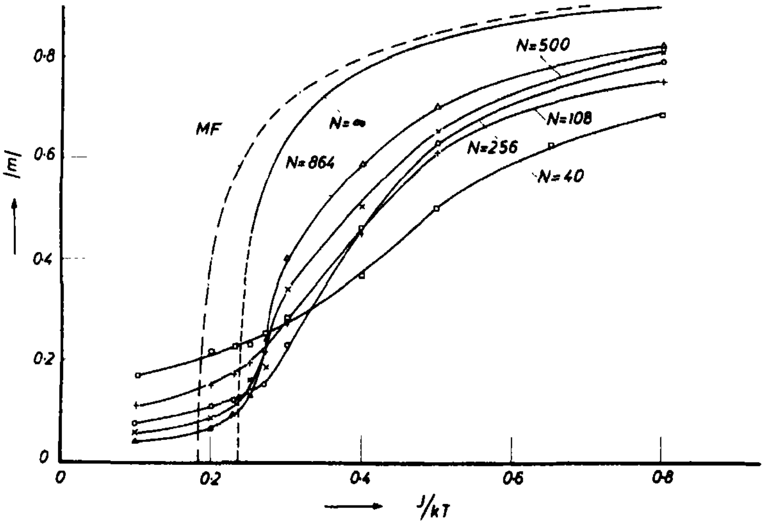

Fig. 4. Absolute values of the magnetization of superparamagnetic particles having the shape of a rectangular block, vs. the reciprocal temperature. For explanation see Fig. 2.

infinite system according to the mean field theory (MF) and with an estimate of the correct function for the infinite system which is taken from the $N = 250$ system with periodic boundary conditions and extrapolated to the known Curie-point. The most remarkable feature is that no phase transition in the usual sense can be observed. Even for a random set of spins the magnetization remains non-zero ($|m|_{\text{random}} \approx 1/\sqrt{N}$) if the number of spins is finite. The magnetization of the finite system strongly depends on the number of spins for most of the temperatures.

The magnetization curves are also distinct functions of the particle shapes. This can be seen very clearly from Fig. 5, where the magnetization is shown for various shapes and for about the same number of spins. In the 'ferromagnetic' temperature region there is a marked shape dependence, while in the 'paramagnetic' region this is not true and the value of the system with periodic boundary conditions is reached. The results for $N = \infty$ contain a certain amount of order even in the paramagnetic region as a consequence of the periodic boundary conditions and are therefore only approximately correct, while the results for the finite systems described here are exact within the model assumed. The 'paramagnetic magnetization' is a simple consequence of the finiteness and has the order of magnitude of $1/\sqrt{N}$.

The internal energy was calculated with the magnetization curves, too. This function shows a similar temperature dependence. Due to correlation effects[2], the value of the energy is to some extent always greater than the square of the relative magnetization. It is not possible to detect any discontinuity in these energy functions and it is quite clear that the specific heat exhibits only a broad peak of finite height instead of any discontinuity. This is also a consequence of the finite size where the transition is smoothed out.

5. CONCLUSIONS

The results discussed above show that for a small magnetic system no Curie-point in the usual sense exists. Therefore, the approximative theories[12, 16, 19] cannot adequately describe the size dependence of the phase transition. In the case of [19] the derivation of a susceptibility series of a finite system is of course a correct and interesting method, but the conclusions concerning the Curie-point are incorrect, mainly because the extrapolation method is based on the assumption that the susceptibility diverges for the Curie-point. However, for a finite system the susceptibility only diverges at $T = 0$[3, 15]. In this sense it is not surprising that there is no

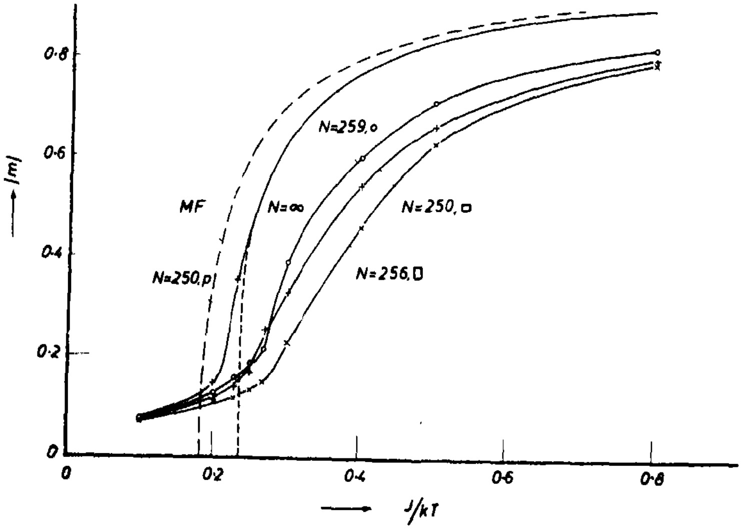

Fig. 5. Absolute values of the magnetization of superparamagnetic particles with different shapes and about the same number of spins, vs. the reciprocal temperature. For explanation see Fig. 2.

clear experimental evidence on a shift of the Curie temperature [16]. With the exact results presented in this paper a new interpretation of the experiments in [3, 12, 16, 20, 21] is possible. Nevertheless a quantitative comparison seems difficult, because in the experiment one has a distinct distribution of particle sizes and shapes.

The theory presented in this paper allows a careful rexamination of previous experiments and theories. The results thus obtained are a valuable source of advice for new experiments.

Acknowledgements—The authors want to thank Professor Ortner for his encouragement and interest.

We express our gratitude to Professor Stetter (Institut für Numerische Mathematik der T. H. Wien) for making the necessary computing time on the IBM-7040 available to us.

REFERENCES

1. BINDFR K. and RAUCH H., *Phys Lett.* **27A**, 247 (1968).
2. BINDER K. and RAUCH H., *Z. Phys.* **219**, 201 (1969)
3. KNELLER E., In *Handbuch der Physik* (Edited by S Flugge), Vol. 18, Part 2 *Ferromagnetismus*, Springer, Berlin-Heidelberg-New York (1966).
4. JACOBS I. S. and BEAN C P., In *Magnetism*, Vol. 3 (Edited by G. T. Rado and H. Suhl). Academic Press, New York (1963).
5. KNELLER E., *Z. Angew. Phys.* **21**, 16 (1966).
6. NEEL L., *Annls Géophys*, **5**, 99 (1949).
7. BECKER J. J., *Trans. AIME* **209**, 59 (1957).
8. BESKOVITZ A. E. and FLANDERS P. J., *Acta Met.* **8**, 823 (1960).
9. KNAPPWOST A. and PAPADIMITRAKI H., *Z. phys. Chem.* **32**, 51 (1962).
10. KNAPPWOST A. and STEIN H. D., *Z. Elektrochem.* **64**, 321 (1960).
11. BEAN C. P. and JACOBS I. S., *J. appl. Phys.* **27**, 1448 (1956).
12. VOGT E., HENNING W. and HAHN A., *Ber. D. Arbeitsgem. Ferromagnetismus*, p. 46 (1958), Riederer, Stuttgart (1959).
13. HAHN A., *Phys. kondens. Mater.* **4**, 20 (1965).
14. THOMAS H., *Z. Angew. Phys.* **21**, 13 (1966).
15. THOMAS H., *Z. Angew. Phys.* **15**, 201 (1963).
16. HELLENTHAL W., *Z. Physik* **170**, 303 (1962).
17. KLEIN M. and SMITH R., *Phys. Rev.* **81**, 378 (1951).
18. VALENTA L., *Czech. J. Phys.* **7**, 127, 136 (1957).
19. LOTTERMOSER M., *Z. Angew. Phys.* **26**, 235 (1969).
20. ABELEDO C. and SELWOOD P. W., *J. appl. Phys.* **32**. Suppl., 229S (1961).
21. KNAPPWOST A. and BURKARD E., *Ber. Bunsenges. phys. Chem.* **68**, 163 (1964).
22. WEST F. G., *J. appl. Phys.* **32** Suppl., 249S (1961).
23. KADANOFF L. P., GÖTZE W., HAMBLEN D., HECHT R., LEWIS E. A. S., PALCIAUSKAS V. V., RAYL M., SWIFT J., ASPNES D. and KANE J., *Rev. mod. Phys* **39**, 395 (1957).
24. RUSHBROOKE G. S. and WOOD P. J., *Mol. Phys.* **1**, 257 (1958).
25. CRITTENDEN E. C. and HOFFMANN R. W., *Rev. mod. Phys.* **25**, 310 (1953).
26. DOMB C. and SYKES M. F., *Phys. Rev.* **128**, 168 (1962).
27. HANDSCOMB D. C., *Proc. Camb. Phil. Soc.* **58**, 594 (1962).
28. HANDSCOMB D. C., *Proc. Camb. Phil. Soc.* **60**, 115 (1964).
29. METROPOLIS N., ROSENBLUTH A. W., ROSENBLUTH M. N., TELLER A. H., and TELLER E., *J. chem. Phys.* **21**, 1087 (1953).

J. Phys. Chem. Solids Pergamon Press 1970. Vol. 31, pp. 399–409. Printed in Great Britain.

AGGREGATION OF DIVALENT METAL IMPURITY IN ALKALI HALIDE CRYSTALS†

J. H. CRAWFORD, Jr.
Department of Physics, University of North Carolina, Chapel Hill, N.C. 27514, U.S.A.

(*Received* 6 *March* 1969)

Abstract—In this paper the processes underlying the aggregation of divalent cation–cation impurity dipoles have been examined in some detail. It is shown that the experimentally observed third-order kinetics which govern the aggregation can be accounted for on the basis of a two-step process: (a) two dipoles come together to form a loosely coupled pair which in turn (b) captures a third dipole to form a trimer. This process can yield a reaction rate proportional to the cube of the dipole concentration only if the dimers are in quasi-equilibrium with the free dipoles, a condition which implies that the energy binding the pair together E_b is rather small (0·15–0·2 eV). A consequence of this kinetic model is that the activation energy for the aggregation reaction E^* is not equal to the energy of motion of the dipole E_M, but rather $E_M - E^* = E_B$. Rough estimates of the interaction energies of the trimer, the planar quadripole form of the dimer, and the linear dimer have been made and it is found that the energy per dipole in the planar quadripole is comparable to that for the trimer which would lead to the expectation that during the first third to one half of the aggregation reaction period a second order process should be observed. It is suggested that the formation of the planar quadripole is inhibited by electrostatic constraints imposed by the motion of the dipoles on the ionic lattice and this inhibiting effect favors relatively the formation and persistence of the loosely coupled pair and hence the two step mechanism of trimer formation.

1. INTRODUCTION

A NUMBER of years ago Dryden and coworkers[1, 2] investigated the kinetics of aggregation of a variety of divalent cations in NaCl and KCl crystals. The experimental approach was straightforward: the concentration of impurity remaining in the crystal in the form of divalent cation–cation vacancy dipoles was followed during an isothermal anneal by periodic measurements of the intensity of dielectric absorption. It was found that during the first stages of aggregation the rate of disappearance of dipoles is proportional to the third power of the dipole concentration; third order kinetics imply that the first aggregation product is a trimer or a cluster of three I–V dipoles. Subsequent investigation of the aggregation process using dielectric absorption[3], electron paramagnetic resonance [4–6] and ionic thermocurrent methods[7] substantiate these early observations. In nearly every case the rate of aggregation was found to be proportional to the cube of the dipole concentration for the early stage. Moreover, Symmonds and Kemp[4] find a resonance signal which they identify as arising from a trimer of dipoles. The stage governed by third order kinetics terminates in a plateau from which further aggregation into higher complexes proceeds much more slowly. The extent of the first stage of aggregation is greater the lower the annealing temperature; this observation has been taken to mean that the plateau is related to the thermal equilibrium concentration of trimers[1].

The strong evidence that the first step in aggregation of divalent metal impurity involves the formation of I–V triplets carries with it a number of unanswered questions. When Dryden[2] first described his work at the Defects in Crystalline Solids Conference in

---

†This work was supported by the U.S. Atomic Energy Commission (Contract No. AT-(40-1)-3677).

A preliminary account of this paper was presented at the Washington Meeting of the American Physical Society (*Bull. Am. phys. Soc.* 13, 659 (1968)) and a more extended version was presented at the International Symposium on Color Centers in Alkali Halides in Rome, September, 1968.

Kyoto attendant discussion reflected much surprise at the third order reaction. Third order reactions are rare simply because of the low probability of the three body encounter. Moreover, the formation of trimers implies that pairs of dipoles are either unstable or much less stable than trimers.

The purpose of this paper is to examine these underlying problems in an attempt to establish a better understanding of the early stages of impurity precipitation. The following points need to be considered: (a) Is there an intermediate to trimer formation? Closely related questions are: (b) What is the significance of the frequency factor and activation energy of the third order process? (c) Is preference for the trimer a result of low stability of the dimer? Treatment of (c) requires a consideration of (d) the probability of a second order process relative to a third order process involving similar reaction volumes and (e) lattice constraints on the formation of clusters of I–V dipoles. Pursuing these various lines of inquiry has convinced the author that the important question is (c). The answer, however, is not a matter of stability of the dimer, but rather the difficulty with which a planar quadripole forms in the rock salt structure. This conclusion follows from the mode of migration of dipoles: They alternately attract and repel each other as they approach to form stable quadripoles and hence move under electrostatic constraints which become large for small separations. Consequences of these lattice constraints for the problem of impurity aggregation in ionic lattices will be discussed.

2. AN ALTERNATIVE TO A PURE THIRD ORDER PROCESS

In view of the small probability anticipated for trimer formation, it is reasonable to search for another process or series of processes which depend upon the third power of the dipole concentration. An obvious candidate is a two-step process which involves (a) the formation of a dimer by the interaction of two I–V dipoles followed by (b) the addition of a third dipole to form a trimer. This possibility has been recently suggested by Cappelletti and DeBenedetti[7].

If one neglects the reverse process in dimer formation, the rates of creation of the intermediate and the final product are

$$\dot{N}_D = k_D N_P^2 = 4\pi D_P r_P N_P^2 \tag{1}$$

and

$$\dot{N}_T = k_T N_P N_D = 4\pi D_P r_D N_P N_D \tag{2}$$

where D_P is the diffusion coefficient of the dipole, N is the atomic concentration of the species indicated by the subscript, r is the appropriate capture radius, the k's are specific rate constants and the subscripts P, D and T refer to dipole, dimer and trimer, respectively.

The expression on the extreme right of equations (1) and (2) comes from the solution of the diffusion equation in spherical geometry after the initial transient has died away. This expression is more appropriate for interactions between entities, one of which moves by atomic steps, than the more familiar one, involving the product of interaction cross section and velocity (σv) which is applicable to gaseous atoms and electron interactions.

The rate of decrease of I–V concentration is then

$$\dot{N}_P = -4\pi D_P N_P (2r_P N_P + r_D N_D) \tag{3}$$

which obviously is not necessarily proportional to N_P^2. If the dimer and trimer are of comparable stability and $r_P \sim r_D$, clearly N_D will build up rapidly until $N_D \sim N_P$ after which creation of trimers will become dominant. Hence dimers are expected to be the dominant product until N_P decreases to a value between one-half and one-third of its initial value. This obviously is contrary to observation since in every investigation the third order process was dominant and only in one instance[7], namely, the aggregation of Sr in NaCl, was there a hint of a second order reaction which could be attributed to the formation of dimers.

The missing ingredient in the above analysis is the decomposition of dipole pairs. If we assume the binding energy for the dimer to be small compared to that for the trimer, quasi-equilibrium between single dipoles and dimers will be established long before the number of trimers becomes appreciable. Under these conditions the concentration of dimers is given approximately by the simple mass action law:

$$N_D \simeq N_P^2K_D = N_P^2AN_L^{-1}\exp[E_B/kT] \quad (4)$$

where N_L is the concentration of cation sites, E_B is the energy of binding between dipoles forming the dimer and A is a constant which includes the effect of entropy change. Now, from equation (2)

$$\dot{N}_T \simeq k_TK_DN_P^3. \quad (5)$$

Since

$$\dot{N}_T = -\tfrac{1}{3}\dot{N}_P$$

we can write

$$\dot{N}_P \simeq -3k_TK_DN_P^3. \quad (6)$$

As indicated above this approximation is better the smaller E_B since the quasi-equilibrium is established more rapidly the smaller N_D in equilibrium. In this oversimplified approach it is also evident that in the limit of $E_B = 0$ this treatment becomes exact since interaction of a third dipole with a random pair is just another way of describing a third order process.

If the two-step process is indeed applicable to the aggregation of I–V dipoles, we should be able to estimate from experimental results the upper limit of E_B, provided the dimer is a quadripole which does not contribute to specimen polarization. The dielectric absorption measurements should reflect N_P reproducibly to at least 5 per cent so that as much as a 5 per cent loss of dipoles in the first step might escape detection. From the data of Cook and Dryden[1] on the aggregation process of 50°C in KCL containing $1{\cdot}4\times10^{-4}$ mole fraction of Ca^{2+}, it is estimated from equation (4) assuming $A \simeq 1$ that $E_B \leq 0{\cdot}16$ eV. Cappelletti and DeBenedetti[7] employed the more precise ITC technique and found direct evidence for a trace of second order reaction in $NaCl:Sr^{2+}$ when the precipitation was carried out at a relatively low temperature. The second order segment would be expected during the initial period when the quasi-equilibrium of the first step is being established.

An alternative possibility is that, instead of a quadripole, the dimer is a loosely coupled, linear pair of dipoles which still exhibits a collective moment and which can reorient in an applied field with much the same time constant as the isolated dipole. If this were the case, the formation of dimers could not be followed conveniently through a decrease in dielectric absorption or decrease in polarization. In view of the small binding energy E_B demanded by experiment this alternative linear dimer configuration is perhaps the more likely one. We shall consider the dimer configuration in greater detail in a later section.

From the temperature dependence of the aggregation rate both the activation energy E^* governing the process and the frequency factor can be obtained. The results obtained for a variety of impurities in both NaCl and KCl are summarized in Table 1. The usual interpretation is that the activation energy E^* is identical with the energy of motion of the coupled pair. However, if the two step model applies this can no longer be correct. Inspection of equations (5) and (6) reveals that the apparent third order rate constant results from the product $k_T\,.\,K_D$. Using equations (2) and (5) one obtains in units of $\sec^{-1}$

$$k_3(\text{apparent}) = 4\pi N_LA^{-1}D_P^0r_D \exp[-(E_M-E_B)/kT] \quad (7)$$

where $D_P = D_P^0\exp[E_M/kT]$. Clearly E^* is not identical with E_M but smaller by the amount E_B. Now E_M can be obtained independently

Table 1. *Kinetic parameters for* M^{2+} *aggregation and diffusion*

System	ω_∞(sec^{-1})	E^* (eV)	E_M (eV)
NaCl:Mn^{2+}	8×10^{17}[a]	0·83[a] 0·78 ± 0·05[b] 0·80 ± 0·05[c]	0·95[d]
NaCl:Cd^{2+}	$2·8\times10^{16}$[e]	0·50 ± 0·04[e]	0·92[f]
NaCl:Ca^{2+}	2×10^{17}[b]	0·92[h]	0·96[g]
NaCl:Pb^{2+}	—	0·80[h]	0·98[i]
NaCl:Co^{2+}	—	0·61[j]	—
KCl:Ca^{2+}	—	0·66[k]	—
KCl:Sr^{2+}	4×10^{13}[a]	0·73[a]	—
KCl:Ba^{2+}	8×10^{15}[a]	0·74[a]	—
KCl:Pb^{2+}	—	0·85[l] 0·75[l]	1·18[m]

[a] COOK and DRYDEN, *Proc. phys. Soc.* **80**, 479 (1962).

[b] DRYDEN, *J. phys. Soc. Japan*, Suppl. III **18**, 129 (1963).

[c] SYMMONDS and KEMP, *Br. J. Appl. Phys.* **17**, 607 (1966).

[d] STEWART and REED, *J. chem. Phys.* **43**, 2890 (1965).

[e] CAPPELLETTI and DeBENEDETTI, *Phys. Rev.* **165**, 981 (1968).

[f] ALLEN, IRELAND and FREDERICKS, *J. chem. Phys.* **47**, 3068 (1967).

[g] MURIN, BANASEVICH and GRUSHKO, *Soviet Phys. Solid-St.* **3**, 1762 (1962).

[h] DRYDEN and HARDY, *J. Phys. C.* (*Solid St. Phys.*) [2] **2**, 603 (1969).

[i] KENESHEA and FREDERICKS, *J. chem. Phys.* **41**, 3271 (1964).

[j] CAPPELLETTI, FIESCHI, MARTEGANI and PIROLA, *J. Phys.* **28**, C4-130 (1967).

[k] CHIBA, UEKI and SAKAMOTO, *J. phys. Soc. Japan* **18**, 1092 (1963); **20**, 1284 (1965).

[l] W. C. COLLINS, Private communication.

[m] ALLEN, IRELAND and FREDERICKS, *J. chem. Phys.* **46**, 2000 (1967).

from the diffusion coefficient of the divalent impurity under the high concentration limit, i.e. under conditions favoring impurity-vacancy association. Hence one way in which to test the two-step hypothesis is to compare E^* obtained from aggregation kinetics with E_M determined from diffusion coefficient measurements under appropriate conditions. There are a few published data available for such a comparison and these values of E_M are listed in the last column of Table 1. Stewart and Reed[8] have used EPR methods to assay the Mn^{2+} concentration in the diffusion front of this ion in NaCl under conditions corresponding to the high concentration limit, i.e. the diffusion of associated I–V pairs. They find $E_M = 0·95$ eV for the Mn^{2+}-vacancy complex, a value 0·15 eV larger than the mean value of E^*. Recently, Dryden and Hardy[9] have measured E^* for NaCl:Pb^{2+} this can be compared with the value of E_M reported by Keneshea and Fredericks[10]. For Pb^{2+} doped NaCl the difference $E_M - E^*$ is 0·18 eV. The energy differences for these two impurities are very close to the value estimated above for E_B of the dimer (0·16 eV) on the basis of the absence of a readily detected second order process during the initial stages of aggregation.

The remaining cases do not conform so closely to expectation: For example in NaCl: Ca^{2+} $E_M - E^* = 0·04$ eV which is probably too small to be significant. Nevertheless, $E_M > E^*$ as required by the two-step model. It should be mentioned that Murin *et al.*[11] in the process of determining E_M, found an energy of association between the Ca^{2+} and the cation vacancy about twice that which has been reported by other workers[12]. Consequently, their value of E_M is somewhat suspect and it would be worthwhile to redetermine E_M for this system. Brebec[13] has recently measured the diffusion coefficient of Ca^{2+} in NaCl for infinite dilution and for 600 ppm Ca^{2+}. His results suggest that in the high concentration limit $E_M = 0·87$ eV, a value lower than E^*. However, this value was measured on a polycrystalline specimen and the low value may result from that fact.

In the two remaining cases, namely, NaCl: Cd^{2+} and KCl:Pb^{2+}, the difference $E_M - E^*$ is much greater than expected. Using the ITC technique Cappelletti and DeBenedetti[7] find that Cd^{2+} aggregates at an extraordinarily high rate even at room temperature with an $E^* = 0·50$, a value some 0·4 eV smaller than E_M as determined by Allen *et al.*[14] and nearly 0·2 eV smaller than the energy of reorientation of the complex. It is difficult to attribute so large a disparity to the binding between two dipoles forming a dimer; according to the above discussion such a large E_B

would require that most of the dipoles would combine to form dimers before the quasi-equilibrium could be established with the result that a second order rather than a third order reaction should be observed. Certainly, however, the large difference cannot be consistent with a simple, one-step third order reaction either since the activation energy of the process is much smaller than that required to move coupled dipoles. A possible alternative is that some other mobile species interacts with the Cd^{2+} and renders the dipole incapable of reorienting; however, it is difficult to see how such a process could occur at a rate proportional to the third power of the Cd^{2+}-vacancy concentration. Similar remarks apply to $KCl:Pb^{2+}$. Using the E_M value of Allen *et al.*[15] and the E^* reported by Dryden and Hardy[9] a difference of 0·33 eV is obtained. Recent measurements by Collins[16] lead to an even greater difference. Once again it is difficult to rationalize such a large disparity in terms of the dimer binding energy unless the pre-exponential constant A in equation (4) is many orders of magnitude less than unity.

In spite of the last two exceptions, it is perhaps fair to say that the available diffusion and aggregation data lend rather strong support to the two-step aggregation process. In any event the data do not support a strictly one-step third order trimer formation process.

It is worthwhile saying a few words about the pre-exponential factors ω_∞ listed in Table 1. They cover an unexpectedly large range of values. An estimate of what might be expected from the two-step model proposed here can be made from equation (7):

$$\omega_\infty \equiv 4\pi N_I A^{-1} D_P{}^0 r_D. \tag{8}$$

According to Lidiard[17]

$$D_P = a^2\omega_1\omega_2/3(\omega_1+\omega_2) \tag{9}$$

where a is the cation–anion distance, ω_1, is the jump probability for the vacancy to move around the impurity (Mode 1) and ω_2 is the jump probability for vacancy–impurity interchange (Mode 2). We make the customary assumption that $\omega_1 \gg \omega_2$ with the result that

$$D_P{}^0 = a^2\nu_2 B/3 \tag{10}$$

where $\nu_2 = \omega_2 \exp[E_2/kT]$ is the attempt frequency of the vacancy–impurity interchange and B is associated with the entropy of motion. Taking $A \simeq 1, B \simeq 1$, $\nu_2 \simeq 10^{13}$ sec^{-1} and $r_D \simeq 10^{-7}$ cm, one obtains $\omega_\infty \simeq 10^{14}$ which falls at the low end of the range of values in Table 1. One implication which might be drawn is that $A \ll 1$ or $B \gg 1$ for certain of the cases considered above. However, to account for the factor of 10^3 between this estimate and some of the ω_∞ values listed in Table 1, an enormous increase of ~ 8 entropy units have to result from dimer formation.

3. THE RELATIVE STABILITY OF DIPOLE PAIRS AND TRIPLETS

In this section we shall make a rough estimate of the relative stability of various configurations of simple dipole aggregates. It is not our purpose to attempt a rigorous calculation of these stabilities since such a task is a difficult undertaking even in the case of the dipole itself[18, 19] in that it involves a knowledge of the interionic potential and a self-consistent evaluation of the displacements of the neighboring ions under the influence of the electric polarization and strain field associated with the imperfection. The complexity of the calculational problem is compounded when two or three dipoles are included in the complex. Rather, our aim here is to obtain a relative estimate of the interaction energy holding dipoles together in simple clusters. To do this we will use a simple point-ion approximation which neglects displacements of neighboring ions and accounts for lattice polarization only in terms of the static dielectric constant for the bulk lattice. These are the same assumptions used by Cook and Dryden[1] in their estimate of the association energy for a trimer.

(a) *The trimer*

As noted above Dryden and coworkers [1, 4] postulate that the trimer forms a six-sided complex on a {111} plane of the cation sublattice as shown in Fig. 1(a). The total electrostatic energy of the array is

$$E_T^{(3)} = -\frac{q^2}{\kappa r_0}\left[6+\frac{3}{2}-\frac{6}{\sqrt{3}}\right] = -4{\cdot}036q^2/\kappa r_0 \quad (11)$$

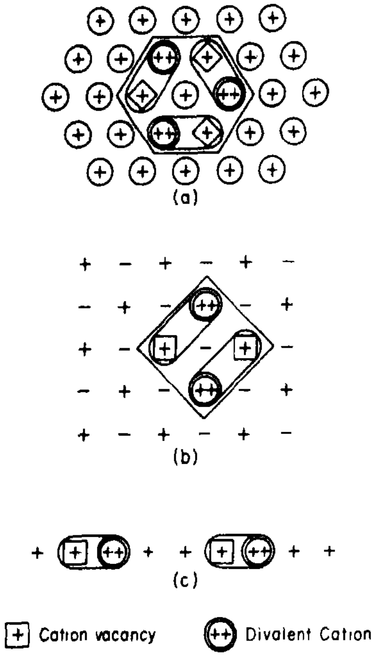

Fig. 1. A schematic representation of various simple dipole clusters. (a) The trimer—a planar hexipole on a {111} plane; (b) the planar quadripole—a dimer and (c) a linear pair of dipoles—a loosely coupled dimer in the ⟨110⟩ direction.

where $-q$ is the electronic charge, κ the static dielectric constant and r_0 is the inter-cation distance. The energy of interaction between the three dipoles is obtained by subtracting the association energy for the dipoles estimated on the same basis:

$$E_I^{(3)} = E_T^{(3)} - 3E_a = 1{\cdot}063e^2/\kappa r_0. \quad (12)$$

For KCl $r_0 = 4{\cdot}44\times 10^{8}$ cm and $\kappa = 4{\cdot}64$ which yield $E_I^{(3)} = 0{\cdot}73$ eV. The corresponding values for NaCl are $3{\cdot}94\times 10^{-8}$ cm, 5·62 and 0·668 eV.

(b) *The planar quadripole form of the dimer*

The most stable form of the dimer is the planar quadripole lying in the {100} plane (Fig. 1(b)). The total electrostatic energy is simply

$$E_T^{(2)} = -\frac{2e^2}{\kappa r_0}\left[2-\frac{1}{\sqrt{2}}\right] = 2{\cdot}586\frac{e^2}{\kappa r_0} \quad (13)$$

and the interaction energy is

$$E_I^{(2)} = E_T^{(2)} - 2E_a = 0{\cdot}586\, e^2/\kappa r_0. \quad (14)$$

The values of E_I for KCl and NaCl are 0·413 and 0·377 eV respectively.

(c) *Linear dipole pairs*

It was indicated earlier that the dipolar pair involved in the two-stage process might be a loosely coupled linear arrangement instead of a dipole. Such a pair aligned in the ⟨110⟩ direction (Fig. 1(c)) has a total electrostatic energy of

$$E_T = -\frac{e^2}{\kappa r_0}\left[\frac{1}{n}+\frac{1}{n+2}-\frac{2}{n+1}+2\right] \quad (15)$$

where n is the number of unit distances (r_0) the pair is separated in the ⟨110⟩ row. The interaction energy is

$$E_I = -\frac{e^2}{\kappa r_0}\left[\frac{1}{n}+\frac{1}{n+2}-\frac{2}{n+1}\right]. \quad (16)$$

The values of E_I for several values of n in KCl and NaCl are tabulated in Table 2.

There are of course other dimer configurations in which the two dimers are not co-linear and whose stabilities are comparable to those listed in Table 2. It is not necessary, however, to use these in the present discussion.

Table 2. The energy of interaction between pairs of dipoles aligned along ⟨110⟩

Separation (n)	E_I for KCl (eV)	E_I for NaCl (eV)
1	0·235	0·214
2	0·059	0·054
3	0·024	0·021

Clearly the above values are not highly reliable. The assumption that the polarization of the lattice can be adequately accounted for on the basis of the static dielectric constant is a crude one. This is obvious from the fact that this assumption gives too high (by a factor of ~ 1·5) a value for the energy of association E_a of the components of the dipole. In addition other factors than purely electrostatic ones are clearly important since Watkins[20] has observed next-nearest-neighbor pairs in NaCl:Mn^{2+}. For this to occur the effect of impurity-ion size coupled with the influence of lattice polarization on the positions of neighboring ions must be strong and such an effect might be expected to carry over to some degree to aggregates of dipoles. However, the rough estimates of the interaction energy given above can probably be relied upon to reflect the relative ranking of the stability of these simple aggregates. We are encouraged in this conclusion by Cook and Dryden's[1] observation that the experimental binding energy of the trimer agreed quite well with the value calculated by the approximation used here.

4. PROBABILITY OF DIMER VS. TRIMER FORMATION

Assuming the above estimates of the interaction energies to be reasonably correct, it is clear that the trimer and planar quadripole have quite comparable stabilities, i.e. the interaction energy per dipole is only 20 per cent smaller for the quadripole than for the hexipole. Therefore, if the aggregation is allowed to proceed in the range of thermal stability of both forms, i.e. under conditions in which the reverse reaction is relatively unimportant compared to the aggregation process, the dimer would be strongly favored because of the kinetics involved. It can be shown from the simple expressions for second and third order kinetics that for dipole concentrations of 10^{-4} mole fraction and capture radii of $\sim 10^{-7}$ cm rates of dimer formation would be initially at least 100 times greater than that of trimers and the disparity would, of course, increase as the aggregation proceeds.

If as appears reasonable from the estimates of the previous section, the stability of these two forms against break-up is comparable, the equilibrium concentration of trimers can be established only late in the reaction and then only by the capture of a dipole by a planar quadripole. This of course is the same as saying that the trimer is formed predominantly by a consecutive reaction rather than by a direct one and this point has already been discussed in connection with the two-step process. The rate of trimer formation will become comparable with the rate of quadripole formation when $r_D N_D \approx r_P N_P$. Since some rearrangement of the quadripole is necessary before the third dipole can be added, one expects the effective value of r_D to be smaller than r_P. This would have the consequence of making quadripole formation the dominant factor in the aggregation reaction virtually insuring that the early stages would obey second order kinetics. There is of course the unlikely possibility that $r_D > r_P$, in which case the reaction would be of mixed order. As pointed out above, the dependence of reaction rate on the third power of the free dipole concentration in a two-step process requires that the dimer be in quasi-equilibrium with the monomer.

Another consequence of the comparable interaction energy per dipole for the quadripole and the hexipole is that the equilibrium concentrations of the two forms are also comparable over most of the temperature range of interest. Simple chemical arguments based upon equilibrium between dipole, dimer and trimer suggest that the energy required to remove a dipole from a trimer is simply $E = E_I^{(3)} - E_I^{(2)} - E_I^{(2)} \simeq 0{\cdot}32\,\text{eV}$. Using this energy and the law of mass action it is readily shown that the equilibrium concentrations of quadripoles and hexipoles are expected to be within a small factor of each other in the range 50°–100°C.

In summary it can be said that the rough estimate of the stabilities of the planar quadripole and the trimer of the preceding section lead one to expect the aggregation process to be characterized by a second order rather than a third order process and that the quadripoles should be nearly as important as the trimers as resultant products of the aggregation.

5. CONSTRAINTS UPON THE FORMATION OF THE QUADRIPOLES

The point we consider in this section is the actual mechanism by which a planar quadripole must form. In moving through the lattice a dipole executes two modes of motion: Mode 1, the motion of the vacancy around the divalent cation, and Mode 2, the interchange of the divalent cation with the vacancy. In order for one dipole to approach another along a ⟨110⟩ direction for example, it must alternately reverse its orientation. If the dipole being approached were held fixed in position and orientation, the mutual interaction would alternate between attractive and repulsive as the dipoles draw together. Obviously, the dipole being approached will not necessarily keep a fixed orientation since it too has some freedom to rotate thereby reducing the repulsive interaction. However, for each successive step of the dipole toward the other there is an irreducible repulsive interaction. To see this we must examine the situation in deeper detail.

Consider two dipoles located near each other on a ⟨110⟩ cation row as shown in Fig. 1(c). They may approach each other either by (a) the dipole on the left inverting by impurity–vacancy interchange (Mode 2) followed by the inversion of the left-hand dipole by rotation (Mode 1) or (b) Mode 1 rotation of the left-hand dipole followed by Mode 2 inversion of the right-hand dipole. The activation energy for Mode 2 (E_2) is expected to be larger than for Mode 1 except perhaps for very small divalent cations[21] so that a given temperature $\omega_1 \gg \omega_2$. In addition, the attractive interaction of the stable arrangement of dipoles opposes both the inversion and the rotation. However, once the impurity reaches the saddle point the dipole moment disappears and rotation of the left-hand dipole can occur freely. Hence to a reasonable approximation one expects the effective activation energy for (a) to be

$$E_{(a)} = E_2 + E_I(n) = E_2 + \frac{e^2}{\kappa r_0} \times \left[\frac{1}{n} + \frac{1}{n+2} - \frac{2}{n+1}\right]. \quad (17)$$

One can readily see, at least in principle, that the activation energy for sequence (b) should be the same since the activation energy opposing the inversion of the right-hand dipole becomes that for the isolated dipole just when the left-hand dipole has rotated to a position for which the attractive interaction is reduced to zero. However, the probability that the rotating dipole will be found in this higher energy state is

$$P_0 = W_0 \exp - [E_I(n)/kT] \quad (18)$$

where W_0 is the statistical weight of the state representing the dipole in the orientation producing no energy of interaction relative to the most stable orientation shown in Fig. 1(c). Since the rate of inversion of the right-hand dipole is the product of the jump probability of the dipole when unopposed by the attractive field of its neighbor and the probability that it will be unopposed, the sequence (b) evidently yields the same activation energy as sequence (a). In real crystals only certain rotational orientations are allowed and these will not necessarily decrease the energy of interaction to zero. However, it can be seen with (a) and (b) that the energy opposing the mutual approach of a pair of dipoles is equal to $-|E_I(n)|$ for the starting configuration assuming of course that mutual polarization between the dipoles does not change the value of E_2.

If the above considerations yield a reasonable approximation, one expects the effective activation energy governing the initial approach of two dipoles to increase with decreasing n as shown schematically in Fig. 2. The amounts of the increments should be reflected in Table 1 for $n = 3$ and $n = 2$. Even more pertinent to the present subject is what occurs when two dipoles attempt to draw together to form a planar quadripole. In Fig. 3 is shown a possible sequence of events which might lead to the formation of a quadripole. Configuration 1 is an obvious candidate for the precursor of the quadripole since the essential requirement is to place a vacancy in a spot which, upon interchange with its impurity ion, will place the two impurity ions on adjacent ⟨100⟩ positions. It can be seen that Configuration 1 does this in the two ensuing steps 2 and 3. A possible abortive rearrangement is shown by Configuration 2′ in which one of the dipoles has spread to a next-nearest-neighbor dipole. Clearly Configuration 2 is unstable and probably is by-passed by the rotation of the left-hand dipole clockwise by 90° as the right-hand dipole goes through the inversion saddle point. The final configuration is then simply achieved by the clockwise rotation of the newly inverted dipole. According to the discussion just above the increase in activation energy for the inversion is just the attractive energy in Configuration 1. Hence the electrostatic constraint opposing quadripole formation appears to be ~0·1 eV; this would decrease the rate of formation by a factor of ~20 over the rate expected in the absence of such a constraint at 100°C. This impedance would prolong the duration of the loosely-bound precursor thereby favoring the capture of a third dipole to form a trimer.

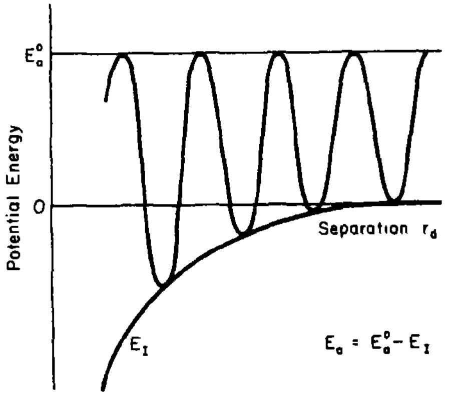

Fig. 2. The energy of interaction between a pair of dipoles as a function of the energy of separation (schematic).

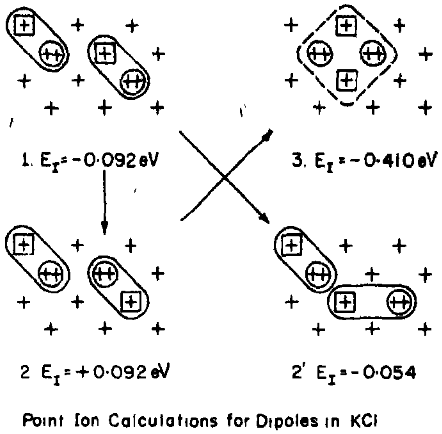
1. $E_I = -0{\cdot}092$ eV
3. $E_I = -0{\cdot}410$ eV
2 $E_I = +0{\cdot}092$ eV
2′ $E_I = -0{\cdot}054$
Point Ion Calculations for Dipoles in KCl

Fig. 3. The sequence of events involved in the formation of a planar quadripole from a loosely coupled precursor. Configuration 1 is one of the necessary starting positions since upon inversion of one of the dipoles a pair of impurity ions is placed in adjacent ⟨100⟩ positions. The process represented by the arrow 2′ is an abortive one in which one of the dipoles transforms to a next-nearest-neighbor configuration.

6. SUMMARY

In this paper we have attempted to account for the rather puzzling evidence that aggregation of I–V dipoles occurs via a third order reaction. It is argued that trimer formation can occur with much greater probability by a two-step process, in which a loosely-coupled pair of dipoles is the intermediate product, than by a three body encounter. The conclusion that the precursor is a loosely-coupled pair, which may itself have a net dipole moment rather than the more stable planar quadripole, arises from the requirement that the precursor pairs must be in quasi-equilibrium with the dipoles before the rate of disappearance of dipoles becomes proportional to the cube of the dipole concentration; this condition is attained earlier the smaller the binding energy of the pair. An important consequence of the two-step model is that the activation energy of aggregation E^* is smaller than the motion energy E_M by the amount of the binding energy of the precursor pair. Examination of existing data for aggregation and for diffusion of dipoles involving a variety of divalent cations in NaCl and KCl reveals that in every case $E_M > E^*$, though in some cases the difference is larger than expected according to the requirement that the precursor pair be loosely-bound.

Consideration of the relative stability of the planar quadripole and the hexipole trimer per dipole suggests that it is comparable in the two forms but slightly larger for the trimer. This also leads to the conclusion that formation of the quadripole should dominate an appreciable part of the aggregation reaction giving rise to a readily detected second order reaction. Therefore, the important question is: Why does the planar quadripole not form? Evidently the determining factor is a kinetic one in that as two dipoles approach each other the mode of motion produces a repulsive interaction during each successive step which is approximately equal to the attractive interaction at the beginning of the act of approach. The amount of this repulsive interaction opposing quadripole formation from the stable pair configuration that immediately precedes it is ~0·1 eV. This is sufficient appreciably to inhibit quadripole formation and strongly favors the trimer formation.

It should be pointed out that rather than being an effect peculiar to the alkali halides, inhibition of certain aggregation products by electrostatic constraints is expected to be quite general. It should occur in ionic crystals whenever transport of impurity is accomplished through the motion of a coupled entity with a large dipole moment which is confined to move on a single sub-lattice such as considered here. If, in addition, the dipole bears a net charge as would be the case for M^{3+}-cation vacancy dipoles in the alkaline earth oxides, the constraints would be large indeed making even the formation of the linear dimer difficult. It will be interesting to see whether evidence for such inhibiting effects can be found in other materials. One possible exception already in the literature should be noted, namely, the aggregation of O^{2-}-anion vacancy dipoles in alkali halides studied by Gümmer [22] in which loss of dipoles occurs via a second order reaction. The difference may well be associated with the different chemical forces involved which are reflected by the very large energy of association of the O^{2-}-vacancy dimer in KCl (0·85 eV).

Acknowledgements—It is a pleasure to acknowledge helpful discussion with W. A. Sibley, L. Slifkin, J. S. Cook, W. C. Mallard, and J. P. Stott.

7. REFERENCES

1. COOK J. S. and DRYDEN J. S., *Proc. phys. Soc.* **80**, 479 (1962).
2. DRYDEN J. S., *J. phys. Soc. Japan*, Suppl. III **18**, 129 (1965).
3. CHIBA Y., UEKI K. and SAKAMOTO M., *J. phys. Soc. Japan* **18**, 1092 (1963); CHIBA Y. and SAKAMOTO M., *J. phys. Soc. Japan* **20**, 1284 (1965).
4. SYMMONDS H. F. and KEMP R. C., *Br. J. appl. Phys.* **17**, 607 (1966).
5. ALZETTA G., CRISPA P. R. and SANTUCCI S., *Nuovo Cim.* **42B**, 100 (1966).
6. SRIVASTAVA K., *Nuovo Cim.* **47B**, 251 (1967).
7. CAPPELLETTI R. and DeBENEDETTI E., *Phys. Rev.* **165**, 981 (1968).
8. STEWART W. H. and REED C. A., *J. chem. Phys.* **43**, 2890 (1965).
9. DRYDEN J. S. and HARDY G. G., *J. phys. C (Solid St. Phys.)* **2**, 603 (1969).
10. KENESHEA F. J. and FREDERICKS W. J., *J. chem. Phys.* **41**, 3271 (1964).

11. MURIN A. N., BANASEVICH S. N. and GRUSHKO Yu. S., *Soviet Phys. Solid-St.* **3**, 1762 (1962).
12. DRYFUS R. W. and NOWICK A. S., *Phys. Rev.* **126**, 1367 (1962).
13. BREBEC G., Private communication.
14. ALLEN C. A., IRELAND D. T. and FREDERICKS W. J., *J. chem. Phys.* **47**, 3068 (1967).
15. ALLEN C. A., IRELAND D. T. and FREDERICKS W. J., *J. chem. Phys.* **46**, 2000 (1967).
16. COLLINS W. C., Private communication.
17. LIDIARD A. B., *Phil. Mag.* **46**, 1218 (1955).
18. BASSANI F. and FUMI F. G., *Nuovo Cim.* **11**, 274 (1954).
19. TOSE M. P. and AIROLDI G., *Nuovo Cim.* **8**, 584 (1958).
20. WATKINS G. D., *Phys. Rev.* **113**, 79 (1959).
21. BUCCI C., *Phys. Rev.* **164**, 1200 (1967).
22. GÜMMER G., *Z. Phys.* **215**, 256 (1968).

J. Phys. Chem. Solids Pergamon Press 1970. Vol. 31, pp. 411–413. Printed in Great Britain.

TECHNICAL NOTE

Piezoemission of gallium antimonide

(*Received* 31 *March* 1969)

PHOTOLUMINESCENCE in GaSb is studied at several temperatures. The splitting of the free exciton line as a function of calibrated uniaxial compressive stress is measured at low temperature. The deformation-potential constants for the valence band are determined: $b = -2$ eV and $d = -4{\cdot}6$ eV.

1. INTRODUCTION

In recent years the infrared optical properties of Gallium Antimonide have been extensively studied by Fan and coworkers. Three absorption peaks (α, β, γ) and a low energy tail have been observed[1] at 4°K in the vicinity of the intrinsic absorption edge of unintentionally doped GaSb (the samples were p-type with approximately 10^{17} holes/cm^3 at room temperature). From magneto-optical studies it has been possible to conclude that the α peak is due to the formation of free excitons and the β and γ ones to the formation of bound excitons. Three emission lines due to the annihilation of the γ exciton and the recombination on two acceptor levels have been observed at 4°K by Johnson *et al.*[2]. The annihilation of the α and β excitons was not observed.

We have studied the emission spectrum at several temperatures and the stress dependence of the free exciton line at 35°K of unintentionally doped samples of GaSb.

2. EXPERIMENTAL RESULTS

The experiments were performed on p-type samples ($p \simeq 10^{17}/\text{cm}^3$) purchased from Cominco Ltd. The stress apparatus and the arrangement for the photoluminescent measurement have already been described in a previous publication[3]. The polarized light study was made with a H-R Kodak polaroid.

1. *Emission*

The observed spectra at 4°K, 20°K and 70°K are shown in Fig. 1. The I_1 line at 778 meV is due to the recombination on the acceptor level which is characteristic of the undoped p-type samples. The line at 796 meV corresponds to the γ peak seen in absorption by Fan. The lines situated at 803 meV and 810 meV at 20°K were not seen previously in the emission experiments of Fan because they were performed at 4°K. The position of the first line (803 meV) is at slightly lower energy than that (805 meV) of the absorption peak β measured by Johnson and Fan. The position of the other line (810 meV) is at the same photon energy as that of the corresponding absorption peak α observed by Johnson and Fan.

Whereas the intensity of the acceptor recombination line varied linearly with the rate of excitation, the intensity of the highest photon energy lines varied quadratically. The linear variation of the intensity of I_1 line indicates that the concentration of free electrons varies linearly with the rate of excitation and is determined essentially by non-radiative recombination processes. The quadratic variation of the intensity of the two highest energy lines is expected for exciton creation if the concentration of free holes, as the concentration of free electrons, varies linearly with the rate of excitation.

At a temperature of about 20°K, the effect of a strong magnetic field on the emission spectrum was studied. Shifts of the two highest energy lines were observed. Up to 20 kG these shifts varied quadratically in the field amplitude; above 20 kG they varied linearly. This behaviour is expected for free and bound excitons. At 50 kG a splitting into two components was observed for the highest energy line. This splitting is attributed to the two spin levels of the electron. We find $|g| \simeq 6$ which is in good agreement with effective mass theory and experimental results of Johnson and Fan on the α absorption peak [1].

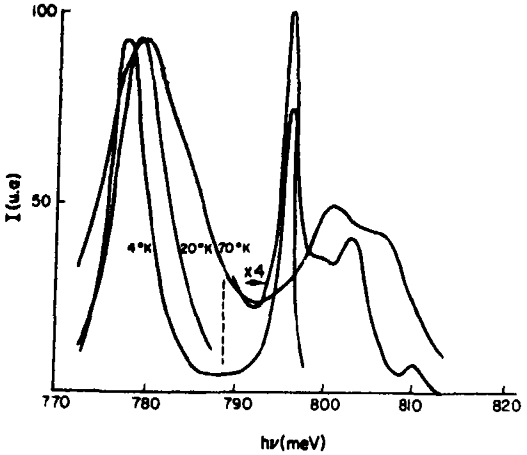

Fig. 1. Emission spectrum of GaSb at low injection level for $T = 4°K$. 20 and 70°K.

2. *Piezoemission*

The change in the energy of free exciton levels under the action of a uniaxial stress is very complicated when taking into account polariton effect, *j-j* electron-hole coupling, variation of the ground state binding energy E_{ex} and longitudinal or transverse polarization. But these effects can be neglected when the stress induced splitting of the valence bands is much greater than E_{ex} so that the splitting of the free exciton ground state is very nearly equal to the splitting of the valence bands.

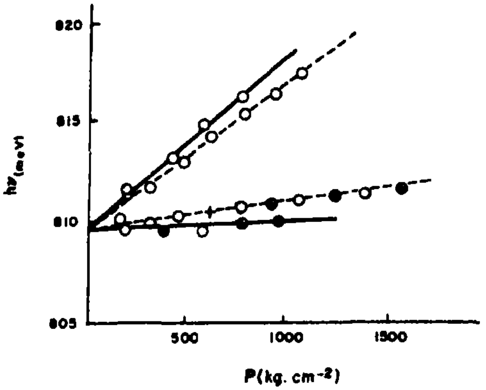

Fig. 2. Position of the maximum of the free exciton emission line vs. the intensity of the applied pressure. ○, $E \perp \sigma$; +, $E // \sigma$; —— $\sigma // (100)$; --- $\sigma // (111)$.

The free exciton positions as a function of stress in the (100) and (111) directions are given in Fig. 2.* As it is expected when the spin-orbit splitting is large compared with the stress induced splitting of the valence bands, the later splitting is linear in the stress. The change ΔE in the mean position (center of gravity) of the two components is roughtly the same for the same intensity of stress ΔP in the (100) and (111) directions. We obtain:

$$\frac{\Delta E}{\Delta P} = 4{\cdot}6 \times 10^{-6}\,\text{eV kg}^{-1}\,\text{cm}^2.$$

In a cubic crystal the value of the band gap variation ΔE with an hydrostatic pressure ΔP_H is three times larger than the value obtained with a uniaxial stress of same intensity:

$$\frac{\Delta E}{\Delta P_H} = 14 \times 10^{-6}\,\text{eV kg}^{-1}\,.\,\text{cm}^2.$$

This value is slightly smaller than the value directly found by Kosiki[4] ($14{\cdot}5 \times 10^{-6}$ eV kg^{-1} . cm^2) for an undoped crystal.

The deformation potentials are calculated using the values of the elastic constants measured by McSkimin *et al.*[5]. The signs are determined by the selection rules in polarized light as in the case of indium antimonide[3]. The lowest energy component is allowed for light polarized both parallel and perpendicular to the stress axis. The highest energy component is only allowed for light polarized perpendicular to the stress axis. We obtain results which are analogous to the case of InSb: the band ($Mj = \pm\frac{1}{2}$) 'goes up' and the band ($Mj = \pm\frac{3}{2}$) 'goes down' for compressive stress. The deformation potentials have also the same order of magnitude. We find: $b = -2$ eV and $d = -4{\cdot}6$ eV.

---

*Unlike our experiments on InSb[3] we can observe the energy component of the line and directly measure the separation of the levels at low stress because the exciton lines in GaSb are sharper than the band to band ones in InSb.

One expects from symmetry that the ratio of the two electric-dipole transition probabilities corresponding to the band ($Mj = \pm\frac{1}{2}$) for parallel and perpendicular polarized light should be equal to 4. The polarization ratio of the lowest energy component is less than 4 because of different light reabsorption in the sample for the two polarizations.*

3. CONCLUSION

By studying the emission spectrum of GaSb as a function of a calibrated uniaxial stress we have measured the deformation potentials of the valence bands. These potentials have approximatively the same values for GaSb as for GaAs[6], GaP[7], InSb[3], Si[8], Ge[8], CdTe[9]: $b \simeq -2$ eV and $\simeq -5$ eV. Furthermore the stress-induced splittings are nearly isotropic. However, in GaSb the splitting in the (100) direction is about 20 per cent larger than in the (111) direction, as in InSb.

C. BENOIT à la GUILLAUME
P. LAVALLARD

Groupe de Physique de l'Ecole Normal Supérieure,
Laboratoire associé au C.N.R.S.,
Faculté des Sciences,
9, quai Saint-Bernard,
Paris 5^e, France

REFERENCES

1. JOHNSON E. J. and FAN H. Y., *Phys. Rev.* **139A**, 1991 (1965).
2. JOHNSON E. J., FILINSKI I. and FAN H. Y., *Proc. Int. Conf. Physics of Semiconductors*, Exeter, p. 375 (1962).
3. BENOIT à la GUILLAUME C and LAVALLARD P., *Proc. Int. Conf. Physics of Semiconductors*, Kyoto, p. 288 (1966).
4. KOSIKI B. B., Ph.D. Thesis, Harvard University.
5. McSKIMIN H. J., BOND W. L., PEARSON G. L. and HROSTOWSKI H. J., *Bull. Am. phys. Soc.* 1, 111 (1956).
6. BHARGAVA R. N. and NATHAN M. I., *Phys. Rev.* **161**, 695 (1967).
7. BASLEV I., *Proc. Int. Conf. Physics of Semiconductors*, Kyoto, p. 101 (1966).
8. BASLEV I., *Phys. Rev.* **143**, 636 (1965).
9. THOMAS D. G., *J. appl. Phys.* **32**, Suppl. 2298 (1961).

---

*It seems that the difference of reabsorption for the two polarizations is responsible for the difference of the position of the maximum of the lines observed in InSb at high pressure [3].

J. Phys. Chem. Solids Pergamon Press 1970. Vol. 31, pp. 415–422. Printed in Great Britain.

RAMAN SPECTRA OF VITREOUS SILICA, GERMANIA AND SODIUM SILICATE GLASSES*

MARVIN HASS
U.S. Naval Research Laboratory, Washington, D. C. 20390, U.S.A.

(*Received* 2 *July* 1969; *in revised form* 14 *August* 1969)

Abstract—The polarized Raman spectra of vitreous silica, germania, and sodium silicate glasses have been obtained in the frequency shift region extending from 10 to 1300 cm^{-1}. The observed spectra of silica and germania have been compared with recent calculations of the vibration spectrum and with the i.r. spectrum. The Stokes–Raman spectrum at low temperatures of vitreous silica decreases markedly in intensity at low frequencies (less than 100 cm^{-1}), but only slightly at higher frequencies (greater than 300 cm^{-1}). The temperature dependence of the Stokes–Raman spectrum is consistent with first-order processes.

1. INTRODUCTION

IN RECENT years polarized Raman spectra obtained with laser excitation sources have proven to be a valuable means of obtaining information about the vibrational spectra of solids. Such spectra provide a great improvement in the low frequency region in which there have been few studies reported for silicate glasses. Furthermore, new calculations of the vibration spectra of simple glasses have recently appeared and these can be compared to the observed Raman spectra. In addition, an examination of the spectrum as a function of temperature would be expected to be quite useful as there are a number of anomalous thermal properties which might be explained by the presence of low frequency modes.

The Raman spectrum of fused silica has been studied by a number of investigators [1–5] of which that due to Flubacher *et al.* [1] is noteworthy for its quality using arc source excitation. A broad low frequency band found earlier by Krishnan [2] was further studied in greater detail in the very low frequency region down to 8 cm^{-1}. A few spectra for GeO_2 have been reported [6] at higher frequencies, but no low frequency data has been given. Raman spectra of sodium silicate glasses have been reported by Wilmot [7], but the low frequency region has not been studied due to experimental difficulties. More data is generally available for the i.r. spectrum of glasses at the present time [8–14]. A useful review of some of the older i.r. and Raman data up to about 1959 has been given by Simon [8].

The calculation of the density of vibrational modes can be carried out by a number of methods. Most of the work in the past has tended to treat the vibrations of SiO_4 structural units or larger units of this type [15, 16]. During the past few years a different approach has been adopted by Bell *et al.* [17]. This method involves considerable computation, but is capable of providing the density-of-states of the vibration spectrum of a realistic model of a vitreous material instead of the eigenfrequencies of a smaller number of units. The starting point of such calculations is the construction of a random model of several hundred atoms of a vitreous material. Such models can be constructed representing vitreous silica based upon certain rules. Radial distribution functions can be calculated with the aid of such models and give fairly good agreement with the observed X-ray and neutron diffraction measurements. While good

---

*Work supported by Advanced Research Projects Agency.

agreement does not necessarily imply that a random model is correct in all details, it does provide a good indication that such an approach is not too different from the actual situation. The next phase consists of a computer calculation of the vibration spectrum of such a system assuming central and non-central nearest neighbor interactions. Since the system consists of several hundred atoms, there are a sufficient number of modes to enable a histogram of the density-of-states to be obtained. Calculations of this nature have greatly increased our understanding of nature of vibrations in vitreous materials and so it is of considerable interest to compare the calculated and observed results. Infrared and Raman spectroscopy currently provide a relatively easy experimental means of determining the vibrational modes of such systems. In order to make a good comparison it is necessary to include the interaction of the electromagnetic radiation with the vibrations, as some modes are much more strongly coupled than others. This has not yet been carried out. To a first approximation it is possible to compare the observed Raman spectrum with the calculated vibration spectrum although the two are not the same.

2. EXPERIMENTAL

The Raman spectra reported here were observed with excitation at 488 nm at an average power level of about 250 mW. A 90° geometry was employed with the incident electric vector perpendicular to the scattering plane. The scattered radiation was analysed with a Spex Model 1400 spectrometer having a 1200 groove/mm grating operating in second order. A polarization scrambler was inserted before the entrance slit to avoid grating polarization effects. The detection system consisted of a cooled ITT FW 130 phototube operating in a photon counting mode. The slit width did not exceed 3 cm^{-1} which was quite adequate for the relatively broad spectra noted here. Some difficulty was encountered due to grating ghosts in the very low frequency region in samples which were not perfectly clear. Usually such effects could be detected by their characteristic appearance.

Commercially available samples of vitreous silica of the following types were employed: Corning 7940, Infrasil, and Suprasil. The vitreous germania and sodium silicate glasses were prepared by Mr. R. J. Ginther of this laboratory.

Low temperature spectra were obtained with the sample mounted on a cold finger in the dewar. An estimate of the sample temperature could be obtained by measuring the ratio of the Stokes to anti-Stokes intensity at around 50 cm^{-1}. This indicated a sample temperature of about 12°K.

3. RESULTS

The Raman spectrum of vitreous silica at room, liquid nitrogen, and liquid helium temperatures is shown in Fig. 1. It can be seen that the low frequency Stokes–Raman spectrum is markedly temperature dependent and this will be discussed later. In Fig. 2 and Fig. 3, the room temperature Raman spectrum of vitreous silica and vitreous germania is compared to calculations of the density of states and with the i.r. spectrum reported previously.

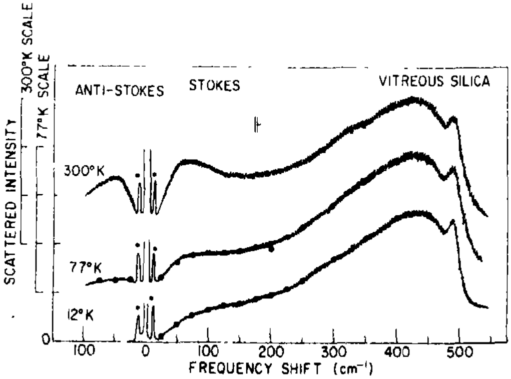

Fig. 1. Raman spectrum of vitreous silica at various temperatures. The dots represent the low temperature spectrum calculated from the room temperature spectrum assuming first-order processes. The sharp bands at ± 13 cm^{-1} marked by (*) are due to grating ghosts.

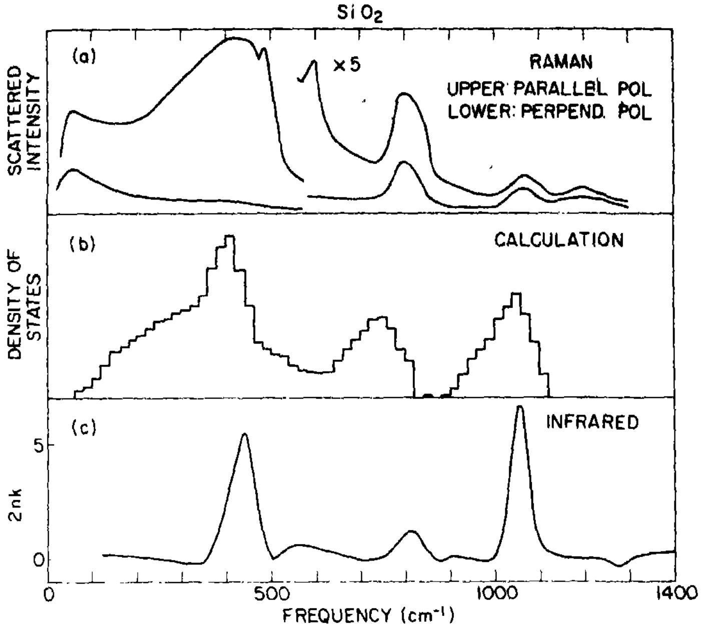

Fig. 2. Comparison of observed Raman spectrum, observed i.r. absorption [12], and calculated density-of-states [17] for vitreous silica.

The maximum scattered intensity for germania is about ten times that of silica. In Fig. 4, a comparison of the room temperature Raman spectra of vitreous silica and sodium silicate glasses of various compositions are given. Here these spectra obtained using a laser

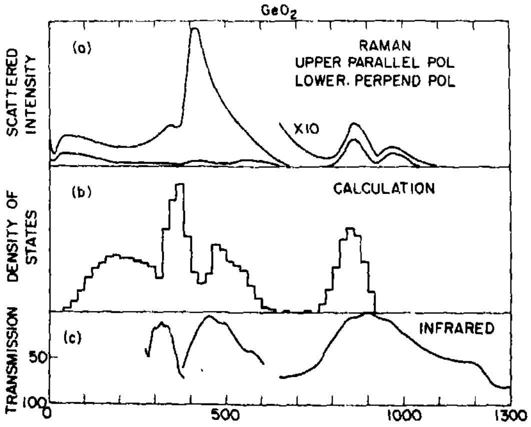

Fig. 3. Comparison of observed Raman spectrum, observed i.r. transmission [6, 14] and calculated density-of-states [17] for vitreous germania.

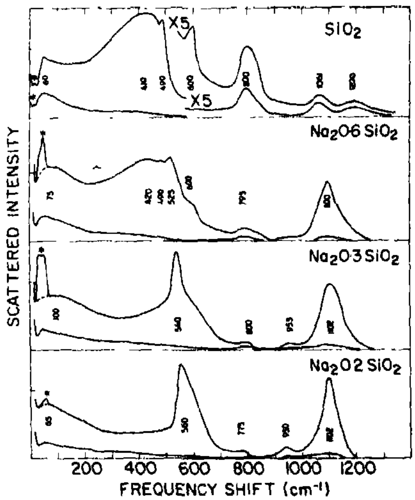

Fig. 4. Polarized Raman spectra of vitreous silica and sodium silicate glasses of various compositions. Upper trace for each material: polarization with electric vector parallel to that of exciting radiation. Lower trace for each material: *polarization with electric vector perpendicular* to that of exciting radiation. The bands indicated by (*) at very low frequencies are believed to be due to grating ghosts and are not characteristic of the sample. The dotted lines in these low frequency regions are more characteristic of the true sample scattering.

excitation source provide superior results in the low frequency region and perhaps show some finer structure elsewhere.

Although three different types of vitreous silica were employed, no differences were noted in the frequency range studied, except possibly for the appearance of a very small band near 975 cm^{-1} in Suprasil. It is well known that the transmission of these glasses varies considerably in the near i.r. at 2·7 μm due to OH impurities and in the region of 180 nm due to metallic impurities. Apparently, these impurities are not present in sufficient concentration to affect the Raman spectrum.

4. DISCUSSION

The interpretation and discussion of these Raman spectra will be divided into the following three parts: (1) the temperature dependence of the Raman spectrum of vitreous silica; (2) Raman spectra of vitreous silica and germania and relation to the i.r. spectra; and (3) spectra of sodium silicate glasses.

1. *The temperature dependence of the spectrum of vitreous silica*

It can be seen from Fig. 1 that the Raman spectrum of vitreous silica is highly temperature dependent in the low frequency region below 100 cm^{-1}, but is only slightly temperature dependent in the higher frequency region above 300 cm^{-1}. The question arises as to whether this temperature dependence stems from some unusual effect or whether it stems from a more straightforward origin. Since the thermal properties of glasses at low temperatures display some anomalies in the heat capacity and thermal conductivity[18], the presence of additional low frequency modes in addition to those predicted from the elastic properties is not unexpected. The occurrence of the broad depolarized low frequency scattering maximum in the Raman spectrum given by Flubacher *et al.* was considered evidence that such modes might indeed exist[1].

A simple approach that has been taken here is to analyse the temperature dependence of these modes in the simplest way. This is to make the *a priori* assumption that they are due to first-order processes. The Stokes-Raman intensity associated with first-order processes is proportional to $1+n_0$, where $n_0 = 1/[\exp(\hbar\omega_0/kT)-1]$ is the Bose population factor[19]. For frequencies of 300 cm^{-1} and above which are typical vibration frequencies, the value of $1+n_0$ does not exceed 1·3 at room temperature. Consequently, the first-order vibrational spectra which are usually encountered have a slight temperature dependence. At 50 cm^{-1} and at room temperature the value of $1+n_0$ is 4·68, giving a substantial temperature dependence. The more common situation used to explain large temperature dependent bands at low frequencies involves second and higher order difference processes. Such processes are more sharply temperature dependent.

In order to see if the data is consistent with first-order processes, the low temperature spectrum has been calculated from the room temperature spectrum as is shown by the dots in Fig. 1. Here the high temperature portions were matched in order to account for a slight change in sample position as the dewar is cooled. The agreement between the observed results and those calculated for first-order processes is quite good.

It might be pointed out that the same single excitation process appears to hold for the i.r. spectrum at room and low temperature [20–22].

This result follows from the single-excitation spectrum for a set of coupled harmonic oscillators. The i.r. vibrational absorption for such a situation is given by $(1+n_0)-n_0$ where $(1+n_0)$ is the probability of absorption and n_0 is the probability of emission[23].

It can be seen from Fig. 1 that the scattered spectrum at low temperatures which is more characteristic of the vibration spectrum of the solid no longer contains a scattering maximum near 50 cm^{-1}. This also is true of the i.r. spectrum at all temperatures. The i.r.

absorption coefficient appears to vary as the square of the frequency between 30 and 100 cm^{-1}, but falls below the frequency squared curve at lower frequencies[20]. The Raman scattering appears to be roughly linear in this frequency range. The origin of the low frequency Raman and i.r. spectrum in vitreous silica is of considerable importance in relation to the anomalous thermal properties. The following possible explanations can be put forward:

(1) The behavior is associated with a random structure and could be explained by calculations carried out using a model. The existing calculations have been based upon a model involving only several hundred atoms. This is not sufficiently large to obtain a low frequency vibration spectrum. In principle, calculations of this type with larger models could be carried out.

(2) The behavior is associated with defects occuring in the random silicate structure. This can be regarded as the breaking of an Si–O linkage. Evidence as to the possibility of a large number (of the order of 1 per cent) of such defects is suggested by considering the number of Schottky defects at the melting temperature[24].

(3) The behavior is associated with foreign impurity centers such as those due to hydrogen, hydroxyl, or metal ions.

While a definitive answer to these possibilities can not be given, some comments can be made. In the first place, the experimental data for the low frequency Raman spectrum appears to be independent of the type of sample. It is known that the concentration of hydroxyl groups in various samples differs as this is readily observed at the stretching frequency in the i.r. Infrasil is more transparent in this spectral region, and thus has a lower hydroxyl concentration. Suprasil is more highly transparent in the u.v. and is believed to be particularly low in metallic impurities. While measurements on these samples have not been carried out in the i.r., there does not seem to be too great a disparity of absorption coefficients among the various investigators and the existing variation might be attributed to difficulties in measurement of unwanted radiation. Consequently, it is felt that foreign impurities do not contribute to the origin of the low frequency Raman or i.r. spectrum. As to whether defects in the random structure or whether the behavior is characteristic of the random structure itself is still an open question.

In view of certain anomalous thermal properties, the presence or absence of low frequency modes presents a number of interesting questions. An estimate of the number of low frequency modes which might account for the anomalous heat capacity has been given[1]. It has been estimated that modes corresponding to about one per cent of the total number and located at low frequencies ($\approx 40\,cm^{-1}$) might account for the heat capacity using a simple model. If most of these modes were located at certain discrete frequencies, they might be observable in the i.r. and Raman spectrum. If broadened they might be difficult to observe. The presence of the low frequency scattering maximum at room temperature has been suggested as evidence for the presence of such modes[1]. The low temperature data presented here indicates much of this scattering is due to a temperature enhancement and not necessarily representative of the true vibration spectrum. It might be noted that this low frequency scattering maximum is more prominent in sodium silicate glasses and that a corresponding increase in the far i.r. absorption in the same frequency region is noted[11, 20].

It has been pointed out that the i.r. reflection spectrum of vitreous silica is temperature dependent in the high temperature region [25]. It is believed that changes in the angle of neighboring silicon–oxygen tetrahedra are important in accounting for these results. A corresponding behavior might be expected in the Raman spectrum in addition to the usual temperature dependent effects associated with first-order processes.

2. *Raman spectra of vitreous silica and germania and relation to the i.r. spectrum and theory*

In order to provide a comparison among the Raman spectrum, i.r. spectrum, and calculations of the vibration spectra, the data has been assembled on a common scale. The results for vitreous silica are shown in Fig. 2 and for vitreous germania in Fig. 3.

The calculated spectra were taken from Fig. 1(a) and 3(a) of the article by Bell *et al.* [17]. The i.r. curve is the imaginary part of the complex dielectric constant ($2nk$) obtained by Miler from reflection spectra[12]. Infrared data for vitreous germania is less common and only the transmission spectra of powders have been reported. The lowest frequency absorption band was taken from Cheremisinov [6] and the two higher frequency bands from Lippincott *et al.*[14].

In general there is fairly good agreement between the positions of the calculated and experimental spectra. Since the input for the calculations involves an estimate of the magnitude of the force constants, some discrepancy with the observed results might be expected. The various bands are tabulated in Table 1.

The highest frequency maximum in the calculated SiO_2 spectrum has been associated with a 'bond-stretching' vibration which has been described by Bell *et al.* as one in which the bridging oxygens move in opposite directions to their Si neighbors, and roughly parallel to the Si–Si lines. Such a motion might be expected to the strongly i.r. active and weakly Raman active. This can be associated with the strong i.r. band at 1061 cm^{-1}. There is a weak depolarized Raman band at this frequency. The small i.r. shoulder and weak Raman band at a slightly higher frequency around 1200 cm^{-1} has not appeared in the calculations. The next stronger lower frequency band near 730 cm^{-1} has been associated with a 'bond-bending' type of motion in which the oxygens move approximately at right angles to the Si–Si lines and in the Si–O–Si planes. This probably corresponds to the Raman band at 800 cm^{-1} and the i.r. band at 811 cm^{-1}. At lower frequencies the bands are not well defined as the modes are no longer localized. The maximum in the spectrum at 410 cm^{-1} is associated with a 'bond-rocking' motion in which the atoms move roughly perpendicular to the Si–O–Si planes. There is a broad strongly polarized Raman band at 410 cm^{-1} and a strong i.r. band at 443 cm^{-1}. The presence of a strong Raman band in GeO_2 at about the same frequency suggests that this band can be largely attributed to motion of the oxygens.

The situation for vitreous germania is not quite as clear. Inspection of Fig. 3 reveals a rather good resemblence between the Raman spectrum and the calculated vibration spectrum in that there is relatively sharp band calculated at 370 cm^{-1} which seems to correspond to a prominent band in the Raman spectrum centered at 412 cm^{-1}. On either side of this band there appears to be sidebands and in both the calculated and observed spectra. One thing which seems a little out of line is that no corresponding i.r. absorption band can be found at 410 cm^{-1}. Consequently it is not known whether to assign the bond-rocking mode to the peak of the i.r. absorption or to the peak of the Raman scattering.

Finally, there is the question of a comparison of the i.r. and Raman spectrum with that obtained from inelastic neutron scattering data[26]. There does not seem to be any relation between the inelastic neutron scattering maxima and those observed by optical methods. The reason for this is not known.

In comparing the experimental spectrum with the calculations, it must be realized that interaction with radiation has not been taken into account. This is not apt to be as serious for the Raman spectrum as the selection rules are not as stringent, especially at lower frequencies. In addition in carrying out calculations there are certain assumptions regarding the nature of the forces and magnitude of the force constants. Such assumptions are more apt to hold for GeO_2 than SiO_2 as

Table 1. *Classification of vibrational modes in vitreous silica and germania*

Silica			Germania			Tentative descriptive assignment
Calc.[17] (cm^{-1})	Raman (cm^{-1})	I.R.[12] (cm^{-1})	Calc.[17] (cm^{-1})	Raman (cm^{-1})	I.R.[6, 14] (cm^{-1})	
	60(b, s, d)			60(b, s, d)		
			200(b, m)	320(m ,p)	315(s)	
410(s)	410(b, s, p)	443(s)	370(s)	412(s, p)		bond rocking
	490(s, p)					
	600(w, p)	568(b, w)				
730(m)	800(w, d)	811(m)	500(m)	560(b, m, p)	564(s)	bond-bending
1040(m)	1065(w, d)	1061(s)	850(s)	862(w, d)	888(s)	bond-stretching
	1200(w, d)	1200(w)		945(w, d)		

b = broad; s = strong; m = medium; w = weak; p = polarized; d = depolarized.

the central mass of the tetrahedron is much heavier than the masses at the vertices. This might be one reason why the calculated and observed Raman spectra for GeO_2 seem somewhat closer than for SiO_2. As far as positions of calculated frequency maxima go, the input force constants to the calculation were rough estimates and a better fit might be found by varying the input parameters. Furthermore, the structures of SiO_2 and GeO_2 have not been established on a definitive basis and this may affect the data. On the whole the agreement obtained so far appears very promising for this type of approach.

3. *Raman spectra of sodium silicate glasses*

The Raman spectra of sodium silicate glasses shown in Fig. 4 are characterized by the appearance of two bands at about 500 cm^{-1} and 1100 cm^{-1} which appear to grow in intensity as the sodium concentration is increased. These major features have been reported earlier[7] and are discussed in the review by Simon[8]. It has been suggested that the lower frequency can be associated with a bending vibration of the Si–O$^-$ non-bridging oxygen group. The sharpness might be attributed to a decoupling from other modes of the random network. The higher frequency at 1100 cm^{-1} can be attributed to bond stretching vibration of the Si–O$^-$ non-bridging oxygen or that of the bond stretching motion of the Si–O–Si bridging group discussed earlier in the section on vitreous silica.

In addition to these more obvious features which are well known, there are a number of finer details to the spectrum not previously reported which may be of some significance. In the first place there seems to be a broad low frequency maximum in all of these sodium silicate glasses. Some difficulty was encountered in observing these due to grating ghosts, but a low frequency scattering maximum at about 60 cm^{-1} is quite evident. As discussed in the first part, much of the intensity in this low frequency region can be attributed to a temperature enhancement and is not characteristic of the true vibration spectrum. However, it does appear that there is a greater amount of scattering for a sodium silicate glass than for vitreous silica. The origin of this low frequency scattering may or may not arise from the same cause as the low frequency i.r. absorption. The latter was discussed by Bagdade and Stolen[20] using a model involving charges distributed in a continuous medium. There is a large change in the far i.r. absorption coefficient (over a factor of 10) between vitreous silica and soft glass. While there does seem to be some change in the Raman scattered intensity between vitreous silica and soft glass, the change is much less than in the i.r. spectrum.

It is of interest to compare the spectrum of $Na_2O{\cdot}6SiO_2$ with that of SiO_2. In SiO_2 there are sharp bands at 489 and 600 cm^{-1}. A band at 489 cm^{-1} and a shoulder at 600 cm^{-1} are observed in the sodium silicate glass and may correspond to bands at the same frequency in vitreous silica. A new band appears at 525 cm^{-1} which might be associated with the formation of non-bridging oxygens.

While the identification of these weaker bands in alkali silicate glasses is still uncertain, it is felt the method of Raman spectroscopy has great merit in investigating problems of this nature.

5. CONCLUSIONS

It has been shown that high quality Raman spectra of simple silicate-type glasses can be obtained and provide useful information about the atomic vibrations in solids. Fairly good agreement is obtained between the observed Raman spectra given here and calculations carried out elsewhere. All of these glasses have a broad low frequency maximum in the scattered intensity. In the case of vitreous silica, spectra at cryogenic temperatures have been obtained and the intensity of this low frequency maximum is greatly reduced. The temperature dependence of the Raman spectrum appears to be consistent with first-order processes in the temperature and frequency range studied.

Acknowledgements—The author wishes to thank Drs. P. Dean, M. Gomez-Rodriguez, H. B. Rosenstock, and C. C. Klick for valuable discussions. The author is also grateful to Mr. R. J. Ginther for preparing some of the samples.

REFERENCES

1. FLUBACHER P., LEADBETTER A. J., MORRISON J. A. and STOICHEFF B. P., *J. Phys. Chem. Solids* **12**, 53 (1959).
2. KRISHNAN R. S., *Proc. Ind. Acad. Sci.* **37**, 377 (1953).
3. HARRAND M., *C. r. hebd. Séanc. Acad. Sci., Paris* **238**, 784 (1954).
4. TOBIN M. C. and BAAK T., *J. opt. Soc. Am.* **58**, 1459 (1968).
5. STOLEN R., Private communication.
6. CHEREMISINOV V. P., *Proc. (Trudy) P. N. Lebedev Physics Institute*, Vol. 25. Nauka, Moscow (1964) (translation: *Optical Methods of Investigating Solid Bodies*, p. 151–163. Plenum Press, New York (1965).
7. WILMOT G. B., Ph.D. Thesis, Massachusetts Institute of Technology (1954).
8. SIMON I., *Modern Aspects of the Vitreous State* (Edited by J. D. Mackenzie), Vol. 1, p. 120. Butterworths, London (1960).
9. SIMON I. and McMAHON H. O., *J. Am. Ceram. Soc.* **36**, 160 (1953).
10. HANNA R. and SU G.-J., *J. Am. Ceram. Soc.* **47**, 597 (1964).
11. HANNA R., *J. phys. Chem.* **69**, 3846 (1965).
12. MILER M., *Czech. J. Phys.* **B18**, 354 (1968).
13. ZARZYCKI J. and NAUDIN F., *Verres Réfract.* **14**, 113 (1960).
14. LIPPINCOTT E. R., VAN VALKENBURG A., WEIR C. E. and BUNTING E. N., *J. Res. natn. Bur. Stand.* **61**, 61 (1958).
15. WADIA W. and BALLOMAL L. S., *J. Phys. Chem. Glasses* **9**, 115 (1968).
16. SU G.-J., BORELLI N. F. and MILLER A. R., *J. Phys. Chem. Glasses* **3**, 167 (1962).
17. BELL R. J., BIRD N. F. and DEAN P., *J. Phys. C (Proc. phys. Soc.)* **1**, 299 (1968).
18. LEADBETTER A. J., *J. Phys. Chem. Glasses* **9**, 1 (1968).
19. LOUDON R., *Adv. Phys.* **13**, 423 (1964).
20. BAGDADE W. and STOLEN R., *J. Phys. Chem. Solids* **29**, 2001 (1968).
21. PLENDL J. N., MANSUR L. C., HADNI A., BREHAT F., HENRY P., MORLOT G., NAUDIN F. and STRIMER P., *J. Phys. Chem. Solids* **28**, 1589 (1967).
22. BOGENS R. K. and ZHUKOV A. G., *Zh. prikl. Spektr.* **4**, 68 (1966).
23. ROSENSTOCK H. B., *J. chem. Phys.* **27**, 1194 (1957).
24. WEEKS R. A., *Interaction of Radiation with Solids* (Edited by A. Bishay), p. 55. Plenum Press, New York (1967).
25. GASKELL P. H., *Trans. Faraday Soc.* **62**, 1493 (1966).
26. EGALSTAFF P. A., *Physics of Non-crystalline Solids* (Edited by J. A. Prins), p. 127. North-Holland, Amsterdam (1965).

J. Phys. Chem. Solids Pergamon Press 1970. Vol. 31, pp. 423–430. Printed in Great Britain.

MAGNETIC AND CRYSTALLOGRAPHIC EVIDENCE FOR LOCALIZATION TO DELOCALIZATION OF V *d*-ELECTRON LEVELS IN $CuCr_{2-x}V_xS_4$ SPINELS

M. ROBBINS, A. MENTH, M. A. MIKSOVSKY and R. C. SHERWOOD
Bell Telephone Laboratories, Incorporated, Murray Hill, N.J. 07971, U.S.A.

(*Received* 12 *June* 1969; *in revised form* 13 *August* 1969)

Abstract – Spinels in the system CuV_2S_4–$CuCr_2S_4$ ($CuV_xCr_{2-x}S_4$) were prepared and studied. CuV_2S_4 is a superconductor and $CuCr_2S_4$ is metallic conducting and ferromagnetic ($T_c = 398°K$). Magnetic measurements indicate that initially from $x = 0$ to $x = 0{\cdot}375$ the substituted vanadium ions exhibit essentially localized *d*-levels and magnetic moments which are magnetically polarized antiparallel to the carriers in the Cu *d*-band and parallel to the localized Cr^{3+} moments. With further addition of vanadium ($x = 0{\cdot}5$ to $x = 2$) it appears that the V *d*-levels broaden into a band which merges with the Cu σ_A^*-band, the total moment of which is polarized antiparallel to the localized Cr^{3+} moments. This behavior is manifested in the unit cell parameters, which increase between $x = 0$ and $x = 0{\cdot}375$ since $r_V3+ > r_{Cr}3+$, followed by a linear decrease, with increasing vanadium content ($x = 0{\cdot}5$ to $x = 2$), to CuV_2S_4. The change from local to band behavior for vanadium occurs over a rather small compositional range ($\Delta x = 0{\cdot}125$). An attempt is made to explain most of the observed properties using Goodenough's[4] band structure models for $CuCr_2S_4$ and CuV_2S_4.

INTRODUCTION

THE ELECTRIC and magnetic properties of chalcogenide spinels containing Cu on the *A* (tetrahedral) sites, have been found to differ markedly from other sulfide and selenide spinels[1–4]. Of particular interest in this work were the spinels CuV_2S_4 and $CuCr_2S_4$. CuV_2S_4 exhibits metallic conduction[2], superconductivity[5], and temperature independent Pauli-paramagnetism[1]. The formal valence distribution in this spinel is reported to be $Cu^{2+}V_2{}^{3+}S_4$[4]. $CuCr_2S_4$ is metallic conducting and ferromagnetic[1] ($T_c = 398°K$) and is also believed[4] to contain the formal valence Cu^{2+} on the tetrahedral sites ($Cu^{2+}Cr_2{}^{3+}S_4$). Goodenough[4] proposed a model for $CuCr_2S_4$ in which localized Cr *d*-levels fall below the top of the valence band and the Cu t_{2g}-levels mix covalently with the anionic valence band orbitals to form an unfilled σ_A^*-band. Thus the magnetic properties of $CuCr_2S_4$ would be due to antiferromagnetic interactions between carriers in the unfilled σ_A^*-band and the localized moments of the Cr^{3+} ions which are ferromagnetically coupled by the nearest neighbor Cr–S–Cr interactions[6]. In the case of CuV_2S_4, the proposed model assumes overlap of copper and vanadium *d*-bands which would be consistent with the observed electric and magnetic properties. In this paper we report the magnetic properties of the system $CuCr_{2-x}V_xS_4$ in which Cr^{3+} (with localized *d*-electrons) are mixed in the *B* sites with V ions (where in CuV_2S_4 the *d*-electrons are presumed to be itinerant).

EXPERIMENT

Preparation and crystallography

All of the materials in this system were prepared by firing pellets of appropriate mixtures of Cu, V, Cr_2S_3, and S in sealed evacuated quartz tubes at 800°C for 48 hr. Single phase spinel compositions were found to form in the complete range between $x = 0$ and $x = 2$ ($CuV_xCr_{2-x}S_4$). Total chemical analyses (to ± 1 wt%) have verified the chemical compositions of materials in this system. Unit cell parameters, obtained by the least square method, as a function of composition are shown in Fig. 1(a). As shown the unit cell size increases with vanadium substitution to a maximum at $x = 0{\cdot}375$. From $x = 0{\cdot}5$ to $x = 2$ (CuV_2S_4) the unit cell size decreases linearly. Although the ionic radius of V^{3+} is larger than Cr^{3+} the unit cell size of CuV_2S_4 has been found[2] to be smaller than that of $CuCr_2S_4$. This is related to the delocalized nature of the *d*-electrons of the vanadium ions in CuV_2S_4, which could result in an apparent vanadium radius (r_{V_d}) which is smaller in this system than its ionic radius. The increase in cell size, which was observed for the initial substitution of V^{3+} for Cr^{3+} ($x = 0$ to $x = 0{\cdot}375$) could be due to the presence of vanadium ions with localized *d*-electrons because $r_{V^{3+}} > r_{Cr^{3+}}$. A similar effect was observed[7] when V^{3+} was substituted for Cr^{3+} in $CdCr_2S_4$ resulting in an increase of the unit cell parameter ($a_{CdCr_2S_4} = 10{\cdot}244$ Å, $a_{CdV_{0.2}Cr_{1.8}S_4} = 10{\cdot}251$ Å). When the concentration of vanadium is increased further ($x = 0{\cdot}5$ to $x = 2$) the observed decrease in cell size may be related to the delocalization of the V-*d* levels (as in CuV_2S_4) which results in a smaller apparent ionic radius (r_V). The variation in unit cell size as a function of composition will be shown to be consistent with the magnetic data.

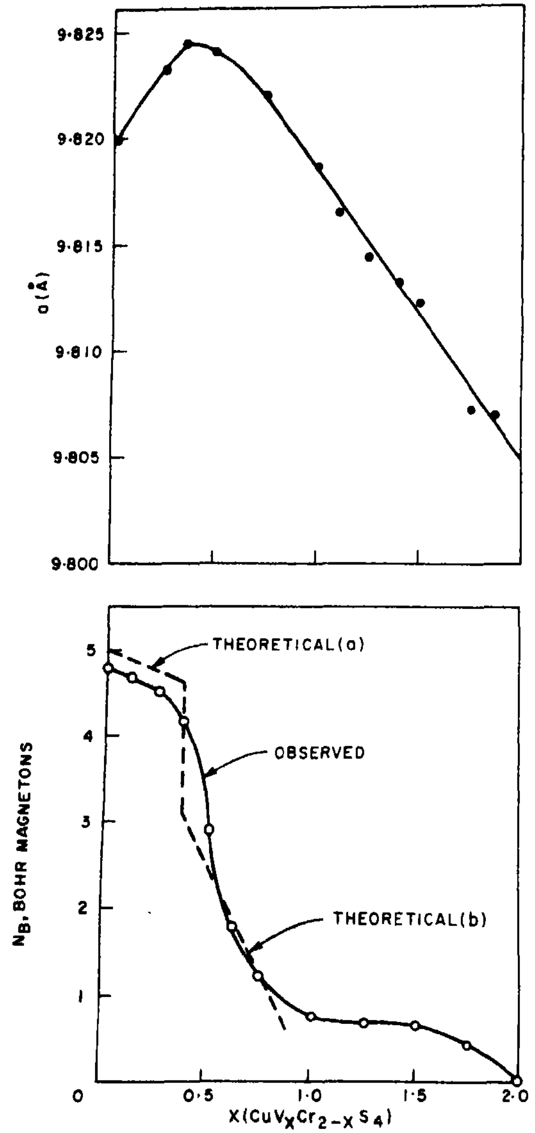

Fig. 1. (a) Unit cell parameters vs. composition (x) for the system $CuV_xCr_{2-x}S_4$. (b) Magnetic moment (Bohr magnetons) measured at 1·5°K and 15 kOe vs. composition (x) for the system $CuV_xCr_{2-x}S_4$.

Magnetic measurements

Measurements of magnetic moment per molecule (N_B) as a function of field, for various values of x, are shown in Fig. 2 and compared to calculated values in Table 1. For $x \leq 0{\cdot}375$ the magnetic moments are in agreement with a model (Fig. 1(b)) which assumes that the V ions are V^{3+} and carry a localized moment which is aligned parallel to the Cr^{3+} moment and, as Cr^{3+}, is coupled negatively (antiferromagnetically) with the moment in the Cu σ_A^*-band as in $CuCr_2S_4$. It is in this compositional region that the unit cell parameter increases as a function of x. The largest cell size is found for $x = 0{\cdot}375$, which is the last sample to contain essentially localized V^{3+} moments. With subsequent vanadium substitution ($x = 0{\cdot}5$, $0{\cdot}625$, $0{\cdot}75$) the magnetic moment decreases sharply to values which can only be accounted for by a model which assumes that the vanadium *d*-levels have combined to form a band which merges with the Cu σ_A^*-band as in

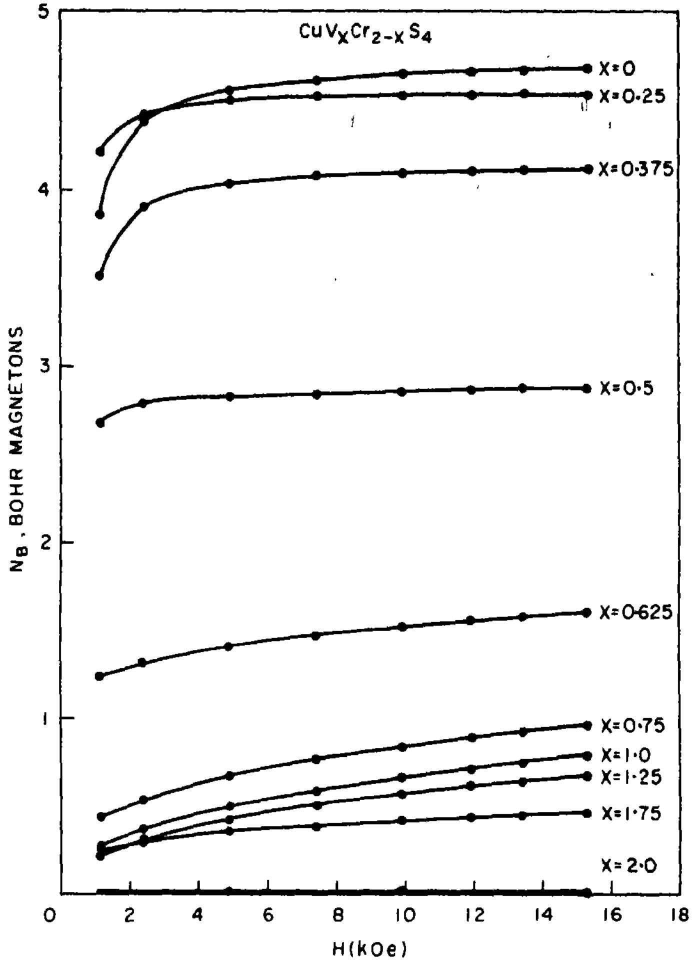

Fig. 2. Magnetic moment vs. field for some compositions in the system $CuV_xCr_{2-x}S_4$.

CuV_2S_4. The vanadium d-electrons would then become identical to and magnetically parallel with the Cu d-electrons, all of which are polarized antiferromagnetically to the localized Cr^{3+} moment. In this compositional region the unit cell parameters decrease linearly between $x = 0{\cdot}5$ and $x = 2$.

The apparent change in the properties of the vanadium ion between $x = 0{\cdot}375$ and $x = 0{\cdot}5$, and further addition of vanadium ($x = 0{\cdot}5$ to $x = 2$) serves to dilute the localized B site (Cr^{3+}) moment and consequently the strength of the long range magnetic interaction between the localized and itinerant electrons. This results in the failure of the localized Cr^{3+} moment to polarize the total potential band moment. Magnetic measurements in fields up to 50 kOe† show that the moment of the material where $x = 1$ increases continuously with field which tends to align the magnetic moment in the band parallel to the Cr^{3+} moment in the direction of the field. Calculations predict that as x increases the moment should decrease until, at $x = 1$, a compensation point (at $x = 1$, $N_B = 0$) should

---

†High field (up to 50 kOe) measurements are being carried out and will be reported in detail at a future date.

Table 1

$CuV_xCr_{2-x}S_4$	Observed moment μ_B (A)	Theoretical moment μ_B (B)	
		a	b
$x = 0$	4·79	5·00	
0·125	4·68	4·875	4·375
0·25	4·53	4·75	3·75
0·375	4·16	4·625	3·125
0·5	2·9	4·5	2·5
0·625	1·8	4·375	1·875
0·75	1·22	4·25	1·25

(A) Obtained by extrapolation to infinite field.

(B) a These moments were calculated assuming the moment of the vanadium ion ($2\mu_B$) is aligned parallel to that of Cr^{3+} and antiparallel to the Cu moment in the band.

b These moments were calculated assuming that the vanadium *d*-electrons are itinerant and like the Cu *d*-electrons are polarized antiparallel to the Cr^{3+} moment.

be reached and for larger values of $x(x > 1)$ the potential moment in the band would be larger than the moment of the localized Cr^{3+} ions. Therefore, if the localized moment were capable of totally polarizing the band moment, ferromagnetism should disappear at $x = 1$ and reappear for $x > 1$. This phenomenon should only be apparent at zero field due to the moment induced by the external field. It is interesting to note that extrapolations to zero field in σ^2 vs. H/σ (Fig. 5) plots[8] results in the disappearance of remenant magnetization in the vicinity of $x = 1$ and the subsequent appearance of zero field remance for $x = 1·5$ and $x = 1·75$. The moments shown as a function of composition in Fig. 1(b) are those measured in a field of 15 kOe. The moment induced by this field may account for our failure to observe zero moment at $x = 1$.

The magnetization as a function of temperature was measured in a field of 15·3 kOe and the results are shown in Fig. 3. The Curie temperatures (T_c) obtained from the point of maximum slope in the magnetization curves are shown as a function of composition in Fig. 4. It should be noted (Fig. 4) that although T_c decreases with increasing vanadium substitution the sharpest decline occurs in the region from $x = 0·25$ to $x = 0·75$ which is where the apparent change in the properties of the vanadium ion takes place.

Effective paramagnetic moments obtained from susceptibility measurements above T_c are shown in Table 2. Since CuV_2S_4 exhibits temperature-independent Pauli paramagnetism, it was assumed that the paramagnetic contribution of the copper and vanadium (where $x \geqslant 0·5$) was temperature independent and the temperature-dependent magnetic suceptibility was due only to the Cr^{3+} ions. It was necessary, therefore, to correct the susceptibility measurements for the temperature-independent contribution. The correction for each composition was the fraction of the susceptibility of CuV_2S_4 corresponding to the vanadium concentration. The observed effective magnetic moments per Cr^{3+} ion are shown in Table 2. The observed values remained fairly constant for the compositions tested and the average value of $3·6\,\mu_B$ is in qualitative agreement with the spin only value of $3·87\,\mu_B$[9] for Cr^{3+}.

DISCUSSION AND CONCLUSIONS

The two compositions where $x = 0·375$ and $x = 0·5$ are critical ones as it is in this region that the transition in the properties of vanadium takes place. Magnetic moments of both of these samples differ somewhat

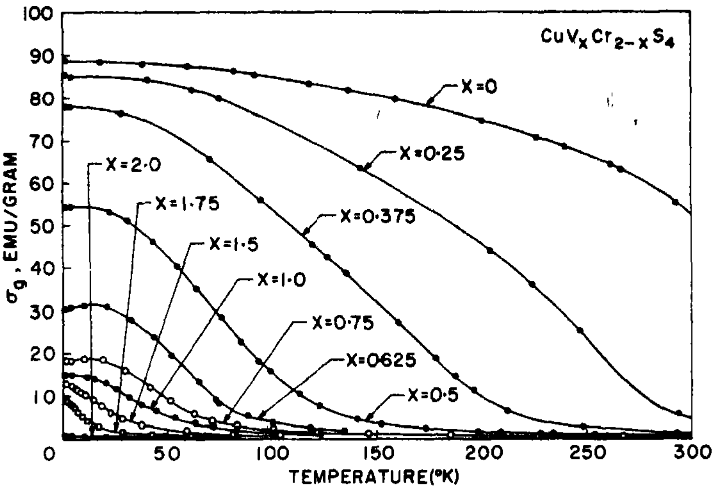

Fig. 3. Magnetic moment at 15 kOe vs. temperature for some compositions in the system $CuV_xCr_{2-x}S_4$.

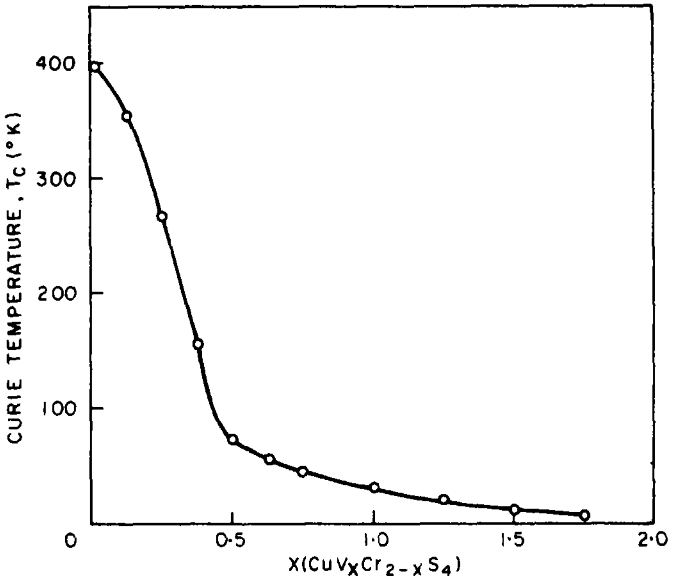

Fig. 4. Curie temperatures obtained from 15 kOe field measurements as a function of composition in $CuV_xCr_{2-x}S_4$.

($\sim 0{\cdot}5\,\mu_B$) from the predicted values. The material where $x = 0{\cdot}375$ is the last to exhibit essentially localized behavior of the V *d*-electrons and its observed moment was lower than that predicted. Whereas for $x = 0{\cdot}5$ the material is the first to exhibit essentially delocalized V *d*-electrons and its observed moment was larger than that predicted. The observed differences may be accounted for by assuming a statistical rather than uniform distribution of vanadium ions in the spinels. In the sample where $x = 0{\cdot}375$ a statistical

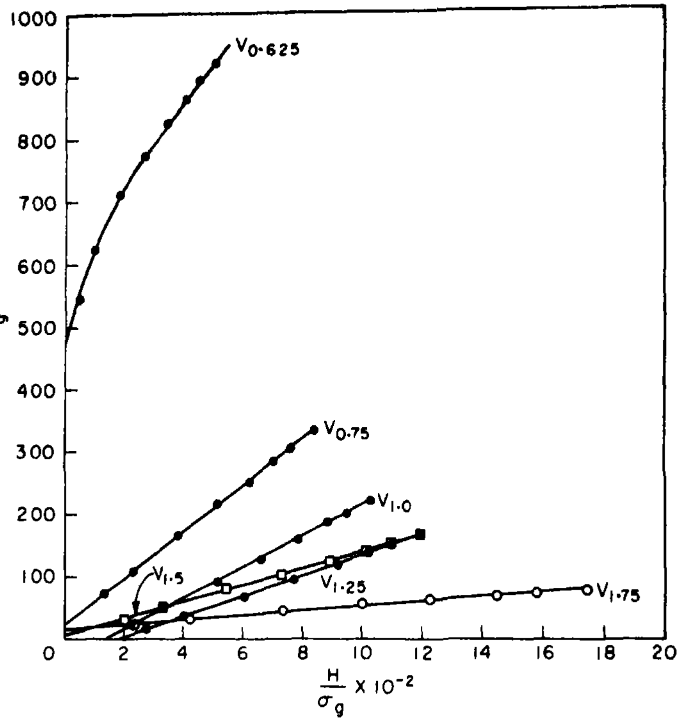

Fig. 5. Moment squared ($\sigma_g{}^2$) vs. H/σ for some compositions in $CuV_xCr_{2-x}S_4$.

Table 2

$CuV_xCr_{2-x}S_4$ x	T_c (°K) (at 15·3 kOe)	Effective paramagnetic moment per Cr^{3+}
0·25	267	—
0·375	155	—
0·5	75	3·66
0·625	57	3·61
0·75	46	3·6
1·00	33	3·5
1·25	22	3·6
1·5	13	3·54
1·75	8	3·8

distribution would result in a smaller distance between some fraction of the vanadium ions causing their *d*-electrons to become itinerant and a lowering of the moment of the material with respect to the predicted moment. In the sample where $x = 0{\cdot}5$ a statistical distribution would result in distances between a fraction of the vanadium ions which are greater than the mean distance for that composition causing them to retain localized magnetic properties. Thus a larger magnetic moment than that predicted would be observed.

The band structure model of Goodenough [4] for $CuCr_2S_4$ and CuV_2S_4 can be used to describe most of the properties of the $CuV_xCr_{2-x}S_4$ system. The partial schematic band structure of $CuCr_2S_4$[4] is shown in

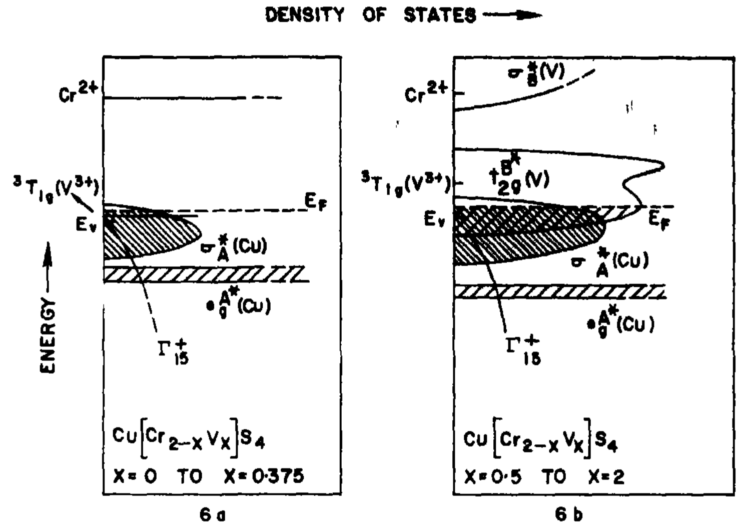

Fig. 6(a and b). Band structure models for the system $CuV_xCr_{2-x}S_4$, adopted from Goodenough [4].

Fig. 6(a) and shows the unfilled Cu σ_A^*-band formed from mixing of Cu d-orbitals with the valence band (lower lying Cr^{3+} d-levels are not shown). As small amounts of V^{3+} $(0 < x \leq 0{\cdot}375)$ are substituted for Cr^{3+}, localized $V^{3+}t_{2g}$-levels are formed near the top of the Cu σ_A^*-band (Fig. 6(a)). In this state the V^{3+} ions increase the unit cell size and exhibit localized magnetic moments which are polarized parallel to Cr^{3+} and antiparallel to the induced moment of the itinerant electrons in the copper band. As the concentration of V^{3+} is further increased $0{\cdot}375 < x \leq 2$ the distance between vanadium ions decreases and the d-levels broaden into a band which merges with the Cu σ_A^*-band (Fig. 6(b)) as described for CuV_2S_4[4]. In this region the cell size decreases and the vanadium moment is delocalized and polarized (with the Cu moment) antiparallel to the Cr^{3+} moment. The effective paramagnetic moment is in agreement with a Cr^{3+} only moment. The transition in properties of the vanadium ion occurs over such a small compositional range $(\Delta x \approx 0{\cdot}125)$ that the change may be described as a discontinuous one similar to the model proposed by Mott [10] to describe the rapid change from semiconducting to metallic conductivity in various substituted metal and oxide solid solutions.

As V^{3+} is substituted in $CuCr_2S_4$ the Curie temperature decreases rapidly with the sharpest decline occuring in the region in which the transition in V^{3+} properties takes place. The sharp decline in T_c, which begins with the initial substitution of V^{3+} for Cr^{3+}, may reflect in part a weaker Cr–S–V superexchange interaction than the original Cr–S–Cr interactions as well as a weakening of the nearest neighbor ferromagnetic Cr–S–Cr interactions due to the initial lattice expansion. For compositions where $x > 0{\cdot}375$ the concentration of ions with localized moments decreases with increasing x leading to weakened magnetic interactions between localized and itinerant d-electrons. Further investigation of the observed itinerant ferromagnetism, the electrical properties, and the persistence of ferromagnetism for relatively small Cr^{3+} concentrations are being conducted.

Acknowledgements – The authors gratefully acknowledge Drs. L. Holmes and G. Knapp for some of the magnetic measurements and for very helpful discussions. We would also like to thank Drs. M. E. Lines and A. C. Gossard for their helpful discussions.

REFERENCES

1. LOTGERING F. K., *Proc. int. Conf. Magnetism*, p. 533, Nottingham, England (1964).
2. BOUCHARD R. J., RUSSO P. A. and WOLD A., *Inorg. Chem.* **4**, 685 (1965).
3. ROBBINS M., LEHMANN H. W. and WHITE J. G., *J. Phys. Chem. Solids* **28**, 897 (1967).
4. GOODENOUGH J. B., *J. Phys. Chem. Solids* **30**, 261 (1969).
5. VAN MAUREN N. H., SCHAEFFER G. M. and LOTGERING F. K., *Phys. Lett.* **25A**, 238 (1967).
6. BALTZER P. K., WOJTOWICZ P. J., ROBBINS M. and LOPATIN E., *Phys. Rev.* **151**, 367 (1966).
7. ROBBINS M., MIKSOVSKY M. A. and SHERWOOD R. C., *J. appl. Phys.* **40**, 2466 (1969).
8. KOUVEL J. S., G. E. Res. Lab. Report No. 57-RL-1799 Research Information Section, Schenectady, New York (Sept. 1957).
9. SELWOOD P. W., *Magnetochemistry*, p. 159. Interscience, New York (1956).
10. MOTT N. F., *Proc. phys. Soc. Lond.* **A62**, 416 (1949); *Nuova Cim. Suppl.* 7, 312 (1958); *Phil. Mag.* **6**, 287 (1961); ANDERSON P. W., In *Solid State Physics* (Edited by F. Seitz and D. Turnbull), Vol. 14. Academic Press, New York (1963).

J. Phys. Chem. Solids Pergamon Press 1970. Vol. 31, pp. 431–446. Printed in Great Britain.

QUANTUM THEORY OF FERROELECTRICITY – I. SPECTRAL ANALYSIS‡

L. NOVAKOVIĆ§
Department of Physics, University of Toronto, Toronto 5, Ontario, Canada

(*Received* 18 *April* 1969; *in revised form* 25 *July* 1969)

Abstract – Using the method of second quantization the proton dynamics in hydrogen-bonded ferroelectrics is formulated. The general expression for the potential energy of the system of protons due to the presence of heavy ions is related to the well-known phenomenological models of Slater, Takagi and Blinc. The diagonal part of the Hamiltonian of the system of protons is represented in terms of the characteristic energies. These energies are calculated assuming the crystal structure KH_2PO_4 and are found strongly dependent on the mass of the proton. The present theory can satisfactorily account for a large isotope effect which concerns the magnitude of the transition temperature. The behaviour of the ferroelectric mode in the vicinity of the transition point is considered. It is possible to test the existence of this mode by measuring an inelastic scattering of neutrons at temperatures close to the transition point.

1. INTRODUCTION

THE FERROELECTRIC (ordered) phase in hydrogen-bonded ferroelectrics such as potassium dihydrogen-phosphate (KH_2PO_4) is characterized by an ordered array of hydrogen atoms. This is well established by the neutron diffraction experiment of Bacon and Pease [1]. At 77°K, i.e. below the transition temperature ($T_c = 122°K$ for KH_2PO_4), Bacon and Pease found that the protons move around one of the two possible equilibrium positions. A free and clear interpretation of this experiment at the temperatures below T_c is given in Fig. 1. Here we bring the environment of a phosphate (PO_4) group together with the other atoms the heights of which are given in Å units. We also mark the four H-atoms surrounding a given phosphate group by 1, 2, 3, 4. It is actually one quarter of the large unit cell which then contains sixteen nonequivalent protons as shown by X-ray or neutron diffraction data[2]. The crystal structure belongs to a tetragonal system which has a center of symmetry. The cell dimensions are $a_1 = a_2 = 7{\cdot}453$ Å, $a_3 = 6{\cdot}959$ Å. Each PO_4 group is connected by four H-bondings to the other groups. The bonds lie almost parallel to either X or Y-directions. The structure consists of two interpenetrating body-centered PO_4 tetrahedra and two interpenetrating body-centered K lattices in such a way that the K and PO_4 sublattices are separated by $a_3/2$ in Z-direction.

At the transition point the crystal undergoes a phase transition which according to Landau's classification may be a second order phase transition, since the crystal changes the symmetry. Also the crystal changes the cell dimensions slightly but the principal change in symmetry is caused by the proton motion. Above the transition point the protons occupy both equilibrium positions with an equal probability. This is directly shown by neutron diffraction. The proton density distribution here looks smoothly distributed over a small distance which is supposed to separate the two equilibrium positions. This distance was measured at various temperatures and it turns out to be about 0·35 Å. The proton density distribution deduced from the neutron diffraction extends along the hydrogen bond in the disordered (paraelectric) phase, while it becomes localized around an asymmetric

---

‡This work was supported by a grant from the National Research Council of Canada.

§On leave of absence from the Boris Kidric Institute of Nuclear Sciences, Belgrade, Yugoslavia.

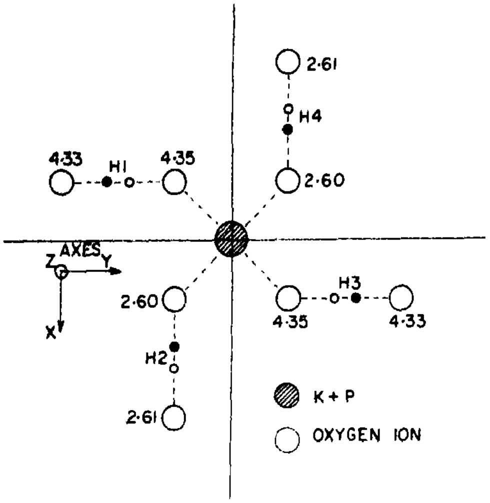

Fig. 1. Environment of any given PO_4 group. The four nonequivalent hydrogen ions are marked by H1, H2, H3, H4. The heights of the oxygen ions are given in Å units. The two equilibrium positions are indicated either by full circles if the hydrogens are close to PO_4 or by open circles if the hydrogens are away from PO_4.

position shifted from the centre of the bond in the ordered (ferroelectric) phase. The direction of the proton shift from the centre of the bond is reversed when the applied field is reversed. This seems to agree with the assumption that the phase transition in KDP is triggered by the order–disorder mechanism.

According to the neutron diffraction every proton takes one of two possible positions in such a way as to ensure that only two protons around a given phosphate group occupy the positions close to the group. All other configurations in which one or three protons, or none or four protons, are attached to the group are assumed to have high configuration energy. The higher configurations seem to play no part in the ferroelectric phase transition. The polarization of the unit cell may be determined from the proton configurations and a state of complete ordering in the proton arrangement is assumed to correspond to the ferroelectric ground state. The magnitude of the saturated polarization P_s in the ordered phase is accounted by the observed values for the displacements of the ions K^+, P^{+5} and O^{-2} along the Z-axis relative to their symmetric positions. Therefore, the hydrogen bondings do not contribute any considerable dipole moments to the saturated polarization so the essential unit of the dielectric properties is the dipole moment of the complex $K^+(PO_4)^-$.

Historically, the first molecular theory of the phase transition in KDP was proposed by Slater[3]. Exactly as the diffraction experiment showed later, Slater assumed that every proton takes only one of two possible positions along the OH. . .O bonding line and from four hydrogen bondings attached to every PO_4 group he assumed only two protons to occupy the 'close' positions, the other two being 'away' from the group. Disregarding higher configurations Slater was able to explain the observed entropy change at the Curie temperature by predicting the first order phase transition although the second order phase transition might be expected from a general and simple classification due to Landau[4]. By taking into account the higher configurations which Slater neglected, Takagi[5] was able to show that the phase transition could be a second order one. Although successful in describing many properties of KDP, the Slater–Takagi model has a serious defect. Commonly characteristic of all the ferroelectric crystals having the hydrogen bonding is a large isotope effect. On deuteration, the Curie temperature is increased by a factor which varies from 1·48 $(C_sH_2A_sO_4)$ to 1·73 (KH_2PO_4), while the Curie constraint C, at least for KDP, changes very little. Concerning the isotope effect on the saturated polarization P_s the most recent measurement of Azoulay *et al.*[6] gives $P_s(KD_2PO_4)/P_s(KH_2PO_4) = 1{\cdot}2$. This effect can only partly be explained by the present theory. There is no isotope effect, however, in the Slater–Takagi model. Here the transition temperature is related only to the energy ϵ (difference between the lowest configurations) where ϵ is assumed to be independent of the mass of the particle.

To explain the large isotope effect Pirrene

[7] treated the whole problem quantum-mechanically by introducing the kinetic energy of the protons. He tried to explain the isotope effect assuming that the protons move freely in a single-minimum potential field. Since the vibrational levels for the deuterons are lower, it may be expected that the transition temperature in deuterated compounds is higher. However, the proton vibrational levels predicted by Pirrene are in disagreement with optical observations. Pirrene's idea is further developed by Blinc[8] in a model where the proton makes a tunnelling motion across the double minimum potential field. It is evident that the tunnelling motion opposes the tendency of obtaining a low energy configuration. If the proton tunnelling really takes place, it should be seen as a splitting of the proton vibrational levels. First experiments by Blinc and Hadzi[9] who analyzed the far infrared absorption data seem to have found the expected vibrational splitting. However, the interpretation of their experiments was questioned by Lazarev and Zaitseva[10] and independently by Barker and Tinkham[11].

In spite of some unclear points the Blinc model was carefully examined and generalized in two exhaustive papers by Tokunaga and Matsubara[12] in order to give a consistent account of various experimental results. The main idea these authors start from is the existence of a proton tunnelling. The phase transition is assumed to be caused by a cooperative ordering in the proton arrangement to which the displacements of heavy ions are strongly coupled. The ferroelectric behaviour of KDP is therefore obtained as a collective effect of several different terms including the ionic displacements, interaction between ions and protons and the kinetic energy of protons. Essentially the same interaction terms are considered independently by the present author in an earlier paper[13] in which the proton frequency spectrum as a function of temperature is calculated. This work was continued in another paper[14] where the elementary excitations of the hydrogen-bonded ferroelectrics are formulated, taking the exact symmetry into account.

The principal purpose of the present paper is the examination of the theoretical conceptions involved in the Blinc model in order to see if it can be established selfconsistently. Some results are not related to the phenomenon of ferroelectricity, rather they give an insight into the nature of the hydrogen bonding in general. In Section 2 we formulate the proton motions in second quantization starting from a complete set of wave functions. In Section 3 we consider the potential energy in relation to the well-known models of Slater, Takagi and Blinc. In Section 4 we calculate the characteristic energies and find that these are in fair agreement with the laser-excited Raman spectra. In Section 5 we consider the so-called ferroelectric mode and its behaviour in the vicinity of the transition point. Generally speaking the present theory can account for the large isotope effect. It also suggests another experiment which may test the existence of the ferroelectric mode. Fundamental distinction between the present theory and the Blinc model is related to the concept of a 'tunnelling' motion. Using the language of second quantization, we never refer to any kind of 'tunnelling' so long as we speak about the properties of a large number of particles.

2. THE PROTON MOTIONS IN SECOND QUANTIZATION

In the present theory the actual motion of the proton is formulated in terms of a system having a large number of particles. The method we use is the method of second quantization which assumes a complete set of orthogonal wave functions. To build up such a set of functions we consider the crystal as a system composed of unit cells. Position of the given proton is described by the vector $\vec{R}_{j\rho}$, where j denotes the unit cell and ρ labels the proton site within the unit cell (Fig. 2).

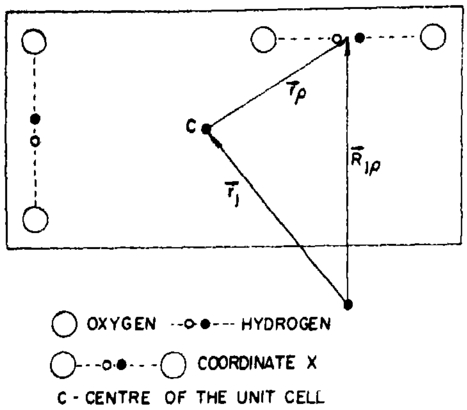

Fig. 2. A simple illustration of the notation used in the text. *C* is the centre of the unit cell, O...O is the coordinate *X*, O and . stand for the oxygen and hydrogen ions, respectively.

We can write

$$\vec R_{jp} = \vec r_j + \vec r_p + \vec x_p \qquad (2.1)$$

where $\vec r_j$ refers to the center of the unit cell, $\vec r_p$ refers to the middle point of the OH...O bonding line, $\vec x_p$ is the position vector of the proton along the OH...O bonding line. For example,

$$\vec x_p = \{x, 0, 0\}, \qquad p = 0, 2$$
$$\vec x_p = \{0, x, 0\}, \qquad p = 1, 3,$$

(see Fig. 1). The crystal lattice is invariant under the transformation

$$\vec R_{jp} \to \vec R_{jp} + m_1\vec a_1 + m_2\vec a_2 + m_3\vec a_3 \qquad (2.2)$$

where m_i are positive or negative integers. and $\vec a_i$ are the fundamental vectors of the ordinary lattice.

Let us denote the complete set of wave functions with $\phi_\alpha(\vec R_{jp})$, where $\alpha = 0, 1, \ldots$ refers to some allowed states at a given proton site. These functions satisfy the condition

$$\int \phi_\alpha^*(\vec R_{jp})\phi_\beta(\vec R_{k\sigma})\mathrm{d}\tau = \delta_{jk}\delta_{p\sigma}\delta_{\alpha\beta}, \qquad (2.3)$$

where $\mathrm{d}\tau$ is the volume element. Suppose that we can write

$$\phi_\alpha(\vec R_{jp}) = u(\vec r_j)v(\vec r_p)\psi_\alpha(\vec x_p), \qquad (2.4)$$

where $u(\vec r_j)$ satisfy the condition

$$u(\vec r_j + m_1\vec a_1 + m_2\vec a_2 + m_3\vec a_3) \equiv u(\vec r_j). \qquad (2.5)$$

It is easy to show that

$$u^*(\vec r_j) \,.\, u(\vec r_k) = \delta_{jk}, \qquad (2.6)$$

if we use the momentum representation in which $u(\vec r_j)$ is given by

$$u(\vec r_j) = N^{-1/2} \sum_p \exp(i\vec p \cdot \vec r_j). \qquad (2.7)$$

Here N denotes the total number of unit cells, and $\vec p$ is a vector of the reciprocal lattice,

$$\vec p = 2\pi\left\{\frac{\nu_1}{N_1} b_1 \; \frac{\nu_2}{N_2} b_2, \frac{\nu_3}{N_3} b_3\right\}, \qquad (2.8)$$

where $b_s (s = 1, 2, 3$ or $x, y, z)$ denote the lengths of the unit cell in the space of the reciprocal lattice. These are related to the lengths a_s of the unit cell in the ordinary lattice by

$$\vec b_1 = \frac{\vec a_2 \times \vec a_3}{v}, \qquad \vec b_2 = \frac{\vec a_3 \times \vec a_1}{v}, \qquad \vec b_3 = \frac{\vec a_1 \times \vec a_2}{v}, \qquad (2.9)$$

$$v = \vec a_1 \,.\, (\vec a_2 \times \vec a_3). \qquad (2.10)$$

Each ν_s in equation (2.8) takes exactly N_s different integer values according to the rule

$$-\frac{N_s}{2} \leq \nu_s \leq \frac{N_s}{2}, \qquad (2.11)$$

where the sign of equality can only be applied if N_s is an even number. Notice that the total number of units cells $N = N_1N_2N_3$. Now using equations (2.7)–(2.11) we obtain

$$u^*(\vec r_j)\, u(\vec r_k) = \sum_{\{\nu_s\}} \exp\left[2\pi i\left(\frac{\nu_1 m_1}{N_1} + \frac{\nu_2 m_2}{N_2} + \frac{\nu_3 m_3}{N_3}\right)\right], \qquad (2.12)$$

$$\vec{r}_j-\vec{r}_k=\sum_{s=1}^{3} m_s\vec{a}_s. \tag{2.13}$$

Equation (2.12) gives 1 if $m_1=m_2=m_3=0$, and 0 if at least one among m_s is different from zero. This completes the proof of the orthogonality condition (2.6).

Next consider the functions $v(\vec{r}_\rho)$ and $\psi_\alpha(\vec{x}_\rho)$. The former functions can be chosen in such a way as to ensure that they are different from zero only in a close neighbourhood around the point $\vec{r}_\rho$ which is placed at the middle of every OH...O bonding line. Taking

$$|v(\vec{r}_\rho)|^2=\delta(\vec{r}-\vec{r}_\rho) \tag{2.14}$$

we obtain

$$\int |v(\vec{r}_\rho)|^2 d^3r=1,$$

$$\int v^*(\vec{r}_\rho)v(\vec{r}_\sigma)d^3\vec{r}=0, \tag{2.15}$$

if $\rho\neq\sigma$. The functions $\psi_\alpha(x)$ we take as follows:

$$\psi_0(x)=C_0[\psi_{RO}(x)+\psi_{LO}(x)], \tag{2.16}$$

$$\psi_1(x)=C_1[\psi_{RO}(x)-\psi_{LO}(x)], \tag{2.17}$$

$$\psi_2(x)=C_2[\psi_{R1}(x)-\psi_{L1}(x)]+\eta_1\psi_1(x), \tag{2.18}$$

$$\psi_3(x)=C_3[\psi_{R1}(x)+\psi_{L1}(x)]+\eta_0\psi_0(x). \tag{2.19}$$

Here

$$\psi_{R0}(x)=\left(\frac{2\xi}{\pi}\right)^{1/4}\exp\left[-\xi\left(x-\frac{a}{2}\right)^2\right], \tag{2.20}$$

$$\psi_{L0}(x)=\left(\frac{2\xi}{\pi}\right)^{1/4}\exp\left[-\xi\left(x+\frac{a}{2}\right)^2\right], \tag{2.21}$$

$$\psi_{R1}(x)=\sqrt{2}\left(\frac{2\xi}{\pi}\right)^{1/4}\sqrt{2\xi}\left(x-\frac{a}{2}\right)\exp\left[-\xi\left(x-\frac{a}{2}\right)^2\right], \tag{2.22}$$

$$\psi_{L1}(x)=\sqrt{2}\left(\frac{2\xi}{\pi}\right)^{1/4}\sqrt{2\xi}\left(x+\frac{a}{2}\right)\exp\left[-\xi\left(x+\frac{a}{2}\right)^2\right], \tag{2.23}$$

where ξ is defined by

$$\xi=\frac{m\omega_{\text{class}}}{2\hbar}. \tag{2.24}$$

m is the mass of the particle, ω_{class} is the characteristic angular frequency of a classical oscillator, $\hbar$ is the Planck constant divided by 2π. The coefficients C_α, η_0 and η_1 are determined from the condition of orthonormality:

$$\int_{-\infty}^{\infty}\psi_\alpha^*(x)\psi_\beta(x)dx=\delta_{\alpha\beta}. \tag{2.25}$$

The result is

$$C_{0,1}=\frac{1}{\sqrt{2}}\left[1\pm\exp\left(-\frac{\eta}{2}\right)\right]^{-1/2}, \tag{2.26}$$

where + and − correspond to C_0 and C_1 respectively. Also we have

$$C_2=\frac{1}{\sqrt{2}}\left[1+(\eta-1)\exp\left(-\frac{\eta}{2}\right)+2\eta\exp(-\eta)\right]^{-1/2}, \tag{2.27}$$

$$\eta_1=2\sqrt{\eta}\exp\left(-\frac{\eta}{2}\right)C_2, \tag{2.28}$$

$$C_3=\frac{1}{\sqrt{2}}\left[1-(\eta-1)\exp\left(-\frac{\eta}{2}\right)+2\eta\exp(-\eta)\right]^{-1/2}, \tag{2.29}$$

$$\eta_0=-2\sqrt{\eta}\exp\left(-\frac{\eta}{2}\right)C_3, \tag{2.30}$$

$$\eta=\xi a^2=\frac{m}{\hbar^2}\left(\frac{\hbar\omega_{\text{class}}}{2}\right)a^2, \tag{2.31}$$

where a denotes the distance separating the two equilibrium positions of the proton.

The energy of the system contains the kinetic energy of the protons and the potential energy due to the presence of heavy ions. If no external field is applied the energy function can be written

$$H=\sum_{j\rho}\left(-\frac{\hbar^2}{2m}\Delta_{j\rho}+U(\vec{R}_{j\rho})\right) \tag{2.32}$$

where

$$\Delta_{jp} = \frac{\partial^2}{\partial x_p^2}+\frac{\partial^2}{\partial y_p^2}+\frac{\partial^2}{\partial z_p^2}. \qquad (2.33)$$

xp, yp, xp are the components of the vector $\vec{x}_p$. The potential energy is assumed to have the form

$$\sum_{jp} U(\vec{R}_{jp}) = -U_0 + \sum_{i} A_i n_i + \sum_{\langle ij\rangle} B_{ij} n_i n_j + \sum_{\langle ijk\rangle} C_{ijk} n_i n_j n_k + \sum_{\langle ijkl\rangle} D_{ijkl} n_i n_j n_k n_l. \qquad (2.34)$$

Here $-U_0$ denotes the total binding energy. A_i, B_{ij}, . . . are various coupling constants, every suffix should be understood as a twofold notation, the quantities n_i, n_j, . . . may take only two values, $n_i = 0,1$. The symbols $\langle ij\rangle$, $\langle ijk\rangle$, are used to indicate that every term is counted only once. The coupling constants are restricted by certain conditions which we shall introduce later.

Using the method of second quantization we can write the total wave function in the form

$$\psi = \sum_{jp\alpha} \phi_\alpha(\vec{R}_{jp})\mathbf{a}_{jp\alpha}, \quad \psi^\dagger = \sum_{jp\alpha} \phi^*_\alpha(R_{jp})\mathbf{a}^\dagger_{jp\alpha} \qquad (2.35)$$

where $\phi_\alpha(\vec{R}_{jp})$ are defined by equation (2.4), and the creation $\mathbf{a}^\dagger_{jp\alpha}$ and annihilation operators $\mathbf{a}_{jp\alpha}$ satisfy the commutation relation

$$[\mathbf{a}_{jp\alpha}, \mathbf{a}^\dagger_{jp\alpha'}]_+ = \delta_{\alpha\alpha'}. \qquad (2.36)$$

It is easily seen that

$$\mathbf{a}^\dagger_{jp\alpha}\mathbf{a}_{jp\alpha} = 0 \text{ or } 1, \qquad (2.37)$$

which reflects the fact that only one proton at a given lattice site (j,p) can be observed in any of the four allowed states $(\alpha = 0,1,2,3)$. Using the above formulas the energy function becomes

$$H = \sum_{jp\alpha\alpha'} \omega(\alpha,\alpha')\mathbf{a}^\dagger_{jp\alpha}\mathbf{a}_{jp\alpha'} \qquad (2.38)$$

$$\omega(\alpha,\alpha') = \int_{-\infty}^{\infty} \psi^*_\alpha(x)\left(-\frac{\hbar^2}{2m}\frac{d^2}{dx^2} - U_0 + An\right)\psi_{\alpha'}(x)dx, \qquad (2.39)$$

where $A_{jp} \equiv A$, $n_{jp} \equiv n$ in the above integral. The energy function in second quantization contains only the single particle terms.

3. THE POTENTIAL ENERGY

Next consider the potential energy of various proton configurations associated with the central phosphate group. To do this we introduce the symmetric variable σ_j by

$$n_j = \tfrac{1}{2}(1-\sigma_j), \qquad (3.1)$$

where j labels the proton sites. If n_j takes the values 0,1 then σ takes the values 1, -1 respectively. Moreover, the potential energy must be a symmetric function with respect to exchange $\sigma_j \rightarrow -\sigma_j$. Therefore we have

$$\sum_{jp} U(\vec{R}_{jp}) = -U_0 + \sum_{\langle jk\rangle} J_{jk}\sigma_j\sigma_k + K\sigma_1\sigma_2\sigma_3\sigma_4, \qquad (3.2)$$

$$J_{12} = J_{23} = J_{34} = J_{41}, \qquad (3.3)$$

$$J_{13} = J_{24}, \qquad (3.4)$$

where j and k denote the proton sites in Fig. 1. On the other hand, the potential energy may also be given by equation (2.34), hence we may have

$$A_j = A, \quad j = 1,2,3,4 \qquad (3.5)$$

$$B_{12} = B_{23} = B_{34} = B_{41}, \qquad (3.6)$$

$$B_{13} = B_{24}, \qquad (3.7)$$

$$C_{jkl} = C, \quad D_{ijkl} = D. \qquad (3.8)$$

The energy levels associated with various configurations are given in Table 1. The protons attached to the phosphate group are marked by $\sigma_j = +$ ('right' position), those

Table 1. Energy levels of the phosphate group

Configuration σ_1 σ_2 σ_3 σ_4	Number of Protons attached to PO_4	Energy compared to the ground state	Energy compared to the first two configurations	Dipole moment in units of μ
$- + - +$	2	$-4J_{12}+2J_{13}+K$	0	2
$+ - + -$	2			-2
$+ + - -$	2	$-2J_{13}+K$	ϵ	0
$+ - - +$				
$- + + -$				
$- - + +$				
$+ - - -$	1	$-K$	w	-1
$- + - -$				1
$- - + -$				-1
$- - - +$				1
$- + + +$	3			1
$+ - + +$				-1
$+ + - +$				1
$+ + + -$				-1
$- - - -$	0	$4J_{12}+2J_{13}+K$	w	0
$+ + + +$	4			0

away from the phosphate group are marked by $\sigma_j = -$ ('left' position). Comparing the third and fourth columns we obtain

$$\epsilon = 4J_{12} - 4J_{13}, \tag{3.9}$$

$$w = 4J_{12} - 2J_{13} - 2K, \tag{3.10}$$

$$w_1 = 8J_{12}. \tag{3.11}$$

Here the energy parameters ϵ, w and w_1 characterize the configurations as compared to the configuration observed by neutron diffraction, $\sigma_1 = \sigma_3 = -$; $\sigma_2 = \sigma_4 = +$.

The various energy levels are related to the various models, and this is illustrated in Fig. 3. Here we bring the well-known and best studied models in the current literature which deal with ferroelectricity in crystals having the structure of KDP. These are the Slater model (where $w = w_1 = \infty$), the Takagi model (where only $w_1 \to \infty$), and the Blinc model.

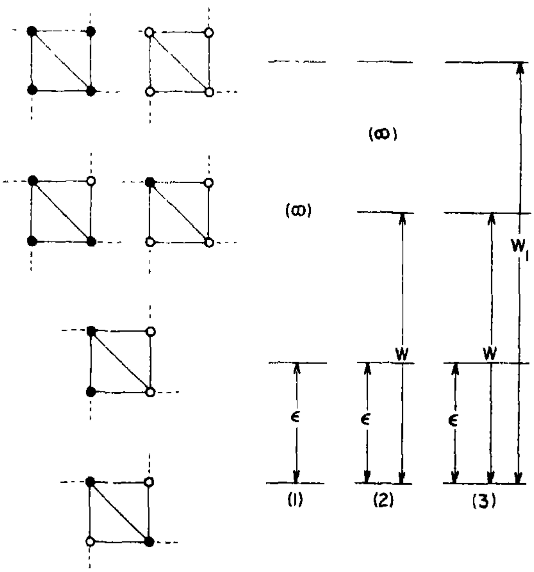

Fig. 3. The various energy levels of the phosphate group in relation to the models due to Slater[1], Takagi[2] and Blinc[3]; ● denotes the proton site close to PO_4, ○ the proton site away from PO_4.

The dipole moment in units of μ (μ is the magnitude of the dipole moment of a $[K^+ - (H_2PO_4)^-]$ complex) for various proton configurations is listed in the last column in

Table 1. Following the original Slater theory of the phase transition we associate the dipole moments to the four proton positions around the central phosphate group as follows: $\mu_1 = \mu_3 = -\mu/2$, $\mu_2 = \mu_4 = \mu/2$. The total dipole moment is then given in the last column. In the original Slater model the crystal has only two states, one is the perfectly ordered state in which all dipoles point in the same direction ($\pm Z$-axis), the other is the completely disordered state in which the dipoles are perpendicular to this direction. No intermediate states are allowed so that the ordered state has the maximum possible dipole moment and polarization, while the disordered state has no net polarization.

Using the Slater model we can compute the transition temperature. Let us assume that there are N phosphate groups and $2N$ hydrogens in the crystal. The perfectly disordered state (dip. moment 0) is distinguished from the perfectly ordered state (dip. moment $\pm 2\mu$) by the energy ϵ.

The probability that all N phosphate groups occupy the energy ϵ is given by

$$P(\beta) = \sum_{j=1}^{N} \exp(-\beta j\epsilon), \qquad (3.12)$$

where $\beta = (kT)^{-1}$, k is the Boltzmann constant, T is the absolute temperature. Now we may define the transition temperature as the temperature at which the probability of all dipoles being perpendicular to the direction a_3 is equal to one, i.e.

$$P(\beta_c) = 1, \qquad (3.13)$$

where $\beta_c = (kTc)^{-1}$, Tc denotes the transition temperature. If we extend the sum (3.12) over $N \to \infty$ then we recover the Slater result

$$\epsilon = kT_c \, . \ln 2. \qquad (3.14)$$

The Slater model cannot explain satisfactorily the large isotope effect which is manifested in deuterated compounds. Since upon deuteration the transition temperature is almost doubled, the energy ϵ should then also be almost doubled. However, this is unacceptable because the energies ϵ, w and w_1 come from an expansion of the potential energy and must not therefore depend on the mass of the proton.

It is possible to relate the energy parameters A, B_{12}, B_{13}, C, and D to the energies ϵ, w and w_1. Using the data in Table 1 and the transformation $n_j = (1-\sigma_j)/2$ we obtain

$$A = -w_1 + w, \quad B_{12} = w_1 - 2w + \epsilon \qquad (3.15)$$
$$B_{13} = B_{12} - \epsilon, \quad C = -w_1 + 4w - 2\epsilon, \quad D = -2C.$$

The above energy parameters are associated with an expansion of the potential energy of the system of protons. So far as we consider a single phosphate group, the energies ϵ, w and w_1 are independent from each other, but when we look at the crystal as a whole, this may not be so. To find a possible relationship between these energies we require that the zeroth order term $(-U_0)$ is the expansions (2.34) and (3.2) be invariant under the transformation $n_j = (1-\sigma_j)/2$. Indeed, setting up $\sigma_j \to 0$ and $n_j \to \frac{1}{2}$ in equations (2.34) and (3.2), we obtain

$$\left[\sum_{jp} U(\vec{R}_{jp})\right]_{\sigma_j \to 0} = -U_0, \qquad (3.16a)$$

$$\left[\sum_{jp} U(\vec{R}_{jp})\right]_{n_j \to \frac{1}{2}} = -U_0 + \left(A + B_{12} + \frac{B_{13}}{2} + \frac{C}{2} + \frac{D}{16}\right)N, \qquad (3.16b)$$

where N denotes the total number of phosphate groups. Equations (3.16a,b) should be equal, hence the second term in equation (3.16b) must vanish. If we insert here the values from equation (3.15) we obtain the following condition:

$$w_1 = 4w - 2\epsilon. \qquad (3.17)$$

This is a remarkable result which shows that the energies of the proton configurations as classified in Table 1 are not mutually independent.

Using the above relation we can re-evaluate the various energy parameters appearing in the expansions (2.34) and (3.2). The result is

$$A=-3w+2\epsilon,\quad B_{12}=2w-\epsilon,\quad B_{13}=B_{12}-\epsilon,$$

$$C=D=K=0, J_{12}=\frac{(2w-\epsilon)}{4};$$

$$J_{13}=\frac{(w-\epsilon)}{2}. \quad (3.18)$$

Suppose now that the system has achieved a thermal equilibrium which can be characterized by an average value of the variable σ_j, say $\langle\sigma_+\rangle$ if $\sigma_j>0$, and $\langle\sigma_-\rangle=-\langle\sigma_+\rangle$. In this case a single proton (e.g. $j=1$ in Fig. 1) has the following potential energy with regard to the phosphate group

$$U_1=(2J_{12}-J_{13})\langle\sigma_+\rangle\sigma_1 \quad (3.19)$$

(the constant term U_0 is omitted). When this proton jumps from one phosphate group to the other its potential energy changes by

$$\Delta U_1=U_1(\sigma_1=+)-U_1(\sigma_1=-). \quad (3.20)$$

Using equations (3.18) and (3.19) we obtain the following change of the potential energy

$$\Delta U_1=(4J_{12}-2J_{13})\langle\sigma_+\rangle=w\langle\sigma_+\rangle, \quad (3.21\text{a})$$

where the thermal average is defined by a self-consistent equation

$$\langle\sigma_+\rangle=-\frac{Tr\sigma_1\exp(-\beta U_1)}{\sum\limits_{\sigma_1}Tr\exp(-\beta U_1)}=th\frac{\beta\Delta U_1}{2}. \quad (3.21\text{b})$$

Equations (3.21a, b) could have been obtained if we started from

$$U_1=An_1+[2B_{12}\langle n\rangle+B_{13}(1-\langle n\rangle)]n_1, \quad (3.22)$$

where

$$\langle n\rangle=\tfrac{1}{2}(1-\langle\sigma_+\rangle). \quad (3.23)$$

By equation (3.18)

$$\Delta U_1=U_1(n_1=0)-U_1(n_1=1) \quad (3.24)$$

gives equations (3.21a, b).

Equations (3.21a, b) are very fundamental relations in the present theory. As we know, any change of the potential energy, if no external forces act on the system, must be equal to the change of the kinetic energy. We shall see later that this condition is sufficient to explain a large isotope effect on the magnitude of the transition temperature.

4. THE CHARACTERISTIC ENERGIES

Write the Hamiltonian (2.38) in the form

$$H=H_0+H_1 \quad (4.1)$$

$$H_0=\sum_{j\rho\alpha}\omega_\alpha\mathbf{a}^\dagger_{j\rho\alpha}\mathbf{a}_{j\rho\alpha}, \quad (4.2)$$

$$\omega_\alpha\equiv\omega(\alpha,\alpha), \quad (4.3)$$

$$H_1=\sum_{j\rho\alpha\neq\alpha'}\omega(\alpha,\alpha')\mathbf{a}^\dagger_{j\rho\alpha}\mathbf{a}_{j\rho\alpha'}, \quad (4.4)$$

where the matrix element $\omega(\alpha,\alpha')$ is given by equation (2.39). We write

$$\omega(\alpha,\alpha')=\Omega(\alpha,\alpha')+An(\alpha,\alpha'), \quad (4.5)$$

$$\Omega(\alpha,\alpha')=\Omega(\alpha',\alpha)=\frac{\hbar^2}{2m}\int_{-\infty}^{\infty}$$

$$\times\frac{d\psi^*_\alpha(x)}{dx}\cdot\frac{d\psi_{\alpha'}(x)}{dx}dx, \quad (4.6)$$

$$n(\alpha,\alpha')=n(\alpha',\alpha)=\int_{-\infty}^{\infty}\psi^*_\alpha(x)n\psi_{\alpha'}(x)dx. \quad (4.7)$$

Using the wave functions (2.16)-(2.19), we obtain

$$\Omega(0,0)=\frac{\hbar\omega_{\text{class}}}{2}C_0{}^2\left[1-(\eta-1)\exp\left(-\frac{\eta}{2}\right)\right], \quad (4.8)$$

$$\Omega(1,1) = \frac{\hbar\omega_{\text{class}}}{2} C_1^2\left[1 + (\eta - 1)\exp\left(-\frac{\eta}{2}\right)\right], \tag{4.9}$$

$$\Omega(0,1) = \Omega(1,3) = \Omega(0,2) = \Omega(2,3) = 0, \tag{4.10}$$

$$\Omega(1,2) = \eta_1\Omega(1,1), \tag{4.11}$$

$$\Omega(0,3) = \eta_0\Omega(0,0), \tag{4.12}$$

$$\Omega(2,2) = \tfrac{3}{2}\,\hbar\omega_{\text{class}}\, C_2^2\left[1 - (1 - 2\eta + \tfrac{1}{3}\eta^2)\exp\left(-\frac{\eta}{2}\right)\right] + \eta_1^2\Omega(1,1), \tag{4.13}$$

$$\Omega(3,3) = \tfrac{3}{2}\,\hbar\omega_{\text{class}}\, C_3^2\left[1 + (1 - 2\eta + \tfrac{1}{3}\eta^2)\exp\left(-\frac{\eta}{2}\right)\right] + \eta_0^2\Omega(0,0). \tag{4.14}$$

Let us define

$$\int |\psi_{R0}(x)|^2 n dx = \int |\psi_{L0}(x)|^2 n dx = 1, \tag{4.15}$$

$$\int \psi^*_{R\mu}(x) n \psi_{L\nu}(x) dx = 0, \quad \mu,\nu = 0,1, \tag{4.16}$$

$$\int |\psi_{R1}(x)|^2 n dx = \int |\psi_{L1}(x)|^2 n dx = 0, \tag{4.17}$$

where the above integrals are extended from $-\infty$ to ∞. Using these integrals the matrix elements (4.7) become

$$n(0,1) = n(1,3) = n(0,2) = n(2,3) = 0, \tag{4.18}$$

$$n(0,0) = 2C_0^2, \tag{4.19}$$

$$n(1,1) = 2C_1^2, \tag{4.20}$$

$$n(1,2) = 2C_1\eta_1, \tag{4.21}$$

$$n(0,3) = 2C_0\eta_0, \tag{4.22}$$

$$n(2,2) = 2C_1^2\eta_1^2, \tag{4.23}$$

$$n(3,3) = 2C_0^2\eta_0^2, \tag{4.24}$$

where the coefficients C_α, η_0 and η_1 are given in Section 2.

We can estimate the order of magnitude of these matrix elements. Taking the value $\hbar\omega_{\text{class}} = 2000\ \text{cm}^{-1}$ ($\simeq 250$ meV) for KDP(p) and the value $a \cong 0{\cdot}40$ Å as derived from the measurement of Bacon and Pease[1] we obtain $\eta \simeq 5{\cdot}34$. We shall assume in the present analysis that the value of η does not depend on the mass of the particle. The nonvanishing matrix elements are listed in Table 2. The first four columns of this table give the diagonal elements, and the effect coming from the off-diagonal elements is given in the last two columns. The energy differences as predicted by the present method are given in Table 3. Here we take $n(0,0) = n(1,1) = 1$, and all the remaining $n(\alpha,\alpha') = 0$.

There has been so far only one experiment on the vibrational spectrum of KDP in the frequency region which is analyzed in the present work. By measuring the laser-excited Raman spectra, Kaminow *et al.*[15] were able to locate three strong proton lines in KDP(p) at the frequencies 2705, 2360 and 1790 (cm^{-1}), and also the deuteron lines in KDP(d) at the frequencies 1990, 1770 and 1370 (cm^{-1}). It can be observed that these frequencies are in agreement with the calculations in Table 3 and Fig. 4.

Next we shall briefly discuss the isotope effect. In a system having a large number of protons there must be established a state of equilibrium in which a change of potential energy is equal to the change of kinetic energy, i.e.

$$\Delta U_1 = \Delta E_{\text{kin}} \tag{4.25}$$

Table 2. The matrix elements $\Omega(\alpha,\alpha')$(in terms of $\hbar\omega_{\text{class}}$) and $n(\alpha,\alpha')$ *are calculated using the value* $\eta = 5{\cdot}34$

$\Omega(0,0)$	$\Omega(1,1)$	$\Omega(2,2)$	$\Omega(3,3)$	$\Omega(1,2)$	$\Omega(0,3)$
0·163	0·350	0·573	1·001	0·069	−0·043
$n(0,0)$	$n(1,1)$	$n(2,2)$	$n(3,3)$	$n(1,2)$	$n(0,3)$
0·935	1·075	0·041	0·065	0·288	−0·362

Table 3. The energy differences as predicted by the present method using $n(0,0) = n(1,1) = 1$, *and the remaining* $n(\alpha,\alpha') = 0$

Units cm^{-1}	ω_{class}	$\lvert A\rvert$	$\omega_1 - \omega_0$	$\omega_2 - \omega_1$	$\omega_3 - \omega_2$
KDP(p)	2000	1000	374	1446	856
KDP(d)	1400	1000	261	1312	599

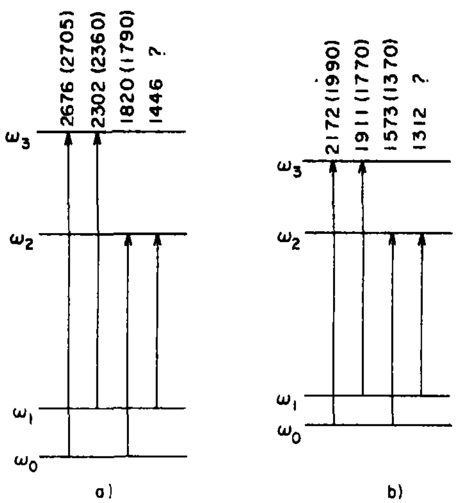

Fig. 4. The characteristic energies in units cm^{-1} calculated for KDP(p)[a] and KDP(d)[b]. The measured laser-excited Raman spectra as quoted by Kaminow *et al.*[15] are given in brackets.

where ΔU_1 is given by equation (3.21a). To calculate $\Delta E_{\rm kin}$ we assume that the proton makes important transitions only between the states with the energies ω_0 and ω_1. Using equations (3.21a) and (4.25) we obtain

$$\Delta E_{\rm kin} = w\,\mathrm{th}\frac{\Delta E_{\rm kin}}{2kT}. \qquad (4.26)$$

We may define the transition temperature by

$$\Delta E_{\rm kin} = \omega_1 - \omega_0,$$

hence

$$\omega_1 - \omega_0 = w\,\mathrm{th}\frac{\omega_1 - \omega_0}{2kT_c}. \qquad (4.27)$$

The isotope effect is most clearly manifested in increasing the transition temperature upon deuteration. If we take

$$(\omega_1 - \omega_0)_p \simeq w \qquad (4.28a)$$

$$(\omega_1 - \omega_0)_p \gg kTcp, \qquad (4.28b)$$

Equation (4.27) leads to

$$\sqrt{2}\,\mathrm{th}\frac{(\omega_1 - \omega_0)_d}{2kT_{cd}} = 1, \qquad (4.29)$$

or

$$kT_{cd} = \frac{(\omega_1 - \omega_0)_d}{\ln 5{\cdot}8}. \qquad (4.30)$$

Taking $(\omega_1 - \omega_0)_d = 261$ cm^{-1} (see Table 3) and using equation (4.30) we obtain $T_{cd} = 215$°K. This agrees fairly well with experiment.

It should be emphasized that the Hamiltonian H_1 given by equation (4.4) may produce slight changes in the energy differences $\omega_\alpha - \omega_{\alpha'}$. These changes are closely related to the lifetimes of the characteristic states and are the subject in one of the following papers.

5. THE FERROELECTRIC MODE

In the present section we shall consider small fluctuations around the well defined energy differences $\omega_\alpha - \omega_{\alpha'}$. In particular, we shall be concerned with the energy difference $\omega_1 - \omega_0$ which is important for a dynamical behaviour of the system of protons as temperature approaches the point T_c. Taking the term $\omega_\alpha \mathbf{a}_{j\alpha}^\dagger \mathbf{a}_{j\alpha}$, $\alpha = 0,1$, from the second quantization and assuming that all σ_j's appearing in the potential energy are dynamical variables, we can write

$$H = \sum_j (\omega_1 - \omega_0)\sigma_{xj} + \sum_{(jk)} J_{jk}\sigma_{zj}\sigma_{zk}, \qquad (5.1)$$

$$\sigma_{xj} = 1 - 2\mathbf{b}_j^\dagger \mathbf{b}_j, \qquad (5.2)$$

$$\sigma_{zj} = \mathbf{b}_j^\dagger + \mathbf{b}_j, \qquad (5.3)$$

where the operators $\mathbf{b}_j^\dagger$ and $\mathbf{b}_j$ create and annihilate a fluctuation at the lattice site j. The representation (5.1)–(5.3) has a physical meaning so long as the thermal average $\langle \mathbf{b}_j^\dagger \mathbf{b}_j \rangle$ is small compared to one. In this case we speak in terms of a set of boson operators satisfying the commutation relation

$$[\mathbf{b}_j, \mathbf{b}_k^\dagger] = \delta_{jk}. \qquad (5.4)$$

Note that for the sake of simplicity we assume one proton per unit cells. The energy parameters J_{jk} are those of Section 2. It is useful to make a transfer from the coordinate representation to the momentum representation; therefore, we introduce a Fourier transform

$$\mathbf{b}_p^\dagger = N^{-1/2} \sum_j \exp(-i\vec{p}\,.\,\vec{r}_j)\mathbf{b}_j^\dagger,$$

$$\mathbf{b}_p = N^{-1/2} \sum_j \exp(i\vec{p}\,.\,\vec{r}_j)\mathbf{b}_j, \tag{5.5}$$

where

$$[\mathbf{b}_p, \mathbf{b}_{p'}^\dagger] = \delta_{pp'}, \tag{5.6}$$

N is the total number of unit cells and $\vec{p}$ is defined by equation (2.8). Clearly we have

$$\mathbf{b}_j^\dagger = N^{-1/2} \sum_p \exp(i\vec{p}\,.\,\vec{r}_j)\mathbf{b}_p^\dagger$$

$$\mathbf{b}_j = N^{-1/2} \sum_p \exp(-i\vec{p}\,.\,\vec{r}_j)\mathbf{b}_{\vec{p}}. \tag{5.7}$$

Next we study the dynamical behaviour of the system of protons at the temperature $T = T_c$. Introduce the following unitary transformation

$$\sigma_x \rightarrow \cos\phi\,\sigma_{x'} + \sin\phi\,\sigma_{z'}$$

$$\sigma_z \rightarrow -\sin\phi\,\sigma_{x'} + \cos\phi\,\sigma_{z'} \tag{5.8}$$

at every lattice site. Here ϕ denotes the angle enclosed by the axis (z,z') and is independent of the lattice sites. The present method should be understood in the sense of the limit $\sin\phi \rightarrow 1$, $\cos\phi \rightarrow 0$. This angle can be determined by a self-consistent equation

$$H_{\text{SCF}} \sin\phi = \omega_1 - \omega_0 \tag{5.9a}$$

$$H_{\text{SCF}} \cos\phi = w\langle\sigma_z\rangle \tag{5.9b}$$

$$w = 4J_{12} - 2J_{13}, \tag{5.9c}$$

where H_{SCF} denotes the magnitude of the self-consistent field. This quantity is determined by

$$H_{\text{SCF}} = w\langle\sigma_{z'}\rangle = w\,\text{th}\,\frac{H_{\text{SCF}}}{2kT}, \tag{5.10}$$

where $T \rightarrow T_c$. At the transition point we have $\langle\sigma_z\rangle = 0$ leading to

$$H_{\text{SCF}}(T = T_c) = \omega_1 - \omega_0, \tag{5.11}$$

and this agrees with equation (4.27).

Using equations (5.2), (5.3) and (5.8) we obtain the transformation

$$\sigma_{xj} \rightarrow (1 - 2\mathbf{b}_j^\dagger\mathbf{b}_j)\sin\phi + (\mathbf{b}_j^\dagger + \mathbf{b}_j)\cos\phi$$

$$\phi_{zj} \rightarrow (1 - 2\mathbf{b}_j^\dagger\mathbf{b}_j)\cos\phi - (\mathbf{b}_j^\dagger + \mathbf{b}_j)\sin\phi. \tag{5.12}$$

With the help of equations (5.12) the Hamiltonian (5.1) becomes

$$H = N(\omega_1 - \omega_0) - 2w\cos^2\phi \sum_p \mathbf{b}_{\vec{p}}^\dagger\mathbf{b}_{\vec{p}}$$

$$+ \sum_p w(\vec{p})(2\mathbf{b}_{\vec{p}}^\dagger\mathbf{b}_p + \mathbf{b}_{-\vec{p}}^\dagger\mathbf{b}_{\vec{p}}^\dagger + \mathbf{b}_{\vec{p}}\mathbf{b}_{-\vec{p}}), \tag{5.13}$$

$$w(\vec{p}) = 2[J_{12}(\vec{p}) - J_{13}(\vec{p}) + J_{14}(\vec{p})]\sin^2\phi, \tag{5.14}$$

$$J_{jk}(\vec{p}) = J_{jk}\exp[i\vec{p}(\vec{r}_j - \vec{r}_k)], \tag{5.15}$$

where we subtracted the term with $\vec{p} = 0$ which is the only contribution coming from the part $\Sigma\,(\omega_1 - \omega_0)\sigma_{xj}$. The first and third order term in the creation and annihilation operators are not considered since their contribution to the above Hamiltonian is proportional only to $\cos\phi$. If $\cos\phi \rightarrow 0$, then $T \rightarrow T_c$ and the system achieves a ground state. Thus the ground state is sharply defined only at the transition temperature. In the present analysis the transition temperature may differ from the Curie temperature which is defined as the point where the dielectric susceptibility becomes infinite.

If we disregard the constant term then the Hamiltonian (5.13) has two major terms; one containing $w\cos^2\phi$ ('unperturbed' energy) and the other containing $w(\vec{p})$ ('perturbational' energy). As $\cos\phi \rightarrow 0$ the unperturbed energy becomes much smaller compared to the perturbation and therefore the use of ordinary perturbation theory becomes unjustified. In order to diagonalize the above Hamiltonian we shall use a linear Bobolubov transformation. For a many-particle system the Bogolubov transformation consists of the set of operators

$$\begin{aligned} \mathbf{B}_p^\dagger &= u(\vec{p})\mathbf{b}_p^\dagger - v(\vec{p})\mathbf{b}_{-\vec{p}} \\ \mathbf{B}_p &= u(\vec{p})\mathbf{b}_{\vec{p}} - v(\vec{p})\mathbf{b}_{-\vec{p}}^\dagger, \end{aligned} \tag{5.16}$$

where $u(\vec{p})$ and $v(\vec{p})$ are even and real functions of the reciprocal lattice vector $\vec{p}$. These operators satisfy the commutation relation

$$[\mathbf{B}_{\vec{p}},\mathbf{B}_{\vec{p}'}^\dagger] = \delta_{\vec{p}\vec{p}'}, \tag{5.17}$$

where we have used the relation

$$u^2(\vec{p}) - v^2(\vec{p}) = 1. \tag{5.18}$$

Clearly we have

$$\begin{aligned} \mathbf{b}_{\vec{p}}^\dagger &= u(p)\mathbf{B}_{\vec{p}}^\dagger + v(p)\mathbf{B}_{-\vec{p}} \\ \mathbf{b}_{\vec{p}} &= u(p)\mathbf{B}_{\vec{p}} + v(p)\mathbf{B}_{-\vec{p}}^\dagger. \end{aligned} \tag{5.19}$$

Suppose that the Hamiltonian (5.13) is written in the form

$$H = N(\omega_1 - \omega_0) - \sum_{\vec{p}} \epsilon(\vec{p})\mathbf{B}_{\vec{p}}^\dagger\mathbf{B}_{\vec{p}}. \tag{5.20}$$

Now applying the operational identity

$$[AB,C] = A[B,C] + [A,C]B$$

we find the following equations of motion

$$\begin{aligned} [H,\mathbf{B}_{\vec{p}}^\dagger] &= -\epsilon(\vec{p})\mathbf{B}_{\vec{p}}^\dagger \\ [H,\mathbf{B}_{\vec{p}}] &= \epsilon(\vec{p})\mathbf{B}_{\vec{p}}. \end{aligned} \tag{5.21}$$

On the other hand, using equations (5.13) and (5.16) we obtain

$$\begin{aligned} [H,\mathbf{B}_{\vec{p}}^\dagger] = {} & (-x(\vec{p})u(\vec{p}) + w(\vec{p})v(\vec{p}))\mathbf{b}_{\vec{p}}^\dagger \\ & +(-x(\vec{p})v(\vec{p}) + w(\vec{p})u(\vec{p}))\mathbf{b}_{-\vec{p}} \end{aligned} \tag{5.22a}$$

$$\begin{aligned} [H,\mathbf{B}_{\vec{p}}] = {} & (x(\vec{p})v(\vec{p}) - w(\vec{p})u(\vec{p}))\mathbf{b}_{-\vec{p}}^\dagger \\ & +(x(\vec{p})u(\vec{p}) - w(\vec{p})v(\vec{p}))\mathbf{b}_{\vec{p}} \end{aligned} \tag{5.22b}$$

$$x(\vec{p}) = w\cos^2\phi - w(\vec{p}). \tag{5.23}$$

Comparing equations (5.22a, b) with equations (5.21) we obtain the determinant

$$\begin{vmatrix} -x(\vec{p}) + \epsilon(\vec{p}) & w(\vec{p}) \\ w(\vec{p}) & -x(\vec{p}) - \epsilon(\vec{p}) \end{vmatrix} = 0 \tag{5.24}$$

which has the solution

$$\epsilon^2(\vec{p}) = x^2(\vec{p}) - w^2(\vec{p}). \tag{5.25}$$

We shall refer to this expression as the dispersion relation for the ferroelectric ground state, i.e. the relation between the frequency of the normal hydrogen vibrational mode and the momentum $\vec{p}$ ('ferroelectric' mode).

For small values of $|\vec{p}|$ this frequency behaves like

$$\epsilon^2(\vec{p}) = -\epsilon_c^2 + Qp^2, \tag{5.26}$$

where $\lim \epsilon_c \to 0$ as $T \to T_c$. Indeed, we expand every function $J_{jk}(\vec{p})$ around the point $p = 0$, by writing

$$\exp[i\vec{p}\,.\,(\vec{r}_j - \vec{r}_k)] = 1 - \tfrac{1}{2}p^2|\vec{r}_j - \vec{r}_k|^2\cos^2\gamma_{jk}, \tag{5.27}$$

$$\gamma_{jk} = \text{angle}\,(\vec{p}, \vec{r}_j - \vec{r}_k). \tag{5.28}$$

There follows the equation

$$\begin{aligned} w(\vec{p}) = {} & w\sin^2\phi - (J_{12}\cos^2\gamma_{12} - J_{13}\cos^2\gamma_{13} \\ & + J_{14}\cos^2\gamma_{14})d^2\sin^2\phi\,.\,p^2 + \cdots \end{aligned} \tag{5.29}$$

where $d = |\vec{r}_j - \vec{r}_k|$ is of the order of 4·5 Å for the crystal under investigation. Now using equations (5.27)–(5.29) we obtain equation (5.26) where

$$\epsilon_c^2 = w^2\cos^2\phi\,(2 - 3\cos^2\phi), \tag{5.30}$$

$$\begin{aligned} Q = {} & 2w\cos^2\phi\sin^2\phi\,(J_{12}\cos^2\gamma_{12} - J_{13}\cos^2\gamma_{12} \\ & + J_{14}\cos^2\gamma_{14})d^2. \end{aligned} \tag{5.31}$$

This completes the formulation of the ferroelectric mode. Notice that $\epsilon(\vec{p})$ was found to behave like[16, 17]

$$\epsilon^2(p) \sim P|T-T_c|+Qp^2 \qquad (5.32)$$

with Q being the temperature independent parameter. According to our equations (5.26)–(5.31) this mode should vanish completely at $T=T_c$. It is possible to reproduce the term $P|T-T_c|$ from our equation (5.26) and (5.30) if $\cos^2\phi$ is assumed to behave like $\cos^2\phi \sim |T-T_c|$ so that $\cos\phi \rightarrow 0$ when $T \rightarrow T_c$. But even in this case the coefficient Q is temperature dependent. following the behaviour $Q \sim |T-T_c|$.

Using equations (5.9a) and (5.10) we can expand H_{SCF} just below the transition point T_c. The result is

$$H_{\mathrm{SCF}} = (\omega_1-\omega_0)(1+\lambda|T-T_c|+\cdots), \qquad (5.33)$$

where the expansion coefficient λ is given by the first derivative

$$\lambda = (\omega_1-\omega_0)^{-1}\left.\frac{dH_{\mathrm{SCF}}}{dT}\right|_{T=T_c} \qquad (5.34)$$

$$= \frac{w(1-z^2)}{T_c[2kT_c-w(1-z^2)]},$$

$$z = \frac{\omega_1-\omega_0}{w}. \qquad (5.35)$$

It can be seen that z is always smaller than 1 and that λ is always positive at the point of the phase transition. Next we expand the functions $\sin\phi$ and $\cos\phi$ in the neighbourhood of $T=T_c$. The result is

$$\sin\phi = \begin{array}{l} 1-\lambda|T-T_c|, \quad T<T_c, \\ 1, T>T_c, \end{array} \qquad (5.36)$$

$$\cos^2\phi = \begin{array}{l} 2\lambda|T-T_c|, \quad T<T_c, \\ 0, \quad T>T_c. \end{array} \qquad (5.37)$$

It is possible to obtain a similar expansion for the ferroelectric mode. For small values of p the frequency $\epsilon(\vec{p})$ can be written

$$\epsilon(\vec{p}) \simeq i\epsilon_c+\sqrt{Q}p \qquad (5{,}38)$$

where ϵ_c is a small imaginary part. Using equations (5.30), (5.31), (5.36), and (5.37) we obtain

$$\epsilon_c = \begin{array}{l} 2w\sqrt{\lambda}|T-T_c|^{1/2}, \quad T<T_c, \\ 0, \quad T>T_c, \end{array} \qquad (5.39)$$

$$\sqrt{Q} = \begin{array}{l} 2\sqrt{\lambda w}|T-T_c|^{1/2}d(J_{12}\cos^2\gamma_{12} \\ -J_{13}\cos^2\gamma_{13}+J_{14}\cos^2\gamma_{14})^{1/2}, T<T_c, \\ 0, \quad T>T_c. \end{array} \qquad (5.40)$$

If $p=0$, the the frequency $\epsilon(\vec{p})$ is purely imaginary and ϵ_c is identical with the damping constant. If $p \simeq p_{\min} = \epsilon_c/\sqrt{Q}$ then the mode can be observed at temperatures close to T_c.

6. DISCUSSION AND CONCLUDING REMARKS

There are several points at which the present theory can be tested by experiment apart from the characteristic energies already compared to the laser-excited Raman spectra.

(i) The arrangement of the four hydrogen atoms around the central phosphate group indicates a coupling between the two sublattices (Fig. 1), one containing the protons $H1$ and $H3$, the other containing $H2$ and $H4$. This coupling is most manifestly seen in the terms $\eta\exp(-\eta/2)$, equations (3.8)–(3.14). It is natural to assume that these terms depend only on the lattice constants but not on the mass of the proton. Therefore, we assume that η has the same value for both crystals. This can be tested by measuring a neutron diffraction on KD_2PO_4. The relation

$$\eta(\mathrm{OD..O}) = \eta(\mathrm{OH..O}) \qquad (6.1)$$

gives

$$\frac{a(\mathrm{OH...O})}{a(\mathrm{OD...O})} = \left(\frac{m_d}{m_p}\right)^{1/4} \simeq 1{\cdot}19, \qquad (6.2)$$

where $m_{p,d}$ is the mass of the proton (deuteron). If we take $a(\mathrm{OH}\ldots\mathrm{O}) \simeq 0{\cdot}40$ Å at low temperatures then we should expect $a(\mathrm{OD}\ldots\mathrm{O}) \simeq 0{\cdot}33$ Å.

(ii) The present method can explain satisfactorily the isotope effect concerning the transition temperature. There is another problem closely related to the mass, namely the saturation value of the spontaneous polarization P_s at low temperatures. It is likely that P_s at $T < T_c$ depends on the thermal average $\langle\sigma_z\rangle$ so that P_s vanishes at T_c and has a maximum at 0°K. Using equations (5.9a–c) we obtain the following values at 0°K

$$H_{\mathrm{SCF}} = w, \tag{6.3a}$$

$$\sin\phi = th\frac{\omega_1-\omega_0}{2kT_c}, \tag{6.3b}$$

$$\langle\sigma_z\rangle = \cos\phi. \tag{6.3c}$$

Numerical calculations are given in Table 4. It may be observed from the third column of this table that the degree of saturation is approximately 30 per cent for KDP(p) and approximately 70% for KDP(d). It is interesting to note that the maximum value for T_c is obtained in the limiting case $\omega_1 \to \omega_0$; there follows from equation (5.10)

$$kT_{c0} = \frac{w}{2} \tag{6.4}$$

$$\langle\sigma_z\rangle_{\max} = 1. \tag{6.5}$$

(iii) The ferroelectric mode can be observed by measuring an inelastic scattering of neutrons. The minimum energy required for the reaction

$$n + H \to n' + H \tag{6.6}$$

to take place can be calculated. Here H denotes the proton bound by the crystal, n and n' denote the neutron before and after the scattering. Using equation (5.26) we obtain the following condition for the reciprocal lattice vector

$$\epsilon^2(\vec{p}) \geqslant 0 \tag{6.7}$$

$$p \geqslant p_{\min} = \frac{\epsilon_c}{\sqrt{Q}} = \frac{\sqrt{w/2}\sqrt{2-3\cos^2\phi}}{d[J_{12}\cos^2\gamma_{12}-J_{13}\cos^2\gamma_{13}+J_{14}\cos^2\gamma_{14}]^{1/2}\sin\phi}. \tag{6.8}$$

Now the wavelength of the neutron is given by $\lambda = 2\pi/p$ so that the maximum value in the neighbourhood of T_c

$$\lambda_{\max} = \frac{2\pi}{p_{\min}} \simeq 2\pi\cdot\frac{d[J_{12}\cos^2\gamma_{12}-J_{13}\cos^2\gamma_{13}+J_{14}\cos^2\gamma_{14}]^{1/2}}{\sqrt{w}}. \tag{6.9}$$

The minimum energy required according to equation (6.8) is given by

$$E_{n'} - E_n = \frac{\hbar^2 p_{\min}^2}{2m_n} \sim 1\ \mathrm{meV}, \tag{6.10}$$

where m_n denotes the mass of the neutron.

Table 4. The values of $\sin\phi$ and $\langle\sigma_z\rangle$ *at the absolute zero using equations* (6.3a–c)

	T_c(°K)	$\sin\phi$	$\langle\sigma_z\rangle = \cos\phi$
KDP(p)	122	0·96	0·3
KDP(d)	223	0·70	0·7

REFERENCES

1. BACON G. E. and PEASE R. S., *Proc. R. Soc.* **A230**, 359 (1955).
2. MEGAW H., *Ferroelectricity in Crystals*, Chap. 3. Methuen, London (1957).
3. SLATER J. C., *J. chem. Phys.* **9**, 16 (1941).
4. LANDAU L. D. and LIFSHITZ E. M., *Statistical Physics*. Pergamon Press, Oxford (1958).
5. TAKAGI Y., *J. phys. Soc. Japan* **3**, 271 (1948).
6. AZOULAY J., GRINBERG Y., PELAH I. and WIENER E. *J. Phys. Chem. Solids* **29**, 843 (1968).
7. PIRENNE J., *Physica* **15**, 1019 (1949).
8. BLINC R., *J. Phys. Chem. Solids* **13**, 204 (1960).

9. BLINC R. and HADZI D., *Molec. Phys.* **1**, 391 (1958).
10. LAZAREV A. N. and ZAITSEVA A. S., *Soviet Phys. solid St.* **2**, 2688 (1961).
11. BARKER A. S. and TINKHAM J., *J. chem. Phys.* **38**, 2257 (1963).
12. TOKUNAGA M. and MATSUBARA T., *Prog. theor. Phys.* **35**, 581 (1966); **36**, 857 (1966).
13. NOVAKOVIC L., *J. Phys. Chem. Solids* **27**, 1469 (1966); *Proc. int. Mtg Ferroelectricity*, Vol. I, p. 127, Prague (1966).
14. NOVAKOVIC L., *Boris Kidric Bull.* **18**, 23 (1967).
15. KAMINOW I. P., LEITE R. C. C. and PORTO S. P. S., *J. Phys. Chem. Solids* **26**, 2085 (1965).
16. VILLAIN J. and STAMENKOVIĆ S., *Phys. Status Solidi* **15**, 585 (1966).
17. PYTTE E. and THOMAS H., *Phys. Rev.* **175**, 610 (1968).

J. Phys. Chem. Solids Pergamon Press 1970. Vol. 31, pp. 447–452. Printed in Great Britain.

SINGULARITIES IN THE AUGER EMISSION SPECTRUM OF METALS

M. NATTA and P. JOYES
Faculté des Sciences, Laboratoire de Physique des Solides.† 91-Orsay, France

(*Received* 9 *July* 1969)

Abstract—As for X-ray transitions, the Fermi statistic can play an important part in the Auger electron emission. This effect should be seen in the neighbourhood of the upper emission edge. We extend the Nozières and De Dominicis model to the Auger effect. The Auger spectrum shows similar singularities; however, the two most probable cases are: a zero upper threshold with either a zero or an infinite derivative. Some experiments are briefly discussed in the last part of this paper.

Résumé—Comme pour les transitions optiques la statistique de Fermi peut jouer un rôle important dans l'émission des électrons Auger. Cet effet doit être visible au voisinage du seuil d'émission supérieur. Nous étendons le modèle de Nozières et De Dominicis à l'effet Auger. Le spectre Auger présente des singularités semblables; cependant les deux cas les plus probables sont ceux d'un seuil supérieur nul avec une dérivée soit infinie, soit nulle. Nous discutons enfin les quelques expériences existantes.

1. INTRODUCTION

THE CURRENT calculations [1, 4] on the Auger emission in metals neglect the dynamical effects consecutive to the sudden switch of the potential associated to the deep hole. The problem is similar to the X-ray emission in metals [5–8]: the conduction electrons not directly involved in the Auger transition screen the potential V. This dynamical screening effect has several consequences [11] that we shall not repeat here. Nozières and De Dominicis [10] have given an exact solution of that problem in the neighbourhood of the X-ray edge for a separable potential V. For the Auger effect the form of the singularity is governed by two opposite factors: on one hand two electrons near the Fermi level (instead of one for the X-ray case) are now involved in the transition, and on the other hand the convolutive product of the density of state by itself starts with a zero value at the edge of the emission spectrum.

2. CALCULATION OF THE AUGER EMISSION NEAR THE UPPER EDGE

(1) *Response function associated to the Auger effect*

Most of the notations used in this paper are taken from the Nozières and De Dominicis paper. Let us first recall their simplified model [8, 9, 10]:

The conduction electrons are assumed to be free, with energy ϵ_k and creation operators $a^+_{k,\sigma}$. Let μ be the Fermi level. Coulomb interaction between conduction electrons is neglected.

The processes participating to the studied emission band are assumed to involve only a single localized deep state $|\psi_0>$ with energy E_0 and creation operator $b^+_\uparrow$.

The presence of the hole gives rise to a scalar potential $V(r)$. This appears in the following Hamiltonian:

$$H = \sum_{k,\sigma}\epsilon_k a^+_{k\sigma}a_{k\sigma} + E_0 b^+_\uparrow b_\uparrow + \sum_{kk'\sigma} V_{kk'}a^+_{k\sigma}a_{k'\sigma}b_\uparrow b^+_\uparrow \tag{1}$$

---

†Associated laboratory to the C.N.R.S.

The originality of the Auger emission is that it involves two electrons of the conduction band (Fig. 1): one electron filling the hole and the other being ejected. This is stated in the interaction potential H_A:

$$H_A = \sum_{k_1, k_2, K, \sigma} a^+_{K\sigma} b^\dagger_\uparrow a_{k_1\uparrow} a_{k_2\sigma} W(\mathbf{K}, \mathbf{k}_1, \mathbf{k}_2) + c.c. \tag{2}$$

We remark that if this term is obviously essential for the Auger transition it has been neglected in the Hamiltonian H; in that sense the ejected electron $|\mathbf{K} >$ is the equivalent of the electromagnetic field for the X-ray radiation.† For the estimation of $W(\mathbf{K}, \mathbf{k}_1, \mathbf{k}_2)$ we shall suppose that the localized state is an S state with wave function $\psi_0(r) = (\pi a^3)^{-1/2} e^{-r/a}$, and the interaction is of Coulomb type screened by a dielectric constant $\epsilon(\mathbf{q}, \omega)$ [3, 4]:

$$W(\mathbf{K}, \mathbf{k}_1, \mathbf{k}_2) = 32e^2 \left(\frac{\pi^3}{\Omega^3 a^5}\right)^{1/2} \frac{1}{\epsilon\left(\mathbf{K} - \mathbf{k}_2, \dfrac{\mathbf{K}^2 - \mathbf{k}_2^2}{2}\right)} \frac{1}{\{(\mathbf{k} - \mathbf{k}_1 - \mathbf{k}_2)^2 + a^{-2}\}^2} \tag{3}$$

Ω is the volume.

The total spin is not affected by this potential. W is not symmetrical with regard to the interchange of $\mathbf{k}_1$ and $\mathbf{k}_2$; however, if the energy E_0 of the localized state is low enough, then for transition where the energy is conserved, W becomes independent of $\mathbf{k}_1$ and $\mathbf{k}_2$.‡ It is then an S potential.

$$W = 32e^2 \left(\frac{\pi^3}{\Omega^3 a^5}\right)^{1/2} \frac{1}{K^6} \tag{4}$$

In this case the summation in (2) being on $\mathbf{k}_1$ and $\mathbf{k}_2$ the terms with spin σ parallel to the spin $\uparrow$ of the localized state will disappear: the ejected electron can then be polarized in the opposite direction to the localized spin.

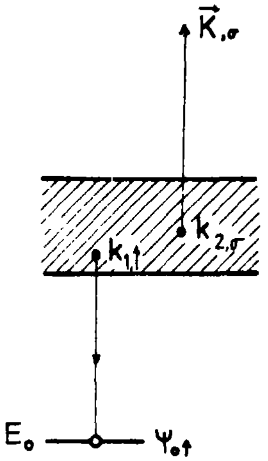

Fig. 1. Auger emission in metals.

In the Born approximation the emission probability of an electron at energy $\epsilon_{K_0} = K_0^2/2$ is twice the real part of the Fourier transform for the frequency $\omega = \epsilon_{K_0}$ of the correlation function:

$$S^e_\omega(t - t') = \sum_{\substack{k_1 k_2 k_3 k_4 \\ |K| = K_0, \sigma}} W^*(\mathbf{K}, \mathbf{k}_1, \mathbf{k}_2) W(\mathbf{K}, \mathbf{k}_3, \mathbf{k}_4) \langle 0 | T\{b(t) a^+_{k_1}(t) a^+_{k_2\sigma}(t) a_{k_3\sigma}(t') a_{k_4\uparrow}(t') b^\dagger_\uparrow(t')\} | 0 \rangle \tag{5}$$

In this expression $|0\rangle$ represents the ground state of the electrons perturbated by the hole. By writing equation (5) we have neglected the scattering of the electron $|\mathbf{K}\rangle$ by the hole, essentially stating that:

$$\langle 0 | a_K(t) a_{K'}^+(0) | 0 \rangle = \delta_{KK'} e^{-i\epsilon_K t}$$

We could also calculate the absorption spectrum; the state $|0\rangle$ would represent then an unperturbated Fermi sea; however, the present experiments are made in emission. *So we shall only discuss the emission case.* We must calculate the function:

---

† In that case the coupling to the X-ray field is described by the perturbation:

$$H_X = \sum_k W a_k^+ b e^{-i\omega t} + c.c.$$

‡ This conclusion holds even if ψ_0 is not an S function.

$$F_{\uparrow\sigma,k_1k_2k_3k_4}(t-t') =$$
$$\langle 0|T\{b_\uparrow(t)a^+_{k_1\uparrow}(t)a^+_{k_2\sigma}(t)a_{k_3\sigma}(t')a_{k_4\uparrow}(t')b^+_\uparrow(t')\}|0\rangle. \tag{6}$$

Let us recall the Green functions defined by Nozières *et al.*[8, 9, 10]:

$$g(t-t') = \langle 0|T\{b(t)b^+(t')\}|0\rangle \tag{7}$$

describes the hole propagation,

$$G_{kk'\sigma}(t-t') = \langle 0|T\{a_{k\sigma}(t)a^+_{k'\sigma}(t')\}|0\rangle \tag{8}$$

is associated to the free electrons.

To the extent that we describe the propagation of the electrons by the function (8) the remaining interaction in (1) is:

$$H_I = -\sum_{kk'\sigma} V_{kk'}a^+_{k\sigma}a_{k'\sigma}b^+_\uparrow b_\uparrow \tag{9}$$

this potential is only effective when the hole is full, therefore for $t > t'$.

The function $F_{\uparrow\sigma k_1k_2k_3k_4}(t-t')$ is given by the set of contributions of the graphs shown on Fig. 2. Following the procedure of Nozières and De Dominicis we can abstract the hole propagation lines --<-- whose contribution is only a factor $\exp(-iE_0(t-t'))$.

We have then a one particule potential. The simplification of a typical graph is shown on Fig. 3.

The total contribution to F is the product of two contributions:

The contribution of the unlinked diagrams which gives $g(t-t')$ as the exponential of the contribution $C(t-t')$ of connected loops.

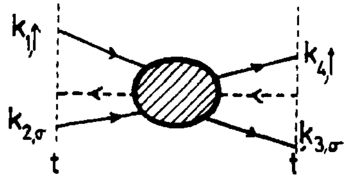

Fig. 2. The correlation function $F_{\uparrow\sigma,k_1k_2k_3k_4}(t-t')$
$--<--g$
$—>—G_{kk'}$.

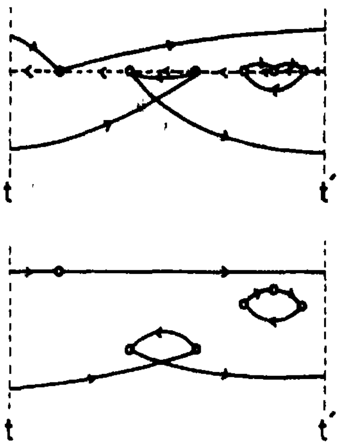

Fig. 3. Reduction to a one body potential problem.

The contribution of the linked diagram which is the product of the contribution of each set of connected diagram taken alone. Moreover there are two possible choices of the extremities. This can be written with Nozières and De Dominicis notations.

$$F_{\uparrow\sigma k_1k_2k_3k_4}(t) = \theta(t)e^{-iE_0t+C(t)}\{L_{k_1k_4}(t)L_{k_2k_3}(t) - \delta_{\uparrow\sigma}L_{k_1k_3}(t)L_{k_2k_4}(t)\} \tag{10}$$

This gives the quantity (with straightforward notations):

$$S^e_\omega(t) = \theta(t)e^{-iE_0t+C(t)}\sum_{\substack{\sigma,1234\\|K|=k_0}} W^*(\mathrm{K},1,2)W(\mathrm{K},4,3)\{L_{14}(t)L_{23}(t)-\delta_{\uparrow\sigma}L_{13}(t)L_{24}(t)\} \tag{11}$$

The formula (11) is exact, the real part of its Fourier transform gives the electron emission probability per unit time at energy ω.

(2) *What are the conditions for the usual calculation to remain correct?*

If the scattering of conduction electron on the hole is neglected and $W(K,k_1,k_3)$ is supposed to be a constant, then the function $S^e_\omega(t)$ can be written:

$$S^e_\omega(t) = \theta(t)e^{-iE_0t}W^2 \sum_{\substack{1,2<k_F\\|K|=K_0}} e^{i(\epsilon_1+\epsilon_2)t} \tag{12}$$

$\nu(E)$ being the density of state of the conduction band, the emission probability is then:

$$P^e(\omega) = (\Omega K/\pi)W^2 \int_{E_1<E_F} \mathrm{d}E_1 \int_{E_2<E_F} \mathrm{d}E_2 \quad \nu(E_1)\nu(E_2)\delta(\omega + E_0 - E_1 - E_2) \quad (13)$$

This is the usual convolutive product. We must remark that whatever the density of state is, this product (13) is always zero at the edge and starts with a non zero finite derivative.

The result (13) will be a good approximation if the potential H_l does not disturb too much the electron motion during a long enough time: let us say ξ_0^{-1}. By a Fourier transform this implies that the changes in frequency must be less than ξ_0 to perturb the electron propagation in the characteristic time ξ_0^{-1}†; because of the Pauli principle only the near by the Fermi level electrons will be perturbated. We can then think that the usual calculation is valid far enough ($\sim \xi_0$) below the emission edge.

(3) *Shape of the emission edge*

The edge singularity is governed by the behaviour of $V_{kk'}$ and $W(K, k, k')$ for ($k, k' \sim k_F$). The calculations are greatly simplified if we take as Nozières and De Dominicis, a separable form for $V_{kk'}$:

$$V_{\mathbf{kk'}} = -V_l u_l(\epsilon_{\mathbf{k}}) u_l(\epsilon_{\mathbf{k'}}) \sum_{lm} Y_m^l(\mathbf{k}) Y_m^{l+}(\mathbf{k'}). \quad (14)$$

In addition $u_l(\epsilon_k)$ is a cut off function more or less centered on the Fermi level such that $u_l(\mu) = 1$ (for instance $u_l(\epsilon) = \exp(-|\epsilon - \mu|/\xi_0)$).

For a large $|E_0|$ the potential W is mainly an S potential; to keep the calculation symmetrical we shall multiply W by $u_0(\epsilon_{k_1})u_0(\epsilon_{k_2})$.

$$W(K,k_1,k_2) = W(K)u_0(\epsilon_{k_1})u_0(\epsilon_{k_2}). \quad (15)$$

Since the calculation in §3 is limited to the singularity which only involves the values of the function at the Fermi level, the approximations on $u_l(\epsilon)$ and W are not essential. Nozières and De Dominicis have shown that with the form (14) the orbital momentum and the spin are preserved along each propagation line of the graph, so that each quantum number (l, m, σ) is an independent channel. For the calculation of $L_{kk'}$ because of particular S behaviour of W we have only to deal with the ($l = 0$) orbital number. We shall not repeat their calculation[10].

Using the X-ray result it follows that:

$$S_\omega^e(t) = -W^2(K)\theta(t)\frac{\nu_0^2}{t^2}(i\xi_0 t)\frac{4\delta_0}{\pi} - 2\sum_l(2l+1) \quad \frac{\delta_l^2}{\pi^2}e^{-i(E_0+\Delta)t+2i\mu t} \quad (16)$$

Setting $\epsilon = \omega + E_0 + \Delta - 2\mu$ the real part of the Fourier transform gives the behaviour of the spectrum near the edge.

$$S^e(\epsilon) = \frac{\nu_0^2 W^2}{(1-\alpha)!}\left(-\frac{\xi_0}{\epsilon}\right)^{4\delta_0/\pi} - 2\sum_l(2l+1)\frac{\delta_l^2}{\pi^2} - 1 \quad (17)$$

where:†

$$\alpha = \frac{4\delta_0}{\pi} - 2\sum_l(2l+1)\frac{\delta_l^2}{\pi^2} \quad (18)$$

and δ_l is the l phase shift associated to the potential V and taken at the Fermi level. The formula (17) fails when $\epsilon \sim \xi_0$. However ξ_0 being a not well defined parameter the connection between the formula (13) and (17) is not possible. The function (17) gives only the behaviour near the edge ($2\mu - E_0 - \Delta$). The phase shifts δ_l obey the Friedel sum rule:

$$\sum_l(2l+1)\delta_l = (\pi/2) \quad (19)$$

---

†ξ_0 is only to be considered as a parameter whose meaning is to be compared to that of Nozières and De Dominicis[10], or to the number N_c defined by Anderson[7] or Friedel[11].

†As ξ_0 is not well defined, the coefficient in (18) is not significant. Equations (16) and (17) only involve δ_0 in the first term of α because of the particular form of W. For other cases the result (17) can easily be extended.

When the hole is deep enough this gives the following results (Fig. 4):

(a) the divergence cases (mainly $\delta_0 = (\pi/2)$) are most improbable.

(b) when only one phase shift δ_l is non-zero for $l \neq 0$, then the behaviour at the edge is proportional to:

$$(-\epsilon)^{1+1/2(2l+1)}$$

This should be the most probable behaviour: zero edge with a zero derivative.

(c) with $\delta_0 \neq 0$, the spectrum can vanish at the threshold with an infinite derivative. This case should be observed to confirm the present theory.

At last let us recall that the ejected electron spin is opposite to the localized electron spin.

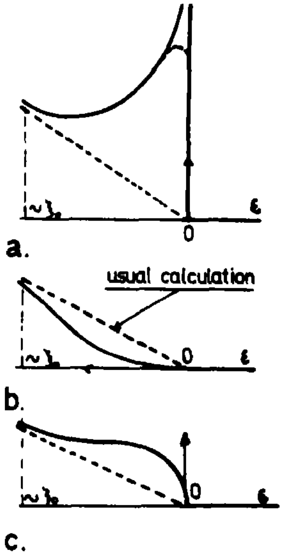

Fig. 4. The three possible shapes of the threshold:
(a) $\delta_0 \leqslant \pi/2$
(b) $\delta_l = \delta_{l,l_0}\delta_{l_0}, l_0 \neq 0$
(c) δ_0 large but $< \pi/2$.

3. DISCUSSION OF AUGER EFFECT EXPERIMENTS

Evidence of secondary electron Auger emission can be shown by several methods: bombardment of metallic targets by photons[12, 13], electrons[14, 15] or ions[16]. Unfortunately, until now, sufficiently precise experiments of this type do not aim at conduction electron studies. The only experiments with the necessary precision and variety are those of Hagstrum *et al.*[1, 2, 17] on the secondary potential emission: a low energy (~ 5 eV) ion beam (He$^+$, Ne$^+$, A$^+$) is directed on the metallic target; at a low enough distance d, an Auger effect occurs: a conduction electron of the metal annihilates the hole of the incident ion while another one is ejected.

It would be then necessary to see what modifications in the Hamiltonians H and H_A are brought by this new geometry. The theory of surface ion neutralization approached by Hagstrum[1] and Heine[3] is by itself a problem, which remains outside the aim of this article. For the present problem, it is complicated by the fact that the spherical symmetry is broken, so that it seems no more possible to write simple formula like (16) and (17), no more than it is possible to give a simple Friedel rule. Nevertheless we can make some remarks:

The d dependence of the new potential H_A shows that the study can be restricted to the case where the ion is close to the surface. Indeed if the particle is at a distance d from the surface, large with respect to its ionic radius, then W is a sum of four terms of the type:

$$\int_{Z_1>0}\int_{Z_2>0} d^3\mathbf{r}_1 d^3\mathbf{r}_2 \frac{e^2}{|r_1 - r_2|}\, \phi_0^+(\mathbf{r}_1) \exp i(\mathbf{k}_1\cdot\mathbf{r}_1 + (\mathbf{k}_2 - \mathbf{K})r_2) \;\#\; \frac{4\pi e^2}{|\mathbf{k}_2 - K|^2}\langle\phi|\mathbf{k}_1\rangle$$

So as a function of the distance W is exponentially decreasing, the largest part of the annihilation is done near the surface. The ion velocity v_l being low† with respect to the Fermi speed v_F, the conduction electrons adiabatically react with the hole. The distance of Auger annihilation can then be defined as the distance d_N where this neutralization is the most probable. This gives rise to a velocity dependent shift $\Delta\{d_N(v_l)\}$ and a broadening of the spectrum. However, it is not possible to make a direct connection between $\Delta(d_N)$ and the shift Δ appearing in $g(t)$ because interatomic interactions were neglected in the Hamiltonian H.

---

†For an ion with 5 eV kinetic energy and mass M: $v_l/v_F \;\#\; (1/60\sqrt{M})$.

When the ion is on the surface, the conduction electron, being more or less speculary reflected, see on the average the same potential than in the bulk case; so we can think that the conclusions of the first paragraph qualitatively hold for the surface emission. We shall apply the formula (17) to Hagstrum's experiments.

Experimental data of reference [2] give results for different energies of incident ions on nickel and copper targets. There is an interesting point: in a range of a few electron-volts under the experimental threshold the intensity is flattened down. Referring to our calculations this 'tail of emission' can correspond to the case (Section 2.3(b)) when the exponent of ϵ is inferior to (-1). As we mentioned our model imperfectly applies to the surface emission, however by means of the quantity $\Delta(d_N)$ it seems possible to explain the shift of the tail.†

---

† A simple argument done on Δ which predicts that the renormalized energy of the hole decreases when d_N decreased (that is to say the speed increases) gives the good variation sign.

Acknowledgements – It is a pleasure to thank Professor J. Friedel and Dr. J. Toulouse for reading the manuscript and useful comments.

REFERENCES

1. HAGSTRUM H. D., *Phys. Rev.* **122**, 83 (1961).
2. HAGSTRUM H. D., *Phys. Rev.* **150**, 495 (1966).
3. HEINE V., *Phys. Rev.* **151**, 561 (1966).
4. JOYES P. and HENNEQUIN J. F., *J. Phys.* **29**, 483 (1968).
5. FRIEDEL J., *Phil. Mag.* **43**, 153 (1952).
6. FRIEDEL J., *Phil. Mag.* **43**, 1115 (1952).
7. ANDERSON P. W., *Phys. Rev. Lett.* **18**, 1049 (1967).
8. ROULET B., GAVORET J. and NOZIERES P., *Phys. Rev.* **178**, 1072 (1969).
9. NOZIERES P., GAVORET J. and ROULET B., *Phys. Rev.* **178**, 1084 (1969).
10. NOZIERES P. and De DOMINICIS C. T., *Phys. Rev.* **178**, 1097 (1969).
11. FRIEDEL J., *Comments on Solid State Physics* **11**, 21 (1969).
12. HENKE B. L., *Norelco Rep.* **14**, 75 (1967).
13. SIEGBAHN K. *et al.*, *Nova Acta Reg. Soc. Scient. Upsala* **20** (1967).
14. HARRIS L. A., *J. appl. Phys.* **39**, 1419 (1968); **39**, 1428 (1968).
15. PALMBERG P. W. and RHODIN T. N., *J. appl. Phys.* **39**, 2425 (1968).
16. HENNEQUIN J. F., JOYES P. and CASTAING R., *C. r. Acad. Sci.* **265**, 312 (1967).
17. HAGSTRUM H. D. and BECKER G. E., *Phys. Rev.* **159**, 572 (1967).

J. Phys. Chem. Solids Pergamon Press 1970. Vol. 31, pp. 453–462. Printed in Great Britain.

SOME OPTICAL PROPERTIES OF Hg_2Cl_2

E. EJDER
Institute of Technology, Department of Solid State Physics, Lund, Sweden

(*Received* 30 *June* 1969)

Abstract – Measurements of diffuse reflexion, absorption, emission and excitation spectra have been made on powders and single crystals of Hg_2Cl_2. The diffuse reflexion and absorption measurements give an absorption edge at 3·5 eV at room temperature and 3·8 eV at 10°K. The fluorescence spectrum consists of four bands at 1·5, 2·2, 2·5 and 3·1 eV with half-widths of 0·2–0·3 eV at 10°K. The excitation spectra have different peaks for the different emissions but also one common excitation region for all emissions (shifted 0·1 eV for one of them). The common region consists of at least three partly overlapping peaks. No dark or photo conductivity was detected. The semiconductor model is rejected and a model which emphasizes the molecular crystal character of Hg_2Cl_2 is suggested. The Seitz–Mott model for the quenching of luminescence is used also to explain the more complicated temperature dependence of the emission intensity. The emissions are believed to be due to energy transfer without mobile electrons and holes after absorption by the host lattice (or a sensitizer) to centres of different kinds.

1. INTRODUCTION

It has been known for a long time that mercurous chloride, Hg_2Cl_2, gives a strong orange-red fluorescence under u.v. excitation at room temperature[1, 2]. A few other investigations have been made of the optical properties of Hg_2Cl_2. Absorption spectra in the infrared have been measured[3–7]. Suchan and Drickamer[8] studied the effect of pressure on the absorption edge and found the value 23 250 cm^{-1} (4300 Å) when no pressure was applied. This is surprising because Hg_2Cl_2 is a white powder. Pringsheim[9] reports that a strong orange-red fluorescence is obtained when mercurous chloride is excited by near u.v. light and that this fluorescence is a general property of the salt to such a degree, that it cannot be ascribed to some accidental impurity. On the other hand it is said that none of the other colourless mercurous salts (sulfate, nitrate, acetate) shows a similar fluorescence. The fluorescence mechanism is unknown and it is not even known whether it is a property of the pure Hg_2Cl_2 crystal or if it is due to impurities. Further it seems that authors who mention the fluorescence have not noticed that Hg_2Cl_2 is one of the rather rare examples of inorganic luminescent molecular crystals. Other examples of such crystals are the solid halogens[10, 11]. The reasons for this investigation have therefore been the scarcity of information on Hg_2Cl_2 and the partly contradictory results.

2. EXPERIMENTAL

The optical measurements described in this paper have been made on several different types of Hg_2Cl_2 samples. Powders from the Merck and BDH Companies with different grain sizes were used as well as small single crystals obtained by sublimation in high vacuum (10^{-5} Torr.) of different powders. The powders were all of reagent grade. No differences in any respect were noted when different samples were used for the measurements.

The low temperature measurements were made mainly in a Sulfrian stainless steel helium cryostat. This was equipped with four windows on quartz (Suprasil) and the samples were mounted on a copper block which was screwed into a copper rod cooled by a surrounding spiral tube through which liquid helium was pumped. By regulating the helium flow rate temperatures between 10°K and 80°K could be obtained at the sample and with liquid nitrogen in the cryostat, the temperature range between 70°K and 300°K was covered. The temperature measurements were made with thermocouples. A Zeiss PMQ II spectrometer consisting of a double monochromator MM 12 with exchangeable glass and quartz prisms, together with a 1P28 photomultiplier or a PbS photoconductor, was used for measuring the fluorescence spectra. The light entering the monochromator was chopped and the amplified signal from the detector was registered by a Moseley 710 IBM recorder. The calibration of the spectral response of the spectrometer and the focusing elements (lenses, mirrors) was made by means of a calibrated tungsten ribbon lamp. The same equipment as for fluorescence investigations was used for the measurement of the spectra of diffuse reflexion and absorption. For absorption and diffuse reflexion spectra, a 30 W H_2 lamp was used and this lamp in conjunction with another Zeiss MM 12 double monochromator was also used for the excitation spectra. The fluorescence was excited by a 90 W long arc Hg lamp with interference filters or a 250 W Xe lamp in conjunction with a Leiss prism monochromator.

The conductivity measurements were made with crystals of the approximate size of 0·5 × 0·5 × 0·5 mm. The contacts were made of painted colloidal silver, indium amalgam or pressure contacts of brass and of indium. The crystal was supported by a Teflon sample holder which also contained a small 25 V battery. A Keithley 602 electrometer was used to detect the current.

3. RESULTS

(a) *Diffuse reflection*

The diffuse reflection spectrum of Hg_2Cl_2 powder was measured between 300°K and 10°K. The spectrum of MgO as a standard substance was measured under the same experimental circumstances. This method of determining the absorption edge has the important advantage of being applicable when a substance is available only as a powder. It has also been shown that the diffuse reflection spectra are not very sensitive to impurity contents[12]. However, there are difficulties in correlating a measured spectrum with the spectral variation of the absorption coefficient obtained in other ways. Different means to define the absorption edge have been suggested. Here ^{10}log (intensity with MgO/intensity with Hg_2Cl_2) vs. photon energy has been drawn. The point where the linear part of the curve bends upwards on the low energy side has been used as absorption edge (Fig. 1). These values of the absorption edge are plotted vs. temperature in Fig. 2. The temperature shift $-dE/dT$ is 17×10^{-4} eV/K at 300°K.

At low temperatures there is apparently a strong increase of the reflectivity around 3·15 eV. However, this effect is caused by a luminescence band which appears at low temperatures and which has its peak at 3·1 eV. This is reported in section 3(c).

(b) *Absorption*

The crystals were so brittle that they could not be ground and polished to the thickness wanted. However, absorption measurements have been made on crystals which had naturally grown to small plates.

^{10}log I_0/I is plotted vs. photon energy for an approximately 50μ thick slice (Fig. 3). Reflexion losses are neglected.

The absorption edge was defined by extra-

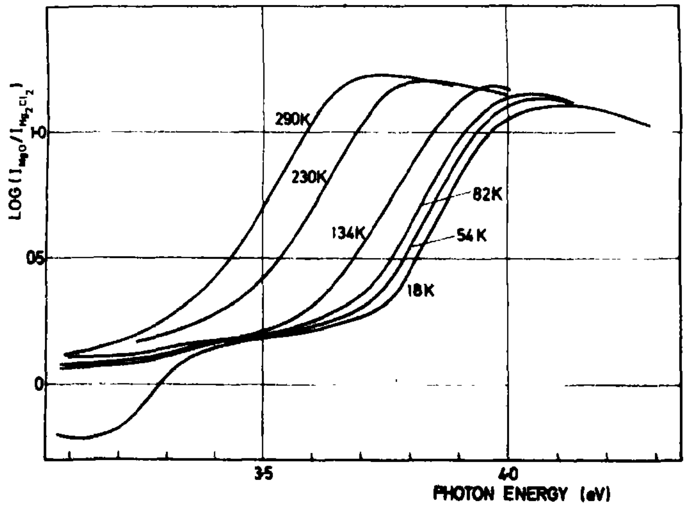

Fig. 1. Diffuse reflexion spectra of Hg_2Cl_2 powder. The strong decrease of the curve for 10°K is due to fluorescence emission 4 which has its peak at 3·1 eV.

polating the linear part of the curve to $\alpha = 0$. The values obtained for the edge are also plotted in Fig. 2. The luminescence emissions (Section 3(c)) did not influence the absorption measurements. A filter with strong absorption in the visible and good transmission in the u.v. part of the spectrum was inserted in the light beam behind the sample. Corrections were made with regard to the u.v. transmission curve of the filter.

(c) *Emission spectra*

The emissions appear at different temperatures, are excited in partially different bands and two of the emissions appear only under certain circumstances. For orientation all of them have been collected in Fig. 4 and denoted from 1 to 4. It should be noted that such a spectrum with all emissions cannot be recorded under constant temperature and excitation wavelength.

Figure 5 shows the spectral distribution of emission 1 at different temperatures. The peak at 1·5 eV (830 nm) has a considerable width especially at high temperatures (300°K), and the emission is therefore seen as orange-red by the eye at this temperature and as red at lower temperatures where the short wavelength tail decreases. The existence of this emission of Hg_2Cl_2 has been known for a long time but no results of more thorough investigations have been published.

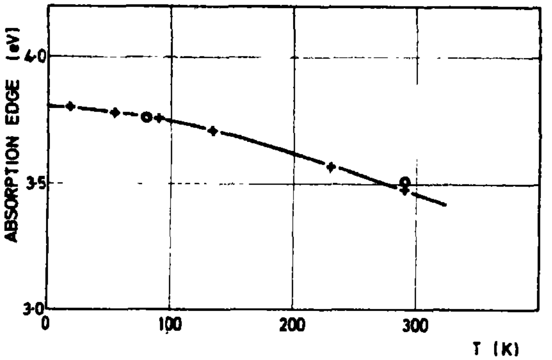

Fig. 2. Absorption edge energy as a function of temperature. Values have been taken from absorption 0 and diffuse reflexion measurements +.

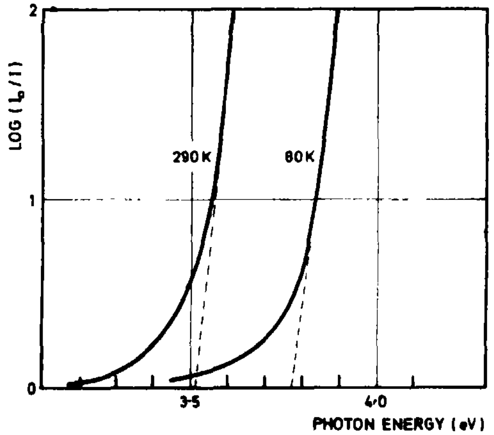

Fig. 3. Absorption spectra of a Hg_2Cl_2 crystal of thickness 50μ. The absorption edge values are plotted in Fig. 2.

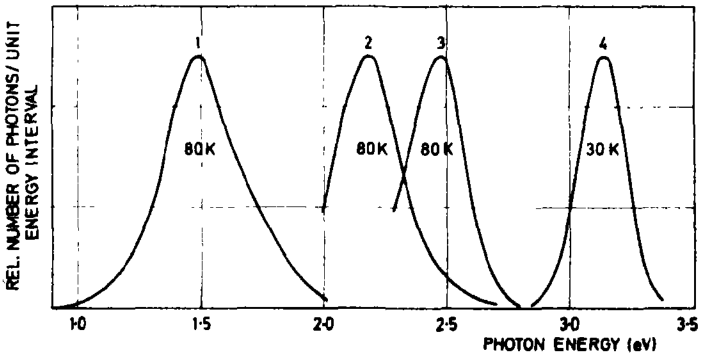

Fig. 4. All fluorescence emissions of Hg_2Cl_2. The emissions are excited under different conditions and have been plotted with the same maximum intensity.

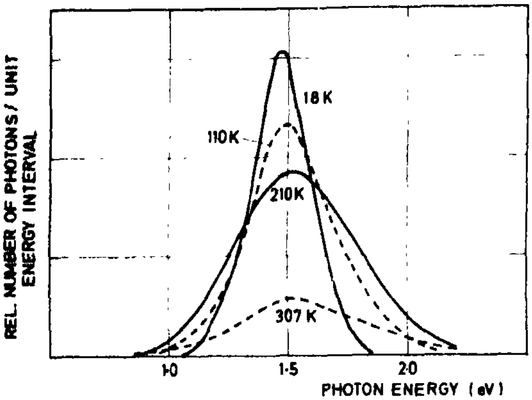

Fig. 5. Emission 1 at different temperatures.

Emission 2 has the peak at 2·2 eV (569 nm), number 3 at 2·5 eV (500 nm) and number 4 at 3·1 eV (397 nm).

Emission 1 is not symmetric, especially not at high temperatures, but emissions 2–4 are symmetric and can be well described by Gaussian curves.

The temperature dependence of the half-widths of the emissions is shown in Fig. 6.

(d) *Excitation spectra*

For each emission the excitation spectrum has been measured over a large temperature interval. A comparison between the excitation spectra of different emissions is given in Fig. 7(a). All curves refer to constant number of photons falling on the specimen per unit energy interval all over the spectral region studied. The excitation intensity was measured with a calibrated spectrometer.

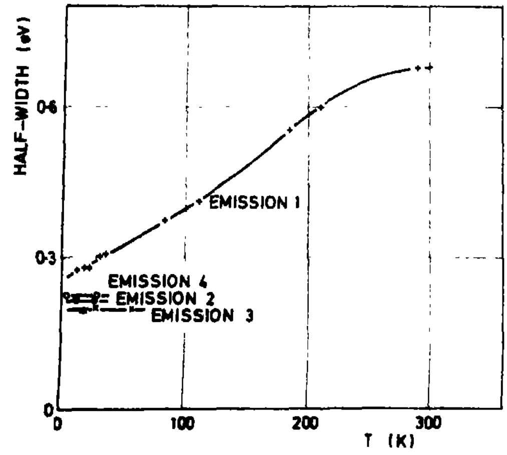

Fig. 6. Half-widths of emissions 1–4 as a function of temperature.

Emission 1 has, at the lowest temperatures, an excitation spectrum with three distinct

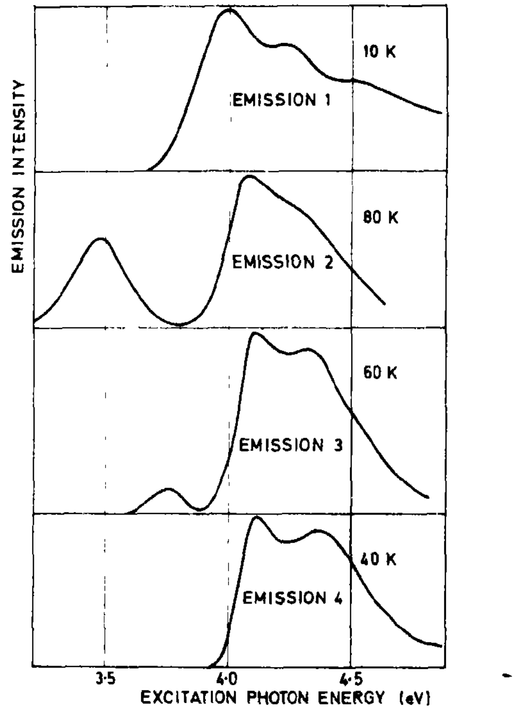

Fig. 7(a). Excitation spectra of all fluorescence emissions. Observe that different temperatures have been used.

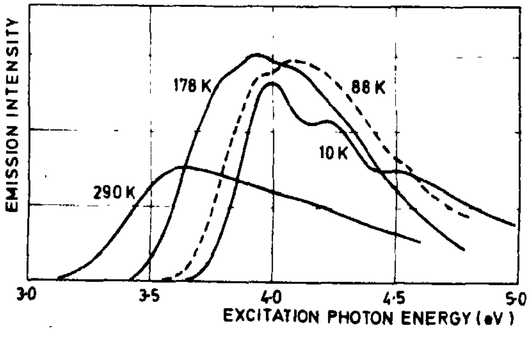

Fig. 7(b). Excitation spectrum of emission 1.

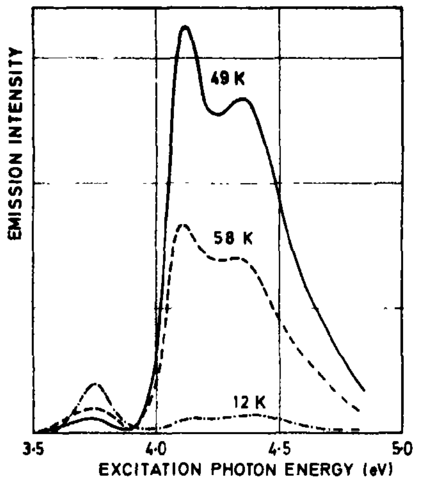

Fig. 7(c). Excitation spectrum of emission 3.

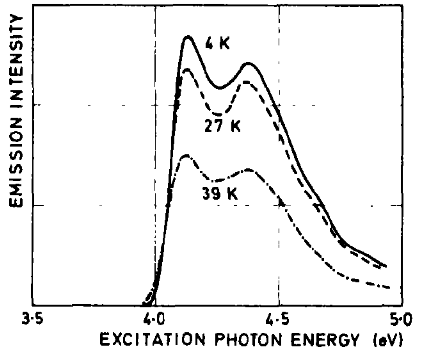

Fig. 7(d). Excitation spectrum of emission 4.

peaks at 4·00, 4·25 and 4·55 eV (Fig. 7(b)). If the peaks are separated, the values of the last two will obviously change slightly. At higher temperatures the structure is less marked and at 290°K there is only a trace of a peak at 4·15 eV. Possibly a new peak appears at about 3·8 eV on the curve for 178°K and it might be this peak which is shifted to 3·65 eV at 290°K. The excitation spectrum of emission 3 (Fig. 7(c)) shows a still more distinct structure at low temperatures. Peaks are found at 4·12 and 4·35 eV. A slight trace of a peak is seen at 4·65 eV. There is also a separate excitation band with the peak at 3·75 eV. Emission 2 has at 80°K a spectrum which is very similar to that of number 3 but due to some special properties of emission 2, the spectrum could be measured only at 80°K (Fig. 7(a)). A separate excitation band is seen with the peak at 3·45 eV. Excitation spectrum 4 (Fig. 7(d)) also has great similarities with No. 3. Peaks are found at 4·13, 4·38 and 4·66 eV, all without correction for the influence of the adjacent peaks.

(e) *Temperature dependence of emission intensity*

The temperature dependence of the integrated emission 1 is shown in Fig. 8. The decrease at low temperatures is due to narrowing down of the band. The peak height is approximately constant at low temperatures.

For emission 2 and 3 different results are obtained if the material is excited with $h\nu <$ 3·9 eV (Fig. 9) or $h\nu >$ 3·9 eV (Fig. 10). Emission 2 has about the same temperature dependence as 3 for excitation energies larger than 3·9 eV. Further investigations of temperature dependence of emission 2 have not been possible for reasons explained in Section 3(f).

In Fig. 10 emissions 3 and 4 are shown when excited in a broad band between 4·1 and 4·6 eV. These measurements are made under

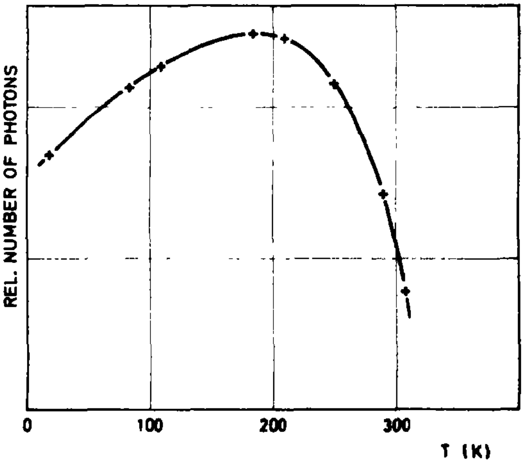

Fig. 8. Temperature dependence of the integrated emission 1 for excitation at 4·0 eV.

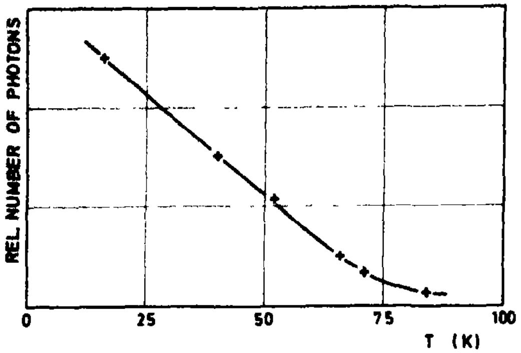

Fig. 9. Temperature dependence of the integrated emission 3 for excitation at 3·75 eV.

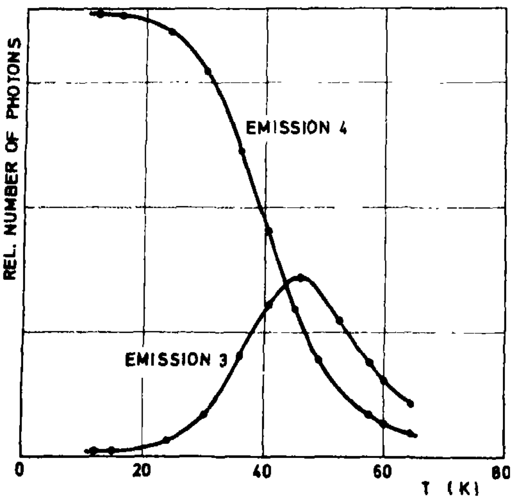

Fig. 10. Temperature dependence of the integrated emissions 3 and 4 for excitation at 4·1 eV.

circumstances when emission 2 is negligible. (No pre-exposure of the sample before cooling.)

(f) *Special properties of emission* 2 *and* 3

If a sample has not been exposed to u.v. radiation at room temperature, emission 3 is very weak at 80°K when excited around 3·75 eV. If, however, the sample is pre-exposed to u.v. light at room temperature, emission 3 is much stronger after cooling. The emission intensity at 80°K is approximately proportional to the pre-exposure time when moderate times and intensities are used. After cooling, the intensity obtained is constant over long periods for constant excitation. If long times and high u.v. intensities are used at room temperature, appreciable photodecomposition of the Hg_2Cl_2-molecules is observed and probably free Hg is formed which can be inferred from the fact that the sample darkens. (Compare with the silver halides AgCl, AgBr, AgI [13, 14].) At low temperatures the process is slower and e.g. at 20°K no darkening has been observed even after several hours with the highest attainable u.v. intensity. This is also in accordance with experiences from silver halides.

Emission 2 shows the same phenomenon but with one important difference; when the sample is excited after pre-exposure at room temperature and cooling, the intensity of emission 2 depends on the pre-exposure time, but decreases exponentially with the time of excitation (Fig. 11). The decay constant is approximately proportional to the excitation intensity. The emission can be recovered only by warming the sample, exposing it to u.v. light, cooling and exciting it again. If the sample is kept for 1 hr at room temperature in darkness after pre-exposure, emission 2 is considerably weaker after subsequent cooling, but still stronger than without pre-exposure. Keeping the sample at 80°K half

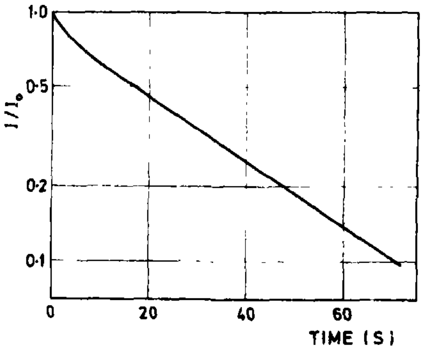

Fig. 11. Intensity of emission 2 as a function of excitation time. The sample was pre-exposed at room temperature and cooled in darkness to 80°K before the excitation. The initial intensity is denoted I_0.

an hour in darkness after exposure at room temperature, did not influence the emission intensity. It has not been possible to make measurements of these phenomena at lower temperatures than 80°K, as no cryostat was available which could cool the sample from room temperature to temperatures below 80°K and up to room temperature again, in reasonable time.

Emissions 1 and 4 are not influenced by pre-exposure.

(g) *Conductivity measurements*

No dark conductivity or photoconductivity has been found. With 25 V over the crystal, the dark current was $<10^{-14}$ A. With a 250 W small arc Xe-lamp carefully focused with a big quartz lens, no detectable current was found ($<10^{-14}$ A).

Measurements of transient photoconductivity with blocking electrodes of Mylar and integrated current measurement was tried, but no photoconductivity was detected.

4. DISCUSSION

Molecular crystals are examples of crystals where the tight-binding model of excitons is applicable. In molecular crystals the binding forces within the molecule is strong in comparison with the van der Waals forces which connect the molecules to a crystal. This means that in such crystals one cannot start with the usual semiconductor model where it is assumed that the electrons are nearly free and then make corrections. Instead we have to start with the opposite point of view and consider the energy levels of a free molecule. The electron levels in the free molecule will appear as excitons in the crystal. The shift of positions and the broadening of the electron levels is due to the crystal binding. Examples of crystals, where at low temperatures we get sharp exciton lines with very little shift in comparison to the free molecule, are antracene and benzene. On the other hand there are substances where an appreciable broadening and shift in position occur, e.g. solid iodine[10, 11].

The excitation spectra of Hg_2Cl_2 begin with a peak, which is rather sharp and the rest evidently also consists of overlapping peaks. These peaks can be interpreted as tight-bound excitons as in antracene or solid iodine[10, 11]. Some investigations have been made in order to determine whether we have energy transfer by bound excitons or transport by independently mobile electrons and holes in conductivity and valence bands.

It was found that the temperature dependence curve of emission 4, i.e. emission intensity vs. temperature, is independent of excitation intensity. However, for a bimolecular process it has been shown that the curve is shifted to higher temperatures with higher excitation intensities. The investigation of emission 4 of Hg_2Cl_2 (Fig. 12) shows that there is a shift of only 0·8°K towards lower temperature when the excitation intensity is increased 166 times. 0·8°K is within the limits of measurement error and the curve can be considered independent of excitation intensity. Therefore, it is concluded that emission 4 is not due to recombination of free charge carriers via a recombination centre. The results of two other experiments also fit into this picture.

No photoconductivity could be detected. This can be explained by the exciton model with no free electrons and holes. However, also with mobile electrons and holes the photoconductivity could be small due to low mobility or short carrier lifetime. Furthermore no influence by secondary light during the excitation or immediately after was found.

If we leave out emission 1 for a while, a model for emissions 2, 3 and 4 may be given. Excitation of the host lattice gives the exciton structure in the excitation spectrum of emission 4. Recombination can then occur in the host lattice or over a centre to which the energy is transferred. When the temperature is lowered, the intensity of emission 4 increases and reaches a constant value at temperatures lower than 20°K. This indicates

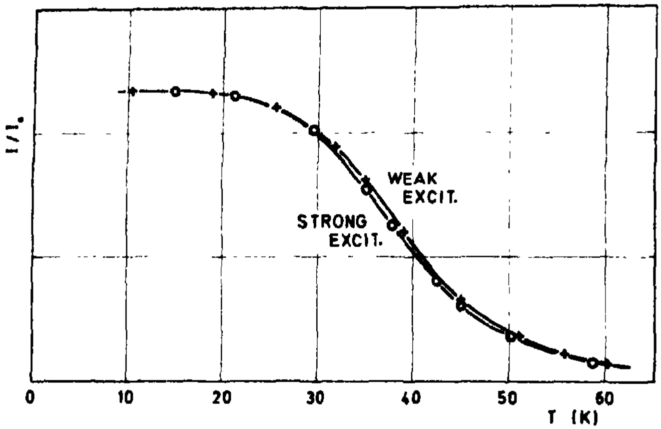

Fig. 12. Temperature dependence of emission 4 at two different excitation intensities. The curves are plotted as I/I_0 where I_0 is the intensity at 0°K (extrapolated)

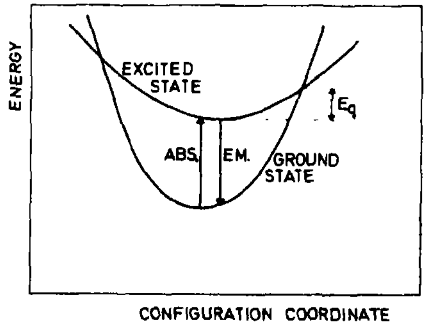

Fig. 13. Schematic drawing showing the potential energy curve vs. a configuration coordinate for a fluorescent centre in its ground and excited states.

that no activation energy is needed for emission 4 and it seems probable, that this emission occurs within the Hg_2Cl_2 molecule. Further, emission 4 cannot be excited for $h\nu < 3{\cdot}9$ eV. In contrast to this, emission 2 and 3 can be excited in one additional band each and when excited there, the intensity increases from the temperature where the emissions first occur down to the lowest temperatures. A process with energy transfer from the host lattice to emission centres seems probable. Examples of such mechanisms can be found in WO_4^{2-} and MoO_4^{2-} compounds. The situation in these compounds has been thoroughly examined by Botden[15] who applied the Mott–Seitz model. If we apply this model to mercurous chloride and assume that emission 4 is due to the Hg_2Cl^2 molecule, we find, if we have a crystal without extra centres, the following situation (Fig. 13).

If U centres (molecules) are excited per unit time interval we have

$$U = p_l a + p_q a$$

where a is the number of excited states and [illegible]d p_q are the probabilities per unit time for [illegible]ited centre to return to ground state with emission of a photon or without photon emission. The quantum efficiency of the luminescence is then

$$I/U = p_l a/(p_l a + p_q a) = p_l/(p_l + p_q)$$
$$I = U/(1 + p_q/p_l).$$

We have: $p_q = c_1 . \exp(-E_q/kT)$ where c_1 is a constant and E_q is the activation energy for thermal quenching. If we assume that p_l is independent of temperature we have:

$$I = U/(1 + c \exp(-E_q/kT)).$$

Taking $I = I_0$ for $T = 0$ this can be transformed to

$$(I_0/I) - 1 = c\,.\exp(-E_q/kT).$$

There is no influence of excitation intensity on the temperature dependence in this model as both fluorescence and quenching is proportional to the excitation intensity.

However, in our case this model is not complete since emission 3 is closely connected to emission 4, as seen in the temperature dependence of the emissions (Fig. 10). This behavior can be incorporated in the Mott-Seitz model by connecting the energy transfer to recombination centres causing emission 3, with a certain thermal activation energy[16, 17] (Fig. 14).

The probability p_t for energy transfer to an emission centre of type 3 will have the form

$$c_2\,.\exp(-E_t/kT)$$

where E_t is the activation energy and c_2 a constant (Fig. 14).

For the intensity of emission 4, I_4, we get

$$I_4/U = p_f a/(p_f a + p_q a + p_t a)$$

$$(I_0/I) - 1 = c_3 \exp(-E_q/kT) + c_4 \exp(-E_t/kT)$$

in the same way as in the treatment of simple thermal quenching. If E_q and E_t are not too closely equal we can neglect one term at high temperatures and the other at low and keep only one term in each region. From Fig. 10 we see that the transfer of energy starts at lower temperatures than thermal quenching. This means that at low temperatures we have approximately:

$$^{10}\log(I_0/I - 1) = {}^{10}\log c_4 - E_q/kT\ {}^{10}\log e.$$

Figure 15 shows the result of plotting the temperature dependence curve of emission 4 as $^{10}\log(I_0/I - 1)$ vs. $1/T$. We find two approximately straight lines corresponding to the two regions of energy transfer and temperature quenching. With corrections with regard to the influence of the small term on the dominating one, we find $E_t = 0{\cdot}01$ eV and $E_q = 0{\cdot}03$ eV. During these measurements it was arranged so that emission 2 did not influence the result (no pre-exposure of the sample before cooling). Emission 2 has probably a similar temperature dependence as emission 3. It was only seen that when emission 2 was present, its intensity increased when the temperature decreased from 60°K, where the emission first appeared and that emission 2

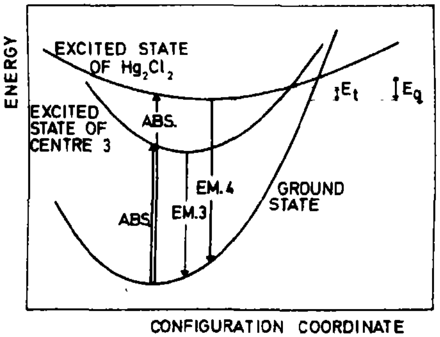

Fig. 14. Schematic drawing showing the potential energy curves vs. a configuration coordinate for the ground and excited states of the Hg_2Cl_2 molecule and centre 3. Differences between the ground states are neglected.

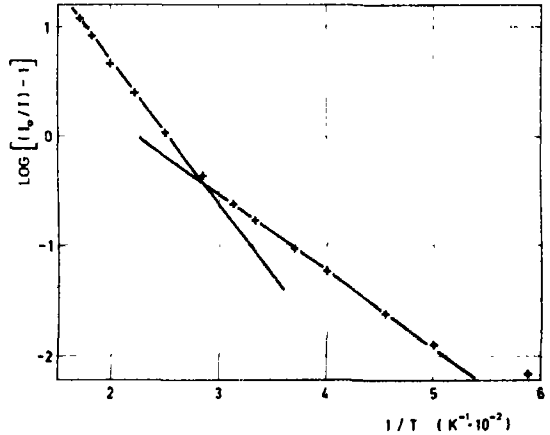

Fig. 15. Temperature dependence curve of emission 4 plotted as log $((I_0/I) - 1)$ vs. T where I_0 is the intensity at 0°K (extrapolated). The thermal activation energies for quenching and energy transfer are calculated from the slopes.

was not present at the lowest temperatures for excitation with $h\nu > 3{\cdot}9$ eV.

All that was said above about energy transfer, is valid for excitation in the region $h\nu > 3{\cdot}9$ eV. Besides this the luminescence of emission 2 and 3 (but not 4) can be excited in specific bands. This corresponds to the transition 2 in Fig. 14. When excited in this band emission 3 increases all the way down to the lowest temperatures used (10°K). This is also in agreement with the model used above, since with this excitation there is no energy transfer, but only excitation and emission in the same centre.

Emission 1 has no connection with the other emissions other than through the fact that the excitation spectra have the same structure at low temperatures. However, excitation spectrum 1 is shifted 0·1 eV to the low energy side. The temperature dependence of emission 1 has no connections with that of the other emissions. It has not been possible to find an explanation for this emission from the measurements made and further investigations are necessary.

An interesting investigation should be the comparison of absorption and emission spectra of Hg_2Cl_2 in its gas and solid states. However, part of the Hg_2Cl_2 molecules in the vapor are dissociated to Hg and $HgCl_2$ when the crystal is heated. It also seems as if there is no suitable solvent for mercurous chloride. Otherwise the absorption spectrum of the solution could have been studied.

More investigations are also needed to determine the nature of centres 2 and 3. From what is said in Section 3(f) about the properties of emission 2 and 3, it can be concluded, that the centres are probably formed by dissociation of the Hg_2Cl_2 molecule. Emission 3 is simply due to formation of stable emission centres. Emission 2 is also due to the forming of centres, but there is a complication. The emission is not constant with time but decreases exponentially. Compare bleaching in alkali halides[18].

Acknowledgements – The author is deeply indebted to Professor H. G. Grimeiss for his guidance and for his continuous interest in this study. He is also grateful to Ch. Särnstrand for the preparation of some of the samples and to Professor B. Aurivillius for valuable discussions.

REFERENCES

1. WILKINSON J. A., *J. phys. Chem.* **13**, 691 (1909).
2. RANDALL J. T., *Nature, Lond.* **142**, 113 (1938).
3. ADAMS D. M., GOLDSTEIN M. and MOONEY E. F., *Trans. Faraday Soc.* **59**, 2228 (1963).
4. POULET H. and MATHIEU J. P., *J. chim. Phys.* **60**, 442 (1963).
5. HADNI A., BOUSTER C., DECAMPS E., MUNIER J. M. and POINSOT P., *Coll. Spectr. Int. 9th. Lyons 1961* **3**, 11 (1962).
6. HADNI A., HENRY C., MATHIEU J. P. and POULET H., *C.r. hebd. Séanc. Acad. Sci., Paris* **252**, 1585 (1961).
7. LECOMTE J., *Boll. Sci. Fac. Chim. Ind. Bologna* **21**, 51 (1963).
8. SUCHAN H. L. and DRICKAMER H. G., *J. Phys. Chem. Solids* **11**, 111 (1959).
9. PRINGSHEIM P., *Fluorescence and Phosphorescence*, p. 501 Interscience, New York (1963).
10. DUMBLETON M. J., *Proc. phys. Soc.* **B68**, 53 (1955).
11. GARLICK G. F. J., *Encyclopedia of Physics*, Vol. 26, p. 16. Springer, Berlin (1958).
12. FOCHS P. D., *Proc. phys. Soc.* **B69**, 70 (1956).
13. BELOUS V. M., BUGRIENKO V. I. and GOLUB S. I., *Opt. Spectry* **17**, 216 (1964).
14. BELOUS V. M., *Opt. Spectry.* **24**, 308 (1968).
15. BOTDEN Th. P. J., *Philips Res. Rep.* **6**, 425 (1951).
16. KRÖGER F. A., *Some Aspects of the Luminescence of Solids*, Chap. 3. Elsevier, Amsterdam (1948).
17. BLASSE G. and BRIL A., *J. electrochem. Soc.* **115**, 1067 (1968).
18. COMPTON W. D. and RABIN H., *Solid State Physics*, Vol. 16, p. 121. Academic Press, New York (1964).

J. Phys. Chem. Solids Pergamon Press 1970. Vol. 31, pp. 463–474. Printed in Great Britain.

ELECTROMIGRATION AND ASSOCIATED VOID FORMATION IN SILVER*†

H. R. PATIL‡ and H. B. HUNTINGTON

Department of Physics and Astronomy, Rensselaer Polytechnic Institute, Troy, N.Y. 12181, U.S.A.

(*Received* 26 *June* 1969)

Abstract – Electromigration in both 99·999 per cent pure silver with about 1 ppm oxygen and 99·99 per cent pure silver with about 40 ppm oxygen (presumably in the form of impurity oxides) has been measured using the vacancy flux method. The method consists of determining local volume changes in specimens subjected to a large d.c. current density ($\sim 10^4 A/cm^2$) and a parabolic temperature distribution, which results from water-cooling the specimen ends. As a result of improved temperature determination, the effective charge for electromigration was found to be about −6·5 e in contrast to the earlier reported value of about −25 e. Microscopic void formation on the cathode side and consequent sample elongation were observed only in the less pure silver and could not be induced in the purer material even when charged individually with oxygen or hydrogen. Some evidence indicated oxygen electromigration to the anode in silver and also an enhancement of the self-electromigration of the latter in the presence of dissolved hydrogen.

1. INTRODUCTION

THE PRESENT investigation is a sequel to the work of Ho and Huntington[1] who measured by the marker motion technique electromigration in high purity silver supplied by Englehard Company. An interesting result of this investigation was that the tubular samples elongated progressively in the course of a run and revealed void formation on the specimen cathode side upon polishing at the conclusion of the run. Sample elongation, void formation and marker velocities were increased when the inert argon ambient was replaced by $5\%H_2 + 95\%A$. It was concluded that the voids were formed by vacancy condensation on the pre-existing impurities in the region of vacancy super-saturation, which happens to be the cathode side in electron conductors. The existence of dissolved hydrogen was surmised to cause enhanced void nucleation and growth. These results on void observation were essentially of preliminary nature and the need for further experiments, particularly under highly purified argon ambient, was pointed out.

In the present experiments electromigration in both essentially oxygen-free and oxygen-bearing silver has been measured, under various ambient conditions, with the object of exploring further the observed phenomenon of cathodic void formation[1]. Some of the results of this investigation pertained to 'hydrogen embrittlement' of silver[2]. The latter was found to introduce in the specimens large dimensional changes extraneous to electromigration itself, which will be the subject of another paper[3]. The results reported here include the following: (i) the effective charge, Z^*, taking into account the improved temperature determination; (ii) the conditions under which microscopic evidence for void formation was obtained; (iii) the direction of electrotransport of interstitial oxygen in silver; and (iv) hydrogen enhancement of self-electromigration in silver.

2. EXPERIMENTAL PROCEDURE

2.1 *Apparatus*

Although the basic experimental approach to measure electromigration in silver was the same as in the earlier work[1], several improvements were made in the apparatus. In order to keep the ambient contaminants at a minimum level, an especially clean specimen chamber was needed. For this purpose an all stainless steel chamber, which could be evacuated and then be filled with high purity dry argon, was designed and fabricated. A gettering system to purify further the 99·995 per cent pure tank argon was also constructed.

---

*Supported by U.S. Atomic Energy Commission.

†This paper is based on a thesis submitted to the Department of Physics and Astronomy at Rensselaer Polytechnic Institute in partial fulfillment of the requirements for the degree of Doctor of Philosophy.

‡Department of Materials Science and Engineering, Cornell University, Ithaca, N.Y. 14850, U.S.A.

A sketch of the chamber, with the specimen mounting assembly, is shown in Fig. 1. It consisted of a 9 in. I.D., 304L stainless steel tube with 9 flanged ports (four of these are not shown in Fig. 1). All the flanges were heli-arc welded to the main tube and contained grooves for viton o-rings. The specimen was held between a fixed clamp and a movable clamp

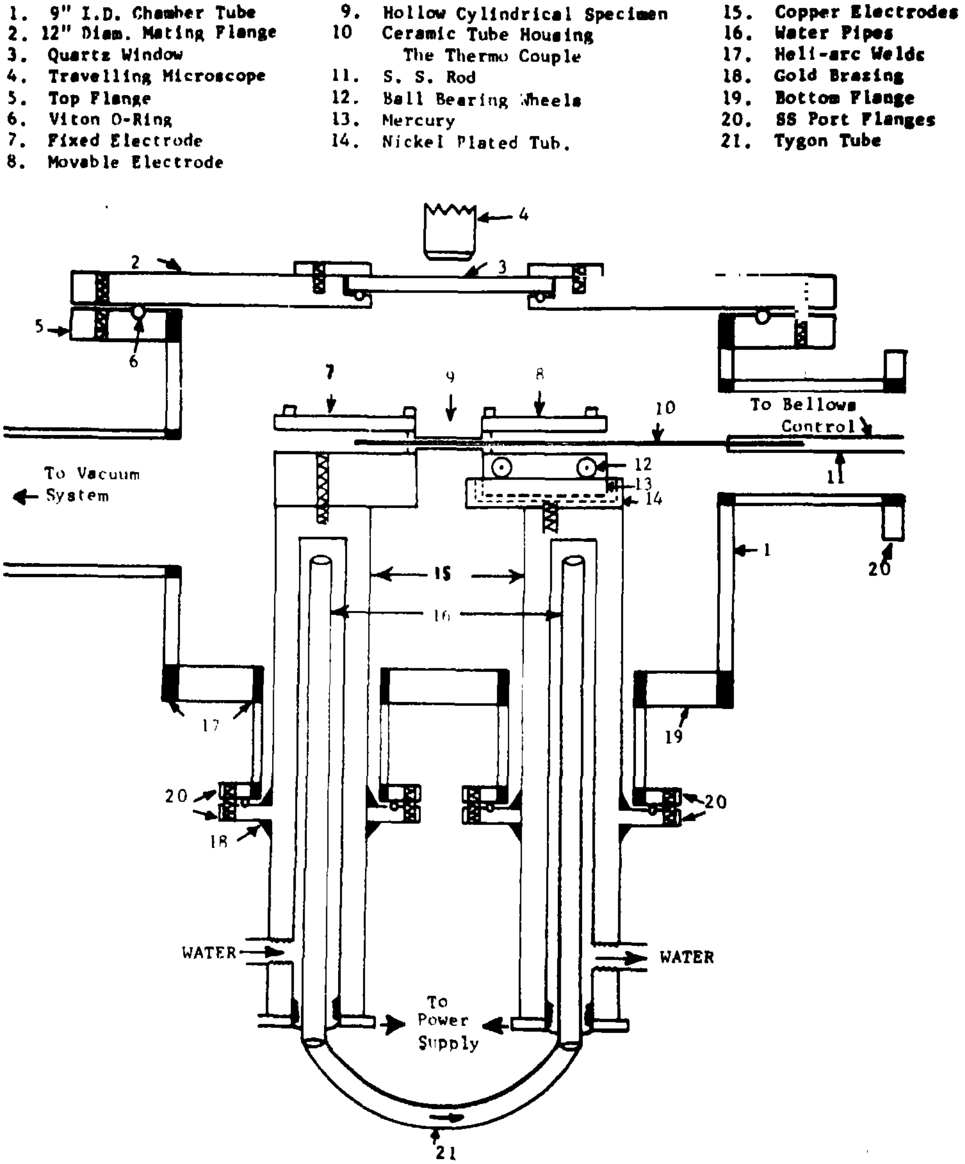

Fig. 1. Chamber with specimen mounting assembly.

which rode on ball-bearing wheels and was partially immersed in mercury contained in a heavy nickel plated tub; the specimen was viewed through the quartz window at the top. Both the fixed clamp and the tub containing mercury were bolted on to OFHC copper electrode rods which were hollowed out from the bottom-end to within $\frac{1}{4}$ in. of the top for water-cooling. Teflon washers (not shown) were used to insulate these electrode rods from the chamber at the two bottom ports. The side port on the right led to an assembly of a bellows and a rod which enabled one to move externally the ceramic tube, housing Pt–Pt10%Rh thermocouple, along the axes of the hollow cylindrical specimens. This arrangement provided a means to measure the temperature distribution in the samples. The port on the left led through a gate valve to the vacuum system, which consisted of a mechanical pump, a fore-line trap, a 2 in. oil-diffusion pump and a liquid nitrogen trap. The remaining side ports (not shown) were for two gas connections, a thermocouple feedthru and a G.E. Trigger Gauge to monitor the high vacuum. Although the maximum possible vacuum for this system was in the range of 10^{-8} Torr, the extensive outgassing of the gettering system permitted vacuum in the range of only 10^{-6} Torr., after several hours of pumping.

The gettering system consisted of a molecular sieve trap for water vapor and a high temperature furnace filled with titanium chips for gettering oxygen and hydrogen. A three phase power supply capable of supplying 1500 d.c. A was used to heat the samples. Three center-tapped, stepdown transformers coupled with six high current silicon diode rectifiers converted the a.c. power, from three saturable core reactors, to d.c. power. The d.c. excitation to the control windings of the saturable core reactors was provided by an amplistat. The input to the latter was a regulated error signal provided by a strip chart recorder with a thermocouple input and processed by a 3-mode controller[4]. This feed-back proportional power control system held the temperature constant normally to within ± 4°C.

2.2 *Material characterization and specimen preparation*

The material used in this investigation was obtained from two different suppliers, Johnson Mathey Company and Englehard Company (hereafter referred to as JM and EH silver) Vacuum fusion gas analysis[5] showed that the 99·999 per cent pure JM silver contained ~ 1 ppm oxygen and the 99·99 per cent pure EH silver contained ~ 40 ppm oxygen, presumably in the form of impurity oxides.

The thin-walled hollow cylindrical samples with massive grips were machined from either $\frac{1}{4}$ or $\frac{5}{16}$ in. rods. The samples were $\frac{31}{32}$ in. in length with O.D. = 0·159 in. and I.D. = 0·125 in. These values were chosen from considerations of capability of the power supply and the requirement that $\Delta r/l$, where Δr is the wall thickness, should be $\leq 0{\cdot}02$ for isotropic dimensional changes[1]. Marks were scribed on the smooth sample surface by a spark erosion technique and were typically 25–50 μ wide, $\sim 50\,\mu$ deep and 30 in number. Samples were thoroughly washed first with acetone and then with alcohol, dried and weighed before mounting in the chamber.

2.3 *Measurements*

After clamping the sample tightly in place, the chamber was sealed properly, evacuated and filled with the desired ambient gas; viz. gettered argon, tank argon, a mixture of hydrogen and argon or a mixture of oxygen and argon. The ambient gas pressure was maintained at ~ 1–$\frac{1}{2}$ atm. The samples were then heated slowly to the operating temperature with the 3-mode controller first in manual and then in automatic operation. The water-cooling of the specimen ends resulted in a parabolic temperature distribution with the maximum at the center.

A Pt–Pt10%Rh thermocouple placed inside a double-holed ceramic tube, movable coaxially within the sample, indicated the temperature along the specimen axis. Careful melting point checks[4] revealed that at high temperatures the internal thermocouple read the sample temperature ~ 60°C too low. The discrepancy arises from the conduction losses in the ceramic tube, which is essentially connected to a heat sink. Calculations based on balancing the heat lost by conduction in the ceramic tube against the heat it receives from the sample through gas conduction and radiation, yielded ~ 31°C for the difference, ΔT, between the sample temperature and the thermocouple reading. However, there are enough uncertain factors in the calculation whose adjustment would provide the flexibility to bring the calculated value in agreement with the observed $\Delta T \sim 60°\mathrm{C}$ (see Appendix). In order to verify further the existence of this large temperature difference, ΔT, an additional experiment was carried out in which an i.r. pyrometer was used in addition to the internal thermocouple. The pyrometer was focussed on an aquadag spot pasted at the center of the sample. The book-value for the emissivity of aquadag[6], 0·8, was used and the losses at the quartz window were corrected for. In the temperature range of interest, 700–900°C, the pyrometer read about 55° ± 10°C higher than the internal thermocouple. This result was in essential agreement with the earlier melting point checks.

The dimensional changes resulting from the current-induced ion and vacancy fluxes in a temperature gradient[7] were measured with a Gaertner traveling microscope equipped with a micrometer filar eye-piece. The longitudinal changes were determined by recording periodically the surface marker displacements relative to the three fiducial marks near the fixed end of the sample. The marker centers were read to an accuracy of $\pm 2\,\mu$. The micrometer filar eye-piece was employed to monitor the transverse changes at each marker position. The uncertainty in the diameter measurements was $\pm 3\,\mu$. At the end of the runs, the samples were potted, polished both mechanically and electrically[4], and examined under an optical microscope (usually at the magnification of 100X).

3. RESULTS AND ANALYSIS

(i) *Self electromigration in silver*

In all the electromigration runs, the mass transport was towards the anode as expected. The typical dimensional changes observed in these experiments are shown in Fig. 2. The marker velocities displayed as functions of position, x, along the sample (Fig. 2(a)) were obtained from straight line plots of displacement vs. time for each marker. The changes in O.D., ΔD_0, corresponding to 8·6 days are shown in Fig. 2(b-1) and need to be corrected for evaporation in the hot central region. The evaporation correction curve, Fig. 2(b-2), was established experimentally* and the sum of the curves 1 and 2 was taken as the actual $\Delta D_0(x)$.

The current induced ion flux[7] at any point in the specimen,

$$\phi_i(x) = N_i V_i(x) \qquad (1)$$

where N_i and V_i are respectively the concentration and the velocity of the ions. The counter flow of vacancies is such that $\phi_i = -\phi_v$, where ϕ_v is the vacancy flux. By virtue of the temperature gradient, non-zero local divergences of these ion and vacancy fluxes exist in the sample, which produce the observed dimensional changes. For N_i independent of both time and position along the sample (which is equivalent to assuming negligible contribution from void formation to

---

*Figure 2(b-2) is readily obtained by symmetrizing the measured curve in Fig. 2(b-1) and forcing ΔD_0 at the center to be zero. However, this procedure cannot be adopted for samples showing cathodic void formation. For this reason, the general shape of curve 2(b-2) was established from measurements at various temperatures on JM samples which showed no significant void formation. For EH runs showing voids on the cathode side, the almost flat, maximum value for curve 2(b-2) was taken to be the negative of the measured ΔD_0 at the center and the general shape established in JM runs was taken as a guide to determine the entire evaporation correction profile.

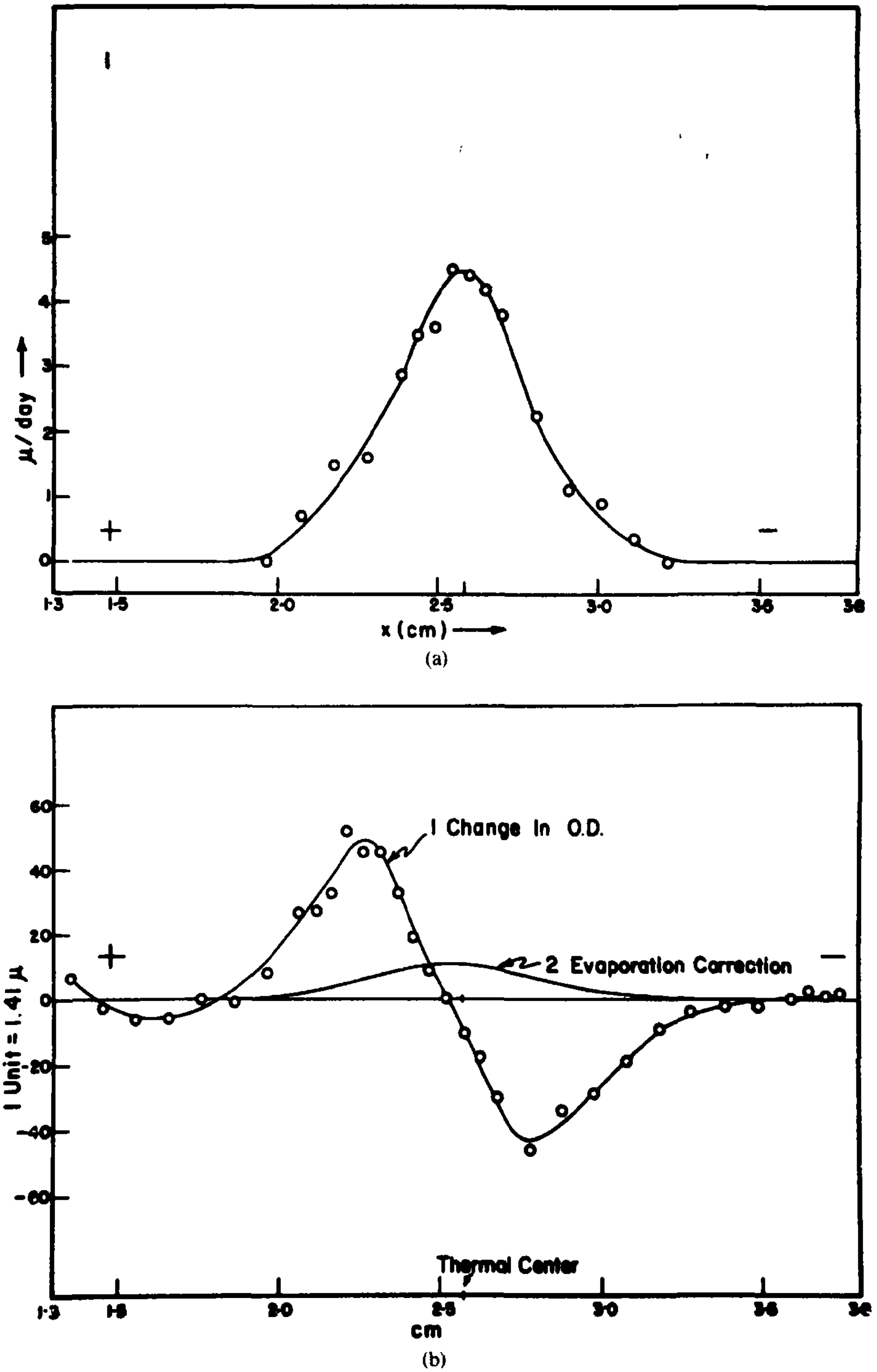

Fig. 2. (a) Marker velocity vs. position (Run No. J7). (b) Diameter change (in 8·6 days) vs. position (Run No. J7).

observed dimensional changes), the mass balance equation leads to

$$\operatorname{div} \phi_i(x) = \operatorname{div}\{N_i V_i(x)\} = N_i \dot{\Delta}(x) \quad (2)$$

where $\dot{\Delta}(x) = \dot{\epsilon}_l(x) + 2\dot{\epsilon}_r(x)$ is the rate of total dilatation at x. $\dot{\epsilon}_l$ and $\dot{\epsilon}_r$ are respectively the longitudinal and transverse strain rates. In the one dimensional case,

$$\frac{\partial V_i(x)}{\partial x} = \dot{\Delta}(x)$$

or

$$V_i(x) = \int_{x_0}^{x} \dot{\Delta}(x')\mathrm{d}x', \text{ where } V_i(x_0) = 0. \quad (3)$$

The slopes determined at various points on the marker velocity vs. x curve (Fig. 2(a)) were taken for $\dot{\epsilon}_l(x)$ and the diameter changes corrected for evaporation (Fig. 2(b)) were divided by the initial O.D., $D_0(x)$, and the time duration of the run to give $\dot{\epsilon}_r(x)$ (it may be noted that proportionate changes take place in I.D., D_i, and the relationship, $\Delta D_i : \Delta D_0 = D_i : D_0$[8], was verified in one of the early runs by polishing away half the sample parallel to its axis and measuring D_i as a function of x). The total dilatation rate, $\dot{\Delta}(x)$, thus determined is shown in Fig. 3(a). The corresponding ion velocities, $V_i(x)$, obtained by graphically integrating equation (3) are shown in Fig. 3(b). Since the temperature is measured as a function of x, the ion velocities are known as functions of T.

It is customary to write, $\dot{\epsilon}_l = \alpha\dot{\Delta}$, where α is the so-called isotropy factor. In cases where α is independent of x, equation (3) yields:

$$V_i(x) = \frac{1}{\alpha}\int_{x_0}^{x} \dot{\epsilon}_l(x')\mathrm{d}x' = \frac{1}{\alpha}V_m(x) \quad (4)$$

where $V_m(x)$ is the velocity of the surface marker at x. However, quite often it turns out that the observed α is either a function of x or approx. a constant different from the isotropic value, $\frac{1}{3}$. The experimental value of α for silver was found to depend on both the frictional and inertial impedence to the movement of the clamp[4] and the purity of the material. For the relatively purer JM material, α was $\sim 0{\cdot}22$ and for the less pure EH material α was close to the isotropic value, $\frac{1}{3}$.

The fact that, in general, α was not a constant made it necessary to measure both longitudinal and transverse dimensional changes so that equation (3) could be used to compute the ion velocities. The latter can be related to the force on the ions, F_i, by the Nernst-Einstein relation,

$$V_i = \frac{DF_i}{kT} \quad (5)$$

where D is the uncorrelated diffusion coefficient and F_i is customarily written as, $F_i = Z^*eE$. Here, Z^* is the effective charge on the ions including both the electrostatic and 'electron wind' effects[7], e is the electronic charge and E is the applied d.c. field. Among the three frequently cited equivalent theoretical expressions for Z^*[7, 9, 10], the one obtained by Huntington[7] reads as follows:

$$Z^* = Z\left[1 - \frac{1}{2}\frac{N_i \rho_d}{N_d \rho}\frac{m^*}{|m^*|}\right] \quad (6)$$

where N_d and ρ_d are respectively the concentration and the resistivity of the defects, ρ is the lattice resistivity and m^* is the charge carrier effective mass. With the use of Ohm's law and the expression $F_i = Z^*eE$, equation (5) is written as,

$$V_i = \frac{D^*Z^*}{fkT}e\rho j \quad (5')$$

where D^* is the correlated diffusion coefficient, f the correlation factor and j the current density in the sample. In the experimental temperature range, ρ/T and Z^* turned out to be only weakly temperature dependent, if at all; and, therefore, a plot $\ln(V_i/j)$ vs. $1/T$ should yield a straight line with negative slope

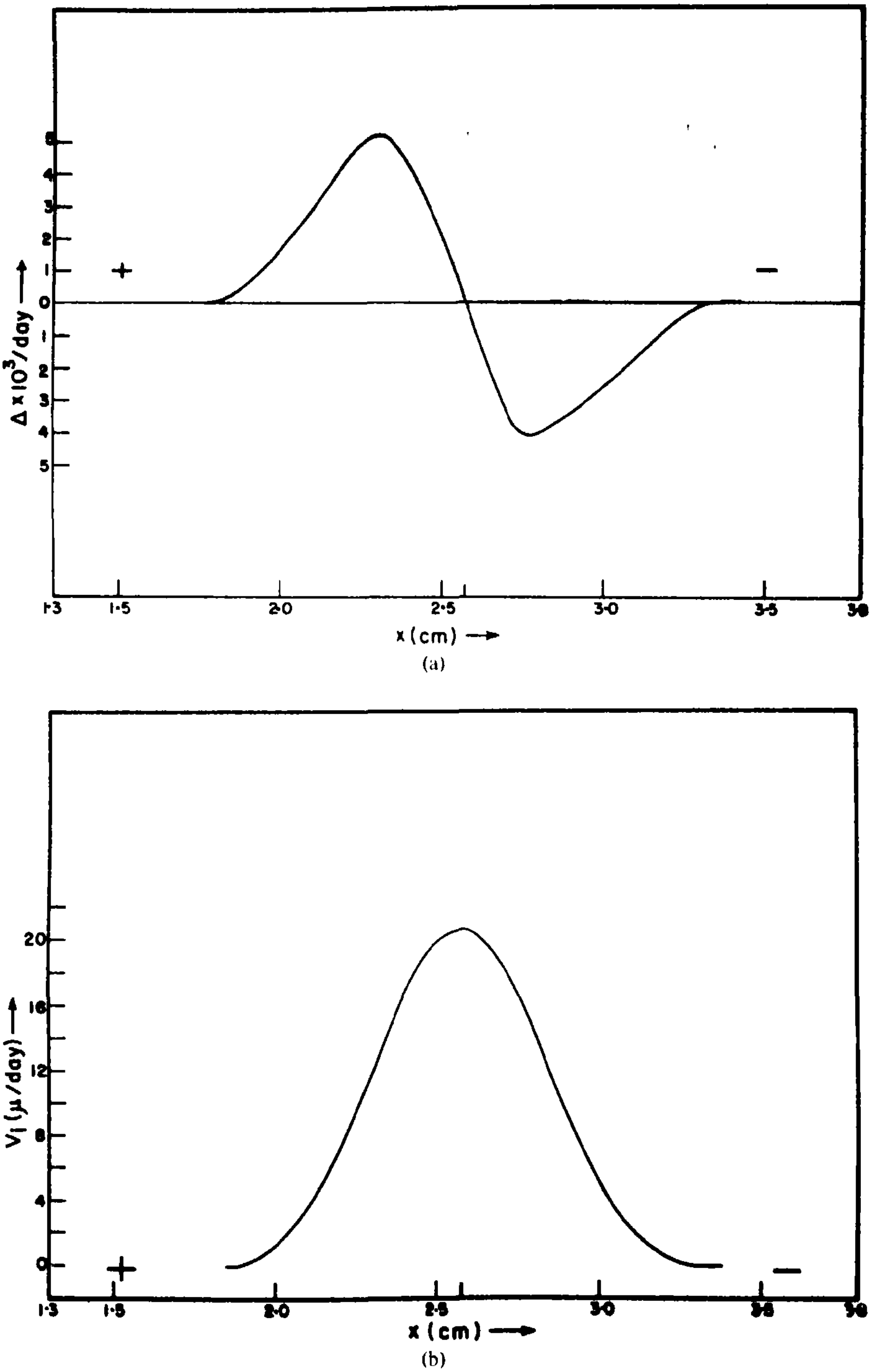

Fig. 3. (a) Total dilatation rate vs. position (Run No. J7). (b) Ion velocity vs. position (Run No. J7).

equivalent to the diffusion activation energy. Figure 4 shows such Arrhenius plots for three runs. The values of V_i in this figure refer only to the specimen anode side, and hence the complications due to cathodic void formation are circumvented. The average activation energy, Q, obtained from the slopes of these lines is $1·95 \pm 0·19$ eV, which agrees well with the self-diffusion value, 1·91 eV[11], as expected. This result also demonstrates the lack of a measurable temperature dependence of Z^*.

The effective charge Z^* at any temperature T can be computed from equation (5′) using the known tracer diffusion constant D^* and the experimental values of V_i. The results of such a calculation are shown in Fig. 5. The average value of Z^* is $-6·5 \pm 1·4$ and no systematic variation with temperature is evident. Although the error limits overlap, it appears that Z^* for the less pure *EH* material is systematically higher than that for the purer JM material. The defect resistivity calculated from equation (6), using the above value of Z^*, is $1·1 \pm 0·2\,\mu\Omega$-cm per cent defect and is in close agreement with the electromigration results for gold[12] and copper[13].

(ii) *Void formation*

The JM silver specimens run in tank argon, 5%H_2 + 95%A, wet argon and 5%O_2 + 95%A ambients did not show a steady elongation

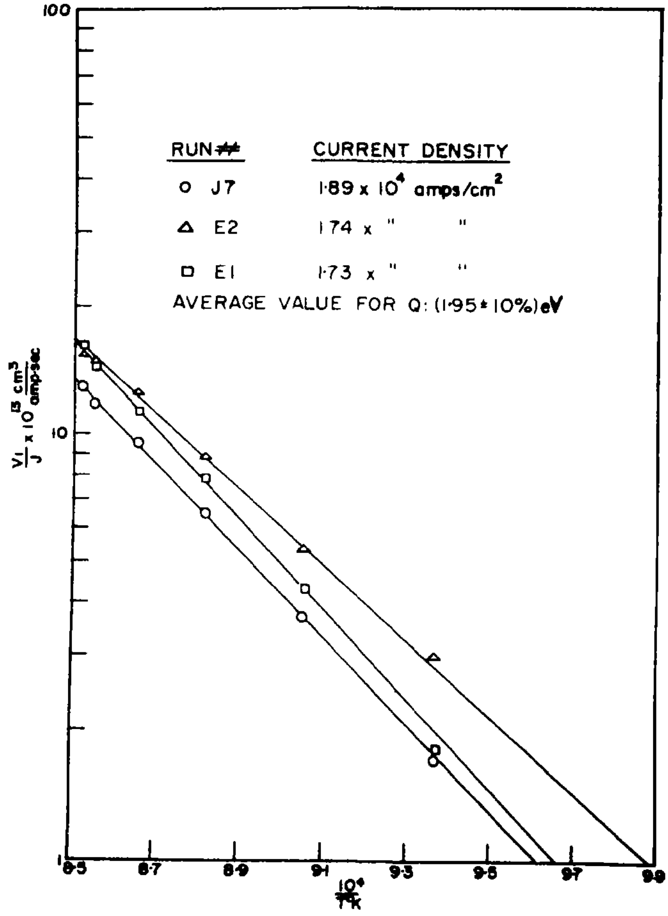

Fig. 4. Results of electromigration in silver.

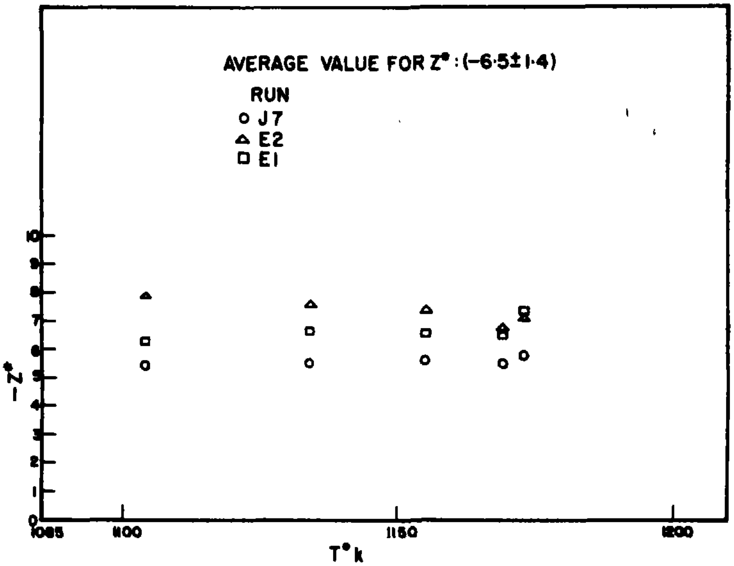

Fig. 5. Effective charge, Z^*, vs. T.

(characteristic of void formation) during the runs; nor did they reveal any microscopic evidence for significant void formation when polished at the conclusion of the runs. However, the oxide-bearing EH silver specimens run in tank argon ambients elongated steadily at the rate of $\sim\frac{1}{2}\,\mu$/day and a small but definite associated void formation was observed on the cathode side of the specimens. No voids were seen on the anode side (Fig. 6(a,b)). Similar results were obtained even when the ambient gas was purified by passing it over hot titanium following a molecular sieve trap. The results of heating the EH samples in a low partial pressure of hydrogen were similar to the 'hydrogen embrittlement' effects[2] on the one hand, and to the swelling caused by the irradiation induced gas bubble coalescence[14], on the other; these results will be reported elsewhere[3].

Although no void formation was observed in JM material impregnated with hydrogen, there was indication of enhanced self-electromigration. In one of these runs, where the ion velocities were determined by measuring both the longitudinal and transverse dimensional changes, $Z^* \sim -14{\cdot}0 \pm 5{\cdot}0$ in contrast to $-6{\cdot}5 \pm 1{\cdot}4$ obtained in runs under pure argon ambients.

In a JM sample run under $5\%O_2 + 95\%A$ ambient, $Z^* \sim -8{\cdot}8 \pm 2{\cdot}5$. Vacuum fusion gas analysis[5], carried out at the end of this run, showed 41 ± 3 ppm and 21 ± 2 ppm oxygen in the specimen anode and cathode halves, respectively. The corresponding numbers for an air-annealed sample were, 100 ± 8 ppm and 39 ± 3 ppm oxygen (the results of gas analysis as to the total amount of dissolved oxygen, are in essential agreement with the calculations based on solubility data). This suggests anode-directed interstitial oxygen electromigration in silver. Additional evidence to indicate a negative electrotransport of dissolved oxygen will be presented in a later paper[3].

4. DISCUSSION

Since silver is an electron conductor the observed anode-directed electromigration is expected. It means that the electron wind force dominates the electrostatic field force. The agreement between the measured diffusion activation energy, $1{\cdot}95 \pm 0{\cdot}19$ eV, and the self-diffusion value, $1{\cdot}91$ eV[11], is also to be expected if the assumption that electromigration is rate limited by bulk diffusion is correct. There appears to be no T-dependence of Z^*.

Although our observations agree in general with those of other investigators[1, 15, 16] the present value of Z^* is considerably lower than the earlier values obtained for Z^* in silver. A nearly T-independent Z^* of about -25 for 99·999 per cent nominal purity *EH* silver was reported by Ho and Huntington[1]. However, their measurements were not corrected for the temperature drop (~ 60°C) at the thermocouple placed inside the coaxial ceramic tube (Section 2). A recalculation of their result, taking into account this temperature correction, yields a Z^* of $-10{\cdot}0\pm0{\cdot}5$, which is somewhat higher than the present value, $-6{\cdot}5\pm1{\cdot}4$. It is possible that the earlier results[1] were influenced, if only marginally, by the 'hydrogen embrittlement' effects, which result from a combination of trace hydrogen in the ambient and some impurity oxides in the specimen material. On the other hand, an especially clean specimen chamber was used in the present work, which made it possible to keep the ambient contaminants at a level low enough to avoid the hydrogen embrittlement effects. The latter are found[3] to introduce in the specimen dimensional changes extraneous to electromigration, which would be reflected in an apparently larger Z^*.

Kuzmenko[15] and Doan[16] have both reported considerably higher Z^* for silver compared to the present result. Kuzmenko's Z^* was $-22{\cdot}2$ at 900°C and decreased slightly with temperature. The scatter in his results was quite large ($-16{\cdot}3$ to $-35{\cdot}8$). Doan also observed a large Z^*, $-16{\cdot}1$ at 889°C, with a rather strong inverse T-dependence. The reasons for the large effective charge values obtained by these investigators are not evident at present and one can only speculate as to some systematic error in their measurements. The present value on the other hand is believed to be correct, since, as a result of the improved temperature determination and the significantly low level of ambient contaminants, the corresponding value of the defect resistivity, $1{\cdot}1\pm0{\cdot}2\ \mu\Omega$-cm/%, is close to that for other noble metals; e.g., for Au[12] and Cu[13] it is $1{\cdot}2\pm0{\cdot}3$ and $1{\cdot}2\pm0{\cdot}2\ \mu\Omega$-cm/%, respectively. Such an agreement is to be expected, since, at high temperature, the defect configuration and the associated scattering cross-sections are likely to be the same in all f.c.c. metals.

The void formation on the cathode side and the associated sample elongation were observed only in the less pure (EH) silver and could not be induced in the purer (JM) material even when charged individually with oxygen or hydrogen. Neither interstitially dissolved oxygen nor hydrogen could by itself produce the dimensional changes corresponding to void formation or any significant microscopic evidence for the latter's production. For void formation, it appears impurity precipitates are important as trapping nuclei to compete for vacancies successfully with the various sinks (e.g. dislocations, grain-boundaries and the surface).

The observed negative electrotransport of interstitial oxygen in silver, like the self migration, implies the dominance of the 'electron wind' force on the oxygen ion. Anode directed electromigration of oxygen in yttrium[17] and β-titanium[18] has also been reported. The apparent increase in Z^* for the oxygen-free material impregnated with hydrogen is quite surprising, since it is not due to an increase in the diffusivity. The latter possibility was investigated by Rothman and Peterson[19] at our request with negative results. The only other alternative would appear to be the influence of a gradient in the hydrogen caused by the electric field which in turn enhances the driving force on the self atoms. Possibly a gradient in the hydrogen density gives rise to a polarization reinforcing the impressed electric field. Additional experiments at various ambient hydrogen partial pressures are planned with a view to explore

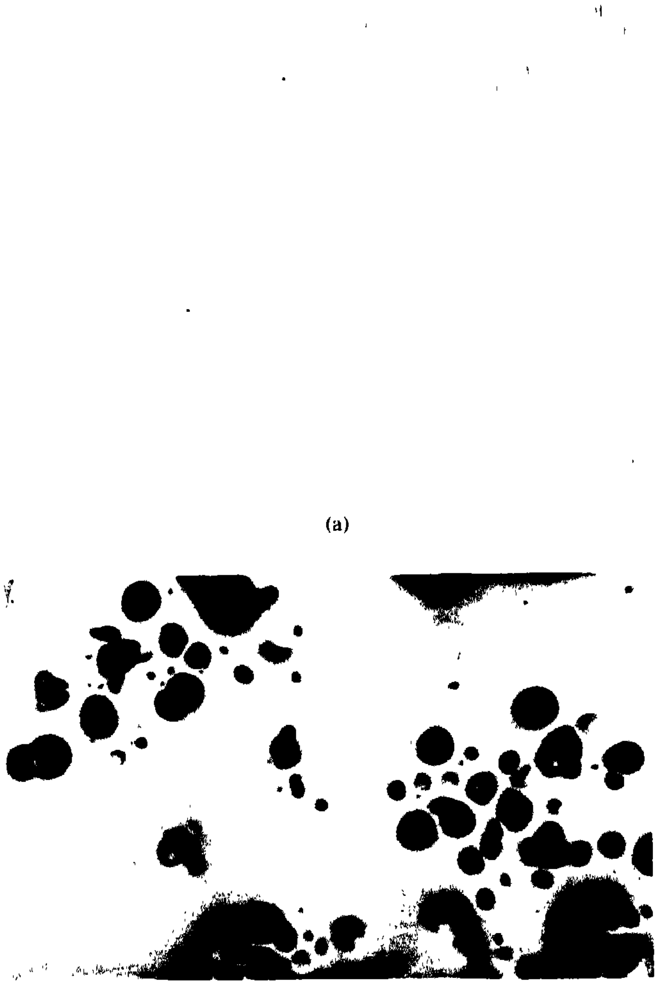

(a)

(b)

Fig. 6. Photomicrographs of anode (a) and cathode (b) regions adjacent to the specimen (EH 1) center; magnification ~ 100 ×.

further the influence of the interstitial on the self-electromigration in silver.

Acknowledgements—We wish to thank Dr. B. H. Kindt and his associates at the M and P laboratory, General Electric Company, Schenectady, New York, for carrying out the gas analysis of our silver specimens. We are indebted to Drs. S. Rothman and N. Peterson of Argonne National Laboratory for investigating the effect of ambient hydrogen on the self-diffusion in silver. The authors acknowledge the helpful discussions with M. D. Feit, J. F. D'Amico, J. L. Routbort and W. Alexander.

REFERENCES

1. HO P. S. and HUNTINGTON H. B., *J. Phys. Chem. Solids* **27**, 1319 (1966).
2. ROGERS H. C., *Science* **159**, 1057 (1968).
3. To be submitted for publication to *J. appl. Phys.*
4. PATIL H. R., Doctoral Thesis, Rensselaer Polytechnic Institute, 1969 (unpublished).
5. The gas analysis results were obtained with a platinum bāth by vacuum fusion at 1900°C at M&P Laboratory, G. E. Co., Schenectady, New York.
6. *Radiation Thermometer Instruction Manual*, IRCON Series 300 HC.
7. HUNTINGTON H. B. and GRONE A. R., *J. Phys. Chem. Solids* **20**, 76 (1961).
8. HO P. S., Doctoral Thesis, Rensselaer Polytechnic Institute (1964).
9. FIKS V. B., *Soviet Phys. solid St.* **1**, 14 (1959).
10. BOSVIEUX C. and FRIEDEL J., *J. Phys Chem. Solids* **23**, 123 (1962).
11. TOMIZUKA C. T. and SONDER E., *Phys. Rev.* **103**, 1182 (1956)
12. GILDER H. M. and LAZARUS D., *Phys. Rev.* **145**, 507 (1966).
13. SULLIVAN G. A., *J. Phys. Chem. Solids* **28**, 347 (1967).
14. BARNES R. S. and NELSON R. S., *Radiation Effects; Met. Soc. Conf.* **37**, 225 (1967).
15. KUZMENKO P. P., *Ukr. Fiz. Zhur.* **7**, 117 (1962).
16. DOAN N. V. and BREBEC G., Internal Rapport CEA-R-3480, Saclay (1968).
17. CARLSON O. N., SCHMIDT F. A. and PETERSON, *J. less-common Metals* **10**, 1 (1966).
18. CLAISE F. and KOENIG P., *Acta metall.* 4, 650 (1956).
19. ROTHMAN S. J. and PETERSON N. L., Private communication.
20. *American Institute of Physics Handbook*, 2nd Edn. McGraw-Hill, New York (1963)

APPENDIX

Effect of conduction losses on temperature determination

We calculate here the temperature difference between the hollow cylindrical specimen and the ceramic tube housing the thermocouple. This difference arises because of conduction losses in the latter. In the steady state, the divergence of the heat efflux due to conduction in the ceramic tube as well as in the thermocouple wires is equated to heat influx due both to gas conduction and radiation. The convection effects are neglected since the gap between the two coaxial cylinders is very small, 0·12 mm. Furthermore, the smallness of the gap enables one to write the radiation term in a rather simple form. With these approximations,

$$-\frac{\mathrm{d}}{\mathrm{d}x}(K_cA_c+2K_tA_t)\frac{\mathrm{d}T_c}{\mathrm{d}x}=\frac{2\pi K_a}{\ln(r_m/r_c)}(T_m-T_c)$$

$$+\frac{2\pi r_m\sigma}{(1/\epsilon_c+1/\epsilon_m-1)}(T_m{}^4-T_c{}^4) \quad \text{(A-1)}$$

where the subscripts c,t,a,m refer to the ceramic, the thermocouple wires, the argon gas and the metal, respectively. K,A,r and ϵ are respectively the appropriate thermal conductivity, cross-sectional area, radius and the emissivity. The first term on the right refers to gas conduction and the second one to radiant heat exchange between the two coaxial cylinders (see CHAPMAN, *Heat Transfer*, MacMillan, New York (1967).

Next we approximate $(T_m{}^4-T_c{}^4)$ by $4[(T_m+T_c)/2]^3(T_m-T_c)$ and take for the various thermal conductivities the values at 1000°K, the temperature midway between the center and the end of the sample. For example, $\bar{K}_c \sim 0{\cdot}0065$ (mullite), $\bar{K}_t \sim 0{\cdot}127$ (Pt–Pt10%Rh) and $\bar{K}_a \sim 10{\cdot}28\times10^{-5}$ cal/sec degcm[20]. For the experimental values, A_c $(4{\cdot}9\times10^{-2}\,\mathrm{cm}^2)$, A_t $(1{\cdot}267\times10^{-4}\,\mathrm{cm}^2)$, r_m (0·159 cm), r_c (0·147 cm), and for reasonable values of ϵ_c $(\sim 0{\cdot}78)$ and ϵ_m $(\sim 0{\cdot}1)$, equation (A–1) becomes:

$$(3{\cdot}55\times10^{-4})\frac{\mathrm{d}^2T_c}{\mathrm{d}x^2}=(86{\cdot}5\times10^{-4}+4{\cdot}81\times10^{-4})(T_m-T_c)$$

or

$$(T_m-T_c)=0{\cdot}0389\frac{\mathrm{d}^2T_c}{\mathrm{d}x^2}. \quad \text{(A-2)}$$

The axial distribution of temperature in a resistively heated-wire (or a hollow cylinder), with the ends held at a fixed low temperature T_0, is a cosine function of position on the axis if radiation and convection losses are neglected in comparison to heat conduction in the wire. The cosine function satisfies the heat equation,

$$K_mJ\frac{\mathrm{d}^2T_m}{\mathrm{d}x^2}=-j^2\rho(T) \quad \text{(A-3)}$$

where K_m is the metal thermal conductivity, J the Joule–Kelvin coefficient, j the current density and $\rho(T)$ the resistivity taken as proportional to the absolute temperature, e.g. $\rho(T)=AT$°K. The temperature at any point in the sample can thus be written as follows:

$$T_m(x)=T_m{}^0\cos\beta x \quad \text{(A-4)}$$

where $\beta^2=j^2A/K_mJ$ and $T_m{}^0\equiv T_m(x=0)$ = the center temperature. Finally, taking the temperature distribution in the ceramic tube to be of the same form as in the sample,

$$T_c(x)=T_c{}^0\cos\beta x. \quad \text{(A-5)}$$

Combining equations (A–2), (A–4) and (A–5) we get,

$$(T_m{}^0-T_c{}^0)=0{\cdot}0389\,\beta^2T_c{}^0.$$

For the experimental values of β^2 ($\sim 0{\cdot}67\ \mathrm{cm}^{-2}$) and $T_c^0 \simeq 1173°\mathrm{K}$,

$$\Delta T^0_{mc} \equiv T_m^0 - T_c^0 \approx 30{\cdot}5\ \mathrm{deg.}$$

This value of ΔT^0_{mc} is only about half of the experimental result ($\sim 60°\mathrm{C}$). However, in addition to the number of approximations involved in the calculation and the uncertainties in the Handbook values of the various physical parameters, the uncertainties in the measurement of r_m and r_c are such that the difference, $(r_m - r_c) \propto \ln(r_m/r_c)$, may vary by a factor of ~ 3. Thus it is possible to bring the calculated ΔT^0_{mc} in good agreement with its observed value simply by adjusting the ratio, (r_m/r_c), within the experimental limits on r_m and r_c (see equation (A-1) and (A-2)). Moreover, it is conceivable that the calculation underestimates the actual ΔT^0_{mc} because of the implicit assumption that the thermocouple junction and the ceramic tube are at the same temperature.

J. Phys. Chem. Solids Pergamon Press 1970. Vol. 31, pp. 475–484. Printed in Great Britain.

MIGRATION SOUS L'EFFET D'UN CHAMP ELECTRIQUE DE ^{110}Ag ET DE ^{124}Sb DANS L'ARGENT†

NGUYEN VAN DOAN et G. BREBEC
Commissariat à l'Energie Atomique, Centre d'Etudes Nucléaires de Saclay, France

(*Received* 24 *February* 1969; *in revised form* 24 *June* 1969)

Résumé – Nous rappelons brièvement les récentes théories concernant l'effet d'un champ électrique sur la migration des défauts ponctuels. Afin de relier les différentes grandeurs physiques du phénomène, nous avons exprimé le flux d'un soluté en fonction des 'valences efficaces' introduites dans la Thermodynamique des Processus Irreversibles. Les résultats expérimentaux montrent que les atomes migrent vers l'anode avec des valences efficaces de l'ordre de -16 pour ^{110}Ag et -95 pour ^{124}Sb vers 900°C. Des estimations sur les résistivités entrant en jeu dans les différentes théories ont été faites afin de comparer leurs prédictions avec les résultats expérimentaux.

Abstract – The most recent theories relative to the influence of an electric field on the migration of point defects in metals are briefly recalled. In order to relate the various physical constants of the phenomenon, the flux of a solute is expressed in terms of 'effective valences' defined in Thermodynamic of Irreversibles Processes. Experimental results show that atoms migrate towards the anode with effective valences of -16 and -95 respectively for ^{110}Ag and ^{124}Sb at temperatures in the region of 900°C. Estimates were made on the resistivities that should be used in the different theories in order to compare their predictions with experimental results.

INTRODUCTION

De nombreux travaux ont été publiés relativement à l'effet d'un champ électrique sur la mobilité des ions métalliques. La quantité mesurée est la valence efficace Z^*, grandeur qui intègre tous les effets du champ électrique: effet électrostatique: une charge Z e placée dans un champ électrique **E** est soumise à une force $\mathbf{F}_S = Z\,e\,\mathbf{E}$, où e est la valeur absolue de la charge de l'électron et Z la valence de l'ion; effet des porteurs de charge: l'interaction des porteurs avec les ions est équivalente à une force $\mathbf{F}_e$. Si les porteurs sont des électrons cette force sera de sens opposé à la précédente. La valence efficace Z^* se définit à partir de la force résultante

$$\mathbf{F}_R = \mathbf{F}_S + \mathbf{F}_e$$

Z^* est telle que: $\mathbf{F}_R = Z^*\,e\,\mathbf{E}$.

Plusieurs auteurs explicitent cette force résultante $\mathbf{F}_R$ en termes de résistivité dans le cas où les porteurs de charge sont des électrons. Le tableau suivant (Tableau 1) groupe les différentes expressions obtenues.

Les différences proviennent des hypothèses de départ[1–3].

La mesure expérimentale de Z^* permet de déterminer $\Delta\rho$ pour chacun des trois modèles; si d'autre part on peut calculer indépendamment cette quantité il est alors possible de préciser la validité relative des hypothèses faites par ces différents auteurs.

Dans la première partie nous rappellerons brièvement comment s'introduisent les valences efficaces d'un point de vue thermodynamique. A l'aide des équations phénoménologiques nous exprimerons les différents flux de matière et nous discuterons du moyen de mesurer Z^*.

Dans la seconde partie nous décrirons le dispositif expérimental utilisé et nous donnerons les résultats obtenus.

Enfins dans la troisième partie nous comparerons nos résultats avec les valeurs calculées de $\Delta\rho$.

---

†Ce travail fait partie d'une thèse de Doctorat ès Sciences qui sera présentée à la Faculté des Sciences d'Orsay par N. V. Doan.

Tableau 1

Modèles	Force exercée sur l'ion du solvant de valence Z	Force exercée sur l'ion du soluté de valence $Z' = Z+z$
Fiks[1]	$-Ze\mathbf{E}\left[\frac{100\,\Delta\rho^{(Z)}}{\rho_0}-1\right]$	$-Ze\mathbf{E}\left[\frac{100\,\Delta\rho^{(Z+z)}}{\rho_0}-1\right]$
Bosvieux et Friedel[2]	$-\frac{1}{2}Ze\mathbf{E}\left[\frac{100\,\Delta\rho^{(Z)}}{\rho_0}-(1+f_0)\right]$	$-\frac{1}{2}Ze\mathbf{E}\left\{\frac{100}{\rho_0}[\Delta\rho^{(z)}+\Delta\rho^{(z+Z)}]-(1+f_0)\right\}$
Huntington [3]	$-\frac{1}{2}Ze\mathbf{E}\left[\frac{100\,\Delta\rho^{(Z)}}{\rho_0}-2\right]$	$-\frac{1}{2}Ze\mathbf{E}\left[\frac{100\,\Delta\rho^{(Z+z)}}{\rho_0}-2\right]$

$\Delta\rho^{(Z)}$ est l'excès de résistivité dû à 1% d'ions du solvant en position de col
$\Delta\rho^{(Z+z)}$ est l'excès de résistivité dû à 1% d'ions du soluté en position de col
$\Delta\rho^{(z)}$ est l'excès de résistivité dû à 1% d'ions du soluté en position stable
ρ_0 la résistivité du solvant pur et f_0 une fonction caractéristique du solvant.

1. THERMODYNAMIQUE DES PHENOMENES DE TRANSPORT SOUS CHAMP ELECTRIQUE

(1) *Expression des flux*

Nous nous bornerons à considérer un alliage métallique A-B où la diffusion est purement lacunaire et qui est soumis à un champ électrique E. Les seuls phénomènes irréversibles observés seront donc des flux de matière, des flux de lacunes et des flux d'électrons (on suppose que la conduction est électronique).

Si tous ces flux sont colinéaires on montre [4] que:

$$\mathbf{J}_A = -\frac{L_{AA}}{T}\frac{\mathrm{d}}{\mathrm{d}x}(\boldsymbol{\mu}_A-\boldsymbol{\mu}_L)-\frac{L_{AB}}{T}\frac{\mathrm{d}}{\mathrm{d}x}(\boldsymbol{\mu}_B-\boldsymbol{\mu}_L) -\frac{L_{Ae}}{T}\frac{\mathrm{d}}{\mathrm{d}x}\boldsymbol{\mu}_e \tag{1-1}$$

$$\mathbf{J}_B = -\frac{L_{BA}}{T}\frac{\mathrm{d}}{\mathrm{d}x}(\boldsymbol{\mu}_A-\boldsymbol{\mu}_L)-\frac{L_{BB}}{T}\frac{\mathrm{d}}{\mathrm{d}x}(\boldsymbol{\mu}_B-\boldsymbol{\mu}_L) -\frac{L_{Be}}{T}\frac{\mathrm{d}}{\mathrm{d}x}\boldsymbol{\mu}_e. \tag{1-2}$$

Les flux $\mathbf{J}_A$ et $\mathbf{J}_B$ sont mesurés ici dans un référentiel lié à la vitesse atomique moyenne **v**. Dans ce référentiel

$$\mathbf{J}_A+\mathbf{J}_B = -\mathbf{J}_L \text{ (flux de lacunes)}$$

avec $\boldsymbol{\mu}_i = \mu_i + q_i \varnothing \quad (i = A, B, L \text{ et } e)$

où μ_i est le potentiel chimique de l'espèce i; q_i sa charge: $\varnothing$ le potentiel électrique au point considéré, $\mathbf{E} = -\partial\varnothing/\partial x$; si $i = L$; $q_L = 0$; si $i = e$, $q_e = -e$, $\mu_e = E_F$ (énergie au niveau de Fermi) et $\mathrm{d}\mu_e/\mathrm{d}x = \mathrm{d}E_F/\mathrm{d}x \simeq 0$.

On définit thermodynamiquement les valences efficaces Z_{A^*} et Z_{B^*} par les relations suivantes[5]

$$L_{Ae} = L_{AA}Z_{A^*} + L_{AB}Z_{B^*} \tag{1-3}$$

$$L_{Be} = L_{BA}Z_{A^*} + L_{BB}Z_{B^*}. \tag{1-4}$$

En utilisant ces deux relations et en tenant compte des expressions des coefficients de diffusion intrinsèques D_A et D_B on montre, qu'à la limite des faibles concentrations de B dans A, le flux $\mathbf{J}_B$ s'écrit:

$$\mathbf{J}_B = -D^A_{B^*}\frac{\partial n_B}{\partial x}+\frac{n_B D^A_{B^*}}{kT}\left[(q_B+Z_{B^*}q_e) + \frac{L_{BA}}{L_{BB}}(q_A+Z_{A^*}q_e)\right]\mathbf{E} \tag{1-5}$$

où $D^A_{B^*} = (kL_{BB}/n_B)$ est le coefficient d'hétérodiffusion de B dans A, n_B est le nombre d'ions B par unité de volume.

Nous avons supposé, pour obtenir (1-5), que μ_L est négligeable en tout point du système c'est à dire que les lacunes sont partout à l'équilibre thermodynamique. On peut vérifier [6, 7] que $(L_{BA}/L_{BB}) < 1$.

D'autre part, dans le cas particulier de l'électromigration de l'Antimoine dans l'argent, $|q_B + Z_{B^*} q_e| \gg |q_A + Z_{A^*} q_e|$. Nous négligerons donc $(L_{BA}/L_{BB})(q_A + Z_{A^*} q_e)$ par rapport à $(q_B + Z_{B^*} q_e)$. Il vient:

$$\mathbf{J}_B = -D_{B^*}^A \frac{\partial n_B}{\partial x} + \frac{n_B D_{B^*}^A}{kT}[q_B + Z_{B^*} q_e]\mathbf{E}. \qquad (1\text{–}6)$$

Cas particulier où B = A* (isotope de *A*) c'est à dire quand on étudie l'influence d'un champ électrique sur la migration des atomes de solvant. Remplaçons *B* par *A* * dans (1–5) il vient:

$$\mathbf{J}_{A^*} = -D_{A^*}^A \frac{\partial n_{A^*}}{\partial x} + \frac{n_{A^*} D_{A^*}^A}{kT}(q_A + Z_{A^*} q_e)$$

$$\left(1 + \frac{L_{A^*A}}{L_{A^*A^*}}\right)\mathbf{E}. \qquad (1\text{–}7)$$

On peut montrer [4] que: $1 + L_{A^*A}/L_{A^*A^*} = 1/f$ où f est le facteur de corrélation pour l'autodiffusion;
donc:

$$\mathbf{J}_{A^*} = -D_{A^*}^A \frac{\partial n_{A^*}}{\partial x} + \frac{n_{A^*} D_{A^*}^A}{fkT}(q_A + Z_{A^*} q_e)\mathbf{E}. \qquad (1\text{–}8)$$

(2) *Equation de Fick généralisée*

Ecrivons l'équation de conservation pour *B* ou *A* * dans le référentiel lié à la vitesse atomique moyenne

$$\frac{\partial n_i}{\partial t} = D_i^A \frac{\partial^2 n_i}{\partial x^2} - D_i' \frac{\partial n_i}{\partial x} \qquad (1\text{–}9)$$

avec $$D_i' = \frac{D_i^A}{f_i kT}(q_i + Z_i^* q_e)E$$

i étant soit *A* * ou *B*; $f_A = f$ et $f_B = 1$.

On peut résoudre cette équation pour la géométrie et les conditions initiales suivantes: une couche mince de *A* * ou de *B* est déposée entre deux échantillons massifs de *A* (géométrie du type 'sandwich'). Dans ces conditions:

$$n_i(x,t) = \frac{Q_i}{2\sqrt{\pi D_i^A t}} \exp - \frac{(x - D_i' t)^2}{4 D_i^A t} \qquad (1\text{–}10)$$

Q_i est la quantité de *i* déposée par unité de surface.

Les abscisses *x* sont mesurées dans le référentiel lié à la vitesse atomique moyenne donc par rapport à la trace de la soudure qui matérialise ce référentiel, $n_i(x,t)$ est maximum quand $x = D_i' t$. La connaissance de l'abscisse du maximum de la courbe permet donc d'atteindre directement D_i' donc Z_i^*.

(3) *Remarque sur les valences efficaces*

On a défini dans l'introduction la valence efficace Z^* par $\mathbf{F}_R = Z^* e\, \mathbf{E}$. Cette définition est en accord avec les phénomènes observés en électrolyse: un ion positif va vers la cathode alors qu'un ion négatif va vers l'anode. Relions-la aux valences Z_{A^*} ou Z_{B^*} définies thermodynamiquement.

On sait, d'après la relation de Nerst-Einstein qu'à une force **F** correspond une vitesse moyenne des particules **V** telle que:

$$\mathbf{V} = \frac{D\mathbf{F}}{kT}$$

où *D* est le coefficient de diffusion. Le flux **J** résultant est: $\mathbf{J} = \mathbf{V}n$, *n* est le nombre de particules par unité de volume qui sont soumises à la force **F**. Avec nos notations, à la valence Z^* correspond le flux:

$$\mathbf{J}_i = \frac{D_i^A n_i}{f_i kT} e Z^* \mathbf{E}. \qquad (1\text{–}11)$$

Ceci n'est que la partie du flux due à l'effet du champ électrique, on peut l'identifier avec le deuxième terme de (1–6) ou de (1–8).

Il vient: si $i = B$; $Z^* = Z_B - Z_{B^*}$

où Z_B est la valence du soluté *B*, par exemple + 5 pour l'antimoine;

$$\text{si } i = A^*; \qquad Z^* = \frac{Z_A - Z_A^*}{f}$$

où Z_A est la valence du solvant, par exemple +1 pour l'Argent. Dans la suite nous ne considérerons que la valence Z^* que est celle couramment utilisée dans la littérature.

(4) *Expression de Z^* en fonction des paramètres mesurables*

On voit facilement que si $x_{\max}$ est l'abscisse du maximum de la courbe $n_t(x)$ on a:

$$Z^* = \frac{kTx_{\max}}{eD_t^A t\rho_0 j} \qquad (1\text{-}12)$$

j est la densité de courant: $\rho_0 \mathbf{j} = \mathbf{E}$.

Remarque: Si l'on ne considère que la valeur absolue de j, E est positif donc le sens positif sur l'axe des x ext imposé de *l'anode vers la cathode*. $x_{\max}$ est donc positif si le maximum est entre la trace de la soudure et la cathode et négatif s'il est entre la soudure et l'anode.

2. DISPOSITIF EXPERIMENTAL-RESULTATS POUR ^{110}Ag ET ^{124}Sb

(1) *Dispositif expérimental* (voir Fig. 1)

Sur des cylindres d'Argent de 10 mm de hauteur et de diamètre compatible avec la puissance du générateur utilisé nous déposons par évaporation sous vide soit ^{110}Ag soit ^{124}Sb. L'Argent, fourni par Jonhson Matthey contient environ 100 ppm d'impuretés. Les cylindres sont préalablement recuits sous vide pendant 20 hr à 800°C. Après l'évaporation ils sont soudés deux par deux en presse[8] ou directement dans l'appareil de champ électrique en plaçant les faces actives l'une contre l'autre. Nous disposons de deux enceintes de travail avec électrodes verticales refroidies à l'eau, l'une alimentée par un générateur de 500 amp, l'autre par un générateur de 2000 amp. Ces deux installations ont chacune un système d'asservissement qui permet de maintenir la température à ±2°C. Dans les deux cas les échantillons sont placés verticalement entre les électrodes, la liaison entre échantillon et électrodes est réalisée par des feuilles souples d'Argent bien recuit.

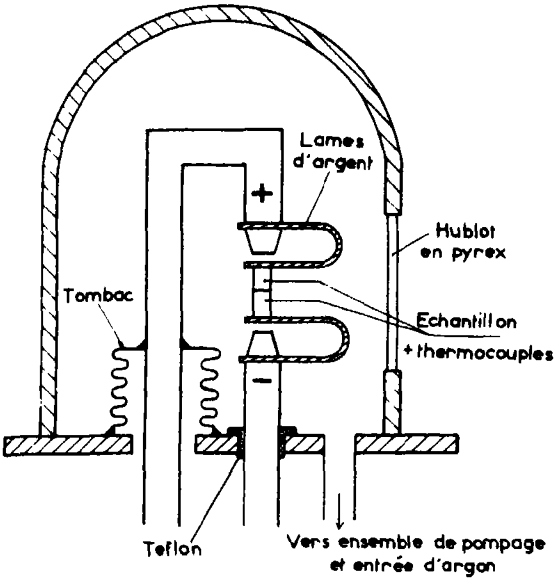
Lames d'argent
+
Hublot en pyrex
Tombac
Echantillon + thermocouples
−
Teflon
Vers ensemble de pompage et entrée d'argon

Fig. 1. Schéma du dispositif expérimental 2000 amp.

L'enceinte du générateur de 2000 amp a une électrode mobile (l'étanchéité est assurée par un soufflet métallique 'Tombac'). Ce dispositif permet de souder les deux extrémités de l'échantillon aux feuilles d'Argent pendant les premières minutes de l'essai après quoi on remonte légèrement l'électrode mobile pour éviter toute contrainte excessive. Nous avons vérifié, en mesurant la distance entre des marques superficielles, qu'avec ce montage il n'y a aucune déformation mesurable de l'échantillon. Bien entendu, pendant la soudure, l'échantillon étant maintenu entre les deux électrodes, sa section augmente. Cette augmentation de section est régulière si l'échantillon est bien vertical. (voir Tableau 2) L'enceinte du générateur de 500 amp n'a pas d'électrode mobile la fixation de l'échantillon aux feuilles d'Argent se fait par l'intermédiaire de petites brides en Argent.

Tous nos essais ont été effectués sous argon purifié sur du Magnésium fondu. La pression d'Argon, de l'ordre de 1 atm, limite l'évaporation de l'Argent. Deux trous de 0,7 mm de diamètre et de 1, 5 à 2 mm de profondeur sont percés dans l'échantillon de part et d'autre de

Tableau 2. Contrôle de l'absence de déformation

		Distance entre les marques superficielles mesurée à température ambiante (en μ)		
T (°C)	t (sec)10^{-6}	Avant l'essai	Après soudure	Après traitement
784	6,018	11.360	11.023	11.025
899	2,517	12.896	12.770	12.768

la couche active à environ 3 mm de celle-ci. Dans chacun d'eux on place l'extrémité d'un couple de 0,5 mm de diamètre du type 'Thermocoax' gainé en acier inoxydable. L'un est utilisé pour la régulation, l'autre permet d'évaluer le gradient de température. Celui-ci est toujours très faible (inférieur à 20°C/cm). L'effet Soret est donc tout à fait négligeable.

La température indiquée par les couples n'est qu'indicative car nous pouvons déterminer avec précision la température moyenne de l'essai par la mesure du coefficient de diffusion[9], soit $D_{\mathrm{Ag}^*}^{\mathrm{Ag}}$, soit $D_{\mathrm{Sb}^*}^{\mathrm{Ag}}$, dont la variation avec T est bien connue[10, 11]. La température ainsi calculée est toujours légèrement supérieure à celle des thermocouples. La différence n'a jamais excédé 10°C.

Les échantillons sont alors découpés au tour ou dans certains cas à la machine à abraser[12] après avoir été convenablement alignés. Cet alignement est réalisé à $\pm 15\mu$. L'épaisseur des tranches enlevées est déterminée par pesée, la position de la trace de la soudure est déterminée optiquement (on révèle facilement l'interface de soudure par attaque chimique dans un bain Na CN–H_2O_2). L'activité des copeaux est mesurée avec un ensemble de comptage γ à 400 canaux préalablement réglé pour l'énergie du rayonnement à mesurer.

Pour déterminer $x_{\max}$ on peut utiliser une méthode graphique ou celle préconisée par Gilder[9].

Si t_S est le temps de soudure, D_S le coefficient de diffusion correspondant à la température de la soudure, t la durée de l'essai et D le coefficient de diffusion on a:

$$D = \frac{1}{4t}\left[\frac{1}{p} - 4D_S t_S\right]$$

où p est la pente de la droite Log (Activité) $= f(x - x_{\max})^2$.
Connaissant D on en déduit:

$$T(°\mathrm{K}) = \frac{Q}{R \operatorname{Log}(D_0/D)}.$$

Q étant l'énergie d'activation et D_0 le facteur de fréquence.

D'après les valeurs publiées dans le Handbook of Physics nous avons utilisé pour loi de variation de ρ_0 (argent) avec T:

$$\rho_0(T) = 1{,}48 + 0{,}69 . 10^{-2}[T - 273] \text{ en } \mu\Omega - \mathrm{cm}.$$

Enfin pour tenir compte de la variation de section de l'échantillon (dilatation plus écrasement pendant la soudure aux lames d'Argent) nous avons utilisé comme coefficient de dilatation linéaire de l'Argent 2, 35 10^{-5}/°C. Si donc S_0 est la section de l'échantillon à la température ambiante T_0 on a:

$$S(T) = S_0[1 + 7{,}05 . 10^{-5}(T - T_0)]$$

$S(T)$ étant la section à la température T de l'essai.

(2) *Résultats* (voir Figs. 2–6)

Les Tableaux 3 et 4 groupent les résultats obtenus. Sur la Fig. 2 nous avons porté Log (v/j) en fonction de $1/T$ pour les 7 essais relatifs à l'antimoine où V est la vitesse de

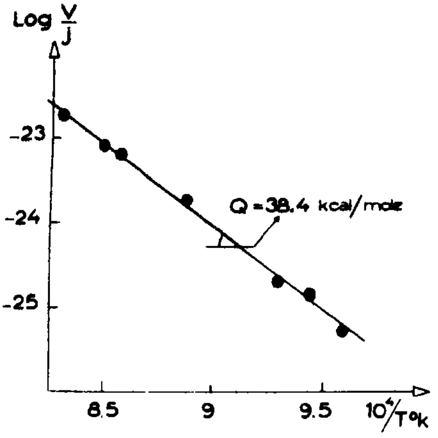

Fig. 2. Variation de Log (v/j) en fonction de $1/T$.

déplacement du maximum et j la densité de courant. D'après (1–12) on voit que:

$$\frac{V}{j} = D\frac{e\rho_0 Z^*}{kT}.$$

La variation de (V/j) est due principalement à D. Si donc on néglige la variation du terme $(\rho_0 Z^*/T)$ le logarithme de (V/j) en fonction de $1/T$ doit être sensiblement une droite de pente $-Q/R$. L'énergie d'activation trouvée est égale à 38, 4 kcal. L'accord est très bon avec les valeurs de Slifkin et al[13, 10] respectivement égales à 39, 4 et 38, 4 kcal. Pour l'Argent 110 l'énergie d'activation trouvée par cette méthode est beaucoup trop faible (30 kcal au lieu de 45). Remarquons que le domaine de température pour les quatre essais relatifs à l'argent n'est que de 56°C, ce qui est peu pour déterminer valablement une énergie d'activation. Notre valeur moyenne de $Z^* \simeq -22$ est du même ordre de grandeur que celle déterminée par Ho et Huntington[14]−25 et celle déterminée par Kuz'menko[15]−27. D'après les différentes théories proposées Z^* devrait, en gros, varier comme $1/\rho_0$ si on admet que $\Delta\rho$ ne varie pas beaucoup avec T.

Il est difficile de se prononcer dans notre cas. Pour l'Antimoine, si la variation de Z^* avec T est vérifiée pour quatre expériences réalisées au dessus de 850°C, elle est moins évidente pour celles faites à plus basses températures; mais on peut penser que, en considérant les courbes de pénétration, la diffusion dans les joints de grain donne lieu à des valeurs apparentes trop faibles de Z^*. Quant à l'argent, si la variation de Z^* paraît très nette, on peut la mettre en doute étant donné que l'énergie d'activation de V/j est trop faible par rapport à celle attendue.

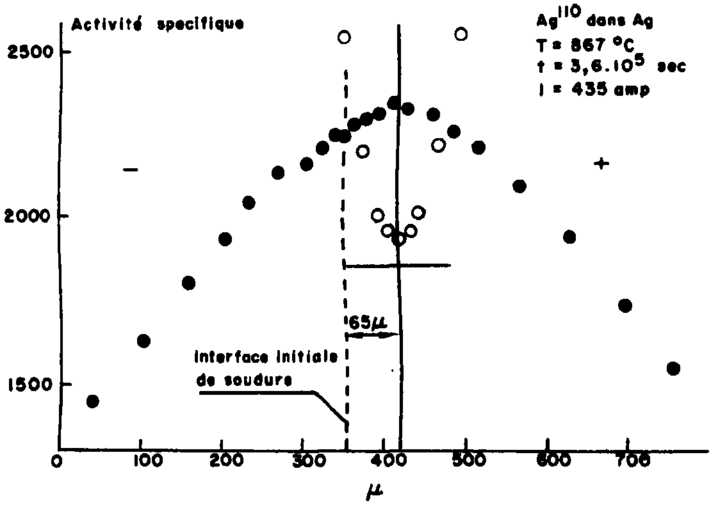

Fig. 3. Courbe de pénétration de ^{110}Ag(no. 2).

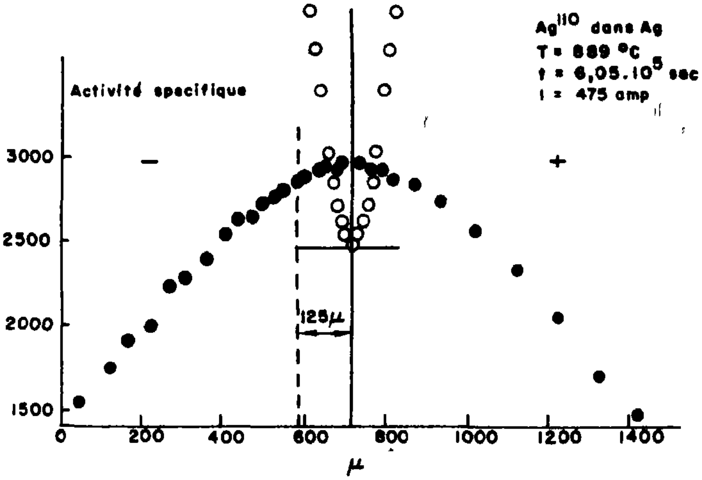

Fig. 4. Courbe de pénétration de ^{110}Ag(no. 4).

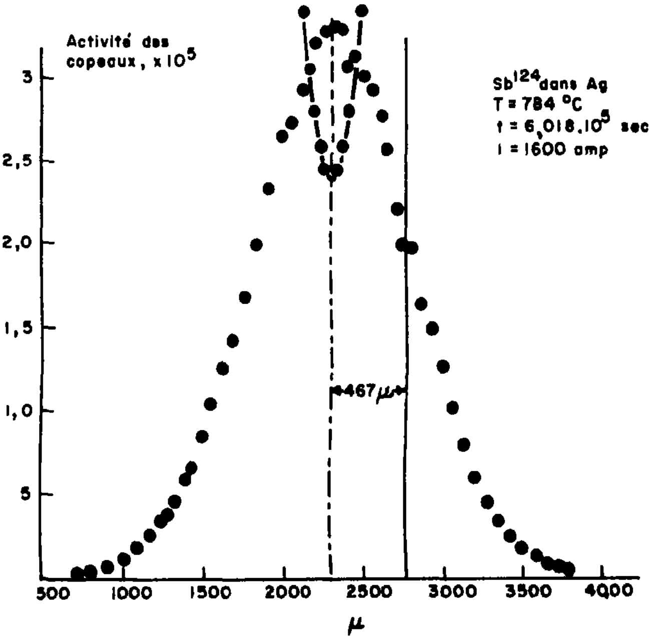

Fig. 5. Courbe de pénétration de ^{124}Sb(no. 2).

3. COMPARAISON ENTRE LES RESISTIVITES MESUREES ET CALCULEES

En utilisant la méthode des pseudo-potentiels[16], comme l'ont déjà fait Huntington *et al.*[17] pour l'aluminium et le cuivre, nous avons pu évaluer les différents termes $\Delta\rho$.

Pour le calcul de $\Delta\rho^{(Z)}$ nous avons pu tenir compte de la relaxation des ions autour de

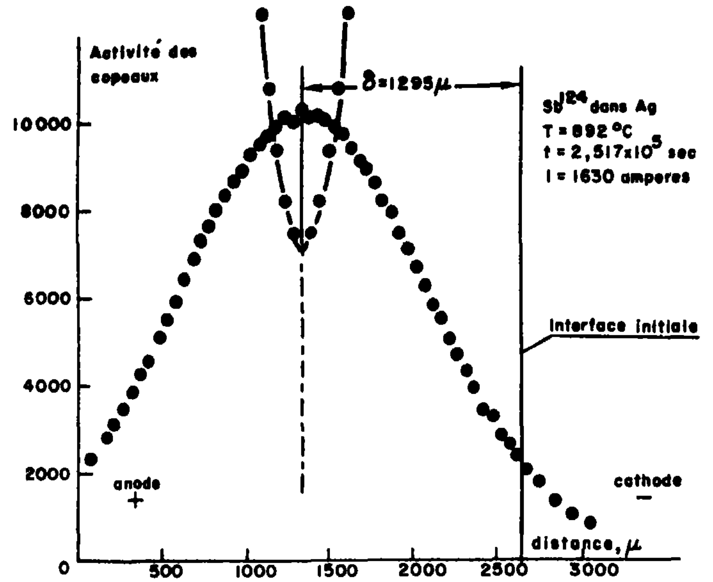

Fig. 6. Courbe de pénétration de ^{124}Sb(no. 5).

Tableau 3. *Valences efficaces de* ^{110}Ag *dans* Ag

T (°C)	Temp. (sec)10^{-5}	Intensité (amp)	Section (mm^2)	x_{max} (μ)	D (cm^2/sec)10^9	Z^*	$\pm\Delta Z^*$
833	5,76	515	7,9	−60	0,76	−27,7	6,9
867	3,6	435	5,51	−65	1,4	−21,5	5,8
875	4,32	460	8,79	−55	1,6	−19,9	5,2
889	6,05	475	5,62	−125	2,0	−16,1	2,7

Tableau 4. *Valences efficaces de* ^{124} Sb *dans* Ag

765	5,184	1.720	29,8	−292	1,42	−90,6	8,7
784	6,018	1.600	31,4	−467	2,00	−100,8	6,5
803	4,961	1.655	25	−577	2,77	−84,1	7,2
852	2,418	427	7,9	−619	6,07	−102	7,0
892	2,517	1.630	25	−1,295	10,8	−95,8	2,9
901	2,367	1.805	28,7	−1,326	12,3	−95,1	3,4
933	1,692	1.450	25,3	−1,215	19,0	−86,5	3,7

l'atome du solvant en position de col en utilisant les valeurs de Johnson et Brown[18]: pour celui de $\Delta\rho^{(Z+z)}$ c'est à dire la résistivité de l'antimoine en position de col dans l'Argent, nous avons dû négliger cet effet n'ayant aucune valeur à notre disposition. Les deux Tableaux 5 et 6 rassemblent les valeurs calculées et celles obtenues à partir des valeurs expérimentales de Z^* suivant les trois modèles de Fiks, Friedel et Bosvieux, et Huntington.

Il est bien difficile de conclure définitivement en faveur de tel ou tel modèle. Malgré tout il nous semble que l'accord est meilleur avec celui de Bosvieux et Friedel.

Tableau 5. Cas de l'electromigration de ^{110}Ag *dans* Ag

Temp. (°C)	$\Delta\rho^{(Z)}$Fiks	$\Delta\rho^{(Z)}$ Bosvieux, Friedel	$\Delta\rho^{(Z)}$ Huntington	$\Delta\rho^{(Z)}$ calculée
833	2,1 ± 0,5	3,9 ± 1	4,2 ± 1	2,47
867	1,7 ± 0,5	3,1 ± 0,9	3,4 ± 1	
875	1,6 ± 0,4	2,9 ± 0,8	3,2 ± 0,8	
889	1,3 ± 0,3	2,3 ± 0,4	2,6 ± 0,6	

Tableau 6. Cas de l'electromigration de ^{124}Sb *dans* Ag

Temp. (°C)	$\Delta\rho^{(z)}+\Delta\rho^{(z+Z)}$ Bosvieux Friedel	$\Delta\rho^{(z)}+\Delta\rho^{(z+Z)}$ calculée	$\Delta\rho^{(Z+z)}$ Fiks	$\Delta\rho^{(Z+z)}$ Huntington	$\Delta\rho^{(Z+z)}$ calculée
765	12,2 ± 1,2	16,4	6,2 ± 0,6	12,4 ± 1,2	9,2
784	13,8 ± 0,9		7,0 ± 0,5	14,0 ± 1,0	
803	11,7 ± 1,0		5,9 ± 0,5	11,8 ± 1,0	
852	14,9 ± 0,6		7,6 ± 0,3	15,2 ± 0,6	
892	14,5 ± 0,5		7,4 ± 0,2	14,8 ± 0,4	
901	14,5 ± 0,5		7,4 ± 0,2	14,8 ± 0,4	
933	13,6 ± 0,6		6,9 ± 0,3	13,8 ± 0,6	

D'autre part, il est intéressant de remarquer que les valeurs expérimentales $\Delta\rho^{(z+Z)}$ déduites des modèles de Bosvieux et Friedel, et de Fiks ne sont pas très différentes de la valeur expérimentale de Linde[19] 7,26$\mu\Omega$ cm/% at., valeur relative à la position stable $\Delta\rho^{(z)}$.

Ce qui tendrait à prouver que la résistivité de l'antimoine varie très peu eu cours d'un saut.

Ceci a également été observé par Hehenkamp[20] et Kuz'menko[21] pour l'antimoine respectivement dans l'Or et dans le Cuivre. Par contre Gilder[19] a obtenu des résultats très différents pour l'Antimoine dans l'Or: il trouve que $\Delta\rho^{(z+Z)}$ est environ deux à trois fois plus grande que $\Delta\rho^{(z)}$.

Signalons que Gilder a étudié l'électromigration de l'Antimoine dans l'Or par la technique de la couche mince, alors que Hehenkamp utilise un alliage Au-Sb entre deux échantillons d'Or pur.

Remerciements—Nous tenons à remercier le Dr. Y. Adda qui n'a pas manqué de nous prodiguer conseils et encouragements tout au long de ce travail. Nous remercions également le Professeur H. B. Huntington et le Professeur J. Friedel pour leurs nombreux commentaires. Nos remerciements vont aussi au Professeur F. Claisse, au Dr. M. Gerl et à M. Bendazzoli, pour leur aide et l'intérêt qu'ils ont portés à cette étude.

REFERENCES

1. FIKS V. B., *Fiz. Tverd. Tela* **1**, 16 (1959); *Soviet Phys. solid St.* **1**, 16 (1959).
2. BOSVIEUX C. et FRIEDEL J., *J. Phys. Chem. Solids* **23**, 123 (1962).
3. HUNTINGTON H. B. et GRONE A. R., *J. Phys. Chem. Solids* **20**, 76 (1961).
4. ADDA Y. et PHILIBERT J., *La diffusion dans les Solides*. P.U.F. Paris (1966).
5. BARANOWSKI B. et CUKROWSKI A. S., *Archiwum Hutnictwa* IX, 31 (1964).
6. HOWARD R. E. et LIDIARD A. B., *Rep. Prog. Phys.* **27**, 161 (1964).
7. NGUYEN VAN DOAN et BREBEC G.. Rapport CEA-R-3480 (1968).
8. ADDA Y., PHILIBERT J., et FARAGGI H., *Rev. Metal.* **54**, 597 (1957).
9. GILDER H. M. et LAZARUS D., *Phys. Rev.* **145**(2), 507 (1966).
10. TOMIZUKA C. T. et SONDER E., *Phys. Rev.* **103**, 1182 (1956).
11. TOMIZUKA C. T., SLIFKIN L. et SONDER E., *Phys. Rev.* **93**, 970 (1954).
12. BENDAZZOLI M. et BEYELER M., Note CEA, 531 (1965).

13. SLIFKIN L., LAZARUS D. et TOMIZUKA C. T., *J. appl. Phys.* **23**, 1405 (1952).
14. HO P. S. et HUNTINGTON H. B., *J. Phys. Chem. Solids* **27**, 1319 (1966).
15. KUZ'MENKO P. P., *Ukr. Fix. Zhns.* **1**, 117 (1962).
16. HARRISON W. A., *Pseudo-Potentials in the Theory of Metals*. Benjamin, New York. (1966).
17. HUNTINGTON H. B., NGUYEN VAN DOAN et FEIT M. (à paraître).
18. JOHNSON R. A. et BROWN E., *Phys. Rev.* **127**, 446 (1962).
19. LINDE J. O., *Ann. Phys.* **15**, 219 (1932).
20. HEHENKAMP Th., HERZIG Ch. et HEUMANN Th., *Intl. Conf. on Vacancies and Interstitials in Metals*. Jülich (1968).
21. KUZ'MENKO P. P., OSTROVSKII L. F. et KOVAL'CHUK V. S., *Soviet Phys. solid St.* **4**, 356 (1962).

J. Phys. Chem. Solids Pergamon Press 1970. Vol. 31, pp. 485–488. Printed in Great Britain.

PARAMAGNETIC DIFFUSE SCATTERING OF NEUTRONS BY A 90 AT.% MANGANESE COPPER ALLOY

E. R. VANCE and J. H. SMITH
Physics Department, Monash University, Victoria, Australia

(*Received* 23 *January* 1969; *in revised form* 24 *June* 1969)

Abstract – Measurements of the paramagnetic diffuse scattering of neutrons by a 90 at.% γ-MnCu alloy were made at temperatures ranging from 150° to 600°K. The observed increase in scattering above the Néel temperature yields a value of $1{\cdot}7 \pm 0{\cdot}3\,\mu_B$ for the localized moment per manganese atom.

1. INTRODUCTION

GAMMA MANGANESE is unstable at room temperature, but the γ-Mn structure can be retained in MnCu alloys which contain more than about 5 at.% of copper by quenching them from the γ-phase field. These alloys become antiferromagnetic and undergo a structure change f.c.c. → f.c.t. ($c/a < 1$) when they are cooled through their transformation temperature, which increases with manganese content to an estimated value of 540°K for pure γ Mn[1].

Other properties of γ Mn have also been deduced by extrapolating the appropriate alloy data. From measurements of the specific heat of MnCu alloys, Zimmerman *et al.*[2] have suggested that the entropy change associated with the magnetic ordering in γ Mn is only half that expected assuming a localized moment model, and that a spin density wave description is more appropriate to the discussion of antiferromagnetism in γ Mn. However, the interpretation of the specific heat curves of magnetic materials is often controversial, as in the studies of α-Mn[3, 4], and Ni[5, 6], and the arguments of Zimmerman *et al.* were by no means conclusive.

The magnetic susceptibilities of γ-Mn alloys with Cu[1] Ni or Pd[7] continue to increase when the alloys are heated above their Néel temperatures. No Curie–Weiss law behaviour is observed, and it has been suggested that these results are inconsistent with a localized moment model. However, additional experimental evidence for the presence of localized moments in paramagnetic materials can be obtained from measurements of the diffuse scattering of neutrons at low angles, although information about the spin coupling can only be obtained by energy analysis of the scattered radiation.

Wilkinson and Shull[8] have shown that when a ferromagnetic or antiferromagnetic material is heated from a temperature which is low compared with its Curie or Néel point to a temperature well into the paramagnetic region, then the increase in the incoherent diffuse scattering of neutrons is given by

$$\frac{\mathrm{d}\sigma}{\mathrm{d}\Omega} = \tfrac{2}{3}S^2\left(\frac{e^2\gamma}{mc^2}\right)^2 f^2 \tag{1}$$

assuming that the ionic moments are localized and due to spin only. S is the spin quantum number of each paramagnetic ion, γ is the magnetic moment of the neutron. f is the magnetic form factor, and the differential scattering cross section is defined in terms of the intensity of the neutrons reaching the counter.

Meneghetti and Sidhu[9] observed paramagnetic neutron scattering from MnCu alloys, with a maximum at 20 at.% Mn. With further addition of manganese, the decrease in paramagnetic scattering corresponded with an increase in the intensity of a diffuse (100) reflexion. This reached a maximum at 50 at.% Mn, and was explained in terms of short range magnetic order.

Hicks and Browne [10] found an increase in the differential cross section of about 150 mb/sr/at in the diffuse scattering of neutrons ($\lambda = 1{\cdot}07$ Å) from an 85 at.% γ-MnPd alloy in a direction $2\theta = 10$ deg when the alloy was heated through its Néel point. The scattering in this direction was at the edge of a large diffuse peak centred about (100) in the neutron diffraction pattern. They attributed this peak to magnon scattering but since spin wave theory is valid only at low temperatures, they invoked a quasi-static model to explain the increased diffuse scattering at $2\theta = 10$ deg when the alloy was heated above its Néel point.

The diffuse (100) peak is not observed in the diffraction pattern of pure γ-Mn prepared by electro-deposition [11], but paramagnetic scattering measurements of this material are not possible since it decomposes rapidly when heated. In principle, measurements could be made in the high temperature range of stability of the gamma phase (1079–1140°C), but the results of this experiment would be difficult to obtain and analyse.

However, by suitable choice of a γ-manganese alloy and of the scattering conditions, the presence or otherwise of paramagnetic scattering in γ-Mn could be inferred.

90 at.% γ-MnCu was chosen because (a) the addition to γ-Mn of 10% Cu produces only a small diffuse (100) peak in the neutron diffraction pattern of the quenched alloy (Fig. 1); (b) the magnetic moment per Mn ion determined at low temperatures by neutron diffraction was almost as large as the value ($2{\cdot}4 \pm 0{\cdot}1\,\mu_B$) estimated for γ-Mn [1]; (c) the Néel point, T_N, (400°K) was such that measurements could be made at temperatures well below this value, and also at temperatures sufficiently high in the paramagnetic region without decomposing the alloy [13].

2. EXPERIMENTAL METHOD

The alloy was prepared by arc melting manganese (4N5) with copper (5N) in an argon atmosphere. The alloy was turned and remelted several times to ensure thorough mixing, and the resulting as-cast ingot was cold-swaged to 1 cm dia. A cylindrical neutron diffraction sample 4 cm long was cut and sealed into an evacuated quartz capsule, then homogenized for 4 days at 1000°C and finally quenched by breaking the capsule under water.

Careful measurements were made of the diffuse scattering of neutrons ($\lambda = 1{\cdot}07$ Å) in

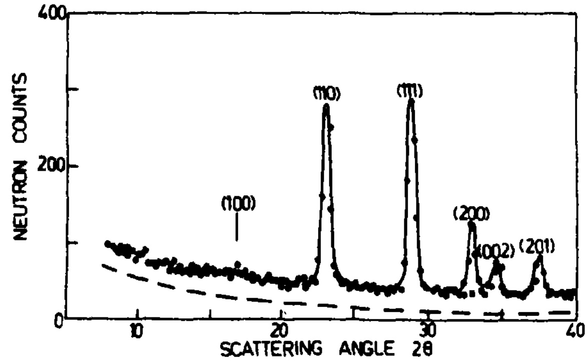

Fig. 1. Neutron diffraction pattern of a 90 at.% γ-MnCu alloy at 300°K. The experimental background is shown by the broken line.

the direction $2\theta = 8$ deg, with the sample maintained at various constant temperatures (±5°K) in the range 150–600°K. The choice of scattering angle was very restricted and the direction $2\theta = 8$ deg was chosen for the following reasons (a) it was sufficiently remote from the (100) diffuse peak, the intensity of which is dependent on temperature[14]; (b) assuming that the magnetic form factor for Mn^{2+} is applicable[11] the value of f^2 in equation (1) is 0·82, and any observed increase in the diffuse scattering above the Néel point would fall rapidly at higher angles; (c) at lower angles, the background scattering due to air and the vanadium windows of the temperature enclosure increases rapidly with decreasing scattering angle, and the separation of any paramagnetic scattering would be more difficult; (d) low angle diffuse scattering from any clusters which might be produced when the alloy was heated would be of significance only at angles much lower than 8 deg[13].

3. RESULTS AND DISCUSSION

The experimental results are shown in Fig. 2. The experimental background scattering has been subtracted, and was estimated using the cadmium difference technique modified to take account of the scattering from the air in the path of the main beam and from the temperature enclosure.

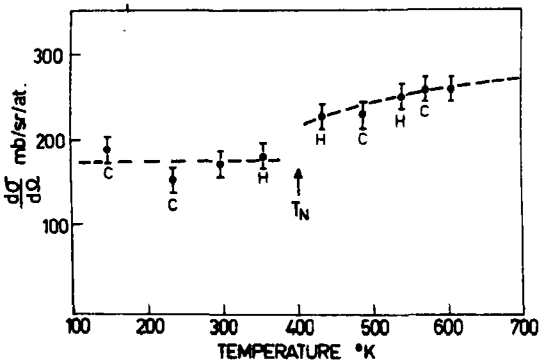

Fig. 2. Temperature dependence of the diffuse scattering of neutrons from a 90 at.% γ-MnCu alloy at 8 deg in 2θ. Points marked H refer to results obtained when the alloy was heated from room temperature. Those marked C refer to those obtained when the alloy was cooled from 600°K. The experimental background has been subtracted.

The remaining scattering, due to the sample only, was normalized relative to itself at $2\theta = 8$ deg, assuming complete nuclear disorder.

At temperatures below T_N, the observed scattering at $2\theta = 8$ deg will be due to contributions from crystal disorder scattering, multiple scattering, isotope and spin disorder scattering. The largest contribution due to crystal disorder was calculated at 119±4 mb/sr/at, and the multiple scattering was deduced by the method of Blech and Averbach[12] to be 15±3 mb/sr/at. The isotope and spin incoherence scattering cross section was calculated as 34±5 mb/sr/at. Temperature diffuse scattering will be concentrated mainly about the Bragg peaks, as discussed below, and so will not contribute to the scattering at $2\theta = 8$ deg. Thus, below T_N, the specimen scattering has been calculated to be 160±10 mb/sr/at.

We now consider possible increases in the diffuse scattering from the specimen at temperatures above T_N. If it is assumed that the atoms vibrate independently, the temperature diffuse scattering increases with increasing scattering angle, and is given by

$$\frac{d\sigma}{d\Omega}(T) = b^2[1-\exp(-2W\sin^2\theta/\lambda^2)] \quad (2)$$

b is the average coherent scattering length per atom and W is the Debye-Waller factor. Assuming a Debye temperature ~300°K, the increased scattering at $2\theta = 8$ deg on heating from 150° to 600°K would not exceed 1 mb/sr/at. This is a maximum value since the atomic vibrations are not independent, and as mentioned previously, the temperature diffuse scattering will be concentrated about the Bragg positions.

Two other possible contributions to the observed increase in low angle scattering were considered. We have found that when quenched γ-MnCu alloys are aged at moderate temperatures (700–900°K), the manganese atoms cluster prior to the precipitation of α-Mn, and this process produces an irreversible increase in the scattering at low angles [13]. Measurements were therefore made both on heating and cooling to check whether any increase in scattering had occurred due to this effect, but no significant change was found (Fig. 2). The assumption of practically complete nuclear disorder is also justified by the results of the low angle scattering measurements of quenched alloys [13].

Another possible contribution to the increased scattering at $2\theta = 8$ deg could arise from the temperature variation of the intensity of the (100) diffuse peak. However, measurements show that this intensity reaches a maximum at the Néel point, but then decreases rapidly at higher temperatures [14].

The observed increase in scattering at 600°K in the direction $2\theta = 8$ deg is therefore assumed to be due to paramagnetic diffuse scattering, and from equation [1], assuming that copper ions make no contribution, the localized moment per Mn atom is $1{\cdot}7 \pm 0{\cdot}3\ \mu_B$.

The assumption of an Mn^{2+} form factor is justified by the relative intensities of the (110) and (201) magnetic peaks observed in the neutron diffraction patterns for the alloy and for γ-Mn [11].

Acknowledgements—This work was part of a project supported by the Australian Institute of Nuclear Science and Engineering, and we wish to thank the staff of the Institute for their assistance. The neutron diffraction work was performed using A.I.N.S.E. equipment installed at the HIFAR reactor of the Australian Atomic Energy Commission. One of us (E.R.V.) was supported by a Monash University Research Scholarship.

REFERENCES

1. BACON G. E., DUNMUR I. W., SMITH J. H. and STREET R., *Proc. R. Soc.* **A241**, 223 (1957).
2. ZIMMERMAN J. E., ARROTT A., SATO H. and SHINOZAKI S., *J. appl. Phys.* **35**, 942 (1964).
3. TAUER K. J. and WEISS R. J., *J. Phys. Chem. Solids* **2**, 237 (1959).
4. SHINOZAKI S., ARROTT A., SATO H. and ZIMMERMAN J. E., *Bull. Am. phys. Soc.* **8**, 66 (1963).
5. HOFFMANN J. A., PASKIN A., TAUER K. J. and WEISS R. J., *J. Phys. Chem. Solids* **1**, 45 (1956).
6. PAWEL R. E. and STANSBURY E. E., *J. Phys. Chem. Solids* **26**, 607, 757 (1965).
7. HICKS T. J., PEPPER A. R. and SMITH J. H., *Proc. phys. Soc. (J. Phys. C) Lond.* **1**, 1683 (1968).
8. WILKINSON M. K. and SHULL C. G., *Phys. Rev.* **103**, 516 (1956).
9. MENEGHETTI D. and SIDHU S. S., *Phys. Rev.* **105**, 130 (1957).
10. HICKS T. J. and BROWNE J. D., *Proc. phys. Soc.* **86**, 139 (1965).
11. SMITH J. H. and VANCE E. R., *Proc. phys. Soc. (J. Phys. C.) Lond.* **2**, 762 (1969).
12. BLECH I. A. and AVERBACH B. L., *Phys. Rev.* **137**, A1113 (1965).
13. SMITH J. H. and VANCE E. R., *J. appl. Phys.* **40**, 4853 (1969).
14. VANCE E. R., SMITH J. H. and SABINE T., *Proc. phys. Soc. (J. Phys. C) Lond.* (To be published).

J. Phys. Chem. Solids Pergamon Press 1970. Vol. 31, pp. 489–502. Printed in Great Britain.

NMR STUDY OF HYDROGEN DIFFUSION IN THE THREE DIFFERENT PHASES OF THE TITANIUM-HYDROGEN SYSTEM*

CHARLES KORN† and **DAVID ZAMIR**
Soreq Nuclear Research Centre, Yavne, Israel

(*Received* 9 *June* 1969)

Abstract—The proton spin lattice relaxation time T_1 has been measured by an NMR pulse technique at 19·00 MHz as a function of temperature in the range 25°–500°C for a series of samples in the α, β and γ phases of titanium hydride. The relaxation mechanism in the α and γ phases was governed primarily by hydrogen diffusion over most of the temperature range. The diffusional activation energy in the γ phase was found to be constant with respect to the hydrogen concentration, having a value of $11{\cdot}7 \pm 0{\cdot}4$ kcal/mole, and the attempt jump frequency was found to be proportional to the available local vacancies. The activation energy behavior is discussed in relation to a previously proposed model for hydrogen diffusion in titanium and the jump attempt frequency is compared to available data on the optical mode of the hydrogen vibrations. Evidence was found for a uniform distribution in the γ phase when the ratio of hydrogen to titanium, x, is greater than 1·6 while clustering takes place at lower ratios. The low temperature γ phase transition concentration at $x = 1{\cdot}6$ was found to be related to the electronic structure from $(T_1)_e$ data. The conduction electrons were the primary cause of relaxation in the γ phase near room temperature and the contribution of this mechanism to the relaxation rate increased with increase in hydrogen concentration. $(T_1)_eT$ ranged from 190 ± 4 sec-°K to $62{\cdot}5 \pm 2$ sec-°K as x (the ratio of hydrogen to titanium atoms) varied from 1·55 to 1·90. The $\alpha+\gamma$, γ phase boundary was found between 25° and 100°C. Diffusion parameters were measured for the α phase and the gradual transition from the $\alpha+\gamma$ to γ region observed. The transition from the $\alpha+\gamma$ to the β phase was observed and a heating–cooling hysteresis effect was displayed. T_1 for the β phase near 450°C of $TiH_{0{\cdot}78}$ was governed mainly by the conduction electrons and a value of $(T_1)_eT = 58 \pm 5$ sec-°K was found.

1. INTRODUCTION

THE ABILITY of the early transition metals to absorb large quantities of hydrogen to form metallic hydrides is well known[1]. These hydrides are generally non-stoichiometric and their phase diagrams have been established by metallurgical methods. The crystallographic structures depend on both hydrogen concentration and temperature, and may differ from that of the pure metal. One interesting feature of the transition metal hydrides is the relatively high rate of diffusion of hydrogen in the metal. The hydrogen diffusion parameters depend on concentration, not only because of variation in the available jump sites but also because of the crystal structure dependence on hydrogen concentration. A convenient method of measuring hydrogen diffusion in hydrides is by nuclear magnetic resonance (NMR)[2–9]. In the present study this method is employed to examine the diffusion properties of hydrogen in the different phases of the titanium-hydrogen system.

Torrey[2] measured the spin lattice relaxation time T_1 of hydrogen in titanium at a single concentration. Stalinsky *et al.*[3] have investigated hydrogen diffusion in the γ phase of titanium in the temperature range of about 50°–150°C using NMR line narrowing. Spalthoff[4] performed similar measurements on a highly concentrated titanium hydride.

---

*The research reported here has been sponsored in part by the Air Force Materials Laboratory through the European Office of Aerospace Research, United States Air Force Contract No. AF 61 (052)-904.

†This paper is based on part of a thesis to be submitted by C. Korn in partial fulfillment of the requirements for the degree of Doctor of Philosophy, Feinberg School of Graduate Studies, Weizmann Institute.

It is generally recognized that the Ti–H system includes the α(h.c.p.), β(b.c.c.) and γ(f.c.c.) phases. The phase diagram, determined principally by metallurgical methods, is presented in Fig. 1. In the present study we have measured the hydrogen spin- lattice relaxation time T_1 in all the phases over a wide temperature range, using the pulse NMR technique. The major factor in the relaxation mechanism is that due to diffusion. Using the well-known formula[10] relating the diffusional relaxation time to the jump frequency, the diffusion parameters have been calculated. Thus we have been able to follow the changes in diffusion properties as related to the different crystal structures of the phases. Moreover, the changes provided us with information on the phase diagram. By separating the diffusional and conduction electron contributions to the spin lattice relaxation time, information can be obtained on the electronic structure of the system.

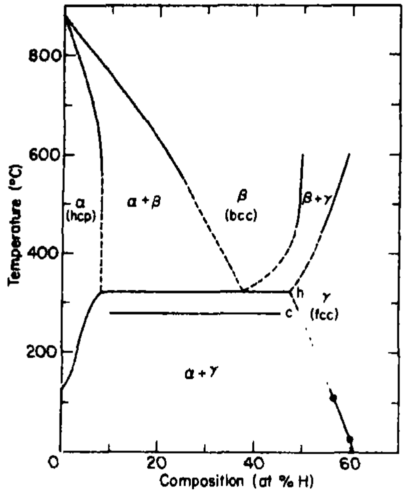

Fig. 1. The Ti–H phase diagram taken from McQuillan [15] and Lenning *et al.*[22]. The high temperature solid lines were obtained by McQuillan from temperature–pressure measurements, and the broken lines are extrapolations from these results. The α to $\alpha+\gamma$ transition line was obtained by Lenning *et al.* using metallurgical methods. The solid γ to $\alpha+\gamma$ transition line was obtained in this study by NMR, and the dotted line is its extrapolation joined to McQuillans curve. A hysteresis effect found by Lenning *et al.*, and confirmed in this study, is shown by the two horizontal lines representing heating (h) and cooling (c).

2. EXPERIMENTAL TECHNIQUES

A. *Sample preparation*

The titanium hydride samples were prepared from sodium-reduced titanium sponge obtained from Johnson Matthey Co. The surface was cleaned by heating the titanium to 950°C under dynamic vacuum conditions until less than 1×10^{-5} mm Hg pressure was recorded.

By exposing the titanium to hydrogen of purity higher than 99·995% and slowly reducing the temperature to ambient over a period of about 8–10 hr, hydrogen was gradually absorbed. In order to ensure homogeneity, cooling was stopped at a given temperature until no more hydrogen was absorbed and an equilibrium state was achieved between hydride and gas. This procedure was repeated at progressively lower temperatures. The amount of hydrogen absorbed was determined from the system volume and the measured pressure. A rough check on the relative concentrations was obtained using the NMR signal intensity.

High hydrogen concentration hydrides were quite brittle and were easily crushed under argon using an alumina mortar and pestle. The fine powder was then passed through a standard 53 μ sieve and sealed into glass ampules containing argon at a pressure of about 1 at. Since samples having low hydrogen concentrations were not brittle, they were prepared by outgassing high concentration powder and rehydriding to the desired concentration.

B. *NMR measurements*

The spin lattice relaxation time T_1 of the hydrogen nuclei was measured at 19·00 MHz using a pulsed NMR apparatus described by Clark[11]. H_1 of more than 20 G was obtained over a 0·5 cm³ volume. This is about twice the low temperature line width. Signals were recorded using a box car integrator which sampled the beginning of the free induction decay for a small fraction of the spin–spin relaxation time T_2. The probe coil was in a crossed coil configuration, wound on lava, and placed within a heavy copper cylinder containing a Kanthal wire heating element. A temperature controller kept the temperature constant to within ±0·2°C, although the overall accuracy of the temperature reading was ±1·0°C. The gradient between sample and thermocouple positions was less than 0·2°C over the entire temperature range.

Most of the T_1 measurements were performed using a 180°–90° pulse sequence. The first pulse flips the magnetic moment over completely. This is followed by a 90° sampling pulse, which is used to measure the exponential growth of the magnetic moment in the direction of the external field over about 1½ decades as a function of time between the two pulses. The time between pulse pairs was taken greater than 10 T_1 except at low temperatures, where T_1 was very long and somewhat shorter times had to be employed. The temperature range covered was about 25°–500°C. At least 20 min was allowed for equilibrium temperature to be attained.

3. RESULTS AND DISCUSSION

We shall discuss each region of the phase diagram separately. Concentration will be designated by the parameter x, giving the ratio of the number of hydrogen atoms to titanium atoms and identifying a hydride of form TiHx.

A. *The γ phase region*

1. *Experimental results.* The spin lattice relaxation time T_1 was measured as function of temperature for several concentrations of hydrogen; the results are shown in Fig. 2. The curves are smooth over the entire temperature range and all display a minimum typical of a diffusion-controlled mechanism[10]. At low temperatures, the curves are ordered according to decreasing concentration along increasing T_1. As the temperature is raised, the curves converge and finally reverse their order.

2. *Discussion of* T_1 *curves.* In order to understand the behavior of these curves as a function of temperature and concentration, let us analyze the different contributions to the spin lattice relaxation.

Generally, several mechanisms contribute to the relaxation rate. Hydrogen diffusion must play a major role, since the T_1 curves display the characteristic minima. We designate this part by $(T_1)_d$. In the present case of nuclei with $I = \frac{1}{2}$, the only other contribution we have to take into account is the conduction electron interaction $(T_1)_e$. Measurements of T_1 down to liquid helium temperature [12] show that relaxation due to paramagnetic impurities is negligible in the present case. We can fit all our data by assuming that T_1 is governed by the sum of the diffusional and electronic contributions:

$$\frac{1}{T_1} = \frac{1}{(T_1)_d} + \frac{1}{(T_1)_e}. \qquad (1)$$

These mechanisms can be separated by making use of their different functional dependence on temperature. $(T_1)_e$ is governed by the Koringa relation[10].

$$(T_1)_e T = \text{const.} \qquad (2)$$

Assuming a correlation function of the form $e^{-\nu t}$, where ν is the jump frequency, the

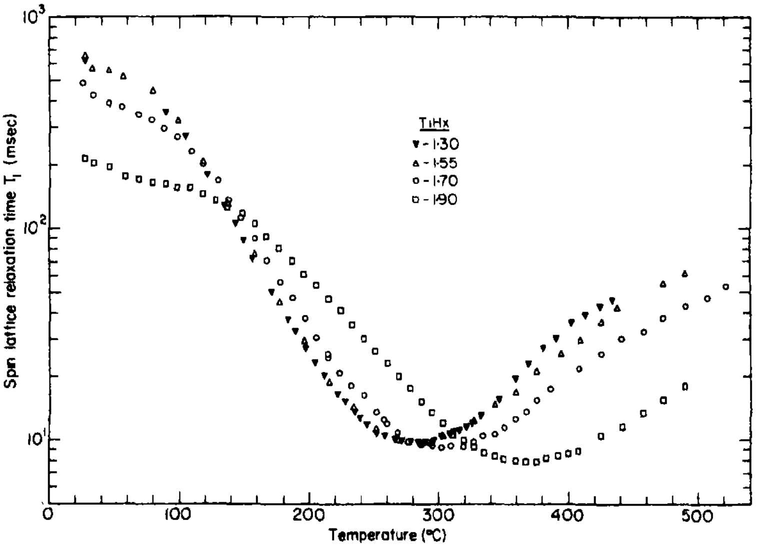

Fig. 2. Temperature dependence of the proton spin lattice relaxation time T_1 of TiHx for various concentrations x in the γ phase. $x = 1{\cdot}81$ has been omitted for the sake of clarity.

standard expression for $(T_1)_d$ is given by:

$$\frac{1}{(T_1)_d} = \tfrac{2}{5}\gamma_I^4\hbar^2 I(I+1)\frac{1}{\omega} \sum_k r_k^{-6}\left(\frac{y}{1+y^2}+\frac{4y}{4+y^2}\right) \qquad (3)$$

where we have written $y = \nu/\omega$. γ_I is the gyromagnetic ratio for protons, $I(=\frac{1}{2})$ is the proton spin, ω is the angular frequency, and $\Sigma_k r_k^{-6}$ is summed over the distance between the hydrogen nuclei. The terms corresponding to proton $-\mathrm{Ti}^{47}$ and Ti^{49} dipole interactions are orders of magnitude smaller and can be neglected. $(T_1)_d$ decreases as $1/y$ for $y \ll 1$, increases as y for $y \gg 4$ and has a minimum at $y = 1{\cdot}624$. Designating this minimum by $(T_1)_d^{\min}$ we obtain:

$$(T_1)_d = 1{\cdot}425(T_1)_d^{\min}\left(\frac{y}{1+y^2}+\frac{4y}{4+y^2}\right)^{-1}. \qquad (4)$$

The diffusion parameters are calculated on the basis of this expression.

The diffusional and electronic contributions to T_1 are separated as follows: For the low temperature region to the left of the minimum, where $(T_1)_d$ is proportional to y and $y = \nu/\omega = (\nu_0/\omega)e^{-E_a/kT}$, we see that $(T_1)_d$ should vary logarithmically with the reciprocal of the temperature. We choose the value of the constant in equation (2) so that, with the help of equation (1), we do indeed obtain a straight line when $(T_1)_d$ is plotted logarithmically as a function of reciprocal temperature. This is illustrated for the case of $\mathrm{TiH}_{1{\cdot}70}$ in Fig. 3. It is seen that a large portion of the relaxation mechanism is indeed due to conduction electrons in the low temperature region.

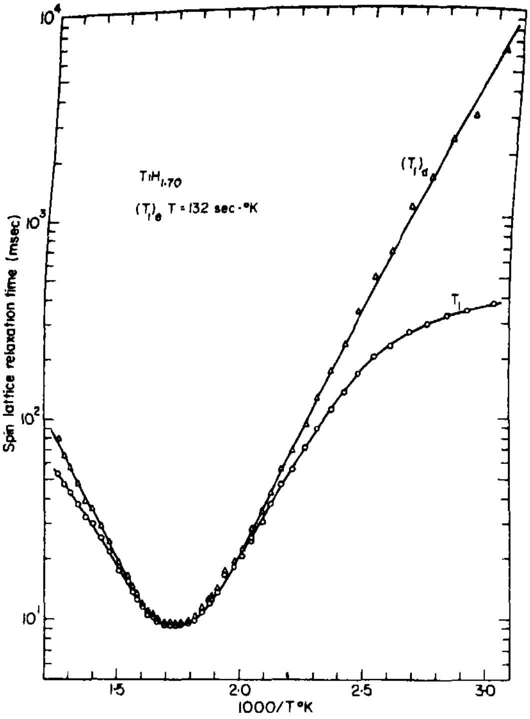

Fig. 3. A typical illustration of how T_1 was broken up into the conduction electron $(T_1)_e$, and hydrogen diffusion $(T_1)_d$, contributions. The experimental curve is designated by T_1. Assuming $(T_1)_eT = 132$ sec-°K and using equation (1), we obtain a straight line for ln $(T_1)_d$ as a function of reciprocal temperature, both above and below the temperature for which T_1 is a minimum.

We can now discuss the relative shapes of the T_1 curves of Fig. 2. The minima occur at higher temperatures for greater hydrogen concentrations. Since a minimum appears when the diffusion jump frequency approaches the NMR resonant frequency, we see that the diffusion falls with increase in concentration. At low temperatures, the major relaxation mechanism is due to the conduction electron interaction. That this interaction becomes stronger at higher hydrogen concentrations is reflected in the fact that at these temperatures the curves are ordered according to decreasing concentration along increasing T_1. As the temperature is raised and the diffusion relaxation mechanism takes over, the curves converge and finally reverse their order, since diffusion is faster at lower hydrogen concentrations. It is seen that T_1 increases very gradually along decreasing temperature in the low temperature region until near 35°C, a faster increase than heretofore appears. This is probably a manifestation of the tetragonal deformation reported at this temperature [13].

Having separated the two relaxation processes, the T_1 data can now be used to obtain

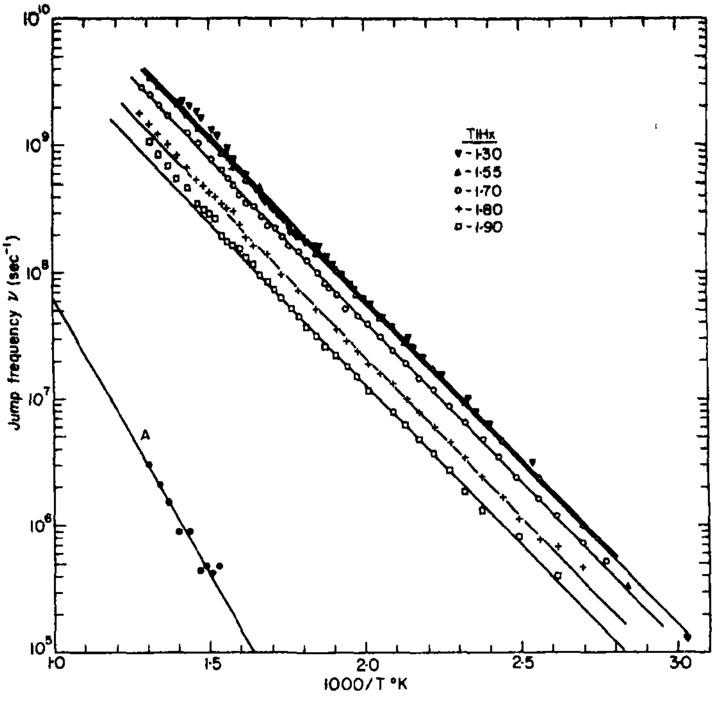

Fig. 4. Temperature dependence of the jump frequency ν for proton diffusion in the γ phase of hydrides having various hydrogen concentrations. A is a straight line drawn through the points obtained by taking the difference between the experimental values of ν and the straight line extrapolation for $x = 1{\cdot}90$. It may indicate the existence of an additional higher activation energy diffusion term.

information on the diffusion parameters, distribution of the hydrogen in the titanium lattice, and conduction electron processes.

3. *Diffusion parameters of hydrogen in the γ phase.* Since $y = \nu/\omega$, the values obtained for $(T_1)_d$ permit ν to be calculated directly as a function of temperature, using equation (4). The results are plotted logarithmically as a function of reciprocal temperature in Fig. 4. An Arrhenius-type relation of the form

$$\nu = Ae^{-E_a/kT} \tag{5}$$

is obeyed. Ea is the diffusional activation energy and A is the diffusion frequency factor. E_a is seen to be a constant, having the value 11·7 kcal/mole for $1{\cdot}3 < x < 1{\cdot}9$ (Fig. 5). This result is in contrast with those obtained by Stalinsky *et al.*[3] who based their calculation of the activation energy on line width narrowing as a function of temperature. There are two significant differences between the

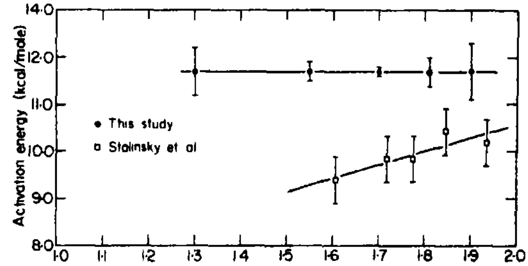

Fig. 5. The activation energy for hydrogen diffusion as a function of concentration. The data of Stalinsky *et al.*[3], obtained from NMR line width narrowing measurements is shown for comparison. The line drawn through the Stalinsky *et al.* data is theirs, and its slope was used by Coogan and Gutowsky[14] to obtain a model of hydrogen diffusion in γ titanium hydride.

results. Firstly Stalinsky's values are consistently lower and secondly he finds that E_a changes with x. The assumed existence of this change was the basis on which Coogan *et al.* [4] developed their electrostatic model of diffusion in titanium hydride. The essential feature of this model is that the hydrogen atom contributes part of its electron to the titanium atoms when it enters the lattice. The properly shielded electrostatic interaction between the charged titanium and hydrogen yields the activation energy E_a. By properly adjusting the shielding factor and the amount of charge each hydrogen atom is assumed to contribute to the titanium, presumably values of E_a can be derived which satisfy either the results obtained by Stalinsky *et al.*, or the higher values obtained in this study. The constancy of E_a with x which we obtained is however another matter. Since according to the theory, the charge contributed to the titanium should increase with the amount of hydrogen absorbed, E_a is thus predicted to increase with x, contrary to our results. It is interesting to note with respect to this question that Pedersen *et al.*[9] obtained a decrease of E_a with x for hydrogen in tantalum. Siting the model of Coogan *et al.*, they took this to support the view that the tantalum was *positively* charged with respect to the hydrogen.

The frequency factor A is plotted as a function of $2-x$ in Fig. 6. Since the maximum value of x is 2, $2-x$ represents the empty available sites which the hydrogen can populate; A is directly proportional to this difference for x larger than 1·6. It is therefore convenient to write $A = (2-x)\nu_0$. For x less than 1·6, A does not attain the magnitude expected from the linear relation. This may be taken as indicating that for $x < 1{\cdot}6$, the hydrogen atoms are not evenly distributed in the γ phase but cluster somewhat so that the number of adjacent available jump sites is not as large as might be expected. There is further support for this supposition, as we shall see later.

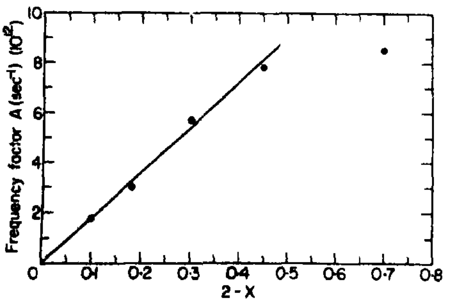

Fig. 6. Frequency factor A as a function of non-occupied hydrogen sites.

The linear variation of A as a function of $2-x$ indicates that ν_0 is independent of x. This is in contrast to the results of Stalinski *et al.*[3] who found ν_0 to increase with hydrogen concentration. Sakamoto *et al.*[15, 16] performed total cross section measurements as a function of neutron energy on a series of titanium hydrides using thermal neutrons. The results show that the hydrogen motion is governed by a single Einstein frequency which is independent of hydrogen concentration. This discrepancy with the results of Stalinsky *et al.* compelled Sakamoto *et al.* to state that the "apparently contradictory result may imply that the jump of diffusion atom is not solely related to the optical vibration frequency but is influenced by the environment in a complex manner". The hydrogen cross section measurements are, however, in accord with the results of this study showing ν_0 to be independent of x, and making it unnecessary to invoke this explanation.

Roughly speaking, we would expect the optical vibrational frequency to be of the same order of magnitude as the diffusional attempt frequency. Following the reasoning of Stalinsky *et al.* A may be written as

$$A = \nu_0{}^0 \frac{n(2-x)}{2}$$

where $\nu_0{}^0$ is the 'true' frequency factor, n is the number of neighboring sites the hydrogen can jump into and $\frac{1}{2}(2-x)$ is the probability that such a site is vacant. For our case $n = 4$. We wish to compare $\nu_0{}^0$ with the optical vibration frequency ν_{0p}. Taking the slope of the line in Fig. 6, we find $\nu_0 = 18 \times 10^{12}$/sec or $\nu_0{}^0 = 9 \times 10^{12}$/sec. The value of ν_{0p} obtained by Sakamoto *et al.*[15, 16] was 33×10^{12}/sec so that $\nu_0{}^0$ and ν_{0p} are indeed of the same order of magnitude.

From the jump frequency curves of Fig. 4, it can be seen that E_a is constant over the entire temperature range for low values of x but deviates towards a larger activation energy in the upper temperature range as x approaches the value 2 (small deviation for $TiH_{1\cdot 81}$, larger deviation for $TiH_{1\cdot 90}$). It is possible that despite the fact that the samples were sealed in small volumes, some outgassing does occur at high x and T. In order to account for the results obtained, outgassing of hydrogen to a pressure of about 10 atm near 450°C would have to be assumed for the volumes of the ampules employed. It is difficult to extrapolate the Ti–H partial pressure curves of McQuillan [17] for this region to see whether this is likely.

The activation energy behavior at elevated temperature and high hydrogen concentration can also be explained by assuming an additional diffusion mechanism to operate yielding a final diffusion equation of the form

$$\nu = (2-x)\nu_0 e^{-E_a/kT} + \nu_0' \mathrm{r}^{-E_a'/kT} \qquad (6)$$

where $E_a' > E_a$. At low temperatures only the first term is significant. When x approaches 2, this term becomes small enough so that the effects of the second term can be felt at high temperatures. A rough estimate of $\nu_0' e^{-E_a'/kT}$ can be obtained from $\nu - (2-x)\nu_0 e^{-E_a/kT}$ by subtracting the values of the extrapolated straight line from the experimental curve for $TiH_{1\cdot 90}$ in Fig. 4. The results shown in the same figure lead to $\nu_0' e^{-E_a'/kT} \approx 2 \times 10^{14}\, e^{-20/kT}$ sec^{-1}.

The origin of the second diffusion term may be explained as follows: We originally wrote the equation governing diffusion as $\nu = Ae^{-E_a/kT}$. On the assumption that A is proportional to the probability of a hydrogen atom finding an available free site, we concluded that A is proportional to $2-x$; this would imply that as $x \to 2$, $\nu \to 0$. However, it is known from general diffusion theory that this is not the case, since there are always thermally produced vacancies. A vacancy will thus exist at a tetrahedral site either because not enough hydrogen was dissolved to fill all the sites (and such vacancies will exist down to $T = 0$°K), or because the site is a thermally excited defect and has a probability proportional to $e^{-E_f/kT}$ of occurring, where E_f is the vacancy formation energy. We can therefore write $A = \nu_0[(2-x) + ce^{-E_f/kT}]$. Hence

$$\nu = \nu_0[(2-x) + ce^{-E_f/kT} x e^{-E_a/kT}$$
$$= (2-x)\nu_0 e^{-E_a/kT} + \nu_0' e^{-E_a'/kT}$$

where $E_a' = E_f + E_a$, giving an equation of type (6) with $E_a' > E_a$.

4. *Distribution of hydrogen in the titanium lattice.* T_1 is very sensitive to the relative position of the nuclei, through a sixth power dependence in the expression $\Sigma_k r_k{}^{-6}$ in equation (3). In fact, since $(T_1)_d{}^{\min}$ is independent of y, this parameter is a good check of theory with experiment. Equations (3) and (4) give:

$$(T_1)_d{}^{\min} = \frac{\omega}{0\cdot 57 \gamma_I{}^4 \hbar^2 I(I+1) \Sigma_k r_k{}^{-6}} \qquad (7)$$

The right hand side of this equation is known once the lattice sites are assumed.

The gamma phase is f.c.c. Second moment [3] and neutron diffraction [18] measurements have located the hydrogen positions at the tetrahedral sites and these form a simple cubic sublattice with a lattice parameter half that of the titanium structure. In general, $\Sigma_k r_k{}^{-6} = 8\cdot 402\mathbf{a}^{-6}$ for a simple cubic lattice. If $\mathbf{a}_0$ is the lattice constant of titanium, then $\mathbf{a} = \mathbf{a}_0/2$ and $\Sigma_k r_k{}^{-6} = 537\cdot 7\mathbf{a}_0{}^{-6}$. Since the probability of a lattice site being occupied is $x/2$ if the hydrogen distribution is uniform, on substituting the appropriate constants, equation (7) becomes:

$$(T_1)_d^{\min} = \frac{10^{-10}(\omega/2\pi)\mathbf{a}_0^6}{1{\cdot}042x} \tag{8}$$

where $(T_1)_d^{\min}$ is in msec, ω in radians/sec and $\mathbf{a}_0$ in Å. Taking into account the lattice expansion due to changes in concentration [19] and temperature [13] and the temperatures at which the $(T_1)_d^{\min}$ values occur, we can obtain a calculated curve of $(T_1)_d^{\min}$ as a function of x. This is shown in Fig. 7, together with the experimental values. Considering that $(T_1)_d$ varies over many orders of magnitude in the temperature range of our measurements, the fit is quite good. If we had assumed for example, that a large proportion of the hydrogen is located at the octahedral sites, there would be a huge discrepancy, with the theoretical $(T_1)_d^{\min}$ values lying far below the experimental points. The small discrepancy that does appear can be ascribed to the simplifying assumption that $(T_1)_d$ is governed by an exponential correlation function [20].

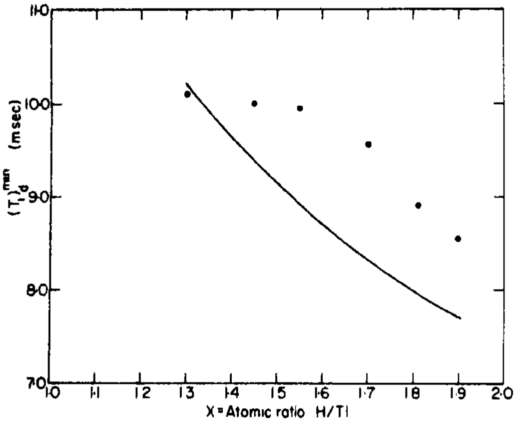

Fig. 7. $(T_1)_d^{\min}$ as a function of hydrogen concentration. The curve is obtained from equation (8), taking into account the effect of hydrogen concentration and temperature on the lattice parameter.

Although we can expect equation (1) to be off by a small factor, the relative values of $(T_1)_d^{\min}$ as a function of x should follow the predicted ones. This is confirmed for $x > 1{\cdot}6$. In this region the experimental points do indeed lie parallel to the theoretical curve. When x is less than 1·6, however, the experimental values of $(T_1)_d$ tend downwards. This is what we would expect if we had clustering, since the stronger interaction resulting from a greater number of proximate neighbors results in a decrease of $(T_1)_d^{\min}$. Here we have a further indication of clustering when $x < 1{\cdot}6$, while for $x > 1{\cdot}6$ an even distribution of the hydrogen nuclei among the tetrahedral sites is confirmed.

Torrey [2] measured T_1 as a function of temperature for a sample $TiH_{1{\cdot}77}$. He found a double minimum which he ascribed to two activation processes due to two interstitial sites, and which Coogan *et al.* [14] explained by two different jump paths between tetrahedral sites. No such double minima were obtained in our measurements for any of the concentrations in the γ phase. Since Torrey measured his sample at a lower frequency, we checked a sample of $TiH_{1{\cdot}70}$ at 10·00 MHz and still found no double minimum. However, we did observe this phenomenon in a sample that was not properly sealed and became oxidized. A close examination of our $(T_1)_d$ curves does show some sort of break in the curvature (Fig. 8) but this is far smaller than the effect found by Torrey.

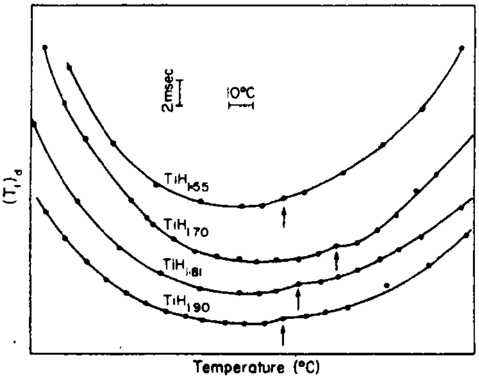

Fig. 8. A closer view of $(T_1)_d$ near the minimum for various concentrations of hydrogen. The curves have been shifted with respect to each other to keep the diagram small. The arrows point to possible breaks in the smooth curvature.

5. *Conduction electron contribution to the spin lattice relaxation.* As shown before, we can separate out the conduction electron contribution $(T_1)_e$ to the relaxation process. The derived values of $(T_1)_eT$ are plotted in Fig. 9 as a function of x. The interaction is seen to increase strongly with x and then level off. This increase in the interaction can be associated with a change in the number of electrons contributed to the conduction band as more hydrogen is added to the titanium. A detailed analysis of the $(T_1)_eT$ behavior will be given elsewhere.

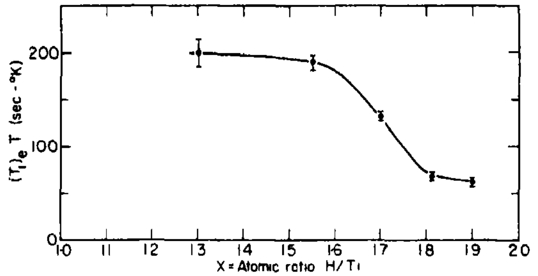

Fig. 9. Conduction electron contribution to the spin lattice relaxation time as a function of hydrogen concentration.

B. *The $\alpha+\gamma$ to γ transition region*

1. *Experimental results.* In order to follow the changes caused by a transition from the $\alpha+\gamma$ region to the pure γ region (see phase diagram of Fig. 1), T_1 was measured as a function of hydrogen concentration across the transition at two temperatures, 24° and 109°C. The results are shown in Fig. 10. T_1 is constant within the experimental error for low x, rises somewhat at higher x, and then drops rapidly at $x = 1{\cdot}6$.

2. *Discussion.* The generally accepted phase diagram of Fig. 1 does not establish the transition line from the $\alpha+\gamma$ to γ regions, although Sidhu *et al.*[18] have indicated that it should be located near $x = 1{\cdot}5$. Below 125°C, practically no hydrogen is located in the α phase titanium, hence, if we designate by x_0 the concentration at the phase transition line, the entire $\alpha+\gamma$ region below this temperature should consist of a mixture of pure α titanium and a γ hydride of *local* composition $TiHx_0$. This is verified by the curves presented in Fig. 10: T_1 remains constant at low x since the hydrogen is always in the same local environment $TiHx_0$; when x exceeds x_0, the local environment changes, resulting in a corresponding influence on T_1. The T_1 vs. x curves show that $x_0 = 1{\cdot}50$ at 24°C and $x_0 = 1{\cdot}33$ at 109°C. These values are transcribed onto the phase diagram of Fig. 1 to give the position of the $\alpha+\gamma$ to γ transition line.

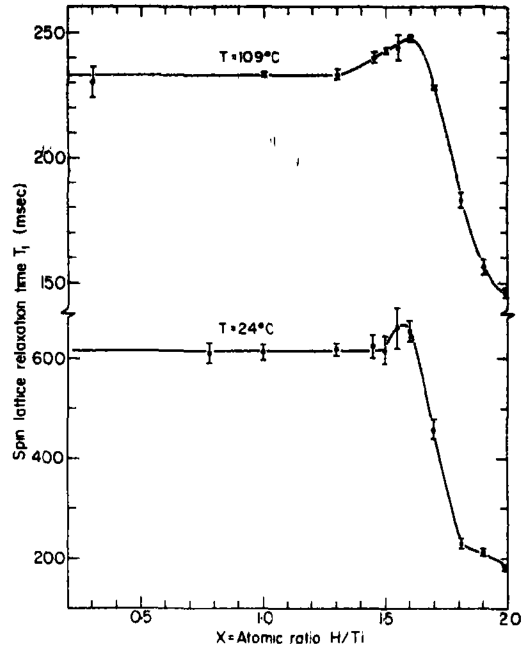

Fig. 10. The spin lattice relaxation time T_1 at 24° and 109°C as a function of hydrogen concentration. Note the change of scale. The constant value of T_1 for low values of x is ascribed to the existence of a single effective local hydrogen concentration in this region. The gradual rise of T_1 is explained by assuming that we have crossed the $\alpha+\gamma$ to γ phase line, so that the local hydrogen concentration is increased and the available neighboring jump sites are decreased resulting in slower diffusion and thus larger T_1. The rapid drop in T_1 is due to the conduction electron relaxation mechanism, which becomes stronger for increasing x, and indicates an 'electronic' change of phase at $x = 1{\cdot}6$.

An overall interpretation of the curves can be as follows: Taking the curve at 109°C as an example, for all $x < 1{\cdot}33$, the hydrogen sits in a constant local concentration of $TiH_{1{\cdot}33}$. At $x = 1{\cdot}33$, all the pure α titanium has been used up and the entire material consists of $TiH_{1{\cdot}33}$. As somewhat more hydrogen is added, it does not distribute itself evenly, but as shown previously, some clustering takes place. Diffusion slows down slightly as some of the available jump sites fill up, causing a small increase in T_1. At $x = 1{\cdot}6$, the hydrogen is distributed uniformly, and the strong conduction electron relaxation mechanism becomes dominant, causing a sharp drop in T_1. $TiH_{1{\cdot}6}$ is probably the low temperature phase transition composition, where the phase is determined by the electronic configuration and is independent of thermal terms. Clustering takes place in the range between what might be an electronic controlled phase change at the composition of $TiH_{1{\cdot}6}$ and the lower concentration thermaly induced phase transition.

C. *The α phase region*

1. *Experimental results.* T_1 of a sample $TiH_{0{\cdot}08}$ was measured as a function of temperature in the range 25°–430°C. From 25° to about 160°C, the values were practically identical to those of the low concentration gamma phase. Between 160° and 320°C it was impossible to derive a simple single value of T_1, since the spin magnetization did not decay exponentially. This is demonstrated by the non-linear character of the logarithmic plot of the signal amplitude as a function of time between pulses (Fig. 11). Above 320°C, the nuclear spin magnetization again followed a simple exponential decay pattern and single values of T_1 could be obtained.

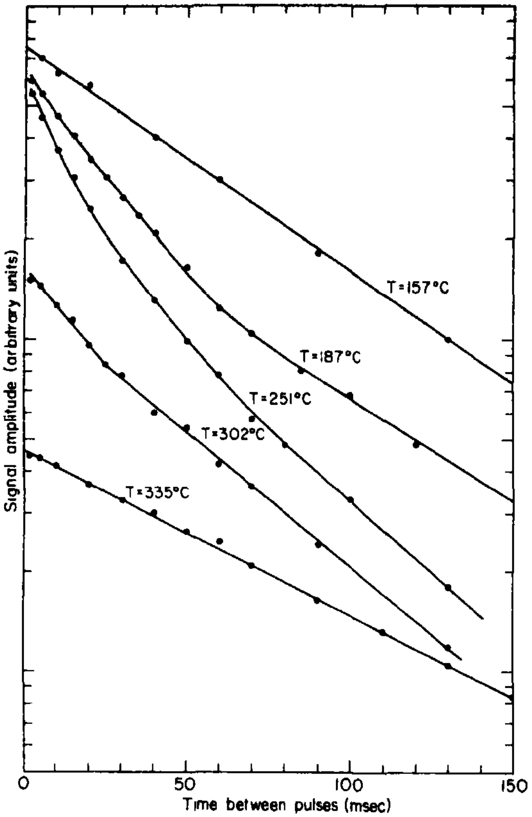

Fig. 11. The change in signal amplitude as a function of time between pulses for a sample $TiH_{0{\cdot}08}$. At low temperatures, almost all of the hydrogen is in the γ phase, resulting in a single T_1 as evidenced by a straight line. Increasing the temperature allows more of the hydrogen to dissolve in the α phase, giving two T_1's (for the α and γ phases respectively) and increases the curvature of the curves. Finally, at high temperatures (e.g. 335°C) all the hydrogen is in the α phase, resulting again in a straight line.

2. *Discussion.* The solubility of hydrogen in the α phase is negligible at temperatures below 125°C and increases to 8 at.% at 320°C. The sample of $TiH_{0{\cdot}08}$ used in these measurements contained the maximum amount of hydrogen in the α phase; even under these conditions, the signal to noise ratio was poor, especially at high temperatures. Below 125°C, the hydrogen is actually situated in the γ phase, having a local concentration of about $TiH_{1{\cdot}4}$. The T_1 vs. temperature curve therefore follows closely that of the previously obtained low concentration γ phase and nothing new is obtained. As the temperature is increased above 125°C, some of the hydrogen begins to dissolve in the α phase, the exact amount being determined by the tie line between the $\alpha+\gamma$ to α and $\alpha+\gamma$ to γ phase transition curves. We were able to detect this removal of hydrogen from the γ phase hydride and its reabsorption in the α phase titanium by

the appearance of two simultaeneous T_1 values, $(T_1)_\gamma$ and $(T_1)_\alpha$, the relaxation time of the hydrogen in the respective phases. Ordinarily, the nuclear spin magnetization decay of our NMR signal is exponential as a function of time of the form e^{-t/T_1}, resulting in a straight line when plotted logarithmically. When signals from two simultaneous phases having different relaxation times are present, the decay is of the form $Pe^{-t/(T_1)_\gamma}+Qe^{-t/(T_1)_\alpha}$ where P/Q is the ratio of the amount of hydrogen in the respective phases. (T_2 is of sufficiently long duration at these temperatures for both phases that it will not influence the assumed decay relation.) This is illustrated in Fig. 11. At low temperature ($T = 157$°C) a straight line is obtained, representing T_1 of the γ phase. At a higher temperature (187°C), some of the hydrogen dissolves in the α phase resulting in an additional component $(T_1)_\alpha$, which, because it is longer than $(T_1)_\gamma$, becomes noticeable at $t > 70$ msec when most of the signal due to the γ phase has already disappeared. With more hydrogen entering the α phase, the factor Q becomes more dominant and the curvature manifests itself at earlier t, until finally all the hydrogen is in the α phase and again a straight line is obtained ($T = 335$°C).

A least square analysis was performed on the data to determine the values of $P, Q, (T_1)_\gamma$, $(T_1)_\alpha$ which give the best fit to the equation $y = Pe^{-t/(T_1)_\gamma}+Qe^{-t/(T_1)_\alpha}$. The results gave values of P, Q and $(T_1)_\gamma$ which followed the general trend expected from the phase diagram and from previous measurements of $(T_1)_\gamma$ in the γ phase, but the spread was too large to verify the α to $\alpha+\gamma$ phase transition curve. In order to obtain useful information on $(T_1)_\alpha$, we performed the calculation again, this time constraining the least square analysis to two degrees of freedom by using the values of $(T_1)_\gamma$ derived from the low concentration gamma phase T_1 measurements and calculating the P/Q ratio from the given $\alpha+\gamma$ to α and $\alpha+\gamma$ to γ phase transition curves.

The values of T_1 for the α phase derived from the least square analysis together with those obtained directly at temperature above 320°C are plotted in Fig. 12. The spread of the data due to the poor signal-to-noise ratio prevents us from obtaining accurate values of the diffusion parameters but a number of conclusions can be drawn.

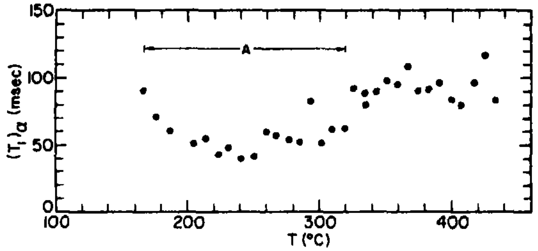

Fig. 12. The proton spin lattice relaxation time $(T_1)_\alpha$ for hydrogen dissolved in the α phase of titanium, using a sample $TiH_{0{\cdot}08}$. Region A is the mixed $\alpha+\gamma$ region where $(T_1)_\alpha$ was obtained from a least square analysis of the signal response.

The fact that there is a minimum, shows that diffusion is a significant factor in the relaxation process at these temperatures. The levelling of the T_1 curve above 360°C is probably due to a conduction electron contribution. An analysis similar to that performed for the γ phase (except that $(T_1)_e T$ is now obtained from the high temperature side), leads to $(T_1)_e T \approx 80$ sec-°K and the diffusion curve shown in Fig. 13. E_a is then found to be roughly 13 kcal/mole. This compares to 12·4 kcal/mole found by Wasilewsky and Kehl [19] from absorption rate measurements.

We can obtain information on the location of the hydrogen in the h.c.p. lattice of the α phase titanium from $(T_1)_d{}^{\min}$, in the same way as was done for the γ phase. Assuming that the hydrogen is situated in either the tetrahedral or the octahedral sites, we calculate $\Sigma_k r_k{}^{-6}$ and see for which assumption equation (7) agrees with the experimental value of $(T_1)_d{}^{\min}$. The lattice parameters of titanium are given by Sidhu *et al.*[18] as $\mathbf{a} = 2{\cdot}952$ Å and $\mathbf{c} = 4{\cdot}689$ Å. Our calculations of $\Sigma_k r_k{}^{-6}$ for the tetrahedral and octahedral sites when $\mathbf{c}/\mathbf{a} = 1{\cdot}5884$, gave $\Sigma_k{}^{\text{tet}} r_k{}^{-6} = 408{\cdot}4\mathbf{a}^{-6}$ and $\Sigma_k{}^{\text{oct}} r_k{}^{-6} =$

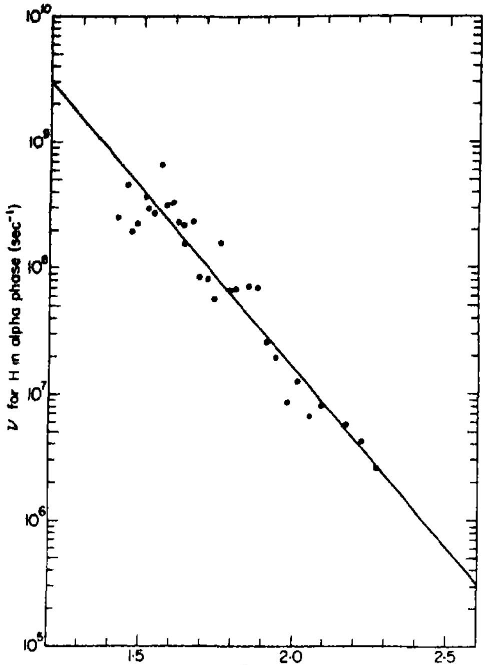

Fig. 13. The temperature dependence of the jump frequency ν for hydrogen in the α phase of titanium.

$18{\cdot}33\mathbf{a}^{-6}$. Since there are two tetrahedral sites and one octahedral site for each titanium atom, the probability of a site being occupied is $x/2$ if we assume the hydrogen to be located in the tetrahedral positions, and x if we assume it to be in the octahedral voids. Equation (7) then yields:

$$(T_1)^{\min}_{d,\mathrm{tet}} = \frac{10^{-10}(\omega/2\pi)\mathbf{a}^6}{1{\cdot}582(x/2)}\,\mathrm{msec}$$

$$(T_1)^{\min}_{d,\mathrm{oct}} = \frac{10^{-8}(\omega/2\pi)\mathbf{a}^6}{7{\cdot}103x}\,\mathrm{msec}$$

where **a** is given in Å. Since in our case $(\omega/2\pi) = 19{\cdot}00$ MHz and $x = 0{\cdot}08$, the final result is $(T_1)^{\min}_{d,\mathrm{tet}} = 19{\cdot}6$ msec and $(T_1)^{\min}_{d,\mathrm{oct}} = 218$ msec. Experimentally we obtained $(T_1)^{\min} \approx 40$ msec at 240°C. Removing the assumed conduction electron contribution of $(T_1)_e T \approx 80$ sec-°K yields $(T_1)_d{}^{\min} \approx 55$ msec. Taking into account the large error in these measurements and the fact that the experimental value of $(T_1)_d{}^{\min}$ for hydrides has been found to be generally larger than that calculated on the basis of equation (7) (see [20]), we must come to the conclusion that the hydrogen is located at the tetrahedral sites of the h.c.p. lattice if the choice is between that position and the octahedral one. Since the experimental value of $(T_1)_d{}^{\min}$ lies between $(T_1)^{\min}_{d,\mathrm{tet}}$ and $(T_1)^{\min}_{d,\mathrm{oct}}$, an exact fit between theory and experiment can of course be made if we assume a small percentage of the hydrogen to be located at the octahedral while the rest are at the tetrahedral sites, but the accuracy of our measurements and that of equation (7) is not sufficient to justify such a quantitative analysis.

D. *Transition to the β phase*

1. *Experimental results.* The spin lattice relaxation time of hydrogen in $\mathrm{TiH}_{0{\cdot}78}$ was measured as a function of both rising and falling temperatures (Fig. 14). For rising temperatures, the T_1 curve flattens out at 240°C, in contrast to the rounding off obtained in the γ phase. At about 340°C, T_1 rises rapidly and then decreases gradually. When the measurements were repeated at decreasing temperatures, a hysteresis effect was observed, the sharp drop in T_1 occurring near 280°C.

2. *Discussion*—(a) *Transition region.* The composition of the β eutectoid has been given as about $\mathrm{TiH}_{0{\cdot}8}$ by Lenning *et al.* [22] and as $\mathrm{TiH}_{0{\cdot}6}$ by McQuillan[17]. Lenning has also observed a hysteresis effect in the change from the $\alpha+\gamma$ to the β phase for rising and falling temperatures from thermal and dilatometer measurements. This hysteresis effect is denoted by the two horizontal lines in the phase diagram. Our results can be explained on the basis of this diagram by assuming that the rapid changes in T_1 are due to the γ to β phase transition. Since the two structures are f.c.c. and b.c.c. respectively, we expect large differences in diffusion rates which in turn influence the magnitudes of T_1. As the temperature is

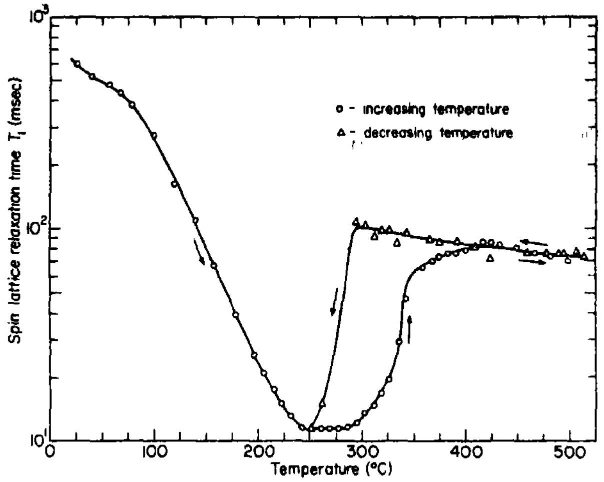

Fig. 14. Temperature dependence of T_1 for a sample $TiH_{0\cdot78}$. The arrows indicate the direction of the sequence of the measurements for heating and cooling.

increased, the change from γ to β phase at 330°C is accompanied by a rise in T_1, while the corresponding phase change for decreasing temperature occurs at about 280°C. Since the T_1 of the $\alpha+\gamma$ region is due primarily to hydrogen in the γ phase, at least part of the hysteresis effect of $\alpha+\gamma \leftrightarrow \beta$ transition must be due to hysteresis between the γ and β phases. The low temperature portion of the curve follows closely the relaxation times of the γ phase measurements. Measurements on samples of $TiH_{0\cdot50}$ at different frequencies show a similar hysteresis effect.

(b) *β phase*. T_1 in the β phase drops slowly with rising temperature; hence, if the relaxation is due to diffusion, we must be on the low temperature side of the minimum. However, in this region we would expect that at a fixed temperature, T_1 would be reduced by a factor of about 4 when ω is halved, as can be seen from equation (3) by taking $y \ll 1$. Measurements of T_1 at 10·00 MHz and other frequencies for a sample of $TiH_{0\cdot5}$ show no such change. We conclude therefore that the relaxation is due to conduction electrons. This is also consistent with the diffusion measurements of Wasilewski and Kehl[21], who obtained the low value of $E_a = 6\cdot6$ kcal/mole giving an extremely high diffusion rate for the open b.c.c. β phase structure and placing $(T_1)_d^{\min}$ at a very low temperature. A rough estimate of $(T_1)_d$ expected from the Wasilewsky and Kehl study can be obtained from their value of $D \approx 0\cdot2\times10^{-4}\,\mathrm{cm^2/sec}$ at 500°C. From the usual relation $D = l^2\nu/6$ where l is the jump distance, and taking $l \approx 5\cdot3$ Å to be the β phase lattice parameter, ν becomes $\sim 10^{11}$/sec. At a frequency $(\omega/2\pi) = 19$ MHz, $y = (\nu/\omega) \approx 10^3$ and from equation (3) we expect a $(T_1)_d$ of the order of thousands of milliseconds, while T_1 is actually in the region of 80 msec. We can therefore conclude that our T_1 in the β phase is due to the conduction electrons. Indeed, over the limited range of our measurements, $1/T_1$ varies linearly with absolute temperature, from which we obtain $(T_1)_eT = 58\pm5$ sec-°K.

4. CONCLUSIONS

Through the study of the proton spin lattice relaxation times, we can draw the following conclusions:

(a) The NMR results confirm the Ti–H phase diagram found before by other methods, and additional points on this phase diagram have been obtained by NMR.

(b) The diffusion constants have been calculated for various phases of the Ti–H system.

(c) The results of this study show E_a for the γ phase to be independent of hydrogen concentration, in contrast to the results of Stalinski *et al.*[3] and the electrostatic model for diffusion of Coogan *et al.* who found E_a to increase linearly with x.

(d) The 'natural' attempt jump frequency ν_0^0 was found to be independent of hydrogen concentration, in agreement with hydrogen cross section measurements [15, 16].

(e) Besides diffusion, the other main mechanism for hydrogen nuclear spin relaxation is the interaction with the conduction electrons. $(T_1T)_e$ was obtained for each phase.

Acknowledgement—We thank Professor S. Alexander for very helpful discussions.

REFERENCES

1. LIBOWITZ G. G., *The Solid State Chemistry of Binary Metal Hydrides*. Benjamin, New York (1965).
2. TORREY H. C., *Nuovo Cim. Suppl.* **9**, 95 (1958).
3. STALINSKY B., COOGAN C. K. and GUTOWSKY H. S., *J. chem. Phys.* **34**, 1191 (1961).
4. SPALTHOFF W., *Z. phys. Chem.* **29**, 258 (1961).
5. HON J. F., *J. chem. Phys.* **36**, 759 (1962).
6. ZAMIR D. and COTTS R. M., *Phys. Rev.* **134**, A666 (1964).
7. NORBERG R. E., *Phys. Rev.* **86**, 745 (1952).
8. SCHREIBER D. S. and COTTS R. M., *Phys. Rev.* **131**, 1118 (1963).
9. PEDERSON B., KROGDAHL T. and STOKKELAND O., *J. chem. Phys.* **42**, 72 (1965).
10. ABRAGAM A., *The Principles of Nuclear Magnetism*. Oxford (1961).
11. CLARK W. G., *Rev. scient. Instrum.* **35**, 316 (1964).
12. EHRENFREUND E., WEGER M., KORN C. and ZAMIR D., *J. chem. Phys.* **50**, 1907 (1969).
13. YAKEL H. L., Jr., *Acta crystallogr.* **11**, 46 (1958).
14. COOGAN C. K. and GUTOWSKY H. S., *J. chem. Phys.* **56**, 110 (1962).
15. SAKAMOTO M., *J. phys. Soc. Japan* **19**, 1862 (1964).
16. KUNITOMI M., HAMAGUCHI Y., SAKAMOTO M., DOI K. and KOMURA S., *J. Phys. (Paris)* **25**, 462 (1964).
17. McQUILLAN A. D. and McQUILLAN M. K., *Titanium*, pp. 210–215. Butterworths, London (1956).
18. SIDHU S. S., HEATON L. and ZAUBERIS D. D., *Acta crystallogr.* **9**, 607 (1956).
19. TRZELIATOWSKY W. and STALINSKY B., *Bull. Acad. polon. Sci.* Classe III **1**, 131 (1953).
20. It can be shown that the experimental points lie between the curves of the theoretical expression of Torrey (*Phys. Rev.* **92**, 962 (1953); *ibid.* **96**, 690 (1954)) which is based on the random walk description, and that of equation (7), with the points lying closer to the latter. The diffusion model of Coogan *et al.*[14] makes the applicability of Torrey's formula questionable in this case. Other examples where the theoretical value of $(T_1)_d^{\min}$ calculated on the basis of equation (7) were found to be lower than the measured results are hydrogen in niobium[6] and hydrogen in tantalum[9]. Pederson *et al.*[9] explain the discrepancy by assuming that the hydrogen–tantalum dipole interaction is reduced by the large quadrupole interaction of the tantalum. This explanation is not applicable in our case since the hydrogen–titanium dipole interaction is small enough to be ignored.
21. WASILEWSKI R. J. and KEHL G.M., *Metallurgia* **50**, 225 (1954).
22. LENNING G. A., CRAIGHEAD C. M. and JAFFEE R. I., *Trans. AIME* **200**, 367 (1954).

J. Phys. Chem. Solids Pergamon Press 1970. Vol. 31, pp. 503–506. Printed in Great Britain.

EFFECT OF BAND STRUCTURE ON THE RUDERMAN–KITTEL–KASUYA–YOSIDA INTERACTION IN THE HEAVY RARE EARTHS

G. BAMBAKIDIS
Lewis Research Center, Cleveland, Ohio 44135, U.S.A.

(*Received* 17 *April* 1969; *in revised form* 26 *May* 1969)

Abstract—The indirect exchange interaction between near-neighbor spins has been calculated for Gd metal near $T = 0$ using electronic energy bands computed by means of the non-relativistic augmented-plane-wave method. The results show that the present accuracy of band-structure calculations does not permit a realistic determination of indirect exchange energies.

THE RKKY (Ruderman–Kittel–Kasuya–Yosida) interaction is generally considered to be the fundamental magnetic interaction between atomic spins in the rare earths. Most treatments have considered the interaction in the context of the free-electron model. Energy-band calculations carried out by others[1, 2] indicate that the energy bands and resulting Fermi surface for the heavy rare earths do not resemble those for free electrons, and various authors[3–5] have discussed the effects of departures from a spherical Fermi surface. In particular Evenson and Liu[5] calculated the **q**-dependent susceptibilities for Gd, Dy, Er and Lu along the symmetry line Γ−A using the relativistic APW energy bands of Keeton and Loucks[2], and were able to identify the occurrence of maxima in the susceptibilities with the experimental magnetic wave vectors in these metals.

We report here a preliminary attempt to calculate the exchange interaction between near-neighbor spins for Gd metal near $T = 0$, using energy bands computed via the non-relativistic APW method[6]. Unfortunately our results indicate that the present accuracy of band-structure calculations does not permit meaningful comparison of calculated exchange energies with those determined by analysing magnon dispersion relations obtained from inelastic neutron-scattering experiments[7].

For two Gd ions *a* and *b* the interaction energy depending on the relative orientation of the spins $\mathbf{S}_a$ and $\mathbf{S}_b$ and arising from the incomplete *f*-shell may be written

$$E_{ab} = 4\phi(\mathbf{R}_{ab})\mathbf{S}_a \,.\, \mathbf{S}_b,$$

where

$$\phi(\mathbf{R}_{ab}) = \frac{1}{\Omega^2} \sum_{\substack{E(\mathbf{k}) \leqslant E_F \\ E(\mathbf{k}') > E_F}} \frac{|J(\mathbf{k},\mathbf{k}')|^2}{E(\mathbf{k}) - E(\mathbf{k}')} e^{i(\mathbf{k}-\mathbf{k}')\,.\,\mathbf{R}_{ab}} \tag{1}$$

$J(\mathbf{k},\mathbf{k}')$ is the exchange integral involving a 4*f* and a conduction electron:

$$J(\mathbf{k},\mathbf{k}') = \Omega \int_{\Omega} d\mathbf{r}_1 \int_{\Omega} d\mathbf{r}_2 \psi_{4f}^*(\mathbf{r}_1)\psi_{\mathbf{k}'}^*(\mathbf{r}_2) \frac{e^2}{|\mathbf{r}_1 - \mathbf{r}_2|} \psi_{4f}(\mathbf{r}_2)\psi_{\mathbf{k}}(\mathbf{r}_1) \tag{2}$$

and $S_a = S_b \doteq \frac{7}{2}$ (units of $\hbar$).

ϕ was evaluated using Roth *et al.*'s[3] prescription obtained by the method of stationary phase:

$$\phi(\mathbf{R}_{ab}) = -\sum_{i,j}{}' \frac{|J(\mathbf{k}_i,\mathbf{k}_j)|^2 m_i^* m_j^*}{16\pi^3 R_{ab}^3 \hbar^4 a_{ij}}$$

$$\Big\{ \cos\,[k_{zi} - k_{zj})R_{ab} + (\theta_i - \theta_j)]$$

$$-\frac{G_{ij}}{R_{ab}}\sin\left[(k_{zi}-k_{zj})R_{ab}+(\theta_i-\theta_j)\right]\Bigg\}, \quad (3)$$

where the sum is over all calipering pairs of points $(\mathbf{k}_i, \mathbf{k}_j)$ on the Fermi surface, and the prime means pairs for which $sn(E_{zi}) = sn(E_{zj})$ are excluded. (The z-axis is taken along $\mathbf{R}_{ab}$). We neglect partial derivatives of E higher than the third. Also, since our intent is to focus attention on the effect of using a more realistic Fermi surface, we neglect the variation of J with $\mathbf{k}_i$, $\mathbf{k}_j$.

We then have

$$G_{ij} = \frac{1}{a_{ij}^2}\left[\frac{E_{zz}^{(i)}}{(E_z^{(i)})^3} - \frac{E_{zz}^{(j)}}{(E_z^{(j)})^3}\right],$$

$$a_{ij} = \left|\frac{E_z^{(j)} - E_z^{(i)}}{E_z^{(j)}E_z^{(i)}}\right|,$$

$$m_i^* = \frac{\hbar^2}{|E_{xx}^{(i)}E_{yy}^{(i)}|^{1/2}},$$

$$\theta_i = -\frac{\pi}{4}\left[sn\left(\frac{E_z^{(i)}}{E_{xx}^{(i)}}\right) - sn\left(\frac{E_z^{(i)}}{E_{yy}^{(i)}}\right)\right].$$

The evaluation of ϕ thus involves the determination of the gradient and second-order partial derivatives of E at calipering points on the Fermi surface.

The muffin-tin potential used in the calculations was constructed from the relativistic HF-SCF charge density for atomic Gd in the configuration $4f^7 6s^2 5d$ obtained by Liberman *et al.*[8]. Thirty-one reciprocal lattice vectors were used in the expansion of the APW wave function. Atomic units ($\hbar = 1$, $m = \frac{1}{2}$, $e^2 = 2$) were used throughout. The accuracy of each eigenvalue $E(\mathbf{k})$ was estimated to be within $\pm 0{\cdot}005\,Ry$. The resulting energy bands were quite similar to those obtained by Dimmock and Freeman [1].

The Fermi level was found by computing the eigenvalues at 126 points in $\frac{1}{24}$ of the primitive B.Z. or 3,024 points in the entire primitive B.Z. The value $E_F = 0{\cdot}394\,Ry$ was obtained with an estimated error of $\pm 0{\cdot}010$ Ry.

The calipering points were obtained by sampling **k**-space near the Fermi surface, The derivatives at each point were obtained with an estimated error of ± 5 per cent in the worst cases.

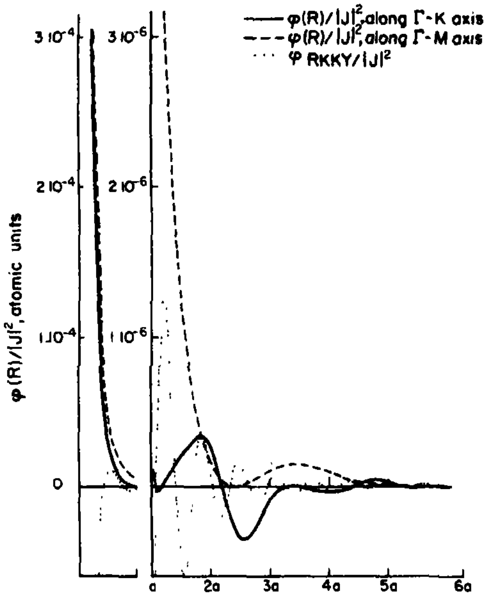

Fig. 1. Indirect exchange interaction $\phi(\mathbf{R})$ in gadolinium, normalized to unit exchange integral $|J|$. $E = 1{\cdot}02\,E_F$. Abscissa is in units of basal-plane lattice constant a. Note scale change at $R = a$.

The results are shown in Fig. 1, where the quantity $\phi(\mathbf{R})/|J|^2$ has been plotted versus $\mathbf{R}$ for $\mathbf{R}$ lying respectively along the directions $\Gamma-\mathrm{K}$ and $\Gamma-\mathrm{M}$ in the crystal. These are the two highest-symmetry directions in the basal plane and contain the nearest and second-nearest basal-plane spins. Also shown is the interaction assuming a free-electron band structure for the conduction electrons. In this case the interaction has simply the isotropic RKKY form,

$$\frac{\phi_{RKKY}(\mathbf{R})}{|J|^2} = \frac{k_F}{32\pi^3 R^3}\left[\cos 2k_F R - \frac{\sin 2k_F R}{2k_F R}\right]. \quad (4)$$

The anisotropy introduced by band-structure effects is quite evident. However, the interaction is positive for nearest-neighbor spins which suggests the spins align themselves in antiparallel, contrary to the observed ferromagnetic ordering pattern in Gd. The free-electron model, on the other hand, is seen to give a negative interaction at the nearest-neighbor distance for Gd (and also for the rest of the heavy rare-earths), which is supported by the ferromagnetism observed in these metals at sufficiently low temperatures. The divergent behavior of all these curves at $R = 0$ is a result of the assumption of constant J and also, in the non-free-electron case, of the use of the asymptotic expression (3) for $\phi(\mathbf{R})$, which samples only points on the Fermi surface. We would expect the finite spread of the $4f$ orbitals to cause $J(\mathbf{k}, \mathbf{k}')$ to approach zero as $|\mathbf{k}\text{-}\mathbf{k}'| \to \infty$ in equation (2) (in the extended-zone scheme). This would be augmented by effective screening of the $4f$-conduction electron exchange. This behavior of J would imply that $\phi(0)$ is finite. Although the portion of the curves for $R < a$ is of little significance here since no two spins in the crystal interact within the nearest-neighbor distance, it has been shown by Watson and Freeman[9] working within the nearly-free-electron model, that the $\mathbf{k}, \mathbf{k}'$ dependence of J has a significant effect, extending out to near-neighbor distances, on the location of the nodes and on the magnitude of the interaction. Enhancement of the interaction due to conduction electron-conduction electron exchange[10] has similar consequences.

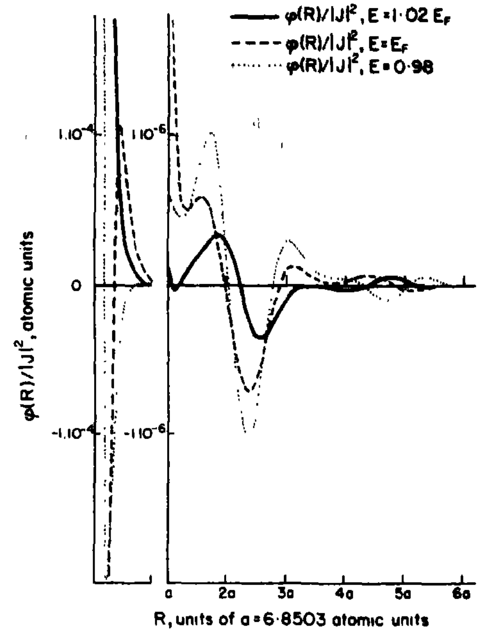

Fig. 2. Sensitivity with respect to energy of the indirect exchange interaction along the $\Gamma - K$ axis in gadolinium. Note scale change at $R = a$.

To check the sensitivity of the results to the Fermi level, the calculation was carried out for the $\Gamma - K$ direction at the computed Fermi level and 2 per cent above and below it, which is of the order of the estimated uncertainty in E_F. The sensitivity of the calculated interaction to the location of the Fermi level, shown in Fig. 2, arises from the rapid variation with E_F of the partial derivatives at the calipering points. Experimentally it is not known how rapidly the interaction changes with E_F but in any case it is evident that to obtain sensible results theoretically, greater precision, to within 0·001 Ry, say, is required in the determination of each eigenvalue. This implies the use of a larger basis set and resulting rapid increase in machine time.

A further limiting factor is the accuracy (~ 0·01 Ry) of the single-electron potential used in the band-structure calculation. It thus appears that until a band calculation can be carried through to the above order of accuracy it will not be possible to assess the reliability of other approximations such as constant J, the stationary-phase method and the use of non-relativistic band structure. In principle, at least, an accurate evaluation of ϕ, as given in equation (1) plus the effect of exchange enhancement, should be relatively stable with respect to E_F and of the correct sign and magnitude for the neighboring spins.

REFERENCES

1. DIMMOCK J. O. and FREEMAN A. J., *Phys. Rev. Lett.* **13**, 750 (1964); FREEMAN A. J., DIMMOCK J. O. and WATSON R. E., *Phys. Rev. Lett.* **16**, 94 (1966).
2. KEETON S. C. and LOUCKS T. L., *Phys. Rev.* **168**, 672 (1968).

3. ROTH L. M., ZEIGER H. J. and KAPLAN T. A., *Phys. Rev.* **149**, 519 (1966).
4. SILVA P. R. P., *Phys. Rev.* **166**, 679 (1968).
5. EVENSON W. E. and LIU S. H., *Phys. Rev. Lett.* **21**, 432 (1968).
6. LOUCKS T. L., *Augmented Plane Wave Method.* Benjamin, New York (1967).
7. HOUMANN J. C. G., *Solid St. Commun.* **6**, 479 (1968).
8. LIBERMAN D., WABER J. T. and CROMER D. T., *Phys. Rev.* **137**, A27 (1965); COWAN R. D., LARSON A. C., LIBERMAN D., MANN J. B. and WABER J., *Phys. Rev.* **144**, 5 (1966).
9. WATSON R. E. and FREEMAN A. J., *Phys. Rev.* **152**, 566 (1966); *ibid.* **178**, 725 (1969).
10. GIOVANNINI B., PETER M. and SCHRIEFFER J. R., *Phys. Rev. Lett.* **12**, 736 (1964).

J. Phys. Chem. Solids Pergamon Press 1970. Vol. 31, pp. 507–516. Printed in Great Britain.

CATHODOLUMINESCENCE OF Er^{3+} IN YGaG AND YAG

J. E. RALPH
Mullard Research Laboratories Redhill, Surrey, England

(*Received* 15 *May* 1969)

Abstract—The cathodoluminescence spectra of Er^{3+} in YGaG and YAG contain various features not normally observed in photoluminescence spectra. These are accounted for in terms of transitions between levels not involving the ground state, energy transfer and self absorption. The $^2P_{3/2}$ splittings of Er^{3+} in YGaG was found to be $54 \pm 4\ cm^{-1}$ and in YAG $121 \pm 4\ cm^{-1}$. Good agreement was found with multiplet splittings obtained by other workers from absorption measurements.

INTRODUCTION

PHOTOLUMINESCENCE measurements on rare earth ions normally involve an excitation energy only a little higher than the emitted energy which it is intended to study. For cathodoluminescence the electron beam energy must be sufficiently high to penetrate beyond any damaged or contaminated surface layer. For YGaG and YAG the penetration of a few microns for the 40 keV electron beam employed was considered to be satisfactory. This incident beam produces secondary electrons of sufficient energy to excite rare earth ions to states well above those normally attainable by optical excitation. Also much higher densities of excited ions can readily be produced than for photoluminescence, so that emitted radiation intensities can be much higher and weak emission line systems more easily studied.

These two factors make it possible using electron excitation to observe transitions between various multiplets not involving the ground state. As a result transitions in the experimentally convenient visible region ($15{,}000$–$25{,}000\ cm^{-1}$) can be observed which give information about the structure of multiplets at much higher energies above the ground state. Also some interesting energy transfer mechanisms come into operation due to the approximate coincidence of the energies of a number of these possible transitions with the energies of transitions involving the ground state. Another effect peculiar to cathodoluminescence is self absorption splitting of some emission lines. This is due to the narrower absorption line of the cool bulk of a single crystal sample superimposed on the broader emission line from the excited region which is normally at a somewhat higher temperature for the beam powers of 1–2 W typically employed.

EXPERIMENTAL

Electron excitation was performed using a converted electron microscope with a beam voltage of 40 kV and a beam current of about 50 μA. The luminescence was analysed by a Jarrell–Ash 0·5 m grating monochromator and detected by a Perkin Elmer 13 Hz amplifying system. For the visible region an IP28 or 9558 photomultiplier was employed and for the infra red a cooled 7102 photomultiplier or an Eastman Kodak lead sulphide cell was used.

Samples were normally rectangular blocks of single crystal YGaG and YAG of about 0·5 cm side and doped with Er^{3+} to between 1 and 10 per cent of the Y^{3+}. These were mounted in indium metal in a recessed copper block attached to a dewar tail. The sample temperature was normally held at 77°K for the experiments reported below.

RESULTS

Figure 1(a) shows the approximate energies of the multiplets of Er^{3+} in YGaG up to 32,000 cm^{-1} and indicates the transitions observed for electron excitation. Only the transitions marked 1,2 and 8 were studied in YAG. Figure 1(b) shows a complete list of the multiplet splittings for Er^{3+} in YGaG which have been obtained by Chamberlain[1] and Cosier[2] by absorption measurements and in the present work. Figures 2, 3 and 4(a) show the 77°K cathodoluminescence spectra due to the transitions $^2P_{3/2} \rightarrow {}^4I_{13/2}$, $^2P_{3/2} - {}^4I_{11/2}$ and $^2P_{3/2} \rightarrow {}^4I_{9/2}$ and the corresponding tables giving line energies and pairs due to the $^2P_{3/2}$ splitting. The mean $^2P_{3/2}$ splitting for Er^{3+} in YGaG was found to be 54 ± 4 cm^{-1} and the mean energies of these levels was 31,583 and 31,529 cm^{-1}. The table in Fig. 4 shows a comparison between the observed spectrum and that predicted using this mean $^2P_{3/2}$ splitting and the $^4I_{9/2}$ levels reported by Chamberlain[1]. The positions of the $^2P_{3/2}$ levels were deduced from Chamberlain's [1] values for the $^4I_{13/2}$ and $^4I_{11/2}$ levels. Figure 4 also shows the effect of concentration of the Er^{3+} on the quenching of the $^2P_{3/2} \rightarrow {}^4I_{9/2}$ emission by energy transfer to the neighbouring $^4S_{3/2} \rightarrow {}^4I_{15/2}$ system. The latter spectrum has been reported by Chamberlain[3] for photoluminescence and will be discussed in more detail below. The considerable reduction in the intensity of the $^2P_{3/2} \rightarrow {}^4I_{9/2}$ system relative to the $^4S_{3/2} \rightarrow {}^4I_{15/2}$ system is clear by comparison of Figs. 4(a) and 4(b). The ratio of the intensity of the

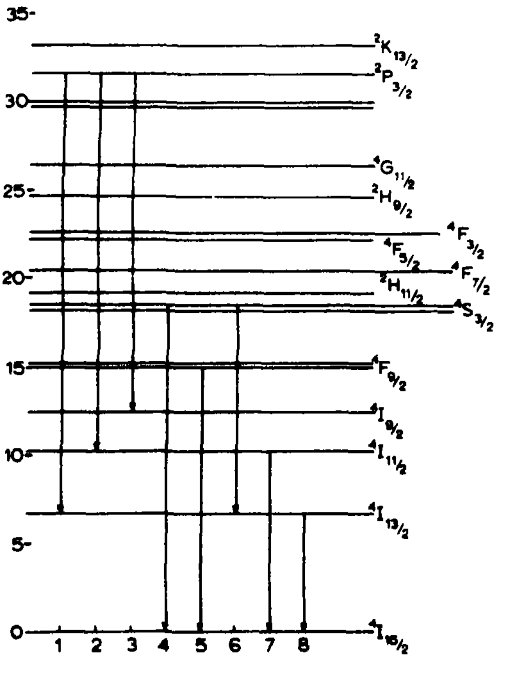

(a)

Multiplet	Energy levels (cm^{-1})	Multiplet	Energy levels (cm^{-1})
• $^4I_{15/2}$	0	(1) $^4I_{9/2}$ (cont)	12588
	45		12734
	74		12762
	419	(1) $^4F_{9/2}$	15310
	434		15336
	491		15348
	525		15509
•(2) $^4I_{13/2}$	6568		15533
	6575	(1) $^4S_{3/2}$	18455
	6594		18431
	6782	(1) $^2H_{11/2}$	19109
	6799		19116
	6825		19166
	6853		19355
(1) $^4I_{11/2}$	10270		19368
	10278		19376
	10367	• $^2P_{3/2}$	31525
	10380		31579
	10397		
	10401		
(1) $^4I_{9/2}$	12323		
	12552		
(1)Chamberlain (2)Cosier • This work			

(b)

Fig. 1. (a) The observed transitions in the cathodoluminescence of Er^{3+} in YGaG. (b) Summary of Er^{3+} in YGaG multiplet splittings.

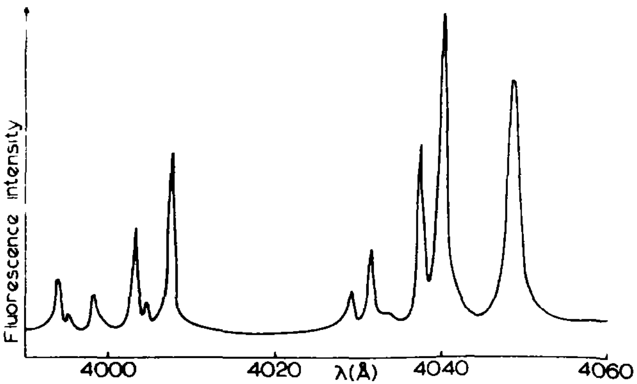

Observed transitions			
Line No.	λ(A)	Energy (cm^{-1})	Separations due to $^2P_{3/2}$ splitting (cm^{-1})
1	3998 2	25011	1 – 4 56
2	3999 0	25006	2 → 5 57
3	4002 2	24986	3 – 6 58
4	4007 2	24965	
5	4008 2	24949	
6	4011 6	24928	
7	4033 2	24794	7 → 10 51
8	4035 6	24779	8 → 11 52
9	4038 0	24765	9 → 12 54
10	4041 5	24743	11 → 13 50
11	4044·2	24727	
12	4046 8	24711	
13	4052 4	24677	

Mean $^2P_{3/2}$ splitting = 54 ± 4 cm^{-1}

$^2P_{3/2}$ levels at 31579 ± 4 cm^{-1}

31525 ± 4 cm^{-1}

Fig. 2. The $^2P_{3/2} \rightarrow {}^4I_{13/2}$ fluorescence spectrum of 1 per cent Er^{3+} in YGaG near 4000 A at 77°K.

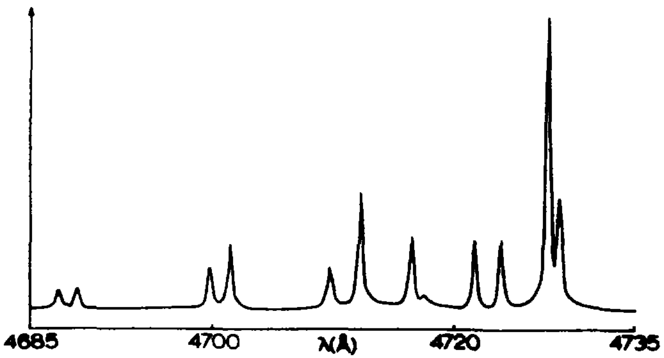

Observed				Predicted
Line No.	λ (A)	Energy (cm^{-1})	Separations due to $^2P_{3/2}$ splitting (cm^{-1})	Energy (cm^{-1})
1	4691·3	21, 316	1 → 3 57	21, 309
2	4692·8	21, 309	2 → 4 57	21, 301
3	4703·8	21, 259		21, 258
4	4705·4	21, 252		21, 247
5	4713 7	21, 215	5 → 9 54	21, 212
6	4716 3	21, 203	6 → 10 52	21, [illegible]
7	4720 5	21, 184	7 → 11 50	21, 182
8	4721 5	21, 180	8 → 12 50	21, 178
9	4725 7	21, 161		21, 158
10	4727 9	21, 151		21, 145
11	4731·7	21, 134		21, 126
12	4732·7	21, 130		21, 124

Mean $^2P_{3/2}$ splitting = 53 ± 4 cm^{-1}

$^2P_{3/2}$ levels at 31586 ± 4 cm^{-1}

31532 ± 4 cm^{-1}

Fig. 3. The $^2P_{3/2} \rightarrow {}^4I_{11/2}$ fluorescence spectrum of 1 Er^{3+} in YGaG near 4700 A at 77°K.

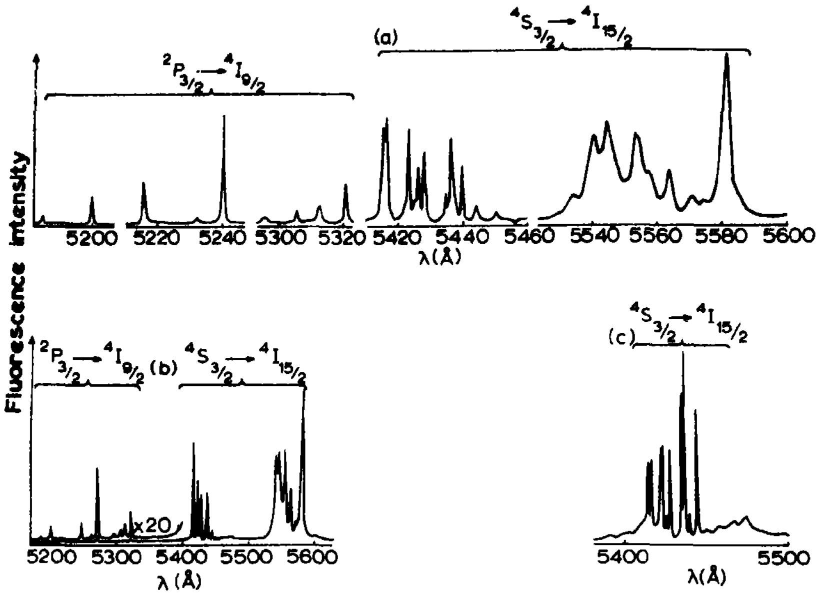

Observed		Predicted
λ(A)	Energy (cm^{-1})	Energy (cm^{-1})
5193	19257	19256
5208	19201	19202
5254	19033	19027
5268	18983	18973
5278	18947	18937
5305	18850	18845
5314	18818	18817
5320	18797	18791
5329	18765	18763
$^2P_{3/2} \rightarrow {}^4I_{9/2}$ Transitions		

Fig. 4. The $^2P_{3/2} \rightarrow {}^4I_{9/2}$ and $^4S_{3/2} \rightarrow {}^4I_{15/2}$ fluorescence spectra of Er^{3+} in YGaG near 5300 A at 77°K. (a) 1 per cent Er^{3+} spectra showing strong $^2P_{3/2} \rightarrow {}^4I_{9/2}$. (b) 10 per cent Er^{3+} spectra showing quenched $^2P_{3/2} \rightarrow {}^4I_{9/2}$. (c) 5 per cent Er^{3+} spectrum showing strong self absorption in the highest energy lines of $^4S_{3/2} \rightarrow {}^4I_{15/2}$.

5750 A line to that of the 5240 A line for an Er^{3+} concentration of 1 per cent is about 1·5 whereas for a concentration of 10 per cent Er^{3+} this ratio is about 35. Figure 4(c) shows the strong differential temperature self absorption splitting mentioned above and this was accentuated in this particular sample by a number of internal reflections of the fluorescence due to irregularities in the sample shape. Figures 5–8 show the energies of the observed lines in the emission spectra arising from transitions between $^4F_{9/2}$ and $^4I_{15/2}$, $^4S_{3/2}$ and $^4I_{13/2}$, $^4I_{11/2}$ and $^4I_{15/2}$ and $^4I_{13/2}$ and $^4I_{15/2}$ for Er^{3+} in YGaG. The transitions to the top of $^4I_{15/2}$ in Figs. 7 and 8 were in many cases too broad to be properly resolved and the predicted positions are indicated by arrows. The important results for Er^{3+} in YAG are shown in Figs. 9–11. From the $^2P_{3/2} \rightarrow {}^4I_{13/2}$ and $^2P_{3/2} \rightarrow {}^4I_{11/2}$ transitions the mean $^2P_{3/2}$ splitting was found to be 121 ± 4 cm^{-1} and the energies of the $^2P_{3/2}$ levels were

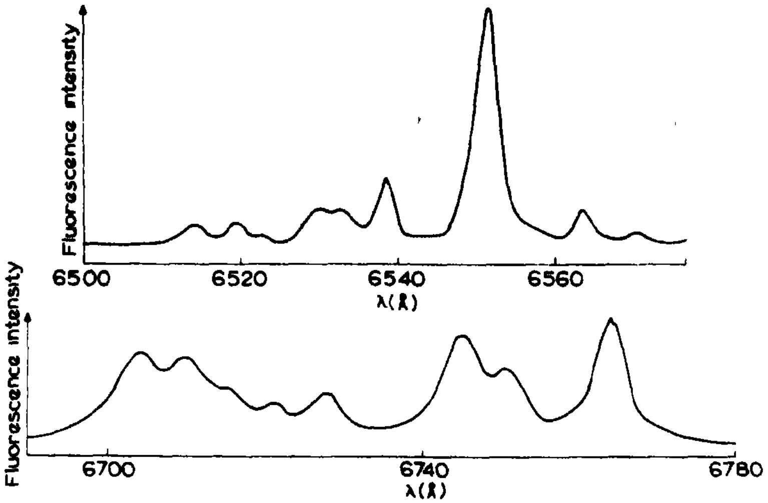

Observed		Predicted
λ(A)	Energy (cm^{-1})	Energy (cm^{-1})
6514	15352	15348
6519	15340	15336
6522	15333	
6530	15314	15310
6533	15307	15303
6539	15294	(15291 (15274
6551 5	15264	(15265 (15262
6563 2	15236	15236
6570	15221	
6704	14916	(14917 (14914
6710	14903	14903
6716	14890	14891
6721	14879	14876
6728	14864	(14857 (14845
6745	14826	14823
6751	14814	(14819 (14811
6764	14784	14785

Fig. 5. The $^4F_{9/2} \rightarrow {}^4I_{15/2}$ fluorescence spectrum of 1 per cent Er^{3+} in YGaG near 6700 A at 77°K.

31,589 and 31,467 cm^{-1}. A comparison with Koningstein's [4] energies for the other levels is shown in the tables where possible.

DISCUSSION

The generally good agreement between predicted transitions and those observed confirms the assignments of the various emission systems, several of which have not been previously reported. The energies of the multiplet levels for Er^{3+} in YGaG obtained from absorption measurements by Chamberlain [1] have been confirmed for $^4I_{15/2}$, $^4I_{11/2}$, $^4I_{9/2}$, $^4F_{9/2}$, $^4S_{3/2}$ and $^2H_{11/2}$ and the splittings

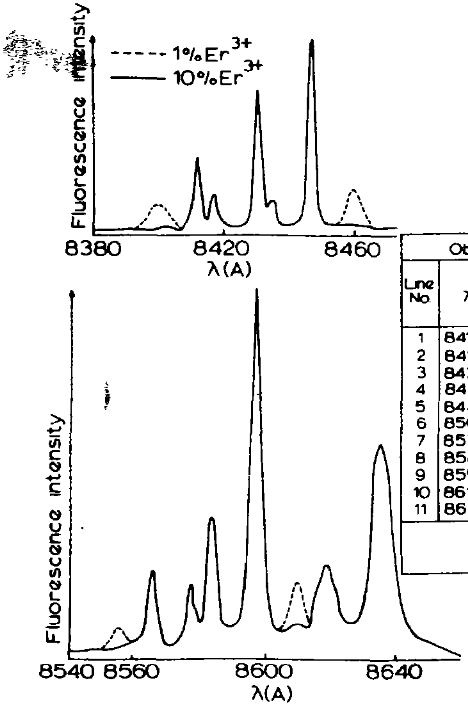

Line No.	Observed transitions λ(A)	Energy (cm^{-1})	Energy separation (cm^{-1})	$^4I_{13/2}$ Energy levels cm^{-1}	Cosiers $^4I_{13/2}$ levels from absorption
1	8411 6	11888	1–3 26	6853	6853
2	8417 0	11881	2–4 25	6825	6840
3	8430 6	11862	3–5 25	6799	6801
4	8434 6	11856		6782	6788
5	8448 0	11837		6594	6596
6	8560 4	11674	6–8 25	6574	6580
7	8578 4	11657	7–9 26	6568	6574
8	8584 4	11649			
9	8597 6	11631	9–10 28		
10	8618 4	11603	10–11 23		
11	8635 4	11580			

Mean $^4S_{3/2}$ splitting = 25 ± 4 cm^{-1}

Fig. 6. The $^4S_{3/2} \rightarrow {}^4I_{13/2}$ fluorescence spectrum of 1 per cent and 10 per cent Er^{3+} in YGaG near 8500 A at 77°K

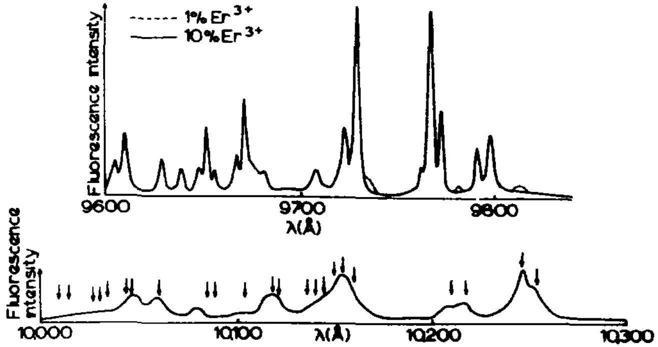

Transitions to bottom of $^4I_{15/2}$			Transitions to top of $^4I_{15/2}$
Observed		Predicted	Predicted
λ(μ)	Energy (cm^{-1})	Energy (cm^{-1})	Energy cm^{-1}
9610·5	10405	10401	10018
9614 5	10401	10387	10022
9632 5	10382	10380	10033
9642·0	10371	10367	10037
9651 0	10362		10039
9655·0	10357	10356	10052
9659·0	10353	10352	10054
9672 0	10339		10067
9675·5	10335	10335	10081
9684·0	10326	10326	10085
9687 0	10323	(10323) (10322)	10112 10126
9703 0	10306	10306	10130
9713 0	10295	10293	10143
9727 0	10281	10278	10147
9733 0	10274	10270	10151
9771 0	10234	10233	10158
9781 0	10224	10225	10161
9796·0	10208	10204	10167
9804·0	10200	10196	10218
			10226
			10253
			10202

Fig. 7. The $^4I_{11/2} \rightarrow {}^4I_{15/2}$ fluorescence spectrum of 1 per cent and 10 per cent Er^{3+} in YGaG near 1·0 μ at 77°K.

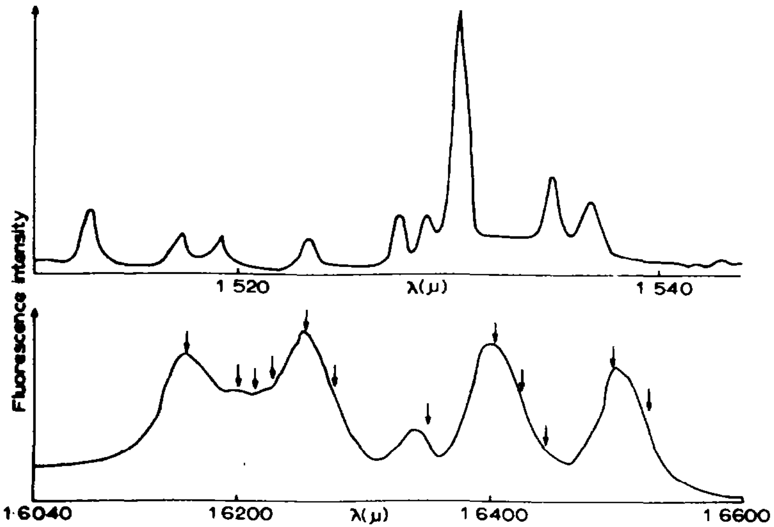

Transitions to bottom of $^4I_{15/2}$			Transitions to top of $^4I_{15/2}$
Observed		Predicted	Predicted
λ(μ)	Energy (cm^{-1})	Energy (cm^{-1})	Energy cm^{-1}
1·5164	6595	6594	6175
1·5206	6576	6575	6160
1·5222	6570	6568	6156
1·5264	6551	6549	6149
1·5308	6533	6530	6141
1·5322	6527	6523	6134
1·5338	6520	6520	6103
1·5382	6501	6501	6084
1·5400	6494	6494	6077
			6050
			6043
			5969

Fig. 8. The $^4I_{13/2} \rightarrow {}^4I_{15/2}$ fluorescence spectrum of 1 per cent Er^{3+} in YGaG near 1·6 μ at 77°K.

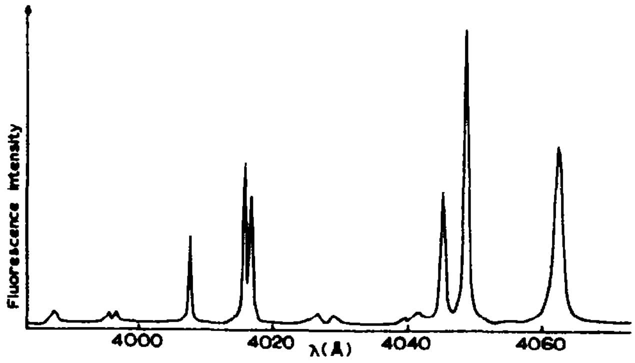

Observed transitions				Energy levels of $^4I_{13/2}$ (cm^{-1})	Koningstein's levels for $^4I_{13/2}$ (cm^{-1})
Line No.	λ(μ)	Energy (cm^{-1})	Energy separation (cm^{-1})		
1	3993·0	25044	1 → 4 125	6882	6949
2	4001·7	24989	2 → 5 124	6800	6858
3	4002·7	24983	3 → 6 122	6781	6766
4	4013·0	24919		6606	
5	4021·7	24865		6600	
6	4022·3	24861		6545	
7	4031·0	24808	7 → 10 118		
8	4043·0	24789	8 → 11 120		
9	4047·3	24708	9 → 12 122		
10	4050·3	24690			
11	4053·7	24669			
12	4067·3	24586			
Mean $^2P_{3/2}$ splitting 122 ± 4 cm^{-1} $^2P_{3/2}$ levels at 31589 ± 4 cm^{-1} 31467 ± 4 cm^{-1}					

Fig. 9. The $^2P_{3/2} \rightarrow {}^4I_{13/2}$ fluorescence spectrum of 1 per cent Er^{3+} in YAG near 4000 A at 77°K.

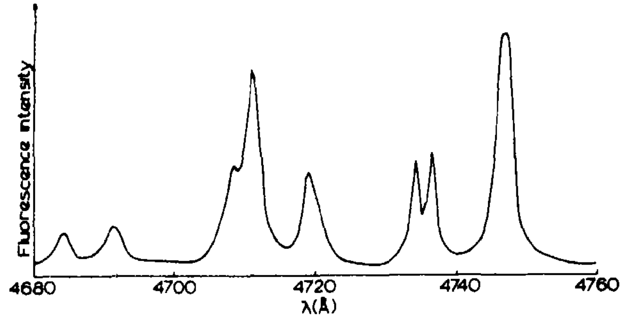

Line No	λ(A)	Energy (cm^{-1})	Energy separation (cm^{-1})	Energy levels of $^4I_{11/2}$ (cm^{-1})	Koningstein's levels for $^4I_{11/2}$ (cm^{-1})
1	4689 3	21325	1 - 4 121	10423	10411
2	4697 7	21292	2 - 5 123	10388	10370
3	4713 7	21215	3 - 6 114	10377	10360
4	4716 0	21204	4 - 7 115	10300	10281
5	4724 0	21169	5 - 8 124	10267	10252
6	4739 0	21101			
7	4742 0	21089			
8	4751 7	21045			
Mean $^2P_{3/2}$ splitting 119 ± 4 cm^{-1}					

Fig. 10 The $^2P_{3/2} \rightarrow {}^4I_{11/2}$ fluorescence spectrum of 1 per cent Er^{3+} in YAG near 4700 A at 77°K.

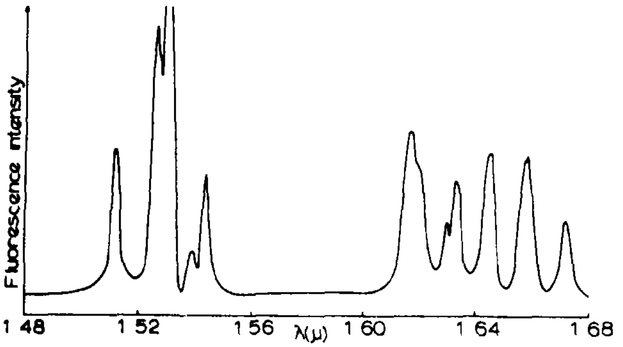

Line No	λ(µ)	Energy (cm^{-1})	Energy separation (cm^{-1})	Energy levels of $^4I_{15/2}$ (cm^{-1})	Koningstein's levels for $^4I_{15/2}$ (cm^{-1})
1	1 514	6605	1 → 2 60	571	568
2	1 528	6545	2 → 4 54	473	460
3	1 532	6527	3 → 5 57	430	424
4	1 541	6491		418	412
5	1 546	6470		75	(140)
6	1 619	6177	6 → 8 50	54	68
7	1 621	6170	7 → 9 55	0	24
8	1 632	6127			0
9	1 635	6115	9 → 10 57		
10	1 647	6072			
11	1 660	6024	11 → 12 50		
12	1 674	5974			
Mean splitting of lowest doublet of $^4I_{13/2}$ = 55 ± 4 cm^{-1}					

Fig. 11. The $^4I_{13/2} \rightarrow {}^4I_{15/2}$ fluorescence spectrum of 1 per cent Er^{3+} in YAG near 1·6 µ at 77°K.

of $^2P_{3/2}$ and $^4I_{13/2}$ established as shown in Figs. 1 and 5.

When the fluorescence spectrum of a level system is excited in the bulk of a single crystal it is clear that self absorption may occur as its passes through the crystal on its way to the detecting system. If the fluorescence transition is to an occupied ground state and if there is no Stokes' shift between emission and absorption energies then such self absorption must occur to some extent. This self absorption would be expected to depend on the geometry of the excitation system and on the concentration of the active ions. Energy transfer between like ions will produce qualitatively the same effect as self absorption on the fluorescence spectrum if some sink exists for the ultimate degradation of the energy after a number of transfers. However energy transfer will not depend on the geometry (e.g. the path of the fluorescence through the sample) but will depend only on the concentration of the active ion. By using electron excitation with a penetration of a micron or so, and by viewing the emission from the excited face of the sample self absorption should be eliminated and only energy transfer processes should be observed. In fact some internal reflection can occur which gives rise to self absorption.

A further difference between energy transfer and self absorption which might be expected[5] is that for the former only an approximated match, to within available phonon energies, between the transitions involved is necessary. However for self absorption the energy match must be to within a line width

A clear example of self absorption due to internal reflection in an irregular sample is shown in Fig. 4(c) for the $^4S_{3/2} \rightarrow {}^4I_{15/2}$ transition in 5 per cent Er^{3+} in YGaG at a nominal temperature of 77°K. The two highest energy lines are split by the corresponding transition in absorption. The splitting rather than a simple intensity reduction arises as pointed out above from the difference in temperature of the bulk and excited regions. The population difference between the lower levels of the $^4I_{15/2}$ ground state is clearly indicated since the highest energy line of Fig. 4(c) shows much stronger self absorption than the next highest and the third highest energy line shows no sign of splitting. The extent of this self absorption is made clear by a comparison of Fig. 4(c) with Fig. 4(b) where internal reflection and hence self absorption were absent. The published photoluminescence spectra of $^4S_{3/2} \rightarrow {}^4I_{15/2}$[3] also show strong self absorption with no splitting even at Er^{3+} concentrations as low as 0·1 per cent Er^{3+}.

A number of unidentified lines were observed in the $^4S_{3/2} \rightarrow {}^4I_{15/2}$, $^4F_{9/2} \rightarrow {}^4I_{15/2}$ and $^4S_{3/2} \rightarrow {}^4I_{13/2}$ spectra for low Er^{3+} concentration. For Er^{3+} concentrations of about 10 per cent these lines disappeared indicating that these also were due to transitions between pairs of high energy multiplets.

The energy transfer between the $^2P_{3/2} \rightarrow {}^4I_{9/2}$ system centred near 19,000 cm^{-1} and the $^4S_{3/2} \rightarrow {}^4I_{15/2}$ system near 18,300 cm^{-1} involves a loss of energy of about 700 cm^{-1}. A phonon assisted sideband spacing of about this energy has been observed in the Er^{3+} fluorescence in several garnets[6] and indicates that this energy difference may be readily absorbed by the lattice during energy transfer between Er^{3+} ions in YGaG and YAG.

CONCLUSIONS

The cathodoluminescence spectrum of Er^{3+} in YGaG and YAG shows several features characteristic of this mode of excitation and these are accounted for in terms of energy transfer and self absorption. The levels of several multiplets are determined and good agreement with the results of other workers was found.

Acknowledgements—Thanks are due to M. J. Smith for assistance with the electron excitation apparatus, to J. L. Page for growing the crystals and to many others for valuable discussions.

REFERENCES

1. CHAMBERLAIN J. R. Unpublished work.
2. COSIER J. P., Mullard Technical Note No. 934.
3. CHAMBERLAIN J. R., PAXMAN D. H. and PAGE J. L., *Proc. phys. Soc.* **89**, 143 (1966).
4. KONINGSTEIN J. A. and GEUSIC J. E., *Phys. Rev.* **136**, 3A, A726 (1964).
5. DEXTER D. L., *J. chem. Phys.* **21**, 836 (1953).
6. BURNS G., GEISS E. A., JENKINS B. A. and NATHAN M. I., *Phys. Rev.* **139**, 5A, A1687 (1965).

J. Phys. Chem. Solids Pergamon Press 1970. Vol. 31, pp. 517–527. Printed in Great Britain.

DIFFUSION OF SULFUR IN GALLIUM PHOSPHIDE AND GALLIUM ARSENIDE*

A. B. Y. YOUNG† and G. L. PEARSON
Stanford Electronics Laboratories, Stanford University, Stanford, Calif. 94305, U.S.A.

(*Received* 19 *May* 1969; *in revised form* 28 *July* 1969)

Abstract—A radiotracer technique was used to study the diffusion of sulfur in GaP and GaAs as a function of temperature, sulfur pressure, and component pressure. The results reported here indicate that the variation of diffusion coefficient with component pressure for sulfur in both GaP and GaAs is not in agreement with a model of vacancy diffusion within a single sublattice. The diffusion coefficient of sulfur in GaP was found to be independent of phosphorus pressure, whereas the diffusion coefficient of sulfur in GaAs varied as $(P_{As_4})^{1/2}$ at low arsenic pressures, and appeared to saturate at arsenic pressures greater than 0·5–1 atm. The results for sulfur in GaP are consistent with diffusion via the divacancy $(V_{Ga}V_P)$ while the diffusion of sulfur in GaAs can be explained by movement via the gallium divacancy $(V_{Ga}V_{Ga})$. The apparent decrease in the diffusion coefficient at high sulfur concentrations can be qualitatively explained by the formation of the complex $(V_{Ga}S_3)$. A plasma reflection technique was used to study the electrically active part of the sulfur-diffused layers in GaAs. At high sulfur concentrations a large percentage of the sulfur in the diffused layer was found to be electrically inactive. This phenomenon is suggested as a possible explanation for the large discrepancy among previously reported values of the diffusion coefficient of sulfur in GaAs.

1. INTRODUCTION

THE DIFFUSION of sulfur in GaAs has been investigated by a number of workers[1–4]. Goldstein measured the temperature dependence of the diffusion coefficients of a number of substitutional impurities in GaAs and concluded that sulfur diffused by means of vacancies within the arsenic sublattice[1]. Vieland carried out a qualitative study of the effect of arsenic pressure on sulfur diffusion in GaAs and concluded that the results were in conflict with the sublattice model proposed by Goldstein[4]. The possibility of the participation of nearest-neighbor gallium vacancies in the diffusion process was suggested by Vieland, but no definite model was proposed. The diffusion of sulfur in GaP has not been reported previously.

In the work reported here, radiotracer methods were used to study the diffusion of sulfur in GaAs and GaP as a function of temperature, sulfur pressure, and component pressure. Particular emphasis was placed on a determination of the *quantitative* dependence of the diffusion coefficient of sulfur in GaAs and GaP on component pressure. These results are not in agreement with the sublattice model of vacancy diffusion.

Although the presence of a large concentration of electrically inactive impurities has been reported previously for melt-grown GaAs[5] and solution-grown GaP[6] crystals that are heavily doped with the group VI donors, S, Se and Te, there appears to have been little consideration of such effects in diffused layers in these materials. In the work reported here, a plasma reflection technique was used to obtain the electron concentration profiles in sulfur-diffused layers in GaAs.

2. EXPERIMENTAL TECHNIQUES

Undoped GaP single crystals were grown by an open tube vapor phase epitaxial process using PCl_3 as the transport agent. The crystals were grown on {111} Ga faces of GaAs seed crystals and were n-type with carrier concentrations of 10^{15}–$10^{16}\,\mathrm{cm}^{-3}$ and mobilities of 80–100 cm²/V-sec. The GaP crystals had a dislocation density of about $10^{6}\,\mathrm{cm}^{-2}$, a density of stacking faults and microtwins of 300–500 cm^{-1}, and contained up to 6 per cent of arsenic on the phosphorus sub-lattice because of contamination from the GaAs seed.

---

*This work was supported by the National Aeronautics and Space administration under grant NGR-05-020-043. One of the authors (ABYY) also acknowledges financial support of the National Science Foundation.

†Present address: Fairchild Semiconductor, Palo Alto, California.

Undoped GaAs single crystals were obtained from the Monsanto Company. These were boat-grown and oriented in the ⟨111⟩ direction. The electron concentration was 10^{15}–$10^{16}\,\mathrm{cm}^{-3}$, the mobility was 4000 cm²/V-sec, and the dislocation density was $1-2\times10^{3}\,\mathrm{cm}^{-2}$.

The crystals were lapped and then mechanically polished with Linde A 0·3 μ alumina. After cleaning and degreasing the samples were etched to remove damage due to the polishing procedure. Typically about 5 μ of material was removed. The etchant for the GaP was 8 g $K_3Fe(CN)_6$: 12 g KOH: 100 ml H_2O and for the GaAs, an 0·15% Br in methanol solution.

Appropriate amounts of radioactive ^{35}S dissolved in spectroquality benzene were pipetted into clean quartz ampoules. After the benzene had been evaporated, the samples were placed in the ampoules along with the appropriate amounts of high purity phosphorus or 6 nine's purity arsenic. In order to minimize surface deterioration and weight losses due to a vapor transport mechanism[2], the samples were sandwiched between two quartz plates[7–9]. Each ampoule was evacuated to approx. 10^{-5} Torr. and sealed off to yield a volume of approximately 1·0 ml. The GaP samples were diffused at temperatures between 1100 and 1300°C, while the GaAs samples were diffused at temperatures between 900° and 1200°C for appropriate times. The furnace temperature was controlled within ±2°C. The diffusion profiles were determined by standard etching, weighing, and counting procedures[10] using the etchants given above. The results were corrected for self-absorption of the 0·167 MeV beta particles in the GaAs or GaP crystals. Absolute values of concentration were obtained by comparing the activity of each etched section with that of a calibrated ^{35}S standard.

The pressures of the various vapor species were calculated from the amounts of sulfur, arsenic, and phosphorus placed in the ampoule together with equilibrium constants given in the literature[11, 12]. The arsenic (or phosphorus) pressure when no excess arsenic (or phosphorus) was added was assumed to be the decomposition pressure for the GaAs (or GaP) solid phase in the binary Ga–As[13] (or Ga–P[14]) system.

The diffusion profiles were well-behaved when the surface concentration was less than $10^{20}\,\mathrm{cm}^{-3}$. These profiles could be fitted to the complementary error function solution of Fick's Second Law,

$$C(x) = C_s \operatorname{erfc}\left[\frac{x}{2\sqrt{Dt}}\right] \tag{1}$$

where $C(x)$ is the impurity concentration at a distance x below the surface, C_s is the surface concentration, D is the diffusion coefficient, and t is the time. The diffusion coefficient was obtained by Hall's method in which normalized profiles $(C/2C_s)$ vs. $(x/\sqrt{t})$ plotted on probability paper yield straight lines whose slopes are related to the diffusion coefficient[15].

3. EXPERIMENTAL RESULTS

Within the GaP or GaAs solidus region, the diffusion conditions can be specified uniquely by the temperature, the sulfur pressure, and the phosphorus or arsenic pressure. The results of experiments in which each of these parameters is varied independently are given in this section.

(A) *Diffusion of sulfur in* GaP

Figure 1 shows the radiotracer profiles of sulfur in GaP when the sulfur vapor density

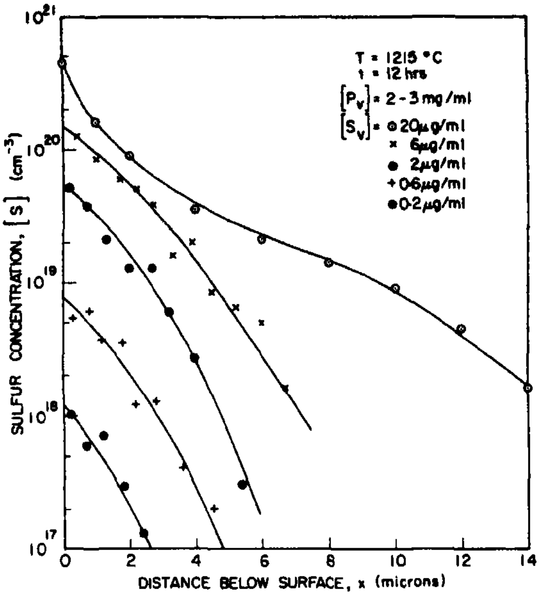

Fig. 1. Diffusion profiles of sulfur in GaP at various sulfur vapor densities.

$[S_v]$, was varied from 0·2 to 20 μg/ml while the temperature and the phosphorus vapor density $[P_v]$ were kept fixed. At surface concentrations below $10^{20}\,\text{cm}^{-3}$ the diffusion profiles can be fitted with complementary error functions so that the diffusion coefficient is independent of sulfur concentration [S].

The upper curve in Fig. 1 is typical of the profiles obtained when C_s is larger than $10^{20}\,\text{cm}^{-3}$. Complementary error functions are no longer obtained and the Boltzmann–Matano technique must be used to evaluate the diffusion coefficient as a function of sulfur concentration. The result of such an analysis is shown in Fig. 2. It is clear that D decreases rapidly with increase in [S] above $\approx 5 \times 10^{19}\,\text{cm}^{-3}$.

Figure 3 shows the dependence of surface concentration C_s on the sulfur vapor density for the diffusion profiles in Fig. 1. It is seen that C_s is proportional to $[S_v]^{1\cdot3}$ which is not in agreement with the usual model for incorporation of sulfur atoms on isolated phosphorus sites.

Figure 4 shows the dependence of D on the phosphorus vapor density $[P_v]$ when the temperature and the sulfur vapor density are kept constant. It is seen that the diffusion coefficient is independent of the phosphorus pressure which is not in agreement with the sublattice model of vacancy diffusion.

Figure 5 shows the temperature dependence

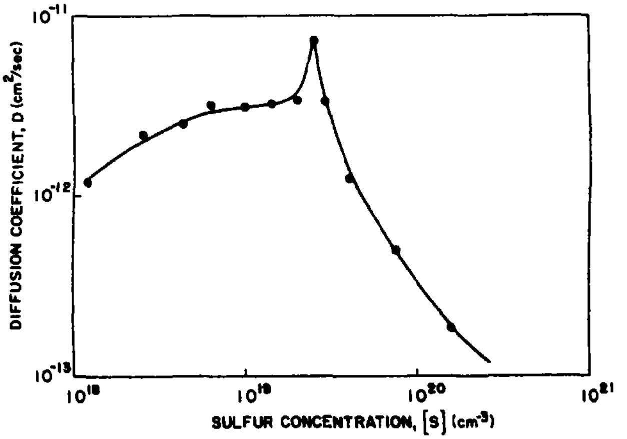

Fig. 2. Concentration dependence of the diffusion coefficient of sulfur in GaP at 1215°C as determined from a Boltzmann–Matano analysis. The data were derived from the high concentration profile in Fig. 1.

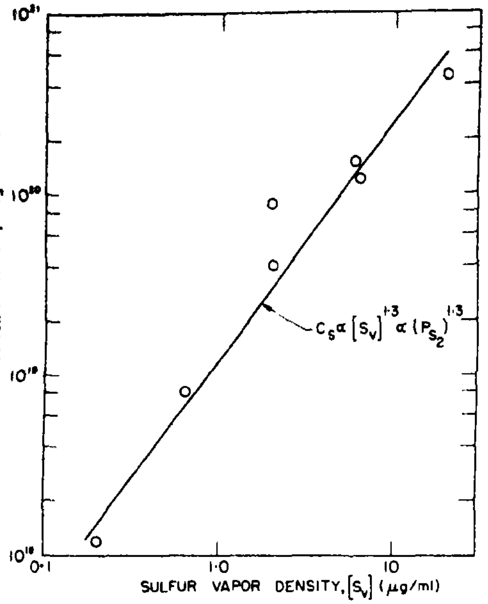

Fig. 3. Dependence of the surface concentration of diffusion profiles in GaP on the sulfur vapor density at 1215°C. $[P_v] = 2$–3 mg/ml ($P_{P_2} \approx 1$ atm).

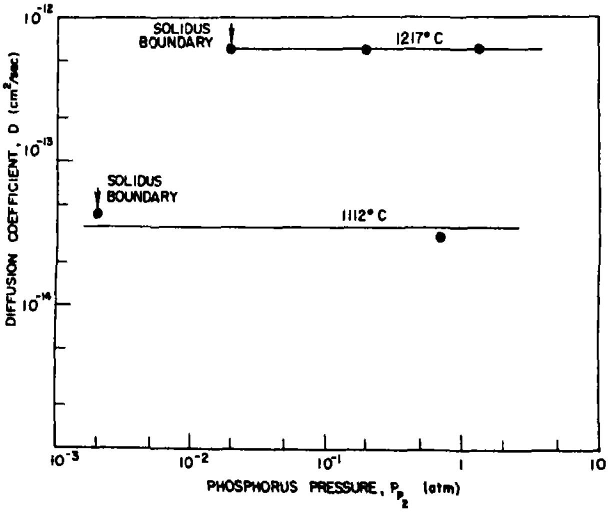

Fig. 4. Dependence of the diffusion coefficient of sulfur in GaP on the phosphorus pressure. $[S_v] = 6\,\mu g/ml$ at 1217°C; $[S_v] = 2\,\mu g/ml$ at 1112°C.

of the diffusion coefficient of sulfur in GaP when $[S_v]$ and $[P_v]$ are kept approximately constant. Fitting the points to a straight line yields the relation

$$D = 3{\cdot}2 \times 10^3 \exp[-4{\cdot}7/kT]\ \mathrm{cm^2/sec}. \quad (2)$$

(B) *Diffusion of sulfur in* GaAs

Figure 6 shows radiotracer profiles of sulfur in GaAs when $[S_v]$ was varied from 0·2 to 6·0 $\mu g/ml$ while temperature and arsenic vapor density $[As_v]$ were kept constant. The nature of the profiles is similar to that reported above for sulfur in GaP with relatively well-behaved profiles at the lower surface concentrations, but with a change in shape for C_s greater than 10^{20} cm^{-3}. Figure 7 shows that a linear relationship is obtained between C_s and $[S_v]$ at the lower surface concentrations. These results are not in agreement with the usual model of incorporation of sulfur atoms on isolated arsenic sites.

Figure 8 shows the dependence of the diffusion coefficient of sulfur in GaAs on arsenic pressure when the temperature and the sulfur vapor density were kept constant. The data were obtained at two temperatures, 1130 and 1003°C. The results at both temperatures are similar in that at low arsenic pressures the diffusion coefficient varies as the square root of the arsenic pressure P_{As_4}.

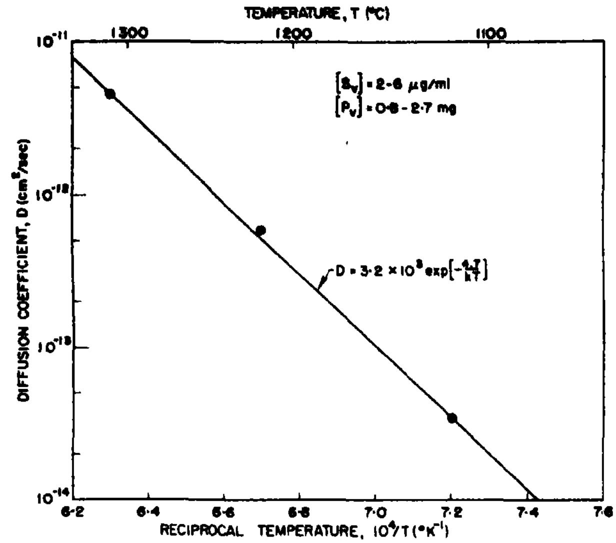

Fig. 5. Dependence of the diffusion coefficient of sulfur in GaP on temperature.

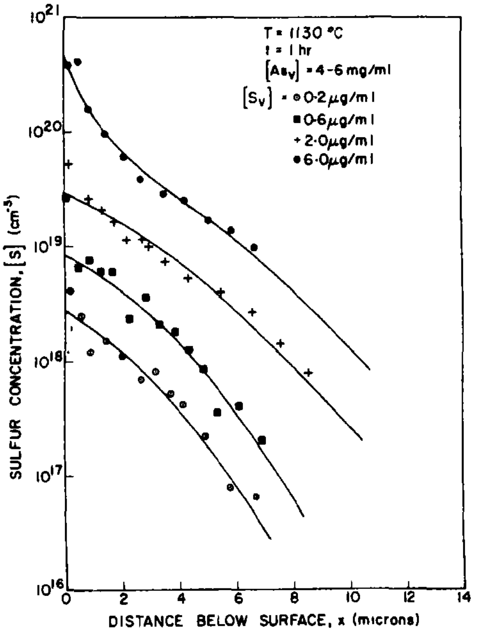

Fig. 6. Diffusion profiles of sulfur in GaAs at various sulfur vapor densities.

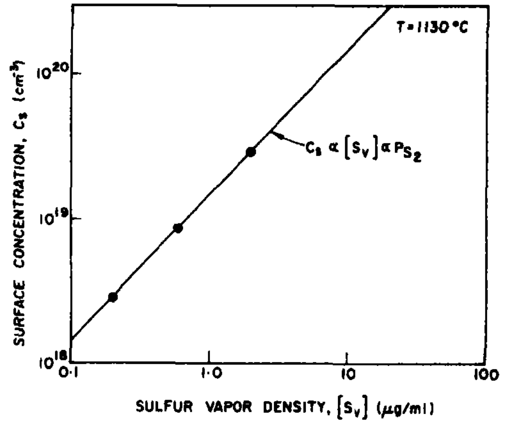

Fig. 7. Dependence of the surface concentration of diffusion profiles in GaAs on the sulfur vapor density at 1130°C. [As$_v$] = 4–6 mg/ml ($P_{As_4} \approx 2$ atm).

Above 0·5–1 atmospheres, however, the diffusion coefficient is relatively independent of P_{As_4}. These results are in agreement with the qualitative findings of Vieland[4]. However, they are not compatible with the sublattice mechanism of diffusion.

Several samples were preannealed in quartz ampoules for 5 days at 1003°C under the same arsenic pressures that were to be used during the diffusion anneal. The samples were then re-encapsulated with appropriate amounts of arsenic and radioactive ^{35}S and

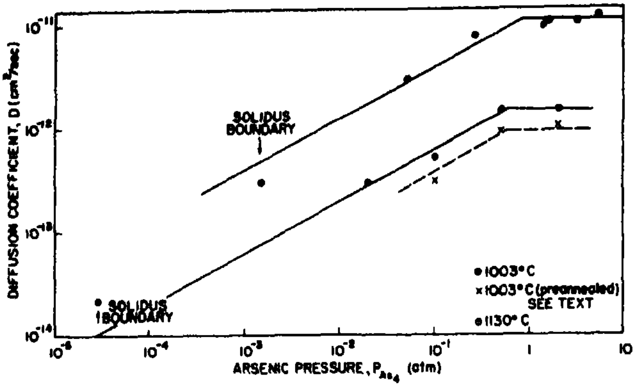

Fig. 8. Dependence of the diffusion coefficient of sulfur in GaAs on the arsenic pressure. $[S_0] = 0{\cdot}2\ \mu g/ml$.

diffused for 12 hr at 1003°C. The results are shown by the dashed curve in Fig. 8. Although these results indicate a slight decrease in diffusion coefficient, the shape of the curve remains the same. Thus it is unlikely that non-equilibrium between the external arsenic vapor and the vacancy concentration in the GaAs crystal is responsible for the knee.

A second possible explanation for the knee is a saturation in the concentration of defects responsible for the diffusion. Although this possibility cannot be ruled out completely, several observations suggest that another explanation must be sought. First, Seltzer[16] studied the diffusion of Mn in GaAs for arsenic pressure up to 5 atm and found no saturation of the diffusion coefficient. This suggests that the concentration of vacancies in the crystal does not saturate at the arsenic pressures corresponding to the knee for sulfur diffusion in GaAs. Second, the arsenic pressure at the arsenic-rich boundary of the GaAs solidus region appears to be an order of magnitude higher than the pressures at the knee [13]. This suggests that a saturation of the defect concentrations due to the presence of a phase boundary is unlikely.

Figure 9 shows the temperature dependence of the diffusion coefficient of sulfur in GaAs. Our experimental data indicate that the diffusion coefficient of sulfur in GaAs at high arsenic pressures is given by the relation

$$D = 1{\cdot}85 \times 10^{-2} \exp(-2{\cdot}6/kT)\ \mathrm{cm^2/sec}. \qquad (3)$$

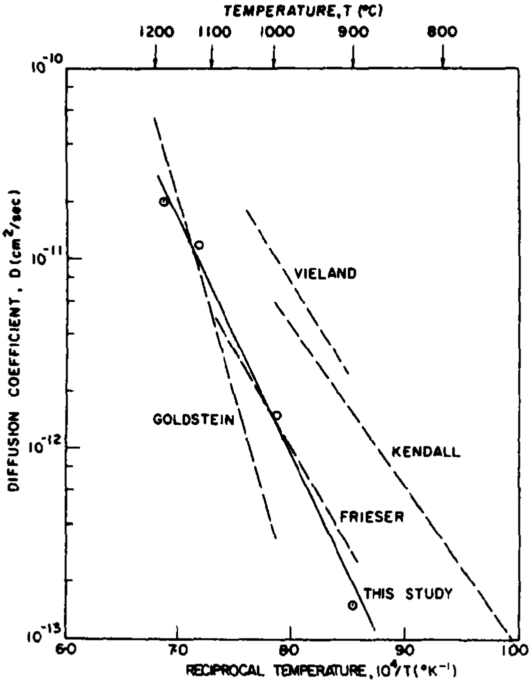

Fig. 9. Dependence of the diffusion coefficient of sulfur in GaAs on temperature as reported by different workers. In this study $[S_0] = 0{\cdot}2\ \mu g/ml$ and $[As_0] = 3$–$5\ mg/ml$.

Also shown in Fig. 9 are the results reported by other workers for the diffusion of sulfur in GaAs[1–4]. A large discrepancy among the different results is apparent. These differences have been discussed previously in the literature and attributed to vapor etching of the samples[2] or enhanced diffusion near the surface as a result of mechanical damage to the crystal[17]. The results reported here indicate that the effects of $[As_v]$ on D may be responsible for some of the observed differences.

Another possible reason for the large discrepancy among different workers is suggested by the following experiment in which the electron and total sulfur concentration profiles were determined simultaneously on a sample of GaAs that had been diffused with sulfur. Before diffusion, the sample and the quartz plates were soaked in a warm aqueous solution of KCN (5 per cent) for 10 min to reduce compensation effects due to copper. The ampoule was quenched in water after the diffusion. The plasma reflection technique was used to determine the electron concentration profile at room temperature. By etching away thin layers of GaAs and measuring the position of the plasma reflection minimum as a function of depth, the electron concentration profile was determined. The relation between the position of the minimum in the reflection spectrum and the electron concentration was taken from the literature[18]. A Perkin–Elmer 621 Grating Spectrophotometer was used in these measurements.

A typical result shown in Fig. 10 indicates that the electron concentration is significantly less than the sulfur concentration at high sulfur concentrations. The maximum electron concentration in the diffused layer varied with diffusion temperature, increasing from 1·6 × 10^{18} cm^{-3} at 900° to 5 × 10^{18} cm^{-3} at 1130°C. However, it appeared to be relatively independent of the surface concentration of sulfur and the arsenic pressure during diffusion.

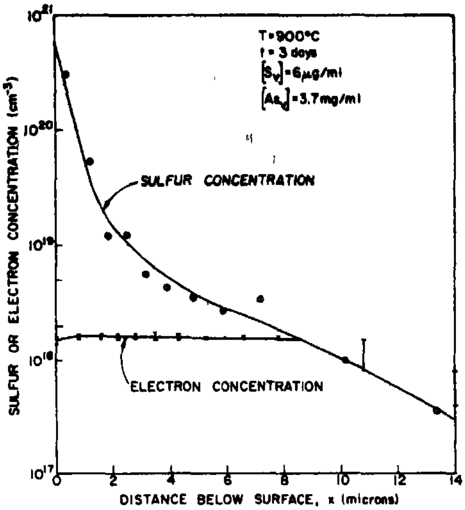

Fig. 10. Comparison of the electron (determined by a plasma reflection technique) and total sulfur (determined by a radiotracer technique) concentration profiles in a diffused layer in GaAs.

The presence of large concentrations of electrically inactive sulfur could explain some of the discrepancies among reported values of the diffusion coefficient of sulfur in GaAs. P–n junction and sheet resistivity techniques were used by several workers[2–4]. Figure 10 indicates that experiments which measure only the electrically active part of the impurity distribution in the diffused layer result in apparent diffusion coefficients that are too high when the surface concentration exceeds the solubility of electrically active sulfur at the diffusion temperature.

4. DISCUSSION

The diffusion of substitutional impurities in III–V compound semiconductors has usually been explained in the literature by a model based on vacancy diffusion within a single sublattice[1]. This model predicts that the diffusion of sulfur in GaAs should be proportional to the concentration of arsenic vacancies $[V_{As}]$ (the vacancies are assumed to be neutral in this discussion). Thus

$$D \propto K_1[V_{As}] = K_2(P_{As_4})^{-1/4} \tag{4}$$

where K_1 and K_2 are equilibrium constants. Similar equations can be written for impurity diffusion on the gallium sublattice, as well as for diffusion in GaP. It is clear that this sublattice model does not agree with our observed pressure dependence of the diffusion coefficient of sulfur in either GaP or GaAs. The findings of other workers on self-diffusion in InSb[2], and the diffusion of Zn in GaAs[10], Zn in GaP[19], Se in GaAs[8], and Mn in GaAs[16] are also in conflict with the sublattice model. The failure of the sublattice model to explain the dependence of the diffusion coefficient on component pressure appears to be a general phenomenon in III–V compound semiconductors.

In the following discussion, models of sulfur diffusion in GaP and GaAs are presented which can explain the quantitative dependence of the diffusion coefficient on component pressure. In addition, a qualitative explanation for the apparent decrease of the diffusion coefficient at high sulfur concentrations is given. Finally, the anomalous dependence of the surface concentrations of the diffusion profiles on the sulfur vapor density is pointed out and possible explanations are discussed.

(A) *Diffusion of sulfur in* GaP

In the work reported here, sulfur diffusion in GaP was found to be independent of phosphorus pressure. Nygren and Pearson[19] have shown that the diffusion rate of Zn in GaP can be changed significantly by varying the phosphorus pressure. Since zinc diffusion at high concentrations is much faster than sulfur diffusion in GaP, it is unlikely that non-equilibrium effects between the external phosphorus vapor and the vacancy concentration in the crystal are responsible for the lack of dependence of sulfur diffusion on phosphorus pressure.

A simple model that can explain the lack of dependence of sulfur diffusion on phosphorus pressure is diffusion by means of divacancies. From simple mass action relations, it can be shown that the concentration of divacancies $[(V_{Ga}V_P)]$ is a function only of temperature and is independent of phosphorus pressure[2]. In the basic jump process, sulfur on a phosphorus site presumably jumps to the phosphorus vacancy end of the divacancy. Although the basic jump to the phosphorus vacancy is exactly the same as in the sublattice model, the presence of the gallium vacancy means that less distortion of the lattice is required during the diffusion process.

The presence of electrically inactive impurities in GaAs and GaP heavily doped with the group VI donors has been attributed to the formation of neutral complexes such as $(V_{Ga}Se_3)$[5, 6, 20] or to the presence of precipitates of Ga_2Se_3[25, 26]. The apparent decrease in the diffusion coefficient of sulfur in GaP at high concentrations can be interpreted qualitatively in terms of the analogous complex $(V_{Ga}S_3)$. If most of the sulfur is in the form of such complexes, but the diffusion flux is by the movement of isolated substitutional S_P^+ donors via divacancies with a diffusion coefficient D_{vv}, the effective diffusion coefficient $\bar{D}$ is given by

$$\bar{D} = D_{vv}\frac{\partial[S_P{}^+]}{\partial[S]} \approx \frac{D_{vv}}{3}\frac{\partial[S_P{}^+]}{\partial[(V_{Ga}S_3)]}, \quad (5)$$

where [S] is the total sulfur concentration. The equilibrium between the mobile and immobile forms of sulfur is

$$3S_P{}^+ + 3e^- + V_{Ga} \rightleftarrows (V_{Ga}S_3). \quad (6)$$

The corresponding mass action equation in the extrinsic region is

$$[(V_{Ga}S_3)] = K_3[S_P{}^+]^6[V_{Ga}]. \quad (7)$$

From equations (5) and (7) it can be shown that $\bar{D}$ is proportional to $[S]^{-5/6}$. Thus the diffusion coefficient should decrease at high sulfur concentrations since a smaller fraction of the total sulfur is free to move. Although the immobile species in this discussion has been taken to be the $(V_{Ga}S_3)$ complex, the same qualitative result would have been obtained for any model which invokes an immobile molecular majority species at high sulfur concentrations. A second phase of Ga_2S_3 (which can be thought of as a macroscopic clustering of isolated complexes) might be responsible for the shape of the diffusion profiles at high sulfur concentrations [21]. It is noted, however, that the diffusion temperature for which the results in Fig. 2 were obtained (1215°C) is considerably higher than the melting temperature of Ga_2S_3 (1090°C) [22]. Under equilibrium conditions at the diffusion temperature, Ga_2S_3 should not exist as a stable solid phase.

(B) *Diffusion of sulfur in* GaAs

The diffusion coefficient of sulfur in GaAs was found to be independent of arsenic pressure above 0·5–1 atm and varied as $(P_{As_4})^{1/2}$ at lower pressures. A simple model that can explain these results is diffusion via the gallium divacancy $(V_{Ga}V_{Ga})$.

Sulfur is assumed to be present in the crystal in two forms. The usual sulfur donor on an arsenic site, $S_{As}^{+} = C_2$, is assumed to be immobile. However, it can interact with a gallium divacancy to form the mobile complex $(V_{Ga}S_{As}^{+}V_{Ga}) = C_1$. This mobile species is assumed to have the diffusion coefficient D_1.

The equilibrium between the mobile and immobile species is given by

$$C_2 + (V_{Ga}V_{Ga}) \rightleftarrows C_1 \tag{8}$$

and the corresponding mass action equation is

$$[C_2][(V_{Ga}V_{Ga})] = K_4[C_1]. \tag{9}$$

The concentration of gallium divacancies is

$$[(V_{Ga}V_{Ga})] = K_5(P_{As_4})^{1/2} \tag{10}$$

and the 'conversion-of-sulfur' equation is

$$[C_1] + [C_2] = [S]. \tag{11}$$

Solving equations (9–11) gives

$$[C_1] = \left[\frac{K_6(P_{As_4})^{1/2}}{1+K_6(P_{As_4})^{1/2}}\right][S] \tag{12}$$

and

$$C_2 = \left[\frac{1}{1+K_6(P_{As_4})^{1/2}}\right][S]. \tag{13}$$

The K's in the above equations are equilibrium constants. The effective diffusion coefficient $\bar{D}$ is

$$\bar{D} = D_1\frac{\partial[C_1]}{\partial[S]} = D_1\left[\frac{K_6(P_{As_4})^{1/2}}{1+K_6(P_{As_4})^{1/2}}\right]. \tag{14}$$

The variation of diffusion coefficient with arsenic pressure predicted by this model is in agreement with the experimental results. At low arsenic pressures, the concentration of gallium vacancies is low. Thus the concentration of the mobile species C_1 is low and the effective diffusion coefficient is small. As the arsenic pressure increases the concentration of C_1 increases and there is a corresponding increase in the effective diffusion coefficient. Finally at some high arsenic pressure, essentially all of the sulfur is in the mobile form and the effective diffusion coefficient saturates at the value D_1, which is simply the diffusion coefficient of the complex C_1.

Although the mass action equations indicate that diffusion via gallium divacancies is a possible mechanism for sulfur diffusion in GaAs, the detailed atomic jump process is not known. It is reasonable, however, to assume that a direct exchange between sulfur on an arsenic site and an arsenic atom at the second-nearest-neighbor position (not an arsenic vacancy as in the sublattice model) can be considerably enhanced in the presence of a gallium divacancy.

Another assignment that predicts the pressure dependence observed in this study is to assume that C_1 is a mobile interstitial donor, S_i^{+}, which can react with an arsenic divacancy $(V_{As}V_{As})$ to form the immobile complex $(S_{As}^{+}V_{As})$. This is essentially a modified version of the interstitial-substitutional model and in the saturation region at high arsenic pressures most of the sulfur would be in interstitial positions. Under our experimental conditions, interstitial concentrations of nearly $10^{19}\,\mathrm{cm}^{-3}$ are implied. This seems rather high in comparison with interstitial solubilities in Ge and Si, and taken together with the rather low values of the diffusion coefficient at high temperatures suggests that sulfur diffusion in is not controlled by an interstitial species.

At high sulfur concentrations, the diffusion profiles are not simple complementary error function. It is likely that the same mechanism discussed above for sulfur in GaP is responsible for the high-concentration diffusion behavior of sulfur in GaAs.

(C) *Solid solubility vs. vapor pressure of gaseous impurities*

The usual model for incorporating sulfur donors from the vapor phase into phosphorus sites in a GaP crystal can be described by the reaction

$$\tfrac{1}{2}\mathrm{S}_2(\text{vapor}) + V_P \rightleftarrows \mathrm{S}_P{}^+ + e^-. \qquad (15)$$

In extrinsic material the mass action equation is

$$[\mathrm{S}_P{}^+] = (K_7)^{1/2}(P_{\mathrm{S}_2})^{1/4}(P_{\mathrm{P}_2})^{-1/4}. \qquad (16)$$

Thus the simple model predicts that the solubility should increase as the fourth root of the sulfur pressure P_{S_2}.

The experimental results presented above indicate clearly that this dependence is not observed. The dependence of the surface concentration on the sulfur pressure for both GaP and GaAs was found to be considerably stronger, as given by the relation $C_s = k[\mathrm{S}_v]^w$, where k_1 is a constant and w is 1·3 for GaP at 1215°C and 1·0 for GaAs at 1130°C. Since the sulfur vapor should be predominantly in the form of diatomic molecules, the relation becomes $C_s = k_2(P_{\mathrm{S}_2})^w$. A limited number of experiments indicated that the profiles scaled as the square root of time and that the surface concentration was relatively independent of time. Thus the assumption of an infinite source seems to be valid and the surface concentration of the diffusion profiles should be equal to the solubility under the diffusion conditions.

Trumbore *et al.*[6] reported that the solubility of sulfur in GaP grown from a gallium-rich solution was proportional to the square root of the mole fraction of sulfur in the solution for sulfur concentrations in the crystal between 2 and $5 \times 10^{19}\,\mathrm{cm}^{-3}$. The anomalous behavior at lower concentrations was later attributed to a non-equilibrium process involving a facet effect[23]. If these results are assumed to be valid, then sulfur in GaP at concentrations less than $5 \times 10^{19}\,\mathrm{cm}^{-3}$ is predominantly an ionized donor on isolated phosphorus sites. At this time, it is diffcult to explain the lack of agreement between our surface concentration measurement and equation (16). Three possible reasons are mentioned below.

One possibility is the formation of a second phase such as the compound $\mathrm{Ga_2S_3}$ at the surface of the sample. This seems unlikely, however, since the anomalous results were obtained at sulfur vapor densities as low as 0·2–0·6 μg/ml and for temperatures much higher than the melting point of $\mathrm{Ga_2S_3}$ (1090°C).

A second reason for the anomalous behavior of surface concentration with sulfur vapor density reported above might be a non-equilibrium steady-state reaction at the surface of the crystal, perhaps caused by the necessity to dissociate the diatomic sulfur vapor into the atomic species. This model has been proposed to explain anamalous effects when Sb is diffused into Ge[24].

A third possibility that should be investigated is a modified gas phase. In the discussion above, it has been assumed that the sulfur in the vapor phase exists as diatomic molecules. This should be true providing there is no interaction between the sulfur and other gaseous species. The need for more detailed information on the gas phase equilibria in the ternary system at high temperatures is evident.

Acknowledgements – The authors gratefully acknowledge helpful discussions with J. W. Allen and D. L. Kendall.

REFERENCES

1. GOLDSTEIN B., *Phys. Rev.* **121**, 1305 (1961).
2. KENDALL D. L., In *Semiconductors and Semimetals* (Edited by R. K. Willardson and A. C. Beer), Vol. 4, p. 198. Academic Press, New York (1968).
3. FRIESER R. G., *J. electrochem. Soc.* **112**, 697 (1965).
4. VIELAND L. J., *J. Phys. Chem. Solids* **21**, 318 (1961). VIELAND L. J., Unpublished data quoted in [17].
5. VIELAND L. J. and KUDMAN I., *J. Phys. Chem. Solids* **24**, 437 (1963),
6. TRUMBORE F. A., WHITE H. G., KOWALCHIK M., LOGAN R. A. and LUKE C. L., *J. electrochem. Soc.* **112**, 782 (1965).
7. GOLDSTEIN B., *Phys. Rev.* **118**, 1024 (1960).
8. FANE R. W. and GOSS A. J., *Solid-St. Electron.* **6**, 383 (1963).
9. VON MUNCH W., *IBM Jl* **10**, 438 (1966).
10. SHIH K. K., ALLEN J. W. and PEARSON G. L., *J. Phys. Chem. Solids* **29**, 379 (1968).
11. *JANAF Thermochemical Tables*. Thermal Laboratories, Dow Chemical Company (1961).
12. STULL D. R. and SINKE G. C., *Thermodynamic Properties of the Elements*. American Chemical Society, Washington, D.C. (1956).
13. ARTHUR J. R., *J. Phys. Chem. Solids* **28**, 2257 (1967).
14. THURMOND C. D., *J. Phys. Chem. Solids* **26**, 785 (1965).
15. HALL L. D., *J. chem. Phys.* **21**, 87 (1953).
16. SELTZER M., *J. Phys. Chem. Solids* **26**, 243 (1965).
17. WEISBERG L. R., *Trans. AIME* **230**, 291 (1964).
18. SCHUMANN P. A. and PHILLIPS R. P., *Solid-St. Electron.* **10**, 943 (1967).
19. NYGREN S. F. and PEARSON G. L., *J. electrochem. Soc.* **116**, 648 (1969).
20. SCHOTTKY G., *J. Phys. Chem. Solids* **27**, 1724 (1966).
21. GOLDSTEIN B., *Solid-St. Electron.* **5**, 411 (1962).
22. LIETH R. M. A., HEIJLIGERS H. J. M. and v.d. HEIJDEN C. W. M., *J. electrochem. Soc.* **113**, 798 (1966).
23. TRUMBORE F. A., KOWALCHIK M. and NASH D. L., *Interl Conf. on Crystal Growth*. Birmingham, England (1968).
24. McNAMARA J. E., *J. electrochem. Soc.* **108**, 199 (1961).
25. ABRAHAMS M. S., BUIOCCHI C. J. and LIETJEN J. J., *J. appl. Phys.* **38**, 760 (1967).
26. KRESSEL H., HAWRYLO F. Z., ABRAHAMS M. S. and BUIOCCHI C. J., *J. appl. Phys.* **39**, 5139 (1968).

J. Phys. Chem. Solids Pergamon Press 1970. Vol. 31, pp. 529–539. Printed in Great Britain.

ELECTRICAL RESISTIVITY OF THE DILUTE *Pd*Co SYSTEM*

GWYN WILLIAMS
School of Mathematical and Physical Sciences, University of Sussex, Brighton, U.K.

(*Received* 2 *June* 1969; *in revised form* 23 *June* 1969)

Abstract—The electrical resistivity of several dilute *Pd*Co alloys has been measured over the temperature range 0·45–300°K. At temperatures well below the ordering temperature the incremental resistivity of the alloy follows a $T^{3/2}$ limiting behaviour, in agreement with the predictions of a theoretical model in which a significant contribution to the low temperature electrical resistivity arises from *s*-electron scattering from excitations of a non single-particle type in the coupled *d*-band-impurity moment system of the alloy. At temperatures immediately below the ordering temperature, a linear decrease of incremental resistivity with decreasing temperature is observed, as would be expected on a molecular field model. On the basis of these two models, the *s*-electron local moment coupling strength in dilute *Pd*Co and *Pd*Fe is compared, and shown to be stronger in the former system. Numerical estimates of this coupling strength are also made on the basis of a theory due to Yosida. In *Pd*Co the magnitude of this coupling strength varies from 0·071 eV (in the 0·098 at.% Co alloy) to 0·133 eV (in the 0·73 at.% Co alloy), almost exactly double the values obtained from a previous investigation on *Pd* Fe alloys of comparable concentration.

Various approaches are used in an attempt to fit the observed concentration dependence of the ordering temperature, and a comparison of these in *Pd* Co and *Pd* Fe enables the relative magnitude of the strength of the *d*-electron local moment coupling in these two systems to be compared.

INTRODUCTION

IN THAT broad class of dilute magnetic alloys (containing < 1 at.% impurity) of which *Cu* Mn is regarded as typical, the onset of magnetic ordering is rather undramatic. The magnetic susceptibility[1, 2], magnetic specific heat[3] and electrical resistivity[2] exhibit a broad maximum at low temperatures. In the latter respect *dilute* alloys of Mn, Fe or Co in Pd are unique,† since the transition to the ordered state produces a sharp anomaly in the electrical resistivity. This takes the form of a rapid decrease of the resistivity with decreasing temperature, below the ordering temperature T_c[4]. This striking difference in behaviour reflects the nature of the ordering in the two types of systems. The former type orders through an indirect coupling via the conduction electrons, induced by the relatively rapid oscillations of an RKKY type interaction[5], to form a 'disordered' antiferromagnetic ground state, whereas the latter type have a well defined ferromagnetic ground state. This difference in behaviour originates from the nearly ferromagnetic, itinerant character of the Pd *d*-band, which manifests itself in an exchange enhancement of the *range* of the induced polarization. This tends to suppress the RKKY oscillations out to relatively large distances[6, 7]. The last point is strongly supported by the neutron diffraction work of Low *et al.*[8], and by the analysis of Mössbauer data on dilute *Pd*Fe[9] and *Pd*Co[10].

We have recently investigated the properties of this ordered state by measuring the electrical resistivity of several dilute *Pd*Fe alloys down to He^3 temperatures[11]. The results were interpreted on the basis of a model in which the low temperature ($T \ll T_c$) electrical resistivity is dominated by *s*-elec-

---

*This work has been sponsored in part by the Air Force Materials Laboratory (AFSC) through the European Office of Aerospace Research (OAR), United States Air Force, under Contract F61052-68-C-0011.

†Magnetization and Mössbauer measurements reveal a similar behavior for these impurities in Pd or Pt (see, for example, SEGAN R., *Phys. Rev.* **160**, 404 (1967)). However, no electrical resistivity measurements have been made on the Pt based alloys.

tron scattering from excitations of a non single-particle type in the coupled *d*-band-impurity moment system. It is the purpose of this paper to report on a similar experimental investigation into the electrical resistivity of the dilute *Pd*Co system, the results of which can be interpreted within the framework of the theoretical model mentioned above, and on the basis of this interpretation to present a comparison of the *Pd*Fe and *Pd*Co systems.

EXPERIMENTAL

Cobalt enters the palladium lattice substitutionally, and disordered f.c.c. solid solutions are formed for cobalt concentrations well in excess of the highest employed in this investigation[12].

The palladium used was of 99·999% purity, and was supplied in the form of sponge by Johnson Matthey & Co. (London). The cobalt was of 99·99% purity, also in the form of sponge, supplied, Koch-Light Ltd. (England).

Initially, a master alloy of approximate composition Pd − 5 at.% Co was prepared by melting the appropriate amounts of the two elements together in a water cooled 'copper-boat induction furnace'[13], surrounded by an inert atmosphere of argon. (This type of induction furnace has several useful advantages for alloy work. During melting, sample levitation occurs, and this considerably reduces the possibility of contamination. In the molten state the alloy constituents are thoroughly mixed by the stirring effects of induced currents, while rapid cooling follows the removal of the r.f. field, as the alloy is lowered back into the water cooled boat.) The master alloy was inverted and remelted five times to ensure homogeneity. It was etched in a solution of nitric acid and hydrogen peroxide, cold-rolled between Melinex sheets[14] to a thickness of about 0·25 mm, sealed in an evacuated silica tube and finally annealed for 24 hr at 1100°C.

Alloys of approximate Co concentration 0·1 at.%, 0·2 at.%, 0·3 at.%, 0·5 at.%, 0·7 at.% and 1·0 at.% were prepared by remelting the master alloy and pure palladium in the necessary proportions. Each alloy was homogenised by inverting and remelting several times. This was followed by etching, cold-rolling between Melinex to thicknesses varying from 0·01 (0·1 at.% Co) to 0·015 cm (1·0 at.% Co); the alloys were then cut into strips 2–3 mm wide and 10 cm long. After cutting the samples were etched, and then finally annealed for 30 hr at 1100°C in the manner described previously. A seventh alloy, of approximate composition Pd–0·1 at.% Fe was also prepared, by diluting part of a Pd–4·6 at.% Fe master alloy previously prepared[11], with the appropriate amount of 'pure' Pd. It was etched, rolled and cut in the manner detailed above, and was annealed with the six *Pd*Co samples.

The samples were mounted in a holder capable of accommodating up to six samples, and a 30 mA current passed through them. Their resistivities were measured using the standard four-probe d.c. potentiometric circuit, incorporating a Tinsley Disselhorst potentiometer and galvanometer amplifier capable of reproducible measurements to 2×10^{-8} V. Using a conventional He^3 cryostat the sample resistivities were measured over the temperature range 0·45–300°K; temperatures below 4·2°K were stabilised and measured to within ± 1 millidegree (using He^4 and He^3 vapour pressures), and above 4·2°K to better than ± 1 per cent (using gas thermometer techniques).

Finally the area to length ratios of the samples were measured by a technique similar to that employed by Dugdale and Basinski[15].

EXPERIMENTAL RESULTS

From the measurements taken it was possible to calculate the absolute resistivities of the various alloys. The general form of the temperature dependence of the electrical resistivity is similar to that reported by Schwaller and Wucher[4], although a detailed comparison with their published data is difficult.

Figure 1 shows the variation, at low temperatures, of the incremental resistivity $\Delta\rho$ $(T)[=\rho(T)_{\text{alloy}}-\rho(T)_{\text{Pd}}]$ of Pd–0·098 at.% Co and Pd–0·10 at.% Fe[16]. In both alloys the transition to the ordered state can be seen. Below the ordering temperature (T_c) the incremental resistivity decreases linearly with decreasing temperature, while at temperatures well below T_c deviations from this linear behaviour are observed. This figure in fact provides an excellent comparison of the two alloy systems; these two alloys have practically identical impurity concentrations and as Fig. 1 indicates, very similar ordering temperatures. Below the ordering temperature both systems exhibit a linear decrease of incremental resistivity with decreasing temperature, but the magnitude of this coefficient is much larger in the *Pd*Co system than in the *Pd*Fe system. In the latter system the transition to the ordered state is exceptionally well defined, and this enables an unambiguous estimate of *an* ordering temperature to be made. The 0·098 at.% Co alloy, however, has a much broader transition, and consequently it is rather more difficult to estimate T_c accurately. The following definition of T_c has therefore been used in the *Pd*Co system: the ordering temperature is taken as the highest temperature at which the linear $(\Delta\rho(T)-T)$ behaviour, mentioned previously, persists.

Figure 2 shows the detailed low temperature behaviour of $\Delta\rho(T)$ in the 0·2 and 0·3 at.% Co alloys, together with inserts showing the behaviour of their resistivities $\rho(T)$ in the vicinity of their ordering temperatures.

Figure 3 reproduces the temperature dependence of $\Delta\rho(T)$ over the entire temperature range examined, for the five more concentrated alloys. The data on Pd–0·10 at.% Fe and Pd–0·098 at.% Co have been omitted from these plots since their incremental resistivities at room temperature are only about 2 per cent of the absolute resistivity of Pd. This means that a change of 0·5 per cent in the area to length ratio of these samples (the estimated maximum error in the measurement of this ratio) produces a 15 per cent change in $\Delta\rho$ at

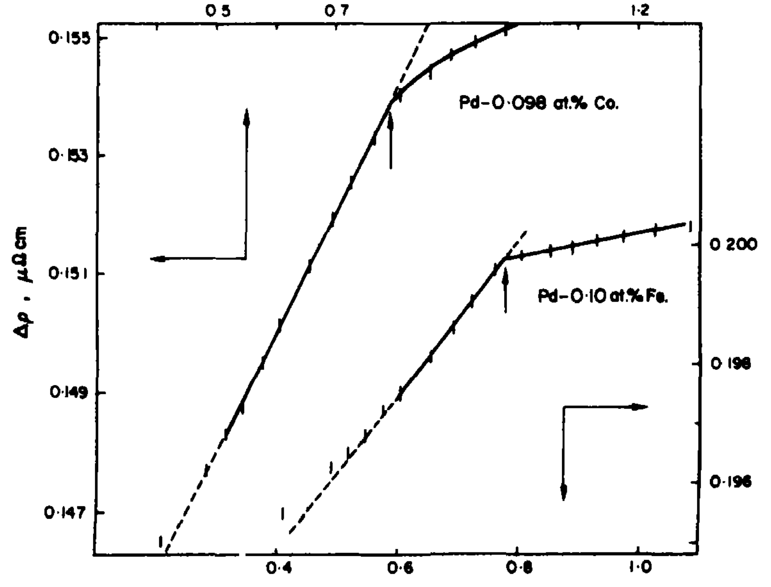

Fig. 1. The incremental resistivity $\Delta\rho(T)$ (in $\mu\Omega$ cm) for Pd–0·1 at.% Fe and Pd–0·098 at.% Co at low temperatures. The vertical error bars correspond to a voltage uncertainty of $\pm 2\cdot 10^{-8}$ V.

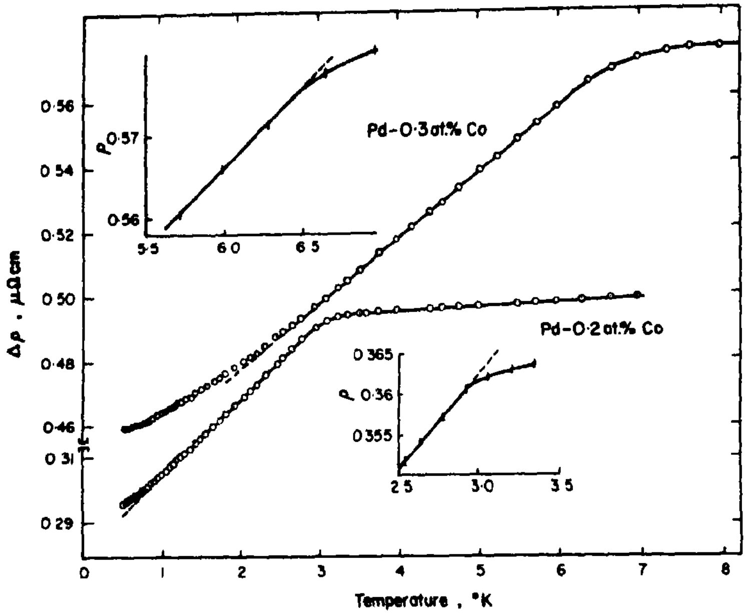

Fig. 2. The low temperature behaviour of the incremental resistivity $\Delta\rho(T)$ (in $\mu\Omega$ cm) for Pd-0·2 and 0·3 at.% Co. The inserts show the behaviour of their resistivities $\rho(T)$ (in $\mu\Omega$ cm) near T_c

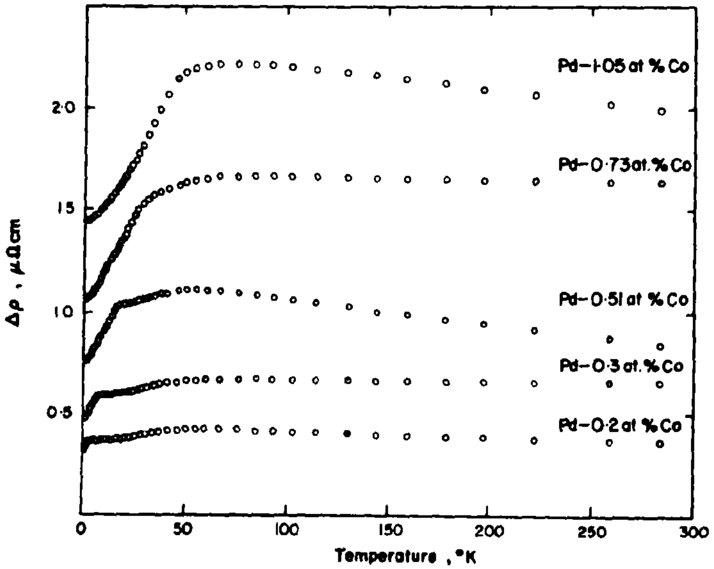

Fig. 3. The incremental resistivities $\Delta\rho(T)$ (in $\mu\Omega$ cm) for Pd-0·2, 0·3, 0·51, 0·73 and 1·05 at.% Co over the entire temperature range examined.

such temperatures. The absolute resistivity of the 'pure' Pd sample, measured at the ice-point, provides a useful check on the measured area to length ratio: the value obtained in this investigation, 9·93(3) ± 0·05 $\mu\Omega$ cms, compares favourably with previous values[17].

DISCUSSION

In relation to the transport properties of Pd and dilute *Pd* Ni alloys, the importance of *s*-electron scattering from spin density fluctuations (paramagnons) in the *d*-band of the Pd host has been demonstrated by the recent work of Schindler and Rice[18]. In alloys of the *Pd*Fe, *Pd*Co type, at temperatures above the ordering temperature, similar considerations should also be important. However, at temperatures below the ordering temperature, a significant contribution to the electrical resistivity should arise from *s*-electron scattering from real spin waves in the coupled *d*-band-impurity moment system. Turner and Long[19] have investigated this type of model theoretically, using the Hamiltonian originally suggested by Doniach and Wohlfarth[20], and their predictions have recently been used to account for the majority of the low temperature properties of the electrical resistivity of dilute *Pd* Fe alloys[11]. A brief description of this model and its predictions follow: in dilute alloys at temperatures well below the ordering temperature, the predicted form of the *incremental resistivity* in the alloy is:

$$\Delta\rho(T) = Ac + \mathrm{B}T^{3/2}/c^{1/2} \qquad (1)$$

(A and B are numerical factors, and c is the impurity concentration). The first term on the right in (1) represents the effects of elastic scattering: both the elastic part of the exchange scattering and the 'potential' scattering arising from the departure of the spin independent lattice potential from perfect periodicity (due to the presence of the impurities) contribute to it. The second term in (1) has three contributions: the first arises from *s*-electron spin flip scattering from *impurity moments* in the coupled *d*-band system. The resulting spin deviation propagates as a spin wave in this coupled system. Electron-magnon scattering in 'pure' ferromagnets contributes a T^2 term to the low temperature electrical resistivity[21], the impurity spins in the coupled *d*-band of the alloy, however, do not possess translational symmetry, and this, Turner and Long claim, results in a limiting $T^{3/2}$ contribution. It is also argued that the contribution from *s*-electron spin flip scattering from interacting *d*-electron–hole pairs in the alloy is reasonably well accounted for, both above and below T_c, by subtracting the Pd resistivity from that measured for the alloy. The second contribution to the second term in (1) comes from the temperature dependence of the elastic part of the exchange scattering, and the third contribution to this term from 'interference' effects between potential and elastic exchange scattering. The former yields a contribution which is proportional to $\langle M^2\rangle$, the mean of the squared magnetization, and the latter, in the strong potential scattering limit is proportional to $\langle M\rangle^2$ the mean magnetization, squared. The dependence of both terms on the magnetization agree with that deduced previously by Yosida[22]. For a system ordering ferromagnetically, both terms lead, in the low temperature limit, to contributions to $\Delta\rho(T)$ which are proportional to $T^{3/2}$.

In transition metal alloys of the type under consideration here, the 'induced' ferromagnetism is a property of the *d*-band, and hence reflects the coupling between the *d*-electrons of the host and the local spin. Thus, as expected, the model of reference [19] gives $T_c \propto |J_{d\text{-local}}|^2$. On the other hand the transport properties of such alloys are predominantly determined by those factors which give rise to the scattering of electrons in the *s*-band. The incremental resistivity of the alloy should therefore reflect the *s*-electron-local moment coupling strength; in fact Turner and Long give the coefficient B (in [1]) $\propto |J_{s\text{-local}}|^2$.

Figures 4–6 show $\Delta\rho(T)$ plotted against

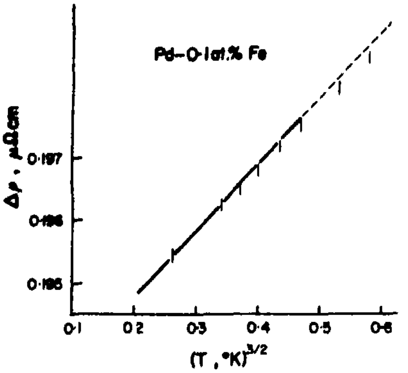

Fig. 4. The incremental resistivity $\Delta\rho(T)$ (in $\mu\Omega$ cm) plotted against $T^{3/2}$ (in $°K^{3/2}$) for Pd 0·1 at.% Fe.

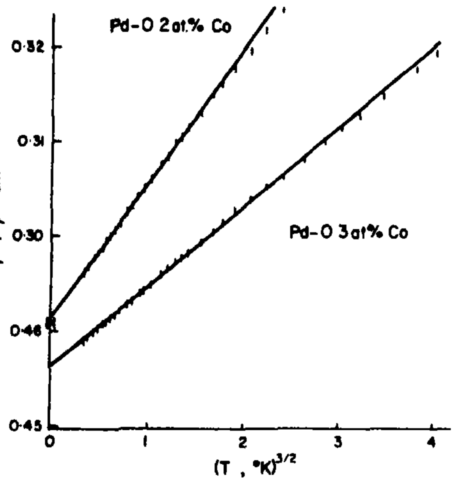

Fig. 5. The incremental resistivities $\Delta\rho(T)$ (in $\mu\Omega$ cm) of Pd–0·2 and 0·3 at.% Co plotted against $T^{3/2}$ (in $°K^{3/2}$). Note the change in zero.

$T^{3/2}$, and it is clear from these that the limiting low temperature form of $\Delta\rho(T)$ in all the alloys examined is that predicted in (1). (The Pd–0·098 at.% Co is not included in these plots since, as Fig. 1 indicates, insufficient points exist at temperatures below ≃ 0·5°K to establish its limiting behaviour with any degree of certainty.) These figures enable $\Delta\rho$ $(T = 0)$ and the coefficient of the $T^{3/2}$ term to be estimated; these, and other parameters, are listed in Table 1. Figure 7 indicates that $\Delta\rho(T=0)$ is linearly proportional to the impurity concentration, as would be expected in this dilute limit. The zero temperature incremental resistivity for Co in Pd is estimated from this figure to be $1{\cdot}40 \pm 0{\cdot}04$ $\mu\Omega$ cm/at.% Co. $\Delta\rho(T = 0)$ for the Pd–0·10 at.% Fe alloy is similarly estimated to be 0·193 $\mu\Omega$ cm, in very good agreement with our previously determined values for the *Pd*Fe system[11]

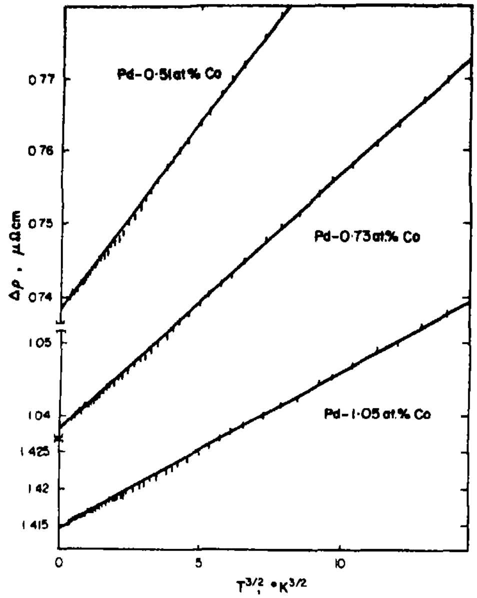

Fig. 6. The incremental resistivities $\Delta\rho(T)$ (in $\mu\Omega$ cm) of Pd–0·51, 0·73 and 1·05 at.% Co plotted against $T^{3/2}$ (in $°K^{3/2}$). Note the change in zero.

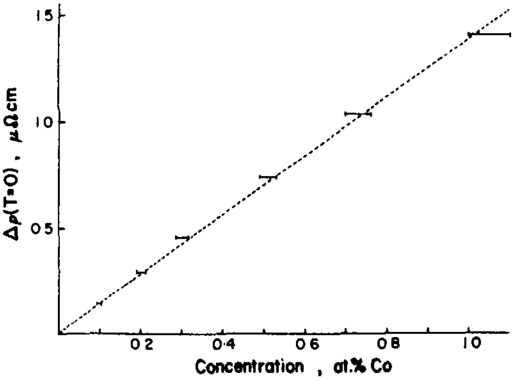

Fig. 7. $\Delta\rho(T = 0)$ (in $\mu\Omega$ cm) plotted against concentration (in at.%). The error bars on the concentration correspond to the values listed in Table 1.

Table 1

Estimated from initial masses	Analysed (at.%)	Taken (at.%)	T_c(°K)	$\Delta\rho(0)$ ($\mu\Omega$ cm)	Coeff. of $T^{3/2}$ term ($\mu\Omega$ cm/°K$^{3/2}$)	Coeff. of linear decrease ($\mu\Omega$ cm/°K)
Pd–0·10 at.% Fe	0·10	0·10 ± 0·005	0·78 ± 0·002	0·1927	$1{\cdot}05(5) \times 10^{-2}$	0·0125
Pd–0·10 at.% Co	0·096	0·098 ± 0·005	0·79 ± 0·01	0·1400	–	0·0209
Pd–0·20 at.% Co	0·19	0·20 ± 0·01	2·95 ± 0·05	0·2914	$1{\cdot}38(0) \times 10^{-2}$	0·0235
Pd–0·30 at.% Co	0·29	0·30 ± 0·015	6·45 ± 0·05	0·4563	$0{\cdot}83(3) \times 10^{-2}$	0·0198
Pd–0·50 at.% Co	0·53	0·51 ± 0·02	16·2 + 0·2	0·7381	$0{\cdot}50(6) \times 10^{-2}$	0·0187
Pd–0·70 at.% Co	0·76	0·73 ± 0·03	27·5 ± 0·3	1·0378	$0{\cdot}34(6) \times 10^{-2}$	0·0194
Pd–1·0 at.% Co	1·09	1·05 ± 0·05	44·0 ± 0·5	1·4144	$0{\cdot}21(5) \times 10^{-2}$	0·0196

(A, in equation (1) being ~ 1·9 $\mu\Omega$ cm/at.% Fe). This previous investigation also indicated that the concentration dependence of the coefficient of the $T^{3/2}$ term is not that predicted in equation (1), but is best represented by Bc^{-1} with B estimated at ~ $1{\cdot}08 \times 10^{-3}$ $\mu\Omega$ cm at.% Fe/(°K)$^{3/2}$. In Fig. 8 the coefficient of the $T^{3/2}$ terms for the five more concentrated *Pd*Co alloys are plotted against c^{-1}; this figure shows that within the experimental error, the concentration dependence of this coefficient is again well represented by Bc^{-1}, with B estimated at $(2{\cdot}7 \pm 0{\cdot}1) \times 10^{-3}$ $\mu\Omega$ cm at.% Co/(°K)$^{3/2}$. Table 1 also contains the coefficients of the linear decrease in $\Delta\rho(T)$ immediately below T_c. These are roughly concentration independent, showing that a molecular field approach provides a reasonably good description of the dilute *Pd*Co system in this temperature region, as was the case in *Pd*Fe. However, the magnitude of B is about a factor of 2·5, and the coefficient of the linear decreases below T_c about a factor of 2 larger in *Pd*Co than in *Pd*Fe. Since the magnitude and concentration dependence of the saturation magentization (and T_c's) of 1 at.% or less of Co or Fe in Pd is quite similar[23, 24, 25], this means that $|J_{s\text{-local}}|$ is much stronger in the *Pd*Co system.

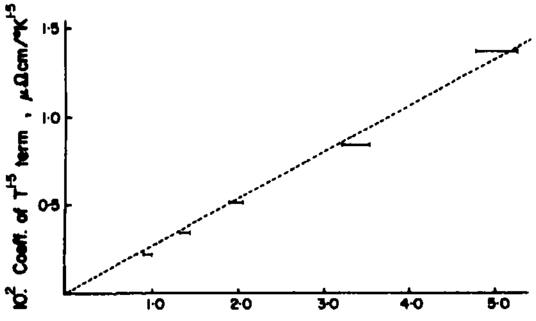

Fig. 8. The coefficients of the $T^{3/2}$ terms (in $\mu\Omega$ cm/°K$^{3/2}$) in Pd–0·2, 0·3, 0·51, 0·73 and 1·05 at.% Co plotted against inverse concentration (in at.%$^{-1}$).

A comparison of the magnitude of $|J_{s\text{-local}}|$ in the two systems is also afforded by the theories of Yosida[22] and Kasuya[21]. For example, Yosida's equation (19) can easily be manipulated to give values for $\Delta\rho(T_c)$ and $\Delta\rho(0)$; these form a pair of simultaneous equations for $|J_{s\text{-local}}|^2$ and V^2 (the deviation of the spin-independent lattice potential from perfect periodicity). For a system ordering ferromagnetically, the resulting quadratic equation yields[26]:

$$|J_{s\text{-local}}|^2 = [2(2S+1)\Delta'\rho(T_c) - \Delta'\rho(0) \pm (8S(2S+1)\Delta'\rho(T_c)\Delta'\rho(0) + \Delta'\rho(0)^2)^{1/2}] (2 \times 5{\cdot}78 \times S(2S+1)^2)^{-1} \qquad (2)$$

S is the 'on site' local spin; $\Delta'\rho(T_c)$ and $\Delta'\rho(0)$ are the incremental resistivities/at.% at the appropriate temperatures. Table 2 lists the values of $\Delta\rho(0)$ and $\Delta\rho(T_c)$, as obtained from the experimental data. However, examination of Fig. 3 reveals that in the *Pd*Co system, $\Delta\rho(T)$ is not independent of temperature above the ordering temperature, while the form of its temperature dependence suggests the same origin as similar effects observed in dilute non-magnetic alloys[15]. In non-magnetic

Table 2

Alloy	$\Delta\rho(T_c)$ ($\mu\Omega$ cm)	Estimated correction ($\mu\Omega$ cm)	Corrected $\Delta\rho(T_c)$ ($\mu\Omega$ cm)	$\lvert J_{s\text{-local}}\rvert$ (eV)	V(eV)	For *Pd*Fe[11]	$\lvert J_{s\text{-local}}\rvert$(eV)
Pd–0·1 at.% Fe	0·1998	0	0·1998	0·034	0·58		
Pd–0·098 at.% Co	0·1539	0	0·1539	0·071	0·51		
Pd–0·20 at.% Co	0·3505	0	0·3505	0·111	0·53	Pd–0·16 at.% Fe	0·051
Pd–0·30 at.% Co	0·5659	0·0054	0·5605	0·129	0·54	Pd–0·23 at.% Fe	0·059
Pd–0·51 at.% Co	0·9981	0·0306	0·9675	0·133	0·54	Pd–0·41 at.% Fe	0·060
Pd–0·73 at.% Co	1·4860	0·1022	1·3838	0·133	0·54	Pd–0·54 at.% Fe	0·064
Pd–1·05 at.% Co	2·0835	0·2835	1·8000	0·105	0·52	Pd–0·78 at.% Fe	0·064

alloys this temperature dependence results from the breakdown of Matthiessen's rule, and is attributed to the existence of several comparable scattering mechanisms with different anisotropies. In the *Pd*Co system these could arise from increasing contributions from modified paramagnon and phonon scattering (compared with impurity spin-disorder scattering) as the temperature increases. *In estimating the magnitude of* $J_{s\text{-local}}$, the observed values of $\Delta\rho(T_c)$ must be corrected for deviation.

Figure 9 shows that within ± 1 per cent, the temperature dependence of $\Delta\rho(T)c^{-1}$ above T_c has the same functional form in all the alloys examined. This suggests that an estimate of the necessary correction can be obtained by measuring the deviation up to the appropriate ordering temperature in Fig. 9, and simply scaling the result for the concentration of the alloy being examined. The results obtained in this way are summarised in Table 2; having used $S(\mathrm{Fe}) = \frac{3}{2}$ and $S(\mathrm{Co}) = 1$[8, 27]. The results obtained from Yosida's approach give $|J_{s\text{-local}}|^2$ to be a factor of 4 larger in *Pd*Co than in *Pd*Fe; a comparison of the coefficients of the $T^{3/2}$ term (well below T_c) gives a factor of 2·5, while the coefficient of the linear decrease below T_c a factor of 2. Each approach thus suggests that the magnitude of the coupling strength between the conduction electrons in the s-band and the local moment is considerably larger in *Pd*Co. The disagreement, in numerical terms, is not too

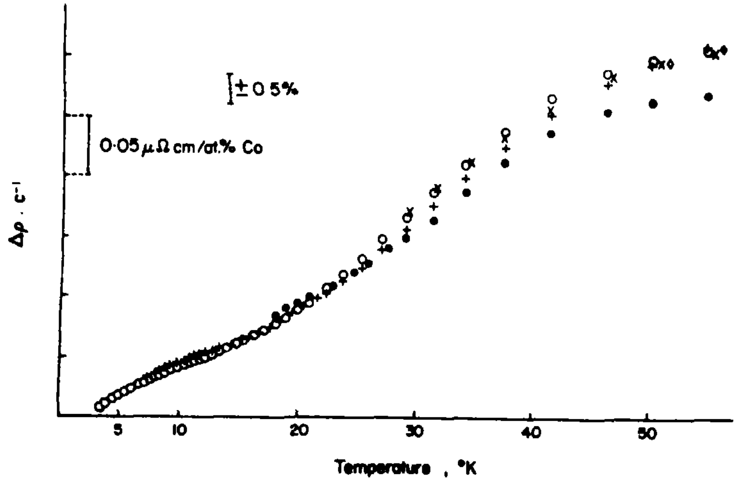

Fig. 9. $\Delta\rho(T)c^{-1}$ (in $\mu\Omega$ cm/at.% Co) plotted against temperature (in °K), above the ordering temperatures: ○ 0·2; + 0·3; ● 0·51; × 0·73; ◊ 1·05 at.% Co.

surprising since each approach, while giving a reasonably good description of the systems in general terms, fail to predict accurately the more subtle effects. For example, the approach of Turner and Long gives the correct temperature dependence of $\Delta\rho(T \ll T_c)$, but incorrectly predicts the concentration dependence of the coefficient of the $T^{3/2}$ terms: application of a molecular field approach immediately below T_c yields a linear decrease of $\Delta\rho(T)$ with decreasing temperature, as observed, but also predicts that the coefficient of this linear decrease should be concentration independent, Table 1 demonstrates that while being nearly concentration independent, some variation does occur. Finally Yosida and Kasuya's approach suggest that $|J_{s\text{-local}}|$ should be independent of concentration, Table 2 indicates that this is not the case. Thus, while agreeing in general terms all three approaches break down in attempting to predict concentration dependences. This could well reflect the molecular field approximation which is used at some stage in each model; this predicts that $T_c \propto c$, Table 1 shows that this is definitely not so.

A careful examination of the values of the ordering temperatures listed in Table 1 indicate that for a given concentration its magnitude is quite close to that in the *Pd*Fe system[11]. In both systems T_c has a complicated dependence on concentration, and as yet no single approach has been able to successfully account for the observed dependence over the entire concentration range examined. This again is not unexpected since in these alloys the impurity concentration ranges over a decade (0·1 – 1·0 at.%), and the most dilute alloys examined are very near the limiting concentration necessary for the appearance of ferromagnetism[25]. For impurity concentrations greater than about 0·15at.%, Fig. 10 indicates that the relation:

$$T_c = T_0 \,.\, c^n \tag{3}$$

is reasonably well obeyed in both *Pd*Fe and *Pd*Co. From this figure $n = 1{\cdot}55 \pm 0{\cdot}08$ in both systems, while $T_0 = 51 \pm 2°\text{K}/(\text{at.}\%)^n$ in *Pd*Fe, and $T_0 = 43 \pm 2°\text{K}/(\text{at.}\%)^n$ in *Pd*Co. In equation (1), before inserting the molecular field splitting of the *d*-band (which gives $T_c \propto c$), the form of the $T^{3/2}$ term is:

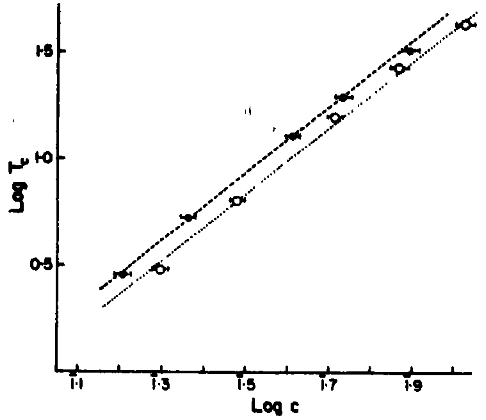

Fig. 10. Log_{10} (T_c (in °K)) plotted against $\log_{10}$ concentration (in at.%)): ○ *Pd*Co; ● *Pd*Fe.

$$cB^1\left(\frac{T}{T_c}\right)^{3/2}$$

using $T_c \propto c^{1\cdot5}$ (as suggested by Fig. 10) yields $Bc^{-5/4}\,T^{3/2}$, in much closer agreement with the observed concentration dependence of this term. Following the remarks made in the opening section concerning the exchange enhancement of the range of the induced polarization, it seemed a reasonable alternative to attempt to fit the observed ordering temperatures to the formula of Trousdale *et al.*[9]. This is based on a model in which the induced polarization has a spatial variation given by $\exp(-r^2\sigma^{-2})$, σ being a characteristic range. This leads to:

$$T_c \propto \exp\left[-\text{constant}\left(\sigma^2 c^{2/3}\right)^{-1}\right]. \tag{4}$$

Figure 11 shows that in the dilute *Pd*Fe system the concentration dependence of T_c reasonably well described by equation (4), for concentrations in the range 0·1 at 0·8 at.% Fe. In *Pd*Co however, the above relationship breaks down for concentrations again below

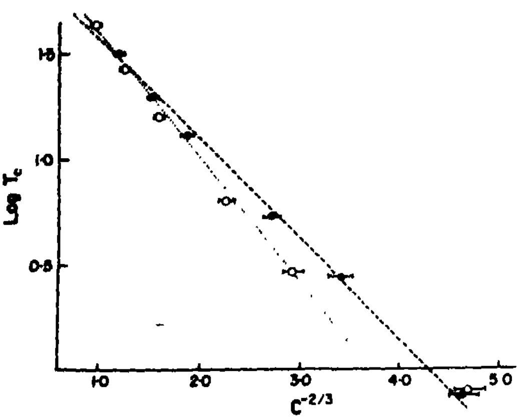

Fig. 11. Log$_{10}$ (T_c (in °K)) plotted against $c^{-2/3}$ (in at.%$^{-2/3}$). ○ *Pd*Co: ● *Pd*Fe.

about 0·15 at.%. Figure 11 also indicates that above this lower limit the range of polarization in the two alloy systems is approximately the same, in agreement with the neutron diffraction data on low concentration alloys[8].

As previously mentioned, the magnitude of the ordering temperature reflects the coupling strength between the *d*-electrons of the host and the local spin, $J_{d\text{-local}}$. Reference [19] gives:

$$kT_c = \frac{|J_{d\text{-local}}|^2 cSN(0)}{24K_0^4(Z/2)^{2/3}} \tag{5}$$

S is on the 'on site' impurity spin; c the concentration; $N(0)$ the 'unenhanced' density of *d*-states of one spin orientation at the Fermi level; Z the number of d holes per atom, and K_0^{-2} $(= 1 - IN(0))$ the Stoner parameter (I being the intra-atomic Coulomb interaction for *d*-electrons). Table 3 lists the values obtained for $|J_{d\text{-local}}|$ using equation (5), with $N(0)K_0^{-2}$ estimated at $\leqslant 12$/eV per atom (from the low temperature magnetic susceptibility of Pd); $Z = 0{\cdot}36$[26], $K_0^2 = 0{\cdot}14$[28], and with $S(\text{Co}) = 1$, $S(\text{Fe}) = \frac{3}{2}$, as previous. This table indicates the $|J_{d\text{-local}}|$ is about 10 per cent larger in *Pd*Co than *Pd*Fe. The concentration dependence of this parameter again reflects the molecular field approximation used to obtain equation (5).

The increased coupling of both *s*- and *d*-electrons to the impurity spins in *Pd*Co means that in this alloy system the transport properties should be rather more sensitive than in *Pd*Fe to *d*-band 'fluctuations'. The latter could be of the spin density type, or simply a natural consequence of the random nature of these alloys, which results, especially in low concentration alloys, in *small* statistical fluctuations in the impurity density (in distances of the order of the inter-impurity spacing) and hence in the 'local' magnetization (molecular field). Such considerations provide a ready explanation of the relative 'width' of the transition in the two systems, and of the increased temperature dependence of the resistivity (above T_c but below 5°K) in the low concentration alloys[29]. A possible alternative explanation of the transition 'width' in terms of macroscopic short range order in the spatial distribution of the Co impurities is ruled out by the fact that: (i) the *Pd* Fe and *Pd* Co alloys were subjected to exactly the same heat treatment; (ii) the annealing procedure itself should disperse any such order.

Table 3

Alloy	T_c(°K)	$\lvert J_{d\text{-local}}\rvert$(eV)	Alloy[11]	T_c(°K)	$\lvert J_{d\text{-local}}\rvert$(iV)
Pd–0·1 at.% Fe	0·78	0·063			
Pd–0·098 at.% Co	0·79	0·079	Pd–0·16 at.% Fe	2·8	0·095
Pd–0·2 at.% Co	2·95	0·107	Pd–0·23 at.% Fe	5·4	0·110
Pd–0·3 at.% Co	6·45	0·129	Pd–0·41 at.% Fe	13·0	0·128
Pd–0·5 at.% Co	16·2	0·157	Pd–0·54 at.% Fe	20·1	0·139
Pd–0·73 at.% Co	27·5	0·171	Pd–0·78 at.% Fe	32·6	0·147
Pd–1·05 at.% Co	44·0	0·180			

SUMMARY

It has been found that at temperatures well below the ordering temperature (T_c), the electrical resistivity of dilute *Pd*Co alloys follow the behaviour predicted on the basis of a model in which a significant contribution to $\Delta\rho(T)$ arises from s-electron scattering from spin waves in the coupled impurity moment-d-band system of the alloy. At temperatures immediately below T_c a molecular field approach provides a reasonably good description of the system. A comparison of the behaviour of the dilute *Pd*Co and *Pd*Fe systems within the framework of these two models suggests a larger magnitude for $|J_{s\text{-local}}|$ in the former system. This is borne out by numerical estimates of this parameter in two systems, using a theory due to Yosida and Kasuya. A comparison of the ordering temperatures in the two systems indicates that $|J_{d\text{-local}}|$ is similarly increased.

This increased coupling of both s- and d-electrons to the impurity spins in *Pd*Co is forwarded as a possible explanation of the increased 'width' of its transition (compared with *Pd*Fe), and of the increased low temperature resistivity in the paramagnetic region.

Similar measurements are being carried out on dilute *Pd*Mn alloys.

Acknowledgements—We would like to thank Dr. J. W. Loram for originally suggesting this topic of research, for continued discussion, and for his many informative suggestions concerning the interpretation of the experimental data. Dr. R. E. Turner and Mr. P. D. Long are also thanked for communication and discussion of their results prior to publication, as is Dr. P. J. Ford for many helpful comments on experimental points.

REFERENCES

1. OWEN J., BROWNE M., KNIGHT W. D. and KITTEL C., *Phys. Rev.* **102**, 1501 (1956).
2. SCHMITT R. W. and JACOBS I. S., *J. Phys. Chem. Solids* **3**, 324 (1957).
3. DE NOBEL J. and DU CHATENIER F. J., *Physica* **25**, 969 (1959); ZIMMERMAN J. E. and HOARE F. E., *J. Phys. Chem. Solids* **17**, 52 (1960).
4. COLES B. R., WASZINK J. H. and LORAM J. W., *Proc. int. Conf. Magnetism*, Nottingham 1964. I.P.P.S., London (1965); SCHWALLER R. and WUCHER J., *Compt. Rend.* **B264**, 1007 (1967).
5. YOSIDA K., *Phys. Rev.* **106**, 893 (1957),
6. GIOVANNINI B., PETER M. and SCHRIEFFER J. R., *Phys. Rev. Lett.* **12**, 736 (1964).
7. KIM D. J. and SCHWARTZ B. B., *Phys. Rev. Lett.* **20**, 201 (1968).
8. LOW G. G. and HOLDEN T. M., *Proc. phys. Soc.* **89**, 119 (1966).
9. TROUSDALE W. L., LONGWORTH G. and KITCHENS T. A., *J. appl. Phys.* **38**, 922 (1967).
10. DUNLAP B. D. and DASH J. G., *Phys. Rev.* **155**, 406 (1967).
11. WILLIAMS G. and LORAM J. W., *J. Phys. Chem. Solids* **30**, 1827 (1969).
12. HANSEN M., *Constitution of Binary Alloys*, p. 491. McGraw-Hill, New York (1958).
13. STERLING H. F. and WARREN R. W., *Metallurgia* **67**,24 (1963).
14. MELINEX, A form of plastic, supplied by Imperial Chemical Industries, Herts, England.
15. DUGDALE J. S. and BASINSKI Z. S., *Phys. Rev.* **157**, 552 (1967).
16. Analysis of the alloys was carried out by Daniel Griffiths & Co., London.
17. BATES L. F. and UNSTEAD P. B., *Proc. int. Conf. Magnetism*, Nottingham 1964. I.P.P.S., London (1965), give $\rho_{Pd}(273°\text{K}) = 10{\cdot}04 \pm 0{\cdot}15\ \mu\Omega$ cm.
18. SCHINDLER A. I. and RICE M. J., *Phys. Rev.* **164**, 759 (1967).
19. TURNER R. E. and LONG P. D., To be published.
20. DONIACH S. and WOHLFARTH E. P., *Proc. R. Soc.* **A296**, 442 (1967).
21. KASUYA T., *Progr. theor. Phys.* **22**, 227 (1959).
22. YOSIDA K., *Phys. Rev.* **107**, 396 (1957).
23. BOZORTH R. M., WOLFF P. A., DAVIS D. D., COMPTON V. B. and WERNICK J. H., *Phys. Rev.* **122**, 1157 (1961).
24. CLOGSTON A. M., MATTHIAS B. T., PETER M., WILLIAMS H. J., CORENZWIT E. and SHERWOOD R. C., *Phys. Rev.* **125**, 541 (1962).
25. CRANGLE J. and SCOTT W. R., *J. appl. Phys.* **36**, 921 (1965).
26. The numerical factor of 5·78 appearing in equation (2) is the result of using an effective mass approach, with $m^*/m = 2{\cdot}2$ (VUILLEMIN J. J., *Phys. Rev.* **144**, 396 (1966)). With 0·36 s-electron per atom, the same approach gives $E_f \simeq 1{\cdot}5$ eV.
27. CABLE J. W., WOLLAN E. O. and KOEHLER W. C., *Phys. Rev.* **138**, 755 (1965).
28. SHIMIZU M., TAKAHASHI T. and KATSUKI A., *J. phys. Soc. Japan* **18**, 240 (1963).
29. The Pd–0·10 at.% Fe and Pd–0·098 at.% Co alloys have been re-examined to higher measuring currents in the temperature range 1·3–4·2°K. An increased temperature dependence of $\Delta\rho$ in the latter compared with the former alloy has been observed. A more detailed description of this investigation will be published at a later date.

J. Phys. Chem. Solids Pergamon Press 1970. Vol. 31, pp. 541–547. Printed in Great Britain.

DEFORMATION POTENTIAL CONSTANTS OF ACCEPTOR IMPURITIES IN InSb

R. SHARAN and E. L. HEASELL
Electrical Engineering Department, University of Waterloo, Waterloo, Ontario, Canada

(*Received* 27 *March* 1969; *in revised form* 16 *June* 1969)

Abstract—The i.r. absorption, associated with optical transitions from shallow acceptor-levels to the conduction band in *p*-type and compensated *n*-type Indium Antimonide is reported. Under the application of uniaxial stress the degenerate acceptor ground state is split into two, two-fold degenerate states. The derivative of the optical absorption spectrum under stress shows three pronounced maxima. One maximum is attributed to an indirect L–O phonon assisted process, the remaining two are interpreted as arising from acceptor level-conduction band transitions. The analysis of the data yields values of the acceptor impurity deformation potentials: $|b'| = 1{\cdot}1$ eV, $|d'| = 4{\cdot}3$ eV. The polarisation dependence of the absorption has been used to show that the sign of both these coefficients is negative.

INTRODUCTION

THE UTILITY of uniaxial stress techniques arises from the splitting of unperturbed degenerate energy levels induced by the action of a shear strain. Such splitting was observed accidently in optical absorption studies of the excitonic transitions in germanium[1]. In subsequent work calibrated uniaxial stress was applied and the direct exciton and indirect absorptions in silicon and germanium were studied[2, 3].

InSb is an essentially direct band gap material and a study of the direct absorption threshold requires very thin crystals which are unsuitable for stressing. The study of the piezo-emission partially avoids this difficulty and the values of the deformation potential constants of free holes have been measured[4].

Optical transitions from the acceptor level to the conduction band are allowed in InSb and have been observed in absorption studies[5]. We report the behaviour of such transitions under uniaxial deformation and the values of the deformation potential constants for Cd and Zn. A preliminary report of part of this work was presented previously[6].

THEORY

The band structure of InSb has been calculated by Kane[7]. The main features are: (1) the conduction and light-mass hole bands are non-parabolic, (2) the heavy-mass hole band has its maxima displaced in $\langle 111 \rangle$ directions from the center of the Brillouin zone, and (3) the spin-orbit splitting of the valence band at $k = 0$ is large ($\approx 0{\cdot}9$ eV) compared to the band gap ($\approx 0{\cdot}22$ eV at 77°K). It has been shown by cyclotron resonance experiments[8] that the amplitude and the displacement of maxima of the heavy-hole mass band in k-space is important only at very low temperatures (< 4°K). At higher temperatures it is a good approximation to treat the valence band of InSb as germanium-like and to ignore the effect of the spin-orbit split off band. Thus we take the maxima of the valence bands at $k = 0$ to be four-fold degenerate (including spin).

The shallow acceptor impurity states in InSb can be treated within the effective mass approximation[9], where their wave functions can be written in the form:

$$\psi(r) = \sum F_j(r)\phi_j(r)$$

The $\phi_j(r)$ are the Bloch functions of the valence band edge in the unperturbed crystal, the $F_j(r)$ are the envelope functions and the sum runs over all the valence band states at $k = 0$.

Since $\phi_j(r)$ for the valence band in InSb is four-fold degenerate, so is the linear combination (1). When uniaxial stress is applied to the crystal the four-fold degenerate valence band splits into two two-fold degenerate bands[10], leading to a similar splitting of the four-fold degenerate ground state of the acceptor impurity[11].

The expression for the energy separation of the split bands of the acceptor level has been given by Bir *et al.*[11] in terms of the crystal strain and impurity deformation potential constants, a', b' and d': a' is the deformation potential constant for hydrostatic pressure, b' and d' correspond to uniaxial stress applied parallel to $\langle 100\rangle$ and $\langle 111\rangle$ crystal directions respectively. The splitting of the levels is given by

$$E_{A,1,2} = -a'\epsilon \pm [E_{\epsilon'}]^{1/2} \tag{2}$$

where the term $[E_{\epsilon'}]^{1/2}$ for specific deformations is given in Table 1.

Table 1. Splitting of the acceptor state with uniaxial stress (s_{ij} are the compliance coefficients and χ is the applied stress)

	$\chi \| [001]$	$\chi \| [111]$	$\chi \| [110]$
$\dfrac{[E_{\epsilon'}]^{1/2}}{\chi}$	$\lvert b'(s_{11}-s_{12})\rvert$	$\left\lvert\dfrac{d'}{2\sqrt{3}}s_{44}\right\rvert$	$\frac{1}{2}\left\lvert(b')^2(s_{11}-s_{12})^2 + 3\left(\dfrac{d'}{2\sqrt{3}}s_{44}\right)^2\right\rvert^{1/2}$

The donor ionization energy of shallow impurities in InSb is very small and we restrict our discussion to the optical absorption due to transitions from shallow acceptor levels to the conduction band. A theoretical analysis of such transitions, in the case of GaAs, is available in literature[12, 13].

If the impurity concentration and the temperature are held constant, the absorption coefficient may be written in the form:

$$\alpha_i(h\nu) = f\frac{(h\nu - E_g + E_{Ai})^{1/2}}{h\nu} \tag{3}$$

where E_g is the band gap, E_{Ai} is the acceptor ionization energy and f a constant. When uniaxial stress is applied E_{Ai} splits giving rise to two subsidiary thresholds in the absorption curve.

By taking the equations quoted by Dumke and (3), the theoretical derivative absorption curves were synthesised using the values E_{Ai} as adjustable parameters. It was found that the values corresponding to a 'best fit' were closely equal to the photon energies of the corresponding minima in the spectra. The latter has been used as giving a direct measure of the acceptor level splittings. This choice differs from that proposed by Balslev[3], however, Balslev was interpreting an indirect process, and numerical analysis supports the present assignment of the split energy levels.

The expression for the direct absorption due to allowed transitions is similar in form to equation (3) with $E_{Ai} = 0$. The $(h\nu - E_g)^{1/2}$ dependence of α, implies a sharp threshold. However, the measured absorption edge in InSb[14] shows a tail on the low-photon energy side of the absorption edge due to 'indirect' transitions involving the absorption of longitudinal optical phonons[15]. The absorption due to the acceptor-conduction band process is small and to detect it a differential wavelength modulation technique has been used.

EXPERIMENTAL METHODS

To enhance the sensitivity with which small changes of absorption can be detected a method similar to that described by Balslev[3] has been employed. In the present system the conventional beam chopper of a Perkin Elmer model-99 monochromator is disabled and the exit mirror is vibrated around its mounting axis by means of a small loudspeaker-type drive. A small portion of the dispersed spectrum is scanned across the exit slit of the monochromator. By synchronously detecting the resultant amplitude modulation at the detector we retrieve a signal which is proportional to $\exp\{-\alpha d\}.(d\alpha/d\lambda)$. This modulation technique has the advantage that the point of focus upon the detector is stationary.

In the measurements to be described the dispersing element was an NaCl prism, and the detector a thermocouple, (Reeder type RP-3W, having an NaCl window). The detected signal was matched by a transformer (AM-1) and preamplifier (CR-4) to a lock-in amplifier (HR-8) (Princeton Applied Research Corp.). The derivative signal was displayed directly on an X–Y recorder, the X-displacement being obtained from a linear potentiometer coupled to the drive drum of the monochromator.

The monochromator was calibrated over the relevant range by comparison with the absorption spectrum of polystrene, water vapour and CO_2. The interpolation of wavelengths was made by means of a computer adaptation of the procedure described by Filler and Indyk[16].

The mechanical stressing system was similar to that described by Fritzsche[17]. The stressing jig was mounted in the tail section of a conventional optical drawer. In the present experiments liquid nitrogen was used in the inner dewar section, and the specimen temperature was 99°K. Loads were applied by a mechanical lever system. The system was checked for residual friction by both room temperature tests, using strain gauges attached to a dummy sample, and by successsive loading and unloading cycles during measurement. The reproducibility of the observed spectra was within the experimental resolution of the system.

A final check on system reproducibility is provided by measurement of the splitting in three stress directions, ⟨100⟩, ⟨111⟩ and ⟨110⟩, the latter orientation providing a check for the consistency of deformation potentials obtained from the first two.

The specimens used were single crystal p- and n-type InSb, oriented by back reflection Laue methods as follows:

χ	X	Y	Z
⟨111⟩	$\langle 1\bar{1}0\rangle$	$\langle 11\bar{2}\rangle$	⟨111⟩
⟨001⟩	⟨100⟩	⟨010⟩	⟨001⟩
⟨110⟩	⟨110⟩	$\langle 1\bar{1}0\rangle$	⟨001⟩

where χ is the stress direction, Z the long axis of the sample, X and Y the width and thickness respectively (approx. 14 mm × 5 mm × 1 mm). Samples were polished by standard metallographic methods. No difference in optical behaviour was found between polished and chemically etched specimens.

Samples adjacent to those used for optical measurements were retained for Hall effect and resistivity measurements. The p-type material was Cd-doped with a carrier concentration of $1{\cdot}8\,.\,10^{14}\,cm^{-3}$ at 77°K. The n-type material had a carrier concentration of $2{\cdot}8\,.\,10^{14}$ at 77°K.

EXPERIMENTAL RESULTS

Typical results for various orientations and stresses are shown in Figs. 1–3.

The broad features of all results using unpolarised radiation are similar. Three major peaks develop as the stress is increased from

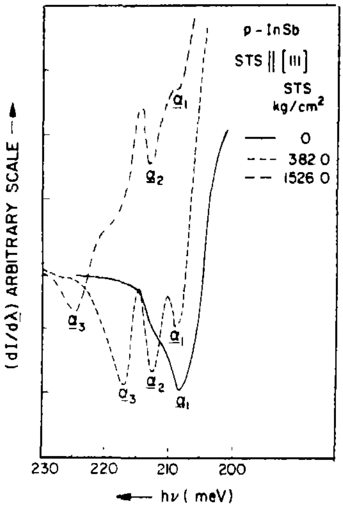

Fig. 1. Derivative transmission spectra of Cd-doped p-InSb at 99°K for stress parallel to [111]. Sample thickness = 0·92 mm.

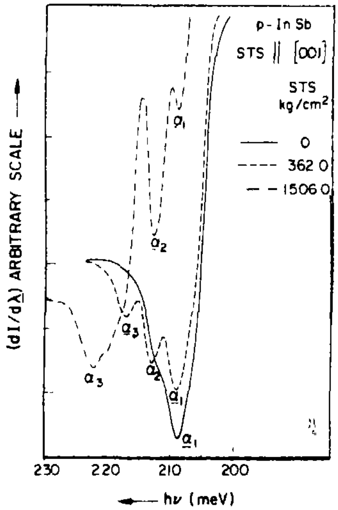

Fig. 2. Derivative transmission spectra of Cd-doped p-InSb at 99°K for stress parallel to [001]. Sample thickness = 0·98 mm.

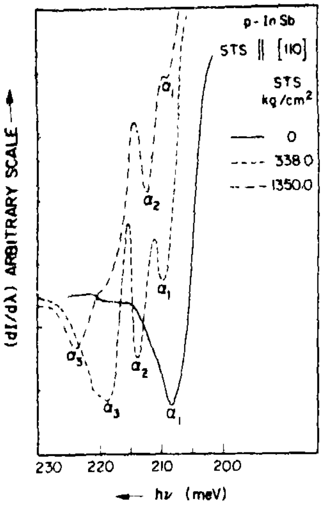

Fig. 3. Derivative transmission spectra of Cd-doped p-InSb at 99°K for stress parallel to [110] Sample thickness = 0·101 mm.

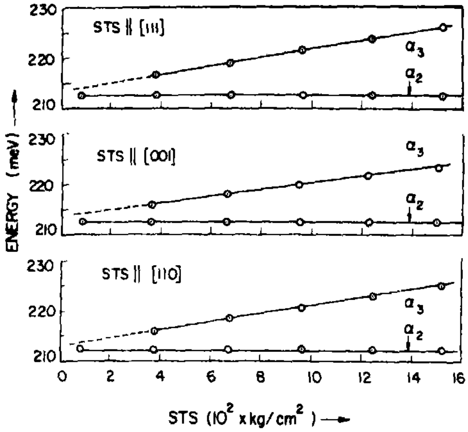

Fig. 4. Splitting energy vs. stress for p-InSb at 99°K for stress parallel to [111], [001] or [110] crystal directions.

zero. Only the peak labeled α_3 shows a substantial shift as stress is increased.

The presence of the peak α_1 both at zero and finite applied stress is associated with transitions involving the participation of an L–O phonon. The position of the minimum of α_1 agrees well with that calculated from Dumke's theory[15] taking the L–O phonon energy as 25 meV[18].

The remaining peaks α_2 and α_3 are interpreted using equation (3) to derive the expression for $(dI/d\lambda)$.

Using the experimental curves the values of E_{A1} and E_{A2} have been obtained at each stress and a plot of these is given in Fig. 3 for Cd-doped material.

Using the relevant expressions for $\langle 001 \rangle$ and $\langle 111 \rangle$ oriented materials and the slopes from Fig. 4, we obtain:

$$|b'| = (1{\cdot}04 \pm 0{\cdot}1)\,\text{eV}$$
$$|d'| = (4{\cdot}4 \pm 0{\cdot}1)\,\text{eV}$$

respectively. If these plots are extrapolated to zero stress they cut the energy axis at 212·2 and 212·8 meV. The energy gap at 99°K is 222·3 meV[14] and hence the acceptor ionisation energy is obtained as $E_A = 9{\cdot}8 \pm 0{\cdot}3$ meV.

In p-type material the latter value may be checked by measurement of the Hall effect vs. temperature. The results of fitting the carrier concentrations deduced from such measurements, vs. $(1/T)$ °K^{-1}, to a simple, single impurity level model is shown in Fig. 5. The two curves shown at the lower temperatures indicate the effect of two different surface treatments, CP4-A and H-100[9] etching. The latter measurements yield an acceptor ionisation energy of 9·7 ± 0·3 meV.

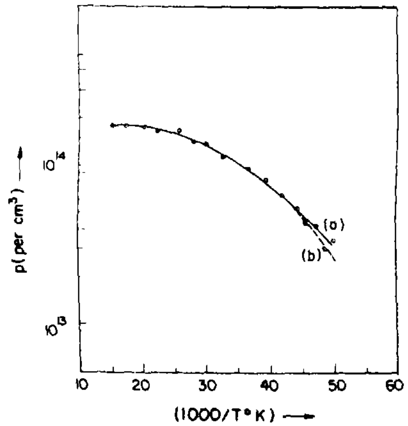

Fig. 5. Carrier concentration of p-InSb as a function of temperature (a) sample etched in CP4 (b) sample etched in CP4 and H100.

This result agrees well with that given by Putley[20], when the latter's numerical values are modified to include a hole effective mass of approximately $0{\cdot}4\,m_0$[8].

If we consider the splitting with stress in the $\langle 110\rangle$ direction, and substitute for $|d'|$, we obtain a check on internal consistency from the new value of $|b'|$ calculated. Such a substitution leads to $|b'| = 1{\cdot}1$ eV, which agrees, within experimental error, with the value obtained directly.

The results of measurements on n-type InSb are given in Figs. 6 and 7. In this case we assume that the transitions occur between partially compensating acceptor levels and tentatively ascribe these to Zn, a known residual impurity in InSb[21]. The interpretation of these results leads to the values

$$|b'| = (1{\cdot}1 \pm 0{\cdot}1)\,\text{eV}$$
$$|d'| = (4{\cdot}3 \pm 0{\cdot}1)\,\text{eV}.$$

Using $|d'|$ and the results of measurements made with $\langle 110\rangle$ applied stress we find $|b'| = 1{\cdot}0$ eV in satisfactory agreement with the direct result. The extrapolated ionisation energy of the residual impurity is $(9{\cdot}7 \pm 0{\cdot}3)$ meV which is indicative of a group II acceptor impurity.

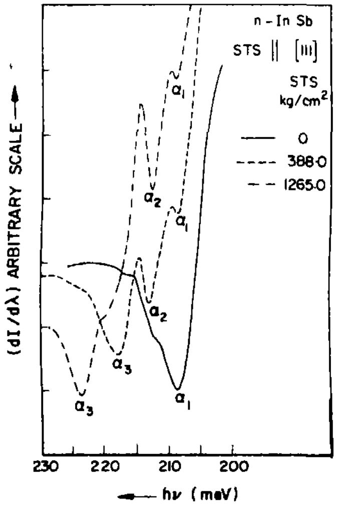

Fig. 6. Derivative transmission spectra of n-InSb at 99°K for stress parallel to [111]. Sample thickness = 0·97 mm.

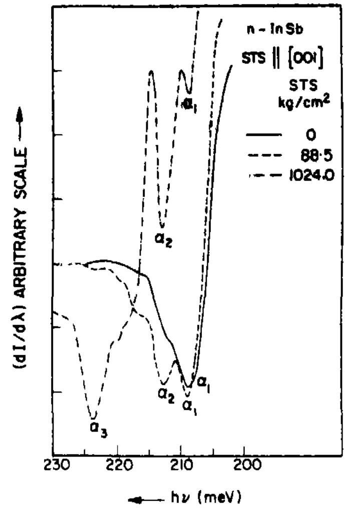

Fig. 7. Derivative transmission spectra of n-InSb at 99°K for stress parallel to [001]. Sample thickness = 0·94 mm.

The polarisation dependence of the absorption is similar in both p- and n-type material. In the unstressed material the four-fold degenerate valence band Γ_8 is split away from $k = 0$; the upper band may be represented by $J = 3/2$, $M_J = \pm\frac{1}{2}$, the lower by $J = 3/2$, $M_J = \pm 3/2$. In the present treatment of the acceptor impurity we consider only the ground state wave function, whose symmetry is unaffected by the hydrogen-like envelope function $F(r)$[9], and retains the same angular momentum quantum numbers for the acceptor impurity wave-functions. Under stress the four-fold ground state at $k = 0$ splits into two-fold degenerate states $M = \pm 3/2$; $M = \pm 1/2$. The rules for dipole transitions then give

$$\begin{aligned}
&M = \pm 1/2\ (\text{valence}),\\
&\qquad M = \pm 1/2\ (\text{conduction}),\ \Delta M = 0, \pm 1\\
&M = \pm 3/2\ (\text{valence}),\\
&\qquad M = \pm 1/2\ (\text{conduction}),\ \Delta M = \pm 1.
\end{aligned}$$

Thus both transitions are allowed for light polarised perpendicular to the stress direction, whereas only the $M = \pm 3/2$ (valence) → $M = \pm 1/2$ (conduction) transitions occur for parallel polarisation.

The polariser used was a Perkin Elmer wire grid type having an NaCl substrate. The experimental results for stress parallel to *⟨001⟩ and ⟨111⟩ are shown in Figs.* 8 and 9. In both orientations with $E||\chi$ the α_3 peak is suppressed while for α_2 little relative change is found. Since α_3 lies above α_2 in photon energy we may conclude that the $J = 3/2$, $M = \pm 1/2$ level moves to higher energy, the $J = 3/2$, $M = \pm 3/2$ level, to lower energy. Thus both b' and d' have negative signs.

We can also obtain from the present measurements a value for the quantity $(c+a')\epsilon/\chi = (3{\cdot}5 \pm 0{\cdot}4)$ eV kgm^{-1} cm^2. Bir *et al.*[11] have shown that a' and a (the deformation potential for free holes) have the same value. However, the value of $3(c+a')\epsilon/\chi$ is only two thirds of the observed change of band gap with hydrostatic pressure[22]. A similar discrepancy has been reported in Ge by Balslev[3].

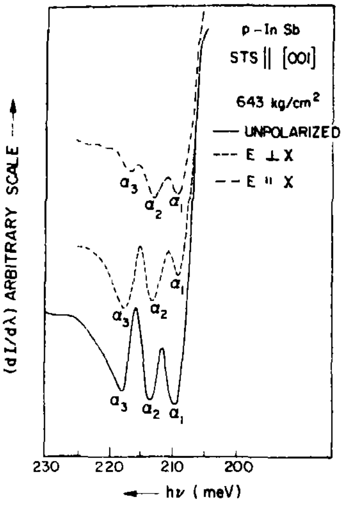

Fig. 9 Polarization dependence of p-InSb for stress parallel to [001]. Spectra for unpolarized light and light polarized parallel and perpendicular to the stress axis are shown.

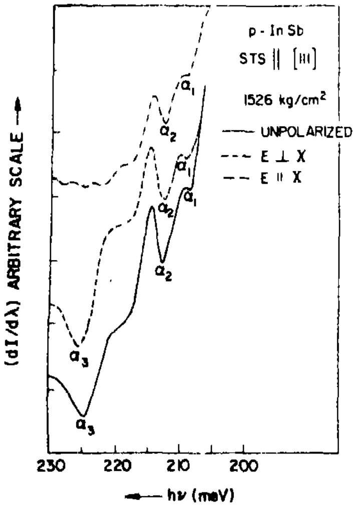

Fig. 8. Polarization dependence of p-InSb for stress parallel to [111]. Spectra for unpolarized light and light polarized and perpendicular to the stress axis are shown.

The available experimental values of the various deformation potentials in InSb (eV) are:

$(a+c)$	b	d	b'	d'
$-7{\cdot}2$	$-2{\cdot}0$	$-6{\cdot}0$	$-1{\cdot}04$(Cd) $-1{\cdot}10$(Zn)	$-4{\cdot}4$(Cd) $-4{\cdot}3$(Zn)

The values of b and d quoted are from piezo-emission studies[4] since these seem less subject to interpretive difficulties than piezo resistance measurements[10].

REFERENCES

1. ZWERDLING S., LAX B., ROTH L. M. and BUTTON K. J., *Phys. Rev.* **114**, 80 (1959); MACFARLANE G. G., McLEAN T. P., QUARRINGTON J. E. and ROBERTS V., *Phys. Rev. Lett.* **2**, 252 (1959); KLEINER W. H. and ROTH L. M., *Phys. Rev. Lett.* **2**, 334 (1959).
2. GLASS A. M., *Can. J. Phys.* **43**, 12 (1965).
3. BALSLEV I., *Phys. Rev.* **143**, 636, (1966).
4. GUILLAUME C. B. and LAVALLARD P., *Proc. Int. Conf. Phys. Semiconductors, Kyoto* (1966); *J. phys. Soc. Japan* **21**, 288 (1966).
5. JOHNSON E. J. and FAN H. Y., *Phys. Rev.* **139**, A1991 (1965).

6. SHARAN R. and HEASELL E. L., *Proc. Int. Conf. Phys. Semiconductors, Moscow* p. 1194 (1968).
7. KANE E. O., *J. Phys. Chem. Solids* **1**, 249 (1957).
8. BAGGULEY D. M. S., ROBINSON M. L. A., and STRADLING R. A., *Phys. Lett.* **6**, 143 (1963); ROBINSON M. L. A., *Phys. Rev. Lett.* **17**, 963 (1966).
9. KOHN W., In *Solid State Physics*, Vol. 5, p. 257. Academic Press, New York (1957).
10. PICUS G. E. and BIR C. L., *Soviet. Phys. solid St.* **1**, 1675 (1960). BIR C. L. and PICUS G. E., *Soviet Phys. solid St.* **3**, 2221 (1962).
11. BIR C. L., BUTIKOV E. I. and PICUS G. E., *J. Phys. Chem. Solids* **24**, 1467 (1963).
12. EAGLES D. M., *J. Phys. Chem. Solid* **16**, 76 (1960).
13. DUMKE W. P., *Phys. Rev.* **132**, 1998, (1963).
14. MAKELUNG O., *Physics of III-V compounds* (Translated by D. Meyerhofer). Wiley, New York (1964).
15. DUMKE W. P., *Phys. Rev.* **108**, 1419 (1957).
16. FILLER A. S. and INDYK L., *J. opt. Soc. Am.* **51**, 572 (1961).
17. CUEVAS M. and FRITZSCHE, *Phys. Rev.* **137**, 1847 (1965).
18. HALL R. N. and RACETTE J. H., *J. appl. Phys.* **32**, 2078 (1961).
19. HENNEKE H. L., *J. appl. Phys.* **36**, 296 (1965).
20. PUTLEY E. H., In *The Hall Effect and Related Phenomena*, p. 3, 131. Butterworths, London (1960).
21. HULME K. F. and MULLIN J. B., *Solid-st. Electron.* **5**, 211 (1962).
22. BRADLEY C. C. and GEBBIE H. A., *Phys. Lett.* **16**, 109 (1965).

J. Phys. Chem. Solids Pergamon Press 1970. Vol. 31, pp. 549-557. Printed in Great Britain.

DETERMINATION DE LA FONCTION DE DISTRIBUTION DE PAIRE DU CUIVRE LIQUIDE PAR DIFFRACTION DE NEUTRONS

M. BREUIL et G. TOURAND
Service de Physique du Solide et de Résonance Magnétique,
Centre d'Etudes Nucléaires de Saclay,
BP. n°2, 91-Gif-sur-Yvette

(*Received* 18 *February* 1969; *in revised form* 3 *June* 1969)

Résumé – Le facteur de structure du cuivre liquide a été déterminé par diffraction de neutrons à trois températures différentes (1150°, 1300°, 1450°C). La variation du maximum de $i(k)$ a été étudiée de 1086° à 1492°C faisant apparaître une dèpendance linéaire en $1/T$. La fonction de distribution de paire $g(r)$ et la fonction de corrélation directe $c(r)$ ont été obtenues par transformation de Fourier et le potentiel de paire $V(r)$ en a été déduit à l'aide des équations de Percus–Yevick et de la chaîne hyper tressée. Ces deux approximations ne conviennent pas au cas du cuivre liquide, mais la partie répulsive du potentiel est en bon accord avec un modèle de sphéres dures de coeur $\sigma = 2{,}2$ Å.

Abstract – The structure factor of liquid copper has been determined for three different temperatures (1150°, 1300°, 1450°C) by neutron diffraction. The variation of the maximum of $i(k)$ with temperature has been studied from 1086° to 1492°C and shows a linear dependence with $1/T$. The pair distribution function $g(r)$ and the direct correlation function $c(r)$ have been obtained by Fourier transformation and the pair potentiel $V(r)$ was derived from these using the Percus–Yevick and hypernetted chain equations. These two approximations are not applicable to liquid copper but the repulsive part of the potential is in good agreement with a hard sphere model of core $\sigma = 2{\cdot}2$ Å.

1. INTRODUCTION

Les paramètres thermodynamiques d'un liquide (pression, volume, chaleur spécifique, température, etc . . .) peuvent être déterminés à partir de deux fonctions[1–3]; d'une part, la fonction de distribution de paire $g(r)$ qui dépend de la densité du liquide et de sa température et d'autre part le potentiel décrivant les interactions atomiques dans le liquide. Nous supposons ici que ce potentiel peut être mis sous la forme d'une somme de potentiels de paire, c'est-à-dire que

$$U = \sum_{i,j} V|\vec{r}_i - \vec{r}_j|.$$

Cette hypothèse est usuelle dans l'étude des fluides en mécanique statistique classique mais pose peut-être un problème dans le cas par exemple des métaux de transition liquides. Actuellement, il n'existe pas de méthode expérimentale permettant de déterminer le potentiel de paire $V(r)$. Mais des mesures de diffraction de Rayons X ou de neutrons permettent d'obtenir une bonne connaissance de la fonction de distribution de paire $g(r)$. En effet, $g(r)$ décrit l'arrangement statistique des atomes dans le liquide et détermine ainsi la distribution angulaire de l'intensité diffusée.

Dans le cas des neutrons, si $I(K)$ est l'intensité totale diffusée par l'échantillon liquide, $I_{\text{coh}}(k)$ la partie cohérente de cette intensité et $I_{\text{coh}}(\infty)$ la valeur que prend $I_{\text{coh}}(k)$ lorsque k est suffisamment grand pour que les effets d'interférence ne puissent plus être observés, on peut définir une fonction $i(k)$ de l'intensité diffusée par la relation:

$$i(k) = \frac{I_{\text{coh}}(k)}{I_{\text{coh}}(\infty)} - 1. \tag{1}$$

Dans ces expressions, on a posé $k = 4\pi/\lambda \sin\theta$. θ est l'angle de Bragg et λ la longueur d'onde du rayonnement monochromatique utilisé.

On peut alors montrer que la fonction $i(k)$ possède les propriétés suivantes:

$a-$
$$1+i(0)=k_BT\rho_0\beta \tag{2}$$

β est le coefficient de compressibilité isotherme du liquide et ρ_0 sa densité atomique moyenne exprimée en nombre d'atomes par unité de volume.

$b-$ $i(k)$ est reliée à $g(r)$ par une relation de transformée de Fourier soit [4–7]:

$$\frac{\rho(r)}{\rho_0}=g(r)=1+\frac{1}{2\pi^2\rho_0 r}\int_0^\infty k\,i(k)\sin kr\,dk \tag{3}$$

oú $\rho(r)$ est la densité atomique à la distance r d'un atome de référence.

De plus, on peut définir comme l'ont fait Zernicke et Ornstein [8] une fonction de corrélation directe $c(r)$ par la relation;

$$c(r)=\frac{1}{2\pi^2\rho_0 r}\int_0^\infty\frac{k\,i(k)}{1+i(k)}\sin kr\,dk. \tag{4}$$

Les relations (3) et (4) fournissent donc $g(r)$ et $c(r)$ à partir des valeurs de $i(k)$ mesurées expérimentalement. Il existe alors diverses approximations qui relient $g(r)$ et $c(r)$ au potentiel de paire $V(r)$. Celles qui ont fourni les meilleurs résultats pour les quantités thermodynamiques, notamment dans le cas de l'argon [9] au voisinage du point triple et qui sont aussi les plus simples à interpréter numériquement sont [10]:

1. L'approximation 'Hyper Netted Chain' HNC qui fournit une relation simple entre $g(r)$, $c(r)$ et $V(r)$ à savoir:

$$V(r)=k_BT[g(r)-1-c(r)-\mathrm{Log}\,g(r)]. \tag{5}$$

2. L'équation de Percus-Yevick qui fournit aussi une relation simple reliant $g(r)$, $c(r)$ et $V(r)$ soit:

$$V(r)=k_BT\,\mathrm{Log}\left[1-\frac{c(r)}{g(r)}\right]. \tag{6}$$

Dans le travail présenté ici, nous avons déterminé $i(k)$ pour le cuivre à diverses températures et nous en avons déduit les fonctions $g(r)$ et $c(r)$ à ces températures. Puis, à l'aide des modèles HNC et PY nous avons tenté de déterminer le potentiel de paire $V(r)$. Nous verrons alors que ces approximations ne donnent pas de résultats corrects pour le cuivre, rejoignant en cela les conclusions auxquelles aboutissait North pour le plomb [11].

2. DISPOSITIF EXPERIMENTAL

Nous avons utilisé le dispositif classique d'un des spectromètres du réacteur EL3 à Saclay dont le faisceau de neutrons monochromatique a une longueur d'onde $\lambda = 1,138$ Å. Les hautes températures nécessaires à ces expériences ont été obtenues au moyen d'un four à induction de haute fréquence permettant d'atteindre 2000°C. Les inducteurs sont disposés de manière à être situés en dehors des faisceaux incident et diffusés. L'échantillon de cuivre utilisé, de forme cylindrique et de dimensions: diamètre = 10 mm et hauteur = 60 mm est placé dans un creuset en tantale. Celui-ci est placé dans un tube cylindrique de quartz de 30 mm de diamètre à l'intérieur duquel on fait un vide dynamique poussé ($p \simeq 10^{-6}$ mm Hg).

Grâce à ce montage, le faisceau de neutrons ne traverse, en dehors du creuset contenant l'échantillon, qu'une faible épaisseur de quartz amorphe et faiblement absorbant. La température est mesurée à l'aide de thermocouples $W/Ré$ placés à la base du creuset au voisinage immédiat du liquide. Plusieurs étalonnages effectués sur divers matériaux et en particulier lors de la fusion du cuivre à 1083°C ont montré que l'erreur dans la mesure de la température est ≤ 2°C. Celle-ci est très finement régulée par action continue sur la tension du générateur haute fréquence de sorte que ses fluctuations sont extrêmement faibles et de l'ordre de 1° à 1500°C. De plus, au dessus de la température de fusion, des contrôles ont montré que les gradients de température radiaux et longitudinaux sont négligeables. Enfin, pour éviter l'évaporation du cuivre, le creuset est fermé à l'aide d'une pièce de tantale de forme spéciale. Grâce à ce dispositif, les vapeurs de cuivre se condensent de sorte que la quantité de cuivre irradiée par le faisceau de neutrons est constante durant toute la durée de l'expérience.

3. LA DETERMINATION EXPERIMENTALE DE i(k) ET LES MESURES EFFECTUEES

On commence par déterminer l'intensité totale $I(2\theta)$ diffusée par l'échantillon liquide. Compte tenu du montage expérimental décrit ci-dessus, ceci se fait de la manière habituelle en mesurant:

1. l'intensité diffusée par le creuset plein soit $I_1(2\theta)$;
2. l'intensité diffusée par le creuset vide à la même température soit $I_2(2\theta)$;
3. l'intensité diffusée par le tube de quartz seul soit $I_3(2\theta)$ et en effectuant la différence I_1-I_2-I_3 corrigée des facteurs d'absorption.

La Fig. 1(A) montre la courbe $I(2\theta)$ obtenue à $T = 1150°C$. On détermine ensuite la partie cohérente de cette intensité soit $I_{coh}(2\theta)$ en remarquant que la diffusion nucléaire incohérente et la diffusion multiple étant isotropes, il suffit de retrancher des valeurs obtenues pour $I(2\theta)$ une quantité constante que l'on détermine à l'aide de l'équation (2) car $i(0)$ est connue[12].

Pour trois valeurs de la température: *1150°, 1300° et 1450°C* nous avons déterminé la spectre de diffusion du cuivre depuis $2\theta = 1°10'$ jusqu'à $2\theta = 116°$ soit pour k variant de 0,11 $Å^{-1}$ jusqu'à 9,4 $Å^{-1}$.

A 1150°C les mesures ont été faites avec un pas de 6′ soit dix comptages par degré, à 1300°C, six comptages par degré et à 1450°C, quatre comptages par degré. Ces comptages duraient assez longtemps pour obtenir une bonne précision statistique.

Enfin pour neuf autres valeurs de la température comprises entre 1086° et 1492°C, nous avons étudié les variations du maximum

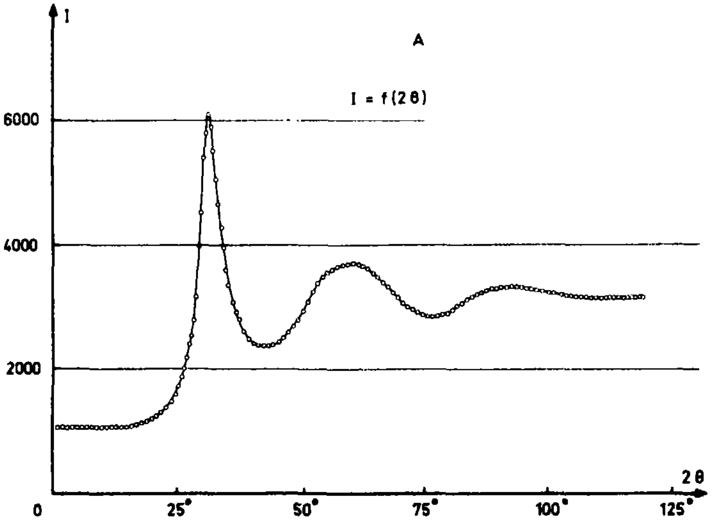

Fig. 1(A). Variation de l'intensité totale diffusée par l'échantillon de cuivre liquide en fonction de l'angle de Bragg, 2θ à $T = 1150°C$.

de $i(k)$ soit $i(k_0)$ dans les mêmes conditions expérimentales.

4. RESULTATS OBTENUS

(a) *Fonction* i(k)

La Fig. 1(B) montre les variations de $i(k)$ pour $T = 1150°$, 1300° et 1450°C et le Tableau 1 fournit les valeurs numériques correspondantes. On remarque que la position des maximums de $i(k)$ reste pratiquement inchangée quand la température varie. De plus le premier maximum se produit pour $k = k_0 = 3\ \text{Å}^{-1}$. Dans le cuivre solide, la première raie de Bragg (111) apparaît exactement à la même valeur k_0. Ce résultat semble assez général et peut être dû au fait qu'il s'agit d'une structure compacte CFC.

Enfin pour $k < 2{,}5\ \text{Å}^{-1}$, les trois courbes $i(k)$ sont très semblables entre elles.

Pour $k = 0$, la valeur de $i(0)$ mesurée[12] à partir de l'équation (2) est:

$$i(0) = -0{,}984.$$

Il est important de remarquer que les mesures de $i(k)$ sont assez imprécises. Cette imprécision due aux mesures statistiques, aux corrections de facteur d'absorption, à la nécessité d'effectuer des différences entre des termes dont les ordres de grandeur sont souvent assez voisins etc... ne nous paraît pas susceptible d'être améliorée de façon très nette en l'état actuel des techniques expérimentales. L'erreur est d'environ 4% au voisinage de $k = k_0$ et atteint 7% quand on s'éloigne de k_0.

(b) *Fonction* g(r)

La Fig. 2 montre les variations de $g(r)$ aux trois températures considérées. Les positions des extrémums de $g(r)$ ne varient pas avec la température. Ces courbes montrent bien que la zone de densité atomique maximale qui correspond au premier pic de $g(r)$ est située à 2,55 Å. Ceci est équivalent à la distance entre plus proches voisins dans

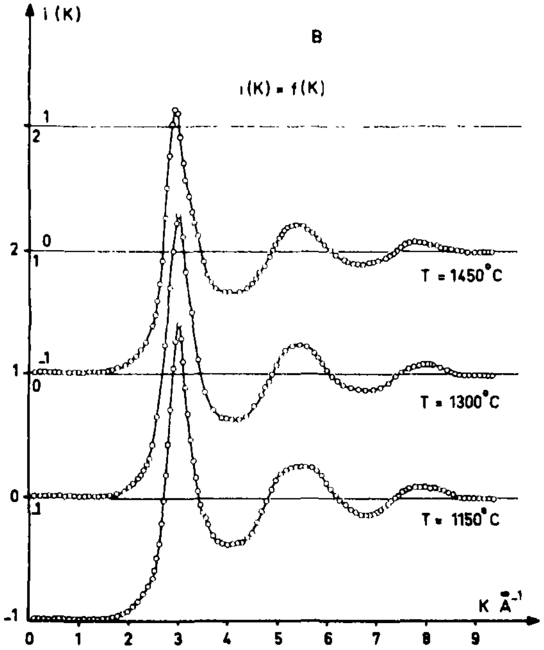

Fig. 1(B). Variation de la fonction $i(k)$ à différentes températures.

Tableau 1. *Valeurs numériques de la fonction* i(k) = f(k, T) *aux températures*: 1150°C, 1300°C, 1450°C

	T				T		
k Å^{-1}	1150°C	1300°C	1450°C	k Å^{-1}	1150°C	1300°C	1450°C
0,106	−0,981	−0,982	−0,985	3,96	−0,371	−0,350	−0,324
0,193	−0,983	−0,983	−0,989	4,05	$\boxed{-0{,}373}$	$\boxed{-0{,}356}$	−0,326
0.289	−0,985	−0,981	−0,989	4,14	−0,363	−0,358	$\boxed{-0{,}329}$
0,385	−0,977	−0,979	−0,978	4,23	−0,360	−0,357	−0,329
0,482	−0,980	−0,978	−0,984	4,36	−0,325	−0,336	−0,317
0,578	−0,984	−0,986	−0,983	4,45	−0,289	−0,305	−0,280
0,674	−0,984	−0,984	−0,992	4,54	−0,248	−0,268	−0,238
0,770	−0,990	−0,980	−0,981	4,67	−0,135	−0,175	−0,171
0,866	−0,988	−0,981	−0,984	4,75	−0,057	−0,125	−0,118
0,962	−0,983	−0,990	−0,985	4,93	0,089	−0,013	0,016
1,058	−0,986	−0,982	−0,976	5,01	0,156	0,040	0,082
1,154	−0,983	−0.981	−0,977	5,10	0,197	0,080	0,133
1,250	−0.985	−0,981	−0,989	5,18	0,228	0,125	0,177
1,346	−0,985	−0,988	−0,988	5,27	0,250	0,168	0,197
1,441	−0,981	−0,986	−0.987	5,35	0,256	0,227	0,200
1,54	−0,974	−0,985	−0,977	5,44	$\boxed{0{,}261}$	$\boxed{0{,}244}$	$\boxed{0{,}205}$
1,63	−0.972	−0,977	−0,960	5,52	0,261	0,222	0,204
1,73	−0,960	−0,960	−0,950	5,69	0,261	0,151	0,158
1,82	−0,952	−0,955	−0,945	5,77	0,240	0,128	0,135
1,92	−0,931	−0,945	−0,933	5,93	0,172	0,048	0,067
2.01	−0,913	−0,913	−0,904	6,01	0,127	0,013	0,039
2,11	−0,876	−0,870	−0,867	6,17	0,040	−0,042	−0,018
2,20	−0,833	−0,824	−0,827	6,25	−0,000	−0,064	−0,045
2,30	−0,778	−0,764	−0,776	6,41	−0.052	−0,098	−0,080
2,39	−0,717	−0,685	−0,704	6,57	−0,103	−0,111	−0,098
2,48	−0,605	−0,575	−0,600	6,72	$\boxed{-0{,}134}$	−0,116	$\boxed{-0{,}100}$
2,58	−0,412	−0,346	−0,401	6,87	−0,128	$\boxed{-0{,}120}$	−0,093
2,67	−0,130	−0,010	−0,084	7,02	−0,108	−0,108	−0,082
2,76	0.254	0,355	0,265	7,17	−0,065	−0,084	−0,070
2,86	0,766	0,794	0,766	7,32	−0,014	−0,037	−0,033
2,90	1,045	0,979	1,010	7,46	0,034	0,004	0,017
2,95	1,269	1,212	$\boxed{1{,}140}$	7,60	0,076	0,033	0,051
3,00	$\boxed{1{,}411}$	$\boxed{1{,}282}$	1,105	7,74	0,097	0,055	0,068
3,09	1,135	1,096	0,810	7,88	0,096	0,075	$\boxed{0{,}073}$
3,14	0,954	0,893	0,699	8,01	$\boxed{0{,}098}$	$\boxed{0{,}088}$	0,059
3,23	0,560	0,544	0,429	8,14	0,095	0,083	0,049
3,32	0,239	0,279	0,211	8,27	0,088	0,063	0,038
3,41	0,031	0,074	0,035	8,33	0,077	0,056	0,028
3,50	−0,120	−0,084	−0,094	8,40	0,070	0,041	0,023
3,60	−0,208	−0,186	−0,190	8,46	0,060	0,034	0,019
3,69	−0,288	−0,265	−0,252	8,52	0,053	0,022	0,011
3,78	−0,343	−0,311	−0,293	8,58	0,044	0,007	0,004
3,87	−0,363	−0,335	−0,315	>8,70	≃0	≃0	≃0

le cuivre solide, distance qui varie entre 2,55 Å et 2,60 Å suivant la température.

(c) *Fonction* i(k$_0$) = f(T)

Une étude complète de la variation de $i(k_0)$ en fonction de la température a été effectuée et le Tableau 2 ci-dessous indique les différentes valeurs obtenues.

La Fig. 3 montre les variations de $i(k_0)$ en fonction de $1/T$ où T est alors la température absolue.

Dans le domaine de température étudié,

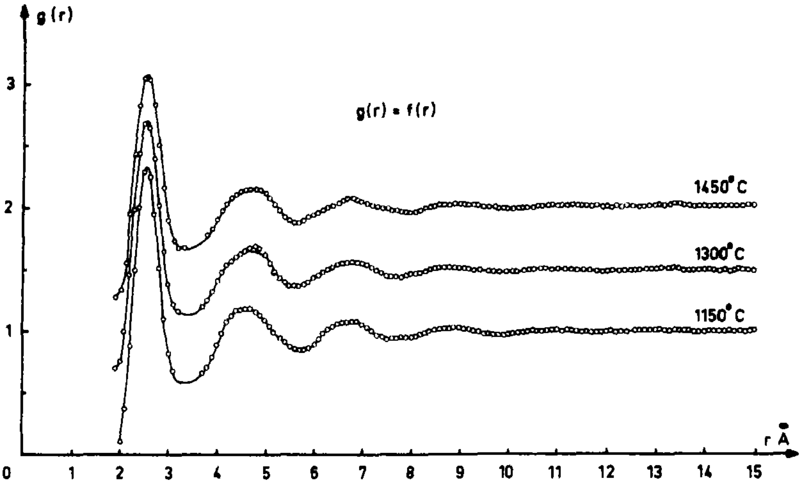

Fig. 2. Variation de la fonction $g(r)$ aux trois températures considérées.

Tableau 2. *Valeurs mesurées de* $i(k_0)$ *en fonction de la température de* 1086°C *à* 1492°C

T°C	1086	1107	1129	1150	1156	1183	1236	1290	1300	1344	1450	1492
$i(k_0)$	1,56	1,54	1,54	1,41	1,50	1,45	1,36	1,26	1,29	1,20	1,14	1,13

ces variations sont bien représentées par l'équation:

$$i(k_0) = 2{,}65\,\frac{10^3}{T} - 0{,}39,$$

qui montre qu'au-dessus de la température de fusion, l'intensité du premier pic décroît comme $1/T$.

(d) *Fonction* c(r)

La Fig. 4 montre ses variations pour les trois températures considérées ici. Pour $r = 0$; on trouve $c(0) = -78$ pour $T = 1150°$ et 1450°C et $c(0) = -80$ pour $T = 1300$°C. La fonction $c(r)$ dépend très fortement des valeurs de $i(k)$ pour k petit c'est-à-dire $< 2{,}5$ Å^{-1}. Ainsi la précision sur $i(k)$ n'est pas assez grande pour pouvoir déterminer correctement $c(r)$ pour $r > 2{,}5$ Å. La Fig. 5 exprime bien ceci en montrant, pour $T = 1300$°C, trois courbes $c(r)$ 'possibles' obtenues en faisant varier, à l'intérieur des barres d'erreur expérimentale la fonction $i(k)$ pour $k < 2{,}5$ Å^{-1}. La courbe 1 de la Fig. 5 correspond aux valeurs de $i(k)$ données dans le Tableau 1 et à la Fig. 4 pour $T = 1300$°C.

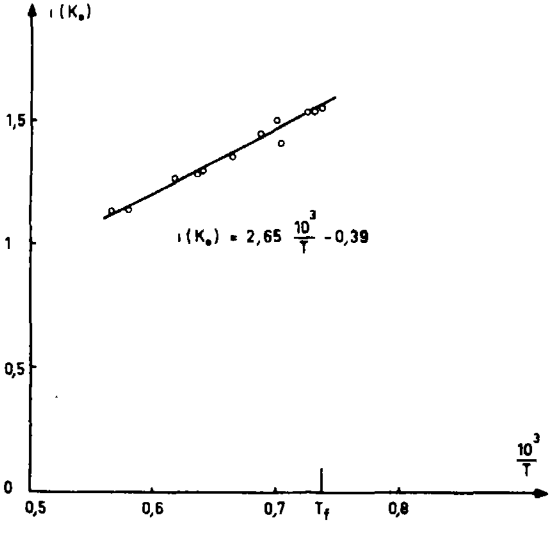

Fig. 3. Variation de $i(k_0)$ en fonction de $1/T$.

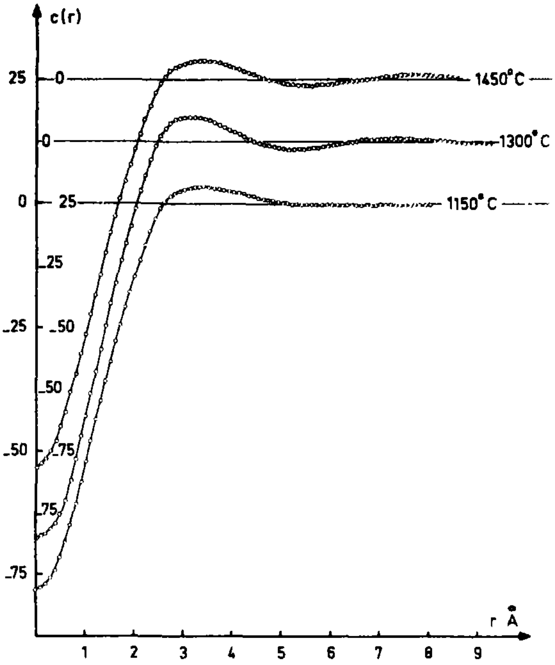

Fig. 4. Variation de la fonction $c(r)$ aux trois températures considérées.

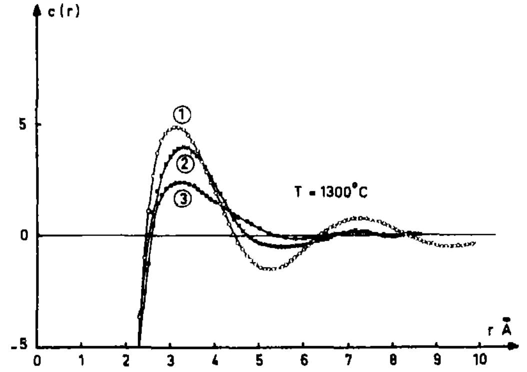

Fig. 5. Variation de la fonction $c(r)$ pour trois valeurs 'possibles' de la fonction $i(k)$ pour $k < 2{,}5$ Å^{-1} et pour une température de 1300°C. La courbe 1 correspond aux valeurs de $i(k)$ données dans le Tableau 1.

5. DISCUSSION

A partir des résultats obtenus pour $g(r)$ et $c(r)$ nous avons tenté de déterminer le potentiel de paire $V(r)$ à partir des équations de Percus-Yevick et de la chaîne hyper tressée.

Equation de Percus-Yevick

La Fig. 6 montre les potentiels ainsi obtenus. Pour les valeurs de r comprises approximativement entre 2,6 et 4,5 Å, nous avons obtenu $g(r) < c(r)$ de sorte que l'équation de Percus-Yevick ne nous a pas permis de déterminer le potentiel de paire $V(r)$. Ceci se produit pour les trois expériences indépendantes réalisées à des températures différentes. De plus, à $T = 1300$°C les trois fonctions $c(r)$ 'possibles' représentées sur la Fig. 5 conduisent à un résultat identique. Il est à noter que pour la forme III de leur fonction de corrélation directe $c(r)$. North *et al.*[11] obtiennent un résultat semblable dans le cas du plomb.

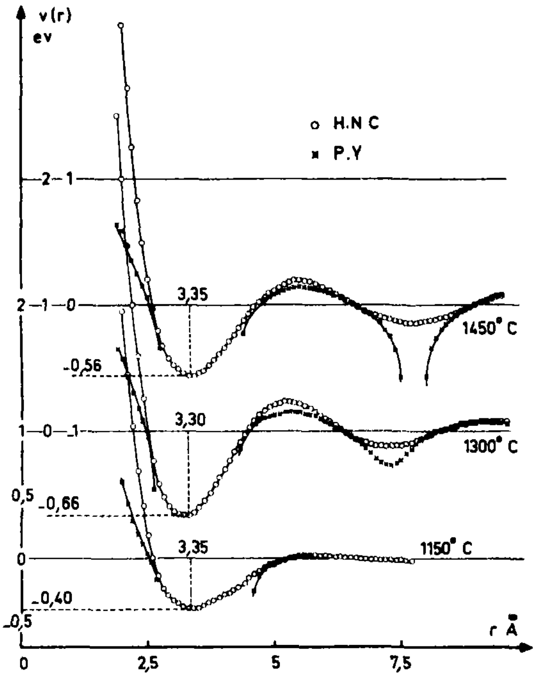

Fig. 6. Représentation de la fonction $V(r)$ obtenue par les équations HNC et P.Y. aux trois températures considérées. Les valeurs de $c(r)$ utilisées sont celles représentées sur la Fig. 4.

Equation HNC

L'équation HNC (5) nous fournit la fonction $V(r)$ représentée également sur la Fig. 6. Les valeurs de $c(r)$ utilisées sont celles représentées sur la Fig. 4. Plusieurs raisons donnent à penser que les potentiels ainsi obtenus ne représentent pas correctement les interactions atomiques dans le cuivre liquide:

1. On remarque que pour les trois potentiels obtenus, le minimum se produit pour $r = r_m \simeq 3{,}35$ Å. Le maximum de $g(r)$ a lieu pour $r = 2{,}55$ Å, valeur qui correspond bien à la distance entre plus proches voisins. Comme les deux distances doivent être sensiblement identiques, on en conclut que la valeur obtenue pour r_m est nettement trop élevée.

2. Le minimum ϵ de $V(r)$ varie suivant les cas entre 0,4 et 0,65 eV. Cette valeur est trop forte car si on calcule $g(r)$ en prenant $\epsilon \simeq 0{,}5$ eV[13, 14] on obtient des valeurs correspondant à l'état solide.

La Fig. 7 montre pour $T = 1300$°C les potentiels $V(r)$ déduits de l'équation HNC et correspondant aux trois formes possibles de $c(r)$ montrées sur la Fig. 5. Il est ainsi clair qu'il est difficile de conclure quant à l'existence d'oscillations de longue portée dans le potentiel de paire $V(r)$.

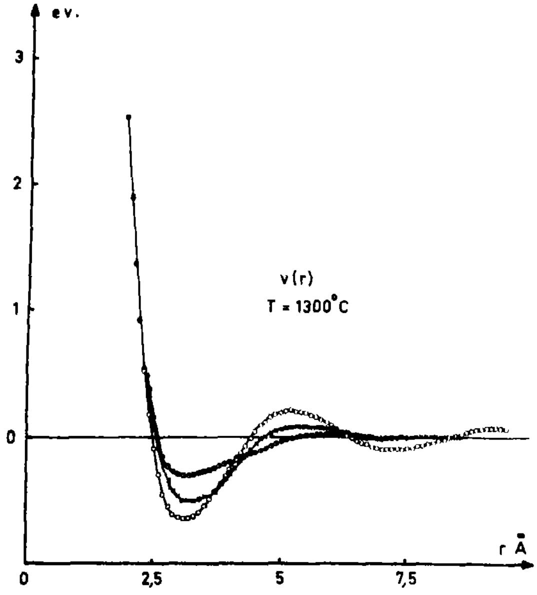

Fig. 7. Variation à $T = 1300$°C du potentiel $V(r)$ déduit de l'équation HNC et correspondant aux trois formes possibles de $c(r)$ montrées sur la Fig. 5.

De plus, même en faisant varier $i(k)$ dans les limites tolérées par l'expérience, les potentiels $V(r)$ fournis par l'équation HNC présentent toujours les mêmes caractéristiques (r_m et ϵ trop grands) qui les rendent inacceptables pour décrire les interactions atomiques dans le cuivre liquide.

6. CONCLUSION

Nous avons mesuré expérimentalement la fonction $i(k)$ du cuivre liquide à diverses températures et nous en avons déduit la fonction de distribution de paire $g(r)$ et la fonction de corrélation directe $c(r)$ à ces mêmes températures par inversion de Fourier. Une étude de la dépendance en température du maximum de $i(k)$ a montré que celui-ci suit une loi en $1/T$.

A partir des valeurs de $g(r)$ et de $c(r)$ nous avons essayé de déterminer le potentiel de paire $V(r)$. Les résultats fournis par les équations approchées de Percus–Yevick et de HNC n'étant pas satisfaisants, nous sommes amenés à conclure que ces approximations ne conviennent pas au cas du cuivre liquide, rejoignant en cela les conclusions auxquelles aboutissent North *et al.*[11] dans le cas du plomb.

Par une succession de transformations de Fourier, Schiff[15] a vérifié que nos résultats expérimentaux sont compatibles avec la condition $g(r) = 0$ pour $r < 2$ Å[16, 17]. La Fig. 8 compare la courbe $i(k)$ expérimentale à une courbe $i(k)$ qui ferait pratiquement disparaître les oscillations de $g(r)$ pour r petit.

La partie répulsive du potentiel correspond donc bien à un modèle de sphères dures de diamètre $\sigma = 2{,}2$ Å, mais il n'est pas possible de conclure quant à l'existence d'oscillations

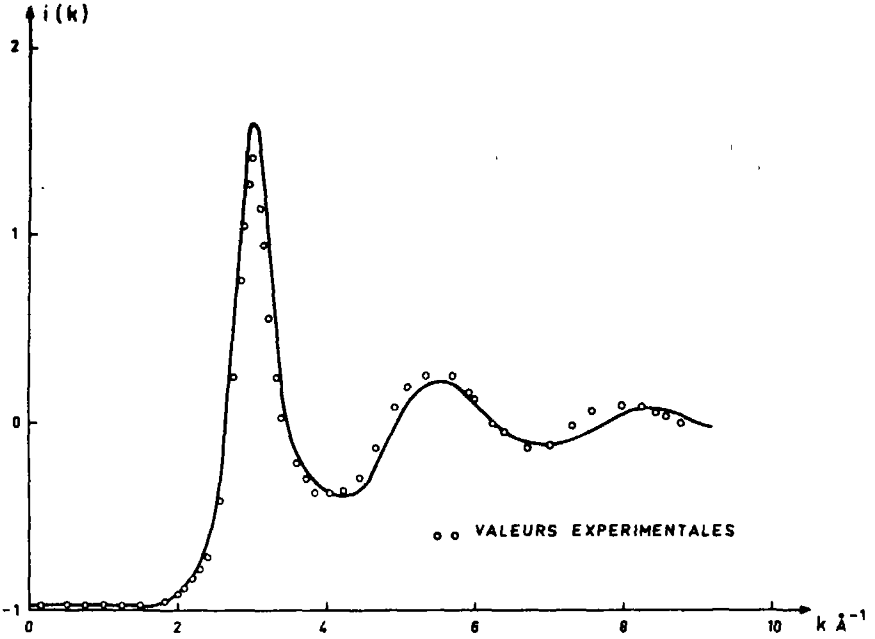

Fig. 8. Comparison des courbes $i(k)$ expérimentale et théorique.

de longue portée. Il semble bien qu'actuellement on soit davantage en mesure de déterminer la partie répulsive du potentiel que sa partie asymptotique. Nous avons entrepris de nouvelles expériences concernant certaines terres rares (La,Ce) et plusieurs métaux de transition (Ni, Fe, Cr)[18] pour étudier en particulier une influence possible de l'anisotropie des liaisons électroniques sur les courbes de diffusion $i(k)$.

Remerciements—Les auteurs remercient vivement Madame F. Cyrot pour de nombreuses et fructueuses discussions, D. Schiff qui a bien voulu nous communiquer la courbe n° 8 et Monsieur M. Tournarie qui s'est chargé de la programmation des calculs de transformée de Fourier effectués sur l'ordinateur IBM 360/75 du C.E.N., Saclay.

REFERENCES

1. YVON J., *La Théorie Statistique des Fluides et l'Equation d'Etat.* Act. Sci. Ind. Hermann, Paris (1935).
2. BORN M. et GREEN H. S., *Proc. R. Soc.* **A190**, 455 (1947).
3. GREEN H. S., *Molecular Theory of Fluids*, North-Holland, Amsterdam (1952).
4. ZERNICKE F. et PRINS J., *Z. Phys.* **41**, 184 (1927).
5. DEBYE P. et MENKE H., *Phys. Z.* **31**, 797 (1930).
6. GINGRICH N. S. *Rev. mod. Phys.* **15**, 90 (1943).
7. GUINIER A., *Théorie et Technique de la Radiocristallographie.* Dunod, Paris (1956).
8. ZERNICKE F. et ORNSTEIN L. S., *Proc. Acad. Sci. Amst.* **17**, 793 (1914).
9. LEVESQUE D., *Physica* **32**, 1985 (1966).
10. RICE S. A. et GRAY P., *The Statistical Mechanics of Simple Liquids.* Wiley, New York (1965).
11. NORTH D. M., ENDERBY J. E. et EGELSTAFF P. A., *Proc. phys. Soc. C*, série 2, **1**, 1075 (1968).
12. EGELSTAFF P. A., *Comptes Rendus de la Conférence de Brookhaven.* Taylor, London (1966).
13. de BOER J., *Rep. Progr. Phys.* **12**, 355 (1949).
14. MONTROLL E. W. et MAYER J. E., *J. chem. Phys.* **9**, 626 (1941).
15. SCHIFF D., Communication privée.
16. RAHMAN A., *J. chem. Phys.* **42**, 10, 3540 (1965).
17. KAPLOW R., STRONG S. L. et AVERBACH B. L., *Phys. Rev.* **138A**, 1336 (1965).
18. BREUIL M. et TOURAND G., *Phys. Lett.* **29A**, 506 (1969).

J. Phys. Chem. Solids Pergamon Press 1970. Vol. 31, pp. 559–565. Printed in Great Britain.

ÜBER DIE PRÄPARATION UND DAS SUPRALEITENDE VERHALTEN VON $CeRu_2$ UND SEINER Gd-, Mn-, Fe-, Co- UND Ni-HALTIGEN MISCHPHASEN

M. WILHELM und B. HILLENBRAND
Forschungslaboratorium Erlangen der Siemens AG, Erlangen, Germany

(*Received* 16 *May* 1969)

Zusammenfassung – Durch geeignete Glühbehandlung wurden einphasige Proben von $CeRu_2$ und homogene Mischkristalle des Typs $Ce_{1-x}Gd_xRu_2$ und $CeRu_{2-x}Me_x$ (Me = Mn, Fe, Co, Ni) hergestellt. Reines $CeRu_2$ hat einen Sprungpunkt von 6,2°K. Die T_c-Absenkung bei Zusatz von Gd ist proportional zur 4. Potenz der $GdRu_2$-Konzentration. Bis etwa 13 Mol.% $GdRu_2$ sind die Mischkristalle supraleitend ($T_c \approx 3{,}8$°K), bei höheren Konzentrationen werden die Proben ferromagnetisch. Bei Zugabe von $CeMe_2$ erfolgt eine praktisch lineare T_c-Absenkung, die für Me = Fe und Mn etwa 10 mal größer ist als bei Me = Co und Ni. Geringe Mengen Fe in dem für die Präparation verwendeten Cer wurden durch Zonenschmelzen entfernt.

Abstract – Single phase samples of $CeRu_2$ and homogeneous mixed crystals of the formula $Ce_{1-x}Gd_xRu_2$ and $CeRu_{2-x}Me_x$ (Me = Mn, Fe, Co, Ni) have been prepared by means of an appropriate annealing process. Pure $CeRu_2$ becomes superconducting at $T_c = 6{,}2$°K. In mixed crystals $Ce_{1-x}Gd_xRu_2$, T_c decreases proportional to the fourth power of the $GdRu_2$ concentration. Superconductivity extends up to the amount of about 13 mol.% $GdRu_2$ ($T_c \approx 3{,}8$°K); alloys exceeding this concentration are ferromagnetic. When adding $CeMe_2$ a linear depression of T_c has been observed. The gradient of this depression is about one order of magnitude greater with Me = Fe or Mn than with Me = Co or Ni. Small amounts of iron which were present in the available cerium metal have been removed by zone melting.

1. EINLEITUNG

DER EINFLUß magnetischer Ionen auf verschiedene Eigenschaften eines Supraleiters wie T_c, die Energielücke, den Meißnerzustand, die Magnetisierungskurve und die kritischen Felder ist in den letzten zehn Jahren Gegenstand zahlreicher experimenteller und theoretischer Untersuchungen gewesen. Es zeigte sich, daß die Theorie, die von Abrikosov und Gorkov[1] aufgestellt und von einer Reihe von Autoren weiterentwickelt wurde, die experimentellen Ergebnisse qualitativ und meist auch quantitativ recht gut beschreibt. So findet sich z. B. in fast allen untersuchten Systemen eine starke T_c-Absenkung schon bei geringen Zusätzen magnetischer Ionen, und bei Beimengungen von ca. 1 Mol.% ist die Supraleitung meist ganz unterdrückt.

Eine Ausnahme macht offensichtlich die Mischkristallreihe $Ce_{1-x}Gd_xRu_2$. Hier wurde von Matthias, Suhl und Corenzwit[2] nur ein schwacher T_c-Abfall mit wachsender $GdRu_2$-Konzentration gefunden. Bei 1 Mol% geben die Autoren sogar eine leichte T_c-Erhöhung an. Auch bei Bozorth, Davis und Williams[3] ist T_c nur wenig von dem $GdRu_2$-Gehalt abhängig. Beide Autorengruppen finden außerdem, daß in einem gewissen Konzentrationsbereich Proben zunächst ferromagnetisch (FM) und dann supraleitend (SL) werden. Die Angaben über die Präparation sind spärlich. In [2] fehlen sie ganz, in [3] wurden die Proben offensichtlich aus der Schmelze abgeschreckt; röntgenographisch wurde festgestellt, daß es sich um feste

Lösungen handelt, die manchmal noch Spuren von elementarem Ru enthalten. Von Matthias und Mitarbeitern[2] wird auch die Möglichkeit nicht ausgeschlossen, daß SL und FM nicht im gleichen Volumenelement vorkommen. Theoretische Überlegungen[4] schließen eine Koexistenz von SL und FM nicht aus.

Wir haben die Untersuchungen an $CeRu_2$ und an Gd-, Mn-, Fe-, Co- und Ni-haltigen Mischkristallen dieser Verbindung aufgegriffen, um das anomale T_c-Verhalten näher zu untersuchen. Die Literaturwerte für T_c von reinem $CeRu_2$ schwanken zwischen 5°K[2, 3] und 6°K[5] und lassen vermuten, daß die Präparationsmethode bzw. der Reinheitsgrad der Ausgangssubstanzen von Einfluß ist. Sorgfältige metallographische Untersuchungen sind auch die Voraussetzung, um in der Frage der Koexistenz von SL und FM im gleichen Volumenelement entscheiden zu können. Vor allem sollte sichergestellt werden, daß die Verteilung der Legierungspartner in den Mischphasen homogen erfolgt ist.

Die intermetallischen Verbindungen $CeRu_2$, $CeFe_2$, $CeCo_2$ und $CeNi_2$ sind kubische Laves-Phasen vom $MgCu_2$-Typ; $GdRu_2$ kristallisiert hexagonal im $MgZn_2$-Gitter [6–8]. $CeCo_2$ wird unterhalb 1,4°K supraleitend[9]; $GdRu_2$ und $CeFe_2$ sind ferromagnetisch mit Curie-Temperaturen von rund 80° bzw. 235°K[6, 10]. $CeNi_2$ weist temperaturunabhängigen Paramagnetismus auf[11]. Eine intermetallische Verbindung $CeMn_2$ ist nicht bekannt.

2. AUSGANGSSTOFFE UND PRÄPARATION

Als Ausgangsstoffe für die von uns hergestellten Verbindungen und Mischkristalle dienten Ce 99,9%*, Fe 99,998%, Co 99,998% und Ni 99,998% (Koch Light Laboratories Ltd.), Gd 99,9% (Johnson, Matthey u. Co., Ltd.) und Ru 99,99% (W. C. Heraeus GmbH).

Von diesen Metallen wurde Cer wegen seines bei rund 0,1% liegenden Fe- und Si-Gehaltes einer nachträglichen Reinigung durch Zonenschmelzen unterworfen. Es wurde 10–20 mal im wassergekühlten Kupferschiff unter Argon mit einer Geschwindigkeit von 0·5 mm/min gezogen. Das Schmelzen des Cers erfolgte mittels Induktionsheizung. In nachgereinigtem Cer konnten durch Spektralanalyse keine metallischen Verunreinigungen mehr nachgewiesen werden.

Zur Synthese der reinen Laves-Phasen wurden der Formel AB_2 (A = Ce, Gd; B = Fe, Co, Ni, Ru) ensprechende Mengen der Elemente mittels Induktionsheizung auf wassergekühltem Kupfer unter Argon verschmolzen. $CeFe_2$, $CeCo_2$, $CeNi_2$ und $CeRu_2$ bilden sich peritektisch. Um den unvollständigen Ablauf der peritektischen Reaktion zu beenden, wurden die nach Abschrecken ihrer homogenen Schmelzen erhaltenen Proben von $CeRu_2$ 15 min bei 1330°C, von $CeFe_2$ und $CeNi_2$ 48 h bei 720°C bzw. 780°C und von $CeCo_2$ 60 min bei 950°C getempert. Abbildung 1 zeigt das typische Abschreckgefüge von $CeRu_2$: Die weißen Kristalle rühren von primär ausgeschiedenem Ru her; sie sind umgeben von grauem $CeRu_2$, an dessen Rändern sich – im Bild schwarz – die eutektische Restschmelze aus β-Ce und $CeRu_2$ anschließt[12]. Änlich sehen die Abschreckgefüge der übrigen Ce-haltigen kubischen Laves-Phasen aus. Stets werden durch rasches Abkühlen der Schmelzen auf wasserdurchflossener Kupferunterlage dreiphasige Gefüge aus Ce-armen Primärkristallen, der gewünschten Laves-Phase und eutektischer Restschmelze besthend aus Laves-Phase und einer Ce-reichen intermetallischen Verbindung bzw. elementarem Ce erhalten. Abbildung 2 zeigt das Korngefüge von $CeRu_2$ nach dem Tempern; Ru und eutektische Restschmelze sind verschwunden.

$GdRu_2$ kristallisiert dagegen offenbar als Verbindung mit offenem Maximum, da das Abschreckgefüge bereits einphasig erscheint und überschüssiges Ru nicht in Form primärer

---

*Reinheitsgrade nach Angaben der Lieferfirmen.

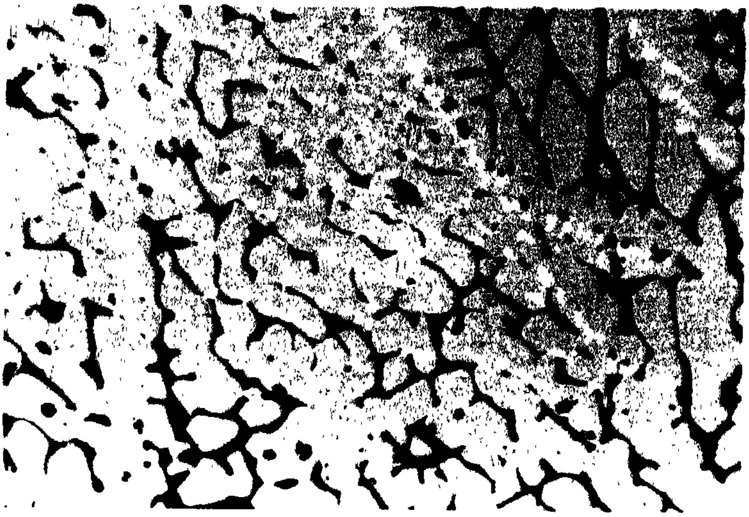

Abb. 1. Gefüge einer von 1800°C abgeschreckten $CeRu_2$Probe: primäre Ru-Kristalle (weiß), $CeRu_2$ (grau), eutektische Restschmelze aus β-Ce und $CeRu_2$ (schwarz); 200 mal.

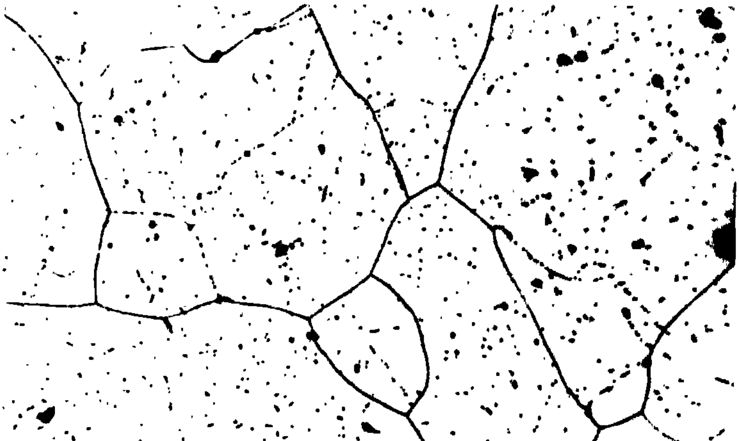

Abb. 2. Korngefüge von $CeRu_2$ nach 15 min bei 1330°C; die schwarzen Punkte rühren von Ceroxid-Einschlüssen her; 200 mal.

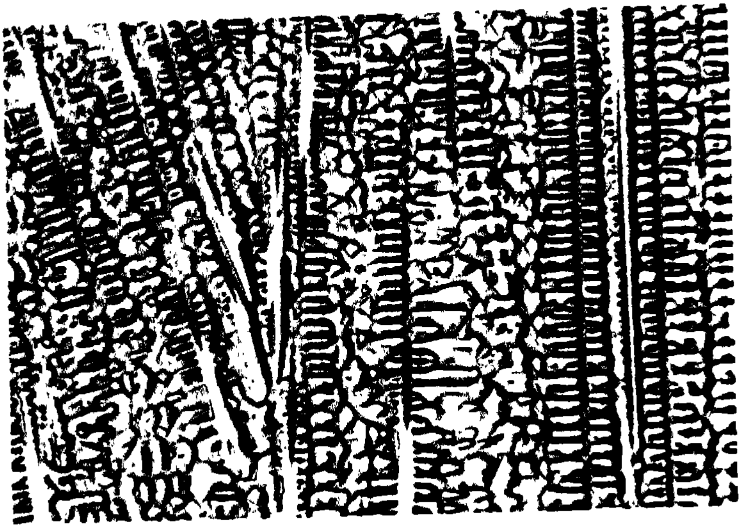

Abb. 3. Dendritisches Abschreckgefüge des Mischkristalls $Ce_{0.9}Gd_{0.1}Ru_2$; durch Ätzen sichtbar gemachte inhomogene Verteilung von Gd in $CeRu_2$; 200 mal.

Dendriten ausgeschieden wird, sondern ein Eutektikum mit $GdRu_2$ bildet.

Mischkristalle vom Typ $Gd_xCe_{1-x}Ru_2$ und $CeRu_{2-x}Me_x$ (Me = Fe, Co, Ni) wurden durch Verschmelzen entsprechender Mengen Ce, Ru und $GdRu_2$ bzw. $CeMe_2$ hergestellt. Mn-haltige Mischphasen wurden in direkter Synthese aus Ce, Ru und Mn bzw. bei kleinen Mn-Gehalten aus Ce, Ru und einer Vorlegierung $CeRu_{1,9}Mn_{0,1}$ erhalten. Die Werte für x schwankten bei den Gd-haltigen Mischkristallen zwischen 0,01 und 0,25, bei den Me-haltigen zwischen 0,002 und 0,2. Die abgeschreckten Legierungen vom Typ $Gd_xCe_{1-x}Ru_2$ wurden 15 min bei 1330°C, dann 90 min bei 1350°C, Legierungen vom Typ $CeRu_{2-x}Me_x$ 90 min bei 1310°C geglüht.

Legierungen mit $\geqq 10$ Mol.% $GdRu_2$ enthielten bereits nach dem Abschrecken von 1800°C erheblich weniger Ru und eutektische Restschmelze als Legierungen mit kleineren Gd-Gehalten bzw. als reines $CeRu_2$. Wurden polierte Proben in 20 proz. HNO_3 etwa 2 min lang elektrolytisch geätzt ($i = 50\ mA/cm^2$), entstanden Gefügebilder von Art der Abb. 3, die typisch sind für sog. Zonenkristalle. Die Erstarrung der Legierung erfolgte so rasch, daß sich während der Kristallisation auftretende Unterschiede der Gd-Konzentration durch Diffusion nicht ausgleichen konnten. Nach dem Tempern hatte sich eine Gd-Verteilung eingestellt, die keinen bevorzugten Ätzangriff bestimmter Bereiche mehr erlaubte. Geätzte Probenanschliffe entsprachen ganz der Abb. 2. Unterschiedlicher Ätzangriff von Gd-haltigen Mischkristallen im abgeschreckten Zustand wurde selbst bei Legierungen mit 1 Mol.% $GdRu_2$ noch beobachtet. Auch Mischphasen vom Typ $CeRu_{2-x}Me_x$, deren Schmelzen rasch abgekühlt worden sind, entwickeln beim anodischen Ätzen in HNO_3 das typisch dendritische Gefüge der Zonenkristalle.

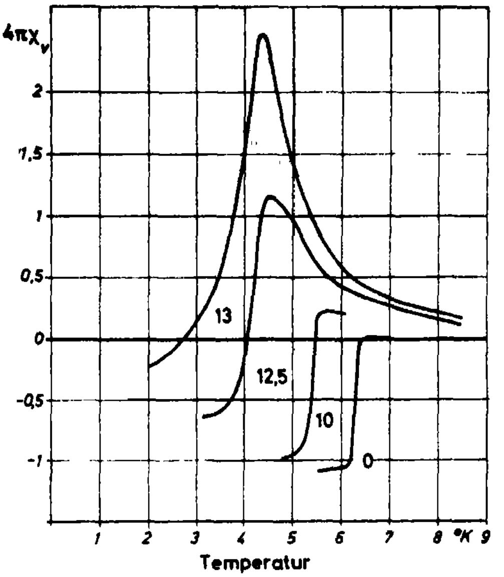

Abb. 4. Änderung der Anfangssuszeptibilität in Mischkristallen $Ce_{1-x}Gd_xRu_2$ als Funktion der Temperatur; Kurvenparameter ist die Konzentration an $GdRu_2$ in Mol.%.

Ein wesentlicher Unterschied zwischen den abgeschreckten Mischkristallen vom Typ $Gd_{0,1}Ce_{0,9}Ru_2$ und $CeRu_{1,9}Me_{0,1}$(Me = Fe, Co, Ni) besteht darin, daß bei letzteren Korngrenzen stets mit Kristallbereichen zusammenfallen, die infolge unterschiedlichen Angriffs der Ätzlösung die größten Niveauunterschiede aufweisen. Häufig werden an diesen Stellen sogar Ausscheidungen metallischer Phasen beobachtet. Möglicherweise kommt es infolge Anreicherung von Eisen, Kobalt oder Nickel in den Randbezirken der Körner zur Segregation Fe-, Co- bzw. Ni-haltiger Phasen. Abschreckgefüge der Gd-haltigen Mischkristalle weisen dagegen keine Anreicherung von Fremdphasen an Korngrenzen auf. Der Verlauf ihrer Korngrenzen steht auch in keinem Zusammenhang mit dem Ätzmuster der anodisch oxydierten Proben. Es liegt nahe anzunehmen, daß Fe, Co und Ni mit Verteilungskoeffizienten $k < 1$, Gd dagegen mit $k > 1$ in $CeRu_2$ eingebaut werden.

Alle Mischphasen zeigten noch das kubische Gitter der $CeRu_2$-Matrix.

3. MESSMETHODE

Die Sprungtemperaturen T_c und Curie-

Temperaturen θ_c wurden magnetisch mit Hilfe der Anfangssuszeptibilität bestimmt. Dazu wurden die Präparate, die gepulvert mit einer Teilchengröße von 10 bis 100 μ vorlagen, in eine Spule gesteckt und deren Induktivitätsänderung als Funktion der Temperatur gemessen. Die Meßfrequenz betrug 860 Hz, die Magnetfeldamplitude einige Zehntel Oe.

Bei Übergang der Probe zur *SL* erniedrigt sich die Induktivität der Spule. Mit Hilfe eines Nb-Stäbchens wurde die Induktivitätsabnahme pro supraleitendes Volumen bestimmt und mit diesem Wert die Induktivitätsänderungen normiert. Es wird dann das Verhältnis $\chi_v/|\chi_{SL}| = 4\pi\chi_v$ gewonnen, wobei χ_v die gemessene mittlere Volumensuszeptibilität und $|\chi_{SL}| = 1/4\pi$ die Volumensuszeptibilität eines *SL* ist. Bei nichtmagnetischen Proben ist $-4\pi\chi_v = (V_{SL})/(V_0)$ (V_{SL} = supraleitender Volumenteil, V_0 = Gesamtvolumen der Probe). Diese Beziehung ist allerdings nicht sehr genau, weil einmal der Packungsfaktor der Pulverpräparate nicht bekannt ist und weil die Meßspule relativ kurz und weit ist, so daß die Bewertung des Volumenelementes einer Probe noch von seiner Lage auf der Spulenachse etwas abhängt. T_c ist definiert als die Temperatur, bei der der halbe Übergang erfolgt ist. Wenn vor Einsatz der *SL* eine paramagnetische Vorverstimmung vorlag, wurde die Übergangshöhe vom Induktivitätsmaximum aus genommen.

Bei Proben mit höherem Gd-Gehalt trat ein Induktivitäts-, d.h. Suszeptibilitätsmaximum auf. Bis zu den tiefsten uns erreichbaren Temperaturen blieb eine paramagnetische Verstimmung. Die Temperatur des Maximums nannten wir dann θ_c. Vorläufige Curiepunktsbestimmungen nach der Forrer-Weiß-Methode bzw. $H/M./.M^2$-Methode lieferten die gleichen Curie-Temperaturen mit Abweichungen $\leqq 0,3$°K.

4. ERGEBNISSE

(a) *Substitution auf* Ce-*Plätzen*

In Abb. 4 sind einige Beispiele für Sprungkurven wiedergegeben. Bei niedrigem Gd-Gehalt betragen die Übergangsbreiten etwa 0,2°–0,3°K, und es wird offensichtlich das Gesamtvolumen supraleitend. Bei höheren Gd-Gehalten zeigte sich eine paramagnetische Vorverstimmung, der Übergang wird breiter, und es wird auch nicht mehr $4\pi\chi_v \approx -1$, wie es bei vollständiger Volumensupraleitung sein sollte. Für das zuletztgenannte Ergebnis kann es mehrere Gründe geben. Vielleicht

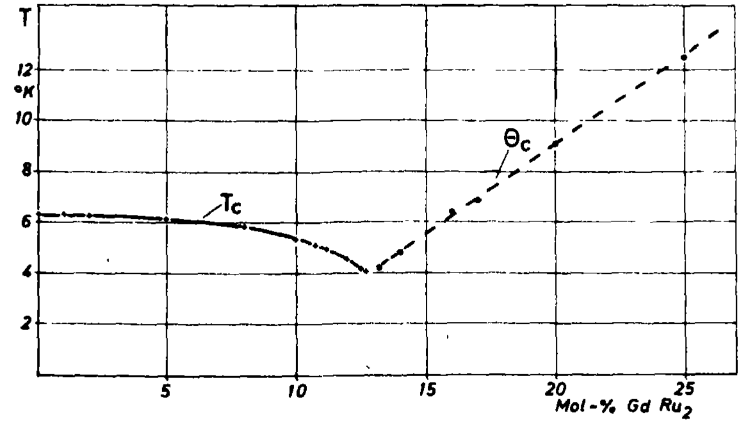

Abb. 5. Verlauf der Sprungtemperatur T_c und der Curie-Temperatur θ_c als Funktion der GdRu$_2$-Konzentration im System Ce$_{1-x}$Gd$_x$Ru$_2$.

war die Temperatur nicht tief genug, doch erwecken die Übergangskurven nicht diesen Eindruck. Trotz der kleinen Feldamplituden kann das Feld lokal an Spitzen in die Probenkörner eindringen, und wegen der paramagnetischen Eigenschaften dieser Volumenanteile wird χ_v dann angehoben. Aus dem Wert $(4\pi\chi_v)_{\text{max.}} = 6$ bei Probe 184 T (siehe Abb. 7) kann man abschätzen, daß mehr als 12 Volumenprozent vom lokal eindringenden Feld erfaßt sein müßten, um $4\pi\chi_v$ auf-0,2 zu bringen, wie es bei der Probe mit 13,0 Mol% $GdRu_2$ der Fall ist (Abb. 4). Das scheint uns reichlich viel. Eine andere mögliche Ursache wird weiter unten angeführt.

In Abb. 5 ist links T_c gegen die Gd-Konzentration c in Mol.% aufgetragen. Man sieht, daß für $c \rightarrow 0$ T_c mit horizontaler Tangente einmündet. Es zeigte sich, daß T_c mit der 4. Potenz der Konzentration abfällt. Empirisch gilt also die Relation

$$T_c = T_{c0} - \alpha c^4 \qquad (1)$$

mit $\alpha = 0{,}835 \cdot 10^{-4}$ (°K/(Mol.%)^4.

Daraus errechnet sich, daß T_c bei $c_{kr} =$ 16,5 Mol.% verschwindet.

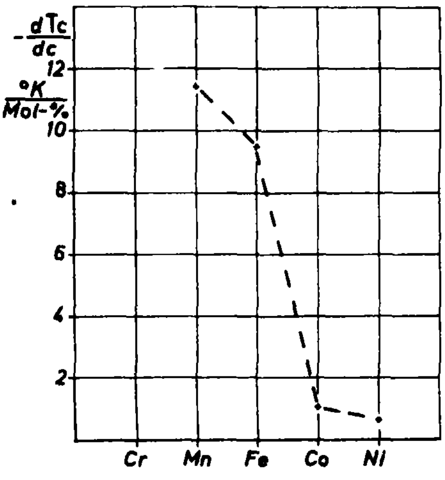

Abb. 6. Gradient der T_c-Absenkung in Mischkristallen $CeRu_{2-x}Me_x$ (Me = Mn, Fe, Co, Ni).

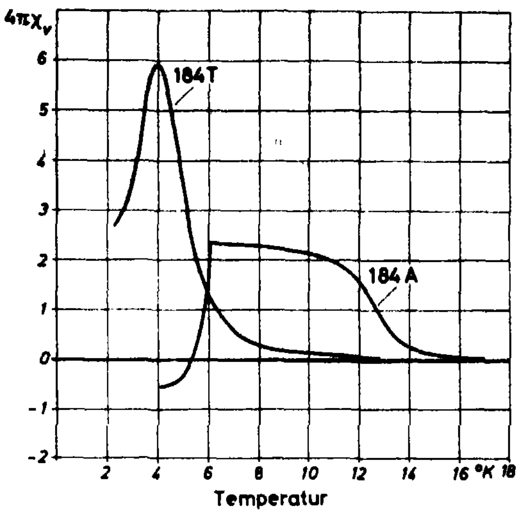

Abb. 7. Anfangssuszeptibilität $4\pi\chi_v$, als Funktion der Temperatur für eine durch Glühen homogenisierte (184°T) und eine abgeschreckte Probe (184°A) der Zusammensetzung $Ce_{0,86}Gd_{0,14}Ru_2$.

(b) *Substitution auf* Ru-*Plätzen*

Nimmt man Substitutionen auf Ru-Plätzen vor, so ist der Einfluß auf T_c wesentlich größer. Wir erhielten bei Zusatz von Ni, Cr, Fe und Mn T_c-Absenkungen, die linear von der Konzentration abhängen. In Abb. 6 sind die Steigungen $-(dT_c/dc)$ bei Zusatz dieser Elemente aufgetragen. Bei Ni und Co, die offensichtlich keine lokalen Momente bilden, ist $-(dT_c/dc)$ von der Größenordnung 1, bei Fe und Mn dagegen ca. 10. Bei Fe und Mn liegt also ein Verhalten vor, wie man es bei Zusatz magnetischer Ionen zu einem *SL* gewohnt ist.

(c) *Magnetisches Verhalten*

In Abb. 5 ist auch θ_c als Funktion der $GdRu_2$-Konzentration aufgetragen. Die Meßpunkte liegen auf einer Geraden, deren Verlängerung die Abszisse bei 8 Mol.% schneidet. Die Molekularfeldbeschreibung [13] liefert Curie-Temperaturen, die linear von der Konzentration magnetischer Ionen abhängt, doch sollte die Gerade durch den Nullpunkt gehen. Die Proben, für die ein θ_c angegeben ist, behalten auch bis 1,8°K ein $\chi_v > 0$. Eine Sonderstellung nimmt die Probe mit 13,2 Mol.% ein. Die Temperatur, bei der für diese Probe die Suszeptibilität ein Maximum hat, liegt einerseits auf der θ_c-Geraden, andererseits aber auch auf der Kurve, die T_{max} verbindet. T_{max} ist dabei die Temperatur, bei der die Suszeptibilität wegen der paramagnetischen Vorverstimmung vor dem Übergang in die *SL* ein Maximum annimmt (siehe Abb. 4). Außerdem ist die Suszeptibilität bei 1,8°K praktisch wieder Null geworden. Bei 13,2 Mol.% $GdRu_2$-Gehalt liegt man offensichtlich an der Stelle, wo T_c und θ_c aneinanderstoßen. Der Übergang in den supraleitenden bzw. ferromagnetischen Zustand bei gegebener Konzentration c_0 erfolgt in einem Temperaturintervall $\Delta T \neq 0$, *z. B.* deswegen, weil statistische Konzentrationsschwankungen in den für die *SL* bzw. den FM charakteristischen Volumina auftreten. (Für die *SL* ist das charakteristische Volumen etwa ξ^3, $\xi =$ Kohärenzlänge). Bereiche mit $c > c_0$ werden ferromagnetisch, mit $c < c_0$ supraleitend, wobei noch mit einer zusätzlichen Komplikation durch den Proximity-Effekt zu rechnen ist. Insgesamt ist aber dort, wo *SL* und *FM* aneinanderstoßen, mit einem Gemenge von supraleitenden und ferromagnetischen Volumenanteilen zu rechnen; das mag mit dazu beitragen, daß bei höheren $GdRu_2$-Konzentrationen $4\pi\chi_v$ nicht mehr den Wert -1 erreicht (Abb. 4). Diese Erklärung schließt ein, daß ferromagnetische Volumenanteile erst bei tieferer Temperatur oder gar nicht mehr supraleitend werden. In diesem Zusammenhang soll erwähnt werden, daß bei der Konzentration, bei der $T_c = \theta_c$ wird, auch $|dT_c/dc| = (d\theta_c/d_c)$ ist.

Ein räumliches Nebeneinander von Gd-reicheren und Gd-ärmeren Bereichen erhält man, wenn man die Proben einfach aus der Schmelze abschreckt (Abb. 3). Mit der Probe 184 (14 Mol.% $GdRu_2$) wurde folgendes Experiment gemacht: Nach dem Abschrecken aus der Schmelze wurde eine Hälfte zerpulvert und vermessen (184 A), die andere Hälfte wurde wie üblich homogenisiert, zerpulvert und dann vermessen (184 T). In Abb. 7 ist für diese Proben $4\pi\chi_v$ als Funktion der Temperatur aufgetragen. Probe 184 T zeigt das normale Verhalten der homogenen Proben, ein Maximum der Suszeptibilität, die eindeutig im paramagnetischen Bereich bleibt (θ_c von 184 T liegt etwas unterhalb der θ_c-Geraden in Abb. 5, vermutlich wurde das Gd bei der Probenteilung ungleich aufgeteilt). Wenn *SL* auf der Verlängerung der T_c-Kurve (Abb. 5) auftreten würde, so müßte bei etwa 3°K eine deutliche Abnahme von $4\pi\chi_v$ erfolgen. Probe 184 A zeigt einen starken Suszeptibilitätsanstieg, der eine maximale, lokale $GdRu_2$-Konzentration von 23 Mol.% vermuten läßt. Bei etwa 5,8°K erfolgt ein Übergang in die *SL*, dazu gehören 8 Mol.% $GdRu_2$, $4\pi\chi_v$ erreicht nicht den Wert 1, doch ist das auch nicht zu erwarten, wenn ferromagnetische Bereiche in dem Pulverpräparat nicht abgeschirmt werden.

5. DISKUSSION

Das auffälligste Verhalten von $CeRu_2$ und seiner Mischkristalle besteht darin, daß bei Substitution von magnetischen Ionen (Gd) auf Ce-Plätzen nicht die in *c* lineare T_c-Absenkung auftritt, die von der Theorie vorhergesagt wird, sondern daß $(dT_c/dc) = 0$ ist. (Bei 1 Mol.% $GdRu_2$ war T_c um 0,05°K höher als bei reinem $CeRu_2$. Ob hier ein echtes Maximum vorliegt, wie es Matthias et al.[2] angeben, oder ob es sich um Schwankungen des Reinheitsgrades der Proben handelt, ist hier nicht von Bedeutung, da der Effekt sehr klein ist). Andererseits bringen Fe und Mn auf Ru-Plätzen eine drastische T_c-Absenkung, selbst die unmagnetischen Co- und Ni-Ionen erniedrigen T_c beträchtlich. Das legt die Annahme nahe, daß die Supraleitung auf das Ru-Untergitter beschränkt ist und daß sie durch Elektronen zustande kommt, die nicht gleichmäßig im Kristall verteilt sind, sondern auf das Ru-Untergitter konzentriert sind. Dafür kommen d-Elektronen in Frage, da diese im allgemeinen stärker lokalisiert sind als s- und p-Elektronen. In $LaAl_2$, das dieselbe Kristallstruktur wie $CeRu_2$ hat, übt Gd einen drastischen Einfluß auf T_c aus [14]. Doch sind beim Al keine d-Elektronen vorhanden. In $Y_{1-x}Gd_xOs_2$[15] gibt es d-Elektronen, und man beobachtet eine in c lineare T_c-Absenkung. Doch handelt es sich um eine hexagonale Laves-Phase mit zwei nicht äquivalenten Os-Plätzen. Weiter sind über die Präparation keine Angaben vorhanden, und (dT_c/dc) ist mit 0,23 (°K/Mol.%) sehr klein. Eine analoge Vorstellung ist auch für Supraleiter entwickelt worden, die in der A15-Struktur kristallisieren, z. B. Nb_3Sn. In diesem Fall soll die Supraleitung an die linearen Nb-Ketten gebunden und von d-Elektronen getragen sein[16]. In $CeRu_2$ sind ebenfalls lineare Ru-Ketten vorhanden.

Warum wir für T_c ein c^4-Gesetz beobachten, können wir nicht erklären. Vielleicht ist es Zufall und die Folge einer Überlagerung verschiedener Ursachen.

Ob Koexistenz von SL und FM im gleichen Volumenelement vorliegt, können wir mit unseren bisherigen Messungen noch nicht entschieden, doch scheint es uns, daß die Literaturangaben darüber im System $Ce_{1-x}Gd_xRu_2$ auf inhomogener Probenzusammensetzung beruhen. Zur Frage der Koexistenz sind noch eine Reihe weiterer Experimente geplant.

Annerkennung – Herrn Professor Dr. Peter, Genf, danken wir für zahlreiche, wertvolle Diskussionen.

LITERATUR

1. ABRIKOSOV A. A. und GORKOV L. P., *Soviet Phys. JETP* **12**, 1243 (1961).
2. MATTHIAS B. T., SUHL H. und CORENZWIT E., *Phys. Rev. Lett.* **1**, 449 (1958).
3. BOZORTH R. M., DAVIS D. D. und WILLIAMS A. J., *Phys. Rev.* **119**, 1570 (1960).
4. GORKOV L. P. und RUSINOV A. I., *Soviet Phys. JETP* **19**, 922 (1964).
5. SMITH T. F. und HARRIS I. R., *J. Phys. Chem. Solids* **28**, 1846 (1967).
6. COMPTON U. B. und MATTHIAS B. T., *Acta crystallogr.* **12**, 651 (1959).
7. FULLING W., MÖLLER K. und VOGEL R., *Z. Metallk.* **34**, 253 (1942).
8. NOWOTNY H., *Z. Metallk.* **34**, 247 (1942).
9. LUO H. L., MAPLE M. B., HARRIS I. R. und SMITH T. F., *Phys. Lett.* **27A**, 519 (1968).
10. FARREL J. und WALLACE W. E., *J. chem. Phys.* **41**, 1524 (1964).
11. SKRABEK E. A. und WALLACE W. E., *J. appl. Phys.* **34**, 1356 (1963).
12. OBROWSKI W., *Z. Metallk.* **53**, 736 (1962).
13. SATO H., ARROTT A. und KIKUCHI R., *J. Phys. Chem. Solids* **10**, 19 (1959).
14. MAPLE M. B., *Phys. Lett.* **26A**, 513 (1968).
15. SUHL H., MATTHIAS B. T. und CORENZWIT E., *J. Phys. Chem. Solids* **11**, 346 (1959).
16. SHULL C. G. und WEDGWOOD F. A., *Phys. Rev. Lett.* **16**, 513 (1966); LABBÉ J., BARISIC S. und FRIEDEL J., *Phys. Rev. Lett.* **19**, 1039 (1967).

J. Phys. Chem. Solids Pergamon Press 1970. Vol. 31, pp. 567–571. Printed in Great Britain.

THE INVESTIGATION OF THE VIBRATIONAL SPECTRUM, OPTICAL CONSTANTS AND IONICITY OF BOND OF $CdGeAs_2$ IN CRYSTAL AND AMORPHOUS PHASES BY I.R. REFLECTION

L. B. ZLATKIN, YU. F. MARKOV, A. I. STEKHANOV* and M. S. SHUR
A. F. Ioffe Physical Technical Institute, USSR Academy of Sciences, Leningrad, U.S.S.R.

(*Received* 9 *January* 1969)

Abstract – I.R. reflectivity is investigated in the frequency region from 2 to 75μ for $T = 295°K$. The measurements show that the changes of the vibrational spectrum take place in the region of the lattice reflection while clear correlation exists in the regions of small (less than 25 μ) and large (higher than 60 μ) wavelengths between the optical constants of $CdGeAs_2$ in crystal and amorphous phase.

The dispersion of the refractive index and dielectrical constant is calculated by Kramers–Kronig and dispersion analysis and the vibrational frequencies have been determined. The qualitative and quantitative parameters of the ionicity of the bond have been estimated. The chemical bond in $CdGeAs_2$ is ionic-covalent with larger degree of covalent part.

INTRODUCTION

THE INVESTIGATION of the physical properties of ternary diamond-type semiconductor compounds is interesting because of the prospects of their practical application. It especially concerns $CdGeAs_2$ (the space group $D_{2d}{}^{12}$, $a = 5{\cdot}943 \pm 0{\cdot}001$ Å, $c/a = 1{\cdot}888$) an isoelectronic analogue InAs and GaAs which is the first diamond-type compound obtained in the amorphous phase.

$CdGeAs_2$ was obtained in crystal and amorphous phase at the laboratory of Professor N. A. Goryunova. The sample preparation was described in paper [1].

The investigated monocrystals of $CdGeAs_2$ had p-type conductivity. The hole concentration and mobility taken from Hall measurements are:

$$p = 4.10^{16}\,\mathrm{cm^{-3}},\ \mu_p = 240\,\mathrm{cm^2/V.sec}$$

the bulk amorphous samples n-type conductivity in the region of $10^{-6} - 10^{-7}\,\Omega^{-1}\,\mathrm{cm^{-1}}$.

This investigation of the i.r. reflection spectra of $CdGeAs_2$ in crystal and amorphous modifications has been carried out with the aim of studying the vibrational spectra of the crystal and amorphous phases, determining longitudinal and transverse optical frequencies and optical constants and analysing on the base of the results obtained the type of chemical bond.

1. THE OVERDAMPED LATTICE VIBRATIONS FOR THE DIAMOND-TYPE SEMICONDUCTORS IN THE AMORPHOUS PHASE

$CdGeAs_2$ has been recently obtained in the amorphous phase which has apparently the tetrahedral atomic coordination. The absence of the distant order in this compound was shown by X-ray method [1].

The i.r. reflection spectra of $CdGeAs_2$ in crystal and amorphous phases have been investigated (for angles of incidence near the normal) in spectral region from 2 to 75μ (Fig. 1).

The measurements in the region $2 \div 25\mu$ were made on the spectrometer ИКС-12 and in the region $20 \div 75\mu$ on the longwave i.r. vacuum spectrometer. The scattering light in the investigated region is not higher than 1 per cent.

The complete understanding of the character of the vibrational spectrum changes in transition from crystal to amorphous phase is not yet attained. In particular it is not clear

---

*Deceased.

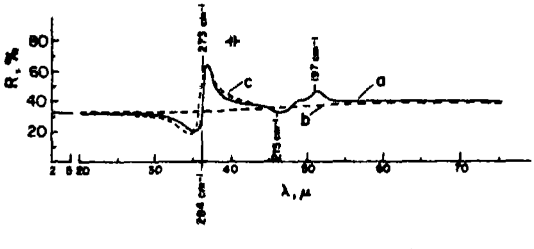

Fig. 1. The i.r. reflectivity spectra for $CdGeAs_2$ ($T = 295°K$). (a) Crystals; (b) amorphous phase; (c) the theoretical curve for the crystal obtained from the dispersion analysis.

whether these changes are considerable or they correspond to the comparatively small shifts and widening of the vibrational bands.

For example a comparative investigation of the density of states $g(\omega)$ for the vibrational spectrum of crystal and amorphous selen[2] has shown that the changes in $g(\omega)$ during the transition from the crystal to amorphous phase correspond to the comparatively small shifts of the maxima of $g(\omega)$.

It can be seen from our experimental data that the vibrational bands are observed only for the crystal $CdGeAs_2$ and are overdamped for $CdGeAs_2$ in amorphous phase (Fig. 1). In the latter case there is only smooth increase of the reflectivity which begins from 35μ, i.e. just from the point where the dispersion connected with the lattice vibrations begins in the crystal. This increase of the reflectivity in amorphous $CdGeAs_2$ results from the addition of the ionic component of the polarization to the electronic one.

The absence of dispersion in the region of lattice vibrations shows that the changes of the vibrational spectra during the transition crystal-amorphous state can be radical.

This result can be connected with the absence of the distant order in the amorphous phase.

2. EXPERIMENTAL DETERMINATION AND CALCULATION OF THE OPTICAL CONSTANTS BY THE KRAMERS-KRONIG AND DISPERSION ANALYSIS

The values of optical ϵ_0 and static ϵ_∞ dielectric constants for the crystal and amorphous phases (see Table 1) were determined directly from the reflectivity spectra.

It should be noted that in [3] the dispersion of refractive index n was determined using the prism method for the crystal ($n = 3{\cdot}4$) and amorphous ($n = 3{\cdot}8$) $CdGeAs_2$ in the regions from 3 to $3{\cdot}5\mu$ and from 2 to 3·5 for crystal and amorphous phases correspondingly. Our results corroborate the data[3] for the amorphous, but not for the crystal phase.

Using Kramers-Kronig and dispersion analysis it is possible to determine the dispersion of real and imaginary parts of the dielectrical constant the refractive index and also the vibrational frequencies.

These two methods supplement each other because the dispersion analysis permits to calculate the optical constants using the approximate (fitted to experimental one) reflectivity and the Kramers-Kronig analysis permits to calculate the approximate values of the optical constants using the exact (in the investigated spectral region but extrapolated beyond its limits) reflectivity.

All the calculations were provided on the BZSU-2 computer. In the Kramer-Kronig calculations the phase angle θ for the reflectivity was determined by equation[4]:

$$\theta(\omega) = \frac{2\omega}{\pi}\int_0^\infty \frac{\ln[\tau(\omega') - \tau(\omega)]}{\omega^2 - \omega'^2} d\omega' \quad (1)$$

where $\tau = \sqrt{R'}$, ω is the frequency. Out of the boundaries of the investigated region we extrapolated reflectivity by the constant values. After the calculation of $\theta(\omega)$ the optical constants were determined:

$$\left.\begin{aligned} n &= \frac{1-\tau^2}{1+\tau^2-2\tau\cos\theta} \\ k &= \frac{2\tau\sin\theta}{1+\tau^2-2\tau\cos\theta} \\ \epsilon' &= n^2 - k^2 \\ \epsilon'' &= 2nk \end{aligned}\right\} \quad (2)$$

The error of the method has been estimated in [5]. It is not more than a few per cent except maybe the small values of k $\leqslant$ 0·1. From that obtained by the Kramers-Kronig method frequency dependence of the optical constants for $CdGeAs_2$ crystal it is possible to determine the vibrational frequencies ω_{l_0} and ω_{t_0} (see Table 1). The zero's of $\epsilon'(\omega)$ function correspond to the frequencies of the longwave optical vibrations and the maxima of $\epsilon''(\omega)$ correspond to the frequencies of the longwave transverse vibrations.

The dispersion analysis has been made for the main (the largest) reflectivity maxima (Fig. 1(c)). The calculation has been carried out using the scheme given in [6]. The optical constants of the crystal obtained from the dispersion analysis (Figs. 2(c),3(c)) corroborate the optical constants obtained from the Kramers-Kronig analysis (Figs. 2(a),3(a)) in the corresponding spectral range though the dispersion analysis made in the approximation of one dispersional oscillator masks the 'non-Lorentz' form of the band which can be seen clearly from the optical constants obtained from the Kramers-Kronig analysis (Fig. 3(a)).

In the region of small wave-lengths (up to 25μ) and large ones (more than 60μ) the clear correlation exists between the optical constants of $CdGeAs_2$ in the crystal and amorphous phase.

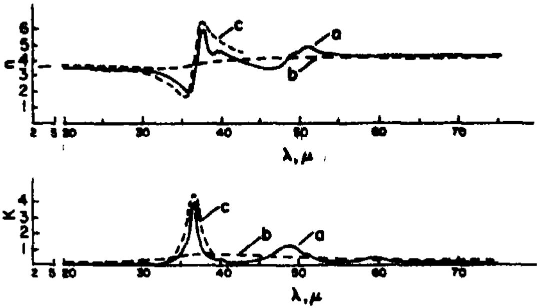

Fig. 2. The dispersion of the real(n) and imaginary (k) part of the refractive index. (a) The curves for the crystal obtained from the Kramers-Kronig analysis; (b) the curves for the amorphous phase obtained from the Kramers-Kronig analysis; (c) the curves for the crystals obtained from the dispersion analysis.

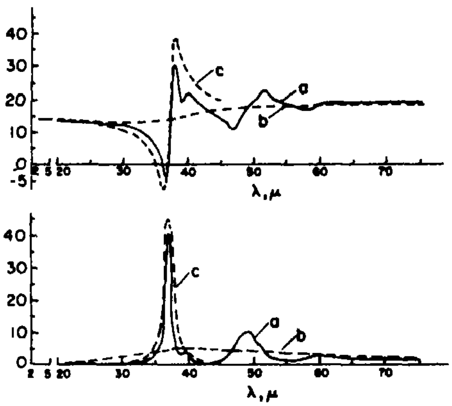

Fig. 3. The dispersion of real (ϵ') and imaginary (ϵ'') part of the dielectrical constant. Abbreviations (a–c) are the same as for Fig. 2.

But as was mentioned in Section 1 the dispersion due to the lattice vibrations is practically absent in the vitreous phase.

Table 1

						Calculated using Kramers-Kronig analysis		Calculated using dispersion analysis		
Compound	Structure	ϵ_0	ϵ_∞	$\Delta\epsilon = \epsilon_0 - \epsilon_\infty$	n	ω_{l_0}	ω_{t_0}	ω_{l_0}	ω_{t_0}	$\frac{e^*}{e}$
$CdGeAs_2$	chalcopyrite	18·7 ±0·5	14·3±0·3	4·4	3·78	278	270	286	270	0·65
$CdGeAs_2$	amorphous	18·2 ±0·5	14·3±0·3	3·9	3·78					
InAs†	sphalerite	14·55±0·3	11·8±0·1	2·7	3·43					0·56
GaAs†	sphalerite	13·13	11·10	2	3·33					0·51

†See Ref. [8].

3. THE DAMPING OF THE DISPERSIONAL OSCILLATOR

The problem of the changes of the vibrational spectrum due to the transformation from crystal to amorphous phase is closely connected with the problem of the band-width has been determined by the phonon life-time. (The life-time in the ideal crystals corresponds to phonon–phonon interaction.)

After investigating $ZnSnP_2$[5] with ordered (chalcopyrite structure) and statistical (sphalerite structure) atoms positions and $CdGeAs_2$ with the large disorder of atoms (amorphous phase) it becomes natural to compare the change of parameter γ characterizing the damping of the dispersional oscillator and connected with the phonon life-time (see Table 2).

This comparison shows that parameter γ is increased with the increase of lattice disorder. It is possibly connected with the decrease of the phonon life-time due to the large scattering in the disordered lattice.

Table 2

Compounds	Structure	γ
$ZnSnP_2$	chalcopyrite	0·06
$CdGeAs_2$	chalcopyrite	0·04
$ZnSnP_2$	sphalerite	0·11
CdGeAs	amorphous phase	> 1

4. THE TYPE OF CHEMICAL BOND

Using the obtained optical constants it is possible to estimate the degree of the bond ionicity in $CdGeAs_2$.

The qualitative estimation can be made using the difference $\Delta\epsilon = \epsilon_0 - \epsilon_\infty$ (see Table 1) which characterizes the contribution of the ionic polarization into the dielectric constant and correspondingly is comparatively large for the ionic crystals and small for the covalent ones. The small value of $\Delta\epsilon$ is sufficient but not essential indication of the covalent bond but the large value of $\Delta\epsilon$ is essential but not sufficient indication of the large ionicity. Indeed the theoretical calculations carried out by Tolpygo[7] for Sic show that the large value of $\Delta\epsilon$ can be observed for the compounds with covalent bonds if the atoms of different kinds have unequal deformation of the electronic orbits due to the lattice vibrations (see also [9,10]).

The obtained value of $\Delta\epsilon$ for $CdGeas_2$ is close to the corresponding values for InAs and GaAs (Table 1) which shows that the bond ionicity is rather small in the ternary diamond-type compound.

As a quantative criterion of the ionicity the dynamical effective charge is usually used. It is possible perhaps to suppose that in crystals with a comparatively simple structure there is a correlation between the 'dynamical effective' charge and 'the effective charge'. In the crystals with a rather complex structure the whole number of limited optical modes can exist and it is necessary to introduce the 'dynamical effective charge' for the every optical mode. That is why it is more difficult to trace such a correlation.

$CdGeAs_2$ crystals have a chalcopyrite structure. The theoretical-group analysis for such a structure[5] shows that two non-degenerate (B_2-type) and six two-fold degenerate (E-type) normal vibrations are i.r. active. In the spectrum (Fig. 1) we observed a considerably small number of bands. Perhaps some of the bands have the small intensity or the structure of the bands can not be solved. It would be possible to consider this problem in detail after the measurements with the polarized light. We estimate the dynamical effective charge using Szigeti formula for the most intensive band:

$$\frac{e^*}{e} = \frac{3\omega_{t_0}}{(\epsilon_\infty + 2)e}\left(\frac{\Delta\epsilon M}{Y\pi N_0}\right)^{1/2}. \qquad (3)$$

Here e^*/e is the ratio of the ionic dynamical effective charge to the electronic charge, N_0 is the number of the ionic pairs in the unit of volume, M is a reduced mass, ω_{t_0} is the frequency of the optical transverse vibration.

ω_{t_0} is determined from the Kramers–Kronig and dispersion analysis data (see Table 1). It is impossible to determine ω_{t_0} from Lyddane-Sachs-Teller relation because in this case several optical modes appear. We also supposed that the ionic charge of Cd and Ge is equal and that the most intensive band corresponds to the vibration of the effective cation sublattice as a whole against the anion sublattice. We assumed the effective cation mass equal to the geometrical average value of the masses of Cd and Ge.

The obtained value $e^*/e = 0{\cdot}65$ for $CdGeAs_2$ crystal is close to the corresponding values for A^3B^5-type compounds which have the effective dynamic charge[8] from 0·42 for InSb to 0·66 for InP which shows that the bond ionicity for $A^2B^4C_2^5$ compounds is approximately the same as for A^3B^5.

Thus the chemical bond of $CdGeAs_2$ is possibly ionic-covalent with a larger covalent component.

Acknowledgements—In conclusion the authors wish to express their gratitude to A. S. Borschevsky and E. O. Osmanov for preparing the samples and N. A. Goryunova and A. I. Gubanov for the discussion of the results.

REFERENCES

1. VAIPOLIN A. A., GOZYUNOVA N. A., OSMANOV E. O. and RUD J. V., *Dokl. Acad. Nauk SSSR* **160**, 633 (1965).
2. KHOTOV B. A., OKUNEVA N. U., REGEL A. R. and SHACKH-BUDAGOV A. L., *Fizika tverd. Tela* **9**, 1227 (1967).
3. TAUC J., ŠTOURAČ L., VORTIČEK V. and ZAVETOVA M., *Intl. Conf. Phys. of Semiconductors*. Moscow 1968.
4. STERN F., *Solid St. Phys.* **5**, 15 (1963).
5. ZLATKIN L. B., MARKOV J. F., STEKHANOV A. I. and SHUR M., *Phys. Status Solidi.* **32**, 473 (1969).
6. SPITZER W. G., KLEINMAN D. A. and WALSH D., *Phys. Rev.* **113**, 127 (1959).
7. TOLPYGO. *Fiz. tverd. Tela* **2**, 2655 (1960).
8. HASS M., In *Semiconductor and Semimetals* (Edited by R. K. Willardson and A. C. Beer) Vol. 3, Chap 1. Academic Press, New York (1967).
9. ZALLEN R., *Phys. Rev.* **173**, 824 (1968).
10. CHEN J. and ZALLEN R., *Phys. Rev.* **173**, 833 (1968).

J. Phys. Chem. Solids Pergamon Press 1970. Vol. 31, pp. 573–574. Printed in Great Britain.

TECHNICAL NOTE

The high pressure compressibility and Grüneisen parameter of strontium titanate*

(*Received* 27 *May* 1969; *in revised form* 8 *August* 1969)

AT TEMPERATURES above 108°K, $SrTiO_3$ is a paraelectric material crystallizing in the cubic perovskite structure. We have measured the compressibility of $SrTiO_3$ and fitted the data to the Murnaghan equation of state. In addition, the Grüneisen parameter calculated from our high pressure compressibility data is compared to the Grüneisen parameter calculated from the zero pressure values of the compressibility, thermal expansion, heat capacity at constant volume, and molar volume.

Data were obtained by means of a diamond anvil high-pressure X-ray diffraction camera described elsewhere[1]. Pressures were determined by observing the shift of the diffraction lines of a 'marker', a material with known compressibility, mixed with the $SrTiO_3$. In this work, CsBr, Al, and V were used as 'markers'. For CsBr, Bridgman's [2] compressibility data were used; for Al and V, the data of Rice *et al.*[3] were used. The $SrTiO_3$ was prepared at this laboratory and was at least 99·99 per cent pure. Samples were prepared for loading in the diamond anvil high-pressure cell by first mixing the $SrTiO_3$ with the appropriate 'marker' and then pressing the powder to about 8 kbar. A small chip from the resultant wafer was used as the high-pressure sample.

In Fig. 1, the relative volume $V/V_0 = a^3/a_0^3$ is plotted vs. pressure where V_0 and a_0 are the unit cell volume and lattice parameter, respectively, at atmospheric pressure. At 298°K and 1 bar, the lattice parameter, a_0, of $SrTiO_3$ is 3·9051 Å[4]. The dashed line in Fig. 1 is an extrapolation of the initial compressibility of $SrTiO_3$ determined from the elastic constants[5] and the solid curve was obtained by a least squares fit of our data to the Murnaghan equation of state[6],

$$P = \frac{B_0}{B_0'}\left\{\left(\frac{V_0}{V}\right)^{B_0'} - 1\right\},$$

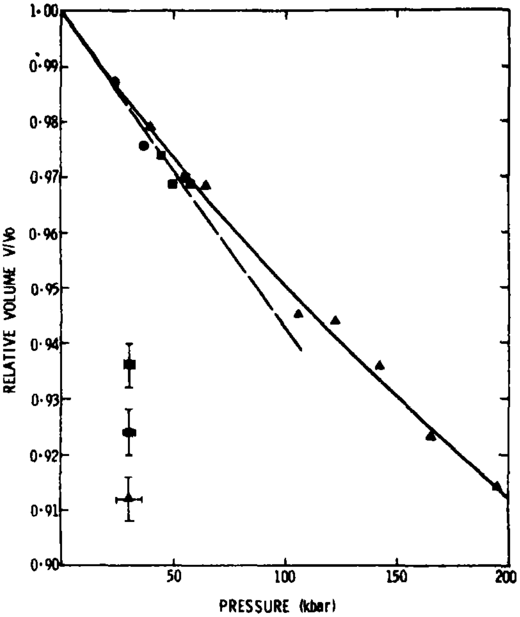

Fig. 1. Relative volume vs. pressure for $SrTiO_3$. Three 'markers', CsBr (●), Al (■), and V (▲), were used to determine pressure. The error bars at the bottom of the figure indicate the uncertainty for each of the 'markers.'

---

*This work was supported by the U.S. Atomic Energy Commission.

where the initial bulk modulus is

$$B_0 = \left\{ -V\left(\frac{\partial P}{\partial V}\right)_T \right\}_{P=0},$$

and the corresponding pressure derivative

$$B_0' = \left\{ \left(\frac{\partial B}{\partial P}\right)_T \right\}_{P=0}.$$

The elastic constants of Bell and Rupprecht [5] were used to calculate $B_0 = 1{\cdot}76 \times 10^3$ kbar and the best fit to our data was obtained with $B_0' = 4{\cdot}4$.

One can determine the Grüneisen parameter for $SrTiO_3$ from the Grüneisen relation[7]

$$\gamma = \frac{\alpha V_m}{\beta C_v},$$

where α is the volume thermal expansion, V_m is the molar volume, β is the compressibility, and C_v is the specific heat at constant volume. At room temperature and atmospheric pressure, the values of the various parameters are $\alpha = 2{\cdot}6 \times 10^{-5}\,{}^\circ K$[8], $\beta = 5{\cdot}67 \times 10^{-13}\,cm^2/dyne$[5], $C_v = 20{\cdot}7$ cal/mole-°K[9] and $V_m = 35{\cdot}7\,cm^3$/mole; using these values, one calculates $\gamma = 1{\cdot}89$. The B_0' obtained from the least squares fitted Murnaghan equation can be used to calculate the Grüneisen parameter by an independent method; Anderson[10] has shown that

$$\gamma = \frac{B_0' - 1}{2}.$$

As mentioned previously, the data was best fit with $B_0' = 4{\cdot}4$, and thus $\gamma = 1{\cdot}7$, in reasonable agreement with the value calculated above.

Acknowledgements—The $SrTiO_3$ sample used in this investigation was kindly provided by J. E. Hesse and J. Matsko of this laboratory. The authors gratefully acknowledge the technical assistance of Clarence Huddle.

Albuquerque,
New Mexico 87115,
U.S.A.

L. R. EDWARDS
R. W. LYNCH

REFERENCES

1. LYNCH R. W., *J. chem. Phys.* **47**, 5180 (1967).
2. BRIDGMAN P. W., *Proc. Am. Acad. Arts. Sci.* **76**, 1 (1945).
3. RICE M. H., McQUEEN R. G. and WALSH J. M., *Solid St. Phys.* **6**, 1 (1965).
4. WYCOFF R. W. G., *Crystal Structures*, p. 394. Wiley, New York (1964).
5. BELL R. O. and RUPPRECHT G., *Phys. Rev.* **129**, 90 (1963).
6. MURNAGHAN F. D., *Proc. natn. Acad. Sci. U.S.A.* **30**, 244 (1944).
7. KITTEL C., *Introduction to Solid State Physics*, p. 154. Wiley, New York (1956).
8. KRIKORIAN O. H., University of California Radiation Laboratory Report UCRL-6132 (1960).
9. COUGHLIN J. P. and ORR R. L., *J. Am. chem. Soc.* **75**, 530 (1953).
10. ANDERSON O. L., *Phys. Rev.* **144**, 553 (1966).

Sandia Laboratories,

J. Phys. Chem. Solids **Pergamon Press 1970. Vol. 31, pp. 575–596. Printed in Great Britain.**

DEFECTS IN CRYSTALLINE QUARTZ: ELECTRON PARAMAGNETIC RESONANCE OF E' VACANCY CENTERS ASSOCIATED WITH GERMANIUM IMPURITIES*

F. J. FEIGL†
Materials Research Center and Department of Physics, Lehigh University, Bethlehem, Penna. 18015, U.S.A.

and

J. H. ANDERSON
Department of Physics, University of Pittsburgh, Pittsburgh, Penna. 15213, U.S.A.

(*Received* 27 *June* 1969; *in revised form* 25 *August* 1969)

Abstract—Magnetic resonance measurements on crystalline quartz doped with germanium indicate E_1' and E_2' trapped electron centers can be produced by low energy ionizing radiation (50 kVp X-rays). Most of these vacancy-related centers are associated with substitutional Ge impurities rather than Si host cations. Analyses of detailed spectroscopic data in terms of non-bonding s–p hybrid orbitals formed from atomic Si or Ge orbitals, as appropriate, effectively account for the basic paramagnetic responses. Two distinct but quite similar EPR spectra of the E_1'-type associated with Ge impurities are observed, each characteristic of a specific treatment (X-irradiation and heating). A single-oxygen-vacancy E-defect model for E' center geometry is proposed. The model is based on the spectroscopic data and experimental results on generation and bleaching of paramagnetic vacancy centers in α-SiO$_2$:Ge. The various E_1' and E_2'-type magnetic centers are pictured as modifications of this basic E defect. These result from interposition of common impurities (hydrogen in particular) and trapping of electrons or holes.

1. INTRODUCTION

THREE paramagnetic defects produced by low energy ionizing radiation in crystalline quartz doped with 10–1000 ppm Ge have been studied via electron paramagnetic resonance (EPR) spectrometry. Analysis of the complex resonant absorption spectra of these 'color centers' indicates that the unpaired-spin electronic configurations responsible for the paramagnetism are associated with a germanium impurity ion. In particular, a parameterization of the orientation dependence of the EPR absorptions in terms of suitable spin Hamiltonians suggests that the centers are analogues of the E_1' and E_2' trapped electron centers in pure crystalline quartz[1, 2] with a Ge atom substituted for the central Si atom in the E defect structures. Thus, these centers should be significant in the continuing attempt to delineate radiation-produced structural defects and defect center paramagnetism in covalent solids[3]. In this respect, the present centers differ from other impurity-related centers previously investigated in normal[4] and Ge-doped[5, 6] quartz. The radiation-produced paramagnetism of the latter centers can be characterized as an impurity paramagnetism (the net-unpaired-spin electronic configuration responsible for the paramagnetism is stabilized by the impurity ions—in the absence of these ions, no analogues of the magnetic electronic configurations would exist).

---

*Research supported by U.S. Air Force Office of Scientific Research and U.S. Navy Office of Naval Research.

Based on a dissertation submitted by Frank J. Feigl to the University of Pittsburgh in partial fulfillment of the requirements for the Ph.D. degree.

†National Science Foundation Cooperative Graduate Fellow and A. W. Mellon Foundation Pre-Doctoral Fellow, University of Pittsburgh.

The existence of Ge-substituted E' centers will be of interest in connection with current experimental efforts on electronic relaxation processes in quartz[7–9] and on defect structures in thin SiO_2 films[10, 11].

2. SPECTROSCOPY OF E' CENTERS

The specimens used in the present investigation were taken from hydrothermally grown synthetic quartz boules[12, 13] obtained from three different sources.* For the spectroscopic measurements, rough-cut blanks were aligned by Laue back reflection techniques and rectangular parallelepipeds $5 \times 10 \times 1{\cdot}5\ \mathrm{mm}^3$, with their short dimension perpendicular to the crystallographic (00·1) planes (so-called 'z-plates'), were cut from the blanks. These were then X-irradiated and subjected to slective bleaching treatments described in detail in the appendix. The specimens were then mounted on a teflon rod inside a TE_{011} cylindrical microwave cavity resonant at approximately 9350 MHz. Two perpendicular experimental rotation axes permitted arbitrary orientation of the specimen in the d.c. polarizing magnetic field The EPR spectrometer used was a conventional high sensitivity equipment; an electronically stabilized klystron source, reflection microwave bridge, and single crystal detection were employed. Resonant absorption spectra were obtained at fixed microwave frequency by linearly sweeping the d.c. polarizing field, and 125 kHz sinusoidal modulation of the polarizing field was employed to take full advantage of the phase sensitive detection technique[14]. All measurements were made at room temperature.

All angles (e.g. Tables 1–4) are given with respect to a coordinate system in which the z-axis is the α-SiO_2 c-axis (the threefold optic axis [0001]), and the x-axis is the α-SiO_2 positive crystallographic axis, that is, the negative electric axis ([$2\bar{1}\bar{1}0$] parallel to a twofold a-axis)[15]. The loci of the crystalline c and a axes were determined by X-ray Laue photographs and from oscilloscope observation of the EPR spectra (i.e. from the symmetry of physical responses). The remaining ambiguity – the sense of the twofold axis – was resolved by piezoelectric effect determinations[16]. All specimens used in the present investigation were left handed crystals. The handedness of the specimens was determined from optical rotation measurements[17]. The polar angle θ is thus given with respect to the [0001] pole, the azimuthal angle ϕ with respect to the positive crystallographic axis [$2\bar{1}\bar{1}0$], which is the electronegative axis. For right handed specimens, ϕ is positive when counterclockwise in the x–y plane, as viewed from positive z. For left handed specimens, ϕ is positive when clockwise in the x–y plane. This convention (right hand) coordinate system for RHα-SiO_2, left hand coordinate system for LHα-SiO_2), if used consistently, results in azimuthal specifications which are valid in magnitude and sign for both right and left quartz.* The situation is summarized in Fig. 1.

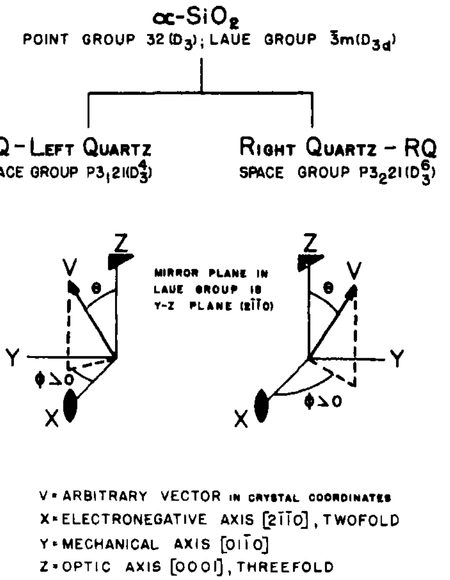

α-SiO₂
POINT GROUP 32 (D₃); LAUE GROUP 3̄m (D₃d)
LQ – LEFT QUARTZ
SPACE GROUP P3₁21 (D₃⁴)
RIGHT QUARTZ – RQ
SPACE GROUP P3₂21 (D₃⁶)
Z
V
θ
Y
φ > 0
X
MIRROR PLANE IN
LAUE GROUP IS
Y-Z PLANE (2̄1̄10)
Z
V
θ
Y
φ > 0
X
V = ARBITRARY VECTOR IN CRYSTAL COORDINATES
X = ELECTRONEGATIVE AXIS [2̄1̄10], TWOFOLD
Y = MECHANICAL AXIS [011̄0]
Z = OPTIC AXIS [0001], THREEFOLD

Fig 1. Coordinate systems in low-quartz (α–SiO_2). The vector V refers to a 'direction' in the quartz structure (for example, an Si–O bond axis) or to a 'direction' of an anisotropic physical property (for example, a principal vector of a spin Hamiltonian tensor). The X, Y, and Z axes are parallel to crystalline a, b, and c axes, respectively. For RQ, $+X \parallel +a$; for LQ, $+X \parallel -a$.

A detailed discussion of EPR spectroscopy in α-SiO_2:Ge is contained in the Appendix.

A. [Ge(III)e^-] *and* [Ge(IV)e^-] *centers*

The spin Hamiltonian relevant to two of the previously unreported centers is:

$$\mathscr{H} = \sum_R \Big\{\mathbf{H}\cdot\mathbf{g}_R\cdot\mathbf{S}+\mathbf{S}\cdot\mathbf{A}_R\cdot\mathbf{I} + \sum_t \left(\mathbf{S}\cdot\mathbf{A}_R{}^t\cdot\mathbf{I}^t+\gamma^t\hbar\mathbf{H}\cdot\mathbf{I}^t\right)\Big\} \qquad (1)$$

---

*Dr. John H. Mackey, Jr. and Mr. Baldwin Sawyer provided many of the research specimens used in the investigation. Specimens were cut from Bell Telephone Laboratory, Clevite Corporation, and Sawyer Research Products quartzes.

*The vexing question of coordinates in quartz has long been one of the main obstacles to communication of results. Twenty years ago Cady described the problem as running like a crack through an otherwise perfect crystal. The situation has not really changed. Reference[15] contains pertinent information, and Fig. 1 a summary of the conventions used in the present work. The present conventions are based on the earlier (Cady) Standard. Any statement regarding the *sense* of the conventional crystallographic axis a applies to right quartz and must be reversed for left quartz.

The first term is the anisotropic Zeeman interaction, the next represents an interaction involving the magnetic minority nucleus Ge^{73} (with A_R representing an anisotropic hyperfine interaction). The final term arises from magnetic Si^{29} isotopes, located in several Si sites t in the defect environment, which exhibit hyperfine interactions with the electronic magnetic moment. The $\sum_R$ indicates a summation over terms related by the symmetry operations of the Laue group D_{3d} of α-SiO_2[18]. For the centers of interest, $S = \frac{1}{2}$ (see Appendix).

The results of fitting the experimental data to the Hamiltonian (1) are listed in Table 1 for the two centers of interest.* Some preliminary comments can be made. One is that, on the basis of the spectroscopic information, the centers appear to be quite similar. The essential differences are in the magnitude of the hyperfine interactions. Unfortunately, the Ge^{73} absorptions for the [Ge(III)e^-] center were too weak to permit detailed analysis, but the c-axis splittings were sufficient to provide an estimate of the hyperfine parameters. Since the two centers arise from different heat treatments of the specimen subsequent to irradiation, as discussed in Section 3B, it is reasonable that they may be modifications of a common basic defect structure.

A second point is that the centers may be assumed to consist of an electron or hole localized primarily on a Ge kernel (giving rise to the large Ge^{73} splittings) and overlapping to a much lesser extent Si sites in the neighborhood of the Ge-impurity (giving rise to the several Si^{29} hyperfine doublets).

The third point suggested by the data on [Ge(III)e^-] and [Ge(IV)e^-] in Table 1 is the similarity between these centers and the E_1' trapped electron center observed by Weeks and detailed by Silsbee in neutron and γ-irradiated quartz crystals.

For convenience the data of Silsbee on the E_1' center in Ge-free quartz are exhibited in Table 2[19]. This center, which has been attributed by Silsbee to an electron occupying an orbital localized on a Si site, is characterized by spin Hamiltonian tensors quite similar to those of the [Ge(III)e^-] centers exhibited in Table 1. On the basis of this similarity, the centers responsible for the [Ge(III)e^-] and [Ge(IV)e^-] absorptions are presumed to consist of structures fundamentally identical to [Si(E_1)e^-], with a Ge atom entering the paramagnetic structure substitutionally for the central Si atom.

This correlation implies that the Ge-related centers involve a lattice defect. The fact that the [Si(E_1)e^-] defect has been observed in very pure fused silica as well as crystalline quartz implies that it is not associated with any impurity.* The absence of any hyperfine multiplets due to impurity nuclei supports this conclusion. This leaves two possibilities: (1) the localized states are associated with defects of the SiO_2 lattice (Si or O interstitials or vacancies, e.g.), or (2) localized lattice distortions provide orbitals which may accommodate electrons or holes produced by ionizing radiation (self trapped holes in 'molecular' orbitals, for example). The stability of the centers and symmetry arguments eliminate the second possibility, and the

---

*The nomenclature for magnetic defects is that of MACKEY J. H., Jr., *J chem. Phys.* **39**, 74 (1963). The notation (inside the square brackets denotes a host) ion or substitutional impurity, the charge carrier trapped (e^+ or e^-), and the presence of interstitial ions (after a virgule). The parenthetical symbols distinguish centers of similar basic composition. Mackey's terminology, developed for substitutional impurity centers, has been extended here to lattice defect centers. In this case, the parenthetical symbol may be used to designate a lattice defect structure. Thus, [Ge(III)e^-] describes a trapped electron localized on a Ge substitutional impurity, as does [Ge(IV)e^-]. The parenthetical III and IV indicate that two distinct centers of this type exist, and further that the centers involve lattice defects characterized as III and IV. [Si(E_2)e^-/H^+] describes a trapped electron localized on an Si ion adjacent to an E_2 defect and an H^+ interstitial ion. A simpler terminology, for lattice defect centers which do not involve substitutional impurities, is that of R. A. Weeks. In Weeks's notation, a magnetic center consisting of a single electron trapped at an E_2 defect is designated E_2'.

*Impurities common to most or all of the specimens examined in this study have high-abundance magnetic isotopes. This point is discussed in Ref.[1].

Table 1A. *Spin Hamiltonian parameters for* [Ge(III)e^-] *center in* α-SiO$_2$:Ge

[Ge(III)e^-]

Principal values and principal directions of spin Hamiltonian tensors
Present investigation

Zeeman g-tensor	2·0011 (113°, 50°)	1·9950 (52°, 340°)	1·9939 (47°, 116°)
Ge^{73} strong hfs		not measured directly (c-axis data only)	
Si^{29} weak hfs	9·85 × 10^{-4} cm^{-1} (66°, 83°)		7·65 × 10^{-4} cm^{-1} axially symmetric
Si^{29} weak hfs	9·15 × 10^{-4} cm^{-1} (146°, 97°)		7·01 × 10^{-4} cm^{-1} axially symmetric

c-Axis orientation data, *Present investigation*

Zeeman g_c	1·9955
Ge^{73} strong hfs	228 G
Si^{29} weak hfs	9·1 G; 8·6 G
Si^{29} very weak hfs	1·5 G; 0·5 G (?)

All directions are specified as (θ, ϕ), according to Fig. 1. The estimated errors are $\pm 0{\cdot}0003$ for g-values, 10^{-5} cm^{-1} for weak hyperfine constants. and ±3° for all directions. 'c-Axis data' refers to data obtained with H parallel to [0001], the crystalline c-axis.

Table 1B. *Spin Hamiltonian parameters for the* [Ge(IV)e^-] *center in* α-SiO$_2$:Ge

[Ge(IV)e^-] center

Principal values and principal directions of spin Hamiltonian tensors, *Present investigation*

Zeeman g-tensor	2·0010 (114°, 49°)	1·9942 (53°, 339°)	1·9935 (47°, 114°)
Ge^{73} strong hfs	268 × 10^{-4} cm^{-1} (113°, 50°)		241 × 10^{-4} cm^{-1} axially symmetric
Si^{29} weak hfs	9·61 × 10^{-4} cm^{-1} (67°, 85°)		7·55 × 10^{-4} cm^{-1} axially symmetric
Si^{29} weak hfs	10·58 × 10^{-4} cm^{-1} (146°, 96°)		8·21 × 10^{-4} cm^{-1} axially symmetric

c-Axis orientation data, *Present investigation*

Zeeman g_c	1·9951
Ge^{73} strong hfs	262 G
Si^{29} weak hfs	10·6 G; 8·5 G
Si^{29} very weak hfs	1·2 G; 0·8 G (?)

All directions are specified as (θ, ϕ), according to Fig. 1. The estimated errors are $\pm 0{\cdot}0003$ for g-values, $\pm 10^{-3}$ cm^{-1} for strong hyperfine constants, $\pm 10^{-5}$ cm^{-1} for weak hyperfine constants, and ±3° for all directions. 'c-Axis data' refers to data obtained with H parallel to [0001], the crystalline c-axis.

[Se(E_1)e^-] center must be associated with defects in the quartz lattice*. The [Ge(III)e^-] and [Ge(IV)e^-] centers must then also be presumed to be associated with defects in the SiO$_2$ lattice. Presumably, this defect involves at least an oxygen vacancy[1, 2, 19].

Thus, the Ge atom is, in a sense, incidental to the basic paramagnetic defect. The E_1'

---

*This point is central to all analyses of E' centers. It is discussed in some detail in Ref. [1].

Table 2. Spin Hamiltonian parameters for the [Si(E_1)e^-] *center in* α-SiO$_2$

[Si(E_1)e^-] center			
Principal values and principal directions of spin Hamiltonian tensors (Silsbee[19])			
Zeeman g-tensor	2·00176	2·00049	2·00029
	(114°, 50°)	(52°, 339°)	(45°. 114°)
Si^{29} strong hfs	424×10^{-4} cm^{-1}		364×10^{-4} cm^{-1}
	(113°, 50°)		axially symmetric
Si^{29} weak hfs	$8{\cdot}61 \times 10^{-4}$ cm^{-1}		$6{\cdot}89 \times 10^{-4}$ cm^{-1}
	(55°, 83°)		axially symmetric
Si^{29} weak hfs	$9{\cdot}15 \times 10^{-4}$ cm^{-1}		$7{\cdot}34 \times 10^{-4}$ cm^{-1}
	(141°, 106°)		axially symmetric
c^*Axis orientation data, Silsbee[19]			
Zeeman g_c	2·0007		
Si^{29} strong hfs	400 G		
Si^{29} weak hfs	9 G; 8 G		
Si^{29} very weak hfs	0·7 G; 0·4 G (?)		
Principal values and principal directions of spin Hamiltonian tensors, *Present investigation*			
Zeeman g-tensor	2·0017	2·00048	2·00021
—	(114°, 48°)	(47°, 343°)	(53°, 118°)
c-Axis orientation data, *Present investigation*			
Zeeman g_c	2·0006		
Si^{29} weak hfs	9·2 G; 8·3 G		
Si^{29} very weak hfs	0·7 G		

All direction are specified as (θ, ϕ), according to Fig. 1. The estimated errors in Silsbee's data (quoted from Silsbee[19]) are ±0·0002 absolute, ±0·00005 relative for g-values, $\pm 2 \cdot 10^{-4}$ cm^{-1} for strong hyperfine constants, $\pm 5 \cdot 10^{-6}$ cm^{-1} for weak hyperfine constants, and ±2° for g-tensor and strong hyperfine directions, ±4° for weak hyperfine directions. The estimated errors in the *Present investigation* data are ±0·0003 absolute, ±0·0001 relative for g-values, and ±6° for g-tensor directions. 'c-Axis data' refers to data obtained with H parallel to [0001], the crystalline c-axis.

defect is produced in crystalline quartz by ionizing irradiation or particle bombardment. The electron orbital for the unpaired spin is relatively well localized on an Si atom position in the crystal, and this atomic position may be occupied by either a Si host atom or a Ge impurity atom without introducing marked changes in the angular characteristics of the orbital functions.

The [Ge(III, IV)e^-] centers are clearly distinguished from the impurity-related paramagnetic centers previously observed in crystalline quartz. Both the trapped-hole aluminum impurity centers [Ale^+], and the trapped electron Germanium impurity centers, [Ge(A)e^-/M$^+$] and [Ge(C)e^-/M$^+$], have been tentatively analyzed in terms of models in which the impurities are located in normal Si positions in the α-SiO$_2$ matrix[4, 5, 6]. These centers may involve additional impurity ions (e.g. M$^+$ = Na$^+$ or Li$^+$ for the [Ge(A)e^-/M$^+$] centers), and in general are characteristic of the impurity content of the quartz and not of structural defects in the α-SiO$_2$ lattice.

The final entry of Table 2 represents data obtained on a center observed during the present investigation. This center could be produced in samples containing no measurable Ge impurity (as determined by spectrochemical analysis and by the absence of any EPR absorptions from Ge-related A and C

centers), and is thus assumed to be associated with the SiO_2 lattice. This assumption is further justified by the fact that any significant unpaired spin density on impurity atoms present in the quartzes used should produce characteristic hyperfine splittings on the primary absorptions (since all the impurities common to specimens which were investigated possess a single magnetic isotope in dominant abundance). Such characteristic hyperfine splittings were not observed. The center occurred with weak intensity relative to Ge centers in Ge-doped quartzes. The spectral absorptions were overlapped by those from the $[\mathrm{Ge(III)}e^-]$ center at most orientations, so full spectroscopic data were not obtained. Any conclusions regarding this center would thus be tentative. However, the data obtained are consistent with those of Silsbee on the $[\mathrm{Si}(E_1)e^-]$ center. This is the first reported evidence of $[\mathrm{Si}(E_1)e^-]$ generation by X-irradiation in crystals. The center has been observed previously in 1 MeV γ-irradiated crystals and in neutron irradiated crystals.

B. $[Ge(\mathrm{E}_2)e^-/H^+)$ *centers*

Table 3 gives the results of fitting observed spectroscopic data to the spin Hamiltonian

$$\mathscr{H} = \sum_R \Big\{\mathbf{H}\,.\,\mathbf{g}_R\,.\,\mathbf{S}+\mathbf{S}\,.\,\mathbf{A}_R\,.\,\mathbf{I} + \sum_l \left(\mathbf{S}\,.\,\mathbf{A}_R{}^l\,.\,\mathbf{I}^l+\gamma^l\hbar\mathbf{H}\,.\,\mathbf{I}^l\right) + \mathbf{S}\,.\,\mathbf{A}_R{}^p\,.\,\mathbf{I}^p+\gamma^p\hbar\mathbf{H}\,.\,\mathbf{I}^p\Big\}. \qquad (2)$$

This is identical to the Hamiltonian (1) with the exception of the final two terms. These two terms arise from a proton in the defect environment. $\mathbf{A}_R{}^p$ again represents an anisotropic hyperfine interaction and $\gamma^p\hbar\mathbf{H}\,.\,\mathbf{I}^p$ a proton Zeeman term. This proton interaction represents the major observed difference between the present center and the two centers described in Table 1. The justification of the assignment of the hyperfine splitting to a proton is given in the Appendix.

The Hamiltonian given above contains terms involving hyperfine interactions (represented by $\mathbf{A}_R{}^l$) with neighboring Si^{29} ions in the defect environment. Weak doublets

Table 3. *Spin Hamiltonian parameters for the* $[\mathrm{Ge}(E_2)e^-/\mathrm{H}^+]$ *center in* $\alpha\text{-}SiO_2:Ge$

$[\mathrm{Ge}(E_2)e^-/\mathrm{H}^+]$ center

Principal values and principal directions of spin Hamiltonian tensors, *Present investigation*

Zeeman g-tensor	2·0009	1·9952	1·9943
—	(131°, 208°)	(49°, 167°)	(68°, 277°)
Ge^{73} strong hfs		not measured directly (c-axis data only)	
H^1 hfs	$1{\cdot}02\times10^{-4}$ cm	$-0{\cdot}32\times10^{-4}\ \mathrm{cm}^{-1}$	$-0{\cdot}55\times10^{-4}\ \mathrm{cm}^{-1}$
	(130°, 203°)	(57°, 145°)	(57°, 260°)

c-Axis orientation data, *Present investigation*

Zeeman g_c	1·9976
Ge^{73} strong hfs	270 G
Si^{29} very weak hfs	1·3 G; 0·7 G
H^1 hfs	0·17 G

All directions are specified as (θ, ϕ), according to Fig. 1. The estimated errors are ±0·0003 for g-values, $\pm10^{-5}\ \mathrm{cm}^{-1}$ for the proton hyperfine constants, and ±3° for g-tensor directions, ±6° for proton hyperfine directions. 'c-Axis data' refers to data obtained with H_{DC} parallel to [0001], the crystalline c-axis.

centered on the primary spectra were observed at certain orientations, and data are given for the crystal optic (c) axis parallel to the d.c. polarizing field. From the spectra examined in the present analysis, it is not possible to definitively analyze such superhyperfine splittings. The complexity of EPR spectra in Ge-doped quartz prohibited detailed identification of the Si^{29} doublets at a sufficient number of orientations (see Appendix).

The Ge^{73} splitting could also only be measured with the crystal oriented such that its c-axis was parallel to the polarizing magnetic field, as indicated in Table 3.* The simple structure of the Ge^{73} multiplet indicated that $S = \frac{1}{2}$ (see Appendix). As described above the present results were obtained at room temperature on a research specimen obtained from a synthetic quartz boule, using standard high sensitivity X-band EPR techniques.

The data contained in Table 3 lead to the following preliminary conclusions. First, the center may be presumed to consist of an electron or hole localized primarily on a Ge kernel (giving rise to the large Ge^{73} splittings) and overlapping to a much lesser extent a proton located in the vicinity of the defect. The hyperfine interaction with the proton is highly anisotropic and small (much less than the proton Zeeman interaction at a polarizing field of approximately 3300 Oe).†

There are two relatively simple explanations for a center of the type described. The first is that the present center is a proton-compensated analogue to the $[Ge(A)e^-/M^+]$ or $[Ge(C)e^-/M^+]$ centers described by Anderson and Weil[5] and Van Wieringen and coworkers[6]. These centers consist of an electron trapped primarily on a Ge-impurity and exhibiting weak anisotropic hyperfine interactions with a nearby Na^+ or Li^+ ion (designated as M^+). This class of magnetic centers is presently understood to involve Ge substituted at a normal Si lattice site (hence bonded to four oxygens).

An alternative explanation, and one that will be defended in this paper, is that the observed center is related to previously studied structural defects in the quartz lattice. The proposition is that the present center is properly designated as $[Ge(E_2)e^-/H^+]$, a Ge-substituted analogue of the center $[Si(E_2)e^-/H^+]$ described by Weeks[2]. The spectroscopic parameters of the E_2' center in high-purity crystalline quartz are exhibited in Table 4. These numbers are recalculated from Weeks' published data and differ slightly from his published parameters[2]. The recalculation was done to exhibit explicitly the full g-tensor and proton hyperfine anisotropy that is manifest in Weeks' data. This facilitates detailed comparison with Table 3 parameters on $[Ge(E_2)e^-/H^+]$ and with spectroscopic analyses of E_1' centers. The deviations from axial symmetry, which were neglected by Weeks, are in fact quite small.

The general similarity of the spectroscopic data in Tables 3 and 4 justifies the assertion that the two centers are analogues. In particular both are presumed to be E_2' defects, in Weeks' terminology, consisting of an electron trapped at a defect structure designated as E_2. The defect presumably involves at least an oxygen vacancy[1, 2]. Weeks' measurements indicated that the E_2 defect may, and generally does, involve an interstitial proton. However, his spectra, and the relaxation measurements of Castle and Feldman[7] exhibit responses from an E_2 defect which was presumably identical to that described in Table 4, but without the compensating proton. No such response was positively identified in the present work. The complex background observed in the spectra from Ge-doped specimens could have masked a weak singlet located at the proton doublets' average position. The present experiments thus

---

*This was a signal intensity problem. As discussed in the Appendix, the ten Ge^{73} hyperfine lines are three times more intense for the c-axis parallel to polarizing field orientation than for any other orientation.

†Detailed data and discussion of this point are contained in the Appendix.

Table 4. Spin Hamiltonian parameters for the $[\mathrm{Si}(E_2)e^-/\mathrm{H}^+]$ *center in* α-$\mathrm{SiO_2}$:Ge

$[\mathrm{Si}(E_2)e^-/\mathrm{H}^+]$ *center*			
Principal values and principal directions of spin Hamiltonian tensors (Adapted from Weeks[2])			
Zeeman g-tensor	2·0020 (120°, 208°)	2·0007 (67°, 133°)	2·0005 (39°, 253°)
$\mathrm{Si^{29}}$ strong hfs		not measured directly (c-axis data only)	
$\mathrm{H^1}$ hfs	$1{\cdot}5\times10^{-4}\,\mathrm{cm^{-1}}$ (126°, 215°)	$-0{\cdot}1\times10^{-4}\,\mathrm{cm^{-1}}$ (44°, 257°)	$-0{\cdot}2\times10^{-4}\,\mathrm{cm^{-1}}$ (70°, 140°)
c-Axis orientation data, Weeks[2]			
Zeeman g_c	2·0009		
$\mathrm{Si^{29}}$ strong hfs	412 G		
$\mathrm{Si^{29}}$ very weak hfs	1·0 G, 0·8 G; 0·4 G		
$\mathrm{H^1}$ hfs	0·4 G		

All directions are specified as (θ, ϕ), according to Fig. 1. The estimated errors in computing the principal values and directions from the published data are ±0·0001 for g-values, $10^{-5}\,\mathrm{cm^{-1}}$ for proton hyperfine constants, and ±5° for g-tensor directions, ±10° for proton hyperfine directions. 'c-Axis data' refers to data obtained with H_{DC} parallel to [0001], the crystalline c-axis.

neither confirm nor preclude the existence of a defect structure of the type $[\mathrm{Ge}(E_2)e^-]$.

Thus, the paramagnetic structure E_2' can be produced in crystalline quartz by ionizing irradiation or particle bombardment. The electron orbital for the unpaired spin is relatively well localized on an Si atom position in the crystal. This site, which may be distinct from a normal lattice position because of distortions associated with the lattice defect[20], may be occupied by either an Si host ion or a Ge impurity ion. The Ge ion is in this sense incidental to the present defect. As with the $[\mathrm{Ge(III, IV)}e^-]$ defects, this clearly distinguished the present center from previously studied magnetic defects related to impurities in quartz. These last remarks must be qualified by the explicit assertion that the $[\mathrm{Si}(E_2)e^-/\mathrm{H}^+]$ center was *not* observed in the present experiments. X-irradiation does not produce $[\mathrm{Si}(E_2)e^-/\mathrm{H}^+]$ centers in measurable concentration in α-$\mathrm{SiO_2}$, although it will produce $[\mathrm{Si}(E_1)e^-]$.*

The identification of the present center as $[\mathrm{Ge}(E_2)e^-/\mathrm{H}^+]$ is reinforced by experiments on generation and stability of the magnetic response, discussed in Section 3B.

C. *Interpretation of spectroscopic data*

The spectroscopic data for each of the E'-type vacancy centers in α-$\mathrm{SiO_2}$ are quite similar. This can be made evident by analyzing the data in terms of a very simple model of the wave function for the unpaired electron. Basically, the hyperfine constants and g-shifts are normalized to appropriate parameters derived from data on atomic Si or Ge. The logic has been discussed in detail by Silsbee[19], and in particular by Watkins and Corbett[21–23]. The procedure will be presented here in outline only.

The wave function for the E' unpaired electron is constructed as a linear combination of atomic orbitals centered on the several atoms neighboring the defect (vacancy or vacancies):

$$\psi_E = \sum \eta_j\psi_j. \tag{3}$$

This expansion would include terms on the central silicon or germanium atom, on the shell of oxygen atoms surrounding the central cation (three or less, depending on the number of oxygen vacancies), on the next shell of silicon atoms, etc. For the majority of E_2 centers, the expansion also involves a proton in the defect environment.

---

*See Section 2A on E_1'-type centers.

It is evident from the spectroscopic data that the dominant term in the expansion (3) is the atomic orbital ψ_0 on the central atom site.

$$\psi_0 = \alpha_0\phi_{ns} + \beta_0\phi_{np} \tag{4}$$

ψ_0 is here approximated as hybrid *nsnp* atomic orbital, with $n = 3$ for Si-related E' defects and $n = 4$ for Ge-related E' defects. The Si^{29} and Ge^{73} strong hyperfine interactions can be analyzed in the approximation that they are determined solely by ψ_0. The axially symmetric form assumed by the interaction parallel and perpendicular to the p-orbital axis is expressed by interaction constants a_0 and b_0 that

$$A_{\parallel} = a_0 + b_0 \tag{5}$$

$$A_{\perp} = a_0 - \frac{b_0}{2}. \tag{6}$$

The constants a_0 and b_0 relate to the isotropic Fermi contact interaction

$$a_0 = \left(\frac{8\pi}{3}\right) g_e\beta_e g_n\beta_n\eta_0{}^2\alpha_0{}^2|\phi_{ns}(0)|^2 \tag{7}$$

and the anisotropic dipole–dipole interaction

$$b_0 = (\tfrac{4}{5}) g_e\beta_e\gamma_n\beta_n\eta_0{}^2\beta_0{}^2\langle r_{np}^{-3}\rangle \tag{8}$$

respectively.

The E' center wave functions can thus be related to atomic s, p wave functions on the central cation by comparing experimental values for a_0 and b_0 obtained from Tables 1–4 with values of $|\phi_{ns}(0)|^2$ and $\langle r_{np}^{-3}\rangle$ for atomic Si or Ge, as appropriate. Values of $\langle r_{np}^{-3}\rangle$ are obtained from the estimates of Barnes and Smith[24], corrected for relativistic effects. Values for $|\phi_{ns}(0)|^2$ are obtained by scaling the corrected Barnes–Smith values of $\langle r_{np}^{-3}\rangle$ by the ratio $|\phi_{ns}(0)|^2/\langle r_{np}^{-3}\rangle$ obtained from Hartree–Fock calculations. Values of $|\phi_{ns}(0)|^2/\langle r_{np}^{-3}\rangle$ for Si^{29} are adapted from Watkins and Corbett[22]; values for Ge^{73} are extrapolated from Watkins and Corbett[22] and Elkins and Watkins[23]. The value of $|\phi_{4s}(0)|^2_{Ge}$ derived thus agrees quite closely with that estimated by Kohn and Luttinger[25]. The results are

$$\text{silicon: } |\phi_{3s}{}^{(0)}|^2_{Si} = 32 \times 10^{24}\,\text{cm}^{-3}$$

$$\langle r_{3p}^{-3}\rangle_{Si} = 16 \times 10^{24}\,\text{cm}^{-3}$$

$$\text{germanium: } |\phi_{4s}(0)|^2_{Ge} = 84 \times 10^{24}\,\text{cm}^{-3}$$

$$\langle r_{4p}^{-3}\rangle_{Ge} = 38 \times 10^{24}\,\text{cm}^{-3}$$

The results of substituting these last numbers plus $(A_{\parallel})_0$ and $(A_{\perp})_0$ from Tables 1–4 into equations (5)–(8) are summarized in Table 5. The quantities $A_{\parallel}$ and $A_{\perp}$ for the strong hyperfine interactions have not been determined directly for the centers $[Ge(III)e^-]$, $[Ge(E_2)e^-/H^+]$, and $[Si(E_2)e^-/H^+]$. The estimates in Table 5 were obtained from the c-axis hyperfine positions*, assuming the principal axis systems for **g** and **A** in equations (1) and (2) to be identical. This is quite reasonable for the g-tensor symmetry and the large hyperfine splittings measured[26].

Within the limitations of the model and the errors in the atomic wave function estimates, the wave function parameters in Table 5 suggest that the unpaired electron in all of the magnetic E' centers is strongly localized in an s–p hybrid orbital on a single cation (either a normal Si or substitutional Ge). The simplest picture is an electron in an sp^3

Table 5. Wave function coefficients of the unpaired electron orbital for magnetic E′ *centers in* α-SiO_2:Ge

Center	Hyperfine constants a_0 (10^{-4} cm^{-1})	 b_0 (10^{-4} cm^{-1})	Wave function coefficients α_0^2	 β_0^2	 $100\eta_0^2$ (% of total w.f.)
E_1': $[Si(E_1)e^-]$	384	40	0·31	0·69	87
E_1': $[Ge(III)e^-]$	218	16	0·37	0·63	91
E_1': $[Ge(IV)e^-]$	250	18	0·38	0·62	103
E_2': $[Si(E_2)e^-/H^+]$	400	50	0·28	0·72	103
E_2': $[Ge(E_2)e^-/H^+]$	250	14	0·43	0·57	89

The first two columns list a_0 = isotopic contact and b_0 = dipolar hyperfine constants, computed from the hfs parameters in Tables 1–4. The last three columns list atomic wave function coefficients calculated from a_0 and b_0, using text equations (7) and (8). The anomalies in the final column ($\eta_0^2 > 1{\cdot}00$) presumably result from neglecting core polarization corrections to the atomic hyperfine constants.

---

*The calculation of Ge^{73} hyperfine constants is discussed in the Appendix.

non-bonding directed orbital facing an oxygen vacancy.

This picture is reinforced by the basic symmetry of the EPR responses. The g-tensor symmetry approximates that expected from an electron in broken tetrahedral coordination (g-tensor approximately axial with $\Delta g_{\parallel} \approx 0$ and $\Delta g_{\perp}$ small)[19, 22]. In this approximation, the g-tensor and strong hyperfine tensor unique axes for $[Si(E_1)e^-]$ and [Ge(III or IV)e^-] are parallel to an Si–O bond. The deviation from the Si–O direction calculated from X-ray crystallographic studies has the same magnitude as the error estimated for the reduced spectroscopic parameters (Tables 1–3). The situation is illustrated in Fig. 2.

For the E_2' centers, the considerations of Weeks[2] on defect geometry cannot be reproduced. The data $[Ge(E_2)e^-/H^+]$ again place the unique g tensor axis parallel to an Si–O bond (the Si_0–O_{III} bond in Fig. 2). In this case, the discrepancy exceeds the estimated error. The unique spectroscopic axis for $[Si(E_2)e^-/H^+]$ deviates significantly (20°) from the appropriate bond direction. The obvious assignment of the source of this discrepancy is to the charge compensating proton. For $[Ge(E_2)e^-/H^+]$, the unique axis of the proton hyperfine tensor is approximately parallel to the unique axis of the g-tensor. Within the uncertainty of present measurements, they can be regarded as identical. The same conditions exist with regard to the $[Si(E_2)e^-/H^+]$ center. Within the experimental error, the proton axis and g-tensor axis are parallel, but the presumed error is, in fact, rather large.

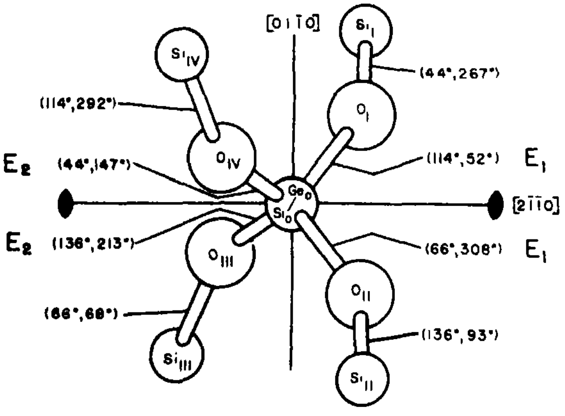

Fig. 2. The geometry of the bonding tetrahedron in α-quartz. The angular specifications are (θ, ϕ), defined in Fig. 1. Small spheres are Si or Si-substituted Ge; large spheres are oxygen. The Si–O directions labelled E_1 and E_2 are approximately parallel to the unique principal axes of the g-tensors for E_1'- and E_2'-type magnetic defects. As explained in the text, this refers to the approximation that the g-tensors are axially symmetric.

The simplest interpretation consistent with all available data is that the E_2' center electron is localized in a directed orbital along the Si–O direction indicated in Fig. 2. This geometry can be more or less distorted (more for $[Si(E_2)e^-/H^+]$, less for $[Ge(E_2)e^-/H^+]$). The distortion is attributed to the effect of the associated charge-compensating proton. The study of A and C centers in Ge-doped quartz indicates that metallic impurities tend to occupy interstitial positions along the c-axis channels in quartz[5, 26]. In these cases, there is presumably no associated lattice defect (the centers consist of a substituted impurity plus an interstitial, but no unoccupied lattice sites). For E_2' defects, it is reasonable to assume that the proton exists somewhere between the vacant oxygen site and the c-axis channel position.

The two Si–O bonds just cited are not equivalent under the symmetry operations appropriate to α-SiO_2. The four near neighbor oxygens of a given silicon define a distorted tetrahedron and are symmetry related in pairs only. The point symmetry about an Si atom site is thus C_{2v}, with one of the crystalline a-directions as the twofold axis. This is clearly evident for the Si_0 atom of Fig. 2. For a given silicon, there are two 'long' Si–O bonds (1·611 Å interatomic spacing) and two 'short' Si–O bonds (1·604 Å interatomic spacing). The principal spectroscopic direction for E_1' centers is parallel to a 'short' Si–O bond, and that for E_2' centers approximately parallel to a 'long' Si–O bond.

As mentioned above, the g-shift tensors for E' centers are consistent in a first approximation with the broken tetrahedral coordination model. Closely related calculations on E' centers in undoped quartz and on E centers in phosphorus doped silicon have been described in some detail[21–23]. These proceed on the assumption that the g-shift data can be treated in terms of a localized 'molecule' made up of the central defect cation (Si or Ge) and the three nearest neighbors (oxygens in the present case). Again, the unpaired defect electron is presumed to occupy a non-bonding sp hybrid on the cation, with the remaining hybrids used in normal covalent bonding with $2p$ orbitals on the oxygens (see Fig. 3). In the first approximation, the g-shifts result from the admixture into the nonbonding orbital ψ_0, via spin–orbit coupling, of bonding orbitals ψ^+, and antibonding orbitals ψ^-.

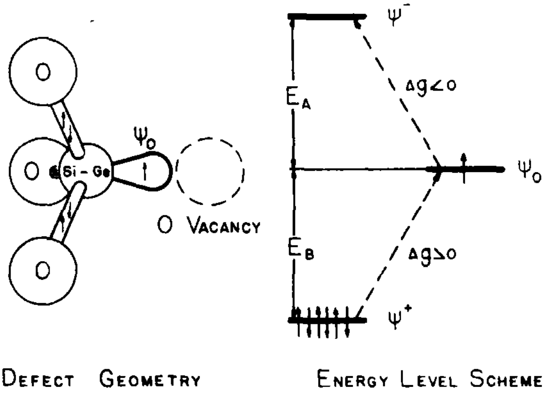

Fig. 3. A molecular model for g-tensor calculation on E' centers. The model assumed an unpaired electron localized in' a non-bonding orbital ψ_0 along an Si–O band direction. The hybrid s–p orbital ψ_0 is directed toward an oxygen vacancy. The g-shifts are presumed to arise via spin-orbit coupling to normal bonding orbitals ψ^+ and antibonding orbitals ψ . This simplified model assumes three degenerate bonding and antibonding orbitals (and hence a non-distorted bonding tetrahedron). In the diagram, electron occupancy is indicated by arrows representing spin states.

The result of calculations on this model is an axially symmetric g-tensor oriented along the broken bond axis. The g-shift for field orientations perpendicular to the symmetry axis arises from incomplete cancellation of the contributions from admixtures of ψ^- (yielding negative g-shifts) and ψ^+ (yielding positive g-shifts). For E defects in silicon, Watkins and Corbett[22] attribute the incomplete cancellation to difference in bonding and antibonding energies ($E_b \neq E_a$) and to stronger matrix elements between ψ_0 and ψ^+ than between ψ_0 and ψ^-. They assign this last factor in part to a core orthogonalization correction. For α-SiO_2, Silsbee[19] and Ruffa[20] assume that $E_a \approx E_b$, and Silsbee assigns the incomplete cancellation for $[Si(E_1)e^-]$ to matrix element differences for the two contributions. In particular, the partially ionic character of the Si–O bond implies an excess of oxygen $2p$ wave function in the bonding orbital and a correspondingly larger fraction of silicon sp^3 wave function in the antibonding orbital. Since, in this approximation, only the sp^3 orbitals on the central defect cation contribute to the g-shifts, the partial ionicity of the α-SiO_2 system result in dominant g-shift contributions from the antibonding matrix elements.

The negative g-shifts results from an expression of the form

$$\Delta g_\perp \approx |\lambda_{np}|\left\{\frac{(1-\gamma)(1-\delta)}{E_b}-\frac{(1+\gamma)(1+\delta)}{E_a}\right\}\beta_0{}^2. \quad (9)$$

The parameters γ and δ account for core orthogonalization and the partially ionic character of the Si–O bonds. Proper application of the g-shift expression (9) to the present problem requires a relatively detailed picture of the partially ionic bonding and antibonding orbitals for both normal Si and Si-substituted Ge in the α-SiO_2 structure. This will not be attempted here.

The observed departure of $g_\parallel$ from the free electron value and the departure of the g-tensor from axial symmetry cannot be reconciled with the simple picture of broken tetrahedral coordination. The present results emphasize these particular difficulties: the deviations from $\Delta g_\parallel = 0$ and axial symmetry are much stronger for the Ge-related E' centers.

A simple normalization of the g-shift data to atomic parameters can be effected, based on the result (9). The simplest attack, invoking the similarity of electron configurations for atomic Si and Ge (see[27]) and the structural and thermodynamic similarity of α-SiO_2 and crystalline GeO_2[15], presumes that γ, δ and $E_a = E_b \approx E$ are not significantly changed by substituting Ge for Si in α-SiO_2. In this case

$$\frac{\Delta g_\perp(Si)}{\Delta g_\perp(Ge)} \approx \frac{\lambda_{3p}(Si)}{\lambda_{4p}(Ge)} \quad (10)$$

that is, the g-shifts vary as the ratio of the atomic spin orbit parameter λ_{np}. These parameters are obtained from the interval relations cited by Fowler[27, 28]: $\lambda_{3p}(Si) \approx 0{\cdot}03$ eV, $\lambda_{4p}(Ge) \approx 0{\cdot}20$ eV.

Table 6 is a summary of g-shift data for the several E' centers (from Tables 1–4) and a compilation of normalized g-shift ratios (10). The g-shift data manifest the basic similarity of the two Si related E' centers and the three Ge related E' centers. The normalized ratios

Table 6. *g-shifts and normalized g-shifts* ($\Delta g/\lambda$) *for magnetic* E′ *centers, calculated from Tables* 1–4

$\Delta g_i = 2{\cdot}0023 - g_i$ *for E′ centers in* α-SiO$_2$:Ge

Center	Δg_1	Δg_2	Δg_3
$[\mathrm{Ge(III)}e^-]$	12×10^{-4}	73×10^{-4}	84×10^{-4}
$[\mathrm{Ge(IV)}e^-]$	13×10^{-4}	81×10^{-4}	88×10^{-4}
$[\mathrm{Ge}(E_2)e^-/\mathrm{H}^+]$	14×10^{-4}	71×10^{-4}	80×10^{-4}
$[\mathrm{Si}(E_1)e^-]$	5×10^{-4}	18×10^{-4}	20×10^{-4}
$[\mathrm{Si}(E_2)e^-/\mathrm{H}^+]$	3×10^{-4}	16×10^{-4}	18×10^{-4}

Center	$\Delta g_1/\lambda$ (cm)	$\Delta g_2/\lambda$ (cm)	$\Delta g_3/\lambda$ (cm)
$[\mathrm{Ge(III)}e^-]$	8×10^{-7}	46×10^{-7}	53×10^{-7}
$[\mathrm{Ge(IV)}e^-]$	8×10^{-7}	51×10^{-7}	55×10^{-7}
$[\mathrm{Ge}(E_2)e^-/\mathrm{H}^+]$	9×10^{-7}	44×10^{-7}	50×10^{-7}
$[\mathrm{Si}(E_1)e^-]$	19×10^{-7}	69×10^{-7}	77×10^{-7}
$[\mathrm{Si}(E_2)e^-/\mathrm{H}^+]$	12×10^{-7}	62×10^{-7}	69×10^{-7}

For the normalized g-shifts, $\lambda = \lambda_{3p}(\mathrm{Si}) = 260\,\mathrm{cm}^{-1}$ for Si-related centers, and $\lambda = \lambda_{4p}(\mathrm{Ge}) = 1600\,\mathrm{cm}^{-1}$ for Ge-related centers. The atomic spin–orbit coupling parameters were obtained from Moore[27].

reflect the basic similarity of the Si and Ge related centers: most of the differences in the g-shifts are eliminated by normalization to atomic spin–orbit parameters.

The qualitative success obtained from a grossly simplified model in estimating a zero-order electronic ground state (from strong hyperfine data) and first order corrections (from g-shift data) can be taken as encouraging evidence that 'molecular orbital' calculations on these defects should be pursued. Such calculations would concentrate on the effects of detailed symmetry, partial ionicity, core polarization and orthogonalization, and bonding-antibonding energies on the hyperfine and g-shift parameters.

In this connection, the several 'weak' and 'very weak' hyperfine interactions observed in E' center EPR spectra are of great interest. These interactions should provide information on term coefficients η_j, α_j and β_j, for $j \neq 0$, in the wave function expansions (3) and (4). Unfortunately, the first step in such an analysis cannot be effected from the simplified model presented thus far. It has not been possible to fit the principal axes of the weak Si^{29} hyperfine interactions for E'_1 centers into the bonding tetrahedron of α-SiO$_2$. Within the volume indicated in Fig. 2, the unique hyperfine tensor axes for weak Si^{29} interactions lie closest to Si$_{\mathrm{II}}$–O$_{\mathrm{II}}$ and Si$_{\mathrm{III}}$–O$_{\mathrm{III}}$ bond directions. The discrepancies are large, however (10–20 degrees). The hyperfine energies presumably arise from direct overlap and direct dipole–dipole interaction as well as overlap core polarization and exchange core polarization effects. The several contributions can vary in sign as well as amplitude, and it is not unreasonable that strong displacements of hyperfine axes from bond directions might result if these competing effects were of comparable magnitude.

None of the very weak Si^{29} interactions have been analyzed in detail. This is a serious deficiency, since observed splittings at favorable orientations have the same magnitude as the direct nuclear Zeeman term. In this circumstance, the number of Si^{29} neighbors which are responsible for a given complex of very weak doublet splittings can only be determined by careful analysis[29].

The weak and very weak Si^{29} interactions, and the details of the g-tensor, constitute the 'hard test' of any model for geometry and electronic wave function of E' centers in α-SiO_2. In the absence of detailed information on the very weak Si^{29} doublets and quantitative understanding of the weak Si^{29} hyperfine interactions, no significant use can be made of the Si^{29} hyperfine structure of the EPR spectra.

Failure to make detailed quantitative use of Ge^{73} and Si^{29} hyperfine data precludes spectroscopic definition of the distinction between [Ge(III)e^-] and [Ge(IV)e^-]. These differ only in several hyperfine amplitudes, which are approximately 10 per cent higher for the [Ge(IV)e^-] center. The detailed similarity of the two centers suggests that they are closely related modifications of the same basic center, involving at least a single oxygen vacancy. Since all principal directions of the spin Hamiltonian tensors are identical, no gross configuration changes are presumed to be involved. Results on generation and bleaching of E' centers, presented in the Section 3B, offer a clear distinguishing characteristic for these two centers.

3. SINGLE VACANCY MODELS FOR E' CENTERS

The available data on Si-related and Ge-related E' centers suggest a single oxygen vacancy model for these magnetic defect structures. The geometries of the various E_1' and E_2' centers are quite similar. In particular, the orientations of the localized orbitals for the unpaired electrons, as deduced from magnetic resonance responses, have been explained in terms of the single vacancy structure in Section 2 of this paper. Further, all details of the various E_1' and E_2' resonance spectra which can presently be explained in some detail are consistent with relatively simple modifications of a single oxygen vacancy. Those features of the EPR spectra which cannot presently be analyzed (the several Si^{29} doublets, in particular) are not inconsistent with this simplified model, as has been shown in Section 2. The electrically neutral oxygen vacancy, which would be the E' center precursor, is designated as E.

A. *The* E *defect in* α-SiO_2

Figure 4 exhibits the single oxygen vacancy model proposed for the E-defect in α-SiO_2.

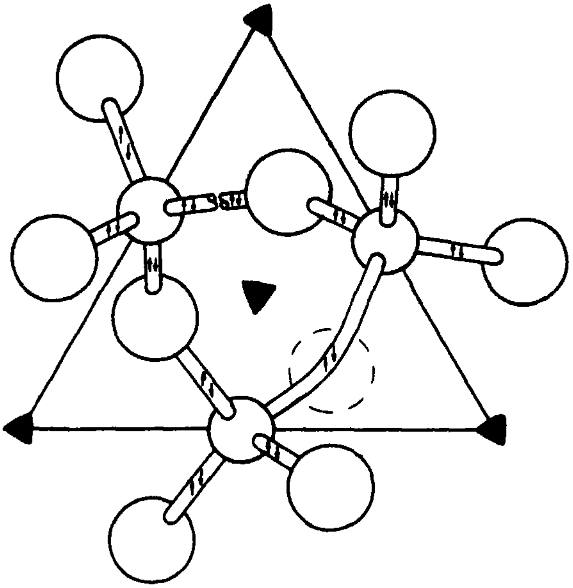

Fig. 4 A model for the E-defect in α-quartz. The quartz structure is viewed along a threefold axis. The locations of threefold screw axes perpendicular to the plane of the diagram are indicated by dark triangles. The three twofold rotation axes parallel to the plane of the diagram form an equilateral triangle. Small spheres represent silicons, large spheres oxygens. The oxygen vacancy is indicated by a broken circle. Electron occupancy is indicated by arrows representing spin states.

This figure represents the α-SiO_2 structure viewed along the three fold optic axis c. It is highly schematic. The E-defect, with the oxygen far removed from its original lattice position, is presumed electrically neutral. This involves assignment of electronic states to two valence-shell electrons not involved in normal bonds (one from each Si-atom adjacent to the missing oxygen).

The electrons are presumed paired, hence the structure is diamagnetic (a spin singlet state). Because of the existence of 'long' and 'short' Si–O bonds in normal SiO_2, there is no reason to expect symmetrical distribution of the electronic density over both Si-atoms adjacent to the missing oxygen.

To the authors' knowledge, no direct response has been identified as arising from the center just proposed. Optical transitions from the ground state just described to an excited state have not been identified, and the only possible triplet state magnetic resonance signal[30] has not beeen analyzed in detail. The properties of the neutral E defect in the partially covalent system α-SiO_2, if it is a stable center, would be of great interest.

Of present concern is the structure of magnetic E' centers. These are presumed to arise as modifications of the neutral E defect by trapping of charge carriers (electrons, holes, and ionic impurities). Thus, the neutral E defect is presented as the structural precursor of the several E' centers. Within the scope of the present investigation, this relationship between the E defect and the E' centers is a *logical* one.

B. *Generation and bleaching of* E′ *magnetic centers*

Table 6 contains a summary of experimental results on generation and bleaching of E' centers in α-SiO_2. These data clarify the identifications made in Section 1. Of primary present interest is the effect of X-irradiation on quartz[31]. In Ge-free quartz, room temperature X-irradiation produces no E' centers. Subsequent heat treatment at 600°K produces measurable (by EPR) concentrations of $[Si(E_1)e^-]$. This center is bleached by heat treatment at 700°K.

In Ge doped quartz, the situation is considerably more complex[31]. The Si-related E_1' center is observed just as in Ge-free quartz, but the Ge-related E' centers and the $[Ge(A,C)e^-/M^+]$ centers greatly complicate the magnetic resonance spectra. The several Ge-related A and C centers are produced by X-irradiation. The following sequence is observed for Ge-related E' centers.

i. The $[Ge(IV)e^-]$ center is produced by room temperature X-irradiation. The $[Ge(IV)e^-]$ center is unstable at room temperature and bleaches completely if specimen is heated to 400°K. There is no Si-related analogue to this center.

ii. The $[Ge(E_2)e^-/H^+]$ center is produced by room temperature X-irradiation, and is bleached if the specimen is heated to 500°K. The behavior of $[Ge(E_2)e^-/H^+]$ in X-irradiated quartz is very similar to the behavior of $[Si(E_2)e^-/H^+]$ in γ-irradiated samples[32]. The generation and bleaching studies therefore reinforce the identification of these centers as analogues.

iii. If X-irradiated Ge-doped quartz is heated to 600°K, the EPR spectrum exhibits responses from $[Si(E_1)e^-]$, $[Ge(III)e^-]$, and a 'hole' resonance not of present interest. All other magnetic responses are bleached. Both $[Si(E_1)e^-]$ and $[Ge(III)e^-]$ are bleached if the specimen is heated to 700°K. The generation and bleaching studies thus enable identification of $[Ge(III)e^-]$ as the true analogue to $[Si(E_1)e^-]$.

Except for the E_1' type $[Ge(IV)e^-]$ center, there is a close parallel between Si and Ge related E' centers.

The simplest model consistent with the spectroscopic analyses and formation kinetics is that the entire class of spectroscopically similar Si and Ge related E' centers are modifications of the electrically neutral single oxygen vacancy E defect. This picture is similar to the first models for E' defects proposed by Weeks and Nelson[32]. In Ge-free quartz, the room temperature stable center appears to be an electrically neutral three electron center compensated by an interstitial proton. This is the $[Si(E_2)e^-/H^+]$ center. The $[Ge(E_2)e^-/H^+]$ center is the analogue in Ge-containing quartz. In addition, the presence of substitutional Ge at the 'short bond' terminus of an oxygen vacancy stabilizes the [Ge(IV)e^-] center. This center is presumed to be an uncompensated three electron defect. It is electrically negative and unstable at room temperature. No analogue to this magnetic structure has been observed in Ge-free quartz.

The [Si(E_1)e^-] and [Ge(III)e^-] centers are high temperature quenched-in defects. It is possible that these centers represent half of a Frenkel defect (the other half being an interstitial oxygen). These are the only 'electron' defects ($\Delta g < 0$) stable above 600°K in α-SiO_2:Ge[31]. The spectroscopic similarity of [Ge(III)e^-] and [Ge(IV)e^-] suggests that these centers are quite similar, and hence that [Si(E_1)e^-] and [Ge(III)e^-] are three electron defects. This suggestion is, however, only tentative. Detailed kinetic studies are necessary to determine the difference between [Ge(III)e^-] and [Ge(IV)e^-]. One possible difference is association with a secondary defect (for example, the degree of separation from an interstitial oxygen).

The results summarized in Table 7 are thus useful in clarifying the spectroscopic measurements. The conclusions derived pertain to the ionic and electronic structure of the E' centers, and their relation to an electrically neutral single oxygen vacancy. The existing data are not sufficient to support a model of generation and bleaching kinetics more detailed than that just outlined.

As noted in Section 2 on spectroscopy, the model of E' centers as modifications of a single oxygen vacancy defect does not explain the complex Si^{29} hyperfine structure of the EPR spectra. Analysis of this structure has been critical to the argumentation for previously proposed divacancy models for E' centers[2]. The logic, though convincing, is circumstantial. It presumes that Si^{29} hyperfine energies of order 10^{-3} cm^{-1} results from the interaction of an electron and a Si^{29} nucleus across an oxygen vacancy and that hyperfine energies of order 10^{-4} cm^{-1} result from transferred hyperfine interaction across two Si–O bonds. This assignment has not been justified.

A final point relevant to the proposal of a single vacancy rather than a multiple vacancy model for E' centers is the observed effect of cation substitution in quartz. It might be

Table 7. Production and bleaching of magnetic E′ *centers in* α-SiO_2 *and* α-SiO_2:Ge

Center	Production	Bleaching
[Ge(IV)e^-]	50 kVp X-rays (300°K)[a]	Heat to 400°K[a] (unstable at 300°K[a])
[Si(E_2)e^-/H$^+$]	Co^{60} γ-rays (300°K)[b]	Heat above 525°K[b]
[Ge(E_2)e^-/H$^+$]	50 kVp X-rays (300°K)[a]	Heat to 500°K[a]
[Si(E_1)e^-]	50 kVp X-rays (300°K) plus heat to 600°K[a] Co^{60} γ-rays (300°K) plus heat to 575°K[b]	Heat to 700°K[a] Heat to 675°K[b]
[Ge(III)e^-]	50 kVp X-rays (300°K) plus heat to 600°K[a]	Heat to 700°K[a]

The references cited are:
(a) FEIGL F. J., Dissertation, University of Pittsburgh, unpublished (1965);
(b) WEEKS R. A. and NELSON C. M., *J. Am. Ceram. Soc.* **43**, 399 (1960).
Weeks' data on high temperature bleaching of [Si(E_2)e^-] are rather sparse; these measurements were incidental to his studies.

assumed that odd electron centers associated with single vacancies are not stable in covalent crystals, and that divacancy centers are the simplest structures that form stable magnetic electron traps. This assumption appears to underlie previous models for E' centers[2]. In this event, the presence of substitutional impurities might be expected to stabilize single vacancy magnetic centers. This situation is observed in doped elemental Si[33]. Such is not observed in α-SiO$_2$. The most commonly observed defects in Ge-doped quartz are the charged and neutral isoelectronic electron traps (the $[\mathrm{Ge(I,II)}e^-]$ centers[34] and the $[\mathrm{Ga(A,C)}e^-/\mathrm{M}^+]$ centers[5, 6], respectively) and the $[\mathrm{Al}e^+]$ impurity center. The latter is presently identified as a trapped hole associated with a Si-substituted Al in a normal lattice site[35]. The overall symmetry of the former centers is not consistent with single oxygen vacancy defects.

Thus, there is no evidence that Ge or Al stabilizes a class of vacancy related defects not observed in association with host cations. In this circumstance, the observation of E' centers associated with Ge impurities is in itself support for the single vacancy character of E defects.

4. CONCLUSION

X-irradiation of α-SiO$_2$:Ge results in the production of several vacancy related centers of the E' type associated with Si-substituted Ge impurities. Analysis of the electronic paramagnetic resonance response of these centers indicates that the unpaired electron occupies a nonbonding orbital strongly localized on the Ge impurity. Comparison of spectroscopic data for the several Si and Ge related E_1' and E_2' centers indicated that the basic electronic structure of all these centers is quite similar. A single oxygen vacancy model for the entire E' class of centers is adequate to explain much of the spectroscopic and kinetic data.

The single oxygen vacancy model represents a great simplification of current understanding of radiation defects in α-quartz. If subsequent calculations and experimental testing verify the model, the question of why no magnetic states occur in α-SiO$_2$ in connection with single vacancy defects is eliminated. While significantly more complicated that defect structures in covalent group IV elements, the single vacancy defect in partially covalent α-SiO$_2$ might be amenable to theoretical attack via currently developing techniques[3].

Acknowledgements—The authors should like to thank Professor W. Beall Fowler and Dr. John A. Weil for discussions of various aspects of this work. The advice and assistance of Professors R. C. Turner and Clyde A. Hutchison, Jr., in spectrometer design and construction is greatly appreciated. This work benefitted from support of materials research at Lehigh via the University's Materials Liaison Program.

REFERENCES

1. WEEKS R. A., *J. appl. Phys.* **27**, 1376 (1956).
2. WEEKS R. A., *Phys. Rev.* **130**, 570 (1963).
3. LIDIARD A. B., *Comments Solid St. Phys.* **1**, 112 (1968).
4. GRIFFITHS J. H. E., OWEN J. and WARD I. M., *Defects in Crystalline Solids: Report of the Bristol Conference*, p. 81. The Physical Society, London (1955).
5. ANDERSON J. H. and WEIL J. A., *J. chem. Phys.* **31**, 427 (1959).
6. VAN WIERINGEN J. S., HAVEN Y. and KATS A., *Magnetic and Electric Resonance and Relaxation: Proceedings of the XIth Colloque Ampere, Eindhoven 1962* (Edited by J. Smidt). North-Holland Publishing, Amsterdam (1963).
7. CASTLE J. G., Jr., FELDMAN D. W., KLEMENS P. G. and WEEKS R. A., *Phys. Rev.* **130**, 577 (1963).
8. BOZANIC D. A., MERGERIAN D. and MINARIK R. W., *Phys. Rev. Lett.* **21**, 541 (1968).
9. SCAVUZZO R. J., Dissertation, University of Pittsburgh, unpublished (1968).
10. FOWKES F. M. and BURGESS T. E., *Surf. Sci.* **13**, 184 (1969).
11. GROVE A. S., *Physics and Technology of Semiconductor Devices*, Chap. 12, New York (1967).
12. LAUDISE R. A. and NIELSEN J. W., *Solid St. Phys.* **12**, 149 (1961).
13. BALLMAN A. A. and LAUDISE R. A., *Hydrothermal growth*, in *The Art and Science of Growing Crystals* (Edited by J. J. Gilman). Wiley, New York (1963).
14. POOLE C. P., Jr., *Electron Spin Resonance*. Interscience, New York (1967).
15. IRE Committee on Piezoelectric Crystals, *Proc. IRE* **37**, 1378 (1949); CADY W. G., *Piezoelectricity*. McGraw-Hill, New York (1946).

16. MASON W. P., *Piezoelectric Crystals and Their Application to Ultrasonics*. Van Nostrand, New York (1950).
17. ROBERTSON J., *Introduction to Physical Optics*, 2nd Edn, p. 286. Van Nostrand, New York (1938).
18. WYCKOFF R. W. G., *Crystal Structures*, 2nd Edn, Vol. I, pp. 312–314, 405. Interscience, New York (1963).
19. SILSBEE R. H., *J. appl. Phys.* **32**, 145 (1961).
20. RUFFA A. R., *Phys. Status Solidi* **29**, 605 (1968).
21. WATKINS G. D. and CORBETT J. W., *Phys. Rev.* **121**, 1001 (1961); *Disc. Faraday Soc.* **31**, 86 (1961).
22. WATKINS G. D. and CORBETT J. W., *Phys. Rev.* **134**, A1359 (1964).
23. ELKIN E. L. and WATKINS G. D., *Phys. Rev.* **174**, 881 (1968).
24. BARNES R. G. and SMITH W. V., *Phys. Rev.* **93**, 95 (1954).
25. KOHN W. and LUTTINGER J. M., *Phys. Rev.* **97**, 883 (1955).
26. GADE S., Dissertation, University of Pittsburgh unpublished (1965).
27. MOORE C. E., *Atomic Energy Levels*, circular 467, National Bureau of Standards, Washington, D.C.
28. FOWLER W. B., *Physics of Color Centers* (Edited by W. B. Fowler), p. 136. Academic Press, New York (1968).
29. WEIL J. A. and ANDERSON J. H., *J. chem. Phys.* **35**, 1410 (1961).
30. WEEKS R. A. and ABRAHAM M. M., *Bull. Am. Phys. Soc.* **10**, 374 (1965).
31. FEIGL F. J., Dissertation, University of Pittsburgh, unpublished (1965).
32. NELSON C. M. and WEEKS R. A., *J. Am. Ceram. Soc.* **43**, 396 (1960); WEEKS R. A. and NELSON C. M., *J. Am. Ceram. Soc.* **43**, 399 (1960).
33. WATKINS G. D. and CORBETT J. W., *Disc. Faraday Soc.* **31**, 86 (1961).
34. MACKEY J. H., Jr., *J. Chem. Phys.* **39**, 74 (1963).
35. O'BRIEN M. C. M. and PRYCE M. H. L., *Defects in Crystalline Solids: Report of the Bristol Conference*, p. 88. The Physical Society, London (1955).
36. KATS A., *Philips Res. Repts.* **17**, 133 (1962).
37. WEIL J. A. and ANDERSON J. H., *J. chem. Phys.* **28**, 864 (1958).
38. BLEANEY B., *Phil. Mag.* **42**, 441 (1951).

APPENDIX: EPR ABSORPTION SPECTROSCOPY IN α-SiO$_2$

The greatest obstacle to acquisition of data on the Ge-related E' centers was the complexity of the electron paramagnetic resonance absorptions of Ge-doped quartz in the spectral region involved ($2{\cdot}0023 \geqslant g \geqslant 1{\cdot}9915$), i.e. approximately 3330–3350 Oersted for a microwave frequency of 9350 MHz. The centers designated [Ge(A)e^-/M$^+$], [Ge(C)e^-/M$^+$] and [Ge(I)e^-], previously studied in detail by Anderson and Weil[5], Van Wierengen and coworkers[6], and Mackey[34], all lie in this region and are generally of sufficient intensity to mask the absorption lines of present interest. Proper treatment of the specimen prior to spectroscopic measurement is thus very important in studying the [Ge(III)e^-] and [Ge(IV)e^-] centers. 'Proper treatment' in the present instance means a particular sequence of specimen treatments (X-irradiation, optical illumination, heating) that will selectively depress the intensity of the dominant EPR absorption from [Ge(A or C)e^-/M$_+$] and/or selectively enhance the absorption of the center being studied. These treatments are of interest in themselves, since they are central to any detailed description of the generation and destruction of defect structures and the interactions between such structures. However, with respect to spectrometry, they constitute recipes for the production of various entities (the E' centers in Ge-doped quartz), and it is useful to state them here.

All of the specimens were given irradiation doses of 4–10 hr with a target to specimen distance of approximately 5 cm. The tungsten target X-ray tube was run at 50 kVp 15 ma and a 0·004 in. beryllium window was between target and specimen. These relatively large irradiation dosages served to suppress the A and C absorption intensities relative to that of the other centers[31]. The following treatments are specific to a given center.

i. To observe the [Ge(IV)e^-] center absorptions, a specimen irradiated as just described is illuminated with high-intensity ultraviolet light. The [Ge(IV)e^-] center is stable under such illumination, while the A and C centers are bleached. Room temperature spectroscopy on [Ge(IV)e^-] is complicated by the instability of this center (see Table 7).
ii. To observe the [Ge(III)e^-] center absorptions, the irradiated specimen was heated slowly (10°/min) to 600°K, and cooled quickly (50°/min) to room temperature. This treatment bleaches the A and C centers and enhances the [Ge(III)e^-] absorption intensities.
iii. Spectrometry of the [Ge(E_2)e^-/H$^+$] center was performed on a hydrogen-diffused specimen. Replacement of the alkali impurity content by H$^+$, via electrolytic ion exchange[31, 36], greatly reduced the interference from [Ge(A, C)e^-/M$^+$]. The specimen was 'aged' at room temperature to reduce [Ge(IV)e^-] absorptions.

The primary magnetic resonance absorptions from the E' type centers being studied ([Ge(III, IV)e^-]) were of a particularly simple sort. A given center exhibits a single absorption line whose spectral position (d.c. polarizing magnetic field to resonance microwave frequency ratio) varies with orientation of the specimen in the polarizing field. In a given plane of rotation of the polarizing field, the quantity

$$g^2(\theta) = \left(\frac{h\nu}{\beta H}\right)^2$$

exhibits a $\cos 2\theta$ dependence. Thus, at fixed microwave frequency ν, the polarizing field at resonance, H, varies as $H^{-2} \alpha \cos 2\theta$. θ is the angle between the polarizing field and the position of a resonance field extremum in the plane. The lines were narrow (approximately 0·1 Oe, which approaches the limits of resolution of the type of spectrometer system utilized) and the variation in spectral position is within a small range (0·5 per cent, or, at fixed

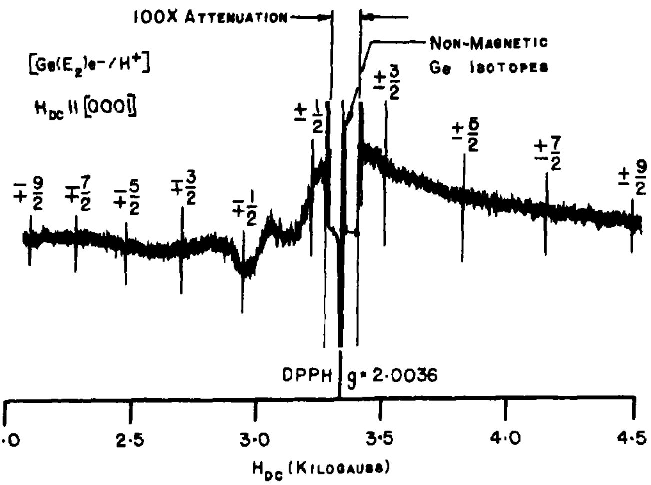

Fig. 5. A tracing of the derivative of the microwave absorption spectrum vs. magnetic field for $[\mathrm{Ge}(E_2)e^-/\mathrm{H}^+]$ center absorptions. The individual components of the ten line Ge^{73} hyperfine decad are labelled by nuclear spin projection numbers.

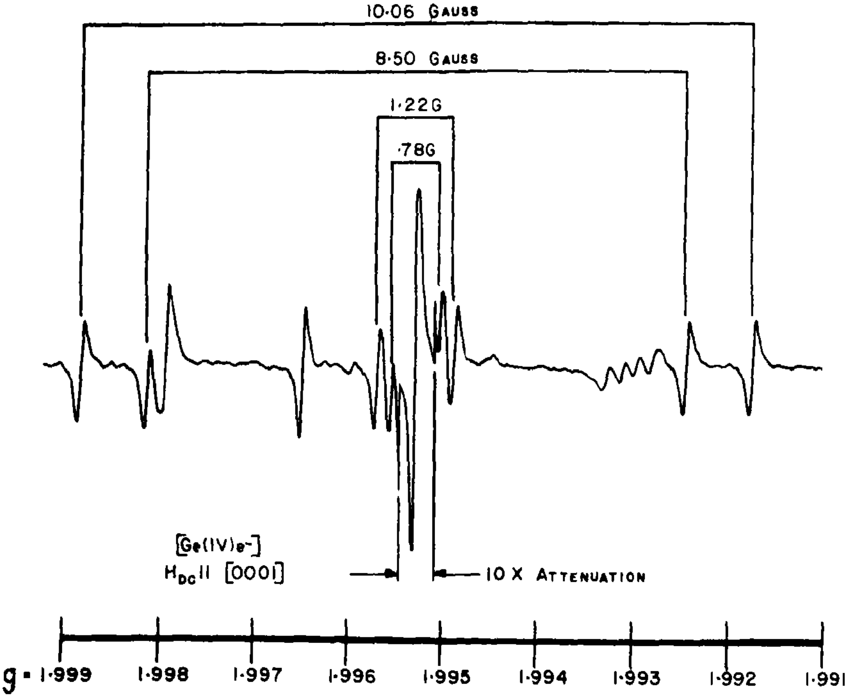

Fig. 6. A tracing of the derivative of the microwave absorption spectrum vs. magnetic field for $[\mathrm{Ge(IV)}e^-]$ center absorptions. The magnetic field axis is labelled in terms of g-values at the bottom of the diagram (magnetic field increases to the right). Four Si^{29} hyperfine doublets are indicated at the top of the diagram.

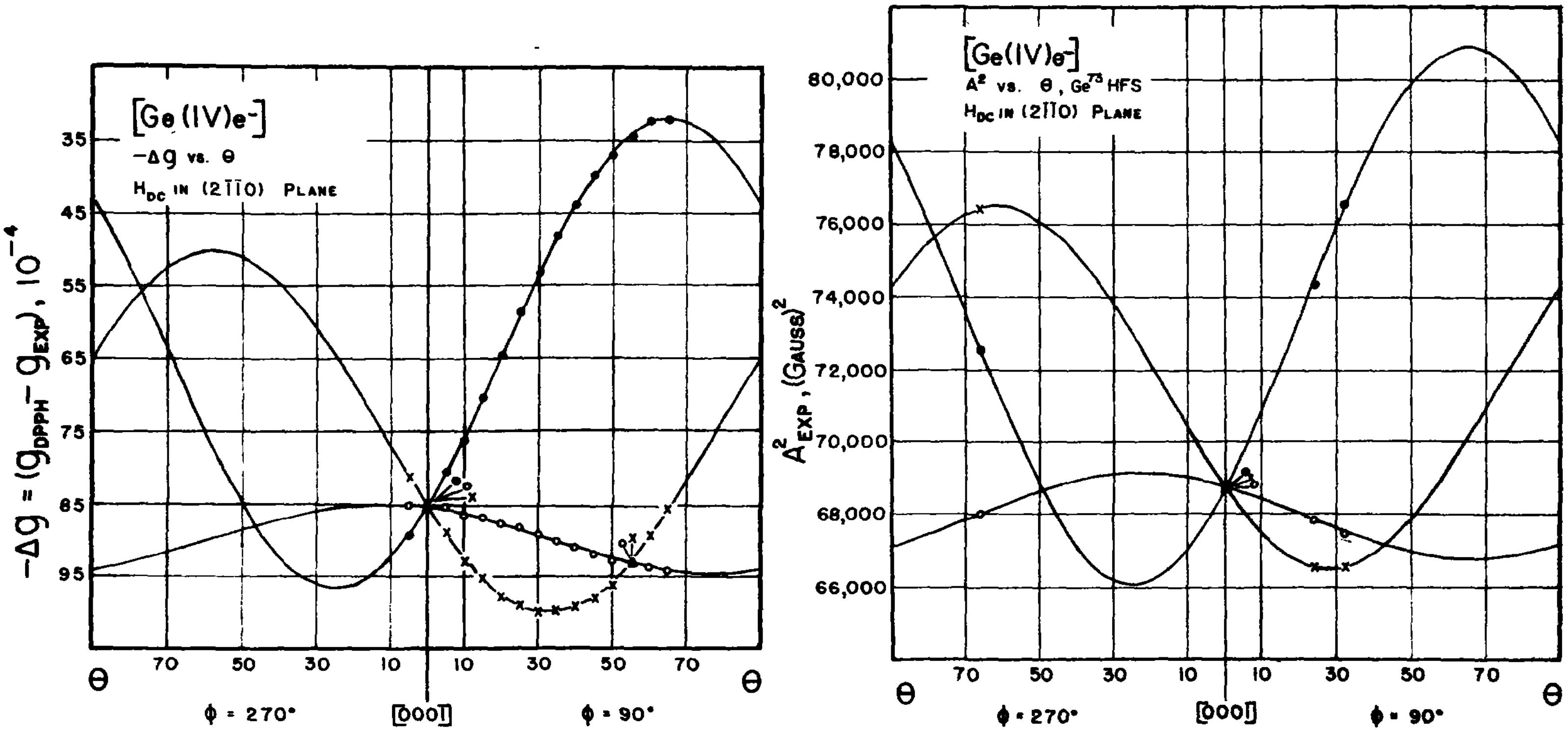

Fig. 7. Variation of experimental spectroscopic parameters for $[\mathrm{Ge(IV)}e^-]$ centers. The quantity θ is the angle between the crystal c-axis [0001] and the polarizing field, with the field in a mirror plane of the crystal, $(2\bar{1}10)$. (a) Δg vs. θ, where Δg is the experimental g-shift relative to a DPPH standard. (b) A^2 vs. θ, where A^2 is determined from H_M, the magnetic field positions of the Ge^{73} hyperfine components. M is the nuclear spin projection member ($M = \frac{9}{2}, \frac{7}{2}, \ldots -\frac{7}{2}, -\frac{9}{2}$).

$$A^2 \propto \left(\frac{H_M - H_{-M}}{2M}\right)^2.$$

frequency of 9350 Mc/sec, 15 Oe variation about a mean value of approximately 3340 Oe).

There are two factors which complicate these simple basic spectra: the symmetry of quartz, and the presence of minority isotopes of the several atomic species involved which possess nuclear moments, and which thus produce hyperfine (and superhyperfine) multiplets.

The point group of α-SiO_2 is D_3, consisting of a threefold screw axis (the *c*-axis) and three twofold axes perpendicular to *c* (the *a*-axes). A given direction associated with the SiO_4 bonding tetrahedron of quartz will be reproduced at six different spatial orientations in the quartz lattice structure. Thus, a given *type* of magnetic defect will exhibit six absorption lines for a general orientation of the polarizing field with respect to the crystal axes. Each absorption arises from one of the symmetry-related orientations of the SiO_4 bonding tetrahedron.

While complicating the basic spectra, the multiplication of spectral lines produced by the quartz symmetry simplified the experimental determination of the orientation dependence. A complete analysis in terms of the standard spin Hamiltonian formulation requires, in general, a determination of the spectral positions in three different planes (with respect to the crystal axes)[37]. In quartz, observation of the orientation dependence with the field maintained in a fixed plane with respect to the crystal axes will in general give information relative to six distinct planes of rotation of the field relative to the SiO_4 bonding tetrahedron.

This procedure provides more than sufficient information, and hence the experimental and mathematical task can be further simplified by a judicious choice of crystal orientation. The symmetry group relevant to EPR is actually the Laue group of α-SiO_2, D_{3d}. This group possesses three so-called 'mirror planes', i.e. planes of reflection symmetry, containing the *c*-axis and a *b*-axis (the *b* or mechanical axis of quartz is perpendicular to the *a* and *c* axes already defined, as illustrated in Fig. 1). If the polarizing magnetic field is at some arbitrary orientation in a mirror plane, a magnetic defect will in general exhibit three absorption lines, each line arising from defects associated with bonding tetrahedra which are related by reflection in the mirror plane. Thus, observation of the spectral behavior of the resonant absorptions with the polarizing field restricted to a mirror plane will yield information on the orientation dependence in three distinct planes. This is sufficient for complete specification of the *g*-tensor ellipsoid.

The least complex spectra are observed with the polarizing field parallel to the crystal *c*-axis[0001]. For this orientation, all symmetry related directions in the

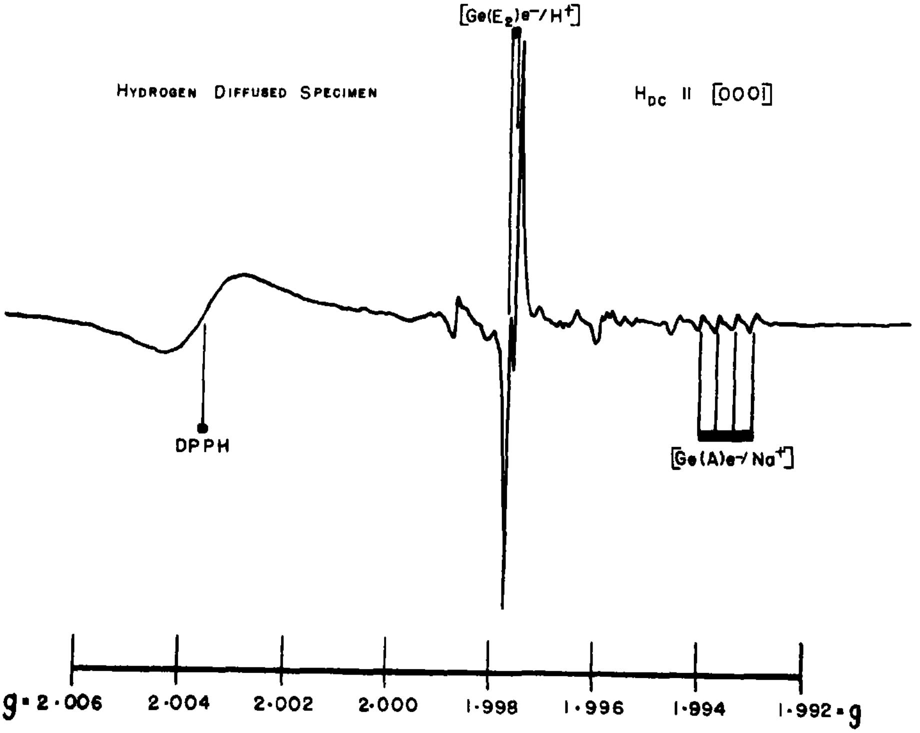

Fig. 8. A tracing of the derivative of the microwave absorption spectrum vs. magnetic field for $[Ge(E_2)e^-H^+]$. center absorptions. The magnetic field axis is labelled in terms of *g*-values at the bottom of the diagram (magnetic field increases to the right). The proton doublet is indicated at the top of the diagram.

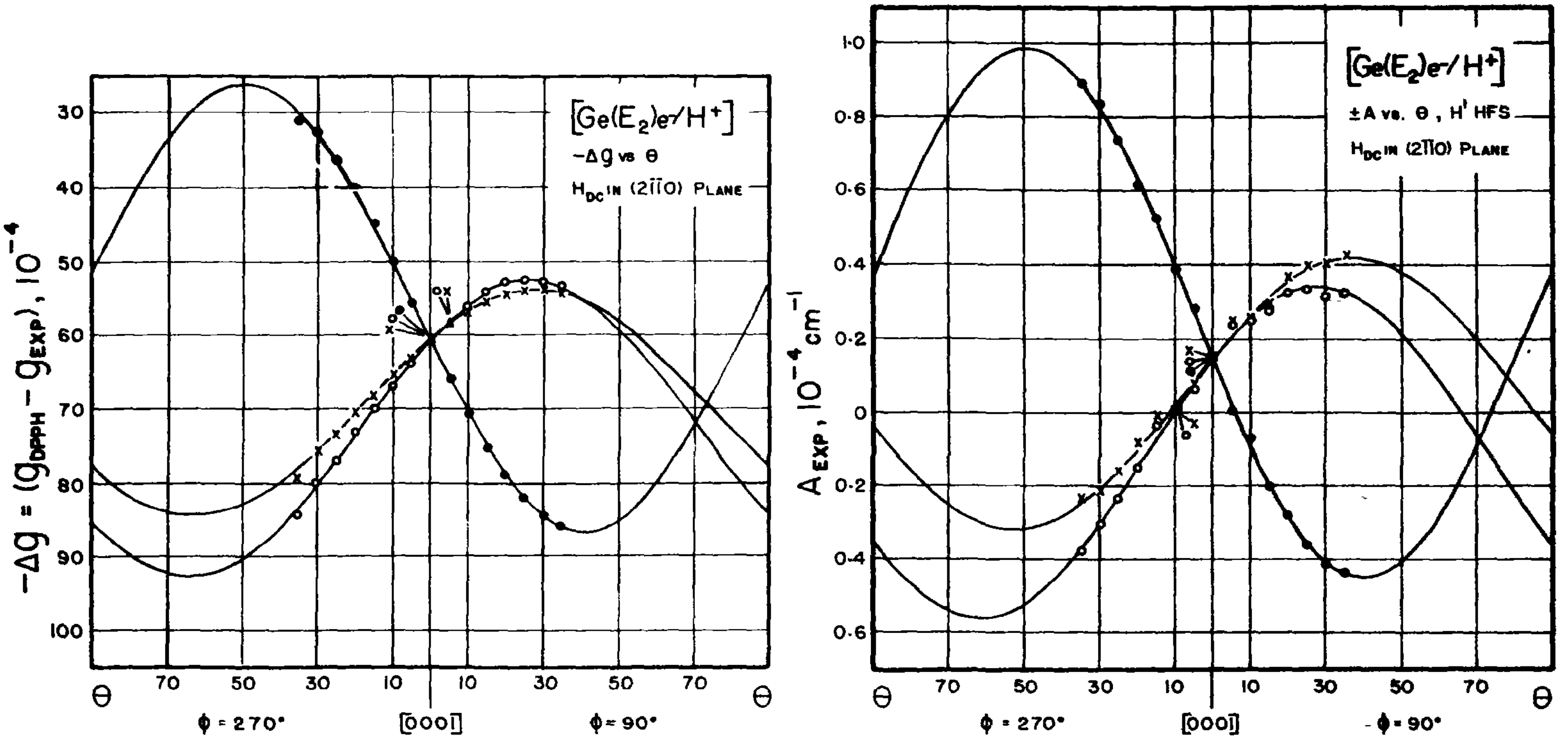

Fig. 9. Variation of experimental spectroscopic parameters for [Ge(E_2)e^-/H$^+$] centers. The quantity θ is the angle between the crystal c-axis [0001] and the polarizing field, with the field in a mirror plane of the crystal. (2$\bar{1}\bar{1}$0). (a) Δg vs. θ, where Δg is the experimental g-shift relative to a DPPH standard. (b) A vs. θ, where A is proportional to ΔH, the separation in field of the proton hyperfine components.

crystal are equivalent (that is, they all form the same angle with the polarizing field). These so called 'c-axis spectra' also contain the strongest spectral absorptions, and spectroscopic data for the c-axis orientation (H_{DC} parallel to [0001]) are presented in Tables 1–4 for reference.

The second complicating factor is the existence of hyperfine multiplets arising from magnetic nuclear species in the defect environment. The isotopes relevant to the present situation are those associated with the quartz lattice (Si^{29} – 4·7 per cent abundant with spin $\frac{1}{2}$) and the impurity of interest (Ge^{73} – 7 per cent abundant with spin $\frac{9}{2}$). The Si^{29} nuclei produce a hyperfine doublet each component of which should occur with an intensity relative to the primary absorptions of 2·35/95·3 = 2·51 per cent. The Ge^{73} nuclei produce a hyperfine decade. In the simplest instance, these lines would appear as ten equally spaced, equal intensity absorptions centered on the primary absorption. Each component of the Ge^{73} multiplet would have an intensity of 0·7 per cent of the primary absorption. Because of the magnitude of the Ge^{73} hyperfine interaction, the hyperfine decad is actually characterized by uneven spacing, unequal intensities, and a shifted center of mass relative to the primary absorption. A Ge^{73} hyperfine spectrum is illustrated in Fig. 5.

Figure 6 exhibits a c-axis EPR spectrum from [Ge(IV)e^-] centers in quartz. Figure 7 exhibits the angular variation of relevant experimental parameters for the [Ge(IV)e^-] centers. The analysis of these data resulted in Table 1 entries for [Ge(IV)e^-].

The analysis of Ge^{73} hyperfine data was performed using a modification of Bleaney's perturbation theory treatment[38]. Because of the magnitude of the Ge^{73} splittings, the perturbation theory results are not sufficient to reproduce experimental line positions to high accuracy. However, within the accuracy of our measurements (1 per cent), the Bleaney results are adequate. The hyperfine constants presented in Table 1 are sufficiently accurate to make the analysis of Table 5 reasonable. The experimental data was fit to all ten members of the Ge^{73} hyperfine decads. The hyperfine constants quoted in Table 5 for [Ge(III)e^-] were obtained by *assuming* that the Ge^{73} hyperfine tensor was axially symmetric and co-axial with the g-tensor. This assumption is quite reasonable[26]. The number of spin Hamiltonian parameters is thus reduced to two ($A_{\parallel}$ and $A_{\perp}$ of Section 2C). These are determined by the observed hyperfine splittings and the shift of the center of mass of the hyperfine decad for the c-axis orientation. However, it must be pointed out that, unlike the [Ge(IV)e^-] data, the symmetry of the main hyperfine interaction for [Ge(III)e^-] could not be verified experimentally.

The absence of large second order splittings of the Ge^{73} hyperfine lines is a direct confirmation of the spin $\frac{1}{2}$ character of the electronic state[38].

The very weak (1 Oe ≅ $10^{-4}\,cm^{-1}$) Si^{29} hyperfine doublets (Fig. 6) have not been measured in sufficient detail to permit analysis. The splittings observed at several orientations are of the same magnitude as the direct nuclear Zeeman interaction. Thus, the number of Si^{29} nuclei producing this hyperfine structure is not unambiguously determined[29].

For [Ge(E_2)e^-/H^+], the general features of the EPR spectra are similar to that just described. The outstanding difference is the doublet character of the primary response. This is illustrated in Fig. 8 for a c-axis orientation. Fig. 9 exhibits the angular variation of the g-tensor (mean position) and experimental hyperfine constant (doublet separation) in the mirror plane. The existence of the doublet structure and the vanishing of the doublet splitting at angular positions separated by less than 90° indicate the presence of a 100 per cent abundant spin $\frac{1}{2}$ nucleus with direct Zeeman interaction much greater than the observed doublet splittings. The only two such isotopes are H^1 and F^{19}. Specimen analyses do not reveal significant F^{19} impurity concentrations in the specimens used. Furthermore, [Ge(E_2)e^-/H^+] concentrations are enhanced by replacement of alkali impurities by H^+ via electrolytic ion exchange[31, 36]. The doublet hyperfine structure is thus assigned to an interstitial proton.

J. Phys. Chem. Solids Pergamon Press 1970. Vol. 31, pp. 597–600. Printed in Great Britain.

ELECTRICAL PROPERTIES OF METAL SURFACE BARRIERS ON THE LAYER STRUCTURES OF GaS AND GaSe

A. H. M. KIPPERMAN and H. F. VAN LEIDEN*
Department of Physics, Eindhoven University of Technology, Eindhoven, The Netherlands

(*Received* 29 *May* 1969; *in revised form* 19 *August* 1969)

Abstract – Barrier energies and I–V curves of several contact metals on *n*-type GaS are studied. The dependence of barrier energy on the work function of the metal can be interpreted by means of chemical interaction with the GaS.

INTRODUCTION

THE INVESTIGATION of electrical transport properties of the high ohmic (10^8–$10^6\,\Omega$ cm) semiconductors GaS and GaSe is hampered because of difficulties in controlling the contact properties. Contacts used in literature on GaS and GaSe are: indium contacts on GaS and GaSe, checked for ohmic behaviour [1]; evaporated Au on GaSe and GaTe[3], [4]; soldered Cu on GaSe[5] and alloyed In–Hg contacts on GaS[6]. Recently, Kurtin and Mead[7] have studied the properties of surface barriers on *p*-type GaSe by a photoresponse method.

We determined the barrier energies of the contacts on *n*-type GaS by measuring the photoresponse in a backwall technique. In addition, current–voltage (I–V) curves of the contacts were obtained by means of voltage probes (in darkness). All the measurements were carried out at room temperature. To avoid differences in bulk properties of the crystals we took them all from one ampulla (the GaS platelets have been grown by vapour transport [8]).

Together with the metal contacts to be investigated gold contacts were evaporated without breaking the vacuum, thus having a reference on each sample.

We found that in our case on GaS as well as in that of Kurtin and Mead on GaSe the relation between the barrier energies and the metal work functions shows a dependence on whether the heat of formation of the considered metal–sulphur (selenium) compound is greater or smaller than that of gallium sulphide (selenide).

SAMPLE PREPARATION

Without any surface treatments the crystals, thin platelets, were mounted in a mask on a small furnace in a high vacuum plant. The evaporation of the contact material occurred from Mo and W boats in a vacuum better than 10^{-5} Torr, argon atmosphere. During the first moments of evaporation a shutter was used to intercept surface impurities from the metal. Because of the better sticking on the surface of the sample, its temperature was raised to 300°C during evaporation. We also evaporated on cold (30°C) samples for purposes of comparison.

For the contact configuration see inset in Fig. 1.

EXPERIMENTS

The high resistances of the samples neccessitated the use of electrometers for the voltage and the current measurements (Keithley 610B and 417 respectively). The light source was a quartz halogen lamp

---

**Present address:* Philips Gloeilampenfabrieken Eindhoven, Netherlands.

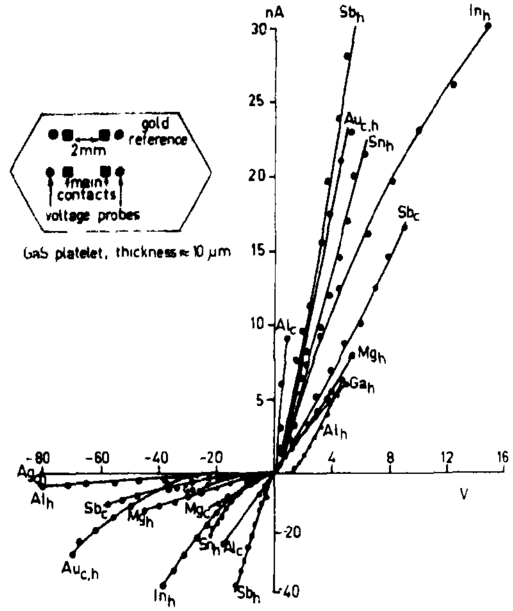

Fig. 1. Current-voltage curves of several contacts on n-type GaS; forward scales are expanded five times. Inset: configuration of the contacts on each sample, including gold as the reference. Subscripts: c, 'cold'; and h, 'hot'.

combined with narrowband interference filter (Balzers B20). Intensity was calibrated with a Si-photodiode (Siemens BPY11) in a short circuit arrangement.

n-*Type GaS*

The I–V curves of the main contacts are presented in Fig. 1. The strong blocking contacts as Au, Ag and Cu constantly showed fluctuations and also current creep during several hours after the reverse voltage was applied.

Figure 1 shows that the temperature during the evaporation of the contacts is very important for their behaviour. Especially the reverse currents of the base metals Al, Mg and Sb appear to be different for 'hot' and 'cold' evaporated contacts, while the same curves were measured for Au contacts. A nearly ohmic I–V curve is obtained in the case of 'hot' evaporated Sb contacts.

Barrier energies were measured by the photoresponse method[9]. At a constant number of incident photons the curves of the square root of the photocurrents vs. photon energy are straight lines. The intercept of the $h\nu$-axis corresponds to the barrier energy ϕ_B i.e. the energy difference between the Fermi level and the GaS conduction band at the interface.

Owing to the fact that the main contacts were of the same material, the photocurrents opposed each other. Therefore a voltage was applied across the sample so that the reverse contact determined the photocurrent. By switching the polarity the barrier energy of the other contact was achieved. The dark-current consequent upon this voltage was compensated. At the end of our experiments we measured a Ag contact in combination with an ohmic contact (Sb) with and without the voltage applied. In both cases we found the same barrier energy, therefore we conclude that barrier lowering due to image force is of no importance.

In Fig. 2 we have plotted the barrier energies

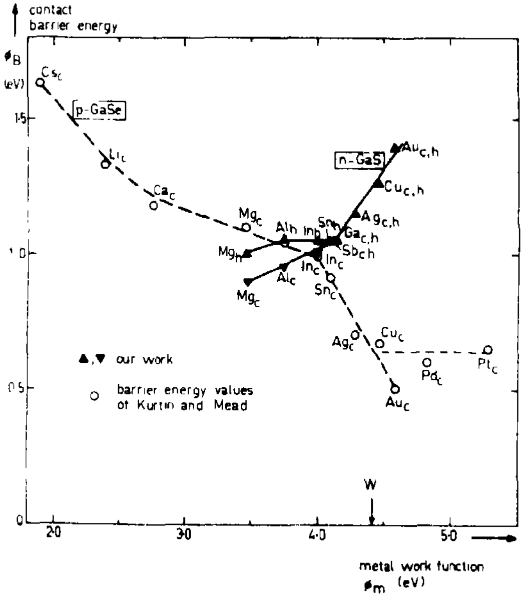

Fig. 2. Barrier energies of contacts on n-GaS and p-GaSe vs. work functions of the contact metals: the work function of tungsten is also indicated. Subscripts: c, 'cold'; and h, 'hot'.

on n-GaS vs. the work functions of the metals ϕ_m[10], together with the barrier energies on p-GaSe, measured by Kurtin and Mead.

p-*Type GaS*

Preliminary measurements of 'hot' contacts on p-GaS indicated a behaviour opposite to that of the n-type samples.

Nearly linear I–V curves showed Au, Ag and Cu contacts. The voltage drop across each of the contacts is less than a few per cent of the applied voltage. Sb contacts showed a blocking non-linear I–V curve.

DISCUSSION

The crystals had been grown as thin platelets, about 10 μm in thickness and had a perfectly clean surface. When they were exposed to air only a very small amount of impurities adhered because of the presence of a Van der Waals bond on the surface.

Apart from this, cleaving of the samples prior to deposition is not recommended, because of the large number of surface states that will arise. This statement is supported by the investigations of Turner and Roderick on metal–silicon Schottky barriers[11] and the electron microscope pictures of cleaved GaS and GaSe samples published by Basinski *et al.*[12]

Therefore, the surfaces of our samples were neither etched nor cleaved prior to deposition of the contact metal.

Comparison of the curves of the gold reference contacts did not indicate the presence of surface leakage.

Some remarks should be made about the I–V curves in Fig. 1. The forward curves have been influenced by the ohmic voltage drop of the bulk between main contact and voltage probe.

As to the reverse direction we tried to find out if the current increase might be caused by tunnelling through the barrier. Especially Sb_h shows a nearly ohmic behaviour, in contrast with Sb_c which was evaporated on the same surface of the sample without breaking the vacuum. According to Zalm[13] the log I vs. $V^{-1/2}$ curve will be linear for high voltages if tunnelling is the main transport mechanism. So we plotted the reverse currents for several contact metals in Fig. 3 and came to the conclusion that tunnelling is likely.

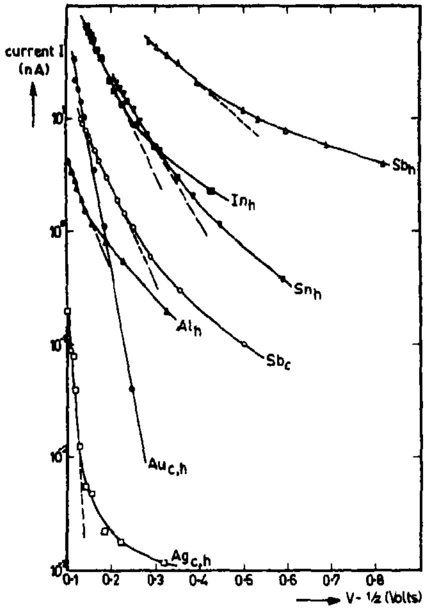

Fig. 3. Reverse current vs. voltage$^{-1/2}$ curves of several contacts on n-type GaS to show tunnelling according to Zalm[13]. Subscripts: c, 'cold'; and h, 'hot'.

It was impossible to determine the saturation owing to the rapid onset of the tunnelling.

The main contacts on each sample proved to have the same barrier energies; moreover, the barrier energies of all reference contacts (gold) were equal. This indicated that if there are any differences in surface conditions, they do not influence the barrier height and so we may compare the results obtained on several samples.

Considering the curves of Fig. 2 there are three remarkable points:

there is a sharp kink in both the GaS and GaSe curve;

the barrier energies of 'hot' contacts of the base metals on GaS are as good as fixed at the Ga value;

the slopes of the curves of *p*-GaSe and *n*-GaS are equal in the same intervals of ϕ_m.

We will explain these points considering the chemical interaction of the contact metal and the sulphur (selenium) atoms in the GaS (GaSe) lattice.

Comparing the heats of formation[14] of GaS (GaSe) and the sulphide (selenide) compounds of the contact metals we find three regions of reactivity:

1. Au, Ag, Cu, Pt and Pd will not react with the S or Se because of the much lower heats of formation of these compounds compared with GaS or GaSe.
2. Sn and Sb may react; the heats of formation have about the same values as GaS or GaSe.
3. Al, In, Mg, Ca, Li and Cs will react with the S or Se and consequently leave behind a very thin layer of Ga at the interface.

The thin Ga layer will change the effective work function of the contact metal. When, in the 'hot' case, more Ga is formed by the reaction, the barrier energy is equal to that of the Ga contacts.

The crystal surfaces of GaS and GaSe are equal, viz. a closed packed layer S (or Se) and a Van der Waals bond to the next S (or Se). Moreover, the chemical nature of S and Se is nearly the same; so equal slopes may be expected.

The slope of right hand parts of the curves in Fig. 2 is 0·8 both for GaS and for GaSe. In terms of uniform density of surface states according to Cowley and Sze[15] this means 2×10^{12} states (eV^{-1} cm^{-2}), while Kurtin and Mead have calculated 7×10^{12}. It should be pointed out, however, that the latter plotted the barrier energy vs. the electronegativity of the metal (Pauling units).

A remark should be made on the deviating points in Pt and Pd in Fig. 2. Because Pt and Pd are difficult to evaporate, we suppose that a small amount of the tungsten filament is evaporated too, thus lowering the work functions of the Pt and Pd contacts.

Acknowledgement—The authors wish to thank Professor Dr. F. van der Maesen for his constant interest and many helpful discussions.

REFERENCES

1. BUBE R. H. and LIND E. L., *Phys. Rev.* **119**, 1535 (1960).
2. BUBE R. H. and LIND E. L., *Phys. Rev.* **115**, 1159 (1959).
3. FISCHER G. and BREBNER J. L., *J Phys. Chem. Solids* **23**, 1363 (1962).
4. LEUNG P. C., ANDERMAN G. and SPITZER W. G., *J. Phys. Chem. Solids* **27**, 849 (1966).
5. GUSEINOV G. D. and RASULOV A. J., *Phys. Status Solidi* **18**, 911 (1966).
6. KIPPERMAN A. H.M. and Van der LEEDEN G. A., *Solid St. Commun.* **6**, 657 (1968).
7. KURTIN S. and Mead C. A., *J. Phys. Chem. Solids* **29**, 1856 (1968).
8. LIETH R. M. A., Van der HEIJDEN C. W. M. and Van KESSEL J. W. M., *J. cryst. Growth* **5**, 251 (1969).
9. FOWLER R. H., *Phys. Rev.* **38**, 45 (1931).
10. MICHAELSON H. B., *J. appl. Phys.* **21**, 536 (1950).
11. TURNER M. J. and RODERICK E. H., *Solid. St. Electron.* **11**, 291 (1968).
12. BASINSKI Z. S., DOVE D. B. and MOOSER E., *H.P.A.*, **34**, 373 (1961).
13. ZALM P., *Phil. Res. Rep.* **11**, 423 (1956).
14. KUBASCHEWSKI O., EVANS E. L. L. and ALCOCK C. B., *Metallurgical Thermochemistry.* Pergamon Press, Oxford (1967).
15. COWLEY A. M. and SZE S. M., *J. appl. Phys.* **36**, 3212 (1965).

J. Phys. Chem. Solids Pergamon Press 1970. Vol. 31, pp. 601–612. Printed in Great Britain.

SURVEY ANALYSIS OF IMPURITIES IN GALLIUM ARSENIDE BY INSTRUMENTAL NEUTRON ACTIVATION

K. B. WOLFSTIRN
Bell Telephone Laboratories, Incorporated, Murray Hill, N.J. 07971, U.S.A.

(*Received* 30 *April* 1969; *in revised form* 13 *August* 1969)

Abstract—The major advantages of activation analysis over almost all other analytical techniques are the avoidance of errors due to impurities in the chemical reagents employed in the procedure and high sensitivity in the determination of selective trace elements. A nondestructive investigation was made of six doped gallium arsenide crystals (Cr, O, Si, Ge) grown by the Bridgman, Czochralski and eutectic epitaxy techniques. The detection in the parts per billion to parts per million range and identification of radioisotopes of impurity elements having relatively short ($t_{1/2} \leq 0{\cdot}5$ day) and moderately long ($t_{1/2} \geq 2-250$ days) half-lives was considered. The specific resistivity range from 0·003 to $10^8 \Omega$ cm was studied No direct correlation was established between resistivity and spectrum intensity except for one heavily Si-doped crystal. All gallium arsenide crystals contained silicon at levels of $4{\cdot}3 \times 10^{16}$–$4{\cdot}7 \times 10^{17}$ atoms/cm^3. Other impurities detected were indium, gold, germanium and zinc at concentrations $< 3 \times 10^{16}$ atoms/cm^3; none of these were consistent contaminants. Phosphorus and indium were identified in a Ge-epitaxy layer on a Si-doped GaAs substrate. Semi-insulating Cr-doped gallium arsenide cyrstals were analyzed for chromium and found to contain $9{\cdot}8 \times 10^{17}$–$1{\cdot}59 \times 10^{18}$ Cr/cm^3. The chromium activation analysis results do not appear to bear any relationship with the concentrations derived from the electrical measurements and suggest the existence of an inhomogeneous second phase. Improvements in the instrumental technique are discussed which can lead to the determination of additional elements for trace characterization of bulk and solution grown gallium arsenide.

INTRODUCTION

IT IS IMPORTANT to check the purity of bulk semiconductor crystals for the following reasons: (1) device advances are based on the ability to produce, measure, and control highly pure materials and the knowledge of the trace elements present is important in explaining their role in electronic processes; (2) commonly employed crystal growth conditions can lead to impurity incorporation and distribution of a rather complex nature. Trace element studies of impurities in gallium arsenide[1, 2, 3] indicate that many elements are present below 10^{16} atoms/cm^3 (i.e. Ca, Cu, Mg, Al, Ni, Fe, K, S). The mass spectrometric work of Brice *et al.*[1] shows carbon, oxygen and nitrogen as the only consistently high concentration impurities in gallium arsenide. They report small amounts of many elements in both Bridgman and pulled crystals. A bulk concentration $> 10^{18}$ cm^{-3} oxygen in gallium arsenide is reported by Bailey and Ross[4] using the $^{16}O(T,n)^{18}F$ reaction. Ahearn *et al.* [3] detected sixteen elements in their mass spectrographic analysis of zone and Bridgman grown gallium arsenide. They concluded that surface absorption of impurities from various pretreatments accounted for most of their observations. Kern[5] grew gallium arsenide crystals by the horizontal Bridgman technique in neutron activated quartz boats. The impurities transferred to the gallium arsenide from the quartz were silicon, copper, gallium, antimony and gold at $\leq 10^{16}$ atoms/cm^3. A neutron activation study by Bujdoso *et al.*[6] of Bridgman grown gallium arsenide showed impurity concentration gradients along the length of the ingot for silver, cobalt, iron, indium and zinc. Green *et al.*[7] determined the short-lived isotopes of silicon, zinc and magnesium in gallium arsenide at concentrations of 10^{-9}–10^{-7} g using neutron activation analysis and radiochemical separations. They established also that the thermal neutron flux density

(4×10^{13} neutrons/cm^2/sec) was not modified by the gallium arsenide matrix during an irradiation.

The objective of this work was the determination of the chromium concentration of Cr-doped gallium arsenide crystals and also to compare the purity of different as-grown samples by instrumental neutron activation analysis. Gallium arsenide synthesized by the horizontal Bridgman, Czochralski, and eutectic epitaxy[8] techniques was analyzed. The elements present were identified after irradiation without chemical separations from the energy of the beta and gamma radiations emitted and half-life measurements.

The fundamental principles and general techniques of activation analysis have been extensively described in the literature[9]. Activation analysis using neutrons as the irradiating media, has been widely used in analyzing for trace impurities in solids[10]. Neutron activation analysis is capable of giving the required sensitivity for many elements and has been used to determine impurity characterization in germanium[11], silicon [12] and gallium arsenide[13] in the parts per million or parts per billion range. Other features tending to make the technique attractive are: (1) elimination of reagent characterization common to many other analytical techniques, (2) most sample handling can be done after the activation step minimizing contamination problems and (3) lack of interference from neighboring elements since the decay properties of radioactive isotopes are unrelated to their chemical properties. Gallium and indium, for example, are related on the basis of similar chemical properties but have dissimilar radioactive properties.

The use of post-growth activation analysis for the III-V compounds can require laborious procedures for the simultaneous determination of several elements in the sample. The matrix elements themselves contain readily activated elements yielding complicated gamma-ray spectra because of the production of several radioactive isotopes each of which has a number of gamma-ray energies in its characteristic spectrum. In order to sort out and identify the component gamma-ray lines, it is necessary either to employ elaborate and time consuming chemical separations or to resort to indirect methods such as the synthetic analysis of the spectrum with the use of matrix standards and spectrum standard curves. The latter approach of post-spectrometer data analysis to separate gamma and/or beta-ray energies was used here.

EXPERIMENTAL

A. *Activation*

Thermal-neutron (slow neutron) activation is very pertinent to the preparation of radiotracers because stable isotopes of many elements have an (n,γ) reaction that produce a radioisotope of the same element. Fast neutrons with energies higher than thermal are normally present in nuclear reactors and the reactions (n,p), (n,α) and $(n,2n)$ can also occur. Table 1 details the nuclides that might be present when gallium arsenide is bombarded with thermal and fast neutrons along with the characteristics of the radionuclides. The activity produced when one milligram of each element is irradiated by a flux of thermal and fast neutrons for 12 hr also is included in Table 1, column 6.

The properties of the gallium arsenide samples used in this study are listed in Table 2. The crystals were randomly selected to provide variety as to growth method (Bridgman, Czochralski and solution), dopant (Cr, O, Ge, and Si), and resistivity (0·003–$10^8\Omega$ cm). They were prepared for activation in the following way in order to minimize preactivation contamination of materials which might lead to significant errors in the results. The surface of a 50–100 mg weight sample of each gallium arsenide crystal was lapped on #600 Aloxite paper, etched twice in 5% bromine in methanol, rinsed in methanol, lapped with a slurry of alumina powder in water followed by two final etches in bromine and alcohol, rinsed

Table 1. GaAs *nuclear data*

Nuclear reaction	Half-life[a]	Type of decay[b] and major radiation energy (MeV)		Decay product (stable)	Activation cross section (barns)[c]	Specific activity after irradiation[d] (dis/sec/mg)
Matrix						
^{69}Ga(n,γ)^{70}Ga	20 m	β^-	1·65	Ge	1·4[e]	$1{\cdot}85 \times 10^{8}$
		γ	0·17			
^{71}Ga(n,γ)^{72}Ga	14·1 h	β^-	0·96	Ge	5·0[e]	$1{\cdot}52 \times 10^{8}$
		γ	0·63,0·84			
^{69}Ga(n,2n)^{68}Ga	68 m	β^+	1·90	Zn	0·55[f]	$2{\cdot}8 \times 10^{4}$
		γ	0·81–1·88			
^{69}Ga(n,p)^{69}Zn	14 h	IT	0·44	Ga	0·024[f]	$1{\cdot}1 \times 10^{2}$
^{71}Ga(n,p)^{71}Zn	3·9 h	β^-	1·5	Ga	0·0005[g]	$2{\cdot}6 \times 10^{1}$
		γ	0·39,0·49,0·61			
^{69}Ga(n,α)^{66}Cu	5·1 m	β^-	2·63	Zn	0·105[f]	$4{\cdot}0 \times 10^{3}$
		γ	0·83,1·04			
^{71}Ga(n,α)^{68}Cu	30 s	β^-	3·5	Zn	—	—
		γ	0·81–1·88			
^{75}As(n,γ)^{76}As	26·5 h	β^-	2·97	Se	4·5[e]	$2{\cdot}0 \times 10^{8}$
		γ	0·56–2·7			
^{75}As(n,2n)^{74}As	18 d	β^+	0·90	Ge	0·55[f]	$2{\cdot}8 \times 10^{4}$
		β^-	1·36	Se		
		γ	0·60,0·64–2·53			
^{75}As(n,p)^{75}Ge	82 m	β^-	1·20	As	0·118[f]	$5{\cdot}0 \times 10^{1}$
		γ	0·07–·63			
^{75}As(n,α)^{72}Ga	14·1 h	β^-	0·96	Ge	0·123[f]	$5{\cdot}2 \times 10^{1}$
		γ	0·63,0·84			
		γ	0·56–2·7		—	—
Impurities						
^{197}Au(n,γ)^{198}Au	2·7 d	β^-	1·37	Hg	98·8[e]	$5{\cdot}7 \times 10^{12}$
		γ	0·41			
^{50}Cr(n,γ)^{51}Cr	27·8 d	γ	0·32	Mn	17[e]	$2{\cdot}8 \times 10^{7}$
^{70}Ge(n,γ)^{71}Ge	11·4 d	EC		As	3·2[e]	$4{\cdot}6 \times 10^{7}$
^{113}In(n,γ)^{114}In	50·1 d	IT		Sn	8[e]	$2{\cdot}5 \times 10^{7}$
		γ	0·19			
^{31}P(n,γ)^{32}P	14·3 d	β^-	1·71	S	0·19[e]	$2{\cdot}3 \times 10^{7}$
^{30}Si(n,γ)^{31}Si	2·7 h	β^-	1·47	P	0·4[e]	$1{\cdot}85 \times 10^{6}$
^{64}Zn(n,γ)^{65}Zn	245 d	EC		Ga	0·46[e]	$8{\cdot}1 \times 10^{5}$
		γ	1·11			

[a] s, seconds; m, minutes; h, hours; d, days.

[b] β^+, positron emission; β^-, negatron emission; γ, photon, IT, internal-conversion electron; EC, electron capture.

[c] One barn equals 10^{-24} cm^2.

[d] Activity in dis/sec/mg of the element, assuming natural abundance ratios for the isotopes, immediately after 12 hr irradiation at thermal neutron flux of $2{\cdot}5 \times 10^{13}$ neutrons/cm^2/sec and fast neutron flux of 2×10^{10} neutrons/cm^2/sec. (The ratio of thermal to fast neutron flux depends upon the position of target material in the core. Union Carbide, Tuxedo, New York, Private communication).

[e] GOLDMAN D. T., *Chart of the Nuclides*. General Electric Co. Schenectady, New York (1964, 1965).

[f] PAUL E. B. and CLARKE R. L., *Can. J. Phys*. **31**, 267 (1953); COHEN B. L., *Phys. Rev*. **81**, 184 (1951).

[g] CHATTERJEE A., *Nucleonics* **23**, 112 (1965).

in methanol and blot dried on filter paper. Each specimen was cleaved and ~ 20 mg weight sample sealed in an evacuated quartz ampoule (10^{-4} Torr). Samples to serve as comparative standards were prepared by sealing separately in quartz weighed quantities of arsenic oxide, chromium, copper, gallium oxide, germanium and silicon. To minimize

Table 2. Properties of GaAs *crystals*

Crystal	Dopant	Type	Reported carrier concentration (cm^{-3}) 25°C	Reported resistivity (Ω cm) 25°C
BH-465[a]	Cr	Semi-insulating	–	3×10^8
BH-548[a]	Cr	Semi-insulating	–	5×10^7
HB-G1185[b]	O	Semi-insulating	–	6×10^7
HB-G1051[b]	Undoped	*N*	$7{\cdot}6 \times 10^{15}$	0·23
C2-547[a]	Si	*N*	$7{\cdot}0 \times 10^{17}$	0·003
7A[c]	Ge	*P*	$1{\cdot}1 \times 10^{19}$	0·006

[a] Czochralski grown crystal.
[b] Horizontal Bridgman crystal.
[c] Eutectic epitaxy[8].

random flux distributions, the gallium arsenide crystals and standard elements were irradiated for 12 hr in the same core position of the Union Carbide reactor facility at Tuxedo, New York at a flux of $2{\cdot}5 \times 10^{13}$ neutrons/cm²/sec.

B. *Detection*

1. ***Beta spectrometry.*** The induced activity produced was measured by means of gas-flow counting and scintillation detection. Proportional gas-flow counting provides high sensitivity for beta radioactivity measurements and minimizes interfering gamma radiation from activated impurities. The counting rates were corrected according to standard radiochemical techniques. The counts per minute per milligram of gallium arsenide were plotted semilogarithmically as a function of time. Graphical resolution of the decay curves into the components made it possible to determine half-lives. The maximum beta energy of the resolved components was determined by absorption measurements with aluminum and lead absorbers. These parameters aided in the identification of beta-radiation emitting nuclides like silicon and germanium. The concentration and rate of decay of silicon in the gallium arsenide crystals was determined by the comparator procedure described below. The analysis was started as soon as the samples were received from the irradiation facility.

Silicon-31 ($t_{1/2}$ 2·7 hr) is the only silicon radioisotope to be considered, as it decays mostly by the emission of beta particles (1·47 MeV) which can be measured by proportional gas-flow counting. Comparator standards containing the same weight of gallium and arsenic as in the test samples were counted under identical conditions to those used for the gallium arsenide crystals. The activities of simulated gallium, arsenic and silicon comparator standards with silicon concentrations from 10^{-9} to 10^{-5} g were used for the calculation of the silicon content of the gallium arsenide crystals. Each gallium arsenide sample and standard was measured every 45 min for 12 hr to establish the decay rate.

Table 3 lists the appropriate beta emissions from the three elements[14]. It is obvious that the matrix interferes with the silicon determination since both gallium and arsenic have

Table 3. β-Ray energy distribution

Isotope	Type of decay	Particle energy (MeV) and distribution
Arsenic-76	β^-	0·30– 1·9%
		0·55– 0·9%
		1·20– 6·6%
		1·75– 3·6%
		2·41–30·6%
		2·97–56·4%
Gallium-72	β^-	0·67–41%
		0·96–35%
		1·51– 7%
		1·94– 7%
		2·53– 5%
		3·17– 5%
Silicon-31	β^-	1·47–100%

beta emissions > 1·47 MeV. The activity observed by the selective use of aluminum absorbers of known thickness and stopping power minimized this difficulty. Table 4 lists the aluminum absorbers used along with their stopping power in MeV. The activity of the standard containing gallium and arsenic only was compared with standards containing known amounts of gallium, arsenic and silicon. The Si–Ga, As standards exhibited two component decay for absorbers in the energy range from 1·2 to 2·0 MeV. A typical absorption–decay curve for absorption at 1·4 and 2·0 MeV for one GaAs crystal (HB-1051) is shown in Fig. 1. The faster decaying component with a measured 3·3 hr half-life was attributed to ^{31}Si. Gallium (14·1 hr) and arsenic (26·5 hr) were the major contributors in the composite slower decaying component during the initial 12 hr devoted to the silicon analysis. Each short-lived component became less significant as time passed. Longer-lived activities from impurities like germanium (11 days) and phosphorus (14·3 days) predominated in the residual curves of some crystals.

Table 4. *β-Ray absorption*

Aluminum absorber	Range in Al		Stopping power energy (MeV)
	Thickness (mm)	Mg cm^{-2}	
15	1·85	495	1·2
16	2·11	560	1·3
17	2·39	625	1·4
18	2·67	701	1·5
19	3·30	861	1·8
20	3·73	961	2·0

The possibility that the observed half-life (3·3 hr) and beta energy (1·5 MeV) might be assigned to ^{71m}Zn from the fast neutron (*n,p*) reaction on ^{71}Ga instead of to ^{31}Si was discredited on the following basis. The smaller cross section and lower flux density for the Zn reaction results in a lower specific activity (Table 1, column 6) even when consideration is given to the larger number of matrix atoms compared to silicon as an impurity. Consideration was directed at detecting the ^{71m}Zn interference-reaction product by a spectrum scan of pure gallium. Failure to detect gamma-ray peaks at 0·39, 0·49 and 0·61 MeV in the appropriate peak intensity ratios with an ~ 4 hr half-life indicated ^{71}Zn was not present at a measureable concentration.

2. *Gamma spectrometry*. The scintillator for gamma detection was a well-type 3 in.

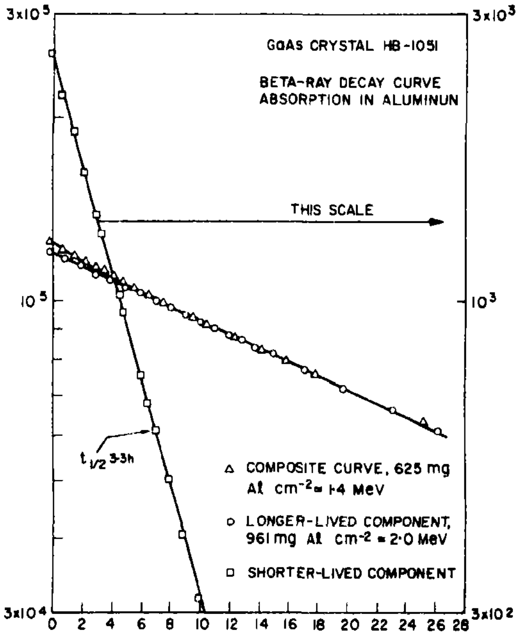

Fig. 1. Beta-ray decay curve for undoped GaAs crystal HB 1051: (△) composite decay curve β-ray absorption in aluminum, 625 mg Al cm^{-2} ≃ 1·4 MeV; (○) longer-lived component β-ray absorption in aluminum 961 mg Al cm^{-2} ≃ 2·0 MeV (composed mostly of ^{76}As); (□) shorter-lived component, $t_{1/2}$ = 3·3 hr ≃ 2·3 × 10^{-8}g Si.

thallium-activated sodium iodide crystal. The counting geometry was varied to accommodate samples too radioactive to count in the standard well-position. Initially the samples were counted with a polystyrene cap (0·7 g/cm^2) covering the NaI detector because of the beta-ray continuum from the matrix elements. Spectra was plotted from a print-out in terms of counting rate per minute as a function of channel number and gamma-ray energy as transmitted from a multi-channel differential pulse-height analyzer. Energy calibration of the spectrometer was made with gamma rays from suitable radioactive reference sources. Each channel is equal to approximately 0·01 MeV when the energy scale is 1 MeV.

Radioactive standards used in the gallium arsenide investigation were prepared by dissolving the activated elements in appropriate solvents and making up to known volumes. The spectra, decay scheme and energy characteristics of aliquots of these primary standards at counting rates similar to the unknowns were observed. This last consideration is important because there will likely be some count-rate dependent gain or zero shifts between spectra if the activities of standards and samples differ by a large factor.

RESULTS AND DISCUSSION

Figure 2 shows the half-life and calculated detector sensitivity in micrograms of a number of elements irradiated at a flux of 2·5 × 10^{13} neutrons/cm^2/sec for 12 hr. Oxygen, nitrogen, hydrogen and carbon have been deleted from the scheme of elements on Fig. 2. These particular elements are insensitive to the (n,γ) nuclear reaction considered here. Therefore, their presence as possible impurities in gallium arsenide was not evaluated. The detection sensitivities listed on Fig. 2 will be halved for each half-life delay. The activated gallium arsenide crystals were allowed to decay for 24 hr after removal from the reactor before the radioanalysis was undertaken. In this way, the high radiation levels of the short-lived ^{72}Ga (14·1 hr) and ^{76}As(26·5 hr) nuclides were decreased somewhat as was the sensitivity of detecting the presence of other fast decaying impurities. The radioactive decay measurements and spectrum scanning were continued for 130 days following neutron bombardment.

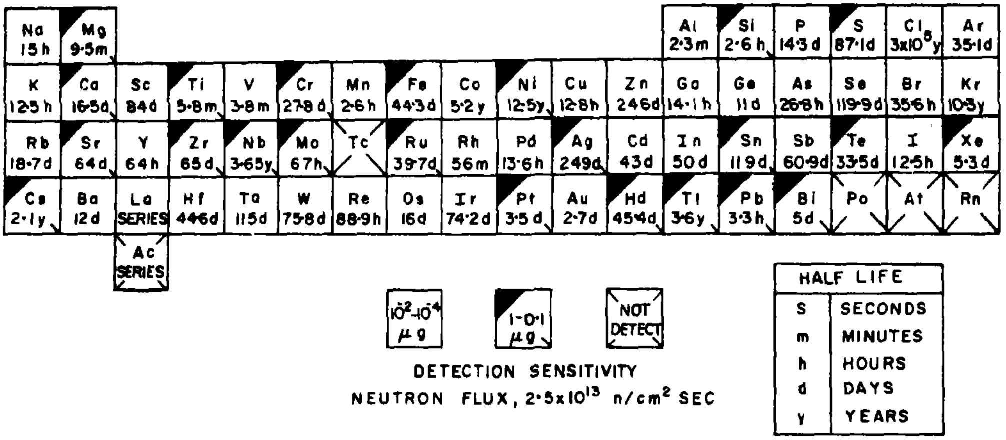

Fig. 2. Detection sensitivity for elements irradiated with 2·5 × 10^{13} neutrons/cm^2-sec for 12 hr. Those shown in open boxes are readily detected by activation analysis. Elements in quarter filled corner squares are detectable only if present in the higher concentrations indicated. Some are not detected and are so indicated by corner hatches. The detection sensitivity could be increased by longer irradiation times or higher fluxes. Conversely they will be halved for each half-life delay.

The silicon analysis was an exception to this procedure. The beta (max. 1·47 MeV) decay measurements of ^{31}Si were started immediately and terminated in 12 hr.

Since each radioactive isotope in the sample has a different half-life and a characteristic set of gamma energies, the graph presented by the differential analyzer is really the sum of all the elements in the sample. Typical spectra from a chromium-doped gallium arsenide crystal taken 72 hr and 24 days after bombardment are shown in Figs. 3 and 4 respectively. Some peaks can be readily associated with certain elements, others are composites and more difficult to unravel. The practive of spectrum stripping was employed, using the primary standard solutions, the pulses due to known elements are subtracted from the sum graph. The resulting spectra becomes less confusing, remaining elements stand out and are identified by using a table of standard spectra and energies[15]. The integrated areas under the respective peaks were calculated to obtain absolute counting rates. Concentrations of the detected elements were determined from the total activity and solution of the neutron activation equation.

$$m = \frac{A_t \, . \, N}{\Theta \, . \, K \, . \, \sigma_{ac} f (1 - e^{-\lambda T_1}) (e^{-\lambda T_2})} \qquad (1)$$

where

m = the mass of the element present in grams

A_t = measured activity in counts per second at time t due to the element

N = atomic weight/Avogadro's number

Θ = isotopic abundance of the target element

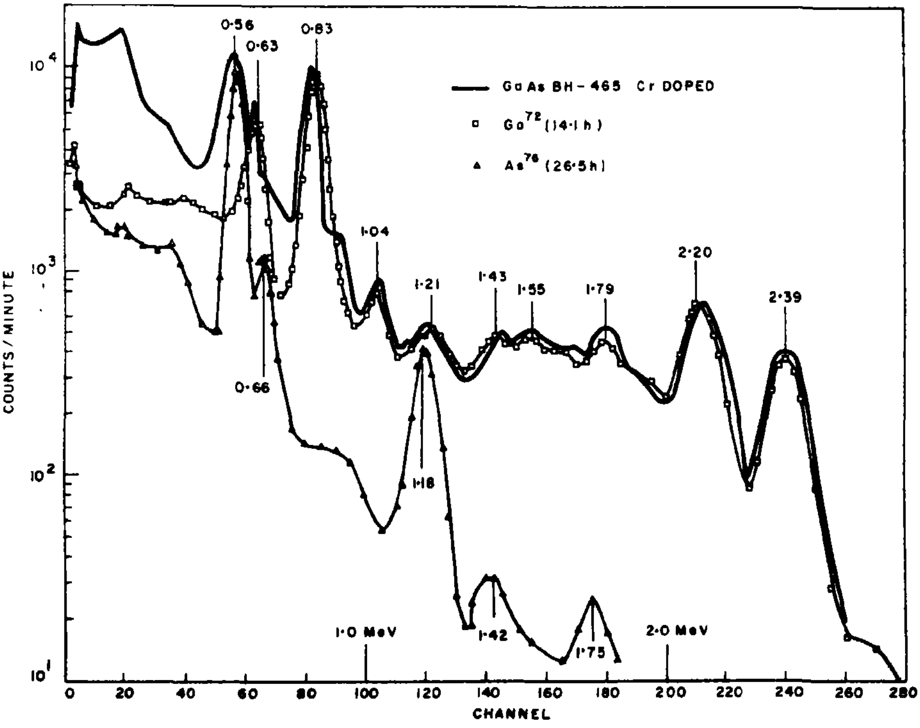

Fig. 3. Experimental composite gamma spectrum (solid line) for Cr-doped GaAs crystal (BH-465) 72 hr after irradiation. Activity in counts/min is plotted against channel number. Standard spectra ^{72}Ga (□) and ^{76}As (△) are included with peak energies shown in MeV.

K = efficiency of the counter for measuring the induced radioactivity

σ_{ac} = activation cross section[16] for neutron capture by the target material, square centimeters per atom per neutron

f = flux of neutrons per square centimeter per second

λ = disintegration constant of the radioactive material

T_1 = the irradiation time, duration of exposure to neutron flux

T_2 = decay time between irradiation and counting

Copper and arsenic were used as the flux monitors and the thermal neutron activity induced was measured by the absolute counting of ^{64}Cu and ^{76}As. Assuming a thermal neutron cross section[16] of 415 barns for ^{64}Cu and for ^{76}As, it was possible to calculate the flux in which the monitors were exposed and similarly the gallium arsenide samples.

In addition to other γ-ray peaks, spectrum stripping of the matrix elements ^{72}Ga and ^{76}As revealed two prominent gamma peaks at 0·51 ($\beta^+\beta^-$ annihilation peak) and 0·60 MeV decaying with a half-life of 17·5 ± 0·4 day in all gallium arsenide crystals (Fig. 4) and the arsenic standard. Successive layers of gallium arsenide were removed from each of the crystals by chemical etching in bromine-methanol solution until only 10 per cent (by weight) of the crystal remained undissolved. The spectra reproduced identically indicating a homogeneous distribution. A search[17, 18] of probable isotopes with the determined gamma energies and half-life indicated ^{121}Te or ^{74}As as likely candidates. However, tellurium was eliminated because (1) production of ^{121}Te sufficient to give the observed activity is improbable when the irradiation time, flux, isotopic abundance and cross section for the ^{120}Te (n,γ) ^{121}Te reaction is considered, (2) other tellurium isotopes more favorable to the (n,γ) reaction were not identified, (3) the active species emits two strong lines and the relative intensity ratios in the sample spectra do not check the known values for ^{121}Te. Arsenic has only one stable isotope, arsenic-75, in 100 per cent natural abundance. As a major constituent of gallium arsenide, it is present several orders of magnitude above the total amounts of contaminant. Therefore, the observed γ-ray peaks seem to be associated with ^{74}As resulting from the $(n,2n)$ fast neutron reaction on ^{75}As (Table 1). The irradiation time, flux and cross section for the fast neutron reaction (0·5 barn, ~ 0·1 that for

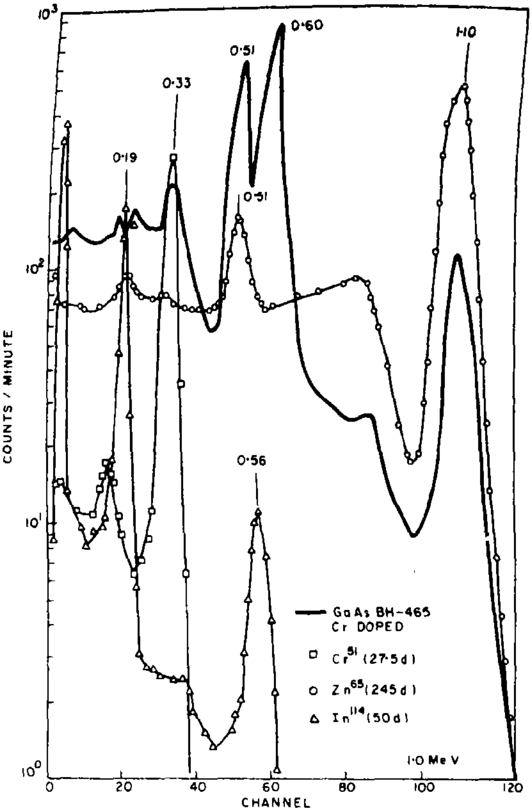

Fig. 4 Experimental composite gamma spectrum for Cr-doped GaAs crystal (BH-465) 24 days after irradiation (solid line) plotted as activity in counts/min vs. channel number. The standard spectra[15] for ^{51}Cr (□), ^{65}Zn (○), and ^{114}In (△) are included for comparison with the peak energies shown in MeV. The two peaks at 0·51 and 0·60 MeV, associated with ^{74}As are labelled on the experimental spectrum.

thermal neutrons) are favorable to its production and observation. The observed intensity of the gamma peak ratios are also consistent with reported values[15] as is its half-life[17]. This interference spectrum was subtracted from each curve of the gallium arsenide analysis.

Figure 3 shows the comparison of the experimental composite spectrum of a Cr-doped gallium arsenide crystal (BH-465) with the individual standard spectrum from ^{72}Ga and ^{76}As. Counts per minute are plotted against channel number for a measurement taken 72 hr after neutron bombardment when the gallium and arsenic nuclides dominate the curve. At this stage in the analysis, counting rates associated with the gallium arsenide matrix are stripped from the experimental spectrum. The residuals are plotted and scanned for γ-peaks. The areas under significant peaks are calculated. Identification of the observed γ-peaks was based largely on the energies of the lines, the relative peak intensity ratios of the active species and finally the half-life determination. For those cases where primary standards were not used, peak area activities were converted to concentration through equation (1).

Figure 4 shows the experimental spectrum for the same Cr-doped crystal taken 24 days later when the ^{72}Ga and ^{76}As had decreased below the detection limit. The maximum gamma energy peaks in MeV are noted. The experimental composite spectrum shows the interfering ^{74}As peaks and the impurities indium (0·19 MeV), chromium (0·32 MeV) and zinc (1·1 MeV). The ^{114}In, ^{51}Cr and ^{65}Zn taken from standard spectra curves[15] are included on the figure for comparison.

Table 5 gives the results of the crystal analyses. It also lists the measured gamma or beta energy and half-life of the resolved impurity. The high chromium concentrations reported for crystals BH-465 and BH-548 of $9{\cdot}8\times10^{17}$ and $1{\cdot}59\times10^{18}$ atoms/cm^3 respectively seem inconsistent with the electrical data in Table 2. Chromium has been reported to have a deep lying level in GaAs with an ionization energy of 0·8 eV[19]. On this basis, $\sim10^{18}$ Cr/cm^3 might be expected to be partly electrically active at 25°C with about 10^{12}/cm^3 uncompensated free carriers ($p\sim10^3\,\Omega$ cm). Therefore, no direct relation can be established between the quantity of the impurity and the value of specific resistivity reported as 10^7–$10^8\Omega$ cm. Little is reported about the chromium solubility in gallium arsenide. Work by Selway[20] and in this laboratory on the diffusion of chromium in gallium arsenide indicate C_0 concentrations from $\sim3\times10^{16}$ to $\sim3\times10^{18}$ atoms/cm^3 in the temperature range 870–1100°C. The semi-insulating behavior in the presence of so large an impurity concentration might be explained if Cr is an amphoteric impurity in GaAs and results in autocompensation. Its existence as a separate phase in the crystal has been suggested by Cronin and Haisty[21].

The high germanium concentration, $6{\cdot}6\times10^{21}$ Ge/cm^3, in the Ge-doped epitaxial layer grown on silicon doped GaAs crystal C2-547 is due to precipitated germanium in the crystal. Photomicrographs after angle lapping showed a number of peaks at the surface which are attributed to germanium regrowth[22]. These enriched areas would give the layer an abnormally high germanium concentration. It is interesting that phosphorus and indium were found as impurities in the Ge-epi layer removed from the gallium arsenide substrate by lapping. Neither of these elements were detected in the substrate. This suggests neutron activation as a possible method for evaluating the purity of epitaxial grown material, since impurity distribution in doped epitaxial layers may be determined by concentration profiles.

All the crystals described in this work had silicon contamination at levels ranging from $4{\cdot}3\times10^{16}$ to $4{\cdot}7\times10^{17}$ atoms/cm^3 (±75 per cent). Although primary standards were used, interference and the short half-life of ^{31}Si adversely affects the accuracy. Crystal C2-547 had the highest concentration and was

Table 5. Impurity elements in GaAs *as detected by neutron activation analysis*

Impurity	Radio nuclide	Measured gamma energy MeV (± 3%)	Measured half-life^{f} (± 5%)	GaAs crystals (atoms/cm^{3})^{d} BH-465^{a}	BH-548^{a}	HB-1185	HB-1051	C2-547
Cr	^{51}Cr	0·32	27·0^{d}	$9·84 \times 10^{17}$	$1·59 \times 10^{18}$	–	–	–
Si	^{31}Si	1·26.1·48^{b}	3·3 h	$6·4 \times 10^{16}$	$8·1 \times 10^{16}$	$4·3 \times 10^{16}$	$2·3 \times 10^{17}$	$4·7 \times 10^{17}$
Au	^{198}Au	0·41	2·7 d	$1·1 \times 10^{16}$	–	$2·7 \times 10^{16}$	–	–
Ge	^{71}Ge	EC(0·23^{e})	11 d	–	–	–	$8·7 \times 10^{15}$	$6·62 \times 10^{21c}$
P	^{32}P	1·70^{b}	14·3 d	–	–	–	–	$1·1 \times 10^{16c}$
Zn	^{65}Zn	1·11	235 d	$1·4 \times 10^{16}$	$2·1 \times 10^{16}$	–	–	–
In	^{114}In	0·19	50·5 d	–	–	$2·5 \times 10^{16}$	–	$3·1 \times 10^{16c}$

[a] Cr doped.

[b] Maximum beta energy.

[c] Ge epi layer grown on GaAs substrate. Crystal 7A (Table 2).

[d] Cr, Ge concentration determined by comparison with primary standards (± 5%). Au, P, Zn, In calculated from equation (1) (± 60%). Si determinations made using primary standards (± 75%) for ^{31}Si.

[e] Electron capture decay.

[f] h, hour; d, day.

purposely doped (Table 2) while the crystal with the lowest silicon concentration (HB-1185) was oxygen doped. This observation is consistent with Woods and Ainslie[23] who have investigated the role oxygen plays in reducing silicon contamination of gallium arsenide. No other impurities were detected in crystal C2-547 and 1 : 1 correlation between the silicon concentration and carrier concentration exists.

Small quantities ($< 3 \times 10^{16}$ atoms/cm^3) of a number of elements were found in all the crystals. Specifically identified were germanium, gold, indium and zinc. None were found to be consistent contaminants. Only the germanium concentration was determined from a primary standard. The $\sim 10^{16}$ Ge/cm^3 found in crystal HB-1051 is believed to be in excess of the amount transmuted as a result of the β^- nuclear reaction on gallium.

The activation analysis results in Table 5 appear to be unrelated to the electrical data in Table 2 with the exception perhaps of the silicon-doped crystal, C2-547. These data show that the resistivity could be subject to suspect if regarded as an unbiased purity index. A similar finding through a combination of activation and autoradiographic analysis has been reported for semiconductor grade silicon[24]. Localized concentrations of mercury and sulfur were found in 107Ω cm n-type zone refined material. Martin[24] also detected and located nonuniform distributions of copper and gold on the surfaces of silicon diodes that had little effect on the reverse current characteristics.

Impurities other than those listed in Table 5 may be present but because of either a short half-life (i.e. Na, K, Cu, Mn, Mg, Al, Li, B) or low sensitivity of detection, (i.e. Ca, Ni, Sn, Fe) would not be resolved under the described experimental conditions unless present at $\geqslant 10^{17}$–10^{18} atoms/cm^3. Both these limitations could be more favorably presented if rapid chemical separation methods for gallium and arsenic were employed and longer irradiation times were used.

The technique of activation analysis offers considerable promise for the analytical measurement of trace elements owing to the high sensitivity which becomes available at high flux levels. The method is free from the errors due to impurities in the chemical reagents employed in the procedure and has the additional advantage of etching the surface of a sample between activation and processing in order to remove any contamination. The problem of distinguishing the induced radioactivity due to one element in the presence of other activities can be resolved in several ways. In classical activation analysis, the approach involves the complete radiochemical purification of the induced activities, and the separation of the individual radioactive element from all other radioactivities present. Such a procedure is a time consuming and often a strenuous task. Another approach involves the use of the gamma-ray spectrometer where the radioactive element may be distinguished in terms of its gamma-ray spectrum. When the matrix contains several radioactivities, such as in the case of gallium arsenide, the spectrometer has difficulty in distinguishing and sorting the energies present. One or two simple processes of radiochemical purification could be sufficient to improve the usefulness of the spectrometer when complex mixtures are analyzed. With the use of simple separations the scope and sensitivity of the activation method can be extended so as to be useful as a post-crystal growth characterization tool. The application of a solid state detector, Ge(Li), to the nondestructive analysis of gallium arsenide might allow wider application of the technique because of its higher resolution relative to NaI scintillators. These approaches are presently under consideration.

CONCLUSION

An instrumental survey analysis of impurities in Bridgman, Czochralski and eutectic epitaxy grown gallium arsenide crystals lead to the following conclusions:

1. Semi-insulating Cr-doped GaAs contained $9\cdot8 \times 10^{17}$ and $1\cdot59 \times 10^{18}$ Cr/cm^3, some quantity of which exists in the crystal in an electrically neutral or compensated state.

2. Silicon is a consistent contaminant in the crystals surveyed at levels of $4\cdot3 \times 10^{16}$–$4\cdot7 \times 10^{17}$ atoms/cm^3.

3. Small quantities of other impurities, germanium, gold, indium and zinc not exceeding 3×10^{16} atoms/cm^3 were found to be intermittent bulk contaminants.

4. A Ge-epitaxial layer grown on an *n*-type GaAs substrate had phosphorus and indium as impurity constituents at $1\cdot1 \times 10^{16}$ and $3\cdot1 \times 10^{16}$ atoms/cm^3 respectively.

5. No 1 : 1 correlation was established between spectra intensity and reported resistivity except for a heavily Si-doped crystal.

6. Chemical separations and increased detection sensitivity could make activation analysis a useful and powerful tool for purity evaluation of bulk and solution grown GaAs.

Acknowledgements—The author is indebted to B. Schwartz for suggesting the project be undertaken and for his comments on the manuscript. Grateful acknowledgement is made also to N. Schwartz and J. D. Struthers for valuable comments, to F. E. Rosztoczy and D. T. Lassota for supplying the Ge-doped GaAs sample, and to J. V. Dalton for use of the multi-channel analyzer and associated equipment.

REFERENCES

1. BRICE J. C., ROBERTS J. A. and SMITH G., *J. mat. Sci.* **2**, 131 (1967).
2. GILBERT E. N. and ARTYUKHIN P. I., *Izv. Sib. Old. Akad. Nauk. SSSr, Ser. Khim. Nauk* **2**, 90 (1967).
3. AHEARN A. J., MALM D. L., SOBERS R. G. and WHELAN J. M., Private communication.
4. BAILEY R. F. and ROSS D. A., *Analyt. Chem.* **35**, 791 (1963).
5. KERN W., *J. electrochem. Soc.* **109**, 200 (1962).
6. BUJDOSO E., MISKEI M. and ORMOS GY., *Proc. Conf. Appl. Phys. Chem. Methods Chem. Anal.*, Budapest **2**, 262 (1966).
7. GREEN D. E., HESLOP J. A. B. and WHITLEY J. E., *Analyst* **88**, 522 (1963).
8. ROSZTOCZY F. E., *J. electrochem. Soc.* **115**, C328 (1968).
9. BOWEN H. J. M. and GIBBONS D. *Radioactivation Analysis*. Clarendon Press, Oxford (1963).
10. KOHN A., *Metall. Rev.* **3**, 143 (1958).
11. MORRISON G. H. and COSGROVE J. F., *Analyt. Chem.* **28**, 320 (1956).
12. MORRISON G. H. and COSGROVE J. F., *Analyt. Chem.* **27**, 810 (1955); KANT A., CALI J. P. and THOMPSON H., *ibid* **28**, 1867 (1956).
13. HARVEY J. T. and SMITH A. J., A.M.L. Report B/122 (M) (1957); HESLOP J. A. B. and CLARKE H. B., A.M.L. Report B/155 (M) (1957).
14. WILSON B. J. (ed.), *The Radiochemical Manual*. Radiochemical Centre, Amersham (1966).
15. HEATH R. L., *Scintillation Spectrometry Gamma Ray Spectrum Catalogue*, Vol. 2. IDO-16880 TIB-4500 (1964).
16. The nuclear cross section is proportional to the probability that the bombarding particles will activate the target nuclei. Values from *Chart of the Nuclides*. General Electric Co., Schenectady, New York (1965).
17. LEDERER C. M., HOLLANDER J. M. and PERLMAN I., *Table of Isotopes*, 6th edn. Wiley, New York (1967).
18. CLARK H. M. and NEIL D. E., *A Table of Radionuclides Arranged According to Half-Life*, USAEC-3144. Federal Clearinghouse, Virginia (1955).
19. HEATH D. R., SELWAY P. R. and TOOKE C. C., *Br. J. appl. Phys.* Ser. 2 **1**, 29 (1968).
20. SELWAY P. R., Research Report AD-826232 (1967).
21. CRONIN G. R. and HAISTY R. W., *J. electrochem. Soc.* **111**, 874 (1964).
22. ROSZTOCZY F. E., Private communication.
23. WOODS J. F. and AINSLIE N. G., *J. appl. Phys.* **34**, 1469 (1963).
24. MARTIN J., *1968 International Conference on Modern Trends in Activation Analysis, Gaithersburg, Maryland (1968)*. NBS Special Publ 312, Vol. 1 p. 517 (1969).

J. Phys. Chem. Solids Pergamon Press 1970. Vol. 31, pp. 613–618. Printed in Great Britain.

ISOTOPIC EFFECTS ON THE THERMAL EXPANSION OF LITHIUM HYDRIDE*

J. L. ANDERSON, J. NASISE, K. PHILIPSON† and F. E. PRETZEL (deceased)
Los Alamos Scientific Laboratory, University of California, Los Alamos, N.M., 87544, U.S.A.

(*Received* 7 *August* 1969)

Abstract—The effect of substitution of one isotope for another in the LiH molecule has been investigated between −196° and 240°C. The isotope effect on lattice parameter, a_0, density, and coefficient of thermal expansion shows a definite trend whereby the lighter isotopes have larger lattice parameters and smaller coefficients of thermal expansion that the heavier isotopes. These effects are more pronounced when the lighter element is the one undergoing substitution. At the lower temperature the effect is relatively large but diminishes at the higher temperature. It is demonstrated that the lattice parameter for the isotopic lithium hydrides can, at any temperature, be related by the linear expression

$$a_0 = A\mu^{-1/2} + B.$$

These isotopic effects are discussed within the framework of the theories of Ubbelohde and London.

INTRODUCTION

UBBELOHDE[1] pointed out in 1935 that the substitution of one isotope for another, in a solid chemical compound, will lead to differences in the rotational and vibrational frequencies of the molecules, without producing any significant change in the structure of the potential energy of the solid. These substitutions cause changes in the lattice constant, a_0, and in the coefficient of thermal expansion, α, of the solid. These changes can be related directly to the vibrational frequencies of the molecules, which in turn are a function of the reduced mass, μ. Hence, isotopic substitution of hydrogen isotopes should be especially effective in such studies. Lithium hydride, which has a NaCl crystal structure, is a particularly convenient compound to use in an investigation of isotope effects. Due to its low molecular weight and reduced mass, both properties experience observable changes on substitution of either hydride or lithium ions. There have been several investigations in the past few years of these isotopic effects on the lithium hydride molecule[2–6]. The present work expands both the isotopic compositions investigated and the temperature range studied.

EXPERIMENTAL

The lattice parameters of ^{n}LiH, ^{n}LiD, ^{6}LiH, ^{6}LiD and ^{7}LiT were determined by X-ray diffraction at −190° and 25°C. This also permitted the calculation of an average coefficient of thermal expansion, $\bar{\alpha}$, over this 215° temperature interval. Densities of ^{6}LiH, ^{6}LiD, ^{7}LiH and ^{7}LiD were determined, by flotation, over the 25°–140°C and 140°–240°C temperature intervals. From these density measurements, lattice parameters and $\bar{\alpha}$'s could be calculated. It was possible to convert the low temperature ^{n}LiH and ^{n}LiD values to 'pure' ^{7}LiH and ^{7}LiD values for comparison with the 25°–240°C data on ^{7}LiH and ^{7}LiD.

Samples

The crystals used in this experiment came from several sources. The ^{n}LiH, ^{n}LiD, ^{7}LiH, ^{7}LiD and ^{6}LiH were prepared in this laboratory using the technique developed by Pretzel [6]. The ^{6}LiD was prepared by and purchased from the Y-12 Plant, Oak Ridge, Tenn. This material was then recrystallized and annealed in the apparatus used for growing single crystals. The ^{7}LiT was actually $^7LiT_{0.88}H_{0.12}$ purchased from Mound Laboratory, Miamisburg, Ohio. This was in the form of small (~2–3 mm on a side) crystals when received, and was used with no further treatment. Again, using Vegard's rule, the values obtained for this material were converted to 'pure' ^{7}LiT values.

---

*Work done under the auspices of the U.S. Atomic Energy Commission.

†Guest Scientist, Los Alamos Scientific Laboratory Summer Student Program. *Present address:* University of California, Berkeley, California.

Apparatus

The X-ray diffraction data were obtained on powder of ~50 micron average particle size. The diffraction pattern was obtained with a vacuum X-ray diffractometer stage attached to a Philips-Norelco X-ray diffractometer. The apparatus and technique have been discussed previously[7, 8]. Measurements of lattice parameters were taken at −190°±1°C and at 25°±1°C. These temperatures were measured with a chromel–alumel thermocouple attached to the stage adjacent to the sample. The low temperature was maintained by flowing liquid nitrogen through the stage. X-radiation from a Cr target was used to determine the diffraction pattern over the 100–160 degree back reflection region. This yielded the (220), (311), and (222) lines for the isotopic LiH's. From the maxima of these diffraction lines, the lattice parameters were calculated with an IBM-704 program using Hess's modified least-squares extrapolation [9].

Because of the low electron densities of the lithium and hydride ions, LiH is quite transparent even to soft Cr X-radiation. As the temperature is increased the diffraction lines become quite weak and diffuse[5, 12] with a resultant loss of precision in determining a_0. For this reason the X-ray diffraction technique was less desirable in the 25°–240°C temperature range. A flotation technique was therefore used to determine crystal densities over this temperature range. Here, carefully dried liquids, with a density at the temperature of interest, closely matching that of the LiH crystal were calibrated so that the density and coefficient of thermal expansion of the liquid were accurately known over the temperature range of interest. Prior to calibration, these liquids were outgassed carefully by freezing in liquid N_2, evacuating the volume over the frozen liquid, isolating this section of the apparatus and allowing the liquid to warm in vacuum to room temperature. This process was repeated a sufficient number of times to insure adequate outgassing. A small (~2 mm on an edge) crystal of the isotopic LiH was then sealed in a quartz tube containing the dried, outgassed liquid. This tube was then placed in a regulated temperature bath, and the temperature of the bath varied until the crystal was suspended in the liquid. Then, knowing the density of the liquid at that temperature, the density of the crystal was known. The temperature of the bath was controlled to ±0·05°C which, for most liquids used, corresponded to ~±0·005 per cent density variation. The temperature was measured using a Pt resistance thermometer calibrated by NBS and a Mueller bridge calibrated by the electronics Group, LASL. The ice point was daily measured with this thermometer as a check on stability and reproducibility of the thermometer.

The liquids used as flotation liquids were inert, dried liquids. Benzene, octane, heptane, DC-556 silicone fluid and several DC-200 silicone fluids were used. All liquids used in this work were dried by storing over crystalline LiH and Linde 5A molecular sieve. The liquids were stored, over the drying agents, at a temperature equal to the highest flotation temperature expected.

The measured densities could then be converted to lattice constants. These values were then used to calculate average values of the coefficient of thermal expansion, $\bar{\alpha}$, over the temperature interval of interest.

RESULTS

The lattice parameters of ^{6}LiH, ^{6}LiD, ^{n}LiH, ^{n}LiD and ^{7}LiT were measured at −190° and 25°C. The flotation densities of ^{6}LiH, ^{6}LiD,

^{7}LiH and ^{7}LiD were measured at temperatures near 25°, 140° and 240°C. There was a definite isotope effect observed in both lattice parameter and coefficient of thermal expansion. Table 1 lists the reduced mass, μ, $\mu^{-1/2}$ and lattice constants at −190°, 25°, 140° and 240°C.

It was demonstrated that, at any given temperature, T, the lattice constant, a_0, for the isotopic series could be related by the expression $a_0 = A\mu^{-1/2} + B$[11], where: μ = reduced mass; A and B are constants. Figure 1 is a plot of this relationship at −190°, 25°, 140° and 240°C. This plot was used to convert the a_0 for ^{n}LiH and ^{n}LiD to a_0 values for 'pure' ^{7}LiH and ^{7}LiD at −190° and 25°C. It will be noted that as the temperature is increased, the slope of this line approaches zero. If indeed there was no isotope effect, the slope should, at all temperatures, be zero. This decreasing slope implies that the effect of isotopic substitution is reduced at higher temperatures. Table 2 lists the slopes of these lines at the temperatures studied. It will be noted that the isotope effect is such that the lighter isotopes result in a higher lattice constant. This is a result of the lower reduced mass of these isotopic compositions, and will be discussed in more detail in the next section.

Table 1. *Reduced mass and lattice parameters for isotopic* LiH

Isotopic composition	μ	$\mu^{-1/2}$	Lattice parameters			
			−190°C	25°C	140°C	240°C
^{6}LiH	0·8632	1·0763	4·0666	4·0851	4·1013	4·1218
^{7}LiH	0·8814	1·0652	4·0657	4·0829	4·1005	4·1224
^{6}LiD	1·5095	0·8139	4·0499	4·0708	4·0888	4·1110
^{7}LiD	1·5649	0·7993	4·0477	4·0693	4·0893	4·1119
^{7}LiT	2·1094	0·6886	4·0403	4·0633	–	–

Table 2. $a_0 = A\mu^{-1/2} + B$

Temperature (°C)	A
−190	0·0665
25	0·0523
140	0·0464
240	0·0407

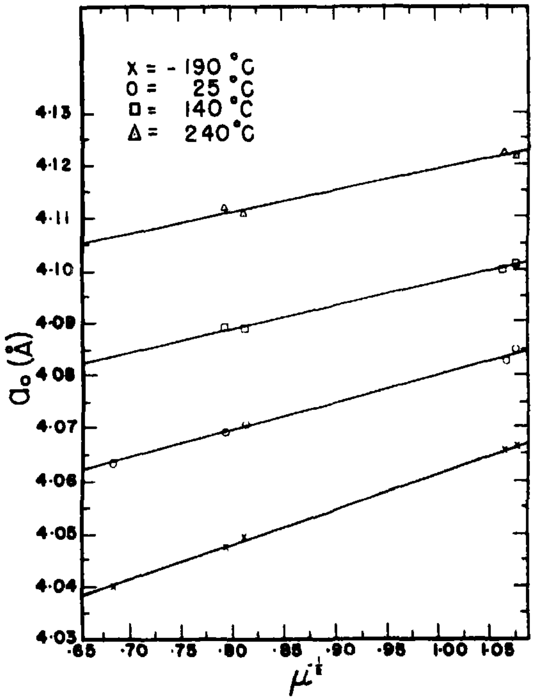

Fig. 1. $a_0 = A\mu^{-1/2} + B$ for isotopic lithium hydride at −190°, 25°, 140° and 240°C.

Table 3 lists the measured coefficients of thermal expansion over the temperature ranges −190°–240°C. Here, contrary to the effect found with lattice constants, the heavier isotopes have the larger coefficients of thermal expansion. Table 4 lists the ratios of the $\bar{\alpha}$'s for these same temperature intervals. Several points should be emphasized about Tables 3

Table 3. $\bar{\alpha}$*'s* × 10^6 *for isotopic* LiH

Isotopic composition	−190°–25°C	25°–140°C	140°–240°C
^{6}LiH	21·0 ± 0·3	34·4 ± 0·8	50·0 ± 1·0
^{7}LiH	19·8 ± 0·4	37·4 ± 0·4	53·3 ± 0·6
^{6}LiD	24·0 ± 1·0	38·4 ± 1·8	54·3 ± 1·0
^{7}LiD	24·8 ± 0·4	42·9 ± 1·0	55·0 ± 1·4
^{7}LiT	26·4 ± 0·5	–	–

and 4. There is a definite discrepancy in $\bar{\alpha}$ for ^{6}LiH compared to $\bar{\alpha}$ for ^{7}LiH in the −190° to 25°C range. There is no reasonable explanation for the higher value of ^{6}LiH over ^{7}LiH. It would be expected that the difference would be small due to the closeness of the reduced masses of ^{6}LiH and ^{7}LiH; however, the reversal appears to be anamolous. Table 4 shows that for any given combination the ratio α light/α heavy approaches 1 as the temperature is increased. Again, all ratios should be exactly one if no isotope effect were present. The greater the relative mass differences between isotopes under study, the lower the ratio α light/α heavy. This is especially noticeable in comparing ^{7}LiH with ^{7}LiT. Conversely, when comparing the data for ^{6}Li and ^{7}Li it is seen that the ratios are all close to one, indicating very little effect.

Table 4. *Ratio of* $\bar{\alpha}$*'s for isotopic* LiH

Ratio	−190°–25°C	25°–140°C	140°–240°C
$\frac{\bar{\alpha}H}{\bar{\alpha}D}$ for ^{6}Li	0·879	0·896	0·921
$\frac{\bar{\alpha}H}{\bar{\alpha}D}$ for ^{7}Li	0·805	0·872	0·969
$\frac{\bar{\alpha}^6\mathrm{Li}}{\bar{\alpha}^7\mathrm{Li}}$ for H	1·060	0·920	0·982
$\frac{\bar{\alpha}^6\mathrm{Li}}{\bar{\alpha}^7\mathrm{Li}}$ for D	0·972	0·895	0·987
$\frac{\bar{\alpha}H}{\bar{\alpha}T}$ for ^{7}Li	0·750	–	–
$\frac{\bar{\alpha}D}{\bar{\alpha}T}$ for ^{7}Li	0·932	–	–

DISCUSSION

If one looks at the curve of potential energy of interaction (the Morse curve) of two particles, it would appear that the equilibrium distance between the particles would be independent of isotopic substitution. Due to the quantum effect leading to zero point oscillations, however, there is an isotope effect. The energy of the zero-point oscillation is proportional to $\mu^{-1/2}$. The lower the value of μ, the higher the energy and, hence, due to the anharmonicity of the potential curve, the greater the equilibrium separation distance between the two interacting particles.

As one isotope is substituted for another, the relative change in μ is greater when light molecules are involved, if the element undergoing isotopic substitution is the lighter element, and in particular, if the element undergoing isotopic substitution is hydrogen.

Several groups have investigated the isotope effect in LiH[2, 3, 4, 5]. These studies have in general been limited to a comparison of ^{n}LiH vs. ^{n}LiD over the −196° to 25°C temperature interval. These studies have indeed shown the lattice parameter of LiH to be greater than that of LiD, whereas the coefficient of thermal expansion of LiD is greater than that for LiH. Our results are in excellent agreement with these literature values.

A formal review of isotope effects and a theoretical treatment of such effects can be found in the papers by Kogan[12, 13]. These papers give a theoretical treatment which will explain the larger a_0 for the lighter isotopes and the larger heat capacity and thus, according to the Gruneisen ratio, a higher coefficient of thermal expansion for the heavier isotopes.

This treatment, in the framework of the Debye theory of solids, demonstrates that these isotope effects should disappear at higher temperatures. Following Ubbelohde[1], Kogan gives the following expression for relating the lattice parameters of LiH and LiD:

$$\frac{a_{\mathrm{LiH}}-a_{\mathrm{LiD}}}{a_{\mathrm{LiH}}}=\alpha\Delta T=\frac{\alpha}{C}\Delta E$$

where ΔE and C are derived from Debye's theory with $\theta_{\mathrm{LiH}}=815°\mathrm{K}$[1] and $\theta_{\mathrm{LiD}}=611°\mathrm{K}$. For this calculation a 25°C α of 32×10^{-6}/deg was used[5]. The calculation gives:

$$\frac{\Delta a}{a}=0{\cdot}23\times10^{-2}$$

compared to an experimental value of

$$\frac{\Delta a}{a}=\frac{a_{\mathrm{LiH}}-a_{\mathrm{LiD}}}{a_{\mathrm{LiH}}}=0{\cdot}33\times10^{-2}.$$

This value of $0{\cdot}33\times10^{-2}$ is in substantial agreement with the reported value of Brückner *et al.*[4]. The discrepancy perhaps implies that the Debye temperatures of LiH and LiD are not sufficiently well known.

London[14] has derived an expression, based on thermodynamic relationships, which will more nearly describe the observed isotope effect. This more rigorous treatment has been adequately discussed by Kogan[12, 13] and Brückner[4]. London[14] derives an expression denoting the change in molar volume induced by isotopic substitution as:

$$\frac{\Delta V}{V}=\frac{\alpha}{C_v}\left(U-E_0-TC_v\right)\left[\frac{\mathrm{d}\ln\nu_k}{\mathrm{d}\ln M}\right]\frac{\Delta M}{M}$$

$$=\frac{a}{C_v}\left[\epsilon_0-T\left(C_v-\frac{U-U_0}{T}\right)\right]\left[\frac{\mathrm{d}\ln\nu_k}{\mathrm{d}\ln M}\right]\frac{\Delta M}{M}$$

where

ν_k = lattice frequency

ϵ_0 = zero point energy $=2(9/8\ R\theta)$ for a two atom solid

α = coefficient of thermal expansion

C_v = heat capacity and

$U_0=\epsilon_0+E_0$ = crystal energy at zero point.

The difficulty is in assessing the manner in which $(\mathrm{d}\ln\nu_k)/(\mathrm{d}\ln M)$ changes. London quotes Kellermann's[13] work on NaCl as a basis for stating that

$$\left[\frac{\mathrm{d}\ln\nu_k}{\mathrm{d}\ln M}\right]=-\frac{1}{2}\frac{1}{1-(M/m)^x}$$

with

$$\tfrac{1}{2}<x<1$$
$$x\approx1\ \text{for}\ T\gg\theta$$
$$x\approx\tfrac{3}{4}\ \text{for}\ T\ll\theta$$

where

M = mass number of atoms in the sublattice that are substituted.

m = mass number of atoms in the sublattice that are not substituted.

Integrating between M_1 and M_2 and making the above substitution for $\mathrm{d}\ln\nu_k/\mathrm{d}\ln M$, London shows

$$\frac{V_{\mathrm{LiH}}-V_{\mathrm{LiD}}}{V_{{}^n\mathrm{LiH}}}=\frac{1}{2}\frac{\alpha_n}{C_{vn}}\left(U_n-E_{on}-TC_{vn}\right)\times\frac{\mu'_n}{x}\left(\frac{1}{M_1^{\,x}}-\frac{1}{M_2^{\,x}}\right)$$

where the subscript n refers to the natural material, on which most of the thermodynamic measurements have been made.

Using the Debye θ's listed above, and the tables of Landolt and Börnstein[16] to determine U_n-E_{on}, a value of $x=0{\cdot}8$, as suggested by Brückner[4], and a 25°C value of $\alpha=32\times10^{-6}$ for ^{n}LiH, one calculates:

$$\frac{\Delta V}{3V}=\frac{\Delta a}{a}=0{\cdot}31\times10^{-2}$$

as compared to the experimental value of $a_{\mathrm{LiH}}-a_{\mathrm{LiD}}/a_{\mathrm{LiH}}=0{\cdot}33\times10^{-2}$. This comparison is, indeed, quite acceptable; however, this agreement must be carefully interpreted. Due to the approximations used, this agreement may be fortuitous.

As Brückner[4] suggested, one is able to compare the ratio $\alpha_{LiH}/\alpha_{LiD}$ by repeating the calculation of equation (1), using first the LiH values and second the LiD values for the terms carrying n in the formula. At 298°K this calculated ratio is 0·80. Experimentally, the value $\bar{\alpha}_{LiH}/\bar{\alpha}_{LiD}$ for the $-190°$–25°C $\bar{\alpha}$ was 0·81. This value approaches 1·0 at the higher temperatures.

The values of a_0 and $\bar{\alpha}$'s determined experimentally are in very good agreement with those determined earlier[3, 4, 5]. This work serves to expand the composition range and temperature intervals studied. It has been shown that the zero point energy E_0 is greater for light isotopes, hence a_0 is larger for the light isotopes. This is due to an inverse dependence of E_0 on the reduced mass of the system. This in turn means a larger effect is detected upon substitution of the lighter element in a binary molecule, i.e. changing hydrogen isotopes causes a larger difference in properties than does changing lithium isotopes.

The Debye theory predicts a larger heat capacity for the heavier element ($C_{heavy} > C_{light}$), then by the Gruneisen relation, $\alpha = \gamma C_v/3BV$, it is expected that $\alpha_{heavy} > \alpha_{light}$. The difference in physical properties resulting from isotopic substitution becomes much less pronounced as the temperature is increased, and should eventually become negligible. It has also been demonstrated that at any temperature there is a linear decrease in lattice parameter as μ, the reduced mass, increases.

Acknowledgements—The authors are indebted to Dr. Dwayne T. Vier for his support and helpful discussions during the course of this investigation. We appreciate the help of Ermil Thrasher who grew the ^{7}LiH and ^{7}LiD crystals and performed the recrystallization and annealing of the ^{6}LiH and ^{6}LiD.

REFERENCES

1. UBBELOHDE A. R., *Trans. Faraday Soc.* **82**, 525 (1936).
2. ZINTL E. and HARDER A., *Z. Phys. Chem.* **28B**, 478 (1935).
3. KOGAN V. S. and OMAROV T. G., *Fiz. Tverd. Tela* 7, 933 (1965).
4. BRÜCKNER W., KLEINSTÜCK K. and SCHULZE G.E.R., *Phys. Status Solidi* **14**, 297 (1966).
5. SMITH D. K and LEIDER H. R., *J. appl. Cryst.* 1, 246 (1968).
6. ANDERSON J. L., NASISE J., PHILIPSON K. and PRETZEL F E., *Abstracts Southwest Regional Meeting*. American Chemical Society, Austin, Texas (1968).
7. PRETZEL F., RUPERT G. N., MADER C. L., STORMS E. K., GRITTON G. V. and RUSHING C. C., *J. Phys. Chem. Solids* **16**, 10 (1960).
8. PRETZEL F. E. and PETTY R. L., *Phys. Rev.* **123**, 464 (1961).
9. PRETZEL F. E. and ANDERSON J. L., *Los Alamos Scientific Laboratory Rep.* LA-3501-MS (1966).
10. HESS J. B., *Acta Crystallogr.* **4**, 209 (1951).
11. VIER D. T., Private communication.
12. KOGAN V. S., *Soviet Phys. Usp.* **5**, 951 (1963).
13. KOGAN V. S. and OMAROV T. G., *J. exp. theor. Phys. (U.S.S.R.)* **47**, 789 (1964).
14. LONDON H., *Z. phys. Chem.* (N.F.) **16**, 302 (1958).
15. KELLERMANN E. W., *Phil. Trans. R. Soc. (London)*, Ser. A **238**, 513 (1940).
16. LANDOLT H. H. and BORNSTEIN R., *Physikalisch-Chemische Tabellen*, p. 702. Springer, Berlin (1927).

J. Phys. Chem. Solids Pergamon Press 1970. Vol. 31, pp. 619–634. Printed in Great Britain.

ULTRASONIC PARAMETERS IN THE BORN MODEL OF THE SODIUM AND POTASSIUM HALIDES

R. W. ROBERTS*
Case Western Reserve University, Cleveland, Ohio 44106, U.S.A.
and
CHARLES S. SMITH
University of North Carolina, Chapel Hill, N.C. 27514, U.S.A.

(*Received* 1 *August* 1969)

Abstract – Available experimental data at 295°K on the ultrasonic elastic constants and their temperature variation, the specific heat, and the thermal expansion of the sodium and potassium halides have been collected and inspected for smoothness in each sequence when plotted against nearest neighbor distance. In the same way, ultrasonic data on the pressure derivatives of the elastic constants have been reviewed and, in the case of NaBr, NaI, KF and KI, measured. The resulting smooth thermodynamic data have been used to obtain values of the constant volume temperature coefficient of the isothermal bulk modulus, $d\ln B_T/dT)_V$ and of $dB_T/dP)_T$. The former is found to be roughly constant at $-0\cdot7\times10^{-4}\text{deg}^{-1}$ for both halide sequences. It arises in the vibrational entropy of the crystal and appears as a correction in expressions giving the repulsive exponent in the two-parameter empirical Born model. The usual procedure of using compression data to obtain $d\ln B_T/dT)_V$ results in an erratic correction that occasionally amounts to more than 10 per cent of the repulsive parameter; on the other hand, the ultrasonically based correction is strikingly smooth at about 2 per cent. Experimental values of $dB_T/dP)_T$ are nearly invariant among these eight alkali halides at a value of 5·4. The Born model correctly predicts this magnitude but also predicts a systematic trend with repulsive exponent significantly greater than that found. Born–Hildebrand equations of state based on the ultrasonic parameters should provide improved estimates of $V(P)$ relations; these do compare fairly well with X-ray data for NaF, NaCl and NaI to pressures on the order of the bulk modulus. Neither comparison with experiment will distinguish, however, for the whole group between the version of the Born model based on a power law repulsive potential and that based on an exponential law.

INTRODUCTION

THIS research has its origins in recent papers by Tosi[1]; Drickamer *et al.*[2], Anderson[3] and Swenson[4] dealing with the equation of state of solids. Although the subject of the binding energy of the alkali halides is one of the oldest in solid state science, modern advances in experimental technique provide refined empirical parameters and additional experimental tests of the theory of ionic crystals. This paper deals with empirical parameters in the Born model of ionic crystals that are based on the single crystal elastic constants and their first pressure derivative.

Tosi[1] reviews the theory of ionic crystals in detail. In particular, he gives an excellent comparison of the parameters, describing the important repulsive interaction, that are derived from several different versions of the classic Born model and also gives a good discussion of both the Hildebrand and the Mie–Gruneisen methods of making the necessary correction for thermal effects. Drickamer *et al.*[2] report X-ray measurements of the compressions of several alkali halides to very high pressures and compare these results, following Tosi, with the Born model in the Hildebrand approximation. Anderson[3] points out that ultrasonic measurements at modest pressures, inserted in the Murnaghan equation of state, give very good estimates of the compressions at high pressures for a wide variety of solids, including one alkali halide, NaCl. Swenson[4] discusses thermal contributions to the equation of state of solids and shows specifically that, when ultrasonic values of both the temperature dependence and the pressure dependence of the elastic constants of single crystals are combined to yield the constant volume temperature coefficient of the isothermal bulk modulus, $\xi = d\ln B_T/dT)_V$, consistently small values of ξ occur for almost all solids. Swenson points out that this fact has good theoretical foundation and that it permits broad generalizations and extrapolations to be made. It will be shown in this paper that ξ appears explicitly and naturally in the Hildebrand correction for thermal effects in the Born model and that Swenson's observations have surprisingly important consequences in that model.

---

*Now at the University of North Carolina, Chapel Hill, North Carolina.

The pressure derivatives of the single crystal elastic constants of NaF [5] and of NaCl and KCl [6] have been previously reported from our laboratory. Similar studies of KBr and KI have been published by Reddy and Ruoff and of KF and NaBr by Koliwad *et al.* [7]. Of the eight sodium and potassium halides, only NaI had not been studied at the inception of this work; these measurements were undertaken and are reported here. One expects the thermodynamic properties of the alkali halides to vary smoothly and monotonically in each sequence as the halogen ion is changed. For example, each elastic constant, C, varies smoothly, approximately as d_0^{-4}, when plotted against nearest neighbor distance, d_0. The various pressure derivatives, dC/dP, vary much less rapidly with halogen (i.e., d_0) than do the C's themselves, but nevertheless, the plots of dC/dP from the sources listed above were unsatisfactory, being erratic by amounts that were considerably beyond the experimental uncertainty. For this reason, the pressure derivatives of the elastic constants of NaBr, KF and KI have been measured independently in our laboratory and are also reported here, the test of a smooth plot now being met. Thus the experimental pressure data that are the main concern of this paper come from one laboratory for seven of the eight Na and K halides, the exception being KBr.

Auxiliary elastic and thermodynamic data are needed in the reduction of experimental observations to values of dC/dP, in the transformation of the ultrasonic adiabatic bulk modulus, B_s, and its temperature and pressure derivatives to the corresponding quantities for the isothermal modulus, B_T, and in the determination of the thermal corrections in the Born model. These data have been chosen from the literature using the same criteria as above for dC/dP. Each type of data has been required to plot smoothly with d_0, and each type has been taken from a common source for all eight alkali halides. These data are given explicitly in a later section because the sources differ in some cases from the traditional ones, for example those quoted by Tosi; the numerical differences are not large, but are sometimes significant. Key points in this research have been the analysis of the complete Na and K sequences and the availability of smooth data from a common source for each sequence.

The analysis presented in a later section of the paper shows that the quantity ξ that appears in the thermal correction to the Born model is far more consistent in the Na and K sequences when it is based on ultrasonic data than when it is obtained from direct compression determinations of the compressibility, $K_T(T,P)$, as has been usual heretofore. Moreover, ξ is consistently small as Swenson predicts, and in this respect is also widely different from the compression ξ. As a consequence, the Born model empirical parameters based on ultrasonic ξ vary smoothly in the sequences and are substantially different from the compression parameters.

These ultrasonic Born model parameters are used in later sections of the paper to predict the quantities $(dB_T/dP)_{P=0}$ and $V(P)$ in two versions, one based on a power law repulsive potential and the other on an exponential law. A comparison of both versions with experimental values of the two quantities is given. The comparison is fairly good in magnitude, but not sufficiently good in detail to distinguish between the two laws for these alkali halides as a group.

EXPERIMENT

Single crystals of NaI and KI were obtained from the Harshaw Chemical Company in the form of 0·6 in. dia. cylinders oriented in the [110] direction and approximately 1 in. long. Similar NaBr and KF samples were obtained from Semi-Elements, Inc., and an additional [110] specimen of KF was cut from a cleavage cube from Optovac, Inc. Supplementary specimens of NaBr, KF and KI oriented in the [100] direction and a duplicate [110] sample of NaBr were likewise obtained in order to provide cross checks and duplicate data. All of these materials, except KI, were found to be deliquescent. This, plus their tendency to crack from thermal or mechanical shock, required that various precautionary measures be taken in working with these materials. Final acoustic surfaces were prepared by lapping opposite ends of the samples flat and parallel with muslin slightly wet with methanol. Paraffin wax was found satisfactory as a seal material to bond both X- and Y- cut quartz transducers onto the samples.

The orientation and the perfection of the single crystals were carefully checked by back reflection Laue patterns made on *both* ends of the specimens. Mosaic spread was found in two NaBr samples, both of which were rejected on this basis. The final acoustic surfaces of the specimens were found to be within 0·5° of the desired [100] or [110] direction. No correction was made for this slight misalignment.

The changes in arrival time with pressure of the three independent [110] acoustic waves were measured using electronic and pressure techniques employed in recent ultrasonic work of this laboratory and well described in previous publications[5, 6]. The end experimental quantity for each wave is $d\ln t_n/dP = d\ln t/dP$, where t_n denotes the appropriate nth echo arrival time and t without subscript the transit time. Zero pressure arrival times were determined using the elastic constant data of Haussühl[8], with the exception of NaBr where they were directly measured using the buffer technique. Pressure data was taken uniformly on all waves to 1 kbar in $\frac{1}{8}$ kbar increments on the upstroke and the interleaving $\frac{1}{8}$ kbar decrements on the downstroke. The values finally adopted for the $d\ln t/dP$ are based on the averaged results of two to four separate pressure runs on each wave of each specimen.

Even though the maximum pressure was restricted to a modest 1 kbar, the $t_n(P)$ data showed a slight nonlinearity, especially in the more compressible materials. For this reason, dt_n/dp at zero pressure was obtained by fitting a quadratic to the raw data by the method of least squares. No formal error analysis was performed on the least squares slopes of the data. The precision on each $d\ln C/dP$ is set at $\pm 0{\cdot}1 \times 10^{-3}$ kbar^{-1}, however, from the repeatability of independent pressure runs.

Internal checks on the dC/dP quoted in the next section were made experimentally in the cases of NaBr, KF and KI. In these three materials, measurements of dC_{11}/dP were made on [100] crystals and are compared with the dC_{11}/dP computed from the [110] data as follows: for NaBr, the measured and calculated dC_{11}/dP are respectively 11·75 and 11·73; for KF, 12·70 and 12·27 and for KI, 13·39 and 13·50.

RESULTS

The $d\ln t/dP$ and the pressure coefficients of the elastic constants, $d\ln C/dP$, are given in Table 1 for NaBr, NaI, KF and KI. The $d\ln C/dP$ of C'_{11}, C' and C_{44} were computed from the $d\ln t/dP$ by means of the relation

$$\frac{d\ln C}{dP} = \frac{1}{3B_T} - 2\frac{d\ln t}{dP} \tag{1}$$

evaluated at zero pressure, the required values of the isothermal bulk modulus being given in the next section. These $d\ln C/dP$, Haussühl's C's (except NaBr) and the relation $B_s = C'_{11}$

Table 1. Values of the measured dlnt/dP *and of* dlnC/dP *at* 295°K; t *is the acoustic wave transit time. Units are* 10^{-3} *kbar*$^{-1}$

	NaBr	NaI	KF	KI
$d\ln t/dP$				
C'_{11}	− 9·5	−13·0	− 5·7	−16·9
C'	−15·8	−21·2	− 9·8	−24·5
C_{44}	− 1·4	− 3·0	+ 2·3	+ 4·8
$d\ln C/dP$				
C'_{11}	20·7	28·2	12·5	36·7
C'	33·2	44·6	20·6	52·0
C_{44}	4·6	8·2	− 3·4	− 6·6
B_s	25·6	33·8	16·7	45·0

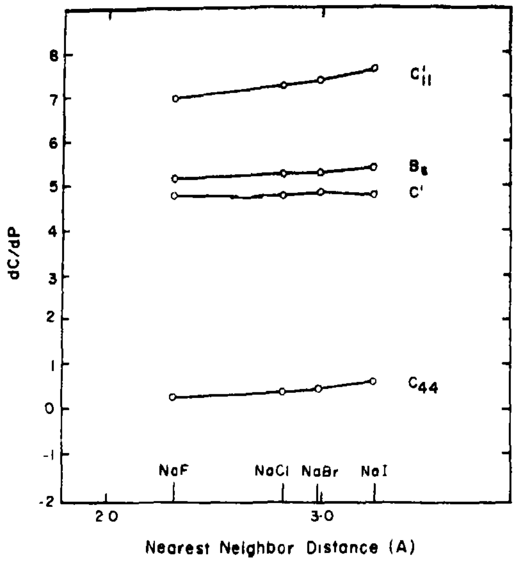

Fig. 1. The pressure derivatives of the elastic constants of the sodium halides vs. nearest neighbor distance.

$-C_{44}-C'/3$ were used to obtain the values of $d\ln B_s/dP$ that are also tabulated.

The *dC/dP* are the central experimental quantities in this work and are given for all of the sodium and potassium halides in Table 2. The values for NaF, NaCl and KCl are those previously reported from our laboratory. The NaI results given here are the first for that material. These, plus our own determination for NaBr, KF and KI result in *dC/dP* data being now available from one laboratory for all of these materials except KBr. The [110] *dC/dP* of KBr were calculated from the data given by Reddy and Ruoff[9] for C_{11}, C_{12} and C_{44}.

Plots of the *dC/dP* for the sodium and potassium halides are given in Figs. 1 and 2. All derivatives for both sequences plot smoothly within the experimental precision quoted. The essential feature of these *dC/dP* is that each derivative is nearly constant throughout each sequence but with a slight and real upward trend when plotted against nearest neighbor distance.

The Na and K sequences are shown in separate figures for clarity; a careful comparison of the two is worthwhile. The value of dC_{44}/dP is small for both sequences, a salient characteristic of the NaCl structure [5], but is positive for the Na sequence and negative for K. The pressure derivative of B_s

Table 2. Values of dC/dP *for the sodium and potassium halides at* 295°*K*

	NaF[5]	NaCl[6]	NaBr	NaI
C'_{11}	6·98	7·24	7·36	7·61
C'	4·79	4·79	4·83	4·80
C_{44}	0·205	0·37	0·46	0·61
B_s	5·18	5·27	5·29	5·40

	KF	KCl[6]	KBr[7]	KI
C'_{11}	6·59	6·83	6·95	7·23
C'	5·25	5·61	5·68	6·03
C_{44}	−0·43	−0·39	−0·328	−0·244
B_s	5·26	5·34	5·38	5·47

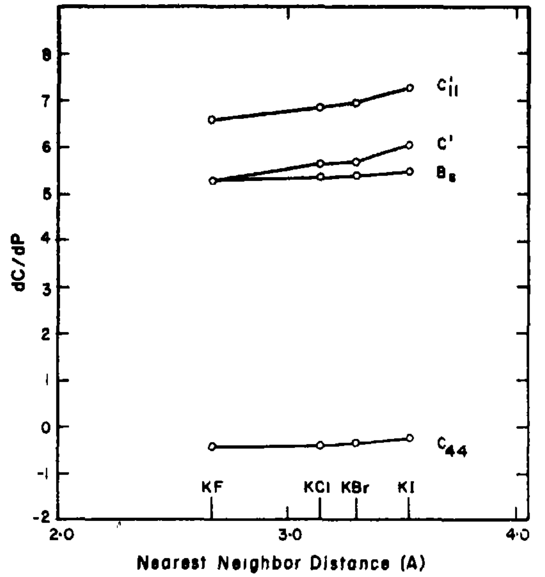

Fig. 2. The pressure derivatives of the elastic constants of the potassium halides vs. nearest neighbor distance.

lies above that of C' in Na, but below in K. We call particular attention to the fact, important in this paper, that the two plots for dB_s/dP very nearly superimpose.

DERIVED QUANTITIES

In this section the pressure derivatives of the elastic constants displayed in the last section are used to obtain two derived quantities that pertain to the Born model of ionic crystals. This process requires auxiliary thermodynamic data at room temperature, as does the Born model itself which is treated in the following section. Before proceeding, a careful selection of these basic data was made, using the same criteria of the previous section. Data of a given kind were as nearly as possible taken from a single reference. Where more than one source was available, the data set that plotted most smoothly with nearest neighbor distance was adopted. The complete basic data selected are given in Table 3. The temperature is 295°K for these data and all subsequent derived quantities.

Lattice constants quoted in Bureau of Standards publications [10] were used to compute the nearest neighbor distance d_0 and the molecular volume Ω_0. This source of d_0 was also adopted by Tosi. The d_0 enter as d_0^4 in the Born model requiring very precise values of this fundamental parameter.

The values of the volume coefficient of thermal expansion, β, were kindly supplied to us by Dr. Richard K. Kirby who has made a critical evaluation of the available measurements of this quantity. The single exception is KF, for which a 295°K value of β was estimated from the thermal expansion data reported by Henglein [11] at −131°C and −40°C. These adopted values of β at 295°K are slightly different from the −40°C values that have been used heretofore [1] in the Born model.

The room temperature specific heats, C_p, are from the published results of Brönsted [12] who measured average specific heats over the

Table 3. Basic data for the sodium and potassium halides at 295°K

	d_0 (10^{-8}cm)	Ω_0 (10^{-24}cm^3 molecule^{-1})	B_s (kbar)	C_P (10^{-16}erg deg^{-1} molecule^{-1})	β (10^{-4}deg^{-1})	γ	$T\beta\gamma$ (10^{-2})	B_T (kbar)
NaF	2·317	24·88	485	7·671	0·96	1·51	4·28	465
NaCl	2·820	44·85	250	8·289	1·19	1·62	5·70	240
NaBr	2·989	53·41	207	8·463	1·26	1·65	6·12	199
NaI	3·236	67·77	159	8·609	1·37	1·71	6·91	151
KF	2·674	38·24	316	8·116	(1·02)	1·52	4·57	305
KCl	3·146	62·27	182	8·421	1·11	1·49	4·89	175
KBr	3·300	71·87	154	8·581	1·16	1·50	5·13	148
KI	3·533	88·20	122	8·602	1·23	1·54	5·58	117

20° interval from 0°C to room temperature. These average C_p were adjusted to 295°K by the addition of 0·08 cal/mole per degree.

The most recent ultrasonic work of Haussühl [8] is the source of the adiabatic bulk moduli. The B_s were computed using the elastic constants reported by Haussühl at 295°K and the relation $B_s = C'_{11} - C_{44} - C'/3$. Multiple sources available for most of the B_s show only very small differences. Published results from this laboratory in four cases show at most a 1 per cent difference from the values of Haussühl, and this, curiously, for NaCl. In addition, Haussühl's B_s differ at most by 2 per cent from the original values of Spangenburg[13] used by Tosi and others.

The final column of numbers in the table of basic data are the isothermal bulk moduli, B_T, that are essential in the Born model and in the equation of state. The B_T were obtained using the relation $B_s/B_T = 1 + T\beta\gamma$. The Grüneisen constant, $\gamma = \Omega\beta B_s/C_p$, and $T\beta\gamma$ are also tabulated with the basic data for reference.

Ultrasonic temperature coefficients of the adiabatic elastic constants are also given by Haussühl[8], who *measured* $d\ln C/dT$ rather than obtaining it from $C(T)$ measurements followed by graphical differentiation. A slight adjustment of these temperature coefficients to 295°K was made since Haussühl reports his values at 0°C. Plots of Haussühl's $d\ln C/dT)_p$ for C'_{11}, C' and C_{44} are given in the Appendix. The quantity $d\ln B_s/dT)_P$ was computed from these values, Haussühl's elastic constants, and the relation $B_s = C'_{11} - C_{44} - C'/3$, and is shown in Fig. 3. These values of $d\ln B_s/dT)_P$ are the best available to date, but still show some irregularity when plotted against d_0. This remaining irregularity in the $d\ln B_s/dT)_P$ manifests itself in later work.

A temperature coefficient of the bulk modulus $d\ln B_s/dT)_P$ arises from a constant volume (intrinsic) temperature dependence $d\ln B_s/dT)_V$ and a dependence arising solely from changes in crystal volume. These considerations are made quantitative using the selected basic data and the identity

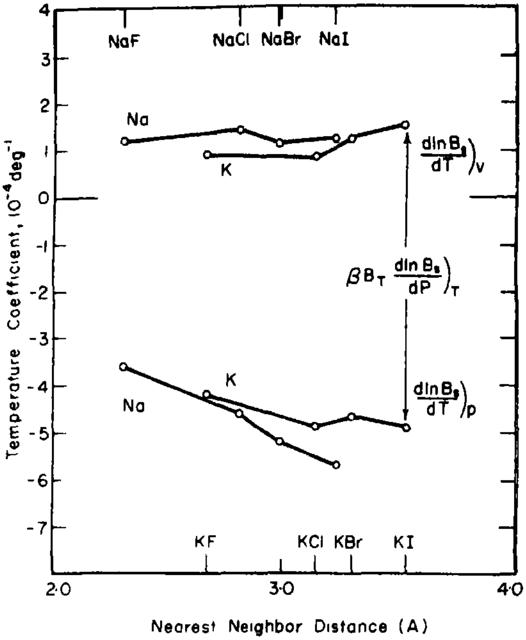

Fig. 3. The temperature coefficients at constant pressure and at constant volume of the adiabatic bulk modulus. The upper curves are the $d\ln B_s/dT)_V$ which result from this analysis. The separation between the two coefficients represents the contribution to $d\ln B_s/dT)_P$ from purely volume effects.

$$\left.\frac{d\ln B_s}{dT}\right)_P = \left.\frac{d\ln B_s}{dT}\right)_V - \beta B_T \left.\frac{d\ln B_s}{dP}\right)_T. \quad (2)$$

The separate contributions to the $d\ln B_s/dT)_P$ are displayed graphically in Fig. 3 for the sodium and potassium halides. The $d\ln B_s/dT)_V$ are found to be small, positive and roughly constant at $+1 \times 10^{-4}$deg^{-1} for all these materials. The graph reveals that $d\ln B_s/dT)_P$ is dominated by the effect of dimension changes in all eight cases.

Values of the intrinisc temperature coefficient of the *isothermal* bulk modulus, $\xi = d\ln B_T/dT)_V$, are required to make a thermal correction in the Hildebrand approximation of the Born model where ξ appears as the isothermal pressure derivative of βB_T. A useful relation containing ξ is obtained by differentiating the identity

$$B_s - B_T = \frac{T}{V} C_V \gamma^2 \qquad (3)$$

and by assuming that γ has no intrinsic temperature dependence at room temperature. The approximate relation [4] is

$$\left.\frac{B_s}{B_T}\frac{d\ln B_s}{dT}\right)_V - \xi = \beta\gamma\left[1+\left.\frac{d\ln C_V}{d\ln T}\right)_V\right]. \qquad (4)$$

The quantity $d\ln C_V/d\ln T)_V$ is small compared with unity for these materials; it was evaluated for a Debye solid using the C_V inferred from Table 3. *The values of ξ computed using* equation (4) are plotted against d_0 in Fig. 4.

The ultrasonic ξ are small, negative and roughly the same at $-0{\cdot}7 \times 10^{-4}\text{deg}^{-1}$ for all eight materials. They are about equal in magnitude to the $d\ln B_s/dT)_V$, but are interestingly of opposite sign. The plots of the intrinsic temperature coefficients of B_s and B_T possess irregularity that may be traced directly to the experimental $d\ln B_s/dT)_P$ in Fig. 3. The remaining irregularity in the $d\ln B_T/dT)_V$ appears to be large only because the quantity itself is so small; it cannot be removed by any adjustment of the input data that we would care to defend.

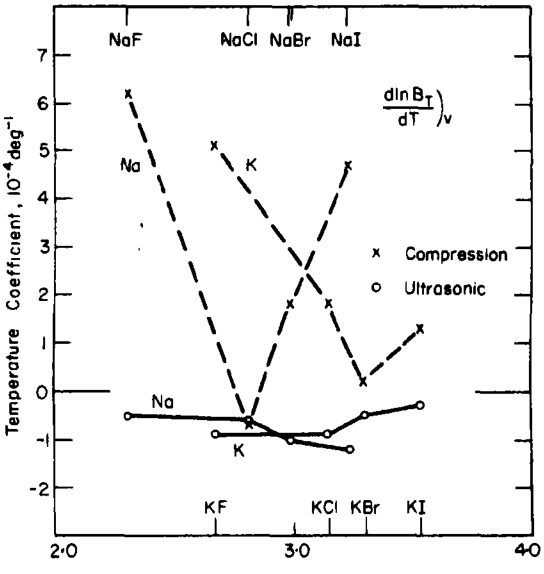

Fig. 4. Derived ultrasonic $d\ln B_T/dT)_V$ of the sodium and potassium halides vs. nearest neighbor distance. Included for comparison are the $d\ln B_T/dT)_V$ obtained from the compression data and commonly used in the Hildebrand approximation.

The values of ξ reported in this work are derived from the results of *ultrasonic* measurements. Values of ξ for these materials may also be calculated using compression measurement data quoted by Tosi [1]. The compression values of ξ are included in Fig. 4 for comparison. These vary widely from large *positive to small and even negative values. A* curious singularity occurs for NaCl where the one negative value is in good agreement with the ultrasonic ξ. Clearly the ultrasonic ξ are preferable; their use in the Born model has surprising consequences.

The final derived quantity of interest is the pressure derivative of the *isothermal* bulk modulus, dB_T/dP. This number will be shown in a later section to provide a very critical test of possible expressions for the lattice potential. The required equation is

$$\left.\frac{dB_T}{dP}\right)_T - \left.\frac{dB_s}{dP}\right)_T = T\beta\gamma\left[1-\frac{2\xi}{\beta}-\left.\frac{d\ln C_V}{d\ln V}\right)_T\right]. \qquad (5)$$

This has been shown to be exact by Swenson [4] and is mostly in terms of quantities known as a result of this investigation. The $d\ln C_V/d\ln V)_T$ are small and were evaluated for a Debye solid using the relation

$$\left.\frac{d\ln C_V}{d\ln V}\right)_T = \gamma\left.\frac{d\ln C_V}{d\ln T}\right)_V. \qquad (6)$$

The dB_T/dP and the contributions to equation (5) are given in Table 4. As usual, there is little difference between the (isothermal) pressure derivatives of the isothermal and adiabatic bulk moduli. In all eight materials, the dB_T/dP is larger in magnitude than dB_s/dP by about $2T\beta\gamma$. This difference is to be compared with the plausible first approximation

Table 4. The pressure derivatives of the isothermal bulk moduli as computed using equation (5). 295°K, zero pressure

	$\left.\frac{dB_T}{dP}\right)_T$	=	$\left.\frac{dB_s}{dP}\right)_T$	+	$T\beta\gamma$ [ ]
NaF	5·25	=	5·18	+	0·07
NaCl	5·38	=	5·27	+	0·11
NaBr	5·44	=	5·29	+	0·15
NaI	5·58	=	5·40	+	0·18
KF	5·38	=	5·26	+	0·12
KCl	5·46	=	5·34	+	0·12
KBr	5·47	=	5·38	+	0·09
KI	5·56	=	5·47	+	0·09

made by Swenson[4] that $dB_T/dP)_T - dB_s/dP)_T = T\beta\gamma$.

BORN MODEL

Several purely volume-dependent expressions for the lattice energy of an ionic solid have been referred to collectively as the Born model. The simplest of these are of the form

$$W_L(V) = -\frac{\alpha e^2}{d_0}\left(\frac{V_0}{V}\right)^{1/3} + W_{RL}(V), \quad (7)$$

where the first term on the right is the Coulomb energy of the ionic lattice per molecule and α is Madelung's constant. The repulsive energy, $W_{RL}(V)$, arises principally from the repulsive overlap of nearest neighbor electron clouds, but in this work will represent the composite of all non-Coulomb energies, both attractive and repulsive, that are present in the real lattice. The forms that have been used for $W_{RL}(V)$ are the power law and the exponential law, which are respectively

$$W_{RL}(V) = A\left(\frac{V_0}{V}\right)^{n/3} \quad (8)$$

and

$$W_{RL}(V) = D\exp\left\{-\frac{d_0}{\rho}\left[\left(\frac{V}{V_0}\right)^{1/3} - 1\right]\right\}. \quad (9)$$

Values of the empirical parameters A, n, D, and ρ have been published elsewhere[1]. A restudy of these will be made in this section using the more recent ultrasonic data to replace the compression data that has previously been used in their evaluation. An examination of the one parameter n, similar to that made of $\xi = d\ln B_T/dT)_V$, will provide a satisfactory illustration of the differences between ultrasonic and compression Born parameters; the other parameters can be quickly obtained once n is known. The latter part of this section will provide a critical comparison of the alternatives for W_{RL} presented by equations (8) and (9), which is made possible with the aid of the ultrasonic values of dB_T/dP.

The equations involving W_L needed to evaluate the repulsive parameters follow from an approximate expression for the Helmholtz free energy

$$A(V,T) = W_L(V) + W_{VIB}(T) - TS(V,T) \quad (10)$$

in which the vibrational energy of the lattice has been assumed to be purely temperature dependent. The Hildebrand equation is the isothermal volume derivative of equation (10) and is written as

$$P = -\frac{dW_L}{dV} + T\beta B_T \quad (11)$$

with use of the identity $dP/dT)_V = \beta B_T$. This is properly speaking, an equation of state in the Hildebrand approximation, a fact which will be pursued in detail in the next section. For the present a second equation is needed. Use of equation (11) and the definition of the isothermal bulk modulus $B_T = -dP/d\ln V)_T$ yields

$$B_T = V\frac{d^2W_L}{dV^2} + \xi T B_T. \quad (12)$$

The term $\xi T B_T$, where $\xi = d\ln B_T/dT)_V$, follows at once from the differentiation of $T\beta B_T$ by using $dP/dT)_V$ to replace βB_T and interchanging the order of differentiation.

The thermal contributions to these equations are relatively small. The thermal pressure, $T\beta B_T$, has values of 3–15 kbar for the materials being studied. The volume derivative of the thermal pressure gives a thermal contribution to B_T in equation (12) which amounts to -2 per cent of B_T for a typical value of $\xi = -0{\cdot}7\times 10^{-4}\mathrm{deg}^{-1}$.

Equations (11) and (12), when evaluated at zero pressure, are the two simultaneous equations needed to evaluate two repulsive parameters if either the power law or the exponential law is used for W_{RL}. The solutions are

$$An = D\left(\frac{d_0}{\rho}\right) = \frac{\alpha e^2}{d_0}[1-T\beta\Lambda], \quad (13)$$

$$\frac{d_0}{\rho} = n+1 = \frac{4+3\Lambda\{1-\xi T\}}{[1-T\beta\Lambda]} - 2, \quad (14)$$

where the quantity $\Lambda = 3\Omega_0 B_T/(\alpha e^2/d_0)$ and all other quantities appearing in these equations have been evaluated at zero (atmospheric) pressure. The term $[1-T\beta\Lambda]$ arises through use of equation (11) and because of a non-zero thermal pressure is about 10 per cent less than unity. The term $\{1-\xi T\}$ enters through the expression for the bulk modulus and is typically 2 per cent greater than unity. If thermal corrections were neglected, the brackets would reduce to unity with $d_0/\rho = 2+3\Lambda$, the uncorrected result.

The values $n+1$ that were computed from equation (14) with the aid of the selected basic data in Table 3 and with the ultrasonic values of ξ are shown in Fig. 5. Also shown in the figure are the values of $n+1$ for these materials that have been computed from the values of ρ quoted by Tosi [1] who used compression data (equivalent to ξ) to make the necessary thermal correction to equation (14). The comparison reveals that with the exception of NaCl, the ultrasonic n are systematically higher than the compression n. The almost linear upward trend that the ultrasonic values show throughout both halide sequences is a marked improvement over the compression values, especially in the sodium sequence. The parameter ξ is in a large part responsible for these differences. The compression values of $\{1-\xi T\}$ are mostly *less* than unity by occasionally 10 per cent with fluctuations in accordance with Fig. 4. A close comparison of Fig. 4 and Fig. 5 reveals that in fact much of the observed irregularity in ξ, Fig. 4, carries over to Fig. 5 in both compression and ultrasonic versions. The singular ultrasonic-compression agreement in ξ noted earlier for NaCl is clearly seen again in Fig. 5.

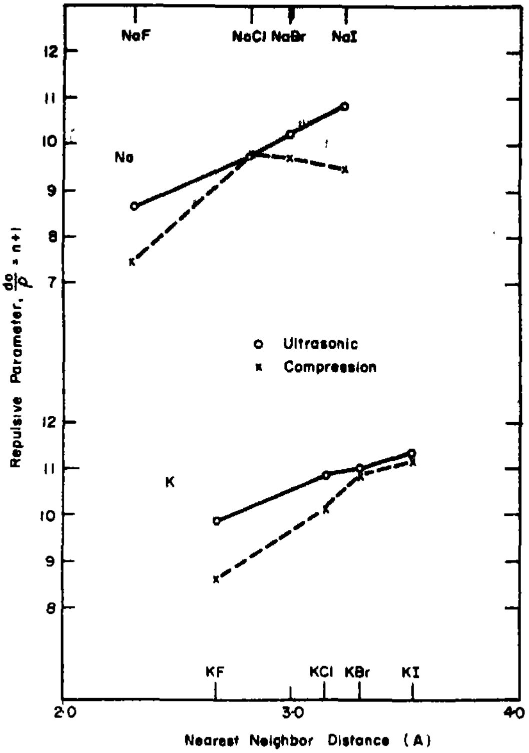

Fig. 5. Born model repulsive parameters, $d_0/\rho = n+1$, for the sodium and potassium halides vs. nearest neighbor distance. Values using both ultrasonic and compression $d\ln B_T/dT)_V$ in the Hildebrand approximation are shown.

Values of A and n for the power law form of W_{RL} are given in Table 5. The values of the exponential law parameters follow quickly from the relations $d_0/\rho = n+1$ and $D = An/(n+1)$.

A critical test of an expression for the lattice

Table 5. The power law repulsive parameters

	A (10^{-12}erg molecule^{-1})	n
NaF	2·139	7·68
NaCl	1·510	8·73
NaBr	1·339	9·21
NaI	1·145	9·81
KF	1·576	8·91
KCl	1·193	9·86
KBr	1·111	10·02
KI	0·993	10·38

energy is the value of dB_T/dP predicted by the expression at zero pressure because dB_T/dP corresponds to the third volume derivative of the lattice energy and hence is heavily weighted by the short range interaction. The first and second volume derivatives (corresponding to the pressure and bulk modulus, respectively) are automatically satisfied at zero pressure by either choice of repulsive potential, since these derivatives have been used to determine the repulsive parameters. Such a test is made possible by the availability of the ultrasonic dB_T/dP in Table 4.

Differentiation of equation (12) with respect to pressure gives an analytic expression for dB_T/dP as a function of volume. If the thermal contributions to P, B_T and dB_T/dP are neglected and if the power law is used for $W_{RL}(V)$, the result evaluated at zero pressure is the extremely simple expression

$$\frac{dB_T}{dP}=\frac{n+7}{3} \tag{15}$$

The exponential law yields an expression for dB_T/dP at zero pressure which is non-linear in d_0/ρ and slightly more complicated. If thermal effects are included, a typically 3 per cent larger prediction of dB_T/dP results, but the expressions for dB_T/dP are considerably more complex, and not functions of n (or d_0/ρ) alone.

The comparison with experiment of the power law and exponential law predictions of dB_T/dP is made in Fig. 6 where the abscissa is $d_0/\rho = n+1$. The power law prediction is 10 per cent larger than the exponential and of course varies linearly with n. The *magnitudes* of the ultrasonic values of dB_T/dP are predicted well enough by the models, with the power law being perhaps a trifle better. But the *trend* of the experimental dB_T/dP differs quantitatively from the trend of the model curves, the experimental dB_T/dP being *nearly invariant* to n, with an average value of 5·4. Theory and experiment thus differ systematically as n increases within each halide sequence. The difference is most pronounced at small n values. For NaF the power law and the exponential law predictions fall below the ultrasonic $dB_T/\mathrm{d}P$ by 10 per cent and 20 per cent respectively.

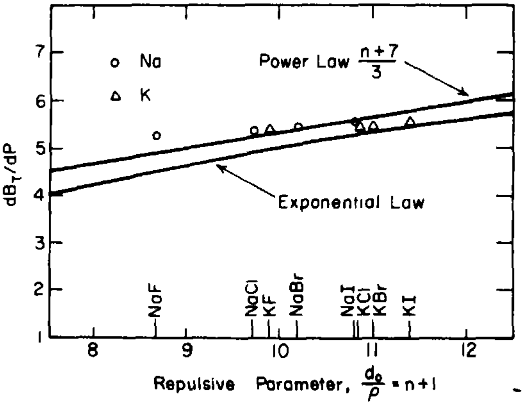

Fig. 6. The ultrasonic dB_T/dP of the sodium and potassium halides vs. repulsive parameter $d_0/\rho = n+1$. The solid curves are the power law and the exponential law predictions of dB_T/dP.

We have ignored thermal corrections in equation (15) and hence in the ordinates of the model *curves* of Fig. 6 because a detailed examination showed that there was much cancellation of them leaving only a residual that could be estimated to be small. This does not mean that thermal effects are absent in Fig. 6; they are present in the abscissa of that figure! The *data* ordinates of course include the residual thermal effect and the *points* have been plotted against $d_0/\rho = n+1$ values that fully take account of thermal effects, Table 5. It should be noted that had the compression parameters of Fig. 5 been used in Fig. 6, the data would have plotted far less smoothly, the sodium sequence would not even have been monotonic, and the discrepancy between experiment and model in NaF would have been doubled.

This comparison with experiment of the power law and exponential law predictions of dB_T/dP does not distinguish between the two forms for W_{RL} as we had hoped. It does display the intrinsic differences between the two versions of the repulsive energy and this difference recurrs in the equation of state to be discussed next.

EQUATION OF STATE

Ultrasonic data and derived parameters including ξ, when used with the Born model, should provide improved estimates of the $V(P)$ relations for ionic solids to pressures of the order of the bulk modulus. Direct X-ray measurements by Drickamer[2] and co-workers make possible comparisons of these ultrasonic Born equations of state with experiment for NaF, NaCl and NaI.

The required analytic expressions follow from the Hildebrand equation (11) of the previous section after the repulsive parameters have been determined by the use of it and equation (12) evaluated at zero pressure. In this section, we shall be concerned exclusively with the *isothermal* bulk modulus which will here be denoted simply by B when it is a function; B_0 will denote its value at zero pressure and similarly for other quantities. Pressures are conveniently expressed in terms of the *reduced* pressure, P/B_0, which is obtained by combining the Hildebrand equation with the evaluated form of equation (11). The exact expressions are,

$$\frac{P}{B_0}=\frac{1}{\Lambda}\left\{[1-T\beta_0\Lambda]\left(\frac{V_0}{V}\right)^{(n+3)/3}-\left(\frac{V_0}{V}\right)^{4/3}\right\} + T\beta\frac{B}{B_0} \tag{16}$$

for the power law and

$$\frac{P}{B_0}=\frac{1}{\Lambda}\left\{[1-T\beta_0\Lambda]\left(\frac{V_0}{V}\right)^{2/3} \times \exp\left\{-\frac{d_0}{\rho}\left[\left(\frac{V}{V_0}\right)^{1/3}-1\right]\right\}-\left(\frac{V_0}{V}\right)^{4/3}\right\} + T\beta\frac{B}{B_0} \tag{17}$$

for the exponential law. The quantity $\Lambda = 3\Omega_0 B_0/(\alpha e^2/d_0)$ has been evaluated at zero pressure. The thermal pressure, $T\beta B$, is formally volume dependent in these equations and this volume dependence has been taken into account in equation (12), where the volume *derivative* of $T\beta B$ appears as a thermal contribution to the bulk modulus. The volume *variation* of $T\beta B$ has been ignored, however, in computing P/B_0 from equations (16) and (17).

The comparisons of these Hildebrand equations of state for NaF, NaCl and NaI with Drickamer's X-ray data are made in Figs. 7, 8 and 9. Drickamer tabulates smoothed data in the form P vs. V/V_0; the values P/B_0 have been calculated using the *ultrasonic* bulk moduli. If the graphs are superimposed, the smoothed compression data in reduced form are found to be surprisingly invariant among these three materials that have widely different bulk moduli. The origin of the slight scatter in the smoothed NaF compression data is not known.

The two versions of the reduced Hildebrand equation are also shown in the figures. They must begin together at zero pressure and have the same zero pressure slope. This initial slope is $B_0 d(V/V_0)/dP$ evaluated at zero pressure and by definition of B_0 should have a value of -1. The actual slopes differ slightly from -1 because of a small effect noted later. At high pressures, however, the power law consistently falls above the exponential. This difference is about 15 per cent of the pressure at $P/B_0 = 1$. That a power law predicts a more incompressible solid at high pressures is to be expected from Fig. 6, where it is observed that

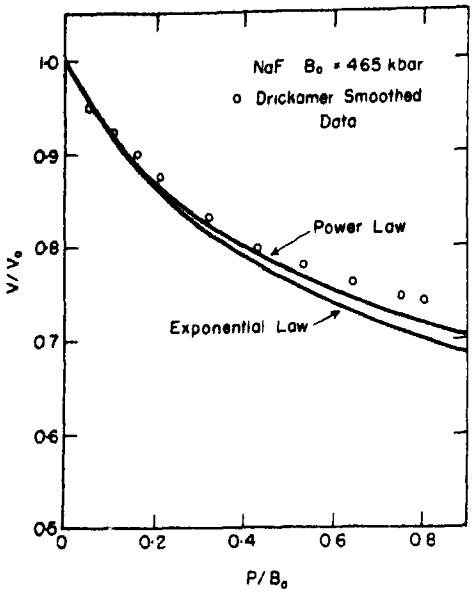

Fig. 7. The Hildebrand equation of state of NaF for the power law and the exponential law. All required repulsive and thermal parameters were evaluated using ultrasonic data.

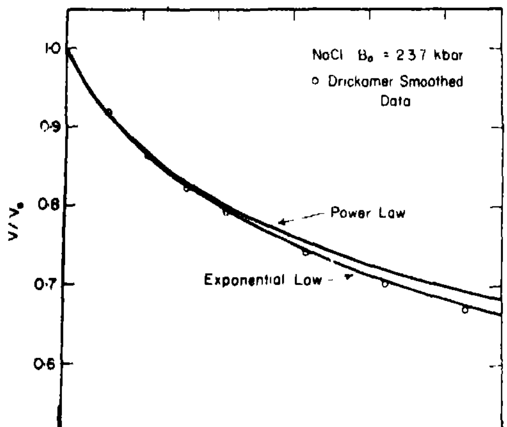

Fig. 8. The Hildebrand equation of state of NaCl for the power law and the exponential law. All required repulsive and thermal parameters were evaluated using ultrasonic data.

the power law also predicts about a 10 per cent larger dB/dP than does the exponential law.

The P/B_0 values given by the power law equation of state at a given V/V_0, e.g. 0·7, increase in the order NaF, NaCl, NaI, which is the same order as the n values and hence of the Born model dB/dP given by $(n+7)/3$ for these three materials. A similar trend among the exponential law curves is also observed. This trend toward larger predicted P/B_0 in the sequence is in contrast to the approximate invariance of the reduced X-ray data, and of the experimental ultrasonic dB/dP.

Leaving aside these details, the overall agreement with experiment is fairly good, considering the magnitude of the pressure at which modest failure begins to occur. The power law equation fits the NaF data well, though it falls low at the higher pressures. The exponential fits the NaCl data very well indeed. The power law and exponential law curves both fall slightly high, however, with respect to the NaI data.

Several alterations of the foregoing analysis could conceivably reconcile these ultrasonic equations of state with experiment, or perhaps significantly affect the observed trends. The effect of possible experimental error in the various input data—especially the bulk modulus—ought to be considered. Van der Waals energy terms arising from dipole-dipole and dipole-quadrupole interaction energies could be included in the expression for W_l. The pressure variation of $T\beta B$, heretofore neglected, should be dealt with as a possible source of systematic error, and the Mie-Gruneisen equation of state could be used in place of the Hildebrand equation.

As for the bulk modulus, values of B_s determined from independent measurements in this laboratory differ very slightly from the B_s of Haussühl, the largest discrepancy being 1 per cent in NaCl. It may be shown that $+\Delta P/P \cong +2(\Delta B_0/B_0)$ at $P/B_0 = 1$. A 1 per cent error in B_0 would thus induce only a 2 per cent error in the pressure. Any alteration of B_0 to another acceptable ultrasonic value would at best lead to a slight improvement in NaCl and NaF and a very slight worsening in NaI.

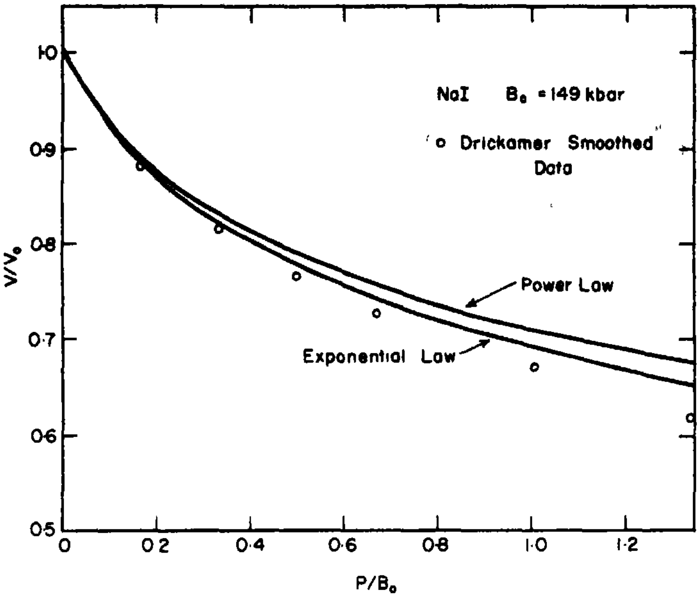

Fig. 9. The Hildebrand equation of state of NaI for the power law and the exponential law. All required repulsive and thermal parameters were evaluated using ultrasonic data.

The inclusion of Van der Waals terms in W_L leads to equations of state for NaI which predict 5 kbar smaller pressures at $P/B_0 = 1$. This 3 per cent improvement for NaI was determined by comparing equations of state both with and without the Van der Waals inclusion. The correction will always be negative and will be even smaller in NaF and NaCl where the Van der Walls coefficients are much smaller.

No account has been taken of the pressure variation of $T\beta B$ in constructing the graphs, because the precise manner in which βB varies at high pressure is not known. The *ultrasonic* $d(T\beta B)/dP$, which equals ξT, is at most $-0{\cdot}03$ for NaF, NaCl and NaI. In the (low) range of pressures where $T\beta B$ varies linearly with pressure, the change in $T\beta B$ due to its pressure variation will be $\Delta T\beta B = \xi TP$ or a 3 per cent negative correction to P/B_0. The neglect of this variation has therefore made the initial slope of the plotted curves 3 per cent smaller in magnitude than the correct value, -1.

The Mie–Gruneisen equation is appropriate as an alternative to the Hildebrand equation in the case of materials with high Debye temperatures[1]. The Mie–Gruneisen pressure was computed for NaF at $V/V_0 = 0{\cdot}8$ using the repulsive parameters quoted by Tosi and was found to be 10 kbar less than the Hildebrand pressure computed on the same basis. This result is only a 2 per cent change in P/B_0 and the use of the Mie–Gruneisen equation surprisingly would worsen the agreement. Even though NaF has the highest Debye temperature of these three materials, this alteration of the Born model is minor in its effect on the equation of state.

Hildebrand equations for NaF, NaCl and NaI in the exponential version previously have been compared with the X-ray data by Drickamer *et al.*[2]. Their treatment included Van der Waals terms, and used different input data in some cases, but the most noteworthy difference between Drickamer's analysis and the present one is their use of the compression values of the temperature and pressure variation of the compressibility (equivalent to ξ) quoted by Tosi. For NaCl, compression ξ

and ultrasonic ξ are seen to be in good agreement in Fig. 4, whereas the NaF and NaI ultrasonic ξ differ considerably from the compression values which are positive and comparatively quite large. It is not surprising then that the NaCl equation of state (exponential) obtained by Drickamer differs little from the ultrasonic equation of state deduced from this work. Both fit the data well.

Drickamer was unable to obtain a NaF fit, however, in contrast to the reasonable ultrasonic fit of Fig. 7. This large discrepancy between the present NaF analysis and that performed by Drickamer is believed to lie in the pressure variation of the thermal pressure $T\beta B$. If the pressure *derivative*, $T\xi$, of the thermal pressure corresponding to a *large* $\xi = 6{\cdot}2\times10^{-4}\text{deg}^{-1}$ is included in equation (12) but the pressure *variation* neglected in equation (11), the initial slope of equation (17) would in magnitude be 18 per cent larger than -1. Drickamer's NaF curve has a slope at zero pressure which differs from -1 by nearly this amount. We too have included the derivative and neglected the variation of $T\beta B$ in our analysis, but the ultrasonic $T\xi$ is small (and of opposite sign) as already noted.

This same situation exists for NaI, where the compression $\xi = +4{\cdot}7\times10^{-4}\text{deg}^{-1}$ is positive and quite large compared with the ultrasonic value. Contrary to the foregoing argument however, the Drickamer treatment agrees very well with the X-ray data. There is, however, another major difference between Drickamer's analysis of NaI and the present one. The bulk modulus Drickamer used in obtaining the repulsive parameters was 167 kbar in contrast to the 10 per cent smaller ultrasonic value of 151 kbar used in this work. This difference is nearly sufficient to compensate for the effect of neglecting the variation with pressure of $T\beta B$ in equation (11). It is interesting to note that Drickamer expresses surprise both at his failure to fit the Born model to NaF and at his success with NaI. The present analyses reverse the situation.

In summary, the ultrasonic Born equations of state in the Hildebrand approximation agree reasonably well with X-ray data when the ultrasonic values of ξ and B_0 are used, especially in view of the magnitude of the pressures to which the comparison is made. The possible modifications to the treatment, described above, result only in nominal shifts of the equations of state relative to the data and these shifts have neither the correct signs nor magnitudes to reconcile significantly the remaining discrepancies between the model and the data. The largest alteration in the Hildebrand equation for a given material occurs in the switch from an exponential to a power law repulsive energy. The equation of state comparison does not, however, distinguish between the two laws for these three materials as a group, just as the dB_T/dP comparison failed to distinguish between them for the whole group of eight. The slight trend away from better power law agreement in NaF toward better exponential law agreement as one progresses through the sodium halide sequence is perhaps significant. It suggests that a repulsive energy of a different *form*, probably involving more than two empirical parameters, is needed to obtain a higher degree of refinement.

We conclude this section with some remarks on the Murnaghan equation of state (MES) which is wholly phenomenological and is based on the assumption that the bulk modulus can be represented adequately by a linear function of the pressure, $B(P) = B_0(1+B_0' P/B_0)$, where B_0' is the dB_T/dP of this paper. Anderson[3] has used the MES, among others, in conjunction with ultrasonic B_0 and B_0' to extrapolate $V(P)$ to high pressures. He has in fact published a comparison of experimental $V(P)$ data with the MES based on the same ultrasonic data of Bartels and Schuele [6] used for NaCl in this paper. This comparison and those for other materials are very good up to pressures given by $P/B_0 \cong \frac{1}{2}$. The MES follows from the integration of the definition of the bulk modulus under the assumption stated, and in reduced form is

$$-\int_{V_0}^{V}\frac{dV}{V}=\int_0^{P/B_0}\frac{dP/B_0}{(1+B_0'P/B_0)}. \quad (18)$$

The MES in the *reduced* form used in this paper is thus a function of B_0' alone. We have already remarked that B_0' is essentially the same for all the sodium and potassium halides; moreover the reduced MES is insensitive, at $P/B_0 < \frac{1}{2}$, to the small although systematic variation in B_0' among materials shown in Table 4 and Fig. 6. It follows that the reduced MES is the *same* for all these alkali halides and is, in effect, a law of corresponding states, an observation for which we are indebted to our colleague O. K. Rice.

It has already been remarked that the $V(P)$ data of Drickamer *et al.*[2] for NaF, NaCl and NaI superimpose fairly well when plotted in reduced form; however, close inspection shows that the NaF smoothed points, Fig. 7, lie systematically a bit higher than those for the chloride and iodide. The 'universal' reduced MES fits best just these NaF data points and hence is systematically high by a small amount with respect to NaCl and NaI. The point may or may not be significant, but is at least a good way of remembering a small but systematic discrepancy.

Acknowledgements—This research was directly supported by the Atomic Energy Commission at both Case Western Reserve University and the University of North Carolina. The background support of the Carbon Products Division of the Union Carbide Corporation at Case Western Reserve University and of the Advanced Research Projects Agency at the University of North Calorina is also acknowledged. Professor D. E. Schuele patiently supervised the terminal stages of the experimental work at Case Western Reserve University and also made helpful comments on the manuscript as did Dr. J. Ross Macdonald. The authors are grateful to Dr. Richard K. Kirby who supplied critically evaluated values of the thermal expansion coefficients.

REFERENCES

1. TOSI M. P., *Solid State Physics* (Edited by F. Seitz and D. Turnbull), Vol. 16, p. 1. Academic Press, New York (1964).
2. DRICKAMER H. G., LYNCH R. W., CLENDENEN R. L. and PEREZ-ALBUERNE E. A., *Solid State Physics* (Edited by F. Seitz and D. Turnbull), Vol. 19, p. 135. Academic Press, New York (1966).
3. ANDERSON O. L., *J. Phys. Chem. Solids* **27**, 547 (1966).
4. SWENSON C. A., *Thermal Contributions to the Equation of State of Solids*, USAEC Rept. IS-870 (1964); also *J. Phys. Chem. Solids* **29**, 1337 (1968).
5. MILLER R. A. and SMITH C. S., *J. Phys. Chem. Solids* **25**, 1279 (1964).
6. BARTELS R. A. and SCHUELE D. E., *J. Phys. Chem. Solids* **26**, 537 (1965).
7. KOLIWAD K. M., GHATE P. B. and RUOFF A. L., *Phys. Status. Solidi* **21**, 507 (1967).
8. HAUSSÜHL H., *Z. Phys.* **159**, 223 (1960).
9. REDDY P. J. and RUOFF A. L., *Physics of Solids at High Pressures* (Edited by C. T. Tomizuka and R. M. Emrick), p. 510. Academic Press, New York (1965).
10. *National Bureau of Standards Circular 539*, Vols. *1-10*. U.S. Government Printing Office, Washington, D.C. (1953).
11. HENGLEIN F. A., *Z. Electroch.* **31**, 424 (1925).
12. BRÖNSTED J. N., *Z. Electroch.* **20**, 554 (1914).
13. SPANGENBURG K., *Naturwissenschaften* **43**, 394 (1956).

APPENDIX

The temperature coefficients at constant pressure and at constant volume of adiabatic elastic constants C_{11}', C' and C_{44} are given in Figs. 10, 11 and 12. The values of $d\ln C/dT)_V$ were computed at 295°K using Haussühl's $d\ln C/dT)_P$ and the identity

$$\left.\frac{d\ln C}{dT}\right)_P=\left.\frac{d\ln C}{dT}\right)_V-\beta B_T\left.\frac{d\ln C}{dP}\right)_T. \quad (A1)$$

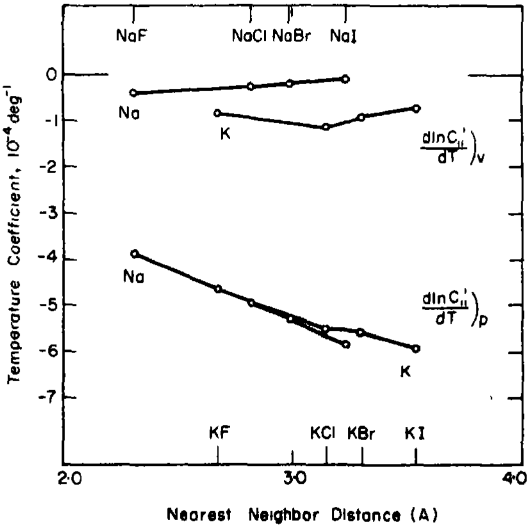

Fig. 10. The temperature coefficients of the adiabatic elastic constant C_{11}' of the sodium and potassium halides at 295°K vs. nearest neighbor distance.

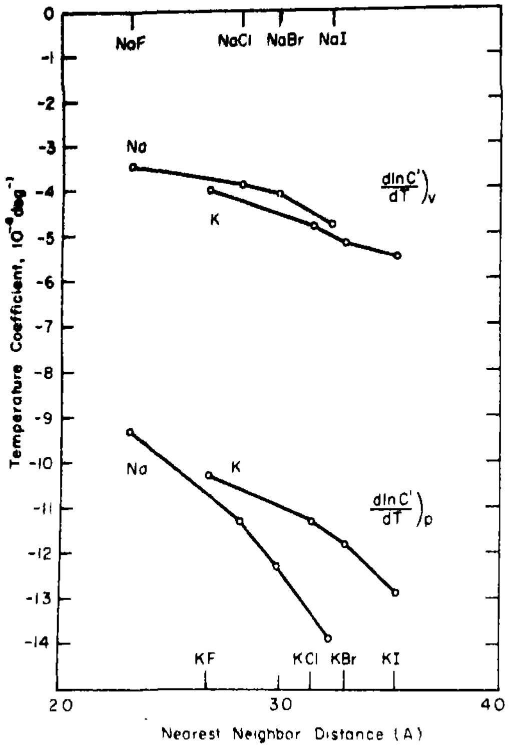

Fig. 11. The temperature coefficients of the adiabatic elastic constant C' of the sodium and potassium halides at 295°K vs. nearest neighbor distance.

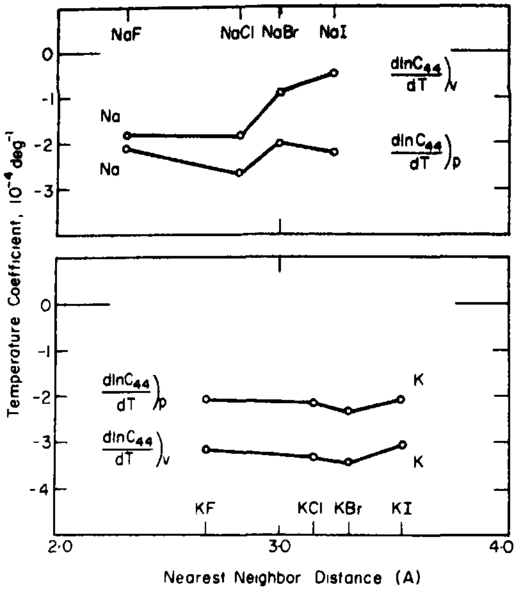

Fig. 12. The temperature coefficients of the adiabatic elastic constant C_{44} of the sodium and potassium halides at 295°K vs. nearest neighbor distance.

The $d\ln C/dT)_V$ are negative in all cases and small, especially the longitudinal $d\ln C'_{11}/dT)_V$ that are nearly zero. The graphical separation of the two coefficients represents the contribution to $d\ln C/dT)_P$ resulting from the volume change owing to thermal expansion. This effect dominates the constant volume effect for C'_{11} and C', but not for C_{44}. Specifically, the $d\ln C/dT)_V$ of the potassium halides are larger in magnitude than the $d\ln C_{44}/dT)_P$ because the dC_{44}/dP of this sequence are negative.

J. Phys. Chem. Solids Pergamon Press 1970, Vol. 31, pp. 635–638, Printed in Great Britain.

MAGNETIC PROPERTIES OF ACr_2Se_4 (A = Fe, Co, Ni) AND $NiCr_2S_4$*

B. L. MORRIS†, P. RUSSO and A. WOLD
Department of Physics and Chemistry, and Division of Engineering, Brown University, Providence R.I. 02912, U.S.A.

(*Received* 28 *July* 1969)

Abstract—The magnetic susceptibilities of ACr_2Se_4 (A = Fe, Co, Ni) and $NiCr_2S_4$ are reported. $CoCr_2Se_4$ has a sharp peak in its susceptibility at 199°K and the other three compounds have broad maxima in their susceptibilities between 210 and 270°K. The unusual shapes of the thermomagnetic curves are explained as a result of competing antiferro- and ferromagnetic interactions.

INTRODUCTION

RECENTLY, the electrical and magnetic properties have been reported [1-4] for a number of isostructural transition metal chalcogenides with the formula AB_2X_4 (A = Fe, Co, Ni: B = Ti, V; X = S, Se) and the Cr_3S_4 structure [5]. All of these compounds show metallic conductivity and small, negative Seebeck coefficients typical of metals. It has also been shown that magnetic ordering occurs in those compounds where A = Fe; $FeTi_2S_4$ has complex magnetic properties[3], while the other three materials are antiferromagnetic[2]. Pauli paramagnetic behavior was observed for those compounds where A = Ni or Co.

Neutron diffraction studies have shown that the compounds $FeCr_2Se_4$[6] and $NiCr_2S_4$[7] are antiferromagnetic at 4·2°K. However, the thermomagnetic curve of $NiCr_2S_4$ does not resemble that of a 'classical' antiferromagnetic compound[8]. The susceptibility does not have a sharp peak at the Néel point and does not show Curie–Weiss behavior above this point. It is of interest, therefore, to extend these studies to include the thermomagnetic curves for the compounds ACr_2Se_4 (A = Fe, Co, Ni) all of which have the Cr_3S_4 structure. In addition, the magnetic properties of $NiCr_2S_4$ are presented.

$FeCr_2S_4$ and $CoCr_2S_4$ normally crystallize with the spinel structure. However, it has been found that when they are subjected to a pressure of 10 bars at 530°C, they transform to the Cr_3S_4 structure. In this form they show antiferromagnetic behavior[8], whereas in the spinel phase they are ferrimagnetic[9].

The Cr_3S_4 structure is intermediate between the NiAs($B8_1$) and CdI_2(C6) types and the comparison is shown in Fig. 1. The NiAs structure has all the octahedral sites in the close-packed hexagonal anion sublattice occupied by cations, whereas in the AB_2X_4 (Cr_3S_4) structure one quarter of the cations are removed and the resulting vacancies confined to alternate metal layers, and ordered within these layers. The holes occur in layers perpendicular to the *c* axis and this is shown in Fig. 2.

EXPERIMENTAL

The materials were prepared by reaction of stoichiometric amounts of the high-purity elements* in evacuated silica tubes. Three successive oneweek firings at 800°C, with intermediate grindings, were necessary to achieve homogeneity. In order to prepare

---

*This work was supported by A.R.P.A. and the U.S. Army Research Office, Durham.

†Now at N.A.S.A. Electronics Research Center, Cambridge, Massachusetts, U.S.A.

*Spectroscopic grade Fe, Co, Ni, Cr, S, Se was obtained from Gallard-Schlesinger Corp., New York.

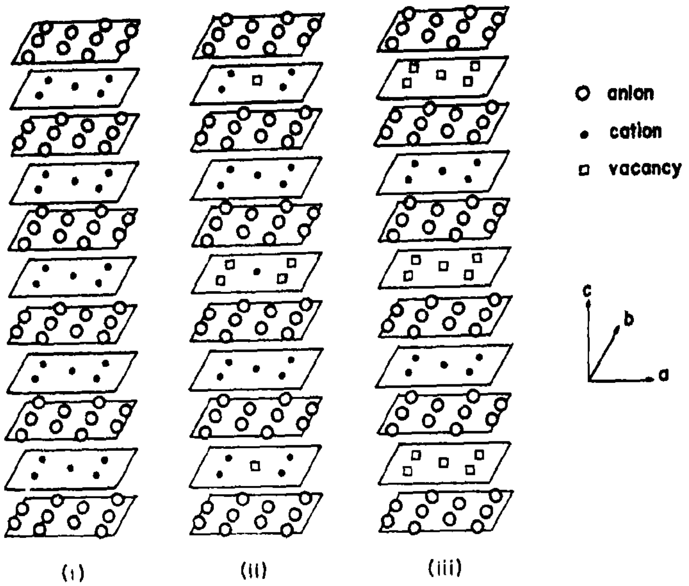

Fig. 1. Comparison of Cr_3S_4 structure (ii) with NiAs (i) and CdI_2 (iii).

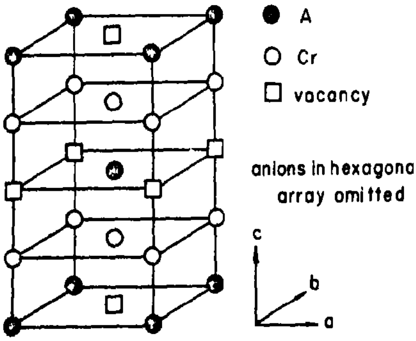

Fig. 2. Cation substructure of ACr_2Se_4 (A = Fe, Co, Ni).

samples suitable for electrical measurements, the products were pressed into bars at a pressure of 10,000 psi and then sintered in evacuated silica tubes at 800°C for 10 days.

Crystallographic parameters were determined on powder samples using a Norelco diffractometer with monochromatic radiation (AMR-202 focusing monochrometer) and a high-intensity copper source.

The magnetic measurements were performed on a Faraday balance which has been described elsewhere[10]. Measurements were made between 5 and 300°K in fields up to 10 kOe. Electrical resistivity measurements were made between 80 and 300°K using a Keithley model 503 milliohmeter. Seebeck measurements were made using a cold junction at 0°C and a hot junction at about 40°C.

RESULTS

The lattice parameters and Seebeck coefficients are given in Table 1. Every peak in the X-ray patterns for the ternary chalcogenides could be indexed on a monoclinic cell. All observed reflections satisfy the conditions $h+k+1 = 2n$ (n = integer) which is required

Table 1. Monoclinic lattice parameters and Seebeck coefficients

Compound	a (Å)	b (Å)	c (Å)	β (deg)	α (u.v./deg)
$FeCr_2Se_4$	6·27	3·62	11·85	90·92	41
$CoCr_2Se_4$	6·27	3·62	11·62	90·75	−37
$NiCr_2Se_4$	6·22	3·59	11·53	91·00	−21
$NiCr_2S_4$	5·94	3·42	11·14	91·30	−117

by the space group $I2/m$[1]. The cell parameters are in agreement with those reported by Jellinek[1] and Chevreton[11]. No trace of a second phase was evident in the X-ray patterns of the products.

The magnetic susceptibility curves are shown in Fig. 3 and Fig. 4. $CoCr_2Se_4$ exhibits a sharp peak in $\chi(T)$ at 199°K. Above this temperature the susceptibility decreases with increasing temperature, but $1/\chi$ vs. T does not give a straight line, and so cannot be used to determine a paramagnetic moment. The susceptibility of $FeCr_2Se_4$ has a maximum near 260°K, and that of $NiCr_2Se_4$ has a broad maximum near 210°K. The susceptibility of $NiCr_2S_4$ reaches a maximum from 220 to 270°K and in this range the susceptibility is independent of temperature. At lower temperatures, 5°K to about 130°K, the susceptibilities of all four compounds increase as the temperature decreases, but $\chi(T)$ does not obey the Curie–Weiss law in this region.

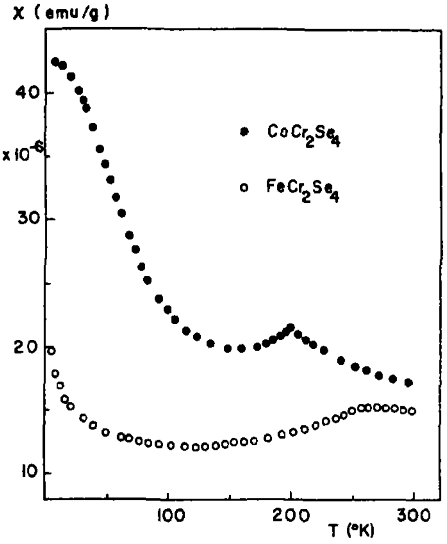

Fig. 3. Magnetic susceptibilities of $FeCr_2Se_4$ and $CoCr_2Se_4$.

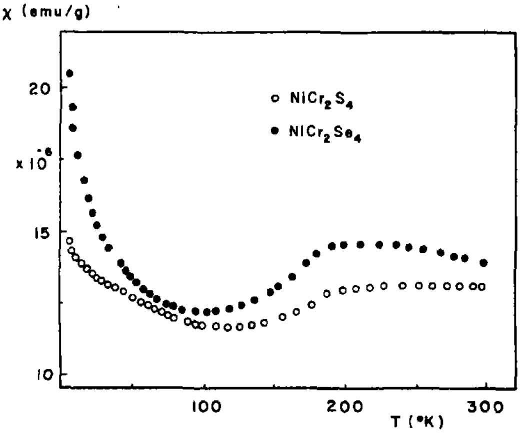

Fig. 4. Magnetic susceptibilities of $NiCr_2Se_4$ and $NiCr_2S_4$.

DISCUSSION

The electrical resistivity measurements were made on pressed, sintered bars, and semiconducting behavior was observed for all four compounds. However, the activation energies observed, about 0·01 eV, were much smaller than those usually measured for semiconducting compounds. Since well sintered bars were not obtained, the results may be, in large measure, caused by grain boundaries. The Seebeck voltages shown in Table 1 are not influenced by grain boundaries, and appear to be somewhat higher than those usually reported for metallic materials.

Neutron diffraction studies on $FeCr_2Se_4$[6] and $NiCr_2S_4$[7] show that they are antiferromagnetic at 4·2°K with a spin propagation vector $\mathbf{k}_0 = (\frac{1}{2}, 0, \frac{1}{2})$. The direction for the spin s for $NiCr_2S_4$ is $\theta \simeq 45°$ and $\phi \simeq 58°$, where θ is the angle of s with $(10\bar{1})$, and $90°\text{-}\phi$ is the angle with b of the projection of s on $(10\bar{1})$. For $FeCr_2Se_4$ $\theta \simeq 55°$ and $\phi \simeq 0°$, that is s is nearly along the c axis ($\theta = 61° 55'$, $\phi_c = 0°$). In $NiCr_2S_4$ the measured moment is reduced by 30 per cent with respect to the spin-only moment, and in $FeCr_2Se_4$ the reduction is 14 per cent. Covalent mixing is given as the reason for these reductions.

In the absence of neutron diffraction data, it is difficult to interpret completely the results presented in this paper. However, the thermomagnetic curve for $NiCr_2Se_4$ is so similar to those of $NiCr_2S_4$ and $FeCr_2S_4$ that it is undoubtedly also antiferromagnetic. $CoCr_2Se_4$, which has a sharp peak in the thermomagnetic curve at 199°K is also believed to be antiferromagnetic, since the rise in the susceptibility below 160°K is also present in the other three materials.

Andron and Bertaut[7] have shown that the total exchange integral in $NiCr_2S_4$ may be written as the sum of five different superexchange interactions. The experimentally determined magnetic structure is stable only if certain of these interactions are negative (antiferromagnetic) and the others positive (ferromagnetic). It is probable that the unusual shapes of the thermomagnetic curves found for $NiCr_2S_4$ and the related selenides result from such competing interactions.

REFERENCES

1. MORRIS B. L., PLOVNICK R. H. and WOLD A., *Solid St. Commun.* 7, 291 (1969).
2. MORRIS B. L., PLOVNICK R. H., JOHNSON V. and WOLD A., *J. appl. Phys.* **40**, 1299 (1969).
3. PLOVNICK R. H., VLASSE M., PERLOFF D. WOLD A., *J. Phys. Chem. Solids* **29**, 1935 (1968).
4. BOUCHARD R. and WOLD A., *ibid.* **27**, 591 (1966).
5. JELLINEK F., *Acta. Crystallogr.* **10**, 620 (1957).
6. CHEVRETON M. and ANDRON B., *Compt. rend.* **264** 316 (1967).
7. ANDRON B and BERTAUT E. F., *J. Phys.* **27**, 619 (1966).
8. TRESSLER R. E. and STUBICAN V. S., *J. Am. ceram. Soc.* **51**, 391 (1968).
9. LOTGERING F. K. *Philips Res. Rep.* **11**, 190 (1956).
10. MORRIS B. L. and WOLD A., *Rev. scient. Instrum.* **39**, 1937 (1968).
11. CHEVRETON M., *Acta Crystallogr.* **16**, 22A (1963).

J. Phys. Chem. Solids Pergamon Press 1970. Vol. 31, pp. 639–646. Printed in Great Britain.

NONSTOICHIOMETRY AND ELECTRONIC DEFECTS IN Co_2SiO_4 AND IN $CoAl_2O_4$–$MgAl_2O_4$ CRYSTALLINE SOLUTIONS

C. GRESKOVICH and H. SCHMALZRIED
Institute for Theoretical Metallurgy, Universität Clausthal, West-Germany

(*Received* 24 *July* 1969)

Abstract – Electronic defects and their relation to nonstoichiometry in Co_2SiO_4 and in $CoAl_2O_4$–$MgAl_2O_4$ crystalline solutions were established by tensi-volumetric measurements between oxygen partial pressures of 2.10^{-1} and 10^{-4} atm in the temperature range 1100–1150°C. The results were consistent with doubly ionized cobalt vacancies and an equivalent number of electron holes. For an oxygen partial pressure of 1 atm and a temperature of about 1150°C, the mole fraction of cobalt vacancies (δ) in $Co_{2-\delta}SiO_4$ and $Co_{1-\delta}Al_2O_4$ was approximately 10^{-4} and 10^{-3}, respectively. There was an exponential decrease in vacancy and defect electron concentration with increasing $MgAl_2O_4$ content in crystalline solutions with $CoAl_2O_4$ at constant p_{O_2}. The standard free energy change for the defect reaction increased linearly in this quasibinary system with the mole fraction of $MgAl_2O_4$.

1. INTRODUCTION

IN THE LAST few years point defect thermodynamics has been extended from the case of binary compounds to ternary ionic crystals [1, 2]. Especially through the application of electrical conductivity measurements, self diffusion measurements and coulometric titration the most probable types of disorder have been elucidated in several ternary compounds [3–6].

In this paper, a comparison is made between the nature of electronic defects in Co_2SiO_4 crystallizing in the olivine structure, and $CoAl_2O_4$ crystallizing in the spinel structure. Furthermore, the effect of a replacement of Co^{2+} by Mg^{2+} on electronic defects in the crystalline solution $CoAl_2O_4$–$MgAl_2O_4$ is studied.

It has been ascertained that the ionic majority defects in $CoAl_2O_4$ consist of Co-vacancies and Al-interstitials, in agreement with other aluminates [3]. Therefore, it is possible to dissolve Al_2O_3 in cobalt aluminate to a certain degree which is temperature dependent. X-Ray intensity measurements [7] show that $CoAl_2O_4$ is essentially a normal spinel below 1100°C, with $Co^{2+}(3d^7)$ and Al^{3+} ions occupying tetrahedral and octahedral lattice sites in the almost close packed oxygen ion structure of the spinel lattice, respectively. The structure of Co_2SiO_4 can be described as isolated SiO_4^{4-}-tetrahedra linked by Co^{2+}ions which are in an octahedral oxygen environment. A deviation from the metal to nonmetal ratio 3:4 in these ternary oxides will result in electronic defects in the same way as is generally accepted for the binary transition metal oxides, e.g. $Co_{1-\delta}O$. In both cases this deviation from stoichiometry is a function of the oxygen partial pressure. For cobalt oxide it is known that at high defect concentrations and low temperatures, single ionized cation vacancies and electron holes in the form of Co^{3+}-ions are present, whereas at small defect concentrations doubly ionized vacancies and a corresponding number of holes are present [5, 8, 9]. The defect concentrations in most cases are too small to be detected quantitatively by chemical analysis. Hence, physical methods are employed to study the electronic defect concentrations, i.e. optical or electrical measurements.

By analogy one may expect that $CoAl_2O_4$ and Co_2SiO_4 exhibit the same kind of electronic defects as does $Co_{1-\delta}O$ as a function of the oxygen partial pressure p_{O_2}. It is appropriate to indicate this by $Co_{1-\delta}Al_2O_4$ and $Co_{2-\delta}SiO_4$. The concentration of electronic defects, however, should be lower in the ternary compound as compared with $Co_{1-\delta}O$. This is because in the ternary compound a cobalt cation has fewer Co-nearest neighbours which are at greater distances, and therefore there is a reduction in the resonance stabilization of the electronic defects as discussed by Zintl[10].

The present investigation shall establish the nature as well as the equilibrium concentrations of the electronic defects in $Co_{1-\delta}Al_2O_4$ and $(Co, Mg)_{1-\delta}Al_2O_4$, both equilibrated with Al_2O_3, and in $Co_{2-\delta}SiO_4$, equilibrated with SiO_2, as a function of the oxygen partial pressure. In this way all independent thermodynamic variables are unambiguously fixed. In order to accomplish the investigation a symmetrical tensi-volumetric apparatus according to Meurer was constructed[11] which accurately can measure a 10^{-7} change in the number of moles of oxygen.

2. EXPERIMENTAL PROCEDURES

CoO was prepared by the decomposition of analytical grade $Co(NO_3)_2 \cdot 6H_2O$. The other starting materials were chemically pure SiO_2, Al_2O_3 and MgO. The binary oxide mixtures leading to $CoAl_2O_4$ with an excess of 10 mole% Al_2O_3 and Co_2SiO_4 with an excess of 2 mole% SiO_2 were fired in air at 1200°C for 5 days, ground and refired two more days at the same temperature. An excess of binary oxide was necessary in order to fix the activity of Al_2O_3 and SiO_2 at unity. $MgAl_2O_4$ was prepared at 1350°C for 7 days, ground and refired for additional 7 days at 1350°C. Crystalline solutions between $CoAl_2O_4$ and 20, 40 and 60 mole% $MgAl_2O_4$ were prepared in air at 1300°C for 5 days. Since the equilibrium concentrations of defects for these compounds were determined within the temperature range of 1100–1150°C, all specimens were initially equilibrated in air for 5 days at their respective working temperature.

For the determination of electronic point defects in nonstoichiometric crystals, a tensi-volumetric apparatus was constructed and is schematically shown in Fig. 1. A highly sensitive micromembrane manometer[12] is the actual measuring device. It transforms pressure differences across the membrane into electrical units by means of capacitance change. The pressure measuring range is 2.10^{-4} to 2.10^{-1} Torr, and is valid for pressure differences of less than 10 Torr across the membrane.

The measurement of the change in oxygen content of a ternary oxide sample as a function of oxygen pressure proceeds as follows: Firstly, a sample of known weight is sealed in a quartz tube (2) and equilibrated in dry air at a known temperature and pressure. Then the oxygen partial pressure is changed to a predetermined value in the overall system, and the two identical fused silica tubes (2) and (3), one containing the sample, are connected via the micromembrane manometer. This procedure takes about 15 sec. The starting point is found by extrapolation. Equilibration of the nonstoichiometric oxide in the lower oxygen pressure environment proceeds by the release of oxygen which causes an increase in pressure on the sample side of the system. The change in pressure (Δp) is recorded as a function of time (t). Equilibrium is indicated by no further pressure change with time.

Proceeding from a lower to a higher total

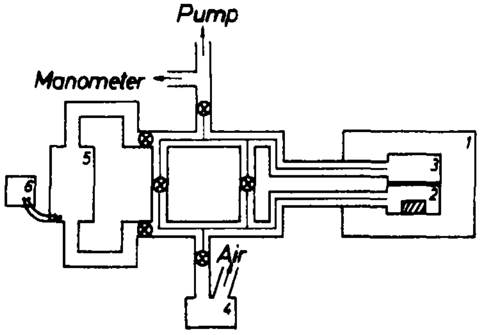

Fig. 1. A schematic representation of the tensi-volumetric apparatus. (1) Furnace, (2), (3) Fused silica tubes, (4) Dewar with dry ice, (5) Pressure measuring condenser, (6) Recorder, (x) Stopcocks.

pressure of air can easily be accomplished, but adsorption effects and small pressure changes due to thermal fluctuations sometimes produce irregularly shaped (Δp vs. t) curves above 80 Torr. However, the absolute value of Δp was essentially the same for the same p_{O_2} change, i.e. from a low to high and from a high to low p_{O_2} value.

The gas on the sample side of the symmetrical system in Fig. 1 can be described by the ideal gas law. A change in pressure caused by a change in the number of moles of gaseous oxygen (Δn_{O_2}) can be expressed as

$$\Delta p = \left(\frac{RT}{V}\right) \cdot \Delta n_{O_2} = K \Delta n_{O_2}. \qquad (1)$$

In order to determine the exact value of the constant K at a given furnace temperature, a $NiO_{1+\gamma}$ single crystal was used as a standard calibration specimen since it is a well-known oxygen excess semiconductor[12–14]. The actual values $\gamma(p_{O_2})$ taken for calibration are those of Sockel[5]. A change in p_{O_2} over a known amount of $NiO_{1+\gamma}$ causes a known change in excess oxygen ($\Delta\gamma$) which is

$$\Delta\gamma = \frac{2\Delta n_{O_2} \cdot M_{NiO}}{m_{NiO}} \qquad (2)$$

where M_{NiO} and m_{NiO} equal the molecular and actual weight of NiO, respectively. Substitution of equation (2) into equation (1) and solving for the constant $(RT/V) = K$, one obtains

$$\left(\frac{RT}{V}\right) = K(T) = \frac{2M_{NiO} \cdot \Delta p}{\Delta\gamma \cdot m_{NiO}}. \qquad (3)$$

Since all terms on the right hand side of equation (3) are known, $K(T)$ can be determined. Cobalt aluminate[27] and cobalt silicate[19] are both metal deficient p-type semiconductors. Then, instead of writing $CoAl_2O_{4+\gamma}$ and $Co_2SiO_{4+\gamma}$ for ternary compounds with excess oxygen, one may write $Co_{1-\delta}Al_2O_4$ and $Co_{2-\delta}SiO_4$ as well, where $\delta \cong \gamma$, if $\gamma \ll 1$. The calculation of δ from γ can easily be performed if the activity of SiO_2 or Al_2O_3 is kept constant during oxidation or reduction. Thus the working equation used for the calculation of the changes in oxygen content, which is the cobalt vacancy concentration δ, can be written as

$$\Delta\delta = \frac{2}{K} \cdot \frac{M_{Co_2SiO_4}}{m_{Co_2SiO_4}} \cdot \Delta p. \qquad (4)$$

Δp is the total change of pressure after a pressure jump, expressed in atmospheres.

Polycrystalline powders (5–15 g) of the specimens were used because with small grain sizes equilibrium was usually attained in less than 12 hours in the temperature range 1100°–1150°C after a p_{O_2} change. To determine if sample surface effects (i.e. surface adsorption or desorption) contributed substantially to the Δp measurements, the Co_2SiO_4 powder was removed from the apparatus and sintered at 1340°C for 4 days so that the average grain diameter was enlarged from 125 to 300 μ. The total values before and after the enlargement of grain size deviated only by 2% for the same p_{O_2} change and temperature. Adsorption and desorption effects originating from the total glass surface on the upper half of the system (see Fig. 1) were neutralized by similar effects on the lower half because of the symmetrical construction of the tensi-volumetric apparatus.

3. RESULTS AND DISCUSSION

3.1 *Defect concentrations in nonstoichiometric* $Co_{2-\delta}SiO_4$

A typical experimental curve for equilibration after an oxygen pressure jump over $Co_{2-\delta}SiO_4$ is shown in Fig. 2. Although the kinetic process proceeding towards equilibrium is diffusion controlled as will be substantiated later, grain size, shape and distribution deviate the curve from the parabolic rate law.

There are two methods for calculating the absolute concentration of cobalt vacancies

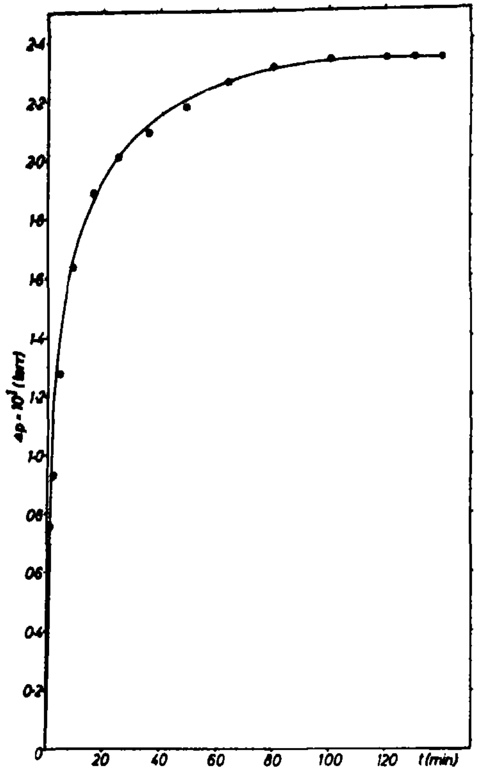

Fig. 2. Change in pressure $\Delta p \propto \Delta n_{O_2}$ as a function of time for 12·4 g of $Co_{2-\delta}SiO_4$ at 1145°C for the p_{O_2} jump from $2 \,.\, 10^{-1}$ to $2{\cdot}26 \,.\, 10^{-2}$ atm.

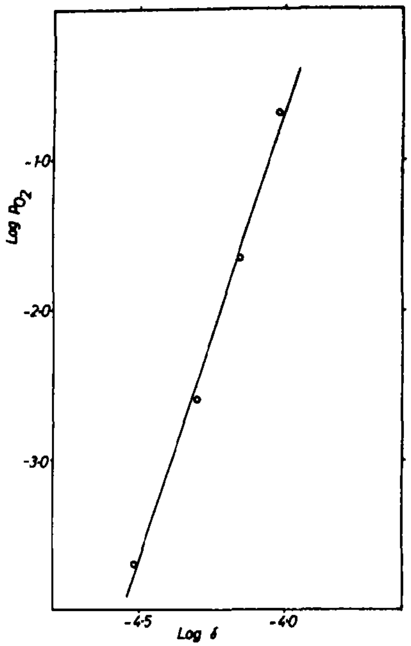

Fig. 3. Partial pressure of oxygen p_{O_2} as a function of the cobalt deficiency δ in $Co_{2-\delta}SiO_4$ at 1145°C.

(δ) in thermodynamic equilibrium as a function of the partial pressure of oxygen. Firstly, one can choose several vacancy concentrations (δ_0') at the lowest p_{O_2} value and add the experimental increments Δδ to it for the corresponding Δp_{O_2}-increments. Accept as the correct δ_0 that value which gives the best linear fit. A plot of log p_{O_2} as a function of log δ is shown in Fig. 3, where the slope (Δ log p_{O_2}/Δ log δ) is equal to 6. This same method was used for $CoAl_2O_4$ and its crystalline solutions with $MgAl_2O_4$. Secondly, Wagner's method[15] can be used for determining the absolute concentration of defects from measurements involving only changes in concentration. The application of this method to the data again results in a slope of 6.

According to the information given in Fig. 3, the interaction of gaseous oxygen with $Co_{2-\delta}SiO_4$ can be expressed by the chemical equation

$$\tfrac{1}{2}O_2(g) + 3Co_{Co} = V''_{Co} + 2Co^{\bullet}_{Co} + CoO, \Delta G_5{}^0 \qquad (5)$$

where in accord with Kröger's notation[16] Co_{Co} is a divalent cobalt ion on its regular lattice site, V''_{Co} is a doubly ionized vacancy of a regular cobalt ion, $Co^{\bullet}_{Co}$ is a Co^{3+} ion or a positive hole (⊕) on a regular cobalt site, CoO is cobalt oxide dissolved in the cobalt silicate lattice and $\Delta G_5{}^0$ is the standard free energy change for reaction (5). Upon consideration of the charged defects in equation (5), the relationship for electrical neutrality reads

$$x_{Co^{\bullet}_{Co}} = 2x_{V''_{Co}} = 2\delta \qquad (6)$$

where x is the fraction of defects per molecule Co_2SiO_4. The corresponding equilibrium condition under the assumption of negligible defect interaction reads

$$K_5 = \frac{4x^3{}_{V''_{Co}} \cdot a_{CoO}}{p_{O_2}^{1/2}} = \exp(-\Delta G_5{}^0/RT) \qquad (7)$$

where K_5 is the equilibrium constant for equation (5). The activity of CoO for Co_2SiO_4 in equilibrium with SiO_2 is calculated, by knowing the standard free energy of formation of Co_2SiO_4 from CoO and SiO_2[17, 18], as 0·64 at $T = 1200$°C. From equation (7) it is seen that the concentration of vacancies is proportional to $p_{O_2}^{1/6}$, provided that a_{CoO} is kept constant.

For $p_{O_2} = 1$ atm, $x_{V''} = 1{\cdot}3 \,.\, 10^{-4}$ and $T = 1145$°C, $\Delta G_5{}^0 = +73$ kcal.

Recently[19] the chemical diffusion coefficient for equilibration of highly dense $Co_{2-\delta}$-SiO_4 after a p_{O_2} change was determined to be $6 \,.\, 10^{-8}$ cm²/sec at 1200°C. Since the majority diffusing species (i) are Co-vacancies and positive holes, the fluxes can be expressed as

$$j_i = -\frac{D_i c_i}{RT} \cdot \operatorname{grad} \eta_i \qquad (8)$$

where j_i is given in moles/cm² sec, D_i is the selfdiffusion coefficient of species i, c_i the concentration and η_i the electrochemical potential. Evaluation of the flux equations leads to the conclusion that the chemical diffusion coefficient virtually equals 3 times the vacancy selfdiffusion coefficient. The relationship between the selfdiffusion coefficient of cobalt vacancies (D_V) and cobalt ions ($D_{Co_{Co}}$) under the assumption of negligible correlation effects is given by

$$D_{Co_{Co}} \cdot x_{Co_{Co}} = D_{V''_{Co}} \cdot x_{V''_{Co}}. \qquad (9)$$

For small concentrations of defects, one obtains

$$D_{Co_{Co}} \approx \tfrac{1}{2} D_{V''_{Co}} x_{V''_{Co}}, \quad x_{Co_{Co}} \approx 2. \qquad (10)$$

In air at 1200°C the value of the selfdiffusion coefficient for octahedral divalent cobalt ions is $5 \,.\, 10^{-13}$ cm²/sec. This value agrees satisfactorily with the diffusion coefficient derived from the kinetic equilibration curve in Fig. 2, assuming diffusion control and knowing the average grain size.

3.2 *Defect concentrations in nonstoichiometric* $Co_{1-\delta}Al_2O_4$ *and its crystalline solutions with* $MgAl_2O_4$

The concentration of cobalt vacancies as a function of p_{O_2} for $Co_{1-\delta}Al_2O_4$ and crystalline solutions between $Co_{1-\delta}Al_2O_4$ and 20, 40 and 60 mole% $MgAl_2O_4$ is given in Fig. 4. The concentration of cobalt vacancies in $Co_{1-\delta}Al_2O_4$ at one atmosphere of oxygen is about $1{\cdot}5 \,.\, 10^{-3}$. In comparison to $Co_{2-\delta}SiO_4$, the concentration of cobalt vacancies which are located on the tetrahedral lattice sites in $Co_{1-\delta}Al_2O_4$ is more than one order of magnitude larger at the same partial pressure of oxygen. The slopes ($\Delta \log p_{O_2}/\Delta \log \delta$) of all the lines in Fig. 4 are essentially parallel

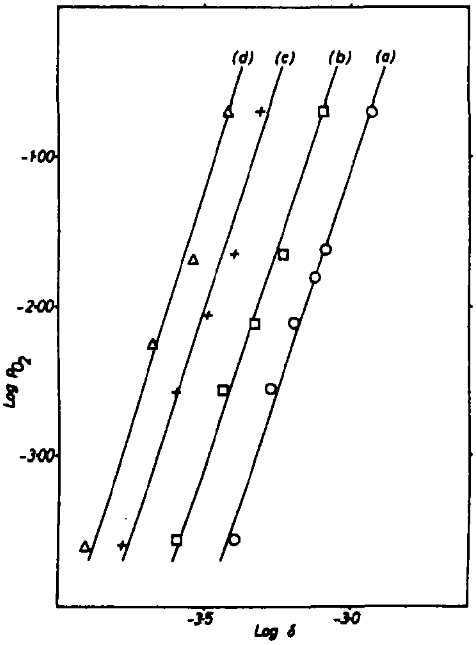

Fig. 4. Partial pressure of oxygen p_{O_2} as a function of the cobalt deficiency δ at 1120°C for (a) $CoAl_2O_4$, (b) $CoAl_2O_4$ + 20 mole% $MgAl_2O_4$, (c) $CoAl_2O_4$ + 40% $MgAl_2O_4$ and (d) $CoAl_2O_4$ + 60% $MgAl_2O_4$.

and equal to 6, indicating that the defect model is practically the same as expressed in equation (5) where defects now occur on the tetrahedral sublattice in the spinel structure. After consideration of the electrical neutrality condition, the equilibrium condition is the same as given in equation (7). In the case of cobalt magnesium aluminate however, the mole fraction of cobalt ions on their regular tetrahedral sites is included in the equilibrium condition as a variable which changes with the mole fraction of $MgAl_2O_4$ dissolved in $Co_{1-\delta}Al_2O_4$. Therefore one has to write

$$x_{Co_{Co}} = 1 - x_{MgAl_2O_4} \quad (11)$$

under the assumption that $MgAl_2O_4$ is essentially a normal spinel below 1350°C and there is a direct substitution of Mg^{2+} ions for Co^{2+} ions in the tetrahedral sublattice. In typical ionic crystals like $MgAl_2O_4$, Mg^{2+} and Al^{3+} have noble gas ion configurations over the p_{O_2} range and electronic defects can be neglected. Thus, as the p_{O_2} is increased it is only the oxidation of Co^{2+} to Co^{3+} ions accompanied with the production of cation vacancies which occurs in the crystalline solutions between $Co_{1-\delta}Al_2O_4$ and $MgAl_2O_4$.

In addition, the activity of CoO dissolved in the spinel crystalline solutions can be approximated as

$$a_{CoO} = a^0_{CoO} \cdot x_{Co_{1-\delta}Al_2O_4} \quad (12)$$

where a^0_{CoO} is the activity of CoO dissolved in pure $Co_{1-\delta}Al_2O_4$ in equilibrium with Al_2O_3. From the standard free energy of formation of $Co_{1-\delta}Al_2O_4$ from its binary oxides[20], the calculated value of a^0_{CoO} is approximately 0·17 at 1200°C.

The calculation of $\Delta G_5{}^0$ as a function of the mole fraction of $MgAl_2O_4$ dissolved in $Co_{1-\delta}Al_2O_4$ can be accomplished with equation (7) and with equations (11) and (12) as approximations. These results are plotted in Fig. 5. Within the region $0 < x_{MgAl_2O_4} < 0{\cdot}6$ the data can be described by the equation

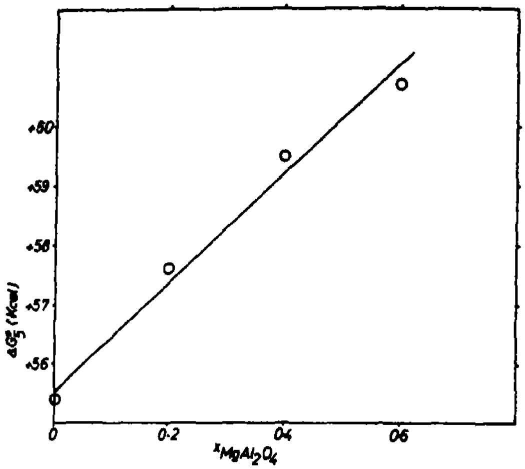

Fig. 5. The dependence of the standard free energy change for defect formation (equation (5)) in the $CoAl_2O_4$-$MgAl_2O_4$ system as a function of $x_{MgAl_2O_4}$ at 1120°C and one atmosphere of oxygen.

$$\Delta G_5{}^0 = \Delta G_5{}^0(CoAl_2O_4)_{x_{MgAl_2O_4}=0} + (9{\cdot}4 \pm 0{\cdot}4) \cdot x_{MgAl_2O_4}\,[\text{kcal}]. \quad (13)$$

It appears that there is a moderate linear dependence of $\Delta G_5{}^0$ on $x_{MgAl_2O_4}$. In the quasi-binary system CoO–MgO Zintl[10] found a strong dependence of ΔG^0 on the mole fraction of MgO which is caused by a rather sharp decrease in the concentrations of cation vacancies and positive holes with increasing MgO in crystalline solution.

The logarithm of the concentration of cation vacancies (log δ) as a function of $x_{MgAl_2O_4}$ in crystalline solution with $Co_{1-\delta}Al_2O_4$ is given in Fig. 6 for an oxygen partial pressure of 1 atmosphere (δ-values extrapolated from Fig. 4). In the region $0 < x_{MgAl_2O_4} < 0{\cdot}6$ the curve approximates a linear behavior. This slow exponential decrease in (δ) or (Co_{Co}) with increasing $x_{MgAl_2O_4}$ is only 1/3 as large as that found in the quasibinary system CoO–MgO [10]. An explanation of this exponential decrease in positive hole concentration and of its absolute magnitude in the quasi-binary system $Co_{1-\delta}Al_2O_4$–$MgAl_2O_4$ and the quasi-binary system $Co_{1-\delta}O$–MgO can be provided

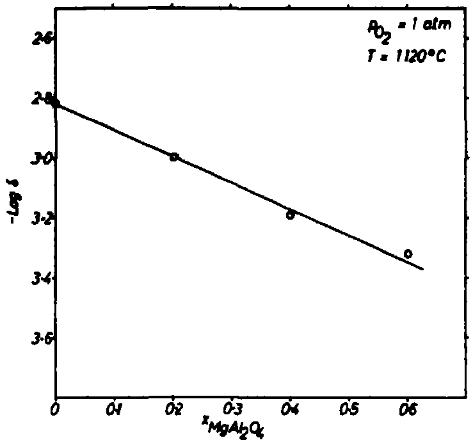

Fig. 6. Mole fraction of cobalt vacancies in the $CoAl_2O_4$–$MgAl_2O_4$ system as a function of $x_{MgAl_2O_4}$ at 1120°C and one atmosphere of oxygen.

through the consideration of a quantum-mechanical resonance effect and crystal chemistry.

Firstly, the $\Delta G_5{}^0$ value for equation (5) can be split into an enthalpy change ($\Delta H_5{}^0$) and an entropy change ($\Delta S_5{}^0$) since

$$\Delta G_5{}^0 = \Delta H_5{}^0 - T\Delta S_5{}^0. \qquad (14)$$

If it is assumed that most of the entropy change for the chemical reaction given by equation (5) is caused by the transfer of 1/2 mole O_2 from the ideal gaseous state to one mole of oxygen ions on the lattice sites, then in addition $\Delta S_5{}^0$ contains vibrational entropy terms which remain approximately constant with the addition of $MgAl_2O_4$ in crystalline solution. Finally if the change in ΔpV is assumed to be negligible then it is the increase in the energy change ($\Delta E_5{}^0$) of the crystal with the addition of $MgAl_2O_4$ that causes the exponential decrease in the concentration of $Co^{\cdot}_{Co}$.

It is known from the hopping electron model [21–23] that electrons and electron holes are mobile over equivalent lattice sites which in turn means these electrons have a somewhat low delocalization energy. In the virtually pure normal spinel $Co_{1-\delta}Al_2O_4$ each tetrahedral Co^{3+} ion or defect electron is surrounded by four nearest neighbour tetrahedral Co^{2+} ions, and the actual electronic state can be thought of in terms of a resonance phenomenon. Stabilization of the defect electron by resonance is greatest when the individual forms contributing to the resonance state are identical in energy[24]. However, the substitution of a Mg^{2+} ion for a Co^{2+} ion strongly disturbs the quantum-mechanical resonance effect because the ionization potential for the Mg^{2+} ion is so large and the concentration of Mg^{3+} ions can be neglected without any significant error. As the concentration of tetrahedral Mg^{2+} ions increases, the resonance effect is rapidly weakened so that there is a decrease in the concentration of Co^{3+} ions and vacancies.

Deviations from stoichiometry in the systems Cu_2S–Ag_2S[25], Cu_2Se–Ag_2Se[26], CoO–NiO[10] and CoO–MgO[10] have already been explained by a quantum-mechanical resonance effect. The exponential decrease in the concentration of Co^{3+} ions is smaller in the system $CoAl_2O_4$–$MgAl_2O_4$ than in CoO–MgO probably because there are 12 nearest neighbours about each cation in the sodium chloride structure whose distance between nearest cations is about 3 Å. Under the assumption of ideal close packing the distance between nearest neighbour tetrahedral cations in the spinel structure is about 3·5 Å. Although the larger number of nearest neighbours and their closer spacing most likely facilitates electron exchange between cobalt ions in CoO the presence of a foreign ion like Mg^{2+} causes a stronger disturbance to the resonance effect in the CoO–MgO system. Secondly, the small degree of ion interchange which exists in pure $Co_{1-\delta}Al_2O_4$ at 1100°C may be sufficient to place the cobalt aluminate without addition of magnesium aluminate already in a disturbed resonance state.

Finally some general comments can be made with regard to the concentration of vacancies (δ) in the metal deficient cobalt compounds $Co_{1-\delta}O$, $Co_{1-\delta}Al_2O_4$ and $Co_{2-\delta}$-

SiO_4. For an oxygen partial pressure of 1 atmosphere and a temperature of 1150°C, the δ-values for the above nonstoichiometric compounds are approximately 10^{-2}, 10^{-3} and 10^{-4}, respectively. Although the defect equations for all three compounds can be formulated similarly as equation (5), very little can be said as to why, for example, (δ) is larger in $Co_{1-\delta}Al_2O_4$ than in $Co_{2-\delta}SiO_4$. An answer to this question can be provided only if the various energy terms which compose $\Delta E_5{}^0$ are exactly known. This means that the Madelung, repulsion, polarization, van der Waals and crystal field stabilization energies must be known for the lattices or ions under consideration.

Acknowledgements—The authors wish to thank H. Meurer for his help in designing some of the experimental apparatus. One of the authors (C. G.) wishes to acknowledge the receipt of a NSF postdoctoral fellowship which made this work possible. Financial support of the "Deutsche Forschungs-gemeinschaft" is also appreciated.

REFERENCES

1. SCHMALZRIED H. and WAGNER C., *Z. phys. Chem.* **31**, 198 (1962).
2. SCHMALZRIED H., *Progress in Solid State Chemistry*, Vol. 2. Pergamon Press, Oxford (1965).
3. MORKEL A. and SCHMALZRIED H., *Z. phys. Chem.* **32**, 76 (1962).
4. WALTERS L. C. and GRACE R. E., *J. phys. Chem. Solids* **28**, 239 (1967).
5. SOCKEL H.-G. and SCHMALZRIED H., *Ber. Bun. phys. Chem.* **72**, 745 (1968).
6. GEORGE W. L. and GRACE R. E., *J. Phys. Chem. Solids* **30**, 881 (1969); *J. Phys. Chem. Solids* **30**, 889 (1969).
7. SCHMALZRIED H., *Z. phys. Chem.* **28**, 203 (1961).
8. WAGNER C. and KOCH E., *Z. phys. Chem.* **B32**, 439 (1936).
9. FISHER B. and TANNHAUSER D. S., *J. electrochem. Soc.* **111**, 1194 (1964).
10. ZINTL G., *Z. phys. Chem.* **48**, 340 (1966).
11. MEURER H., Thesis, Clausthal University (1969).
12. BAUMBACH H. H. v. and WAGNER C., *Z. phys. Chem.* **B24**, 59 (1934).
13. MITOFF S. P., *J. chem. Phys.* **35**, 882 (1961).
14. TRETJAKOV J. D. and RAPP R. A., *Nonstoichiometry and Defect Structures in Pure Nickel Oxide and Lithium Ferrite Trans. Met. Soc. AIME*, in print (1969).
15. DÜNWALD H. and WAGNER C., *Z. phys. Chem.* **B22**, 212 (1933).
16. KRÖGER F. A., *The Chemistry of Imperfect Crystals*. North-Holland, Amsterdam (1964).
17. NAVROTSKY A., Personal communication, Clausthal (1968).
18. AUKRUST E. and MUAN A., *J. Am. Cer. Soc.* **46**, 7 (1963).
19. GOTTSCHALCK H., *Diplomarbeit*, Technical University of Clausthal (1968).
20. SCHMALZRIED H., *Z. phys. Chem.* **25**, 178 (1960).
21. BOER J. H. de and VERWEY E. J. W., *Proc. phys. Soc.* **49**, 66 (1937).
22. MOTT N. F., *Proc. phys. Soc.* **62A**, 416 (1949).
23. MILLER R. C., HEIKES R. R. and MAZELSKY R., *J. appl. Phys.* **32**, 2202 (1961).
24. COTTON F. A. and WILKENSON G., *Advanced Inorganic Chemistry*. Interscience, New York (1962).
25. WERNER A., *Z. phys. Chem.* **47**, 267 (1965).
26. VALVERDE N., *Z. phys. Chem.* **61**, 92 (1968).
27. SCHMALZRIED H., *Ber. Bun. phys. Chem.* **67**, 93 (1963).

J. Phys. Chem. Solids Pergamon Press 1970. Vol. 31, pp. 647–654. Printed in Great Britain.

LOW TEMPERATURE GRÜNEISEN PARAMETER OF RbI FROM ELASTICITY DATA*

JOHN J. FONTANELLA and D. E. SCHUELE
Case Western Reserve University, Cleveland, Ohio 44106, U.S.A.

(*Received* 8 *July* 1969)

Abstract—The elastic constants and their pressure derivatives of rubidium iodide were measured at 295° and 195°K by the ultrasonic pulse-echo technique. The results are:

	$\frac{dC_{11}}{dP}$	$\frac{dC_{12}}{dP}$	$\frac{dC_{44}}{dP}$
295°K	13·16	1·66	−0·51
195°K	12·83	1·78	−0·55

The low temperature Grüneisen parameter was calculated and found to be negative in agreement with that predicted by G. K. White on the basis of thermal expansion data. These results can be understood qualitatively via a simple Born model.

INTRODUCTION

THEORETICAL treatments of the thermal properties of insulators are usually based on the Quasi-Harmonic Model[1]. In this approximation that portion of the internal energy which is due to thermal excitations is a function of 3N normal modes of vibration, $\omega_j(\mathbf{k})$, which depend upon volume only. Writing the Helmholtz free energy and applying the thermodynamic relation:

$$P = -\left(\frac{dF}{dV}\right)_T \tag{1}$$

an equation of state is obtained. Indigenous to the equation of state, then, is the variation of the normal modes with volume. The pertinent anharmonic parameter is defined to be:

$$\gamma_j = -\frac{d\ln\omega_j}{d\ln V} \tag{2}$$

and is known as the mode gamma.

If the thermodynamic relation:

$$\left(\frac{dP}{dT}\right)_V = \beta B_T \tag{3}$$

is applied to the equation of state, and the Grüneisen gamma is defined as:

$$\gamma_g = \frac{\sum_{i=1}^{3N} c_i\gamma_i}{\sum_{i=1}^{3N} c_i} \tag{4}$$

one arrives at the Grüneisen relation:

$$\beta B_T = \frac{C_v\gamma_g}{V} \tag{5}$$

where β is the volume coefficient of thermal expansion, B_T is the isothermal bulk modulus, C_v/V is the heat capacity per unit volume, and c_i is the Einstein heat capacity of the ith normal mode. Thus, the Grüneisen gamma can be obtained both from the thermodynamic data via equation (5), and from the microscopic relation, equation (4), once the mode gammas are known.

The motivation for the present research was the negative low temperature value for

---

*Work supported in part by the Atomic Energy Commission.

the Grüneisen parameter determined by White[2] from thermal measurements. Such a consequence has interesting implications on the lattice excitations as will be seen.

THE EXPERIMENT

Sample

All measurements were done on a (110) single crystal supplied by Professor W. B. Daniels of Princeton University. Because of the softness and hygroscopic nature of rubidium iodide, it was difficult to maintain smooth, parallel surfaces. As a result, it became necessary to lap the crystal during the course of the experiment. This was accomplished by cementing the crystal into a stainless steel lapping ring with phenyl salicylate (salol) and smoothing the faces on successive grinding surfaces of 2/0, 3/0, and 4/0 Carborundum Flexbac Polishing paper. It was found that lubricating the paper with a little kerosene helped eliminate scratches. The resulting faces were parallel to within a part in a thousand. The length of the crystal was 0·777 ± 0·0005 cm for the pressure derivatives and 0·653 ± 0·0005 cm for the elastic constant measurements.

In both cases of the experiment the crystal was oriented with X-rays using the back reflection Laue technique. The elastic constants were measured with the crystal within 30′ of the (110) plane. The pressure derivatives, however, were done with the crystal off 3° in the basal plane and orientation corrections were applied to account for this as will be noted later.

Apparatus and procedure

A description of the ultrasonic pulse-echo technique is given in the review article by Daniels and Smith[3]. The zero pressure elastic constants were measured using the buffer-rod technique[4]. The buffer rod was a single crystal of sodium fluoride in the shape of a circular cylinder with diameter of 2 cm and length 8 cm. The measurements were made by determining the time between the first buffer echo, first crystal echo, second crystal echo, and, in the case of C_{44}, a third crystal echo. The delay times were read on a Tektronix 547 Oscilloscope and the readings were reproduced to within two tenths of a nano-second. Salol seals were used at room temperature, and Nonaq stopcock grease was used at dry ice temperature. A mixture of Freon and dry ice was used as the low temperature bath. It was noted that the bath temperature was about five centigrade degrees colder than the −78°C sublimation point of dry ice, and all of the data has been converted by linear interpolation to the dry ice temperature. A Chromel–Alumel thermocouple, calibrated at the mercury freezing point, was used to monitor the bath temperature.

A description of the pressure system and measurement used in this experiment is given in the paper by Wong[10]. Typical data runs are shown in Fig. 1. The maximum pressure allowed was 1600 bars in order to avoid the phase transition from face-centered cubic to simple cubic which occurs in the region 3430–3650 bars[7].

RESULTS

The basic data used in the reduction of experimental results are listed in Table 1. The low temperature lattice constant and x-ray density are calculated from room temperature data obtained from the National Bureau of Standards tables[18] using a numerical integration of a smoothed curve of White's thermal expansion coefficient[2]. The adiabatic bulk modulus is that determined from the measured elastic constants, and the isothermal bulk modulus is calculated from this using:

$$\frac{B_s}{B_T} = 1 + \frac{TV\beta^2 B_s}{C_p}. \qquad (6)$$

The three independent modes for a (110) crystal yield C_{11}', C_{44}, and C'. These are related to C_{11} and C_{12} by the relations:

$$C'_{11} = \frac{C_{11}+C_{12}+2C_{44}}{2} \tag{7a}$$

$$C' = \frac{C_{11}-C_{12}}{2}. \tag{7b}$$

Elastic constants

The measured elastic constants appear to be correct to within 0·5 per cent which places the uncertainty on C_{12} at about 4 per cent. The results are listed in Table 2 along with previous determinations and thermal extrapolations which are needed for later analysis. Of particular interest is the agreement between the 4·2°K values of Lewis *et al.*[14] and our temperature extrapolation to $\theta_0/5$. In general the results are good, agreeing in most cases to within 1 per cent. The larger discrepancies are probably due to crystal orientation since rubidium iodide is a highly anisotropic crystal with anisotropy factor 0·258 at room temperature calculated from:

$$A = \frac{2C_{44}}{C_{11}-C_{12}}. \tag{8}$$

Pressure derivatives

Table 3 is a compilation of the pressure data. The first column comes directly from experiment where t is the transit time. The second column is obtained by taking the pressure derivative of:

$$X_i = \rho v_i^2 = \frac{4L^2}{t_i^2}\rho \tag{9}$$

and making the appropriate thermodynamic association:

$$\frac{\mathrm{d}\ln X_i}{\mathrm{d}P} = \frac{1}{3} - 2\frac{\mathrm{d}\ln t_i}{\mathrm{d}P}. \tag{10}$$

The third column lists the pressure derivatives of the effective elastic constants. The above quantities were obtained directly from the measurements and thus correspond to the case where the crystal was off orientation three degrees in the basal plane. The fourth column, however, contains the values of the pressure derivatives of the elastic constants C_{11}, C_{12}, and C_{44} obtained from the off orientation values by a procedure to be outlined while the other values quoted are calculated from the above.

The secular equation can be written in the following form:

$$X^3 + A_1X^2 + A_2X + A_3 = 0 \tag{11}$$

where the roots are the quantities expressed in equation (9). The coefficients A_1, A_2, and A_3 are functions of the elastic constants and the direction cosines of the propagation direction. Specifically, $A_1 = -(C_{11}+2C_{44})$, while the coefficient A_2 involves products of elastic constants and A_3 contains triple products of elastic constants. Thus, the pressure derivative can be written:

$$\frac{\mathrm{d}X_i}{\mathrm{d}P} = -\frac{X_i^2\frac{\mathrm{d}A_1}{\mathrm{d}P} + X_i\frac{\mathrm{d}A_2}{\mathrm{d}P} + \frac{\mathrm{d}A_3}{\mathrm{d}P}}{3X_i^2 + 2A_1X_i + A_2}. \tag{12}$$

The quantity $\mathrm{d}X_i/\mathrm{d}P$ is identified with the off orientation pressure derivatives where i denotes the three polarizations. The pressure derivatives of the coefficients can be written as linear combinations of the pressure derivatives of the elastic constants. In functional form we now have:

$$\frac{\mathrm{d}X_i}{\mathrm{d}P} = D_i\frac{\mathrm{d}C_{11}}{\mathrm{d}P} + E_i\frac{\mathrm{d}C_{12}}{\mathrm{d}P} + F_i\frac{\mathrm{d}C_{44}}{\mathrm{d}P} \tag{13}$$

where D_i, E_i and F_i are functions of the elastic constants, X_i, and the direction cosines. By matrix inversion the above set of equations can be solved for the pressure derivatives of the elastic constants. These manipulations including the determination of the off axis ρv_i^2 were carried out by a computer program written by our colleague Dr. Robert Hankey. The uncertainty in the pressure derivatives, by conservative estimate, is thought to be no more than 5 per cent.

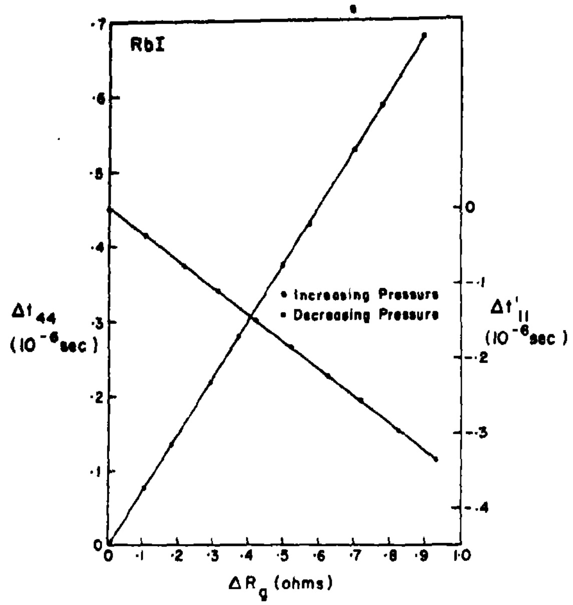

Fig. 1. Typical data runs showing the anomalous behavior of the shear mode t_{44}. Δt_{44} refers to the second echo at 195°K while $\Delta t'_{11}$ refers to the second echo of the longitudinal mode at 295°K.

Table 1. Basic data used in reduction of experimental results. The low temperature lattice constant and densities were calculated using a numerical integration of a smoothed curve of White's thermal expansion data. The bulk moduli are from the experiment and low temperature values are from a linear extrapolation to $\theta_0/5$.

Data	295°K	195°K	22°K	0°K
Molecular weight	212·39	212·39	212·39	212·39
Lattice constant [18] (Å)	7·341	7·313	7·273	7·273
X-ray density [18] ρ expansion coefficient α (g/cm^3)	3·565	3·607	3·666	3·666
Linear thermal [2] (10^{-7} deg^{-1})	392	380	76	0
Heat capacity at [17] c_p constant pressure (cal mole^{-1} atom^{-1} deg^{-1})	6·3	6·15	2·08	0
Adiabatic bulk modulus (10^{11} dy/cm^2)B_s	1·125	1·176	1·264	1·264
Isothermal bulk modulus (10^{11} dy/cm^2)B_T	1·070	1·137	1·263	1·264

Table 2. Elastic constants of rubidium iodide in units $10^{11} dy/cm^2$

Description	C'_{11}	C_{44}	C'	C_{11}	C_{12}	B_s
Author 295°K	1·762	0·2780	1·078	2·562	0·406	1·125
Author 195°K	1·862	0·2832	1·210	2·789	0·369	1·176
Author temperature extrapolation to 22°K	2·035	0·2923	1·438	3·182	0·305	1·264
Lewis *et al.*[14] 4·2°K	—	0·292	—	3·210	—	—
Lewis *et al.*[14] 295°K	1·729	0·2776	1·111	2·562	0·34	1·081
Reinitz[13] 295°K	1·749	0·276	1·067	2·54	0·407	1·118
Bolef and Menes[12] 300°K	1·722	0·287	1·13	2·56	0·31	1·06
Haussühl[11] 295°K	1·755	0·278	1·106	2·583	0·37	1·108

Table 3. Pressure and temperature derivatives of rubidium iodide. The first two columns are in units 10^{-12} cm^2/dy, dC_i/dP is dimensionless, and the temperature derivatives are in units 10^8 dy/cm^2-deg. The tabulated digits are for purposes of completeness only and not all figures should be considered significant

Wave	Temperature	$\frac{d\ln f_i}{dP}$	$\frac{d\ln X_i}{dP}$	$\frac{dX_i}{dP}$		$\frac{dC_i}{dP}$	Author $\frac{dC_i}{dT}$	Haussühl[11] $\frac{dC_i}{dT}$
X'_{11}	295°K	−18·45	40·02	7·140	C'_{11}	6·896	−1·00	−1·123
	195°K	−17·06	37·05	7·006		6·748		
X_{44}	295°K	10·78	−18·44	−0·5128	C_{44}	−0·5135	−0·0524	−0·0573
	195°K	11·21	−19·49	−0·5522		−0·5529		
X'	295°K	−24·54	52·20	5·510	C'	5·754	−1·32	−1·36
	195°K	−20·83	44·59	5·266		5·525		
	295°K				C_{11}	13·164	−2·27	−2·428
	195°K					12·826		
	295°K				C_{12}	1·656	0·37	0·322
	195°K					1·776		
	295°K				B_s	5·492	−0·51	−0·595
	195°K					5·459		

Temperature derivatives

The temperature derivatives listed are obtained from two points widely separated in temperature and exhibit reasonable agreement Haussühl[11]. In fact they show the trend expected in that they are all slightly less negative which is probably due to the low temperature nature of our effective derivative whereas Haussühl quotes 273°K. This points out the slight curvature with temperature that elastic constants exhibit.

Grüneisen parameter

The temperature variation of the Grüneisen parameter is shown in Fig. 2. The values were calculated from the following data: thermal expansion due to White[2], heat capacity by Clusius *et al.*[17], our bulk modulus, and the

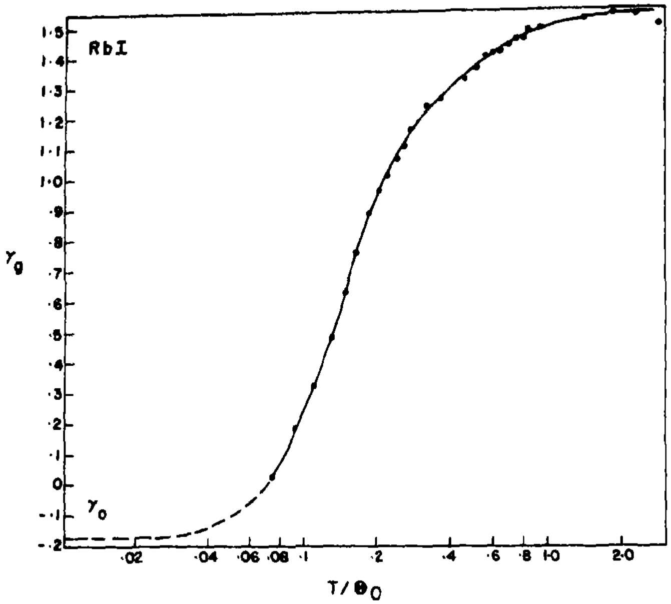

Fig. 2. Grüneisen gamma as a function of temperature.

density as a function of temperature calculated as previously mentioned.

The overall variation exhibited by rubidium iodide is like that of the other alkali halides with the exception of lithium fluoride. The interesting feature is the negative value at low temperatures, which reflects the negative thermal expansion coefficient in this temperature region and the large change, about 1·7, from the limiting high temperature value to the limiting low temperature value.

The zero temperature thermodynamic Grüneisen parameter was obtained in the following way. In the low temperature region the linear expansion coefficient can be expressed as:

$$\alpha = AT^3 + BT^5$$

where A and B are fitting parameters. The capacity is expanded giving:

$$C_v = eT^3 + fT^5 + \ldots \tag{15}$$

with

$$e = \frac{12\pi^4 R}{5\theta_0^3} \tag{16}$$

R is Boltzmann's constant, and θ_0 is the Debye temperature. In this limit of very low temperatures, then, we can write:

$$(\gamma_0)_{\text{Thermo}} = \frac{3AVB_s}{2e}. \tag{17}$$

Analyzing his low temperature data. White arrived at the value: $A = -0{\cdot}25 \times 10^{11}$. Substituting this and our value for the adiabatic bulk modulus into equation (17) yields

$$(\gamma_0)_{\text{Thermo}} = -0{\cdot}178.$$

The low frequency mode gammas can be calculated from the pressure derivatives of the elastic constants and thus the low temperature limiting value of $(\gamma_0)_{\text{Elas}}$ can be obtained from the microscopic expression. This has been done using the computer program of Schuele and Smith[8]. In Table 4 the mode gammas for the principal directions in a cubic crystal are listed. These show a wide variation for the different modes. We note in particular the large negative value for

Table 4. Mode gammas for the three principal crystal directions

Gamma	Mode	295°K	195°K
C'_{11}	(110) Long.	1·93	1·89
C'	(110) Trans.	2·69	2·43
C_{44}	(110) Trans.	−1·15	−1·28
C_{11}	(100) Long.	2·58	2·47
C_{44}	(100) Trans.	−1·15	−1·28
C^l	(111) Long	1·55	1·56
C_t	(111) Trans.	2·25	2·04

the C_{44} mode and its becoming more negative with a lowering of temperature.

At low temperatures the dominant modes are those having small sound velocities. For rubidium iodide with its large anisotropy, the dominant modes are those with C_{44} character. Thus the average Grüneisen parameter will be heavily weighted with these modes which show a negative mode gamma. The values of $(\gamma_0)_{\text{Elas}}$ are listed in Table 5 along with the volume extrapolated value $(\gamma_0(V_0))_{\text{Elas}} = -0{\cdot}195$ (in the spirit of the Quasi-Harmonic approximation). Thus, comparison between the thermal value and the elastic data is excellent.

Table 5. The relevant values of the low temperature Grüneisen parameter. The Debye temperature was calculated from the tables of de Launay[9] *using the temperature extrapolated elastic constants*

White $(\gamma_0(V_0))$ Therm.	Author $(\gamma_0(V_0))$ Elastic	Author $(\gamma_0)_{195}$	Author $(\gamma_0)_{295}$	Author $(\theta_0)_{0°\text{K}}$	Clusius *et al.*[17] (θ_0)
−0·178	−0·195	0·0296	0·193	108°K	100–118°K

Pressure derivatives of the elastic constants at lower temperatures would have been desirable to the volume extrapolation. However, rubidium iodide has properties which makes these measurements quite difficult.

DISCUSSION

Rubidium iodide exhibits a negative thermal expansion coefficient at low temperatures which is thought to persist to absolute zero where it must vanish. This results in a low temperature limiting value of the Grüneisen parameter which is negative and is now also confirmed by these elasticity measurements.

In the alkali halides, the trend to lower values of γ_0 at low temperatures is related to larger ion sizes. This trend can be semi-quantitatively understood by means of a simple Born model. In this model the repulsive range parameter increases as one goes down the columns in the periodic table for either the alkali metal or halogen atom. The effect of this increase in the repulsive range parameter is to make more negative the mode gammas for the C_{44} type modes. These concepts have been discussed by Barron[16] and Blackman [5, 6] and a simplified version has been given by Smith *et al.*[15].

REFERENCES

1. LIEBFRIED G. and LUDWIG W., *Solid State Physics* (Edited by F. Seitz and D. Turnbull), Vol. 12, p. 275. Academic Press, New York (1961).
2. WHITE G. K., *Proc. R. Soc.* **A286**, 204 (1965).
3. DANIELS W. B. and SMITH C. S., *The Physics and Chemistry of High Pressures*, p. 50. Society of Chemical Industry, London (1963).
4. McSKIMIN H. J., *J. acoust. Soc. Am.* **33**, 606 (1961).
5. BLACKMAN M., *Proc. phys. Soc., Lond.* **B70**, 827 (1957).
6. BLACKMAN M., *Phil. Mag.* **3**, 831 (1958).
7. DANIELS W. B. and SKOULTCHI A. I., *J. Phys. Chem. Solids* **27**, 1247 (1966).
8. SCHUELE D. E. and SMITH C. S., *J. Phys. Chem. Solids* **25**, 801 (1964).
9. de LAUNAY J., *J. chem. Phys.* **30**, 91 (1959).
10. WONG C. and SCHUELE D. E., *J. Phys. Chem. Solids* **29**, 1309 (1968).
11. HAUSSÜHL S., *Z. Phys.* **159**, 223 (1960).

12. FOLEF D. I. and MENES M., *J. appl. Phys.* **31**, 1010 (1960).
13. REINITZ K., *Phys. Rev.* 123, 1615 (1961).
14. LEWIS J. T., LEHOCZKY A. and BRISCOE C. V., *Phys. Rev.* **161**, 877 (1957).
15. SMITH C. S. SCHUELE D. E. and DANIELS W. B. *Proc. 1st int. Conf Physics of Solids at High Pressure* (Edited by C. Tomizuka), p. 496. Academic Press, New York (1965).
16. BARRON T. H. K., *Phil Mag.* **46**, 720 (1955); *Ann. Phys. N.Y.* **1**, 77 (1957).
17. CLUSIUS K., GOLDMANN J. and PERLICK P., *Z. Naturf.* **4a**, 424 (1949).
18. Circ. No. 539. *N.B.S.* 4, 43 (1955).

J. Phys. Chem. Solids Pergamon Press 1970. Vol. 31, pp. 655–667. Printed in Great Britain.

A MÖSSBAUER-EFFECT STUDY OF PARAMAGNETIC RELAXATION OF Er IMPURITIES IN Zr

L. L. HIRST†
Physik-Department, Technische Hochschule München, München, Germany

(*Received* 7 *July* 1969)

Abstract—Mössbauer emission spectra of dilute Er impurities in Zr, in the paramagnetic state with zero external field, have been measured at various temperatures from 4·2°K to 35°K. At the lowest temperatures, due to the slow relaxation of the electronic moment, a splitting into five lines is seen, which transforms into a single-line pattern by about 35°K as the relaxation rates increase. To quantitatively interpret these spectra it is necessary to treat the coupled system of paramagnetic moment plus nuclear spin as the basic resonant system, where the off-diagonal elements of the hyperfine coupling must be included. Such a theory has been worked out and yields a good fit to the data over the entire temperature range. The paramagnetic relaxation information determined from such a fit is the same as could in principle be obtained from paramagnetic resonance, but the Mössbauer-effect measurements are more sensitive and are feasible at much higher temperatures. At low temperatures the relaxation is dominated by an exchange coupling, J_{s-f}, to the conduction-electron spins. The product $|J_{s-f}N_E|$, where N_E is the density of states, is determined to be 0·034. At higher temperatures ($\geqslant$ 20°K) evidence is seen for relaxation processes proceeding via higher crystal-field levels.

1. INTRODUCTION

A PRELIMINARY report has recently been given[1] of the observation of Mössbauer hyperfine splitting in Er^{166} impurities in Zr metal, in the paramagnetic state without external field. This splitting occurs because of the slow relaxation of the electronic moment at liquid helium temperatures, and disappears at temperatures higher than about 35°K as the relaxation rates increase. The purpose of the present paper is to present the higher-temperature data in more detail together with the theoretical interpretation and fits for the relaxation phenomena.

Paramagnetic hyperfine splitting by a localized moment is a very simple effect in principle. At temperatures low enough for the relaxation rates to be small, the spin of the electronic moment and the nuclear spin in the ground or excited state, coupled by the hyperfine interaction, constitute an isolated quantum-mechanical system having certain energy levels, whose spacings correspond to the various lines of the recoilless gamma resonance spectrum. At higher temperatures the relaxation forces of the host act on the electronic-nuclear system to produce transitions among its levels, yielding characteristic changes in the form of the lines and eventually transition to a one-line spectrum. A detailed analysis of the low-temperature splitting pattern observed in Er–Zr has been carried out in a separate paper[2], in which the electronic ground state and the hyperfine interaction tensor between the electronic ground doublet and the nuclear spin were unambiguously deduced. In the present paper we can therefore take the point of view that the structure and internal properties of the system of electronic plus nuclear spin are known, and can regard this system as a probe for investigating the fluctuating fields present in the host which cause the relaxation effects. Such an investigation is of particularly great interest for the present case involving a metallic host, since the dominant relaxation interaction at low temperatures should be the exchange coupling between the local electronic moment and the conduction-electron spins. This interaction is of fundamental interest to the study of magnetism in metals, yet is simple enough in form to be amenable to quantitative analysis. The Mössbauer technique offers a particularly powerful method for its study.

---

†*Present address*: Institut für Theoretische Physik an der Universitat, Frankfurt, W. Germany.

Although relaxation phenomena in the Mössbauer effect have been studied in insulators and in concentrated metallic systems for some time, no previously available theory is capable of treating the case of Er–Zr except in certain limiting cases. The largest part of the present paper will be devoted to working out such a theory. The principal features of the problem are that it is necessary to treat the electronic moment and nuclear spin as constituting a single resonant system, and that the nuclear-electronic hyperfine interaction is not diagonal. We will show that it is possible to give a solution which is exact to second order in time-dependent perturbation theory, valid over the entire range from fast to slow relaxation, and capable of practical evaluation. Once the problem has been correctly set up, the formal solution by means of density-matrix methods originally developed for the theory of magnetic resonance is straightforward. In the presentation, an effort has been made to emphasize the physical basis of the theory rather than the formal methods. A Section discussing the relation of the present theory to some previous ones is also included.

2. EXPERIMENTAL RESULTS

In order to obtain a workable recoil-free intensity in a dilute alloy, the Mössbauer spectra were measured using Er^{166}–Zr as the source, together with a single-line absorber of ErAl_2 held at 77°K. The sources were prepared by neutron irradiation of dilute (0·2 at. %) alloys of Ho–Zr. Source preparation and other experimental details are discussed more fully in Ref. [2]. The source could be held at temperatures above 4·2°K by partially evacuating the source chamber to reduce thermal contact with the surrounding He bath. The source temperature was measured with a Au–Co vs. Cu thermocouple, which also automatically controlled a small ohmic heating coil to maintain the temperature at a pre-set value. The experimental spectra at various temperatures are shown in Fig. 1, together with the theoretical fits which will be obtained in what follows.

The following features of the experimental results should be noted: (1) Although the quadrupole interaction is very small [2], the lines at low temperature are not equally spaced. This is a characteristic feature of paramagnetic hyperfine splitting when the magnetic hyperfine interaction is not diagonal [3, 4]. (2) With increasing temperature, some of the lines shift by an appreciable

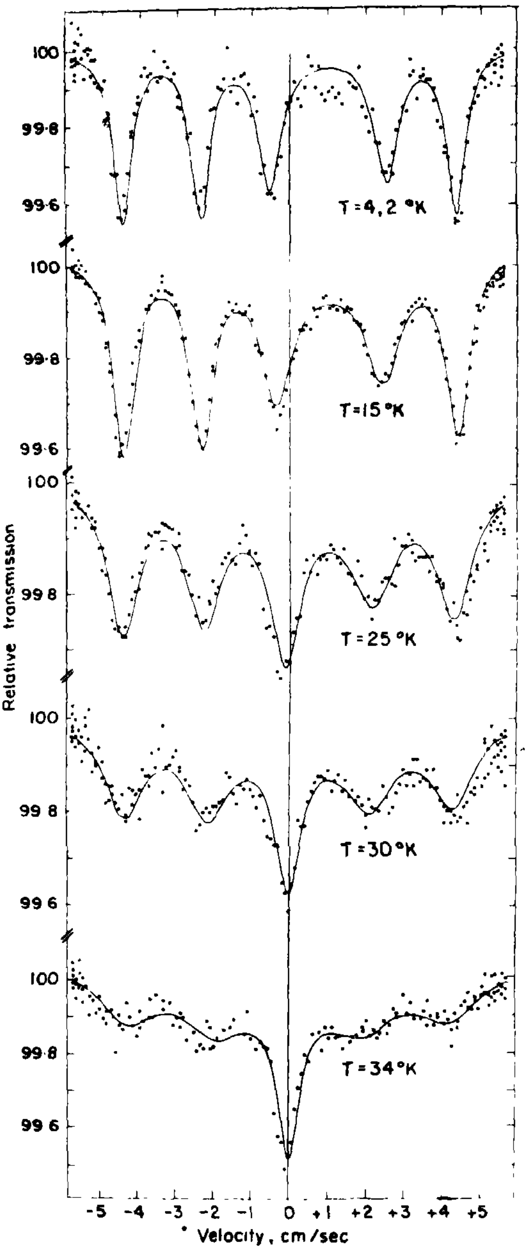

Fig. 1. Mössbauer emission spectra for Er^{166} as a dilute paramagnetic impurity in Zr, together with the theoretical fits.

amount; nevertheless they do not shift continuously toward the center in the same way as would be expected for a magnetic phase transition in a concentrated system in the fast-relaxation limit. (3) In most previous models of paramagnetic relaxation behaviour, and for inhomogeneity broadening as well, one expects the outer lines to show the greatest broadening and reduction in depth. Here, however, the 2nd and 4th lines show slightly more broadening than the 1st and 5th lines at intermediate temperatures such as 25°K; and at the lowest temperatures it is the inner lines (3rd and 4th) which show broadening. These features follow from the correct theory.

Even at the lowest experimental temperature of 4·2°K the spectrum shows some relaxation broadening. The theoretical extrapolation to zero relaxation gives a width (half width at half maximum) of 2·7 mm/sec for all five lines, which limit has already been practically reached by the leftmost two lines at 4·2°K. This residual width is three times the natural width. On the basis of additional measurements with a single-line $HoAl_2$ source it is believed that most or all of the extra width originates in the one-line absorber, but it was impossible to determine the absorber width accurately since the width of the $HoAl_2$ source in turn was uncertain.

3. THE RELAXATION THEORY

We are interested in the Mössbauer effect at the nucleus of a paramagnetic ion in a magnetically dilute substance, in which the paramagnetic moment may be viewed as being only weakly perturbed by its surroundings. Although Mössbauer relaxation phenomena have been seen in magnetically concentrated materials subject to magnetic ordering[5], the dilute approximation is a good one for most cases in which relaxation effects on a magnetic hyperfine splitting are observed.

Since the hyperfine splitting is dominated by the interaction of a nucleus with the electronic moment of its own ion, it is normally not consistent to regard this same interaction as being a weak perturbation on the nucleus when discussing the effects of relaxation on a resolved hyperfine splitting; instead, it is necessary to treat the nucleus plus paramagnetic moment as a strongly-interacting, coupled system, which is then subject to weak perturbing forces from the lattice or from other spins. In practice, for a Mössbauer nucleus in a paramagnetic ion, the relaxation forces coupled directly to the nuclear spin will be negligible compared to those coupled to the electronic moment. Nevertheless, in the coupled-system approach, it is necessary to consider the relaxation forces as operating on the system as a whole. Similarly, the gamma-transition process must be considered to operate on the system as a whole even though it is directly coupled to the nucleus only. Furthermore, in the coupled-system theory we cannot use a simple transition-rate description even in terms of eigenstates of the coupled system. For example, suppose we think of a relaxation force as generating a transition between definite states of the coupled system with the nucleus in the excited state. We are still left with the question, what is simultaneously happening in the ground-state system which is at the other end of the gamma-radiation process? Clearly we cannot think of the ground-state relaxation transitions as something completely independent, since the same electronic moment is involved, yet the description of the relaxation as a transition between definite excited-system energy eigenstates does not constitute a well-defined description in the ground-state system. Difficulties of this sort compel us to abandon the simple transition-rate picture and turn to the more powerful density-matrix formalism. This yields a solution which we will be able to interpret in terms of relaxation transitions among certain equivalent elementary oscillators, instead of among eigenstates of the system.

We begin our formal development by considering a nucleus which is recoillessly absorbing gamma radiation. The energy absorption spectrum is described by the imaginary part of an electric or magnetic multipole susceptibility of the nucleus, where the type of multipole corresponds to the particular gamma transition in question. This susceptibility is given by the Fourier transform of $\langle\langle M(t)M(0)\rangle\rangle$, where M is an operator for the appropriate dynamic (very high frequency) multipole moment of the nucleus. Actually, the correct expression for the sample as a whole is $\Sigma_p \int d\Omega_r P(\mathbf{r}, p)\ \langle\langle M^{\mathbf{r},p}(t)\, M^{\mathbf{r},p}(0)\rangle\rangle$, where $\mathbf{r}$ is the direction of the gamma momentum relative to the local crystal axes, p enumerates two polarization directions normal to $\mathbf{r}$, and $P(\mathbf{r}, p)$ is a normalized distribution corresponding to the experimental arrangement. For simplicity we will drop the polarization indices and restore them at the end of the calculation. The multipole operator M will depend on the coordinates of the individual nucleons, but its detailed form need not be considered; all that is needed is its angular-momentum transformation rules, which are specified by the multipole type. The Heisenberg-representation operator is $M(t) = \exp(iHt)\, M \exp(-iHt)$, where the total Hamiltonian H introduces a dependence of $M(t)$ upon the extranuclear environment. Since M functions as a transition operator, the matrix elements which contribute to $\langle\langle M(t)\, M(0)\rangle\rangle$ are $M(t)_{a,b}$ where a denotes a state including (among other things) the nucleus in the internal excited state, and b includes the nucleus in the ground state, or vice versa. The double brackets denote an ensemble average, and our problem is to solve for the time dependence of the ensemble average of these off-diagonal M elements. If one wishes to consider the spectrum of recoilless emission, the same formal expression is applicable, since according to the fluctuation-dissipation theorem[6] one may regard spontaneous emission as forced radiation driven by the zero-point fluctuations of the vacuum.

We separate the total system into a 'resonant system' and a remaining part, referred to as the lattice or the thermal bath, which may be assumed to stay in good thermal equilibrium. As explained above, in the dilute paramagnetic problems we wish to consider the resonant system will consist of the nucleus and the electronic moment of a single impurity (which may be subject to time-independent Zeeman fields or crystalline electric fields). The interaction between the bath and the resonant system in the Schrödinger representation is taken to be $H_I = \Sigma_q K^q F^q$, where the F^q are operators involving the bath variables and the K^q involve the resonant-system variables. Since we assume the relaxation forces to be coupled to the electronic moment, the K^q will actually involve the electronic variables (usually expressed by an effective spin) only.

We now proceed to eliminate the bath variables by thermal averaging to obtain an equation of motion for $M(t)$, which is regarded as a matrix having as dimensionality the number of degrees of freedom of the resonant system. This is the familiar density-matrix formalism in a representation where the operator $M(t)$ is time-dependent and the density matrix of the resonant system, σ_0, is time independent. We give the derivation only in brief outline, since the basic methods are well known[7]. The total Hamiltonian is $H = H_0 + H_B + H_I$, where H_0 is the Hamiltonian of the resonant system (including the nuclear internal energy), H_B is the Hamiltonian of the bath, and the interaction H_I has been given above. H_0 and H_B commute, and the products of their eigenstates form a basis for the total physical system. We define

$$M^*(t) = \exp[-i(H_0 + H_B)t]\, M(t) \times \exp[i(H_0 + H_B)t]. \qquad (1)$$

The basic idea is that $M^*(t)$ is only weakly time-dependent since motion induced by H_0 and H_B has been removed. The motion of $M^*(t)$ is given by

$$i(\mathrm{d}/\mathrm{d}t)M^*(t) = [M^*(t), H_I^*(t)] \qquad (2)$$

where

$$H_I^*(t) = \exp[-i(H_0 + H_B)t]\, H_I \times \exp[i(H_0 + H_B)t].$$

(This definition is different from that appropriate in the representation where the density matrix contains the time dependence.) By integrating equation (2) in an iterative approximation we obtain

$$(\mathrm{d}/\mathrm{d}t)M^*(t) = -\int_0^\infty \mathrm{d}\tau[H_I^*(t), [H_I^*(t-\tau), \times M^*(t)]]. \qquad (3)$$

In this equation we introduce matrix elements with respect to eigenstates of H_0 and take an ensemble average over the bath states to obtain

$$\begin{aligned}(\mathrm{d}/\mathrm{d}t)M^*_{ad}(t) = \sum_{q,b,c} (\tfrac{1}{2}) \{ & -K^{-q}_{ab} K^q_{bc} M^*_{cd}(t) \\ & \times J_q(\omega_{cb}, T) \exp[-i(\omega_{ab}+\omega_{bc})t] \\ & + K^{-q}_{ab} M^*_{bc}(t) K^q_{cd} J_q(\omega_{dc}, T) \\ & \times \exp[-i(\omega_{ab}+\omega_{cd})t] \\ & + K^q_{ab} M^*_{bc}(t) K^{-q}_{cd} J_q(\omega_{ab}, T) \\ & \times \exp[-i(\omega_{ab}+\omega_{cd})t] \\ & - M^*_{ab}(t) K^q_{bc} K^{-q}_{cd} J_q(\omega_{bc}, T) \\ & \times \exp[-i(\omega_{bc}+ w_{cd})t]\}. \qquad (4)\end{aligned}$$

Here the spectral density is defined as the Fourier transform of the autocorrelation function of the bath variable F^q in the thermal-equilibrium bath at temperature T:

$$J_q(\omega, T) = \int_{-\infty}^{\infty} \mathrm{d}\tau \exp(-i\omega\tau) \langle\langle F^{-q}(0) F^q(\tau)\rangle\rangle \qquad (5)$$

where $F^q(\tau) = \exp(iH_B\tau)\, F^q \exp(-iH_B\tau)$. The spectral density is of fundamental importance since it summarizes the totality of information about the relaxation forces in the host which can be obtained from measurement of any kind of paramagnetic relaxation phenomena in the resonant system. $J_q(\omega, T)$ represents the probability that the bath give a quantum $\hbar\omega$ into the resonant system via the coupling K^q. It satisfies the important identity $J_q(-\omega, T) = \exp(\hbar\omega/kT)\; J_q(\omega, T)$ which describes the tendency of the bath to return the resonant system to thermal equilibrium.

In addition to relaxation effects, we must also include a decay term to describe the effect of the gamma-resonance process itself on the motion[8]. In principle this term should describe only the excited-state natural lifetime of the nucleus itself, but in practice it will usually be permissible also to include inhomogeneity broadening and the linewidths of both source and absorber, in place of the rigorously correct folding of the spectrum with a spectrometer resolution function. Adding this term to equation (4) and rewriting in terms of $M(t)$ we obtain as our final equation of motion

$$(\mathrm{d}/\mathrm{d}t)M_{ad}(t) = (i\omega_{ad} - \Gamma)\, M_{ad}(t) + \text{(four terms)}$$

where the remaining four terms are the right side of equation (4) with M^* replaced by M and the explicit phase factors deleted.

We can simplify the solution of this differential equation by regarding each combination of bra and ket indices as forming a single state-pair index[7]: for example, $M_{ab}(t) \rightarrow M_i(t)$. With this convention we can regard $M(t)$ as a column vector and equation (6) becomes a matrix equation

$$(\mathrm{d}/\mathrm{d}t)\mathbf{M}(t) = (i\omega' + \mathbf{R})\mathbf{M}(t) \qquad (7)$$

where the definition of the relaxation matrix $\mathbf{R}$ is obvious from equations (4) and (6) and where $(\omega')_{i,j} = [(E_a - E_b)/\hbar + i\Gamma]\delta_{i,j}$, where $\delta_{i,j}$ is the Kronecker delta, if i corresponds to the state pair a, b. The solution of equation (7) is obtained by matrix exponentiation: $\mathbf{M}(t) = \exp[(i\omega' + \mathbf{R})t]\mathbf{M}(0)$.

We can now compute the correlation function $G(t) = \langle\langle M(t)M(0)\rangle\rangle$. Since the averaging of the bath variables has already been performed, the ensemble average reduces to a trace with σ_0, the density matrix of the resonant system. σ_0 describes the initial preparation of the system and is a thermal-equilibrium distribution if we are considering an absorber or the distribution immediately after a beta decay and quasi-instantaneous electronic re-arrangement if we are considering a source.† In both cases it is diagonal: $(\sigma_0)_{bb} = W_b$, where W_b will be non-zero only for states with the nucleus in the ground or excited state for the case of absorber or source respectively. Thus we have

---

†These statements may not hold if the system is prepared unconventionally, e.g. using coincidence techniques or with application of r_f power.

$$G(t) = \sum_{a,b} W_b\, M_{ba}(t)\, M_{ab}(0) = (\mathbf{M}(t))^{\dagger}\, \mathbf{W}\, \mathbf{M}(0)$$

where in the last form we have written W_b as a diagonal matrix in an obvious way. The absorption or emission spectrum is proportional to the real part of $\int_0^\infty \mathrm{d}t \exp(i\omega t)\, G(t)$, which gives

$$I(\omega) = -Re\{(\mathbf{M}(0))^{+}(i\omega\mathbf{E} - i\omega' + \mathbf{R})^{-1} \times \mathbf{W}\,\mathbf{M}(0)\} \qquad (8)$$

where **E** is the unit diagonal matrix. We must now reconsider polarization and angular-distribution effects. Our equation of motion solution is the same no matter which particular component of the radiation operator M we are discussing, so all that is necessary is to re-attach the polarization indices $\mathbf{r}, p$ to the $M_i(0)$ operators. If only one value of **r** contributes, equation (8) will furnish the answer immediately. When there is **r**-averaging, however, it is better to handle it in formal analogy to the density matrix by defining

$$D_{j,i} = \sum_{p} \int \mathrm{d}\Omega_{\mathbf{r}}\, P(\mathbf{r}, p)\, \mathrm{M}_j^{\mathbf{r},p}(0)\, (M_i^{\mathbf{r},p}(0))^{*}. \qquad (9)$$

Then we have

$$I(\omega) = -Re\, Tr\{\mathbf{D}\,(i\omega\mathbf{E} - i\omega' + \mathbf{R})^{-1}\, \mathbf{W}\}. \qquad (10)$$

Equation (8) or (10) represents our final result for the frequency spectrum, and may be straightforwardly evaluated in cases of interest. We may give a heuristic and graphic interpretation of this formal solution as follows. In Fig. 2 we schematically indicate a set of coupled-system energy levels (actually those appropriate to the Er–Zr problem). The possible gamma transitions in the coupled system, which we will refer to as elementary oscillators, are indicated by downward lines; each elementary oscillator corresponds to a unique pair of states, described by a state-pair index, i, and corresponding to a row or column in our matrix notation. The oscillator i has radiation amplitude $M_i^{\mathbf{r},p}(0)$ in direction **r** with polarization p. In general, the frequencies, intensities, and radiation patterns of the various oscillators will be different. The elements of the relaxation matrix must be thought of as corresponding not to transition rates between eigenstates, but rather to switching rates between the elementary oscillators. Two such $R_{i,j}$ elements are indicated schematically by the wavy lines in Fig. 2. There are also diagonal **R** elements related to the off-diagonal ones. The effect of relaxation is to cause groups of connected oscillators to broaden and shift when the switching rates are moderately slow, and to merge into a single narrow line at a weighted-mean frequency when the switching rate is fast. The switching corresponds to a switching of amplitude, not of intensity, and it has a phase 'memory' so that one has narrowing, instead of uncertainty-principle broadening, in the fast-switching limit.

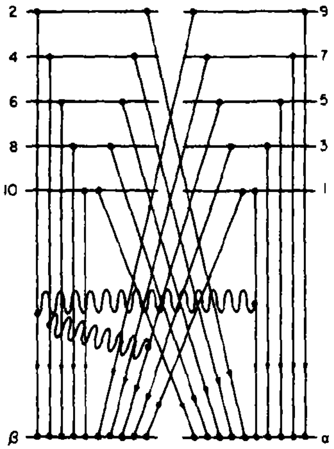

Fig. 2. Schematic representation of the eigenstates of the coupled nuclear-paramagnetic system in Er–Zr. The ten upper levels involve the 80·6 keV excited nuclear state. Downward lines with arrows denote the gamma transitions (elementary oscillators) between pairs of individual levels. The wavy lines symbolize two of the possible relaxation coupling terms.

4. EXAMPLES OF RELAXATION BEHAVIOR

In the present section we will give some details of the application of the results of Section 3, particularly for the case of Er–Zr but with reference to some other cases. The discussion is intended to provide a concrete example of the formalism and to bring out some of the reasons for the sort of relaxation behavior which is observed.

The formal solution is of wide validity. For example, it can be used for a formal treatment of the entire $J = 15/2$ manifold of states in Er^{166}, as is necessary for analysis of relaxation processes involving the ground doublet but proceeding via higher crystal-field levels[9]. For the present, however, we wish to avoid complexity by restricting our treatment to the ground doublet only. To justify this we invoke the following theorem, which is intuitively reasonable and will be proved elsewhere[9]. Provided that the remaining crystal-field levels are at sufficiently high energy, their effect on the hyperfine spectrum is equivalent to that of an extra paramagnetic relaxation, i.e. of an extra spectral density acting on the ground doublet. It can also be shown[9] that under these same conditions the initial preparation of the source is approximately equivalent to an equal population of all coupled-system states formed from the ground doublet and the excited nucleus.

To further simplify, we will neglect the small quadrupole interaction in Er–Zr and will also use $(A_\perp/A_z) \equiv \epsilon$ as the basis of a power-series expansion to order ϵ^2, where $\mathbf{A}$ is the magnetic hyperfine tensor coupling the excited-state nuclear spin to the effective spin $S = \frac{1}{2}$ of the electronic ground doublet. (The actual value[2] of ϵ is $\pm 0{\cdot}21$.) These approximations are for purposes of discussion only and the actual theoretical spectra have been obtained by direct computer evaluation of equation (10) without approximations. Using the small-ϵ approximation, the coupled-system energy eigenvalues, and the eigenstates in terms of the basis states $|I_z, S_Z\rangle$, are easily found as listed in Table 1 and schematically represented in Fig. 2. The states can be divided into those consisting predominantly of $S_z = -\frac{1}{2}$, which are on the left in Fig. 2, and those predominantly of $S_z = +\frac{1}{2}$, on the right. The elementary oscillator amplitudes $M_i^{r,\sigma}(0)$ consist of a sum of products of an electronic overlap with a nuclear transition matrix element. The oscillators connecting states of parallel predominant S_z, indicated by vertical lines in Fig. 2, all have electronic overlap parts approximately unity, while those connecting oscillators of opposite predominant S_z, indicated by diagonal lines, have overlap parts of order ϵ and hence are relatively weak. In the important special case when all directions $\mathbf{r}$ are equally sampled, as in our experiments, the evaluation of the directional averaging in equation (9) is made simple by the cancellation of interference terms between amplitudes corresponding to different types of nuclear transition, that is, between amplitudes generated by different spherical-tensor components of the nuclear-transition operator which connects the excited-state spin $\mathbf{I}_a$ with the ground-state spin $\mathbf{I}_g$. Using these considerations and Table 1, the weighting matrix D of equation (9) can easily be found.

The physical origin of the relaxation forces will be discussed in Section 4. For the present, we assume only that they are intrinsically isotropic in terms of their coupling to the total electronic angular momentum $\mathbf{J}$, and that their frequency spectrum is 'white' over frequencies of the order of the hyperfine splitting. This yields an isotropic spectral density $J(\omega, T) \approx J(0, T)$ but an anisotropic coupling tensor $\mathbf{K}$ when projected onto the electronic ground doublet: $(K^z, K^\pm) = (g_z S^z, g_\perp S^\pm/\sqrt{2})$, where the electronic $\mathbf{g}$ tensor satisfies $g_\perp/g_z = A_\perp/A_z = \epsilon$. Calculating the relaxation-matrix elements from equation (4), we see that the lowest-order off-diagonal K^z contributions are of order ϵ while the lowest-order $K^\pm$ contributions are of order ϵ^2; however, the former connect strong elementary oscillators to weak ones while the latter connect pairs of strong oscillators. This means that

Table 1. *Approximate eigenstates and energies of the coupled nuclear-paramagnetic system in* Er–**Zr**. *Basis states are* $|\mathbf{I}_Z, \mathbf{S}_Z\rangle$

Excited states ($E_{\text{nuc}} \approx 80{\cdot}6$ keV)	Energy
$\|1\rangle = \|2, +\rangle$	$E_{\text{nuc}} + A_z$
$\|2\rangle = (1 - 2\epsilon^2/9)\,\|2, -\rangle - (2\epsilon/3)\,\|1, +\rangle$	$E_{\text{nuc}} + A_z(-1 - 2\epsilon^2/3)$
$\|3\rangle = (1 - 2\epsilon^2/9)\,\|1, +\rangle + (2\epsilon/3)\,\|2, -\rangle$	$E_{\text{nuc}} + A_z(\frac{1}{2} + 2\epsilon^2/3)$
$\|4\rangle = (1 - 3\epsilon^2)\,\|1, -\rangle - \sqrt{6}\,\epsilon\,\|0, +\rangle$	$E_{\text{nuc}} + A_z(-\frac{1}{2} - 3\epsilon^2)$
$\|5\rangle = (1 - 3\epsilon^2)\,\|0, +\rangle + \sqrt{6}\,\epsilon\,\|1, -\rangle$	$E_{\text{nuc}} + A_z(3\epsilon^2)$
$\|6\rangle = (1 - 3\epsilon^2)\,\|0, -\rangle + \sqrt{6}\,\epsilon\,\|-1, +\rangle$	$E_{\text{nuc}} + A_z(3\epsilon^2)$
$\|7\rangle = (1 - 3\epsilon^2)\,\|-1, +\rangle - \sqrt{6}\,\epsilon\,\|0, -\rangle$	$E_{\text{nuc}} + A_z(-\frac{1}{2} - 3\epsilon^2)$
$\|8\rangle = (1 - 2\epsilon^2/9)\,\|-1, -\rangle\ (2\epsilon/3)\,\|-2, +\rangle$	$E_{\text{nuc}} + A_z(\frac{1}{2} + 2\epsilon^2/3)$
$\|9\rangle = (1 - 2\epsilon^2/9)\,\|-2, +\rangle - (2\epsilon/3)\,\|-1, -\rangle$	$E_{\text{nuc}} + A_z(-1 - 2\epsilon^2/3)$
$\|10\rangle = \|-2, -\rangle$	$E_{\text{nuc}} + A_z$

Ground states	Energy
$\|\alpha\rangle = \|+\rangle$	0
$\|\beta\rangle = \|-\rangle$	0

the K^z-induced transitions will be more important at low temperatures where the spectral density is small, whereas the $K^\pm$-induced transitions between the strong lines will be dominant at higher temperatures where the larger spectral density can compensate the ϵ^2 factor.

Specifically, the most important $K^\pm$ contributions are

$$R_{1\alpha,2\beta} = R_{2\beta,1\alpha} = R_{9\alpha,10\beta} = R_{10\beta,9\alpha} = g_\perp^2/2 = \epsilon^2 g_z^2/2 \quad (11)$$

$$R_{2\alpha,4\beta} = R_{4\beta,2\alpha} = R_{7\alpha,8\beta} = R_{8\beta,7\alpha} = g_\perp^2/2 = \epsilon^2 g_z^2/2 \quad (12)$$

plus some diagonal R elements. The elements of equation (11) plus corresponding diagonal elements, taken alone, give two identical submatrices of $(i\omega\mathbf{E} - i\omega' + \mathbf{R})$ which describe the broadening of the two outer lines of the low-temperature gamma spectrum and their merging into a central line at the zero-velocity position. The elements of equation (12) give a similar but separate broadening and merging of the 2nd and 4th lines. The behavior in each two-oscillator sub-problem is similar to that shown by the well-known model of Anderson[10] for fine-structure collapse in NMR. Since the $R_{i,j}$ elements are equal in the two sub-problems but the frequency difference between the 2nd and 4th lines is smaller than that between the 1st and 5th lines, one expects the broadening and merging of the inner pair to set in before that of the outer pair.

The most important K^z contributions are

$$R_{4\alpha,5\alpha} = -R_{4\beta,5\beta} = R_{6\beta,7\beta} = -R_{6\alpha,7\alpha} = -g_z^2\sqrt{\tfrac{3}{2}}\,\epsilon \quad (13)$$

plus symmetric elements $R_{5\alpha,4\alpha} = R_{4\alpha,5\alpha}$, etc., and diagonal elements. These contributions, taken alone, describe a tendency of the 3rd and 4th lines from the left in the low-temperature spectrum to broaden and shift toward one another. However, in this case there is an important difference: due to the unequal strengths of the coupled elementary oscillators, expressed by the asymmetric weighting factors $M_i^{rp}(0)$, the 3rd and 4th lines do not tend to merge into a collapsed line halfway between them in the fast-relaxation limit of the sub-problem. Rather, this limit yields two narrow lines, one somewhat to the right of the original position of the 3rd line (exactly at the zero-velocity position, in fact) and one somewhat to the left of the original 4th-line position.

On the basis of the foregoing simplified discussion, we thus expect the following relaxation behavior as a function of increasing temperature: at a fairly low temperature, due to the K^z coupling, the 3rd and 4th lines tend to first broaden and then narrow again, having taken up new positions somewhat nearer to one another. (Actually there is also a similar but smaller effect involving the 2nd and 5th lines which we have ignored.) Then, at higher temperatures, due to the $K^\pm$ coupling, first the 2nd and 4th, and then the 1st and 5th lines tend to broaden and collapse into a central narrow line. Computer evaluation of equation (10) shows these conclusions to be correct except that, due to the finite value of ϵ, the second phase begins before the first can be completed. It should be clear that a qualitative discussion of this sort can be useful but is not a satisfactory substitute for a full computation. This is especially true since the matrix inversion operation in equation (10) is highly non-linear, with the consequence that the effects of various $R_{i,j}$ elements are not additive.

The actual computations for the case of Er-Zr were carried out by means of a computer program into which the hyperfine coupling constants determined in Ref.[2] were fed to yield the necessary coupled-system eigenstates and matrix elements. The only theoretical unknowns are the phenomenological width in the absence of relaxation, which is fixed by the 4·2°K data as mentioned in Section 2, and a spectral density specifying the strength of the relaxation forces at each temperature. The most time-consuming operation is the matrix inversion in equation (10), but this is simplified by the fact that many off-diagonal elements of $\mathbf{R}$ vanish, yielding submatrices which can be inverted separately. A spectrum with 200 velocity points could be computed with about 5 sec computing time per set of input parameters. The best-fit theoretical curves obtained at each temperature are shown with the experimental points in Fig. 1. The corresponding values of the spectral density will be given, and their significance discussed, in Section 6.

We have mentioned that the relaxation matrix $\mathbf{R}$ usually has many vanishing off-diagonal elements, so that the elementary oscillators of Fig. 2 break up into groups having no connection with one another, each group corresponding to a submatrix of $\mathbf{R}$. This constitutes a computational convenience, but it also corresponds to an important feature of our relaxation model. In the fast-relaxation limit each connected group of oscillators will yield a single narrow line at the intensity-weighted mean frequency of the group. It can happen that the weighted mean frequencies of the various groups differ from the zero-velocity position, so that in a certain fast-relaxation limit one sees a resolved splitting into 'ghost' lines which do not correspond to real hyperfine energy levels. Of course, at sufficiently high temperatures more relaxation channels must open up, corresponding to a breakdown in the approximate submatrix structure appropriate to low temperatures and resulting in collapse into a single line. According to the above discussion, there is a tendency for this 'ghost' line phenomenon to occur in Er-Zr at moderately low temperatures (≈ 15°K) where the K^z relaxation coupling is dominant, but it is not very striking since the ghost-line positions lay near those of the real energy levels, and since the K^z coupling does not remain dominant to a sufficiently high temperature. In Fig. 3 we show theoretical relaxation spectra computed for a simple model which has been contrived to illustrate the phenomenon more clearly. The basic requirement for the ghost-line effect to be pronounced is that the dominant relaxation coupling be of very high symmetry. Since this is usually not the case in practice, it will be difficult to find experimentally such a clear example of the phenomenon as is shown in Fig. 3. Nevertheless it should be kept in mind that the relaxation behavior for paramagnetic ions with non-diagonal hyperfine interaction will often exhibit some tendency in this direction.

5. COMPARISON TO OTHER RELAXATION THEORIES

There exists a considerable body of theoretical literature concerning relaxation phenomena in the Mössbauer effect. Concerning the more general formal aspects of the subject we especially recommend consulting Refs.[8] and [11], where approaches similar to the present one have been used. The desirability of treating the electronic moment as part of the quantum-mechanical resonant system has been widely understood, and several formalisms capable of doing so have been published[12, 13]. These results, however, were not carried far enough to yield explicit solutions or fits to experimental data. In the present section we are interested in comparison with some previous theories in which actual computations and fits have been made, with special emphasis on the domains of validity of the respective theories.

The conceptually simplest relaxation problem arises when it is possible to approximate the influence of the electronic moment on the nucleus by an effective classical field, so that the nucleus alone may be taken as the quantum-mechanical resonant system. A good example occurs when the magnetic ion containing the Mössbauer nucleus is part of a magnetically concentrated substance below its ordering temperature[14, 15, 16]. In this case the time-average hyperfine field will constitute a large static effective field and the fluctuations about the average value will normally have a fast enough correlation time and a small enough net effect to be treated as a perturbation. Such theories, when the magnetic part of the hyperfine interaction is dominant, normally yield a spectrum of equally-spaced lines in which the outer lines are the first to be weakened and broadened by relaxation. Sufficiently fast relaxation results in a single narrow central line.

In the case of Mössbauer resonance in the

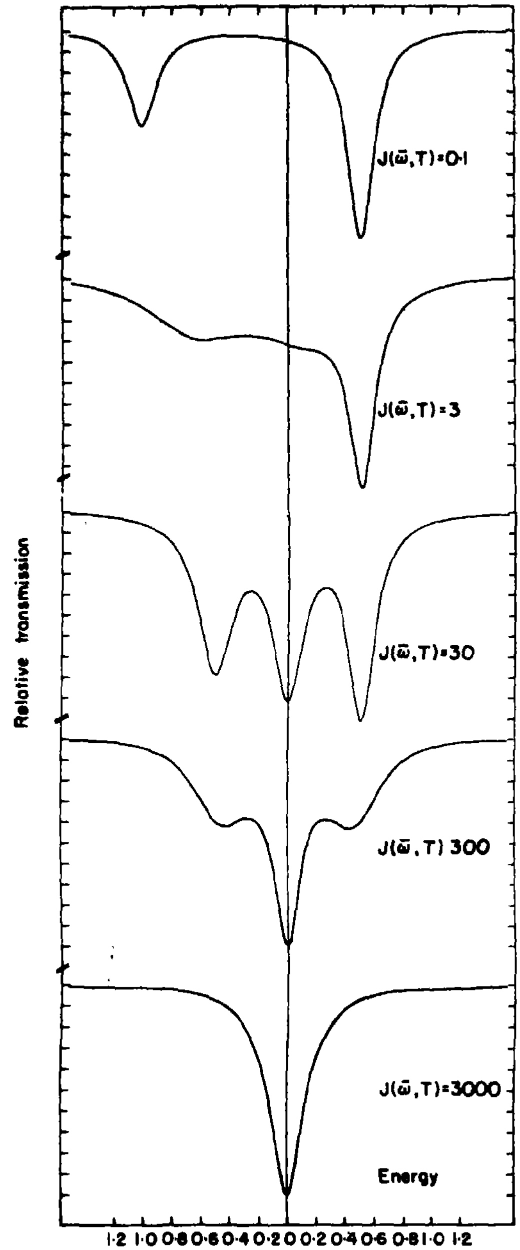

Fig. 3. Theoretical relaxation spectra for a model chosen to illustrate the 'ghost line' effect. We consider an isotropic electronic doublet $S = \frac{1}{2}$ and a $1 \rightarrow 0$ nuclear transition with magnetic hyperfine interaction of strength unity, $\mathbf{I}.\mathbf{S}$, in the excited state. The natural linewidths are 0·1 (*HWHM*). *The relaxation coupling tensor is taken* to be $(K^z, K^\pm) = (S^z, (0{\cdot}03/\sqrt{2})S^\pm)$. For weak relaxation (uppermost curve) one sees lines corresponding to the real energy levels of the system in the excited state, *which correspond to the two values* $F = \frac{3}{2}, \frac{1}{2}$ of the total effective angular momentum $\mathbf{F} = \mathbf{I} + \mathbf{S}$, with degeneracies 4 and 2 respectively. For intermediate spectral density strength, where only K^z coupling is important, three 'ghost' *lines appear which do not correspond to real* energy levels. Finally for large spectral densities the K^+ relaxation terms come into play to give a single narrow line.

paramagnetic state where the magnetic hyperfine interaction is diagonal, the effect of the electronic moment on the nucleus is also equivalent to that of an effective field, which can take on the values $\pm H_{\mathrm{eff}}\hat{z}$ only. This may be described as an *adiabatic* time-dependent effective-field model, since the effective field has no perpendicular component and is thus unable to induce nuclear spin-flip transitions. The time average of the effective field will vanish in the absence of an external field, and in cases of interest the correlation time characterizing its fluctuations will be comparable with the nuclear Larmor time corresponding to $|H_{\mathrm{eff}}|$. This means that the frequency spectrum of the random motion of H_{eff} is not 'white' as it would be in the limit of a short correlation time. In order to proceed using the effective field approximation, it is necessary to introduce a phenomenological stochastic model[7, 10]. for the frequency spectrum of H_{eff}. This should be compared with the coupled-system method, in which the electronic moment is treated as part of the quantum-mechanical resonant system so that the frequency spectrum of its motion need not be explicitly found. In the coupled-system method, random forces enter the picture at the stage of the interaction of the coupled system with the thermal bath, where the fast-correlation approximation is always valid in practice. Although the stochastic method is capable in principle of yielding exactly the correct Mössbauer spectrum, this requires that exactly the correct stochastic model be found. In practice, the stochastic method as applied to this problem introduces an approximation without any appreciable gain in simplicity as compared to the coupled-system method, so it would appear that the latter is to be preferred. The coupled-system method with diagonal hyperfine interaction constitutes a special case of the present theory, which has been treated extensively by Wickmann and others[11, 3, 17]. The theoretical spectra again show that the outer lines are the first to be affected by relaxation in the simplest cases, although in practice this simplicity may be obscured by the superposition of several lines having different intrinsic intensities and also by different thermal populations of the electronic states[11].

In the case of Mössbauer resonance in the paramagnetic state where the magnetic hyperfine interaction is *not* diagonal, to represent the effect of the electronic moment on the nucleus by a time-dependent effective field would result in a non-adiabatic model, since the effective field would now have perpendicular components capable of inducing nuclear spin flips. We wish to emphasize that, aside from the practical difficulties of solution which are introduced by this non-adiabatic aspect[18], the effective-field model is no longer capable, even in principle, of yielding a correct solution. This is immediately obvious since even in the limit of very slow motion of the effective field the correct level scheme and gamma spectrum cannot be reproduced [3, 4]. The source of the difficulty is that the motion of the electronic moment now has a phase-coherent component due to its interaction with the nuclear spin in addition to the random component due to interaction with the thermal bath, so it cannot adequately be described by a stochastic model. In order for a non-adiabatic stochastic effective-field model to be correct it is necessary that the effective field in question really correspond to a classical field, that is to a field representing the combined effect of a large number of quantum-mechanical degrees of freedom. As applied to the problem of paramagnetic Mössbauer spectra with non-diagonal hyperfine interaction, the stochastic effective-field model may be considered as as being complimentary to the present one in the sense that it becomes valid in the limit of a very large, and hence classical, paramagnetic moment, where the present theory remains formally valid but becomes unwieldy. It is of course possible to treat the present problem by stochastic methods if one takes the whole nuclear-paramagnetic system as the resonant object and represents its surroundings stochastically-described random forces. It has been pointed out to the author by M. Blume (private communication; M. Blume and M. Clauser, to be published) that such a treatment is implicitly contained in Ref. [12]. Retaining only the first term in a cumulant expansion in the stochastic treatment is equivalent to the physical assumption of a temperature bath remaining always in good equilibrium which we have used in obtaining the density matrix equation of motion. The present derivation offers advantages of directness and simplicity when the assumption of a temperature bath in good equilibrium is well justified, as in our experiment, but the results of the two treatments should be the same.

In conclusion, we emphasize that as compared to the other relaxation models reviewed, the theory of Section 3 yields a considerably wider variety of relaxation behavior. As was seen in the example of Er–Zr, the effect of relaxation can manifest itself initially anywhere in the spectrum, not necessarily on the outer lines, depending on the details of the problem. Furthermore, once relaxation has started, it need not continue simply as a monotonic tendency for each line to broaden and transfer its weight directly toward a narrow central line; instead it can exhibit the 'ghost line' phenomenon or other more complicated forms of behavior. Of course, in all cases a single narrow line must finally result at sufficiently high temperature.

6. THE *s–f* EXCHANGE INTERACTION IN Er–Zr

In metals at low temperatures the paramagnetic relaxation of the localized moment is expected to be dominated by its exchange coupling to the conduction-electron spins. If we assume a short-range, delta-function type of coupling

$$H_l = -2J_{s-f}(\Lambda-1)\,\mathbf{s}\,.\,\mathbf{J}\,\delta(\mathbf{r}_s-\mathbf{r}_f)$$

and non-interacting conduction electrons with a density of states (including twofold spin degeneracy) per atomic volume of N_E, equation (5) can be evaluated straightforwardly to yield a spectral density, for $|\hbar\omega| \ll kT$,

$$J(\omega,T) = (\pi/2)[(\Lambda-1)/\Lambda]^2(J_{s-f}N_E)^2\,kT. \quad (14)$$

Here $\Lambda = \frac{6}{5}$ is the Landé factor.

Reality is a good deal more complicated than this simple model. In the first place, the *s–f* interaction, which contains contributions both from an exchange integral[19] and from interband mixing effects[20], actually has a finite range in real space, i.e. a wavenumber dependence, as has been investigated by Watson and co-workers[19, 20, 21] in first-principle calculations using Hartree–Fock rare-earth ion wavefunctions and orthogonalized plane wave conduction electron states. They find that $J_{s-f}(\mathbf{k},\mathbf{k}') \approx J_{s-f}(|\mathbf{k}-\mathbf{k}'|)$ decreases as a function of $|\mathbf{k}-\mathbf{k}'|$, typically goes through zero at a value of $|\mathbf{k}-\mathbf{k}'|$ in the vicinity of $2k_F$, and tends to oscillate for large $|\mathbf{k}-\mathbf{k}'|$. When this dependence is taken into account, the $(J_{s-f})^2$ which appears in equation (14) is replaced by a mean value with $\mathbf{k}$ and $\mathbf{k}'$ averaged over the Fermi surface. The $\mathbf{k}$ dependence thus affects the relaxation rate less drastically than it does the long-range spatial spin-density distribution (dominated by $|\mathbf{k}-\mathbf{k}'| \approx 2k_F$) which was emphasized in Refs. [19] and [21]. The effect of the $\mathbf{k}$ dependence is to give a smaller relaxation rate as compared to the zero-range assumption.

One should also take into account the band structure of the conduction electrons. Zr has a valence configuration $5s^2\,4d^2$ and according to APW calculations by Loucks[22] the band structure is qualitatively similar to that found by Freeman and co-workers[23] for Tm, so the *s–f* interaction problem for a rare earth impurity in Zr should be similar to the same problem for pure rare earth metals. At present, however, very little is known about the effects of band structure on J_{s-f}. It is not even certain whether the interaction with *s*-like or with *d*-like bands should be more important, since the 4*f*–4*d* radial overlap is large but there could be an angular cancellation. The band structure could result in a strong directional dependence of $J_{s-f}(\mathbf{k}, \mathbf{k}')$ in **k** space, but this will not result in any anisotropy of the spectral density so long as the $\mathbf{s}.\mathbf{J}$ form of coupling is preserved for each **k**, **k**′.

It is to be expected that an interaction between conduction electrons will also be present, which will enhance the effects of J_{s-f} on magnetic relaxation[24, 25, 26]. Evaluation of this effect in a complicated band structure is very difficult, however. Analysis of analogous effects in nuclear magnetic relaxation in normal (non-transition) metals[25] indicates that the relaxation rates are enhanced by up to a factor 2.

It appears therefore that the estimation from first principles of the effective strength of the *s*–*f* interaction is very uncertain at the present time. However, one can be more confident that the proportionality of the spectral density to the temperature, which is due to the Fermi statistics, remains correct. It is true that this temperature dependence can in principle be upset by band effects (if they introduce very sharp structure into the density of states) or by electron–electron interactions (if they tend to drive the system ferromagnetic) but it seems very unlikely that such effects could manifest themselves over the temperature range up to 35°K where our data is taken. We shall thus interpret the data using equation (14), where it is understood that $(J_{s-f})^2$ now represents an appropriately weighted and enhanced average over **k**. The appropriate weighted value of J_{s-f} could be somewhat different in other types of experiment, but not, as we have emphasized in Section 3, in other paramagnetic relaxation experiments.

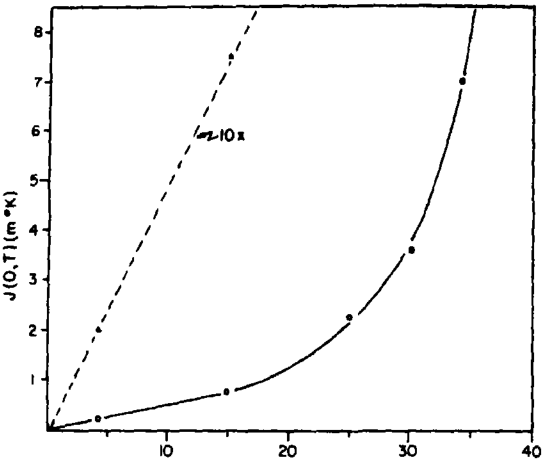

Fig. 4. Values of the effective spectral density $J(0, T)$ acting on the ground electronic doublet in Er–Zr at various temperatures, corresponding to the best-fit theoretical spectra in Fig. 1. The two lowest-temperature points are also shown magnified 10×.

In Fig. 4 are shown the spectral-density values corresponding to the relaxation fits of Fig. 1. From the slope of this curve in the range 4°–15°K, where it is linear, we obtain $|J_{s-f}N_E| = 0{\cdot}034$. If the value $N_E = 0{\cdot}66$/eV calculated by Loucks[22] be adopted, one obtains $|J_{s-f}| = 0{\cdot}05$ eV.

High-temperature deviations of the apparent spectral density from proportionality to *T* are to be expected when relaxation proceeding via the higher crystal-field levels comes into play. We tentatively attribute the high-temperature effects seen in Fig. 4 to transitions via crystal-field levels lying at energies of 30°–50°K above the ground doublet, driven predominantly by the *s*–*f* exchange coupling [27] at intermediate temperatures and predominantly by phonons[28] at the highest temperatures. These effects will be considered in detail elsewhere[9].

7. CONCLUSIONS

We have experimentally measured and theoretically interpreted the recoilless nuclear gamma emission spectrum of Er^{166} as a dilute impurity in Zr metal. To obtain the Mössbauer spectrum under the influence of relaxation, we have solved the motion of the coupled system of nucleus and paramagnetic moment. The eigenstates of this system are known from previous analysis of the low-temperature splitting pattern. Hence the relaxation fits at each temperature involve only one important theoretical unknown, which is a spectral density describing the effective strength of the fluctuating fields in the host which act on the electronic moment and are responsible for the relaxation. This theory yields a good fit to the data.

The success of the relaxation theory in reproducing the details of the experimentally measured spectra in Er–Zr is gratifying, but it ought not to be surprising, since our calculation represents the solution of a well-grounded model without any assumptions of a heuristic or arbitrary nature. The real importance of the method is not that it permits the Mössbauer spectra to be fitted, but rather that it permits measurement of the relaxation forces. The information so obtained is the same as could in principle be determined by EPR, but the Mössbauer method offers important practical advantages, especially in the fact that its sensitivity is not reduced, as is that of EPR, by the presence of metallic conductivity. This permits measurements in metals to be extended to much higher temperatures than would be feasible with EPR, where sensitivity problems are severe at any temperature. Temperature control is also easier in the Mössbauer method since the heat leak to the sample can be made very small.

Since the relaxation at low temperatures is dominated by the s–f exchange interaction, the basic quantity determined by our measurements is the product of a mean s–f exchange strength and a density of states: $|J_{s-f}N_E| = 0{\cdot}034$.

Acknowledgements—The author thanks Professor R. L. Mössbauer for suggesting this problem, and for the hospitality of his laboratory. He is grateful to E. R. Seidel for experimental advice and assistance, as well as for his interest in the theoretical problem. The support of a stipendium from the Bundeswissenschaftsministerium is gratefully acknowledged.

REFERENCES

1. HIRST L. L., SEIDEL E. R. and MÖSSBAUER R. L., *Phys. Letters* **29A**, 673 (1969).
2. HIRST L. L. and SEIDEL E. R., *J. Phys. Chem. Solids*, **31**, 857 (1969).
3. WICKMANN H. H., KLEIN M. P. and SHIRLEY D. A., *Phys. Rev.* **152**, 345 (1966).
4. SEIDEL E. R., KAINDL G., CLAUSER M. J. and MÖSSBAUER R. L., *Phys. Lett.* **25A**, 328 (1967).
5. ZINN W. and WIEDEMANN W., *J. appl. Phys.* **39**, 839 (1968).
6. CALLEN H. B. and WELTON T. A., *Phys. Rev.* **83**, 34 (1951).
7. ABRAGAM A., *Principles of Nuclear Magnetism*. Clarendon Press, Oxford (1961).
8. BRADFORD E. and MARSHALL W., *Proc. Phys. Soc.* **87**, 731 (1966).
9. HIRST L. L., To be published.
10. ANDERSON P. W., *J. Phys. Soc. Japan* **9**, 316 (1954).
11. WICKMANN H. H., In *Mössbauer-Effect Methodology* (Edited by I. J. Gruverman), Vol. 2, p. 64. Plenum Press, New York (1966).
12. GABRIEL H., BOSSE J. and RANDER K., *Phys. Status Solidi* **27**, 301 (1968); GABRIEL H., *Phys. Status Solidi* **23**, 195 (1967).
13. AFANASEV A. M. and KAGAN Yu., *Zh. Eksper. Teor. Fiz.* **45**, 1660 (1963); Engl. transl. *Sov. Phys. J.E.T.P.* **18**, 1139 (1964).
14. WEGENER H., *Z. Phys.* **186**, 498 (1965).
15. VAN DER WOUDE F. and DEKKER A. J., *Phys. Status Solidi* **9**, 755 (1965); **13**, 181 (1966).
16. LEVINSON L. M. and LUBAN M., *Phys. Rev.* **172**, 268 (1968).
17. NOWIK I., *Phys. Lett.* **24A**, 487 (1967).
18. BLUME M. and TJON J. A., *Phys. Rev.* **165**, 446 (1968); TJON J. A. and BLUME M., *Phys. Rev.* **165**, 456 (1968).
19. WATSON R. E. and FREEMAN A. J., *Phys. Rev.* **152**, 566 (1966).
20. WATSON R. E., KOIDE S., PETER M. and FREEMAN A. J., *Phys. Rev.* **139**, A167 (1965).
21. WATSON R. E., In *Hyperfine Interactions* (Edited by A. J. Freeman and R. B. Frankel). Academic Press, New York (1967).
22. LOUCKS T. L., *Phys. Rev.* **159**, 544 (1967).
23. FREEMAN A. J., DIMMOCK J. O. and WATSON R. E., *Phys. Rev. Lett.* **16**, 94 (1966); WATSON R. E., FREEMAN A. J. and DIMMOCK J. P., *Phys. Rev.* **167**, 497 (1968).
24. MORIYA T., *J. Phys. Soc. Japan* **18**, 516 (1963).
25. NARATH A. and WEAVER H. T., *Phys. Rev.* **175**, 373 (1968).
26. BURR C. R. and ORBACH R., *Phys. Rev. Lett.* **19**, 1133 (1967).
27. HIRST L. L., *Phys. Rev.* In press.
28. ORBACH R., *Proc. Roy. Soc. (London)* **A264**, 485 (1961).

J. Phys. Chem. Solids **Pergamon Press 1970. Vol. 31, pp. 669–684. Printed in Great Britain.**

PROPRIETES MAGNETIQUES DES OXYSULFURES DE TERRES RARES

G. QUEZEL*, R. BALLESTRACCI et J. ROSSAT-MIGNOD
C.E.N.-G. et C.N.R.S., Chemin des Martyrs, Grenoble, France

(*Received* 3 *July* 1969)

Résumé—Nous avons étudié systématiquement les propriétés magnétiques des oxysulfures de terres rares T_2O_2S, pour des températures comprises entre 2° et 700°K. Les composés où T = Ce, Pr, Nd, Sm, Eu, Er, Tm restent paramagnétiques jusqu'aux plus basses températures que nous avons atteintes expérimentalement; ceux où T = Gd, Tb, Dy, Ho et Yb s'ordonnent antiferromagnétiquement, avec des températures de Néel comprises entre 2,5°K (Ho) et 7,7°K (Tb): nous avons précisé les propriétés dans le domaine ordonné par l'étude des structures magnétiques par diffraction neutronique et par celle des propriétés métamagnétiques induites dans des champs élevés.

Abstract—The magnetic properties of the rare earth oxisulfides have been systematically studied in the temperature range 2–700°K. Compounds with T = Ce, Pr, Nd, Sm, Eu, Er, Tm are paramagnetic to the lowest temperatures we have reached experimentally; those with T = Gd, Tb, Dy, Ho, Yb are ordered antiferromagnetically, with a Néel temperature between 2·5°K (Ho) and 7·7°K (Tb). The magnetic properties in the ordered state have been studied by neutron diffraction and metamagnetic transitions have been investigated in high magnetic fields.

1. INTRODUCTION

DANS LE cadre d'une étude sur les interactions magnétiques entre ions terre rare trivalents et sur le comportement de ces ions dans un champ cristallin de symétrie C_{3v}, nous avons effectué une série de mesures magnétiques sur les composés T_2O_2S, où T représente une terre rare trivalente variant de Ce à Yb, ainsi que l'yttrium.

Les oxysulfures de terres rares, préparés à 1000°C par sulfuration contrôlée des oxydes T_2O_3, cristallisent dans le système hexagonal [1, 2]; la structure cristalline peut se décrire dans le groupe d'espace $P\bar{3}m1-D^3_{3d}$[3], et l'ion magnétique est placé dans un site de symétrie ponctuelle C_{3v}.

Les propriétés magnétostatiques ont été étudiées sur des échantillons polycristallins à l'aide de plusieurs techniques expérimentales:

dans la zône de température 2–700°K, par une balance de translation d'un type analogue à celle décrite par Cohen[4], dans un champ magnétique de 9500 oersted,

dans la zône des très basses températures, correspondant au domaine ordonné pour un certain nombre de composés, par une méthode d'extraction axiale[5], mise au point dans notre laboratoire par Mollard,

enfin, nous avons réalisé des études en champs magnétiques élevés (75 Koe), sur l'appareillage réalisé par Feron[6].

2. PROPRIETES PARAMAGNETIQUES

Tous les oxysulfures T_2O_2S présentent des propriétés paramagnétiques jusqu'à des températures voisines de l'hélium liquide; certains d'entre eux restent paramagnétiques jusqu'aux températures les plus basses atteintes avec notre appareillage, c'est-à-dire environ 2°K.

Dans tous les cas où la correction était importante, nous avons retranché le diamagnétisme des ions, suivant les valeurs données par Selwood[7]; nous avons par ailleurs mesuré, à différentes températures, la susceptibilité diamagnétique de Y_2O_2S, que nous avons trouvée en bon accord avec la valeur calculée (χ_M mesurée: $70 \,.\, 10^{-6}$ pour χ_M calculée: $86 \,.\, 10^{-6}$ u.é.m).

---

*Ce travail fait partie d'une thèse de Doctorat ès Sciences Physiques, enregistrée au Centre de Documentation du C.N.R.S. sous le Numéro A0 3319, qui sera soutenue prochainement par G. Quezel.

Nous avons reporté (Fig. 1) les valeurs des susceptibilités molaires χ_M à la température de 293°K, en même temps que les valeurs rassemblées par Schieber[8] pour les oxydes T_2O_3; l'accord avec la courbe classique établie par Hund et Van Vleck est excellent. On remarque cependant que la valeur du χ_M de Ce_2O_2S est très inférieure à celle de Ce_2O_3.

L'oxysulfure Ce_2O_2S reste paramagnétique jusqu'aux plus basses températures obtenues dans nos expériences; la courbe $(1/\chi)(T)$ présente une forte concavité vers l'axe des T au-dessous de 150°K environ. La constante de Curie C_M, évaluée dans la zône linéaire, est inférieure à la valeur calculée pour l'ion libre Ce^{3+} (C_M mesurée = 0,73; C_M calculée = 0,82) (Fig. 2). Nous avons observé par ailleurs, au cours des mesures faites à moyenne température (300° à 600°K, sous pression réduite d'hélium), une décroissance continue de la susceptibilité, accompagnée d'un changement d'aspect du produit. Bien que l'analyse aux R.X. ne nous ait pas permis d'identifier le composé formé, nous pensons que la décroissance de χ_M est due à la transformation de Ce^{3+} en Ce^{4+}, isoélectronique de La^{3+} et donc non magnétique.

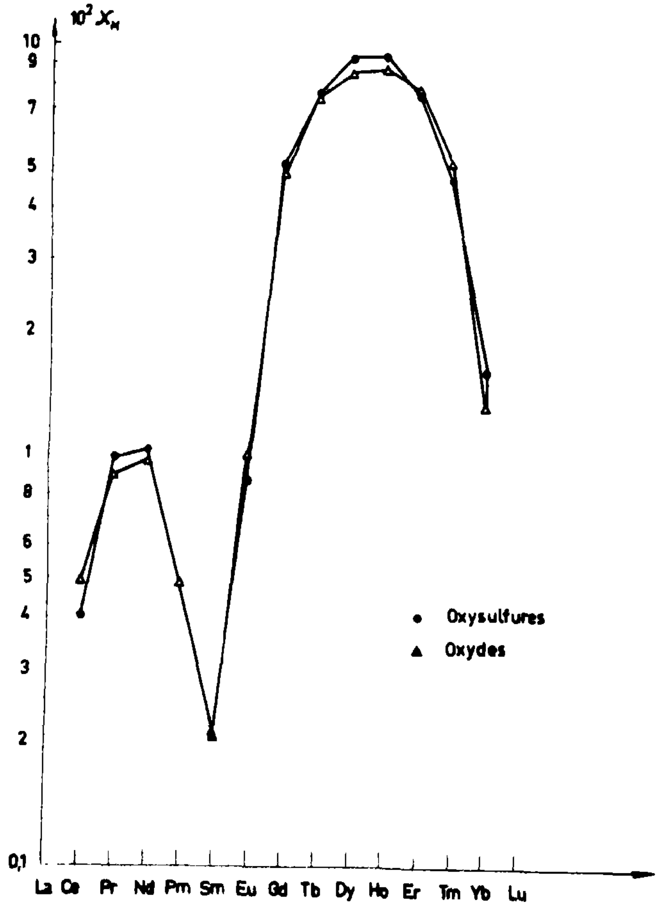

Fig. 1. Valeurs de la susceptibilité molaire des oxysulfures et des oxydes de Terres Rares à 293°K.

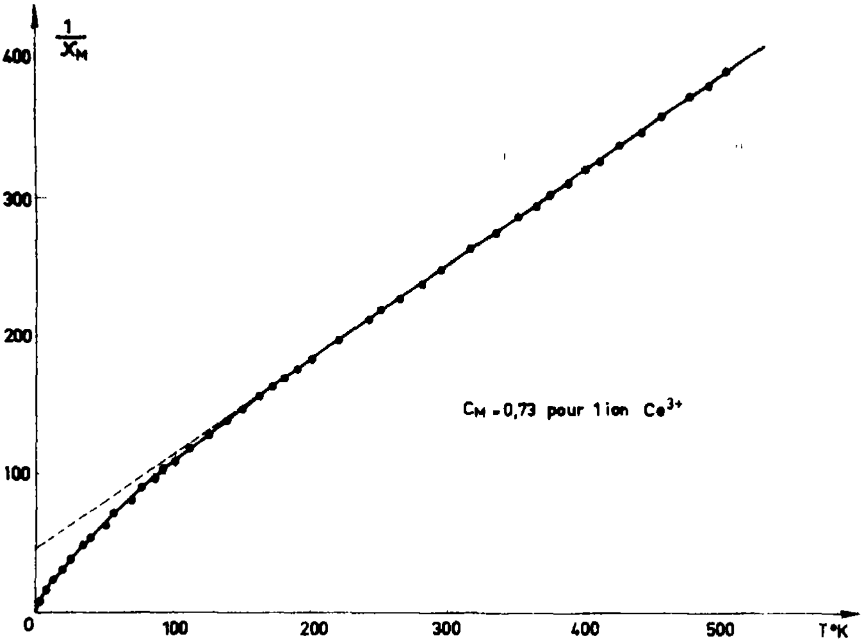

Fig. 2 Inverse de la susceptibilité molaire en fonction de la température pour l'oxysulfure de Ce.

L'oxysulfure de Néodyme reste paramagnetique jusqu'à la température de 2°K; la courbe $(1/\chi)(T)$ correspond à une loi de Curie–Weiss jusqu'à une température voisine de 10°K, avec une constante de Curie correspondant à la constante théorique de l'ion libre (C_M mesuré = 1,62; C_M théorique = 1,63). Au-dessous de $T = 10$°K, la susceptibilité augmente rapidement et la courbe $(1/\chi)(T)$ s'incurve vers l'axe des T (Fig. 3).

L'oxysulfure Pr_2O_2S obéit également à une loi de Curie-Weiss au voisinage de la température ambiante, avec une constante de Curie mesurée égale à la valeur théorique de l'ion libre Pr^{3+} (C_M mesuré = 1,61 : C_M théorique = 1,60). La courbe $(1/\chi)(T)$ s'incurve vers l'axe des T au-dessous d'une température de 150°K environ, contrairement à l'oxysulfure PrOS étudié antérieurement [9] (Fig. 4), ou à l'oxyde Pr_2O_3 étudié par Kern [10].

Les oxysulfures de Sm et d'Eu restent paramagnétiques jusqu'à la température de 2°K; les courbes $(1/\chi)(T)$ ne sont pas des droites de Curie–Weiss. Nous avons montré ailleurs [11] que la partie basse température de la courbe de Eu_2O_2S s'expliquait par la présence de 1% environ d'ions divalents Eu^{2+}. On constate par ailleurs que la courbe $(1/\chi)(T)$ de Sm_2O_2S passe par un maximum étalé au voisinage de $T = 350$°K (Fig. 5).

Les oxysulfures de Gd, Tb, Dy et Ho suivent une loi de Curie-Weiss entre la température ambiante et des températures voisines de celles de l'hélium liquide, où apparaît un ordre antiferromagnétique [11]. Les constantes de Curie observées correspondent avec une très bonne approximation à celles que l'on calcule pour les ions libres T^{3+} correspondants. Les températures de Curie paramagnétiques sont comprises entre −8° et −18°K.

Les mesures magnétiques effectuées sur Er_2O_2S montrent un comportement paramagnétique jusqu'à 2°K; la température de Curie paramagnétique, voisine de −7°K, semble indiquer des interactions d'échange comparables à celles de Ho_2O_2S ou de Yb_2O_2S: cependant, un diagramme de diffraction neutronique, réalisé à la température de

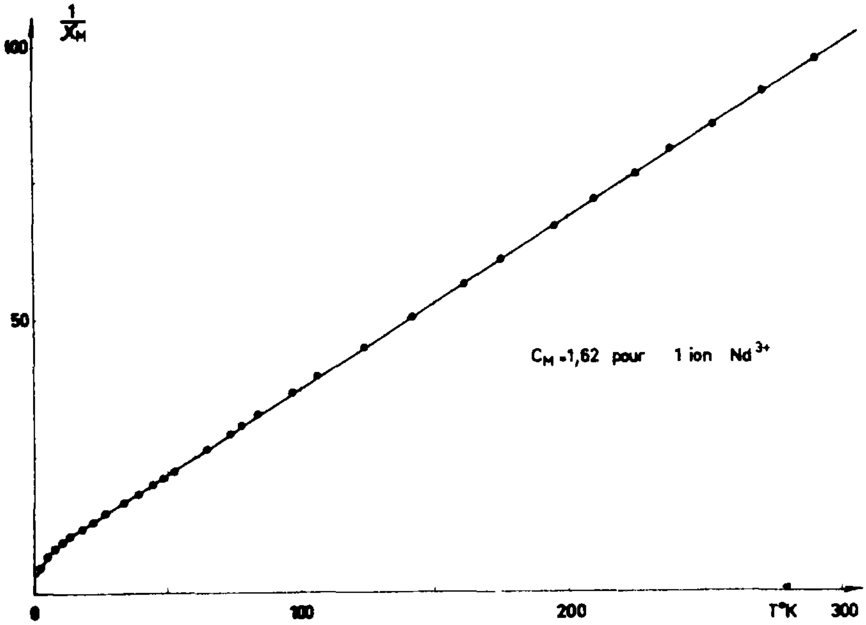

Fig. 3. Inverse de la susceptibilité molaire en fonction de la température pour l'oxysulfure de Nd

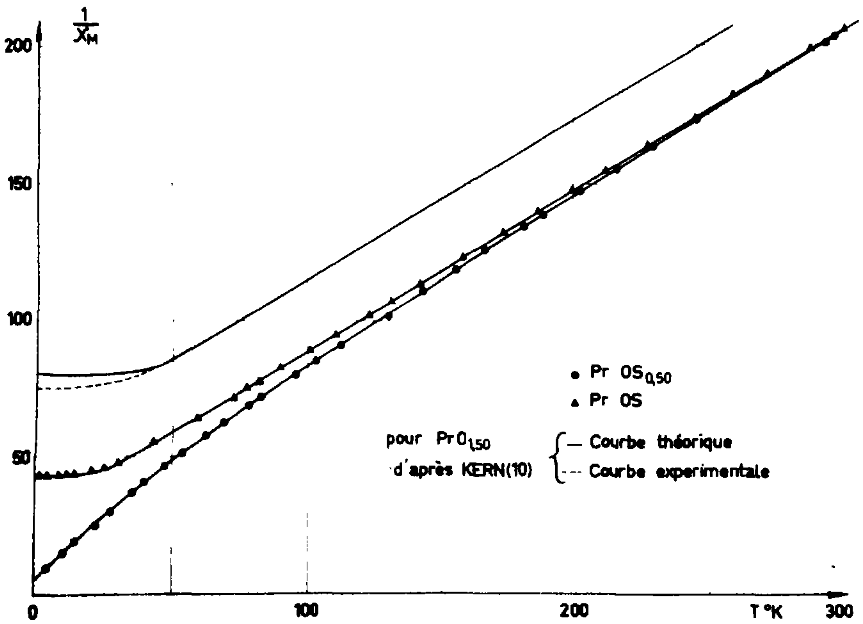

Fig. 4. Inverse des susceptibilités moléculaires en fonction de la température pour les oxysulfures de Pr.

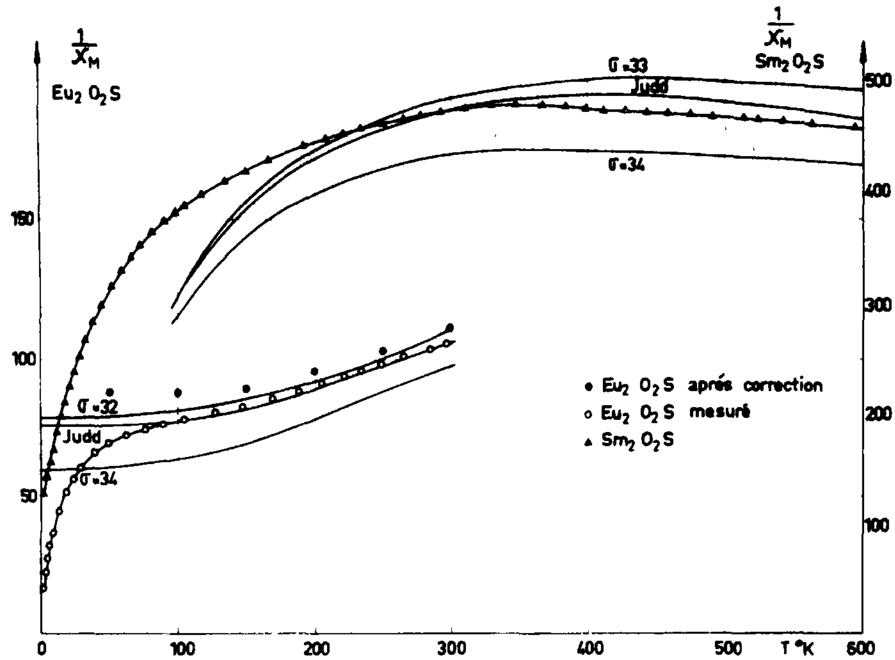

Fig. 5 Inverse des susceptibilités molaires en fonction de la température pour les oxysulfures de Sm et d'Eu.

0,3°K dans un cryostat à ^{3}He n'a révélé la présence d'aucune raie de surstructure magnétique. La courbe $(1/\chi)(T)$ présente, au-dessous de $T = 30$°K, une légère concavité vers l'axe des ordonnées, tandis que la concavité s'inverse au-dessous de $T = 15$°K (Fig. 6). La constante de Curie est égale à celle calculée pour l'ion libre (C_M mesurée = 11,62 : C_M théorique = 11,57).

L'oxysulfure de Tm suit la loi de Curie-Weiss entre la température ambiante et 30°K avec une constante de Curie correspondant à la valeur théorique de l'ion libre. (C_M mesurée = 7,14 : C_M théorique = 7,10). Au-dessous de $T = 20$°K, la courbe présente une concavité tournée vers l'axe des ordonnées, et la susceptibilité devient sensiblement constante au-dessous de 8°K (Fig. 7).

L'oxysulfure d'Ytterbium reste paramagnétique jusqu'à une température voisine de 3°K; la courbe $(1/\chi)(T)$ présente une forte concavité tournée vers l'axe des T, au-dessous de $T = 100$°K. Elle semble ensuite linéaire jusque vers 350°K, mais la constante de Curie que l'on calcule dans cet intervalle est nettement supérieure à celle de l'ion libre (C_M observée = 2,84; C_M théorique = 2,57). Entre 550 et 700°K, nous obtenons de nouveau une représentation linéaire, et la constante de Curie est égale à celle de l'ion libre (C_M mesurée = 2,55). La température de Curie paramagnétique, définie par cette portion de courbe, vaut $\theta_p = -6,5$°K environ (Fig. 8).

3. PROPRIETES ANTIFERRO ET METAMAGNETIQUES

Les oxysulfures de Gd, Tb, Dy, Ho et Yb deviennent antiferromagnétiques à basse température, avec des températures de Néel comprises entre 2,5°K (Ho) et 7,7°K (Tb); l'allure très différente des courbes de susceptibilités, mesurées dans un champ fixe de 9500 oe (voir par exemple la Fig. 9 pour Ho_2O_2S et Tb_2O_2S) nous a incités à étudier l'aimantation des oxysulfures de Tb, Dy, Ho et Yb en

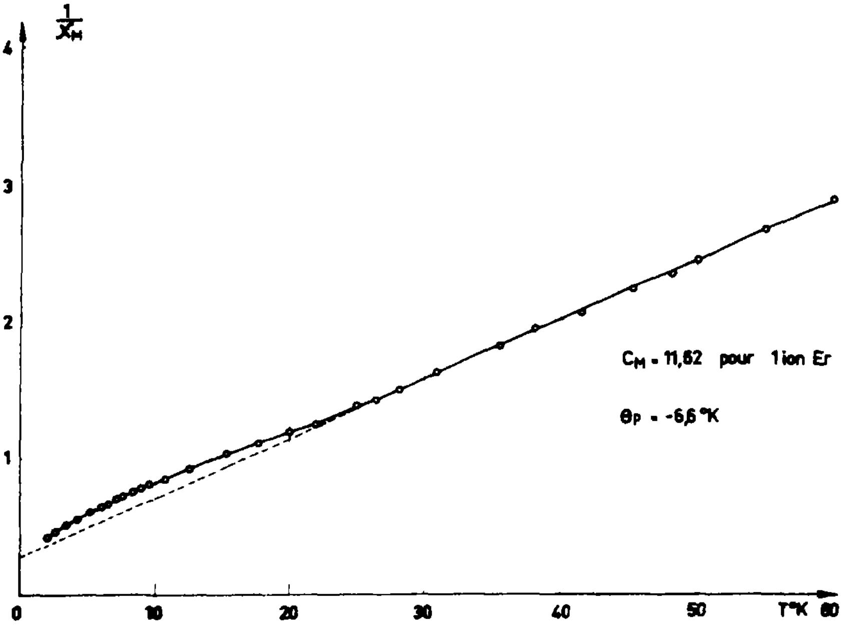

Fig. 6. Inverse de la susceptibilité molaire en fonction de la température pour Er_2O_2S.

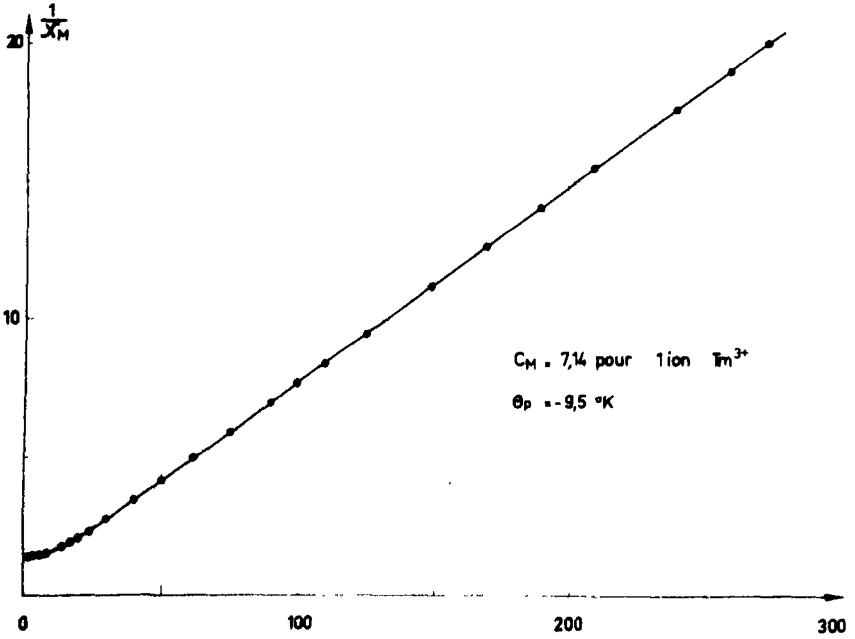

Fig. 7. Inverse de la susceptibilité molaire en fonction de la température pour Tm_2O_2S.

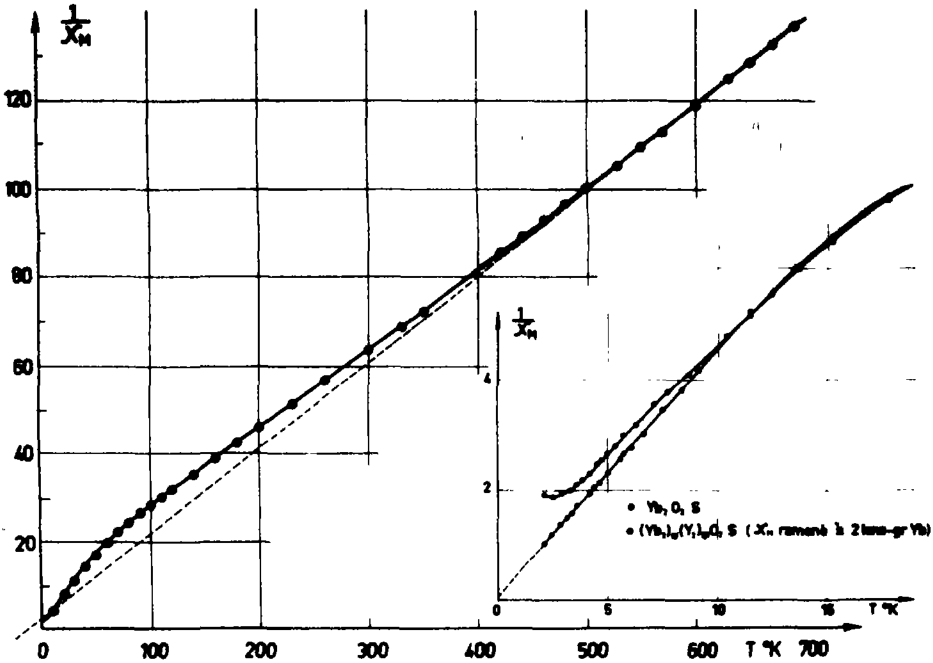

Fig. 8. Inverse de la susceptibilité molaire en fonction de la température pour Yb_2O_2S.

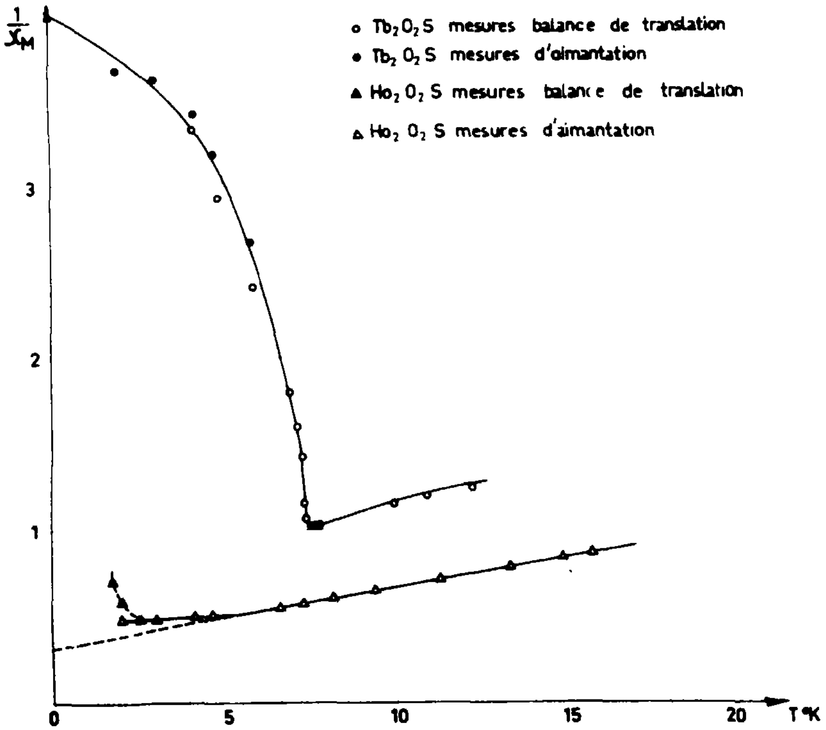

Fig. 9. Transitions antiferromagnétiques pour Tb_2O_2S et Ho_2O_2S.

fonction du champ magnétique appliqué, pour des températures inférieures à la températures d'ordre, et pour des champs atteignant 75 kOe.

Pour Tb_2O_2S, les courbes de la Fig. 10 montrent une transition antiferro-ferromagnétique; nous définirons le champ seuil comme la valeur de H au point d'inflexion des courbes $\sigma(H)$: dans le cas de Tb_2O_2S, il atteint des valeurs relativement élevées ($T = 4{,}2°K$: $H_S = 31500$ Oe). La saturation n'est pas atteinte dans un champ de 75 000 oe: une extrapolation en champ infini, en employant la loi classique d'approche à la saturation en $1/H^2$, nous donne la valeur: $\sigma_S = 7{,}38\ \mu_B/$atome, en bon accord avec la valeur attendue théoriquement.

constante au-dessous de la température de Néel. Le moment à saturation, obtenu par extrapolation en champ infini, vaut environ 8,2 μ_B/atome, en bon accord avec les valeurs obtenues par diffraction neutronique[11].

L'oxysulfure de Dy a un comportement complexe; on distingue nettement, sur la courbe $\sigma(H)$ tracée à $T = 1{,}134°K$* (Fig. 12), deux transitions: l'une se produit pour un champ seuil H_{S1} voisin de 19000 Oe, l'autre pour H_{S2} voisin de 35000 Oe. Le moment à saturation, obtenu par extrapolation en champ infini, est légèrement inférieur au moment théorique (à $T = 1{,}134°K$, $\sigma_S = 8{,}6\ \mu_B/$atome); il est cependant très supérieur au moment calculé à 1,5°K par diffraction neutronique (4,41 μ_B)[11].

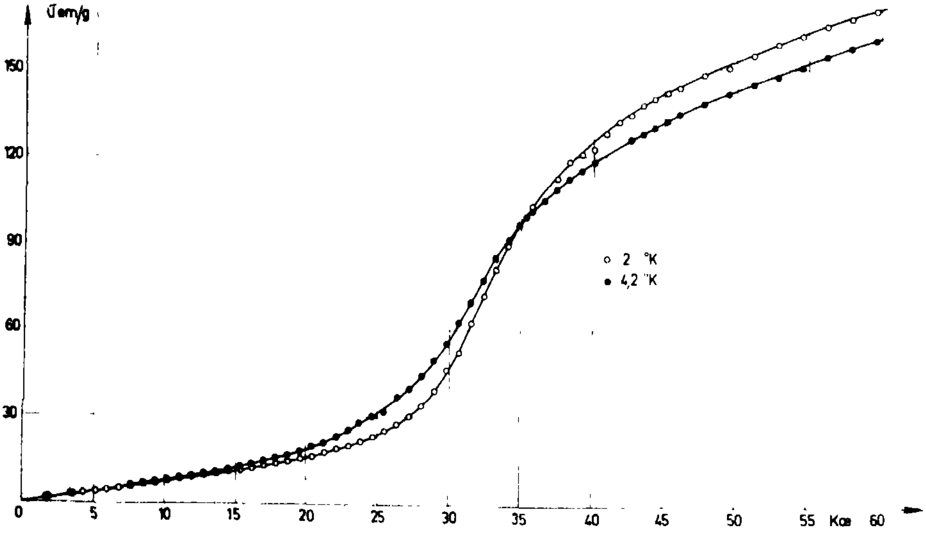

Fig. 10. Aimantation de Tb_2O_2S en fonction du champ appliqué.

Dans le cas de Ho_2O_2S, la courbe d'aimantation est très différente (Fig. 11): le champ seuil est beaucoup plus faible ($T = 1{,}8°K$: $H_S = 6000$ Oe) que pour Tb_2O_2S; d'autre part, $\sigma(H)$ est sensiblement linéaire entre 9000 et 15000 oe et la susceptibilité ($\Delta\sigma/\Delta H$), calculée dans cette région, est presque exactement égale à la susceptibilité maximale observée au point de transition ($(\Delta\sigma/\Delta H) = 1{,}97$ pour $\chi_{T_N} = 1{,}99$), ce qui indique qu'elle correspond à la susceptibilité perpendiculaire,

La courbe de susceptibilité de Yb_2O_2S indique l'apparition d'un ordre antiferromagnétique au-dessous de $T = 3°K$; les mesures d'aimantation en fonction du champ appliqué, réalisées aux températures de 4,2°, 2,65° et 1,9°K, confirment l'existence de cet ordre: les courbes obtenues pour les températures inférieures à la température d'ordre ont

---

*Nous remercions Filippi et Manhes qui ont effectue la manipulation sur leur appareillage.

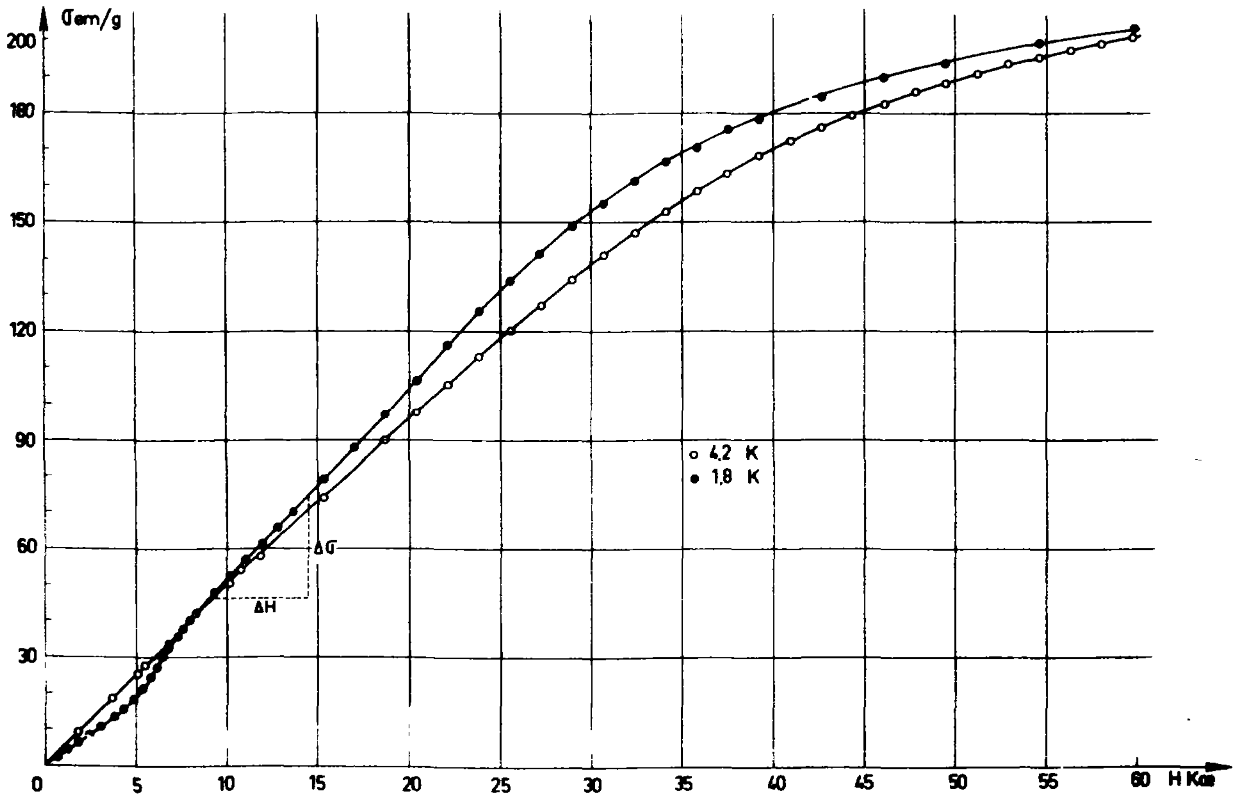

Fig. 11. Aimantation de Ho_2O_2S en fonction du champ appliqué.

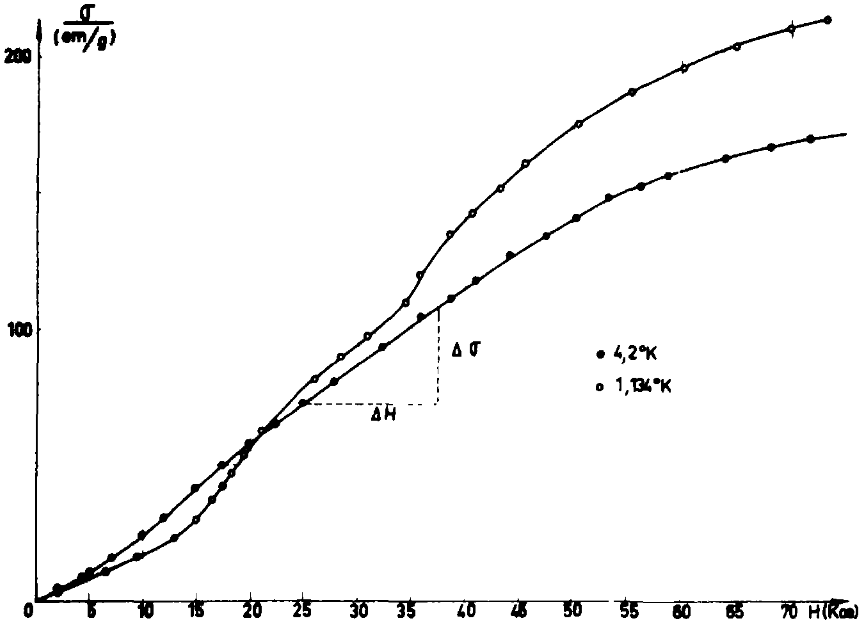

Fig. 12. Aimantation de Dy_2O_2S en fonction du champ appliqué.

en effet une allure analogue à celles de Ho_2O_2S. Une étude par diffraction de neutrons, à la température de 1,5°K, a permis de déterminer la structure magnétique[12].

4. DISCUSSION DES PROPRIETES PARAMAGNETIQUES

Les propriétés paramagnétiques s'interprètent dans le cadre général de la théorie de Van Vleck, appliquée aux ions Terres Rares placés ici dans un potentiel électrostatique de symétrie C_{3v}. Les calculs détaillés concernant les paramètres de champ cristallin et l'interprétation des résultats magnétiques seront publiés ailleurs.

La méthode générale consiste à déterminer les niveaux d'énergie de l'ion magnétique et à calculer ensuite la perturbation apportée par le champ magnétique appliqué H. On sait que, dans le cas des ions terres rares, l'énergie de couplage spin-orbite est en général très supérieure à l'énergie due à l'interaction avec le champ électrique créé par les anions voisins, les niveaux d'énergie sont donc définis par un nombre quantique J, et le champ cristallin lève la dégénérescence d'ordre $2J+1$ du niveau J. Les propriétés magnétiques de l'ion sont étroitement liées à la largeur de ce multiplet de champ cristallin.

Cas de Gd, Tb, Dy, Ho, Er

Les propriétés paramagnétiques des oxysulfures de Tb, Dy, Ho et Er s'interprètent simplement dans ce modèle: l'étude des courbes $\chi T(T)$ montre que la constante de Curie expérimentale coincide avec celle de l'ion libre dès que les températures sont supérieures à quelques dizaines de degrés K; par ailleurs, la loi de Curie-Weiss est suivie rigoureusement entre 300° et 20–30°K, les constantes de Curie mesurées coïncidant exactement avec celles que l'on calcule pour l'ion libre. On déduit de ceci que la largeur totale du multiplet de champ cristallin ne dépasse pas quelques dizaines de degrès K. D'autre part, pour ces ions, le premier niveau excité, très éloigné du fondamental (voir par exemple[13]) n'est pas peuplé aux températures atteintes expérimentalement.

Dans ces conditions, tous les niveaux de champ cristallin sont également peuplés, si bien que les ions se comportent en moyenne comme une assemblée d'ions libres, et leur susceptibilité se calcule alors par la formule classique[14]:

$$\chi = \frac{C}{T+\theta_p} \text{ avec } C = \frac{N\mu_B{}^2 g^2}{3k} J(J+1)$$

g est le facteur de Landé de l'ion libre et J le nombre quantique correspondant au niveau fondamental.

Au-dessous de 20°K, les énergies d'échange entre ions magnétiques deviennent comparables à kT: les courbes expérimentales montrent un comportement antiferromagnétique. Par ailleurs, il est nécessaire de faire intervenir explicitement cette interaction dans la détermination des niveaux d'énergie.

Le cas du Gd, dont le niveau fondamental $^8S_{7/2}$ est insensible au premier ordre à l'action du champ cristallin, est identique à celui de l'ion libre.

Cas de Tm *et de* Pr

Dans le champ cristallin hexagonal de symétrie C_{3v}, l'état fondamental $^3H_6$ de l'ion Tm^{3+} est décomposé en 9 niveaux, 4 doublets et 5 singulets; aux très basses températures, la susceptibilité tend vers une constante α, où α représente le paramagnétisme constant de Van Vleck dans la formule

$$\chi_M = \frac{C_M}{T+\theta} + \alpha.$$

La constante de Curie C_M est donc nulle, ce qui implique un singulet en niveau fondamental.

Le niveau fondamental $^3H_4$ de l'ion Pr^{3+} est décomposé par le champ cristallin en trois singulets et trois doublets; la susceptibilité croissant vers les basses températures montre que le niveau fondamental est cette fois un doublet: cette situation est différente de celle que l'on rencontre dans l'oxyde Pr_2O_3 (symétrie D_{3d})[10] ou dans l'oxysulfure PrOS (symétrie C_{4v}) que nous avons étudié précédemment. Ce résultat semble par contre habituel en symétrie C_{3v}, comme le montrent les études réalisées sur le nitrate double de Pr et de Mg[15, 16]. On remarque que la déviation à la loi de Curie-Weiss commence à une température voisine de 100°K, ce qui implique une largeur totale du multiplet de champ cristallin assez grande (quelques centaines de °K).

Cas du Nd *et du* Ce

Les ions Nd^{3+} et Ce^{3+} présentent la dégénerescence de Kramers et le doublet fondamental est magnétique jusqu'aux plus basses températures; l'effet du champ cristallin semble relativement faible dans le cas du Nd^{3+}, tandis qu'il est beaucoup plus important pour le Ce^{3+}; ceci se place dans la ligne générale des résultats que nous avons obtenus, qui montre que la largeur du multiplet de champ cristallin croît avec les J décroissants [17].

Cas de Yb

L'oxysulfure d'ytterbium ne suit une loi de Curie-Weiss, avec la constante de Curie C_M correspondant à l'ion libre Yb^{3+}, que pour des températures supérieures à $T = 550$°K; ceci montre que le multiplet de champ cristallin est très dilaté, puisqu'il faut atteindre une température relativement élevée pour que les niveaux soient également peuplés. Au-dessous de 550°K, le dépeuplement des niveaux les plus élevés se traduit par une diminution de susceptibilité, avec un terme de paramagnétisme constant important; aux très basses températures le doublet fondamental est seul occupé, mais l'énergie d'échange entre les ions Yb^{3+} devient prépondérante et le composé s'ordonne. Pour déterminer la constante de Curie à basse température, ainsi que le paramagnétisme constant α, nous avons étudié la susceptibilité paramagnétique de la solution solide $(Yb_2)_{0.1}(Y_2)_{0.9}O_2S$, où les interactions entre ions magnétiques deviennent effectivement négligeables (Fig. 8).

Cas de Sm *et* Eu

Le comportement paramagnétique des composés contenant des ions Sm^{3+} ou Eu^{3+} a été expliqué pour la première fois par Van Vleck et ses collaborateurs[14, 18]; il résulte du faible écartement énergétique des niveaux du terme fondamental, ce qui entraine, dans le calcul des susceptibilités, les deux conséquences bien connues:

— la formule simple de Hund

$$\chi_M = \frac{Ng_J{}^2\mu_B{}^2J(J+1)}{3kT}$$

où N est le nombre d'Avogadro, doit être remplacée par la somme:

$$\chi_M = N\frac{\sum_J |g^2{}_J\mu_B{}^2J(J+1)_{/3kT} + \alpha_J(2J+1)\exp(-E_{J/kt})}{\sum_J (2J+1)\exp(-EJ/kT)} \text{ où } J$$

prend les différentes valeurs possibles du terme fondamental (de 0 à 6 pour Eu, de $\frac{5}{2}$ à $\frac{15}{2}$ pour Sm).

—le terme du second ordre, α_J (paramagnétisme constant de Van Vleck) devient très important, car il contient des termes proportionnels à $(1/E_{J+1} - E_J)$. Il faut remarquer qu'il est également nécessaire de tenir compte des effets de champ cristallin, lorsque la perturbation est importante: c'est effectivement le cas de Sm[19], où la courbe de susceptibilité s'écarte des allures de courbe de l'ion libre pour T inférieur à 200°K environ; par contre, l'état fondamental $J = 0$ de l'ion Eu^{3+} est insensible à l'action du champ cristallin, et la perturbation sur le premier niveau excité $J = 1$, situé à environ 500°K du fondamental est certainement faible, si bien que les niveaux d'énergie sont ceux de l'ion libre, en première approximation.

Le calcul de la susceptibilité, à température moyenne, nécessite donc la connaissance du multiplet fondamental de l'ion libre, que l'on peut obtenir expérimentalement par émission de fluorescence ou par absorption infra-rouge (voir par exemple [19,20]), ou que l'on peut calculer théoriquement grâce à la formule de Goudsmit[21] et à la règle de Landé[22]

Formule de Goudsmit:

$$\Delta E = \frac{8\pi^4me^2}{c^3h^5}\frac{2L+1}{n^3l(l+1)(2l+1)}(Z-\sigma)^4$$

où ΔE est la largeur totale du multiplet, Z le nombre atomique, m et e la masse et la charge d'un électron, h la constante de Planck, n le nombre quantique principal, c la vitesse de la lumière, l le nombre quantique orbital d'un électron et L le nombre quantique orbital de l'ion, et σ une constante d'écran.

La règle de Landé:

$$E_{J-1} - E_J = AJ$$

permet de calculer les différences d'énergie entre les différents termes du multiplet.

La formule de Goudsmit nécessite la connaissance de la constante d'écran σ: les mesures de la susceptibilité magnétique, très sensible à la valeur de σ, permettent de la préciser; par ailleurs, Judd[23] a montré, par un calcul au 2e ordre sur les positions des niveaux, que la règle de Landé devait se modifier de la façon suivante:

$$E_{J-1} - E_J = aJ + bJ^3.$$

Les courbes de susceptibilité, calculées par Arajs[24] pour différentes valeurs de la constante d'écran ainsi que pour les écartements donnés par Judd ont été reportées sur la figure 5: on constate que, dans le cas de Sm_2O_2S, les valeurs expérimentales se placent au voisinage de la courbe calculée à partir des valeurs de Judd; l'augmentation de χ_M constatée expérimentalement au-dessus de 350°K environ correspond au peuplement du premier niveau excité ${}^6H_{7/2}$, situé à 1500°K au-dessus du fondamental ${}^6H_{5/2}$. Nos résultats semblent confirmer les écartements calculés par Judd, qui sont également en bon accord avec les observations spectroscopiques.

Dans le cas de Eu, par contre, il est impossible, avec nos résultats, de trancher entre les courbes obtenues pour $\sigma = 32$ ou 33 et avec les valeurs de Judd: ceci est dû pour une part à l'incertitude expérimentale liée à la correction que nous devons apporter à nos mesures par suite de la présence d'ions Eu^{2+}[11] et pour une autre à l'intervalle de températures trop réduit de notre étude: on remarque en effet[24] que les désaccords sur les énergies des niveaux ^7F_J calculées avec $\sigma = 32, 33$ ou par la méthode de Judd ne sont importants que pour les termes supérieurs du multiplet. Par ailleurs, pour un calcul rigoureux, il est nécessaire de tenir compte de l'effet du champ cristallin sur le premier niveau excité $^7F_1$.

5. DISCUSSION DES PROPRIETES DANS LE DOMAINE ORDONNE

Les mesures magnétostatiques révèlent la présence d'un ordre antiferromagnétique dans cinq oxysulfures (Gd, Tb, Dy, Ho, Yb); nous avons étudié par diffraction neutronique ceux pour lesquels la section efficace d'absorption des neutrons par la terre rare est suffisamment faible. Les structures magnétiques de Tb_2O_2S, Dy_2O_2S, Ho_2O_2S et Yb_2O_2S ont été décrites précédemment[11, 12].

L'interprétation des variations de l'aimantation en fonction du champ appliqué peut se faire de façon semi-quantitative à l'aide d'un modèle simple d'antiferromagnétisme à deux sous-réseaux, dans le cadre de la théorie macroscopique du champ moléculaire, conformément aux idées proposées dès 1936 par L. Néel[25].

Le calcul, que l'on effectue pour un corps uniaxe, où l'énergie d'anisotropie est décrite par $W = k_1 \sin^2\theta$ (θ angle du moment magnétique avec l'axe de facile aimantation Δ), consiste à écrire l'énergie du système en présence d'un champ magnétique appliqué H, et à minimiser cette énergie pour obtenir les solutions d'équilibre du système (voir par exemple Herpin[26]). Les résultats obtenus se résument de la façon suivante:

- dans le cas où H est perpendiculaire à Δ, la seule solution stable est une solution 'oblique', où les moments des deux sous-réseaux sont également inclinés sur la direction du champ; l'aimantation varie linéairement avec le champ appliqué,
- dans le cas où H est parallèle à Δ, le calcul conduit à un système de trois relations entre H, K_1, n_1, M_T, θ et θ' où n_1 est le coefficient de champ moléculaire qui mesure l'interaction avec les proches voisins, M_T l'aimantation d'un sous-réseau à la température T, et θ et θ' les angles que font les moments des sous-réseaux avec Δ.

On obtient ainsi trois solutions d'équilibre possible: arrangement antiferromagnétique (A), arrangement ferromagnétique (F), arrangement 'oblique' (0). Le diagramme de stabilité de ces solutions (Fig. 13) montre la possibilité de deux types de transitions, leur éventualité étant liée au rapport entre l'énergie d'anisotropie et l'énergie d'échange dans le corps:

- anisotropie "forte" soit $\frac{K_1}{2n_1M_T^2} > \frac{1}{2}$: transition directe $A \rightarrow F$
- anisotropie "faible" $\frac{K_1}{2n_1M_T^2} < \frac{1}{2}$: transition $A \rightarrow 0$, puis $0 \rightarrow F$.

Nous allons appliquer cette théorie simple à deux exemples, Ho_2O_2S et Tb_2O_2S. Il faut remarquer que nos résultats ont été obtenus sur des échantillons polycristallins, où les cristallites sont orientés au hasard. Nous observons donc un effet moyen, et la définition des champs seuil est délicate: nous avons une incertitude importante sur leur mesure, et les valeurs obtenues, notamment pour les coefficients d'anisotropie, ne sont que des ordres de grandeur.

Ho_2O_2S

Nous sommes ici dans le cas de 'l'anisotropie faible', (Fig. 11); la transition observée

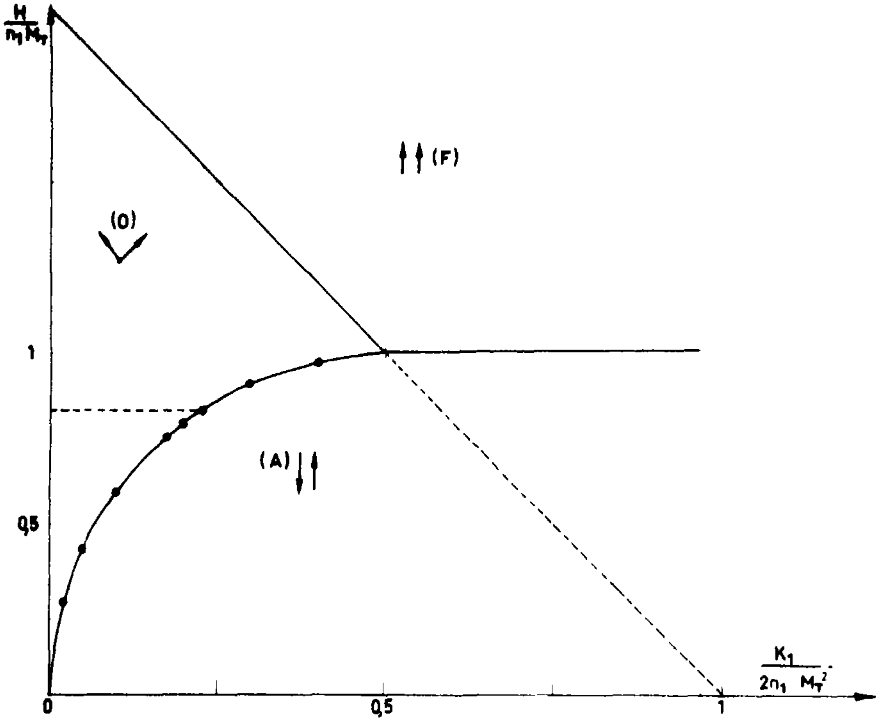

Fig. 13. Diagramme d'équilibre des structures antiferromagnétiques ferromagnétiques et obliques.

à 1,8°K pour $H_S = 6000$ oe correspond à une rotation de la direction d'antiferromagnétisme et donc à l'apparition de la solution 'oblique'.

Nous pouvons, dans la théorie utilisée jusqu'à présent, évaluer les coefficients de champ moléculaire n_1 et n_2, définis en écrivant que le champ agissant sur un atome du sous-réseau 1 vaut $\mathbf{H}_{m_1} = -n_2\mathbf{M}_2 - n_2\mathbf{M}_1$; en portant les valeurs de θ_p(8°K) et de T_N(2,5°K) dans les relations classiques $\theta_p = (C_M/2)(n_1 + n_2)$ et $T_N = (C_M/2)(n_2 - n_1)$ où C_M est la constante de Curie relative à l'ensemble des deux sous-réseaux, nous obtenons:

$$n_1 = 0{,}375;\quad n_2 = 0{,}31.$$

Nous remarquons également que dans cette théorie la susceptibilité à la température de Néel vaut $\chi_{TN} = (1/n_1)$: nous trouvons ainsi:

$$n_1 = 0{,}50.$$

En utilisant une valeur moyenne pour n_1, et en prenant pour M_T la valeur expérimentale trouvée à 1,8°K par extrapolation en champ infini, nous pouvons utiliser le graphique de la Fig. 13 pour déterminer K_1.

$$K_1 = 5\,.\,10^7\ \text{ergs/mole}$$

$$\text{ou } K_1 = 0{,}13\,.\,10^6\ \text{ergs/g}.$$

Tb_2O_2S

La Fig. 10 montre l'existence d'une transition directe $A \rightarrow F$: nous sommes cette fois dans le cas de 'l'anisotropie forte'. En utilisant les résultats expérimentaux de la courbe tracée à 4,2°K, il est possible de calculer n_1 à partir de la relation $(H_S/n_1M_T) = 1$ (Fig. 13); pour K_1, toutefois, nous n'obtenons que l'inégalité $(K_1/2n_1M_T^2) > \frac{1}{2}$ soit $K_1 > 1{,}3\,.\,10^9$ ergs/mole.

Pour évaluer K_1, nous pouvons utiliser une formule également dérivée de la théorie pré-

Tableau 1. *Valeurs des coefficients de champ moléculaire et des constantes d'anisotropie*

	n_1 obtenu par			K_1 (en 10^6 ergs/g) obtenu par	
	Champ seuil	$\frac{1}{\chi_{T_N}}$	$\frac{2}{C}(\theta_p + T_N)$	Champ seuil	Extrapolation de $1/\chi_M$
Dy_2O_2S		0,9	0,75		0,33
Tb_2O_2S	0,79	1,03	1,05	>3,4	7,9
Ho_2O_2S		0,50	0,375	0,13	

cédente: la susceptibilité au zéro absolu s'écrit, en effet:

$$\frac{1}{(\chi_M)_{T=0}} = \frac{3}{2}\left|\frac{1}{(\chi_M)_{T_N}} + \frac{2K_1}{M_0^2}\right|$$

soit $K_1 = 3 \,.\, 10^9$ ergs/mole ou $K_1 = 7{,}9 \,.\, 10^6$ ergs/g.

Cette valeur est environ 20 fois plus forte que celle qu'on a obtenue pour Ho_2O_2S.

Nous avons également évalué les coefficients de champ moléculaire n_1 et n_2 définis plus haut; nous trouvons, avec

$$\theta_p = 17°\text{K et } T_N = 7{,}7°\text{K}:$$

$$n_1 = 1{,}05;\ n_2 = 0{,}4.$$

On remarque que la valeur de n_1 concorde parfaitement avec la valeur expérimentale $1/(\chi_M)_{T_N} = 1{,}03$, et qu'elle est en accord raisonnable avec celle que nous obtenons par la méthode du champ seuil.

Dy_2O_2S

La courbe d'aimantation complexe de Dy_2O_2S (Fig. 12) ne permet pas une interprétation de ce type. Nous pouvons évaluer K_1 en considérant la valeur de $1/\chi_M$ extrapolée au zéro absolu, en n_1 et n_2 par les formules classiques utilisées plus haut; les valeurs obtenues sont consignées dans le Tableau 1, avec celle de Tb_2O_2S et Ho_2O_2S.

Remarque

On peut songer à d'autres mécanismes pour expliquer le métamagnétisme de Ho_2O_2S et Dy_2O_2S: en particulier, Mareschal *et al.*[27] et Holmes *et al.*[28] ont étudié des oxydes doubles de Terres Rares et de métaux de transition a structure pérovskite déformée et ils ont montré que le champ magnétique produisait un renversement des moments le long de la direction de facile aimantation Δ, sans que Δ s'oriente perpendiculairement à H ('spin flip'). Une étude par diffraction neutronique sur des échantillons polycristallins de Ho_2O_2S et de Dy_2O_2S, dans un champ magnétique variant de 0 à 16000 oe, a montré que ce mécanisme ne se produisait pas ici.

6. CONCLUSION

L'étude entreprise sur des échantillons polycristallins d'oxysulfures de terres rares T_2O_2S a permis de mettre en évidence l'influence du champ cristallin sur les propriétés paramagnétiques des ions T^{3+}; dans le domaine ordonné, les différentes transitions induites par le champ magnétique ont conduit à l'évaluation des constantes d'anisotropie et des paramètres macroscopiques de champ moléculaire: malgré les limites de la théorie simple à deux sous-réseaux utilisée, et malgré les incertitudes expérimentales importantes sur les champs seuils des transitions, la cohérence des résultats obtenus est satisfaisante.

Note: dans toute cette étude, les susceptibilités magnétiques et les coustantes de Curie sont évaluées en uém cgs par mole.

REFERENCES

1. FLAHAUT J., GUITTARD M. et PATRIE M., *Bull. Soc. Chim. France* 990 (1958).

2. COLLIN G. et LORIERS J., *C.r. hebd. Séanc Acad. Sci. Paris* **260**, 5043 (1965).
3. ZACHARIASEN W. H., *Acta crystallogr* **2**, 60 (1949).
4. COHEN J., *C.r. hebd. Séanc. Acad. Sci. Paris* **246**, 3425 (1959).
5. WEISS P., *J. Phys., Paris* **4**, 473 (1905).
6. FERON J., Thèse, Grenoble (1969).
7. SELWOOD, *Magnetochemistry*, p. 78. Interscience, New York (1956).
8. SCHIEBER, *Experimental Magnetochemistry*, p. 303. North-Holland, Amsterdam (1967).
9. BALLESTRACCI R., Thèse, Grenoble (1967).
10. KERN S., *J. chem. Phys.* **40**, 1, 208 (1964).
11. BALLESTRACCI R., BERTAUT E. F. et QUEZEL G., *J. Phys. Chem. Solids* **29**, 1001 (1968).
12. BALLESTRACCI R. et ROSSAT-MIGNOD J., *Solid St. Commun.* **7**, 1011 (1969).
13. ELLIOT R. J. et STEVENS K. W. H., *Proc. R. Soc.*, **A218**, 553 (1953).
14. VAN VLECK J. H., *The Theory of Electric and Magnetic Susceptibilities*. Oxford (1932).
15. RAUCKHORST W. H. et FENICHEL H., *J. Phys. Chem. Solids* **29**, 2231 (1968).
16. SCOTT P. C. et JEFFRIES C. D., *Phys. Rev.* **127**, 32 (1962).
17. TRAMMEL G. T., *Phys. Rev.* **131**, 932 (1963).
18. VAN VLECK J. H. et FRANK A., *Phys. Rev.* **34**, 1494 (1929) et FRANK A., *Phys. Rev.* **39**, 119 (1932).
19. ROSSAT-MIGNOD J., BALLESTRACCI R., QUEZEL G., LINARES C. et TCHEOU F., *J. Phys. Chem. Solids* **30**, 2679 (1969).
20. GOBRECHT H., *Ann. Phys.* **31**, 755 (1938) *Ann. Phys.* **28**, 673 (1937).
21. GOUDSMIT S., *Phys. Rev.* **31**, 946 (1928).
22. CONDON E. V. and SHORTLEY G. H., *The Theory of Atomic Spectra*, p. 193. Cambridge University Press, Cambridge (1935).
23. JUDD B. R., *Proc. phys. Soc.* **A69**, 157 (1956).
24. ARAJS S., *Phys. Rev.* **120**, 756 (1960) et *Phys. Rev.* **122**, 14 (1961).
25. NÉEL L., *Ann. Phys.* **5**, 232 (1936).
26. HERPIN A., *Théorie du Magnétisme*, PUF 1968, p. 491.
27. MARESCHAL J., SIVARDIERE J., de VRIES G. F. et BERTAUT E. F., *J. appl. Phys.* **39**, 1364 (1968).
28. HOLMES L., SHERWOOD R. et VAN UITERT L. G., *J. appl. Phys.* **39**, 1373 (1968).

J. Phys. Chem. Solids Pergamon Press 1970. Vol. 31, pp. 685–700. Printed in Great Britain.

ONE PHONON ABSORPTION FROM ALUMINIUM COMPLEXES IN SILICON COMPENSATED BY LITHIUM OR ELECTRON IRRADIATION

S. D. DEVINE and R. C. NEWMAN
J. J. Thomson Physical Laboratory, Whiteknights, Reading RG6 2AF, England

(*Received* 16 *June* 1969)

Abstract—Silicon containing 10^{19} atom cm^{-3} of aluminium has been compensated by (a) lithium diffusion and (b) irradiation by 1·5 MeV electrons. The one phonon band mode absorption has been measured in both types of sample which contain $Al^{-}(s)$–$Li^{+}(i)$ and $Al^{-}(s)$–$Al^{2+}(i)$ pair defects respectively; the latter centre has been identified by EPR measurements. In the lithium compensated sample in-band resonances were observed at 520 cm^{-1} due to Li and at 469 cm^{-1} and 431 cm^{-1} due to the paired $Al^{-}(s)$. A resonant mode at 242 cm_{-1} has been ascribed to the vibrations of $Al^{2+}(i)$ in the irradiated sample and this is compared in detail with the similar lithium mode. This sample also showed marked absorption features characteristic of the critical point structure of the silicon density of states. These measurements are compared with neutron scattering data and previously measured one phonon absorption. The initial removal rate of $Al^{-}(s)$ by the irradiation as determined from resistivity measurements had the very high value of 2 atom per electron -cm. Interesting surface effects were also observed in these measurements and related to the diffusion of defects; the activation energy of diffusion of $Al^{2+}(i)$ has been estimated to be about 1·2 eV. These results give further information about the products of the electron irradiation damage process, and also about the one phonon absorption associated with vacancy and interstitial impurity complexes.

INTRODUCTION

THE PRESENCE of a defect in a homopolar crystal such as silicon modifies the normal modes of vibration and destroys the translational symmetry of the lattice. The modified modes may be either similar to the unperturbed modes of the perfect lattice (Band modes) or be at higher frequencies than the Raman frequency ω_M when light impurities are present (Localized modes). In general, there will be corresponding one-phonon absorption which is in the form of a continuum up to ω_M[1, 2] and discrete lines at the frequencies of any localized modes[1, 3, 4]. The simplest model used to describe this absorption is that of Dawber and Elliott[5, 6] who considered defects consisting of isolated impurities of different mass from the host lattice atoms, but where all force constants were unchanged. The band mode absorption for this model was shown to be proportional to the density of states of the unperturbed lattice multiplied by a frequency dependent dipole moment which is characteristic of the mass of the impurity. An 'in-band resonance' or 'pseudolocalized mode' can occur if a resonant vibrational mode of the impurity happens to fall at a frequency where the density of lattice modes is very small. More general types of defects, including for example changes in force constants, have been shown to lead to similar effects[7, 8]. That is, the absorption is expected to show peaks corresponding to the critical point structure of the density of states of the pure host lattice as well as to other features characteristic of the impurity. In principle therefore, the one phonon band mode absorption may be used to study particular defects as well as the more commonly investigated localized mode structure arising from light atoms.

Such effects have been very elegantly demonstrated by Angress, Goodwin and Smith [1, 2] in a study of the i.r. absorption of silicon containing boron and various donor impurities. In particular, by comparing the spectra of compensated samples containing B/P, B/As or B/Sb, they were able to assign some of the absorption peaks in the band mode region to the presence of specific impurities. For example a strong and relatively sharp peak at 441 cm^{-1} was unambiguously related to an in-band resonance due to phosphorus. Other features were however common to all samples, and could be related to critical points of the phonon dispersion curves.

A major problem in these studies is that the free carrier absorption associated with the electrically active impurities has to be eliminated in order that the much weaker vibrational absorption can be detected. This can be achieved by using compensated samples which have been prepared in previous investigations by (a) growing them with almost equal concentrations of donor and acceptor impurities and subsequently producing complete compensation by electron irradiation[1, 2, 9] or by lithium diffusion[10], (b) by lithium diffusion alone to form ion pairs with grown-in acceptor impurities[11–13] or (c) by irradiation with fast neutrons[1, 2].

It has also been shown that electron irradiation of silicon containing low concentrations of aluminium leads to the formation of interstitial aluminium double donors[14, 15]. This suggests the possibility that silicon doped with aluminium alone may be compensated by this process. In this paper we show that this is indeed the case even when the aluminium concentration is as high as 10^{19} cm^{-3}. At this level there is appreciable one-phonon band mode absorption which will be described in detail and related to the defects present in the same samples as determined by the electron paramagnetic resonance (EPR) technique. The latter measurements showed that all the $Al^{2+}(i)$ ions were paired with normal substitutional aluminium acceptors[14] and hence the one phonon absorption has to be interpreted in terms of defect pairs[8], rather than isolated impurities[5, 6]. Consequently the one-phonon band mode absorption arising from $Al^{-}(s)$–$Li^{+}(i)$ ion pairs has also been investigated due to the similar nature of the defect centres in the two cases. The latter samples were prepared by a simple lithium diffusion process which is known to lead to complete ion pairing, both from electrical measurements[16] and by analogy with the observed local mode absorption in boron doped crystals[11–13, 17]. The present results are therefore of considerable interest from two points of view: they represent the first examples of observed band mode absorption from pairs of impurities in a semiconductor and secondly the results obtained from the electron irradiated sample shed further light on the damage process itself.

2. DETAILS OF SAMPLES AND TREATMENTS

2.1 *Aluminium concentration*

The single crystal material used in this investigation was prepared by the temperature gradient zone melting process[18] to obtain high aluminium and low oxygen concentrations respectively. The room temperature resistivity measured by the standard four probe technique was $1{\cdot}1 \times 10^{-2}$ Ω-cm. Conversion of this value into a concentration [C] of aluminium was complicated by the large scatter in previously reported data[19]. Thus from the results of Horn[20], who related the resistivity of various samples doped with boron to their boron contents, a value of $[C] \simeq 4 \times 10^{18}$ cm^{-3} was obtained. Horn's results were reanalysed later by Carlson[21], who concluded that the concentrations originally quoted should have been higher by about 20–30 per cent because too large a value of the hole mobility had been assumed. However, the boron concentrations were only determined by *direct* chemical methods for two samples containing approximately 0·3 and 0·1 at. per cent boron, and the concentrations in the other less highly doped crystals, relevant to the present problem, were obtained by an extrapolation process. These results are not in very good agreement with those of Backenstoss[22] who measured the resistivity in several samples containing gallium at a rather lower level and determined the gallium concentration by the neutron activation process. In addition, a comparison of different acceptor impurities was made to find the effect of differing acceptor ionization energies. Unfortunately the concentrations of impurities used in this work, which has been substantiated by the later investigation of Fuller, Doleiden and Wolfstirn[23], were smaller than in the present aluminium doped crystal. Extrapolation of the curves of Backenstoss would however indicate [C] $\simeq 2 \times 10^{19}$ cm^{-3}, which is *five* times greater than our first estimate and still four times greater than the value obtained with Carlson's correction. It is not clear how to make a definitive choice between these values, although it is thought that the latter measurements are the more reliable particularly in view of the discussion presented in Section 7. Consequently, a compromise value of [C] $\simeq 10^{19}$ cm^{-3} will be adopted at this stage. It is clear that estimates of the defect introduction rates produced by the electron irradiation (Section 5) and the apparent charges of defects giving rise to the observed i.r. absorption (Section 7) are subject to an uncertainty directly related to that of [C] itself. It is for this reason that this somewhat lengthy discussion has been given.

2.2 *Details of irradiation*

Two samples about 1 mm in thickness, nominally held at room temperature on a water cooled block, were irradiated with 1·5 MeV electrons at a current density of 12·4 μA/cm^2 in successive stages. The maximum temperature rise as monitored by a thermocouple in contact with the samples was 30°C. After each dose of irradiation the resistivity of one of the samples with ground faces was remeasured (see Fig. 1) and the transparency of the second sample, which had optically polished faces, was checked in the wavelength range 5–20 μm. For doses greater than about 6×10^{18} electrons cm^{-2}, the measured resistivity did not appear to increase as rapidly as was expected from an interpolation of the measurements for the lower doses. This was found to be due at least in part to surface effects, since a significantly higher resistivity was measured after the removal of a relatively thin surface layer by grinding; the higher values are those shown in Fig. 1. After the total dose of $1 \cdot 3 \times 10^{19}$ electrons cm^{-2} the apparent change in resistivity after grinding was from 50 to 100 Ω-cm. Similar effects were also apparent in the optical measurements on a second sample. A low background absorption was only obtained after regrinding and repolishing the surfaces. It is concluded from these results that the total irradiation dose of $1 \cdot 3 \times 10^{19}$ electrons cm^{-2} given to these samples is sufficient to remove essentially all of the free carriers (holes) originally present, but that the process is less efficient near the surfaces than in the bulk.

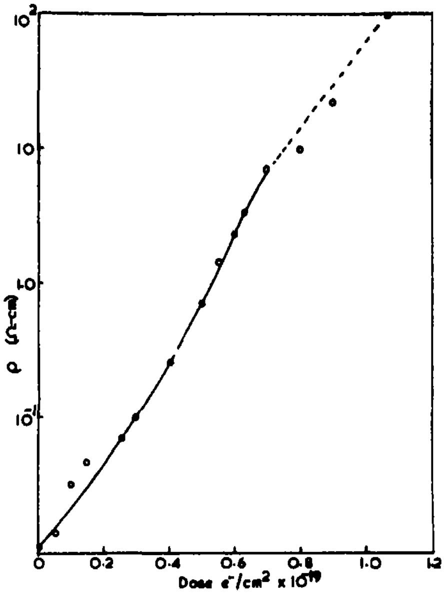

Fig. 1. Variation of sample resistivity as a function of electron irradiation dose.

2.3 *Lithium diffusion*

Samples were saturated with lithium according to a process similar to that described by Spitzer and Waldner[12]. Wafers were coated with a lithium suspension in oil and pre-alloyed at 600°C in an argon atmosphere. The main diffusion was carried out at about 850°C for several hours and the samples were cooled to room temperature in a few minutes. These samples showed some small residual free carrier absorption which could be largely removed by a very small dose of electron irradiation of up to 10^{18} electrons cm^{-2}.

3. I.R. MEASUREMENTS

Measurements were made on the irradiated and lithium compensated Al/Si samples from the absorption edge to 400 cm^{-1} using a Grubb Parsons Spectromaster double beam grating spectrometer. In the region from 550 to 100 cm^{-1} an f/4 Czerny Turner single beam vacuum grating spectrometer was used to obtain spectra at 300 and 80°K with a resolution of 2 cm^{-1} at short wavelengths and 5 cm^{-1} at the longer wavelengths. No absorption was detected at 9 μm due to oxygen[24], at 12 μm due to oxygen-vacancy complexes[25] or at 10 μm due to lithium–oxygen pairs[13]. Similarly there was no detectable local mode absorption due to carbon[3, 4, 26]. The results confirm that the method of sample growth used did not lead to the introduction of carbon and oxygen impurities.

Very strong absorption was present in the irradiated Si/Al sample from the absorption edge to about 4 μm with an absorption coefficient of more than 100 cm^{-1}. The one phonon spectra of both types of Si/Al samples are shown in Fig. 2 together with that of a neutron irradiated sample of pure silicon with which comparison will be made in a later section[27].

A measurement of the absorption at 550 cm^{-1} of the irradiated sample at 77°K showed that the free carrier absorption coefficient was not greater than 3 cm^{-1} and further measurements at higher energies showed that the background absorption was decreasing with increasing wavelength. It follows that the absorption coefficient due to free carriers at energies lower than the Raman edge is probably everywhere less than 3 cm^{-1}. This enables us to estimate the total integrated absorption for this sample up to the Raman frequency as

$$\int_0^{\omega_m} \alpha(\bar{\nu}) d\bar{\nu} = 2 \times 10^3 \ cm^{-2}.$$

At room temperature the form of the spectrum was unchanged in every respect except for a broadening of some of the features and a very marked increase in the background absorption both above and below the Raman frequency. The high background absorption necessitated the use of larger slitwidths to obtain the measurements and this could well have accounted for the apparent broadening of the lines. Because of this high background absorption it was not possible to estimate whether the remaining integrated absorption up to the Raman edge at room temperature was identical with that at low temperature. However the two sets of measurements were not inconsistent with this possibility.

The lithium compensated sample showed a relatively low background absorption with $\alpha = 3 \ cm^{-1}$ at room temperature and consequently only a few measurements were carried out at 77°K. The integrated absorption up to the Raman edge in this sample, after subtracting a reasonable contribution for free carrier effects and that due to intrinsic two phonon processes, was $10^3 \ cm^{-2}$. Thus the impurity induced absorption in this sample was only about one half of that in the former. The absorption in the lithium compensated sample may well have been smaller if it had not received a small dose of irradiation. However, under these circumstances the free carrier absorption was very large and would have made an estimate of the remaining integrated absorption totally unreliable.

4. EPR MEASUREMENTS

Measurements were carried out at X-band with a sample mounted on the side of a rectangular H_{011} cavity fabricated from pyrophyllite and with a slot cut adjacent to the sample so that it could be illuminated with tungsten light from a small bulb in the micro-

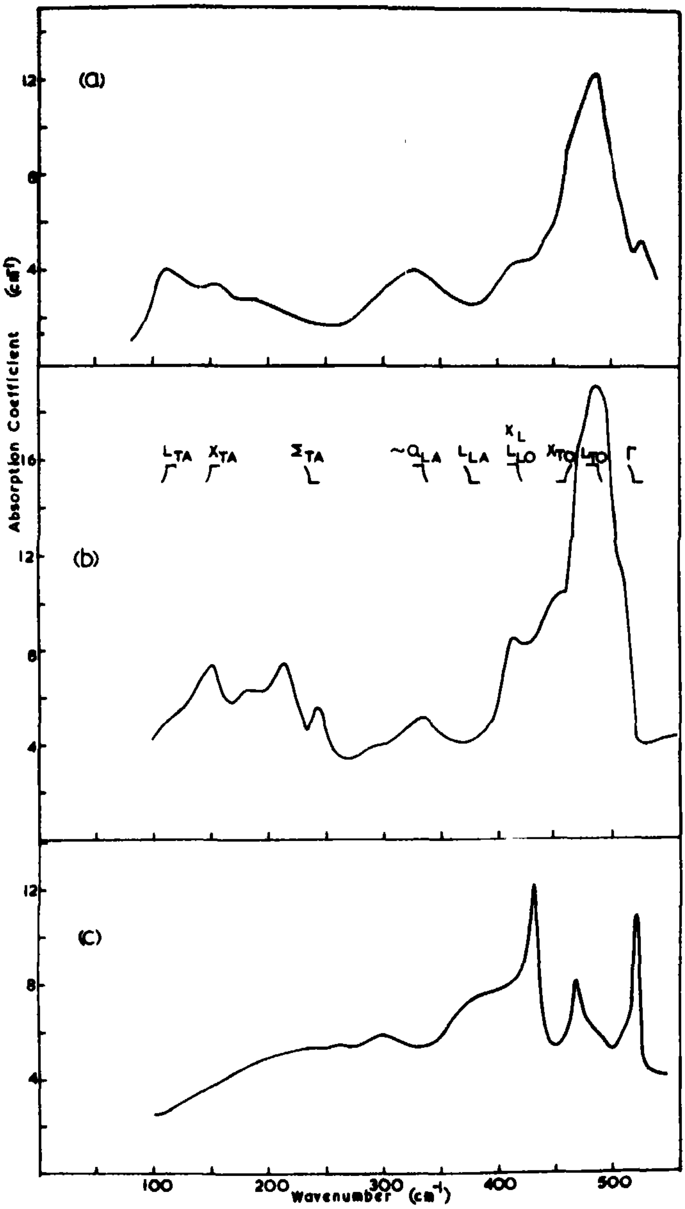

Fig. 2. I.r. spectra (a) Pure silicon after fast neutron irradiation to a dose of 9·3 × 10^{18} neutrons cm^{-2} (300°K)[27]. (b) Aluminium doped silicon after 1·5 MeV electron irradiation to a dose of 1·1 × 10^{19} electrons cm^{-2} (77°K). (c) Aluminium doped silicon compensated by lithium diffusion (300°K).

wave assembly. 100 kc/sec modulation was used with the spectrometer tuned for absorption which gave rise to absorptionlike recorder traces rather than the usual derivative of absorption due to rapid passage effects[15] at 4·2°K.

It should be made clear that the purpose of these measurements was to attempt to establish the nature of some of the defects present in the *same* samples as had been used in the i.r. measurements. Thus specially oriented samples were not examined and no detailed angular variations have been carried out. In spite of this limitation, the results obtained were quite unambiguous in certain respects.

A typical spectrum obtained with a random sample orientation relative to the direction of the magnetic field is shown in Fig. 3. The spectrum consists of six distinct groups of closely spaced and incompletely resolved lines, together with an extra absorption line at 3350 G ($g = 2$). It may be noted immediately that there is *no* spectrum present due to isolated $Al^{2+}(i)$ impurities (Si-G 18,[14] see Table 1) which consists of six 'approximately' equally spaced lines[15] due to the hyperfine interaction of the s-state electron with the 100 per cent abundent Al^{27} (I 5/2) nucleus. Illumination of the sample with tungsten light also failed to give any indication of the presence of the [V + Al] pair spectrum described previously by Watkins[15]. The main spectrum with the six groups of lines could be fitted to the spin Hamiltonian

$$\mathcal{H} = \beta S \cdot \mathbf{g} \cdot H + \sum_j S \cdot \mathbf{A}_j \cdot I_j$$

where the parameters are those appropriate to the $Al^-(s)$–$Al^{2+}(i)$ centre[14] (SiG 19); these are reproduced in Table 1 together with those for $Al^{2+}(i)$ (SiG 18) and a similar pair spectrum SiG 20 also observed previously by Watkins[14]. It is seen that although the pair centres are anisotropic, as is required by their C_{3v} symmetry, the differences in the magnitudes of the various parameters along the two principal axes are very small; thus to a very good approximation the centres may be regarded as being isotropic with averaged parameters. The width of each group of lines is determined by the hyperfine parameter of the substitutional aluminium ion in the pair and should be about five times the value of the relevant hyperfine parameter. The measured

Table 1. *EPR parameters for* Al^{2+}(i) *and aluminium pair spectra*[14]

	Model	g	A(cm^{-1})	Nucleus
SIG 18	$Al^{2+}(i)$	2·0019 isotropic	A^i 440·6	$Al^{27}(i)$
SiG 19	$Al^{2+}(i) + Al^-(s)$	2·0006 2·0009 2·0009	$A^i_\parallel = 396{\cdot}0$ $A^i_\perp = 392{\cdot}8$	$Al^{27}(i)$ [111]
		[111]	$A^s_\parallel = 13{\cdot}3$ $A^s_\perp = 12{\cdot}0$	$Al^{27}(s)$ [111]
SiG 20	$Al^{2+}(i) + Al^-(s)$	2·0014 2·0025 2·0025	$A^i_\parallel = 389{\cdot}5$ $A^i_\perp = 386{\cdot}5$	$Al^{27}(i)$ [111]
		[111]	$A^s_\parallel = 42{\cdot}7$ $A^s_\perp = 42{\cdot}2$	$Al^{27}(s)$ [111]

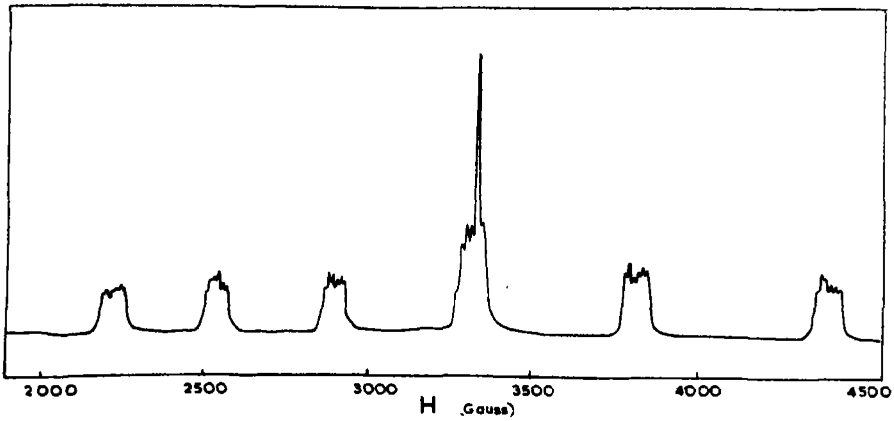

Fig. 3. EPR spectrum of irradiated aluminium doped silicon at 4·2°K and 9·3 Gc/s; random orientation.

widths were all in the range 65–75 G which are consistent with a value of $A_s \simeq 12\cdot5 \times 10^{-4}\,\mathrm{cm}^{-1}$ (SiG 19), giving an expected width of 65 G, but *not* with $A_s \simeq 42\cdot5 \times 10^{-4}$ (SiG 20). A value of $A_t \simeq 388 \times 10^{-4}\,\mathrm{cm}^{-1}$ leads to an overall spread in the positions of the groups of lines which is also in agreement with the observations. The value of $A_t \simeq 441 \times 10^{-4}\,\mathrm{cm}^{-1}$ for Al^{2+}(i) (SiG 18) is sufficiently different compared with that for the SiG 19 spectrum for there to be no possibility of the transitions due to the former centre being obscured by the presence of a somewhat stronger pair spectrum.

The origin of the second spectrum centred on $g \simeq 2$ has not been determined, although it appears to have $S = 1/2$ as there were no obvious fine structure effects. The centre could well involve a vacancy for reasons discussed in the following section, but [V + O] and [V + carbon] centres can be ruled out as neither the irradiated nor the lithium diffused samples showed any detectable amounts of oxygen or carbon. A possibility not inconsistent with the i.r. absorption measurements is that it is due to divacancies.

Finally, it is recognised that the absence of the [V + Al] spectrum may have been due to saturation effects, although this is thought to be unlikely in such a heavily doped sample. However, the method of observation was not ideal and further measurements using somewhat different techniques would be necessary to arrive at an unambiguous conclusion. Alternatively, the illumination of the present sample by the tungsten lamp may have been quite ineffective because of the exceedingly strong i.r. absorption in the relevant spectral region (see Section 3); that is, [V + Al] centres may have been present but kept in darkness due to absorption from divacancies for example.

5. THE DEFECTS PRESENT IN THE IRRADIATED SAMPLES

Before discussing the nature of the centres in our irradiated samples, it will be helpful to review briefly the results of Watkins relating to more lightly aluminium doped crystals in the 10^{5}–$10^{16}\,\mathrm{cm}^{-3}$ range[14, 15]. After irradiation of oxygen free samples with 1·5 MeV electrons at room temperature, the EPR technique was used to reveal aluminium vacancy pairs [V + Al] and isolated interstitial aluminium double donors Al^{2+}(i). These results were clarified by other irradiations carried out with the sample at 4·2°K. At this temperature, the production rate of Al^{2+}(i) was found to have the same value of 0·03 centres/cm^3 per electron/cm^2 as that of isolated primary vacancies. To explain this result it was suggested that the primary interstitial silicon atoms were mobile even at 4·2°K and became trapped by substitutional aluminium impurities. The two atoms were than assumed to interchange positions, leaving the aluminium in an interstitial site. On annealing these samples at 170°K, the isolated vacancies became mobile and were also trapped by substitutional aluminium atoms to give [V + Al] complexes. A rather surprising result was that the concentration of the Al^{2+}(i) centres did not decrease during this treatment, showing that they did not recombine with the mobile vacancies. The centres in these annealed samples were thus the same as those produced by a room temperature irradiation and no further changes occurred until the sample temperature was raised to about 200°C. An anneal in this range led to a decrease in the strength of the [V + Al] and the isolated Al^{2+}(i) centres and the formation of pairs of two different types (Table 1).

These latter results are easily understood if it assumed that the Al^{2+}(i) ions became mobile in this temperature range, as was originally suggested by Watkins[14] and that they then form ion pairs with Al^{-}(s). It is interesting to note that 200°C is close to the maximum temperature for which such pairs might be expected to remain stable. Application of the law of mass action

$$\frac{[\mathrm{Al}^-(\mathrm{s})-\mathrm{Al}^{2+}(\mathrm{i})]}{[\mathrm{Al}^-(\mathrm{s})][\mathrm{Al}^{2+}(\mathrm{i})]}=A\exp(-\Delta E/kT)$$

to the case where the total aluminium atom fraction is 2×10^{-7}, requires the binding energy ΔE to be about 0·8 eV for half of the aluminium ions to be paired assuming[17] a value of $A\sim10^{-1}$. This is not unreasonable since the binding is due to a Coulomb interaction

$$\Delta E=q_1q_2/\epsilon r$$

where $q_1=-e$ and $q_2=2e$ and where a value of $\Delta E\simeq0{\cdot}4$ eV has been obtained for B^-–Li^+ pairs[17] with $-q_1=q_2=e$.

The difference between these results and those described in Section 4 can then only be due to the very different impurity levels present in the two types of sample. This is not unexpected, since an increase in the impurity concentration has two important effects which are not entirely unrelated: (a) in a given time a diffusing impurity ion is more likely to encounter a substitutional negative ion trap purely on a statistical basis and (b) the mobile ion is more likely to be within the "capture radius" of the substitutional ion[28]. The latter quantity R is defined so that the interaction energy at this distance is equal to the thermal energy kT; that is $R=-q_1q_2/\epsilon kT$. From the above arguments that $\Delta E\simeq0{\cdot}8$ eV, it is easily seen that $R\simeq70$ Å at $T\simeq50$°C, if the closest distance of approach of the ion pairs is taken as 2·6 Å which is the value for B^-–Li^+ pairs[17] (N.B. the ionic radius of Al^{2+} and Li^+ are very similar as discussed below). In any case, it is clear that R is very much greater than the mean separation of aluminium ions r_0 of only 17 Å in the present samples so that correlated ion pairing is to be expected to be complete in a time given by[28]

$$\tau=\epsilon kTr_0^3/3Dq_1q_2=(4\pi NRD)^{-1}$$

where D is the diffusion coefficient of the Al^{2+}(i) and N is its concentration; it has been assumed here that the concentration of Al^-(s) is greater than that of Al^{2+}(i). This expression is also applicable to the samples used by Watkins[14] on the assumption of correlated pairing and hence it may be used to obtain some estimate of the activation energy of D. The ratio of the aluminium concentrations is about 10^4 and so it follows that

$$D(50°)\tau_1\simeq10^{-4}D(200°\mathrm{C})\tau_2$$

where τ_2 was the time of the anneal given in the Watkins experiment, and τ_1 the time the present sample was at 50°C during its irradiation. τ_1 was of the order of 100 hr and it is assumed that $\tau_2\simeq1$ hr to give $D(50°\mathrm{C})\simeq10^{-6}D(200°\mathrm{C})$, which in turn yields an activation energy of 1·25 eV. This is typical of values found previously for interstitial iron [29], gold and copper ions[30] but is significantly larger than the value[31] of 0·66 eV for Li^+(i). This difference would then explain the lack of ion pairing in Watkins samples at lower temperatures.

During a study of B–Li ion pairing, Pell and Ham[28] observed a surface effect similar to that described in Section 2. They ascribed this to diffusion of mobile lithium ions to the external surface where they presumably combined with oxygen and were 'lost'. As a result, the surface of the sample remained p-type with a low resistivity due to the presence of uncompensated boron impurities. Similar behaviour has also been observed previously at much higher temperatures, where substitutional diffusion occurs, in compensated samples containing aluminium and phosphorus; in this case it is the aluminium which diffuses out of the sample[32]. It follows that the present surface effects may be attributable to out diffusion of interstitial aluminium ions. However, it may be that primary interstitial silicon atoms diffuse to the surface rather than to impurity atoms in a thin surface layer to give essentially the same result. In either case, these observations are obviously of very considerable significance to measurements of the irradiation damage process itself based purely on changes in electrical conductivity, particularly if very thin samples are used.

Since our samples contained interstitial ions, there must have been a corresponding number of vacancies present in some form. If the concentration of [V + Al] centres was negligible it seems most likely that clustering of the vacancies occurred since no other impurities were present to act as vacancy traps. The simplest cluster is the divacancy which gives rise to strong electronic absorption bands at 1·8, 3·3 and 3·9 μm depending upon the position of the Fermi level in the band gap[33]. The present samples showed exceedingly intense absorption throughout this region of the spectrum and hence this centre could well have been present; this would also not be inconsistent with the observed $g \simeq 2$ EPR spectrum[14]. The difference between these samples and those of Watkins is not so clear in this context. However the production rate for divacancies could be much higher due to the very much higher aluminium content of the samples; such effects have been noted previously in relation to oxygen impurities[34] and more recently by us[35] in crystals containing high concentrations of carbon. The presence of vacancy centres is also indicated by the substantial increase in free carrier absorption during a 20 min isochronal anneal at about 200°–230°C, the samples became completely opaque again after an anneal at 260°C. This behaviour is almost certainly to be ascribed to reconversion of $Al^{2+}(i)$ to normal $Al^{-}(s)$ sites by recombination with vacancies. In fact, annealing in this temperature range could be predicted; since the $Al^{-}(s)$–$Al^{2+}(i)$ pairs would dissociate completely at about 250°C if the estimated parameters given above are reasonably accurate.

Although there was no evidence for the presence of any other centres, it is interesting to speculate that some recombination of transient [V + Al] centres with Al(i) did take place at the temperature of irradiation to produce pairs of substitutional aluminium ions. Evidence for this type of centre in samples containing boron has been obtained from a study of its localized modes of vibration[9, 36]. Unfortunately the corresponding [Al–Al] centre would only be expected to make a small contribution to the one phonon band mode absorption and would not be detectable; likewise the centre is probably not paramagnetic. [Al(s)–Al(s)] or residual isolated Al(s) centres must be present however to achieve overall charge neutrality in the crystal because each interstitial Al ion is a double donor and it is extremely unlikely that there will be a *double* negative charge associated with each vacancy; this would require for example $[V + V]^{4-}$ which appears to be unrealistic.

Finally, we shall consider the introduction rates of the defects in the present crystals. For each aluminium acceptor transferred to an interstitial site ($Al^{2+}(i)$) there is a direct nett loss of three holes from the valence band. It will be further assumed that the simultaneously created vacancy also acts as a hole trap to give a total loss of four holes per displacement. Since a total dose of $1{\cdot}3 \times 10^{19}$ electrons cm^{-2} removed essentially all of the carriers, it follows that the *average* displacement rate of aluminium atoms is about 0·2 cm^{-1}. If it is further assumed that there is no significant change in the hole mobility after the initial electron dose of 5×10^{17} cm^{-2}, then the initial displacement rate is found to be about 1·5 aluminium atoms cm^{-3} per electron cm^{-2}. This value may be compared with the "high" value of 0·03 cm^{-1} obtained by Watkins[14] in his less highly doped samples. This present value is not however unusually high in heavily doped crystals since Angress *et al.*[1] have previously reported a loss of 10^{19} atom cm^{-3} of both boron and phosphorus from unperturbed substitutional sites after an electron dose of only 5×10^{18} cm^{-2} in crystals containing both impurities in an original concentration of 5×10^{19} cm^{-3}. This corresponded to a 20 per cent reduction in the absorption co-efficients of i.r. absorption bands directly attributable to these impurities. Watkins has already pointed out that impurities play a very significant role in determining the nature of the irradiation damage[14, 37]. It is now seen that the damage process is almost *completely dominated* by the impurities when these are present in a higher concentration. In fact, if the initial aluminium content of our samples were as high as $2 \times 10^{19}\,\mathrm{cm}^{-3}$ (see Sections 2 and 7) the experimental introduction rates above would have to be doubled. Thus the present defect introduction rates would be very close to the *maximum* values possible[38] for vacancy-interstitial pair formation by electrons with energies in the range 1·5–2 MeV.

6. FREQUENCY DEPENDENCE OF I.R. ABSORPTION

Inspection of Fig. 2 shows that the i.r. absorption of the electron irradiated sample is quite different from that of a sample which has been compensated by a lithium diffusion, although the former closely resembles that of the neutron irradiated pure crystal. In the lithium compensated crystal, all the substitutional aluminium impurities are expected to be paired with interstitial lithium ions by analogy with the behaviour of compensated crystals containing boron[11–13]. Similar pairing of substitutional aluminium with interstitial aluminium ions has also been shown to occur in the irradiated sample and it is for this reason that the two types of spectra will be compared both in terms of their frequency dependence and their absolute integrated absorption.

6.1 *Effects due to the silicon lattice*

In the introduction it was pointed out that some features of one phonon band made absorption are expected to be closely related to the critical points in the phonon dispersion curves for pure silicon, while other features will be quite specific to particular impurities in particular configurations. These two contributions may be distinguished, at least in principle, by comparison of spectra from samples containing quite different defects. The former contribution to the present observations will now be considered in more detail.

Phonon dispersion curves for silicon have been obtained from neutron scattering measurements[39] along the directions *X*, *L*, and Σ in reciprocal space and certain well-defined critical points are thereby immediately determined (Table 2). These curves are however incomplete for the line Σ as both the *TA* and *TO* modes should be split into two curves

Table 2. Critical point energies and assignments for the silicon lattice

Critical point assignments	Phonon dispersion curves (cm^{-1})	Additional critical points (cm^{-1})	*Critical point energies* Electron irradiated Si/Al (cm^{-1})	Neutron irradiated Si (cm^{-1})	*B*/*P* doped Si (cm^{-1})
Γ	518		520	517	520
L_{TO}	489		487	485	491
X_{TO}	463		460	460	462
L_{LO}	420				425
X_{L}	412		415	416	
L_{LA}	378		~ 375	~ 375	376
near Q_{LA}		340	335	334	331
Σ_{TA_1}	228		235		
Q_{TA}		209	212	212	
(?) Σ_{TA_2}		~ 162	164		
X_{TA}	150		150	152	
L_{TA}	114		112	112	

because of symmetry considerations, whereas only single curves have been determined from the experimental observations. In addition, topological and symmetry arguments indicate that there are critical points for other directions in reciprocal space. For example Bilz *et al.*[40], show that the *LA* frequency at *L* will be a maximum so that any path connecting *X* to *L* for this branch must pass through a critical point as the frequency at *X* is greater than that at *L*. The high density of states calculated at 340 cm^{-1} by Dolling and Cowley[41] is probably due to the contribution of these critical points. In addition, along the line *Q* in the hexagonal face of the Brillouin zone, both the *TA* and the *TO* branches are split into pairs[42]. As a consequence it has been shown that at least one branch of each pair must have a maximum or a minimum which will give rise to at least one critical point. The frequencies of these points are unknown, although the frequency of the Q_{TO} critical points are expected to lie just below L_{TO}, somewhere near 480 cm^{-1}. Similarly, the frequencies of the Q_{TA} critical points are expected to be near 200 cm^{-1}. The peak in the calculated density of states at 209 cm^{-1}[41] is likely to be the maximum along one of the *TA* branches. These additional critical points are also listed in Table 2.

Topological arguments have been used to determine the form of the frequency dependence of the density of states curve around the critical points listed[39, 42]. The corresponding one phonon absorption is expected to have a similar frequency dependence. Features in the spectrum of the irradiated Si/Al may now be related to the critical point structure discussed above as shown in Table 2 and Fig. 2. The correctness of these assignments is indicated by the fact that the one phonon spectra of samples containing other impurities also show similar features at very similar energies; data for compensated boron doped and neutron irradiated silicon respectively are also shown for comparison in Table 2. All three types of sample show a peak near 340 cm^{-1} supporting the conclusion that this corresponds to the critical point of the LA branch already discussed. The spectrum of neutron irradiated silicon at 77°K obtained by Balkanski and Nusimovici[43] shows a very small peak at 212 cm^{-1} which probably corresponds to the line at 214 cm^{-1} observed in our electron irradiated sample. This would imply that the latter line is not due to an in band resonance but that it should be assigned to the critical point along Q_{TA}.

The lithium compensated Si/Al spectrum however shows no features that are obviously due to critical point contributions. This has also been found in a previous investigation of silicon containing boron–lithium ion pairs[11].

6.2 *In-band resonances due to impurities*

The assignments made in the previous section cannot account for the peaks at 242 cm^{-1} and the shoulder at 455 cm^{-1} in the electron irradiated sample, or the three sharp lines in the lithium compensated sample (see Fig. 2). It will be convenient to discuss the lithium compensated sample first, since the Al–Li system is analagous to the now well understood B–Li system and the absorption due to the lithium is expected to be similar in the two cases.

6.2.1 *Lithium compensated Si/Al.* The line observed at 520 cm^{-1} (Fig. 2), briefly referred to previously by Spitzer and Waldner[12], is to be ascribed to the vibrations of interstitial lithium ions paired with substitutional aluminium acceptors. A similar line has also been observed in compensated silicon containing either gallium or boron, and Spitzer and Waldner[12] have shown that the strength of this line increases linearly with boron content in the latter samples. The frequency of this vibrational mode is not very dependent on the type of acceptor present as shown in Table 3, presumably because the interaction is predominantly coulombic and of a similar magnitude for all three types of ion pairs. The vibrations of an isolated lithium inter-

Table 3. ***Resonant frequencies of*** ^{6}***Li and*** ^{7}***Li isotopes paired with acceptor impurities in silicon***

*B–^{7}Li	522 cm^{-1}	*Ga–^{7}Li	515 cm^{-1}	Al–^{7}Li	520 cm^{-1}
B–^{6}Li	534 cm^{-1}	Ga–^{6}Li	521 cm^{-1}	Al–^{6}Li	525 cm^{-1}

*Spitzer and Waldner[12].

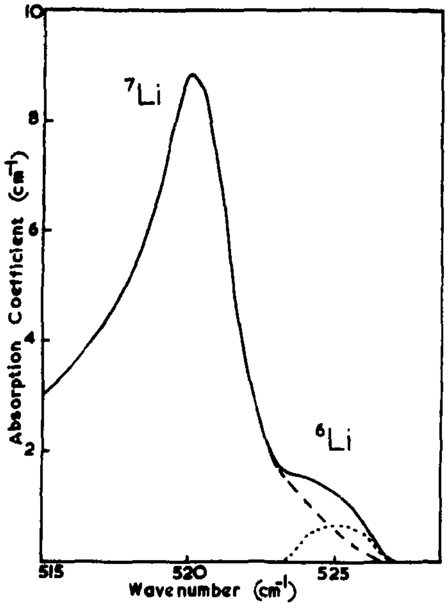

Fig. 4. Absorption near the Raman edge due to ^{6}Li and ^{7}Li isotopes paired with aluminium.

stitial ion should be triply degenerate because of the tetrahedral symmetry. When ion pairing occurs the symmetry is lowered to C_{3v}, and there should be two modes which predominantly involve motion of the lithium ion. It follows that two absorption bands should be observed. However the second band has not been detected in measurements extending to 350 cm^{-1}[11] and neither has a band due to isolated lithium interstitial ions[44]. It may be that these modes occur at frequencies where the density of lattice modes is very high.

From the frequency of the lithium resonances, Elliott and Pfeuty[8] have calculated that the force constant for the interstitial lithium ion should have the value $\beta \sim 23$ kergs cm^{-2}, which is less than half that of a substitutional silicon atom (56 kergs cm^{-2}). It will be shown that a similar value of the force constant may also be appropriate to the interstitial Al^{2+}.

The line in the present sample showed a shoulder at 525 cm^{-1} (80°K) which is almost coincident with the position of the Raman frequency at this temperature (Fig. 4). The ratio of the estimated absorption in this peak to the main peak at 520 cm^{-1} was about 1 : 13. It is therefore reasonable to attribute these two peaks to the vibrations of the naturally occurring ^{6}Li and ^{7}Li isotopes, in which case, the ratio should be 1 : 12·35. The isotope shift of 5 cm^{-1} is then very close to that of 6 cm^{-1} found for the Ga–Li system[12]. However both these systems lead to a smaller splitting than is found in boron doped samples. In the latter case, the ^{6}Li vibrational frequency is in the local mode region whereas in the former case the ^{6}Li and ^{7}Li peaks are both in the band mode region. This could well be the reason for the apparent discrepancy.

It would appear that the two strong lines at 469 cm^{-1} and 431 cm^{-1} have to be ascribed to in-band resonances of Al(s) paired with lithium since these lines are neither present in the irradiated sample, nor in samples containing boron–lithium pairs[11]. The latter result, together with the fact that such lines are not produced by an electron irradiation of lithium doped silicon[44], precludes the possibility that they are due to lithium vibrations. The occurence of two lines separated by 38 cm^{-1} is what might be expected because of the C_{3v} symmetry of the centre, and the previously observed splitting of the triply degenerate localized mode of boron when it is similarly paired with an interstitial lithium ion. In the latter system, the separation of the two localized modes is 94 cm^{-1} but their centre of gravity is the same to within experimental error as that of isolated boron[11, 12]. If this result were also true for the present sample it would lead to an estimate of 456 cm^{-1} for the position of the isolated aluminium in-band resonance. It is interesting to note that this frequency is somewhat higher than that of 441 cm^{-1} observed previously for isolated phosphorus impurities [1, 2] which would imply that the vibrational force constants for these two impurities would be of a very similar magnitude.

Reference to Fig. 2 shows that the resonant line at the higher frequency is the weaker of the two which is contrary to the observations on the localized vibrational modes of the boron–lithium system where the higher frequency line has been assigned to the doubly degenerate mode[11, 12]. The present results are not necessarily inconsistent with this interpretation since (a) reversals in relative intensities have been observed in other pair spectra in the local mode region[9, 10] and (b) the present lines are in the band region and occur at frequencies where the density of states will be different. In the latter context the low energy lines falls in a region between the optic and acoustic modes where the density of states is expected to be small, whereas the other line falls in a region where the density of states is expected to be higher. This result could then in itself account for the observations.

6.22 *Irradiated Si/Al sample.* In Section 5, it was concluded that this sample definitely contained Al(s)$^-$–Al(i)$^{2+}$ pairs, almost certainly contained some residual Al(s)$^-$ atoms, probably Al(s)$^-$–Al(s)$^-$ pairs and must contain vacancies in an unknown configuration. The expected contribution to the absorption of each of these will now be considered.

It will be shown first that the assignment of the peak at 242 cm^{-1} to paired interstitial aluminium ions leads to conclusions which are entirely consistent with those obtained for interstitial lithium ions. Since the mass of aluminium is close to that of silicon, the calculations of Elliott and Pfeuty[8] giving the energy of the in-band resonance of a silicon interstitial as a function of its nearest neighbours force constants, are pertinent. An energy of 242 cm^{-1} leads to a force constant $\beta = 21$ kergs cm^{-2} which is essentially identical with that found for interstitial lithium. In fact the ratio of the frequencies of vibrations for these two ions should then be in proportion to the inverse square root of their masses if both peaks are genuine pseudo-localized modes; this is almost exactly so. The similarity of the force constants for the two ions is perhaps not too surprising since they both exist in a positive charge state and both have similar ionic radii. The radius of Li$^+$ is known to be 0·60 Å, while the radii of Al^{3+} and Al$^+$ have been given by Pauling[45] as 0·50 and 0·72 Å respectively.

It might be expected that the absorption from the substitutional aluminium in the paired configuration could also be determined by analogy with the lithium–aluminium pair centre. In this case the coulomb interaction is expected to be twice as great as in the latter, and this might then lead to absorption peaks near 483 and 407 cm^{-1} respectively; it has again been assumed that the centre of gravity of the substitutional in-band resonance is not shifted as a result of the interaction. Such lines are not observed but a line near 480 cm^{-1} would be obscured by the strong TO critical point absorption, while 407 cm^{-1} is close to the critical points X_L and L_{LO} at 410 cm^{-1}.

The in-band resonance due to isolated substitutional aluminium has been estimated to occur at 456 cm^{-1}. It can be seen in Fig. 2 that there is a shoulder at 455 cm^{-1} which could be interpreted in this way. If this is so, the closeness of these two values must be regarded as being very fortuitous. However this shoulder could be due to quite different effects. Balkanski and Nusimovici[43] have reported a shoulder in the absorption coefficient of a neutron irradiated sample at 449 cm^{-1}, while an electronic absorption line due to aluminium should occur at 445 cm^{-1}.[46]. The other one phonon absorption arising from the isolated substitutional aluminium might be expected to follow the density of states of pure silicon fairly closely because of the similarity of the mass of the aluminium and silicon atoms[5, 6].

Similar considerations would apply to Al(s)–Al(s) pairs if they are present except that the acoustic modes would be favoured relative to the optic modes.

While no calculations have been made for the absorption expected from vacancies, either in isolation or in complexes with other impurities, their presence would certainly be expected to contribute to the overall absorption. Further comments relating to this will be made in Section 7.

7. THE MAGNITUDE OF THE I.R. ABSORPTION

7.1 *An optical determination of the aluminium concentration*

In the previous section it was established that the frequency of vibration of lithium ions paired with aluminium was very similar to that of lithium paired with boron; for the ^{7}Li isotope both frequencies were lower than the Raman frequency[47]. It follows that to a good approximation the concentration of Al–Li pairs in the present sample may be obtained by comparison with the corresponding data for B–Li pairs given by Spitzer and Waldner[12]. These authors calibrated the relevant ^{7}Li mode for a wide range of boron concentrations where there was no ambiguity over the interpretation of the room temperature resistivity measurements. These measurements in fact established a linear relationship for the strength of this band with boron content of the sample. If this calibration is applied to the present Al–Li sample, the aluminium concentration is found to be $2\times10^{19}\,\text{cm}^{-3}$. This is at the upper limit of that given in Section 2.

7.2 *Total integrated absorption*

7.2.1 *Theory.* The total integrated absorption arising from an impurity of mass M' may be characterized by an apparent charge η according to the relation

$$\int\alpha(\omega)\mathrm{d}\omega = \frac{2\pi^2\eta^2 D}{ncM'}$$

where D is the impurity concentration, c is the velocity of light, and n the refractive index of silicon. The quantity η is related to the effective charge e^* by

$$\eta = \Lambda e^*$$

where Λ is the effective field. Leigh and Szigeti[48] have shown that for a substitutional impurity in a homopolar crystal such as silicon, Λ is expected to be a much smaller factor than that given by the usual Lorentz expression, and that the static charge on the impurity atom is almost insignificant in determining the magnitude of the integrated absorption. What is important however is the charge sharing between the impurity and its nearest neighbours which then also contribute to the absorption.

These authors go on to show that there is another contribution to the total absorption not included above. This is due to long range polarization effects which only occur when charged impurities are present. In the present samples pairing of the charged impurities has been shown to occur, and it is therefore likely that these effects will be small due to the relative short range of the resulting dipolar fields. In any case, the calculated contributions from this process to the total absorption is of the order of 2 per cent of that observed even if no pairing had occurred.

These theoretical ideas have been developed for substitutional impurities and have been substantially verified by various measurements [1, 2]. However, there is at present no corresponding theory for vacancies and interstitial impurities.

7.2.2 *The measured absorption.* In the Li–Al sample the integrated absorption of 10^3 cm^{-2} (Section 3) leads to $\eta = 2{\cdot}4\,e$ per impurity pair assuming an aluminium concentration of $2\times10^{19}\,\text{cm}^{-3}$. From these measurements alone it is not possible to determine the relative contributions to the absorption of the interstitial lithium and substitutional aluminium respectively. Neither can comparison be made with the B–Li system since there have been no complete measurements in the band mode region. The total absorption in the irradiated aluminium doped sample was twice as large, although in this case the actual impurity concentration was only half as great. Since the expected impurity centres in the sample would not be expected to give rise to anomalously large values of η, it follows that the marked increase in the absorption must be associated with irradiation damage centres. In this context it may be noted that the spectral form of the present absorption is very similar to that produced in pure silicon by irradiation with fast neutrons (see Fig. 2). The latter samples are known to contain a high concentration of di-vacancies as determined by the strength of an absorption band in the region 3·3 μm[33, 49] although it has not been established to what extent these centres contribute to the one phonon absorption. It has been inferred that vacancies must be present in the irradiated aluminium sample and it has also been shown that there is very strong absorption in the region 3 μm. Although it is tempting to assume that these various observations are related in an obvious way, it is clear that further measurements are necessary before any definite conclusions can be made.

8. CONCLUSIONS

It has been demonstrated that appreciable one-phonon absorption is produced by the presence of $Al^{-}(s)$–$Al^{2+}(i)$ and $Al^{-}(s)$–$Li^{+}(i)$ pairs of impurities in compensated silicon. The absorption consists of characteristic in-band resonances as well as a continuum up to the Raman frequency. It has been profitable to consider these two systems together because a substitutional aluminium atom paired with a positively charged interstitial ion is involved in both types of crystal, thus enabling a detailed comparison to be made of the behaviour of the two interstitial ions. A complete comparison of these results with theory is not possible because no calculations have been made for the expected band mode absorption for this type of impurity pair.

Measurements of integrated absorption were a factor of two greater in the irradiated sample compared with the sample compensated by lithium diffusion, although the impurity content of the former was obviously smaller. It is therefore concluded that some of the absorption should be attributed to irradiation defects. In particular, the question naturally arises as to what absorption would be expected from vacancies or clusters of vacancies. It should again be noted that there are no theoretical estimates for these types of defect.

The present results have also given further information about the nature of the resulting damage in the electron irradiated sample. It has been shown that the initial removal rate of aluminium atoms from substitutional sites is approximately equal to the expected rate of generation of silicon intersitial atoms. These results imply that the nature of the defects produced will be governed wholly by the type of the impurities initially present when their concentration is of the order of 10^{19} cm^{-3}. The present observations of ion pairing taken together with previous results of Watkins have allowed an estimate to be made for the activation energy of diffusion of Al^{2+} ions. The binding of such an ion to a substitutional aluminium acceptor has also been estimated by comparison with results obtained previously for B–Li pairs. The values of the parameters so obtained have then lead to a self consistent explanation of all related observations.

Acknowledgements—One of us (S.D.D.) acknowledges the financial support of the University Grants Committee and the Ministry of Technology and the experimental facilities available to him as a member of Dr. S. D. Smith's group. Thanks are due to R. S. Smith for carrying out the electron irradiation of the samples, to J. Whitehouse for his assistance with the EPR measurements and to R. L. Rouse of AEI/GEC for supplying the crystal. Thanks are also due to Professor E. W. J. Mitchell for his interest in the work and for the electron irradiation facilities.

REFERENCES

1. ANGRESS J. F., GOODWIN A. R. and SMITH S. D., *Proc. R. Soc.* **287A**, 64 (1965).
2. ANGRESS J. F., GOODWIN A. R. and SMITH S. D., *Proc. R. Soc.* **308A**, 111 (1968).
3. NEWMAN R. C. and WILLIS J. B., *J. Phys. Chem. Solids* **26**, 373 (1965).
4. NEWMAN R. C. and SMITH R. S., *J. Phys. Chem. Solids* **30**, 1493 (1969).
5. DAWBER P. G. and ELLIOTT R. J., *Proc. R. Soc.* **273**, 222 (1963).
6. DAWBER P. G. and ELLIOTT R. J., *Proc. phys. Soc.* **81**, 453 (1963).
7. SLATER J. Ph.D. Thesis, University of Reading (1968).
8. ELLIOTT R. J. and PFEUTY P., *J. Phys. Chem. Solids* **28**, 1789 (1967).
9. NEWMAN R. C. and SMITH R. S. In *Localized Excitations in Solids* (Edited by R. F. Wallis), p. 177. Plenum Press, New York (1968).
10. TSEVETOV V., ALLRED W. and SPITZER W. G. In *Localized Excitations in Solids* (Edited by R. F. Wallis), p. 185. Plenum Press, New York (1968).
11. BALKANSKI M. and NAZAREWICZ W., *J. Phys. Chem. Solids* **27**, 671 (1966).
12. SPITZER W. G and WALDNER M., *J. appl. Phys.* **36**, 2450 (1965).
13. CHRENKO R. M., McDONALD R. S. and PELL E. M., *Phys. Rev.* **138A**, 1775 (1965).
14. WATKINS G. D. In *Radiation Effects in Semiconductors*, p. 97. Dunod, Paris (1965).
15. WATKINS G. D., *Phys. Rev.* **155**, 802 (1967).
16. MAITA J. P., *J. Phys. Chem. Solids* **4**, 68 (1958).
17. SPITZER W. G., *Phys. Rev. Lett.* **14**, 223 (1965).
18. PFANN W. G., *Trans. AIME* **203**, 961 (1965)
19. CONWELL E. M., *Proc. I.R.E.* **46**, 1281 (1958); see also CHAPMAN P. W., TUFTE O. N., ZOOK J. D. and FONG D., *J. appl. Phys.* **34**, 3291 (1963).
20. HORN F. H., *Phys. Rev.* **97**, 1521 (1955).
21. CARLSON R. O., *Phys. Rev.* **100**, 1075 (1955).
22. BACKENSTOSS G., *Phys. Rev.* **108**, 1416 (1957).
23. FULLER C. S., DOLEIDEN F. H and WOLFSTIRN K., *J. Phys. Chem. Solids* **13**, 187 (1960).
24. KAISER W., KECK P. H. and LANGE C. F. *Phys. Rev.* **101**, 1264 (1956).
25. CORBETT J. W., WATKINS G. D., CHRENKO R. M. and McDONALD R. S., *Phys. Rev.* **121**, 1015 (1961).
26. BAKER J. A., TUCKER T. N., MOYER N. E. and BUSCHERT R. C., *J. appl. Phys.* **39**, 4365 (1968).
27. ANGRESS J. F., SMITH S. D. and RENK K. F., In *Lattice Dynamics* (Edited by R. F. Wallis), p. 467. Pergamon Press, Oxford (1965).
28. PELL E. M. and HAM F. S., *J. appl. Phys.* **32**, 1052 (1961).
29. STRUTHERS J. D., *J. appl. Phys.* **27**, 1560 (1956).
30. BOLTAKS B. I. and SOZINOV I. I., *J. Tech. Phys. (Moscow)* **28**, 679 (1958).
31. FULLER C. S. and SEVERIENS J. C., *Phys. Rev* **92**, 1322 (1953); *ibid.* **96**, 21 (1954).
32. BULLOUGH R., NEWMAN R. C. and WAKEFIELD J., *Proc. I.E.E.* **106B**, Suppl. No. 15, 277 (1959).
33. CHENG L. J., CORELLI J. C., CORBETT J. W. and WATKINS G. D., *Phys. Rev.* **152**, 761 (1966).
34. FAN H. Y. and RAMDAS A. K., In *Proc. Int. Conf. on Semiconductor Physics, (Prague) Czech Acad. Sci.* p. 309. Prague (1961).
35. BEAN A. R., NEWMAN R. C. and SMITH R. S., *J. Phys. Chem. Solids*, In Press.
36. NEWMAN R. C and SMITH R. S., *Phys. Lett.* **24A**, 671 (1967).
37. WATKINS G. D. In *Radiation Effects in Semiconductors* (Edited by F. L. Vook). p. 67. Plenum Press, New York (1968).
38. MITCHELL E. W J., In *Radiation Effects in Semiconductors*, p. 367. Dunod, Paris (1965).
39. DOLLING G. In *Inelastic Scattering of Neutrons in Solids and Liquids*, Vol. 2, p. 23. I.A.E.A., Vienna (1963).
40. BILZ H., GEICK R. and RENK K F. In *Lattice Dynamics* (Edited by R. F Wallis), p. 355. Pergamon Press, Oxford (1965).
41. DOLLING G. and COWLEY R. A., *Proc. phys. Soc.* **88**, 463 (1966).
42. JOHNSON F. A. and LOUDON R., *Proc. R. Soc.* **A281**, 274 (1964).
43. BALKANSKI M. and NUSIMOVICI M., *Phys. stats Solid* **5**, 635 (1964).
44. YOUNG R. C., WESTHEAD J. W and CORELLI J C., *J. appl. Phys.* **40**, 271 (1969).
45. PAULING L. In *The Nature of the Chemical Bond*, p. 514. (1960). Cornell University Press, Ithaca.
46. HROSTOWSKI H. J. and KAISER R. H., *J. Phys. Chem. Solids* **4**, 148 (1958).
47. PARKER J. H. Jr., FELDMAN D. W. and ASHKIN M., *Phys. Rev.* **155**, 712 (1967).
48. LEIGH R. S. and SZIGETI B., *Proc. R. Soc.* **A301**, 211 (1967); *Phys. Rev. Lett.* **19**, 566 (1967); In *Localized Excitations in Solids* (Edited by R. F. Wallis). p. 159. Plenum Press, New York (1968).
49. FAN H. Y. and RAMDAS A. K., *J. appl. Phys.* **30**, 1127 (1959).

J. Phys. Chem. Solids Pergamon Press 1970. Vol. 31, pp. 701–705. Printed in Great Britain.

FORMATION AND STRUCTURE OF H′ CENTERS*

G. J. DIENES
Brookhaven National Laboratory, Upton, N.Y. 11973, U.S.A.
and
R. D. HATCHER
Queens College, Flushing, New York, U.S.A.
and
R. SMOLUCHOWSKI
Princeton University, Princeton, N. J. 08540, U.S.A.

(*Received* 8 *August* 1969; *in revised form* 30 *October* 1969)

Abstract – *The theoretically predicted cross-sections for the formation of H′-centers out of H-centers in* KCl and KBr and for the trapping of H-centers at Na impurities are in good agreement with the values obtained experimentally by Itoh. Two H-centers joined along a[110] direction can have nine possible configurations. Their energies have been calculated using a somewhat simplified model with the result that in the lowest state the two H-centers are perpendicular to each other and lie in a (001) plane. In the highest state they are co-linear.

1. INTRODUCTION

THE FORMATION of a new band, H′, in proximity of the known H band was first observed in KCl and KBr crystals, upon prolonged X-ray irradiation at low temperatures, by Faraday and Compton[1]. Further studies by Itoh *et al.*[2, 3] have shown that initially the concentration of H′-centers is proportional to the square of the concentration of H-centers and that later it saturates. This lead them to suggest that the H′-center is a pair of H-centers. H-centers are anticenters of F-centers and are produced by a crowdion-like motion of the displaced halogen as first proposed by Howard *et al.*[4] and later used in other mechanism such as Pooley's[5]. Thus the efficiency of the 2H→H′ reaction during irradiation is proportional not only to the effective cross-section σ of the H-centers for this reaction but also to the mean path of the interstitialcy. The experimentally determined parameter $\beta = \lambda\sigma$ is a volume which can be deduced either from the relative rate of growth of H and H′ bands or from the saturation value. The experimental[3] values of β are $1{\cdot}2\times10^3$ and $2{\cdot}5\times10^3$ for KCl and $1{\cdot}4\times10^3$ and $2{\cdot}7\times10^3$ for KBr expressed in units of the elementary lattice cubes d^3. In the first section of this paper the effective cross-section of H-centers is calculated and the product $\sigma\lambda$ compared with experiment under the assumption that the H′centers are stable and that there is no back reaction. In the second section the structure of the various H′ configurations is analyzed.

2. FORMATION OF H′-CENTERS

The stability and the structure of H-centers and of their immediate neighborhood has been investigated in considerable detail by Dienes *et al.*[6]. At that time, however, no particular attention was paid to more distant neighbors which may be of importance for the present problem. Thus the calculations have been repeated using the same methods and numerical values as previously[6] It was first established that displacements in other than the close-packed cubic directions decrease very rapidly with distance. This per-

---

*Work supported in part by the U.S. Atomic Energy Commission.

mitted directing the main effort at calculating displacements in the cubic directions including up to 10-th neighbors. As shown in Fig. 1 in four equivalent directions the ions are displaced outward while in the remaining two equivalent directions they are displaced inward. The calculated displacements are shown in Fig. 2 for KCl and KBr. The displacements do not fall on a smooth curve with the positive ions being displaced relatively more than the negative ones. It should be pointed out that the inclusion of these additional ions alters the total energy of the H-center only by about one per cent and thus all the earlier conclusions[6] concerning the stability of these centers are valid.

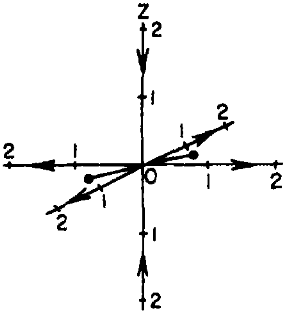

Fig. 1. Strain pattern around an H-center.

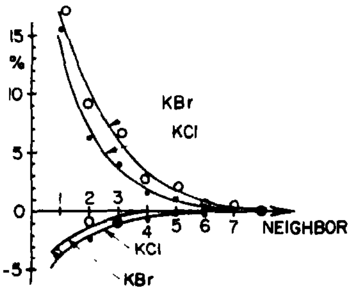

Fig. 2. Displacements of neighbors of an H-center along cubic directions. Positive (outward) displacements along x and y axes, negative (inward) displacements along z-axis (see Fig. 1). Only first neighbors have a significant displacement in non-cubic directions. Displacements expressed as percentage of interionic distance. Note that positively charged neighbors are relatively more displaced while the negatively charged neighbors are less displaced than the mean strain indicated by the curves. Full dots KCl, open dots KBr.

If the strain pattern surrounding an H-center were approximately spherical with a radius r then the effective cross-section σ would be given by $(2r)^2\pi$. This is not the case, however, and thus the relationship between the displacements shown in Fig. 2 and the interaction between a moving and a stationary H-center has to be investigated in detail. First of all the mean displacement of an ion in KCl or KBr from its ideal lattice site near 4°K is given essentially by its zero point amplitude which is about 0·3 per cent of the interionic distance d. It is thus reasonable to assume that at this temperature the effective strain pattern surrounding an H-center in KCl should be cut off at the 7th neighbor in the four equivalent cubic directions and at the 5th neighbor in the two other cubic directions. It follows that an H-center moving, as a crowdion, in a $\langle 110\rangle$ direction presents a cross-like strain pattern, perpendicular to that direction, with one arm $(7/\sqrt{2})d$ and the other $5d$ long. A stationary H-center presents two kinds of strain patterns as viewed from various $\langle 110\rangle$ directions: one of them has arms $(7/\sqrt{2})d$ and $5d$ long while the other one has arms $(7/\sqrt{2})d$ and $7d$ long. The second pattern occurs in twice as many $\langle 110\rangle$ directions as the first. The interaction between two such cross-like patterns is illustrated in Fig. 3 for patterns with arms $5d$ long. The dotted line is the locus of the center of cross A when one of its arms comes within a distance d of the stationary cross B and thus the area enclosed is the required cross-section. A similar pattern is easily obtained when the arms of the crosses are not equal. Taking a properly weighted average of the two kinds of strain patterns of the stationary H-center one obtains $\sigma = 208\,d^2$ for KCl and $\sigma = 283\,d^2$ for KBr.

The strain pattern illustrated in Fig. 1 suggests that if only an elastic interaction were present then for certain mutual orientations the two H-centers would repel rather than

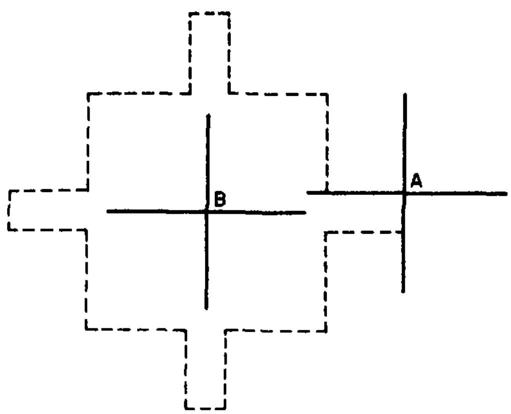

Fig. 3. Cross-section for interaction of identical strain patterns *A* and *B* (see text). The <110> direction is normal to the plane of the figure.

attract. It is reasonable to assume, however, that once two H-centers are close enough they may reorient themselves into other configurations of lower energy. Reorientation of free H-centers[7] does not occur below about 10°K but in proximity of other H-centers, their mobility may be greatly increased.

The most direct estimate of the length of the path of the displaced halogen as an interstitialcy in KBr has been obtained by Itoh *et al.*[8] from the observed stabilizing effect of chlorine impurities. The result is $\lambda \sim 10d$. No similar measurements in KCl, doped for instance with KF, have been made. The various studies[9, 10] of α-center formation and stability in $SrCl_2$ doped KCl do not permit an unambiguous interpretation in terms of a mean path of the interstitialcy. Behr *et al.*[11] expressed a belief that in KCl this path is about $6d$ long. Recent studies by Balzer[12] of the spontaneous recombination of vacancies and interstitials suggest a value of about 7. Combining these various results one obtains for $\beta = \sigma\lambda$ the value $1{\cdot}46 \times 10^3\ d^3$ for KCl and $2{\cdot}70 \times 10^3\ d^3$ for KBr which compare favorably with the experimental values $1{\cdot}2 - 2{\cdot}5 \times 10^3\ d^3$ and $1{\cdot}4 - 2{\cdot}7 \times 10^3\ d^3$ respectively.

An H-center travelling through a KCl or KBr lattice may encounter not only other H-centers to form H′-centers but also other impurities. In particular it may encounter a Na^+ substitutional ion. According to Douglas' calculations[13] the nearest Cl^- to Br^- neighbors of the Na^+ ion are displaced inward by about $0{\cdot}04\,d$ while the next nearest, K^+, neighbors are displaced outward by about $0{\cdot}002\,d$. Using the same criteria as above one obtains for the stationary strain pattern as viewed from a ⟨110⟩ direction a rectangle $d\sqrt{2}$ long and about one atom wide. The cross-section for interaction with a moving H-center obtained in the same manner as above is about $20\,d^2$. It follows that the parameter β for H′-center formation should be 10 times greater than a similar parameter for the capture of H-centers at Na^+ impurities both in KCl and in KBr. Itoh *et al.*[3] data indicate that for KBr this ratio is 9·4 for the lower and 18 for the higher value of β. Thus also here the agreement between theory and experiment is satisfactory within the limits of the available information. It would be interesting to see whether parameters β are temperature dependent and whether this dependence could be explained in terms of a progressive cut-off of the calculated strain patterns or of the increasing instability of H′-centers.

3. CONFIGURATION AND ENERGY OF H′-CENTERS

It is interesting to analyze the various possible configurations which can arise when two H-centers are nearest neighbors along a[110] direction. The problem is analogous to that of O_2^- centers in KCl and KBr[14, 15]. The basic method of calculation was the same as that used in the early study[6] of H-centers. In order to compare the energies of the various configurations two quantities were kept constant: The size i.e. the separation between the two chlorine ions in each Cl_2^- molecule and the separation of the two H-centers. The orientation of the two H-centers was different in each case but it was kept fixed while the surrounding lattice was permitted to relax.

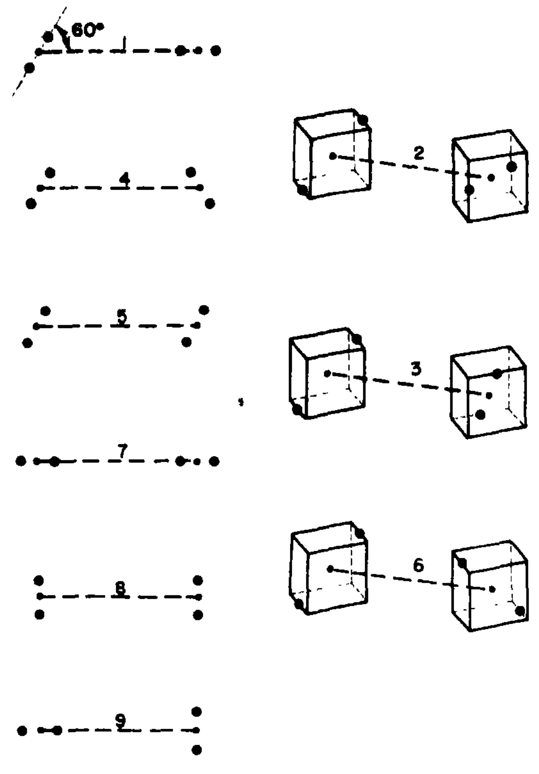

Fig. 4. Possible configuration of two H-centers forming an H′-center. The small cubes are meant to aid in visualizing the orientation of the H-centers and are not to be confused with the elementary cubes of the lattice.

The various possibilities are illustrated in Fig. 4 using notation introduced in the study of O_2^- centers[14]. Depending upon the symmetry of the configuration a number of parameters was necessary to describe the displacements of the neighboring ions. Case 3 required 45 parameters while case 7 only 6. The results are given in Table 1. It is interesting to note that relaxation did not alter much the sequence of energies and that cases 5, 6 and 8 are very close to each other. The relaxation lowers the energies uniformly by about 3·5 to 3·8 eV except for case 3 where it is only 2·7 eV. The lowest energy corresponds to a configuration in which the two H-centers lie in a (001) plane and are perpendicular to each other.

Table 1. *Energies (relative to the perfect lattice, in* eV*) of the various possible H′-centers with and without relaxation*

Configur-ration	Molecular orientation	Common plane	No relaxation	With relaxation
9	$[110]-[\bar{1}\underline{1}0]$	(001)	7·54	3·85
2	$[1\underline{0}1]-[1\underline{1}0]$		7·64	3·99
8	$[1\bar{1}0]-[110]$	(001)	7·75	4·08
5	$[101]-[10\underline{1}]$	(111)	7·70	4·12
6	$[101]-[101]$		7·75	4·14
4	$[101]-[0\bar{1}1]$	(111)	7·83	4·20
1	$[101]-[110]$	(111)	7·83	4·32
3	$[101]-[011]$		7·66	4·96
7	$[110]-[110]$	(hkl)	11·87	8·10

A more detailed calculation in which both the size of each of the constituent H-centers and also their orientation would be permitted to relax was not made because of the enormous increase in complexity and in the number of variable parameters. Only the high symmetry case 7 was re-calculated permitting the two H-centers to adjust their size but not their orientation. Its final energy turned out to be comparable to that of the unrelaxed case 3 and thus still one of the highest. It is interesting to note that the sequence of configurations here obtained is quite different from that deduced for O_2^- centers[14] which for KCl is 1, 8, 5, 6, 9, 2, 7, 3 and 4 while for KBr is 1, 9, 7, 8, 5, 6, 2, 3 and 4. In all these calculations only the elastic energy was taken into account and no quantum mechanical corrections included. The latter are known to affect the configuration of H-centers themselves[6]. The present case is prohibitively complicated for a complete quantum mechanical treatment and the use of simplified models for configurations of such low symmetry appears too arbitrary to lead to meaningful results.

The absolute magnitudes of the energies in Table 1 are undoubtedly too high because of the neglect of the above mentioned relaxations. As far as the sequence of various configurations is concerned, configurations 8, 5 and 6 are so close to each other that their order could be changed if the relaxations were to decrease the energies by, say, a factor of 2. The order of the remaining configurations, for which the energy difference may go down to 5 per cent in some cases, probably would not change since the computations themselves are good to 0·01 eV. For the same reason, in comparing the energy of the most stable H′-center, 3·85 eV, with the energy of two isolated H-centers in KCl, 2·8 eV[6], it should not be concluded that the H′-center is unstable relative to the H-center. As mentioned above, a more detailed calculation for the H′-centers is rather prohibitive because of low symmetry.

It is also of interest to compare the energy of an H-center with that of a neutral Cl_2 molecule inserted interstitially in the KCl lattice. A calculation was carried out for an interstitial Cl_2 molecule oriented in a [100] direction with the two nuclei located symmetrically in adjacent cells (dumbbell configuration across a face). The nearest neighbors (those located in the plane perpendicular to the midpoint of the molecular axis) and the next nearest neighbors (at the corners of the cubes) were allowed to relax. The molecular interaction between the two Cl nuclei was represented by a Morse function fitted to the potential energy vs. distance curve for the free molecule. The calculations showed that the nearest neighbors are displaced outward by about 10 per cent and the next nearest neighbors by 5 per cent, and that the interstitial Cl_2 molecule is slightly expanded in the KCl lattice (from $r = 2{\cdot}0$ Å to $r = 2{\cdot}2$ Å, where r is the internuclear distance in the molecule). The energy of this configuration is 2·1 eV relative to the perfect crystal. A similar calculation showed that if the interstitial Cl_2 molecule is confined to one cell in a [100] orientation the molecule is compressed slightly ($r = 1{\cdot}9$ Å) and the energy rises to 2·7 eV.

The interstitial Cl_2 molecule, according to these calculations, has a lower energy (2·1 eV) than two H-centers (2·9 eV) or two isolated neutral chlorine interstitials (3·6 eV). These results support the idea that the final state of the H-center is the interstitial Cl_2 molecule.

REFERENCES

1. FARADAY B. J. and COMPTON W. D., *Phys. Rev.* **138**, A893 (1965).
2. ITOH N., KAWAMATA T., HIRAO T. and KANZAKI H., *J. phys. Soc. Japan* **23**, 453 (1967).
3. ITOH N. and SAIDOH M., *Phys. Status Solidi* **33**, No. 2 (1969).
4. HOWARD R. E., VOSKO S. and SMOLUCHOWSKI R., *Phys. Rev.* **122**, 1406 (1961).
5. POOLEY D., *Proc. Phys. Soc.* **87**, 245, 257 (1966).
6. DIENES G. J., HATCHER R. D. and SMOLUCHOWSKI R., *Phys. Rev.* **157**, 692 (1967).
7. BACHMANN K., Thesis, Eidgenössische Technische Hochschule, Zürich (1968).
8. ITOH N., ROYCE B. S. H. and SMOLUCHOWSKI R., *Phys. Rev.* **138**, A1766 (1965).
9. BEHR A., PEISL H. and WAIDELICH W., *J. Phys.* **28**, C4-163 (1967).
10. GIULIANI G. and REGUZZONI E., *Phys. Status Solidi* **25**, 437 (1968).
11. BEHR A., PEISL H. and WAIDELICH W., *Phys. Lett.* **24A**, 379 (1967).
12. BALZER R., Thesis, Technische Hochschule, Darmstadt (1969).
13. DOUGLAS T. B., *J. chem. Phys.* **45**, 4571 (1966).
14. SHUEY R. T. and BEYELER H. U., *J. appl. Math. Phys.* **19**, 278 (1968).
15. VON WALDKIRCH T., ZELLER H. R. and KÄNZIG W., *Helv. Phys. Acta* **40**, 823 (1967).

J. Phys. Chem. Solids Pergamon Press 1970. Vol. 31, pp. 707–711. Printed in Great Britain.

SOME OBSERVATIONS ON THE LUMINESCENCE OF β-Ga_2O_3

G. BLASSE and A. BRIL
Philips Research Laboratories, N. V. Philips' Gloeilampenfabrieken, Eindhoven, The Netherlands

(*Received* 8 *August* 1969; *in revised form* 28 *October* 1969)

Abstract—The compound β-Ga_2O_3 shows at least three different emission bands depending on the choice of the dope. At room temperature, an efficient blue emission is found for undoped Ga_2O_3 and Ga_2O_3 containing cations with a charge higher than three. Greenish emission is found for Ga_2O_3 doped with Be or with a combination of Li (or Be) and one of the ions causing the blue emission. At liquid nitrogen temperature an u.v. emission band is observed for practically all compositions.

1. INTRODUCTION

LEVERENZ[1] mentions the emission of α-Ga_2O_3 under cathode-ray excitation. The β-modification, however, has not been investigated. Its crystal structure was reported by Geller[2]. There are two kinds of Ga^{3+} ions present, one in octahedral, the other in tetrahedral coordination. Further three different types of O^{2-} ions can be distinguished. According to Tippins[3] β-Ga_2O_3 shows photoconductivity for band-edge excitation. Lorenz *et al.*[4] showed that β-Ga_2O_3 is an n-type semiconductor. The resistivity of the samples depends strongly on the atmosphere during the preparation. The dominant donor species was assumed to be an anion vacancy. Recently Wanmaker and Ter Vrugt[5] found that gallate spinels are efficient phosphors under ultraviolet (u.v.). and cathode-ray (c.r.) excitation. In this paper we report on the luminescence of doped and undoped β-Ga_2O_3. No efficient phosphors based upon this lattice are known to the authors except for β-Ga_2O_3-Dy with efficient Dy^{3+} emission [6].

2. EXPERIMENTAL

Samples were prepared by usual techniques. Ga_2O_3 was used with a purity of 99·99% (Alusuisse). Spectrochemical analysis showed the following impurities: Al (0·5 ppm), Si (10 ppm), Sn (3 ppm), Zn (2 ppm), Cu and Pb (0·1 ppm). The dope concentration was varied from 0·1–1·0 atomic per cent. Firing was carried out in alundum crucibles.

Samples were checked by X-ray analysis and their optical properties were determined as described previously[7].

3. RESULTS

At least three types of emission were observed for doped and undoped β-Ga_2O_3, viz. broad emission bands with maxima at about 365, 420 and 500 nm. In the following these bands will be called the ultra-violet (u.v.), blue and green band, respectively. All samples showed a long rise and afterglow (usually with a green colour) especially under u.v. excitation. A number of representative dopes are compiled in Table 1.

3.1 *Emission spectra*

Table 1 shows the influence of the dopant on the emission colour. Undoped and doped β-Ga_2O_3 show in general a blue emission at room temperature (Fig. 1) (it should be kept in mind that undoped Ga_2O_3 contains impurities in the ppm range). An exception is the Be-doped Ga_2O_3 with mainly green emission (Fig. 2) and Si-doped Ga_2O_3 (fired in N_2) with u.v. and blue emission (Fig. 3). A double dope consisting of Li (or Be) with one of the dopes giving blue emission results in (mainly) green-emitting phosphors (Fig. 4). The phos-

Table 1. Luminescence of β-Ga_2O_3

Composition	Dominant emission band* 300°K	77°K	$q(\%)$† (250–270 nm)	$\eta(\%)$‡ (20 kV)
Ga_2O_3 (fired in O_2)	B	UV	20	2·5
Ga_2O_3 (fired in N_2)	B	UV	40	4
Ga_2O_3-Si (fired in O_2)	B	UV	40	3
Ga_2O_3-Si (fired in N_2)	UV/B	UV	20	1
Ga_2O_3-P	B	UV	45	4
Ga_2O_3-B	B	UV/B	40	3
Ga_2O_3-Mo	B	UV	35	3
Ga_2O_3-W	B	UV	35	3
Ga_2O_3-Nb	B	UV	30	3
Ga_2O_3-Sn	B	UV	20	2
Ga_2O_3-Be (fired in N_2)	G	UV	30	2
Ga_2O_3-Be (fired in O_2)	G	UV	15	1
Ga_2O_3-Li, Si (fired in N_2)	G	UV/G	40	3
Ga_2O_3-Li, Si (fired in O_2)	G	UV/G	25	2
Ga_2O_3-Li, P	G	UV/G	50	3
Ga_2O_3-Li, W	G	UV/G	40	3
Ga_2O_3-Li, Sn	G	UV/G	30	3
Ga_2O_3-Be, Si	G	UV/G	30	2
Ga_2O_3-Be, W	G	UV/G	30	2

*B: blue (~ 420 nm); UV: ultra-violet (~ 365 nm); G: green (~ 500 nm)

†Quantum efficiency for 250–270 nm excitation at room temperature (the maximum of the excitation band is at shorter wavelengths. The maximum quantum efficiency in the u.v. region is about 1·4 times the value in the table).

‡Radiant efficiency for c.r. excitation at room temperature.

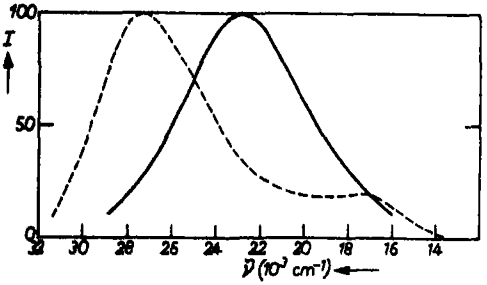

Fig. 1. Spectral energy distribution of the emission of Ga_2O_3 (254 nm excitation) at 300°K (———) and 77°K (- - - -). I gives the radiant power per constant wavenumber interval in arbitrary units.

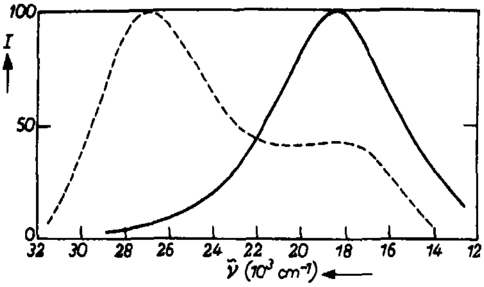

Fig. 2. Spectral energy distribution of the emission of Ga_2O_3-Be (254 nm excitation) at 300°K (———) and 77°K (- - -).

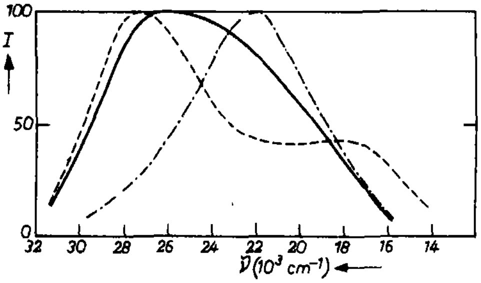

Fig. 3. Spectral energy distribution of the emission of Ga_2O_3-Si (fired in N_2) at 300°K (———) and 77°K (- - -) and of Ga_2O_3-Si (fired in O_2) at 300°K (-.-.-) and 77°K (- - -) (254 nm excitation).

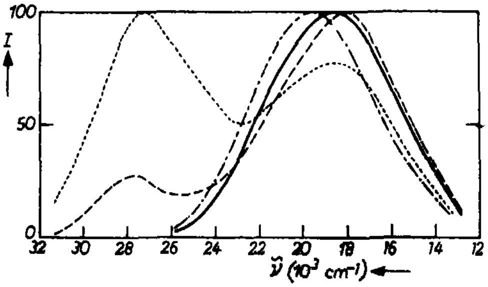

Fig. 4. Spectra energy distribution of the emission of Ga_2O_3-Be, Si at 300°K (———) and 77°K (- - -) and of Ga_2O_3-Li, Si at 300°K (-.-.-) and 77°K (· · ·) (254 nm excitation).

phor Ga_2O_3-Be itself gives the same emission; Ga_2O_3-Li, however, shows the blue emission. Usually the two dopes were added in such a ratio that they can substitute for Ga^{3+} ions without vacancy formation (e.g. $Li^+ + 2Si^{4+} = 3Ga^{3+}$). This exact ratio, however, is not necessary to obtain the green emission.

The firing atmosphere had a drastic influence on the emission of Ga_2O_3–Si. Under oxidizing conditions it is blue, under reducing conditions it contains also the u.v. band (Fig. 3). This effect was observed only for Si-doped samples.

Decreasing the temperature from room temperature to liquid N_2 temperature brings about marked changes in the emission spectra. In the blue- as well as in the green-emitting samples a new band appears, viz. the u.v. band (observed at room temperature only for Ga_2O_3–Si, fired in N_2). At the same time the intensity of the blue or green band decreases. In Fig. 5 the temperature dependence of the green emission of Ga_2O_3–Li, Si is given as an example. From room temperature to liquid N_2 temperature the emission colour changes, therefore, either from blue to violet or from green to blue (Figs. 1–4). In many cases the emission spectra consist of more than one emission band (see e.g. Fig. 3, where at room temperature the emission of Ga_2O_3–Si, fired in N_2, contains the u.v. and the blue band; at liquid N_2 temperature the green band is observed too).

Also Ga_2O_3–Dy, at room temperature an efficient Dy^{3+}-phosphor[6], shows at liquid N_2 temperature only the u.v. band emission. The characteristic Dy^{3+} emission has nearly completely disappeared.

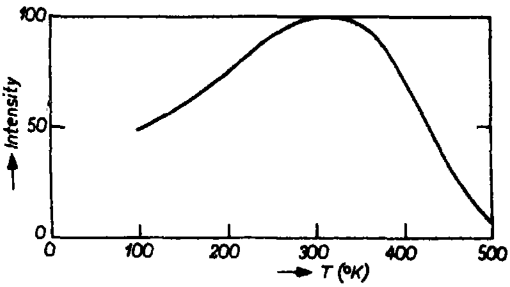

Fig. 5. Temperature dependence of the intensity of the green emission band of Ga_2O_3–Li, Si under 254 nm excitation.

3.2 *Decay and afterglow*

In Fig. 6 the decay-curve of the u.v. emission band of Ga_2O_3–Si is given for cathode-ray excitation. The curves for the blue and green emission band of other samples are similar. These curves are clearly not exponential. The main decay is very fast: the intensity of the emission falls to 50 per cent of its original value in about 30 nsec. Within the experimental error this value is equal for the u.v., blue and green emission band. In addition a long afterglow was observed. The intensity of this afterglow increases with decreasing current density. As an example we give some data for the blue emission band of Ga_2O_3–Si: For cathode-ray excitation the intensity at 80 μsec after a 20 μsec pulse amounts to 13 per cent

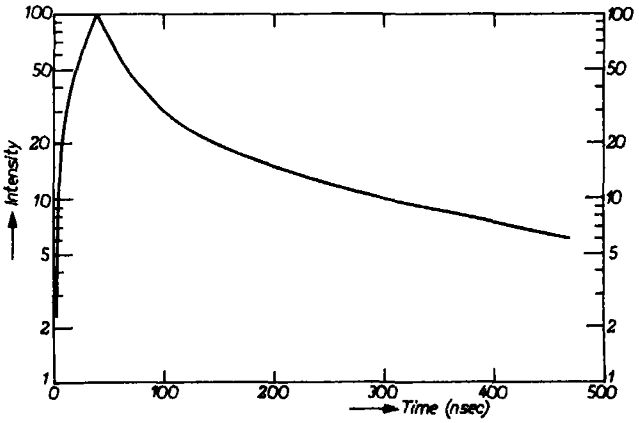

Fig. 6. Rise and decay of the ultraviolet emission (λ < 390 nm) of Ga_2O_3–Si (fired in N_2) under cathode-ray excitation. Pulse time 40 nsec.

of the maximum intensity for 0·01 $\mu A/cm^2$ and to 3 per cent for 10 $\mu A/cm^2$.

Similar phenomena are observed for ultraviolet excitation. For Ga_2O_3–Be, for example, the intensity of the emission falls to 50 per cent of its original value in 0·1–10 sec depending on the excitation density. The rise and decay under u.v. excitation are very much slower than under cathode-ray excitation because the excitation density is much higher in the latter case.

3.3 *Excitation spectra and efficiency*

Due to the long rise and afterglow, measurement of the excitation spectra is difficult. All samples show a strong excitation band peaking at about 260 nm. This band corresponds to the absorption edge of β-Ga_2O_3 (*Fig. 7*). The excitation spectra contain also a number of very weak bands at longer wavelengths (Fig. 7). These bands were found for all Ga_2O_3 samples and also for a number of Ga^{3+} compounds. Due to their weakness measurements such as those recorded in Fig. 7 have a qualitative meaning only. The green emission could be excited in all bands shown in Fig. 7, the blue emission only in the bands in the region 220–260 nm and 290–310 nm. In the diffuse reflection spectra we could not find any absorption bands corresponding to the weak excitation bands.

Quantum efficiencies were measured for 250–270 nm excitation and are reasonably high (up to 50 per cent, see Table 1). Since the maximum of the excitation band is at shorter wavelengths, the maximum quantum efficiency in the u.v. region is higher (up to 70 per cent). Radiant efficiencies for c.r. excitation vary from 1 to 4 per cent (see Table 1). In many cases we found a dependence of the efficiency on the firing atmosphere. Undoped Ga_2O_3 shows higher efficiencies if fired under reducing conditions and so does Ga_2O_3–Li, Si. On the other hand, Ga_2O_3–Si shows higher efficiencies if fired under oxidizing conditions (Table 1). In the latter case, however, the emission spectrum changes also.

4. DISCUSSION

The present results indicate that β-Ga_2O_3 has properties similar to those of the ZnS-type of phosphors. This is not surprising because other oxides of $3d^{10}$ ions are also known to show emission of this type: ZnO fired under reducing conditions shows a green emission (ascribed to anion vacancies) and ZnO doped with Ga^{3+} or Cl^- shows an orange emission (ascribed to cation vacancies)[8]; GeO_2 (rutile modification) shows yellow emission (ascribed to anion vacancies)[9].

An explanation of the fluorescence of β-Ga_2O_3 may be even more difficult than in the

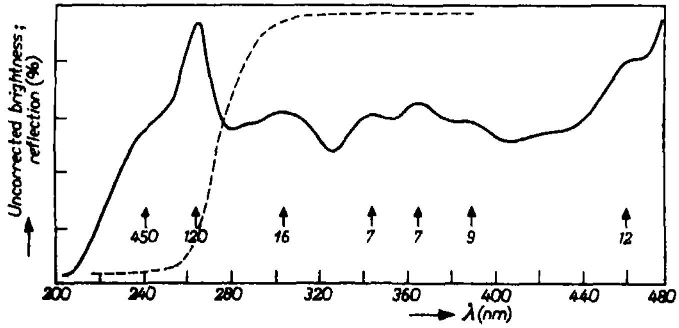

Fig. 7. Diffuse reflection spectrum (– – –) and excitation spectrum of the green emission band of Ga_2O_3–Li, Sb. The excitation spectrum curve is an uncorrected recorder curve. Correction factors are indicated in the figure (with arrows). The zero-point curve should be estimated from the recorder curve.

case of compounds like ZnS and ZnO due to the fact that the structure of β-Ga_2O_3 contains two crystallographic sites for gallium and three for oxygen. The number of different defects can, therefore, be very high, even in pure β-Ga_2O_3, so that an interpretation of the present results seems not to be feasible at the moment.

REFERENCES

1. LEVERENZ H. W., *An Introduction to Luminescence of Solids*, p. 222. Wiley, New York (1950).
2. GELLER S., *J. chem. Phys.* **33**, 676 (1960).
3. TIPPINS H. H., *Phys. Rev.* **140**, A316 (1965).
4. LORENZ M. R., WOODS J. F. and GAMBINO R. J., *J. Phys. Chem. Solids* **28**, 403 (1967).
5. WANMAKER W. L. and TER VRUGT J. W., *J. electrochem. Soc.* **116**, 871 (1969); *Phillips Res. Rep.* **24**, 201 (1969).
6. HERBERT W. C., MINNIER H. B. and BROWN J. J., *J. electrochem. Soc.* **115**, 104 (1968).
7. BRIL A. and WANMAKER W. L., *J. electrochem. Soc.* **111**, 1363 (1964); BRIL A., BLASSE G. and DE POORTER J. A., *J. electrochem. Soc.* In press.
8. KRÖGER F. A. and VINK H. J., *J. chem. Phys.* **22**, 250 (1954).
9. SARVER J. F. and HUMMEL F. A., *J. electrochem. Soc.* **108**, 195 (1961).

Note added in proof. After submission of this paper the blue and green emission of β-GA_2O_3 have also been reported by HERBERT W. C., MINNIER H. B. and BROWN J. J., *J. electrochem. Soc.* **116**, 1019 (1969).

J. Phys. Chem. Solids Pergamon Press 1970. Vol. 31, pp. 713–727. Printed in Great Britain.

ENTROPIES OF MIXING OF SOLIDS WITH A RETROGRADE SOLIDUS*

ROBERT BENZ
Los Alamos Scientific Laboratory, University of California, Los Alamos, N.M. 87544, U.S.A.

(Received 4 June 1969; in revised form 12 September 1969)

Abstract – Molar entropies of mixing for elemental and compound phases at the composition extreme in retrograde solidi are calculated from available thermodynamic data on the respective liquid solutions and the tentative assumption that the partial molar entropy of mixing of the solid solvent is zero. Calculated values of $S_2^{M(s)}$, the partial molar entropy of mixing of the solute or dissolved component, for the elemental phases agree with the available experimental data demonstrating the usefulness of the method of calculation for dilute solid solutions. For compound phases, the calculated values of $S^{M(s)}$, the integral molar entropy of mixing, are more positive than that as calculated from published values of entropies of formation. The differences are attributed in part to the neglect of the partial molar entropy of mixing of the solid solvent. For the compounds CaF_2, CdTe, PbTe, UN, UP, and US, the differences are too great to be attributed to assumptions in the calculations. Arguments are presented suggesting that these discrepancies are due in part to errors in the accepted entropy values for formation of the compounds and/or of phase transition of the constituent elements.

USEFULNESS of an approximate method for calculation of the entropies of mixing at the extreme composition of binary solids with a retrograde solidus is discussed. The composition ranges of such solids are quite narrow, consequently, direct experimental data on the entropies of mixing are difficult to obtain and published data are sparse.

PREVIOUS WORK

A solidus is retrograde when the temperature coefficient of solubility of a component in the solid coexisting with a fixed liquid phase exhibits a sign reversal. A retrograde solidus has been reported to occur in a number of binary phase systems. Published data[1–79] are listed in Table 1 with the solute element designated by 2. The other element is designated by 1. Other solidi that may be retrograde are Ge(+ As)[6], Si(+ As)[6], Ge(+ Au)[77], Si(+ B)[6], Ge(+ Bi)[31], Si(+ Bi)[6], CdSe(+ Cd)[41], Ge(+ Co)[77], Si(+ Co)[6], Ge(+ Fe)[77], Ge(+ Mn)[77], Si(+ Mn)[6], Si(+ P)[6], Ge(+ S)[77], Si(+ S)[6], SnS(+ S)[78–9], Ge(+ Se)[77], SnSe(+ Se)[79], Ge(+ Sn)[6], SnTe(+ Sn)[41], Ge(+ Te)[77], and Ge(+ Tl)[31], but these are not listed in Table 1 because of the apparent need for additional experimental investigation.

Symbols of Wagner[80] are employed. Atomic fractions of component $i = 1$ and 2 are designated X_i, partial molar entropies and enthalpies by $\bar{S}_i$ and $\bar{H}_i$, respectively, and the partial molar entropies of mixing by S_i^M. Integral molar entropy of mixing and integral molar free energy of mixing are represented by S^M and G^M. The above quantities for liquid and solid phases are distinguished by the superscripts (l) and (s), respectively.

Thermodynamic implications of a retrograde solidus have been investigated by several authors. Meijering[81] examined cases of retrograde solubility known at the time with an equation equivalent to equation (2) (below), estimated entropies of fusion, and the assumption of ideal entropies of mixing for the solid and liquid phases. From the available liquidus data, he predicted a retrograde solidus in several binary systems. Some anomalies in his

---

*This work was done under the auspices of the U.S. Atomic Energy Commission.

Table 1. *Compositions of the solidus and liquidus at the temperature of maximum retrograde solubility*

		Solidus extremum			Liquidus	
Solid phase	Dissolved component, 2	$X_2^{(s)*}$	Temp. (°C)	Ref.	$X_2^{(l)*}$	Ref.
Ge	Ag	$2{\cdot}3 \times 10^{-8}$	875	1	0·22	2
Si	Ag	4×10^{-6}	1350	3	0·15	2
Ge	Al	0·0097	675	4	0·47	2
Si	Al	0·0004	1200	5, 6	0·35	2
Co	Au	0·025	1200	7	0·44	7
Si	Au	2×10^{-6}	1300	8, 9, 28	0·18	2
Ag	Bi	0·027	500	12, 12b	0·35	2
Au	Bi	0·0006	900	12	0·12	2
Bi_2Te_3	Bi	0·4027	560	13	0·496	13
Cu	Bi	3×10^{-5}	800	10, 11, 2	0·60	2
CaF_2	Ca	0·34	1330	14	0·38	14, 15
Cu	Cd	0·026	650	16, 17	0·37	2
CdTe	Cd	0·50003	900	18	0·90	19
Ge	Cd	5×10^{-5}	840	20	0·50	2
Zn	Cd	0·015	300	21–23 cf. 24	0·56	2
Ge	Cu	7×10^{-7}	880	25, 26	0·18	27, 2
Si	Cu	3×10^{-5}	1300	25, 28	0·20	2
Si	Fe	7×10^{-7}	1300	28	0·17	2
Ge	Ga	0·011	700	29, 4	0·60	2, 30
Si	Ga	0·0008	1200	6, 31	0·50	2
HgSe	Hg	0·5001	350	76		
Ge	In	9×10^{-5}	800	6, 31	0·38	2
Si	In	4×10^{-5}	1330	31	0·32	2
Ge	Li	0·00017	800	32	0·13	32
Si	Li	0·0013	1185	33, 34	0·37	2
Ge	Ni	$1{\cdot}8 \times 10^{-7}$	880	35	0·16	2
Si	O	$3{\cdot}4 \times 10^{-5}$	1410	36, 37	(0·004)	37
Ag	Pb	0·028	650	12, 38, 39, 23	0·37	2
Au	Pb	0·001	900	12	0·12	2
Ge	Pb	$1{\cdot}1 \times 10^{-5}$	870	6	0·35	2
PbS	Pb	0·5004	1050	40	0·65	2, 41
(PbSe)	Pb	0·5004	1000	41	0·65	41, 42
PbTe	Pb	0·50003	790	43–45	0·82	46, 47
PbS	S	0·5002	900	40, 79	0·63	40
Au	Sb	0·011	600	48	0·23	2
Ge	Sb	0·0002	880	25, 29, 31	0·25	49, 50
Si	Sb	0·0013	1320	6, 31	0·25	2
Al	Sn	0·002	620	51	0·19	2, 52
Si	Sn	0·0011	1200	6, 53	0·98	75
CdTe	Te	0·5004	1060	18, 19	0·55	19
CoTe	Te	0·66	800	54	0·84	54
PbTe	Te	0 50013	700	43–45, 79	0·68	2, 55
SnTe	Te	0·51	600	56, 57	0·69	2
ThN	Th	0·51	2000	58[(1)]	0·89	58
ThP	Th	0·50	2300	59	0·75	59
(ThAs)	Th	0·50	2400	60	0·68	60
Ag	Tl	0·075	550	12	0·70	61
Au	Tl	0·009	800	12	0·23	2
UC	U	0·51	2000	62–65	0·87	66–69
UN	U	0·50	2200	70[2]	0·91	70, 71
(UP)	U	0·50	2200	72	0·81	72

Table 1 *(cont.)*

Solid phase	Dissolved component, 2	Solidus extremum			Liquidus	
		$X_2^{(s)*}$	Temp. (°C)	Ref.	$X_2^{(l)*}$	Ref.
(UAs)	U	0·50	2200	73	0·81	73
US	U	0·50	2000	74	0·86	74
Ge	Zn	$1{\cdot}1 \times 10^{-4}$	800	29, 6	0·40	2
Si	Zn	$1{\cdot}2 \times 10^{-6}$	1320	6	0·22	75

1. Part of the Th that had been previously identified as precipitate was subsequently found to have been inclusions. With the assumption that the ThN phase in products annealed at 1400° is stoichiometric, the extreme N/Th ratio at the Th-saturated ThN solidus was redetermined microscopically as 0·975 ± 0·015 at 2000°.

2. Reported analyses for U as determined by ignition in air at 800° are in error due to an incorrect formula, U_3O_8, assumed for the product. Corrected for this systematic error, the N/U ratio of the UN congruent melting composition is 1·00 ± 0·03 as based upon ignition analyses and 0·995 ± 0·005 as based upon microscopic analyses. The extreme N/U ratio of U-rich UN has been subsequently determined microscopically as 0·99 ± 0·01.

calculated results were attributed by him to $S^{M(s)}$ values being greater than his assumed ideal values. Thurmond and Struthers[25] reported data on retrograde solubilities of Sb in Ge, Cu in Si, and Cu in Ge based upon measurements of distribution coefficients. From the results, they represent S_2^M as a sum of two terms, (1) configuration (random mixing) term and (2) a large positive composition-independent term. Hodgkinson[26] arrived at virtually the same results for solutions of Cu in Ge based upon electrical resistance measurements on quenched specimens. According to Hodgkinson, the composition-independent term is associated with vibrational entropy. The data interpreted according to these authors result in large positive values for $H_2^{M(s)}$ (partial molar enthalpy of mixing of the solute, 2). Thurmond and Struthers suggested this is a general characteristic of solid solutions with a retrograde solidus. Miller and Komarek[41] reported liquidus curves for the Pb–PbS, Pb–PbSe, and Pb–PbTe systems. From inflections in their smoothed curves, they suggested that the liquids deviate from ideal solutions in the positive direction at temperatures only slightly above that at which the maximum solid solubility occurs.

CALCULATIONS

Relation between partial molar entropies at the temperature of maximum retrograde solubility

General differential equations describing a liquidus and a solidus in a binary system as first derived by Schootky, Ulich, and Wagner [80, 82] may be written, respectively

$$\frac{\mathrm{d}}{\mathrm{d}T}X_2^{(l)} = -\frac{X_1^{(s)}\Sigma_1 + X_2^{(s)}\Sigma_2}{[X_2^{(l)} - X_2^{(s)}]\left(\dfrac{\partial^2 G^{M(l)}}{\partial X_2^{(l)2}}\right)} \qquad (1)$$

$$\frac{\mathrm{d}}{\mathrm{d}T}X_2^{(s)} = -\frac{X_1^{(l)}\Sigma_1 + X_2^{(l)}\Sigma_2}{[X_2^{(l)} - X_2^{(s)}]\left(\dfrac{\partial^2 G^{M(s)}}{\partial X_2^{(s)2}}\right)} \qquad (2)$$

where $\Sigma_1 = (\bar{S}_1^{(l)} - \bar{S}_1^{(s)})$ and $\Sigma_2 = (\bar{S}_2^{(l)} - \bar{S}_2^{(s)})$ denote entropies of transfer for the respective components from the phase s to l. The equations as given by Schottky, Ulich, and Wagner are expressed in terms of the heats of transfer, $\Lambda_1 = \bar{H}_1^{(l)} - \bar{H}_1^{(s)}$ and $\Lambda_2 = \bar{H}_2^{(l)} - \bar{H}_2^{(s)}$, instead of Σ_1 and Σ_2. These quantities are related under equilibrium conditions by the following equations: $\Lambda_1 = T\Sigma_1$ and $\Lambda_2 = T\Sigma_2$ where T denotes temperature in degrees Kelvin. For a retrograde solidus, there exists a temperature, denoted by T^*, at which the solubility is a maximum so that $(\mathrm{d}/\mathrm{d}T)X_2^{(s)}=0$. and, therefore, from equation (2),

$$X_1^{(l)*}\Sigma + X_2^{(l)*}\Sigma_2 = 0. \qquad (3)$$

In what follows, for each element we shall adopt a single reference state, the normal state, that is common to both the solid and liquid solutions of a given binary system; therefore, we may replace the entropies of transfer in equation (3) by the appropriate differences in the partial molar entropies of mixing to obtain the equation

$$X_1^{(l)*}[\mathrm{S}_1^{M(l)}(X_2^{(l)*}) - \mathrm{S}_1^{M(s)}(X_2^{(s)*})]$$
$$+X_2^{(l)*}[\mathrm{S}_2^{M(l)}(X_2^{(l)*}) - \mathrm{S}_2^{M(s)}(X_2^{(s)*})] = 0, \qquad (4)$$

valid at temperature T^*. In equation (4), $\mathrm{S}_i^{M(l)}(X_2^{(l)*})$ for the liquid and $\mathrm{S}_i^{M(s)}(X_2^{(s)*})$ for the solid phases are written explicitly as functions of the liquidus and the solidus atomic fractions, respectively, at temperature T^*. We shall omit the explicit expression of $X_2^{(l)*}$ and $X_2^{(s)*}$ in the subsequent discussion and write simply $\mathrm{S}_i^{M(l)}$ and $\mathrm{S}_i^{M(s)}$ as well as $\mathrm{S}^{M(l)}$ and $\mathrm{S}^{M(s)}$, respectively, for the liquid and solid phases remembering that the entropies of mixing are to be evaluated at the respective liquidus and solidus composition, unless specifically stated otherwise. Solving for $\mathrm{S}_2^{M(s)}$ in equation (4) gives

$$\mathrm{S}_2^{M(s)} = \mathrm{S}_2^{M(l)} + \frac{X_1^{(l)*}}{X_2^{(l)*}}[\mathrm{S}_1^{M(l)} - \mathrm{S}_1^{M(s)}]. \qquad (5)$$

The integral molar entropy of mixing of the solid can be written, correspondingly, as

$$\mathrm{S}^{M(s)} = \mathrm{S}^{M(l)} + (X_2^{(l)*} - X_2^{(s)*})[\mathrm{S}_1^{M(s)} - \mathrm{S}_2^{M(s)}]. \qquad (6)$$

Equations (5) and (6) are, in our discussion, basic equations relating the entropies of mixing of the liquid and solid solutions coexisting at temperature T^*. The object of this note is to delineate the usefulness and limitations of equations (5) and (6) for calculation of $\mathrm{S}_2^{M(s)}$ and $\mathrm{S}^{M(s)}$ values, respectively, from a knowledge of the phase diagram, available information on the entropies of mixing of the liquids, and estimated $\mathrm{S}_1^{M(s)}$ values.

A qualitative relation that we shall subsequently use and with which experimental results at T^* must be consistent can be seen with equations (1) and (3). Elimination of Σ_1 from equations (1) and (3) gives

$$\frac{\mathrm{d}}{\mathrm{d}T}X_2^{(l)} = \frac{\left[\dfrac{X_2^{(l)*}}{X_1^{(l)*}} - \dfrac{X_2^{(s)*}}{X_1^{(s)*}}\right]X_1^{(s)}\Sigma_2}{[X_2^{(l)*} - X_2^{(s)*}]\left(\dfrac{\partial^2 G^{M(l)}}{\partial X_2^{(l)2}}\right)} \qquad (7)$$

valid at the temperature T^*. From equation (7), it follows that $\Sigma_2 = (\bar{\mathrm{S}}_2^{(l)} - \bar{\mathrm{S}}_2^{(s)}) < 0$ and, remembering equation (3), $\Sigma_1 = (\bar{\mathrm{S}}_1^{(l)} - \bar{\mathrm{S}}_1^{(s)}) > 0$. Thus, in contrast to entropies of the pure elements in the liquid and solid states, $\bar{\mathrm{S}}_2$ is more positive for the solid than for the coexisting liquid phase at T^*, the temperature of maximum retrograde solubility.

RESULTS

Evaluation of the entropies of mixing for the liquids composition at temperature T*.

The standard reference states are defined as the pure elements in their normal states at the temperature T^*. For the prescribed calculations, we shall need $\mathrm{S}_1^{M(l)}$, $\mathrm{S}_2^{M(l)}$, and $\mathrm{S}^{M(l)}$ values at $X_2 = X_2^{(l)*}$ and the temperature $T = T^*$. Values as computed† from published experimental data are listed in columns 6 to 8 of Table 2 for the elements in the reference states as shown in columns 1 and 2. The values which are selected for the subsequent calculations are indicated by asterisks.

---

†For extrapolation as a function of temperature as employed in the calculations, the entropies of mixing are assumed to be constant. Some of the values listed in columns 6 to 8 of Table 2 are enclosed in parentheses to indicate a lesser reliability that results from either scatter in the original data, possible determinant error in the experimental method, or because the published data pertain to remote conditions and an extended extrapolation as a function of temperature and/or composition is necessary to obtain the quantities under the appropriate conditions. Entropies of transition at temperature T^* are calculated with the values of entropies of normal transition as tabulated by Stull and Sinke[111] and others[112–114]. The entropies of fusion at the normal melting point are corrected to $T = T^*$ with heat capacity values as given by

Entropy values as calculated with the assumption that the entropy of mixing of the liquid components is ideal, are listed in Columns 3 to 5 of Table 2. They are all reasonably close to the published experimental values suggesting that the calculated values are reasonable approximations in the cases for which experimental data are lacking. For the cases that experimental data are lacking, the ideal entropies of mixing as listed in Columns 3 to 5 of Table 2 are adopted in the subsequent calculations.

Evaluation of the entropies of mixing of the solidus composition at the temperature T*

For the cases of elemental phases with retrograde solidi, the extreme solubility, $X_2^{(s)*}$, does not exceed 0·03 except for the case of Ag–Tl for which $X_2^{(s)*} = 0{\cdot}075$. With some degree of confidence, then the approximation

$$S_1^{M(s)} \approx 0 \tag{8}$$

can be made for the elemental solid phases.

For the compound phases with retrograde solidi, the analysis of $S_1^{M(s)}$ is more complicated because (1), by virtue of being a compound, the solution is no longer dilute with respect to either component 1 or 2 and (2) the normal state of component 1 need not be solid at temperature T^*. Consider the process of solidification of component 1, if it is not already a solid in its reference state, and then of dissolution of component 1 in a sufficiently large quantity of the solid solution with $X_2^{(s)} = X_2^{(s)*}$. The net entropy change can be written for one gram atom of component 1 as the sum of the entropy changes of the individual reactions as follows:

$$S_1^{M(s)} = -\Delta S_{v1}(T^*) - \Delta S_{f1}(T^*) + S_1^{M(s\bullet)}, \tag{9}$$

if component 1 is gaseous,

$$S_1^{M(s)} = -\Delta S_{f1}(T^*) + S_1^{M(s\bullet)}, \tag{10}$$

if component 1 is liquid,

$$S_1^{M(s)} = S_1^{M(so)}, \tag{11}$$

if component 1 is solid in its normal reference state at temperature T^*. In equations (9) to (11), $S_1^{M(s\bullet)} = [\bar{S}_1^{(s)}(T^*) - S_1^{\bullet(s)}(T^*)]$ and $S_1^{M(so)} = [\bar{S}_1^{(s)}(T^*) - S_1^{o(s)}(T^*)]$, representing the partial molar entropies of mixing of component 1, explicitly indicate by the superscripts (s●) or (so) whether component 1 is referred to a superheated or normal solid state, respectively. In the absence of a tested method for calculation of $S_1^{M(s\bullet)}$ and $S_1^{M(so)}$, these terms are omitted and tentative calculations are made with the approximation equations

$$S_1^{M(s)} \approx -\Delta S_{v1}(T^*) - \Delta S_{f1}(T^*), \tag{9a}$$

if component 1 is gaseous,

$$S_1^{M(s)} \approx -\Delta S_{f1}(T^*), \tag{10a}$$

if component 1 is liquid, and

$$S_1^{M(s)} \approx 0, \tag{11a}$$

Kubaschewsky, Evans and Alcock[114] if listed, otherwise the small temperature correction is neglected. Entropies of vaporization at T^* are approximated in all cases as the value of the entropy of vaporization at 1 atm pressure. Arsenic and phosphorus form complex mixtures of associated gaseous molecules at temperatures near the boiling points. For these cases, the Trouton-rule value of 22 e.u. is adopted for the entropy of vaporization of the diatomic molecules at the pertinent temperatures. Sulfur and selenium also form associated molecules on vaporization, but for these cases, the values are taken as given by Kubaschewski, Evans, and Alcock[114]. The reference temperature exceeds the critical temperature for the elements arsenic (1047°)[115], fluorine (−129°)[111] nitrogen (−147°)[111], oxygen (−118°)[111], phosphorus (721°) [115], and sulfur (1040°)[115], and there is no experimental significance to a pure hypothetical liquid state as a reference for these elements. The entropy change suffered by these elements upon formation of the gas is approximated as the sum of the normal entropies of fusion and of evaporization. This is emphasized by brackets enclosing the calculated results. Any error introduced by this artifact is expected to yield over estimates for the entropies of vaporization and, therefore, to not alter the final conclusions.

Table 2. Molar entropies of mixing the liquidus composition at the temperature of maximum retrograde solubility

Component and reference state		Entropies of mixing, e.u.						
		Ideal			Experimental (lit.)			
1	2	S_1^M	S_2^M	S^M	S_1^M	S_2^M	S^M	Ref.
Ge(s)	Ag(s)	6·5	5·3	6·2				
Si(s)	Ag(l)	7·5	3·8	7·0				
Ge(s)	Al(l)	7·3	1·5	4·6				
Si(s)	Al(l)	8·2	2·1	6·0				
Co(s)	Au(l)	3·4	1·6	2·6				
Si(s)	Au(l)	7·6	3·4	6·8				
Ag(s)	Bi(l)	3·1	2·1	2·7	3·1	2·6	2·9	83, 84
					3·2	3·3	3·3	85
					3·8	2·8	3·3	86
					4·0	2·3	3·2†	88
Au(s)	Bi(l)	2·5	4·2	2·7	3·2	4·3	3·3†	89
Te(l)	Bi(l)	1·4	1·4	1·4				
Cu(s)	Bi(l)	4·0	1·0	2·2	4·7	1·7	2·9	90
					5·0	1·5	2·9	91
					4·5	1·4	2·7	92
					4·6	1·2	2·6†	93
F_2(g)	Ca(l)	[−8·2	1·9	−4·4]				
Cu(s)	Cd(l)	3·0	2·0	2·6	3·1	2·5	2·9	94
					2·8	1·7	2·4†	95
					2·8	1·2	2·2	96, 97
					2·6	0·3	1·7	98
					3·3	0·0	2·1	87
Te(l)	Cd(g)	4·6	−22·8	−20				
Ge(s)	Cd(g)	7·4	−21·6	−7·1				
Zn(s)	Cd(s)	4·0	3·7	3·8	4·1	3·7	3·8	99
					7·0	3·5	5·0	100
					3·9	3·6	3·7	101
					4·0	3·7	3·8†	102
					4·0	3·7	3·8	103
Ge(s)	Cu(s)	6·4	5·7	6·3				
Si(s)	Cu(l)	7·6	3·2	6·7				
Si(s)	Fe(s)	7·6	5·3	7·2				
Ge(s)	Ga(l)	7·8	1·0	3·7				
Si(s)	Ga(l)	8·7	1·4	5·1				
Ge(s)	In(l)	7·0	1·9	5·0				
Si(s)	In(l)	8·0	2·3	6·2				
Ge(s)	Li(l)	6·3	4·1	6·0				
Si(s)	Li(l)	8·2	2·0	5·9				
Ge(s)	Ni(s)	6·3	5·6	6·2				
Si(s)	O_2(g)	[7·2	1·9	7·2]				
Ag(s)	Pb(l)	3·2	2·0	2·8	3·3	1·6	2·7	104
					3·0	1·7	2·5†	105
					3·5	3·1	3·4	106
Au(s)	Pb(l)	2·5	4·2	2·7	2·6	7·8	3·3	107
					2·6	6·6	3·0†	87
Ge(s)	Pb(l)	6·9	2·1	5·2				
S_2(g)	Pb(l)	[−12·1	0·9	−3·7]				
Se(g)	Pb(l)	−10·3	0·9	−3·0				
Te(l)	Pb(l)	3·4	0·4	0·9				
Pb(l)	S_2(g)	2·0	−13·3	−7·6				
Au(s)	Sb(s)	2·7	8·2	4·0	2·7	8·6	4·1†	108
Ge(s)	Sb(l)	6·6	2·8	5·6				

Table 2. (*cont.*)

Component and reference state 1	2	Entropies of mixing, e.u. Ideal S_1^M	S_2^M	S^M	Experimental (lit.) S_1^M	S_2^M	S^M	Ref.
Si(s)	Sb(l)	7·8	2·8	6·5				
Al(s)	Sn(l)	3·1	3·3	3·1				
Si(s)	Sn(l)	15·1	0·0	0·3				
Cd(g)	Te_2(g)	−21·4	−8·6	−14·3				
Co(s)	Te(l)	6·0	0·3	1·2				
Pb(l)	Te(l)	2·3	0·8	1·3				
Sn(l)	Te(l)	2·3	0·7	1·2				
N_2(g)	Th(l)	[−4·3	0·2	−0·3]				
P_2(g)	Th(l)	[−8·2	0·6	−1·6]				
As_2(g)	Th(l)	[−8·7	0·8	−2·3]				
Ag(s)	Tl(l)	4·7	0·7	1·9	(3·5	1·1	1·8)	109
					5·7	1·0	2·4†	110
Au(s)	Tl(l)	2·7	2·9	2·8	2·8	4·1	3·1†	89
					(2·5	4·6	3·0)	109
C(s)	U(l)	9·1	0·3	1·4				
N_2(g)	U(l)	[−3·9	0·2	−0·2]				
P_2(g)	U(l)	[−7·7	0·4	−1·2]				
As_2(g)	U(l)	[−7·7	0·4	−1·2]				
S_2(g)	U(l)	[−10·3	0·3	−1·2]				
Ge(s)	Zn(l)	7·0	1·8	4·9				
Si(s)	Zn(g)	7·7	−20·1	+1·6				

†Published data as used in calculations.

if component 1 is solid in its normal state of reference at temperature T^*. Subsequently, the validity of this procedure is tested by comparison of the calculated results with the available experimental data.

Values of $S_2^{M(s)}$ and $S^{M(s)}$ as calculated with equations (5) and (6), the data given in Tables 1 and 2, and the appropriate approximations for $S_1^{M(s)}$ as given in equations (8) and (9a) to (11a) are listed in Columns 3 to 5 of Table 3.

DISCUSSION

Elemental phases

For comparison, the only pertinent experimental data on the entropies of mixing the solid elemental phases seem to be those reported by Thurmond and Struthers[25] and Hodgkinson[26] on the Cu–Ge, Cu–Si, and Sb–Ge solutions. Values of $S_2^{M(s)}$ as calculated from their data are listed in Column 6 of Table 3. Our calculated and the reported $S_2^{M(s)}$ values agree in that they are all strongly positive indicating that the described method of calculation is profitable.

In analogy to equations (9) to (11) for component 1, the entropy of mixing of component 2 can be written

$$S_2^{M(s)} = -\Delta S_{v2}(T^*) - \Delta S_{f2}(T^*) + S_2^{M(s\bullet)}, \quad (12)$$

$$\approx -\Delta S_{v2}(T_{v2}) - \Delta S_{f2}(T_{f2}) + S_2^{M(s\bullet)}, \quad (12a)$$

$$S_2^{M(s)} = -\Delta S_{f2}(T^*) + S_2^{M(s\bullet)}, \quad (13)$$

$$\approx -\Delta S_{f2}(T_{f2}) + S_2^{M(s\bullet)}, \quad (13a)$$

or

$$S_2^{M(s)} = S_2^{M(so)} \quad (14)$$

if component 2 is, respectively, a gas, liquid, or *solid in its normal reference state at the* temperature of T^*. The term $S_2^{M(s\bullet)} = [\bar{S}_2^{(s)} - S_2^{\bullet(s)}]$, is the partial molar entropy of component 2 referred to its superheated solid state and $S_2^{M(so)} = [\bar{S}_2^{(s)} - S_2^{o(s)}]$ is the

Table 3. Entropies of mixing of the solidus composition at the temperature of maximum retrograde solubility

Component and reference state		Entropies of mixing, e.u.					
		Calculated			Experimental		
1	2	S_1^M	S_2^M	S^M	S_2^M	S^M	Ref.
Ge(s)	Ag(s)	0	28	0·0			
Si(s)	Ag(l)	0	46	0·1			
Ge(s)	Al(l)	0	9·7	0·1			
Si(s)	Al(l)	0	17	0·0			
Co(s)	Au(l)	0	5·9	0·2			
Si(s)	Au(l)	0	38	0·0			
Ag(s)	Bi(l)	0	7·8	0·2			
Au(s)	Bi(l)	0	22	0·0			
Cu(s)	Bi(l)	0	3·7	0·0			
Te(l)	Bi(l)	−5·8	8·7	0·3			
F_2(g)	Ca(l)	[−10·3	5·3	−5·0]		−11·0	113
Cu(s)	Cd(l)	0	7·1	0·2			
Te(l)	Cd(g)	−5·6	−22·0	−13·6		(−16·5)	117
						−16·1	118
						−18·0	119
						−16·7	120
						−17·6	121
						−16·7	122
						−17·5	133
Ge(s)	Cd(g)	0	−14	0·0			
Zn(s)	Cd(s)	0	6·8	0·1			
Ge(s)	Cu(s)	0	35	0·0	42		25
					45		26
Si(s)	Cu(l)	0	34	0·0	27		25
Si(s)	Fe(s)	0	42	0·0			
Ge(s)	Ga(l)	0	6·2	0·0			
Si(s)	Ga(l)	0	10	0·0			
Ge(s)	In(l)	0	13	0·0			
Si(s)	In(l)	0	19	0·0			
Ge(s)	Li(l)	0	46	0·0			
Si(s)	Li(l)	0	16	0·0			
Ge(s)	Ni(s)	0	39	0·0			
Si(s)	O_2(g)	[0	1800	0·1]			
Ag(s)	Pb(l)	0	7·4	0·2			
Au(s)	Pb(l)	0	23	0·0			
Ge(s)	Pb(l)	0	15	0·0			
S_2(g)	Pb(l)	[−15·1	2·5	−6·3]		(−10·9)	123
						−9·0	124, 125
						−9·5	126
						−10·3	127
						−7·1	128
Se_2(g)	Pb(l)	−14·2	3·0	−5·6		−9·0	129
Te(l)	Pb(l)	−5·7	2·4	−1·7		−4·5	117
						−6·3	130–1, 124
Pb(l)	S_2(g)	−1·6	−11	−6·4		−10·9	123
						−9·6	124, 125
						−9·5	126
						−10·3	127
						−9·0	128
Au(s)	Sb(s)	0	17	0·2			
Ge(s)	Sb(l)	0	23	0·0	29		25

Table 3. (*cont.*)

Component and reference state		Entropies of mixing, e.u.					
		Calculated			Experimental		
1	2	S_1^M	S_2^M	S^M	S_2^M	S^M	Ref.
Si(s)	Sb(l)	0	26	0·0			
Al(s)	Sn(l)	0	17	0·0			
Si(s)	Sn(l)	0	0·3	0·0			
Cd(g)	Te_2(g)	−25·2	−5·5	−15·3		−21·4	117
						−20·5	118
						−22·9	119
						−21·6	120
						−22·5	121
						−21·6	122
						−22·4	133
Co(s)	Te(l)	0	1·4	0·9			
Pb(l)	Te(l)	−1·8	2·7	0·5		−4·5	117
						−6·0	130–1, 124
Sn(l)	Te(l)	−2·4	2·8	0·3		−4·5	117
						−3·3	132
N_2(g)	Th(l)	[−10·0	0·9	−4·4]			
P_2(g)	Th(l)	[−11·5	1·7	−4·9]			
As_2(g)	Th(l)	[−17·1	4·8	−6·2]			
Ag(s)	Tl(l)	0	2·7	0·2			
Au(s)	Tl(l)	0	12·0	0·1			
C(s)	U(l)	0	1·7	0·8		−1·8	134
						−0·7	135
N_2(g)	U(l)	[−10·0	0·8	−4·7]		−10·8	136–8
P_2(g)	U(l)	[−11·5	1·3	−5·3]		−10·9	139
As_2(g)	U(l)	[−17·1	2·6	−7·3]			
S_2(g)	U(l)	[−15·1	1·1	−7·0]		−12·1	140
Ge(s)	Zn(l)	0	12	0·0			
Si(s)	Zn(g)	0	7·2	0·0		−11·6	141–2

analogous quantity with component 2 referred to its normal solid state at temperature T^*. For the elemental phases under consideration, these quantities may be written quite generally as

$$S_2^{M(s\bullet)} = -R \ln X_2^{(s)} + S_2^{E(s)}(X_2^{(s)}) \quad (15)$$

and

$$S_2^{M(so)} = -R \ln X_2^{(s)} + S_2^{E(s)}(X_2^{(s)}), \text{respectively,} \quad (16)$$

where $S_2^{E(s)}(X_2^{(s)})$ is the partial molar excess entropy of component 2 in crystals of component 1. The latter quantity is subsequently written as $S_2^{E(s)}$ without explicit statement of the dependence on $X_2^{(s)}$. If $X_2^{(s)} \ll 1$, one has practically a limiting value for $S_2^{E(s)}$ when $X_2^{(s)} \rightarrow 0$. This is the quantity denoted as σ by Thurmond and Struthers. The quantity $S_2^{E(s)}$ is important in conjunction with considerations of statistical mechanics. This has been pointed out by Zener[116]. In his paper, Zener calculated the quantity $S_2^{E(s)}$, denoted by him as ΔS_v, from the temperature dependence of the solubility of component 2 in crystals of component 1 coexisting with virtually pure crystals of component 2. He showed that theoretical considerations for 13 different cases of dilute solid solutions lead to the conclusion that $S_2^{E(s)}$ is positive.

By way of comparison with Zener's results, values of $S_2^{E(s)}$ were computed with equations (15) and (16) from the $S_2^{M(s)}$ values listed in

Column 4 of Table 3 at $X_2^{(s)} = X_2^{(s)*}$ for the elemental phases. Values thus obtained for the solutes show no systematic dependence on interatomic distances (International Crystallographic Tables values) with the various solvents such as would be expected if the size and vibrational considerations of Zener were alone sufficient to account for the $S_2^{E(s)}$ values. Furthermore, both positive and negative $S_2^{E(s)}$ values occur in contrast to the exclusively positive values occurring in the cases examined by Zener[116]. Thus, in general, $S_2^{E(s)}$ is a quantity more complex than that which occurs in the cases examined by Zener and electronic as well as (positive or negative) vibrational effects can contribute appreciably to $S_2^{M(s)}$ of dilute solid solutions.

Compounds. For comparison with our calculated results, experimental $S^{M(s)}$ values as computed from published standard molar entropies of formation are listed in column 7 of Table 3. In the single case of PbS, our values of −6·3 e.u. agrees fairly well with the value of −7·1 e.u. as calculated from data reported by Colin and Drowart[128]. In all other cases, our calculated $S^{M(s)}$ values listed in Column 5 are significantly more positive than the experimental ones. The differences are largest, exceeding at least 4 e.u. for the compounds CaF_2, CdTe, PbTe, UN, UP, and US. The differences are too great to be attributed to collapse of the assumption of ideal entropies of mixing of the liquid elements.

Possible sources of error that could give rise to the differences are (1) the entropies of vaporization of components i at the temperature T^* above the normal boiling point, $\Delta S_{vi}(T^*)$, are greater than the normal entropies of vaporization, $\Delta S_{vi}(T_{vi})$, as has been suggested by Kubaschewski, Evans, and Alcock,[114] (2) errors in the phase diagrams, (3) the terms $S_1^{M(se)}$ and $S_1^{M(so)}$ that have been neglected in equations (9–11) are appreciable, and (4) errors in the accepted entropy values for the formation of compounds and/or of phase transition of the elements.

The first possibility could be valid only for those cases that $T^* > T_{vi}$, $i = 1$ and/or 2, viz. the cases of the compounds CaF_2, CdTe, PbS, PbSe, UN, UP, and US. Even in these cases, this possibility is an unlikely explanation because the observed differences would require that the quantity

$$(\Delta S_{vi}(T^*) - \Delta S_{vi}(T_{vi})) = \int_{T_{vi}}^{T^*} [C_{pi}^{(g)} - C_{pi}^{(l)}] \frac{dT}{T},$$

have a rather large positive value for $T^* > T_{vi}$. This quantity is as a rule negative, however, because the factor $(C_{pi}^{(g)} - C_{pi}^{(l)})$ is as a rule negative with a common value of approximately −2·3 cal/deg-g atom [114] at temperatures near the normal boiling points. Thus, the integral is negative at temperatures near the normal boiling points and in order to account for the observed differences, a reversal in sign with relatively large positive values of $(C_{pi}^{(g)} - C_{pi}^{(l)})$ at higher temperatures would be required. This seems unlikely.

Second, the possibility of errors in the phase diagram is very real. Uncertainties in the T^* values from which the $X_2^{(l)*}$ values as listed in Table 1 are deduced from reported phase diagrams can contribute appreciably to uncertainties in the calculated $S^{M(l)}$ values as listed in Table 3. With reasonable assumed values for the margins of uncertainty in the T^* and the $X_2^{(l)*}$ values, however, the large differences under discussion cannot be accounted for in this way.

Third, in the absence of quantitative data on $S_1^{M(se)}$ and $S_1^{M(so)}$ in equations (9–11), these terms were omitted in the calculations of the molar entropies of mixing of solids. Reasonable limitations on signs and extreme magnitudes of these terms can be estimated for compound phases. The physical basis for the terms can be described qualitatively as contributions from changes in vibrational, free-electron, configurational (lattice defect), and magnetic entropies. In view of the apparent order in and the near-stoichiometry of the compounds under consideration, changes in configurational entropy will be relatively small and may be neglected. The major contributions to $S_1^{M(s\bullet)}$ or $S_1^{M(so)}$ arise, then, from changes in the physical origins which are the same as those leading to the term $S_2^{E(s)}$ in equations (15) and (16), applicable to dilute solid solutions. At the elevated temperatures of interest, changes in magnetic entropies will be negligible and changes in only the vibrational and the free-electron entropies need be contemplated. Now the resultant sum of these contributions must be negative in order to account for the observed differences. Qualitatively, appreciable negative changes in vibrational entropy may be expected for the formation of the compounds under discussion because their melting points are considerably greater than those of the constituent elements. From the available melting points and heat capacities of the solid elements and compounds the extreme value for the vibrational contribution to the partial molar entropies of mixing of the compounds is estimated to be no more negative than -6 e.u. Negative changes in free-electron entropies may, also, be expected at least for the ionic and semi-conductor compounds that are formed from metallic elements. Contributions from free-electrons are estimated by consideration of the extreme model in which the compounds contain no free electrons (ionic) and are formed from metallic constituents that, in the pure elemental state, are assumed to be an ideal solution of distinguishable-valence free electrons (equal in number to the number of valence electrons) and ion cores. This model should lead to an over estimate of the entropy change arising from electrons which are in fact indistinguishable. For formation of compounds in such a model, the entropy change due to changes in free-electron concentrations ranges in value from -2 e.u. for divalent Cd and Ca to -4 e.u. for sexvalent U. Taking the two contributions additively then we expect the $S_1^{M(s\bullet)}$ or $S_1^{M(so)}$ terms in equations (9–11) to be no more negative in value than -10 e.u.

That the $S_1^{M(s\bullet)}$ and $S_1^{M(so)}$ terms are indeed negative at the atomic fractions, $X_2^{(s)*}$, and temperatures, T^*, of interest is evident from the experimental standard molar entropies of compound formation that are referred to the constituent elements both in the solid state at 25°, ΔS_f^0 (25°). Values of $S^{M(s)}$ (25°) as calculated from the available ΔS_f^0 (25°) values with the equation $2S^{M(s)}(25°) = \Delta S_f^0(25°)$ are listed in Column 2 of Table 4. The phases are all monocompounds with virtually no range of composition at 25°. Neglecting small temperature dependences of entropies, the partial molar entropy of mixing of component 2 at $X_2^{(s)} = X_2^{(s)*}$, as referred to the super-heated solid state of pure 2, may be written.

Table 4. Values of $S^{M(s)}$ *for some binary compounds at 25° and estimated algebraic lower bounds for* $S_2^{M(s)}(T^*)$ *and upper bounds for* $S_1^{M(s)}(T^*)$ *referred to the constituent elements all in the solid state*

Formation reaction	$S^{M(s)}$(25°), e.u.	Ref.	Compn. 2	l.b. $S_2^{M(s)}$, e.u.	u.b. $S_1^{M(s)}$, e.u.
Cd(s) + Te(s) = CdTe(s)	−0·8	117	Teg	7·0	−8·6
Pb(s) + S(s) = PbS(s)	−0·65	124	Pbl	2·8	−4·1
Pb(s) + Se(s) = PbSe(s)	−0·4	129	Pbl	2·8	−5·6
Pb(s) + Te(s) = PbTe(s)	−0·6	117	Tel	6·6	−7·8
Sn(s) + Te(s) = SnTe(s)	+0·1	117	Tel	6·5	−6·6
U(s) + C(s) = UC(s)	+0·4	135	Ul	2·4	−1·5
U(s) + P(s) = UP(s)	+0·6	139	Ul	2·4	−1·2
U(s) + S(s) = US(s)	−0·5	141	Ul	2·4	−3·4

$$S_2^{M(s)} \approx \Delta S_{f2}(T_{f2}) - R\ln X_2^{(l)*} + (\bar{S}_2^{(s)}(X_2^{(s)*}) - \bar{S}_2^{(l)}(X_2^{(l)*})). \quad (17)$$

In equation (17), the expression in parentheses is always positive according to our earlier discussion of equation (7). Omission of this term then gives the equation of a lower bound for $S_2^{M(s)}$ at the temperature T^*,

$$\text{l.b.}S_2^{M(s)} = \Delta S_{f2}(T_{f2}) - R\ln X_2^{(l)*}. \quad (17a)$$

Values of $\text{l.b.}S_2^{M(s)}$ as calculated with equation (17a) and corresponding algebraic upper bounds of $S_1^{M(s)}$, u.b. $S_1^{M(s)}$, are listed in Columns 5 and 6, respectively, of Table 4. These values are all negative, thus, within the described approximation, the available standard entropies of formation yield u.b. $S_1^{M(s)}$ and, a fortiori, $S_1^{M(s)}$ values that are indeed all negative.

Values of $S_1^{M(se)}$ or $S_1^{M(so)}$ as needed to bring the calculated (Column 5 of Table 3) into agreement with the experimental (Column 7 of Table 3) $S^{M(s)}$ values were calculated. Considerable uncertainty exists in the values thus deduced. Positive statements can be made only about the largest values of -150 for CaF_2, -100 to -150 for CdTe, -23 for PbSe, up to -36 for PbTe, -18 for UN and UP, and -14 e.u. for US. Of these values, the extremely large negative values for CaF_2 and CdTe may be due in part to erroneous T^* and/or $X_2^{(l)*}$ values as listed in Table 1 leading to too narrow of solid-liquid two-phase regions in the respective phase systems. Even allowing for possible errors in the T^* and $X_2^{(l)*}$ data for the above named compounds, all the values are more negative than our estimated limiting value of -10 e.u. The latter differences are too great to attribute the differences between the calculated and experimental $S^{M(s)}$ values to neglect of the $S_1^{M(se)}$ and $S_1^{M(so)}$ terms in equations (9–11).

Summarizing the results for the compounds, there is considerable uncertainty in the $S^{M(s)}$ values calculated as described above with equation (6). The principal uncertainty stems from the second and third of the four possible sources of error as considered above. However, the differences between the calculated and experimental $S^{M(s)}$ values for the compounds CaF_2, CdTe, PbTe, UN, UP, and US seem too great to be attributed to the approximations in our calculations suggesting that there exist errors in the accepted values for the entropies of formation of these compounds and/or of phase transition of their constituent elements.

Acknowledgement—The author thanks C. Wagner for a stimulating written discussion.

REFERENCES

1. BUGAI A. A., KOSENKO V. E. and MISELIUK E. G., *Zh. tekh. Fiz.* **27**, 1671 (1957).
2. HANSEN M. and ANDERKO K., *Constitution of Binary Alloys*. McGraw-Hill, New York (1958).
3. BOLTAKS B. I. and HSÜEH SHIH-YIN, *Fiz. Tverd. Tela* **2**, 2677 (1960).
4. TRUMBORE F. A., PORBANSKY E. M. and TARTAGLIA A. A., *J. Phys. Chem. Solids* **11**, 239 (1959).
5. NAVON D. and CHERNYSHOV V., *J. appl. Phys.* **28**, 823 (1957).
6. TRUMBORE F. A., *Bell System Tech J.* **39**, 205 (1960).
7. RAUB E. and WALTER P., *Z. Metallk.* **41**, 234 (1950).
8. COLLINS C. B., CARLSON R. O., and GALLAGHER C. J., *Phys. Rev.* **105**, 1168 (1957).
9. BOLTAKS B. I., KULIKOV G. S. and MALKOVICH R. SH., *Fiz. Tverd. Tela* **2**, 2395 (1960).
10. VOCE E. and HALLOWES A. P. C., *J. Inst. Metals* **73**, 323 (1947).
11. BASSI G., *Z. Metallk.* **48**, 394 (1957).
12. RAUB E. and ENGEL A., *Z. Metallk.* **37**, 76 (1946); (b). *ibid.* **41**, 485 (1950).
13. BREBRICK R. F., *J. Phys. Chem. Solids* **30**, 719 (1969).
14. LICHTER B. D. and BREDIG M. A., *J. electrochem. Soc.* **112**, 506 (1965).
15. ROGERS P. S., TOMLINSON J. W., and RICHARDSON F. D., "Metal-Molten Salt Solutions. I. Phase Equilibria in the Systems $Mg + MgCl_2$ and $Ca + CaF_2$." Physical Chemistry of Process Metallurgy, V. 8, Pt. 2, *Intern. Symp. sponsored by the Met. Soc. AIME* (Edited by G. R. St. Pierre), p. 909, Interscience, New York (1961).
16. RAUB E., *Z. Metallk.* **38**, 119 (1947).
17. SULONEN M., *Z. Metallk.* **55**, 543 (1964).
18. DE NOBEL D., *Philips Res. Rep.* **14**, 361, 430 (1959).

19. LORENZ M. R., *J. Phys. Chem. Solids* **23**, 939 (1962).
20. KOSENKO V. E., *Fiz. Tverd. Tela* **1**, 1622 (1959).
21. JENKINS C. H. M., *J. Inst. Metals* **36**, 63 (1926).
22. STOCKDALE D., *J. Inst. Metals* **44**, 75 (1930).
23. HANSEN M., *Der Aufbau der Zweistofflegierungen*. Springer, Berlin (1936).
24. BRAY H. J., *J. Inst. Metals* **87**, 49 (1958).
25. THURMOND C. D. and STRUTHERS J. D., *J. phys. Chem.* **57**, 831 (1953).
26. HODGKINSON R. J., *Phil. Mag.* **46**, 410 (1955).
27. REYNOLDS J. and HUME-ROTHERY W., *J. Inst. Metals* **85**, 119 (1956).
28. STRUTHERS J. D., *J. appl. Phys.* **27**, 1560 (1956).
29. THURMOND C. D., TRUMBORE F. A. and KOWALCHIK M., *J. chem. Phys.* **25**, 799 (1956).
30. SAVITSKIY YE. M., BARON V. V. and TYLKINA M. A., *Zh. Neorg. Khim.* **3**, 763 (1958).
31. KOZLOVSKAYA V. M. and RUBINSHTEIN R. N., *Fiz. Tverd. Tela* **3**, 3354 (1961).
32. PELL E. M., *J. Phys. Chem. Solids* **3**, 74 (1957).
33. PELL E. M., *J. Phys. Chem. Solids* **3**, 77 (1957).
34. FULLER C. S. and REISS H., *J. chem. Phys.* **27**, 318 (1957).
35. WERTHEIM G. K., *Phys. Rev.* **115**, 37 (1959).
36. HROSTOWSKI H. J. and KAISER R. H., *J. Phys. Chem. Solids* **9**, 214 (1959).
37. ABRIKOSOV N. Kh., LIANG TS'UN-WU, and SHASHKOV YU. M., *Izvest. Akad. Nauk SSSR, Otdel. Tekh. Nauk, Met. i Toplivo*, No. 6, p. 65 (1960).
38. RAUB E. and POLACZEK-WITTEK A. V., *Z. Metallk.* **34**, 93 (1942).
39. RAUB E. and ENGEL A., *Z. Elektrochem.* **49**, 89 (1943).
40. BLOEM J. and KROEGER F. A., *Z. phys. Chem.* **7**, 1 (1956).
41. MILLER E. and KOMAREK K. L., *Trans. met. Soc. AIME* **236**, 832 (1966).
42. SEIDMAN D. N., *Trans. Met. Soc. AIME* **236**, 1361 (1966).
43. BREBRICK R. F. and ALLGAIER R. S., *J. chem. Phys.* **32**, 1826 (1960).
44. SCANLON W. W., *Phys. Rev.* **126**, 509 (1962).
45. BREBRICK R. F. and GUBNER E., *J. chem. Phys.* **36** 1283 (1962).
46. GRAVEMANN H. and WALLBAUM H.-J., *Z. Metallk.* **47**, 433 (1956).
47. PELZEL E., *Metall.* **10**, 717 (1956).
48. OWEN E. A. and ROBERTS E. A. O., *J. Inst. Metals* **71**, 213 (1945).
49. RUTTEWIT K. and MASING G., *Z. Metallk.* **32**, 52 (1940).
50. STOEHR H. and KLEMM W., *Z. anorg. all. Chem.* **244**, 205 (1940).
51. PHILLIPS H. W. L., *Annotated Equilibrium Diagrams of Some Aluminum Alloy Systems*, No. 25. Inst. Metals (1959).
52. CAMPBELL A. N. and KARTZMARK R., *Can. J. Chem.* **34**, 1428 (1956).
53. TRUMBORE F. A., ISENBERG C. R., and PORBANSKY E. M., *J. Phys. Chem. Solids* **9**, 60 (1958).
54. DUDKIN L. D. and DYUL'DINA K. A., *Zh. Neorg. Chem.* **4**, 2313 (1959).
55. MILLER E., KOMAREK K., and CADOFF I., *Trans. met. Soc. AIME* **215**, 882 (1959).
56. BREBRICK R. F., *J. Phys. Chem. Solids* **24**, 27 (1963).
57. BREBRICK R. F. and STRAUSS A. J., *J. chem. Phys.* **41**, 197 (1964).
58. BENZ R., HOFFMAN C. G. and RUPERT G. N., *J. Am. chem. Soc.* **89**, 191 (1967).
59. JAVORSKY C. A. and BENZ R., *J. nucl. Mater.* **23**, 192 (1967).
60. BENZ R., *J. nucl. Mater.* **25**, 233 (1968).
61. RAUB E., *Z. Metallk.* **40**, 432 (1949).
62. WILLIAMS J., SAMBELL R. A. J. and WILKINSON D. W., *J. less-common Metals* **2**, 352 (1960).
63. BUCKLEY S. N., "The Formation and Properties of Sub-Stoichiometric Uranium Monocarbide," AERE-R3872, Sci. Admin. Off. At. Energy Res. Estab., Harwell, Berkshire, England (1961).
64. MAGNIER P. and ACCARY A., *Carbides in Nuclear Energy* (Edited by L. E. Russell), Vol. 1, p. 22. MacMillan, New York (1964).
65. GUINET P., VAUGOYEAU H. and BLUM P. L., *C. r. hebd. Séanc. Acad. Sci., Paris* **261**, 1312 (1965).
66. CARTER J. H., CT-609 (1934). U.S. At. Energy Comm., Tech. Inform. Services, Wash. 25, D.C.
67. SNOW A. I., CT-954 (1943), *ibid.*
68. MALLETT M. W., GERDS A. F. and NELSON H. R., *J. electrochem. Soc.* **99**, 197 (1952).
69. STORMS E. K., *Thermodynamics*, Vol. 1, Intern. At. Energy Agency, Vienna, 1966, p. 309, *ibid. The Refractory Carbides*. Academic Press, New York (1967).
70. BENZ R. and BOWMAN M. G., *J. Am. chem. Soc.* **88**, 264 (1966).
71. BUGL J. and BAUER A. A., *J. Am. ceram. Soc.* **47**, 425 (1964).
72. BENZ R. and WARD C. H., *J. inorg. nucl. Chem.* **30**, 1187 (1968).
73. BENZ R. and TINKLE M. C., *J. electrochem. Soc.* **115**, 322 (1968).
74. BENZ R. (not published).
75. THURMOND C. D. and KOWALCHIK M., *Bell System Tech. J.* **39**, 169 (1960).
76. BREBRICK R. F. and STRAUSS A. J., "Homogeneity Range and Concentration-pressure Isotherms for HgSe," *II–VI Semiconducting Compounds, 1967 Intern. Conf.*, (Edited by D. G. Thomas), p. 425. Benjamin, New York (1967).
77. TYLER W. W., *J. Phys. Chem. Solids* **8**, 59 (1959).
78. ALBERS W., HAAS C., VINK H. J. and WASSCHER J. D., *J. appl. Phys.* **S32**, 2220 (1961).
79. ALBERS W., HAAS C. and VINK H. J., *Philips Res. Rep.* **18**, 372 (1963).
80. WAGNER C., *Thermodynamics of Alloys*. Addison-Wesley, Reading, Mass. (1952).
81. MEIJERING J. L., *Philips Res. Rep.*, **3**, 281 (1948).
82. SCHOTTKY W., ULICH H., and WAGNER C., *Thermodynamik*, p. 511. Springer, Berlin (1929).
83. GREGORCZYK Z., *Roczniki Chem.* **34**, 621 (1960).

84. GREGORCZYK Z., *ibid.* **35**, 307 (1961).
85. VECHER A. A. and GERASIMOV YA. I., *Dokl. Akad. Nauk SSSR* **141**, 381 (1961).
86. ALDRED A. T. and PRATT J. N., *Trans. Faraday Soc.* **59**, 673 (1963) as reviewed in [87].
87. HULTGREN R., ORR R. L., ANDERSON P. D. KELLEY K. K., *Selected Values of Thermodynamic Properties of Metals and Alloys*. Wiley, New York (1963).
88. RAYNOR J. B., *Ber. Buns. phys. Chem.* **67**, 629 (1963).
89. KLEPPA O. J., *J. Am. chem. Soc.* **73**, 385 (1951).
90. KLEPPA O. J., *J. Am. chem. Soc.* **74**, 6047 (1952).
91. NIKOL'SKAYA A. V., LOMOV A. L., and GERASIMOV YA. I., *Zh. Fiz. Khim.* **33**, 1134 (1959).
92. OELSEN W., SCHUERMANN E., and BUCHHOLZ D., *Arch Eisenhuetten* **32**, 39 (1961).
93. LOMOV A. L. and KRESTOVNIKOV A. N., *Izv. Vysshikh Uchebn. Zavedenii Tsvetn. Met.* **7**, 84 (1964).
94. JELLINEK K. and ROSNER G. A., *Z. phys. Chem.* **152**, 67 (1931).
95. SCHNEIDER A. and SCHMID H., *Z. Elektrochem.* **48**, 627 (1942).
96. RICCOBONI L., GENTA V. and FIORANI M., *Ricerca scient.* **23**, 408 (1953).
97. RICCOBONI L., GENTA V., FIORANI M., and VALENTI V., *Gass. Chim. Ital.* **84**, 982 (1954).
98. NIKOL'SKAYA A. V., OTOPKOV P. P., and GERASIMOV YA. I., *Zh. Fiz. Khim.* **31**, 1007 (1957).
99. TAYLOR N. W., *J. Am. chem. Soc.* **45**, 2865 (1923).
100. KOTOV E. I., *Vestnik Akad. Nauk Kazakh S.S.R.* **6**, No. 1 (46), 37 (1949) as quoted in CA 47:9084c (1953).
101. SANO K., OKAJIMA K. and TATSUO S., *Mem. Fac. Eng. Nagoya Univ.* **5**, 299 (1953).
102. BOHL R. W. and HILDEBRANDT V. D., *J. Am. chem. Soc.* **79** 2711 (1957).
103. WYNNEMER D. J. and PRECKSHOT G. W., *Trans. met. Soc. AIME* **221**, 186 (1961).
104. EREMENKO V. N., *Ukrain. Khim. Zhur.* **23**, 6 (1957) as quoted in CA 51:11015b.
105. TERPILOWSKI J., *Arch. Hutnictwa* **2**, 289 (1957).
106. ALDRED A. T. and PRATT J. N., *Trans. Faraday Soc.* **57**, 611 (1961).
107. KLEPPA O. J., *J. Am. chem. Soc.* **71**, 3275 (1949).
108. WEIBKE F. and SCHRAG G., *Z. Elektrochem.* **46**, 658 (1940).
109. KLEPPA O. J., *J. phys. Chem.* **60**, 446 (1956).
110. TERPILOWSKI J., KUNDYS E., and SLABY H., *Arch. Hutnictwa* **6**, 137 (1961).
111. STULL D. R. and SINKE G. C., *Thermodynamic Properties of the Elements*. Am. Chem. Soc., Wash. 6, D.C. (1956).
112. KELLEY K. K., U.S. Bur. Mines Bull. 383, U.S. Gov. Printing Off., Wash. 25 D.C. (1935).
113. WICKS C. E. and BLOCK F. E., U.S. Bur. Mines Bull. 605, U.S. Gov. Printing Off., Wash. 25, D.C. (1963).
114. KUBASCHEWSKI O., EVANS E. LL. and ALCOCK C. B., *Metallurgical Thermochemistry*. Pergamon Press, Oxford (1967).
115. *Gmelins Handbuch d. Anorgan. Chem.*, Verlag Chem., GmbH., Weinheim Bergstr., No. 17 (1952); No. 9 (1953); 16 (1964).
116. ZENER C., *Thermodynamics in Physical Metallurgy*, p. 16. Am. Soc. Metals, Cleveland, Ohio (1950).
117. MCATEER J. H. and SELTZ H., *J. Am. chem. Soc.* **58**, 2081 (1936).
118. KORNEEVA I. V., BELYAEV A. V. and NOVOSELOVA A. V., *Zh. Neorg. Khim.* **5**, 241 (1960). Knudsen vapor pressure (450–650°) data are analyzed for congruent vaporization and the assumed reaction $CdTe(s) = Cd(g) + \frac{1}{2}Te_2(g)$.
119. LORENZ M. R., *J. Phys. Chem. Solids* **23**, 1449 (1962).
120. GOLDFINGER P. and JEUNEHOMME M., *Trans. Faraday Soc.* **59**, 2851 (1963).
121. BREBRICK R. F. and STRAUSS A. J., *J. Phys. Chem. Solids* **25**, 1441 (1964).
122. TERPILOWSKI J. and RATAJCZAK E., *Bull. Acad. Polon. Sci., Ser. Sci. Chim.* **12**, 355 (1964).
123. JELLINEK K. and DEUBEL A., *Z. Elektrochem.* **35**, 451 (1929).
124. KELLEY K. K. and KING E. G., U.S. Bur. Mines Bull. 592, U.S. Gov. Printing Off., Wash. 25, D.C. (1961).
125. KELLEY K. K., U.S. Bur. Mines Bull. 476, U.S. Gov. Printing Off., Wash. 25, D.C. (1949).
126 SUDO K., Science Repts., *Research Inst. Tohoku Univ.* **A2**, 325 (1950)
127. STUBBLES J. R. and BIRCHENALL C. E., *Trans. met. Soc. AIME* **215**, 535 (1959).
128. COLIN R. and DROWART J., *J. chem. Phys.* **37**, 1120 (1962).
129. FINCH C. B. and WAGNER J. B., Jr., *J. electrochem. Soc.* **107**, 932 (1960).
130. BREBRICK R. F. and STRAUSS A. J., *J. chem. Phys.* **40**, 3230 (1964).
131. KELLEY K. K., U.S. Bur. Mines Bull. 584, U.S. Gov. Printing Off., Wash. 25, D.C. (1960).
132 BREBRICK R. F. and STRAUSS A. J., *J. chem. Phys.* **41**, 197 (1964).
133. DROWART J. and GOLDFINGER P., *J. chim. Phys.* **55**, 721 (1958).
134. ALCOCK C. and GRIEVESON P., *Thermodynamics of Nuclear Materials*, p. 563. Intern. At Energy Agency, Vienna (1962).
135. "The Uranium-Carbon and Plutonium-Carbon Systems; A Thermochemical Assessment." Tech. Reps. Sers. No. 14, A Panel Rep. 1962, Intern. At. Energy Agency, Vienna, 1963, p. 37.
136. WESTRUM E. F., Jr. and BARBER C. M., *J. chem. Phys.* **45**, 635 (1966).
137. COUNSELL J. F., DELL R. M., MARTIN J. F., *Trans. Faraday Soc.* **62**, 1736 (1966).
138. SPEIDEL E. O. and KELLER D. L., BMI-1633, Battelle Memorial Inst., Columbus 1, Ohio (1963).
139. COUNSELL J. F., DELL R. M., JUNKISON A. R. and MARTIN J. F., *Trans. Faraday Soc.* **63**, **72** (1967).

140. CATER E. D., RAUH E. G., and THORN R. J., *Thermodynamics of Nuclear Materials*, p. 487; Intern. At. Energy Agency, Vienna (1962), *J. chem. Phys.* **48**, 538 (1968).
141. WESTRUM E. F., Jr. and GRONVOLD F., *Thermodynamics of Nuclear Materials*, *ibid.*, p. 3.
142. MACLEOD A. C. and HOPKINS S. W. J., *Proc. Brit. Ceram. Soc.* **8**, 15 (1967).

J. Phys. Chem. Solids Pergamon Press 1970. Vol. 31, pp. 729–737. Printed in Great Britain.

ELECTRICAL CONDUCTIVITY OF ADDITIVELY COLORED POTASSIUM CHLORIDE*

ROBERT E. SEEVERS† and ALLEN B. SCOTT
Department of Chemistry, Oregon State University, Corvallis, Oregon 97331, U.S.A.

(*Received* 27 *June* 1969; *in revised form* 12 *September* 1969)

Abstract—The conductivity of colored KCl crystals was found to be greater than that of uncolored crystals over the range from 150° to 550°C. The electronic transport number, determined to be 0·96 at 400°C, indicates that the increased conductivity was due to ionized F centers. Plots of log σ vs. $1000/T$ were linear, with two different slopes depending on the prior treatment of the sample. If gold contacts were evaporated onto freshly cleaved crystals rectification was observed. The rectification could be eliminated by either heating the colored crystals for five minutes at temperatures greater than approximately 500°C, after applying the contacts, or by sanding the crystals prior to applying the contacts. Accompanying the elimination of rectification was a decrease in the conductivity and an increase in the activation energy for conduction, from 1·13 to 1·22 eV. Curves of σ, at a given temperature, vs. $\sqrt{n_t}$ were found to be linear. From the above observations and the theory of rectifying contacts, the thermal ionization energy for F centers was calculated to be not less than 2·04 eV. Comparison of the calculations with experiment lead to the conclusion that the concentration of negative-ion vacancies in colored crystals was much less than the equilibrium concentration in uncolored crystals.

1. INTRODUCTION

THE MOBILITY of F centers, and the electrical conductivity of additively colored alkali halide crystals, has received considerable attention [1–7]. There remains disagreement, not only concerning the interpretation of the temperature coefficient of conductivity, but also upon the source of carriers.

Mott and Gurney[3] treated the experiments of Smakula[2], assuming that thermal ionization provides conduction electrons in a concentration small compared to that of negative-ion vacancies produced by intrinsic disorder, and showed that in the region of intrinsic ionic disorder the electronic conductivity due to F centers should vary approximately as $\exp[-(E_F-\frac{1}{2}E_S)/kT]$, where E_F is the thermal ionization energy of F centers and E_S is the energy for formation of a pair of separated Schottky defects.

Shamovskii, Dunina and Gosteva[4] studied the temperature range in which ionic conductivity was extrinsic. In this range, if the negative-ion vacancy concentration is established by the Schottky equilibrium, the electronic conductivity should vary approximately as $\exp[-(E_F-E_S)/kT]$. Since E_F and E_S are both undoubtedly in the neighborhood of 2 eV, the expected temperature coefficient of conductivity is about zero. These authors, however, found a large positive coefficient, corresponding to an activation energy of 1·03 eV and concluded that the conductivity varied as $\exp(-E_F/2kT)$. This result follows from the assumption that the number of conduction electrons and number of negative-ion vacancies are equal, that is, that all negative-ion vacancies are produced by F center ionization. It must be noted that, since $E_F \simeq E_S$, the activation energy $E_F-\frac{1}{2}E_S \simeq E_F/2$, so that the temperature coefficient of conductivity alone will not distinguish between the assumption of Mott and Gurney and that of Shamovskii *et al.*

Maycock[7] assumed the electronic conductivity to vary as $\exp(-E_F/kT)$, which implies a temperature-independent concentration of negative-ion vacancies.

---

*Supported by the National Science Foundation.

†*Present address*: Department of Chemistry Southern Oregon College, Ashland, Oregon 97520, U.S.A.

On the other hand, Jain and Sootha[5, 6] interpret the increased conductivity of colored crystals as being due to thermionic emission from colloidal metal particles.

The experiments described here were carried out using purified crystals of low extrinsic conductivity. In this way, the regions of both extrinsic and intrinsic ionic conductivity could be investigated using relatively low F center concentrations and moderate temperatures. Colloid formation was avoided, so that there was no possibility of thermionic emission from metal particles. Transport number measurements were made to show whether, in fact, the conductivity is due to ionized F centers. The dependence of conductivity upon F center concentration was determined, which allows a choice of proper interpretation of the temperature coefficient to be made.

In addition some information upon the effects at the electrodes, during d.c. measurements, was obtained which, in conjunction with the theory of rectifying contacts, is of assistance in interpreting some of the experimental results.

2. EXPERIMENTAL

Crystals containing from $1\cdot3\times10^{16}$ F centers cm^{-3} to $2\cdot5\times10^{17}$ F centers cm^{-3} were used. The crystals were grown under an HCl and argon atmosphere, by the Kyropoulos method, from potassium chloride which had been purified by ion exchange. The process of purification was similar to that developed by Fredericks, Rosztoczy and Hatchett[8]. The crystals were additively colored using potassium metal. The F center concentration, n_F, was found by the use of the Smakula equation in the form

$$n_F = 0\cdot97\times10^{16} A_F \text{ cm}^{-3}$$

where A_F is the absorbance per cm at the maximum of the F band at room temperature.

A stainless steel conductivity cell, having a guard ring to eliminate the effect of surface conduction, was used. A purified argon atmosphere was maintained in the cell during measurements.

A Marshall Company furnace, controlled to ±0·5°C by a Barber–Coleman series 620 power controller and a Wheelco model 407 temperature regulator, was used in heating the cell. The temperature was measured by means of a chromel–alumel thermocouple, calibrated at the steam point of water and the freezing points of cadmium and aluminum. Conductivity measurements were made after the temperature had remained constant for at least 10 min. This proved sufficient to insure that thermal equilibrium had been established.

The circuit consisted of the conductivity cell, a Keithley model 241 regulated d.c. power supply and a Keithley model 610A electrometer connected in series. All electrical leads were of shielded coaxial cable to maintain a low noise level.

The samples were prepared by cleaving the colored crystals to dimensions of approximately $15\times15\times1\cdot5$ mm^3 after which gold contacts were evaporated onto the surfaces. Gold has been found in this laboratory to provide stable ohmic electrodes for use with uncolored alkali halide crystals and was chosen for this reason. As will be seen, a correction is necessary for rectification occurring with colored crystals.

The d.c. conductivity was calculated from the measured current density and the applied electric field strength. Polarization effects were slight and were observed only at low temperatures. The final current, after polarization had reached a maximum was used in calculating the conductivity, following the argument of Sutter and Noweick[9].

3. RESULTS

3.1 *Freshly cleaved samples*

In Fig. 1 log σ has been plotted vs. $1000/T$ for two crystals containing different concentrations of F centers and compared with the data for an uncolored crystal. A more complete correspondence with theory might be made by plotting $\log \sigma T^{-3/4}$ (see equation (4)) as ordinate; however, this is hardly warranted because of the uncertainty in the temperature coefficient of the electronic mobility. At lower temperatures the curves for the colored crystals are linear, with a slope corresponding to an activation energy of 1·13 eV. In the present work it was found that the low-temperature conductivity varied considerably between two samples of the same crystal; however, the high-temperature conductivity was found to be reproducible if crystals thicker than about 1·5 mm were used.

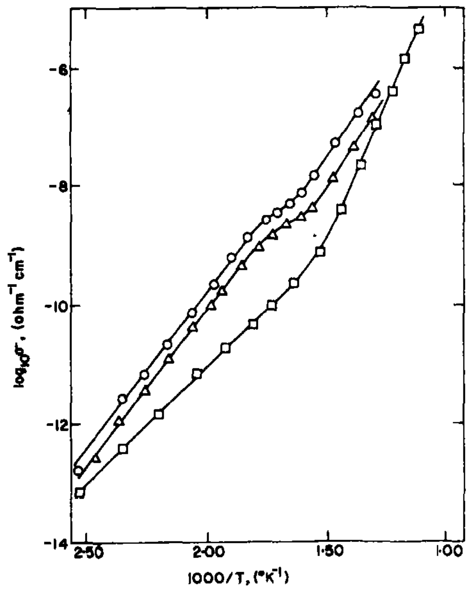

Fig. 1. The conductivity of additively-colored KCl crystals. The contacts were applied to freshly cleaved samples. *F* center concentrations: ○ – 1·2 × 10^{17} cm^{-3}, △ – 1·3 × 10^{16} cm^{-3}, □ – 0.

3.2 *The effect of heating before measurements*

When gold contacts were evaporated onto freshly cleaved samples and then the samples were heated at approximately 500°C (that is, at the upper end of the temperature range of measurements on the colored crystals) for five minutes, after which they were quenched to room temperature, their behavior was changed remarkably. After this treatment plots of log σ vs. 1000/*T* were reproducible and practically linear up to the point of intersection with the intrinsic curve for uncolored crystals. The conductivity at high temperatures was the same as the high-temperature conductivity characteristic of crystals which had not been heated and quenched. This behavior is shown in Fig. 2 where log σ is plotted vs. 1000/*T* for two crystals containing different concentrations of *F* centers. The slope in this case corresponds to an activation energy of 1·22 eV. Also shown for comparison is an uncolored crystal.

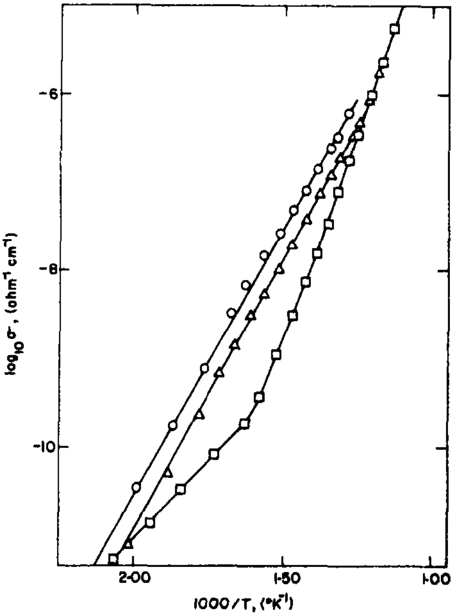

Fig. 2. The conductivity of additively-colored KCl crystals. After applying the contacts the crystals were heat-treated before conductivity measurements were made. *F* center concentrations: ○ – 1·8 × 10^{17} cm^{-3}, △ – 4·1 × 10^{16} cm^{-3}, □ – 0.

In colored samples, some departure from linearity at high temperatures was observed if thin crystals were used, or if the heating period was extended. This was avoided by using crystals of approximately 1·5 mm thickness and limiting the preheating period to 5 min. Presumably the cause of the nonlinearity was diffusion of *F* centers out of the crystals at high temperatures. If thick crystals were used the relative loss in 5 min was negligible.

3.3 *The effect of sanding crystal surfaces*

It was found that sanding the crystal surfaces with size O Monox polishing paper, before evaporating on the gold contacts, had, in nearly every case, the same effect as heating and quenching. Again the low temperature-conductivity was decreased until the log σ vs. $1000/T$ became an extension of the high-temperature conductivity curve exhibited by freshly cleaved crystals. It was also found that Ohm's law was accurately obeyed for the sanded or heated crystals, whereas rectification was observed for the freshly cleaved samples. This behavior is shown in Fig. 3 where we have plotted the current vs. voltage for a sanded crystal and for a crystal prepared by evaporating gold contacts onto the surfaces after sanding one face while leaving the other freshly cleaved.

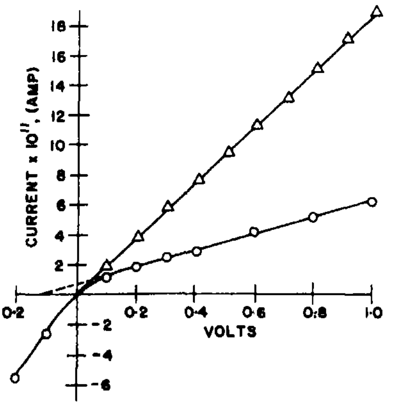

Fig. 3. The rectifying behavior of contacts applied to freshly cleaved samples and the obedience to Ohm's law for crystals sanded before applying contacts. ○ – freshly cleaved sample. △ – sanded sample.

3.4 *Dependence of σ on* F *center concentration*

Having found that the conductivity of sanded or preheated crystals, as well as the high-temperature conductivity of the freshly cleaved crystals, was reproducible, we determined the dependence of the conductivity on the F center concentration. This dependence is exhibited in Fig. 4, where we have plotted the total conductivities at $1000/T = 1{\cdot}5$, for several crystals containing different concentrations of F centers. vs. the square root of the F center concentration. The conductivity is seen to be proportional to $n_F^{1/2}$ to a good degree of accuracy.

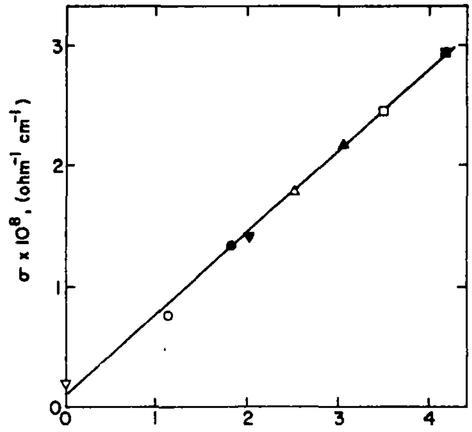

Fig. 4. Dependence of conductivity upon the square root of F center concentration at $1000/T = 1{\cdot}5$. F center concentrations: ○ – $1{\cdot}3 \times 10^{16}$, ● – $3{\cdot}4 \times 10^{16}$, ▼ – $4{\cdot}1 \times 10^{16}$, △ – $6{\cdot}5 \times 10^{16}$, ▲ – $9{\cdot}5 \times 10^{16}$, □ – $1{\cdot}2 \times 10^{17}$, ■ – $1{\cdot}8 \times 10^{17}$, ▽ – $0\ \text{cm}^{-3}$.

3.5 *Transport measurements*

An experiment was conducted to measure the transport number for ionized F centers. The procedure was to sandwich a colored crystal between two uncolored crystals and to place all three in the conductivity cell in the usual manner. The cell was then heated to the desired temperature and a potential applied across the crystals. After a measured length of time it was found that the boundary between the colored and uncolored regions had moved away from the negative electrode. The distance that the boundary had moved, denoted d, was determined by slicing the uncolored layer from the colored crystal and measuring its thickness with a micrometer.

The F center transport number, t_F, is the ratio of the charge transported by F centers to the total charge transported, or

$$t_F = \frac{den_F}{Jt},$$

where J is the current density, e is the electronic charge, and t is the time. For a crystal having $n_F = 9{\cdot}5 \times 10^{16}\,\mathrm{cm}^{-3}$, t_F at 400°C was found to be 0·96.

4. DISCUSSION

4.1 *Transport numbers*

The transport number for ionized F centers was sufficiently close to unity to show that in these experiments, the conductivity of the colored crystals was practically all due to F centers.

The concentration of F centers was too low for colloid formation within the temperature range of interest; in fact, in the highly purified material used, the rate of colloid formation was too low to be observed even in the concentration and temperature range in which colloid can be formed rapidly in commercial KCl crystals[10]. Consequently, we may disregard thermionic emission from metal particles as a source of carriers in these experiments.

4.2 *Effects of preheating and sanding*

Consider the region in Fig. 1 at $1000/T \gtrsim 1{\cdot}75$ for freshly-cleaved samples. In this region conduction occurs between both electrodes by an almost completely electronic mechanism. The contacts are non-ohmic because the crystals are behaving as n-type semiconductors with work functions less than the work function of the gold contacts[11]. At $1000/T \simeq 1{\cdot}75$ the rate of loss of F centers due to diffusion becomes significant, creating a layer at the crystal-electrode interface which is nearly void of F centers. Eventually the layer reaches the point where its thickness exceeds the mean distance that an electron travels between traps. At this point the conductivity in the barrier layer becomes almost entirely ionic. Such a point in Fig. 1 would correspond to $1000/T \simeq 1{\cdot}6$.

For values of $1000/T \lesssim 1{\cdot}6$ conduction occurs in two parts. Between the electrodes and the colored portion of the crystal the current is ionic and is carried by migrating vacancies. In the colored portion of the crystal the current is carried by electrons. Electronic conduction through the colored region could only be possible if accompanied by a movement of the forward and trailing boundaries between the two regions. If this were not the case there would be a charge build-up at these two boundaries. In order for the forward boundary to advance the conduction electrons must overcome a potential barrier and penetrate the uncolored region of the crystal. These electrons only move a relatively short distance before becoming trapped at negative-ion vacancies, forming new F centers in the previously uncolored region.

Heating the crystals at approximately 500°C causes the loss of F centers at the surfaces to occur before the measurements are begun and hence the conductivity is that exhibited in Fig. 2. There is no region where a transition from electronic to electronic-plus-ionic conductivity occurs. The contacts are ohmic since the evaporated gold is in contact with the uncolored portion of the crystal. We believe the reduced conductivity, at a given temperature, and the apparent increase in activation energy, arises from the potential barrier for penetration of the uncolored crystal by electrons. The uncolored layers then may be extremely thin, which may account for the observed reproducibility of measurements after the heat treatment.

Sanding caused the same effect as heating since polishing the surfaces before applying the contacts generated sufficient heat to cause evaporation of F centers at the surfaces.

4.3 *Relation of conductivity to theory*

Let n be the concentration of electrons freed by thermal ionization of F centers. For a semiconductor with donor concentration n_F, with donor ionization energy E_F, the concentration n of conduction electrons is given by [12]

$$\frac{nn_\alpha}{n_F} = (2\pi m^* kT/h^2)^{3/2}\exp(-E_F/kT) = CT^{3/2}\exp(-E_F/kT) \qquad (1)$$

where n_α is the concentration of α centers (that is, negative-ion vacancies), m^* is the electron effective mass, E_F is the thermal ionization energy for F centers, and the other symbols have their usual significance.

In the region of intrinsic ionic conductivity, it is logical to suppose that $n_\alpha \gg n$, and that n_α is established by the Schottky equilibrium, so that n should be given at equilibrium by

$$n = \frac{n_F}{N}CT^{3/2}\exp(-\Delta s/2k)\exp[-(E_F-\Delta h/2)/kT] \qquad (2)$$

where N is the concentration of anion sites, and Δs and Δh are respectively the entropy and enthalpy for formation of a Schottky pair. In the region of extrinsic ionic conductivity, the equilibrium value of n should be

$$n = \frac{n_F n_\pi}{N^2}CT^{3/2}\exp(-\Delta s/k)\exp[-(E_F-\Delta h)/kT] \qquad (3)$$

where n_π is the concentration of positive-ion vacancies established by the presence of impurities.

The conductivity is given in each case by

$$\sigma = e\mu n$$

where μ and e are the electronic mobility and charge, respectively. We assume that μ is independent of n_F in the temperature range of interest, although it is known that at much lower temperatures, where the lifetime of F' centers is appreciable, the apparent mobility varies inversely with n_F. If this were the case here, σ according to equation (3), for example would then be independent of n_F, and in the case of equation (4) to be given later, σ would vary *inversely* as $\sqrt{n_F}$.

Equations (2) and (3) fail to represent the experimental results. We may calculate from (2), for example, the conductivity for a desired F-center concentration at any temperature in the range for intrinsic ionic conductivity, using the measured activation energy of 1·1 eV for $(E_F-\Delta h/2)$, with $\exp(-\Delta s/2k) \simeq 0{\cdot}07$ [13], $\mu = 1{\cdot}5\ \mathrm{cm}^2\ \mathrm{V}^{-1}\ \mathrm{sec}^{-1}$ [14], and taking m^* as the free electron mass, a good approximation for alkali halides. At 667°K, the calculated value, with $n_F = 10^{17}\ \mathrm{cm}^{-3}$, is $\sigma \simeq 10^{-14}\ \Omega^{-1}\ \mathrm{cm}^{-1}$, which is more than six orders of magnitude lower than observed. An even lower value of μ should probably be used, as the value above corresponds to room temperature.

Further, according to equation (3), the slope of the electronic conductivity curves, in the region of extrinsic ionic conductivity, should be governed by an activation energy $E_F - \Delta h$. Since E_F is believed to be somewhat less than the optical ionization energy (2·2 eV for F centers in KCl) and Δh is 2·3 eV [13], the slope should be about zero if the equation applies. Clearly the result, both of this experiment and that of Shamovskii *et al.* [4], is in disagreement with equation (3). It is possible that departure from equilibrium (for example, the freezing-in of α centers in excess of the equilibrium concentration) may occur at sufficiently low temperatures; however, no hysteresis effects upon warming or cooling, attributable to this cause, were found even at the lowest temperatures used (120°C).

Finally, the equations predict that σ should vary with n_F, whereas according to Fig. 4 it varies in fact with $\sqrt{n_F}$. Some error in the curve of Fig. 4 may result from the circumstance that sanding or preheating is thought to introduce a thin layer of uncolored material of higher resistivity than that of the colored crystal. The effect of this error is such that if the conductivity of the colored portion were actually linear with n_F, the measured conductivity would appear sublinear. The reproducibility of measurements with several samples of the same concentration, and the accurate linearity Fig. 4, lead us to believe this error is small, however.

The linearity of σ with $\sqrt{n_F}$ has not been previously demonstrated, although it may be seen to hold roughly in the case of the two lowest concentrations studied by Shamovskii *et al.* Those authors proposed that the α-center concentration characteristic of the host crystal is reduced to zero by additive coloration with saturated vapor. The α-center concentration after coloration is then only that due to ionization, in which case $n = n_\alpha$, and equation (1) becomes

$$n = n_F^{1/2}C^{1/2}T^{3/4}\exp(-E_F/2kT). \quad (4)$$

Again we may calculate the conductivity by means of (4), using 1·1 eV for $E_F/2$ in this case. For $n_F = 10^{17}\,\text{cm}^{-3}$ at 667°K, $\sigma \simeq 2\times 10^{-9}\,\Omega^{-1}\,\text{cm}^{-1}$, which is within an order of magnitude of the observed value. Equation (4) also predicts the observed variation of σ with $\sqrt{n_F}$, as well as the fact that no difference in slope of the conductivity curves, between the regions of intrinsic and extrinsic ionic conductivity, should occur.

We conclude, then, that the data are best represented by equation (4), which implies that in additively colored KCl the concentration of α centers is not established by the Schottky equilibrium, but rather is only that produced by the ionization of F centers.

This surprising result agrees with that of Shamovskii *et al.* The reason is unknown. The coloration by alkali-metal vapor is apparently irreversible with respect to re-establishment of an equilibrium number of α centers; however, it is well known that the coloration proceeds reversibly with respect to the pressure of alkali-metal vapor[15]. Shamovskii *et al.* contend that high-temperature disorder in KCl is predominantly of the Frenkel type and that negative-ion vacancies are irreversibly destroyed by coloration; this contention appears to us to be inconsistent with the available evidence upon ionic transport in alkali halides[13].

4.4 *Thermal ionization energy of* F *centers*

To obtain E_F from the low-temperature slopes of curves such as those of Fig. 1 it was necessary first to correct for the effect of the non-ohmic contacts. For applied voltage large compared to e/kT, equations given by Dekker[16] for current in the 'reverse' direction at a semiconductor-metal rectifying contact reduce to

$$J = [\mu en(V_0+V)/x_0]\exp(-eV_0/kT)$$

where V is the applied potential difference across the contact, x_0 and V_0 are the thickness and heights respectively of the potential barrier resulting from loss of electrons from the semiconductor to the metal, and n is the concentration of conduction electrons in the bulk of the semiconductor. By extrapolation of the linear portion of the curve through the circles of Fig. 3, V_0 is found to be +0·11 V. Since n varies as $\exp(-E_F/2kT)$, it is clear that the conductivity across the contact varies as $\exp[-(eV_0+E_F/2)/kT]$. Depending upon the resistance of the contact relative to the body of the crystal, the observed activation energy should be corrected by subtracting between 0·0 and 0·11 eV. If we use the maximum correction this gives $\frac{1}{2}E_F = 1{\cdot}13 - 0{\cdot}11 = 1{\cdot}02$ eV, which compares favorably with the activation energy, 1·03 eV, reported by Shamovskii *et al.*[4], and 1·00 eV reported by Smakula[2]. This yields the ionization energy, $E_F = 2{\cdot}04$ eV.

4.5 *Comparison with experiments of Jain* et al.

Quantitative comparison with the published results of Jain and Sootha[5, 6] is difficult since their data is presented in the form of ratios of σ_c/σ_n, where σ_c is the conductivity of the colored crystal and σ_n is that of the uncolored crystal. The values of σ_n are not reported explicitly and can only be inferred from the stated purity. The contribution to the conductivity due to color centers is $\sigma_c - \sigma_n$, so that we see no physical significance in the ratios, and in fact the use of ratios may obscure the information sought because of the dependence of σ_n on temperature.

Those authors [6] find no increase in conductivity, due to coloration, below 250°C. This we believe due to high extrinsic ionic conductivity of their uncolored materials. The purest crystals used, judging from the conductivity of the uncolored material, were stated to contain $< 10^{-6}$ mole fraction of divalent ion impurities. At 250°C, 10^{-6} mole fraction of divalent ions, estimating from the data of Kelting and Witt [17], impart to KCl a conductivity of the order of $10^{-10}\,\Omega^{-1}\,\mathrm{cm}^{-1}$. This is comparable to the excess electronic conductivity which we observe; at lower temperatures the extrinsic ionic conductivity would clearly predominate.

In a recent paper, Jain and Jain [18], using highly pure KBr, have reported electronic conductivity due to additive coloration, at temperatures above 100°C; a maximum in σ_c/σ_n occurs at about 180°C.

Jain and coworkers rule out conduction due to F center ionization because (a) the ratio σ_c/σ_n remains unity until the temperature exceeds about 300°C in KCl where F centers are known to form colloids rapidly at sufficiently high n_F in impure crystals, (b) the ratio falls again above about 450° as colloids become unstable with respect to F centers, (c) the ratio in KBr at 180°C is sublinear with n_F, and (d) measurements of the mobility of F centers in KBr at high temperature by Smakula [2], extrapolated to 180°C, show that ionized F center conduction would not be 'appreciable'.

We believe that (a) the ratio σ_c/σ_n remains unity below 300°C in their experiments because of the high extrinsic ionic conductivity of the KCl crystals used, (b) the fall in the ratio above 450°C may be in large degree due to surface bleaching near the electrodes and to the change of slope of the log σ_n vs. T^{-1} curve, and that (c) the sublinearity of σ_c/σ_n with n_F in KBr, although not accurately determined, may in fact be due to the proportionality we have found between σ and $\sqrt{n_F}$. While the extrapolation of Smakula's data is unreliable when carried out over such an extreme temperature range, we find, by extrapolation to 180°C and taking $n_F = 10^{17}\,\mathrm{cm}^{-3}$, that σ for KCl is of the order of 10^{-11} and for KBr, $10^{-9}\,\Omega^{-1}\,\mathrm{cm}^{-1}$. The first of these agrees well with our observation; the second is surely appreciable compared to the ionic conductivity of KBr of the purity stated by Jain and Jain, which we estimate from the data of Grundig [19] to be of the order of $10^{-13}\,\Omega^{-1}\,\mathrm{cm}^{-1}$.

We do not exclude the possibility that a significant proportion of the currents observed by Jain and coworkers were in fact due to thermionic emission from colloids, although it is quite clear that the data of Fig. 1 yield peaks in the curve of σ_c/σ_n similar to those of Jain and Sootha, due both to the evaporation of F centers from the surface of the crystal and to the transition from extrinsic to intrinsic ionic conduction in the uncolored crystal, even though no colloidal centers are present. In fact, when such curves were constructed using our data, a curve of log n_F vs. $1000/T'$, where T' is the temperature of the maximum, formed an extension of the curve in Fig. 3 of reference [5]. Further, the analysis of Jain and Sootha [5] led to a value for the enthalpy of formation of colloid from F centers more than twice that found by direct study of the temperature-variation of equilibrium F-center concentration [10].

Acknowledgements—The authors had the benefit of several helpful discussions with Professors H. Pick and S. C. Jain, to whom thanks are due. The assistance of a National Defense Education Act Fellowship, awarded to one of us (R. E. S.) during a portion of this work is gratefully acknowledged.

REFERENCES

1. STASIW O., *Gött. Nachr.* p. 387 (1933).
2. SMAKULA A., *Gött. Nachr.* p. 55 (1934).
3. MOTT N. F. and GURNEY R. W., *Electronic processes in ionic crystals*. Oxford University Press, London (1948).
4. SHAMOVSKII L. M., DUNINA A. A. and GOSTEVA M. I., *Soviet phys. Solid St.* **2**, 2252 (1960).
5. JAIN S. C. and SOOTHA G. D., *J. Phys. Chem. Solids* **26**, 267 (1965).

6. JAIN S. C. and SOOTHA G. D., *Phys. Rev.* **171**, 1075 (1968).
7. MAYCOCK J. N., *J. appl. Phys.* **35**, 1512 (1964).
8. FREDERICKS W. J., ROSZTOCZY F. E. and HATCHETT J. *U.S. Dept. Comm., Tech. Serv.*, AD 407, 600 (1963).
9. SUTTER P. H. and NOWICK A. S., *J. appl. Phys.* **34**, 734 (1963).
10. SCOTT A. B., SMITH W. A. and THOMPSON M. A., *J. phys. Chem.* **57**, 757 (1953).
11. AZAROFF L. V., *Introduction to Solids*. McGraw-Hill, New York (1960).
12. PUTLEY E. H., *The Hall Effect and Related Phenomena*. Butterworths, London (1960).
13. BEAUMONT J. H. and JACOBS P. W. M., *J. chem. Phys.* **45**, 1496 (1966).
14. KALABUKHOV N. P. and SIDYAKIN V. G., *Soviet phys. Solid St.* **2**, 2309 (1960).
15. SCHULMAN J. and COMPTON W. D., *Color Centers in Solids*. Macmillan, New York (1962).
16. DEKKER A. J., *Solid State Physics*. Prentice Hall, Englewood Cliffs (1957).
17. KELTING H. and WITT H., *Z. Phys.* **126**, 697 (1949).
18. JAIN S. C. and JAIN V. K., *Phys. Rev.* **181**, 1312 (1969).
19. GRUNDIG H., *Z. Phys.* **182**, 477 (1965).

J. Phys. Chem. Solids Pergamon Press 1970. Vol. 31, pp. 739–751. Printed in Great Britain.

ELECTRON IRRADIATION DAMAGE IN SILICON CONTAINING CARBON AND OXYGEN

A. R. BEAN, R. C. NEWMAN and R. S. SMITH
J. J. Thomson Physical Laboratory, Whiteknights, Reading RG6 2AF, England

(*Received* 27 *August* 1969)

Abstract—Infra-red absorption bands have been measured in the range 1–25 μm for a large number of silicon samples containing oxygen and carbon impurities after various doses of irradiation at room temperature by 2 MeV electrons. Measurements have been made of the removal rates of oxygen and carbon from normal unperturbed interstitial and substitutional sites respectively, and similar results are presented for the growth of the *A*-centre and divacancy bands. The presence of oxygen increases the carbon removal rate as defined above and likewise the presence of carbon increases the removal rate for oxygen and leads to a large increase in the rate of formation of divacancies. It is concluded that carbon traps interstitial silicon atoms and is then itself ejected into interstitial sites in the manner previously found for group III impurities. The interstitial carbon appears to be mobile at room temperature and a large number of new vibrational bands have been observed. Several new bands thought to be of electronic origin and involving carbon atoms have also been detected.

1. INTRODUCTION

IT IS NOW well known that when silicon is irradiated with electrons in the energy range 1·5–2 MeV, a large variety of defects are produced depending upon the temperature of the irradiation and the nature of the impurities which may be present[1, 2]. From these results, a general pattern of the damage process has emerged. The primary defects are vacancies and interstitials which may either remain as close pairs, recombine or dissociate. In the latter situation the vacancies and intrinsic interstitials, which are both mobile at low temperatures, then migrate until they are trapped by a crystal defect such as an impurity atom. The resulting centres which have been identified so far include the single vacancy V[1], the divacancy [V-V] [3–6] and vacancies paired with various impurities namely [V-P][7], [V-As][8], [V-Sb][8], [V-Al][9] and [V-O][10, 11]. When a silicon interstitial is trapped by an impurity, it appears that the impurity is ejected into an interstitial site and the silicon atom returns to a normal substitutional site. The resulting interstitial impurity atom may itself become mobile only at a much higher temperature, in the range 0°–300°C, as inferred from observations of ion pairing[1, 2]. So far, this type of reaction has only been definitely established for Al and Ga impurities which act as donors when they occupy interstitial sites; there is also less direct evidence for similar effects with B impurities[1, 12]. Thus it appears that Group III acceptors may act as traps for either primary vacancies or silicon interstitials, whereas Group V impurities have only been observed to trap vacancies.

Most of these positive identifications have been obtained by the EPR technique, although the divacancy has associated electronic transitions which have been correlated with the EPR results[6]. A correlation of EPR data has also been made with the infra-red local mode absorption band of the [V-O] centre [10, 11]. The vibrational frequency of this band is sensitive to isotope substitution, and this fact, together with other properties of such optical absorption lines, can lead to a determination of further microscopic properties of defect centres in favourable cases. For non-paramagnetic centres this may be the only technique available for their examination. As a specific example, this method has allowed measurements to be made of the rate of removal of oxygen atoms from their normal isolated interstitial sites as a result of irradiation treatments[13].

In this paper, the effect of electron irradiation on silicon containing carbon impurities will be examined. Carbon, like oxygen, is a light impurity which gives rise to a localized mode of vibration and is frequently present in nominally pure crystals grown by either the floating zone or Czochralski techniques [14–21].

Carbon is however different from oxygen since various measurements have indicated that it occupies substitutional sites[15, 17, 21]. Hence the question arises as to whether it behaves like an acceptor impurity and is capable of trapping both intrinsic interstitials and vacancies, or whether it behaves like a Group V impurity and can only trap vacancies. Previously, it was shown that a room temperature irradiation led to a reduction in the concentration of carbon atoms which occupy unperturbed lattice sites since the strength of the corresponding localized mode absorption was reduced as a result of this treatment. It is now clear that the interpretation of this observation, taken in isolation, is ambiguous since either of the above possibilities could be operative.

It has also been shown by the local mode technique that when carbon and oxygen are simultaneously present in a crystal, a fraction of the impurities form close pairs, probably of two distinct types[19, 20]. It was suggested that the carbon atom occupied either a second or third neighbour substitutional site from the interstitial oxygen in these centres although the arrangements were not determined unambiguously. What is important in the context of the present work is that pairing has been shown to occur and so it seems reasonable that other types of carbon–oxygen complexes may form as a result of irradiation treatments. There have in fact been some recent measurements to support these ideas; absorption bands observed at 922 and 932 cm^{-1} after a low temperature irradiation were ascribed to vibrations of carbon–oxygen defect centres which were however unstable at room temperature[13].

The present work will be concerned solely with room temperature irradiations and will involve quantitative measurements of the rates of removal of carbon and oxygen from their normal unperturbed sites. Quantitative measurements will also be given of the rates of growth of previously reported irradiation damage bands. In addition, a very large number of new bands of vibrational origin have been observed, together with several new electronic transitions. Examination of a large number of samples has allowed these bands to be classified in a general sense but because of the complexity of the results, no serious attempt has been made at this stage to identify the microscopic properties of any of the centres formed.

2. EXPERIMENTAL

The single crystals used in this investigation were all high resistivity *p*-type, grown by either a melt-back technique (oxygen free) or by the Czochralski technique (oxygen content about 2×10^{18} atom cm^{-3})[19, 20]. The former crystals contained natural carbon (1·1%^{13}C), while the pulled samples contained either natural carbon or a mixture of ^{12}C and ^{13}C in approximately equal concentrations. The carbon content of the samples was determined by room temperature measurements of either the fundamental (16·5 μm) or second harmonic local mode transitions used in conjunction with the previously established calibrations which are all in very close agreement[19–21]. Similarly, the concentration of oxygen in normal isolated interstitial sites was determined by measurements of the 9 μm band at 77°K[13]. In order to do this, a correspondence between the absorption at 290° and 77°K had first to be established in a carbon-free crystal. This was necessary because in samples containing a high concentration of carbon there is significant absorption due to [C-O] pairs in the same spectral region[20], and it will be shown in a later section that other new bands are produced in this same region as a result of the electron irradiation treatment given to the samples; at room temperature these various bands are not resolved. It has now been shown by an analysis of lithium diffusion experiments[22, 23] and direct radiochemical methods[24, 25] that the original calibration of the 9 μm band[26] is almost certainly in error by a factor of two. That is, for a given integrated absorption in the band the amount of oxygen actually present in the samples is twice as great as has been previously assumed; a survey of these results has now been given by Pajot[27]. The quoted concentrations of oxygen in the present samples therefore relate to this modified calibration and it follows that all oxygen contents quoted in our previous publications should be doubled[19, 20].

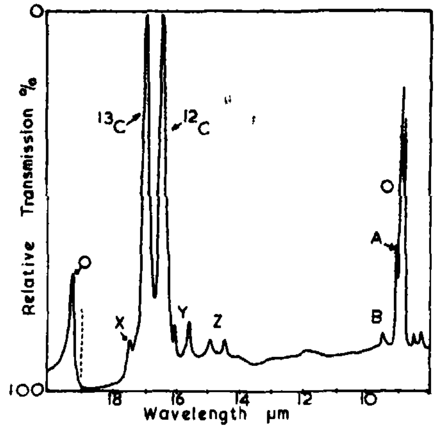

Fig. 1. Relative transmission at 80°K of an as-grown sample containing 2×10^{18} oxygen/cm^3 and 10^{18} atom/cm^3 each of ^{12}C and ^{13}C vs undoped floating zone crystal. Lines A,B,X,Y and Z are due to C-O pairs, the vertical dashed line indicates the position of the Raman frequency.

Most of the infra-red measurements were carried out at 77°K with the sample clamped to a cold finger of a liquid nitrogen cryostat. The differential technique was employed extensively with a similarly mounted sample of high purity prepared by the floating-zone technique and of the same thickness in the reference beam of a double beam grating spectrometer[20]. This allowed weak bands with absorption coefficients of the order of 0·04 cm^{-1} to be detected. Such a spectrum of the relative transmission of an as-grown Czochralski sample is shown in Fig. 1, where the lines X, Y, Z, A and B are due to the previously reported [C-O] pairs[20]. The method of determining the absorption coefficient of bands in such experiments has been given elsewhere[20].

Measurements of the absorption due to divacancies were made in the same way. Since in our spectrometer arrangement, white light falls on the sample, bands at 1·8 μm (1·69 μm 80°K) and 3·6 μm were observed simultaneously[6] although the band at 3·6 μm could be eliminated by placing a germanium filter in front of the light source. The concentration of divacancies present was estimated from the previously established correlation of the introduction rate for these centres determined from simultaneous infra-red and EPR measurements[6], although there appears to be some ambiguity about the temperature at which the former were carried out. These results led to an oscillator strength of $f = 0{\cdot}05$ for the 1·8 μm band which will be used in the present work; it has now been shown that the integrated absorption in this band does not change significantly between 300° and 77°K. The above value was determined on the assumption that there was no local field correction and consequently a similar assumption is made now; it then follows that the two sets of measurements are at least self-consistent.

A few infra-red measurements were also made using a non-differential technique with the sample cooled to liquid helium temperature. Electron irradiations were carried out at 2 MeV using the Reading Van de Graaff accelerator with current densities in the region of 15 μA/cm². The samples were mounted on a thin aluminium window in a brass cell, through which water was passed to maintain a sample temperature less than about 40°C. To ensure that damage was nearly uniform throughout the 2 mm thick specimens, each sample was irradiated equally on both sides; all doses referred to below are for the integrated flux on one side only.

Half-hour isochronal anneals were carried out up to 500°C in air, the samples being placed in unsealed silica tubes and quenched into ethanediol. Anneal temperatures were measured and maintained to ±3°C.

3. RESULTS FOR REMOVAL AND PRODUCTION OF KNOWN CENTRES

3.1 *Removal rates of oxygen and carbon*

The concentrations of both oxygen and carbon remaining in normal unperturbed interstitial and substitutional sites respectively both decreased with increasing doses of irradiation as shown in Fig. 2 for two samples with very different carbon concentrations. The decrease in the 9 μm band is of course now well known[13], while the result for carbon verifies our earlier observations[19]. In samples containing a low carbon concentration (the lowest was less than 10^{17} cm^{-3}), the oxygen removal rate was very small and saturation occurred at about the same integrated flux as that which effectively removed *all* the carbon from normal sites.

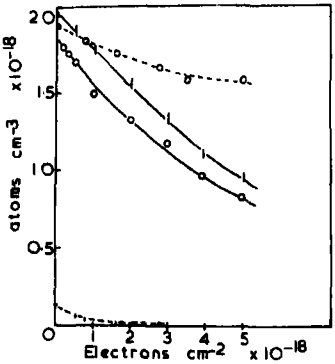

Fig. 2. The removal of oxygen and carbon from unperturbed lattice sites as a function of irradiation dose. Dashed lines for a sample containing 2×10^{18} oxygen atoms/cm^3 and $1{\cdot}3 \times 10^{17}$ carbon atoms/cm^3, continuous curves for a sample containing 2×10^{18} cm^{-3} of both oxygen and carbon. Experimental points for oxygen are indicated by circles and for carbon by vertical dashes.

For the low-carbon sample shown in Fig. 2, this dose was about 2×10^{18} electrons cm^{-2} which removed about $1{\cdot}3 \times 10^{17}$ carbon atom cm^{-3} and $2{\cdot}4 \times 10^{17}$ oxygen atom cm^{-3}. When the carbon content was higher, saturation effects were hardly noticeable and there was still a high removal rate of both oxygen and carbon even when the total dose had reached 5×10^{18} cm^{-2}. At this dose, about 10^{18} carbon atoms cm^{-3} had been removed and the corresponding concentration for oxygen was $1{\cdot}2 \times 10^{18}$ cm^{-3}. It is clear from these results that the impurity removal rate is very sensitive to the concentration of impurities present, the highest rates being about 0·2 atom cm^{-3} per electron cm^{-2} for both oxygen and carbon, with a slightly higher rate for oxygen than carbon in all cases. It is concluded that the presence of carbon has a *drastic* effect on the removal rate of oxygen as summarized in Fig. 3.

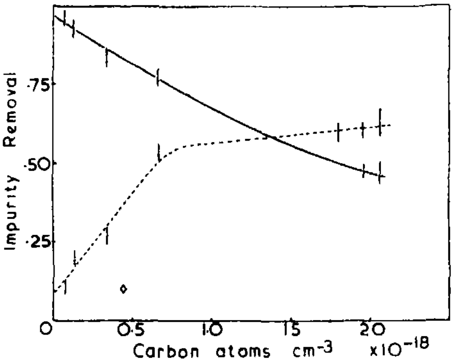

Fig. 3. Fraction of carbon (continuous curve) and oxygen (dashed curve) impurities removed by a total dose of 5×10^{18} electrons cm^{-2} for samples containing 2×10^{18} oxygen atoms/cm^3 and various carbon contents. The diamond indicates the result for carbon removal in an oxygen free sample.

Unfortunately, the removal rate of carbon as a function of oxygen content could not be determined as crystals with a constant carbon concentration and variable oxygen contents were not available. However, in the 'oxygen-free' samples the carbon removal rate was very small, corresponding to about 10 per cent of an initial concentration of 4×10^{17} cm^{-3} after a total dose of 5×10^{18} electrons cm^{-2}. This result in itself is therefore valuable since it implies that the removal rate of carbon is dependent on the concentration of oxygen present.

Before proceeding with a description of the damage bands produced by these treatments, it will be helpful to consider briefly the implications of these results. As stated in Section 1, it is now well known that isolated interstitial oxygen centres present in as-grown crystals are very efficient traps for mobile vacancies. For example, it has been demonstrated that the presence of oxygen can even inhibit the formation of [V-Al][9] and [V-P][7] centres. Hence if carbon were being removed from normal substitutional sites predominantly as a result of the formation of [V-C] centres, then the rate of formation of this centre should *decrease* when oxygen is present and likewise the removal rate of oxygen should decrease when carbon was present. In fact, the observations are just the opposite of this. This is explicable if carbon atoms act predominantly as traps for mobile silicon interstitials and are themselves ejected into interstitial sites[1]. It then follows that the rate of recombination of intrinsic silicon interstitials with vacancies would be reduced and the rate of formation of centres involving trapped vacancies should be enhanced. In the next section, results will therefore be given for the rate of formation of the known [V-O] and [V-V] centres in these same crystals.

It should be pointed out at this stage that it is not implied that no [V-C] centres form, since it is reasonable to expect this defect to be produced in the absence of oxygen or when the concentration of carbon is of the same order as that of oxygen. In fact, there is some evidence that such centres may be produced (Section 4).

To complete this section it should be noted that the irradiation appeared to have *no* appreciable effect on the strength of the vibrational bands previously ascribed to carbon–oxygen pairs[20] present in as-grown material (bands X, Y, Z, A and B in Fig. 1). This result is rather surprising since it implies that such centres either do not act as traps for vacancies or interstitials or they are equally effective traps for both types of defect in all of the samples examined. This result is in agreement with the observations of previous irradiations carried out at low temperatures[13].

3.2 *Growth of damage bands*

3.2.1 *The A-centre* [*V-O*]. Spectra in the region of 8–13 μm of two samples containing high and low carbon concentrations respectively after an electron dose of 5×10^{18} cm^{-2} are shown in Fig. 4. The strongest line in this region produced by the irradiation is that due to the [V-O] centre at 12 μm. The absorption in this band was measured as a function of dose for two samples, as in Fig. 2, and the results are shown in Fig. 5. The most striking feature is that the introduction rate for this centre is not greatly different, indicating that the number of vacancies trapped by isolated oxygen atoms is little affected by the presence of carbon; this is again in agreement with previous results[13]. In fact, the initial introduction rate is higher in the absence of carbon, although the concentration of these

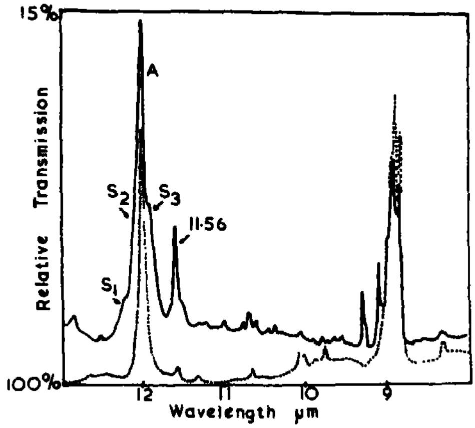

Fig. 4. Relative transmission at 80° of two samples containing 2×10^{18} oxygen atoms/cm^3 after an electron dose of $5 \times 10^{\,8}$ cm^{-2} vs. undoped floating zone crystal. Dashed trace for sample with less than 10^{17} carbon atoms/cm^3; continous trace for sample with 2×10^{18} carbon atoms/cm^3.

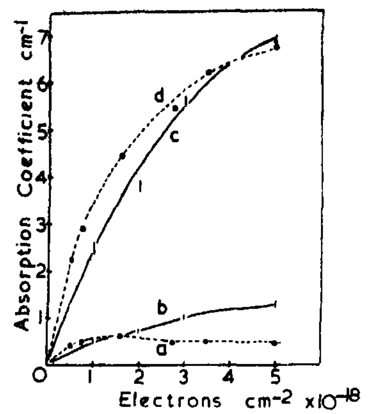

Fig. 5. Peak absorption coefficient at 80°K of 11·56 μm (curves a and b) and 11·98 μm (curves c, d) bands as a function of irradiation dose. Dashed and continuous curves for samples containing $1{\cdot}3\times10^{17}$ and 2×10^{18} cm^{-3} of carbon respectively; both samples contained 2×10^{18} oxygen atoms/cm^3.

centres tends to saturate at a dose of about 5×10^{18} cm^{-2}, when the concentrations are approximately equal in all samples examined. From the known correlation of this band with EPR data[10, 11], the maximum absorption observed corresponds to about $3{\cdot}5\times10^{17}$ centres cm^{-3}, with an estimated accuracy of a factor of two[11]. In the sample containing less than 10^{17} atom cm^{-3} of carbon the loss of oxygen from normal sites, as measured by the 9 μm band, was estimated to be about $2{\cdot}2\times10^{17}$ cm^{-3}: these values are therefore not inconsistent. An extrapolation of the curve of Fig. 3 to zero carbon content would lead to an expected reduction in the strength of the integrated absorption of the 9 μm oxygen band, of about 12 cm^{-2}, (about 9 per cent) whereas the corresponding growth of the integrated absorption in the A-band would be about 22 cm^{-2}. This difference implies that the apparent charge[28–30] may not be the same for the two oxygen configurations. Since the numbers of *A*-centres produced is virtually independent of carbon concentration, it is clear that these results do not provide an explanation of the fate of vacancies produced by irradiation of the samples containing high carbon concentrations.

3.2.2 *The divacancy (1·8 μm) Band.* The growth of the 1·8 μm band due to divacancies, as a function of fluence, is shown in Fig. 6 for the same two samples as above. In the high carbon sample the growth remains linear up to the maximum dose given of 5×10^{18} electrons cm^{-2}; at this dose the absorption corresponds to a concentration of about 4×10^{17} centres cm^{-3}[6]. The number of vacancies involved is thus 8×10^{17} cm^{-3}, while the number paired with oxygen is about $2{\cdot}5\times10^{17}$ cm^{-3}, giving a *total* vacancy concentration observed optically of about 10^{18} cm^{-3}. It is important to note that this corresponds closely with the *loss* of carbon from isolated substitutional sites of about $9{\cdot}10^{17}$ atoms cm^{-3} in the same sample; a comparison of Figs. 3 and 7 shows this to be approximately true for all samples. This result then further indicates that carbon is ejected into interstitial sites by the irradiation, since the number of interstitials would be expected to equal the number of observed vacancies. It follows that a lower production rate for divacancies should occur in the samples of low carbon doping, where the carbon removal is lower. This is indeed the case as seen in Fig. 6. In this

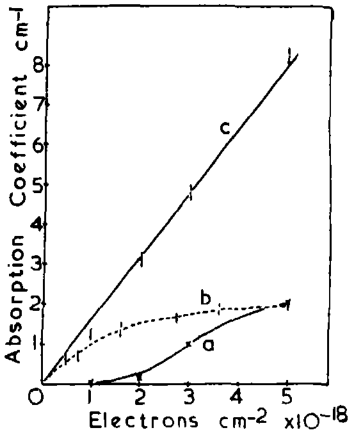

Fig. 6. Peak absorption coefficient at 80°K of 1·69 μm divacancy band (curves b and c) and 2·54 μm band (curve a) as function of irradiation dose for the same samples as in Fig. 5.

sample the production of divacancies tends to saturate at a dose of about 2×10^{18} electrons cm^{-2}, which corresponds to the fluence at which effectively all the carbon has been removed from normal substitutional sites (Fig. 2). The resulting divacancy concentration as a function of carbon content after a dose of 5×10^{18} electrons cm^{-2} is shown in Fig. 7. This shows an almost linear variation but the line does *not* pass through the origin. This implies that divacancies can be produced in the absence of carbon but with a much reduced introduction rate; this reduction in 'pure' samples is now well known[6, 31].

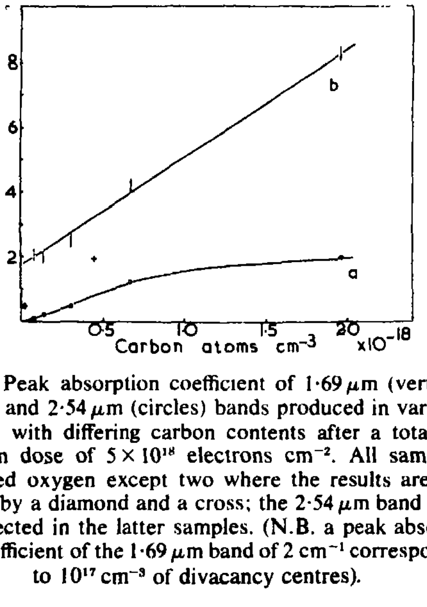

Fig. 7. Peak absorption coefficient of 1·69 μm (vertical dashes) and 2·54 μm (circles) bands produced in various samples with differing carbon contents after a total irradiation dose of 5×10^{18} electrons cm^{-2}. All samples contained oxygen except two where the results are indicated by a diamond and a cross; the 2·54 μm band was not detected in the latter samples. (N.B. a peak absorption coefficient of the 1·69 μm band of 2 cm^{-1} corresponds to 10^{17} cm^{-3} of divacancy centres).

3.3 *Overall model of processes*

These results for removal and production rates lead to a very 'simple' overall picture of the damage process. The primary silicon interstitials are assumed to be trapped very efficiently by substitutional carbon atoms provided they do not recombine first with primary vacancies or divacancies as would appear to be the case in 'oxygen-free' material. When oxygen atoms are present, they trap vacancies and somehow this leads to a higher production rate for divacancies, as has been noted previously[31]. Thus the simultaneous presence of the two impurities acts so as to separate the two intrinsic defects and inhibit their mutual annihilation. These results are in themselves quantitative, but leave unanswered at this stage the question of the fate of the interstitial carbon atoms. The fact that oxygen is lost from normal interstitial sites at almost the same rate as carbon from substitutional sites strongly suggests that interstitial carbon atoms are mobile under the conditions of the irradiation and that they then form complexes with interstitial oxygen atoms. It is therefore expected that a series of new absorption bands should be produced corresponding to this type of centre which could clearly have many modifications. Various new bands have in fact been observed in these samples and will be discussed in more detail below.

4. OTHER DAMAGE BANDS

Damage bands formed in the 'oxygen-free' sample will be discussed first since these might be expected to be relatively simple. The bands observed were of two types: (a) A series of peaks in the regions between 13·6 and 14·2 μm, and between 18·1 and 18·9 μm which appeared to be vibrational in origin, and (b) structure at 1·28 μm, the strength of which decreased with increasing temperature of observation, and is therefore thought to be due to electronic transitions of a defect centre (Fig. 8). The latter centre was only observed in 'oxygen-free' samples or in crystals where the carbon content was of the order of 10^{18} cm^{-3}. It therefore seems possible that it may be due to electronic transitions of a [V-C] centre, although this assignment is obviously very tentative. The vibrational bands were also observed with greater intensity in the pulled crystals which in general contained a higher carbon content. In samples of this latter type containing ^{12}C and ^{13}C, there was slight broadening of the structure at 14·0 μm towards lower energies

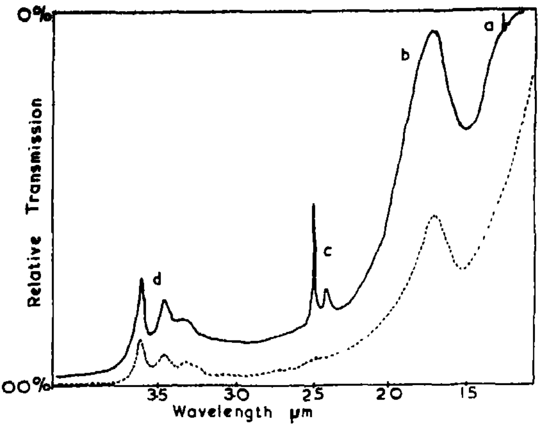

Fig. 8. Relative transmission at 80°K of the irradiated samples shown in Fig. 4. Band a at 1·28 μm, c at 2·54 μm, and b and d due to divacancies.

together with some other small changes in the form of the absorption (Fig. 9). No clear isotope effects were observed and it was therefore concluded that the bands in both the 14 and 18·5 μm regions arose from clusters of atoms rather than single atoms or pairs (see Section 5).

In the samples containing oxygen, another new band thought to be of electronic origin was observed at 2·54 μm. The growth of this band as a function of dose is shown in Fig. 6 for the high-carbon sample. The introduction rate is initially rather small but becomes greater at larger doses; the reason for this behaviour is not understood. The strength of this band after a total dose of 5×10^{18} electrons cm^{-2} is shown in Fig. 7 and it is seen that it increases with increasing carbon content of the sample, and that the line passes through the origin whereas that of the divacancy centre does not. It would seem that this centre involves both oxygen and carbon and possibly another defect, but again it would be dangerous to ascribe any definite model at this stage. The annealing behaviour of this band was unusual in that it showed a very marked increase in strength after the sample had been heated at temperatures below 200°C, whereas after a higher temperature anneal it rapidly vanished; no vibrational bands which could be correlated with this electronic band have been found (details of the positions, annealing behaviour, strengths and tentative assignments of all bands observed are given in Tables 1 and 2). Annealing the irradiated samples in the region of 200°C also produced several other new sharp bands which appeared to be electronic in origin. Those in the region of 3·2 μm were found only in those samples which originally exhibited the 1·28 μm band, while the 4·03 μm band was detected only in those samples which contained both oxygen and carbon; the strength of this latter band also appeared to correlate with the concentration of carbon present. A band at 6·5 μm was only observed in one sample of high carbon content.

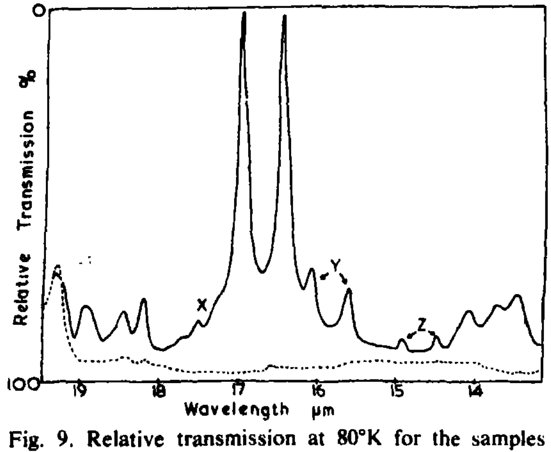

Fig. 9. Relative transmission at 80°K for the samples shown in Figs. 4 and 8, showing structure produced in the 14 μm and 18·5 μm regions.

A great many bands of vibrational origin were observed in the samples containing both carbon and oxygen, some of which have already been mentioned in connection with Fig. 9. Many of these bands were very weak and consequently no details will be given except for the data in Table 2. Between 9 μm and 12 μm, a number of sharp absorption lines all much weaker than that due to the [V-O] centre were found in samples containing a low concentration of carbon[32]. The intensities of these bands increased fairly

Table 1. *Electronic bands*

Wavelength (μm)	Wave no. (vacuum) (cm^{-1})	Anneal type, temperature (°C)	Maximum peak intensity, (cm^{-1})	Interpretation	References
1·262	7923	i 220	0·5	C-V ?	
1·284	7787		2·7		
1·689	5918	i 250	8·3	V_2	[3, 4]
3·306	3024		0·3		
3·464	2886		0·8		
3·614	2766		1·2		
2·467	4053	iii 160, 220	0·7	O, C	
2·541	3935		3·3		
3·072	3249	iii 180, 260	0·1	C.	
3·153	3170		0·2		
3·211	3108		0·1		
4·029	2481	iii 180, 360	0·8	C, O	
6·520	1530	iii 180 340	0·9	C, O	

Anneal types; (i) band anneals out at T°C without prior growth (ii) band grows on heating at T°C, and is stable at 500°C (iii) band grows on heating at T_1°C, and disappears at about T_2°C

uniformly for a fixed dose of irradiation with increasing carbon concentration, provided this was less than about 5×10^{17} cm^{-3}. With higher carbon contents, these bands were weaker again but numerous other weak bands then appeared in the same region of the spectrum. Further discussion will therefore be limited to a few of the more prominent lines, some of which have been reported in previous publications.

In all pulled crystals other than that with the lowest carbon content of 8×10^{16} atom cm^{-3}, bands were observed at 11·56, 8·96, 13·48 and 18·20 μm with comparable intensities. Except for the 13·48 μm band, these appeared to saturate at relatively low doses; the strength of the well-known[31] 11·56 μm band is shown as a function of integrated flux in Fig. 5. This band, together with others in the same spectral region, was examined at liquid helium temperature to see if the presence of ^{13}C led to any isotopic splitting. All the results were negative. Unfortunately this cannot be taken as evidence that carbon is not involved in these centres, since a similar negative result has been found previously for lines A and B (Fig. 1) due to [C-O] pairs in as-grown material[20]. Vibrations in this spectral region would predominantly involve motion of the oxygen atom and a negligibly small isotopic splitting would be expected unless the oxygen were bonded directly to the carbon atom (for further discussions of such effects see [33]). Hence the possibility that the 11·56 μm band is for example an *A*-centre perturbed by a nearby carbon atom cannot be ruled out; all that can be stated is that the strength of this band is negligible in samples with the very *lowest* carbon content of less than 10^{17} atom cm^{-3}. Clearly what is needed is an examination of a series of samples with even lower carbon contents than those used in the present work because of the rapid saturation of these centres. In this case however, measurement of the actual carbon content would be very difficult.

Another feature of the present work was the observation of satellite lines around the *A*-band as shown in Fig. 4. It seems likely that lines S_1 and S_2 are the same as those found previously by Ramdas and Rao in annealed samples which had been irradiated by neutrons[32]. They also reported a third satellite S_3 which also appeared after annealing. It is not clear whether this is the same band as that shown at 11·88 μm (Fig. 4) and which appeared to correlate with the carbon content of the present samples; the reason for the

Table 2. Vibrational bands

Wave-length (μm)	Wave-number (vacuum) (cm^{-1})	Anneal types temper-ature (°C)	Maxi-mum peak intensity (cm^{-1})	Inter-pretation	Ref.
13·6–14·2	735–704	*	0·5	C	
18·12	551·7	unchanged	0·15	C	
18·46	541·5	i 240	0·4	C	
18·60	537·6	unchanged	0·1	C	
18·92	528·5	*	0·4	C	
8·962	1115·5	i 340	0·7	O, C ?	
9·260	1079·6	unchanged	0·3	O, C ?	
9·271	1078·3	i 340	0·8	O, C ?	
9·415	1061·9	ii 360	0·2	O, C ?	
9·631	1038·0	i 250	0·1	O, C ?	
9·696	1031·1	i 250	0·06	O, C ?	
9·773	1023·2	i 180	1·0	O	[32]
9·956	1004·1	ii 450	0·1	O	[32, 34]
10·031	996·6	i 250	0·4	O	
10·097	990·1	ii 450	0·2	O	[34]
10·256	974·7	ii 450	0·3	O	]32, 34]
10·351	965·9	ii 400	0·2	O, C ?	[32, 44]
10·426	958·9	i 250	0·1	O, C ?	[32, 44]
10·476	954·4	ii 350	0·1	O, C ?	[32]
10·577	945·3	i 300	0·2	O, C	
10·651	938·7	i 200	0·6	O	
10·686	935·6	i 250	0·2	O, C	[43]
10·744	930·6	ii 400	0·2	O, C ?	
10·989	909·8	ii 450	0·2	O	[32, 34]
11·179	894·3	iii 330,480	0·8	O (O$_2$V)	[32, 34]
11·476	871·2	i 350	0·2	O, C ?	
11·556	865·2	i 350	1·8	O, C ?	[31, 32]
11·876	841·8	i 480	1·1	O, C ?	[32, 44]
11·975	834·9	i 350	7·7	O (O–V)	[10, 11]
12·006	832·7	iii 280,400	2·0	O	[32, 44]
12·063	828·8	iii 280,400	1·4	O	[32, 44]
12·486	800·7	i 350	0·15	O	
12·801	781·0	i 350	0·15	O	
13·48	741·5	i 340	0·6	C, O	
18·20	549·2	i 350	0·6	C, O	

*Apparent superposition of bands with more than one annealing stage observed in the range 250–350°C.

uncertainty is that this band did not grow on annealing in the same way as the S$_1$ and S$_2$ satellites in this previous work. In pulled crystals with a high carbon content, a band was observed at 9·27 μm which also increased in strength with increasing carbon content. The origin of this band is also obscure since no corresponding satellites due to perturbed vibrations of isolated substitutional carbon could be found.

As described by Corbett, Watkins and McDonald[34], the anneal of the *A*-band above 300°C was found to be associated with the rise of a band at 11·18 μm which they suggested might be due to a dioxygen-vacancy complex. We observed the 11·18 μm band to rise to only one-tenth of the peak absorption of the *A*-band, with the oxygen 9 μm band recovering some 30 per cent between 300° and 380°C. In this same temperature range the 8·96, 9·27, 11·56, 13·48 and 18·20 μm bands also annealed out, while the carbon–oxygen bands *A* and *B* (Fig. 1) were observed to more than double in strength, although heating an unirradiated specimen for similar periods at these temperatures was not found to produce significant growth.

The results of this section may be summarized by stating that a room temperature irradiation of samples containing carbon and oxygen leads to the formation of a very large number of bands which do not appear to be correlated with one another. This is readily understood if interstitial carbon atoms are assumed to be mobile under the conditions of irradiation and form pairs or more complicated complexes with oxygen and with themselves. This general result would then be consistent with the more quantitative details presented in the previous section.

5. CONCLUSIONS AND DISCUSSION

It has been shown that the presence of carbon in a pulled crystal leads to a very significant increase in the rate of production of divacancy centres. Since very appreciable amounts of carbon are simultaneously removed from normal substitutional sites, it has been inferred that carbon is ejected into interstitial sites as a result of the irradiation. When oxygen is absent, these processes are less efficient and it has been suggested that [V-C] centres may be formed. These results indicate that the behaviour of carbon is like that of group III substitutional acceptor elements in silicon. The present results have gone further and indicated that the interstitial carbon atoms are mobile at room temperature (40°C) at least under the conditions of irradiation used in the present experiments. This has been inferred by the anomalously high removal rate of oxygen from normal interstitial sites which cannot be accounted for in terms of an increased introduction rate of [V-O] centres; instead a series of new bands have been observed which are almost certainly to be attributed to [C-O] complexes.

It is interesting to speculate on the origin of the new bands formed on the oxygen-free samples on the basis of these conclusions. If [V-C] centres and mobile interstitial carbon are formed simultaneously, then some recombination of these centres is to be expected and in the simplest situation pairs of substitutional carbon atoms [C-C] might be expected to form. Such centres would be similar to those described previously both experimentally[35, 36] and theoretically [37, 38] for [B-B] pairs. It has been shown that the infra-red active localized modes of vibration of such pairs are at lower frequencies than for the isolated impurity; for example, the $[^{11}B\text{-}^{11}B]\Gamma_2^-$ mode occurs at 552·5 cm^{-1} while the corresponding band for $[^{10}B\text{-}^{10}B]$ is at 570·1 cm^{-1}[35, 36]. Due to the similarity of the force constants between carbon-silicon and boron-silicon respectively for the isolated substitutional impurities[20], the band due to $[^{12}C\text{-}^{12}C]$ would be expected to lie at about 530 cm^{-1} which is very close to the region where absorption was observed (Table II and Fig. 9). However, in the carbon doped samples, simple sharp lines were not observed and it would appear that further clustering, perhaps involving carbon interstitials occurs. There is another similarity, since in the boron doped crystals lines were observed at 733·0 and 760·0 cm^{-1} due to single ^{11}B and ^{10}B atoms respectively[35, 36]. The origin of these lines is still somewhat obscure but it has been tentatively suggested that they involve boron in interstitial sites; a fuller account of these observations will be given elsewhere[39]. The corresponding position for ^{12}C would then be around 716 cm^{-1}, which is again in the region where broad band absorption was observed (Table 2 and Fig. 9). No sharp single line was observed, but a shift of the broad structure towards lower energies was noted when C^{13} was present. It seems reasonable therefore to relate these two sets of observations and to conclude that they arise from the same types of defects, although these are obviously more complex in the samples containing carbon. It would then follow that interstitial carbon atoms have a greater tendency to form clusters than interstitial boron atoms at 40°C. Consequently, a simpler situation should prevail if the irradiation of the carbon doped samples were carried out at lower temperatures.

When oxygen is present, the situation is clearly much more complex since interstitial carbon atoms may be trapped in a variety of sites near interstitial oxygen atoms, [V-O] centres or even [V-V] centres. At this stage, it is worth stating that the vibrational frequencies associated with [V-C] centres would be expected to be rather low due to the "loss" of one C-Si bond, and any associated absorption could well fall in the band mode region below the Raman frequency (estimated to be at 525 cm^{-1} at 77°K)[40]; no such absorption was detected.

Evidence for the high mobility of interstitial carbon atoms at room temperature may also be inferred from other recent work of Vook and Stein[13], in relation to the formation of bands involving oxygen. These authors irradiated samples containing both oxygen and carbon at 80°K. Bands were observed at 922 and 932 cm^{-1} which were dependent on the simultaneous presence of both impurities and were attributed to a trapped silicon interstitial at a carbon-oxygen complex. This was thought to be a different centre from that giving rise to the 1103 cm^{-1} band, since this band was not reduced in strength as a result of the irradiation, in agreement with the present observations. The important point however, was that the 922 and 932 cm^{-1} bands annealed out on warming the sample above 250°K as had been observed previously[41–43], and they were not produced by a room temperature irradiation. It could well be that this is the temperature at which carbon interstitials become mobile and this leads to the formation of more complex centres. Stein and Vook did not report any new bands in an oxygen free sample containing $1{\cdot}3\times10^{17}$ carbon atoms cm^{-3}, but since the total dose given was only $7{\cdot}7\times10^{17}$ of 2 MeV electrons cm^{-2}, this result is not too surprising. The structure observed in the present samples in the 14 μm and 18 μm regions was only easily detected after a dose of $5\times10^{18}\,cm^{-2}$ and where the initial carbon content was $4{\cdot}5\times10^{17}\,cm^{-3}$.

Some further comments will now be made about some of the other bands produced in the present experiments. Satellites to the [V-O] band have been reported by Ramdas and Rao[32], in samples after neutron irradiation but *not* after electron irradiation. They suggested that these satellites arose as a result of more complex centres resulting from the more extensive type of damage to be expected in the former case. Satellites S_1 and S_2 have now been observed in the present samples which are identified from both their wavelengths and annealing behaviour; the situation for the third satellite S_3 at 11·88 μm is less clear as its annealing behaviour did not conform to that reported previously[32]. The relative intensity of these lines has now been found to vary with different samples immediately after irradiation and also after differing annealing treatments, so that they must arise from different centres. In the samples studied, the strength of the satellite at 11·88 μm appeared to correlate with carbon content, but this was not so for the other two lines. In any case, it is now clear that extensive neutron damage is not necessary for their formation. The intensities of other bands in the 9–12 μm region are apparently not uniquely determined by the carbon content, as seen by comparing Table 2 and Fig. 4 with Fig. 1 of Ramdas and Rao[32]. It would seem that further low temperature irradiations and annealing treatments are necessary to clarify the results.

It is concluded finally that the presence of carbon in silicon has a very marked influence on the nature of the damage produced by 2 MeV electrons. Since carbon is a neutral impurity, its presence may often go undetected, although a pulled crystal not deliberately doped with this impurity has now been found with a carbon content of 2×10^{18} atom cm^{-3}. This figure is unusually high, but concentrations of only one order of magnitude smaller are quite common. Clearly, this must be taken into account in future irradiation damage studies, as has been pointed out previously[13, 19, 32].

Acknowledgements—The authors wish to thank R. L. Rouse of A.E.I./G.E.C. for supplying the silicon crystals used in this investigation. Two of us A.R.B. and R.S.S. thank the S.R.C. for research studentships. Thanks are also due to Professor E. W. J. Mitchell for his interest in this work and for providing the laboratory electron irradiation facilities.

REFERENCES

1. WATKINS G. D. In *Radiation Effects in Semiconductors*, p. 97. Dunod, Paris (1965).
2. WATKINS G. D. In *Radiation Effects in Semiconductors* (Edited by F. L. Vook). p. 67. Plenum Press, New York (1968).
3. WATKINS G. D. and CORBETT J. W., *Phys. Rev.* **138**, A543 (1965).
4. CORBETT J. W. and WATKINS G. D., *Phys. Rev.* **138**, A555 (1965).
5. BEMSKI G., SZYMANSKI B. and WRIGHT K., *J. Phys. Chem. Solids* **24**, 1 (1963).
6. CHENG L. J., CORELLI J. C., CORBETT J. W. and WATKINS G. D., *Phys. Rev.* **152**, 761 (1966).
7. WATKINS G. D. and CORBETT J. W., *Phys. Rev.* **134**, A1359 (1964).
8. ELKIN E. L. and WATKINS G. D., *Phys. Rev.* **174**, 881 (1968).
9. WATKINS G. D., *Phys. Rev.* **155**, 802 (1967).
10. WATKINS G. D. and CORBETT J. W., *Phys. Rev.* **121**, 1001 (1961).
11. CORBETT J. W., WATKINS G. D., CHRENKO R. M. and McDONALD R. S., *Phys. Rev.* **121**, 1015 (1961).
12. WATKINS G. D. Private communication.
13. VOOK F. L. and STEIN H. J., *Appl. Phys. Lett.* **13**, 343 (1968).
14. SCHINK N. *Solid State Elect.* **8**, 767 (1965).
15. NEWMAN R. C. and WAKEFIELD J., *J. Phys. Chem. Solids* **19**, 230 (1961).
16. NEWMAN R. C., *Proc. phys. Soc.* **76**, 993 (1960).
17. NEWMAN R. C. and WAKEFIELD J., In *Metallurgy of Semiconductor Materials* (Edited by J. B. Schroeder), Vol. 15, p. 201. Interscience, New York (1961).
18. BULLOUGH R. and NEWMAN R. C. *Prog. Semiconductors* **7**, 101 (1963).
19. NEWMAN R. C. and WILLIS J. W., *J. Phys. Chem. Solids* **26**, 373 (1965).
20. NEWMAN R. C. and SMITH R. S., *J. Phys. Chem. Solids* **30**, 1493 (1969).
21. BAKER J. A., MOYER N. E., TUCKER T. N. and BUSCHERT R. C., *J. appl. Phys.* **39**, 4365 (1968).
22. PELL E. M., *Phys. Rev.* **119**, 1222 (1960).
23. IGLITSYN M. I., KEKELIDZE G. P. and LAZEREVA G. V., *Soviet phys. Solid St.* **6**, 2508 (1965).
24. NOZAKI T., TANAKA S., FURUKAWA M. and SAITO K., *Nature* **190**, 39 (1961).
25. ALEKSANDROVA G. I., DEMIDOV A. M., KOTELNIKOV G. A., PLESHAKOVA G. P., SHUKOV G. V., CHOPOROV D. Ya and SHMANENKOVA G. I., I.A.E. 1165, Inst. At. Energii Gosudarsevennyi Komitet po Ispol'zovaniyn At. Energii SSSR, Moskova (1966).
26. KAISER W. and KECK P. H., *J. appl. Phys.* **28**, 882 (1957).
27. PAJOT B., *Solid State Electronics* **12**, 923 (1969).
28. LEIGH R. S. and SZIGETI B., *Proc. R. Soc.* **301A**, 211 (1967).
29. LEIGH R. S. and SZIGETI B., *Phys. Rev. Lett.* **19**, 566 (1967).
30. LEIGH R. S. and SZIGETI B., In *Localized Excitations in Solids* (Edited by R. F. Wallis), p. 159. Plenum Press, New York (1968).
31. FAN H. Y. and RAMDAS A. K., in *Proc. Int. Conf. of Semiconductor Physics* (Prague) Czech Acad. Sci. p. 309 (1961).
32. RAMDAS A. K. and RAO M. G., *Phys. Rev.* **142**, 451 (1966).
33. PAJOT B. and DELTOUR J. P., *Infrared Phys.* **7**, 195 (1967).
34. CORBETT J. W., WATKINS G. D. and McDONALD R. S., *Phys. Rev.* **135A**, 1381 (1964).
35. NEWMAN R. C. and SMITH R. S. *Phys. Lett.* **24A**, 671 (1967).
36. NEWMAN R. C. and SMITH R. S., In *Localized Excitations in Solids* (Edited by R. F. Wallis), p. 177. Plenum Press, New York (1968).
37. ELLIOTT R. J. and PFEUTY P., *J. Phys. Chem. Solids* **28**, 1789 (1967).
38. PFEUTY P., In *Localized Excitations in Solids* (Edited by R. F. Wallis), p. 193. Plenum Press, New York (1968).
39. NEWMAN R. C. and SMITH R. S., To be published.
40. PARKER J. H., Jr., FELDMAN D. W. and ASHKIN M., *Phys. Rev.* **155**, 712 (1967).
41. WHAN R. E., *Appl. Phys. Lett* **8**, 131 (1966).
42. WHAN R. E., *J. appl. Phys.* **37**, 3378 (1966).
43. WHAN R. E. and VOOK F. L., *Phys. Rev.* **153**, 814 (1967).
44. RAMDAS A. K. and FAN H. Y., *J. phys. Soc. Japan* **18**, Suppl. II, 33 (1963).

J. Phys. Chem. Solids Pergamon Press 1970. Vol. 31. pp. 753–761. Printed in Great Britain.

HIGH MOBILITY OF HEAVY RARE GASES IN POTASSIUM HALIDES AT LOW TEMPERATURES (20–100°C)

Hj. MATZKE*
Chemistry Department, CCR Euratom, Ispra (Va), Italy

and

C. JECH†
Institute for Materials Research, McMaster University, Hamilton/Ontario, Canada

(*Received* 14 *January* 1969; *in revised form* 26 *August* 1969)

Abstract – A new process in the release of the heavy rare gases Kr, Xe, and Rn from potassium halides at temperatures well below those of normal volume diffusion (i.e. between about ambient temperature and 100°C) is described. The process comprises a part of the total gas only and is enhanced by low gas concentration and proximity of the gas to the surface. The activation enthalpy of this release process, ΔH, is $1{\cdot}0 \pm 0{\cdot}2$ eV. The release mechanism is compatible with the gas coming to rest in high mobility sites, e.g. interstitial positions, part of it escaping to the surface and part getting trapped in sites similar to normal substitutional sites, in divacancies or vacancy clusters, at pre-existing defects or at radiation damage.

1. INTRODUCTION

THE DIFFUSION of rare gases in solids has been studied extensively in the past decade, originally because of the problems that fission gases create in nuclear fuels, e.g. in the swelling of such fuels. Later, the studies have been extended to 'model substances', systems with a similar structure as that of fuel materials, e.g. to potassium-halides representing uranium carbide, UC. At present, results on gas release from crystalline solids are interesting from two aspects, first because of their contribution to a general understanding of the behaviour of rare gases in solids, and secondly, because of the possible implications to reactor fuel comportment.

Earlier studies showed that usually various different processes contribute to the overall release of rare gases from solids that hence proceeds in various stages. Rare gas atoms can thus migrate via a normal volume diffusion process, but they can also interact with different defects, e.g. vacancy clusters, radiation damage, pre-existing defects, or other gas atoms etc. All these interactions lead to a delay in release. To obtain physically meaningful diffusion parameters from release data, the different processes have to be seperated, a task which was not always performed in the older studies. The present investigation is a contribution towards such a separation of different processes, and is concerned with a release process at abnormally low temperatures.

A previous study (1) of inert-gas-diffusion, mainly involving Kr and Xe, in ion-bombarded KCl, KBr, and KI has shown that the bulk release of the gases consists either of two distinguishable processes, depending on bombardment dose and gas concentration, or else of low- and high-dose limits of what is possibly, though not necessarily, a single process. The low-dose process or limit (called Stage II A) appeared to represent undisturbed volume diffusion of the gas, whereas the high dose process or limit (Stage II B) appeared to be correlated with transient gas–gas or gas-damage interactions.

---

*Present address: European Institute for Transuranium Elements, D-75 Karlstruhe, Postfach 2266, Germany.

†On leave of absence from the Institute of Physical Chemistry, Praha.

Though the low-dose process or limit (Stage II A) was compatible with volume diffusion and showed a fairly well-defined activation enthalpy, ΔH, there were sometimes indications of it being composite with another process occurring at *lower* temperatures. For example, in KCl Tesla-labelled with Kr to very low doses[1], a second release peak at 130°C appeared in addition to the normal one at around 190°C. A similar behaviour was also observed for KCl in [2], where the temperature width of the release peak was excessive, and for KCl and KBr in [3, 4], where there was sometimes an unexplained step in the release curves at 50° to 100°C.

The present study investigates, separates and analyses this low-temperature release process (also referred to as Stage I release, see Section 5). Most results will be reported for KCl, and KBr and KI will only occasionally be referred to as the three potassium halides KCl, KBr, and KI show a nearly identical behaviour.

2. EXPERIMENTAL

The experiments were performed with single crystals of KCl, KBr, and KI obtained variously from Harshaw (Cleveland, USA) or Korth (Kiel, Germany). Plates of about $10 \times 10 \times 2$ mm^3 were prepared by cleaving and the cleavage faces labelled with rare gas by ion bombardment. Three types of bombardment were used: (a) Xenon was introduced at various energies (1, 5 and 40 keV) and doses (8×10^{10}, 4×10^{13}, 2×10^{16} ions/cm^2) using the Chalk River electromagnetic mass-separator*[5]. For details see [4]. (b) Low-energy Kr- and Xe-bombardments were performed in a Tesla discharge apparatus[2]. The resulting energies and doses can only be estimated[1] to be roughly 1 keV, and 3×10^{13} ions/cm^2 for 0·6 sec. discharges, and 2×10^{14} ions/cm^2 for 9 sec. discharges. (c) Very low concentrations of Em were achieved by implanting 5×10^6 to 1×10^7 Ra-224 atoms/cm^2 from a Th-228 recoil source at energies between 50–100 keV. Em-220 is then formed by radio-active decay at a concentration of 4×10^{-3} of that of Ra-224.

Following the bombardments, release measurements were carried out in three different ways: (a) specimens labelled with the mass-separator were step-heated, i.e. alternately heated isothermally in air with hold times of 5 min and then cooled to room temperature for counting. The annealings were spaced at intervals of $\geqslant 75$°C and therefore the effect of step-heating could be neglected [6]. (b) Specimens labelled with the Tesla-discharge apparatus were heated with a linear temperature rise of 10°C/min in streaming dry N_2 and the rate of gas release was continuously recorded[2]. (c) Specimens labelled with Em were transferred into a vacuum-cryostat which contained a solid state α-detector connected to a multi-channel-analyzer. The detector was shielded with thermally insulated Al-foils from both directly emitted α-particles and from recoil atoms. The counting rate was therefore predominantly due to those Em-atoms that diffused from the sample and around the Al-shieldings. The sample temperature could be varied between $-170°$ to $+150$°C. Counting was done at the α-energy of Em-220 (6·28 MeV) for fixed periods of time, usually 1 hr, with the cryostat being disconnected from the vacuum system.

3. THEORETICAL

The mathematics needed for evaluation of both isochronal curves (fractional release, F, vs. temperature, T, for fixed annealing periods, t) and of release-rate curves (dF/dt vs. T) have been published before[1, 4, 6]. Essentially, correlations between the activation enthalpy, ΔH, and some readily recognized temperature are established. Such a temperature might be that of the maximum of the release peak, T_{max}, for dF/dt vs. T curves or e.g. that of $F = 0{\cdot}5$ for F vs. T curves.

---

*These bombardments were performed during the stay of one of the authors (Hj. M.) at the Chalk River laboratories in September 1967.

References [4, 6] contain also the mathematics needed to deduce diffusion coefficients from isothermal experiments.

In addition to the mathematics of normal volume diffusion, the appropriate solution of the diffusion equation for diffusion with irreversible trapping[6] will be needed, i.e. the solution for the case where part of the gas diffuses freely to the surface whereas another part gets trapped at some defect. The relevant diffusion equation is

$$\partial C/\partial t = (D/\lambda^2)(\partial^2 C/\partial x^2) - DC/L^2\lambda^2 \quad (1a)$$

$$\text{with } \partial m/\partial t = DC/L^2\lambda^2 \quad (1b)$$

where C is the concentration of mobile gas, m the concentration of gas in traps and L is the diffusion trapping length or spacing of trapping centers in units of the mean atomic spacing, λ.

As has been shown before[6], the fraction, F_l, of gas atoms that will escape without getting trapped is given by

$$F_l^{-1} = 1 + R/\ln 2L \quad (2)$$

where R = median range of the gas, i.e. location of the gas atoms beneath the surface. Equations (1) and (2) are valid both for gas moving via normal sites or getting trapped in deep traps (e.g. radiation damage), and for part of the gas coming to rest in high mobility sites and the rest ending up in *either* normal sites *or* deep traps.

With the aid of these formulae, the present results can be evaluated, i.e. it can be checked whether or not the release kinetics are compatible with ideal volume diffusion and, if so, ΔH's can be deduced, provided the range of the ions is known or can be estimated. Here, the range values published in [1, 7, 8] were used. In addition, an indication can be obtained on the spacing of defects acting as traps for gas atoms.

4. RESULTS

(a) *Mass-separated beams of Xenon*

Figure 1 shows isochronal release curves from KCl bombarded with mass-separated beams of Xe-ions at 1 and 5 keV, and three different gas concentrations corresponding to ion doses of 8×10^{10}, 4×10^{13}, and 2×10^{16} ions/cm². Data for a higher energy of 40 keV and the same doses are taken from[1] and

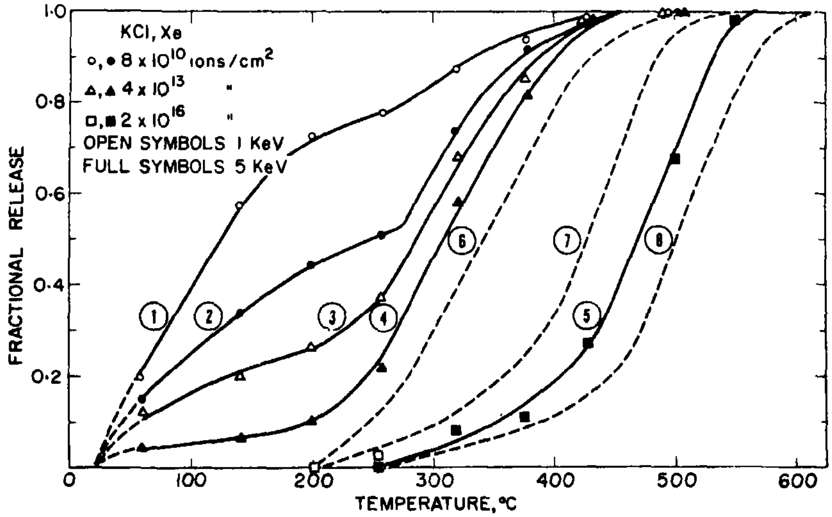

Fig. 1. Release (F vs. T-curves) of Xe from KCl single crystals following ion bombardment at 1 and 5 keV energy and doses of 8×10^{10}, 4×10^{13}, and 2×10^{16} ions/cm². The dashed curves for the same three doses and 40 keV ions are for comparison and are taken from[1].

shown as dashed lines. Qualitatively, the following two features are evident:

(i) The release curves for energies of 1 and 5 keV and doses of 8×10^{10} ions/cm^2 are composite. The (sigmoidal) release curve 6 for 40 keV ions and the low dose of 8×10^{10} ions/cm^2 has previously been interpreted[1] as being representative for undisturbed bulk diffusion (or Stage IIA, with an activation enthalpy, ΔH, of $33{\cdot}5 \pm 3$ kcal/mole or $1{\cdot}45 \pm 0{\cdot}15$ eV/atom). A shift of this release curve towards lower temperatures without appreciable change in shape is expected for the smaller energies (smaller ranges and hence smaller diffusion distances) if the same volume diffusion process is still operative at the lower energies. Examples for such a shift have been given previously (Fig. 1 of [9]). The second part of curves 1–4 above about 230°C and comprising about 20, 50, 70, or 90 per cent residual release is roughly compatible with this bulk diffusion process. The first part of the curves 1–4 below about 230°C represents then a different release process that occurs at temperatures *below* normal bulk diffusion.

(ii) At the highest dose of 2×10^{16} ions/cm^2, no indication of this release process was observed. The two data points for 1 keV energy and curve 5 for 5 keV energy are seen to closely resemble curve 8 (40 keV, 2×10^{16} ions/cm^2) which previously [1] has been explained as being due to retarded release of trapped gas due to gas-gas or gas-damage interactions (or Stage IIB). In fact, no gas was released below 230°C.

(b) *Tesla-labeling*

Figure 2 shows some typical release curves for KCl and KBr and a linear heating rate (dF/dt in arbitrary units vs. temperature, T). A total number of 15 runs was performed using both Kr and Xe. All these runs yielded the following results:

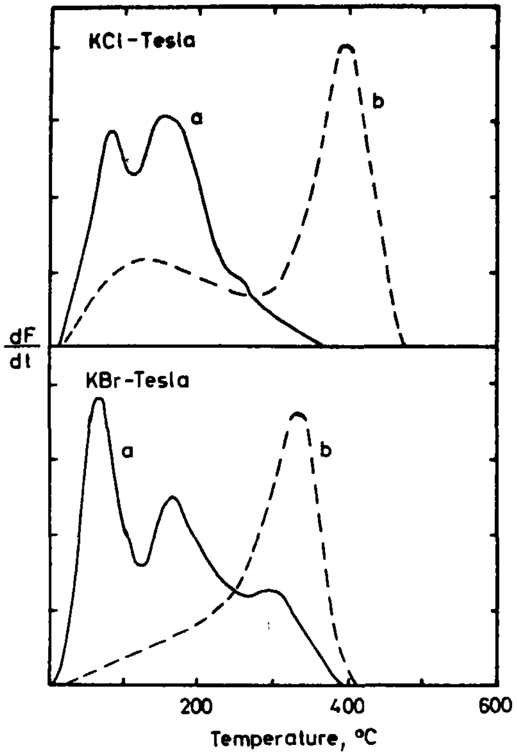

Fig. 2. Release (dF/dt vs. T-curves) of heavy rare gases from Tesla-labeled KCl and KBr single crystals. Curves (a) are for 0·3 sec exposure and Xe; curves (b) for a 9·0 sec prebombardment with (inactive) Kr before labeling for 0·3 sec with (radioactive) Xe.

(i) The release curves for low dose bombardments (0·1–0·3 sec duration of the discharge) were always composite, i.e. two peaks were observed for all these runs (see Fig. 2, curves a). The second peak at around 150 to 200°C has previously been interpreted [1] to be due to volume diffusion (or Stage IIA) with activation enthalpies of $33{\cdot}5 \pm 3$ kcal/mole ($1{\cdot}45 \pm 0{\cdot}15$ eV/atom) for KCl, 32 ± 2 kcal/mole ($1{\cdot}4 \pm 0{\cdot}1$ eV/atom) for KBr, and 29 ± 2 kcal/mole ($1{\cdot}25 \pm 0{\cdot}1$ eV/atom) for KI. Therefore, the first peak at temperatures of around 70°–90°C must again be due to a fast process occurring at temperatures *below* those of normal bulk diffusion.

(ii) At higher bombardment doses, as indicated for Xe in Fig. 2, curves b, and reported for both Kr and Xe in [1], the release peak at low temperatures was completely suppressed, and the peak for normal volume diffusion to a great extent. Rather, a new peak was observed at much higher temperatures. This peak was previously [1] attributed to trapping in the form of gas-gas or gas-damage interactions (or Stage II B).

Table 1 summarizes the temperatures for release peaks and Table 2 the deduced activation enthalpies, ΔH, for both the new low temperature release process and the two limits (see [1]) for low doses (normal volume diffusion involving mobility of vacancies (or Stage IIA)) and high doses (trapping involving gas-gas or gas-damage interactions (or Stage IIB)).

Since the diffusion process studied occurs in the outermost atom layers, one might argue that it could be affected by reactions of the halide with humidity. Therefore, a separate series of experiments was performed by measuring the room temperature release of Kr-85 from KCl that was (a) stored in a desiccator but exposed to the ambient air during counting; (b) stored and counted in a desiccator; (c) stored and counted in a static vacuum (10^{-3} Torr). Six different crystals were used and the release was followed for time periods of up to 3 *d*. In agreement with the results of Fig. 2, an amount of gas roughly compatible with that of the low temperature peaks (30–50 per cent for different crystals) was released if the bombardment dose was low (0·1 sec bombardment). No acceleration in release was observed for crystals exposed to the ambient air. Therefore, the presence of humidity did not seem to be responsible for the low temperature release (Stage I). No release at room temperature was observed for high dose bombardment which is in agreement with the results of Fig. 2, and, in addition, is another argument against any influence of humidity.

The release curves for crystals stored in the desiccator (conditions a and b) represented the theoretically expected time dependence of the release for constant diffusion coefficients of $2{\cdot}2$–$3{\cdot}6 \times 10^{-18}$ cm^{2}sec^{-1}, respectively. This scatter has to be regarded of little importance

Table 1. Temperatures (°C) for release peaks with Tesla bombardments

	Low temp. release (Stage I)		Low dose limit (Stage IIA)		High dose limit (Stage IIB)	
Material	Kr	Xe	Kr	Xe	Kr	Xe
KCl	120	90	190	165	380	395
KBr	120	70	155	170	280	330
KI	—	n.f.	150	150	230	255

n.f. = process not found

The table contains two apparent inconsistencies: (a) Stage I release of Xe occurred at lower temperatures than Stage I release of the smaller Kr. (b) Stage I release was observed for KCl and KBr, but not for KI. Both these observations, however, are probably artifacts due to the inherent difficulties of labeling at room temperature and observing the subsequent low temperature release. The sample surface gets slightly heated during labeling. Because of technical reasons, the labeling pressure for Kr was higher than that for Xe leading to a slightly higher temperature. Therefore, some Kr might have been released *during* labeling causing a change in the shape of the range distribution as well as in the shape of the release curve. Similarly, Stage I release from KI may go to completion *during* bombardment since the release temperatures decrease with decreasing melting point, and hence very low release temperatures ($\leqslant$ 50°C) would be expected for KI.

*Table 2. Observed activation enthalpies (ΔH's, eV)**

Gas and target	Type of bombardment	Low temp. release (Stage I)	Low dose limit (volume diffus.) (Stage IIA)	High dose limit (trapping)^{b} (Stage IIB)
Kr–KCl	Tesla	1·1	1·3	1·9
Xe–KCl	Tesla	1·0	1·3	2·0
Xe–KCl	1 keV	1·1	1·6$^{(a)}$	n.d.
Xe–KCl	5 keV	1·0	1·6$^{(a)}$	2·0
Xe–KCl[1]	40 keV	n.f.	1·4	1·8
Em–KCl	recoil	0·8	1·5	n.d.
Kr–KBr	Tesla	1·1	1·2	1·6
Xe–KBr	Tesla	1·0	1·3	1·8
Xe–KBr[1,4]	40 keV	n.f.	1·3	1·6
Kr–KI	Tesla	n.f.	1·2	1·5
Xe–KI	Tesla	n.f.	1·2	1·5
Xe–KI[1]	40 keV	n.f.	1·2	1·5
Kr–NaCl[9]	Tesla	n.f.	1·5	2·4
Xe–NaCl[9]	Tesla	n.f.	1·6	2·4
Xe–NaCl[9]	40 keV	n.f.	1·6	2·1

*The ranges used for calculating ΔH's are based on refs. (1, 7, 8, 9). The uncertainties due to the assumed range of k_0, i.e. 10^{15-1} sec^{-1} where k_0 is the pre-exponential diffusion rate constant ($k_0 = 2\,D_0/\lambda^2$, λ = mean atomic spacing), are about ±0·1 eV; a further uncertainty of about ±0·1 eV arises due to the scatter in the data.

[a] This value may be high because of the overlapping of the low temperature release process with release due to volume diffusion in F vs. T-type curves.

[b] These are *apparent* values since kinetics different from those of volume diffusion are indicated for the high dose limit (see [9]).

n.d. = ΔH not determined. n.f. = process not found.

since the diffusion coefficients for normal volume diffusion (Stage IIA) would be lower by 6 to 7 orders of magnitude (see Section 5).

(c) *Emanation recoil-labeling*

Some KCl-single crystals were recoil-labeled with Ra-224 from a Th-228 source. The Ra was then diffused into the crystals to a median depth of about 0·2 μm and the crystals were placed in the cryostat mentioned in Section 2(c). Since the Em-isotope employed, Em-220, has a half-life of 54 sec, and is continuously generated by the decay of Ra-224, the time scale of the diffusion is in the order of 1–3 min, independent of the heating time. Figure 3 shows the results of various runs. The first counts were obtained between about −80° and −70°C, and were probably due to the onset of desorption of recoil atoms. Some recoil Em-atoms escape with a low remaining energy and have therefore a sticking factor < 1 in the aluminum shielding. These atoms will get adsorbed on the cold KCl or the supporting copper rod, and will be desorbed if temperatures of −80° to −70°C are reached. With further increases in temperature, the release rate was constant, until about 30°–40° C were reached. Between about 40 to 100°C, a release process occurred comprising about 1 per cent of the total gas. Then, a saturation up to about 120°C and a second release process were indicated. With the reactor irradiated crystals, the first release process between 40° to 100°C was absent. However, when these

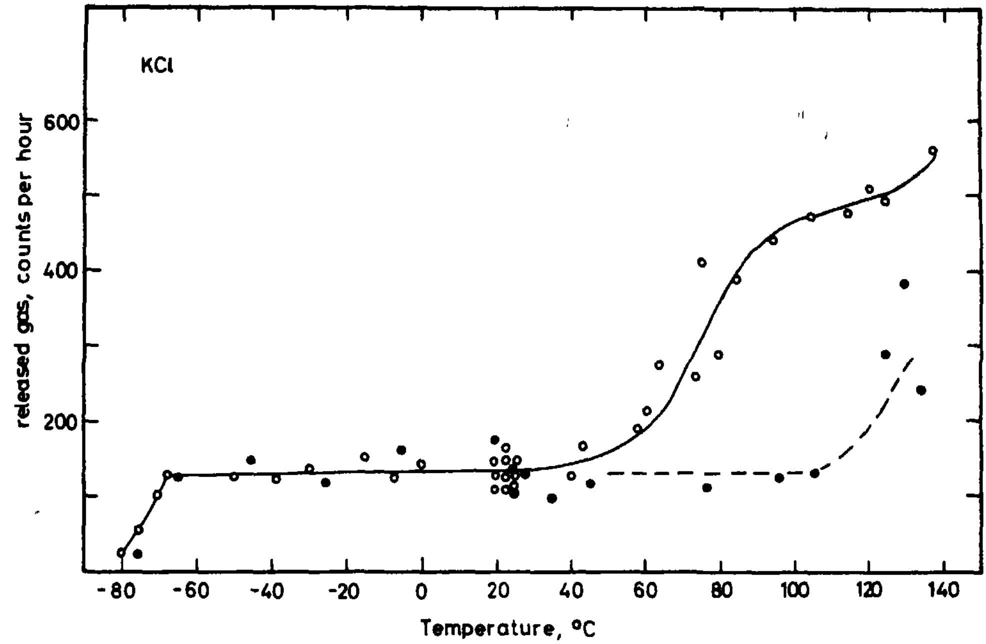

Fig. 3. Release of Em-220 from KCl single crystals between −80 and +140°C. The open symbols are for as received KCl, the full ones for reactor irradiated crystals (2×10^{16} nvt). The low temperature release process is absent in reactor irradiated specimens.

reactor irradiated crystals were annealed for about 30 min at 200°C to anneal the *F*-centers and to restore the transparency of the samples, release curves similar to those of unirradiated specimens and showing a low temperature process between about 40–100°C were obtained.

5. DISCUSSIONS

Diffusion constants for the mobility of rare gases are usually determined by measuring the integral concentration of gas that leaves a solid, i.e. the release of the gas. Since, in the last years, this release has been realized to consist of various competing processes involving different mechanisms and kinetics, a physically meaningful interpretation of release data is only possible if these different processes can be separated. To this end, a division of the overall release into Stages was suggested [e.g. 4, 10, 11]. In this system, Stage II was defined as gas release which occurs within the temperature range of volume self-diffusion of the matrix atoms, whereas Stage I is most simply described as any gas release occurring well below this temperature range.

The present study proves the existence of such a low temperature or Stage I release for the three rare gases Kr, Xe, and Rn in the alkali-halides KCl and KBr. Three different experimental techniques were used to separate this process from Stage II release which, depending on time scale (heating schedule), and diffusion distances used, started at about 200–250°C (ion bombardment with mass separation) or about 120°C (Tesla labeling) nevertheless representing the same diffusion process with a constant activation enthalpy of e.g. 1·45±0·15 eV for KCl[1]. Again, depending on the same experimental conditions, the new Stage I process started between about room temperature (Tesla labeling) or 40°C (release of Em and ion bombardment) and hence well below the temperatures of normal volume diffusion (Stage II). An activation enthalpy, ΔH, of 1·0±0·2 eV was deduced for this new process*. At room temperature, D-values of about $2\text{–}3 \times 10^{-18}\,\text{cm}^2\,\text{sec}^{-1}$ were implied for Stage I release, whereas the calculated D-value for volume diffusion (Stage IIA) at room temperature would be about 10^6 to 10^7 times smaller. Conversely, the temperature corresponding to a D of $2\text{–}3 \times 10^{-18}\,\text{cm}^2\text{sec}^{-1}$ and Stage IIA release would be 150°C instead of room temperature. Therefore, the experimental results show a clear separation of Stage I from Stage II and constitute thus evidence for the existence of Stage I-type release of heavy rare gases in the alkali halides KCl and KBr.

Before discussing the mechanism of the new release process, we want to recall the present knowledge on Stage II release. For this release and *low* doses, a mechanism involving the mobility of the gas in small stable vacancy clusters, e.g. divacancies, was suggested on the basis of studies of doping[1, 4], α-channeling and proton-scattering[12]. At *high* doses, trapping in the form of gas-gas or gas-damage interactions was proposed to have occurred; the release was retarded in time or shifted towards much higher temperatures thus indicating a high *apparent* activation enthalpy (see Table 2). Hence, the new low temperature process (Stage I) must be due to another new mechanism of mobility.

There are three more features of this release process that may help to explain its mechanism (a) it is dominant at *low doses* and is suppressed at high doses, (b) it is absent in reactor irradiated crystals but is present following pre-annealing of such crystals, (c) it comprises a part of the total gas only.

These observations seem to be compatible with a model where the gas comes to rest in high mobility sites and part of it escapes to the surface whereas another part gets trapped. Such a model satisfies feature (c) by definition, and can explain features (a) and (b) with the aid of equation (2): the fraction released in Stage I, F_I, decreases at constant energy (hence constant R) with increasing bombardment dose and equals zero in reactor irradiated crystals due to a decrease in L, the spacing of trapping centers. Pre-annealing of the reactor irradiated crystals leads to annealing of defects and to an increase in L and, therefore, Stage I release can be observed again. F_I decreases also if higher bombardment energies are used at constant dose since then the range R of the ions is increased.

Equation (2) yields also indications for L, the diffusion trapping length appropriate to the low temperature release. For Tesla labeling of 0·1–0·3 sec duration corresponding to an estimated 2×10^{13} ions/cm²; F_I is about 0·5 and hence

$$L \approx 1{,}4R \approx 10 \pm 2 \text{ atom layers.}$$

This implies that each incident 1 keV ion produces roughly 10 traps that are stable at room temperature. Since halide or potassium interstitials are mobile much below room temperature[13], many of these traps may be vacancy clusters. The values of L deduced from Fig. 1 are of the same order and are about 35 atom layers for the low dose of 8×10^{10} ions/cm² and 3 atom layers for the dose of 4×10^{13} ions/cm².

As to the mechanism of the low temperature release, the most probable high diffusivity position would be an interstitial position. Theoretical calculations (14) are available for the light rare gas, argon, and potassium halides. According to these calculations, the migration enthalpy of an interstitial argon atom would be small (0·15–0·34 eV) but single vacancies would act as comparatively deep traps with binding energies between 0·8 to

---

*This release process may in fact have a certain (but limited) *range* in activation enthalpies rather than a well defined single value, as indicated by the presence of a two peak release process even following a room temperature release experiment. Though a 24 hr exposure at 20°C is equivalent to a 5 min heating to 65°C, the room temperature release would comprise the part of the gas having lower ΔH's whereas the subsequent release on heating wou[illegible] due to gas occupying sites with slightly higher ΔH[illegible] The indicated spectrum of ΔH's would, however, fal[illegible] the above range of 1·0 ± 0·2 eV.

1·5 eV. The present results are dealing with heavy rare gases. Therefore, the activation enthalpy for interstitial motion may be slightly higher.* It is at present, however, not possible to decide whether a pure interstitial process or an interstitial migration with trapping in single vacancies are dominant. Single vacancies do not seem to be *normal* equilibrium sites for the heavy rare gases (see above) and might therefore be high diffusivity positions, especially in combination with proximity of the gas to the surface.

The only other system where a fast *release* process at (and even below) room temperature was observed, is Em/UC[15, 16]. This process was attributed to an interstitial mechanism, since vacancies are not mobile in UC at such low temperatures. High *mobilities* of Xe and Kr in W at and below room temperature, however, have in addition been deduced from range studies and were attributed to a process involving interstitial migration and subsequent trapping[17–19]. As in the present study, preexisting defects suppressed this mobility. Finally, an abnormally long range implying a similar effect was observed in the system Kr/NaCl[20], and indicated in the systems Xe/NaCl and Xe/KBr[7]. Fast release processes starting slightly *above* room temperature were previously reported[10, 21, 22] with W, Al_2O_3, Nb_2O_5, SiO_2, and TiO_2. These releases were always connected to surface proximity of the gas.

Acknowledgements—The experimental help of the team of the Chalk River electromagnetic mass separator is gratefully acknowledged. Special thanks are due to D. C. Santry (AECL, Chalk River). The authors are further grateful to Prof. R. Kelly (McMaster University, Hamilton) for discussions.

REFERENCES

1. KELLY R., JECH C., and MATZKE Hj., *Phys. Status Solid* **25**, 641 (1968).
2. JECH C., *Phys. Status Solid* **2**, 1299 (1962).
3. KELLY R., MATZKE Hj., *J. nucl. Mat.* **17**, 179 (1965).
4. MATZKE Hj., *Z. Naturf.* **22a**, 507 (1967).
5. DAVIES J. A., BROWN F. and McCARGO M., *Can. J. Phys.* **41**, 829 (1963).
6. KELLY R. and MATZKE Hj., *J. nucl. Mat.* **20**, 171 (1966).
7. WHITTON J. L. and MATZKE Hj., *Can. J. Phys.* **44**, 2905 (1966).
8. KELLY R., *Proc. Conf. Application of Ion Beams to Semi-Conductor Techn.*, p. 201 Grenoble, (1967).
9. MATZKE Hj., RICKERS G. and SØRENSEN G., *Z. Naturf.* **24a**, 820 (1969).
10. KELLY R. and BROWN F., *Acta metall.* **13**, 169 (1965).
11. KELLY R. and JECH C., *J. nucl. Mat.* **30**, 122 (1969).
12. MATZKE Hj. and DAVIES J. A., *J. appl. Phys.* **38**, 805 (1967).
13. e.g. SONDER E. and TEMPLETON L. C., *Phys. Rev.* **164**, 1106 (1967).
14. NORGETT M. J. and LIDIARD A. B., AERE-Harwell Rep. TP 332 (1968).
15. MATZKE Hj., *J. nucl. Mat.* **30**, 107 (1969).
16. MATZKE Hj., *Solid St. Commun.* **7**, 549 (1969).
17. DAVIES J. A. and JESPERSGÅRD P. J., *Can. J. Phys.* **44**, 1631 (1966).
18. HERRMANN H., LUTZ H. and SIZMANN R., *Z. Naturf.* **21a**, 365 (1966).
19. DAVIES J. A., ERIKSSON L. WHITTON J. L., *Can. J. Phys.* **46**, 573 (1968).
20. SØRENSEN G., University of Aarhus, Personal communication (1968).
21. KORNELSEN E. V. and SINHA M. K., *Can J. Phys.* **46**, 613 (1968).
22. JECH C. and KELLY R., *Proc. Br. ceram. Soc.* **9**, 259 (1967).

**Note added in proof.* Recent calculations (M. J. Norgett, private communication, 1970) for the systems Kr/KCl and Xe/KI have again yielded activation enthalpies for interstitial gas mobility in the range 0·2–0·3 eV, thus favouring a contribution of vacancies to the present release process.

J. Phys. Chem. Solids **Pergamon Press 1970. Vol. 31, pp. 763–769. Printed in Great Britain.**

THE RESISTIVITY OF DILUTE *Au* Co ALLOYS*

J. W. LORAM, P. J. FORD and T. E. WHALL
University of Sussex, School of Mathematical and Physical Sciences, Brighton, England

(*Received* 26 *March* 1969; *in revised form* 26 *August* 1969)

Abstract – Measurements are presented of the resistivity of Au containing between 0·005 and 3 per cent Co between 0·5° and 300°K. The results are consistent with a Kondo Temperature of around 400°K for the most concentrated *Au* Co alloys. At low temperatures the resistances vary approximately linearly with temperature, with a slope proportional to (concentration)$^{1\cdot 5}$. Possible explanations for this unusual concentration dependence are discussed, and it is concluded that this results from a Kondo temperature which decreases with increasing concentration.

INTRODUCTION

THE PROPERTIES of dilute *Au* Co and *Cu* Co alloys differ in many important respects from the properties of the noble metals containing other transition metal impurities, and the magnetic state of the Co atoms in these hosts is far from clear. In particular, previous measurements[1] have failed to demonstrate the existence of a resistance minimum in alloys containing less than 0·4 at. per cent Co. A minimum has, however, been observed in higher concentration alloys, and Domenicali and Christenson[2] have shown that the resistivities of Au containing 2·1 per cent and 4·3 per cent Co vary approximately linearly in log T between room temperature and 1000°K, and flatten off at lower temperatures (when plotted against log T) in a manner considered to be characteristic of the formation of a spin compensated state. Their curves suggest that the Kondo temperature T_K of the *Au* Co system is around 400°K. A similar value may be derived from the thermoelectric power of a Au 2·1 per cent Co alloy[3], which exhibits a large negative peak at around 300°K. If this is a correct interpretation of these results, then the Kondo temperature of *Au* Co is similar to that of *Au* V[4].

A value for the effective *s-d* exchange integral J can be derived, if it is assumed that $T_K = E_F e^{-1/Jn(E_F)}$ ($n(E_F)$ is the density of conduction electron states at the Fermi Energy E_F). Taking $T_K = 400°\text{K}$, then $Jn(\text{E}_F) = 0{\cdot}20$ and $J = 0{\cdot}62$ eV. To investigate this system in more detail at low temperatures, we have measured the resistivity of a series of *Au* Co alloys containing between 0·005 at. per cent Co and 3 at. per cent Co between 0·5°K and 300°K. A preliminary report on some of these results has been published previously[5].

EXPERIMENTAL METHOD

The materials used for the preparation of the alloys were 99·9999 per cent pure Au(Cominco) with an estimated Fe content of 0·4 ppm, and 99·99 per cent pure Co (Koch Light Industries) containing less than 50 ppm of Fe. The alloys were prepared by melting together suitable proportions of pure Au and a Au 3 at. per cent Co master alloy, in a water cooled copper boat induction furnace. All the alloys were inverted and remelted several times to ensure good homogeneity. They were then annealed in vacuo for six hours at 950°C and quenched rapidly into iced water. After cold rolling between melinex sheets to a thickness of 0·06 mm, they were cut into strips 3 mm wide and 10 cm long, and etched in aqua regia to remove surface contamination. They were finally reannealed and

---

*This work has been sponsored in part by the Air Force Materials Laboratory (AFSC) through the European office of Aerospace Research (OAR), United States Air Force, under Contract F61052-68-C-0011.

quenched as before. A pure Au specimen prepared in an identical manner was found to have a resistance ratio of 800, and from the Kondo term in the resistivity, was found to contain approximately 0·5 at ppm Fe in solution. It is therefore hoped that the alloys contain a similar low level of Fe impurity.

The solubility of Co in Au[6] is 19 at. per cent at 950°C, falling to 3 at. per cent at 650°C, and is negligible at room temperature. The linear dependence of the residual resistivity $\Delta\rho_0$ (where $\Delta\rho_0 = \rho_{\text{Alloy}}(1°\text{K}) - \rho_{\text{Au}}(1°\text{K})$) on nominal concentration c, shown in Fig. 1, demonstrates that very little Co has precipitated during the annealing process, but the very low room temperature solubility makes it likely that some clustering of the Co atoms will have occurred, particularly in the more concentrated alloys. The value of $\Delta\rho_0/c = 5·75\ \mu\Omega$ cm|at. per cent is in good agreement with the value found by other authors[1, 7].

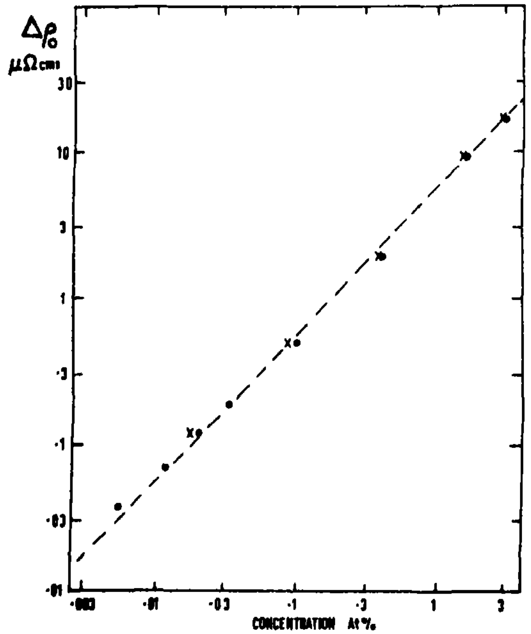

Fig. 1. Residual resistivity $\Delta\rho_0 = \rho_{\text{Alloy}}(1°\text{K}) - \rho_{\text{Au}}(1°\text{K})$ versus Co concentration in at. per cent. Closed circles indicate concentrations estimated from the initial weights of the materials, and crosses indicate the concentrations as determined by chemical analysis. The dashed line represents $\Delta\rho_0\,\mu\Omega$ cm $= 5·75 \times$ (concentration in at. per cent).

The resistances were measured by a four terminal potentiometric technique in a conventional He_3 cryostat. Six specimens, one pure and five alloys, were measured simultaneously over the temperature range 0·5°–300°K. Below 4°K, temperatures were stabilized and measured to better than 2 mdeg. Above 4°K, the temperature was stabilized to better than 0·1 per cent and was measured with an uncertainty of less than 0·5 per cent of the temperature.

Accuracy of resistance measurement is limited, in the more dilute alloys, by the accuracy of potential measurement. To develop a sufficiently large potential across the 0·005, 0·01, 0·02, 0·03 at. per cent Co specimens to enable their very small temperature dependences to be determined, a measuring current of 1 amp was used. To overcome the effects of joule heating, they were immersed in the He_4 bath, and measurements on these alloys were limited to the temperature range 1·3–4·2°K.

The determination of the resistivity from the resistance requires an accurate knowledge of the length and cross sectional areas of the specimens. The distances between the shallow depressions on the specimens left by the potential knife edges were measured with a travelling microscope. They were then cut at the knife edge marks and weighed accurately. The average cross sectional area between the potential marks could then be determined from the mass and density (obtained from lattice spacing data[8]). This procedure enables the length/area to be determined to better than 0·5 per cent.

RESULTS AND DISCUSSION

In Fig. 2. the excess resistivity $\Delta\rho = \rho_{\text{Alloy}}(T) - \rho_{\text{Au}}(T)$ is plotted against temperature between 0° and 300°K. Low temperature results are presented in more detail in Fig. 3 for the 0·4, 1·6 and 3 per cent alloys and in Fig. 4 for the more dilute alloys. It is evident from these results that the resistivity varies

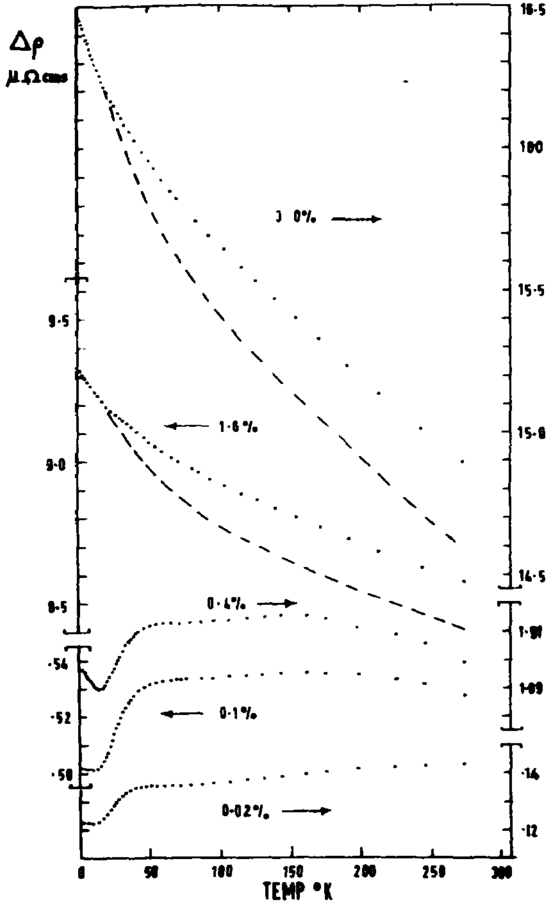

Fig. 2. $\Delta\rho$ vs. temperature for *Au* Co alloys. Co concentrations and relevant resistivity scales are indicated in the figure. (Note the expanded resistivity scale for the three most dilute alloys.) Dots represent experimental points; the effect of applying a correction of Matthiessen's Rule is shown by the dashed curves.

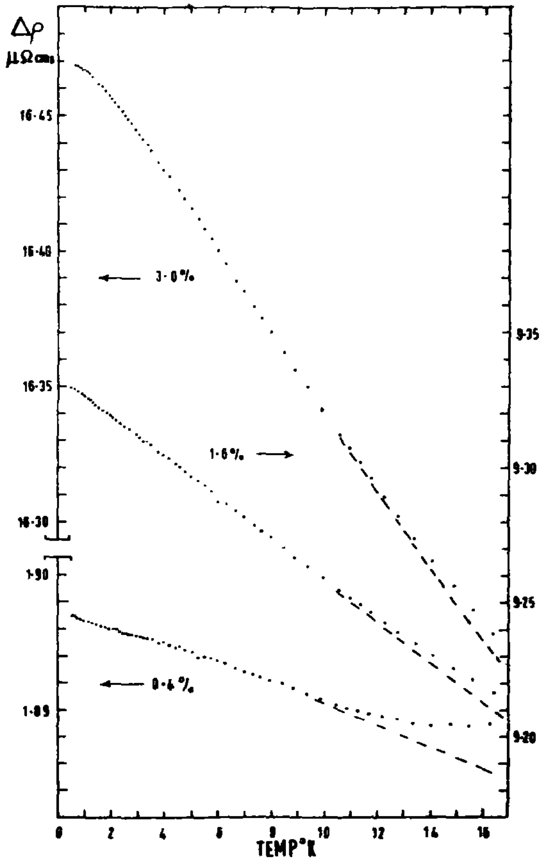

Fig. 3. $\Delta\rho$ vs. temperature for *Au* Co alloys. Co concentrations and relevant resistivity scales are indicated in the figure. (Note the expanded scale for the 0·4 at. per cent alloy.) Dots represent experimental points; the effect of applying a correction to Matthiessen's Rule is shown by the dashed curves.

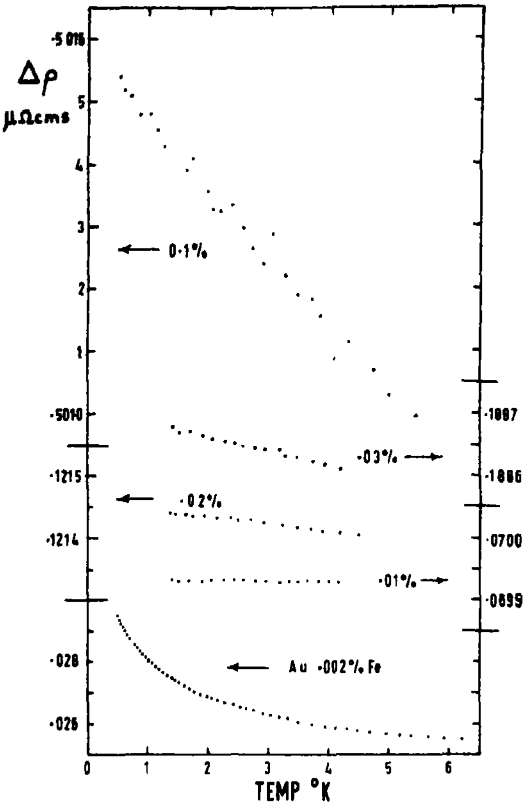

Fig. 4. Δρ vs. temperature for *Au* Co alloys containing 0·01, 0·02, 0·03 and 0·1 per cent Co. The resistivity of an Au ·002 at. per cent Fe alloy is included for comparison. (Note different resistivity scale for this alloy.)

almost linearly with temperature at low temperatures for all alloys except the most concentrated. This is in contrast with the behaviour of *Au* V[4] and *Cu* Fe[9] which tend to an approximately quadratic temperature dependence well below T_K. The results are also in better agreement with the linear dependence predicted by Anderson[10] than the quadratic dependence derived by Nagaoka [11] and the more complicated dependences predicted by Appelbaum and Kondo[12] and by Hamann[13] for $T \ll T_K$.

The linear dependence is observed for concentrations down to 0·02 at. per cent Co. This can be readily distinguished from the effects of Fe impurity scattering which exhibits the characteristic logarithmic temperature dependence shown in Fig. 4 for a Au 0·002 at. per cent Fe alloy. The temperature dependence may, however, be affected at the lowest temperatures by the presence of a few parts per million of Fe. In the Au 3 at. per cent Co alloy, the resistance tends to flatten off below 3°K, suggesting that magnetic ordering effects are becoming significant at this concentration.

In the 3 and 1·6 at. per cent alloys the slopes of the curves decrease at higher temperatures and tend to the logarithmic dependence found by Domenicali and Christenson about 300°K, as is shown in Fig. 5. For the alloys containing 0·4 at. per cent and less of Co, Δρ passes through a minimum at around 13°K and a broad maximum at higher temperatures. The very rapid increase in the excess resistance above 10°K, when phonon scattering is becoming significant, is typical of the breakdown of Matthiessen's Rule which is found in alloys

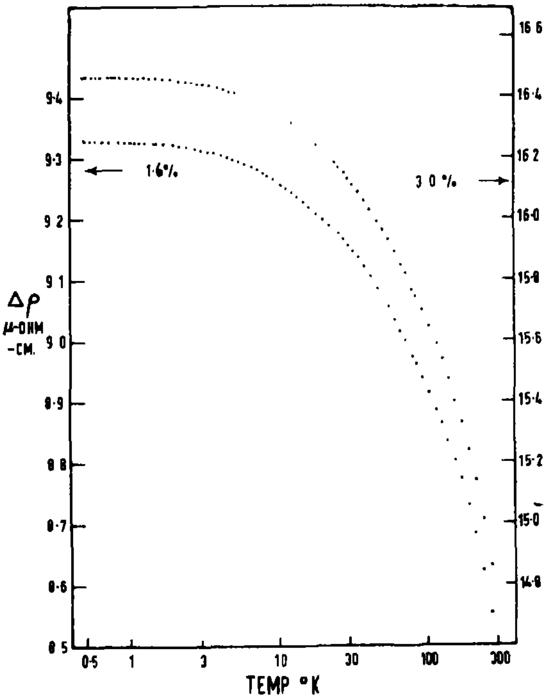

Fig. 5. Δρ vs. log *T* for concentrated *Au* Co alloys. Co concentrations and relevant scales are indicared in the figure.

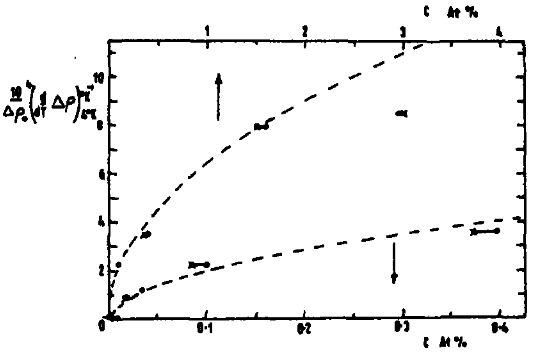

Fig. 6. Fractional slope at 4°K, $10^4/\Delta\rho_0\,(d/dT\Delta\rho)_{4°K}$ vs. concentration *c* at. per cent. Arrows indicate the relevant concentration scales for the high and low concentration alloys. Closed circles represent concentrations estimated from initial weights of materials, crosses represent concentrations determined by chemical analysis. The relation $1/\Delta\rho_0\,(d/dT\,\Delta\rho)_{4°K} = 6{\cdot}4\times10^{-4}\,c^{0\cdot5}$ is represented by the dashed curve.

containing non-magnetic[14] and magnetic [15] solutes.

There are several causes for this breakdown. The most important arises when different scattering mechanisms of comparable magnitudes have different *k*-dependences (*k* being the wave vector of the conduction electrons). The competing scattering processes in the present case are those due to phonons and impurities. Kohler[16] has shown that the deviation from Matthiessen's Rule can be written

$$\Delta\rho = \rho_i + \Delta(T)$$

where

$$\Delta(T) = \frac{\beta\rho_i\,\gamma\rho_p}{\beta\rho_i + \gamma\rho_p}$$

ρ_i and ρ_p are the impurity and phonon resistivities, and β and γ depend on the relative anisotropies of the two scattering processes, and may be temperature dependent. In [15] it is shown that this relation holds approximately, up to 50°K; for a wide range of transition metal solutes in Au, with β and γ taken to be constant, and for high concentration alloys [14, 15] this may be a reasonable approximation up to room temperature. For the alloys containing 0·4 at. per cent Co and less, the deviation is consistent with the above expression, but the correction is too large to permit a reliable estimate of the impurity resistivity above 20°K. For the 1·6 and 3 at. per cent alloys, it is fractionally much smaller, and the effect of applying such a correction with $\gamma = 1{\cdot}2$ and $\beta = 0{\cdot}02$ is shown by the dashed curves in Figs. 2 and 3. These values for β and γ are consistant with values found for other alloys of comparable residual resistivity [15], but while γ is probably correct to within ±20 at. per cent, β may be in error by as much as a factor of two.

A striking feature of the results is the non-linear concentration dependence of the low temperature slope $d/dT\,\Delta\rho$. A graph of $1/\Delta\rho_0\,(d/dT\,\Delta\rho)_{4°K}$ against *c* is shown in Fig. 6, and it can be seen that this quantity varies approximately as $c^{0\cdot5}$ for $0{\cdot}02 < c < 3$ at. per cent Co. (The rather low value for the 3 at. per cent alloy may be due to the effects of magnetic ordering at 4°K.) Thus the slope varies as $c^{1\cdot5}$ in this concentration range. A concentration and temperature dependence similar to that found here for *Au* Co has been seen in the resistivity of *Cu* Co alloys[17] containing 0·5, 1 and 2 at. per cent Co; and a non-linear magnetoresistance was observed in the same alloys. The specific heat at 5°K has been found to vary as $c^{1\cdot5}$ in *Au* Co[18] and c^2 in *Cu* Co [19]. The thermoelectric power is approximately linear in temperature and independent of concentration below 16°K in both of these systems[20, 21]. Hildebrand[22] has shown that the high temperature susceptibility (measured up to 600°K) can be represented by a Curie–Weiss law, with an effective moment of $4{\cdot}6\,\mu_B$ and a negative Curie temperature which decreases approximately linearly with concentration from 247°K for Au 0·3 at. per cent Co to 87°K for Au 3·5 at. per cent Co. The low temperature magnetisation, measured by Le Guillerm *et al.*[23], is a very non-linear function of field and concentration, and remanance is observed in alloys containing more than 2 at. per cent Co. Very similar effects are observed in *Cu* Co alloys[22, 23].

Evidently, the temperature dependence of the Kondo scattering per impurity increases as the mean separation between Co atoms decreases. This differs from the behaviour observed in other dilute magnetic alloy systems such as *Cu* Cr[24] where the effect of increasing magnetic interaction (due to increasing concentration) is to terminate the Kondo scattering. Such an effect is observed here only in the 3 at. per cent alloy, below 3°K, and may be expected when the RKKY interaction energy becomes comparable with T_{K^0}.

To explain this unusual concentration dependence, Caroli[25] has suggested that Co atoms may be on the verge of magnetism, being nonmagnetic when isolated, but becoming magnetised when in close proximity to other Co atoms. Since the number of neighbouring pairs in a dilute random alloy is proportional to c^2, properties depending on the presence of a magnetic moment on the Co atoms would increase with at least this power of the concentration. This explanation, while accounting qualitatively for most of the low temperature properties, is inconsistent with the concentration (and temperature) independent moment found at high temperatures by Hildebrand[22], and the concentration independent low temperature thermopower[20, 21].

It is unlikely that the large value of the effective moment can be ascribed to single Co atoms. Taking $g = 2$, a moment of $4{\cdot}6\,\mu_B$ corresponds to a spin of 1·85. Such a spin value would involve the improbably large number of at least 2·7 *s* and *p* like electrons in the screening of each Co atom. As enhanced moments of the kind observed in, for instance, *Pd* Co, are unlikely to exist in noble metal based alloys, it seems probably that the Co atoms are present in clusters, as suggested by Le Guillerm *et al.*[23], and that these clusters remain intact up to at least 600°K. As the moment is concentration independent (at least for c > 0·3 at. per cent), the number of Co atoms in a cluster must also be independent of concentration, and the number of clusters proportional to concentration. If this is the case, *Au* Co is evidently not a simple random alloy.

If the clusters remain intact to temperatures in excess of 600°K, the interaction between the members of the cluster must be very strong and Kondo scattering from the individual Co atoms in the cluster will be suppressed. However, Béal-Monod[26] has shown that a strongly coupled pair of magnetic impurities, whilst not giving rise individually to temperature dependent Kondo scattering, will scatter as a single spin, and exhibit a Kondo resistivity whose magnitude depends on the nett spin of the pair and on their separation. As the resistivity and thermopower suggest that the system undergoes a transition to a spin compensated state at a rather high temperature, it must be tentatively presumed that the whole cluster becomes spin compensated, with each member of the cluster retaining its full magnetic moment.

The concentration dependence of the low temperature properties can be understood qualitatively if the Kondo temperature, or the width of the scattering resonance, decreases with concentration. Nagaoka[27] has shown that such an effect may be expected to result from the long range of the conduction electron spin polarisation associated with the spin compensated state. He finds that the Kondo temperature, and properties of the system at or above T_K, do not depend on the concentration, as the amplitude of the spin compensating cloud is small at high temperatures. At very low temperatures compared with T_K, correlations between spin compensated states may be expected when the concentration exceed $c_0 > n(E_F)T_K$. (In the present system, with $T_K \sim 400°\mathrm{K}$, $c_0 \sim 1$ per cent.) Nagaoka shows that the width Δ of the resonance will decrease when c exceeds c_0, leading to an increase in the temperature dependent scattering per impurity for $T \ll T_K$. This is in qualitative agreement with the observed behaviour, though neither the temperature nor concentration dependence predicted by Nagaoka fit the present results.

CONCLUSIONS

The high temperature resistivity, thermopower and magnetic susceptibility demonstrate that *Au* Co undergoes a transition to a spin compensated state at a rather high temperature, though the susceptibility suggests that it is probably tightly bound clusters of Co atoms which undergo the transition. The present results also indicate that at concentrations sufficiently small for interactions of the RKKY type to be negligible, and for $T \ll T_K$, correlations between Co atoms (or clusters) increase the temperature dependence of the resistivity. (Similar effects have also been observed in the resistivity of *Cu* Fe and *Au* V [28].) There is at present no satisfactory theoretical explanation of this effect. However, the concentration dependence of the low temperature properties can be understood in general terms if it is assumed that T_K(or Δ) decreases with increasing concentration, and this conclusion is strongly supported by the linear decrease of the Curie temperature with concentration found by Hildebrand[22]. The one property which does not seem to fit in with this picture is the thermopower, which is independent of concentration at low temperatures[20].

Since the linear slope of the low temperature resistivity per impurity does not tend to a constant value at low concentrations (as does the Curie temperature[22]) but apparently tends to zero, it may be concluded that a linear temperature dependence is not characteristic of isolated Co atoms (or clusters) at temperatures very low compared with T_K. The actual temperature dependence in alloys sufficiently dilute for correlations between Co atoms to be negligible is very difficult to establish because of uncertainties due to the breakdown of Matthiessen's Rule, and the possible presence of minute amounts of Fe impurity. However, the present results are more consistant with a parabolic temperature dependence[11, 12] for the resistivity, than with the expression given by Hamann[13], which predicts that the slope of the resistivity becomes infinite as the temperature tends to zero.

Acknowledgements—We would like to thank Mr. R. J. White for his assistance in the preparation of some of the alloys, and the Analytic Laboratory of Imperial College, London, for their analysis.

REFERENCES

1. VAN DEN BERG G. J., VAN HERK J. and KNOOK B., *Proc. 10th Int. Conf. on Low Temperature Physics*, Vol. 4, p. 272. Moscow (1966).
2. DOMENICALI C. and CHRISTENSON E. L., *J. appl. Phys.* **32**, 2450 (1961).
3. POWELL R. L., CAYWOOD L. P. and BUNCH M. D., *Temperature, its Measurement and Control in Science and Industry* (Edited by Herzfeld), Vol. 3, Part 2., p. 65. Reinhold, New York (1962).
4. KUMÉ K., *J. phys. Soc. Japan* **23**, 1226 (1967).
5. FORD P. J., WHALL T. E. and LORAM J. W., *Proc. 11th International Conference on Low Temperature Physics*, Vol. 2, p. 1246 (1968).
6. HANSEN M., *Constitution of Binary Alloys*. McGraw-Hill, New York (1958).
7. GERRITSEN A. N., *Physica* **25**, 489 (1959).
8. PEARSON W. B., *A Handbook of Lattice Spacings*. Pergamon Press, Oxford (1967).
9. DAYBELL M. D. and STEYERT W. A., *Phys. Rev. Lett.* **18**, 398 (1967).
10. ANDERSON P. W., *Phys. Rev.* **164**, 352 (1967).
11. NAGAOKA Y., *Phys. Rev.* **138**, 1112 (1965).
12. APPELBAUM J. A. and KONDO J., *Phys. Rev. Lett.* **19**, 906 (1967).
13. HAMANN D. R., *Phys. Rev.* **158**, 570 (1967).
14. DUGDALE J. S. and BASINSKI Z. S., *Phys. Rev.* **157**, 552 (1967).
15. WHALL T. E., LORAM J. W., WHITE R. J. and FORD P. J., To be published.
16. KOHLER M., *Z. Phys.* **126**, 495 (1949).
17. JACOBS I. S. and SCHMITT R. W., *Phys. Rev.* **113**, 495 (1959).
18. CRANE L. T., *Phys. Rev.* **125**, 1902 (1962).
19. CRANE L. T. and ZIMMERMAN J. E., *Phys. Rev.* **123**, 113 (1961).
20. MACDONALD D. K. C., PEARSON W. B. and TEMPLETON I. B., *Proc. R. Soc.* **A266**, 161 (1962).
21. KJEKSHUS A. and PEARSON W. B., *Can. J. Phys.* **40**, 98 (1962).
22. HILDEBRAND E., *Ann. Phys.* **30**, 593 (1936).
23. LE GUILLERM J., TOURNIER R. and WEIL W., *Proc. 8th International Conference on Low Temperature Physics*, p. 236. Butterworth, New York (1963).
24. DAYBELL M. D. and STEYERT W. A., *Phys. Rev. Lett.* **20**, 195 (1968).
25. CAROLI B., *J. Phys. Chem. Solids* **28**, 1427 (1967).
26. BÉAL-MONOD., *Phys. Rev.*, To be published.
27. NAGAOKA Y, *J. Phys. Chem. Solids* **27**, 1139 (1966).
28. STAR W. M. and BOERSTOEL B. M., *Phys. Lett.* **29A**, 26 (1969).

J. Phys. Chem. Solids **Pergamon Press 1970. Vol. 31, pp. 771–775. Printed in Great Britain.**

APPLICATION OF THE ELECTRON TEMPERATURE MODEL TO LOW-TEMPERATURE NON-OHMIC TRANSPORT IN GaAs

RICHARD S. CRANDALL
RCA Laboratories Princeton, N.J. 08540, U.S.A.

(*Received* 25 *August* 1969)

Abstract – The electron temperature model and a theory involving a direct solution of the Boltzmann equation are compared with experiment. The experimental data are the field dependence of the conductivity and Hall constant at 4·23°K in GaAs. Only the theory involving a direct calculation of the distribution function appears to explain the experimental observations. This result is surprising since the electron density is about 4 orders of magnitude above that required to justify the electron temperature model.

INTRODUCTION

THE MOST widely used model of hot electron phenomena is the electron temperature model (ETM)[1–4]. In this model the electron distribution function is assumed to be Maxwellian with an effective electron temperature. This model was originally proposed by Fröhlich[1] who assumed that interelectronic collisions were sufficiently strong to enforce an internal equilibrium of the electron gas, thus justifying the concept of an electron temperature. Stratton[3] extended the calculations of Fröhlich and Paranjape [2] to include a variety of scattering mechanisms and lattice temperatures.

The advantage of the ETM is that the Boltzmann transport equation need not be solved. This simplification allows many problems that would otherwise be avoided because of their complexity, to be at least investigated for their physical content.

The ETM, however, has no rigorous justification. That strong electron-electron scattering maintains a Maxwellian (Fermi) distribution is only an assumption. This assumption has not been proven because of the difficulty of solving the transport equation for arbitrary electric fields in the presence of electron-electron collisions. Despite this, however, the ETM continues to be extensively applied. In most comparisons with experiment, the ETM agrees well with the experiment. Even with carrier densities orders of magnitude below that required for its justification, it can give a fairly good account of some rather complicated results[5].

In this article we use both the ETM and a direct solution of the Boltzmann equation [6] to analyze some Hall effect measurements in n-type GaAs at low temperature[7]. We find that even though the ETM gives fairly good agreement with the field dependence of the electron mobility, it does not fit the field dependence of the Hall constant. The direct solution however, gives good agreement with both the Hall constant and the mobility. This result is surprising since for the conditions in these measurements the usual criterion for the ETM is met[8].

RESULTS

The experimental details which are described in another publication by the author [7], are outlined below. In Fig. 1 the results of measurements of the electric field dependence of the Hall effect in *n*-type epitaxial GaAs at 4·2°K are shown. In this material the impurity density is so high that the donors do not freeze

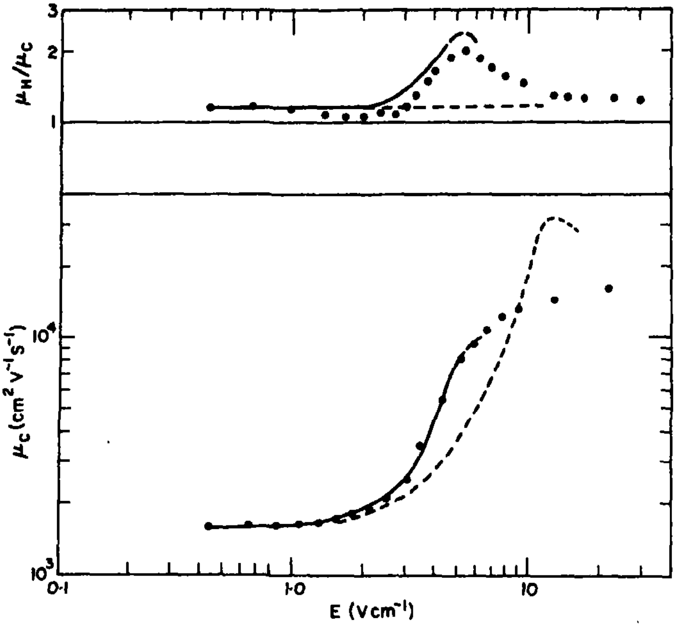

Fig. 1. The conductivity mobility μ_c and the ratio $\mu_H\mu_c^{-1}$ vs. electric field at 4·23°K. The solid line is for the BES calculation; the dashed line is for the ETM. The parameters are the same in both calculations. The dots are experimental data.

out down to the lowest temperatures. This result is similar to the case of InSb where donor freeze out is not observed[9]. The conductivity mobility μ_c was not measured directly, but was obtained from the measured conductivity by the relation $\mu_c = \sigma(ne)^{-1}$. The ratio $\mu_H\mu_c^{-1}$ was similarly obtained from the measured Hall constant R_H using the relation: $\mu_H\mu_c^{-1} = R_H ne$. Here n is $3{\cdot}5 \times 10^{15}$ cm^{-3}. The carrier density was obtained from measurements of the ohmic Hall constant at room temperature. The dots are experimental data. The dashed curves were obtained from the ETM. The solid curves were calculated from the direct solution of the Boltzmann equation (BES). We assumed that the electron scattering is due to ionized impurities and acoustic phonons interacting via both piezoelectric and deformation potentials. Screening of the electron-phonon as well as the electron-impurity interactions was taken into account. These assumptions give a consistent picture of both the ohmic and non-ohmic transport[7]. In both theories the parameters are the same and given in [7]. The theoretical curves are shown only in their region of validity; i.e. at fields where the optical phonon does not make a significant contribution to the scattering.

DISCUSSION

At this point a brief mention of the two theories and their approximations is in order. Both theories begin with the Boltzmann equation. The assumption is made that the electron distribution function $f(\mathbf{k})$ can be adequately represented by

$$f(\mathbf{k}) = f_0(\epsilon) + \mathbf{k} \cdot \mathbf{f}_1(\epsilon) \qquad (1)$$

where $f_0(\epsilon)$ depends on energy ϵ and is the symmetric part of $f(\mathbf{k})$, and $\bar{f}_1(\epsilon)$ is in the direction of the electric field E. The wave vector is **k**. Then it is straightforward to show in the relaxation time approximation that

$$f_1(\epsilon) = -\frac{e}{m}\hbar\tau\mathbf{E}\frac{\partial f_0(\epsilon)}{\partial\epsilon} \tag{2}$$

where τ is the momentum relaxation time.

Here the similarity between the two theories ends. In the ETM the assumption is made that $f_0(\epsilon)$ is of Maxwellian form but with an effective electron temperature T^*. The electron temperature is found from the energy balance relation: the power input to the electron gas is equated to the power lost to the phonons.

The criterion for the use of the ETM, as given by Fröhlich and Paranjape[8] is that the rate of loss of energy to the phonons is equal to the rate of energy exchange within the electron gas. This gives a critical density:

$$n_c \sim \epsilon^{1.5}m^{1.5}s^2\epsilon_0^2(4\pi kTe^4\tau)^{-1} \tag{3}$$

where m is the electron mass, s the sound velocity, ϵ_0 the dielectric constant, k Boltzmanns constant, T the lattice temperature, e the electron charge and τ the momentum relaxation time for phonon scattering. In our case we use a composite relaxation time for the two electron-phonon interactions [6, 7]. Using this expression we find that at 4·2°K the carrier density of $3{\cdot}5\times10^{15}\,\text{cm}^{-3}$ is at least 4 orders of magnitude above the critical concentration. It would thus seem that if the ETM were justified at all, it would at least be justified under these circumstances.

As Fig. 1 shows, the ETM does not give a very good fit to the data. Of course, we have used the parameters with the ETM calculation that gave the best fit for the BES. Referring now to the μ_c curve; we could change the parameters to improve the fit of the ETM curve, however, it would still not give as good a fit as the BES solution. The ETM curve at high fields would still be a factor of two higher than the experimental data.

But even with the above adjustment, the serious defect in the ETM fit is that it can not explain the field dependence of the ratio $\mu_H\mu_c^{-1}$. As we shall show below, it is the non-Maxwellian shape of the proper distribution function that is responsible for the field dependence of $\mu_H\mu_c^{-1}$.

To show clearly the non-Maxwellian shape of the proper electron distribution, we refer to Fig. 2. In this figure the number density dn/dϵ is plotted vs. electron energy. This quantity is the product of the symmetric part of the electron distribution function and the

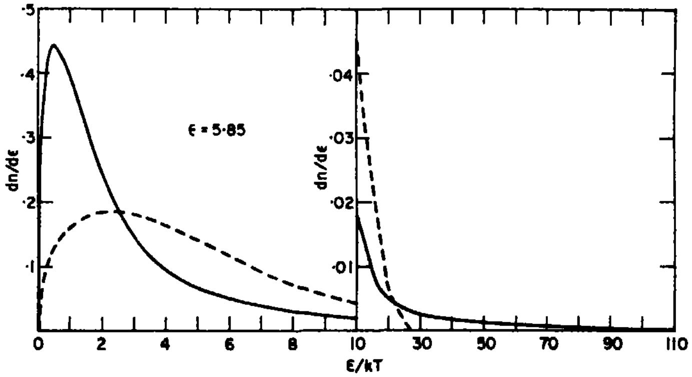

Fig. 2. The number density dn/dϵ vs. normalized energy $\epsilon = \epsilon/kT$ from ETM and BES calculations for an average energy of 5·85 kT. The lattice temperature is 4·23°K. The solid line is for the BES calculation; the dashed line is the ETM. The tails of the distributions are shown by the scale at the right. Note the scale change at $\epsilon = 10$.

square root of the dimensionless density of states parameter $\epsilon = \epsilon/kT$. The calculation of the function $dn/d\epsilon$ for the BES was outlined in [7]. For the ETM

$$\frac{dn}{d\epsilon} = \epsilon_1^{1/2} \exp(-\epsilon_1), \tag{4}$$

where $\epsilon_1 = \epsilon T(T^*)^{-1}$.

Both distributions have an average energy of $5{\cdot}85\,kT$; T is 4·23°K. The electric field is $5\ \mathrm{V\,cm^{-1}}$ for the BES. There are two important differences between the two curves: the maximum of $dn/d\epsilon$ is shifted little from the ohmic value of $\epsilon = 0{\cdot}5$ for the case of the BES model; whereas, for the ETM, the maximum is at $\epsilon = 2{\cdot}93$. The other difference is the long tail on the number density for the BES model. This tail, which contains a small fraction of the free electrons, makes a large contribution to the current. We can understand these differences in the two distribution functions when we consider that the mobility is determined by ionized impurity scattering, whereas the energy loss is to acoustic phonons (the electron-phonon interaction is primarily via the piezo-electric potential). Since the ionized impurity scattering time increases roughly as the cube of the electron velocity v, the rate of energy gain from the electric field increases as roughly v^3. The energy loss rate to the acoustic phonons increases only linearly with velocity. Therefore, electrons in the tail of the distribution gain energy faster than they lose it and accelerate to higher energy. What keeps the electrons from 'running away' is the deformation potential interaction. At energies above about 0·009 eV ($\sim 20\,kT$) the deformation potential interaction dominates and the energy loss rate increases as v^3. If we had considered only ionized impurity scattering and the deformation potential e-p interaction, the distribution function would remain nearly Maxwellian. The long tail would be absent, because there would be no unstable state for the high velocity electrons. This is the reason that the electron temperature model works so well in germanium.

We now argue why the long tail on the distribution function produces the structure in the $\mu_H \mu_c^{-1}$ curve. The Hall mobility depends on the average of the square of the scattering time, $\langle \tau_s^2 \rangle$, whereas μ_c depends on $\langle \tau_s \rangle$. Because τ_s increases with increasing energy, the average of τ_s^2 weights the tail of the distribution more heavily than does $\langle \tau_s \rangle$. Therefore, as the tail of the distribution increases with increasing electric field, we find that $\mu_H \mu_c^{-1} = \langle \tau_s^2 \rangle \langle \tau_s \rangle^{-2}$ increases. We can speculate that $\mu_H \mu_c^{-1}$ decreases at high fields because the distribution function changes from one that is spread out in energy to one that has most of the electrons concentrated just below the optical phonon energy. Since this distribution occupies a narrow range in energy space, $\mu_H \mu_c^{-1}$ approaches unity.

The reason that the theoretical curves in Fig. 1 are not extended above about $5\ \mathrm{V cm^{-1}}$ is that the theory is inappropriate at higher fields because it predicts that a significant fraction of the electrons are at energies where scattering due to optical phonon emission should be important. The solid portion of the BES curve in Fig. 1 is for fields where electrons of energy greater than the optical phonon energy do not contribute to the calculated current or energy. In the region represented by the broken portion of the curve, up to 5 per cent of the total number of electrons can emit optical phonons. Since these electrons lose most of their energy and momentum by optical phonon emission, they do not contribute significantly to the current. We have, therefore, approximated optical phonon scattering in our theory by omitting any contribution to the current by those electrons whose energy is greater than the optical phonon energy. Of course this procedure is inappropriate when these optical-phonon-scattered electrons become a sizeable fraction of the total electron density. This approach does, however, indicate when optical phonon emission becomes important. The experimental and theoretical terminations of the rapid mobility rise are in good agreement. This same cutoff procedure was used with the ETM. Since there is no long tail on the Maxwellian (Fermi) distribution, the field is higher before the optical phonon emission becomes important. The electron temperature at this field is about 10 times the lattice temperature. This corresponds to an average energy of 15 kT, whereas with the BES distribution, the average energy is about 5·9 kT when the optical phonon becomes important. Thus, the ETM gives a much hotter distribution than the BES.

It is indeed surprising that we find such good agreement between theory and experiment when electron-electron (*e-e*) scattering is omitted. If we take the limit of *e-e* scattering strong enough to enforce a Maxwellian distribution then, we can not fit the data. This is doubly puzzling since the experimental carrier density is 4 orders of magnitude above that needed for the ETM to be justified.

One usually considers that *e-e* scattering removes the asymmetry of the distribution. Since the main change in the calculated distribution in the high field region is an increase in the tail and not an increase in the asymmetry (the assymmetry actually decreases), *e-e* scattering must reduce the tail to be effective. This tail can be reduced if high energy electrons share their energy with low energy electrons. However, this process will not completely reduce the tail. Even with *e-e* scattering the long tail will persist, since it arises because the mean free time between scattering events increases faster with increasing energy than does the energy loss rate. The scattering rate for *e-e* collisions decreases with increasing energy. All that we can conclude from this qualitative discussion is that the distribution is probably in between the BES and the ETM distributions. Since we found that the BES solution gave good agreement with experiment and the ETM did not, the distribution is probably closer to the BES than to a shifted Fermi distribution.

SUMMARY

On comparing the electron temperature model and a direct solution of the Boltzmann equation with experiment, it was found that the direct solution gave a good fit to the data whereas the electron temperature model gave a poor fit. For the experimental conditions the electron temperature model should have been valid.

REFERENCES

1. FRÖHLICH H., *Proc. R. Soc.* **A188**, 532 (1947).
2. FRÖHLICH H. and PARANJAPE, B.V., *Proc. phys. Soc.* **B69**, 21 (1956).
3. STRATTON R., *Proc. R. Soc.* **A242**, 355 (1957); *Proc. R. Soc.* **A246**, 406 (1958).
4. CONWELL E. M., In *Solid State Physics* (Edited by F. Seitz, D. Turnbull and H. Ehrenreich), Suppl. 9. Academic Press, New York (1967).
5. MATZ D. and GARCIA-MOLINER F., *J. Phys. Chem. Solids* **26**, 551 (1965).
6. CRANDALL R. S., *Phys. Rev.* **169**, 585 (1968).
7. CRANDALL R. S. and GWOZDZ P., *Bull. Am. phys. Soc. Ser. II* **13**, 406 (1968); R. S. Crandall, to be published.
8. Reference [2], p. 23.
9. SANDERCOCK J. R., *Solid St. Commun.* **5**, 229 (1967).

J. Phys. Chem. Solids **Pergamon Press 1970. Vol. 31, pp. 777–781. Printed in Great Britain.**

THERMODYNAMIC PROPERTIES OF DILUTE MAGNETIC ALLOYS*

C. S. TING
Department of Physics, University of California, San Diego, La Jolla, Calif. 92037, U.S.A.

(*Received* 19 *August* 1969)

Abstract—The free energy of a dilute magnetic alloy is obtained on the basis of Suhl's theory from which the temperature dependent entropy and specific heat of the system are calculated at all temperature ranges. The zero temperature entropy we obtain is in agreement with Zittartz's calculation, which is based upon Nagaoka's formulation, and our specific heat results are in qualitative agreement with the experimental data given by Daybell and Steyert.

THE specific heat of dilute magnetic alloys was first calculated by Bloomfield and Hamann[1] and then by Zittartz and Müller-Hartmann[2]. Both of the calculations are based upon Nagaoka's formulation[3]; their results yield predictions in qualitative agreement with experiment, for example, Cu(Fe) and Cu(Cr) systems[4, 5]. However, the temperature-dependent entropy change due to the presence of the magnetic impurity in a non-magnetic metal host cannot be easily obtained from Nagaoka's formulation. In both of the above mentioned papers, the authors have made the entropy calculations only for $T = 0$; their results are different from each other. In the present note, we use Suhl's formulation[6, 7] to compute the entropy and the specific heat of a dilute magnetic alloy. This method has been used by Kondo[8] to obtain an expression for free energy to fourth order in powers of J, where J is the coupling constant between conduction electrons and the magnetic impurity. For a dilute magnetic alloy, we may neglect the interaction between two impurities. It is reasonable to assume that there is only one impurity at the origin, then the interacting Hamiltonian is of the form

$$H' = J \sum_{kk'} \Big\{ (\mathrm{C}^{+}_{k\uparrow}\mathrm{C}_{k'\uparrow} - \mathrm{C}^{+}_{k\downarrow}\mathrm{C}_{k'\downarrow})\,\mathrm{S}_z + \mathrm{C}^{+}_{k\uparrow}\mathrm{C}_{k'\downarrow}\,\mathrm{S}_- + \mathrm{C}^{+}_{k\downarrow}\mathrm{C}_{k'\uparrow}\,\mathrm{S}_+ \Big\} \tag{1}$$

where S_z and S_+ are components of the spin operator associated with the impurity; $\mathrm{C}^{+}_{k\sigma}$ and $\mathrm{C}_{k\sigma}$ are the creation and annihilation operators of the conduction electrons. If we introduce the current density operator $j_\sigma = [\mathrm{H}', \mathrm{C}^{+}_{k\sigma}]_-$, then the ground state average of (1) can be expressed in terms of a product of the current density operators. The current density in turn can be expressed by the T-matrix[6]:

$$T_{k\sigma,\uparrow} = {}^-\langle k\sigma | j^{+}_{\uparrow} | 0\rangle, \qquad T_{k\sigma;\uparrow} = {}^-\langle k\sigma | j_{\uparrow} | 0\rangle,$$

where $|0\rangle$ is the ground state and $|k\sigma\rangle^-$ is the incoming scattering intermediate eigenstate. On making use of the method as described in [7], the thermodynamic average of (1) is given by [8]

$$\langle \mathrm{H}' \rangle = -\frac{1}{\mathrm{J}} \lim_{x\to\infty} x t(x) + \mathrm{JS(S+1)} \int \rho(x)\mathrm{d}x \tag{2}$$

where $\rho(x)$ is the density of states function, $t(x)$ is the spin nonflip scattering amplitude. It satisfies the following coupled integral equations:

$$t(z) = \int_{-1}^{1} \mathrm{d}x\, \rho(x) \frac{|t(x)|^2 + \mathrm{S(S+1)}|\tau(x)|^2}{z - x} \tag{3}$$

---

*Research sponsored by the Air Force Office of Scientific Research U.S. Air Force, under Grant No. AF-AFOSR-610-67.

$$\tau(z)=J+\int_{-1}^{1}\mathrm{d}x\,\rho(x)\,\frac{\tau(x)\,t^*(x)+\tau^*(x)\,t(x)-|\tau(x)|^2\tanh x/2T}{z-x}\quad\cdot\tag{4}$$

where we choose the density of states function $\rho(x)=\rho(0)\sqrt{1-x^2}$, with the Fermi level at the center of the band. The solution for $t(x)$ is well known and is given by [7, 9]

$$t(x)=\frac{1}{2\pi i\rho(x)}\left\{1-\frac{1}{F(x)}\exp\left[\frac{\mathrm{i}}{2\pi}\rho(x)\int_{-1}^{1}\frac{\mathrm{d}y}{\rho(y)}\,\frac{\ln(1/(|F(y)|^2)+a(y))}{y-x}\right]\right\}\tag{5}$$

with $a(x)=4\pi^2\mathrm{S}(\mathrm{S}+1)\,\rho^2(x)$

$$F(x)=\frac{J}{1-J\gamma(x,T)-iJ\pi\rho(x)\tanh x/2T}$$

$$\gamma(x,T)=P\int_{-1}^{1}\rho(y)\,\mathrm{d}y\tanh y/2T\,\frac{1}{y-x}\tag{6}$$

if we approximate $\tanh y/2T$ by $+1$ for $y>2T$, -1 for $y<-2T$ and $y/2T$ for $|y|\leqslant 2T$, then $\gamma(x)$ can be proved to have the form

$$\gamma(x,T)=\rho(x)\left\{2\ln(1+\rho(x))-\ln(x^2-4T^2)+\frac{x}{2T}\ln\left|\frac{x-2T}{x+2T}\right|\right\}.\tag{7}$$

At $x=0$, $\mathrm{F}(x)$ is a function of temperature only. It will become divergent as the temperature approaches T_K 'Kondo temperature', from (6) and (7), $T_K=\exp(-1/2J)$. It is not difficult to see that at $T>T_K$, $F(z)$ is analytic on the physical sheet of the complex energy plane except with a cut along the real axis from -1 to $+1$; however, it has a pair of complex poles on the unphysical sheet, at $T=T_K$. These two poles meet at the origin and enter into the physical sheet at $T<T_K$. From (6) the positions $\pm i\Delta$ of the poles on the physical sheet satisfy the equation

$$1-J\int_{-1}^{1}\mathrm{d}x\,\rho(x)\tanh x/2T\,\frac{1}{x\mp i\Delta}=0.\tag{8}$$

On making use of the analytical properties of $F(x)$, (5) can also be proved to have the expression

$$t(x)=\frac{1}{2\pi i\rho(x)}\left\{1-\frac{x(1+\Delta^2)^{1/2}-i(1-x^2)^{1/2}\Delta}{x(1+\Delta^2)^{1/2}+i(1-x^2)^{1/2}\Delta}\times\exp\left[\frac{i\rho(x)}{2\pi}\int_{-1}^{1}\frac{\ln(1+a(y)\,|F(y)|^2)}{\rho(y)\,(y-x)}\mathrm{d}y\right]\right\}.\tag{9}$$

By Feynman's theorem, the free-energy shift is given by

$$\Delta F=\int_0^J\frac{dJ'}{J'}\langle\mathrm{H}'\rangle_{J'}.\tag{10}$$

Multiplying x on both sides of equation (9), and putting $x\rightarrow\infty$, from (2) and (10), we readily have

$$\Delta F=-\int_0^J\frac{\mathrm{d}J'}{J'^2}\left\{\frac{\Delta}{\pi(1+\Delta^2)^{1/2}}+\frac{1}{4\pi^2}\int_{-1}^{1}\mathrm{d}x\left[\frac{\ln(1+a(x)|F(x)|^2)-a(x)J'^2}{\rho(x)}\right]\right\}.\tag{11}$$

Since $\Delta^2\ll 1$, if we neglect it in the denominator of the first term of (11), then (11) is exactly the only one obtained by Kondo[8]. From (8), we have $\Delta=2\exp(-1-1/J)$ at $T=0$. It is easy to show that the first term of (11) gives a contribution to the ground state energy shift $\Delta F^{(1)}=\Delta E^{(1)}=-2\Delta/\pi$. Kondo calculated the second term of (11) by expanding the integrand in powers of J. The fourth order free energy shift which can also be obtained by perturbation theory[9] gives a logarithmic temperature term

$$\Delta F^{(4)} = 16\pi^2 J^4 \rho^4(0)\, \mathrm{S}(\mathrm{S}+1)\, T \ln(1/T).$$

Because of this logarithmic behavior, it gives a fourth order term to the reduction of entropy of conduction electrons

$$\Delta \mathrm{S} = -16\pi^2 J^4 \rho^4(0)\, \mathrm{S}(\mathrm{S}+1) \ln(1/T).$$

The unperturbed entropy which comes from the $(2\mathrm{S}+1)$-fold degeneracy of the impurity spin is $\ln(2\mathrm{S}+1)$. Whether the cancellation of the total entropy is complete at $T = 0$ or not, and how it varies with temperatures are questions which can not be answered by expanding the free energy in powers of J. Therefore, one has to make a nonperturbative calculation for (11). However, the main difficulty associated with (11) is the complicate T and J dependences of Δ, which makes the computation tedious. As we will see later, it is very convenient to substitute (5) into (2), then the free energy can be written as

$$\Delta F = J\mathrm{S}(\mathrm{S}+1)\int_{-1}^{1} \rho(x)\mathrm{d}x - \frac{1}{4\pi^2}\int_0^J \frac{\mathrm{d}J'}{J'^2}$$
$$\int_{-1}^{1} \mathrm{d}x \frac{\ln J'^2 + \ln[1/(|F(x)|^2) + a(x)]}{\rho(x)}. \qquad (12)$$

The integration over J' can be carried out easily for equation (12), the result is

$$\Delta F = J\mathrm{S}(\mathrm{S}+1)\int_{-1}^{1} \rho(x)\mathrm{d}x - \frac{1}{4\pi^2}$$
$$\int_{-1}^{1} \frac{\mathrm{d}x}{\rho(x)}\left\{A(x,T)\left[\pi - 2\tan^{-1}\frac{((1/J) - \gamma(x,T))}{A(x,T)}\right]\right.$$
$$+2\left(\frac{1}{J} - \gamma(x,T)\right) - \left(\frac{1}{J} - \gamma(x,T)\right)$$
$$\left.\times \ln\left[\left(\frac{1}{J} - \gamma(x,T)\right)^2 + A^2(x,T)\right] + \frac{2}{J}\ln\left(\frac{1}{J}\right) - \frac{2}{J}\right\} \qquad (13)$$

where $A(x,T) = [a(x) + \pi^2\rho^2(x)\ \tanh^2 x/2T]^{1/2}$. The entropy shift of conduction electrons can be obtained by taking the derivative of (13) with respect to temperature, that is $\Delta\mathrm{S} = -\partial F/\partial T$

$$\Delta \mathrm{S} = \frac{1}{4\pi^2}\int_{-1}^{1}\frac{\mathrm{d}x}{\rho(x)}\left\{\pi - 2\tan^{-1}\right.$$
$$\left.\frac{((1/J) - \gamma(x,T))}{A(x,T)}\right\}\frac{\mathrm{d}A(x,T)}{\mathrm{d}T} - \frac{1}{4\pi^2}\int_{-1}^{1}\frac{\mathrm{d}x}{\rho(x)}$$
$$\ln\left[\left(\frac{1}{J} - \gamma(x,T)\right)^2 + A^2(x,T)\right]\frac{\mathrm{d}}{\mathrm{d}T}\left[\frac{1}{J} - \gamma(x,T)\right] \qquad (14)$$

where

$$\frac{\mathrm{d}A}{\mathrm{d}T} = -\frac{\pi^2\rho^2(x)}{2A(x,T)}\frac{x}{T^2}\tanh\frac{x}{2T}\,\mathrm{sech}^2\frac{x}{2T}$$
$$\frac{\mathrm{d}}{\mathrm{d}T}\left[\frac{N}{J} - \gamma(x,T)\right] = \frac{\rho(x)}{T}\left\{2 + \frac{x}{2T}\ln\left|\frac{2T - x}{2T + x}\right|\right\}.$$

Let us examine the entropy reduction of conduction electrons at $T = 0$. It is not difficult to show that the second term of (14) gives no contribution to the entropy as $T \to 0$. The contribution to the first term of (14) is essentially coming from the integration over a small region near the Fermi surface. This region of integration is in the order of magnitude T. At $T = 0$, it is very easy to show that (14) becomes

$$\Delta\mathrm{S}(T = 0) = \lim_{T\to 0}\frac{\pi}{4}\int_{-1}^{1}\frac{\rho(x)\,\mathrm{d}x}{A(x,T)}\frac{x}{T^2}$$
$$\times \tanh\frac{x}{2T}\,\mathrm{sech}^2\frac{x}{2T}$$

with the change of variable $y = x/2T$, and perform the integration, one has

$$\Delta\mathrm{S}(T = 0) = -(2\mathrm{S}+2)\ln(2\mathrm{S}+2) + 2\mathrm{S}\ln 2\mathrm{S}$$
$$-2(2\mathrm{S}+1)\ln(2\mathrm{S}+1).$$

This is exactly the result that Zittartz and Müller-Hartmann obtained for the entropy reduction at $T = 0$. Here we have also done the numerical computations for $\Delta\mathrm{S}$ at finite temperatures. The results are shown in Fig. 1

for three different Kondo temperatures, where we put the Boltzmann constant $K_B = 1$, Fermi energy $\epsilon_F = 1$, and the impurity spin $S = \frac{1}{2}$. ΔS is in the unit of K_B/atom. From Fig. 1, we readily see that the entropy reduction becomes bigger and less dependent on the coupling constant as the temperature gets lower. At $T = 0$, $\Delta S = -0{\cdot}523$, it is a coupling constant independent quantity. For spin $\frac{1}{2}$ impurity, the unperturbed entropy is equal to ln 2(= 0·69). Hence, the entropy shift of the conduction does not completely compensate the entropy due to the degeneracy of the impurity spin states.

The specific heat can be obtained by doing the calculation of $C_v = T\, \partial\Delta S/\partial T$

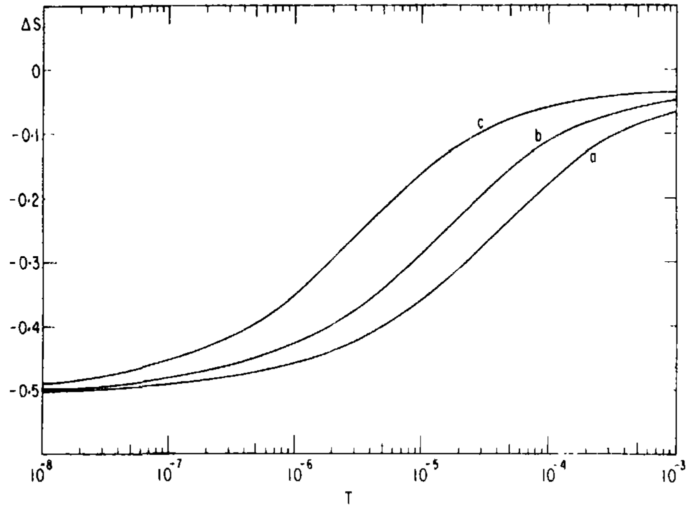

Fig. 1. Variation of the entropy shift ΔS as a function of temperature. For curve a, the Kondo temperature T_K is set equal to $1{\cdot}234 \times 10^{-4}$. For curve b, $T_K = 4{\cdot}539 \times 10^{-4}$. For curve c, $T_K = 1{\cdot}013 \times 10^{-5}$. The impurity spin $S = \frac{1}{2}$ for the three curves.

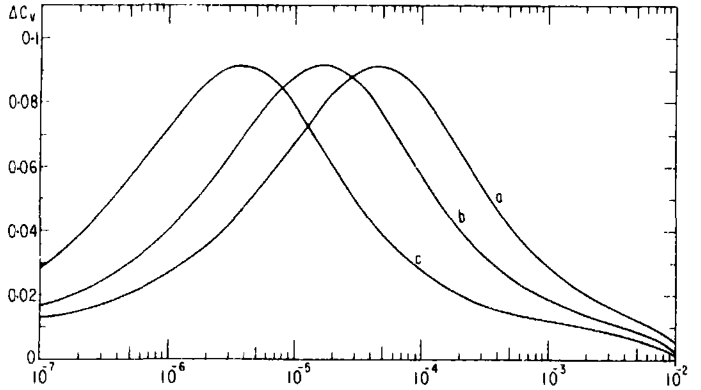

Fig. 2. Variation of the specific heat C_v as a function of temperature. For curve a, the Kondo temperature T_K is set equal to $1{\cdot}234 \times 10^{-4}$. For curve b, $T_K = 4{\cdot}539 \times 10^{-4}$. For curve c, $T_K = 1{\cdot}013 \times 10^{-5}$. The impurity spin $S = \frac{1}{2}$ for the three curves.

$$C_v = \frac{1}{4\pi^2}\int_{-1}^{1}\frac{\mathrm{d}x}{\rho(x)}\left\{\pi - 2\tan^{-1}\frac{(1/J-\gamma(x,T))}{A(x,T)}\right\}T\frac{\mathrm{d}^2A(x,T)}{\mathrm{d}T^2}$$

$$-\frac{1}{2\pi^2}\int_{-1}^{1}\frac{\mathrm{d}x}{\rho(x)}\left\{\frac{\frac{\mathrm{d}A^2(x,T)}{\mathrm{d}T}\cdot T\frac{\mathrm{d}}{\mathrm{d}T}\left[\frac{1}{J}-(x,T)\right]}{A^2(x,T)+(1/J-(x,T))^2}\right\}$$

$$+\frac{1}{2\pi^2}\int_{-1}^{1}\frac{\mathrm{d}x}{\rho(x)}\frac{T\left(\frac{1}{J}-\gamma(x,T)\right)\left(\frac{\mathrm{d}A(x,T)}{T}\right)^2}{A^2(x,T)+(1/J-\gamma(x,T))^2}$$

$$-\frac{1}{4\pi^2}\int_{-1}^{1}\frac{\mathrm{d}x}{\rho(x)}T\frac{\mathrm{d}^2}{\mathrm{d}T^2}\left[\left(\frac{1}{J}-\gamma(x,T)\right)\right]$$

$$\cdot\ln\left[\left(\frac{1}{J}-\gamma(x,T)\right)^2+A^2(x,T)\right]$$

$$-\frac{1}{2\pi^2}\int_{-1}^{1}\frac{\mathrm{d}x}{\rho(x)}T\left\{\frac{\mathrm{d}}{\mathrm{d}T}\left(\frac{1}{J}-\gamma(x,T)\right)\right\}^2$$

$$\times\frac{(1/J)-\gamma(x,T)}{(1/J-\gamma(x,T))^2+A^2(x,T)} \tag{15}$$

with

$$\frac{\mathrm{d}^2A(x,T)}{\mathrm{d}T^2} = -\frac{\pi^4\rho^4(x)}{4A^3(x,T)}\frac{x^2}{T^4}\tanh^2\frac{x}{2T}\operatorname{sech}^2\frac{x}{2T}$$

$$+\frac{\pi^2\rho^2(x)}{2A(x,T)}\left[\frac{2x}{T^3}\tanh\frac{x}{2T}\operatorname{sech}^2\frac{x}{2T}\right.$$

$$\left.-\frac{x^2}{T^4}\operatorname{sech}^2\frac{x}{2T}+\frac{3x^2}{4T^4}\operatorname{sech}^4\frac{x}{2T}\right]$$

$$\frac{\mathrm{d}^2}{\mathrm{d}T^2}\left[\frac{1}{J}-\gamma(x,T)\right] =$$

$$-\rho(x)\frac{1}{T}\left\{\frac{x}{T}\ln\left|\frac{2T-x}{2T+x}\right|+4\frac{2T^2-x^2}{4T^2-x^2}\right\}.$$

We have done the numerical computation for (15) for three different Kondo temperatures; the results are shown in Fig. 2. The feature of our numerical results seems in qualitative agreement with Cu(Fe)[4] and Cu(Cr)[5] data are the shape of the C_v curve and the position of the C_v peak at $T_{\mathrm{Max}} \sim 1/3\, T_K$. The height of the C_v peak seems independent of the coupling constant J.

Acknowledgement—The author wishes to thank Professor H. Suhl for suggesting this problem and for his continuous guidance.

REFERENCES

1. BLOOMFIELD P. E. and HAMANN D. R., *Phys. Rev.* **164**, 856 (1967).
2. ZITTARTZ J. and MÜLLER-HARTMANN E., *Phys. Lett.* **26A**, 284 (1968); *Z. Phys.* **212**, 380 (1968).
3. NAGAOKA Y., *Phys. Rev.* **138**, A1112 (1965).
4. DAYBELL M. D. and STEYERT W. A., *Phys. Rev. Lett.* **18**, 398 (1967).
5. DAYBELL M. D., PRATT W. P. Jr. and STEYERT W. A., *Phys. Rev. Lett.* **22**, 401 (1969).
6. SUHL H., *Phys. Rev.* **138**, A515 (1965); *Physics* **2**, 39 (1966).
7. SUHL H. and WONG D., *Physics* **3**, 17 (1967).
8. KONDO J., *Prog. theor. Phys.* **40**, 695 (1968).
9. KONDO J., *Prog. theor. Phys.* **40**, 683 (1968).

J. Phys. Chem. Solids Pergamon Press 1970. Vol. 31, pp. 783–791. Printed in Great Britain.

ELECTRICAL CONDUCTIVITY OF Li DOPED MnO

C. CREVECOEUR and H. J. DE WIT
Philips Research Laboratories, N.V. Philips' Gloeilampenfabrieken, Eindhoven, The Netherlands

(*Received* 11 *August* 1969)

Abstract—Electrical resistivity, thermoelectric force and dielectric losses has been measured on Li doped MnO as a function of temperature. We have found that the slopes of $\log \rho$ and α vs. $1/T$ are quite different which can be explained by a hole mobility increasing exponentially with temperature. The depth of the Li acceptors is about 0·4 eV, the activation energy of the mobility of holes is about 0·3 eV. The movement of holes around a Li-ion is also thermally activated. The small polaron character of the holes is thought to be connected with Jahn–Teller deformations caused by the holes.

INTRODUCTION

BESIDES the problem of why NiO, CoO and MnO are semiconductors and not metals, even the question of how electrical conduction takes place has not yet been resolved. Charge carriers may move in some sort of a narrow band or, in terms of Holstein's theory [1] be small polarons, more or less strongly coupled with the lattice. Numerical calculations on Holstein's small polaron theory[2] indicate that only a large coupling constant will make it possible to decide from combined Seebeck effect—and resistivity measurements whether the charge carriers move thermally activated through the lattice. We have therefore studied the properties of *p*-type MnO for which a strong coupling constant can be expected, on account of the Jahn–Teller deformation of the high spin $3d^4$ state of the hole (Mn^{3+}).

MnO has been the subject of several investigations. Some of those referring to electrical properties will be listed below. The electrical conduction in Li-doped MnO was first discussed by Heikes and Johnston[3]. From conductivity measurements near room temperature it was decided that the large temperature coefficient of the resistivity could be explained by a thermally activated diffusion of holes. Miller and Heikes[4] felt that this model was supported by mechanical loss measurements performed at low frequencies on $Li_xMn_{1-x}O$ samples. Hed and Tannhauser[5] concluded from combined electrical and thermogravimetric measurements on MnO at high temperatures to a thermally activated mobility of holes, the activation energy being 0·37 eV. The oxygen pressure was varied between 10^{-1} and 10^{-18} atm, the temperature between 1400 and 1800°K. They constructed a phase diagram which was used in our investigation.

Hall effect measurements were performed by Nagels and Denayer[7] on lightly doped single crystals of MnO. The Hall mobility of the holes varies from $5 . 10^{-3}$–$8 . 10^{-3}$ cm^2/Vsec when going from 150 to 500°C. They concluded that the decrease of the resistance on going from 20 to 800°C is almost entirely due to the increase of the charge carrier concentration. The Hall measurements are in agreement with those obtained on polycrystalline samples[8]. A study of Ali, Fridman, Denayer and Nagels[9] includes measurements on the thermoforce of slightly doped single crystals, treated at 800°C in atmospheres with different oxygen concentrations. Again it was concluded that the increase of the conductivity with temperature is almost completely determined by the increase of the charge carrier concentration; that treatment of the crystals in atmospheres containing oxygen as well as radiation with neutrons, introduces donors in MnO and that the acceptor level lies 0·64 eV above the valence band.

We have investigated the temperature

dependence of the Seebeck coefficient and the resistivity in the temperature region 200–1400°K and also the dielectric properties of the Li centre at low frequencies (10^5–10^{-2} Hz) and low temperatures (300–77°K).

Sample preparation

MnO was prepared by decomposing $MnCO_3$ for some hours in a mixture of hydrogen gas (25 per cent) and nitrogen gas (75 per cent) at 800°C. Li doped MnO was obtained by heating an intimate mixture of Li_2CO_3 and MnO at 800°C, for 2 hr in technical nitrogen (containing about 100 ppm oxygen), and 1 hr in a mixture of H_2 and N_2. After milling, the Li-containing MnO powder was pressed into disks and bars, packed in platinum foils and fired at 1200°C for 24 hr in Al_2O_3 boats in a CO/CO_2 mixture. In order to prevent donors (e.g. Li compensated by oxygen vacancies) the CO/CO_2 ratio was chosen so that at 1200°C $[V_{Mn}]$ was of the same order of magnitude as [Li]. The oxygen pressure amounted to 10^{-6}–10^{-11} atm. To prevent oxydation the CO/CO_2 mixture was sometimes replaced by a H_2/N_2 mixture when cooling below 1000°C. This did not influence the measurements however.

Single crystals were prepared in two ways. In the first one a molten zone was drawn through a sintered bar. The molten zone was obtained in the manner of Kooy and Couwenberg[10] by focussing light from a Xenon arc. H_2/N_2 gas flowed rapidly around the sample to prevent precipitation of evaporated MnO on the quartzglass tube surrounding the MnO bar. In reducing atmospheres beautiful whiskergrowth on the rods was observed.

Crystals were also obtained by the Verneuil method. A gas mixture of 1 l/min oxygen and 4 l/min hydrogen was used. The MnO powder was doped with Li. Finally the crystals were heated in a CO/CO_2 atmosphere at 1200°C.

The ceramic samples had a density of 90–95 per cent of the ideal value. No second phase was observed on polished samples. The crystals prepared with the floating zone technique were of a poorer quality than the Verneuil crystals. Polished samples of both types of crystals show Mn_3O_4 as small isolated isles in the MnO. The presence of such Mn_3O_4 inclusions were reported by Loh and Newman[11].

The main impurity in the ceramic samples is Si introduced during milling. Later on it was found that the samples contain also carbon to an amount of 50 weight ppm, making the accurate determination of the Mn^{3+} concentration by chemical methods impossible. Table 1 gives a survey of the analysis. The crystal was not analysed. Dielectric measurements showed the presence of Li, the concentration being < 0·1 at per cent.

Measurements

Contacts on the samples were made with painted Pt from Degussa for high temperature resistivity and thermoelectric measurements.

At low temperatures painted silver contacts were used for dielectric measurements and In Hg contacts for resistivity and thermoelectric measurements.

Resistivity was measured on bars and disks using four electrodes. At low temperatures the Seebeck coefficient was obtained by measuring the thermal e.m.f. and the tempera-

Table 1

Marking	Sample	$[Li^+]$ at %	$[Mn^{3+}]$ at %	Impurities (wt. %)
◐	ceramic	0·03		0·001 Si; 0·001 Fe; 0·004 Na
○	ceramic	0·1	0·09–0·05	0·003 Si; 0·001 Fe; 0·003 Na
◒	ceramic	5	6	0·1 Na
●	crystal	< 0·1	—	—

ture difference between two copperblocks to which the MnO sample was soldered. Above room temperature bars were clamped between Pt blocks and thermocouples were mounted in holes near the ends in the sample.

For the dielectric measurements at low frequencies (< 1 Hz) the current through and the voltage over the specimen were directly recorded as a function of time. Changes in the phase difference were calculated by a least square analysis. The loss angle at 77°K was put equal to zero.

RESULTS

Figure 1 shows the temperature dependence of the resistivity of different $Li_xMn_{1-x}O$ samples, $3 . 10^{-4} < x < 5 . 10^{-2}$. Because the possible influence of Mn_3O_4 is discussed, the resistance of a sample of Mn_3O_4 to which 0·02 wt. per cent Li was added, is included in Fig. 1 (dotted line).

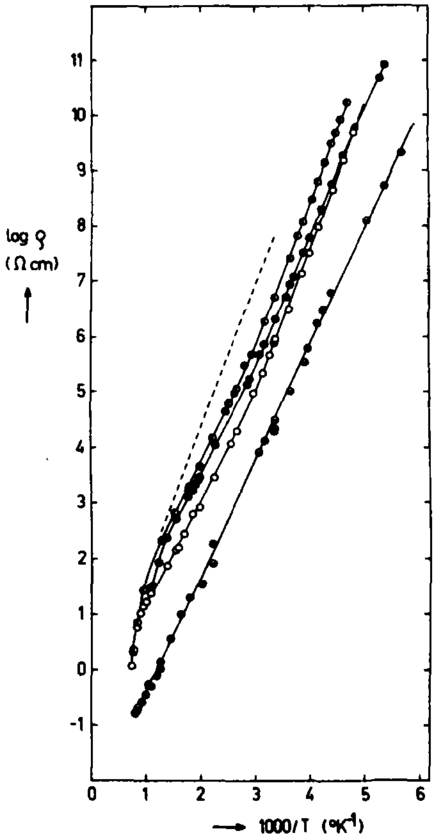

Fig. 1. Log resistivity as a function of reciprocal temperature for MnO containing different amounts of Li. ● Single crystal; ◐ 0·03 at per cent Li; ○ 0·1 at per cent Li; ◒ 5 at per cent Li.

Near room temperature a.c. measurements were carried out in the frequency range 20 kHz–2 MHz. The a.c. resistivities do not differ from the d.c. values. Near room temperature thin insulating layers are not present.

The value of the resistivity and its variation as a function of temperature are in agreement with measurements done by Nagels *et al.*[7] and Ali *et al.*[9].

Figure 2 presents thermoelectric measurements as a function of temperature on the same samples as mentioned in Fig. 1. Partial oxidation of a sample $Li_xMn_{1-x}O$ with $x = 10^{-3}$ to Mn_3O_4 in CO_2 at 1000°C for 1 hr did not change the Seebeck coefficient and the resistivity at room temperature. α increases for all samples when T decreases. This behaviour is in disagreement with that reported by Ali *et al.*[4]. They find a Seebeck

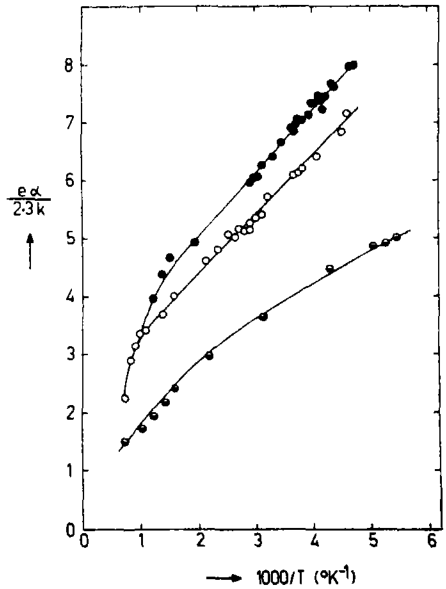

Fig. 2. Thermoelectric power in units (2·3k/e) vs. reciprocal temperature of MnO containing different amounts of Li. Markings as in Fig. 1.

coefficient which is almost independent of temperature. We have no explanation of the lack of agreement between the two sets of measurements.

In earlier publications[12, 13] it was shown that holes in $Li_xMn_{1-x}O$ as well as in $Li_xCo_{1-x}O$, bound at low temperatures to a Li^+ ion, move thermally activated around it. Figure 3 shows the temperature dependence of the relaxation time of the Li^+-Mn^{3+} and Li^+-Co^{3+} dipoles at low temperatures.

DISCUSSION

The curves of $\log\rho$-$1/T$ and α-$1/T$ attract attention by not running parallel. This behaviour is different from what has been found recently for NiO and CoO. The first question is whether this is an intrinsic property of MnO or that it has to be ascribed to inhomogeneities (barriers, second phase etc.). Three observations are against inhomogeneities:

(1) The difference in slope is found in single and polycrystalline samples.

(2) The presence of thin isolating layers between the grains of the polycrystalline samples does not appear from a.c. measurements.

(3) Thin conducting layers between grains or on the surface of the crystals, having a conductivity comparable to that of the bulk are improbable because of the high specific resistivity of Mn_3O_4. This is confirmed by the specimen which was treated in a much higher oxygen pressure than the other specimens, where Mn_3O_4 was distinctly present, but which still showed the same thermoelectric force and electrical resistivity at room temperature.

When the difference in slope is looked upon as an inherent property of the material, it still has to be decided whether electric transport is brought about by one single or by two types of charge carrier. Intrinsic conductivity at low temperatures is ruled out by the large band gap of MnO. In NiO impurity conduction lowers the electrical resistivity and the thermoelectric force, the more so at higher acceptor concentrations. Indeed we find for MnO a low thermoelectric force, which decreases when the dope increases, not faster however than expected from the increase of the number of holes in the valence band. Neither does the electrical resistivity bend down at low temperatures.

Impurity conduction was not found in Li-doped CoO[14]. The movement of a hole around a Li ion is hampered by a barrier which must be overcome by thermal activation. It is likely that this barrier also prevents charge carriers jumping from one Li centre to another. As the movement of holes around Li ions in MnO also needs a thermal activation[11] we do not expect impurity conduction in MnO.

It appears therefore that none of the known corrupting effects can be invoked to explain the difference in slope of $\log\rho$ and α and we feel inclined to hold one single type of charge carrier responsible for the observed behaviour. The immediate consequence is that the mobility of the holes is strongly dependent on temperature. The measurements, particularly those obtained on MnO doped with 0·1 at. per cent Li, will be analysed in the following from this viewpoint.

Thermoelectric force

The thermoelectric force of holes only is given by[15]

$$\alpha = \frac{k}{e}\left(\frac{E_F}{kT} + A\right) = \frac{k}{e}\left(\ln\frac{N_v}{p} + A\right)^*.$$

The temperature dependence of α is mainly determined by the temperature dependence

---

*The following symbols have been used: ρ specific resistivity; α thermoelectric force; T temperature; k Boltzmann's constant; e electronic charge; E_F Fermi level; A transport term connected with the kinetic energy of the free holes; N_v density of states of the valence band or level; p, N_A, N_D concentrations of free holes, acceptors and donors respectively, E_A ionisation energy of the acceptor with respect to the valence level; g degree of degeneracy; μ mobility of holes; q the activation energy of the movement of holes through the lattice; τ relaxation time of a hole near a Li-ion; a the lattice constant of MnO.

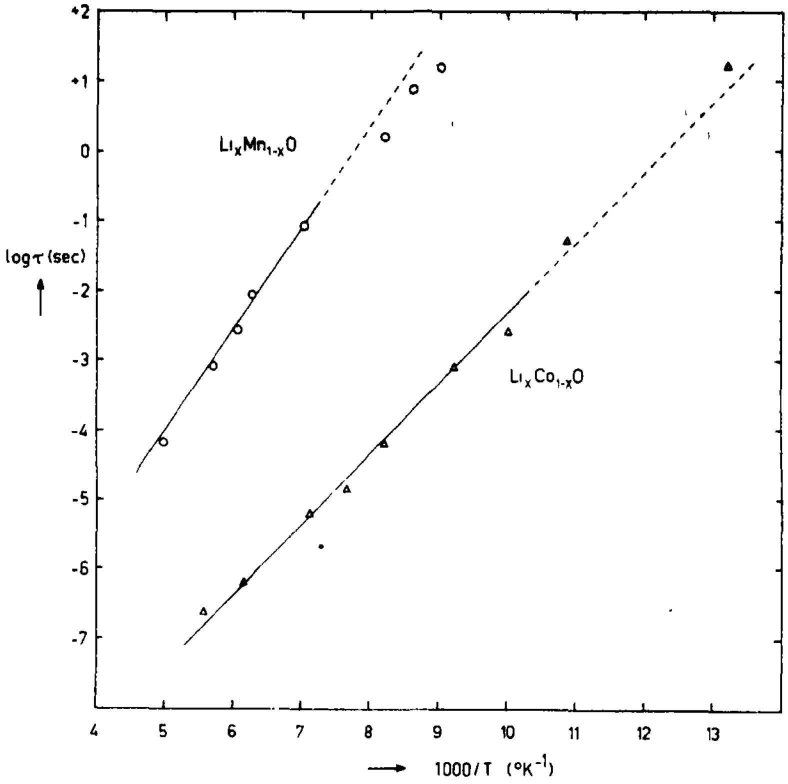

Fig. 3. Log τ of $Li_xMn_{1-x}O$ (○) and $Li_xCo_{1-x}O$ (△) as a function of reciprocal temperature. $x = 10^{-3}$.

of the concentration of holes. For low doped samples and below 500°K, α-$1/T$ is a straight line with a slope of 0·2 eV. This activation energy represents E_A or $E_A/2$. In Fig. 4 $e\alpha T$ is plotted as a function of T. When $A = 0$, $e\alpha T$ gives the Fermi level E_F. $e\alpha T$ increases with increasing T over the whole temperature region measured. Such behaviour can be expected for a heavily compensated semiconductor or for a semiconductor with a very low compensation. In the first case

$$e\alpha T = E_A - kT\left(\ln\frac{N_A - N_D}{N_D}\right) + AkT.$$

A positive slope can only (disregarding AkT) be obtained when $N_D > N_A/2$ and N_D must be almost equal to N_A in order to obtain the high slope observed in Fig. 4. For $T \to 0$, $e\alpha T \to E_A$. In the other case (low compensation, $p > N_D$) $e\alpha T$ is given by

$$e\alpha T = E_A/2 + \tfrac{1}{2}kT \ln N_V/N_A + AkT.$$

For $T \to 0$, $e\alpha T \to E_A/2$. With decreasing temperature p will ultimately become lower than Nd and $e\alpha T$ is expected to change its slope and to point to E_A. That this is not seen in Fig. 4 implies that even at 200°K p is still larger than Nd. (The high resistivity makes measurements of α at still lower temperatures impossible).

We believe that MnO is not heavily compensated for the following reasons:

(1) Chemical analysis shows that the impurity content is lower than the dope

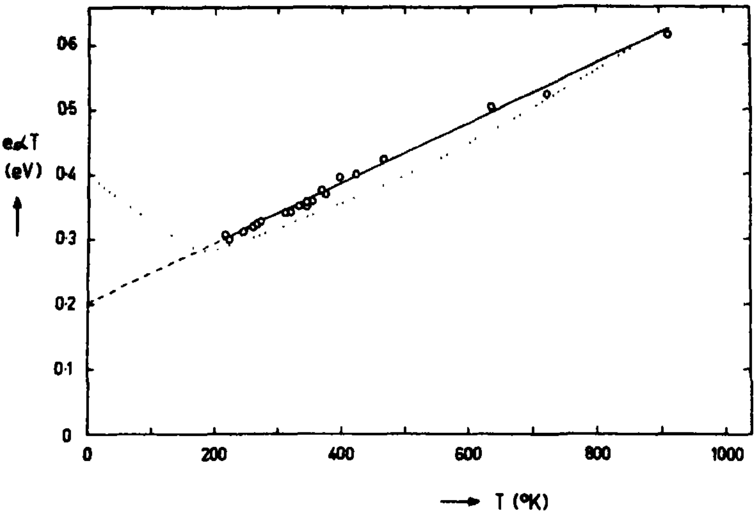

Fig. 4. $e\alpha T$ as a function of temperature for the MnO sample containing 0·1 at. per cent Li. The dotted line has been calculated, see text.

concentration by at least a factor of ten. Active oxygen analysis gives an oxygen concentration too high for $N_D \approx N_A$.

(2) A high degree of compensation will exhaust the acceptors at relatively low temperatures, which is not observed.

(3) The height of the dipole losses is in agreement with the assumption that N_A holes jump from one Mn nearest neighbour of a Li ion to another.

Thus we decide that compensation in $Li_xMn_{1-x}O$ is low and that the acceptor depth is about 0·4 eV for $x = 10^{-3}$.

Comparison of ρ and α

At 1000°K the conductivity is proportional to the Li concentration. Above 1000°K ionization of Mn vacancies as well as the onset of intrinsic conduction causes a sharp decrease of the resistivity of the low doped samples. Assuming that the Li^+-Mn^{3+} acceptors are fully ionized at 1000°K, we obtain the value of 0.01 cm²/Vsec for the mobility at that temperature.

The temperature coefficient of $\log \rho$ is larger than that of α. Since $\rho = 1/(pe\mu)$ the mobility must increase rapidly with temperature. The temperature dependence of μ can be determined by subtracting $\log \rho$ from α:

$$\frac{e\alpha}{2\cdot 3k} - \log \rho = \log (eN_v e^A) + \log \mu$$

as the first term of the right hand side will be nearly independent of temperature.

A mobility increasing rapidly with temperature is given by the small polaron theory[1] which predicts that μ is proportional to $T^{-3/2} \exp(-q/kT)$. Therefore we have plotted in Fig. 5 the quantity:

$$\frac{e\alpha}{2\cdot 3k} - \log \rho - \tfrac{3}{2} \log (1000/T).$$

The curves for various dopes can, at least at lower temperatures, be represented by straight lines, the slope of which gives values of 0·25–0·30 eV for the activation energy of the hopping process. At higher temperatures the slopes of the mobility curves of the low doped specimens decrease and converge to a single value at 1000°K. It is remarkable that the Hall mobility too flattens down in the same temperature region[8]. With the value of μ at 1000°K, 0·01 cm²/Vsec, for the quantity $N_v e^A$ the value 10^{23}/cm³ is obtained. Assuming

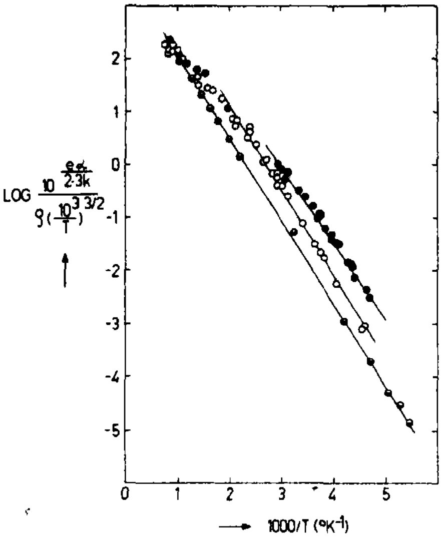

Fig. 5. Temperature dependence of the difference between the thermoelectric power in units ($2{\cdot}3\,k/e$) and log resistivity after correction for $T^{3/2}$. In the small polaron theory the slope of this plot gives the activation energy of the hopping process. To obtain the mobility one has to subtract $\{\log(eN_vA) - 3/2 \log 1000/T\}$ from the value of the ordinate. Markings as in Fig. 1.

$A = 1$, N_v comes near the number of Mn ions per cm^3 ($= 0{\cdot}46 \times 10^{23}$). The degree of compensation can also be calculated. Between 1000 and 200°K the mobility changes by a factor of 10^5 whereas the specific resistivity changes by a factor of more than 10^8. This means that the number of free holes at 200°K is less than 10^{-3} of the dope and since p is greater than N_d at that temperature, the degree of compensation is also less than 10^{-3}.

For the mobility at room temperature the value 3.10^{-5} cm^2/Vsec is obtained.

Note

At low temperature, when the contribution of intrinsic conduction can be neglected, the concentration of holes is determined by the relation

$$p(p+N_D)/(N_A-N_D-p) = N_v/g \exp\left(-\frac{E_A}{kT}\right).$$

With $E_A = 0{\cdot}4$ eV; $N_A = 4{\cdot}6 \,.\, 10^{19}/\text{cm}^3$; $N_d = 4{\cdot}6 \,.\, 10^{15}/\text{cm}^3$; $N_v = 4{\cdot}6 \,.\, 10^{22}/\text{cm}^3$; $g = 1$ and $A = 1$, $e\alpha T$ has been calculated as a function of temperature. This curve is included in Fig. 4.

It is sometimes suggested that for a small polaron conductor $A = 0$. (See for instance Austin and Mott[19]). We can on the other hand manipulate with the degree of degeneracy g. This factor takes into account the number of ways a hole can be exchanged between the valence level and the acceptor level. Because Li is surrounded by twelve Mn ions, each of which may be able to accommodate a hole in a number of ways, the value of g may be quite large.

The influence of g vanishes nearly at high temperature when all the acceptors are ionized; only a factor two, due to spin degeneracy of the valence level remains. For instance a curve calculated with the same set of numbers as above but now with $A = 0$ and $g = 48$ coincides with the experimental one from 200–900°K.

HALL EFFECT

In MnO the Hall mobility of holes varies from $3 \,.\, 10^{-3}$ to $8 \,.\, 10^{-3}$ cm^2/Vsec when going from 350–750°K. This is greater than the drift mobility determined in the preceding sections. Holstein and Friedman[16] have considered the Hall effect of the small polaron. They predict that the Hall mobility of a small polaron is greater than the drift mobility, particularly so at low temperatures because the temperature dependence of the Hall mobility is smaller.

Thus the Hall effect measurements do not contradict the postulate that MnO is a small polaron conductor.

POLARON BAND

Holstein[1] predicts that at low temperatures small polarons do not move by the hopping process but move in a narrow band, the small polaron band.

The consequence is that below a certain transition temperature T_t the mobility starts to increase again. Such an increase is not found down to 200°K.

A transition from hopping to tunnelling is also expected[17] for the movement of holes around the Li$^+$ ions at low temperatures. Measurements of dipole relaxation can be carried out at lower temperatures than d.c. conductivity measurements when low frequencies are used. In Fig. 4 the relaxation time τ for Li$_x$Mn$_{1-x}$O and Li$_x$Co$_{1-x}$O is plotted as a function of $1/T$. In the whole temperature region the movement of holes around the Li ion is thermally activated.

Nothing in this figure indicates the occurrence of tunnelling processes. The mobility of holes around a Li^+ ion is smaller in MnO than in the lattice. The relaxation time at 200°K is $\approx 10^{-4}$ sec, which corresponds to a mobility

$$\mu = \frac{ea^2}{kT} \cdot \frac{1}{\tau} \approx 7\,.\,10^{-10}\,\mathrm{cm^2/Vsec}$$

whereas the extrapolated value of the drift mobility is $1{\cdot}6 \times 10^{-7}\,\mathrm{cm^2/Vsec}$. In MnO the activation energies of the mobility around the Li ion and in the lattice are about equal (0·3 eV).

FINAL REMARKS

MnO has rather remarkable electrical properties. *n*-type MnO[18] which we did not investigate further because of the poor quality of our samples, has a Hall mobility of 10 $\mathrm{cm^2/Vsec}$ at high temperature and shows an increase of it up to 20–40 $\mathrm{cm^2/Vsec}$ at room temperature. *p*-type MnO however has only a mobility of 0·01 $\mathrm{cm^2/Vsec}$ at high temperature, which is also much smaller than the mobilities of holes in CoO (0·3 $\mathrm{cm^2/Vsec}$) and NiO (0·5 $\mathrm{cm^2/Vsec}$). In contrast to these latter two oxides the electrical transport properties of *p*-type MnO indicate a thermally activated mobility of holes.

We suggest that the difference between CoO and NiO on the one hand and MnO on the other is caused by Jahn–Teller deformations brought about by holes in MnO (high spin $3d^4$ configuration). The interaction between holes and lattice may therefore be larger in MnO than in CoO and NiO.

The small polaron mechanism is at present not very much in vogue therefore we consider our interpretation with some misgivings. It is known that the thermoelectric force is very much susceptible to influences that lower its value. Although known influences, such as thin conducting layers and impurity conduction do not seem to work, the present results could also be considered to bring to light a hitherto unknown influence on the thermoelectric force. The more so as the thermoelectric force as a function of $1/T$ keeps the same slope down to the lowest temperature we measured. This makes it impossible to determine the degree of compensation, only an upper limit can be given which turns out to be remarkably low ($< 10^{-3}$). We are not reassured by Heikes *et al.*[3] since their conclusions are based on resistivity measurements near room temperature only. Nor are we comforted by the results of Hed *et al.*[6] because they find a large hopping energy (0·57 eV when corrected for $1/T^{3/2}$) at high temperatures, while our activation energy if present at that temperature is much smaller. The number of holes has been determined from gravimetric measurements on the assumption that the V_{Mn} are fully ionized. The Hall effect measurements at high temperature do not support this assumption however [8]. Hall effect measurements, not being in conflict with our interpretation, are as a matter of fact the main reason why Nagels *et al.*[7] and Ali *et al.*[9] rejected the hopping mechanism. Nevertheless all this is not sufficient to change our opinion and we feel that the evidence amassed in this investigation suggests strongly that *p*-type MnO is an orthodox hopping semi-conductor.

Acknowledgements—Thanks are due to Drs. A. M. J. H. Seuter for preparing single crystals by the Verneuil method and to Dr. H. J. van Daal and Dr. J. D. Wasscher for fruitful discussions on the degeneracy of the Li acceptor in MnO.

REFERENCES

1. HOLSTEIN T., *Ann. Phys.* **8**, 343 (1959).
2. DE WIT H. J., *Philips Res. Rep.* **23**, 449 (1968).
3. HEIKES R. R. and JOHNSTON W. D., *J. chem. Phys.* **26**, 582 (1957).
4. MILLER R. C. and HEIKES R. R., *J. chem. Phys.* **28**, 348 (1958).
5. HED A. Z. and TANNHAUSER D. S., *J. electrochem. Soc.* **114**, 314 (1967).
6. HED A. Z. and TANNHAUSER D. S., *J. chem. Phys.* **47**, 2090 (1967).
7. NAGELS P. and DENAYER M., *Solid St. Commun.* **5**, 193 (1967).
8. NAGELS P., DENAYER M., DE WIT H. J. and

CREVECOEUR C., *Solid St. Commun.* **6**, 695 (1968).
9. ALI M., FRIDMAN M., DENAYER M. and NAGELS P., *Phys. Status Solidi* **28**, 193 (1968).
10. KOOY C., COUWENBERG H. J. M., *Philips tech. Rev.* **23**, 161 (1961).
11. LOH E. and NEWMAN R., *J. appl. Phys.* **32**, 470 (1961).
12. CREVECOEUR C. and DE WIT H. J., *Solid St. Commun.* **6**, 843 (1968).
13. BOSMAN A. J. and CREVECOEUR C., *J. Phys. Chem. Solids* **29**, 109 (1968).
14. BOSMAN A. J. and CREVECOEUR C., *J. Phys. Chem. Solids* **30**, 1151 (1969).
15. BLAKEMORE J. S., *Semiconductor Statistics*. Pergamon Press, Oxford (1962).
16. FRIEDMAN L. and HOLSTEIN T., *Ann. Phys.* **21**, 494 (1963).
17. SEWELL G. L., *Phys. Rev.* **129**, 597 (1963).
18. DE WIT H. J. and CREVECOEUR C., *Phys. Lett.* **25A**, 393 (1967).
19. AUSTIN I. G. and MOTT N. F., *Adv. Phys.* **18**, 42 (1969) Section 8.

J. Phys. Chem. Solids Pergamon Press 1970. Vol. 31, pp. 793–803. Printed in Great Britain.

MAGNETIC STRUCTURES IN THE $Ca_2Fe_{2-x}Al_xO_5$ SYSTEM

S. GELLER, R. W. GRANT and L. D. FULLMER
Science Center, North American Rockwell Corporation, Thousand Oaks, California, U.S.A.

(*Received* 8 *August* 1969)

Abstract – In the $Ca_2Fe_{2-x}Al_xO_5$ system there are two different spin orientations associated with the two different crystal structures. The occurrence of the different magnetic structures, one in magnetic space group Pcm′n′, the other in Ic′m′m′, depends on both x and temperature; increasing both x and temperature tends to favor the Ic′m′m′ structure. Similar to the case of the $CaFe_{2-x}Cr_xO_4$ system, investigated by Corliss *et al.*, there is a large region of x and T in which the two structures appear to coexist, even though the transition from one structure to the other should be first order. In the $Ca_2Fe_{2-x}Al_xO_5$ system a discontinuous 90° spin flip apparently occurs.

1. INTRODUCTION

AT ROOM temperature, there are two different crystal structures[1] in the system $Ca_2Fe_{2-x}Al_xO_5$, $0 \leq x \leq 1.36$. According to Smith[1], for $0 \leq x \leq 0.66$ the structure belongs to space group Pcmn while for $x > 0.66$, it belongs to Icmm. Crystals of $Ca_2Fe_2O_5$ have equal numbers of Fe^{3+} ions in octahedral and tetrahedral coordination[2]. While the structure in Icmm has not been worked out in detail, it is closely related to that in Pcmn and also contains equal numbers of Fe^{3+} ion sites of octahedral and tetrahedral coordination. As in the case of the Al^{3+} ion substituted yttrium iron garnets[3], the Al^{3+} ions prefer (but not exclusively) tetrahedral sites in this system [1,4,5].

The magnetic structure of $Ca_2Fe_2O_5$ has been determined both by Mössbauer spectroscopy[6,7] and by neutron diffraction[8]. The inter- and intrasublattice superexchange interactions are antiferromagnetic and the spins on both sublattices are parallel to the crystallographic c-axis ($c < a < b$). The most probable magnetic space group is Pcm′n′. Subsequent investigations by others have all confirmed this structure[9–11].

We have recently determined[5] the magnetic structure of Ca_2FeAlO_5 and found that it differs significantly from the Pcm′n′ structure. While the nearest neighbor superexchange interactions remain antiferromagnetic, the spins on both sublattices are oriented parallel to the crystallographic a-axis and the most probable magnetic space group is Ic′m′m′. One purpose of the present investigation was to determine how the spin orientations correlated with the crystal structures in the $Ca_2Fe_{2-x}Al_xO_5$ system.

Recently, there has been considerable interest[12,13] in the reorientation of the Fe^{3+} ion spins in some orthoferrites. The two crystal structures existing in the $Ca_2Fe_{2-x}Al_xO_5$ system are related to that of the orthoferrites[6,10]. We have shown[13] that the spin reorientation in $ErFeO_3$ is a continuous and coherent rotation of the Fe^{3+} ion spins. In the $Ca_2Fe_{2-x}Al_xO_5$ system, the spin reorientation depends both on composition (x) and on temperature. Our results indicate that in this system, a discontinuous spin reorientation mechanism is most probable.

2. EXPERIMENTAL

Single crystals of $Ca_2Fe_{2-x}Al_xO_5$ with compositions $x = 0.60$, 0.72 and 0.86 were grown by the Kyropolus technique. A melt contained in an RF heated Pt crucible was allowed to nucleate on a suspended Pt wire. After nucleation occurred, the temperature was kept constant for several hours while the crystallites grew into the melt. The crystals were then removed from the melt and slowly cooled to room temperature.

The crystals grew in thin plates parallel to the *ac* plane. They were mechanically polished to ~ 5 mil and oriented with Buerger precession camera X-ray photography. Powder X-ray diffraction photographs were taken of material adjacent to the single crystal used to determine the spin directions. By comparing these photographs with those of powder specimens of precisely known compositions prepared by solid state reaction techniques, the nominal composition of the single crystals was confirmed to be the same as those of the melts to within $x = \pm 0{\cdot}01$. A careful examination of the photographs also indicated that while some compositional gradient did exist in the single crystals, it was probably not more than $x = \pm 0{\cdot}02$. High temperature powder X-ray diffraction photographs of $Ca_2Fe_2O_5$ were taken with a Bond camera[14] built in this laboratory.

Mössbauer spectra were taken on an automated mechanical constant velocity spectrometer in the transmission mode. Two sources of 14·4 keV (^{57}Fe) resonant radiation were used; a single line source of ^{57}Co in Cu and a linearly polarized gamma ray source of ^{57}Co in a thin foil of α-Fe. The ^{57}Co in α-Fe source was magnetized in the plane of the foil by a small (~ 0·5 kG) permanent magnet and the gamma ray propagation direction, $\mathbf{k}$, was perpendicular to the source magnetization direction, $\mathbf{H}_S$. Both sources were always at room temperature (23°C). For some experiments with single crystal absorbers, a magnetic field of 1·1 kOe was applied in the absorber *ac* plane; the absorber magnetization direction is $\mathbf{H}_A$. Temperatures below and above room temperature were obtained with the absorber in a Dewar (Au-2·1 at.% Co thermocouple) or a small vacuum oven (Fe-Constantan thermocouple) respectively.

3. RESULTS

The spectra of three single crystals near liquid helium temperature taken with the single line source are shown in Fig. 1. The bar diagram indicates the approximate positions of the hyperfine components associated with the octahedral and tetrahedral sublattices as previously established[4,6]. The strong intensity of the $\Delta m = 0$ lines in all these spectra indicates that the spins on both sublattices of the three specimens lie in or near the *ac* plane.

To determine the spin directions within the *ac* plane, we have employed the same technique used previously in the $Ca_2Fe_2O_5$[7] and Ca_2FeAlO_5[5] cases. Sets of spectra with $\mathbf{k} \parallel \mathbf{b}$ and with both $\mathbf{H}_S \parallel \mathbf{a}$ and $\mathbf{H}_S \parallel \mathbf{c}$ were obtained at several temperatures for the three single crystals. In particular, for $x = 0{\cdot}60$, spectra were taken at 15, 296, and 403 K; for $x = 0{\cdot}72$, at 10, 100, 150, 200, and 296 K; and for $x = 0{\cdot}86$, at 8, 150, and 200 K. In Fig. 2 we show, as a representative example of these spectra, the data obtained near liquid helium temperature for $x = 0{\cdot}72$ and $x = 0{\cdot}86$. We use the notation of [7] to identify the absorption lines: the source lines are identified by roman characters in order of ascending energy, while the absorber lines of the individual sublattices are identified by Greek characters in order of ascending energy; [ ] and ( ) indicate the octahedral and tetrahedral sublattices, respectively. Thus the absorption lines at about $-13{\cdot}6$, $-12{\cdot}1$ and $+13{\cdot}9$ mm/sec result from [Fα], (Fα), [Aη], and (Aη), respectively (the latter two are superimposed). The spectra in Fig. 2 of the $x = 0{\cdot}72$ sample clearly indicate that the spins on both the octahedral and tetrahedral sublattices in $Ca_2Fe_{1\cdot 28}Al_{0\cdot 72}O_5$ are parallel to $\mathbf{c}$ at 10 K. However, the intensity of the four absorption lines [Fα], (Fα), [Aη], and (Aη) in the $x = 0{\cdot}86$ sample are nearly equal (see Discussion).

The intensities of the [Fα] and (Fα) lines were also measured as a function of angle between $\mathbf{H}_S$ and $\mathbf{a}(\mathbf{k} \parallel \mathbf{b})$. Examples are given in Fig. 3.

Results of the present magnetic phase

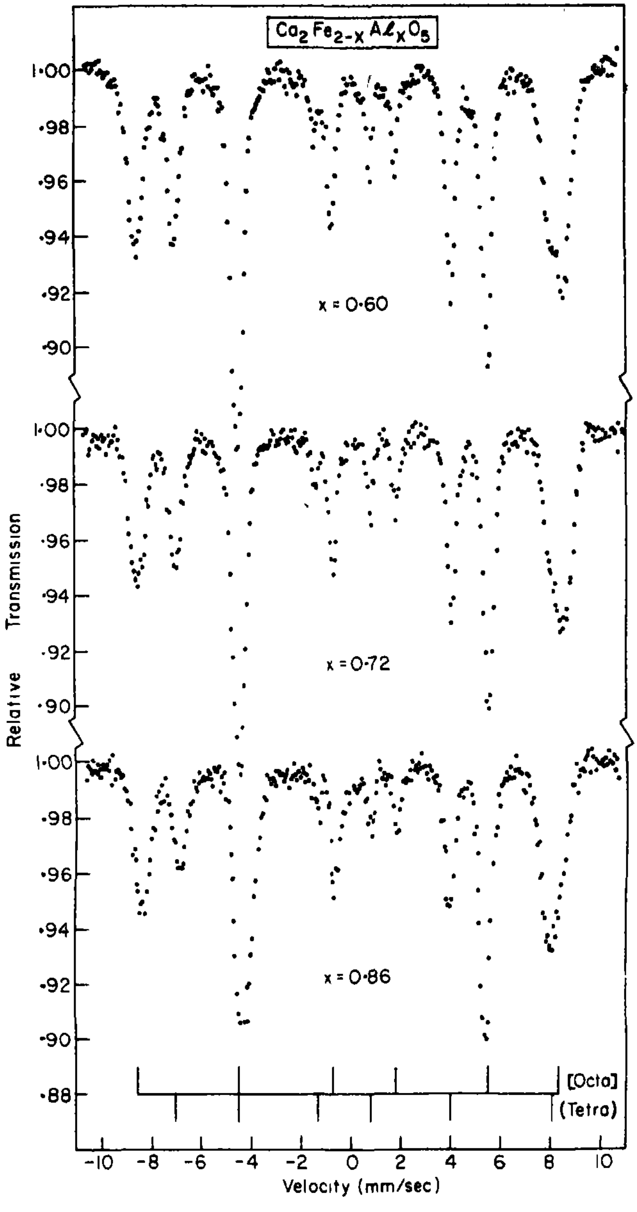

Fig. 1. Mössbauer spectra taken with a ^{57}Co in Cu source (23°C) and single crystal $Ca_2Fe_{2-x}Al_xO_5$ absorbers with $\mathbf{k}\|b$ for specimens with: $x = 0·60$ (15 K), $x = 0·72$ (10 K), and $x = 0·86$ (8 K).

investigation together with those of earlier Mössbauer and neutron diffraction experiments on $Ca_2Fe_2O_5$ and Ca_2FeAlO_5 are shown in Fig. 4. The Néel temperatures (Table 1) defining the paramagnetic-antiferromagnet phase boundary (Fig. 4) were determined (for specimens with $x = 0·50$ and 0·72) as described previously[15].

Increasing either x or T tends to favor spins pointing in the a direction or the Icmm struc-

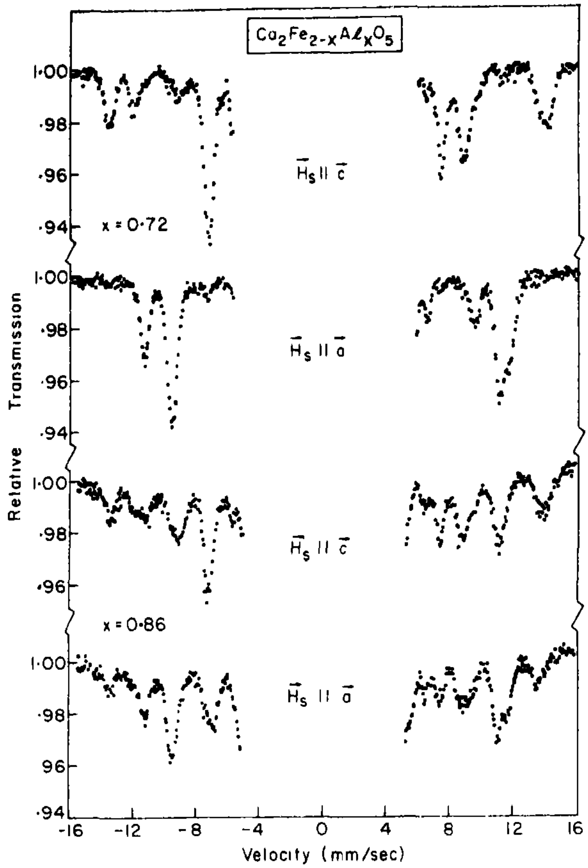

Fig. 2. Mössbauer spectra taken with a ^{57}Co in α-Fe source (23°C). $\mathbf{H}_S \perp \mathbf{k}$, and single crystal $Ca_2Fe_{2-x}Al_xO_5$ absorbers with $\mathbf{k} \parallel \mathbf{b}$ for specimens with: $x = 0{\cdot}72$ (10 K) and $x = 0{\cdot}86$ (8 K). Orientation of $\mathbf{H}_S$ is shown in figure.

Table 1. *Néel temperatures in the* $Ca_2Fe_{2-x}Al_xO_5$ *system*

x	T_N(°C)	Ref.
0·00	457 ± 2	[8, 15]
0·50	295 ± 4	This work
0·72	200 ± 5	This work
1·00	60 ± 15	[5]

ture. A powder X-ray diffraction photograph of $Ca_2Fe_2O_5$ taken at 1125°C, well above the Néel temperature, showed that it still had the Pcmn structure.

According to Fig. 4, in the paramagnetic region the Pcmm–Icmm phase boundary should exist at $0{\cdot}6 \leqslant x \leqslant 0{\cdot}7$. An attempt was made to determine this phase boundary by an

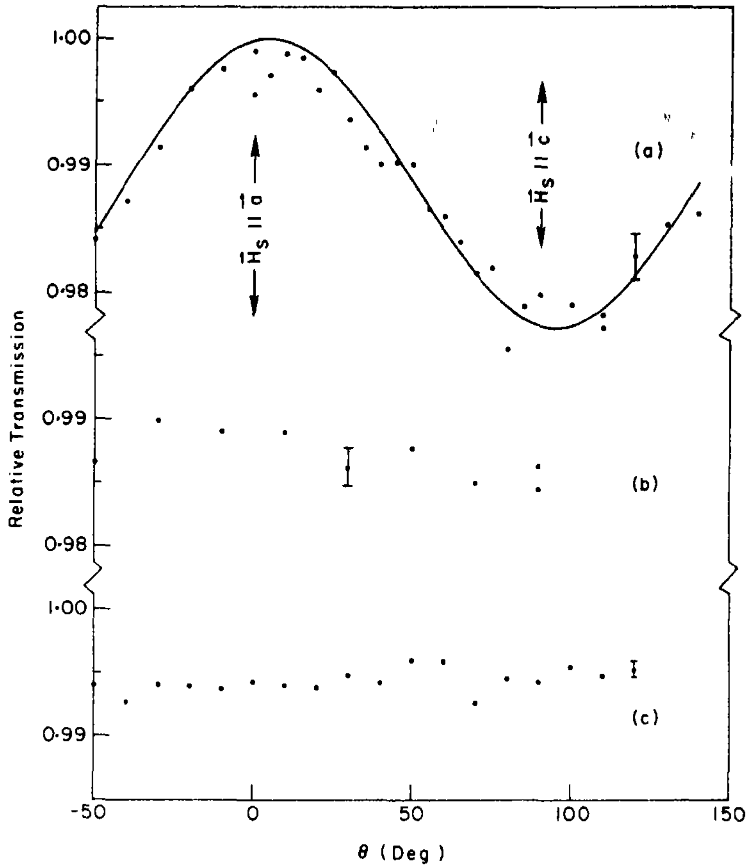

Fig. 3. The relative transmission of the [Fα] line as a function of $\mathbf{H}_S$ orientation. The source was ^{57}Co in α-Fe (23°C), $\mathbf{H}_S \perp \mathbf{k}$; the absorbers were $Ca_2Fe_{2-x}Al_xO_5$ single crystals, $\mathbf{k}\|\mathbf{b}$, $\theta = 0°$ is defined as $\mathbf{H}_s\|\mathbf{a}$. (a) $x = 0{\cdot}72$ (10 K) at $-13{\cdot}68$ mm/sec. (b) $x = 0{\cdot}86$ (24 K) at $-13{\cdot}53$ mm/sec, and (c) $x = 0{\cdot}86$ (90 K) at $-13{\cdot}21$ mm/sec (in this case $\mathbf{H}_A = 1{\cdot}1$ kOe was applied at $\theta = -45°$).

investigation of the quadrupole coupling and the isomer shift as a function of T and x in the paramagnetic region: Mössbauer spectra were taken of specimens with $x = 0{\cdot}0$, $0{\cdot}50$, $0{\cdot}60$, $0{\cdot}72$ and $1{\cdot}00$ at several temperatures; representative examples are given in Fig. 5. Each of the spectra consists of two very broad lines in agreement with other experimental results.* The two broad lines may be decomposed into two sets of quadrupole split doublets associated with (Fe^{3+}) and [Fe^{3+}].

Because the Al^{3+} ions show considerable preference for the tetrahedral sites, the computer-fitted absorption lines are easily assigned to either (Fe^{3+}) or [Fe^{3+}].† The larger isomer shift, δ, and slightly larger quad-

---

*Wittmann[16] has reported a spectrum of Ca_2FeAlO_5 which differs significantly from those of Fig. 5 and with all other spectra of $Ca_2Fe_{2-x}Al_xO_5$ in the paramagnetic region. We are forced to the conclusion that his interpretation of his spectrum is incorrect.

†An estimate of the actual site population was made for the powder specimen with $x = 0{\cdot}50$ (which was quenched from 1225°C) by the same technique used previously for Ca_2FeAlO_5[5]. By comparing corresponding line intensities in a relatively thin absorber (saturation effects were negligible) at 5 K, and assuming equal [Fe^{3+}] and (Fe^{3+}) recoil free fractions, the site population is $Ca_2[Fe_{0\cdot90}Al_{0\cdot10}](Fe_{0\cdot60}Al_{0\cdot40})O_5$.

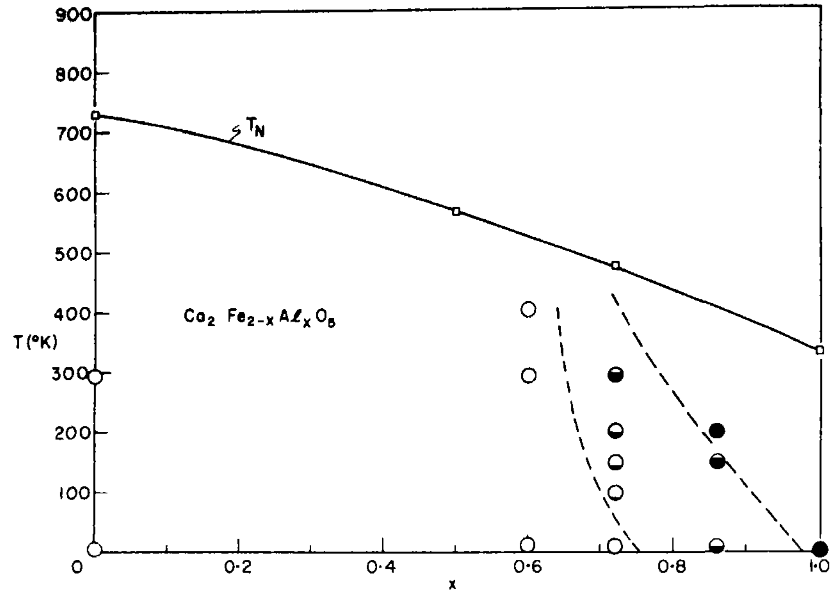

Fig. 4. Magnetic phases in the $Ca_2Fe_{2-x}Al_xO_5$ system. The open symbol ○ indicates spins ‖c (Pcm'n'), ● spins ‖a (Ic'm'm'). The partially filled symbols indicate the fraction of spins along a and c. The Néel temperature dependence on x is indicated.

rupole splittings (peak separation), ΔE_Q, are associated with [Fe^{3+}]. The difference in isomer shift observed at the octahedral and tetrahedral sites, $\delta_0 - \delta_t = 0{\cdot}15 \rightarrow 0{\cdot}20$ mm/sec, is consistent with, and seems to be characteristic of, the shift difference observed in other ferrites and garnets[17]. This shift difference in the $Ca_2Fe_{2-x}Al_xO_5$ system has also been previously observed below T_N [11, 18].

The temperature dependence of ΔE_Q and δ for a specimen with $x = 0{\cdot}60$ (Fig. 6) as well as for specimens with $x = 0{\cdot}50$, 0·72 or 1·00 were linear within experimental error. For this reason, although about three times as many data were obtained, only representative values are given in Table 2. Thus, within the temperature range in which the paramagnetic materials were studied ($\leq 700°C$) it was not possible to observe the effect of the Pcmn/Icmm phase transformation on either ΔE_Q or δ. The results plotted in Fig. 4 suggest that in the paramagnetic region the phase boundary may be a steeply varying function of x. Thus, in the hope of observing the phase boundary, ΔE_Q and δ were plotted as a function of x at various temperatures. For this purpose a straight line was fitted through the temperature dependent ΔE_Q and δ data (as in Fig. 6) and the compositional dependence of ΔE_Q and δ at a specific T was determined (Fig. 7*). These results do not delineate the phase boundary, unlike previous experience[19] in which it was observable from ΔE_Q vs. T. We are forced to conclude that the phase transition has little effect on the immediate surroundings of the Fe^{3+} ions.

The data (Table 2) indicate that increasing Al^{3+} ion substitution increases ΔE_Q somewhat for both Fe^{3+} ion sites, consistent with previous observations[11, 20, 21].

4. DISCUSSION

The most probable magnetic space group for $Ca_2Fe_2O_5$, Pcm'n', restricts the spins on

---

*Similar plots between 300 and 700°C showed a smooth variation of ΔE_Q and δ with x.

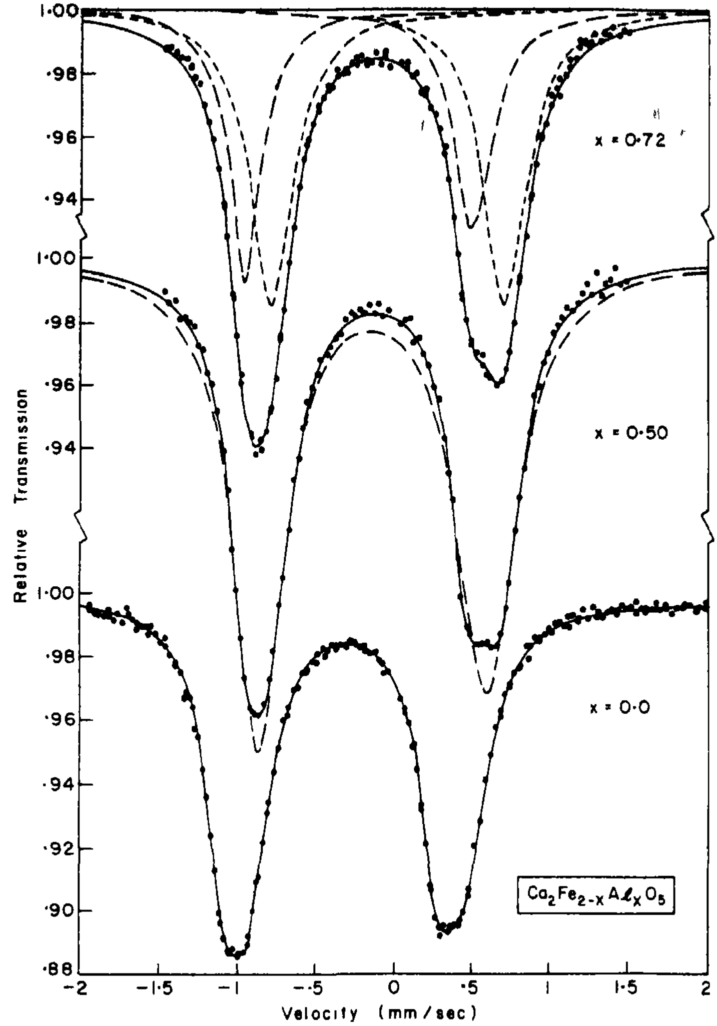

Fig. 5. Mössbauer spectra obtained with a ^{57}Co in Cu source (23°C) and polycrystalline $Ca_2Fe_{2-x}Al_xO_5$ absorbers for specimens with: $x = 0{\cdot}72$ (300°C), $x = 0{\cdot}50$ (310°C), and $x = 0{\cdot}00$ (525°C). The solid curves are a least squares fit by four Lorentz line shapes with the intensity, position and width as variables. The four decomposed curves are indicated in the $x = 0{\cdot}72$ spectrum and for comparison a 'best' fit to a two line spectrum is shown (dashed) in the $x = 0{\cdot}50$ spectrum.

the tetrahedral sublattice to lie in the ac plane. Within experimental error (< 10°) the spins on both sublattices are parallel to *c*[7–10]. In Pcm′n′, the *c*-direction is the only direction within the *ac* plane along which the spins can align without producing a ferromagnetic moment; this direction is probably preferred because of the large inter- and intra-superexchange bond angles. Takeda *et al.*[10] have observed magnetic hysteresis in $Ca_2Fe_2O_5$ on cooling the material in a magnetic field from above the Néel temperature. They interpret this as implying the existence of a weak ferromagnetic moment parallel to *a*. (The effect is

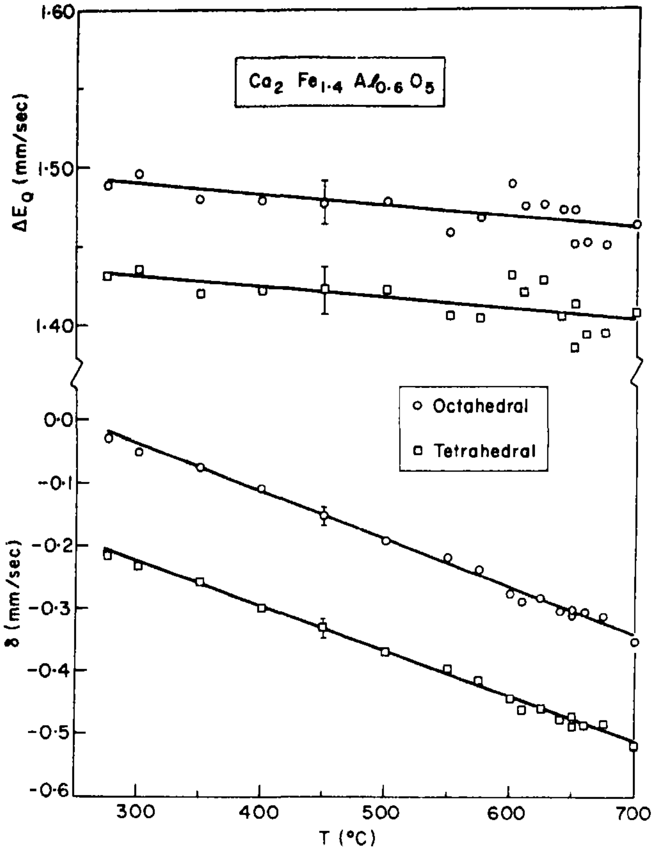

Fig. 6. Temperature dependence of ΔE_Q and δ in $Ca_2Fe_{1.4}Al_{0.6}O_5$.

small and would not be observable by the Mössbauer technique.) The higher symmetry Icmm structure places more restrictions on spin directions. The spins in the tetrahedral sites must point along one of the crystallographic axes while the spins on the octahedral sublattice must be either parallel or perpendicular to *c*.

An important problem to resolve is the nature of the transition from the Pcm′n′ to the Ic′m′m′ structure. The results given in Fig. 2 for the 0·86 specimen suggest three most probable mechanisms: (1) a discontinuous spin flip from *c* to *a* at the Pcm′n′/Ic′m′m′ phase boundary and approximately half the spins are parallel to *a* and half to *c*; (2) because the specimen is a solid solution, a continuous but incoherent spin rotation and the spin directions restricted to the *ac* plane having an appropriate distribution which, in this case ($x = 0{\cdot}86$, $T = 8$ K) is random; (3) a continuous coherent spin rotation, as in $ErFeO_3$ [13]*, with equal numbers of spins oriented at approximately ±45° to **a** and **c**. A fourth possibility, namely that rotation occurs continuously but in magnetic space group Pcm′n′ is quickly ruled out. It would require a large ferromagnetic moment at liquid N_2 temperature which was not observed.

---

*Our preliminary indication of the spin reorientation mechanism in $ErFeO_3$ published in the Collected Abstracts of the Eighth International Congress of Crystallography (Abstr. VI-42) was incorrect.

Table 2. Isomer shifts and quadrupole splittings observed in several $Ca_2Fe_{2-x}Al_xO_5$ materials

x	T (°C)	$\delta_0{}^{(a,b)}$ mm/sec	$\delta_t{}^{(a,b)}$ mm/sec	ΔE_Q(oct)$^{(b)}$ mm/sec	ΔE_Q(tetra)$^{(b)}$ mm/sec
0	525	−0·22	−0·39	1·40	1·38
0·50	310	−0·06	−0·24	1·50	1·43
	400	−0·12	−0·30	1·47	1·42
	500	−0·19	−0·36	1·45	1·41
	600	−0·27	−0·44	1·46	1·42
	675	−0·33	−0·50	1·44	1·42
0·60	275	−0·03	−0·21	1·49	1·43
	400	−0·11	−0·30	1·48	1·42
	500	−0·20	−0·37	1·48	1·42
	600	−0·28	−0·45	1·49	1·43
	700	−0·35	−0·52	1·46	1·41
0·72	225	+0·01	−0·17	1·53	1·46
	300	−0·05	−0·23	1·52	1·45
	400	−0·12	−0·30	1·50	1·44
	500	−0·20	−0·37	1·50	1·44
	650	−0·32	−0·49	1·51	1·43
1·00	100	+0·11	−0·10	1·56	1·51
	200	+0·04	−0·16	1·55	1·49
	393	−0·11	−0·31	1·54	1·49
	500	−0·18	−0·37	1·51	1·47
	675	−0·35	−0·53	1·53	1·46

(a) Isomer shift relative to a ^{57}Co in Cu source (23°C).
(b) Approximate standard deviations ± 0·015 mm/sec.

The third possible mechanism was considered further. The [Fα] and (Fα) intensities were measured as a function of angle between $\mathbf{H}_S$ and $\mathbf{a}$. Some of these results are given in Fig. 3. (Fig. 3c, the specimen was first magnetized at 5 K with $\mathbf{H}_A \| a$, $\mathbf{H}_A$ was rotated to $\theta = -45°$ and the crystal was then warmed to 90 K.) Neglecting saturation, recoil free fraction anisotropy and other small corrections, the expected angular dependence of the [Fα] line intensity for a colinear spin arrangement is[7] proportional to $\cos^2\alpha'$ where α' is the angle between $\mathbf{H}_S$ and the spin direction of the octahedral Fe^{3+} ion. The solid line in Fig. 3(a) is a least squares fit to this function; thus, the octahedral Fe^{3+} ion spins in $Ca_2Fe_{1\cdot 28}Al_{0\cdot 72}O_5$ at 10 K are parallel to c to within ± 5°. The data of Fig. 3b show very little angular dependence, as expected for either of the first two mechanisms given above or for the third mechanism if several magnetic domains are present, so that approximately equal numbers of spins in the specimen are at $\theta = \pm 45°$.

The data in Fig. 3(c) resulted from an attempt to obtain a single magnetic domain assuming that the third mechanism applies. The angular invariance of these data suggests that the third mechanism is not correct. Of the two remaining mechanisms (1 and 2 above), we would guess that the first is the more likely, because it is the simpler of the two. Thus in constructing Fig. 4, the simultaneous existence of the two magnetically ordered phases is postulated. The situation bears similarity to that observed in the $CaFe_{2-x}Cr_xO_4$ system[22]. In the $Ca_2Fe_{2-x}Al_xO_5$ system the difference in crystal structure is ultimately observable by X-ray diffraction, i.e. when x is

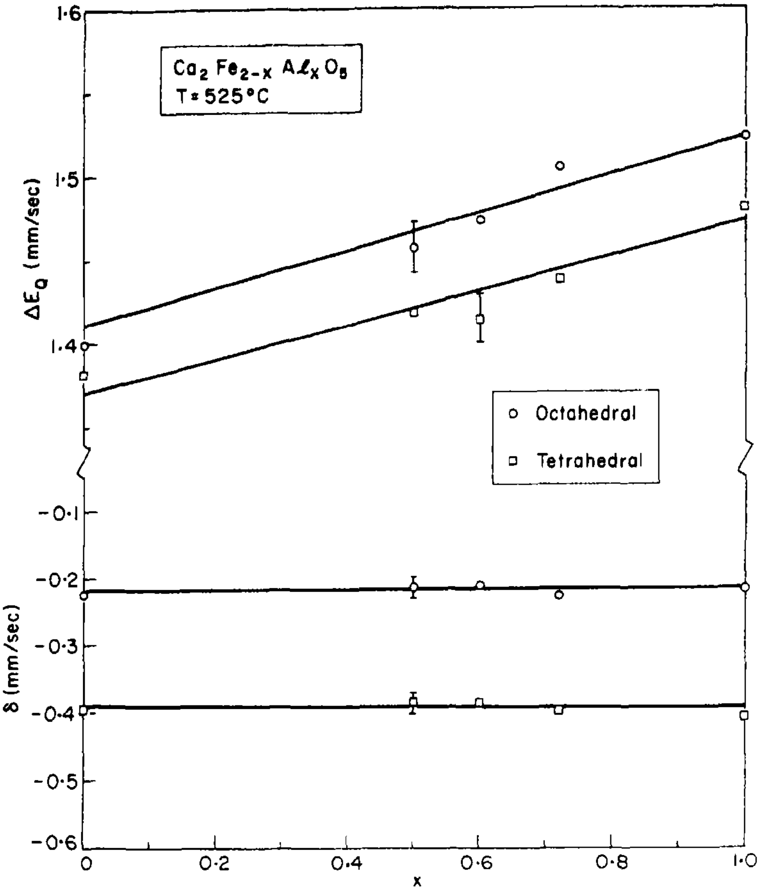

Fig. 7. Compositional dependence of ΔE_Q and δ in the $Ca_2Fe_{2-x}Al_xO_5$ system at $T = 525°C$.

sufficiently large. In the $CaFe_{2-x}Cr_xO_4$ system, the two magnetic structures derive from the same crystal space group.

Because of the large electric field gradient (EFG) present at the Fe^{3+} ion sites in the $Ca_2Fe_{2-x}Al_xO_5$ system, it might be expected that the coexistence of two magnetic phases would be detectable as two sets of hyperfine patterns in the Mössbauer spectrum of such a material; e.g. Ono and Ito[23] have observed two sets of lines in the temperature region near the Morin transition in α-Fe_2O_3. An examination of the spectrum of the $x = 0{\cdot}86$ specim[illegible] K (Fig. 1) shows no indication of more than one set of hyperfine lines per site although we believe that roughly equal amounts of both phases coexist at this temperature. The explanation for this observation requires consideration of the internal magnetic field orientation at both Fe^{3+} ion sites with respect to the EFG at these sites. A detailed analysis of the EFG in $Ca_2Fe_2O_5$ and Ca_2FeAlO_5[24] has shown that, to within experimental error, the EFG at the Fe^{3+} ion sites in all cases is axially symmetric and the unique principal axis of the EFG in all cases is parallel to *b*. Thus at the Pcm'n'/Ic'm'm' phase boundary although the spins flip discontinuously from *a* to *c*, the internal magnetic field remains perpendicular to an essentially axially symmetric EFG and, to within experimental error, no change is observed in the nuclear eigenvalues.

If indeed, there is coexistence of the two distinct phases in this system, and the transition from Pcm'n' to Ic'm'm' is first order, Fig. 4 does not represent a phase diagram. A true phase diagram requires a single line to delineate the phase boundary. This implies that if the crystals were of sufficient 'perfection', the region of coexistence would shrink to a line. Because the crystal structure includes the magnetic structure, this would imply further that at room temperature the Pcmn structure should persist to a value of x somewhat greater than 0·66, i.e. to $x \simeq 0{\cdot}70$.

Acknowledgements – We wish to thank H. Wiedersich and U. Gonser for discussion, G. P. Espinosa for preparing several specimens by solid state reaction and P. B. Crandall, M. Bloombaum and K. Rasmussen for technical assistance.

REFERENCES

1. SMITH D. K., *Acta Crystallogr.* **15**, 1146 (1962) and pertinent references therein.
2. BERTAUT E. F., BLUM P. and SAGNIÈRES A., *Acta Crystallogr.* **12**, 149 (1959).
3. GILLEO M. A. and GELLER S., *Phys. Rev.* **10**, 73 (1958); *ibid. J. appl. Phys.* **29**, 380 (1958); GELLER S., WILLIAMS H. J., ESPINOSA G. P. and SHERWOOD R. C., *Bell Syst. Tech. J.* **43**, 565 (1964).
4. POBELL F. and WITTMANN F., *Phys. Lett.* **19**, 175 (1965).
5. GRANT R. W., GELLER S., WIEDERSICH H., GONSER U. and FULLMER L. D., *J. appl. Phys.* **39**, 1122 (1968).
6. GELLER S., GRANT R. W., GONSER U., WIEDERSICH H. and ESPINOSA G. P., *Phys. Lett.* **20**, 115 (1966).
7. GONSER U., GRANT R. W., WIEDERSICH H. and GELLER S., *Appl. Phys. Lett.* **9**, 18 (1966).
8. CORLISS L. M., HASTINGS J. M., KUNNMANN W. and BANKS E., *Acta Crystallogr. Suppl.*, **21**, A95 (1966).
9. FRIEDMAN Z., SHAKAD H. and SHTRIKMAN S., *Phys. Lett.* **25A**, 9 (1967).
10. TAKEDA T., YAMAGUCHI Y., TOMIYOSHI S., FUKASE M., SUGIMOTO M. and WATANABE H., *J. phys. Soc. Japan* **24**, 446 (1968).
11. WHITFIELD H. J., *Aust. J. Chem.* **20**, 859 (1967); see also GELLER S., GRANT R. W., GONSER U., WIEDERSICH H. and ESPINOSA G. P., *Phys. Lett.* **25A**, 722 (1967).
12. WHITE R. L., *J. appl. Phys.* **40**, 1061 (1969) and pertinent references therein.
13. GRANT R. W. and GELLER S., *Solid State Commun.* **1**, 1291 (1969), and pertinent references therein.
14. BOND W. L., *Rev. scient. Instrum.* **29**, 654 (1958).
15. GRANT R. W., WIEDERSICH H., GELLER S., GONSER U. and ESPINOSA G. P., *J. appl. Phys.* **38**, 1455 (1967).
16. WITTMANN F., *Phys. Lett.* **24A**, 252 (1967).
17. VAN LOEF J. J., *Physica* **32**, 2102 (1966) and pertinent references therein.
18. WITTMANN F. and POBELL F., *Z. Naturf.* **21a**, 831 (1966).
19. GRANT R. W., GELLER S., CAPE J. A. and ESPINOSA G. P., *Phys. Rev.* **175**, 686 (1968).
20. POBELL F. and WITTMANN F., *Z. Angw. Phys.* **20**, 488 (1966).
21. HUDSON A. and WHITFIELD H. J., *J. chem. Soc.* (*A*) 376 (1967).
22. CORLISS L. M., HASTINGS J. M. and KUNNMANN W., *Phys. Rev.* **160**, 408 (1967).
23. ONO K. and ITO A. J., *J. phys. Soc. Japan* **17**, 1012 (1962).
24. GRANT R. W., *J. chem. Phys.* **51**, 1156 (1969).

J. Phys. Chem. Solids Pergamon Press 1970. Vol. 31, pp. 805–815. Printed in Great Britain.

THERMODYNAMICS OF THE Fm3m ⇄ Pm3m TRANSITION IN THE POTASSIUM AND RUBIDIUM HALIDES*

A. J. DARNELL and **W. A. McCOLLUM**
Atomics International Division, North American Rockwell Corporation,
Canoga Park, Calif. 91304, U.S.A.

(*Received* 27 *March* 1969; *in revised form* 5 *August* 1969)

Abstract – The Fm3m ⇄ Pm3m phase transition in the potassium and rubidium halides has been examined by a dilatometric method from 25°C to temperatures near the melting point. The pressure (P_{tr}) and volume change (ΔV_{tr}) measured for these polymorphic transitions were treated by method of least squares. Averages of P_{tr} and ΔV_{tr} at 25° were taken from this work and from data in the literature. These average values of P_{tr} and ΔV_{tr} were used to calculate the $P\Delta V$ work for this transition; the entropy change (ΔS_{tr}) was calculated from the average value of ΔV_{tr} and the temperature coefficient, (dP_{tr}/dT). Data are also given for P_{tr}, ΔV_{tr} and ΔS_{tr} at the triple point (Fm3m ⇄ liquid ⇄ Pm3m). No solid-solid transition was observed in KF below 800°C and 45 kb. The following trends are noted. At constant pressure, the entropy change ΔS (Fm3m → Pm3m) is positive for the potassium salts KCl, KBr and KI; for the rubidium halides it is negative. The transition volume ΔV(Fm3m → Pm3m) in all cases decreases as the temperature increases.

1. INTRODUCTION

THERE HAVE been numerous investigations of the pressure-induced polymorphic transition in the alkali halides since a transition of this type was first discovered in the rubidium halides RbBr and RbI by Slater[1] in 1926. Bridgman found a similar transition in RbCl [2] and in the potassium salts KCl, KBr and KI[3]. Piermarini and Weir[4, 5] also reported the discovery of a solid-solid transition in the fluorides, RbF and KF. Jacobs[6] established, by high pressure X-ray diffraction, that the pressure-induced phase transition in RbI is from the sodium chloride type structure (space group Fm3m) to the denser cesium chloride type structure (space group Pm3m). Other workers[5, 7–9] have shown that this same type of structure change also occurs in RbCl, RbBr, KI and KCl. A recent report by Klement and Jayaraman[10] summarizes the work which has been carried out on the phase transitions in these salts.

Most of the measurements of the polymorphic transition in these salts have been made at room temperature with the exception of the work by Bridgman[3], Pistorius[11, 12] and Pistorius and Snyman[13] at temperatures up to 200°C. We have studied the transition in the potassium and rubidium halides at higher temperatures by the volume discontinuity method[14, 15] to temperatures approaching the triple point between the two solid phases and the liquid phase. Data for the transition pressure (P_{tr}), the transition volume (V_{tr}) and their variation with temperature have been obtained and thermodynamic data were derived from these experimentally measured quantities. These will be presented and discussed in this paper.

2. EXPERIMENTAL

(A) Materials

The salts used in these measurements were Mallinckrodt analytical reagent grade with the exception of RbF which was obtained from the A. D. McKay Co. The fluorides, KF and RbF were dried at 300°C under vacuum ($P < 10^{-6}$ Torr.) for 48 hr. This was followed by treatment with anhydrous HF at a pressure of 1 atm for 24 hr. The chlorides, bromides and iodides of these alkali metals were heated for 24 hr under high vacuum at a temperature of 150°C. The dried salts were compressed into pellets at a pressure of ~ 2 kb. The fluorides, KF and RbF, were

---

*This work was supported by the Research Division of the United States Atomic Energy Commission.

handled in an atmosphere of argon in order to reduce pickup of water.

(B) Apparatus

Use of the piston displacement method for the detection of phase transitions has been described by Bridgman [14], Kennedy and Newton [15], and by Jayaraman *et al.* [16]. Our techniques are similar to those described by the above workers. However, we have extended the temperature range of this piston displacement method from the upper limit of ~ 200°C, imposed by external heating of the compound cylinder apparatus, to temperatures of ~ 1000°C which are attainable with use of the internally heated graphite furnace. In this modification the sample in the form of a cylinder 0·6 cm in dia. by 1·5 cm in length was placed within a cylindrical graphite furnace heating element within the high pressure chamber. The volume of the sample in this case now comprises approximately 20 per cent of the total volume of the pressure chamber.

The transition volume was determined by the piston displacement method. This technique has been used by Bridgman [14] and more recently described by Jayaraman *et al.* [17]. Usually the sample and piston have the same diameter; however, in the technique used here the sample and piston differ in diameter by a factor of two. Thus the sample and internal furnace apparatus must distort or 'flow' in order that the volume change which takes place in the sample be transmitted into a displacement of the piston. The greater reproducibility of the ΔV_{tr} measurements at higher temperatures, i.e. $t > 200$°C, is very probably due to the increase in the plasticity of the furnace parts and of the sample at these higher temperatures.

For pressure calibration the phase transition Bi(I) ⇄ Bi(II) and Bi(II) ⇄ Bi(III) at 25°C were used. We find 25·6 ± 0·2 kb and 27·3 ± 0·2 kb respectively for these transitions. Kennedy and LaMori [18, 19] give 25·38 ± 0·02 kb and 27·0 ± 0·2 kb for these transitions in Bi at 25°C. It was assumed that this calibration holds good at higher temperatures also.

Temperatures were measured with a chromel-alumel thermocouple whose junction was positioned in the geometric center of the salt sample. No corrections for the pressure effect on e.m.f. were made since corrections at pressures below 25 kb are expected to be small, i.e. less than 1% for Cr–Al thermocouples [20].

3. RESULTS AND DISCUSSION

The pressures of this polymorphic transition (P_{tr}) were determined upon compression and decompression at approximately 100° intervals, from 25 to 700°C and in some cases up to 800°C. The results for the salts KCl, KBr and KI are shown in Fig. 1; similarly, results for RbF, RbCl, RbBr and RbI are given in Fig. 2. No phase transition was ob-

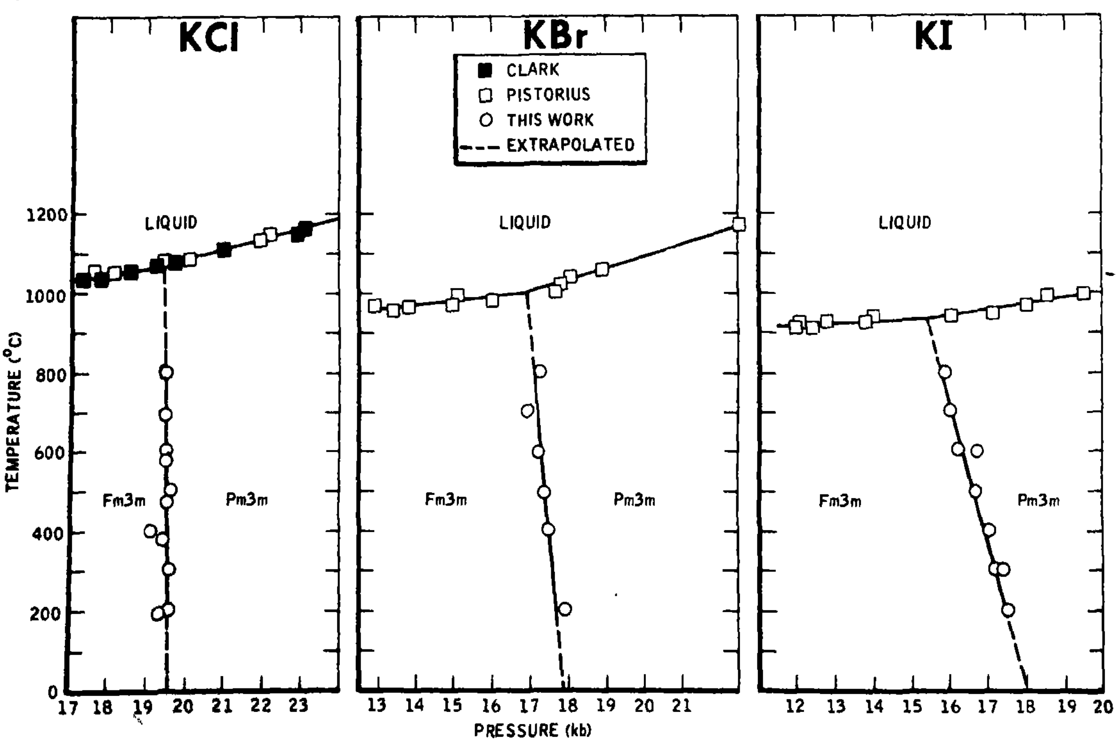

Fig. 1. *PV* diagram for the potassium halides KCl, KBr and KI: ■ – melting point data of Clark (1959). □ – melting point data of Pistorius (1965, 1966). ○ – Fm3m ⇄ Pm3m transition, this work.

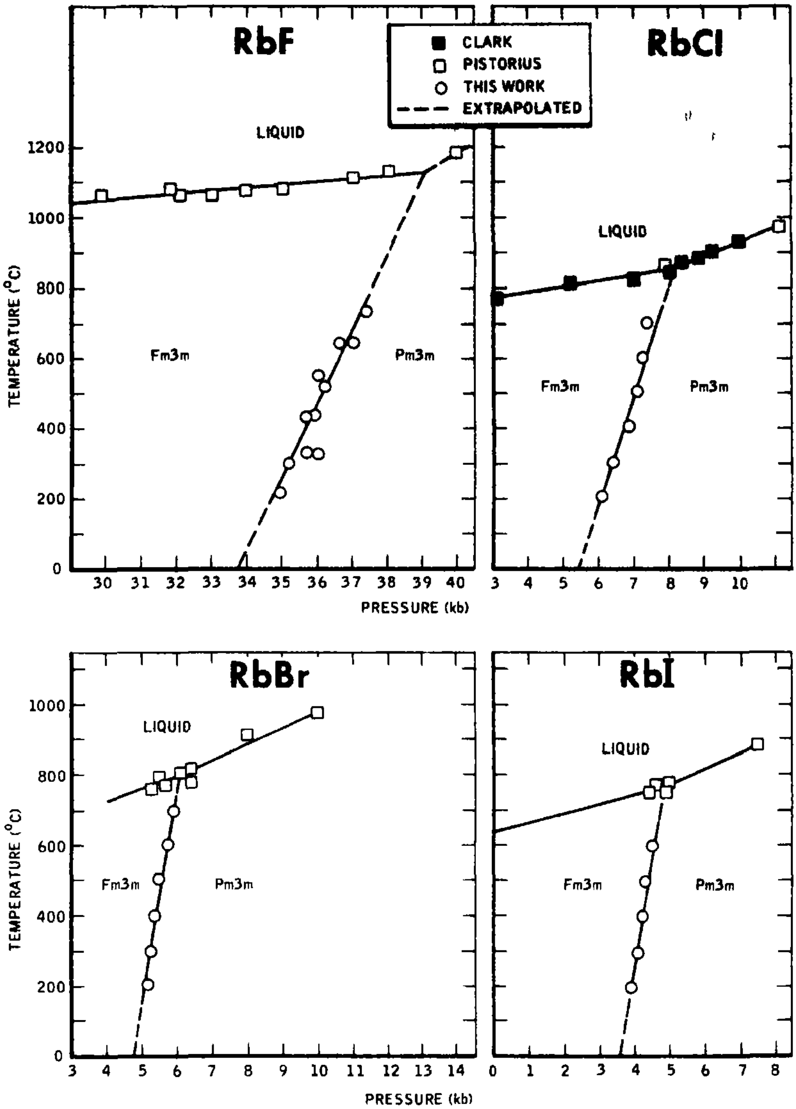

Fig. 2. *PV* diagram for the rubidium halides: □—melting point data of Clark (1959). ■—melting point data of Pistorius (1965, 1966). ○—Fm3m ⇄ Pm3m transition, this work.

served in KF at pressures up to 45 kb and at temperatures up to 800°C.

As in the case of most solid–solid phase transitions[21] these salts also show a hysteresis effect. The width of the hysteresis loop is, in general, less than one kilobar at temperatures greater than 200°C, and becomes larger and less reproducible at temperatures below 200°C. We have assumed that the equilibrium transition pressure is the average of the transition pressures obtained on compression and decompression. In all cases, the equilibrium transition pressure appears, within the experimental accuracy of these data, to be a linear function of the temperature over the interval 200–700°C. These P_{tr} data were treated by method of least squares to obtain the transition pressure as a function of temperature in the form

$$P_{tr}(\text{kb}) = a + bt \qquad (1)$$

where P_{tr} is the Fm3m ⇄ Pm3m transition pressure at a given temperature t (°C). Data for the constants a and b are given in Table 1. The constant b is of particular significance since $b = \mathrm{d}P/\mathrm{d}T$. The values for the transition pressure at 25°C reported in Table 2 were obtained from extrapolation of the high temperature data, by the use of equation (1).

The transition volumes* (ΔV_{tr}, Fm3m → Pm3m) for KCl, KBr and KI at temperatures between 200–800°C are shown in Fig. 3. Similarly, ΔV_{tr} for RbF, RbCl, RbBr and RbI are shown in Fig. 4. The volume change (ΔV_{tr}) appears to be a linear function of temperature at temperatures above 200°C. These data were also treated by method of least squares to obtain the transition volume as a function of temperature in the form

$$\Delta V_{tr}(\text{cm}^3/\text{mole}) = c + \mathrm{d}t. \qquad (2)$$

where ΔV_{tr} is the transition volume at a given temperature t (°C). Values for the constants c and d are given in Table 1. The transition volumes at 25°C reported in Table 3 were obtained from an extrapolation of the high tem-

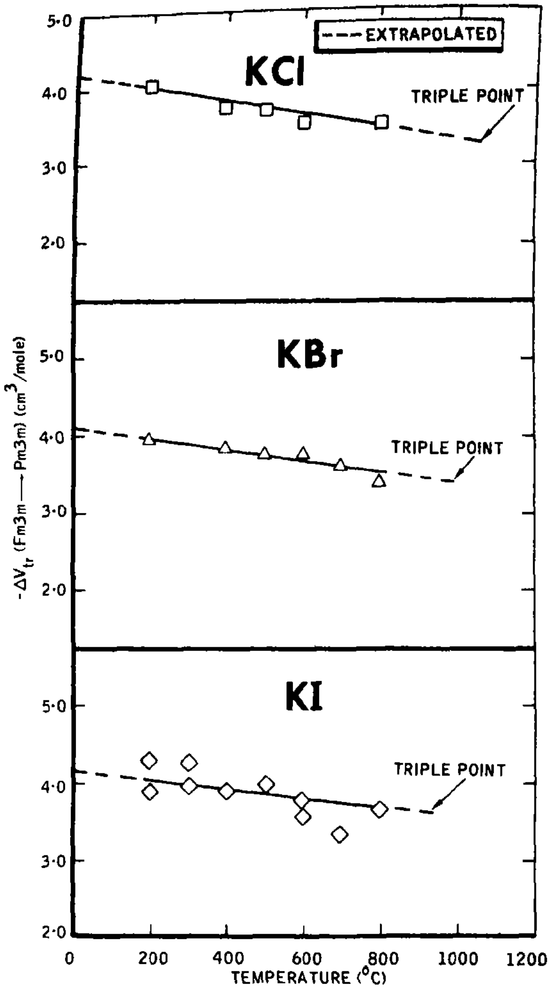

Fig. 3. ΔV(Fm3m → Pm3m) vs. T for KCl, KBr and KI.

Table 1. *Constants for the temperature dependence of the* Fm3m ⇄ Pm3m *transition pressure* [P_{tr}(kb) = $a + bt$] *and the transition volume* Fm3m → Pm3m [ΔV_{tr}(cm³/mole) = $c + dt$] *in the potassium and rubidium halides*

Salt	a (kb)	$b \times 10^3$ (kb/deg)	c (cm³/mole)	$d \times 10^3$ (cm³/mole/deg)
KCl	19·55 ± 0·13	−0·015 ± 0·256	−4·13 ± 0·01	0·830 ± 0·176
KBr	18·02 ± 0·28	−1·186 ± 0·485	−4·19 ± 0·11	0·869 ± 0·201
KI	18·35 ± 0·20	−3·223 ± 0·387	−4·44 ± 0·15	1·211 ± 0·295
RbF	34·37 ± 0·38	+3·723 ± 0·710	−1·84 ± 0·29	0·445 ± 0·513
RbCl	5·61 ± 0·14	+2·800 ± 0·296	−6·96 ± 0·11	2·880 ± 0·269
RbBr	4·88 ± 0·06	+1·371 ± 0·124	−7·47 ± 0·18	1·597 ± 0·366
RbI	3·64 ± 0·05	+1·400 ± 0·115	−8·15 ± 0·10	1·920 ± 0·236

---

*The transition volume vs. temperature data shown in Figs. 3 and 4 are not at constant pressure (except in the special case of KCl where $\mathrm{d}T/\mathrm{d}P \approx 0$) but are at pressures corresponding to the temperatures along the Fm3m ⇄ Pm3m phase boundary.

Table 2. *Transition pressure* (P_{tr}, kb) *for the* Fm3m $\rightleftarrows$ Pm3m *phase change in the potassium and rubidium halides at* 25°C

Salt	Bridgman 1945[25]	Daniels. *et al.* 1966[31]	Kennedy and LaMori. 1962[18]	Knof and Maisch. 1963[26]	Larson. 1965[29]	Piermarini and Weir. 1962[4]	Pistorius. 1964[11, 12]	Pistorius and Snyman. 1964[13]	This work	Average Value
KF						35		14·6 ± 1·3	None observed	
KCl	19·7		18·28 ± 0·21		20·0		19·27 ± 0·08		19·55 ± 0·13	19·4 ± 0·3
KBr	18·0		17·88 ± 0·06		18·5		17·43 ± 0·07		17·99 ± 0·28	18·0 ± 0·2
KI	17·8		17·48 ± 0·24				17·34 ± 0·05		18·27 ± 0·19	17·7 ± 0·3
RbF				33		12		6·1	34·47 ± 0·38	33·8 ± 0·8
RbCl	4·90						5·28		5·68 ± 0·14	5·32 ± 0·24
RbBr	4·50						4·20 ± 0·2		4·92 ± 0·06	4·57 ± 0·35
RbI	3·96	3·54					3·59 ± 0·16		3·68 ± 0·05	3·69 ± 0·11

Table 3. *Transition volume* ($-\Delta V_{tr}$, cm^3/mole) *for the* Fm3m $\rightarrow$ Pm3m *phase change in the potassium and rubidium halides at* 25°C

Salt	Adams and Davis. 1962[8]	Bridgman. 1945[25]	Genshaft *et al.*. 1967[30]	Jacobs. 1938[6]	Jamison. 1957[7]	Nagasaki and Minomura. 1964[9]	Pistorius and Snyman. 1964[13]	Weir and Piermarini. 1964[5]	This work	Average value
KF							1·0	2·49	None Obs.	
KCl		4·20				3·85		6·85	4·11 ± 0·10	4·05 ± 0·17
KBr		4·55						8·35	4·17 ± 0·11	4·36 ± 0·19
KI		4·50			4·50			11·8	4·41 ± 0·15	4·47 ± 0·13
RbF								3·70	1·83 ± 0·29	
RbCl	6·55	6·00	6·30					5·76	6·95 ± 0·11	6·30 ± 0·35
RbBr		6·55						6·60	7·43 ± 0·18	6·86 ± 0·39
RbI	9·65	7·50		7·9				8·26	8·10 ± 0·10	8·28 ± 0·31

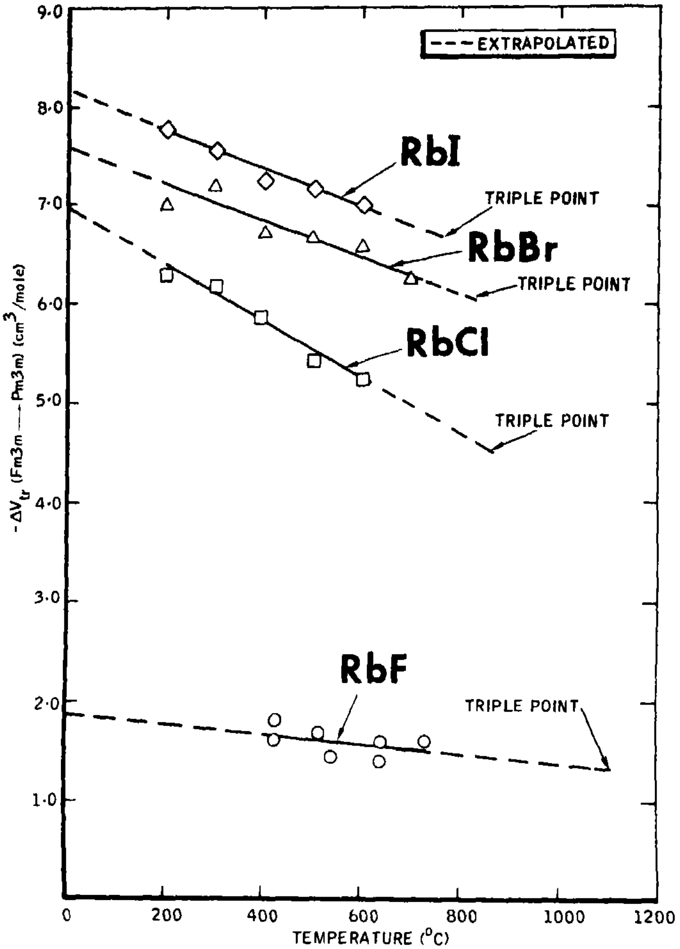

Fig. 4. Δ*V*(Fm3m → Pm3m) vs. *T* for the rubidium halides

perature data by use of equation (2). The pressure-temperature coordinates of the Fm3m ⇄ liquid ⇄ Pm3m triple point for these salts were determined from the intersection of the melting curves of the Fm3m and Pm3m phases at the Fm3m ⇄ Pm3m phase boundary. The melting curves of the Fm3m and Pm3m phases were drawn through the data points of Clark[22] and of Pistorius [23] in order that the intersection of these two curves would fall on the Fm3m ⇄ Pm3m phase boundry obtained in this work. Triple point coordinates obtained for the salts KCl, KBr and KI are shown in Fig. 1; coordinates for the rubidium halides are shown in Fig. 2. These triple point P–T coordinates are compared with the P–T coordinates given by Clark[22] and by Pistorius[23] in Table 4.

Potassium halides

Potassium fluoride was examined at pressures up to 45 kb at approx. 100° intervals from room temperature up to 800°C. However, we fail to find the phase transition reported by Weir and Piermarini[5] and by Pistorius and Snyman[13]. Pistorius *et al.* found the volume change of this transition to be small, i.e. 0·5 per cent. The sensitivity of the method used here is more than adequate to detect a phase transition with such a small

Table 4. *Thermodynamic properties of the* Fm3m → Pm3m *transition in the potassium and rubidium halides at the* Fm3m ⇄ *liquid* ⇄ Pm3m *triple point*

Salt	Clark[22]		Pistorius[23]		This work						
	P (kb)	T (°C)	P (kb)	T (°C)	P (kb)	T (°C)	$-\Delta V_{tr}$ (cm³/mole)	ΔS_{tr} (cal/mole/deg)	$T_{\Delta}S$ (cal/mole)	P (cal/mole)	ΔE (cal/mole)
KF					none observed						
KCl	18·95 ± 0·1	1042 ± 5	18·7 ± 0·7	1050 ± 10	19·5 ± 0·3	1070 ± 10	3·24 ± 0·21	+0·001	17	−1520	−1540
KBr			16·8 ± 1·0	997 ± 10	16·8 ± 0·6	1005 ± 10	3·32 ± 0·18	+0·09	120	−1340	−1460
KI			16·9 ± 1·5	934 ± 15	15·3 ± 0·4	940 ± 15	3·31 ± 0·19	+0·25	308	−1210	−1520
RbF			32	1055	38·5 ± 0·8	1105 ± 15	1·39 ± 0·55	−0·12	−170	−1280	−1110
RbCl	7·80	852	7·80 ± 0·01	852 ± 5	8·1 ± 0·3	870 ± 5	4·45 ± 0·18	−0·30	−344	−860	−520
RbBr			6·1 ± 0·8	808 ± 10	6·0 ± 0·2	830 ± 10	6·15 ± 0·23	−0·20	−222	−880	−660
RbI			5·0 ± 0·8	760 ± 10	4·7 ± 0·2	763 ± 10	6·69 ± 0·16	−0·22	−233	−750	−520

volume change. Since we find no polymorphic change at high temperatures where the transition kinetics would be more favorable, and the fact that Pistorius[23] found no break in the melting curve suggests that KF has no solid-solid transition at pressures below 45 kb.

The Fm3m ⇄ Pm3m transition pressures found for the salts KCl, KBr and KI are compared in Table 2 with the transition pressures reported in the literature. Bridgman has examined this transition in these salts on three separate occasions[3, 24, 25]; however, only the latest of Bridgman's data[25] are given. In general our results for P_{tr} are in good agreement with the published data (Table 2). Average values of P_{tr} were in each case calculated from the data tabulated in Table 2.

Bridgman[3] and Pistorius[11, 12] have examined the effect of temperature on the transition pressure in these salts over the temperature range 25°–200°C. Bridgman[3] gives $+3{\cdot}45$, $-4{\cdot}54$ and $+3{\cdot}33$ bar/deg respectively for the temperature dependence of the transition pressure in KCl, KBr and KI. Pistorius [11, 12], on the other hand, gives $-0{\cdot}25$, $+0{\cdot}55$ and $-1{\cdot}88$ bar/deg for these same salts. These data are compared with the constant b from Table 1, i.e. the value of dP/dT found in this work. The data from these three sources all indicate that the variation of P_{tr} with temperature is small. It is seen that the values of dP/dT found by Bridgman and Pistorius all disagree in sign. The sign of dP/dT however determines the sign of the entropy change, ΔS_{tr} (Fm3m → Pm3m) for this transition in these salts since ΔV_{tr} (Fm3m → Pm3m) is negative in all cases.

The agreement between ΔV_{tr} for KCl, KBr and KI found here and with published data (Table 3) is also relatively good, with the exception of the ΔV_{tr} data given by Weir and Piermarini[5]. Weir *et al.* obtained their transition volume data from high pressure X-ray diffraction studies. Their data, however, are also in disagreement with the ΔV_{tr} data given by Jamieson[7] and by Nagasaki *et al.*[9] for KI and KCl respectively. (The latter data for KI and KCl were also determined from X-ray diffraction studies carried out at high pressures.) These ΔV_{tr} data of Weir *et al.*[5] were not used in the calculation of the average value of ΔV_{tr} for the salts KCl, KBr and KI.

Rubidium halides

Piermarini and Weir[4] report a solid-solid phase transaction in RbF at a pressure between 9 and 15 kb. They give the volume change for this transition as -20 per cent. Knof and Maisch[26] have observed changes in the optical transmission properties of RbF at a pressure of 33 kb, which is similar to the optical effect associated with the Fm3m → Pm3m transition in the potassium halides, KCl and KBr. Pistorius and Snyman[13], on the other hand, report phase transitions in RbF at a pressure of 6·1 kb at a temperature of 20°, and 5·0 kb at 200°C. The latter authors[13] noted that this phase transition in RbF was very sluggish. No indication of the size of ΔV for this transition was given by Pistorius *et al.*[13].

The results from our dilatometric measurements clearly indicate a polymorphic transition in RbF at about 35 kb, in agreement with the results reported by Knof *et al.*[26]. Transition pressure data for RbF are shown in Fig. 2. The transition was very sluggish at 100° and no transition was observed at room temperatures. However, at temperatures above 300°C the transition proceeds as readily as was found in the other alkali halides at 200°C. In the case of RbF, data taken only above 300°C were used in the least squares treatment of P_{tr} and ΔV_{tr} vs. temperature. It was also necessary to modify the experimental arrangement since at temperatures above 400°C RbF reacts with the graphite heater causing it to become relatively non-conducting. Pistorius[23] found Ni to be a satisfactory container for RbF at high temperatures. We therefore isolated our sample from the graphite heater with a thin (0·0025 cm) nickel sleeve. With this modification our measurements were still limited to temperatures below about

750°C since an irreversible change occurs in the resistance of graphite at higher temperatures, presumably from attack by RbF through the nickel foil. Our RbF samples were examined by X-ray diffraction after being removed from the pressure chamber and showed diffraction lines characteristic of only the Fm3m phase. Data for P_{tr} and ΔV_{tr} for this salt at 25°C are given in Tables 2 and 3 respectively.

The pressures obtained for the Fm3m ⇄ Pm3m transition in the rubidium halides are compared with the published values in Table 2. Averages of P_{tr} for each of these salts were calculated from data given in Table 2. However, in the case of RbF only the data of Knof and Maisch[26] were averaged with the data from this work. Pistorius[11, 12] gives the temperature dependence of the polymorphic transition pressure in RbCl, RbBr and RbI as 3·01, 2·19 and 1·94 bar/deg respectively. The agreement with dP/dT found here (b in Table 1) is better than in the case of the potassium salts.

Thermodynamic calculations

The average values of P_{tr} and ΔV_{tr} given in Tables 2 and 3 were used to calculate the thermodynamic properties of this polymorphic transition in these salts at a temperature of 298°K. However in the case of dP/dT, we have used only the values obtained in this work, since our measurements are over a much wider temperature interval (from 400°C to as much as 700°C) than were Bridgman's [24] and Pistorius' [12, 13] work.

At a temperature and pressure where the two polymorphs may be considered to be in equilibrium, then

$$G(\text{Fm3m phase}) = G(\text{Pm3m phase}). \qquad (3)$$

Thus

$$\Delta G = 0 \qquad (4)$$

and at constant temperature and pressure

$$\Delta E = P\Delta V - T\Delta S. \qquad (5)$$

The external $P\Delta V$ work necessary to carry out the Fm3m → Pm3m phase transformation (reversibly) at constant pressure and temperature is calculated from the average values of P_{tr} and ΔV_{tr}. These data for $P\Delta V$ at 298°K are given in Table 5. Data for $P\Delta V$ reported by Weir *et al.*[5] are also shown. The larger values of $P\Delta V$ reported by these authors[5] for the potassium salts arise from the larger transition volumes found by them. On the other hand, good agreement in case of RbF is fortuitous since Weir's much lower value of P_{tr} is compensated for by the larger value of

Table 5. *Thermodynamic properties of the* Fm3m → Pm3m *transition in the potassium and rubidium halides at* 298°K

Salt	ΔS_{tr} Pistorius[11, 12] (cal/mole/deg)	ΔS_{tr}^{*} This work (cal/mole/deg)	$T\Delta S$ This work (cal/mole)	$P\Delta V$ Weir *et al.*[5] (cal/mole)	$P\Delta V$† This work (cal/mole)	ΔE This work (cal/mole)
KCl	+0·03	0·002	6	−3,000	−1880	−1890
KBr	−0·11	0·12	37	−3,300	−1880	−1920
KI	+0·53	0·34	103	−4,500	−1890	−1990
RbF		−0·16	−48	−1,300	−1490	−1440
RbCl	−0·44	−0·42	−125	−700	−800	−675
RbBr	−0·35	−0·23	−67	−700	−750	−680
RbI	−0·38	−0·28	−83	−700	−730	−660

*Average values of ΔV_{tr} in Table 4 were used to calculate these entropies.

†Average value of P_{tr} in Table 1 and average value of ΔV_{tr} in Table 4 were used to calculate this $P\Delta V$ product.

ΔV. The agreement of $P\Delta V$ from this work and from Weir's is, however, relatively good in the case of RbCl, RbBr and RbI.

The entropy change (ΔS_{tr}, Fm3m → Pm3m) was calculated from the Clausius Clapeyron relation. Data obtained for ΔS_{tr} at 298°K are given in Table 5. Similarly, Pistorius[12, 13] has calculated ΔH for this polymorphic transition in these salts from his value of dP/dT and from Weir's and Piermarini's [5] transition volume. As noted above, Weir's value of ΔV_{tr} for the potassium salts are considerably higher than the results found by others (results, on the other hand, for the rubidium salts RbCl, RbBr and RbI are in good agreement, Table 2). The entropy of transformation derived from Pistorius' calculations are -0.44, -0.35 and -0.38 cal/mole/deg respectively for RbCl, RbBr and RbI. The agreement between the ΔS_{tr} calculated by Pistorius[12, 13] and those derived from this work is relatively good for these salts.

Data for the $T\Delta S$ term in equation (5) are given in Table 5 as also the data for the change in internal energy (ΔE) associated with this polymorphic transformation. Similarly, thermodynamic properties for this Fm3m → Pm3m transformation at the triple point are given in Table 4.

Several trends in the transition properties of these salts are noted. From Figs. 4 and 5, it is seen that in all cases studied, the absolute value of transition volume decreases with an increase in temperature. In general, the pressure of the Fm3m ⇄ Pm3m transition is relatively insensitive to temperature for the halides of these two alkali metals. The potassium salts do, however, show a small decrease whereas the rubidium salts show a correspondingly small increase in transition pressure with an increase in temperature. The transition pressure for CsCl is also known to increase with an increase in temperature[27]. Consequently, at constant pressure ΔS-(Fm3m → Pm3m) is positive for the potassium halides and negative for the rubidium halides (and CsCl). Thus in the case of the alkali chlorides, the absolute entropy of the Fm3m phase becomes larger relative to the Pm3m phase as the cation increases in atomic number and therefore in size. A similar trend has been noted[28] in the fusion of the Fm3m phase of these chlorides.

Acknowledgements—The authors are indebted to Dr. S. J. Yosim for his continued interest and many helpful discussions during the course of this work, and to Dr. Maynard Hiller for preparing the samples of KF and RbF.

REFERENCES

1. SLATER J. C., *Proc. Am. Acad. Arts Sci.* **61**, 144 (1926).
2. BRIDGMAN P. W., *Z. Krist.* **67**, 363 (1928).
3. BRIDGMAN P. W., *Phys. Rev.* **48**, 893 (1935).
4. PIERMARINI G. J. and WEIR C. E., *J. chem. Phys.* **37**, 1887 (1962).
5. WEIR C. E. and PIERMARINI G. J., *J. Res. Nat. Bur. Standards* **68A**, 105 (1964).
6. JACOBS R. B., *Phys. Rev.* **54**, 468 (1938).
7. JAMIESON J. C., *J. Geol.* **65**, 334 (1957).
8. ADAMS L. H. and DAVIS B. L., *Proc. nat. Acad. Sci.* **48**, 982 (1962).
9. NAGASAKI H. and MINOMURA S., *J. phys. Soc. Japan* **19**, 1496 (1964).
10. KLEMENT W., Jr. and JAYARAMAN A., In *Advances in Solid State Chemistry* (Edited by H. Reiss) p. 289. Pergamon Press, Oxford, (1966).
11. PISTORIUS C. W. F. T., *J. Phys. Chem. Solids* **25**, 1477 (1964).
12. PISTORIUS C. W. F. T., *ibid.* **26**, 1003 (1965)
13. PISTORIUS C. W. F. T. and SYNMAN H. C., *Z. phys. Chem. Neue Folge* **43**, 1 (1964).
14. BRIDGMAN P. W., *Physics of High Pressures*. Bell, London (1958).
15. KENNEDY G. C. and NEWTON R. C., In *Solids Under Pressure* (Edited by W. Paul and D. M. Warschauer), p. 163. McGraw-Hill, New York (1963).
16. JAYARAMAN A., KLEMENT W., NEWTON R. C. and KENNEDY G. C., *J. Phys. Chem. Solids* **24**, 7 (1963).
17. JAYARAMAN A., KLEMENT W., Jr. and KENNEDY G. C., *Phys. Rev.* **130**, 2277 (1963).
18. KENNEDY G. C. and LAMORI P. N., *J. geophys. Res.* **67**, 851 (1962).
19. KENNEDY G. C. and LAMORI P. N., In *Progress in Very High Temperature Research* (Edited by F. P. Bundy, W. R. Hibbard and H. M. Strong). Wiley, New York (1961).
20. LLOYD F. C., BECKETT C. W. and BOYD F. R., Jr., *Science* **164**, 860 (1969).
21. RAO C. N. R. and RAO K. J., In *Progress in Solid State Chemistry* (Edited by H. Reiss), Vol. 4, p. 131. Pergamon Press, Oxford (1966).
22. CLARK S. P., *J. chem. Phys.* **31**, 1526 (1959).
23. PISTORIUS C. W. F. T., *J. Phys. Chem. Solids* **26**, 1543 (1965).

24. BRIDGMAN P. W., *Proc. Am. Acad. Arts. Sci.* **74**, 21 (1945).
25. BRIDGMAN P. W., *Proc. Am. Acad. Arts. Sci.*, **76**, 1 (1945).
26. KNOF H. and MAISCH W. G., *J. Phys. Chem. Solids* **24**, 1625 (1963).
27. MENARY J. W., UBBLOHDE A. R. and WOODWARD I., *Proc. R. Soc.* **208**, 158 (1951).
28. BAUER S. H. and PORTER R. F., In *Molten Salt Chemistry* (Edited by M. Blander), p. 623. Interscience, New York (1964).
29. LARSON D. B. In *Physics of Solids at High Pressures* (Edited by C. T. Tomizuka and R. M. Emrick), p. 459. Academic Press, New York (1965).
30. GENSHAFT Yu. S., LIVSHITS L. D. and RYABININ Yu. N., *Zh. Tek. Fiziki* **37**, 179 (1967).
31. DANIELS W. B. and SKOULTCHI A. I., *J. Phys. Chem. Solids* **27**, 1247 (1966).

J. Phys. Chem. Solids **Pergamon Press 1970. Vol. 31, pp. 817–823. Printed in Great Britain.**

ANOMALOUS HALL EFFECT IN SEMICONDUCTORS

ANTOINE J. F. BASTIN, COLETTE LEWINER and NOËLLE FAYET
Groupe de Physique des Solides de l'Ecole Normale Supérieure*, Faculté des Sciences de Paris,
9, quai Saint Bernard, Paris V

(*Received* 19 *May* 1969; *in revised form* 28 *July* 1969)

Abstract—The anomalous Hall effect due to the orbital magnetism has been investigated in a weakly doped semiconductor in the presence of a magnetic field. For a collisionless electron gas, we have calculated the conductivity tensor and (besides the usual Hall effect) we have obtained an anomalous current proportional to $\vec{\mathscr{E}} \times \vec{M}$. We find that for $\omega = 0$ no particular affect arises; for finite frequencies, we give the first non trivial term of the anomalous Hall current. We also discuss the influence of the collisions and the conditions for observing the predicted effects experimentally.

1. STATE OF THE PROBLEM

KARPLUS and Luttinger[1] first pointed out that the spin-orbit interaction of polarized conduction electrons gives rise to a current perpendicular to both the electric field and the magnetization, and thus accounted for the d.c. Hall effect in ferromagnetics. Later on, several theories have been proposed [2], [3], [4], where the stress has been put on the influence of various types of scattering. There is still a need for an analysis of the basic influence of an average magnetization on anomalous Hall effects through spin-orbit coupling.

In this paper, we develop a theory which is valid both for finite frequencies and for finite magnetic fields. An average magnetization will be assumed, regardless of its origin (we do not intend to deal only with ferromagnets). We will be chiefly interested in the Hall effect of a collisionless electron gas in crossed electric and magnetic fields and will briefly discuss the influence of collisions in the last part of the paper.

The electron gas is immersed in a constant magnetic field $\vec{H}$, parallel to the z-axis. We apply an r.f. electric field $\vec{\mathscr{E}}\exp(i\omega t)$ parallel to the x-axis. The corresponding perturbation in the Hamiltonian is

$$H_1 = -\frac{e}{i\omega}\vec{\mathscr{E}}\cdot\vec{j}\exp(i\omega t) \qquad (1.1)$$

where $\vec{j}$ is the current operator. In the presence of the magnetic field, $\vec{j}$ includes the gauge current as well as the velocity operator $\vec{\pi}/m$:

$$\vec{j} = \frac{\vec{\pi}}{m} + \frac{e}{mc}\vec{A}. \qquad (1.2)$$

According to the theory of linear response [5], the complex conductivity tensor is given by

$$\sigma_{\alpha\beta}(\omega) = \frac{ie^2}{\hbar\omega}\sum_{\nu}{}' \left[\frac{j^{\alpha}_{\mu\nu}j^{\beta}_{\nu\mu}}{\omega-\omega_{\nu\mu}+i\eta} - \frac{j^{\beta}_{\mu\nu}j^{\alpha}_{\nu\mu}}{\omega+\omega_{\nu\mu}+i\eta}\right] + \frac{ie^2}{m\omega}\delta_{\alpha\beta}. \qquad (1.3)$$

In this expression, μ and ν are *exact eigenstates* of the unperturbed Hamiltonian H_0, and the Σ' stands for the sum over all states but μ. The general expression (1.3) can be simplified if we assume the system is rotationally invariant around σz. The coefficients σ_{xx} and σ_{xy} are then given by

$$\sigma_{xx} = -\frac{2e^2}{i\hbar\omega}\sum_{\nu}{}' \frac{\omega_{\nu\mu}}{\omega^2-\omega^2_{\nu\mu}} j^{x}_{\mu\nu}j^{x}_{\nu\mu} + \frac{ie^2}{m\omega} \qquad (1.4)$$

---

*Laboratoire Associé au Centre National de la Recherche Scientifique.

$$\sigma_{xy} = -\frac{e^2}{i\hbar}\sum_{\nu}{}' \frac{j^x_{\mu\nu}j^y_{\nu\mu} - j^y_{\mu\nu}j^x_{\nu\mu}}{\omega^2 - \omega^2_{\nu\mu}} \tag{1.5}$$

($ie^2/m\omega$ is the gauge current arising from the a.c. vector potential $\vec{\mathscr{E}}/i\omega \exp(i\omega t)$). In the absence of a magnetic field ($\vec{H} = 0$), $\vec{j}_{\mu\nu}$ connects only those states which have the same wave vector index and belong to different bands. Since $\omega_{\mu\nu}$ is a band gap, $\omega \ll \omega_{\mu\nu}$ so that (1.4) reduces to

$$\sigma_{xx} = \frac{2ie^2}{m^2\hbar\omega}\sum \frac{\pi^x_{\mu\nu}\pi^x_{\nu\mu}}{\omega_{\mu\nu}} + \frac{ie^2}{m\omega} = \frac{ie^2}{m^*\omega} \tag{1.6}$$

where m^+ is the usual effective mass tensor. A similar expression holds for σ_{xy}. Usually σ_{xy} vanishes for zero field, because of time-reversal invariance (from the Onsager's relationships). However, even if there is no magnetic field, a magnetization $\vec{M}$ provides a time reversal violation and σ_{xy} can be finite. It must then have only odd terms in $\vec{M}$. The simplest we can imagine is the ferromagnetic effect [1], [3]:

$$\vec{j} = \alpha\vec{\mathscr{E}} \times \vec{M}. \tag{1.7}$$

This may also occur in paramagnetic materials if we imagine that, for times much shorter than the spin relaxation time, we can maintain an average magnetization or if we assume that the spin polarization is due to optical pumping of conduction electrons.

If the spin-orbit coupling is high enough, such as in SbIn, the main part of the magnetism is orbital and involves the same combination ($j^x_{\mu\nu}j^y_{\nu\mu} - j^y_{\mu\nu}j^x_{\nu\mu}$) as σ_{xy}. A detailed calculation (see Appendix A) yields

$$\sigma_{xy} = -2\,ec\frac{M_z}{\bar{\Delta}} \tag{1.8}$$

where $\bar{\Delta}$ is of the order of the band gap, and M_z the z component of the orbital magnetization.

If $\vec{H}$ is finite, things become far less simple. The band structure is deeply alterated by the occurrence of discrete Landau levels. The off-diagonal matrix elements of (1.4) and (1.5) now involve intraband transitions between different Landau levels of the same band, as well as the usual interband terms.

For weak magnetic fields ($\hbar\omega_c^* \ll \bar{\Delta}$), the Landau structure is negligible as compared to the band structure and we do not expect relevant changes in the interband terms. So the main problem will be to evaluate the new intraband terms and the contribution to σ_{xx} and σ_{xy}. We can already predict their order of magnitude since it is well known that a collisionless semiconductor yields a perfect d.c. Hall effect [6] ($\sigma_{xx} = 0$; $\sigma_{xy} = e^2/m^*\omega_c$).

In Section 2, we analyse the situation for $\omega = 0$ and calculate the d.c. conductivity. As a result, we show that no spin-orbit effect arises. In Section 3, we calculate the conductivity at finite frequencies, which needs perturbation theory up to fourth order in $\vec{k}$ and enables us by the way to construct a one-band effective Hamiltonian; its various terms are interpreted and finally we separate the 'normal' and the 'anomalous' part of the Hall effect. In Section 4, we briefly review our results and discuss the influence of collisions; we also suggest ways of looking for experimental observation.

2. D.C. CONDUCTIVITY

Let us first recall a few standard results on the Luttinger and Kohn (hereafter L.–K.) basis [7], [8], defined by

$$|m\vec{k}\rho\rangle = \exp i\vec{k}.\vec{r}|m\rho\rangle \tag{2.1}$$

where $|m\rho\rangle$ is the exact (although unknown) eigenstate of the Hamiltonian H_0 corresponding to the band m and wave vector 0 (ρ stands for the spin variable). In other words,

$$H_0|m\rho\rangle = E_m|m\rho\rangle. \tag{2.2}$$

For the sake of simplicity, we assume that the energy minimum (or maximum in the case of holes) of the band m is located at $k = 0$. It is then clear that, in the L.–K. basis, the Hamiltonian is off-diagonal by terms of first order in $\vec{k}$ at least.

The current operator may be written as

$$\vec{j} = \frac{\vec{\pi}}{m} + \frac{e\vec{A}}{mc} = \frac{i}{\hbar}\left[H_0, \vec{r}\right]. \qquad (2.3)$$

In the L.–K. basis, the matrix elements of $\vec{r}$ and $\vec{\pi}$ are given by

$$\langle n\vec{k}\rho|\vec{r}|n'\vec{k}'\rho'\rangle = i\vec{\nabla}_k\delta(\vec{k}-\vec{k}')\delta_{nn'}\delta_{\rho\rho'} \qquad (2.4)$$

$$\langle n\vec{k}\rho|\vec{\pi}|n'\vec{k}'\rho\rangle = \vec{\pi}_{n\rho,n'\rho'}\delta(\vec{k}-\vec{k}') + \hbar\vec{k}\delta(\vec{k}-\vec{k}')\delta_{nn'}\delta_{\rho\rho'}. \qquad (2.5)$$

In principle, a function of $\vec{r}$ can be replaced by a function of $i\vec{\nabla}_{k}$. However, this equivalence between $\vec{r}$ and $i\vec{\nabla}_{k}$, as shown by (2.4), is not strictly rigorous. The δ-function in (2.4) is not exactly the standard δ-distribution insofar as $\vec{k}$ and $\vec{k}'$ have to be restricted to the first Brillouin zone. Since we intend to restrict ourselves to small carrier densities in the conduction band, relevant $\vec{k}$ vectors will remain smaller than the Brillouin zone scale so that no trouble will occur with the identity of $\vec{r}$ and $i\vec{\nabla}_{k}$. We are then able to consider $\vec{A}$ as a function of $i\vec{\nabla}_{k}$ and to define

$$\bar{\vec{k}} = \vec{k} + \frac{e\vec{A}}{\hbar c}. \qquad (2.6)$$

This yields for the matrix elements of $\vec{j}$ and H_0:

$$\langle n\vec{k}\rho|\vec{j}|n'\vec{k}'\rho'\rangle = \frac{\vec{\pi}_{n\rho,n'\rho'}}{m}\delta(\vec{k}-\vec{k}') + \frac{\hbar}{m}\bar{\vec{k}}\delta_{nn'}\delta(\vec{k}-\vec{k}') \qquad (2.7)$$

$$\langle n\vec{k}\rho|H_0|n'\vec{k}'\rho'\rangle = \left(E_n + \frac{\hbar^2\bar{\vec{k}}^2}{2m}\right)\delta_{nn'}\delta_{\rho\rho'}. + \beta\vec{H}\,.\,\vec{\sigma}_{n\rho,n'\rho'} + \frac{\hbar}{m}\vec{\pi}_{n\rho,n'\rho'}\,.\,\bar{\vec{k}} \qquad (2.8)$$

In the free electron case, $\vec{j}$ obeys the usual equation of motion

$$[\mathscr{H}, \vec{j}] = \frac{ie\hbar}{mc}\vec{j}\times\vec{H}. \qquad (2.9)$$

For a semiconductor crystal, we can also derive an exact relationship between H_0 and $\vec{j}$. We proceed as follows: according to (2.7), we separate $\vec{j}$ into two parts, $\vec{j}^d$ and $\vec{j}^{od}$ which are respectively diagonal and off-diagonal in the L.–K. basis. We verify that

$$[H_0, j^{dx}] = i\hbar\omega_c j^y \qquad (2.10)$$

$$[H_0, j^{dy}] = -i\hbar\omega_c j^x \qquad (2.11)$$

with $\omega_c = eH/mc$ (m is the *free* electron mass). Equations (2.10) and (2.11), established within the L.–K. basis, are valid in any representation. In the basis constructed on the eigenbasis of H_0, they become

$$\omega_{\mu\nu}j^{dx}_{\mu\nu} = i\omega_c j^y_{\mu\nu} \qquad (2.12)$$

$$\omega_{\mu\nu}j^{dy}_{\mu\nu} = -i\omega_c j^x_{\mu\nu} \qquad (2.13)$$

On comparing (1.4) and (1.5) with (2.12) and (2.13), we see that, for $\omega = 0$

$$\sigma_{xx} = \frac{ie^2}{m\omega} + \frac{e^2}{\hbar\omega\omega_c}\sum_{\nu}{}' \left[j^x_{\mu\nu}j^{dy}_{\nu\mu} - j^{dy}_{\mu\nu}j^x_{\nu\mu}\right].$$

The commutator $[j^x, j^{dy}]$ is equal to $-i\hbar\omega_c/m$. It follows that

$$\sigma_{xx} = 0 \qquad (2.14)$$

as predicted in Section 1. Similarly,

$$\sigma_{xy} = \frac{e^2}{i\hbar\omega_c^2}\left[j^{dy}, j^{dx}\right] \qquad (2.15)$$

which yields

$$\sigma_{xy} = \frac{e^2}{m\omega_c} \qquad (2.16)$$

or, for the whole conduction band,

$$\sigma_{xy} = \frac{ne^2}{m\omega_c} \qquad (2.17)$$

where n is the carrier density in the conduction band. Our result (2.17) seems to be exact. However it has two failures. Since it means that every collisionless crystal exhibits a perfect d.c. Hall effect, it would imply the occurence of the Hall effect in insulators and we know this is wrong. Furthermore, in the limit $\omega_c \rightarrow \infty$, the lattice band structure is negligible against $\hbar\omega_c$ and every electron will contribute to a Hall conductivity $Ne^2/m\omega_c$ (N being the total electron density).

The limitation of (2.17) comes from the L.-K. formalism, which becomes wrong when one works near a Brillouin zone edge (or when open orbits do exist), as we mentioned above. Such a limitation occurs for $\omega_c = 0$ in an insulator because every level in every band is occupied; for a semiconductor or a metal, it becomes effective when $\hbar\omega_c$ is of the order of magnitude of a band width. Otherwise, (2.17) holds.

3. CONDUCTIVITY AT FINITE FREQUENCIES

The equations of motion (2.10) and (2.11) are no longer useful for $\omega \neq 0$ because of the factor $\omega_{\mu\nu}^2/(\omega^2 - \omega_{\mu\nu}^2)$ in the intraband terms. We are compelled to look for an approximate procedure. The latter will be an expansion of (1.4) and (1.5) in powers of $\vec{k}$.

We shall try to calculate σ up to order $\bar{k}^0$. It is then necessary to consider separately the interband and the intraband terms in (1.4) and (1.5). In the interband terms, the energy $\omega_{\mu\nu}$ is finite; we neglect ω, and it is enough to know the current matrix elements up to order $\bar{k}^0$. In the intraband terms, we have

$$\omega \sim \omega_c \sim \bar{k}^2$$

since in the quantum regime ω_c is comparable to the transverse kinetic energy. Hence, the energy denominator in (1.5) is of order $\bar{k}^4$. The corresponding matrix elements of $\vec{j}$ are of order $\bar{k}$. The leading term of σ_{xy} is thus of order $\bar{k}^{-2}$ and corresponds to the usual Hall effect. In order to achieve an accuracy of order $\bar{k}^0$ in σ, the matrix elements of $\vec{j}$ should be known up to order $\bar{k}^3$ while $\omega_{\mu\nu}$ should be calculated up to order $\bar{k}^4$.

Such an accuracy implies a detailed knowledge of the *exact* eigenstates μ, ν appearing in (1.4) and (1.5); as such, the L.-K. basis is not sufficient. What is required is a canonical transformation

$$\tilde{H}_0 = e^{-S} H_0 e^S \qquad (3.1)$$

which diagonalizes the Hamiltonian to the required order. The matrix element $\vec{j}_{\mu\nu}$ can be obtained as the matrix element of the transformed operator $\vec{j}$ between the two L.-K. states. The problem is reduced to the elimination of the perturbation $\vec{k}.\vec{\pi}$ in (2.8).

The second order expansion of $\tilde{H}_0$ is quite standard[7] and yields, for a cubic crystal:

$$\tilde{H}_{0\mu\mu} = \left(\frac{\hbar^2}{2m^*}\bar{k}^2 + E_\mu\right) - \vec{\mu} . \vec{H} \qquad (3.2)$$

where the effective mass tensor is given by

$$m^2\left(\frac{1}{m^*} - \frac{1}{m^*}\right) = 2 \sum_\nu \frac{\pi_{\mu\nu}^\alpha \pi_{\mu\nu}^\alpha}{\omega_{\mu\nu}}; \ \alpha = x, y, z \qquad (3.3)$$

and the orbital magnetic moment $\vec{\mu}$ is:

$$\mu_z = \frac{g-2}{2}\mu_\beta \sigma_z = \frac{i\beta}{m} \cdot \frac{\pi_{\mu\nu}^x \pi_{\nu\mu}^y - \pi_{\mu\nu}^y \pi_{\nu\mu}^x}{\omega_{\mu\nu}}. \qquad (3.4)$$

From (3.2), one gets the well-known result:

$$\sigma_{xx} = \frac{ie^2}{m^*\omega} \cdot \frac{\omega^2}{\omega^2 - \omega_c^{*2}} \qquad (3.5)$$

$$\sigma_{xy} = \frac{e^2}{m\omega_c} \cdot \frac{\omega_c^{*2}}{\omega_c^{*2} - \omega^2}. \qquad (3.6)$$

The fourth order expansion is obtained by a similar procedure. For an isotropic system (cubic crystal), we may guess the form of $\tilde{H}_0$ by using symmetry arguments. Since

$\tilde{H}_0$ is even in $\vec{\bar{k}}$ and ω_c is of order 2, we may expect only terms of the form

$$\bar{k}^2(\vec{\mu}\cdot\vec{H})$$
$$(\vec{\bar{k}}\cdot\vec{\mu})(\vec{\bar{k}}\cdot\vec{H}).$$

There are also terms in $\bar{k}^{x4}$, $\bar{k}^{y4}$, $\bar{k}^{z4}$, $\bar{k}^{x2}\bar{k}^{y2}$, $\bar{k}^{x2}\bar{k}^{z2}$, $\bar{k}^{y2}\bar{k}^{z2}$, which represent deviations from spherical and parabolic energy bands; they can be reduced to the well-known dependence of m^+ upon $\vec{\bar{k}}$[9]. Since this effect is irrelevant in our theory, we drop the corresponding terms. We are then left with

$$\tilde{H}_{0\nu\nu} = E_\nu + \frac{\hbar^2\bar{k}^2}{2m^*} - \vec{\mu}\,.\,\vec{H} + \gamma\vec{\bar{k}}^2(\vec{\mu}\,.\,\vec{H}) + \delta(\vec{\bar{k}}\,.\,\vec{\mu})(\vec{\bar{k}}\,.\,\vec{H}). \quad (3.7)$$

Intermediate calculations are outlined in Appendix B and give, for a two-band model:

$$\gamma = \frac{\hbar^2}{\Delta}\left(\frac{1}{m^*} - \frac{2}{m}\right) \quad (3.8)$$

$$\delta = \frac{\hbar^2}{m\Delta}. \quad (3.9)$$

The fourth term in (3.7) may be regarded either as an alteration of $\bar{k}^2$ by $(\vec{\mu}\,.\,\vec{H})$ or as an alteration of $(\vec{\mu}\,.\,H)$ by $\bar{k}^2$. In the latter case, it is equivalent to a $\vec{k}$ dependence of the g-factor and confirms the conclusions of Lax *et al.*[9]. In the former one, the system behaves as if the effective mass were m^{**} with

$$\frac{1}{m^{**}} = \frac{1}{m^*}\left(1 + \frac{2\gamma m^*}{\hbar^2}\,\vec{\mu}\,.\,\vec{H}\right). \quad (3.10)$$

Since m^{**} is spin-dependent, it follows that spin-up and spin-down electrons have slightly different cyclotron frequencies.

The fifth term of (3.7) can account for combined resonances for the $(\vec{\bar{k}}\,.\,\vec{H})$ induces transitions between Landau levels and $(\vec{\bar{k}}\,.\,\vec{\mu})$ induces a spin-flip.

It is now quite straightforward to compute $\vec{\tilde{r}}, \vec{\tilde{j}}$ and σ_{xy}. We give the result for a two-band model; the general case can be treated exactly in the same spirit but the explicit expressions would be uselessly involved. Since

$$\vec{r}_{\mu\nu} = -i\vec{\nabla}_{\bar{k}}\delta_{\mu\nu} \quad (3.11)$$

we get:

$$\tilde{x}_{\mu\mu} = -i\frac{\partial}{\partial k_x} + \frac{i\hbar^2}{2m^2\Delta^2}\sum_{\nu\alpha}(\pi^x_{\mu\nu}\pi^\alpha_{\nu\mu} - \pi^\alpha_{\mu\nu}\pi^x_{\nu\mu})\,.\,\bar{k}^\alpha \quad (3.12)$$

and similar expressions for $\tilde{y}$. From

$$\vec{\tilde{j}} = \frac{i}{\hbar}[\tilde{H}_0, \vec{\tilde{r}}] \quad (3.13)$$

one obtains

$$j^\alpha_{\mu\mu} = \frac{\hbar\bar{k}^\alpha}{m^{2+}}\left(1 - \frac{\vec{\mu}\,.\,\vec{H}}{\Delta}\right) + \frac{\delta\mu^\alpha}{\hbar}\,(\vec{\bar{k}}\cdot\vec{H}). \quad (3.14)$$

When (3.14) is inserted in (1.5), the m^{**} in the current operator cancels the m^{**} which is included in the Landau level spacing and the second term of (3.14) does not contribute. This means that the fourth order terms in $\tilde{H}_0$(3.7) do not contribute to σ_{xy}, as far as the intraband terms are concerned.

The interband part of σ_{xy} is already known from (1.8). The intraband part is then

$$\sigma^{(1)}_{xy} = \left(\frac{e^2}{m\omega_c} - 2ec\frac{\mu^z}{\Delta}\right)\frac{\omega_c^{*2}}{\omega_c^{*2} - \omega^2}. \quad (3.15)$$

From (3.15), (1.8), (3.5), we obtain, for the whole conduction band,

$$\sigma_{xx} = \frac{ine^2}{m^*\omega}\cdot\frac{\omega^2}{\omega^2 - \omega_c^{*2}}$$
$$\sigma_{xy} = \frac{ne^2}{m\omega_c}\cdot\frac{\omega_c^{*2}}{\omega_c^{*2} - \omega^2} - 2ec\frac{M^z}{\Delta}\frac{\omega^2}{\omega^2 - \omega_c^{*2}}. \quad (3.16)$$

We recover, in the limit $\omega \to 0$, the result (2.14), (2.17), i.e. the well known Hall effect whereas for $\omega_c = 0$, we get the result (1.8).

4. CONCLUSIONS

σ_{xy} may also read

$$\sigma_{xy}=\frac{ne^2}{m}\cdot\frac{1}{\omega_c^{*2}-\omega^2}\left[\frac{\omega_c^{*2}}{\omega_c}+\frac{\hbar(g-2)}{2\Delta}\langle\sigma_z\rangle\omega^2\right]. \tag{4.1}$$

For an a.c. electric field, (4.1) shows the existence of an anomalous Hall effect, linked to the existence of a non-zero $(g-2)$. This is precisely the influence of the average magnetization through spin-orbit coupling which we looked for.

We would like now to discuss the orders of magnitude of this effect and the possibility of looking for its experimental observation.

We are primarily interested in materials such as SbIn for two reasons: the collision time is not too disastrous, so our model is likely to be valid in a wide range of frequencies; besides, the Landé g-factor is about 50, which provides high values of M^z.

Although the above calculations are intended to apply to a collisionless system, we may hope to obtain a good account of the collisions merely by replacing ω by $(\omega-i/\tau)$, as in the standard theories of electrical conductivity. σ_{xy} then

$$\sigma_{xy}=\frac{ne^2\tau}{m}\cdot\frac{\omega_c^{*2}}{\omega_c^{*2}\tau^2+(1+i\omega\tau)^2}$$

$$\left[\frac{1}{\omega_c}-\frac{\hbar g}{2\Delta}\langle\sigma_z\rangle\frac{(1+i\omega\tau)^2}{\omega_c^{*2}\tau^2}\right] \tag{4.2}$$

of course, (4.2) reduces to (4.1) if $\omega\tau \gg 1$ (which can be achieved at microwave frequencies). In a magnetic field of several kG, it is easy to have all spins parallel to $\vec{H}$. If we take the numerical values of SbIn ($\Delta=0{\cdot}27$ eV; $g=50$; $m^*=0{\cdot}013$ m) and a frequency of 10^{11} Hz, the normal part and the anomalous part in (4.1) are of the same order of magnitude so, in principle, they could be separated.

Another way of observing the anomalous effect is to have strictly $\omega_c=0$ so that σ_{xy} reduces to its anomalous part:

$$\sigma_{xy}=\frac{ne^2\tau}{m}\cdot\left(-\frac{\hbar g}{2\Delta\tau}\langle\sigma_z\rangle\right) \tag{4.3}$$

In order to have a non-zero $\langle\sigma_z\rangle$ even for $\omega_c=0$, the conduction electrons can be optically pumped; so far no experiment has been made on SbIn but values of 10^{-2} for $\langle\sigma_z\rangle$ are likely to be obtained; if so, $\omega_c=0$ actually means

$$|\vec{H}| \leqslant 10^{-3}\,\mathrm{G}$$

which can be achieved.

Acknowledgements—The authors are most grateful to Professor P. Nozières for suggesting this problem and for helpful discussions.

REFERENCES

1. KARPLUS R. and LUTTINGER J. M., *Phys. Rev.* **95**, 1154 (1954).
2. LUTTINGER J. M., *Phys. Rev.* **112**, 739 (1958).
3. GUREVICH L. E. and YASSIEVICH I. N., *Soviet Phys. solid St.* **4**, 209 (1963).
4. KAGAN Yu and MAKSIMOV L. A., *Soviet Phys. solid St.* **7**, 422 (1965).
5. NOZIERES P., *Le Problème à N Corps*, p. 36. Dunod, Paris (1963); *Theory of interacting Fermi Systems*. Benjamin, New York Amsterdam (1964).
6. LAX B. and MAVROIDES J. G., In *Solid State Physics*, Vol. 110 (Edited by F. Seitz and D. Turnbull) Academic Press, New York (1960).
7. YAFET Y., In *Solid State Physics* (Edited by E. Seitz and D. Turnbull), Vol. 14. Academic Press, New York (1963).
8. LUTTINGER J. M. and KOHN W., *Phys. Rev.* **97**, 864 (1955).
9. LAX B., MAVROIDES J. G., ZEIGER H. J. and KEYES R. J., *Phys. Rev.* **122**, 31 (1961).

APPENDIX A

According to (1.5)

$$\sigma_{xy}=-\frac{e^2}{i\hbar}\sum_{\nu}{}'\frac{j^x_{\mu\nu}j^y_{\nu\mu}-j^y_{\mu\nu}j^x_{\nu\mu}}{\omega^2-\omega^2_{\nu\mu}} \tag{A.1}$$

as for σ_{xx}, j^x and j^y, apart from purely diagonal matrix elements which are excluded by the Σ', connect only two different bands. Assuming that ω is much smaller than the band gap, we obtain

$$\sigma_{xy}=\frac{e^2}{i\hbar m^2}\sum\frac{\pi^x_{\mu\nu}\pi^y_{\nu\mu}-\pi^y_{\mu\nu}\pi^x_{\nu\mu}}{\omega^2_{\mu\nu}}. \tag{A.2}$$

The orbital moment $\vec{\mu}$ is connected to matrix elements of $\vec{\pi}$ [7]
by

$$\sum \frac{\pi^x_{\mu\nu}\pi^y_{\nu\mu} - \pi^y_{\mu\nu}\pi^x_{\nu\mu}}{\omega_{\mu\nu}} = -i\,\mu^z \frac{m}{\beta}. \tag{A.3}$$

If only two bands are considered, then

$$\sigma_{xy} = -2ec\frac{\mu_z}{\Delta} \tag{A.4}$$

where Δ is the band gap. More generally, σ_{xy} retains the same shape, since μ^z is connected to the antisymmetric combination $(\pi^x\pi^y - \pi^y\pi^x)$. Instead of $\omega_{\mu\nu}$, we introduce an 'average' band gap $\bar{\Delta}$ and we can write

$$\sigma_{xy} = -2ec\frac{\mu_z}{\bar{\Delta}} \tag{A.5}$$

per electron, of for the whole conduction band

$$\sigma_{xy} = -2ec\frac{M_z}{\bar{\Delta}} \tag{A.6}$$

$\vec{M}$ being the orbital magnetization.

APPENDIX B

We have to diagonalize

$$H_{0\mu\nu} = \left(E_\mu + \frac{\hbar^2\bar{k}^2}{2m}\right)\delta_{\mu\nu} + \frac{\hbar}{m}\vec{\pi}_{\mu\nu}\,.\,\vec{\bar{k}} \tag{B.1}$$

up to fourth order in $\bar{k}$. The procedure is straightforward: the unitary transformation $\exp S$ should be such that

$$\tilde{H}_0 = (\exp - S)H_0(\exp S) \tag{B.2}$$

has no off-diagonal interband elements of order $\leqslant 2$. (We do not explicitly separate the spin components: what is written as a scalar has to be handled as a 2×2 spinor.) Equation (B.2) may be expanded as

$$\tilde{H}_0 = H_0 + [H_0,S] + \tfrac{1}{2}[[H_0,S],S] + \tfrac{1}{6}[[[H_0,S],S],S] + \ldots \tag{B.3}$$

The first order part of S must cancel the first order off-diagonal elements of H_0, and so on. For a two band model, the explicit result is

$$S_{\mu\nu} = -\frac{\hbar}{m}\frac{1}{\omega_{\mu\nu}}\sum_\alpha \pi^\alpha_{\mu\nu}\bar{k}^\alpha - \frac{\hbar^3\omega_c}{im\omega^2_{\mu\nu}}(\pi^x_{\mu\nu}\bar{k}^y - \pi^y_{\mu\nu}\bar{k}^x)$$
$$+\frac{4}{3}\frac{\hbar^3}{m^3}\frac{1}{\omega^3_{\mu\nu}}\sum_\alpha\sum_\beta\sum_\gamma \pi^\alpha_{\mu\nu}\pi^\beta_{\nu\mu}\pi^\gamma_{\mu\nu}\bar{k}^\alpha\bar{k}^\beta\bar{k}^\gamma. \tag{B.4}$$

We have used extensively the following identity

$$[\bar{k}^x, \bar{k}^y] = \frac{im\omega_c}{\hbar}. \tag{B.5}$$

By making use of (B.1), (B.3), (B.4), (B.5) and (A.3), one obtains

$$\tilde{H}_{0\,\mu\mu} = E_\mu + \frac{h^2\bar{k}^2}{2m^*}\left[1 + \frac{2\vec{\mu}\,.\,\vec{H}}{\Delta}\left(1 - \frac{2m^*}{m}\right) - \frac{\hbar^2}{2\Delta}m^*\right.$$
$$\left.\left(\frac{1}{m^*} - \frac{1}{m}\right)^2 k^2\right] - \vec{\mu}\,.\,\vec{H} + \frac{\hbar^2}{m\Delta}(\vec{\bar{k}}\,.\,\vec{\mu})(\vec{\bar{k}}\,.\,\vec{H}) \tag{B.6}$$

(pure c-numbers have been deliberately omitted).

J. Phys. Chem. Solids Pergamon Press 1970. Vol. 31, pp. 825–843. Printed in Great Britain.

DIFFUSION OF VACANCIES AND VACANCY PAIRS IN NaCl†‡

VAUGHN C. NELSON§ and ROBERT J. FRIAUF
University of Kansas, Lawrence, Kansas 66044, U.S.A.

(*Received* 4 *November* 1968; *in revised form* 18 *July* 1969)

Abstract—Measurements are reported for pure NaCl crystals of intrinsic ionic conductivity (550°–800°C), diffusion of Na tracers (640°–790°C), and diffusion in a d.c. electric field of Na tracers (600°–770°C) and Cl tracers (690°, 770°C). The diffusion measurements in a field represent the first quantitative application of this technique to alkali halides and afford a direct determination of Na tracer drift mobilities from the observed displacement of the diffusion profile. A general experimental check is provided by showing that the sum of the cation and anion mobilities agrees with the total conductivity.

The results can be interpreted satisfactorily in terms of contributions to diffusion of *both* cations and anions from *both* free vacancies and neutral vacancy pairs. The best fit of all available conductivity, diffusion, and mobility data gives $D_c^*(\mathrm{Na}) = 182 \exp(-2\cdot10/kT)$ and $D_{pr}^*(\mathrm{Na}) = 1130 \exp(-2\cdot35/kT)$, with D_0 in cm²/sec and W in eV; vacancy pairs contribute nearly 40 per cent of the Na diffusion at the melting point. This fit gives an essentially constant anion transport number of 0·34 and an activation energy for cation diffusion by single vacancies of 2·10 eV; both of these are noticeably larger than previous values. It is also found that $D_{pr}^*(\mathrm{Na})$ is 6 to 7 times larger than $D_{pr}^*(\mathrm{Cl})$, just slightly above the limit imposed by the theory of correlation factors, which means that cation jumps into a vacancy pair have a much higher frequency than anion jumps, contrary to theoretical predictions. The diffusion data for vacancy pairs are not compatible with previously reported high temperature dielectric loss measurements. These data also rule out any appreciable contribution from cation Frenkel defects, but difficulty in fitting the conductivity suggests that vacancy triplets may make a small contribution.

1. INTRODUCTION‖

OBSERVATIONS of ionic conductivity and diffusion in alkali halides have been explained for many years by the presence of Schottky defects[1]. For some time attention was focussed almost exclusively on cation vacancies [2–4], and there seemed to be a fairly simple and complete picture[5]. More recent diffusion[6–8], transport number[9, 10], and conductivity experiments[11–14], however, have shown that there is an appreciable contribution of anion vacancies throughout the intrinsic region, in some cases exceeding 50 per cent at the melting point. A tangible contribution of vacancy pairs to transport processes was first seen in anion diffusion in crystals doped with divalent positive ions[15–17], and additional evidence for vacancy pairs seemed to be provided by observations of a relaxation peak in the dielectric loss at high temperatures[18–21]. Then an attempt to check the Einstein relation for diffusion of Na in NaCl revealed a small extra amount of diffusion that was tentatively attributed to vacancy pairs[22], and similar results were observed for self-diffusion in TlCl[23]. Finally the results in this paper will show that vacancy pairs do, indeed, make an appreciable contribution to cation diffusion in NaCl, amounting to 40 per cent at the melting point.

We are thus led to consider the following

---

†Work supported by the U.S. Atomic Energy Commission. This is Technical Report COO-1197-32.

‡This work is based in part on a thesis submitted by V. C. N. in partial fulfillment of the requirements for the Ph.D. degree.

§*Present address*: West Texas State University, Canyon, Texas 79015, U.S.A.

‖Preliminary accounts of this work have been presented in *Mass Transport in Oxides* (Edited by J. B. Wachtman, Jr. and A. D. Franklin), p. 9. National Bureau of Standards Special Publication 296, Washington, D.C. (1968), and in *Color Centers in Alkali Halides*, 1968 International Symposium, Rome, p. 218 (1968).

contributions to diffusion and ionic conductivity in a pure crystal at high temperatures.

$$D^*(\mathrm{Na}) = D_v^*(\mathrm{Na}) + D_{pr}^*(\mathrm{Na}) \qquad (1)$$

$$D^*(\mathrm{Cl}) = D_v^*(\mathrm{Cl}) + D_{pr}^*(\mathrm{Cl}) \qquad (2)$$

$$\sigma_v(\mathrm{Cl}) = \sigma_v(\mathrm{Na}) + \sigma_v(\mathrm{Cl}). \qquad (3)$$

The free vacancy contributions $D_v^*(\mathrm{Na})$, $\sigma_v(\mathrm{Na})$ and $D_v^*(\mathrm{Cl})$, $\sigma_v(\mathrm{Cl})$ are related by the Einstein equations

$$\begin{aligned} D_v^*(\mathrm{Na}) &= f_v(kT/N_0e^2)\sigma_v(\mathrm{Na}), \\ D_v^*(\mathrm{Cl}) &= f_v(kT/N_0e^2)\sigma_v(\mathrm{Cl}), \end{aligned} \qquad (4)$$

where N_0 is the total number of molecules per unit volume in the crystal and $f_v = 0{\cdot}78146$ is correlation factor for vacancy diffusion on a f.c.c. lattice[24, 25]. The vacancy pair contributions, $D_{pr}^*(\mathrm{Na})$ and $D_{pr}^*(\mathrm{Cl})$ to cation and anion diffusion, respectively, are not necessarily equal[25, 26], however, (see Section 2B) and thus there remain four independent terms on the right hand side of equations (1–3). Hence the measurement of the three directly observable quantities $D^*(\mathrm{Na})$, $D^*(\mathrm{Cl})$, and σ on the left hand side is not sufficient to determine the defect contributions uniquely, and some additional experiments are needed.

In previous work the vacancy pair contribution to anion diffusion was separated from the free vacancy contribution by adding divalent positive ions to suppress the concentration of free anion vacancies[15–17]. In the present work the contribution of free vacancies is distinguished from that of vacancy pairs in a pure crystal by applying an electric field during diffusion. The free vacancies should drift along the field because of their charge, thereby giving an independent measure of their mobility, whereas the vacancy pairs should be unaffected by the field because of their electric neutrality. A few previous measurements have been made of diffusion of ions in an electric field[27, 28], but in only one case has this method been used to distinguish between charged and neutral defects [27]. Most of the experiments reported here are for cation diffusion, but two check points have also been obtained for anion diffusion.

Recently several additional types of charged defects have been postulated because of difficulty in fitting the conductivity curve with Schottky defects only[29, 30]. By using our diffusion and drift mobility measurements we are able to show that the presence of cation Frenkel defects[29] is unlikely but that a small contribution from vacancy triplets[30] is possible.

2. THEORY

A. *Ionic conductivity, diffusion and drift mobility*

The theory of ionic defects has been reviewed by Lidiard[31], and we shall follow his notation for the most part. In the intrinsic region free cation and anion vacancies are present with mole fractions $x_c = x_a = x_0$ given by the Schottky equilibrium.

$$x_cx_a = x_0^2 = \exp(s_s/k)\exp(-h_s/kT). \qquad (5)$$

The cation vacancies have a jump frequency†

$$\nu_c = 12\nu_0 \exp(\Delta s_c/k)\exp(-\Delta h_c/kT), \qquad (6)$$

and the microscopic diffusion coefficient and mobility are given by

$$d_c = \tfrac{1}{6}\nu_c a^2 = \tfrac{1}{3}\nu_c a_0^2,\quad \mu_c = \tfrac{1}{3}(ea_0^2/kT)\nu_c, \qquad (7)$$

where $a = \sqrt{2}a_0$ is the jump distance (a_0 is half the lattice parameter). These are clearly related by the microscopic Einstein equations [1].

$$d_c/\mu_c = d_a/\mu_a = kT/e. \qquad (8)$$

---

†Notice that ν_c is the total jump frequency for the vacancy in accordance with the first expression for d_c in equation (7). For simplicity of notation we shall use the same attempt frequency $\nu_0 = 4{\cdot}91 \times 10^{12}$Hz for all types of jumps[29].

The contributions to cation diffusion and ionic conductivity are

$$D_v^*(\mathrm{Na}) = f_v x_c d_c, \quad \sigma_v(\mathrm{Na}) = eN_0 x_c \mu_c = \sigma_c, \tag{9}$$

and these combine to give the macroscopic Einstein relation of equation (4).

The mole fraction of vacancy pairs is given by

$$x_{pr} = 6 \exp(s_{pr}/k) \exp(-h_{pr}/kT), \tag{10}$$

and it has been emphasized by Lidiard[32] that this concentration is independent of the impurity content of the crystal. The frequency for a cation jump into a vacancy pair is†

$$\nu_c' = 4\nu_0 \exp(\Delta s_c'/k) \exp(-\Delta h_c'/kT). \tag{11}$$

The microscopic diffusion coefficient may be defined as

$$d_c' = \tfrac{1}{6}\nu_c' a^2 = \tfrac{1}{3}\nu_c' a_0{}^2, \tag{12}$$

and the macroscopic diffusion coefficient[25] is then

$$D_{pr}^*(\mathrm{Na}) = f_c' x_{pr} d_c'. \tag{13}$$

It is interesting to compare the contributions to diffusion to be expected from vacancy pairs and free vacancies. If the temperature variation of f_c' is neglected for the moment, we have

$$D_{pr}^*(\mathrm{Na})/D_v^*(\mathrm{Na}) \approx C \exp(-W/kT),$$

with

$$W = (h_{pr} - \tfrac{1}{2}h_s) + (\Delta h_c' - \Delta h_c).$$

With upper limits of $h_s = 2{\cdot}17$ eV from[29] and $\Delta h_c = 1{\cdot}01$ eV from our work, and with $h_{pr} = 1{\cdot}27$ eV and $\Delta h_c' = 1{\cdot}46$ eV from theory [33], we find $h_{pr} - \tfrac{1}{2} h_s = 0{\cdot}18$ eV and $\Delta h_c' - \Delta h_c = 0{\cdot}45$ eV. Both of these quantities are positive, which means that the relative contribution of vacancy pairs should *increase* as temperature increases. The first term shows that even the relative concentration of vacancy pairs increases (free vacancies are formed more rapidly than vacancy pairs can dissociate because the binding energy $\Delta h_b = h_s - h_{pr} = 0{\cdot}91$ eV is less than $\tfrac{1}{2} h_s$), and the larger activation enthalpy for vacancy pair jumps enhances the effect considerably. Similar conclusions follow for anion vacancies with $\Delta h_a' - \Delta h_a = 1{\cdot}27[33] - 1{\cdot}00$ (our work) $= 0{\cdot}27$ eV. Thus we expect the largest contributions of vacancy pairs to appear at the very highest temperatures approaching the melting point.

We shall also need an expression for the drift mobility of a radioactive tracer ion in an electric field E_0. We may obtain this by considering the particle current densities for vacancies and ions,

$$J_{\mathrm{vac}} = N_0 x_c \mu_c E_0, \quad J_{\mathrm{ion}} = N_0 \mathrm{M}_v(\mathrm{Na}) E_0, \tag{14}$$

where $\mathrm{M}_v(\mathrm{Na})$ is the macroscopic mobility for cations.† These current densities must be equal since every time a vacancy moves one direction an ion moves in the opposite direction, and we obtain immediately

$$\mathrm{M}_v(\mathrm{Na}) = x_c \mu_c = \sigma_v(\mathrm{Na})/eN_0. \tag{15}$$

This result is to be contrasted to equations (9) and (13) for diffusion, where correlation factors appear. The absence of a correlation factor in equation (15) is clear from the 'vacancy wind' effect described above and is also deducible from other treatments of correlation factors[34]. The conductivity can now be expressed very simply in terms of the macroscopic mobilities,

$$\sigma = \sigma_c + \sigma_a = eN_0 [\mathrm{M}_v(\mathrm{Na}) + \mathrm{M}_v(\mathrm{Cl})]. \tag{16}$$

---

†It is assumed that the cation comes from one of the four neighboring positions that will leave the vacancy pair bound after the jump. Dissociation jumps are not considered.

†The use of M (capital μ) for macroscopic mobilities is analogous to the use of D for macroscopic diffusion coefficients.

B. *Correlation factors for vacancy pairs*

A vacancy pair moves through the lattice by a kind of tumbling motion that involves a mixed sequence of both cation and anion jumps with frequencies ν_c' and ν_a'. Hence there is a relationship between the contributions to cation and to anion diffusion; the interdependence enters through the correlation factors, which are functions of the frequency ratio $\phi' = \nu_a'/\nu_c'$.

$$f_c' = f_{pr}(\phi'),\ f_a' = f_{pr}(1/\phi'). \qquad (17)$$

The function $f_{pr}(\phi')$ for the NaCl structure has been calculated by several authors[25, 26] and is shown in Fig. 1. The limiting behavior is[10]

$$\lim_{\phi'\to 0} f_{pr}(\phi') = b\phi',\quad \lim_{\phi'\to\infty} f_{pr}(\phi') = f_v. \qquad (18)$$

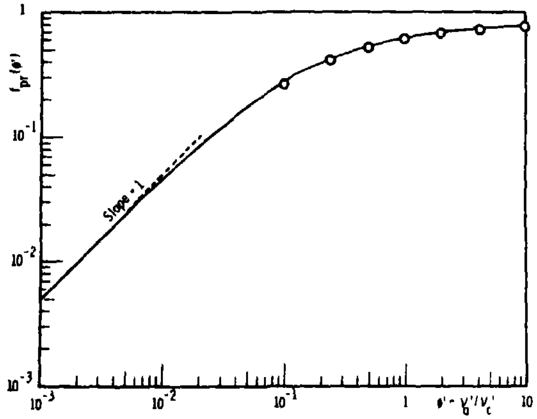

Fig. 1. Correlation factor vs. frequency ratio for diffusion by vacancy pairs on the NaCl lattice. ——— Howard[26]. ○ Compaan and Haven[25].

Howard's[26] value of b has been corrected from 5·0 to 4·4 by extrapolation of the more accurate results of Compaan and Haven [25].

The ratio of anion to cation diffusion by vacancy pairs is given by

$$\frac{D_{pr}^*(\mathrm{Cl})}{D_{pr}^*(\mathrm{Na})} = \frac{f_a' x_{pr} d_a'}{f_c' x_{pr} d_c'} = \frac{\phi' f_{pr}(1/\phi')}{f_{pr}(\phi')} \equiv F(\phi'). \qquad (19)$$

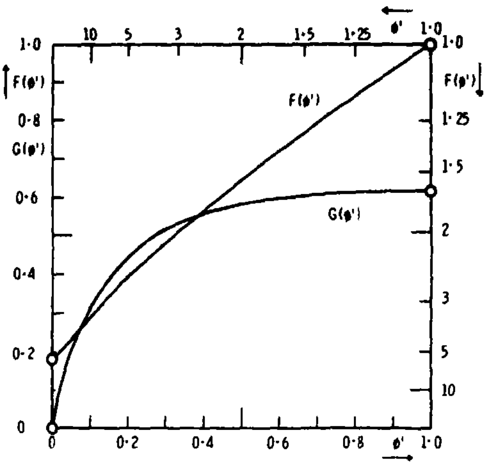

Fig. 2. Functions for diffusion by vacancy pairs on the NaCl lattice. $F(\phi')$ is the ratio of anion to cation diffusion. $G(\phi')$ is the correction factor for the sum of anion and cation diffusion.

The function $F(\phi')$ is shown in Fig. 2 and has the following properties:

$$F(1/\phi') = 1/F(\phi')$$

$$\lim_{\phi'\to 0} F(\phi') = f_v/b = 0{\cdot}178,$$

$$\lim_{\phi'\to\infty} F(\phi') = b = f_v = 5{\cdot}6.$$

When both $D_{pr}^*(\mathrm{Cl})$ and $D_{pr}^*(\mathrm{Na})$ can be determined experimentally, these limits provide a check for the consistency of the interpretation of the experimental results.† In favorable cases it may even be possible to determine ϕ' as a function of temperature by using equation (19) in reverse.

In other situations it may be possible to determine only the sum of the two vacancy pair contributions to diffusion[22, 23] or the sum of the two jump frequencies $\nu_c' + \nu_a'$. The latter possibility occurs if the interpretation of the high temperature dielectric loss peak in terms of vacancy pairs is correct[21]. A treatment similar to that given by Lidiard for cation vacancy-divalent ion complexes

---

†Lidiard[32] previously gave limits of 0·26 = 1/3·8 because of a smaller estimate of $b = 3$ from the results of Compaan and Haven[25]. More recently Haven[10] quoted values similar to those given here.

[35] shows that the relaxation time for vacancy pairs is

$$\tau = (\nu_c' + \nu_a')^{-1}. \tag{20}$$

A partial analysis in these circumstances may be made by considering

$$D_{pr}^*(\mathrm{Na}) + D_{pr}^*(\mathrm{Cl}) = \tfrac{1}{3} a_0{}^2 x_{pr}(\nu_c' + \nu_a') G(\phi') \tag{21}$$

with

$$G(\phi') = [f_{pr}(\phi') + \phi' f_{pr}(1/\phi')][1+\phi']^{-1}. \tag{22}$$

This function is also shown in Fig. 2 and has the following properties.

$$G(1/\phi') = G(\phi'), \lim_{\phi' \to 0} G(\phi') = (b + f_v)\phi'$$

$$G_{\max} = G(\phi' = 1) = f_{pr}(\phi' = 1) = 0{\cdot}6189.$$

These results show that the total contribution of vacancy pairs is always diminished to some extent by the correlation factors[23], even in the most favorable case of $\phi' \sim 1$, and the diminution becomes appreciable when ϕ' is outside the range of 0·1–10.

C. *Diffusion equations*

The diffusion experiments are performed by placing a very thin layer containing radioactive tracers between two flat crystal slabs, which are much thicker than $\langle x \rangle$ or x_{rms} defined below. A steady electric field is applied perpendicular to the initial interface, and the tracer current then contains a drift term from equation (14) as well as the usual term from the concentration gradient

$$J_x^* = -D^*(\partial n^*/\partial x) + n^* \mathrm{M}_v E. \tag{23}$$

If E is independent of x (but not necessarily of t), the diffusion equation becomes

$$\frac{\partial n^*}{\partial t} = D^*\left(\frac{\partial^2 n^*}{\partial x^2}\right) - M_v E\left(\frac{\partial n^*}{\partial x}\right). \tag{24}$$

The solution for the initial and boundary conditions described above is

$$n^*(x,t) = [B/(4\pi D^* t)^{1/2}] \exp[-(x-x_0)^2/4D^*t] \tag{25}$$

where B is the initial amount of tracer per unit area. When M_v and E are independent of time

$$x_0(t) = M_v E t, \tag{26}$$

and when M_v and E vary with time

$$x_0(t) = \int_0^t M_v(\tau) E(\tau) \mathrm{d}\tau. \tag{27}$$

The average and root-mean-square displacements are

$$\langle x \rangle = B^{-1} \int_{-\infty}^{\infty} x n^*(x,t) \mathrm{d}x = x_0, \tag{28}$$

$$x_{rms}^2 = B^{-1} \int_{-\infty}^{\infty} (x - x_0)^2 n^*(x,t) \mathrm{d}x = 2D^*t. \tag{29}$$

Thus the field produces a drift of the diffusion profile that is proportional to the mobility but does not influence the amount of spreading.

In order to maintain a steady electric field in an ionic crystal, a steady current must pass through the electrodes, and this often causes some deterioration of the crystal near the electrodes. Furthermore the contact between the two crystal slabs is initially not very good and gradually improves during the rather long times (~ 20 hr) involved in diffusion measurements. For both of these reasons the field near the interface is likely to undergo variations with time, and it is necessary to determine the average field defined by the integral in equation (27) as follows[23]. A silver coulometer is inserted in series with the voltage source and the crystal, and $E = I/\sigma A$ is expressed in terms of the steady current I, the area of the crystal A, and the conductivity σ. Also E is applied only while the crystal is maintained at a constant temperature so that M_v and σ may be taken outside the integral. Then

$$x_0 = (M_v/\sigma A)\int_0^t I(\tau)\mathrm{d}\tau = M_vQ/\sigma A, \quad (30)$$

where Q is the total charge measured by the coulometer. After x_0 is determined from the displacement of the diffusion profile, M_v is calculated directly from equation (30).

In the experimental diffusion profiles there often seems to be a small discontinuity in both concentration and concentration gradient at the interface between the two crystals (see Fig. 3). An attempt was made to obtain corresponding features in the solutions of the diffusion equations by introducing a barrier to diffusion at the interface.

$$[-D^*(\partial n_1^*/\partial x)+M_vEn_1^*]_{x=+0} = D^*H(n_1^*-n_2^*)$$
$$= [-D(\partial n_2^*/\partial x)+M_vEn_2^*]_{x=-0} \quad (31)$$

where n_1^* and n_2^* are the solutions for $x > 0$ and $x < 0$ respectively. The strength of the barrier is determined by the parameter H: when $H = 0$ there is no current flow across the interface and the barrier is complete; when $H = \infty$ the current flow is unrestricted and $n_1^*(0) = n_2^*(0)$ as for no barrier. The solution without a field is given in Carslaw and Jaeger[36], and a similar method was used to obtain a solution with a field. When a barrier is present the simple solution in equation (25) must be multiplied by the following correction factors.

$$\begin{Bmatrix} C_1 \\ C_2 \end{Bmatrix} = \begin{Bmatrix} 2 \\ 0 \end{Bmatrix} \mp \begin{Bmatrix} (F+b) \\ H \end{Bmatrix} (H+F)F^{-1}(\pi D^*t)^{1/2} \exp u^2 \, erfc\, u$$
$$- \begin{Bmatrix} (F-b) \\ H \end{Bmatrix} (H-F)F^{-1}(\pi D^*t)^{1/2} \exp z^2 \, erfc\, z, \quad (32)$$

where

$$\begin{Bmatrix} u \\ z \end{Bmatrix} = (4Dt)^{-1/2}|x| + (Dt)^{1/2}(H \pm F).$$
$$F = (H^2+b^2)^{1/2}, b = x_0/2Dt.$$

Curves obtained from this solution are shown in Fig. 3.

3. EXPERIMENTAL

A. *Procedures*†

Conductivity runs were made on crystals of pure NaCl from the Harshaw Chemical Co. and also on crystals grown in this laboratory in air from analytical reagent grade powder. From the upper limit of the extrinsic range for conductivity at 490°C it is estimated that both types of crystals do not contain appreciably more than 1 ppm divalent impurity. Samples for both conductivity and diffusion were cleaved along (100) planes to dimensions of approximately 10 × 10 × 2·5 mm.

The same sample holder was used for both conductivity and diffusion experiments in order to eliminate any difficulty in comparing temperatures. The sample was held by light spring pressure between Pt electrodes, and a Pt vs. Pt–10% Rh thermocouple was welded directly to the bottom electrode. This assembly was mounted in a long quartz tube, which was evacuated to less than 10^{-5} Torr before each experiment and then filled with pure He gas to a pressure of about 1 atm. The furnace temperature was controlled to ±0·2°C with a standard on–off controller.

Electrodes of graphite suspended in isopropyl alcohol (Aquadag) were applied directly to the sample faces for most of the conductivity measurements, and these were quite stable even for several hours at 798°C. No difference in results was obtained for one run with electrodes of dry spectroscopic pure graphite (see Fig. 4). The sample resistance was usually measured at 1 kHz with a General Radio capacitance bridge and decade resistors; frequent checks at 0·27, 10 and 100 kHz showed that polarization effects were not important. Conductivity measurements for different samples differed by up to 2 per cent, but measurements on a single sample were repeatable within 0·5 per cent, whether the temperature was held constant for 30 min or was changing at a rate up to 1°C/min.

---

† More details are available in [37].

For diffusion measurements a thin layer of NaCl containing the tracer was evaporated onto a Harshaw crystal in vacuum. The isotopes used were ^{22}Na (half-life 2·6 yr, carrier free) and ^{36}Cl (half-life 4×10^5 yr, specific activity 15 mc/g). Temperature measurements were made every 10 sec during heating and cooling and every 10 min at the diffusion temperature with a Non-Linear Systems digital voltmeter. An effective diffusion time at the equilibrium temperature T_0 was calculated from these data on punched cards according to

$$t_{\text{eff}} = [D(T_0)]^{-1} \times \int_0^\infty D(T)\,\mathrm{d}t.$$

Since the time at T_0 was usually 10–20 hr (extreme values 2 hr and 8 days), the correction for heating and cooling was only a few per cent of the total time in most cases. After a diffusion run the edges of the sample were removed, and then slices of 6–10 μ were cut with a microtome, weighed on a semimicro balance, and counted with a Geiger–Mueller tube (10,000 counts minimum). With double samples the two samples could be separated at the initial interface with slight pressure from a razor blade, and slices were taken in both samples away from this interface. The error in the diffusion coefficient given by the computer-calculated least squares fit was 1–2 per cent for single samples and 1–4 per cent for double samples.

For diffusion without a field single samples were used in most cases. For experiments with an electric field double samples were used, with the tracer evaporated onto one of the inner faces and Aquadag electrodes applied to the outer faces. In these circumstances the apparent conductivity was initially too small by the order of 50 per cent and showed only gradual improvement with time, and values of the diffusion coefficient from the two sides of the interface differed by 5–10 per cent, even for three trials with double samples without a field. The following attempts were made to improve the contact at the interface, but none showed any particular signs of success. (1) The two samples were prepared by cleaving a single crystal and replacing the two pieces in the same orientation after evaporation of the tracer. (2) The tracer was evaporated onto both of the common faces, and the crystals were then rubbed together before mounting in the sample holder. (3) For one run a layer of Aquadag was placed between the two samples at the interface. (4) For another run a heat pulse up to 798°C was applied in the furnace before stabilizing at the diffusion temperature.

In order to apply and measure the d.c. field and current, the sample was placed in series with a 300 V power supply, a resistance box, an ammeter, and a Ag coulometer. The coulometer consisted of 15 g of $AgNO_3$ in 100 ml of de-ionized water, a pure Ag rod, a porous cup, and a Pt screen that was weighed before and after the run[38]. The total charge usually agreed with the current measured by the ammeter within the expected accuracy of 1 per cent. With approximately 100 V across the sample the current varied from 0·3 mA at low temperatures to 3 mA at high temperatures, giving a total charge of 30–100 C. This caused a displacement of the maximum in the diffusion profile by 40–200 μ in most cases.

B. *Diffusion profiles*

Two diffusion profiles for diffusion with a field are shown in Fig. 3. The upper curve is typical of the more satisfactory results obtained at higher temperatures (690–770°C), and the lower curve is illustrative of the less satisfactory behavior found at lower temperatures (600–660°). The solution of the diffusion equation without a barrier in equation (25) gives a parabola for $\ln n^*$ vs. x, and the least squares fit of this equation gives values of B, D^*, and x_0 and the solid curves in Fig. 3. Because of the break in the diffusion profiles at the interface ($x = 0$) the

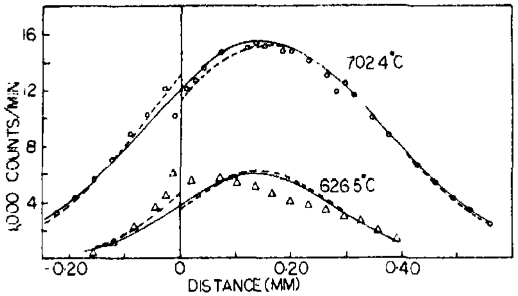

Fig. 3. Diffusion profiles for Na in NaCl with a d.c. electric field. The open circles and triangles give actual points obtained by sectioning for two different runs. The solid curves are the least squares fit without a barrier, equation (25), and the dotted curves are the fit with a barrier, equation (32). The initial interface is at $x = 0$, and the field is applied along the positive axis.

solution with a barrier in equation (32) is also fit by a trial and error procedure in which the four parameters B, D^*, x_0, and H are varied over limited ranges starting from the values with no barrier. A comparison of the two types of fit is shown by the points in Figs. 6 and 7; subsequent calculations are based on the fit without a barrier.

The diffusion profiles at higher temperatures are fit reasonably well, except for an occasional point right at the interface, and the values obtained without and with a barrier are in rather good agreement. The fit at lower temperatures is much less satisfactory, however, and indicates that other phenomena not included in the diffusion equations are occurring in the samples. Observations following passage of the d.c. current confirm this view: there was invariably deposition of salt at the cathode and decomposition of the sample at the anode, and in two cases (Na at 793°C and Cl at 692°C) easily visible holes developed from the anode and extended well into the sample, causing complete or partial shorting of the sample resistance (the holes were filled with graphite). It seems probable that in these extreme cases, and to a lesser extent in all cases, the initial contact at the interface is good on an atomic scale at only a few, sharply defined points, leading to a highly localized concentration of current flow and electric field lines. There is then an enhanced displacement of tracers along these 'tubes' of high electric field, and this causes the extended tail visible in Fig. 3 and the abnormally large diffusion coefficients for the experiments with a field (the open points at the four lowest temperatures in Fig. 6). Unfortunately the spatial distortion of the electric field in the diffusion region near the interface also introduces a further uncertainty into the determination of the tracer drift mobilities, for this invalidates the assumption made in obtaining the diffusion equation (24) that the field is independent of position. Since the amount of the distortion varies in an unknown way with time as the contact gradually improves during the diffusion run, it appears that the only way to avoid this problem is to obtain a major improvement in the initial contact.

C. *Results*

Conductivity measurements are shown in Figs. 4 and 5.† The results in Fig. 4 show no systematic difference between the Harshaw crystals and ours but do indicate the small variations between samples. In order to simulate conditions for a diffusion run, the sample for Fig. 5 was heated rapidly to 647°C, held there for 17 hr, and then heated slowly to 797°C. The slight break in these results at 647°C shows that there was a small decrease of conductivity during the time the sample was held at this temperature; for many of the diffusion samples there was a comparable decrease, ranging from 3 per cent at 640° to 1 per cent at 750° and occurring mostly within the first 3–5 hr at temperature. A similar behavior was reported by Barr and Schroeder [16], who attributed it to solution of impurities; annealing of dislocations might also give this effect.

Apparent activation energies for intrinsic conductivity were obtained from graphs of

---

†Tables of conductivity, diffusion, and mobility data are available in [37].

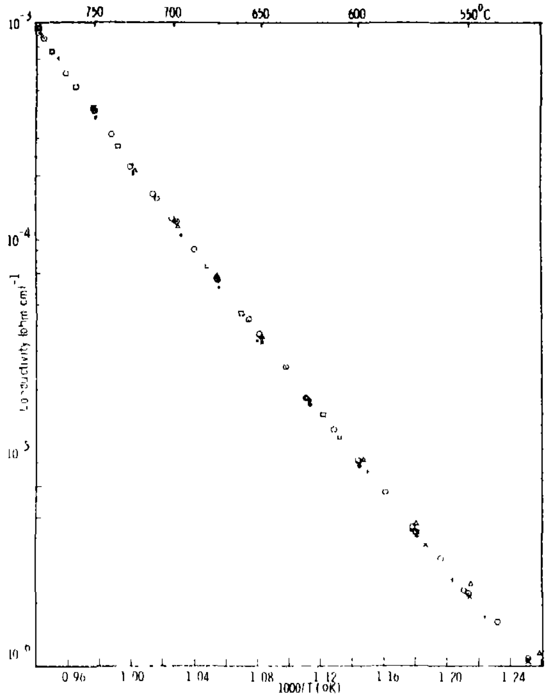

Fig. 4. Intrinsic ionic conductivity for NaCl. ● ○ △ + Harshaw crystals. × ⊙ □ Crystals grown in this laboratory. × and ⊙ are for the same sample with pure carbon electrodes in the first case and Aquadag electrodes in the second. The lower end of the intrinsic range is taken as 550°C, but the changeover to extrinsic behavior (not shown) is centered at about 490°C.

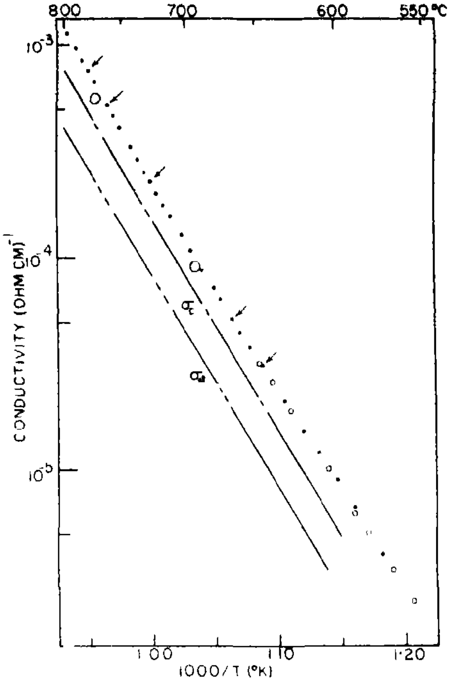

Fig. 5. Conductivity measurements on a Harshaw NaCl crystal. ● increasing temperature, ○ decreasing temperature, ← equilibrium temperatures. The two large open circles show the conductivity calculated from the sum of the cation and anion drift mobilities according to equation (16). The lines labeled σ_c and σ_a show the cation and anion contributions according to the fit of equation (39).

log (σT) vs. $1/T$. The values of 1·92 eV (550–650°C) to 2·19 eV (720–800°C) compare satisfactorily with the previously reported range of 1·84–1·99 eV (550–700°C) [2–5, 22, 39–45].

Diffusion coefficients for Na tracers with and without an electric field are shown in Fig. 6. If the abnormally large values of D^*(Na) with field at low temperatures are excluded, the values with field show no systematic variation from those without field. There are not enough data to warrant a two-exponential fit, as was done by Barr *et al.* for Cl diffusion[16], and the results of Downing were obtained with a different batch of samples, sample holder, and temperature range[22]. Hence the data from this work were fit with a single exponential of the usual form.

$$D(T) = D_0 \exp(-W/kT).$$

Our results are compared to other values in Table 1.

The tracer drift mobility M_v is obtained from the displacement x_0 of the diffusion profile and the average electric field, and gives directly the transport of Na ions through the crystal in an electric field. If we assume that this transport is due entirely to motion of free vacancies, we may convert to the corresponding diffusion coefficient by means of the Einstein relation

$$D_v^*(\text{Na}) = f_v(kT/e)M_v(\text{Na}). \qquad (33)$$

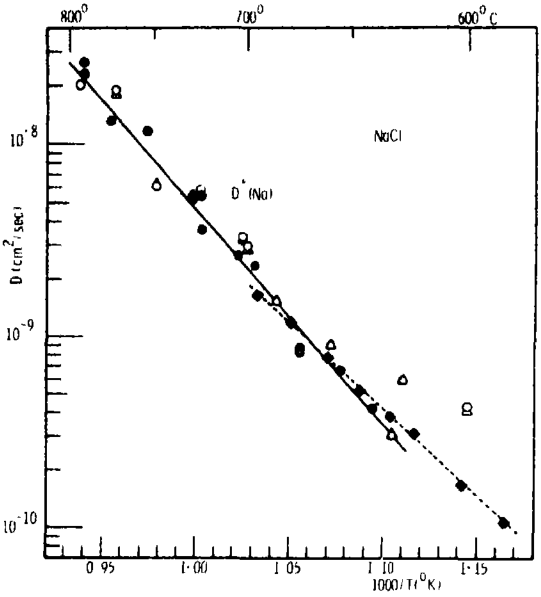

Fig. 6. Diffusion of Na in NaCl. ● without field, this work; ♦ without field, Downing[22]; ○ with field, no barrier (equation (25)); △ with field, with barrier (equation (32)).

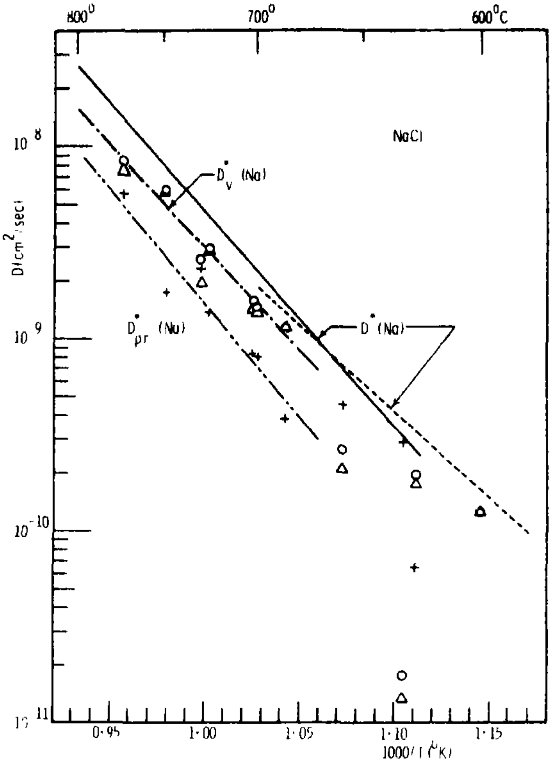

Fig. 7. Diffusion of cations by free vacancies and by vacancy pairs in NaCl. D_r^*(Na) is calculated from the measured tracer drift mobility (equation (33)), and D_{pr}^*(Na) is then obtained by subtraction from D^*(Na) (equation 1). Free vacancies ○ no barrier, △ with barrier. Vacancy pairs: + no barrier. The lines for D^*(Na) are from Fig. 6.

These results are shown in Fig. 7, where it is evident that some additional, neutral transport mechanism is needed to account for the total diffusion coefficient. Our proposal is that vacancy pairs provide this mechanism. The difference between the smoothed value of D^*(Na), represented by the solid line in Fig. 6, and the actual value of D_r^*(Na) at each temperature is therefore indicated by the points labeled D_{pr}^*(Na) in Fig. 7. The least squares fits (with the exclusion of the four lowest temperature points) for D_r^*(Na) and D_{pr}^*(Na) are shown by the dash-dot and dash-dot-dot lines.

$$D_r^*(\mathrm{Na}) = 182 \exp(-2{\cdot}10/kT) \qquad (34)$$

$$D^*(\mathrm{Na}) = 1130 \exp(-2{\cdot}35/kT). \qquad (35)$$

Table 1. *Apparent activation energies for diffusion of* Na *in* NaCl

Ref	Temp. (°C)	D_0 (cm²/sec)	W (eV)
Mapother *et al.*[4]	520–720	4·6†	1·80
Laurent and Benard[7]	600–795	0·5	1·61
Downing and Friauf[22]	585–695	3·2	1·78 ± 0·03
This work	640–790	790	2·23 ± 0·08

†This value is obtained from their graph; the value listed in their table is 3·1.

Two runs were also made with Cl tracers in order to provide an overall check on the experimental technique of measuring drift mobilities, and the corresponding diffusion coefficients $D_r^*(\mathrm{Cl})$ are shown in Fig. 8. There is rather good agreement with Laurance's results[15] and order of magnitude agreement with those of Barr *et al.*[16], and the same is true for $D^*(\mathrm{Cl})$ at the higher temperature.† Values of $D_{pr}^*(\mathrm{Cl})$ shown in Fig. 9 were obtained by subtracting from Laurance's $D^*(\mathrm{Cl})$ according to equation (2). The overall check is provided by comparing $M_r(\mathrm{Na}) + M_r(\mathrm{Cl})$ to the total conductivity according to equation (16). The results are shown by the open circles in Fig. 5; the sum is small by 7 per cent at the lower temperature and 14 per cent at the higher. These errors are well within the possible uncertainties associated with the contact problems at the interface and the non-uniform electric field inside the sample and give a reasonable indication of the general reliability of the present mobility measurements.

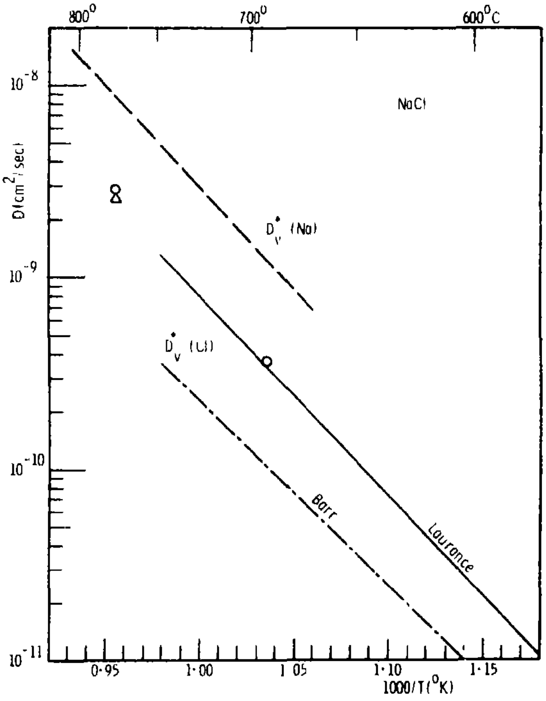

Fig. 8. Diffusion of anions by free vacancies in NaCl. $D_r^*(\mathrm{Cl})$ is calculated from the drift mobility of Cl tracers (equation 33). ○ no barrier, △ with barrier. The lines give the average results of Laurance[15] as calculated by Fuller and Reilly[13] and of Barr et al.[16]. $D_r^*(\mathrm{Na})$ is shown from Fig. 7 for comparison.

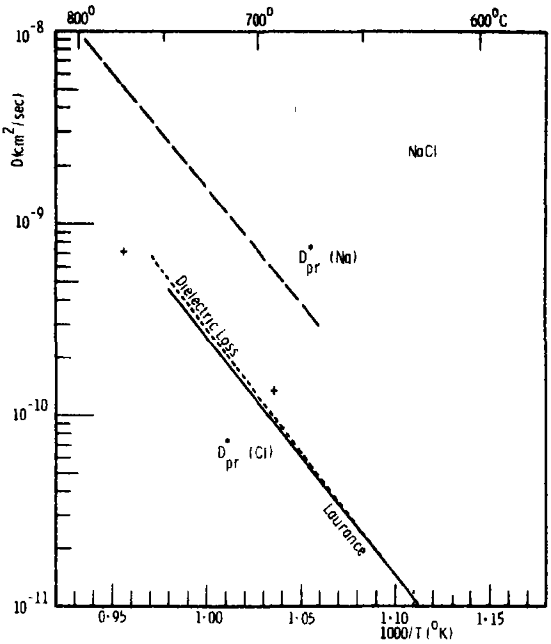

Fig. 9. Diffussion of anions by vacancy pairs in NaCl. The points are obtained (equation 2) by subtracting $D_r^*(\mathrm{Cl})$ from $D^*(\mathrm{Cl})$ given by Laurance[15]. The lines give the average results of Laurance[13, 15], and $D_{pr}^*(\mathrm{Na})$ is shown from Fig. 7 for comparison. The dotted line gives the maximum possible contribution to diffusion calculated from dielectric loss measurements and should be compared to $D_{pr}^*(\mathrm{Na}) + D_{pr}^*(\mathrm{Cl})$.

4. DISCUSSION

A. *Vacancy pairs*

The basic thesis of this paper is that vacancy pairs make an appreciable contribution to diffusion of both cations and anions as expressed in equations (1) and (2). The free vacancy and vacancy pair contributions for cations have been separated by measuring the cation drift mobility in pure crystals and subtracting the corresponding free vacancy diffusion coefficient from the total cation diffusion in Fig. 7. The contributions for anions have been previously separated by studying diffusion of Cl in doped crystals [15, 16], and these results have been confirmed by the two measurements of anion drift mobility shown in Figs. 8 and 9. Thus for the first time data are available for both cation and anion jumps into vacancy pairs, and we shall explore some of the consequences in this section. Since our experimental results for anions are generally in better agreement with those of Laurance[15] as recalculated by Fuller and Reilly[13], we shall use these values for anion diffusion for the following calculations.

---

†At the lower temperature holes developed part way through the sample, the diffusion profile was badly distorted, and the value of $D^*(\mathrm{Cl})$ was abnormally large, as for Na at lower temperatures.

We may first check whether the proposed vacancy pair contributions are compatible within the limits imposed by the theory of correlation factors in equation (19) and Fig. 2. A glance at Fig. 9 shows that $D_{pr}^*(\mathrm{Na})$ is appreciably larger than $D_{pr}^*(\mathrm{Cl})$ at all temperatures, and in the region of direct determination of both quantities (670°–750°C) the ratio $F(\phi')$ varies from 0·14 to 0·17. These values are slightly below the theoretical minimum of 0·178 from Section 2; an extrapolation of $D_{pr}^*(\mathrm{Cl})$ to 790° gives $F = 0{\cdot}179$, which is right at the limit. Thus if we wish to interpret the second mechanism for cation diffusion as being due to vacancy pairs, we must conclude that $F(\phi')$ has essentially its minimum value and that therefore $\nu_a' \ll \nu_c'$. In this case the limiting forms of the correlation factors in equation (18) apply, and we find

$$D_{pr}^*(\mathrm{Na}) = \tfrac{1}{3}a_0^2 b\, x_{pr}\, \nu_a'$$
$$D_{pr}^*(\mathrm{Cl}) = \tfrac{1}{3}a_0^2 f_c\, x_{pr}\, \nu_a'. \qquad (36)$$

The most noteworthy feature of this result is that both cation and anion contributions are governed by the smaller anion jump frequency.

The contribution of vacancy pairs to diffusion may also be compared to the information from high temperature dielectric loss measurements[21]. The height and the frequency of the relaxation peak presumably give the concentration x_{pr} and the sum of the frequencies $\nu_c' + \nu_a'$ according to equation (20). The maximum contribution to $D_{pr}^*(\mathrm{Na}) + D_{pr}^*(\mathrm{Cl})$ can then be calculated from equation (21) using $G_{\max}$. The result is shown by the dotted line in Fig. 9, and it is evident that there is an appreciable discrepancy. The maximum value of $G(\phi')$ should apply only when $\phi' = 1$, and in that case $D_{pr}^*(\mathrm{Na})$ would be equal to $D_{pr}^*(\mathrm{Cl})$, leaving the dielectric loss results too small by at least a factor of two. With $D_{pr}^*(\mathrm{Na})$ actually much larger than $D_{pr}^*(\mathrm{Cl})$, we have $\phi' < 0{\cdot}1$ and $G(\phi') < 0{\cdot}3$, giving an even larger discrepancy. Since the values of x_{pr} calculated from the dielectric loss measurements are already uncomfortably large ($x_{pr} = 0{\cdot}13$ at 790°C), it is not possible to contemplate still larger values. The only way to improve the situation would be to have relaxation frequencies an order of magnitude larger than those observed in the dielectric loss experiments. Perhaps the true vacancy pair relaxation was not observed in those experiments because of the frequency limitation of the measuring apparatus at 10 MHz. In any case it is not possible to reconcile both the diffusion and the dielectric loss measurements with a single, consistent choice of parameters for the vacancy pairs.

(After the manuscript for this paper was completed new information about the dielectric loss measurements was received in private correspondence from D. Miliotis and D. N. Yoon at the University of Illinois, Y. Haven at Wake Forest University, and A. Kessler at Bratislava. In brief it is demonstrated that the dielectric loss peaks reported by Economu and Sastry[21] were artifacts caused by air gaps at the electrodes. According to this interpretation, then, the former dielectric loss measurements give no information about vacancy pairs; thus the discrepancy with the diffusion results is eliminated, but unfortunately the possible assistance in determining the concentration of vacancy pairs is also removed.)

B. *Conductivity*

The conductivity is the sum of at least two terms as written in equation (3), where it is supposed that free cation and free anion vacancies are the only charged defects present in the crystal. When the appropriate temperature dependences are inserted, this equation becomes

$$\begin{aligned}\sigma T &= (N_0 e^2/k)(4\nu_0 a_0^2)\\ &\times\{\exp[(\tfrac{1}{2}s_s+\Delta s_c)/k]\times\exp[-(\tfrac{1}{2}h_s+\Delta h_c)/kT]\\ &+\exp[(\tfrac{1}{2}s_s+\Delta s_a)/k]\exp[-(\tfrac{1}{2}h_s+\Delta h_a)/kT]\}.\end{aligned} \tag{37}$$

Debye–Hückel corrections have not been included because a detailed fit of the conductivity was not the primary aim of this work. Furthermore the elegant treatment of conductivity in NaCl by Allnatt and Pantelis [29] shows that these corrections vary smoothly from 10 to 16 per cent between 600° and 790°C and that their inclusion does not affect the activation enthalpies by more than 0·02 eV.

Two procedures were tried for fitting the conductivity data between 600° and 797°C in Fig. 5 to equation (37).† First conductivity data only were used, it was assumed that the cation contribution was predominant except near the melting point, and both cation and anion parameters were varied to obtain

$$\begin{aligned}\sigma T &= 2{\cdot}0\times10^{9}\exp(-1{\cdot}98/kT)\\ &+1{\cdot}5\times10^{17}\exp(-3{\cdot}77/kT).\end{aligned} \tag{38}$$

Second the cation contribution was calculated from the measured M_p(Na), and then the anion parameters were varied to fit σ.

$$\begin{aligned}\sigma T &= 3{\cdot}6\times10^{9}\exp(-2{\cdot}06/kT)\\ &+2{\cdot}53\times10^{9}\exp(-2{\cdot}08/kT)\end{aligned} \tag{39}$$

From the deviation plots in Fig. 10 it appears that the first procedure gives a better fit, but the extraordinarily large values of the enthalpy and entropy for the anion contribution make this fit clearly untenable. Under the circumstances the second fit is most consistent with all of the available data, and the two terms are shown by the lines in Fig. 5. A noteworthy feature is that the enthalpies are essentially equal for cation and anion motion. This gives a practically constant cation transport number of 0·66, which is somewhat smaller than Haven's [10] measurements (by the Tubandt [2] method) of 0·86 at 690° and 775°C.

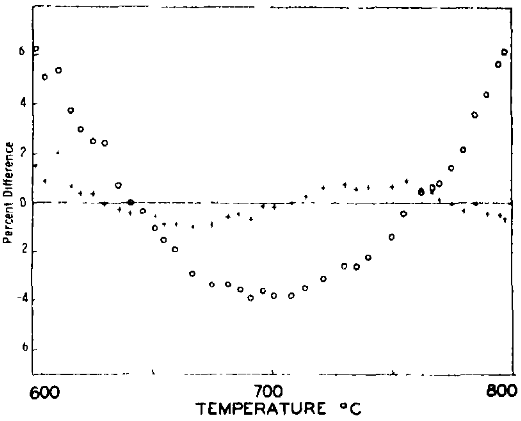

Fig. 10. Deviation plots for conductivity fits in NaCl. The ordinate is $100\times(\sigma_{calc}-\sigma_{obs})/\sigma_{obs}$. + first procedure: fit of conductivity data only. ○ second procedure: cation contribution calculated from the measured drift mobility.

C. *Activation enthalpies and entropies*

Values of these quantities are given in Tables 2 and 3 for comparison to the results of other experiments and of theoretical calculations. For the free vacancy parameters in Table 2 the assignment to particular processes is straightforward if it is assumed that free vacancies are the only charged defects present. Then the cation and anion components of the conductivity represent directly the corresponding contributions to diffusion; data are quoted for diffusion experiments

---

†In both cases it was impossible to include the data between 550° and 600°C without obtaining large systematic deviations; perhaps there is still a small influence of residual impurities at these lower temperatures.

Table 2. Defect parameters for free vacancies in NaCl. *Activation enthalpies* h *are given in* eV *and activation entropies* s/k *in* e.u. *with* $\nu_0 = 4{\cdot}91 \times 10^{12}$ Hz[29]. ***Boldface** entries are measured or evaluated directly; other entries in the same column are calculated from these*

Quantity	Ionic conductivity: intrinsic and extrinsic h	s/k	Ionic conductivity: two exponential fit h	s/k	Diffusion h	s/k	Theory h
Formation h_s	2·12 ± 0·06^{a}	6·2 ± 1·8^{a}	**2·17^{b}**	**2·44^{b}**			**2·12^{h} 1·94^{k} 1·79–2·13^{g}** **1·77^{i,j} 2·1^{m} 2·10^{n}**
Cation jump Δh_c	**0·80 ± 0·02^{a}**	**3·3 ± 0·7^{a}**	**0·66^{b}**	**3·17^{b}**			**0·87^{l} 0·85^{k}**
Anion jump Δh_a			**1·15^{b}**	**9·43^{b}**			**1·11^{i} 0·90^{k}**
Cation diffusion $\frac{1}{2}h_s + \Delta h_c$	**1·86 ± 0·06^{a}**	**6·4 ± 1·7^{a}**	1·75^{b} **2·06^{c}**	4·39^{b} **8·63^{c}**	2·10 ± 0·10^{d}	9·6 ± 1·2^{d}	1·76^{i,j} 1·82^{k}
Anion diffusion $\frac{1}{2}h_s + \Delta h_a$			2·24^{b} **2·08^{c}**	10·65^{b} **8·26^{c}**	**2·07 ± 0·05^{e}** **1·92 ± 0·1^{f}** 2·09 ± 0·3^{g}	**7·5 ± 1·0^{e}** **4·5 ± 1·2^{f}** 8·1 ± 3·1^{g}	2·00^{i,j} 1·87^{k}

[a] Dreyfus and Nowick[5]. Since they used $\nu_0 = 5{\cdot}9 \times 10^{12}$ Hz, their value of Δs_c has been increased by 0·2 e.u. to correspond to the ν_0 used here.

[b] Allnatt and Pantelis[29].

[c] This work, with the cation part determined from the mobility M_p(Na).

[d] This work, with D_r^*(Na) calculated from M_p(Na) (dash–dot line in Fig. 7).

[e] Laurance[15], as recalculated by Fuller and Reilly[13].

[f] Barr *et al.*[16].

[g] This work, by subtraction of M_p(Na) from the conductivity (dotted line in Fig. 8).

[h] Tosi and Fumi[46].

[i] Guccione *et al.*[47].

[j] h_s is calculated from the results in [47] with a lattice energy of 7·88 eV per molecule according to Tharmalingam[48]

[k] Tosi and Doyama[49].

[l] Boswarva and Lidiard[50].

[m] Boswarva and Franklin[51].

[n] Scholz[52].

only where the experimental procedure allows a separation of the free vacancy and vacancy pair contributions.

Our experimental results from the drift mobility give an activation enthalpy for cation diffusion considerably larger than reported previously from conductivity experiments. The discrepancy seems to be larger than our estimated error, but it should also be remembered that the mobility measurements do involve a difficult and still somewhat uncertain experimental technique. The near equality of our enthalpies for cation and anion diffusion seems to substantiate the more recent calculations of Tosi and Doyama[49], who also found similar behavior for KCl and RbCl. Our diffusion enthalpies are still 0·1 to 0·3 eV larger than the theoretical values, but the recent improvements of including van der Waals interactions[50] and displacements for more than the six nearest neighbors of a vacancy[51, 52] appear to remove most of this discrepancy.

For the vacancy pair parameters in Table 3 more interpretation is required before definite assignments can be made. If one of the jump frequencies ν_c' or ν_a' is larger than the other by a factor of 10 or more, then both cation and anion contributions to diffusion are governed by the *smaller* jump frequency, equation (36), whereas the relaxation time observed in dielectric loss measurements is determined almost exclusively by the larger jump frequency, equation (20).

Table 3. *Defect parameters for vacancy pairs in* NaCl. *For units and symbols see Table* 2

Quantity	Dielectric loss		Diffusion		Theory
	h	s/k	h	s/k	h
Formation, h_{pr}	**1·30 ± 0·05**[a]	**10·3 ± 0·6**[a]			1·17[f] **1·27**[g]
Cation jump, $\Delta h'_c$	**1·25 ± 0·05**[a,b]	**2·6 ± 0·6**[a,b]			**1·46**[g]
Anion jump, $\Delta h'_a$					**1·27**[g]
Cation diffusion			**2·35 ± 0·22**[c]	**9·0 ± 2·5**[c]	$h_{pr}+\Delta h'_c = 2{\cdot}73$[g,h]
Anion diffusion			**2·50 ± 0·02**[d]	**10·6 ± 0·1**[d]	$h_{pr}+\Delta h'_a = 2{\cdot}54$[g,h]
			2·37 ± 0·1[e]	**9·6 ± 1·2**[e]	

[a] Economu and Sastry[21].

[b] These values are assigned to the cation jump because D^*_{pr}(Na) > D^*_{pr}(Cl).

[c] This work, by subtracting D^*_r(Na) from D^*(Na) (dash–dot–dot line in Fig. 7).

[d] Laurance[15], as recalculated by Fuller and Reilly[13].

[e] Barr *et al.*[16].

[f] Tosi and Fumi[46] with h_s from[47].

[g] Tharmalingam and Lidiard[33].

[h] Usually the larger of these two values will govern both cation and anion diffusion.

Since our results give D^*_{pr}(Na) > D^*_{pr}(Cl), we have therefore assigned the parameters for the relaxation time to the cation jump. It is still not possible to make any direct estimate of the cation diffusion from this assignment, however, since no information is given about the smaller jump frequency needed in equation (36).

The theory of Tharmalingam and Lidiard [33] indicates that the jump activation enthalpies are somewhat larger for jumps into the vacancy pair than for the corresponding free vacancy jumps, and our results are in general agreement with this conclusion. The theory predicts a larger activation enthalpy for the cation jump into the vacancy pair, however, and this would make $\nu'_c \ll \nu'_a$ and mean that both cation and anion contributions to diffusion should have an activation enthalpy $h_{pr}+\Delta h'_c = 2{\cdot}73$ eV, which is not in agreement with the experimental results. According to our interpretation, on the other hand, we find $\nu'_c \gg \nu'_a$ and therefore expect both contributions to diffusion to have an activation enthalpy $h_{pr}+\Delta h'_a$; within the fairly large error of our results the equality of the two activation enthalpies is confirmed. The value obtained, 2·35–2·50 eV, would agree moderately well with the prediction of theory $h_{pr}+\Delta h'_a = 2{\cdot}54$ eV, but as noted above this interpretation is not consistent unless $\Delta h'_c < \Delta h'_a$.

A brief comment may be made about the activation entropies obtained from experiment. Even though there are no theoretical estimates for direct comparison, many of the reported values seem rather large. A good part of this may be due to the choice of ν_0, which enters directly into the calculation of all jump activation entropies. The value used here is approximately the Debye frequency, that is, roughly the maximum frequency of the acoustic branch of lattice vibrations. It seems quite reasonable that removal of ions to form vacancies or vacancy pairs should give a local mode with a somewhat higher frequency, although the reduction of force constants would tend to oppose this effect. With this uncertainty it is difficult to say much more than that the large entropy values do indicate rather large local influences from the displacement of ions near a vacancy.

D. *Cation Frenkel defects*

Fitting the intrinsic conductivity with the sum of two exponential terms, as in equation (37), has been quite successful for several alkali halides, notably KCl[53] and RbBr[12], but similar attempts for NaCl have encountered considerable difficulty. Our results in equation (38) using conductivity data only, for instance, give completely outlandish values for the anion activation enthalpy and entropy. And even when Debye–Hückel interactions are included, as in the work of Allnatt and Pantelis[29], there are still serious problems. For free anion vacancies they note that their activation energy is too large, and their calculated values of $M_v(Cl)$ are larger than Laurance's[15] observed values by a factor of 2–3 and predict an *anion* transport number of 0·66° at 790°C. For free cation vacancies their calculated values of $M_v(Na)$ are too small by a factor of 1·3–2 compared to our measurements, and their predicted activation energy also seems to be much too small in this case.

All of these results indicate that there is some real difficulty in fitting the conductivity in NaCl. Some of this might be caused by activation enthalpies (and entropies) that vary with temperature or by small errors in conductivity or temperature measurements; either of these effects might have a large influence since this type of analysis, particularly for the anion contribution, is sensitive not only to the position but also to the curvature of the conductivity plot. These effects do not seem to be pronounced for other alkali halides, however, and therefore the possibility of other types of charged defects has been suggested, namely, either cation Frenkel defects[29] or vacancy triplets[30]. We shall consider briefly the bearing of our mobility and diffusion results on these suggestions in the last two sections.

The difficulties mentioned above led Allnatt and Pantelis[29] to introduce cation Frenkel defects, in addition to Schottky defects, and this procedure did give some further reduction in the errors of fitting the conductivity. Furthermore their activation enthalpies of 2·70 eV for formation and 0·75 eV for motion do not appear unreasonable in view of Tharmalingam's[48] theoretical values of 2·63 eV for formation and 0·74 eV for collinear interstitialcy jumps. (Anion Frenkel defects are not considered because of their exorbitant formation enthalpy of 6·38 eV[48].) But the comparison with drift mobilities is still quite unsatisfactory: their predicted cation mobility is a factor 1·4 larger than our measured values, and their anion mobility is a factor 2 smaller than the results of Laurance[15] and our two measurements.

A further difficulty is encountered with the interpretation of the diffusion results when cation Frenkel defects are included. In this case the total drift mobility and diffusion coefficient from charged cation defects are given by

$$M_\sigma(\mathrm{Na}) = M_v + M_i, \tag{40}$$

$$D_\sigma^*(\mathrm{Na}) = (kT/e)(f_v M_v + f_i M_i). \tag{41}$$

The comparison in Fig. 7 has been made by calculating $D_\sigma^*(\mathrm{Na})$ with $f_v = 0{\cdot}781$ as a multiplier for all of $M_\sigma(\mathrm{Na})$. If a smaller multiplier $f_i = 0{\cdot}333$ for the collinear interstitialcy[25] were used for part of $M_\sigma(\mathrm{Na})$, the calculated $D_\sigma^*(\mathrm{Na})$ would be reduced still more, and an even larger contribution to cation diffusion by vacancy pairs would be required. Since our results for $D_{pr}^*(\mathrm{Na})$ are already at the maximum limit compared to $D_{pr}^*(\mathrm{Cl})$, it seems that there should not be any appreciable contribution from cation Frenkel defects.

E. *Vacancy triplets*

In the early stages of the analysis of this work it was thought that vacancy triplets might help to explain two anomalies, namely, the difficulty of fitting the conductivity curve and the 10–15 per cent discrepancy between the sum of the drift mobilities and the total conductivity (Fig. 5). On closer inspection the important result was discovered, as described below, that *no* kind of charged defect can account for the latter discrepancy, although the possibility of additional contributions to conductivity and diffusion might help to explain the former.

Two kinds of vacancy triplets can exist, cation triplets containing two cation vacancies and one anion vacancy as shown in Fig. 11, and anion triplets *mutatis mutandis*. In the simplest possibility the three vacancies form an L on a 45° right triangle on a (100) plane; for each location of the anion vacancy there are 12 equivalent orientations of the cation triplet. For each orientation there are four cation jumps and one anion jump that lead to a new orientation without changing the basic configuration, and these jumps form a connected mesh throughout the lattice, thereby enabling the triplet to migrate in three dimensions and hence to participate in volume diffusion. It also seems quite likely that the three vacancies may form an I along a [100] direction, probably with smaller formation energy than the L form, but it is not possible for the triplet to change between the three equivalent orientations of the I form without going through the L form.

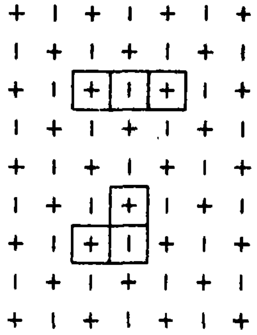

Fig. 11. 'L' and 'I' forms of cation triplets for the NaCl type lattice. Similar forms exist for anion triplets.

In order to determine the contributions of vacancy triplets to conductivity and drift mobilities, let us suppose that the mole fractions of cation and anion triplets are x_{ct} and x_{at} and that the microscopic mobilities are μ_{ct} and μ_{at}. We find

$$\sigma = eN_0(x_c\mu_c + x_a\mu_a + x_{ct}\mu_{ct} + x_{at}\mu_{at}), \quad (42)$$

$$\text{M(Na)} = x_c\mu_c + 2x_{ct}\mu_{ct} - x_{at}\mu_{at}, \quad (43)$$

$$\text{M(Cl)} = x_a\mu_a - x_{ct}\mu_{ct} + 2x_{at}\mu_{ct}. \quad (44)$$

The mobility equations are obtained by the same kind of reasoning used for single vacancies in equations (14) and (15); the cation triplet clearly involves the displacement of two cations for each unit of charge and also drags an anion in the *opposite* direction. The important result is obtained by adding equations (43) and (44) to give, by comparison with equation (42),

$$\sigma = eN_0[\text{M(Na)} + \text{M(Cl)}]. \quad (45)$$

This is the same as equation (16) and shows that this result is valid *no matter what defect mechanisms are present*.†

For vacancy triplets this is most easily seen by regarding a cation triplet as a combination of a cation vacancy and a vacancy pair: as the vacancy pair moves along with the cation vacancy it produces an extra contribution to cation mobility, giving the factor of 2 in equation (43), but it must also cause an equal contribution to anion mobility in the opposite direction, giving the minus sign in equation (44); and the two contributions cancel exactly when the two equations are added together. Thus equation (45) affords a rigorous check of the experimental measurements in all cases—any deviations must be due to experimental errors—but by the same token it does not allow any inferences to be made about the possible absence or presence of additional transport mechanisms.

The vacancy triplets do, however, introduce additional terms in the individual equations (43) and (44) and may consequently influence the observed results of conductivity and mobility measurements. The corresponding contributions to diffusion will all be positive and will involve correlation factors depending on the ratios of pertinent jump frequencies. None of these correlation factors has been calculated, but they will probably all be smaller than f_v except in limiting cases, as for vacancy pairs in Fig. 1. Under this assumption any contribution of anion triplets would call for a larger contribution of vacancy pairs to anion diffusion but smaller to cation diffusion, in analogy to the argument used for cation Frenkel defects. Then the small discrepancy in $D^*_{\nu r}$(Cl)/$D^*_{\nu r}$(Na) would be reduced or eliminated.† The opposite effect would be caused by cation triplets. Thus it appears that vacancy triplets may be making a small contribution to diffusion, with perhaps a slight preference for anion triplets. The presence of additional parameters in equation (42) would also undoubtedly allow a better fit of the conductivity. Even if only the L form of anion triplets is present, however, there are three new free energies (for formation and two jump frequencies); and if the I form is also present, there are two more free energies. Since the measured values of M_σ(Na) are neither extensive nor accurate enough to detect a small curvature in the Arrhenius plot, there is no way to estimate the amount of vacancy triplet contributions from the present data.

---

†It may also readily be shown that the presence of cation or anion Frenkel defects does not alter this result.

5. CONCLUSIONS

The ultimate purpose of conductivity and diffusion measurements in ionic crystals is to identify the atomic transport processes responsible for these phenomena and to determine the corresponding defect parameters. The most accurately known quantities are the total conductivity and the total diffusion coefficient for each kind of ion in the pure crystal. These data have now been supplemented in NaCl with the tracer drift mobility, mostly for cations, reported here and with anion diffusion in doped crystals, reported previously. Further information is potentially available from transport number and dielectric loss measurements, but the experimental method is of doubtful reliability in the first case and the interpretation is uncertain in the second.

The larger part, if not all, of the conductivity is certainly due to the motion of single cation and anion vacancies, and our results do not change this basic view. The diffusion experiments show, however, that some additional, neutral contribution is needed for both cation and anion diffusion; our primary interpretation is based on the most likely possibility, namely, vacancy pairs. We thus obtain a general picture in terms of single vacancies and vacancy pairs that is consistent within experimental error with all available conductivity, diffusion, and mobility measurements. We find that $D^*_{\nu r}$(Na) > $D^*_{\nu r}$(Cl), essentially at the limit imposed by the theory of correlation factors, meaning that $\nu'_c > 10\nu'_a$, contrary to theoretical expectations. In this case we can obtain only $h_{\nu r} + \Delta h'_a$, which has a reasonable value. Unfortunately we cannot use the dielectric loss measurements to separate the formation and motion components for vacancy pairs because the observed frequencies are too low by a factor of ten or more to account for the magnitude of the vacancy pair diffusion with any reasonable values for the concentration; thus the interpretation of the dielectric loss measurements still remains in doubt. For single vacancies we find a somewhat larger contribution from anions than previously deduced from conductivity or transport number measurements and a noticeably larger value for Δh_c for motion of cation vacancies.

The possibility of other kinds of charged defects has also been considered. It seems unlikely that cation Frenkel defects make any appreciable contribution, but there may be a small contribution from vacancy triplets, with a slight preference for anion triplets. In any case it is clear that vacancy pairs must make appreciable contributions to diffusion, and hence the main conclusion will be largely unchanged even if some contribution from additional charged defects is present.

---

†The appreciable discrepancy with the dielectric loss measurements cannot, however, be removed in this way.

Acknowledgements—The authors would like to thank Alan Allnatt and P. Pantelis for useful correspondence and a preprint of their paper, Leslie Barr and R. J. Maurer for stimulating discussion and correspondence, and Alan Lidiard for suggesting vacancy triplets at a symposium on mass transport in oxides. The data analysis and curve fitting were made possible through the cooperation of the University of Kansas Computation Center.

REFERENCES

1. MOTT N. F. and GURNEY R. W., *Electronic Processes in Ionic Crystals*. Oxford University Press, London (1940).
2. TUBANDT C., *Handb. exp. Physik*, Vol. XII, part I, p. 383. Leipzig (1932).
3. ETZEL H. W. and MAURER R. J., *J. chem. Phys.* **18**, 1003 (1950).
4. MAPOTHER D., CROOKS H. N. and MAURER R., *J. chem. Phys.* **18**, 1231 (1950).
5. DREYFUS R. W. and NOWICK A. S., *J. appl. Phys.* **33**, 473 (1962).
6. SCHAMP H. W and KATZ E., *Phys. Rev.* **94**, 828 (1954).
7. LAURENT J F. and BÉNARD J., *J. Phys. Chem. Solids* **3**, 7 (1957); **7**, 218 (1958).
8. BARR L. W., HOODLESS I. M., MORRISON J. A. and RUDHAM R., *Trans. Faraday Soc.* **56**, 697 (1960).
9. KERKHOFF F., *Z. Phys* **130**, 449 (1951).
10. HAVEN Y., *Proc. Br. Ceramic Soc.* **1**, 93 (1964).
11. BEAUMONT J. H. and JACOBS P. W. M., *J. chem. Phys.* **45**, 1496 (1966).
12. DAWSON D. K. and BARR L. W., *Phys Rev. Lett.* **19**, 844 (1967).
13. FULLER R. G. and REILLY M. H., *Phys Rev. Lett.* **19**, 113 (1967).
14. FULLER R. G., REILLY M. H., MARQUARDT C. L. and WELLS J. C., Jr., *Phys. Rev. Lett* **20**, 662 (1968).
15. LAURANCE N., *Phys. Rev.* **120**, 57 (1960).
16. BARR L. W., MORRISON J. A. and SCHROEDER P. A., *J. appl. Phys.* **36**, 624 (1965).
17. FULLER R. G., *Phys. Rev.* **142**, 524 (1966).
18. SASTRY P. V. and SRINIVASAN T. V., *Phys. Rev.* **132**, 2445 (1963).
19. SACK H. S. and SMITH G. C., *J. phys. Soc. Japan* **18**, Suppl. III, 124 (1963).
20. ECONOMU N. A., *Phys. Rev.* **135**, A1020 (1964).
21. ECONOMU N. A. and SASTRY P. V., *Phys. Status Solidi* **6**, 135 (1964).
22. DOWNING H. L., Jr. and FRIAUF R. J., *J. Phys. Chem. Solids* **31**, 845 (1970)
23. FRIAUF R. J., *J. appl. Phys.* **33**, 494 (1962).
24. BARDEEN J. and HERRING C., *Imperfections in Nearly Perfect Crystals* (Edited by W. Schockley). p. 261. Wiley, New York (1952).
25. COMPAAN K. and HAVEN Y., *Trans. Faraday Soc.* **52**, 786 (1956); **54**, 1498 (1958).
26. HOWARD R. E., *Phys. Rev.* **144**, 650 (1966).
27. REDINGTON R. W., *Phys. Rev.* **87**, 1066 (1952).
28. CHEMLA M., *Ann. Phys. (Paris)* **1**, 959 (1956).
29. ALLNATT A. R. and PANTELIS P., *Solid St. Commun.* **6**, 309 (1968).
30. FULLER R. G. and REILLY M. H., *J. Phys. Chem. Solids* **30**, 457 (1969).
31. LIDIARD A. B., In *Handbuch der Physik* (Edited by S. Flügge), Vol. 20, p. 246, Springer-Verlag, Berlin (1957).
32. LIDIARD A. B., *J. Phys. Chem. Solids* **6**, 298 (1958).
33. THARMALINGAM K. and LIDIARD A. B., *Phil. Mag.* **6**, 1157 (1961).
34. MANNING J. R., *Phys. Rev.* **125**, 103 (1962).
35. LIDIARD A. B. (ref.[31]), pp. 314–316.
36. CARSLAW H. S. and JAEGER J. C., *Conduction of Heat in Solids*, 2nd Edn, pp. 363–364. Oxford University Press, London (1959).
37. NELSON V. C., U.S. Atomic Energy Commission Technical Report COO-1197-26 (1967).
38. ROSA E. B. and VINAL G. W., *National Bureau of Standards Bulletin* **13**, 479 (1916).
39. BEAN C. Thesis, Illinois (1952).
40. BIERMANN W., *Z. phys. Chem. (Frankfurt)* **25**, 90 (1960).
41. KOBAYASHI K. and TOMIKI T., *J. phys. Soc. Japan* **15**, 1982 (1960).
42. DREYFUS R. W. and NOWICK A. S., *Phys. Rev.* **126**, 1367 (1962).
43. JAIN S. C. and DAHAKE S. L., *Physics Lett. (Netherlands)* **3**, 308 (1963); *Indian J. Pure Appl. Phys.* **2**, 71 (1964); JAIN S. C. and PARASHAR D. C., *Indian J. Pure Appl. Phys.* **3**, 154 (1965).
44. KANZAKI H., KIDO K., TAMURA S., and OKI S., *J. Phys. Soc. Japan* **20**, 2305 (1965).
45. BROWN N. and HOODLESS I. M., *J. Phys. Chem. Solids* **28**, 2297 (1967).
46. TOSI M. P. and FUMI F. G., *Disc. Faraday Soc.* **23**, 92 (1957)
47. GUCCIONE R., TOSI M. P. and ASDENTE M., *J. Phys. Chem. Solids* **10**, 162 (1959).
48. THARMALINGAM K., *J. Phys. Chem. Solids* **24**, 1380 (1963).
49. TOSI M. P. and DOYAMA M., *Phys. Rev.* **151**, 642 (1966).
50. BOSWARVA J. M. and LIDIARD A. B., *Phil. Mag.* **16**, 805 (1967).
51. BOSWARVA J. M. and FRANKLIN A. D., *In Mass Transport in Oxides* (Edited by J. B. Wachtman Jr., and A. D. Franklin, p. 25. National Bureau of Standards Special Publication 296, Washington, D. C. (1968).
52. SCHOLZ A., *Phys. Status Solidi* **7**, 973 (1964).
53. BEAUMONT J. H. and JACOBS P. W. M., *J. chem. Phys.* **45**, 1496 (1966).

J. Phys. Chem. Solids Pergamon Press 1970. Vol. 31, pp. 845–847. Printed in Great Britain.

SELF-DIFFUSION OF Na IN NaCl†

HARRY L. DOWNING, Jr. and **ROBERT J. FRIAUF**
University of Kansas, Lawrence, Kansas 66044, U.S.A.

(*Received* 4 *November* 1968; *in revised form* 18 *July* 1969)

Abstract – Measurements have been made of the diffusion of Na in pure NaCl from 590° to 690°C by the sectioning method. The results are fit by $D_0 \exp(-W/kT)$ with $D_0 = 3{\cdot}2 \pm 1{\cdot}1$ cm²/sec and $W = 1{\cdot}78 \pm 0{\cdot}03$ eV. Comparison to the ionic conductivity shows an excess diffusion of 10–20 per cent, which is tentatively attributed to vacancy pairs. This conclusion is consistent with the more quantitative results obtained in the preceding paper.

1. INTRODUCTION

THESE experiments were initiated by a desire to provide an accurate check of the correlation factor for diffusion by vacancies in a typical alkali halide crystal. This can be done by comparing the ionic conductivity and the sum of the tracer diffusion coefficients, for it can readily be shown from equations (1) to (4) of [1] that

$$D^*(\mathrm{Na}) + D^*(\mathrm{Cl}) = f_v D_\sigma = f_v (kT/N_0 e^2)\sigma \quad (1)$$

provided that only free vacancies contribute to both diffusion and conductivity. The value of the correlation factor $f_v = 0{\cdot}78146$ for single vacancies on a f.c.c. lattice is well known from theory[2], but it was felt that a direct experimental verification would substantiate the application of the theory to actual physical processes and would also clarify the picture of conductivity and diffusion mechanisms in NaCl[3]. As things turned out, it was not possible to verify the value of f_v in any simple, direct way, presumably because of contributions of vacancy pairs to diffusion, which are not contained in equation (1), and this led to the more extensive work described in the preceding paper[1]. These results are reported briefly here in order to make the data available in the open literature; they supplement the preceding results for $D^*(\mathrm{Na})$ by extending measurements to lower temperatures.

2. EXPERIMENTAL

The techniques for measuring conductivity and diffusion were similar to those used by Nelson[1]. For the purposes of converting from conductivity to diffusion with the Einstein relation as in equation (1) a value of $N_0 = 2{\cdot}23 \times 10^{22}$ cm^{-3} was calculated from $a_0 = 2{\cdot}820$ at 26°C[4]. When sample dimensions measured at room temperature are used to calculate σ and $D^*(\mathrm{Na})$, the corrections for thermal expansion cancel out in equation (1) and therefore do not need to be incorporated explicitly.

The principal experimental differences were the preparation of the samples and the sample holder. The starting material was analytical reagent grade powder from Fisher Scientific Co. containing approximately 10 ppm of polyvalent metal impurities. Crystals were grown in air by withdrawal from the melt in a quartz crucible. By comparing conductivity curves for samples from these crystals with the results of Aschner[5] in the impurity region, it is estimated that our crystals contain 2–3 ppm divalent impurities. The sample holder consisted of a number of pieces of Inconel inside a long Inconel tube. The sample in the form of a flat plate 10 × 10 × 2 mm was held between thick Inconel plates faced with 10 mil Pt sheets, and a chromel–alumel thermocouple was brazed into the bottom plate. 1 mil Pt foils were placed adjacent to Aquadag electrodes on the sample, and thin quartz plates were placed around all four edges of the sample. Thus possible sources of contamination were the alloy (Inconel is 75 per cent Ni), the thermocouple, and the nickel-brazing compound used to attach the Pt sheets and the thermocouple and to make a vacuum-tight seal at the high temperature end of the Inconel tube. The sample holder was evacuated to 1×10^{-5} mm Hg before each experiment and was then filled with about 1 atm of pure He gas.

---

†Work supported by the U.S. Atomic Energy Commission. This is Technical Report COO-1197-33.

‡*Present address:* Drake University, Des Moines, Iowa, U.S.A.

Diffusion coefficients were determined with an accuracy of 2 to 3 per cent and are compared to the conductivity in Fig. 1.† The dotted line is calculated from the average of four conductivity runs, on two samples from each of the two crystals used for these experiments. Since there is no sharp break in the conductivity curve in the temperature range of interest (560–720°C) we presume that the results show intrinsic properties. This is confirmed by the diffusion measurements, which are fit well by

$$D(T) = D_0 \exp(-W/kT) \qquad (2)$$

with $D = 3{\cdot}2 \pm 1{\cdot}1$ cm^2/sec and $W = 1{\cdot}784 \pm 0{\cdot}027$ eV.†

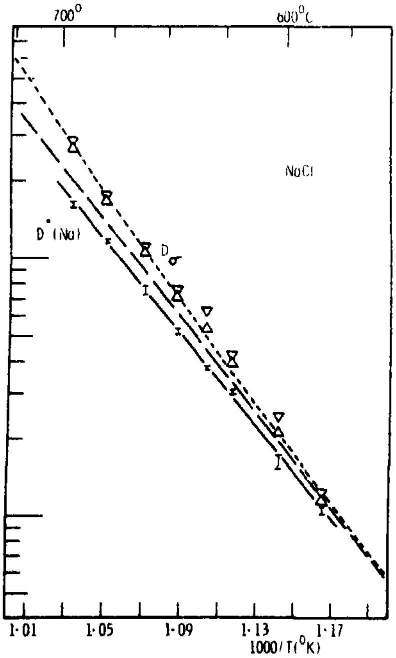

Fig. 1. Diffusion of Na in NaCl. ——I—— Measured with tracers. ------Calculated from average conductivity. Δ and ∇ calculated from conductivity of diffusion sample before and after a run. ——— Measured by Mapother *et al.*[3].

A slightly disturbing feature of the experimental results was a slow change in conductivity during the rather long time (24–48 hr) at constant temperature in a diffusion anneal. There was an increase in conductivity of 5–12 per cent, with most of the increase occurring during the first several hours. This effect is shown in Fig. 1, where the erect and inverted triangles correspond respectively to the conductivity measured at the beginning and at the end of the diffusion anneal. Since this effect was not present in Nelson's work [1] (a slight *decrease* in conductivity was actually observed there), our suspicions that there was some contamination of the sample from the metal parts of the sample holder seem to be confirmed. This effect is not large enough to invalidate the general conclusions but has made it infeasible to attempt a detailed, quantitative analysis with these data.

3. DISCUSSION

Measured values of D^*(Na) from this work and of D^*(Cl) from Laurance[7] are shown together in Fig. 2; although D^*(Cl) is smaller than D^*(Na), it is not completely negligible, especially at the higher temperatures. In order to check the correlation factor according to equation (1), it is therefore necessary to compare the sum of D^*(Na) and D^*(Cl) to $f_v D_\sigma$. The results in Fig. 2 show that $D^*(\mathrm{Na}) + D^*(\mathrm{Cl})$ is larger than $f_v D_\sigma$ by 10–20 per cent

---

†Tables are available in [6].

‡These are compared to other measured values in Table 1 of [1].

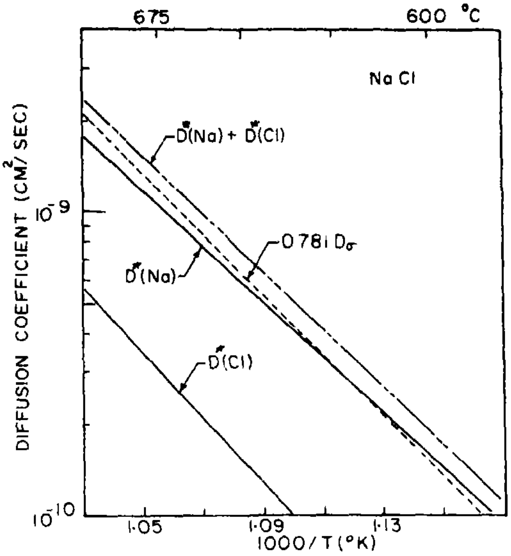

Fig. 2. Diffusion of Na and Cl in NaCl. D^* (Na) and D_σ are taken from Fig. 1. D^*(Cl) is from Laurance [7]

throughout the temperature interval. The possibility of a systematic error in either conductivity or diffusion measurements is ruled out by the check of f_v to within 1–2 per cent in AgCl:Cd, using the same techniques and largely the same equipment as for this work [8]. Hence it is necessary to contemplate an additional transport mechanism in order to account for the extra diffusion, and vacancy pairs were the obvious suggestion at the time these results were obtained [6]. The improved sample holder and new experimental technique of the preceding paper have subsequently allowed a more quantitative treatment of vacancy pairs in NaCl. Although the contact problems at lower temperatures prevent any direct comparison with this work, the fact that D^*_{pr}(Na) is 31 per cent of D^*(Na) at 690°C in Fig. 7 of [1] shows that the predicted amount of vacancy pair diffusion is quite sufficient to account for the results in Fig. 2 of this paper.

Acknowledgements—The authors would like to thank the persons mentioned in the preceding paper for their interest in this work. The data analysis was made possible through the cooperation of the University of Kansas Computation Center.

REFERENCES

1. NELSON V. C. and FRIAUF R. J., *J. Phys. Chem. Solids* **31**, 825 (1970).
2. COMPAAN K. and HAVEN Y., *Trans. Faraday Soc.* **52**, 786 (1956); **54**, 1498 (1958).
3. MAPOTHER D., CROOKS H. N. and MAURER R. J., *J. chem. Phys* **18**, 1231 (1950).
4. WYCKOFF R. W. G., *Crystal Structures*, 2nd Edn, Vol. 1., Chap. III, Table 14C Interscience, New York (1963).
5. ASCHNER J. F., *Phys. Rev.* **94**, 771 (1954).
6. DOWNING H. L., JR., *U.S. Atomic Energy Commission Tech. Rep.* COO-1197-9 (1964).
7. LAURANCE N., *Phys. Rev.* **120**, 57 (1960).
8. GRACEY J. P. and FRIAUF R. J., *J. Phys. Chem. Solids* **30**, 421 (1969).

J. Phys. Chem. Solids Pergamon Press 1970. Vol. 31, pp. 849–855. Printed in Great Britain.

OPTICAL PROPERTIES OF SINGLE CRYSTAL SILICON ARSENIDE*

L. C. E. MILLER† and **C. R. KANNEWURF**
Department of Electrical Engineering, Northwestern University, Evanston, Ill. 60201, U.S.A.

(*Received* 24 *June* 1969)

Abstract – Optical absorption and reflectivity have been studied in single crystal SiAs at 300°K over the wavelength range of 0·3 to 8 μ. Measurements were performed for the incident radiation polarized both parallel and perpendicular to the two-fold axis of symmetry in this monoclinic crystal. From an analysis of the absorption data the following direct transition band gap energies were obtained: 1·48 ± 0·01 eV for $E \| b$ and 1·57 ± 0·01 eV for $E_\perp b$. For $E_\perp b$ an indirect transition was identified with a threshold band gap of 1·45 ± 0·03 eV, but a preference for an allowed or forbidden type transition could not be determined For $E \| b$ an indirect transition could not be clearly identified. The optical measurements indicate SiAs is a semiconductor; all material studied was undoped *p*-type.

INTRODUCTION

ARSENIC has been employed for many years as a doping agent in silicon and germanium semiconductors to produce extrinsic material with n-type conduction, and many papers in the literature describe the investigation of arsenic donor levels in these materials. Generally, the concentration of arsenic is considerably less than 1 per cent by chemical composition, and there is no major change in the diamond cubic crystal structure. If, however, arsenic is added in significant amounts to prepare a stoichiometric binary composition, then new semiconductor structures are formed which have not been thoroughly investigated.

Klemm and Pirscher[1] were the first to present a phase diagram of the Si–As system. From thermal analysis and X-ray studies they established the existence of silicon monoarsenide, SiAs, and silicon diarsenide, $SiAs_2$. The crystal system for SiAs was determined by Schubert *et al.* [2] to be monoclinic. A detailed analysis of the SiAs crystal structure was presented by Wadsten[3], who also found the system to be monoclinic. However, Beck and Stickler [4] have also performed a structure analysis for SiAs, and report the crystal system to be orthorhombic. In a study of the composition and bonding of many crystalline materials characterized as anomalously composed daltonides, Hulliger and Mooser[5] indicate SiAs should show semiconductor behavior with regard to electrical conductivity. Ing *et al.*[6] report that tellurium doped n-type material has an optical band gap of 2·2 eV; these measurements were performed on material with a monoclinic structure in agreement with Wadsten[3]. In the present investigation, single crystal SiAs was prepared, and detailed optical reflectivity and transmission measurements have been performed in the neighborhood of the fundamental absorption edge on undoped material.

SAMPLE PREPARATION

Silicon monoarsenide was synthesized by reacting stoichiometric proportions of the

---

*This research was supported in part by the National Science Foundation, and in part by the Advanced Research Projects Agency of the Department of Defense through the Northwestern University Materials Research Center.

†*Present address:* Bell Telephone Laboratories, Inc., Naperville, Illinois, U.S.A.

elements* in thick wall quartz tubes evacuated to 10^{-4} Torr or better. Synthesis tubes were positioned in level zone furnaces, and the temperature increased over a 6-hr period to 1130°C and maintained at this temperature for periods of 5–7 days. The melting point for SiAs has been reported to be approx. 1083°C [1]. Complete reaction was found to occur particularly if the furnace was elevated at one end, so that the synthesis tube made an angle of 15° with the horizontal during the entire synthesis. Variations in the cooling rate had very little effect on the ingot composition.

The inner ingot material, which was not in contact with the walls of the synthesis tube, was found to be homogeneous with large regions of single crystal development having typical surface dimensions of 1·0 by 0·5 cm. The ingot material develops in a layered structure. Freshly cleaved surfaces do not show any visible reaction with ordinary laboratory atmosphere, even when left exposed for several months.

The appearance of a few thin needle like crystals in some of the ingot synthesis tubes indicated that possibly single crystal material could be grown by vapor transport methods. Such methods had already been employed to obtain material for crystal structure analysis [4, 6]. Attempts to transport ingot material through the temperature gradient of a two zone horizontal furnace in evacuated tubes or with a halogen transporter resulted in varying yields of many extremely thin needle like crystals, some of which developed to a length of 2·5 cm. In other trials, uncombined arsenic and silicon were located in opposite ends of an evacuated horizontal transporter tube, and a few milligrams of iodine added. The latter procedure was employed to prepare extremely thin needle and ribbon like crystals of silicon diarsenide. Consequently, the majority of single crystal samples employed for the optical measurements was obtained directly from ingot material.

CRYSTAL ORIENTATION

In the first detailed crystal structure analysis of SiAs, Wadsten [3] determined the crystal system to be monoclinic with the following description: lattice parameters $a = 15{\cdot}979$, $b = 3{\cdot}668$, $c = 9{\cdot}529$ Å and $\beta = 106{\cdot}0°$; space group $C^3_{2h} - C2/m$; with 12 formula units of SiAs in the unit cell. The same general features had been reported in an earlier paper [2]. The atomic coordination for the silicon atoms is the normal tetrahedral arrangement; the bonding scheme is in agreement with the form suggested by Hulliger and Mooser [5]. The structure is of the layered type with the b axis parallel to the layer planes. The shortest distance between arsenic atoms of adjacent layers is 3·60 Å, which is the longest interatomic distance and is most likely responsible for the ease in cleavage of the crystal in sections parallel to this plane. The structure is isotypic with that of GaTe and GeAs [7]; drawings of the structure type and bonding arrangement are available in the literature [3, 8]. In an independent structure determination of SiAs, Beck and Stickler [4] report the crystal system to be orthorhombic with lattice parameters $a = 6{\cdot}95$, $b = 9{\cdot}25$ and $c = 7{\cdot}70$ Å. They propose that since the material cleaves quite easily, which generally results in large amounts of plastic deformation, the examination of heavily faulted material resulted in the failure to extract from the X-ray data a fully reduced unit cell in the earlier structure determination.

In view of this disagreement, considerable care was taken in the present investigation to determine the crystal orientation for the optical measurements. A number of Debye–Scherrer, as well as single crystal X-ray photographs, were prepared, and the results compared to the work of all earlier structure determinations [9]. Good agreement with Wadsten [3] was obtained for all features of the monoclinic unit cell. From single crystal oscillation photographs, a lattice parameter of 3·65 ± 0·04 Å was obtained with the cleavage plane of crystal containing the axis of rotation; this value confirms the *b* axis which is the axis of 2-fold symmetry in the structure. The *a* and *c* axes determined from single crystal photographs were 15·99 ± 0·16 and 9·63 ± 0·10 Å respectively. In Fig. 1, the orientation is shown of typical single crystal samples with respect to the principal crystallographic directions. With the direction of the *a* and *c* axes, as specified by Wadsten[3], the major surfaces are thus (20$\bar{1}$) type planes. In cleaving single crystal material, usually at least one well defined edge or fracture line would occur on the surface. It was found that this line always developed in the direction of the *b* axis in the (20$\bar{1}$) planes. Thus, the intersection of the (20$\bar{1}$) planes and this secondary cleavage plane uniquely located the direction of the *b* axis in all samples. The crystallographic orientation of the secondary cleavage planes was not successfully determined. All SiAs prepared in the present investigation had this growth orientation and crystal structure.

---

*Silicon was obtained from Gallard-Schlesinger Chemical Manufacturing Corporation, purity: 6-nines; arsenic from the American Smelting & Refining Company, purity: 5-nines +.

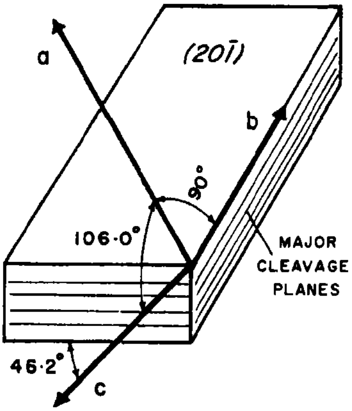

Fig. 1 Growth orientation of single crystal material with respect to the principal crystallographic directions. The *b* axis is perpendicular to the plane formed by the *a* and *c* axes. With the occasional exception of the crystal edge formed by the secondary cleavage plane parallel to the *b* axis, the edges of the samples are rather irregular which is not shown in this figure.

A measured density of 3·81 ± 0·02 g/cm^3 is in good agreement with the calculated density of 3·81 g/cm^3 based on 12 molecules of SiAs per unit cell. Chemical analysis confirmed the composition SiAs; experimental: 27·45 ± 0·05 per cent Si, 72·47 ± 0·05 per cent As; calculated 27·27 per cent Si, 72·73 per cent As. In the X-ray analysis, material scraped from the walls of the growth tube showed a trace of SiO_2 to be present. Occasionally, a trace of elemental arsenic was found on the ingot surface away from the tube walls. However, all samples from the inner regions of the various ingots were found to be free from these impurities.

During the course of the work, some measurements were also made with $SiAs_2$ which has an orthorhombic structure[9]. The lattice parameters, which were all measured from independent oscillation photographs, are $a = 14·57 \pm 0·15$, $b = 10·40 \pm 0·10$, $c = 3·65 \pm 0·04$ Å; these are in good agreement with the corresponding values given by Wadsten[10]. It is interesting to note that the *c* parameter for $SiAs_2$ is within experimental error of the *b* parameter for SiAs; thus, more than a single oscillation photograph might be necessary to distinguish between the two structures. None of the features of the structure for SiAs discussed by Beck and Stickler[4] were observed. In a similar program of measurements on the isotypic GeAs, Rau[11] has found only material with the monoclinic structure.

OPTICAL MEASUREMENTS

Optical reflectivity and transmission measurements were performed with a Zeiss MM 12 monochromator with interchangeable optics, and the associated Zeiss spectrophotometer units over the wavelength range of 0·3 to 8 μ. A discussion of the characteristics of the system employed at this laboratory can be found elsewhere[12]. In the wavelength range of 0·4 to 1·0 μ the resolution of the system varied from 12 to 79 Å. Transmission measurements, using the sample in-sample out technique, and reflectivity measurements, using the comparison technique, were carried out in the standard Zeiss microcell housing with specially prepared mounting units for accommodating samples with small surface areas[12]. In this system the radiation on the sample surface did not exceed 3° from normal incidence.

Reflectivity and transmission measurements were performed with the incident radiation normal to the $(20\bar{1})$ planes, and polarized both parallel and perpendicular to the b axis from 0·3 to 2·2 μ. Unpolarized light was employed from 1·85 to 7·7 μ. All measurements were taken at 300°K. A maximum area of $0{\cdot}4 \times 4$ mm of the sample surface was used, since areas larger than this generally were found to have various imperfections. A plot of the reflection coefficient vs. wavelength is shown in Fig. 2. These data represent reflectivity measurements from several samples with a maximum deviation of ±3 per cent from the average values for both polarizations. On the long wavelength side of the absorption edge beyond 2 μ, the average value of the index of refraction is 3·51.

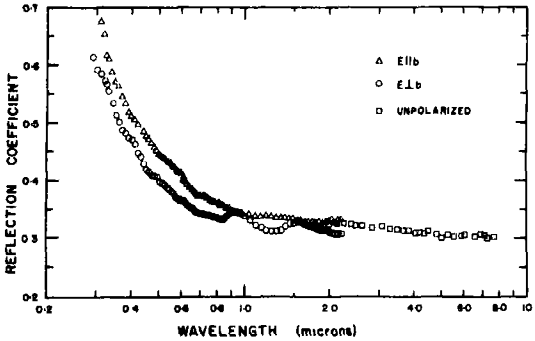

Fig. 2. The reflection coefficient vs. wavelength.

Transmission measurements were performed over the wavelength range of 0·42 to 7·7 μ on many single crystal samples with thicknesses from 0·23 to 342μ. The absorption coefficients, α, were calculated by digital computer procedures using the following expression for the average transmission through semiconductor crystals:

$$T = \frac{(1-R)^2 e^{-\alpha d}}{1 - R^2 e^{-2\alpha d}}$$

where R is the reflection coefficient at normal incidence and d is the sample thickness. Such numerical methods have been discussed by Kahan[13]. Figure 3 shows the variation of the absorption coefficient in the high absorption region for both polarizations of the incident radiation, and Fig. 4 shows the corresponding variation in the low absorption region. In Fig. 3 at the onset of the fundamental absorption edge in the narrow wavelength range of 0·770 to 0·795 μ, the separation of the two curves is less than 42 Å which

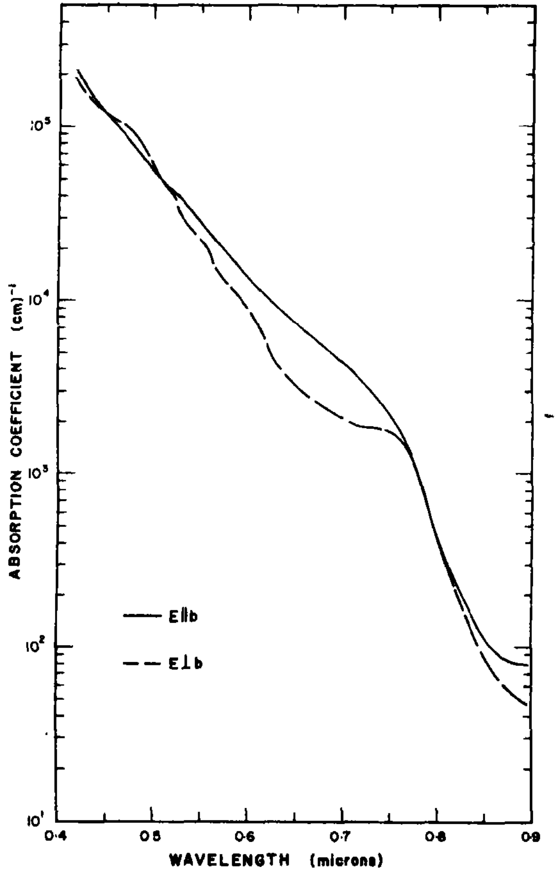

Fig. 3. Absorption coefficient vs. wavelength at 300°K.

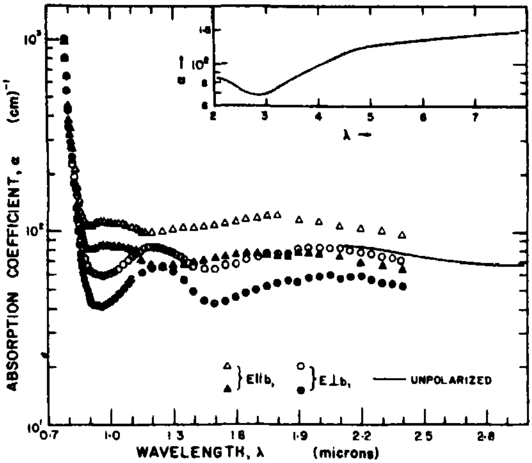

Fig. 4. Absorption coefficient vs. wavelength on the high-transmission side of the fundamental edge. The separation of the two branches for each polarization in the low absorption region indicates the maximum range of variation for all samples The insert figure continues the absorption behavior for unpolarized radiation to longer wavelengths.

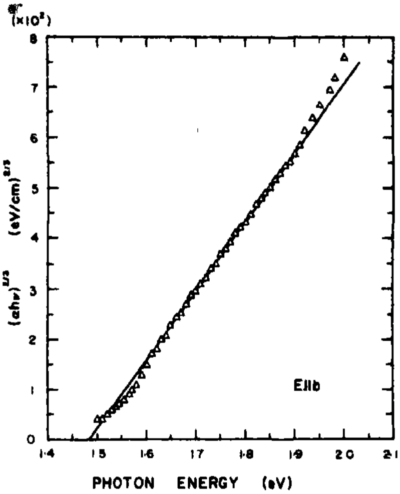

Fig. 5. $(\alpha h\nu)^{2/3}$ vs. photon energy extrapolated to the direct band gap energy value.

was the resolution of the system in this wavelength interval.

In Fig. 4 on the long wavelength side of the absorption edge, the curves are split into two branches for each polarization showing the maximum range of values obtained for different samples examined in this region. The insert section of Fig. 4 continues the absorption coefficient behavior with unpolarized radiation out to 7·7 μ. Some structure is to be noted in the low absorption region, principally, the peak at $\lambda = 1{\cdot}22\,\mu$ (1·02 eV) occurring in the $E_\perp b$ data for all samples.

ANALYSIS AND DISCUSSION

Both curves in Fig. 3 were examined for evidence of direct and indirect band transitions. For direct transitions, the absorption coefficient should vary with photon energy as $(h_\nu - E_g{}^d)^m/h\nu$, where m is 1/2 for allowed transitions and 3/2 for forbidden transitions; the direct band gap is $E_g{}^d$[14]. An analysis of the data for $E \| b$ in Fig. 5 shows a good fit for a forbidden direct transition over the energy interval of 1·6 to 1·9 eV. The extrapolated band gap value is 1·48±0·01 eV. Above 1·9 eV the absorption data for $E \| b$ does not fit any recognized dependence on photon energy.

For $E_\perp b$ the best fit is obtained for an allowed direct transition over a rather narrow energy range as shown in Fig. 6. The extrapolated direct band gap value is 1·57±0·01 eV. In the high absorption region (in Fig. 3) the $E_\perp b$ curve is seen to cross and recross the $E \| b$ curve. In this region at the slight knee in the curve ($\lambda \cong 0{\cdot}48\,\mu$) over the energy interval of 2·45 to 2·75 eV, there is again some evidence for a fit to an allowed

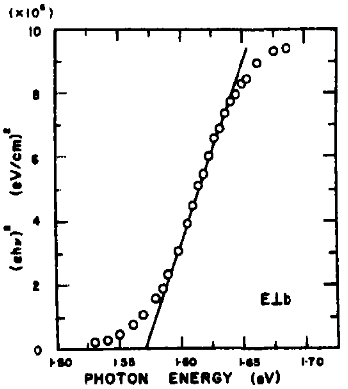

Fig. 6. $(\alpha h\nu)^2$ vs. photon energy extrapolated to the direct band gap energy value.

direct transition dependence on energy with a band transition energy of ~ 2·4 eV, but the reliability of the fit in this region is questionable.

For indirect transitions the absorption coefficient should vary as $(h\nu - E_g{}^i \pm E_p)^n/h\nu$ where n is 2 for allowed and 3 for forbidden transitions; $E_g{}^i$ is the minimum forbidden gap energy and E_p is the energy of the photon being absorbed (+) or emitted (−) in the transition [14]. An analysis of the absorption data for both $E\|b$ and $E_\perp b$ was made to identify indirect transition mechanisms in the low absorption region. Both curves show a fit to an allowed type indirect transition only over an energy interval of less than 0·09 eV; the indirect energy gap is the same for both: $E_g{}^i \leqslant 1{\cdot}47 \pm 0{\cdot}01$ eV. However, just as good a fit is obtained for a forbidden type indirect transition also over an energy interval of 0·09 eV, and the indirect energy gap is again the same for both: $E_g{}^i \leqslant 1{\cdot}42 \pm 0{\cdot}01$ eV. Figure 7 shows the fit for the $E_\perp b$ data to both the allowed and forbidden indirect transition dependence on photon energy. The corresponding plot for the $E\|b$ data, not reproduced here, is nearly identical to Fig. 7.

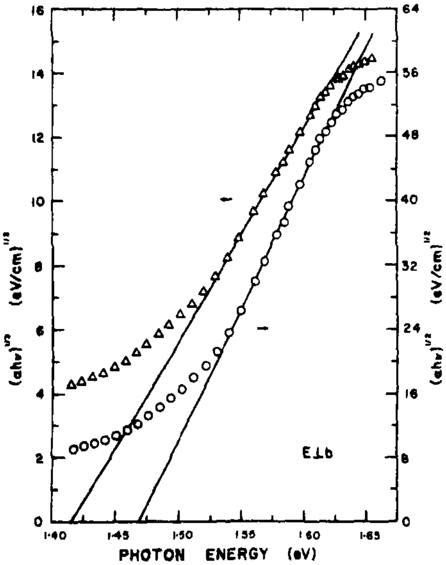

Fig. 7. $(\alpha h\nu)^{1/3}$ and $(\alpha h\nu)^{1/2}$ vs. photon energy extrapolated to the threshold energy for indirect phonon assisted transitions.

The difficulty in obtaining a well defined region for identifying any possible indirect transition is attributed to the rather high level of background absorption, on the order of 10^2 cm^{-1} as shown in Fig. 4. In the case of the $E\|b$ data the band gap energy for an allowed indirect transition is within experimental error of being identical to the direct band gap value; for the forbidden indirect transition the band gap energy is only 0·06 eV less than the direct band gap value. Thus, the establishment of an indirect band gap for $E\|b$ is not clearly resolved from the optical data. For $E_\perp b$ there appears to be an indirect band gap at least 0·1 eV below the direct band gap at approximately 1·45 eV, but a preference for either an allowed or forbidden type transition cannot be determined. Most of the features shown in Fig. 3 for SiAs have been observed by Rau[12] with GeAs which also has a background absorption in the low absorption region at ~ 10^2 cm^{-1}.

Thermoelectric probe tests indicate all material studied to be p-type. Electrical resistivity at 300°K varied from 10 to 450 Ω-cm. Ing *et al.*[6] have performed optical transmission measurements on n-type crystals of SiAs containing about 5 at. % tellurium with an electrical resistivity of $1{\cdot}4 \times 10^3$ Ω-cm. They report an optical band gap of 2·2 eV, but found only an extrinsic activation energy of 0·28 eV from a study of resistivity vs. temperature in the Te doped material. The present authors believe the much higher optical band gap resulted from performing the transmission measurements on extremely thin crystals which did not show any appreciable absorption until well beyond the onset of the fundamental edge.

The optical measurements on undoped material discussed in this paper have shown that SiAs is a semiconductor which is in agreement with the discussion of Hulliger and Mooser[5]. The knee in the absorption curve for polarization of the incident radiation both parallel and perpendicular to the principal crystallographic axis of symmetry at the same wavelength, approximately 0·75 μ, has been identified as belonging to a direct band transition mechanism. The exact nature of lower energy indirect type band transitions is not entirely clear from the above analysis. More extensive electrical measurements are now in progress at this laboratory which would help to clarify this point.

Acknowledgement—The authors would like to thank Dr. J. W. Rau for many helpful discussions during the course of the optical measurements.

REFERENCES

1. KLEMM W. and PIRSCHER P., *A. anorg. Chem.* **247**, 211 (1941).
2. SCHUBERT K., DÖRRE E. and GÜNZEL E., *Naturwiss.* **41**, 448 (1954).
3. WADSTEN T., *Acta chem. scand.* **19**, 1232 (1965).
4. BECK C. G. and STICKLER R., *J. appl. Phys.* **37**, 4683 (1966).
5. HULLIGER F. and MOOSER E., *J. Phys. Chem. Solids* **24**, 283 (1963).
6. ING S. W. Jr., CHIANG Y. S. and HAAS W., *J. electrochem. Soc.* **114**, 761 (1967).
7. PARTHÉ E., *Crystal Chemistry of Tetrahedral Structures.* Gordon and Breach, New York (1964).
8. PEARSON W. B., *Acta Crystallogr.* **17**, 1 (1964).
9. MILLER L. C. E., M.S. Thesis, Northwestern University (1968).
10. WADSTEN T., *Acta chem. scand.* **21**, 593 (1967).
11. RAU J. W., Ph.D. Thesis, Northwestern University (1969), (To be published).
12. RAU J. W. and KENNEWURF C. R., *Zeiss Mitteilungen*, (In press).
13. KAHAN A., *Appl. Optics* **3**, 314 (1964).
14. BARDEEN J., BLATT F. J. and HALL L. H., *Photoconductivity Conference* (Edited by Breckenridge, Russell and Hahn), p. 146. Wiley, New York (1956)

J. Phys. Chem. Solids Pergamon Press 1970. Vol. 31, pp. 857–863. Printed in Great Britain.

A MÖSSBAUER EFFECT STUDY OF LOCAL MOMENTS OF ERBIUM IN ZIRCONIUM

L. L. HIRST and E. R. SEIDEL
Physik-Department der Technischen Hochschule München, München, Germany

(*Received* 23 *June* 1969)

Abstract – By means of the Mössbauer effect, magnetic hyperfine splitting of dilute Er impurities in Zr has been observed in the paramagnetic state, without applied field. From analysis of the fully-resolved splitting seen at 4·2°K, we are able to determine the hyperfine coupling constants between the ground Kramers doublet of the electronic moment and the excited-state nuclear spin. By considering symmetry-imposed limits on the possible values of the electronic g tensor, we are able to show that the magnetic hyperfine coupling constant is at least 15 per cent larger than its value for Er in insulator hosts, which enhancement we attribute to conduction-electron effects. To our knowledge, this is the first measurement of such a conduction-electron contribution in a non-ferromagnetic system, as well as the first observation of magnetic hyperfine splitting in the zero-field paramagnetic state of a dilute alloy.

1. INTRODUCTION

WE HAVE recently briefly reported[1] the observation of resolved Mössbauer magnetic hyperfine splitting of localized Er moments in Zr, in the absence of an external field. The observation of this splitting is possible because the relevant electronic relaxation rates are slow at 4·2°K. At higher temperatures, a characteristic relaxation-induced transformation towards a single-line spectrum sets in, which is essentially complete by 35°K. These relaxation effects are well understood and will be discussed in a separate paper[2]. In the present paper, we give a detailed analysis of the resolved splitting pattern obtained in the slow-relaxation, low-temperature limit. This means we are interpreting the lines of the spectrum as corresponding to energy levels of the isolated, quantum-mechanical system of electronic spin plus excited-state nuclear spin. The analysis has important differences [3] from the case of splitting induced by a classical field acting on the nucleus, and is more complicated; but we will be able to establish a unique solution and to gain a great deal of information about the electronic spin state as well as the intrinsic hyperfine coupling strengths. One can hope to carry through such an analysis successfully whenever, as in the present case, one is working with a reasonably simple gamma transition with an intrinsic linewidth small enough to give good resolution of the individual lines.

The most important specific results of the present paper will be (1) determination of the eigenstates of the coupled system of nuclear and electronic spins, in effective spin language, which is an essential prequisite for correct treatment of the relaxation phenomena; (2) determination of the approximate angular-momentum state vector and g tensor of the electronic ground doublet, which yields information concerning the size of the magnetic moment, EPR resonance frequencies, bulk magnetic properties, etc.; and (3) demonstration that the magnetic hyperfine coupling constant of erbium in zirconium metal is at least 15 per cent larger than in insulator hosts, presumably due to conduction-electron effects.

2. EXPERIMENTAL METHOD AND RESULTS

Since we wish to measure an effect of individual moments, it is essential to work with alloys sufficiently dilute that impurity-impurity interactions be small. For rare earth moments, indirect interactions via conduction electron spins and direct magnetic dipole–dipole interactions are expected to be roughly comparable, and estimates suggest that concentrations should be limited to a few tenths of an atomic percent, although the interaction effects are difficult to evaluate theoretically and have not yet been systematically studied experimentally. With this dilution and for all but the lightest host materials, the electronic photo-absorption will outweigh the resonant nuclear absorption so strongly as to preclude use of the alloy as absorber in a recoilless gamma-resonance experiment; it is necessary instead to use the alloy as source together with a single-line absorber.

We have chosen to work with the 80·6 keV gamma transition of ^{166}Er because it has a relatively simple $2^+ \rightarrow 0^+$ transition with a narrow intrinsic linewidth. ^{166}Ho serves as source for the transition, and the electronic rearrangement to Er structure following the nuclear decay should be essentially instantaneous for our purposes[4]. Zr was chosen as host because Ho is soluble in it to several per cent[5] and because it has an unusually small neutron capture cross section, permitting the whole alloy to be irradiated to activate the Ho. A number of buttons of concentration approximately 0·2 at.% Ho-*Zr* were prepared by arc melting. Slab-shaped samples were sawed from the alloy buttons and etched carefully to remove sawing damage; the final slabs were about 1 mm thick. Although Zr has a cubic beta phase above 860°C, X-ray diffraction showed only the hexagonal alpha phase to be present in our samples. After neutron irradiation of the slabs in the Forschungreaktor München, their recoilless gamma emission spectra were measured, using $ErAl_2$ at 77°K as the single-line absorber. The apparatus and cryostat were of conventional design[6].

3. THE EFFECTIVE SPIN HAMILTONIAN

The principal concern of the present paper is to analyze quantitatively the spectrum observed at 4·2°K (Fig. 1) by interpreting the individual peaks as corresponding to energy levels of the isolated quantum-mechanical system of electronic spin plus excited-state nuclear spin. Actually, the system is not completely isolated: some relaxation coupling to the conduction electron spins persists at 4·2°K and provides a very satisfactory explanation of the differences in widths and depths of the different lines[2]. However, according to the theory such moderate relaxation effects should be accompanied only by very small shifts in the peak positions (not more than 0·03 cm/sec) which may be neglected without appreciable error. For our analysis, accordingly, the energy levels were identified with the line centers as determined from a phenomenological 5-line Lorentzian fit.

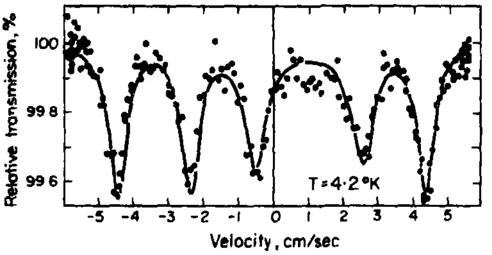

Fig. 1. Mössbauer spectrum of ^{166}Er as a dilute impurity in Zr at 4·2°K. The curve was calculated using the best-fit effective spin Hamiltonian constants of the present paper, together with the relaxation lineshape of [2].

According to theory and empirical observation[7], the Er moment should be well describable as a $4f^{11}$ configuration L–S coupled to give a total angular momentum $J = 15/2$, and split by the crystalline field. The hexagonal C_{3h} point symmetry[†] of the Zr host yields eight Kramers doublets, and previous experience with crystalline fields acting on rare earth ions in metallic hosts[8] suggests an overall splitting of 70–200 cm^{-1}. Thus the *a priori* chances are good that only the ground state doublet is appreciably populated at low temperatures, and experimentally we see no indication of anything more than the 5 lines which a single doublet should give. The most general hyperfine interaction with the ground doublet is

---

[†] We assume the Er to dissolve substitutionally into the Zr lattice; this is expected on metallurgical grounds although we have no direct evidence that it occurs in the present case. The somewhat larger Er ion will cause a distortion of the Zr lattice in its vicinity which should be predominantly radial and hence leave the point symmetry about the Er site unchanged to good approximation.

$$H_{hf} = A_{\parallel} I_z S_z + A_{\perp}(I_x S_x + I_y S_y) + (B/4)[3I_z^2 - I(I+1)]/(2I^2 - I) \qquad (1)$$

where z is the local hexagonal axis, S is an effective spin 1/2, and I is the nuclear excited-state spin. The quadrupole coupling constant B contains contributions both from the lattice (enhanced by anti-shielding)[9] and from the $4f$ shell[10]. Because of symmetry, the quadrupole contribution comes only from the z-z component of the $4f$ quadrupole operator. Since the $4f$ spin is being treated quantum mechanically, the remaining components of the $4f$ quadrupole operator would have to be taken into account except for the fact that they vanish identically (not just as time averages) within a single doublet of a crystalline field having no $V_2^{\pm 2}$ components. The Hamiltonian (1) has trace zero; an additive constant, corresponding to a chemical shift, has not been included since experimentally the sum of the five peak velocities is zero very exactly ($\pm 0{\cdot}01$ cm/sec).

Solving the Hamiltonian is elementary and yields the energy eigenvalues

$$E_1 = A_{\parallel} + B/4. \qquad (2a)$$

$$E_{2,3} = (-A_{\parallel} + B/4 \pm \sqrt{9(A_{\parallel} - B/4)^2 + 16A_{\perp}^2})/4 \qquad (2b)$$

$$E_{4,5} = (-A_{\parallel} - 3B/4 \pm \sqrt{(A_{\parallel} - B/4)^2 + 24A_{\perp}^2})/4. \qquad (2c)$$

These equations may be inverted to give expressions for the three spin-Hamiltonian constants $A_{\parallel}$, $A_{\perp}$, and B in terms of the energies. However, the determination of the constants from the measured energy levels is not trivial since there are a large number of ways in which the experimental levels may be assigned to the theoretical E_i; in fact there are $5!/4 = 30$ possibilities, taking into account that $E_2 > E_3$ and $E_4 > E_5$ by definition. Since their sum is zero, the five experimental levels constitute four independent quantities, and, for each of the 30 possible level orderings, yield determinations of the three constants plus one consistency check. These were worked out and those level orderings discarded which lead to bad consistency checks or to imaginary values of the constants. For those orderings yielding solutions which merited further investigation, the values of the constants were adjusted in each case to locally minimize the mean-square error of a Lorentzian fit to the data, and the optimized fits for the various orderings were compared. The results decided unambiguously in favor of the solution in which the levels are E_1, E_3, E_5, E_4, E_2 (referring to equation (2a–c)) in order of increasing energy; the solution is produced by the best-fit parameters

$$A_{\parallel} = (-4{\cdot}280 \pm 0{\cdot}014)\ \text{cm/sec} = -11{\cdot}50 \times 10^{-6}\ \text{eV} \qquad (3a)$$

$$|A_{\perp}| = (0{\cdot}903 \pm 0{\cdot}015)\ \text{cm/sec} = 2{\cdot}44 \times 10^{-6}\ \text{eV} \qquad (3b)$$

$$(B/4) = (-0{\cdot}021 \pm 0{\cdot}01)\ \text{cm/sec} = -0{\cdot}060 \times 10^{-6}\ \text{eV} \qquad (3c)$$

where the errors given are purely statistical. The corresponding fit has a mean square error slightly less than statistically expected. The second-best solution gave almost twice as great a mean-square error and corresponded to a quadrupole coupling $(B/4) = 9{\cdot}2 \times 10^{-6}$ eV, which we consider inadmissably large (see discussion below). The remaining solutions gave clearly unsatisfactory fits. It should be noted that the relaxation theory [2] depends sensitively on the correct choice of eigenstates for the nuclear-electronic spin system, so its success in reproducing the experimental lineshapes at various temperatures is a further check that the solution we have found is the correct one.

Assuming the total electronic angular momentum, **J**, to be a good quantum number, the magnetic hyperfine interaction can be written more generally as $A_0\mathbf{I}\cdot\mathbf{J}$, where the magnetic hyperfine tensor $(A_\parallel, A_\perp)$ of the effective spin Hamiltonian is related to the magnetic hyperfine coupling constant A_0 by $(A_\parallel, A_\perp) = (g_\parallel, g_\perp)A_0/\Lambda$, where $\Lambda = 6/5$ is the Landé factor. The tensor is what is directly measured but the constant A_0 is the more fundamental quantity since it does not contain crystal-field effects. The exact value of A_0 is an interesting question to which we will shortly return, but we know that since the 4*f* shell is well shielded from the chemical environment it must have *approximately* the value* $A_0 = 1{\cdot}00\times10^{-6}$ eV found for ^{166}Er in insulating hosts[11, 12]. This yields the *g*-values $g_\parallel \approx -14$ and $|g_\perp| \approx 3$.

We wish to emphasize that in the Mössbauer technique the sign of $A_\parallel$, and hence of $g_\parallel$, is experimentally significant†, although, as can be seen from equations (2bc), the sign of $A_\perp$ or $g_\perp$ is not. This is ultimately because the electronic moment is interacting with a quantum-mechanical spin, *I*, rather than with a classical field, and contrasts with the case of EPR where only the absolute values of $g_\parallel$ and $g_\perp$ are significant for the resonance frequency.

4. THE ELECTRONIC STATE

It is now possible to go beyond the effective-spin Hamiltonian analysis to consider the actual angular-momentum state vector of the crystal-field ground doublet. Assuming strong *L-S* coupling so that the total angular momentum, *J*, is a good quantum number, the C_{3h} crystalline field in the hexagonal lattice couples J_z components differing by ±6, so the symmetry-allowed states are of the forms

$$|\pm\rangle = a|\pm 15/2\rangle + b|\pm 3/2\rangle + c|\mp 9/2\rangle \quad (4a)$$

$$|\pm\rangle = a|\pm 13/2\rangle + b|\pm 1/2\rangle + c|\mp 11/2\rangle \quad (4b)$$

$$|\pm\rangle = a|\pm 7/2\rangle + c|\mp 5/2\rangle \quad (4c)$$

where the coefficients *a*, *b*, and *c* may all be taken as real and *c* may be chosen positive. (4a) cannot be the correct form since it gives $g_\perp = 0$. The form (4c) must also be ruled out since it gives $g_\parallel \geqslant -2\,\Lambda(5/2) = -6$, as compared to $g_\parallel \approx -14$ found above. This leaves the form (4b), which is specified by two independent amplitudes after imposing normalization. Only a certain range of *g*-values is generated by states of this form. It is clear that our large negative value of $g_\parallel$ will require $c \approx 1$, with *a* and *b* small. In fact, the value of $g_\parallel$ estimated above is more negative than is allowed. This means that the approximate value used for A_0 was too small and must be increased, with corresponding decreases in the implied values of $g_\parallel$ and $g_\perp$. Numerical analysis, the details of which need not be given, shows that allowed solutions are reached for $A_0 \geqslant 1{\cdot}15\times10^{-6}$ eV. The solutions at the threshold value of A_0, for example, are

$$g_\parallel = -12{\cdot}0,\quad g_\perp = \pm 2{\cdot}55,\quad c = 0{\cdot}98,$$
$$a = \pm 0{\cdot}20,\quad b = 0. \quad (5)$$

---

*So far as we are aware, the sign of the nuclear g factor of the 80·6 keV state in ^{166}Er has not been measured, but according to nuclear theory it must be positive for such a rotational level. Together with the assumed dominance of the 4*f* orbital contribution to the field at the nucleus, this determines a positive sign for A_0.

†We remind the reader that the definition $\mathbf{g}\mathbf{S} = \Lambda\,\mathbf{J}$ fixes the signs of the components of the *g* tensor without ambiguity, so long as $g_\perp \neq 0$, since the condition

$$\Lambda\langle S_z = -1/2|J^+|S_z = 1/2\rangle = g_\perp \begin{pmatrix}0\\1\end{pmatrix}^+ (S^+)\begin{pmatrix}1\\0\end{pmatrix} = 0$$

uniquely determines which state of the Kramers pair must be associated with $S_z = +1/2$.

If one chooses to allow the possibility $g_J = -g_\mu$, then the correct statement is that we have determined the sign of the *g* tensor to be negative. It can be shown that this exhausts the totality of physically significant sign information in the *g* tensor. See BLUME M., GESCHWIND S. and YAFET Y., *Phys. Rev.* **181**, 478 (1969).

The significance of the lower limit on A_0 will be discussed in the next section; for the present, we remark that in view of the expected dominance of the $4f$ orbital contribution to the hyperfine field, we consider it improbable that A_0 can be very much larger than the lower limit. This means that the values given in equation (5) should represent useful approximations to the actual electronic state.

Let us now consider briefly the quadrupole interaction[10]. By using our approximate electronic state of equation (5) we can calculate the $4f$ quadrupole operator to be 0·27 times its value in the fully polarized $J = 15/2$ state. Comparing with the quadrupole interaction measured in erbium metal[13] for a fully polarized $4f$ shell, we deduce $(B/4)_{4f} \approx 0{\cdot}26 \times 10^{-6}$ eV. The quadrupole field gradient from the lattice is just the $A_2{}^0$ coefficient of the crystalline field, multiplied by conventional numbers and the Sternheimer antishielding factor[9]. Inserting these numbers and requiring that the total crystal-field splitting [8] not be more than 300 cm^{-1}, which places a limit on $A_2{}^0$, we calculate $|(B/4)_{\text{latt}}| \leq 0{\cdot}8 \times 10^{-6}$ eV. We have previously invoked these quadrupole-interaction estimates as an additional argument against certain solutions for the effective-spin Hamiltonian constants requiring a very large quadrupole interaction. We may now reverse the argument and combine the measured total quadrupole coupling $(B/4)$ with the calculated $(B/4)_{4f}$ to determine $(B/4)_{\text{latt}} \approx -0{\cdot}3 \times 10^{-6}$ eV, which implies $A_2{}^0 \langle r^2 \rangle \approx -500$ cm^{-1}. To obtain the effective crystal field acting on the $4f$ shell one must multiply this by an electronic shielding factor $(1 - \sigma_2)$, which is rather uncertain since it seems to be sensitive to the chemical environment in a real crystal. Assuming the theoretical value [9, 14] $\sigma_2 \approx 0{\cdot}5$, this value of $A_2{}^0 \langle r^2 \rangle$, if it were the dominant crystal-field term, would correspond to a total splitting of about 100 cm^{-1}.

5. CONDUCTION ELECTRON EFFECTS ON MAGNETIC HYPERFINE COUPLING

In the previous section we established a lower limit on the magnetic hyperfine coupling constant, $A_0 \geqslant 1{\cdot}15 \times 10^{-6}$ eV, the significance of which we will now examine. Bleaney [11] has given an empirical systematization of the data on magnetic hyperfine coupling of lanthanons, including ^{167}Er in insulator hosts, which may be adapted to the present case since the ratio of nuclear moments of ^{167}Er and ^{166}Er has been accurately measured [12]. Following convention, we will usually give the magnetic hyperfine coupling constant in terms of equivalent $\langle r^{-3} \rangle_{4f}$ values, without meaning thereby to imply anything about the actual physical origin of the contributions. For Er in insulator hosts, Bleaney finds a magnetic hyperfine interaction corresponding to $\langle r^{-3} \rangle_{\text{equ}} = (10{\cdot}60 - 0{\cdot}15) a_0{}^{-3}$, where the dominant first term is the shielded orbital $4f$ contribution and the second is a core polarization correction. (For ^{166}Er $\langle r^{-3} \rangle_{\text{equ}} = 10{\cdot}45\, a_0{}^{-3}$ corresponds to $A_0 = 1{\cdot}00 \times 10^{-6}$ eV, or to a field at the nucleus of $7{\cdot}63 \times 10^6$ Oe. if $J_z = 15/2$.) This value is thought to be good to within 2 per cent for various insulator hosts[11], so the presumption is that any larger deviations found in metallic hosts must be due to direct or indirect conduction-electron effects.

There is in fact considerable evidence for such extra contributions, although in some of the earlier references they are not interpreted as A_0 shifts since the insulator A_0 values were not then accurately known. For example, Cohen and Wernick[15] have measured in ErFe$_2$ a magnetic hyperfine splitting corresponding to $\langle r^{-3} \rangle_{\text{equ}} = 11{,}5\, a_0{}^{-3}$, or an extra contribution of 760 kOe. compared to the Bleaney value. A number of other Laves-phase compounds have been studied, and it appears that for a given chemical environment the extra contribution, expressed in Oe, is comparable for various rare-earth ions, whether S-state[16] or non-S-state[15, 17, 18]. The magnitude of this contribution ranges from about -400 to $+800$ kOe, corresponding for ^{166}Er to a shift in A_0 of -5% to $+10\%$. The situation for erbium metal is not entirely clear since there is uncertainty concerning the electronic moment per Er ion. Hüfner *et al.*[13] prefer an interpretation yielding an extra contribution of +120 kOe, but by assigning a smaller value derived from neutron diffraction to the moment, an extra contribution of +700 kOe can be obtained.

The lower limit we have established for A_0 in Er-*Zr* corresponds to $\langle r^{-3}\rangle_{\text{equ}} = 12{\cdot}0\ a_0^{-3}$, an increase of 15% over the insulator-host value, or to an extra field of 1140 kOe. when referred to the $J_z = 15/2$ state. The particularly interesting feature of our result is that, in contrast to the other cases cited, our metal is not ferromagnetic. A specific mechanism which has often been invoked in discussing a conduction-electron contribution to the hyperfine field is the action of a partially polarized conduction-electron band on the nucleus, either directly through the Fermi contact interaction or with a further indirect contribution by induced core polarization. In our case at least, this explanation cannot be correct since there can be no polarization of the band as a whole; the effect must be local.

One possible local mechanism is a charge-screening effect causing the $4f$ shell to distend, but this explanation is considered untenable on theoretical grounds due to the isolation of the $4f$ shell, and because it fails to account for the large conduction-electron effects seen in $4f^7$ S-state ions[16]. More likely is the formation of a localized cloud of conduction-electron polarization, in the vicinity of each ion and due to the ion itself, which then acts back on the nucleus directly and via induced core polarization. In this connection, it should be remembered that the rare earth atom has a $5d^16s^2$ ground-state or low excited-state valence configuration, and that the trivalent ion may tend to form a $5d$ virtual bound state, which would give an enhanced local spin susceptibility.

6. CONCLUSIONS

We hope that the present work has demonstrated some of the power of the recoilless gamma resonance method as a tool for the investigation of localized moments and their hyperfine interactions. Hyperfine splitting in the zero-field paramagnetic state, besides being an interesting phenomenon in itself, can yield detailed information about the electronic state of the moment. In the present case, we were able to determine accurately the magnetic and quadrupole couplings in the effective spin Hamiltonian, fix the sign of $g_\parallel$, and determine the approximate values of $g_\parallel$ and $g_\perp$ and of the state vector of the crystal-field ground doublet, and to estimate the A_2^0 coefficient of the crystal-field potential. In addition, aided by a fortunate value of the g-tensor near a symmetry-determined limit, we were able to establish the presence of an extra positive contribution to the hyperfine field as compared to its value in insulator hosts, which we attribute to the influence of conduction electrons. This appears to be the first time the existence (or non-existence) of such a conduction-electron contribution has been established in a non-ferromagnetic substance, and as such should be very significant for the theory of hyperfine interactions.

It would be particularly interesting if the electronic g values of Er-*Zr* could be directly determined by EPR, which would then completely fix the value of the magnetic hyperfine coupling constant. The relaxation times are sufficiently long to permit such a measurement at 4°K in a high-sensitivity apparatus, provided that a suitable single-crystal sample can be prepared[19].

Acknowledgements—We are grateful to Professor R. L. Mössbauer for suggesting this problem, and for his continued support and interest. One of us (L.L.H) wishes to acknowledge a stipendium from the Bundeswissenschaftsministerium.

REFERENCES

1. HIRST L. L., SEIDEL E. R. and MOSSBAUER R. L., *Phys. Lett.* **29A**, 673 (1969).
2. HIRST L. L., *J. Phys. Chem. Solids*, **31**, 655 (1969).
3. WICKMANN H. H., KLEIN M. P. and SHIRLEY D. A., *Phys. Rev.* **152**, 345 (1966); SEIDEL E. R.,

KAINDL G., CLAUSER M. J. and MÖSSBAUER R. L., *Phys. Lett.* **25A**, 328 (1967).

4. WEXLER S., In *Actions Chimiques et Biologiques des Radiations* (Edited by M. Haissinsky). *8* eme Série. Masson et Cie, Paris (1965).
5. ELLIOTT R. P., *Constitution of Binary Alloys*, 1st Supplement. McGraw-Hill, New York (1965).
6. SEIDEL E. R., Diplomarbeit, Technische Hochschule München (1967).
7. COQBLIN B. and BLANDIN A., *Adv. Phys.* **17**, 281 (1968).
8. ELLIOTT R. J., In *Magnetism* (Edited by G. T. Rado and H. Suhl), Vol. **IIA**, p. 385. Academic Press, New York (1965); WILLIAMS Gwyn and HIRST L. L., *Phys. Rev.* In press; UHRICH D. L., GENIN D. J. and BARNES R. G., *Phys. Lett.* **24A**, 338 (1967); UHRICH D. L., BARNES R. G. and GENIN D. J., *Phys. Rev.* **166**, 261 (1968).
9. STERNHEIMER R. M., *Phys. Rev.* **146**, 140 (1966) and references therein.
10. BARNES R. G., MÖSSBAUER R. L., KANKELEIT E. and POINDEXTER J. M., *Phys. Rev.* **136**, A175 (1964).
11. BLEANEY B., In *Proc. 3rd Int. Symp. on Quantum Electronics* (Edited by P. Grivet and N. Bloembergen), p. 595. Columbia University Press (1964).
12. DOBLER H., PETRICH G., HÜFNER S., KIENLE P., WIEDEMANN W. and EICHER H., *Phys. Lett.* **10**, 319 (1964).
13. HÜFNER S., KIENLE P., WIEDEMANN W. and EICHER H., *Z. Phys.* **182**, 499 (1965).
14. STERNHEIMER R. M., BLUME M. and PEIERLS R. F., *Phys. Rev.* **173**, 376 (1968).
15. COHEN R. L. and WERNICK J. H., *Phys. Rev.* **134B**, 503 (1964).
16. BUDNICK J. I. and SKALSKI S., In *Hyperfine Interactions* (Edited by A. J. Freeman and R. B. Frankel), p. 724. Academic Press, New York (1967); GEGENWARTH R., BUDNICK J. I., SKALSKI S. and WERNICK J. H., *Phys. Rev. Lett.* **18**, 9 (1967).
17. COHEN R. L., *Phys. Rev.* **134**, A94 (1964).
18. NOWIK I., OFER S. and WERNICK J. H., *Phys. Lett.* **20**, 232 (1966).
19. BURR C. R. and ORBACH R., *Phys. Rev. Lett.* **19**, 1133 (1967).

J. Phys. Chem. Solids Pergamon Press 1970. Vol. 31, pp. 865–869. Printed in Great Britain.

t-MATRIX APPROXIMATION IN SPIN WAVE CALCULATION*

W. YOUNG and J. CALLAWAY
Department of Physics, Louisiana State University Baton Rouge, La. 70803, U.S.A.

(*Received* 29 *May* 1969)

Abstract – A Green function method is used to determine the spin wave energy in the itinerant model for a ferromagnet. The self energy used is the t-matrix approximation in a one band model using the Hubbard Hamiltonian. Within this approximation the relevant diagrams for the transverse spin susceptibility are summed and a formal expression is obtained for the spin wave dispersion relation valid for all values of the wave vector $\mathbf{q}$ in the low density limit. This expression reduces, in the appropriate limit, to the RPA result with the bare interaction V replaced by t.

1. INTRODUCTION

THE PROBLEM of calculating the energies and lifetimes of spin waves in ferromagnetic metals has received much attention. Our discussion will be based here on the one band contact interaction Hamiltonian extensively studied by Hubbard[1].

$$H = \sum_{\mathbf{k}\sigma} \epsilon(\mathbf{k})\, a^{+}_{\mathbf{k}\sigma} a_{\mathbf{k}\sigma} + V \sum_{i} n_{i\uparrow}\, n_{i\uparrow}. \quad (1.1)$$

Here the operators $a^{+}_{\mathbf{k}\sigma}$, $a_{\mathbf{k}\sigma}$ create or annihilate an electron in a band state of wave vector $\mathbf{k}$ and spin σ, whose energy is $\epsilon(\mathbf{k})$. The operators $n_{i\uparrow} n_{i\downarrow}$ are number operators referring to a Wannier state centered around lattice site $\mathbf{R}_i$, and we pictorially refer to $n_{i\uparrow}$ as the number of electrons of spin up on lattice site i. The quantity V describes an interaction between electrons of opposite spin on the same site. It is positive and may be large.

The energy and wave function for the completely ferromagnetic state of a system of electrons with the Hamiltonian (1.1) are determined easily since, if the band is less than half full, there is no interaction in this state. If the band is more than half full, we may change from electron to hole operators, and the same conclusion holds except for a change in the zero of energy. The energies of other states cannot be determined so readily; however, there is good evidence that the ferromagnetic state is the ground state for some values of the interaction strength V and some values of the particle density[2–4].

In this work, we consider states with a single reversed spin. These states include spin waves, and our concern will be with the determination of the energies of spin waves. This problem has been studied by several authors[5–8]. For long wave length spin waves, it follows from general considerations that

$$E = D\mathbf{q}^2 \quad (1.2)$$

where $\mathbf{q}$ is the wave vector of the spin wave. A formally exact expression for D has been given by Edwards, and the evaluation of this for a particular band structure has been considered by one of us elsewhere[9]. When $\mathbf{q}$ is not small, the situation is still confused. A number of authors have derived an integral equation from which spin wave energies may be determined. This is

$$1 = V \sum_{\mathbf{k}}^{(0)} \frac{1}{\epsilon(\mathbf{k}+\mathbf{q}) - \epsilon(\mathbf{k}) + V\rho - E}. \quad (1.3)$$

The sum includes occupied states only, as is indicated by the superscript (0) on the summa-

---

*Supported in part by the Air Force Office of Scientific Research.

tion sign. However, this equation is incorrect, as it leads to a result in the long wave length limit which has serious defects, as will be discussed below.

The situation is as follows. Edwards' result for D is, at $T = 0$, the following

$$D = \frac{1}{6N\rho} \sum_{\mathbf{k}}^{(0)} \left[\nabla^2 \epsilon(\mathbf{k}) - 2 \frac{|\nabla \epsilon(\mathbf{k})|^2}{U(\mathbf{k})} \right] + \cdots\cdots \tag{1.4}$$

where N is the number of cells in the crystal, $N\rho$ is the number of electrons, and $U(\mathbf{k})$ is given in the low density limit by

$$U(\mathbf{k}) = t\rho \tag{1.5}$$

where t is an approximate t matrix element and ρ is the particle density. For low densities, t may be approximated by

$$t = \frac{V}{1 + \frac{1}{2}VI} \tag{1.6}$$

where

$$I = \frac{1}{N} \sum_{\mathbf{k}} \frac{1}{\epsilon(\mathbf{k})} \cdot \tag{1.7}$$

The sum here includes only unoccupied states. We see that t is independent of $\mathbf{k}$, however, it depends on particle density through the summation.

In contrast, a small $\mathbf{q}$ expansion of equation (1.3) leads to an expression for D of the form (1.4), however, in this case one has, instead of (1.5)

$$U(\mathbf{k}) = V\rho. \tag{1.8}$$

The difficulties with this approximation become apparent for large V. In this limit (1.8) predicts that for sufficiently large V, D will be positive; that is, the ferromagnetic state will be stable against spin wave excitations, regardless of the particle density. This result cannot be correct. When V is large, the theory becomes in many respects similar to that of a hard sphere Fermi gas, in which the effective interaction is measured by the scattering length rather than the potential strength.

Edwards results apply only to long wave length spin waves at $T = 0°\text{K}$. It is of considerable interest to try to obtain a more adequate expression for spin wave energies which (1) would yield the expression for D with the t matrix in the appropriate limit, and (2) would enable a calculation of the energy for any $\mathbf{q}$, and for finite temperatures, and in addition, would enable an estimate of spin wave lifetimes. It seems plausible that this might be done by replacing V by some appropriately defined t matrix element in (1.3), by including Fermi factors appropriately, and by adding a small imaginary part to the denominator. The replacement of V by t was originally suggested by Izuyama and Kubo[10], but, to our knowledge, a formal justification of such a procedure has not been given. It is the object of this paper to show that this expectation is correct.

2. DIAGRAMMATIC TECHNIQUES

For simplicity the results will be derived for absolute zero. The finite temperature expressions are simple generalizations of this case. We shall assume that the spin wave excitation of wave vector $\mathbf{q}$ is given by $S(\mathbf{q})|\Psi_0\rangle$ where $|\Psi_0\rangle$ is the ferromagnetic ground state described by the equation:

$$|\Psi_0\rangle = a^+_{k_1\uparrow} a^+_{k_2\uparrow} \cdots\cdots a^+_{k_N\uparrow} |0\rangle \tag{2.1}$$

where $|0\rangle$ is the bare vacuum. The operator $S(\mathbf{q})$ is taken to be

$$S(\mathbf{q}) = \sum_{\mathbf{k}\,\mathrm{occ}} a^+_{\mathbf{k}+\mathbf{q}\downarrow} a_{\mathbf{k}\uparrow} \cdot \tag{2.2}$$

The probability amplitude that, if we create a spin wave at time $t = 0$, we find it at a later time t is given by $\chi(\mathbf{q}, t)$ which is defined by

$$\chi(\mathbf{q}, t) = -\langle \Psi_0 | T(S^+(\mathbf{q}, t) S(\mathbf{q})) | \Psi_0 \rangle. \tag{2.3}$$

Figure 1 gives the graphical representation of the function $\chi(\mathbf{q})$.

We define the Fourier transform $\chi(\mathbf{q})$ by

$$\chi(q)=\int_{-\infty}^{\infty}\mathrm{d}t\, e^{iq_0t}\chi(\mathbf{q},t).$$

The pole of $\chi(q)$ gives the energy and lifetime of the spin wave. Note that we have used a four-vector notation i.e. $q=(\mathbf{q},q_0)$.

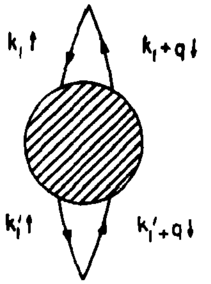

Fig. 1. Graphical representation of $\chi(q)$.

The function $\chi(q)$ is calculated by the usual diagrammatic rules[11] where the free particle Green's functions are given by

$$G_0\uparrow(k)=\frac{1}{k_0-\epsilon_k+i\delta_k};\tag{2.4}$$

$$\begin{aligned}\delta_k&=\delta \text{ for } k \text{ unoccupied}\\&=-\delta \text{ for } k \text{ occupied}\end{aligned}$$

and

$$G_0\downarrow(k)=\frac{1}{k_0-\epsilon_k+i\delta}.\tag{2.5}$$

These expressions follow directly from our definition (2.1) of the ground state. It is observed that there are no hole lines for a down spin particle and this is reflected in the appearance of δ instead of δ_k in the down spin propagator.

The Hamiltonian (1.1) can be rewritten in the Bloch representation as

$$H=\sum_{\mathbf{k},\sigma}\epsilon_{\mathbf{k}}a^+_{\mathbf{k}\sigma}a_{\mathbf{k}\sigma}+\frac{V}{N}\sum_{\mathbf{k}_1,\mathbf{k}_2\mathbf{q}}a^+_{\mathbf{k}_1+\mathbf{q}\uparrow}\,a_{\mathbf{k}_1\uparrow}\,a^+_{\mathbf{k}_2-\mathbf{q}\downarrow}\,a_{\mathbf{k}_2\downarrow}\tag{2.6}$$

The merits and disadvantages of this Hamiltonian have been discussed elsewhere[12]. The form of the interaction in equation (2.6) is such that only particles of opposite spin interact. Because of this and the absence of down spin hole lines the exact up spin propagator $G\uparrow$ is identical to the free up spin propagator $G_0\uparrow$.

The down spin propagator $G\downarrow$ is given by Dyson's equation

$$G\downarrow^{-1}(k)=G_0\downarrow^{-1}(k)-\sum(k).\tag{2.7}$$

The self energy $\Sigma(k)$ will be evaluated in the t matrix approximation, which is exact in the low density limit. Diagrammatically, the approximate Σ is represented by the series of diagrams shown in Fig. 2. Using the standard rules for these graphs we find

$$\sum(k)=\frac{-iVG(l_1)}{1-iVG\downarrow(k_1)G\uparrow(k+l_1-k_1)}\tag{2.8}$$

where for convenience we have adopted the convention that all subscripted variables are to be summed over. Defining the t matrix by the equation

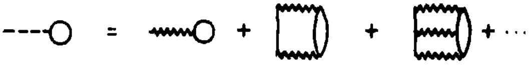

Fig. 2. Down spin self energy insertions.

$$t(k,l)=\frac{V}{1-iVG\downarrow(k_1)G\uparrow(k+l-k_1)}\tag{2.9}$$

we may write

$$\sum(k)=-iG\uparrow(l_1)t(k,l_1).\tag{2.10}$$

Let us now consider the two particle propagator $\chi(q)$. The approximation we make for χ must be consistent with that for Σ. One can readily convince oneself that the series of diagrams in Fig. 3 is the required set. The solid lines in Fig. 3 are, of course, the particle lines dressed according to the self energy

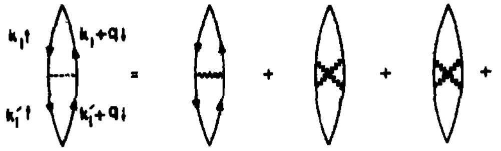

Fig. 3. Irreducible vertex part in $\chi(q)$.

given in equation (2.8). The value of the diagram given in Fig. 3 is the expression

$$iG\uparrow(k_1)G\downarrow(k_1+q)t(k_1,k_1'+q)G\uparrow(k_1') \quad G\downarrow(k_1'+q). \tag{2.11}$$

To evaluate $\chi(q)$ we must iterate the diagram given in Fig. 3 i.e. we must consider the series represented by the graphs in Fig. 4. If we define the vertex function $\Gamma(k,k'+q)$ by the integral equation

$$\Gamma(k,k'+q)=t(k,k'+q)+it(k,k_1+q) \quad G\uparrow(k_1)G\downarrow(k_1+q)\Gamma(k_1,k'+q). \tag{2.12}$$

The contribution to $\chi(q)$ coming from Fig. 4 is the expression (2.11) with Γ replacing t.

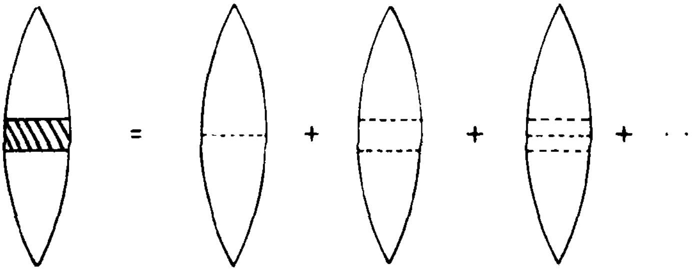

Fig. 4. Contributions to the function $\Gamma(k,k'+q)$.

Adding this to the contribution from the zeroth order graph we have

$$\chi(q)=G\uparrow(k_1)G\downarrow(k_1+q)+iG\uparrow(k_1) \quad G\downarrow(k_1+q)\Gamma(k_1,k_1'+q)G\uparrow(k_1')G\downarrow(k_1'+q). \tag{2.13}$$

The expression (2.13) for the transverse spin susceptibility $\chi(q)$ is the main result of the paper. We shall use this to derive the spin wave energy. It has been shown by one of the authors[9] that the t matrix may be taken to be constant in the low density limit. If we assume this the integral equation (2.12) for Γ is easily solved. Defining $\chi_0(q)$ by the equation

$$\chi_0(q)=G\uparrow(k_1)G\downarrow(k_1+q) \tag{2.14}$$

we obtain

$$\Gamma(k,k'+q)=\Gamma(q)=\frac{t}{1-it\chi_0(q)}. \tag{2.15}$$

Using equations (2.13–2.15) we obtain

$$\chi(q)=\frac{\chi_0(q)}{1-it\chi_0(q)}. \tag{2.16}$$

Expression (2.16) is in exactly the same form as the *RPA* result except that the bare interaction V has been replaced by t.

The dispersion relation for the spin waves is given by

$$1=it\chi_0(q) \tag{2.17}$$

where

$$\chi_0(q)=i\sum_{k\ \mathrm{occ.}}\frac{1}{q_0+\epsilon_{\mathbf{k}}-\epsilon_{\mathbf{k+q}}-tp}. \tag{2.18}$$

Thus we have

$$1=\sum_{k\ \mathrm{occ.}}\frac{t}{tp-q_0-\epsilon_{\mathbf{k+q}}-\epsilon}. \tag{2.19}$$

For small q we may expand the denominator to second order. Using the expansion

$$\epsilon_{\mathbf{k}+\mathbf{q}}-\epsilon_{\mathbf{k}}=(\mathbf{q}\,.\nabla)\,\epsilon\;+\frac{1}{2}(\mathbf{q}\,.\nabla)^2\epsilon_{\mathbf{k}} \quad (2.20)$$

we have

$$q_0=\frac{1}{\rho}\sum_{\mathbf{k}\,\mathrm{occ.}}\frac{1}{2}(\mathbf{q}\,.\nabla)^2\epsilon_{\mathbf{k}}-[(\mathbf{q}\,.\nabla)\epsilon_{\mathbf{k}}]^2/t\rho \quad (2.21)$$

where the gradient operator is taken in k space and the linear terms removed by argument of time reversal symmetry. Furthermore, for cubic crystals we have

$$q_0=\frac{\mathbf{q}^2}{6\rho}\sum_{k\;\mathrm{occ}}\{\nabla^2\epsilon_{\mathbf{k}}-2|\nabla\epsilon|^2/t\rho\}\,. \quad (2.22)$$

The expression for the spin wave energy q_0 is not new and has been derived previously by one of the authors using the formulation given by Edwards. We may observe here that although the expression given by Edwards[8] is exact to order $\mathbf{q}^2$, it is very limited in scope. For instance, it is difficult to determine the lifetime of the spin waves and cannot be generalized to higher temperatures.

From the calculations outlined in this section we are able to give an expression for the spin susceptibility $\chi(q)$ beyond the random phase approximation. If one calculates the t matrix exactly one can determine not only the energy but also the lifetime of the spin waves.

For the finite temperature case, all expectation values are taken with respect to a statistical ensemble. We can apply the procedure developed by Abrikosov, Gor'kov and Dzyaloshinski[13]. The basic result of their development is that physical quantities such as G, χ may be obtained from the corresponding 'thermal' functions by simple analytic continuation. The diagrammatic techniques are the same as those for absolute zero. To convert the previous results to finite temperatures we apply the following prescription:

(1) All energy variables k_0 in the Green's function must be replaced by $i\omega_n=i(2n+1)\pi T$ and q_0 is replaced by $i2n\pi T$, where n is an integer and T is the temperature.

(2) The integration $\int\frac{\mathrm{d}k_0}{2\pi}$ must be replaced by $iT\sum_{n=-\infty}^{\infty}$

(3) The quantity $\chi(q)$ is replaced by $i\chi(q)$.

For instance the finite temperature t matrix is given by

$$t(k,l)=\frac{V}{1+VG\uparrow(k+l-k_1)G\downarrow(k_1)}$$

where

$$G(k_1)=\frac{1}{i\omega_1-\epsilon_{k_1}}$$

In principle one could write down the corresponding dispersion relation for spin waves at finite T. However, the calculation of the quantities are somewhat complicated and will be reported in a later communication.

REFERENCES

1. HUBBARD J., *Proc. R. Soc.* **A276**, 238 (1963).
2. NAGAOKA Y., *Phys. Rev.* **147**, 392 (1966).
3. KANAMORI J., *Proc. theor. Phys.* **30**, 275 (1966).
4. CALLAWAY J., *Phys. Rev.* **140**, A618 (1964).
5. IZUYAMA T., KIM D. and KUBO R., *J. phys. Soc. Japan* **18**, 1025 (1963).
6. ENGLERT F. and ANTONOFF M. M., *Physica* **30**, 429 (1964).
7. ROTH L., *J. Phys. Chem. Solids* **28**, 1549 (1967); *J. appl. Phys.* **39**, 474 (1968).
8. EDWARDS D. M., *Proc. R. Soc.* **A300**, 373 (1967).
9. CALLAWAY J., *Phys. Rev.* **170**, 576 (1968).
10. IZUYAMA T. and KUBO R., *J. appl. Phys.* **35**, 1074 (1964).
11. MATTUCK R. D., *A Guide to Feynman Diagrams in the Many-Body Problem*. McGraw-Hill, New York (1967).
12. HERRING C., *Magnetism* (Edited by G. T. Rado and H. Suhl), Vol. 4. Academic Press, New York (1966).
13. ABRIKOSOV A. A., GOR'KOV L. P. and DZYALOSHINSKI I. E., *Methods of Quantum Field Theory in Statistical Physics*. Prentice Hall, New Jersey (1963).

J. Phys. Chem. Solids Pergamon Press 1970. Vol. 31, pp. 871-872. Printed in Great Britain.

TECHNICAL NOTES

The Debye temperature and temperature-dependent hyperfine coupling constants of Mn^{2+} in SrF_2 and CdF_2

(*Received* 28 *July* 1969; *in revised form* 30 *October* 1969)

A CONVENTIONAL electron spin resonance spectrometer was used to measure the temperature-hyperfine coupling constants of Mn^{2+} at cubic sites in the two crystals: SrF_2 and CdF_2. The sample temperature was varied and controlled by utilizing a Varian-4557 variable temperature accessory. The experimental data are as shown in Fig. 1.

The temperature dependence of the hyperfine coupling constant of Mn^{2+} in the octahedral surrounding was first interpreted by Símanek and Orbach[1]. In their paper, they proposed a mechanism which involves the admixture of the excited $(3d)^4$ ns configurations into the ground $(ed)^5$ configuration by means of the Van Vleck orbit-lattice interaction. This theory is correct only at very low temperatures. However, the phonon-induced effect is much more pronounced at high temperatures. In view of this, Huang used the peaked phonon spectra to calculate the temperature-hyperfine coupling constant of Mn^{2+} in alkali halides[2]. The same theory was later applied to Mn^{2+} in alkali halides[2]. The same theory was later applied to Mn^{2+} in the crystals with the cubic coordination[3]. The temperature dependent part of the hyperfine coupling constant in this case was found to be

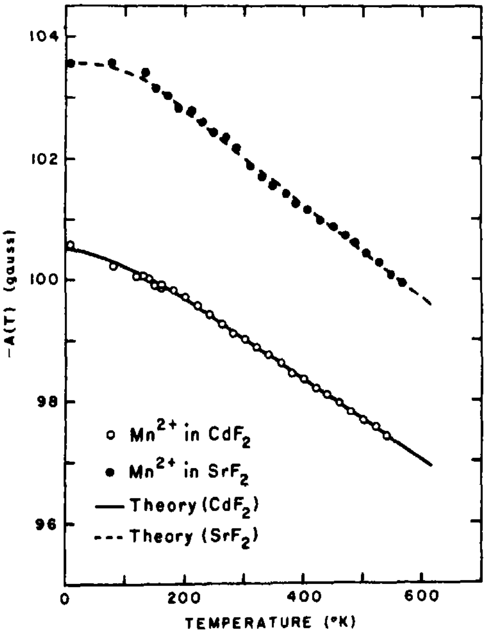

Fig. 1. The hyperfine coupling $A(T)$ of Mn^{2+} in SrF_2 and CdF_2.

$$A'(T) = (\text{const.})\, T^2 \int_0^{T_D/T} x\,\{\exp(x)-1\}^{-1}\,dx \tag{1}$$

with

$$\text{const.} = A(0)KL'$$

$$L' = \{2^7/(2\pi\times 3^6\times 5)\}\,(e\,e_{\text{eff}}/R^4)^2\,(8\pi/\rho)$$
$$\times\,(v_l^{-3}+2v_t^{-3})k_B^2/h. \tag{2}$$

Here $A(0)$ is the hyperfine coupling constant at 0°K. K is a value involving the matrix elements of the electronic radius and has been found to be $1{\cdot}76\times 10^{-10}\,\text{sec}^4/\text{g}^2\,\text{deg}^8$ for Mn^{2+}[2], e_{eff} is the effective charge of a ligand ion, $4R$ is the lattice constants, v_l, and v_t are longitudinal and transverse sound velocities respectively, ρ is the density of the crystal, and T_D is the Debye temperature. Equation (1) was successfully applied to fit the data for Mn^{2+} in CaF_2 and BaF_2[3].

Since both SrF_2 and CdF_2 possess the CaF_2 structure, equation (1) is applicable to our cases. The solid curve is the theoretical curve for SrF_2 obtained by multiplying a scale factor of 5·7 to the theoretical estimate based on equation (1) with [4] $T_D = 380$°K, $R = 1{\cdot}47\times 10^{-8}$, $\rho = 4{\cdot}28\ \text{g/cm}^3$, $v_l = 5{\cdot}40\times 10^5$ cm/

sec, $v_t = 2{\cdot}72 \times 10^5$ cm/sec, and $e_{\text{eff}} = e$. As shown, the theoretical curve fits reasonably well with the experimental points, and we conclude that the theoretical estimate agrees with the experimental data within an order of magnitude[5].

The Debye temperature and elastic constants of CdF_2 are not available at present. However, equation (1) could be used to find the Debye temperature by the proper choice of the constant and T_D. As shown in the dashed curve of Fig. 1, the experimental points could be well fitted with $T_D = 350°$K [6]. This is the first time the Debye temperature is determined by using an ESR spectrometer.

REFERENCES

1. SÍMǍNEK E. and ORBACH R., *Phys Rev.* **145**, 191 (1966).
2. HUANG CHAO-YUAN, *Phys. Rev.* **158**, 280 (1967).
3. HUANG CHAO-YUAN, REICHERT J. F. and GIGANTE J., *Phys. Lett.* **26A**, 219 (1968).
4. GERLICH D., *Phys. Rev.* **136**, A1366 (1964).
5. According to the more detailed theory (HUANG C. Y. and LUE T. J., To be published), equation (1) is accurate within 15% of errors at high temperatures
6. After the completion of this work, Mike Adlerstein informed us that the elastic constants of CdF_2 are almost the same with those of CaF_2. Hence the Debye temperature of CdF_2 can be roughly estimated by considering the masses of these two crystals. The Debye temperature obtained in this manner turns out to be 320°K.

Department of Physics,
Case Western Reserve University,
Cleveland,
Ohio

C.-Y. HUANG
F. RACHFORD
J. A. LOCK
M. A. MOSTROM

J. Phys. Chem. Solids Vol. 31, pp. 872–874.

Magnetically induced nuclear quadrupole interaction in cubic Fe^{2+}: Pseudo-quadrupole interaction

(*Received* 29 *October* 1969)

IN RECENT YEARS there have been several Mössbauer studies [1–4] of nuclear quadrupole interaction of Fe^{2+} in a cubic site symmetry. Ganiel *et al.*[5] attributed the observed quadrupole interaction to distorted spatial distribution of electrons which results because of the interaction of molecular field in a magnetically ordered crystal or of external field in a paramagnetic crystal with Fe^{2+} in cubic crystal field through spin orbit coupling. They presented a detailed theory of octahedral case. Hoy *et al.*[6] have treated similar interaction for Fe^{2+} in tetrahedral crystal field. However, predictions based on these theoretical considerations alone do not explain the observed Mössbauer spectra[6, 7]. In this communication we deal with another additional origin of magnetically induced quadrupole interaction viz. pseudo-quadrupole interaction, here after abbreviated PQI [8, 9].

The Hamiltonian for iron group of substances in the absence of external magnetic field can be expressed as[10]

$$\mathscr{H} = \mathscr{H}_F + V_{\text{crys.}} + \mathscr{H}_{LS} - \gamma\beta_N \bar{H}_n \,.\, \bar{I} + \frac{eQV_{zz}}{4I(2I-1)}[3I_z^2 - I(I+1) + \eta(I_x^2 - I_y^2)] \qquad (1)$$

where $\mathscr{H}_F$ is the free ion part of Hamiltonian, $V_{\text{crys.}}$ is the crystalline field set up by the surrounding diamagnetic charges, $\mathscr{H}_{LS}$ is the spin orbit coupling and remaining part being the hyperfine interaction of magnetic field and electric field gradient set up by electrons at the nucleus with nuclear moments. γ is nuclear gyro-magnetic ratio, β_N is nuclear magneton and H_n is the internal magnetic field. For Fe^{2+}, $\bar{H}_n$ is given by

$$\bar{H}_n = -2\beta\langle r^{-3}\rangle_{3d}\left\{\bar{L} - \frac{1}{42}\left[L(L+1)\bar{S} - \frac{3}{2}\left(\bar{L}\,.\,\bar{S}\right)\bar{L} - \frac{3}{2}\bar{L}\left(\bar{L}\,.\,\bar{S}\right)\right]\right\} + A\bar{S} \qquad (2)$$

where β is Bohr magneton, $\langle r^{-3}\rangle_{3d}$ is the average of r^{-3} for a $3d$ electron and A is a constant. The last term is due to Fermi contact interaction.

In a cubic Fe^{2+}, $V_{zz} = 0$ and therefore no direct quadrupole interaction. On choosing the z-axis parallel to $\bar{H}_n$, we can write magnetic hyperfine interaction as

$$\mathcal{H}_n = 2\gamma\beta\beta_N\langle r^{-3}\rangle_{3d}\left[L_z - \frac{1}{7}S_z + \frac{1}{28}\left(\bar{L}\cdot\bar{S}\right)L_z + \frac{1}{28}L_z\left(\bar{L}\cdot\bar{S}\right)\right]I_z - \gamma\beta_N A S_z I_z. \tag{3}$$

According to Hund's rule, the ground state of Fe^{2+} is ^5D. From group theory arguements it can be seen that ^5D level splits in a cubic crystalline field into an orbital triplet $^5T_2$ and an orbital doublet ^5E. In octahedral symmetry the ground state will be $^5T_2$. The spin orbit coupling will further remove degeneracy[10]. The problem of eigen states and eigen values has been dealt by Low *et al.*[11]. $\mathcal{H}_n$ is very small compared to spin orbit coupling and can therefore be treated as a perturbation to these states. The first order effect of magnetic hyperfine interaction (equation (3)) gives rise to Zeeman splitting of nuclear levels which can be easily evaluated by calculating the matrix elements of $\mathcal{H}_n$ over these eigen states and taking thermal average, provided the relaxation time for thermal transitions between electronic levels is much shorter than the hyperfine field precession time. The second order effect of magnetic hyperfine interaction gives rise to PQI. The perturbation $\mathcal{H}_n$ lifts the degeneracy in first order itself. Hence PQI can be evaluated by calculating square of the matrix elements of $\mathcal{H}_n$ between various eigen states and thermal averaging over various energy levels. We have worked out the pseudo-quadrupole splitting of $I = \frac{3}{2}$ level in Fe^{57m} due to PQI for the case of Fe^{2+} in octahedral cubic symmetry at 0°K. Our results can be expressed as

$$\Delta E_{\pm 3/2 \leftrightarrow \pm 1/2} = \frac{102}{49\lambda}\left(\gamma\beta\beta_N\langle r^{-3}\rangle_{3d}\right)^2 + \frac{1}{2\lambda}\left(\gamma\beta_N A\right)^2 \tag{4}$$

where λ is the spin orbit coupling parameter.

The PQI is large when there are low lying excited states. For example, in praseodymium ethyl sulphate it is several times larger than the true quadrupole interaction[8]. Ghatikar [12] has worked out such a Zeeman-field-dependent PQI in some rare earth trichlorides and has shown it to be quite large compared to direct quadrupole interaction in some cases. In Fe^{2+} case, the excited states are not as narrow as in case of rare earths. PQI therefore is expected to be small in this case. The PQI is a magnetic induced interaction, for in the absence of magnetic hyperfine structure it is zero. It can be argued that in precision Mössbauer experiments PQI should be considered. In favourable cases the contribution of PQI may be quite significant. The detailed theory of the effect in Fe^{2+} in tetragonal crystalline field is in progress.

Acknowledgements —The authors are grateful to Dr. S. C. Mathur for helpful discussions. Financial assistance of the Council of Scientific and Industrial Research, Government of India is acknowledged.

Department of Physics, R. KAMAL
Indian Institute of Technology,
Hauz Khas, New Delhi,
India

R. G. MENDIRATTA*
George C. Marshall Space Flight Center,
Huntsville,
Alabama, U.S.A.

REFERENCES

1. WERTHEIM G. K., GUGGENHEIM H. J., WILLIAMS H. J. and BUCHANAN D. N. E., *Phys. Rev.* **158**, 446 (1967).
2. GANIEL U., KESTIGIAN M. and SHTRIKMAN S., *Phys. Lett.* **24A**, 563 (1967).
3. SIEGWARTH J. D., *Phys. Rev.* **155**, 285 (1967).
4. HOY G. R. and CHANDRA S., *J. chem. Phys.* **47**, 961 (1967).
5. GANIEL U. and SHTRIKMAN S., *Phys. Rev.* **167**, 258 (1968).
6. HOY G. R. and SINGH K. P., *Phys. Rev.* **172**, 514 (1968).
7. HOY G. R., SINGH K. P. and CHANDRA S. *Hyperfine Structure and Nuclear Radiation*, p. 515. North-Holland, Amsterdam (1968).

---

*On leave from the Indian Institute of Technology, New Delhi, India.

8. BAKER J. M. and BLEANEY B., *Proc. R. Soc.* **245**, 156 (1958).
9. BLEANEY B., *Hyperfine Interaction*, p. 1. Academic Press, New York (1967).
10. LOW W., *Solid-St. Phys. Suppl.* 2 (1960).
11. LOW W. and WEGER M., *Phys. Rev.* **118**, 1119 (1960).
12. GHATIKAR M. N., *Proc. R. Soc.* **87**, 727 (1966).

J. Phys. Chem. Solids Vol. 31, pp. 874–875.

Structural stability of inorganic polymorphs

(*Received* 2 *September* 1969; *in revised form* 23 *October* 1969)

BEFORE THE fact arguments over the type of structure which will be stable for particular crystalline chemical species under a set of pressure and temperature conditions have to be based mainly on the thermodynamic or structural evidence. The lowest free energy form, concurrent with the value of the radius ratio of participating atoms, ions or molecules, suggest the stable structure. At the moment no physical arguments exist for predicting the occurrence of one structure or another from knowledge of the properties of the constituent particles. The only a priori statements that can be made at present are from either the phenomenologic, thermodynamic or phase aspects or alternatively from the geometric, packing or structure aspect. Both are qualitative. Quantitative predictions will eventually have to be based on the bonding or physical aspects.

We have recently discovered a relationship between a phsyical and a structural parameter of solids which differentiates between various structures, and adds a new dimension to the radius-ratio concept. Figure 1 shows, for a variety of materials with zincblende, cesium chloride and rocksalt structures, damping vs. radius ratio. Damping of a solid is classically expressed as the width at half intensity of the main transverse optical frequency of the infrared spectrum divided by the value of the frequency itself; $\Delta\nu/\nu_{TO}$. Plendl has recently shown how this damping parameter can be calculated from phsyical quantities and is primarily related to the atomic coordination, a structure factor, the radius ratio and anharmonicity of the binding forces[1]. Values of these experimentally derived or calculated quantities for various solids, are shown in Table 1 and plotted in Fig. 1.

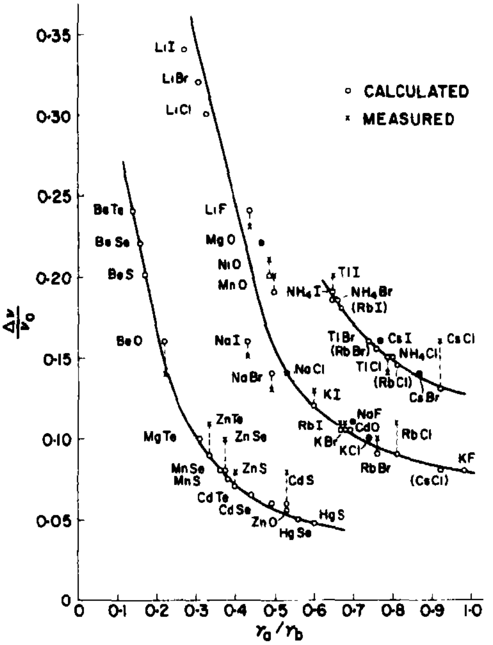

Fig. 1. Damping vs. radius for the structures: ZnS, NaCl and CsCl (CN = 4, 6 and 8, respectively). Crosses experimental values, open circles calculated values.

As was shown earlier, damping may be calculated on the basis of ionic or covalent parameters resulting in different values. The magnitude of the value of the damping factor based on ionic parameters is for any one substance, by far the greater. In the substances of Fig. 1, the ionic character predominates and hence ionic radii were used for all three types of structures considered.

Figure 1 clearly indicates how, depending on the radius ratio, each structure calls for a discrete value of the damping parameter. Although no quantitative deductions are implied, or can be made at this point, it is instructive to note that all three curves have distinct

Table 1. Data used in Fig. 1

Substance	Structure	CN	$\frac{\Delta\nu}{\nu_{TO}}$ Calc.	$\frac{\Delta\nu}{\nu_{TO}}$ Exp.	r_a/r_b
LiF	Rocksalt	6:6	0·24	0·23	0·44
LiCl	Rocksalt	6:6	0·30	–	0·33
LiBr	Rocksalt	6:6	0·32	–	0·31
LiI	Rocksalt	6:6	0·34	–	0·27
NaF	Rocksalt	6:6	0·11	0·11	0·70
NaCl	Rocksalt	6:6	0·14	0·14	0·53
NaBr	Rocksalt	6:6	0·14	0·13	0·49
NaI	Rocksalt	6:6	0·16	0·15	0·43
KF	Rocksalt	6:6	0·08	–	0·98
KCl	Rocksalt	6:6	0·10	0·10	0·74
KBr	Rocksalt	6:6	0·105	0·11	0·68
KI	Rocksalt	6:6	0·12	0·13	0·60
RbCl	Rocksalt	6:6	0·09	0·11	0·81
RbBr	Rocksalt	6:6	0·09	0·10	0·76
RbI	Rocksalt	6:6	0·105	0·11	0·67
(CsCl)	Rocksalt	6:6	0·08	–	0·92
MgO	Rocksalt	6:6	0·22	0·22	0·47
NiO	Rocksalt	6:6	0·20	0·21	0·49
MnO	Rocksalt	6:6	0·19	0·20	0·50
CdO	Rocksalt	6:6	0·105	–	0·69
CsCl	Cesiumchlor.	8:8	0·13	0·16	0·92
CsBr	Cesiumchlor.	8:8	0·14	0·14	0·87
CsI	Cesiumchlor.	8:8	0·16	0·16	0·77
(RbCl)	Cesiumchlor.	8:8	0·145	–	0·81
(RbBr)	Cesiumchlor.	8:8	0·155	–	0·76
(RbI)	Cesiumchlor.	8:8	0·18	–	0·67
TlCl	Cesiumchlor.	8:8	0·15	0·14	0·79
TlBr	Cesiumchlor.	8:8	0·16	–	0·74
TlI	Cesiumchlor.	8:8	0·18	0·20	0·65
NH_4Cl	Cesiumchlor.	8:8	0·15	–	0·80
NH_4Br	Cesiumchlor.	8:8	0·16	0·16	0·73
NH_4I	Cesiumchlor.	8:8	0·19	–	0·65
BeO	Wurtzite	4:4	0·16	0·14	0·22
BeS	Zincblende	4:4	0·20	–	0·17
BeSe	Zincblende	4:4	0·22	–	0·16
BeTe	Zincblende	4:4	0·24	–	0·14
MgTe	Wurtzite	4:4	0·10	–	0·315
MnS	Zincblende	4:4	0·075	–	0·38
MnSe	Zincblende	4:4	0·08	–	0·36
ZnO	Wurtzite	4:4	0·057	–	0·53
ZnS	Zincblende	4:4	0·07	0·08	0·40
ZnSe	Zincblende	4:4	0·08	0·10	0·375
ZnTe	Zincblende	4:4	0·09	0·11	0·335
CdS	Zincblende	4:4	0·06	0·08	0·53
CdSe	Zincblende	4:4	0·06	–	0·49
CdTe	Zincblende	4:4	0·065	–	0·44
HgS	Zincblende	4:4	0·055	–	0·60
HgSe	Zincblende	4:4	0·050	–	0·56

minima below which the structure apparently cannot be stable. If, due to the electronic structure of the elements and the degree of interpenetration of the outer electron shells for a given set of pressure and temperature conditions, the interaction of the electrons results in a higher or lower damping of the lattice vibrations, the structure will not be stable.

Considering the data from well known high pressure transition measurements, we note that within groups of related solids such as alkali iodides, bromides, chlorides and fluorides, the value of the pressure necessary for transition to more highly coordinated structures increases as the position on the damping vs. radius ratio curve goes up.

For LiF, e.g. for which no transition pressure to the cesium chloride structure has been experimentally determined, in spite of measurements to hundreds of kilobars, the increase on damping may well be beyond that physically available under these conditions. For such cases as LiF it might not be possible to obtain the elevated, high pressure, state[2]. Lattice vibrations could become aperiodic and the structure unstable at pressures and temperatures where transition from the basic to the elevated state[2] would otherwise be expected. Until such time when the variation of all essential parameters as a function of pressure and temperature become available, little can be said about the quantitative relationships of structural stability.

A more complete account, including all physical data and references used, may be obtained in report form from the authors.

Bedford, Mass. 01730, J. N. PLENDL
U.S.A.

Kingston, R.I. 02881, P. J. M. GIELISSE
U.S.A.

REFERENCES

1. PLENDL J. N., *Characteristic Energy Absorption Spectra of Solids*, AFCRL-Rep. 1969-0353. Also article in *Far Infrared Properties of Solids*. Plenum Press, New York. To be published (1970).
2. PLENDL J. N. and GIELISSE P. J., *Phys. Status. Solidi* **35**, 151 (1969).

J. Phys. Chem. Solids Vol 31, pp. 876–878.

Photoelastic constants of CaF_2 and BaF_2

(*Received* 21 *May* 1969; *in revised form* 25 *August* 1969)

CALCIUM fluoride and barium fluoride belong to the O_h class of the cubic system in the Schoenflies notation. They have three non-vanishing independent stress-optical constants q_{ij} in Pockels' scheme. All the q_{ij} have been determined for CaF_2 by the pioneer investigator of photoelasticity of crystals, Pockels [1] himself using the Babinet compensator and the interferometric methods. Recently, the photoelastic dispersion of $(q_{11}-q_{12})$ for CaF_2 has been studied by a number of workers *including Ziauddin*[2] *and Michael*[3]. For BaF_2, the only information available with regard to photoelasticity is that due to Jacob and Narasimhamurty[4] who have obtained $(q_{11}-q_{12})$ and q_{44} at wavelength 5893 Å using a Babinet compensator. Schimdt and Vedam [5] reported the effect of hydrostatic pressure on the refractive indices of CaF_2 and BaF_2 at the wavelength 5893 Å.

The authors have now computed all the stress-optical and the strain-optical constants for CaF_2 and BaF_2 by combining the hydrostatic data of Schmidt and Vedam with the stress birefringence data obtained by the previous workers. The strain polarizability constant λ_0 and the effect of temperature on the refractive index have been calculated for both the crystals.

CALCIUM FLUORIDE

Schmidt and Vedam[5] observed the change in refractive index of CaF_2 under uniform hydrostatic pressure to be $2{\cdot}44 \times 10^{-4}$/kb, from which one can arrive at the result,

$$(q_{11}+2q_{12}) = 1{\cdot}66 \text{ brewsters} \qquad (1)$$

taking the index of refraction $n_D = 1{\cdot}434$ for CaF_2. At [illegible]um yellow wavelength, using a birefringent compensator, Ziauddin[2] has determined the value,

$$(q_{11}-q_{12}) = -1{\cdot}45 \text{ brewsters.} \qquad (2)$$

Solving (1) and (2) we get

$$q_{11} = -0{\cdot}413 \text{ brewsters and}$$
$$q_{12} = 1{\cdot}04 \text{ brewsters.}$$

From these values of q_{ij}, the strain-optical constants p_{11} and p_{12} are calculated using the relation,

$$p_{hl} = \sum_{j=1}^{6} q_{hj}c_{lj}. \qquad (3)$$

The elastic constants of CaF_2 have been determined among others by Voigt[6], Huffman and Norwood[7] and Haussuhl[8]. The values reported by them do not differ much. The elastic constants used in these calculations are those due to Voigt. The values of p_{ij} and q_{ij} thus obtained are given in Table 1.

BARIUM FLUORIDE

Schmidt and Vedam[5] reported the change of refractive index due to uniform hydrostatic pressure on BaF_2 to be $6{\cdot}40 \times 10^{-4}$/kb. From this data we get

$$(q_{11}+2q_{12}) = 4{\cdot}01 \text{ brewsters.} \qquad (4)$$

Combining this information with the stress optical data obtained by Jacob and Narasimhamurty[4] i.e.

$$(q_{11}-q_{12}) = -2{\cdot}93 \text{ brewsters} \qquad (5)$$

we get

$$q_{11} = -0{\cdot}617 \text{ brewsters and}$$
$$q_{12} = 2{\cdot}31 \text{ brewsters.}$$

From these values of q_{ij}, the strain-optical constants p_{11} and p_{12} are calculated as for CaF_2. As there is not much difference between the elastic constants obtained by Bergmann [9], Haussuhl[8] and Gerlich[10], the elastic constants used in these calculations are the same as those used by Jacob and Narasimhamurty, namely those due to Bergmann. The index of refraction assumed is $n_D = 1{\cdot}472$ at 5893 Å. The values of the stress-optical and the strain-optical constants thus calculated are given in Table 1.

Using the formula $(n^3/6)(p_{11}+2p_{12}) = L(1-\lambda_0)$ where $L = \frac{(n^2-1)(n^2+2)}{6}$ we have calculated the strain polarizability constant λ_0 at 5893 Å from the values of the strain optical constants given in Table 1 for CaF_2 and BaF_2.

Table 1

Constants \ Substance	CaF_2		BaF_2	
	Ziauddin	Present	Jacob and Narasimhamurty	Present
q_{11} brewsters	—	−0·413	—	−0·617
q_{12} brewsters	—	1·04	—	2·31
$(q_{11}-q_{12})$ brewsters	−1·45	—	−2·93	—
q_{44} brewsters	0·89	—	1·06	—
p_{11}	—	0·0258	—	0·131
p_{12}	—	0·202	—	0·277
$(p_{11}-p_{12})$	−0·164	—	−0·146	—
p_{44}	0·0239	—	0·0264	—
p_{12}/p_{11}	—	8·2	—	2·12

The temperature change of refractive index is due to two factors (Pockels[11]): (1) due to the deformation caused by temperature and (2) due to direct influence of temperature on the refractive index. Thus the thermo-optic behavior can be represented by,

$$\frac{dn}{dt} = \left(\frac{dn}{dt}\right) + \left(\frac{\delta n}{\delta t}\right) \tag{6}$$

Here dn/dt is the observed change in the refractive index due to temperature, (dn/dt) is the factor due to thermal dilatation and $(\delta n/\delta t)$ the true temperature coefficient. The factor due to thermal dilatation can be calculated from the known strain optical data the the known linear thermal expansion coefficients. Sirdeshmukh and Deshpande[12] found the thermal expansion coefficients to be $20{\cdot}01\times10^{-6}$ for CaF_2 and $20{\cdot}07\times10^{-6}$ for BaF_2 at 20°C. From this data we can get the contribution in the change of refractive index due to thermal dilatation as follows:

$$B_{11} - B^{\circ}_{11} = -(p_{11}\alpha_{xx} + p_{12}\alpha_{yy} + p_{13}\alpha_{zz}) \tag{7}$$

i.e.

$$\frac{-2\Delta n}{n^3} = -(p_{11}+2p_{12})\alpha_{xx}$$

$$\therefore \Delta n = \frac{n^3}{2}(p_{11}+2p_{12})\alpha_{xx}. \tag{8}$$

Thus we get

$$\left(\frac{dn}{dt}\right) = -1{\cdot}268\times10^{-5} \text{ for } CaF_2$$

$$\left(\frac{dn}{dt}\right) = -2{\cdot}215\times10^{-5} \text{ for } BaF_2.$$

The effect of temperature on the refractive index of CaF_2 has been studied by Radhakrishnan[13] and Houston *et al.*[14], and of BaF_2 by Houston *et al.*[14] and Malitson[15]. $dn/dt = -1{\cdot}15\times10^{5}$ at 20°C which is the extrapolated value for CaF_2 obtained from Radhakrishnan's results. Houston *et al.* report $dn/dt = -1{\cdot}60\times10^{-5}$ for CaF_2, $-1{\cdot}86\times10^{-5}$ for BaF_2 at 20°C and Malitson finds $dn/dt = -1{\cdot}50\times10^{-5}$ for BaF_2 at 20°C. The true temperature coefficient of refractive index of CaF_2 and BaF_2 have been calculated using equation (6) from the above data. Using Radhakrishnan's value of dn/dt, we get $(\delta n/\delta t) = +0{\cdot}118\times10^{-5}$ per °C for CaF_2 and using Malitson's value of dn/dt we get $(\delta n/\delta t) = 0{\cdot}715 \times 10^{-5}$ per °C for BaF_2 whereas taking the value of dn/dt for both CaF_2 and BaF_2 as obtained by Houston *et al.* we get $-0{\cdot}322 \times 10^{-5}$ and $+0{\cdot}355 \times 10^{-5}$ per °C respectively. Thus the value of $(\delta n/\delta t)$ for CaF_2 calculated from the value of dn/dt as obtained by Houston *et al.* is negative, though the corresponding value for BaF_2 is positive. Hence the other set of values of $(\delta n/\delta t)$ seem to be more probable. The several optical data including the strain polarizability constants are now collected in Table 2.

The most striking conclusion from Table 1 is that both the strain-optical constants p_{11} and p_{12} are positive for CaF_2 and BaF_2 while $(p_{11}-p_{12})$ is negative for both i.e. p_{11} is less than p_{12}, and magnitudes of p_{ij} are higher for BaF_2 than those for CaF_2. Again, both the crystals have q_{11} negative and the magnitudes of q_{11} and q_{12} are higher for BaF_2 than those for CaF_2. The ratio of (p_{12}/p_{11}) is 8·2 for CaF_2, but it is only 2·12 for BaF_2. Thus as we go from CaF_2 to BaF_2, the magnitudes of p_{ij} and q_{ij} are increasing while their ratio (p_{12}/p_{11}) has gone down to $\frac{1}{4}$ roughly. Furthermore, this ratio has been obtained by Pockels as 4·07 while Schmidt and Vedam's values give 7·62. Hence the value of this ratio has to be confirmed directly by ultrasonic experiments.

From Table 2 one can note that the strain-polarizability constant λ_0 for BaF_2 is less than that for CaF_2. The true temperature coefficient $(\delta n/\delta t)$ of BaF_2 is larger than that of CaF_2.

Table 2

Substance / Constants	CaF_2	BaF_2
n_D	1·434	1·472
λ_0	0·704	0·551
$\dfrac{\rho dn}{d\rho}$	0·211	0·364
$\dfrac{\delta n}{\delta t}$	$0{\cdot}118 \times 10^{-5}$/°C	$0{\cdot}715 \times 10^{-5}$/°C

Acknowledgements—One of the authors (K.V.R) is grateful to University Grants Commission, India for the award of a Research Training Scholarship.

Department of Physics,
Osmania University,
Hyderabad—7,
India

K. VEERABHADRA RAO
T. S. NARASIMHAMURTY

REFERENCES

1. POCKELS F., *Lerhrbuch der Kristalloptik.* Teubner, Leipzig and Berlin (1906).
2. ZIAUDDIN M., Ph.D. Thesis, Osmania University, Hyderabad, India (1966).
3. MICHAEL A. J., *J. opt. soc. Am.* **58**, 889 (1968).
4. JACOB P. J. and NARASIMHAMURTY T. S., *Curr. Sci.* **31**, 328 (1962).
5. SCHMIDT E. D. D. and VEDAM K., *J. Phys. Chem. Solids* **27**, 1563 (1966).
6. VOIGT W., *Lehrbuch der Kristallphysik.* Teubner, Leipzig (1910).
7. HUFFMAN D. R. and NORWOOD M. H., *Phy. Rev.* **117**, 709 (1960).
8. HAUSSUHL S., *Phys. Status Solidi* **3**, 1072 (1963).
9. BERGMANN L., *Z. Naturf.* **12A**, 229 (1957).
10. GERLICH D., *Phys. Rev.* **135**, 1331A (1964).
11. POCKELS F., *Ann. Phys.* **37**, 144, 372 (1889).
12. SIRDESHMUKH D. B. and DESHPANDE V. T., *Ind. J. pure appl. Phys.* **2**, 405 (1964).
13. RADHAKRISHNAN T., *Proc. Ind. Acad. Sci.* **A33**, 22 (1951).
14. HOUSTON T. W. *et al.*, *J. opt. Soc. Am.* **53**, 1286 (1963).
15. MALITSON I. H., *J. opt. Soc. Am.* **54**, 628 (1964).

J. Phys. Chem. Solids Vol. 31, pp. 878–883.

Optical properties of chromium rich chromium iron alloys at room temperature*

(*Received* 12 *May* 1969; *in revised form* 20 *August* 1969)

LOW TEMPERATURE specific heat measurements on transition element alloys with electron per atom ratios, e/a, between 5·5 and 7 have been frequently analyzed with a rigid band model. Measured liquid He temperature electronic specific heat coefficients, γ_0, which are in simple systems proportional to the density of states, $N(E)$, follow a similar pattern not only in disordered transition element alloys of V–Fe, Cr–Fe, and Cr–Mn but also in ordered $TiFe_{1-x}Co_x$ and $TiFe_{1-x}$, Ni_x compounds[1].

---

*Work supported by the National Science Foundation.

The rapid increases in γ_0 with e/a for alloys with $e/a \approx 6$ cannot be explained with the concept of impurity states only, because specific heat data over an extended temperature range on pure chromium can be explained only with a sharp minimum in the density of states curve, confirming qualitatively the rigid band model for $e/a = 6$[2]. Figure 1 shows the density of states as calculated from γ_0 and the concept of the rigid band model[2]. This curve was used to calculate quantitatively high temperature specific heat data of pure chromium.

Specific heat measurements give only information on the electronic state in an energy interval of the order of kT. Measurements in the liquid He temperature range give the average density of states $N(E)$ values in an energy interval of $kT = 10^{-4}$ eV. If one measures specific heats at elevated temperatures above 1000°K, then one averages $N(E)$ over an energy interval of the order of 10^{-1} eV. This shows that it is presently not possible to determine features of the electronic structure far below or above the Fermi level from specific heat measurements. Other techniques, as e.g. optical measurements have to be used.

Photons, absorbed in a metal, interact with electrons and excite them into higher states. Different types of electron excitations due to photon interactions are possible. A general survey has been given e.g. by Ehrenreich[3]. For low photon energies, interband and intraband effects are of interest. The former can be found also for intermediate photon energies. Plasma oscillations of electrons are expected

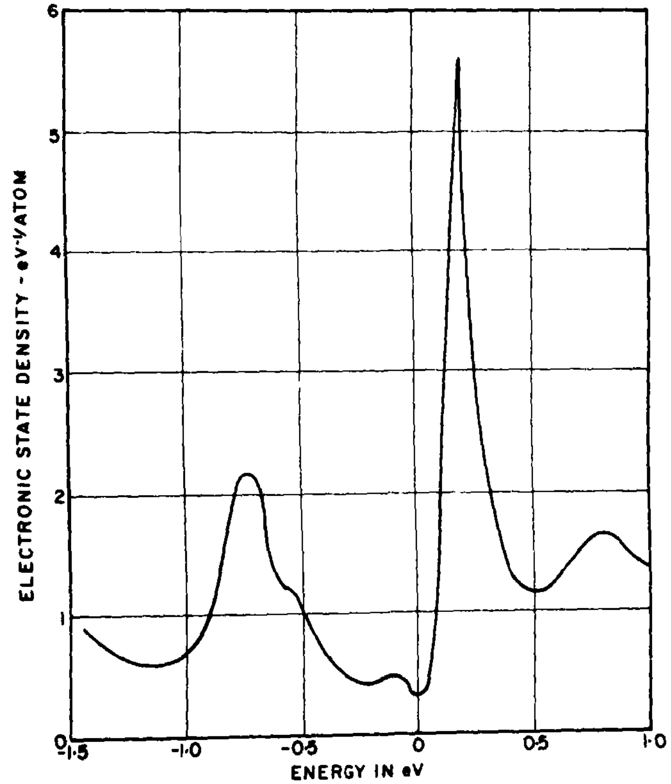

Fig. 1. Ordinate: electronic state density eV⁻¹/atom. Abscissa: energy in Ev. Electronic state density of chromium according to Shimizu *et al.*[2]. Fermi energy level of chromium set equal to zero eV.

for higher energies above those used in our experiments.

Intraband transitions are associated with electron transition inside one band. In interband transitions, electrons jump from one energy band to another band. Intraband absorption in good electrical conductors should lead to a very high reflectance value R close to one. Low energy interband transitions lead to a rapid decrease of R with increasing photon energy (absorption edge).

Optical properties on pure chromium samples have been measured by several authors[4–9]. Lenham *et al.*[4–7] investigated optical properties of transition metals with photon energies below 4 eV. Lenham[7] plotted $2\eta\kappa/\lambda$ as a function of wavelength on log–log paper. Any consistent correlation with λ of the form $2\eta\kappa/\lambda = \text{const}\,\lambda^{\alpha}$ characteristic for intraband relations would give a linear plot with gradient α. He found a nearly linear section in this plot for the majority of transition metals studied only for longer wavelength. For chromium α is 0·74. Deviations from this straight line indicate interband transitions. Its low energy limit is 0·24 eV for chromium. The relatively shallow increase of $\eta\kappa/\lambda$ with decreasing wavelengths indicates according to Lenham, that the energy band with electrons responsible for the interband transition is not parallel to the Fermi energy level. A temperature dependent reflectance anomaly near 10 μm is probably due to the spin density wave associated with antiferromagnetic ordering.

The density of states curve of chromium rich alloys has a sharp minimum at pure chromium[1]. This is due to antiferro-magnetic ordering, as γ_0 measurements on Cr–Mo and Cr–W alloys indicate. The increase of γ_0 with increasing e/a ratio has been associated with filling of e_g states,[10] which are responsible for localized moments and for the onset of ferromagnetism at 10 at.% in Cr. γ_0 reaches a maximum for the alloy with 19 at.% Fe. γ_0 is rather flat (neglecting the γ_0 minimum due to antiferromagnetic ordering) for Cr *V* alloys and increases below $e/a = 5{\cdot}5$ with decreasing e/a values. It has been proposed that d electrons for $e/a < 6$ are of t_{2g} symmetry. Using a simple 3-band model with a conduction band, a e_g-band, and a t_{2g}-band one would expect that photon assisted interband transitions may be possible for t_{2g} electrons. They would be excited to the Fermi level of the conduction band. This transition should be noticeable for photon energy values equal to the difference between Fermi level and the rapid increase in $N(E)$ below E_F. Figure 1 shows this energy difference to be about 0·3 eV. This value agrees within experimental accuracy with the energy associated with the onset of interband transition[7]. $N(E)$ increase with decreasing e/a values and reaches a maximum for e/a between 4 and 5. This maximum is about 0·7–0·8 eV, below the Fermi energy of chromium and should correspond to the high energy end of the absorption edge. One has to conclude that $E(k)$ for the t_{2g}-band is not parallel to the Fermi surface, just as expected for photon assisted electron transitions by Lenham[7]. The 0·3 eV energy difference between chromium and the sudden increase in $N(E)$ is close to the threshold energy value of 0·24 eV given by Lenham. Using the rigid band model, and increase of e/a to 6·46 (23 at.% Fe in Cr) should shift E_F by about 0·25 eV (see Fig. 1). The energy difference for the onset of a noticeable electron transitions should then be found at about 0·5 eV, and the end of the absorption edge (close to 0·8 eV for pure chromium) should move to an energy value of 1 eV for the alloy with 23 at.% Fe. Our measurements of R in the range from 0·5 to 2·4 eV should therefore be able to confirm or reject this simple rigid band model.

EXPERIMENTAL PROCEDURE

The method of measuring the absorption characteristics of the alloy samples is based on measuring the temperature change of the thermally connected sample-black absorber when the sample or black absorber is illuminated by monochromatic radiation[11–12]. Thus for the sample-black absorber with a total heat capacity C, the energy absorbed gives rise to an increase in heat ΔQ, with $\Delta Q = C\Delta T$. The energy absorbed per unit time is $C\dot{T}$. The ratio of the heating rate when the sample is illuminated to the heating rate when the black absorber is illuminated is equal to the sample absorptivity $A = 1 - R$, where R is the sample reflectance for an opaque material.

The 'specimen-black absorber' temperature change is detected by an iron-contantan thermocouple whose output is then amplified by a Keithley Millimicrovoltmeter. The signal is then passed through an active filter which has an upper cutoff frequency of 0·3 Hz, differentiated and recorded on an $x - t$ recorder. The filter is necessary since the Keithley output contains high frequency components superimposed on the *d.c.* level and the process of differentiation enhances these components resulting in a noisy recording signal. A similar system was used before by Chapman[13].

The chromium–iron samples were prepared from high purity chromium chips and Westinghouse puron iron. Appropriate amounts of chromium and iron were melted several times in an arc furnace under an argon atmosphere. The samples were then annealed in a 92%He–8%H_2 atmosphere and quenched. Details of this procedure and sample analysis have been described previously[14].

It is presently not possible to prepare chromium with a 'perfect' surface. The oxide film is very stable and cannot be removed by annealing. Further, the composition of the surface layer will change during such a procedure. This may also occur if one uses argon bombarding for cleaning. Electrolytic polishing may also produce surface films of unknown structure, and the absorptivity may be more characteristic of the film than of the metal. Mechanical polishing by hand was therefore utilized[15], taking the samples down with 600 grit paper; then they were rinsed with distilled water and inspected under a microscope for surface irregularities. A typical finished specimen size was $4 \times 4 \times 0{\cdot}6\ \text{mm}^3$. This procedure should result in rather small surface deformation since the samples are brittle. One has to keep in mind that a relative comparison of the various alloys is made and a systematic error due to an electrically insulating surface film is not critical.

RESULTS AND DISCUSSION

Figure 2 shows the reflectance R of chromium rich alloys as a function of photon energies from 0·5 to 2·4 eV. R drops sharply from values between 0·85 to 0·90 at 0·5 eV to values between 0·6 and 0·7 at 0·7 eV. R stays in this 0·6–0·7 value range for increasing photon energies. Only the R values of pure chromium and of the alloy with 10 at% Fe fell out of this range. Pure chromium reaches lower R and the alloy with 10 at.% Fe reaches higher R values than the other samples. These slight anomalies should be associated with general uncertainties of the measurements. They are not associated with a lack in reproducibility of the data, because it is possible to repeat measurements on one sample within 3 per cent. The details of the $R = R(E)$ curves are therefore 'real'. We are essentially concerned with slopes of $R(E)$ curves. Absolute values of R are not important. Presently it is not possible to interpret the fine features of the curves and to show which feature corresponds to bulk properties or to surface features.

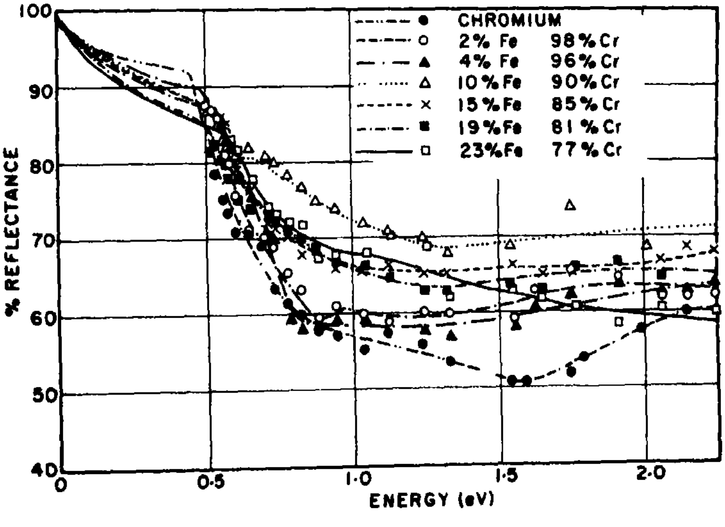

Fig. 2. Ordinate: reflectance in percentage, Abscissa: energy (eV). Reflectance of chromium iron alloys as a function of photon energy.

Reflectance values of some samples bend over into a more horizontal direction with decreasing photon energies. R reaches near 0·5 eV those values expected from d–c resistivity data and the Hagen–Rubens relation for intraband transitions. The change in the slope occurs in the same region as in R values obtained in previous experiments[4–8]. The steep slopes of the $R(E)$ curves in the range from 0·5 to 0·8 eV indicate their association with interband transitions[3]. The slopes extropolate to $R(E) = 1$ for $E = 0{\cdot}3$ eV for practically all alloys. This implies that interband transitions begin for all samples independent of composition near 0·3 eV, if we use the to $R(E) = 1$ extrapolated R value as characteristic for the onset of interband transitions, following the approach by Biondi and Rayne [16]. Only the sample with 10 at.% Fe seems to be an exception. This alloy composition has aside from a rather high room temperature resistivity[17–20], no special characteristic which can be correlated to high reflectance values (The onset of ferromagnetism at liquid He temperature is found near 10 at.% Fe. This sample should be paramagnetic at room temperature[21]. Its high R values are therefore attributed to experimental uncertainties).

This result indicates that a rigid band model cannot be used to analyze the experimental results, because this model predicts a shift of the Fermi energy E_F by about 0·25 eV with the addition of 23 at.% Fe to chromium. Such a shift should move the edge in the reflectance curve by the same amount to higher energies if the absorption edge is associated with transitions from states below the Fermi surface to E_F. Similarly, transitions from E_F to higher states would lead with increasing iron concentration to a shift of the absorption edge to lower photon energy level.

It is therefore proposed that iron impurities form a new energy band at the Fermi level. These states could be 'virtual energy states', similar to those due to nickel impurities in the Cu Ni system[11–12]. There it was proposed that new energy states were responsible for optical absorption phenomena for photon energies of about 4 eV. The states associated with Fe in Cr have to be at least as close as 10^{-3} eV to the Fermi level, else they would not be noticeable in the liquid He temperature specific heat measurements where T ranges from 1·5 to 4·2°K. The concept of 'virtual energy states' has been proposed to explain the effects of small amounts of impurities on physical properties of alloys[22]. The localized wave functions of transition element impurities interact with those parts of the conduction electron wave functions with d-character. This leads to a shift of the energy state of the impurity atom electron from its original energy E_0 to a resonance energy E_r. It will interact strongly with conduction electrons with this energy. 'Virtual energy states' lead to new density of states terms and may be responsible for an additional term in the specific heat which is proportional to the absolute temperature. Therefore this term cannot be separated from the regular electronic specific heat. The theory of virtual energy states has not been expanded to high impurity concentrations, but one may expect that essentially E_r will be independent of E_F. The high resistivity of Cr Fe alloys would indicate that E_r is close to the Fermi level. The same conclusion would be drawn from the rapid increase of γ_0 of Cr Fe alloys with increasing iron concentration, if this would be associated only with impurity 'virtual energy states'. However it is more likely that γ_0 increases with increasing iron concentration because we have both an increase in the regular electronic specific heat, and some contribution to γ_0 from impurity states. The increase in the regular specific heat can be deduced from the interpretation of the high temperature specific heat data of pure chromium, which can be understood only if one assumes that $N(E)$ is close to a minimum in the density of states curve for $e/a \sim 6$[2].

'Virtual energy states' would not necessarily effect the Fermi energy level, only the density of states. Transitions from the t_{2g} electron band to E_F would not change with iron concentration. This would explain the concentrantion independent absorption edge of chromium and chromium iron alloys.

This is naturally not the only way to describe the experimental results. One may postulate that Fig. 1 gives the correct density of states curve for pure chromium. The addition of iron and magnetic ordering is responsible for a shift of the subband associated with localized states. This means that the peak at +0·2 eV in respect to pure chromium in Fig. 1 will move to lower energies. if iron atoms are added to the system. The distance between t_{2g} states and E_F will not change markedly for this model. One may describe this system as a 'semi-rigid' band model.

C. E. McCAIN[*]
K. SCHRÖDER
Department of Chemical Engineering and Metallurgy,
Syracuse University,
Syracuse,
N.Y. 13210, U.S.A

REFERENCES

1. HEINIGER F., BUCHER E. and MULLER J., *Phys. kondens. Mater.* **5**, 243 (1966).
2. SHIMIZU M., TAKAHASHI T. and KATSUKI A., *J. phys. Soc. Japan* **17**, 1740 (1962)
3. EHRENREICH H., *Proc. Int. School of Phys.* Course 34, p. 106. *The Optical Properties of Solids*, Academic Press, New York (1966).
4. LENHAM A. P. and TREHERNE D. M., *J. opt. Soc. Am.* **56**, 1137 (1966).
5. GRAVES R. H. W. and LENHAM A. P., *J. opt. Soc. Am.* **58**, 884 (1968).
6. LENHAM A. P. and TREHERNE D. M., *J. opt. Soc. Am.* **56**, 1076 (1966).
7. LENHAM A. P., *J. opt. Soc. Am.* **57**, 473 (1967).
8. BARKER A. S., Jr., HALPERIN B. I. and RICE T. M., *Phys. Rev. Lett.* **20**, 384 (1968).
9. BOR J., HOBSON A. and WOOD C., *Proc. phys. Soc. Lond.* **51**, 932 (1939).
10. GOODENOUGH J. B., *Phys. Rev.* **120**, 67 (1960).
11. SCHRÖDER K. and ÖNENGÜT D., *Phys. Rev.* **162**, 628 (1967).
12. SCHRÖDER K. and MAMOLA K., *Phys. Rev.* **167**, 658, (1968).
13. CHAPMAN R., *Rev. scient. Instrum.* **40**, 95 (1969).
14. SCHRÖDER K. and McCAIN C. E., *Phys. Rev.* **135**, A149 (1964).
15. PELLS G. P., *J. scient. Instrum.* **44**, 997 (1967).
16. BIONDI M. A. and RAYNE J. A., *Phys. Rev.* **115**, 1522 (1959).
17. ARAJS S. and DUNMYRE G. R., *J. appl. Phys.* **37**, 1017 (1966).
18. SCHRÖDER K., YESSIK M. J. and BAUM N. P., *J. appl. Phys.* **37**, 1019 (1966).
19. RAJAN N. S., WATERSTRAT R. M. and BECK P. A., *J. appl. Phys.* **31**, 731 (1960).
20. NEWMANN M. M. and STEVENS K. W. H., *Proc. phys. Soc. Lond.* **74**, 290 (1959).
21. NEVITT M. V. and ALDRED A. T., *J. appl. Phys.* **34**, 463 (1963).
22. DANIEL E. and FRIEDEL J., *Low Temperature Physics*. (Edited by J. G. Daunt, D. O. Edwards, F. J. Milford and M. Yaqub), p. 933. Plenum Press, New York.

J. Phys. Chem. Solids Vol. 31, pp. 883–886.

Inhomogeneous broadening of edge recombination radiation

(*Received* 30 *July* 1969)

THE CREATION of excitons in an indirect gap material at low temperature gives an absorption coefficient of the form[1]

$$\begin{aligned}\alpha(\omega) &= 0,\ \omega < 0\\ &= \sqrt{\omega},\ \omega \geqslant 0\end{aligned}$$

where the origin of the frequency, ω, is the energy gap plus the relevant phonon energy. The corresponding recombination radiation spectrum is

$$\begin{aligned}I(\omega) &= 0,\ \omega < 0\\ &= \sqrt{\omega}\,\mathrm{e}^{-\beta\omega},\ \omega \geqslant 0\end{aligned} \tag{1}$$

where the origin of ω is moved to the energy gap *minus* the phonon energy, and $\beta = \hbar/kT$. Equation (1) is as would be expected by detailed balance arguments based on the absorption edge[2], although these arguments are not strictly valid when comparing low temperature spectra, due to phonons being emitted in both cases[3]. The same spectral distribution as (1) is found at donor-valence band and acceptor-conduction band ('defect-band') transitions, in direct gap materials, at least[4]. The origin of ω is then the energy gap minus the defect binding energy.

From (1), the peak height, $I(\omega_0)$, occurs at

---

[*] *Present address:* LeMoyne College, Syracuse, New York, U.S.A.

$\omega_0 = 1/2\beta$, and the full width at half height is $\Gamma = 1{\cdot}7953\ldots/\beta$. A sharp spike is then expected at $\omega = 0$ in the limit of low temperature, but the width of this line will be made finite by lifetime broadening and by the inhomogeneous state of the crystal. Since an exciton binding energy is low (~8 meV for Si) its diameter is large (~60 Å in Si on a simple Bohr model). The excitons are therefore expected to thermalise into the perturbed states of the strained lattice as a whole. The observed spectrum is then

$$F(\omega) = e^{-\beta\omega} \int_0^\infty \sqrt{x}\, p(x-\omega)\, dx \qquad (2a)$$

where $p(x)$ is a measure of the spreading out of the density of exciton states. On the other hand, a band-defect transition may be broadened by the defect binding energy being modified by other nearby imperfections in the lattice. If the carriers thermalise into essentially unperturbed lattice states and then make transitions to defects whose binding energies are distributed in a function $q(x)$ the observed spectrum is

$$G(\omega) = \int_0^\infty \sqrt{x}\, e^{-\beta x}\, q(x-\omega)\, dx. \qquad (2b)$$

MacFarlane *et al.*[5] found the absorption edge of Si is perturbed by a Gaussian broadening. In this Note we evaluate equations (2a, b) for Gaussian $p(x)$ and $q(x)$:

$$p(x) = q(x) = \exp(-ax^2) \qquad (3)$$

where the width of the Gaussian is

$$\Gamma_G = 2\sqrt{\frac{\ln 2}{a}}.$$

In this case, the *profiles* of equations (2a, b) are identical, for completing the square of the exponent of (2b) gives

$$G(\omega) = e^{-\beta^2/4a}\, e^{-\beta(\omega-\beta/2a)}$$

$$\times \int_0^\infty \sqrt{x}\, e^{-a[x-(\omega-\beta/2a)]^2}\,.\, dx \qquad (4)$$

$$\propto F(\omega - \beta/2a).$$

One may show the profiles are identical if the Fourier transform of $p(x)$ with respect to k, $T\{p(x), k\}$ has the property:

$$T\{p(x), k\} \propto T\{p(x), k - i\beta\}\, e^{ibk},$$

b constant, which is true for $p = e^{-ax^2}$.

The lineshape equation (2b) with Gaussian $q(x)$ has been evaluated by direct numerical integration and by Gauss–Laguere quadrature [6]. The quadrature method has been found to be sufficiently accurate for $2\beta\Gamma_G > 3{\cdot}5$ when 15 terms are used in the summation. The results are shown in Figs. 1 and 2 for the special case of $T = 20°$K. However, the data are applicable at all T after scaling as may be seen by writing equation (2b) in the reduced form

$$G(\nu) = e^{-\nu^2} \int_0^\infty \sqrt{y}\, e^{-y(r-2\nu)}\, e^{-y^2}\, dy$$

where $\nu = \sqrt{a}\omega$; $r = \beta/a$. Then, for example, the data for $T = 80°$K, $\Gamma_G = 4$ meV may be obtained by expanding the energy scale of the $T = 20°$K, $\Gamma_G = 1$ meV data by a factor of four.

The striking invariance of the high energy side of the spectra may be understood in the important cases where $\Gamma_G < 4kT$ by rewriting equation (4) as

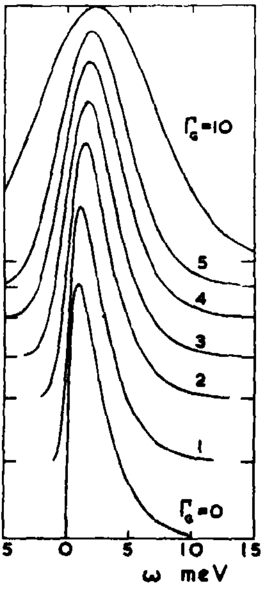

Fig. 1. Profiles of Gaussian broadened recombination radiation spectra at 20°K for Gaussian full widths Γ_G of 0–10 meV.

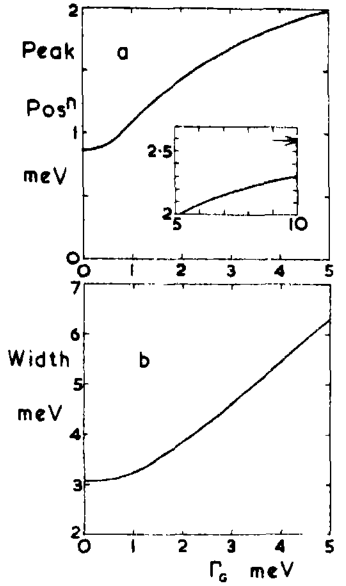

Fig. 2 The peak position (a) and full width at half height (b) of the spectrum after broadening, for Γ_G = 0–5 meV at 20°K. The peak position is measured from the true (unbroadened) threshold and the inset in (a) shows the peak position to Γ_G = 10 meV with the limit of movement arrowed.

$$G(\omega) = \mathrm{e}^{-\beta(\omega-\beta/4a)}\int_{-p}^{\infty}\sqrt{y+p}\,\mathrm{e}^{-ay^2}\,\mathrm{d}y \quad (5)$$

where $p = \omega-\beta/2a$; $y = x-p$. When the integral approximates to $\sqrt{\omega-c}$ where c is a constant, $G(\omega)$ has the *shape* of equation (1). Writing $\sqrt{y+p}$ as a Taylor series expansion about $y = 0$ we may drop all the odd powers of y in the expansion under the condition

$$p \gg \Gamma_G. \quad (6)$$

The integral of (5) is then

$$I = \sqrt{p}\int_{-p}^{\infty}\left\{1-\frac{y^2}{8p^2}-0\,.\left(\frac{y^4}{p^4}\right)\right\}\mathrm{e}^{-ay^2}.\mathrm{d}y$$

which, under the condition (6) is closely proportional to $\sqrt{p}$, or $\sqrt{\omega-\beta/2a}$, as required for the constant high energy side.

In Fig. 3, computed profiles are compared with experimental data for diamond, Si and GaP. The two components shown for diamond derive from the small spin orbit splitting of the valence band[7], and the spectrometer broadening will only substantially affect the lower energy component. For Si, the major broadening is due to fast exciton relaxation [2]. The GaP sample used was grown by SERL by vapour deposition on a GaAs substrate, and so may be strained due to the different lattice sizes.

Since convolution processes are associative, and since two Gaussians of widths Γ_1 and Γ_2 convolve to a third Gaussian of width $\sqrt{\Gamma_1{}^2+\Gamma_2{}^1}$, the profiles will be of the calculated form for any number of independent Gaussian processes. Thus, although in the examples given the spectra are appreciably instrument broadened, the calculations are applicable, and good fits result.

Acknowledgements—The author is grateful to C. D. Mobsby for providing unpublished GaP data, and to E. C. Lightowlers for helpful discussions.

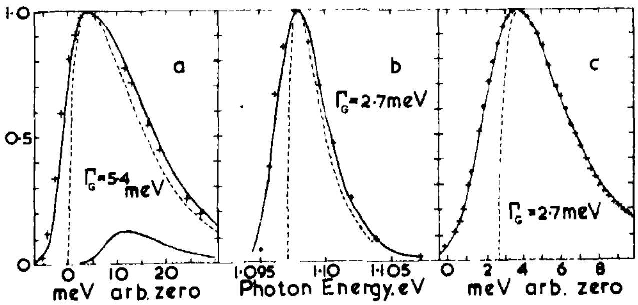

Fig. 3. Fits of the Gaussian broadened spectra to experimental data (+) for (a) the TO phonon of diamond at 100°K[7]; (b) the TO phonon of Si at 18°K[2]; and (c) the LA phonon of GaP at 25·5°K (Mobsby, unpublished). Unbroadened spectra are also shown (---).

Wheatstone Laboratory,
King's College,
Strand,
London W.C.2,
England

GORDON DAVIES

REFERENCES

1. ELLIOT, R. J., *Phys. Rev.* **108**, 1384 (1957). Experimental applications are illustrated by: CLARK C. D., DEAN P. J. and HARRIS P. V., *Proc. R. Soc.* **A277**, 312 (1964); DEAN P. J. and THOMAS D. G., *Phys. Rev.* **150**, 690 (1966).
2. HAYNES J. R., LAX M. and FLOOD W. F., *Proc. Int. Conf. on Semiconductor Physics*, p. 423. Academic Press, New York and London (1960).
3. NELSON D. F. and STURGE M. D., *Phys. Rev.* **137**, A1117 (1965).
4. EAGLES P. M., *J. Phys. Chem. Solids* **16**, 76 (1960).
5. MACFARLANE G. G., MCLEAN T. P., QUARRINGTON J. E. and ROBERTS V., *Phys. Rev.* **111**, 1245 (1958).
6. KOPAK Z. *Numerical Analysis. Chapman and Hall*, London (1955).
7. DEAN P. J., LIGHTOWLERS E. C. and WIGHT D. R., *Phys. Rev.* **140**, A352 (1965).

J. Phys. Chem. Solids Vol. 31, pp. 886–887.

Thermal conductivity and Lorenz ratio of RuO_2

(*Received* 8 *July* 1969)

INTEREST in the conducting transition metal oxides has recently increased as samples permitting sophisticated transport measurements have become available. RuO_2 is an example of such an oxide; it is metallic with a room temperature resistivity of 40 $\mu\Omega$-cm [1–3]. Very pure, small crystals have been grown with a ratio of room temperature to helium temperature resistance greater than 10^4[4]. The de Haas–van Alphen effect[4], magnetoresistance[5], and Azbel'–Kaner cyclotron resonance[6] have been observed in RuO_2. In this note the thermal conductivity and Lorenz ratio of RuO_2 are reported. This is the first measurement of these quantities in a conducting transition metal oxide.

The crystal was grown using oxygen-transport deposition; its dimensions were $4{\cdot}0 \times 0{\cdot}165 \times 0{\cdot}09$ mm.* Thermal conductivity was measured by the axial flow (c axis in the crystal), steady-state method. The temperature gradient was measured with a Au–Co vs. Ag–Au differential thermocouple. Since the sample was quite small and brittle, the leads were attached with some care.* The method of attaching leads was tested on a copper sample of approximately the same size. Measurements on the copper yielded a Lorenz ratio and ideal thermal conductivity in agreement with the literature[7].

It was necessary to correct for radiation from the heater surface, the corrections being larger than those in experiments with more conventional sample sizes. Such corrections were made by suspending the sample and heater from the heat sink by a small nylon chain, thus eliminating the thermal link to the heat sink. The temperature difference between the heater and its surroundings at a given power input was then measured. This procedure yielded the power radiated as a function of temperature. Radiated power was subtracted from input power in determining the thermal conductivity.†

The thermal conductivity of RuO_2 is shown in Fig. 1. The thermal conductivity, K, of metals follows the expression[7, 8]

$$\frac{1}{K} = \frac{\beta}{T} + \alpha T^n \qquad (1)$$

for temperature less than $1{\cdot}5\ T_m$ where T_m is the temperature at which K is a maximum. For RuO_2, this expression holds with $\alpha = 8{\cdot}42 \times 10^{-4}$ cm°K^{1-n}/W and $n = 1{\cdot}66$. This is an unusually low value for n, which typically lies between 2·0 and 3·0[7, 8]. β, for this sample, is 18·1 cm°K^2/W.

The resistivity was measured with the same leads used in the thermal conductivity measurement so that sample geometry did not affect the value obtained for the Lorenz

---

*The ratio of room temperature to helium temperature resistance was 115. Crystals with larger ratios were too smal[illegible]ermal conductivity measurements.

*Each thermocouple junction was glued with GE7031 varnish to a short copper wire which was then attached to the sample with a conducting cement, Emerson and Cuming 56C. The heater and heat sink were similarly connected to the sample.

†At 100°K, 40 per cent of the input power was radiated.

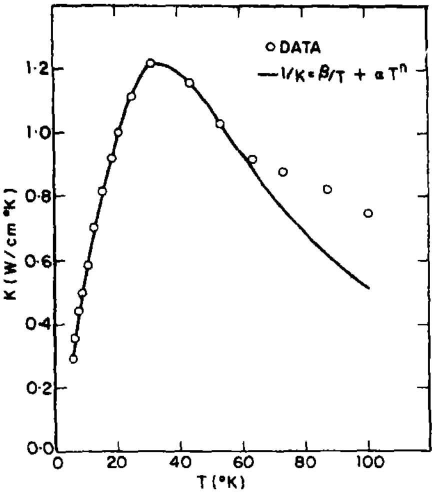

Fig. 1. Thermal conductivity of RuO_2.

ratio. At low temperatures, the Lorenz ratio reached a constant value of $(2{\cdot}60 \pm 0{\cdot}1) \times 10^{-8}\ W\Omega/°K^2$ which is close to the theoretical Lorenz number $2{\cdot}45 \times 10^{-8}\ W\Omega/°K^2$.

Acknowledgements—The author wishes to thank Dr. S. R. Butler for preparing the sample and Mr. Douglas M. Graham for technical assistance.

Central Research Department, J. MILLSTEIN
E. I. du Pont de Nemours,
Experimental Station,
Wilmington,
Delaware, U.S.A.

REFERENCES

1. SCHÄFER, H., SCHNEIDONEIT G. and GERHARDT W., *Z. anorg. allg. Chem.* **319**, 327 (1963).
2. RYDEN W. D., LAWSON A. W. and SARTAIN C. C., *Phys. Lett* **26A**, 209 (1968).
3. ROGERS D. B., SHANNON R. D., SLEIGHT A. W. and GILLSON J. L., *Inorg. Chem.* **8**, 841 (1969)
4. MARCUS S. M. and BUTLER S. R., *Phys. Lett.* **26A**, 518 (1968).
5. MARCUS S. M., *Phys. Lett.* **28A**, 191 (1968).
6. SLIVKA R. T. and LANGENBERG D. N., *Phys. Lett.* **28A**, 169 (1968).
7. WHITE G. K. and WOODS S. B., *Phil. Trans. R. Soc., Ser. A*, **251**, 273 (1958).
8. POWELL R. W., HO C. Y. and LILEY P. E., *Thermal Conductivity of Selected Materials.* (National Standard Reference Series—National Bureau of Standards, 8 (1966) and 16 (1968).

J. Phys. Chem. Solids Vol. 31, pp. 887–890.

Precision lattice parameters and thermal expansion of sodium nitrate

(*Received* 1 *May* 1969; *in revised form* 3 *June* 1969)

SODIUM nitrate, isostructural with calcite, crystallizes in the space group $R\bar{3}C$. It is one of the substances whose physical properties have been widely investigated. However, a perusal of the literature shows that, the agreement between the lattice parameters obtained by various investigators is not good. Consequently, the agreement between the coefficients of thermal expansion is also poor. As the thermal expansion of sodium nitrate is very interesting, in showing a large anisotropy, it is thought worthwhile to determine its precision lattice parameters at various temperatures and evaluate the coefficients of thermal expansion, as a part of a programme of X-ray studies on calcite type compounds.

The thermal expansion of sodium nitrate was studied by the dilatometer method by Kracek[1] from the room temperature to its melting point and by Hulsmann and Bilz[2] from the room temperature to liquid helium temperature. But the dilatometer method is not capable of measuring the anisotropy of thermal expansion.

Austin and Pierce[3] used single crystals to determine the coefficients of thermal expansion by the interference method. They found that $\alpha_\perp$ increased up to 100°C and then showed a decrease up to the melting point. Saini and Mercier[4] found by the X-ray method that $\alpha_\perp$ continued to increase up to 200°C. Thus there were conflicting reports about the behaviour of $\alpha_\perp$. To resolve these discrepancies, Kantola[5] measured the cell parameters of sodium nitrate from room temperature to the melting point using Unicam high temperature camera. More recently, Cherin *et al.*[6] measured the cell parameters of sodium nitrate from room temperature to 200°C. The results obtained by the various investigators are given in Table 1. It may be

Table 1. *Lattice parameters* (Å) *of sodium nitrate at different temperatures*

Temp. (°C)	Saini and Mercier[4]		Kantola and Vilhonen[5]		Cherin *et al.*[6]		Present study	
	a	*c*	*a*	*c*	*a*	*c*	*a*	*c*
25	5·070	16·818	5·071	16·818	5·071 ± 0·002	16·825 ± 0·003	5·0694 ± 0·0002	16·8200 ± 0·001
100	5·075	16·965	5·076	16·97	5·074 ± 0·002	16·976 ± 0·004	5·0726 ± 0·0002	16·9538 ± 0·001
150	5·079	17·084	5·079	17·09	5·075 ± 0·003	17·070 ± 0·004	5·0754 ± 0·0002	17·0638 ± 0·001
200	5·084	17·221	5·082	17·24	5·079 ± 0·003	17·164 ± 0·005	5·0791 ± 0·0002	17·2050 ± 0·001
250			5·085	17·46			5·0871 ± 0·003	17·4703 ± 0·01
300			5·089	17·77			5·0890 ± 0·003	17·6876 ± 0·01

seen from Table 1 that though there is fair agreement between the values of '*a*' at all temperatures, there is good agreement between the values of '*c*' only at room temperature. At higher temperatures, the agreement between the values of '*c*' is rather poor.

The powder specimen of sodium nitrate used in this investigation is prepared from crystals obtained from solution in water of an Analar grade sample. Using a 19 cm high temperature camera, powder photographs are taken with Cu radiation from a Raymax-60 demountable X-ray unit, at different temperatures ranging from the room temperature to the melting point. The experimental details and the method of evaluating the lattice parameters and the coefficients of thermal expansion are given in a recent paper[7].

Reflections 5, 0, 4; 2, 2, 16; 3, 1, 16; 4, 1, 12; and 5, 1, 4 (in terms of hexagonal unit cell) recorded in the Bragg angle region 63°–83°C have been selected for evaluating the lattice parameters using Cohen's[8] analytical method. Above 250°C, as some of the high angle reflections are very much diminished in intensity, a few reflections of Bragg angles between 50° and 73° have also been included. In calculating the lattice parameters independent measurements and calculations have been made using several films.

The lattice parameters obtained at different temperatures are given in Table 1 and shown grap[illegible] in Fig. 1. The data of the other investigators also are shown graphically in Fig. 1 for comparison. The coefficients of

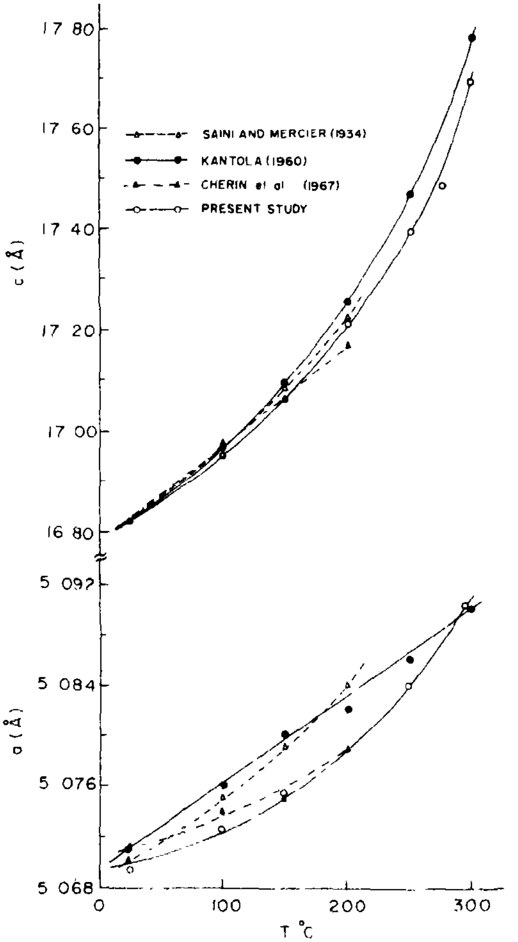

Fig. 1. Lattice parameters of sodium nitrate at different temperatures.

expansion at different temperatures are given in Table 2 and shown graphically in Fig. 2 along with the data obtained by other investigators. The temperature dependence of the coefficients is represented by the following equations:

$$\alpha_{\parallel} = 135{\cdot}60 - 75{\cdot}67 \times 10^{-8}t + 5{\cdot}23 \times 10^{-9}t^2$$
$$\alpha_{\perp} = 6{\cdot}82 + 1{\cdot}44 \times 10^{-8}t + 1{\cdot}82 \times 10^{-10}t^2$$

where t is in °C.

A few photographs recorded at different temperatures are shown in Fig. 3. Figure 3 shows that the displacement of reflections with large l indices, 2, 2, 16; 3, 1, 16 and 4, 1, 12 are much more than those of 5, 0, 4 and 5, 1, 4 the reflections with small l indices. This is on account of the large value of $\alpha_{\parallel}$ when compared with $\alpha_{\perp}$.

Table 2. Coefficients of thermal expansion of sodium nitrate at different temperatures

Temperature (°C)	$\alpha_{\perp} \times 10^6$ Obs.	$\alpha_{\perp} \times 10^6$ Calc.	$\alpha_{\parallel} \times 10^6$ Obs.	$\alpha_{\parallel} \times 10^6$ Calc.
50	8·33	8·00	104·01	111·10
90	9·27	9·60	117·68	120·70
130	11·64	11·78	132·82	130·37
170	14·10	14·54	163·44	161·11
210	18·44	17·89	208·94	212·91
250	22·29	21·82	264·67	279·79
290	25·89	26·32	375·17	364·17

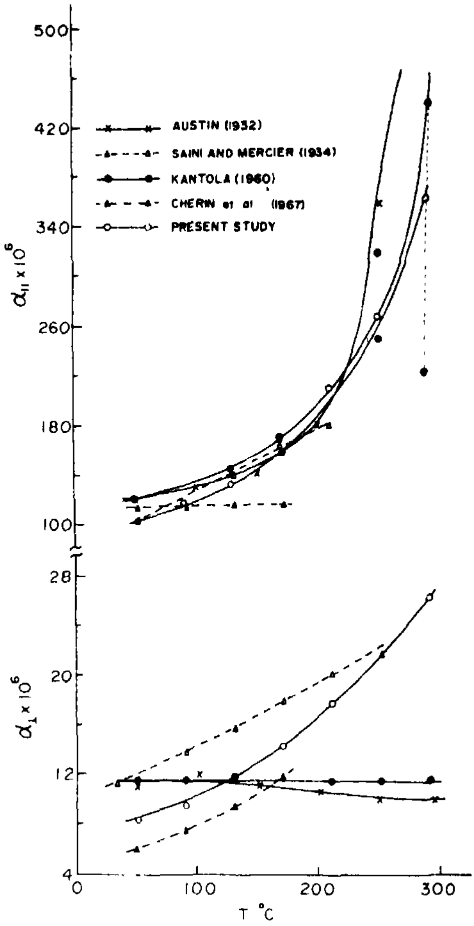

Fig. 2. Thermal expansion coefficients of sodium nitrate at different temperatures.

The lattice parameters at room temperature obtained in the present investigation are compared with the values obtained by other workers in Table 1. There is good agreement between the values obtained by the various investigators.

Table 1 also shows the lattice parameters obtained at different temperatures by various investigators. There is reasonable agreement between the values of the present investigation and those given by Kantola[5]. The values of the '*c*' parameter obtained by Cherin *et al.* [6] at higher temperatures appear to be very much in error probably on account of the single crystal method used by them for higher temperatures.

The coefficients of thermal expansion at 50°C reported by various investigators are shown in Table 3. There is good agreement between the values of the present investigation and the values reported by Austin and Pierce [3] and Kantola[5].

Figure 2 shows that there is good agreement between the coefficients of expansion obtained in the present investigation and the values reported by Kantola[5] up to 250°C. Above 275°C Kantola[5] reported a sudden decrease in the value of $\alpha_{\parallel}$, which has not been observed

Table 3. Comparison of coefficients of thermal expansion of sodium nitrate

Temp. (°C)	Method	Author	$\alpha_\perp \times 10^6$	$\alpha_\parallel \times 10^6$
50	X-ray	Saini and Mercier[4]	10·42	93·60
50	X-ray	Kantola[5]	10·00	120·5
50	Interferometer	Austin and Pierce[3]	11·00	120
50	X-ray	Cherin *et al.*[6]	6·25	127·29
50	X-ray	Present study	8·33	111·10

in the present investigation. It may be mentioned that on account of the low intensity of the high angle reflections above 250°C, it is not possible to get accurate values of the cell parameters above 250°C. Consequently the percentage error in $\alpha_\parallel$ will be very large and this may be the reason for considerable differences between the values of $\alpha_\parallel$ reported by us and those of Kantola above 250°C. Thus the present investigation has shown that both $\alpha_\parallel$ and $\alpha_\perp$ of sodium nitrate continuously increase with temperature upto its melting point.

Acknowledgement—The authors wish to express their grateful thanks to the Council of Scientific and Industrial Research, New Delhi for the sanction of a Research Scheme.

Department of Physics, K. V. KRISHNA RAO
Osmania K. SATYANARAYANA MURTHY
University,
Hyderabad-7,
India

REFERENCES

1. KRACEK F. C., *J. Am. chem. Soc.* **53**, 2609 (1931).
2. HULSMANN O. and BILZ W., *Z. anorg. allg. Chem.* **219**, 357 (1934).
3. AUSTIN J. B. and PIERCE R. H. H., *J. Am. chem. Soc.* **55**, 625, (1932).
4. SAINI H. and MERCIER A., *Helv. phys. Acta* **7**, 267 (1934).
5. KANTOLA M. and VILHONEN E., *Ann. Acad. Sci. Fenn.*, Series AVI **54**, (1960).
6. CHERIN P., HAMILTON W. C. and POST B., *Acta Crystallogr.* **23**, 455 (1967).
7. KRISHNA RAO K. V., NAGENDER NAIDU S. V. and SATYANARAYANA MURTHY K., *J. Phys. Chem. Solids* **29**, 245 (1968).
8. COHEN M. U., *Rev. scient. Instrum.* **6**, 68 (1935).

J. Phys. Chem. Solids Vol. 31, pp. 890–892.

Evidence of deformation twinning in natural diamond crystals

(*Received 2 June 1969*)

1. INTRODUCTION

FRIEDEL and Ribaud[1] observed a relaxation in the birefringence of a diamond crystal which was heated to 1880°C. They interpreted their observation as evidence of plastic flow relieving internal strain. The experiments of Gallagher[2], Bell and Bonfield[3], Penning and de Wind[4] and Peissker *et al.*[5] on crystals of the diamond structure like silicon and germanium have shown that extensive plastic deformation of these crystals occured at temperatures in excess of one-half to two-thirds of their absolute melting temperatures. In the case of diamond itself, slip lines have been produced by Seal[6], Phaal[7] and Evans and Wild[8] and evidence is conclusive that diamond which is hard and brittle at ordinary temperatures becomes ductile when suitably heated. Williams[9], Tolansky and Omar[10] and Tolansky *et al.*[11] have also reported observing slip lines on natural octahedral faces of diamond.

Plastic deformation in crystals can take two distinct forms; *slip* and *deformation twinning*. Slip is fundamental and an essential prerequisite for twinning and Maruyama [12] has shown that their relative probabilities depend on pressure and temperature. Earlier, Seifert[13] had postulated that the twin lamellae in galena was of mechanical origin and formed in nature at high pressure and temperature.

Diamond formed in nature, presumably at high pressure and temperature, and able to slip might twin as well. No evidence however of deformation twinning in diamond has ever been reported. According to Cahn [14], twinning even in materials of the diamond structure requires to be confirmed.

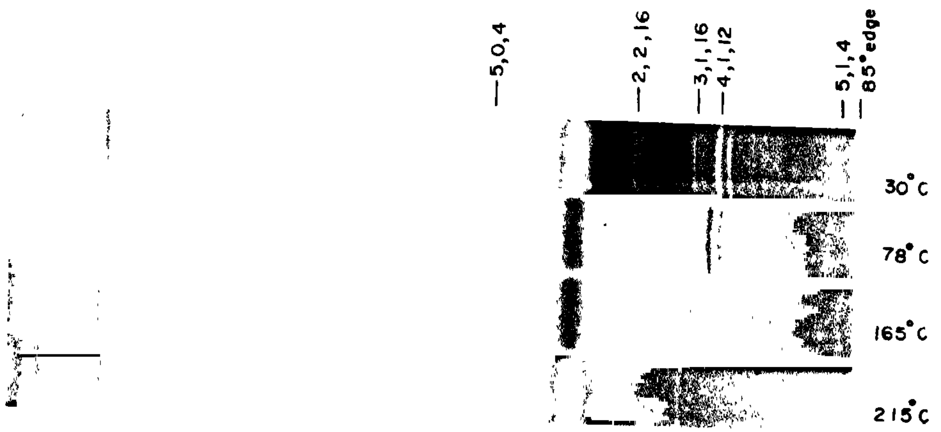

Fig. 3. Powder photographs of sodium nitrate at different temperatures.

In the above background, the observations herein reported are significant as they offer, perhaps for the first time, evidence that deformation twinning occurs in diamond.

2. OBSERVATIONS

The features studied are similar to those studied by Tolansky *et al.*[11] on one crystal. They appear as linear discontinuities on octahedral faces of natural diamond crystals and run parallel to a ⟨110⟩ direction lying in the face. Often they show trigons 'strung' on them—a characteristic first observed by Sutton[15]. The trigons may occur close together or may be far apart. Very often the lines extend right across a whole face and sometimes may be followed round the crystal edge and across one or more adjacent faces. There is *always* a step on the surface, the magnitude of which might vary from line to line as well as along the same line. When multiple lines occur side by side on a crystal, generally the less pronounced of them are also the shorter. Figure 1 brings this out. Line A extends over more than two-thirds the length of the crystal face, whereas B and C which are fainter are also respectively shorter.

Tolansky *et al.*[11] in the crystal studied by them, noted that the lines were strictly straight and parallel giving no suspicion what so ever of any fracture along them. Figure 2 provides an interesting case where after having been sharp and straight for a considerable length, the line unmistakably wriggles towards the right end. Figure 3 shows a wriggling part of a long line passing through two tiny trigons at the two ends. Despite the wriggling, the overall direction seems fairly well maintained. Occasionally after passing through centres of trigons and maintaining their rectilinearity and direction over a considerable length, they change their course and even direction. An example is in Fig. 4. It is interesting to note that towards the left end the line after deviation manages to pass through the centres of some trigons. Another interesting case is in Fig. 5 where the line loses direction, regains it and in the process gets laterally displaced.

The nature of the discontinuity becomes evident when examined at high magnification after tilting the crystal suitably. The appearance of the line as a mere discontinuity undergoes a veritable transformation and its structure unfolds itself. Figure 6 shows at high magnification a small length of a line passing through two trigons side by side. A slight tilt to the crystal surface gave Fig. 7 where the structure of the discontinuity becomes evident. Without doubt it has all the appearance of a twin lamella.

3. CONCLUSION

The formation of twin lamella with step on the surface is proof that the phenomenon is deformation twinning. For slip and twinning, high pressures and temperatures are necessary. It must be mentioned here that in none of the several cases studied, was there any evidence of graphitization on the surface. This suggests according to the Berman–Simon equilibrium curve[16] that the phenomenon could have occurred even as the diamond was formed in nature. The clear evidence of occasional fracture along the lines is consistent with the very intimate relation between fracture and slip and twinning. At the same time, the propagation of the lines without obvious fracture sometimes over considerable lengths need not present any puzzle as we know from the work of Bridgman[17] that high pressure could enhance plasticity and inhibit to a large extent brittle fracture. The propagation of the features through centres of trigons suggests intrinsic weakness in the planes containing trigon centres. This agrees well with the theory of trigon formation around lattice defects proposed by Varma[18].

Churchman[19] has shown that when crystals containing twin lamellae are annealed, the lamellae sometimes disappear leaving the surface steps behind. What would happen in the case of the diamond twins would be an interesting study.

Physics Department,
C. M. College (University of Bihar),
Darbhanga.
Bihar,
India

C. K. R. VARMA

REFERENCES

1. FRIEDEL G. and RIBAUD G., *Bull. Soc. franc. Miner.* **47**, 94 (1924).
2. GALLAGHER C. J., *Phys. Rev.* **88**, 721 (1952).
3. BELL R. L. and BONFIELD W., *Phil. Mag.* **9**, 9 (1964).
4. PENNING P. and DE WIND G., *Physica* **25**, 765 (1959).
5. PEISSKER E., HAASEN P. and ALEXANDER H., *Phil. Mag.* **7**, 1279 (1962).
6. SEAL M., *Proc. int. Conf. Electron Microscopy*, London, p. 513 (1954).
7. PHAAL C. *Phil. Mag.* **10**, 887 (1964).
8. EVANS T. and WILD R. K., *Phil. Mag.* **12**, 479 (1965).
9. WILLIAMS A. F. *The Genesis of Diamond*, p. 462. Benn, London (1932).
10. TOLANSKY S. and OMAR M., *Phil. Mag.* **44**, 514 (1953).
11. TOLANSKY S., HALPERIN A. and EMARA S. H., *Phil. Mag.* **3**, 675 (1958).
12. MARUYAMA S., *J. phys. Soc. Japan* **15**, 1243 (1960).
13. SEIFERT H., *Neues Jb. Miner, Beilageband* (A) 57, 665 (1928).
14. CAHN R. W., Proc. AIME Metallurgical Society Conference, Vol. 25, p. 25, Gainesville, Florida (1963).
15. SUTTON J. R., *Diamond*. Murby, London (1928).
16. BERMAN R. and SIMON F., *Z. Elektrochem.* **59**, 333 (1955).
17. BRIDGMAN P. W., *Studies in Large Plastic Flow and Fracture*. McGraw-Hill, New York (1952).
18. VARMA C. K. R., *Phil. Mag.* **16**, 959 (1967).
19. CHURCHMAN A. T., *J. Inst. Metals* **83**, 39 (954–55).

Fig. 1. (× 200) Line A extends over two-thirds the length of the crystal face and is well pronounced. B and C are shorter and relatively less pronounced.

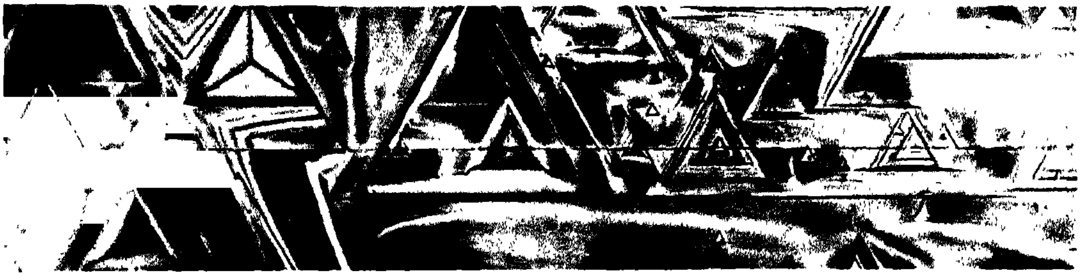

Fig. 2. (× 200) The discontinuity line having been sharp and straight over a considerable length, wriggles towards the right end.

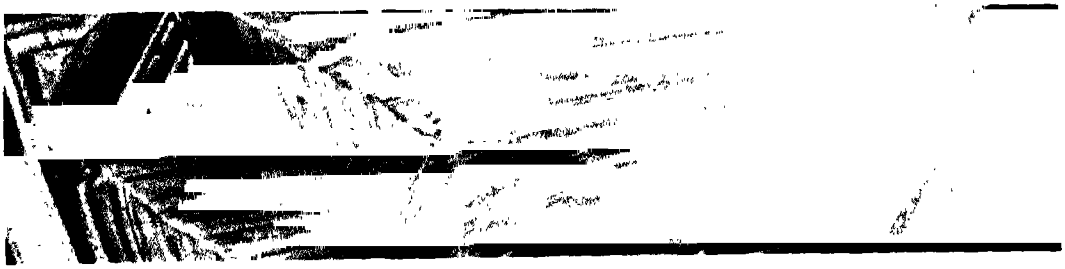

Fig. 3. (× 250) Despite the wriggling, the overall direction of the line seems well maintained.

Fig. 4. (×200) Passing through centres of trigons and maintaining strict rectilinearity and direction over part of its length, a line changes course and direction apparently to pass through a row of trigons on the left.

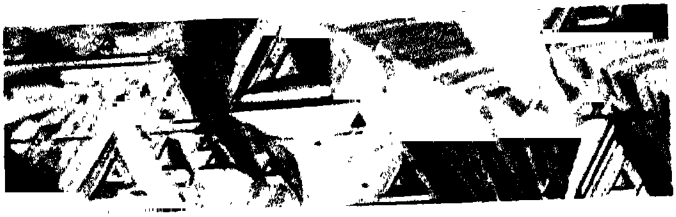

Fig. 5. (×200) A line loses direction, regains it and gets laterally displaced in the process.

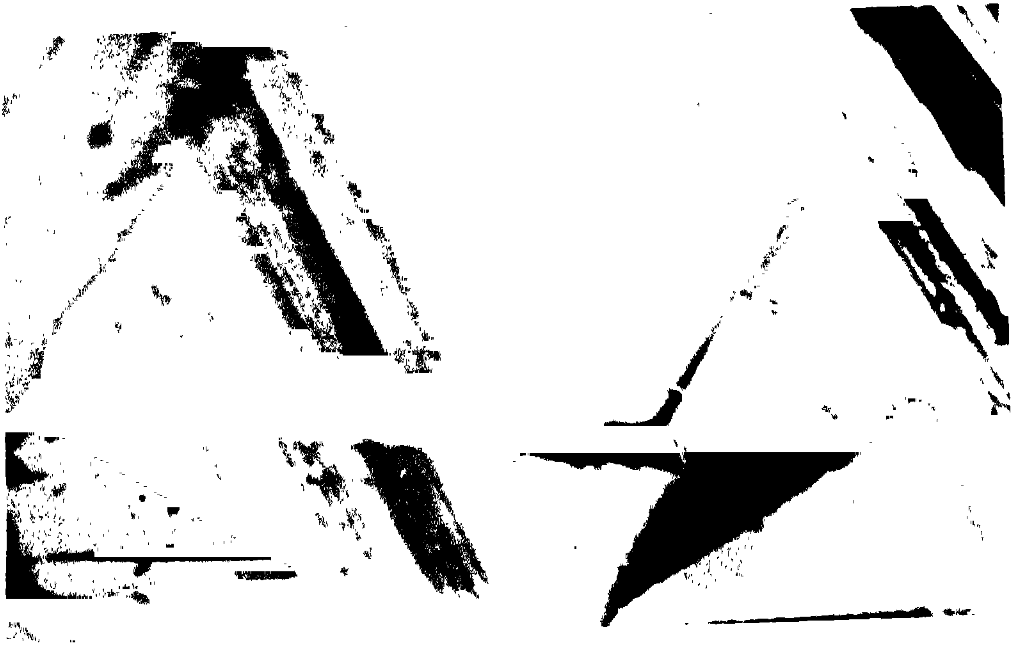

Fig. 6. (×760) A small length of a line passing through two trigons side by side, seen at high magnification.

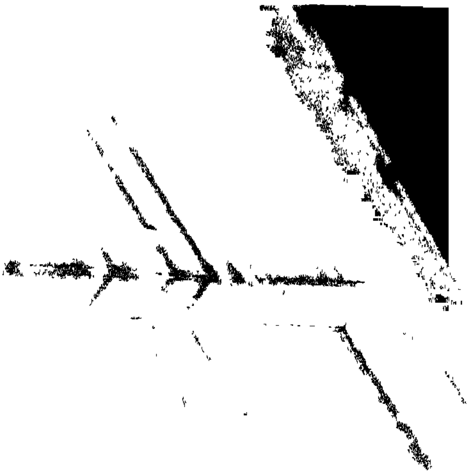

Fig. 7. (× 760) The nature of the discontinuity as a twin lamella becomes abundantly clear.

J. Phys. Chem. Solids Pergamon Press 1970. Vol. 31, p. 893. Printed in Great Britain.

ERRATUM

A. P. BATRA, A. L. LASKAR and L. SLIFKIN: Low temperature suppression by chlorine of diffusion of gold in silver chloride. *J. Phys. Chem. Solids* **30**, 2053 (1969).

THE MISSING fourth line in the Conclusions on page 2058 is:

0·47 eV. At low temperatures, the diffusion is

NOTES FOR CONTRIBUTORS

I. GENERAL

1. Submission of a paper to *The Journal of Physics and Chemistry of Solids* will be taken to imply that it represents original research not previously published (except in the form of an abstract or preliminary report), that it is not being considered for publication elsewhere, and that if accepted it will not be published elsewhere in the same form, in any language, without the consent of the Editor-in-Chief. It should deal with original research work in the field of the physics and chemistry of solids.

2. Papers should be submitted to the appropriate regional editor (all English-language papers to be sent to the U.S. editor).

3. Short communications may be published as "Technical Notes" and will receive somewhat more rapid handling than full length articles. Short communications requiring the maximum speed of publication should be submitted to one of the editors of "Solid State Communications."

II. SCRIPT REQUIREMENTS

1. **Papers** submitted should be concise and written in a readily understandable style. Scripts should be typed and double spaced with good margins on one side of the paper only and submitted in duplicate to facilitate refereeing.

It will be appreciated if authors clearly indicate any special characters used. An abstract not exceeding 200 words, should be provided in the language of the paper. French and German papers should be submitted with English abstract and titles, but if this is not possible the abstract will be translated by the publishers. To conserve space, **authors are requested to mark less important parts of the paper,** such as details of experimental technique, methods, mathematical derivations, etc. **for printing in small type.** The technical description of methods should be given in detail only when such methods are new. Authors will receive proofs for correction when their papers are first set, and **alterations must be restricted to printer's errors.** Other than these, any substantial changes may be charged to the authors.

2. **Illustrations** should not be included in the typescript of the paper, and legends should be typed on a separate sheet. Line drawings which require redrawing should include all relevant details and clear instructions for the draughtsman. If figures are already well drawn it may be possible to reproduce them direct from the originals, or from good photo-prints if these can be provided. It is not possible to reproduce from prints with weak lines. Illustrations for reproduction should normally be about twice the final size required. The lettering should be sufficiently large and bold to permit this reduction. Photographs should only be included where they are essential.

3. **Tables and figures** should be so constructed as to be intelligible without reference to the text. Every table and column should be provided with an explanatory heading. Units of measure must always be clearly indicated. The same data should not be published in both tables and figures. The following standard symbols should be used on line drawings since they are easily available to the printers: ○, ●, +, ×, □, ■, △, ▲, ◇, ◆, ▽, ▼.

4. **References** are indicated in the text by numbers on the line in brackets, and the full reference should be given in a list at the end of the paper in the following form:

1. BARNES R. G., BORSA F. and PETERSON D. *J. appl. Phys.* **36**, 940 (1965).
2. KNIGHT W. D., In *Solid State Physics* (Edited by F. Seitz and D. Turnbull), Vol. 2, p. 93. Academic Press, New York (1957).

Abbreviations of journal titles should follow those given in *World List of Scientific Periodicals* (4th Edn.). It is particularly requested that authors' initials, and appropriate volume and page numbers, should be given in every case.

Footnotes, as distinct from literature references should be indicated by the following symbols—*, †, ‡, §, commencing anew on each page; they should *not* be included in the numbered reference system.

5. Due to the international character of the journal no rigid rules concerning notation and spelling will be observed, but each paper should be consistent within itself as to symbols and units.

THE JOURNAL OF PHYSICS AND CHEMISTRY OF SOLIDS

VOLUME 31, NUMBER 1 1970 JANUARY

CONTENTS

V. A. Rowe and P. A. Schroeder: Thermopower of Mg, Cd and Zn between 1·2° and 300°K . . . 1

P. Raj and S. K. Kulshreshtha: Mössbauer studies of the lithium ferrite–aluminate system . . . 9

D. P. Spitzer: Lattice thermal conductivity of semiconductors: a chemical bond approach . . . 19

Č. Jech and R. Kelly: On the formation of ion-bombardment-induced disorder in zircon, corundum and diamond (Studies on bombardment-induced disorder—II). 41

B. Khurgin, I. Nowik, M. Rakavy and S. Ofer: Spin relaxation phenomena in Mössbauer spectra of magnetically ordered dysprosium intermetallic compounds . 49

P. D. Southgate: *The derivation of recombination rate constants from time-dependent* bulk electroluminescent spectra in compensated GaAs . . . 55

H. Mathieu: Etudes des queues de bandes dans le Ga Sb fortement dopé . . . 67

M. Hirabayashi, S. Yamaguchi, K. Hiraga, N. Ino, H. Sato and R. S. Toth: A new type of long period superlattice with hexagonal symmetry in Au–Cd alloys. . 77

K. Baumann, P. Kocevar and M. Kriechbaum: Anisotropic phonon excitation by hot electrons in *n*-Ge . . . 95

M. E. Lines: The quadratic-layer antiferromagnet . . . 101

R. W. Vaughan, D. D. Elleman and D. G. McDonald: The de Haas–van Alphen effect in white tin . . . 117

P. Novák: Some aspects of the cooperative Jahn–Teller effect in spinel and perovskite systems . . . 125

R. E. Schmunk and D. R. Winder: Lattice dynamics of sodium chloride at room temperature . . . 131

S. B. Palmer: Debye temperatures of holmium and dysprosium from single crystal elastic constant measurements . . . 143

O. V. Kovalev and A. G. Gorbanyuk: Irreducible representations of magnetic groups of quantum-mechanical operators . . . 149

J. F. Verwey: Time and intensity dependence of the photolysis of lead halides . . 163

M. M. Blouke, N. Holonyak, Jr., B. G. Streetman and H. R. Zwicker: Solid solubility of Zn in Si . . . 173

D. C. Finbow, P. Makhurane and P. Gaunt: Lattice distortion, specific heat and antiferromagnetic ordering in AuMn . . . 179

Technical Note:

R. J. Smith and D. A. Otterson: Electrical resistivity of PdH$_x$ system for H/Pd atom ratios to 0·97 . . . 187

PRINTED BY J. W. ARROWSMITH LTD., BRISTOL, ENGLAND